

OFFICE OF THE CHIEF  
OF NAVAL RESEARCH  
Arlington, Virginia 22217-5040

CONF 11331-7



AD-A247 996



Ninth Symposium

(International)

ON

DETONATION

DTIC  
ELECTE  
MAR 20 1992  
S D

Portland, Oregon  
August 23 - September 1, 1980

This document has been approved  
for public release and sale; its  
distribution is unlimited

Best Available Copy



VOLUME II

92-07199



92 3 20 003

Approved for public release; distribution is unlimited.

# PROCEEDINGS Ninth Symposium (International) on Detonation

## VOLUME II

Sponsored by:

Office of Naval Research  
Air Force Armament Laboratory  
Army Armament Research, Development  
and Engineering Center  
Army Ballistic Research Laboratory  
Lawrence Livermore National Laboratory  
Los Alamos National Laboratory  
Naval Sea Systems Command  
Naval Surface Warfare Center  
Office of Naval Technology  
Sandia National Laboratories



Accession For	
NTIS CRA&I	<input checked="" type="checkbox"/>
DTIC TAB	<input type="checkbox"/>
Unannounced	<input type="checkbox"/>
Justification	
By .....	
Distribution /	
Availability Codes	
Dist	Avail and/or Special
A-1	

August 28 - September 1, 1989

---

Red Lion Inn, Columbia River  
Portland, Oregon

---

Approved for public release; distribution is unlimited.

## **REPRODUCTION QUALITY NOTICE**

**This document is the best quality available. The copy furnished to DTIC contained pages that may have the following quality problems:**

- **Pages smaller or larger than normal.**
- **Pages with background color or light colored printing.**
- **Pages with small type or poor printing; and or**
- **Pages with continuous tone material or color photographs.**

**Due to various output media available these conditions may or may not cause poor legibility in the microfiche or hardcopy output you receive.**



**If this block is checked, the copy furnished to DTIC contained pages with color printing, that when reproduced in Black and White, may change detail of the original copy.**

**VOLUME I**  
**CONTENTS**

Page

**SHOCK-TO-DETONATION TRANSITION**

**General Session**

**Cochairmen: Philip Howe and Mohammad Chaudhri**

<b>Combined Pressure Shear Ignition of Explosives</b> V. Boyle, R. Frey, and O. Blake .....	3
<b>Particular Aspect of the Explosive Particle Size Effect on Shock Sensitivity of Cast PBX Formulations</b> H. Moulard .....	18
<b>Particle Size Effects in the Initiation of Explosives Containing Reactive and Non-Reactive Continuous Phases</b> R. L. Simpson, F. H. Helm, P. C. Crawford, and J. W. Kury .....	25
<b>In-Situ Study of the Chemically Driven Flow Fields in Initiating Homogeneous and Heterogeneous Nitromethane Explosives</b> S. A. Sheffield, R. Engelke, and R. R. Alcon .....	39
<b>Decomposition of High Explosives in Shock and Detonation Waves</b> V. E. Fortov, G. I. Kanel, T. N. Fortova, S. I. Malyrenko, and A. V. Utkin .....	50

**Specialist Session**

**Cochairmen: Randall Simpson and Peter Haskins**

<b>Initiation of Explosive Crystals by Shock or Impact</b> C. S. Coffey .....	58
<b>Initiation Threshold of High Explosives in Small Flyer Plate Experiments</b> H. R. Kleinhanß, F. Lungenstraß, and H. Zöllner .....	66
<b>A Two-Dimensional Lagrangian Technique for Shock Initiation Diagnosis</b> Huan Shi and Ding Jing .....	77
<b>Influence of RDX Crystal Shape on the Shock Sensitivity of PBXs</b> A. C. van der Steen, H. J. Verbeek, and J. J. Meulenbrugge .....	83
<b>A Lagrange Gauge Study of the Shock Initiation Process in an Intermolecular Explosive EAK</b> M. Cowperthwaite, J. T. Rosenberg, and A. G. Taliancich .....	89

# VOLUME I

## CONTENTS (Cont.)

Page

### Specialist Session

**Cochairmen: Jerry Wackerle and Robert Setchell**

**Anomalous Shock Sensitivity/Density Relationship for Pressed Booster Explosives from a Small-Scale Gap Test**

R. J. Spear and V. Nanut ..... 98

**Shock Initiation of LX-17 as a Function of Its Initial Temperature**

P. A. Urtiew, L. M. Erickson, D. F. Aldis, and C. M. Tarver ..... 112

**Initiation and Detonation Properties of the Insensitive High Explosive TATB/Kel-F 800 95/5**

C. D. Hutchinson, G. C. W. Foan, H. R. Lawn, and A. G. Jones ..... 123

**Fabry Perot Velocimetry on Detonating LX-17 in Planar and Spherically Divergent Geometries**

K. L. Bahl, R. D. Breithaupt, C. M. Tarver, and W. G. Von Holle ..... 133

**Reaction Rates of PBH-9D Explosive**

Zhao Feng, Sun Chengwei, Chen Peiqi, and Ouyang Denghuan ..... 142

### TIME RESOLVED CHEMISTRY

#### General Session

**Cochairmen: Anatolij Dremin and William Von Holle**

**Pulsed-Laser-Excited Raman Spectra of Shock-Compressed Triaminotrinitrobenzene**

W. M. Trott and A. M. Renlund ..... 153

**Laser Ignition of Explosives: A Mass Spectroscopic Study of the Pre-ignition Reaction Zone**

H. Östmark and H. Nilsson ..... 162

**The Use of Time-Resolved Spectrometries in the Study of Initiation of Explosives at Molecular Level**

A. E. Delpuech ..... 172

**Vibrational Spectroscopic Investigations of Shock-Compressed Liquid Nitrogen and Shock-Compressed Liquid Nitromethane**

D. S. Moore and S. C. Schmidt ..... 180

**Absorption Spectroscopy of Shocked Benzene**

N. C. Holmes, G. Otani, P. McCandless, and S. F. Rice ..... 190

# VOLUME I

## CONTENTS (Cont.)

Page

### INITIATION MODELING

#### General Session

Cochairmen: Pier Tang and John Field

<b>Reaction Rates and the Charge Diameter Effect in Heterogeneous Explosives</b> G. A. Leiper and J. Cooper .....	197
<b>A Shock Initiation Model for Fine-Grained Hexanitrostilbene</b> M. E. Kipp and R. E. Setchell .....	209
<b>A Theoretical Picture of Shock-to-Detonation Transition in a Homogeneous Explosive</b> A. K. Kapila and J. W. Dold .....	219
<b>Chemical Phenomena Associated with the Initiation of Thermal Explosions</b> T. B. Brill and P. J. Brush .....	228

#### Specialist Session

Cochairmen: Kibong Kim and Graeme Leiper

<b>The Lattice Density of States Concept and its Role in Determining the Shock Sensitivity of PETN and Nitromethane</b> R. D. Bardo .....	235
<b>Unified Formulation of the Reactivity of Condensed Explosives</b> R. Cheret .....	246
<b>The Choice Problem of Equation Determining the Condensed Reacting Media Characteristics in Numerical Modeling of Shock Processes</b> V. S. Trofimov .....	250
<b>Global Calibration of Constitutive Relationships in Explosive Reaction Zone</b> Huan Shi and Ding Jing .....	252

### DEFLAGRATION-TO-DETONATION TRANSITION

#### General Session

Cochairmen: Richard Bernecker and Albert van der Steen

<b>DDT - Determination of the Successive Phases of Phenomena</b> M. Samirant .....	259
---	-----

# VOLUME I

## CONTENTS (Cont.)

	<u>Page</u>
<b>Deflagration to Detonation in Granular HMX</b> J. M. McAfee, B. W. Asay, A. W. Campbell, and J. B. Ramsay .....	265
<b>Model Calculations and Experimental Measurements of the Response of HMX Porous Beds to Deflagration and Shock</b> D. F. Aldis, E. L. Lee, R. L. Simpson, and A. M. Weston .....	280
<b>Compressive Combustion of Granular Materials Induced by Low-Velocity Impact</b> M. R. Baer and J. W. Nunziato .....	293
<b>Compaction Wave Acceleration in Granular Energetic Material: Simulation with a Reactive Shock Wave Model</b> D. E. Kooker .....	306
<b>Specialist Session</b> <b>Cochairmen: Douglas Kooker and Henry Moulard</b>	
<b>Combined Experimental and Theoretical Investigations into the Deflagration-to-Detonation Transition</b> H. J. Verbeek and A. C. van der Steen .....	320
<b>Numerical Simulation of Deflagration-to-Detonation Transition for TS 3659 Propellants</b> T. Hsieh and K. Kim .....	329
<b>Dynamic Compaction and Compressive Reaction Studies for Single and Double-Base Ball Propellants</b> B. C. Glancy, H. W. Sandusky, P. J. Miller, and A. D. Krall .....	341
<b>DDT Studies of a High Energy Spherical Ball Propellant</b> R. R. Bernecker .....	354
<b>An Improved Model of the Deflagration-to-Detonation Transition in Porous Beds</b> C. F. Price, A. I. Atwood, and T. L. Boggs .....	363

## EQUATION OF STATE

### General Session

Cochairmen: Claude Fauquignon and Milton S. Shaw

<b>Shock Behavior of Explosives about the C-J Point</b> P. W. Cooper .....	379
---	-----

**VOLUME I**  
**CONTENTS (Cont.)**

	<u>Page</u>
<b>Electrically Enhanced Detonation and Equations of State for Detonation Products</b>	
M. Cowperthwaite .....	388
<b>The Measurement of Electrical Conductivity in Detonating Condensed Explosives</b>	
D. G. Tasker and R. J. Lee .....	396
<b>Synthesis of Ultrafine Diamonds in Detonation Waves</b>	
V. M. Titov, V. F. Anisichkin, and I. Yu. Mal'kov .....	407
<b>Carbon in Detonations</b>	
J. D. Johnson .....	417
<b>Phase Changes in Carbon and Nitrogen Systems: Their Effects on the Detonation Properties of High Explosives</b>	
F. H. Ree and M. van Thiel .....	425
<b>Specialist Session</b>	
<b>Cochairmen: Francis Ree and Katsumi Tanaka</b>	
<b>The Detonation Parameters of New Powerful Explosive Compounds Predicted with a Revised VLW Equation of State</b>	
Wu Xiong, Sun Jian, and Xiao Lianjie .....	435
<b>Theoretical Model of Explosive Detonation Products: Tests and Sensitivity Studies</b>	
G. I. Kerley .....	443
<b>A New Simulation Method for the Efficient Calculation of Benchmarks for Detonation Products Equations of State</b>	
M. S. Shaw .....	452
<b>Calculations of Detonation Pressures for a Homologous Series of Polynitroaliphatic Explosives Using a Fluid Perturbation Equation of State and a New Chemical Equilibrium Computer Program</b>	
F. J. Zerilli and H. D. Jones .....	461
<b>Specialist Session</b>	
<b>Cochairmen: LeRoy Green and Manfred Held</b>	
<b>A Detonation Pressure Measurement System Employing High Resistance Manganin Foil Gauge</b>	
S. Y. Song and J. W. Lee .....	471

# VOLUME I

## CONTENTS (Cont.)

	<u>Page</u>
<b>Heat of Detonation, the Cylinder Test, and Performance in Munitions</b> I. B. Akst .....	478
<b>Theoretical Prediction of High Explosives Efficiency: Application to NTO</b> F. Bugaut, S. Bernard, and R. Chirat .....	489
<b>Determining JWL Equation of State Parameters Using the Gurney Equation Approximation</b> P. J. Miller and K. E. Alexander .....	498
<b>Specialist Session</b> <b>Cochairmen: Gerald Kerley and Douglas Tasker</b>	
<b>Studies about the Equations of State of the Detonation Products</b> N. Carion, J. Avelle, P. Andriot, F. Chaisse, G. Guri, M. T. Kerihuel, and M. Leroy .....	506
<b>Sensitivities of Adiabatic and Gruneisen Gammas to Errors in Molecular Properties of Detonation Products</b> W. Byers Brown and M. Braithwaite .....	513
<b>Reactive Flow Measurements and Calculations for ZrH<sub>2</sub>-Based Composite Explosives</b> M. J. Murphy, R. L. Simpson, R. D. Breithaupt, and C. M. Tarver .....	525

## COMPOSITES AND EMULSIONS

### General Session Cochairmen: Ding Jing and Raymond McGuire

<b>Detonation Characteristics of Gun Propellants</b> B. W. Asay, A. W. Campbell, M. J. Ginsberg, and J. B. Ramsay .....	537
<b>Detonation Properties of Mixtures of HMX and Emulsion Explosives</b> J. D. Renick, P. A. Persson, and J. A. Sanchez .....	545
<b>The Prospects for Composite Explosive</b> Guo Yuxian .....	554
<b>Detonation Velocity and Pressure of the Non-Ideal Explosive Ammonium Nitrate</b> A. Miyake, A. C. van der Steen, and H. H. Kodde .....	560

# VOLUME I

## CONTENTS (Cont.)

	<u>Page</u>
<b>Specialist Session</b>	
<b>Cochairmen: Herbert Richter and James Short</b>	
<b>Shock Sensitivities of Energetically Substituted Benzofuroxans</b> M. L. Chan, C. D. Lind, and P. Politzer .....	566
<b>Detonation and Shock Initiation Properties of Emulsion Explosives</b> J. Lee, F. W. Sandstrom, B. G. Craig, and P.-A. Persson .....	573
<b>Effect of Pressure on Shock Sensitivity of Emulsion Explosives</b> G. Om Reddy and F. P. Beitel, Jr. ....	585
<b>Development of a Model of Reaction Rates in Shocked Multicomponent Explosives</b> K. Kim .....	593
<b>A Model for the Initiation of Heterogeneous High Explosives Subject to General Compressive Loading</b> J. Starckenberg .....	604

## COMPOSITES AND EMULSIONS/UNDERWATER EXPLOSIVES

<b>Specialist Session</b>	
<b>Cochairmen: Leslie Roslund and Algot Persson</b>	
<b>Calculation of Detonation Properties of Emulsion Explosives</b> K. Tanaka, M. Iida, Y. Nakayama, N. Ishiokawa, M. Yoshida, and S. Fujiwara .....	621
<b>Chemistry of Underwater Explosive Detonations</b> D. Carlson, R. Doherty, V. Ringbloom, J. S. Deiter, and G. B. Wilmot .....	626
<b>Estimation of Performance of Underwater Explosives</b> D. A. Cichra and R. M. Doherty .....	633
<b>Underwater Explosion of Emulsion Explosives</b> K. Hattori, Y. Kato, K. Tokita, Y. Fukatsu, N. Mori, and A. Torii .....	640
<b>The Fundamentals of Metal Combustion in Composite Explosives Revealed by High Speed Microphotography</b> W. C. Tao, A. M. Frank, R. E. Clements, and J. E. Shepherd .....	641

**VOLUME I**  
**CONTENTS (Cont.)**

Page

**REACTION ZONE**

**General Session**

**Cochairmen: William Davis and Joseph Foster**

<b>Detonation Reaction-Zone Structure for PBX 9502</b> W. L. Seitz, H. L. Stacy, R. Engelke, P. K. Tang, and J. Wackerle .....	657
<b>Reaction Zone Structure in Supracompressed Detonating Explosives</b> L. G. Green, C. M. Tarver, and D. J. Erskine .....	670
<b>Lagrangian Analysis of MIV Gauge Experiments on PBX 9502 Using the Mass-Displacement Moment Function</b> C. A. Forest, J. Wackerle, J. J. Dick, S. A. Sheffield, and D. R. Pettit .....	683
<b>The Heterogeneous Explosive Reaction Zone</b> C. L. Mader and J. D. Kershner .....	693
<b>Using Small Scale Tests to Estimate the Failure Diameter of a Propellant</b> C. M. Tarver and L. G. Green .....	701

**DETONATION WAVE PROPAGATION**

**General Session**

**Cochairmen: Roger Cheret and Michael Cowperthwaite**

<b>Molecular Dynamics Simulation of the Effect of Molecular Dissociation and Energy Absorption on Detonation Structure in Energetic Solids</b> S. G. Lambrakos, M. Peyrard, and E. S. Oran .....	713
<b>Multiprocess Detonation Model</b> A. N. Dremin, V. Yu. Klimenko, O. N. Davidova, and T. A. Zoludeva .....	724
<b>Detonation Shock Dynamics: A New Approach to Modeling Multi-Dimensional Detonation Waves</b> J. B. Bdzil, W. Fickett, and D. S. Stewart .....	730
<b>Nonequilibrium Effects of Slow Diffusion Controlled Reactions on the Properties of Explosives</b> M. van Thiel and F. H. Ree .....	743
<b>Computation of a Diverging Comp-B Detonation</b> B. G. Bukiet .....	751

# VOLUME I

## CONTENTS (Cont.)

	<u>Page</u>
<b>A Theoretical Analysis of the Sonic Point Properties in a Plane Detonation Wave</b> L. Brun and F. Chaisse .....	757
<b>Specialist Session</b> <b>Cochairmen: Craig Tarver and Patrick Gimenez</b>	
<b>Investigations of the Influence of Polymorphous Transformation on the Process of Detonation of Mixtures Containing HE and Substances Undergoing Transformation</b> E. Wiodarczyk, R. Trebinski, W. Trzcinski, and W. Witkowski .....	766
<b>Examples of Detonation Shock Dynamics for Detonation Wave Spread Applications</b> D. S. Stewart and J. B. Bdzil .....	773
<b>Application of Whitham's Shock Dynamics Theory to the Propagation of Divergent Detonation Waves</b> B. D. Lambourn and D. C. Swift .....	784
<b>Propagation of Detonation Waves from an Impact Region</b> R. S. Lee, W. C. Tao, and L. D. Crouch .....	798
<b>Detonation Wave Propagation in PBXW-115</b> J. W. Forbes, E. R. Lemar, and R. N. Baker .....	806
<b>Specialist Session</b> <b>Cochairmen: Jerry Forbes and James Kennedy</b>	
<b>Non-Steady Flow in a Detonator</b> Jia Quansheng, Chen Fumei, and Wang Tinzheng .....	816
<b>Polysulfone SIP Gage for Flying Plate Explosive Components</b> T. W. Warren and R. R. Weinmaster .....	822
<b>The Effects of Inert Walls on the Velocity of Detonation in EDC35, an Insensitive High Explosive</b> G. Eden and R. A. Belcher .....	831
<b>Experimental and Numerical Study of Oblique Interactions of Detonation Waves with Explosive/Solid Material Interfaces</b> J. Aveillé, N. Carion, J. Vacellier, and J. M. Servas .....	842
<b>Experimental and Numerical Study of Corner-Turning Detonation</b> A. W. Gibb .....	853

## VOLUME II

## CONTENTS

Page

### HOT SPOTS

#### General Session

**Cochairmen: Charles Coffey and Per-Anders Persson**

<b>The Initiation of Fast Decomposition in Solid Explosives by Fracture, Plastic Flow, Friction, and Collapsing Voids</b> M. M. Chaudhri .....	857
<b>Characterization of Defect Microstructure in High Explosives Single Crystals by Synchrotron X-Ray Tomography</b> W. C. Tao and J. H. Kinney .....	868
<b>Cavity Collapse in a Heterogeneous Commercial Explosive</b> N. K. Bourne and J. E. Field .....	869
<b>Response of Composite Propellants to Shock Loading</b> Bai Chunhua and Ding Jing .....	879
<b>Deformation and Explosive Properties of HMX Powders and Polymer Bonded Explosives</b> J. E. Field, M. A. Parry, S. J. P. Palmer, and J. M. Huntley .....	886

#### Specialist Session

**Cochairmen: Paul Cooper and Hyla Napadensky**

<b>Physical and Chemical Nature of Hot Spots in TATB and HMX</b> J. Sharma, B. C. Beard, J. Forbes, C. S. Coffey, and V. M. Boyle .....	897
<b>Hot Spot Formation in a Collapsing Void of Condensed-Phase, Energetic Material</b> P. B. Butler, J. Kang, and M. R. Baer .....	906
<b>Broad Bandwidth Study of the Topography of the Fracture Surfaces of Explosives</b> M. Y. D. Lanzerotti, J. J. Pinto, and A. Wolfe .....	918
<b>Effects of Microballoon Concentration on the Detonation Characteristics of Nitromethane-PMMA Mixtures</b> H. N. Presles, J. Campos, O. Heuzé, and P. Bauer .....	925

**VOLUME II**  
**CONTENTS (Cont.)**

Page

**DETONATION PRODUCTS**

**Specialist Session**  
**Cochairmen: Anita Renlund and Gert Bjarnholt**

<b>Detonation Characteristics of Dense Gaseous Explosive Mixtures</b> P. Bauer, M. Dunand, H. N. Presles, and O. Heuzé .....	933
<b>Detonation Temperature of Some Liquid and Solid Explosives</b> Y. Kato, N. Mori, H. Sakai, T. Sakurai, and T. Hikita .....	939
<b>The Studying of Detonation Temperatures of Solid High Explosives</b> Shi Huisheng, Han Chengbang, Kang Shufang, and Huang Lihong .....	947
<b>Free-Expansion Experiments and Modeling in Detonation: Chemistry and Hydrodynamics on a Laboratory Scale</b> N. R. Greiner and N. Blais .....	953
<b>Detonation Products of Less Sensitive High Explosives Formed Under Different Pressures of Argon and in Vacuum</b> F. Volk and F. Schedlbauer .....	962
<b>Explosive Potential of Carbohydrate-Metal Composites</b> A. J. Tulis, J. L. Austing, W. K. Sumida, D. E. Baker, and D. J. Hrdina .....	972

**CHEMISTRY AND COMPOSITION**

**Specialist Session**  
**Cochairmen: Tom Larson and Fritz Schedlbauer**

<b>A Review of Paramagnetic Resonance Products in Condensed Phase Energetic Materials</b> M. D. Pace .....	987
<b>Properties of Bis(2,2,2-Trinitroethyl-N-Nitro) Ethylenediamine and Formulations Thereof</b> Dong Haishan .....	995
<b>NTO Development at Los Alamos</b> L. B. Chapman .....	1001
<b>Use of Oxynitrotriazole to Prepare an Insensitive High Explosive</b> A. Becuwe and A. Delclos .....	1008

**VOLUME II**  
**CONTENTS (Cont.)**

Page

<b>Effects of Binder Concentration on the Properties of Plastic-Bonded Explosives</b>	
R. D. Steele, L. A. Stretz, G. W. Taylor, and T. Rivera .....	1014

**Specialist Session**  
**Cochairmen: Horst Adolph and Fred Volk**

<b>Chemistry of Nitromethane at Very High Pressure</b>	
S. F. Agnew, B. I. Swanson, J. Kenney, and I. Kenney .....	1019

<b>Decomposition Mechanisms and Chemical Sensitization in Nitro, Nitramine, and Nitrate Explosives</b>	
M. D. Cook and P. J. Haskins .....	1027

<b>Decomposition of Energetic Materials on the Drop-Weight-Impact Machine</b>	
G. A. Buntain, T. L. McKinney, T. Rivera, and G. W. Taylor .....	1037

**SPECIAL INITIATION**

**Specialist Session**  
**Cochairmen: Pai Lu and Christopher Hutchinson**

<b>Behavior of an Unreacted Composite Explosive on Low Velocity Impact</b>	
C. Loupias and A. Fanget .....	1047

<b>Response of Rocket Propellants to Projectile Impact</b>	
S. Y. Ho .....	1052

<b>Characterization of Booster-Rocket Propellants and Their Simulants</b>	
L. J. Weirick .....	1060

<b>Experimental Study and Numerical Modeling of Thermal Initiation and Combustion of High Heterogeneous Explosives</b>	
C. Castille, D. Bainville, P. Reynier, and R. Belmas .....	1070

**Specialist Session**  
**Cochairmen: Edward Lee and Krishna Mohan**

<b>Electrostatic Sensitivity Testing of Explosives at Los Alamos</b>	
T. E. Larson, P. Dimas, and C. E. Hannaford .....	1076

VOLUME II

CONTENTS (Cont.)

	<u>Page</u>
<b>Molecule-Surface Collision Induced Excitation and Dissociation: n,i-C<sub>3</sub>F<sub>7</sub>NO, C<sub>6</sub>F<sub>5</sub>NO, 2-Methyl, 5-Vinyl Tetrazole and C(NO<sub>2</sub>)<sub>4</sub> with MgO(100) Surfaces at E<sub>incident</sub> ≤ 7.5 eV</b> K. Kolodney, P. S. Powers, L. Iwata, H. Reisler, C. Wittig, I. B. Mishra, and C. Capellos .....	1084
<b>Initiation and Propagation in Primary Explosives</b> P. M. Dickson, M. A. Parry, and J. E. Field .....	1100
<b>Prompt Detonation of Secondary Explosives by Laser</b> D. L. Paisley .....	1110
<b>Laser Initiation of Secondary Explosives</b> A. M. Renlund, P. L. Stanton, and W. M. Trott .....	1118

POSTER PAPERS

**Organizer and Chairman: Robert Frey**  
**Cochairmen: Harold Sandusky, John Kury, Philip Stanton,**  
**Allan Anderson, Michel Samirant, and Thomas Boggs**

<b>Intense Electron Beam Detonation of TATB Explosives</b> D. Demske, N. Brazell, W. E. Farley, S. Miller, and R. Warnes .....	1131
<b>Time-Resolved Mass Spectrometry Technique for Studying Fast Transient CHNO Explosive Decomposition Kinetics</b> R. D. Skocypec and K. L. Erickson .....	1140
<b>Laser Ignition of Explosives: Raman Spectroscopy of the Ignition Zone</b> H. Nilsson and H. Östmark .....	1151
<b>The Effect of the Pentafluorothio (SF<sub>5</sub>) Group on the Properties of Explosive Nitro Compounds: New SF<sub>5</sub> Explosives</b> M. E. Sitzmann and D. L. Ornellas .....	1162
<b>Chemistry of Detonation Soot: Diamonds, Graphite, and Volatiles</b> N. R. Greiner and R. Hermes .....	1170
<b>Molecular Models for Explosives: Applications to NTO</b> J. P. Ritchie and E. M. Kober .....	1185
<b>Reaction and Diffusion in Detonation</b> N. J. B. Green, M. J. Pilling, and S. H. Robertson .....	1193

VOLUME II  
CONTENTS (Cont.)

	<u>Page</u>
<b>A Thermochemical Model for Shock-Induced Chemical Reactions in Porous Solids: Analogs and Contrasts to Detonation</b> M. B. Boslough .....	1199
<b>Reactive Modeling in Shock Initiation of Heterogeneous Explosives</b> M. Quidot and J. Groux .....	1217
<b>Reactive Flow Analysis and Its Applications</b> G. A. Leiper and D. L. Kennedy .....	1224
<b>Physical Evidence of Different Chemical Reactions in Explosives as a Function of Stress</b> T. P. Liddiard, J. W. Forbes, and D. Price .....	1235
<b>Towards Developing the Capability to Predict the Hazard Response of Energetic Materials Subjected to Impact</b> C. S. Coffey, D. F. DeVost, and D. L. Woody .....	1243
<b>"Frozen Hot Spots" in Shocked EDC35, an Insensitive High Explosive</b> G. Eden, R. A. Belcher, M. I. Andrew, and W. R. Marlow .....	1253
<b>Deformation and Shock Loading Studies on Single Crystals of Ammonium Perchlorate Relating to Hot Spots</b> H. W. Sandusky, B. C. Glancy, D. W. Carlson, W. L. Elban, and R. W. Armstrong .....	1260
<b>The Influence of Grain Morphology on the Behavior of Explosives</b> S. Dufort, H. Cherin, and P. Gohar .....	1271
<b>Role of Adiabatic Shear Bands in Initiation of Explosives by Drop-Weight Impact</b> V. Krishna Mohan, V. C. Jyothi Bhasu, and J. E. Field .....	1276
<b>Gap Tests as a Method of Discriminating Shock Sensitivity</b> S. A. Aubert, G. H. Parsons, J. G. Glenn, and J. L. Thoreen .....	1284
<b>Shock Sensitivity of Damaged Energetic Materials</b> H. P. Richter, L. R. Boyer, K. J. Graham, A. H. Lepie, and N. G. Zwierzchowski .....	1295
<b>Burning Rates of Two Cast Nitramine Explosives Using a Hybrid Closed Bomb-Strand Burner</b> W. C. Tao, M. S. Costantino, and D. L. Ornellas .....	1310
<b>Explosiveness and Shock-Induced Deflagration Studies of Large Confined Explosive Charges</b> P. J. Hubbard and R. Tomlinson .....	1322

**VOLUME II**  
**CONTENTS (Cont.)**

	<u>Page</u>
<b>Initiation and Detonation Measurements on Liquid Nitric Oxide</b> G. L. Schott, W. C. Davis, and W. C. Chiles .....	1335
<b>Mechanisms of Detonation and Failure in Weak Chemically Sensitized Mining Safety Explosives</b> M. Kennedy and I. D. Kerr .....	1351
<b>Experimental Studies on the Detonation of an Explosive by Multi-Point Initiation</b> Yu Jun, Fu Xinghai, and Zhang Guanren .....	1360
<b>Detonation Properties of Explosive Foams</b> C. J. Anderson, K. Von Rosen, A. W. Gibb, and I. O. Moen .....	1364
<b>F.P.I. Velocimetry Techniques Applied to Various Problems in Detonics</b> P. Gimenez, J. P. Bedoch, C. Saint-Martin, G. Baudin, and Y. de Longueville .....	1371
<b>Detonation Product Equation of State for Baratol</b> J. W. Kury and R. D. Breithaupt .....	1378
<b>Design and Development of Precision Linear Shaped Charges</b> M. G. Vigil .....	1385
<b>Jet Initiation Mechanisms and Sensitivities of Covered Explosives</b> M. Chick, T. J. Bussell, R. B. Frey, and A. Bines .....	1404
<b>Initiation Phenomena with Shaped Charge Jets</b> M. Held .....	1416
<b>Spherical Projectile Impact on Explosives</b> E. N. Ferm and J. B. Ramsay .....	1427
<b>Projectile Impact Initiation of Explosive Charges</b> M. D. Cook, P. J. Haskins, and H. R. James .....	1441
<b>Correlation of Explosive Sensitivity to Compressional Inputs</b> M. Kornhauser .....	1451
<b>Sensitivity of Several Explosives to Ignition in the Launch Environment</b> J. Starckenberg, D. L. McFadden, D. L. Pilarski, K. J. Benjamin, V. M. Boyle, and O. R. Lyman .....	1460
<b>Study of Explosive Shell Fillings with Defects in Simulated Gun Launch Conditions</b> C. Bélanger .....	1480

**VOLUME II**  
**CONTENTS (Cont.)**

	<u>Page</u>
<b>A Computational Assessment of the Role of Shielding in Preventing the Sympathetic Detonation of Munitions</b> J. Starkenberg, T. M. Dorsey, K. J. Benjamin, and A. L. Arbuckle .....	1489
<b>Output Measurements and Modeling of HNS Mild Detonating Fuse</b> R. G. Jungst and M. E. Kipp .....	1510
<b>Detonator Response Measurements with a Standardized Piezoelectric Polymer (PVDF) Gauge</b> L. M. Moore, R. A. Graham, and R. P. Reed, and L. M. Lee .....	1529
<b>Indexes for the Proceedings of the Symposia (International) on Detonation--1951 through 1985</b> S. L. Crane, W. E. Deal, J. B. Ramsay, and B. E. Takala .....	1543
<b>Author Index</b> .....	I-1

## **SESSIONS ON**

## **HOT SPOTS**

**Cochairmen: Charles Coffey**  
**Naval Surface Warfare Center**

**Per-Anders Persson**  
**Center for Explosive Technology Research**

**and**

**Paul Cooper**  
**Sandia National Laboratories**

**Hyla Napadensky**  
**Napadensky Energetics Inc.**

# THE INITIATION OF FAST DECOMPOSITION IN SOLID EXPLOSIVES BY FRACTURE, PLASTIC FLOW, FRICTION, AND COLLAPSING VOIDS

M. Munawar Chaudhri  
Cavendish Laboratory  
University of Cambridge  
Madingley Road,  
Cambridge CB3 0HE  
UNITED KINGDOM

*Several series of high speed photography experiments have been carried out in order to examine the relative importance of the various mechanisms thought to be responsible for producing hot spots and causing initiation of fast decomposition in explosives. Framing rates of up to  $2 \times 10^6 \text{ s}^{-1}$  were used and photographic sequences show that (i) fast fractures in an explosive single crystal do not cause its ignition, (ii) intercrystalline friction is an important mechanism, (iii) rapid compression of gas bubbles down to  $50 \mu\text{m}$  or less in diameter does give rise to initiation, and (iv) the interaction of strong shocks with spherical voids produces fast jets, which can also play a dominant role. We have also discussed rapid plastic flow in an explosive crystal as an effective mechanism when the plastic strains are very high.*

## INTRODUCTION

There are now many high-speed photographic observations which show that in most, if not in all cases, the initiation of a fast reaction or a detonation in an explosive occurs at microscopic regions. Representative examples from experiments employing stimuli, such as low velocity impact, high strength shock waves, unfocused light, and electric field will be found in published reports.<sup>1-4</sup> In the literature, several mechanisms have been proposed for the concentrated dissipation of energy of the stimulus at localized regions resulting in their becoming 'hot spots.' At these regions, the temperature is considerably higher than that of the surrounding explosive material; consequently, the rate of chemical reaction is much higher there. If the conditions for self heating exist, the instability (i.e., initiation of fast reaction) occurs at these regions.

Of the many mechanisms proposed so far, the ones generally considered seriously by investigators are: (i) fracture of explosive

crystals,<sup>5,6</sup> (ii) plastic flow, including dislocation pileups<sup>7</sup> and adiabatic shear flow,<sup>8-11</sup> (iii) friction,<sup>12,13</sup> (iv) adiabatic compression of gas pockets,<sup>12</sup> and (v) shock-void interactions.<sup>2</sup>

It may be said here that, despite a vast amount of research effort, our lack of understanding of the mechanisms of initiation is quite apparent from the fact that we would not be able to predict accurately the initiation behavior of an explosive in an impact or shock experiment even if we were given all its physical and chemical properties. The purpose of this paper is to examine in some depth the various mechanisms in the light of experimental observations.

## INITIATION BY FRACTURE

Fracture studies were made on single crystals of silver azide, lead azide, and PETN. The test crystal was supported on a hard anvil, and the fracture was caused by driving into the crystal a sharp hardened steel chisel at a speed of  $10\text{-}15 \text{ ms}^{-1}$ . The entire fracture process was

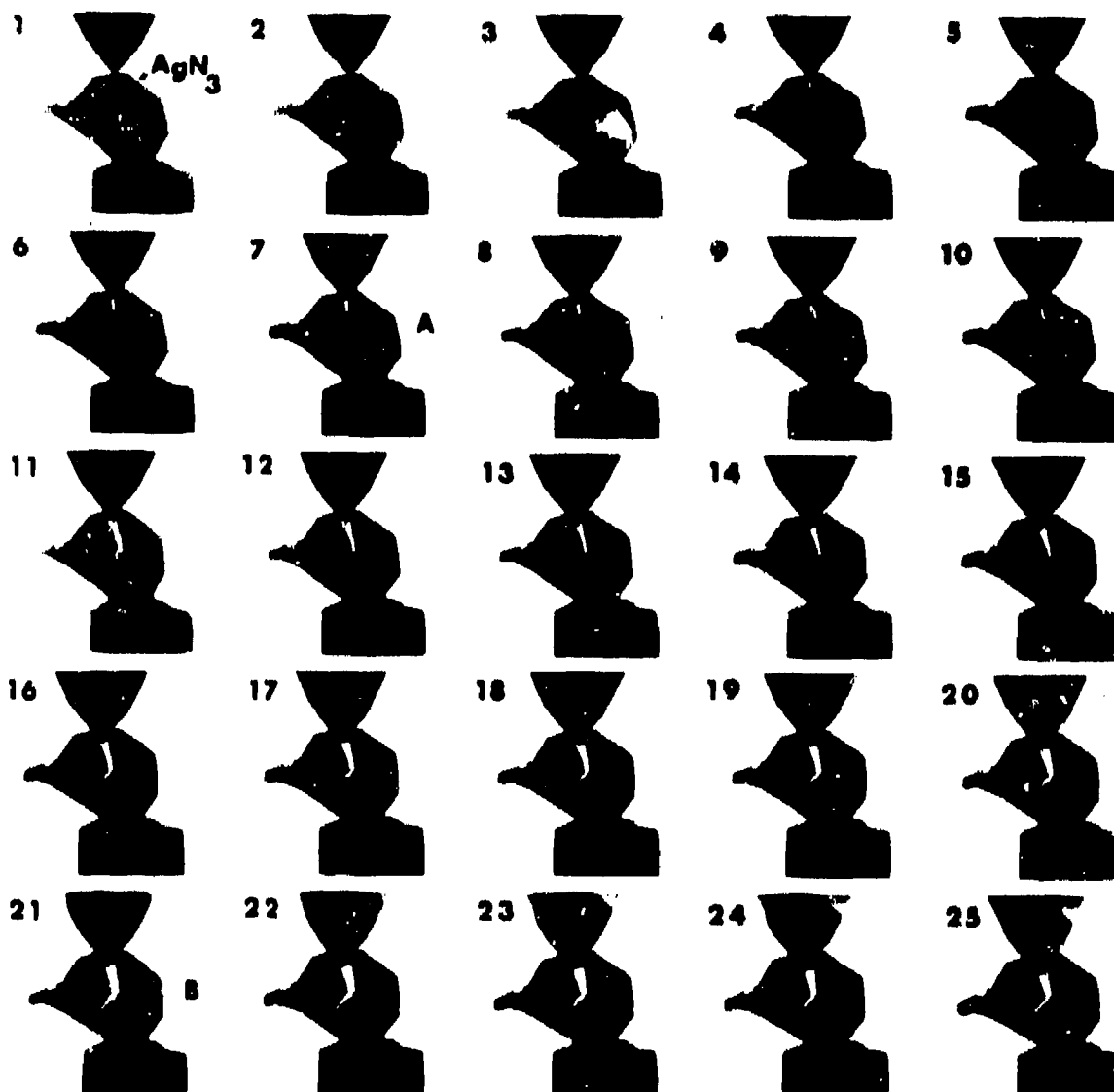


Figure 1. Fast Fractures of Velocity up to  $170 \text{ ms}^{-1}$  in a Single Crystal of Silver Azide are Unable to Cause an Initiation of Explosion. Interframe time:  $2.0 \mu\text{s}$ ; crystal height:  $2.0 \text{ mm}$ .

photographed with a Bockman and Whitley model 189 rotating mirror framing camera using back lighting.

A sequence of photographs showing the formation and growth of fast fractures in a silver azide crystal is given in Figure 1. Frame 1 shows the crystal of size  $2.5 \times 2.0 \times 0.5 \text{ mm}^3$ ,  $2\text{-}3 \mu\text{s}$  before it was impacted with the chisel; the larger faces of the crystal are  $\{010\}$ . Note that as yet no cracking has started. In frame 2, a single crack is initiated immediately below the chisel tip and propagates along cleavage planes, changing its direction of propagation twice. The crack

speed is variable between frames, reaching a maximum value of  $170 \text{ ms}^{-1}$  between frames 11 and 12. An explosion did not take place and the fragments of this crystal were recovered after the experiment. We have shown before that fast fractures ( $800 \text{ ms}^{-1}$ ) in  $\beta$ -lead azide crystals were also unable to cause the initiation of an explosion.<sup>14</sup>

Figure 2 shows a sequence of photographs of the fracture behavior of a single crystal of PETN of height  $6.9 \text{ mm}$ , width  $3.6 \text{ mm}$ , and thickness  $2 \text{ mm}$ . About  $8 \mu\text{s}$  before frame 4, the chisel hits the crystal resulting in the initiation of fracture in frame

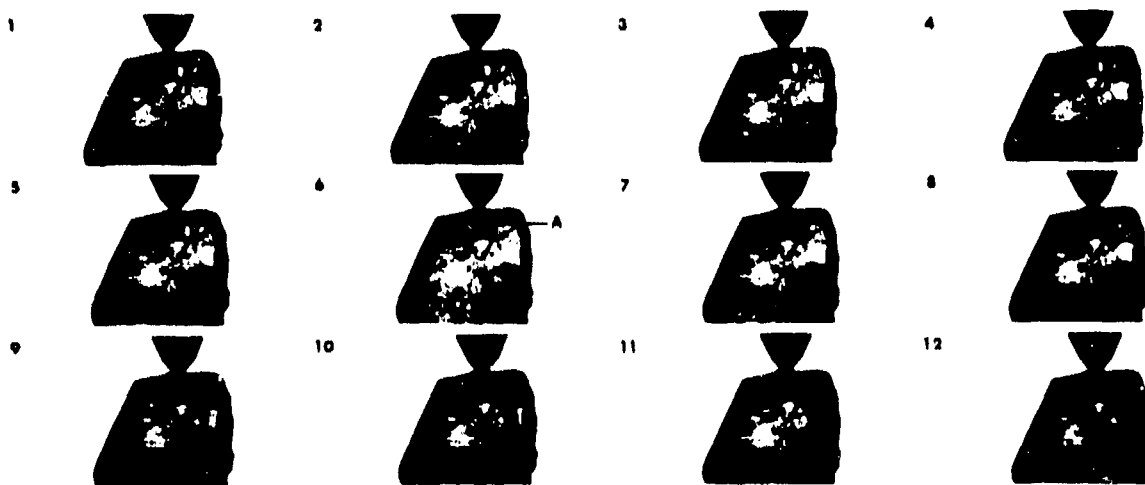


Figure 2. Fast Fractures ( $700 \text{ ms}^{-1}$ ) in a Single Crystal of PETN. Interframe time:  $1.0 \mu\text{s}$ ; crystal height:  $6.9 \text{ mm}$ .

4 at the point of impact. The crack, which appears as a dark line, moves with a velocity of  $\sim 350 \text{ ms}^{-1}$  between frames 4 and 5, and it then accelerates to a velocity of  $600\text{--}700 \text{ ms}^{-1}$  between frames 5 and 6. In frame 6, a second crack appears at the impact site (see A, frame 6), and both reach a maximum velocity of  $\sim 700 \text{ ms}^{-1}$  between frames 6 and 8. In this crystal as well, the cracks appear to change their direction during propagation. The two cracks merge in frame 11. The crystal did not explode and the undecomposed fragments of the crystal were later recovered.

A few experiments were also conducted in which PETN crystals were fractured by the impact of  $0.4 \text{ mm}$  diameter soda-lime glass spheres at a velocity of  $\sim 200 \text{ ms}^{-1}$ . The spheres were accelerated individually using an explosive gun described elsewhere.<sup>15</sup>

A typical sequence of the impact of a glass sphere on a (110) plane of a PETN crystal (size:  $6 \text{ mm} \times 4 \text{ mm} \times 2 \text{ mm}$ ) is shown in Figure 3. The contact occurs in frame 2, and within  $1 \mu\text{s}$  (i.e., frame 3) a fast moving median crack (see Reference 15 for the various crack systems) forms, the leading edge of which is shown with an arrow. This median crack is of a semicircular shape and it probably lies on a cleavage plane containing the load axis. Between frames 2 and 3, the crack velocity is

at least  $1380 \text{ ms}^{-1}$ . In frame 3, the debris (see at d) of the crystal is also ejected at a high speed ( $\sim 300 \text{ ms}^{-1}$ ). Note that initially the debris is ejected at an angle of  $\sim 45^\circ$ , but when the impacting projectile has gone deeper into the crystal, the debris comes out normal to the crystal surface (see frame 19). There was no initiation and fragments of the crystal were recovered afterwards.

The high-speed photographic sequences presented above clearly show that fracture of even a sensitive explosive crystal cannot cause the initiation of a fast reaction. One particular advantage of using silver and lead azides for these experiments is that, if high enough temperatures had been generated at even a microscopic volume at the crack tip, the fast reaction would have been initiated and propagated throughout the rest of the crystal.<sup>16</sup>

It may be emphasized that here we have not dealt with such solids which may produce very reactive free radicals on fracture. However, such solids deserve further investigation regarding their influence on the initiation behavior of explosives.

## INITIATION BY PLASTIC FLOW

The process of plastic flow in a solid is a very efficient (95 percent efficiency) way of

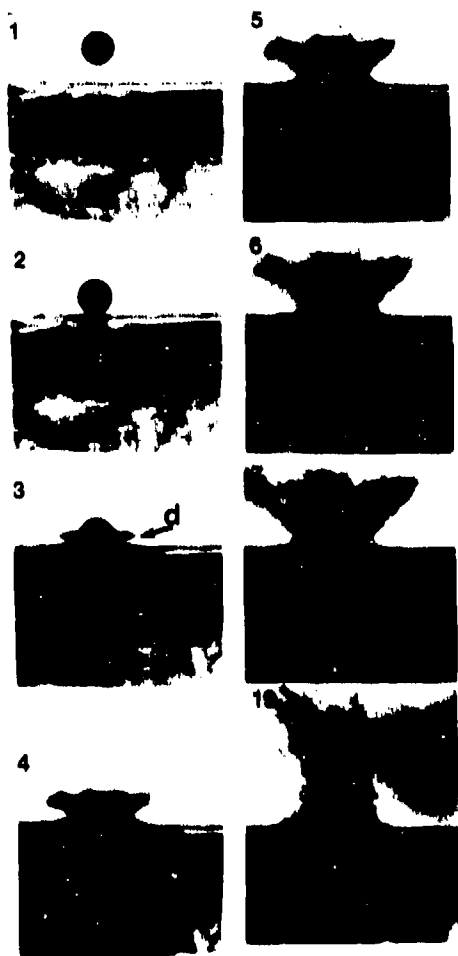


Figure 3. Impact of a 0.4 mm Diameter Glass Sphere on a (110) Surface of a PETN Single Crystal at a Velocity of  $200 \text{ ms}^{-1}$ ; Interframe time:  $1.0 \mu\text{s}$ .

converting the mechanical energy of a stimulus into heat. However, in most crystalline solids, plastic flow occurs inhomogeneously, which means that under transient conditions the temperature rise in a plastically deformed solid is likely to be nonuniformly distributed.

In crystals, the plastic flow occurs along crystallographic slip planes, which give rise to slip bands (these bands are also called shear bands). Such bands can form under both quasi-static and dynamic conditions. In the former, the temperature of the bands may not be very different from that of the regions lying in

between the bands as most of the heat generated in the bands will be conducted away.

Using a simple approach, one can estimate the maximum possible value of the temperature rise in a solid which has been deformed dynamically. We shall assume that the heat generated at a region does not conduct away from it. This type of situation can arise when the deformation is produced in a very short time and when the thermal conductivity of the solid is negligibly small. We shall also assume that the total work of deformation is liberated as heat.

Now, for a solid of uniaxial flow stress  $Y(\epsilon)$ , the amount of work,  $W$ , performed per unit volume in producing a true uniaxial plastic strain of  $\epsilon$  is given by

$$W = \int_0^{\epsilon} Y(\epsilon) d\epsilon . \quad (1)$$

In Equation (1), if we assume, as an approximation,  $Y(\epsilon)$  as being independent of  $\epsilon$ , we get

$$W = Y\epsilon . \quad (2)$$

Accordingly, the temperature rise  $\Delta T$  in the volume will be given by

$$\Delta T = \frac{Y\epsilon}{\rho C} \quad (3)$$

where  $\rho$  is the density and  $C$  is the specific heat of the solid.

As said above, in a solid the deformation is not likely to be homogeneous. Therefore, to predict the temperature distribution, we need to know the magnitude of the plastic strain at different points in the deformed zone. In metals, the strain distribution within locally deformed regions has been estimated by examining the hardness contours of sectioned specimens.<sup>17,18</sup> It is interesting that in metals such as steels, strains of greater than 1 are found only under severe deformation conditions. Whether strains of this magnitude or higher can be produced in explosive crystals, which are very brittle, is not known yet. Nevertheless, in Table 1, we give the predicted values of the maximum temperature rises generated in three explosives, the mechanical and thermal properties of which are available

**Table 1. Calculated Temperature Rise in Various Explosive Crystals Due to Adiabatic Plastic Flow at Different Strains,  $\epsilon$**

Explosive	Temperature Rise (K)		
	$\epsilon=1$	$\epsilon=2.4$	$\epsilon=5$
RDX	20	47	98
$\beta$ -HMX	31	75	156
$\alpha$ -PbN <sub>6</sub>	27	66	137

**Table 2. Uniaxial Yield Stress Values and Thermal Properties of Various Explosives**

Explosive	Y*/MPa	$\rho$ /Mgm <sup>-3</sup>	C/kJ kg <sup>-1</sup> K <sup>-1</sup>
RDX	40	1.81	1.13
$\beta$ -HMX	75	1.91	1.26
$\alpha$ -PbN <sub>6</sub>	50	4.8	0.38

\* Single crystal data taken from Reference 19.

(see Table 2). Note that in these estimated temperature rises we have taken a constant value of the yield stress independent of the temperature and strain rate. It is only an approximation, but in reality the yield stress will drop with increasing temperature. It appears, however, that very little work has been carried out on the variation of the yield stress of various explosive single crystals with varying temperature and strain rate.

It will be seen from Table 1 that even for high plastic strains, the adiabatic temperature rises are not high enough to take any of the three explosives to their ignition points. In order to check our method of estimating the temperature rise, we can compare the theoretical and experimental results in the case of a steel suffering localized deformation. Marchand and Duffy<sup>20</sup> carried out dynamic torsion experiments on a steel (HY-100) having a shear yield stress of  $\sim 500$  MPa. They found that the steel showed 20  $\mu$ m shear bands in which shear strains of the order of  $\sim 10$  were produced. These investigators also measured

the temperature of the sheared bands by using calibrated infrared detectors, and estimated a value of  $\sim 600^\circ\text{C}$ . Taking the density and the specific heat of the steel as  $7.85 \times 10^3 \text{ kg m}^{-3}$  and  $4.92 \times 10^2 \text{ J kg}^{-1} \text{ K}^{-1}$ , we estimate a maximum possible temperature rise of  $\sim 1300^\circ\text{C}$ . This is an overestimate, as we have taken a constant value of the shear stress. In fact, their measurements show that the shear stress drops dramatically to  $\sim 0$  during the rapid shear process. Thus, taking an average shear stress of  $\sim 250$  MPa, our estimated temperature rise will be  $\sim 650^\circ\text{C}$ , which is much closer to the measured value.

An important factor to consider here is the melting point of the solid. It is unlikely that the temperature rise caused by plastic flow or by friction will exceed the melting point of the solid. If the ignition temperature is significantly higher than the melting point, ignition by these processes cannot occur. Of course, under impact or shock loading conditions, high pressures exist and the plastic flow occurs in the presence of these pressures. One is tempted to think that these high pressures will raise the melting point of the solid. If the pressures are purely hydrostatic, then the melting point is most likely to increase. However, under the impact or shock loading conditions, high shear stresses also prevail and these may inhibit any rise of the melting point. It is interesting to note that Mishina et al.<sup>21</sup> report a lowering of the melting point of Wood's metal when it is subjected to shear stresses.

## INITIATION BY FRICTION

Friction between grains of a solid explosive, or between grains and their confining walls is also a very efficient way of converting mechanical energy into heat. As in the case of plastic flow, most of the work of friction is liberated as heat at the friction surfaces. If the coefficient of friction of the rubbing surfaces is known, along with their relevant mechanical properties, one can make a fairly good estimate of the temperature rise due to friction. It is interesting that if one makes an experiment in which the dominant mechanism by which heat can be generated is friction, one can be in a position to predict

whether ignition will occur. Such a situation exists when a column of a solid explosive is impacted with a truncated conical striker. The conical striker is dropped into the explosive vertically and during its penetration the truncated end of the striker picks up explosive particles from the surface and then drags them along into the compact. During this process, the adhered particles rub against the surrounding explosive particles. The temperature rise of these particles due to the friction during the penetration may be calculated using the expression given by Chaudhri.<sup>22</sup>

As an example, the temperature rise is calculated when a conical striker of semi included angle of  $15^\circ$ , mass 0.145 kg, strikes a compact of lead azotetrazole (ignition temperature 493K) with an initial velocity of  $0.5 \text{ ms}^{-1}$ . The average particle size of the compact is  $\sim 25 \mu\text{m}$  and the inter-particle coefficient of friction, measured using the technique of Amuzu et al.,<sup>23</sup> is  $\sim 0.56$ . The predicted temperature rise is shown in Figure 4. Note that initially the temperature rises quite rapidly, and then slows down as the striker penetration increases, reaching a steady state temperature rise of  $\sim 240^\circ\text{K}$  when the penetration is  $\sim 0.4 \text{ mm}$ . This corresponds to an interfacial temperature of  $293 + 240 = 533 \text{ K}$ , which, being higher than the ignition point of lead azotetrazole, should give rise to the ignition of the compact. Similar conclusions have also been drawn by Haskins.<sup>24</sup> Experiments showed that under these

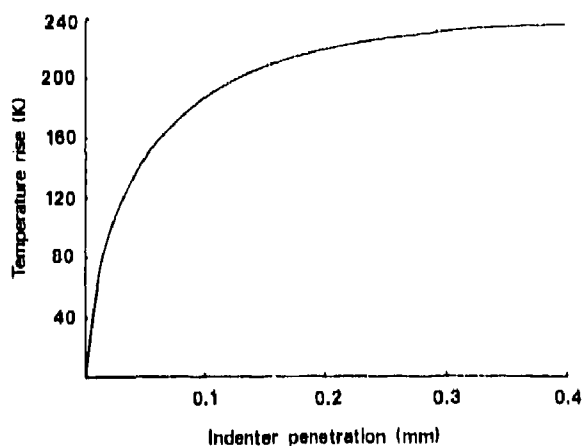


Figure 4. Calculated Temperature Rise Vs. Striker Penetration

conditions initiation of explosion of the lead azotetrazole did occur. Our friction model predicts that the ignition will occur at the tip of the striker when it has penetrated the compact sufficiently. These predictions have been supported by our high-speed photographic experiments. In these, a column of compacted lead azotetrazole was confined between two flat PMMA plates; a needle-shaped metallic striker was then impacted onto the explosive at a velocity of  $\sim 30 \text{ ms}^{-1}$  and the entire event was photographed with a Beckman and Whitley model 189 rotating mirror framing camera using dark field illumination. A typical sequence is shown in Figure 5. Note that the ignition occurs at the tip of the striker after it has penetrated the column by about 0.3 mm.

Situations similar to the one described above may also occur for high-melting point secondary explosives when they are impacted with sharp metal fragments and projectiles. The point being made here is that under suitable conditions, the frictional heating may be more important than any heating due to the shock generated by the impact.

## INITIATION BY BUBBLES AND VOIDS

Gas-filled bubbles and voids play a very important part in controlling the initiation and propagation behavior of all explosives containing them. This fact has been exploited in commercial explosives by adding to them hollow glass or plastic balloons of diameter in the range  $10\text{-}200 \mu\text{m}$ .<sup>25</sup> The sensitization influence of the balloons (or voids) comes from the fact that under a suitable mechanical stimulus the balloons give rise to 'hot spots.' Most investigators are in agreement over this. However, there are major differences of opinion regarding the mechanisms by which the 'hot spots' are formed. We can divide the mechanical stimuli into two types: (i) low strength ones, such as those produced during a low velocity impact of a few  $\text{ms}^{-1}$  or shocks of strength of up to  $\sim 5\text{-}7 \text{ kbar}$ ; and (ii) relatively high strength shocks (pressures:  $15\text{-}20 \text{ kbar}$  and greater), such as those produced by a blasting cap or by the impact of a high velocity projectile. The interaction of low strength shocks with gas-filled balloons quite clearly

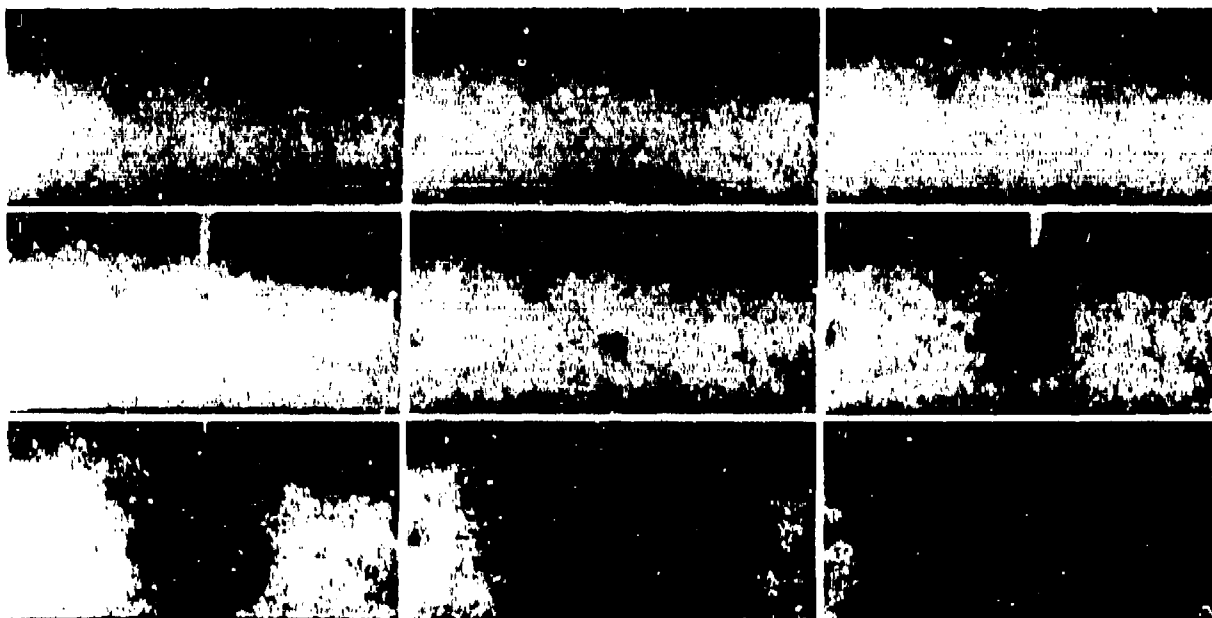


*Figure 5. A Sequence Showing the Location of Initiation When a Conical Striker Penetrates a Column of Compacted Charge of Lead Azotetrazole at a Velocity of  $30 \text{ ms}^{-1}$ . The penetration begins in frame 1 and the initiation (dark zone) occurs in frame 5. Interframe time:  $2.0 \mu\text{s}$ .*

results in the rapid (near adiabatic) collapse of the bubbles, thus giving rise to high temperatures within the contained gas. From their photographic observations of the collapsing bubbles, Bowden and Chaudhri<sup>26</sup> estimate temperatures of up to 1500 K when a 1 mm diameter air bubble in water is collapsed by a shock of only 1 kbar. This temperature rise is high enough to induce the initiation of fast reaction of an  $\text{AgN}_3$  crystal on which it collapses. Much smaller size bubbles of diameter 50-70  $\mu\text{m}$  also cause the initiation of reaction<sup>27</sup> as can be seen in the sequence shown in Figure 6(a). Note from the figure that the ignition in the explosive crystal occurs exactly at the point of contact of the collapsed bubble on the crystal surface. When the collapse of the bubble occurred only a few  $\mu\text{m}$  away from the crystal surface, no initiation took place. When the gas within the bubbles is butane, which has a very low value of  $\gamma$ , the ratio of the specific heats, no reaction takes place due to the collapse process [see Figure 6(b)]. It may be noted that the effect of the  $\gamma$  of the gas is seen only for small (i.e.,  $<300 \mu\text{m}$  diameter) bubbles. These two sequences give very strong support to the theory of the adiabatic heating of the contained gas. Our

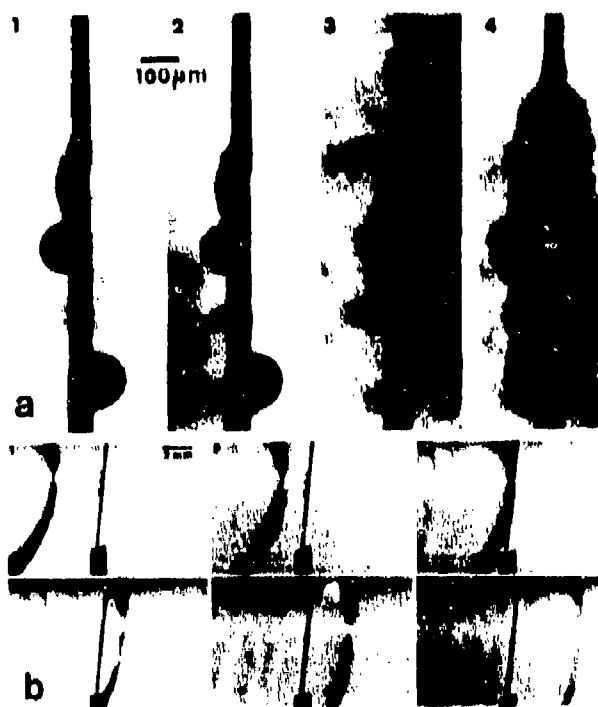


*Figure 6. A Sequence Showing the Importance of the  $\gamma$  of the Gas Contained within Collapsing Bubbles. (a) Argon; interframe time:  $0.6 \mu\text{s}$ . (b) Butane; interframe time:  $1.0 \mu\text{s}$ .*

calculations have also shown that sufficient heat is transferred from gas to the crystal surface within a microsecond.

The collapse of bubbles by relatively weak shocks also produces jets, but their velocities are not high enough to give rise to any significant heating on impact. On the other hand, when the collapse of a void is produced by strong shocks, very fast jets are produced which can play an important role in the initiation process. We have examined the collapse process in water of a 9.5 mm diameter, hollow aluminum sphere having a wall thickness of 250  $\mu\text{m}$  and by using the experimental arrangement which has been described elsewhere.<sup>25</sup> The entire event was photographed with a multiple Kerr Cell camera. A typical sequence is shown in Figure 7. In frame 'O' we can see the PETN charge placed to the right of the aluminum sphere. In frame 1, the water shock (velocity 2900  $\text{ms}^{-1}$ ) has gone over the sphere by about 7 mm and we can see the reflected wave moving towards the expanding detonation products. In the next frame, the initial shock has completely gone over the sphere and another shock,  $S_1$ , appears at the back of the sphere. During the 5  $\mu\text{s}$  after the initial shock hit the back wall of the sphere (i.e., the wall nearest the charge), it has moved in the direction of the shock at a velocity of 1000  $\text{ms}^{-1}$ . In frame 3, part of the back wall has hit the front one and another shock,  $S_2$ , appears around the collapsed hollow sphere, which appears to be generated by the impact of the jet. The jet penetrates the sphere and the latter takes the shape of a dumbbell. The velocity of the secondary shock, as measured from frames 3 and 4, is 2.4  $\text{kms}^{-1}$  (corresponding to a pressure of 10 kbar), but near the point of the jet impact the strength of the shock may be much higher. A rough estimate of the jet velocity is  $\sim 3.5 \text{ kms}^{-1}$ . It appears quite likely that under suitable conditions, the shock produced by the jet impact may even lead the primary shock. Note that Mader's<sup>28</sup> theory predicts regions of high pressures and high temperatures due to shock focusing at a distance of about one diameter of the original sphere and in the direction of the original shock. We have not found any evidence in support of these or any other predictions of the

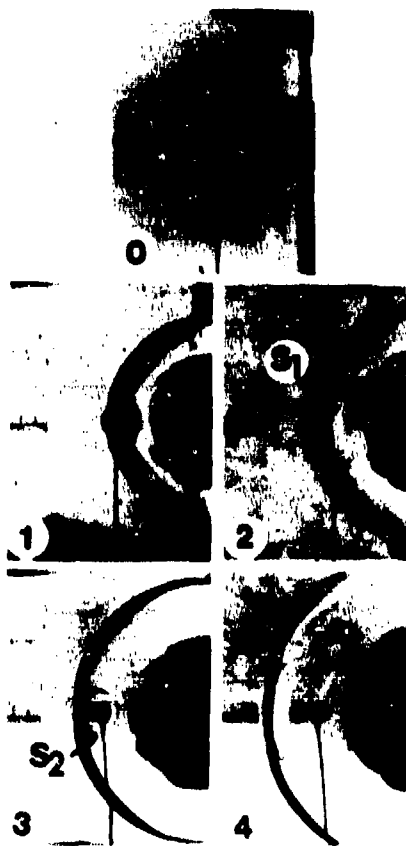


Figure 7. A Sequence Showing the Collapse of a Hollow Aluminum Sphere (Diameter = 9.5 mm, Wall Thickness: 0.25 mm) by a Shock From a 20 g PETN Charge. Frames 3 and 4 show the fast jetting. The times at which the various frames are taken: 1-0  $\mu\text{s}$ ; 2-3  $\mu\text{s}$ ; 4-5  $\mu\text{s}$ ; 4-10  $\mu\text{s}$ ; exposure time for each frame: 0.1  $\mu\text{s}$  (Reference 25).

theory in our bubble-shock wave interaction studies.

As regards the sensitization of an explosive containing voids, when the former is subjected to a relatively strong shock, we believe that the highest temperature hot spots are formed at the point of impact of the jet on the front wall of the void. This is because the temperature of the material of the jet will be higher than that of the initial uncompressed material, as there is always a residual temperature rise after shock compression. Some evidence in support of this can be found in a recent paper.<sup>25</sup>

## CONCLUSIONS

It has been shown experimentally that fast fractures travelling at several hundred  $\text{ms}^{-1}$  in sensitive explosive crystals are unable to cause their explosion. We have interpreted this as being evidence of the lack of high enough temperatures at crack tips. We have also argued that plastic flow, whether localized or not, can only be effective in producing initiation in an explosive crystal if the strains are very high. Whether such high strains in explosive crystals, which are very weak and brittle, can be formed has yet to be seen. Frictional processes have been shown to be relevant for causing initiation in explosive materials, the melting point of which are at least as high as their ignition temperatures. Strong experimental evidence has been provided in support of the adiabatic heating of the gas contained within a collapsing bubble. In the case of the interaction of strong shocks with spherical gas bubbles and voids, fast jets have been shown to form. We have proposed that these jets are the most important factor in the high pressure regime.

## ACKNOWLEDGEMENTS

I should like to thank Dr. J. E. Field of our laboratory for useful discussions. The work was supported in part by the Ministry of Defence (Procurement Executive) and in part by the U.S. Government through its European Research Office. I also thank Dr. J. Roth for correcting my value of the specific heat of  $\beta$ -HMX in the preprint.

## REFERENCES

1. Heavens, S. N. and Field, J. E., "The Ignition of a Thin Layer of Explosive by Impact," *Proceedings of the Royal Society*, Vol. A338, 1974, pp. 77-93.
2. Campbell, A. W.; Davis, W. C.; and Travis, J. R., "Shock Initiation of Detonation in Liquid Explosives," *Physics of Fluids*, Vol. 4, No. 6, 1961, pp. 498-510.
3. Hagan, J. T. and Chaudhri, M. M., "Low Energy Laser Initiation of Beta Lead Azide," *Journal of Materials Science*, Vol. 16, 1981, pp. 2457-2466.
4. Chaudhri, M. M., "High Speed Photography of Electrical Breakdown and Explosion of Silver Azide," *Nature*, Vol. 242, 1973, pp. 110-111.
5. Copp, J. I.; Napier, S. E.; Nash, T.; Powell, W. J.; Skelly, H.; Ubbelohde, A. R.; and Woodward, P., "The Sensitiveness of Explosives," *Philosophical Transactions of the Royal Society*, Vol. 241, 1948, pp. 198-296.
6. Fox, P. G., "The Explosive Sensitivity of the Metal Azides to Impact," *Journal of Solid State Chemistry*, Vol. 2, 1970, pp. 491-502.
7. Armstrong, R. W.; Coffey, C. S.; and Elban, W. I., "Adiabatic Heating at a Dislocation Pile-up Avalanche," *Acta Metallurgica*, Vol. 30, 1982, pp. 2111-2116.
8. Afanas'ev, G. T. and Bobolev, V. K., "Initiation of Solid Explosives by Impact," *Israel Programme for Scientific Translations*, Jerusalem, 1971.
9. Winter R. E. and Field, J. E., "The Role of Localized Plastic Flow in the Impact Initiation of Explosives," *Proceedings of the Royal Society*, Vol. A343, 1975, pp. 399-413.
10. Frey, R. B., "The Initiation of Explosive Charges by Rapid Shear," *Proceedings of the Seventh Symposium (International) on Detonation*, Naval Surface Weapons Center, White Oak, Silver Spring, MD, 1981, pp. 36-42.
11. Howe, P. M.; Gibbons, G.; and Webber, P. E., "An Experimental Investigation of the Role of Shear in the Initiation of Detonation by Impact" *Proceedings of the Eighth Symposium (International) on Detonation*, Naval Surface Weapons Center, White Oak, Silver Spring, MD, 1985, pp. 294-301.
12. Bowden, F. P. and Yoffe, A. D., *Initiation and Growth of Explosion in Liquids and Solids*, Cambridge University Press, London, 1952, pp. 33.

13. Dienes, J. K., "Frictional Hot Spots and Propellant Sensitivity," *Proceedings Materials Research Society Symposium*, Elsevier Science Publishing Co., 1984, pp. 373-383.
14. Chaudhri, M. M., "Shock Initiation of Fast Decomposition in Crystalline Solids," *Combustion and Flame*, Vol. 19, 1972, pp. 419-425.
15. Chaudhri, M. M. and Walley, S. M., "Damage to Glass Surfaces by the Impact of Small Glass and Steel Spheres," *Philosophical Magazine*, Vol. A37, 1978, pp. 153-165.
16. Chaudhri, M. M. and Field, J. E., "Deflagration in Single Crystals of Lead Azide," *Proceedings of the Fifth Symposium (International) on Detonation*, Office of Naval Research, Department of the Navy, Arlington, VA, 1970, pp. 301-310.
17. Williams, G. H. and O'Neill, H., "The Straining of Metals by Indentation Including Work-Hardening Effects," *Journal of the Iron and Steel Institute*, Vol. 182, 1956, pp. 266-273.
18. Chaudhri, M. M. and Gilbert, J. E., "The Plastic Deformation and Hardness Contours of Phosphor Bronze Cones," *Philosophical Magazine*, Vol. A52, 1985, pp. 549-560.
19. Chaudhri, M. M., "Deformation Stress of Highly Brittle Explosive Crystals from Real Contact Area Measurements," *Journal of Materials Science*, Vol. 19, 1984, pp. 3028-3042.
20. Marchand, A. and Duffy, J., "An Experimental Study of the Formation Process of Adiabatic Shear Bands in a Structural Steel," *Journal of Mechanics and Physics of Solids*, Vol. 36, 1988, pp. 251-283.
21. Mishina, H.; Sasada, T.; and Watanabe, K.; "Freezing Point Depression Within a Shear Field and the Effect of a Shear Field on Crystallization of Bi-Pb-Sn-Cd Alloy," *Japan Journal of Applied Physics*, Vol. 25, 1986, pp. 260-262.
22. Chaudhri, M. M., "Stab Initiation of Explosions," *Nature*, Vol. 263, 1976, pp. 121-122.
23. Amuzu, J. K. A.; Briscoe, B. J.; and Chaudhri, M. M., "Frictional Properties of Explosives," *Journal of Physics D: Applied Physics*, Vol. 9, 1976, pp. 133-143.
24. Haskins, P. J., "A Theory of Stab Sensitivity," *R.A.R.D.E. Branch Memorandum*, Sep 1978.
25. Chaudhri, M. M.; Almgren, L-A.; and Persson, A., "High Speed Photography of the Interaction of Shock Waves with Voids in Condensed Media," *Fifteenth International Congress on High Speed Photography and Photonics*, SPIE Vol. 348, 1983, pp. 388-394.
26. Bowden, F. P. and Chaudhri, M. M., "Initiation of Explosion in AgN<sub>3</sub> and  $\beta$ -PbN<sub>6</sub> Single Crystals by a Collapsing Bubble," *Nature*, Vol. 220, 1968, pp. 690-694.
27. Chaudhri M. M. and Field, J. E., "The Role of Rapidly Compressed Gas Pockets in the Initiation of Condensed Explosives," *Proceedings of the Royal Society*, Vol. A340, 1974, pp. 113-128.
28. Mader, C. L., "Initiation of Detonation by the Interaction of Shocks with Density Discontinuities," *Physics of Fluids*, Vol. 8, 1965, pp. 1811-1816.

## DISCUSSION

W. B. SUDWEEKS, Ireco Inc.  
West Jordan, Utah

How would you expect your results to change if you studied glass or plastic microballoons instead of gas bubbles?

## REPLY BY M. M. CHAUDHRI

In the case of my experiments in which I collapsed small gas bubbles on individual single crystals of silver azide, the initial water shock was just about 1-2 kbar in strength. I have not yet studied the interaction of such a

weak shock with a glass or plastic microballoon, though we have done so for mm size glass balloons (see Reference 25). I believe that the static fracture strength of a glass microballoon is higher than 1 kbar (of course, this strength depends upon the wall thickness and the type of glass). I, therefore, wonder if the weak water shock will collapse the glass microballoon. If it does not, the gas inside it (I believe the pressure inside a glass microballoon is less than 1 bar at room temperature) will not be heated and I would not expect an initiation of reaction in the silver azide crystal. If the strength of the water shock is high enough to collapse the glass microballoon, the initiation of fast reaction in the crystal is only possible if the heated gas makes thermal contact with the crystal surface. In the case of a plastic microballoon resting on a silver azide crystal, the weak water shock will collapse the microballoon, but, perhaps without breaking it. Assuming that it is so, the gas within the bubble may only heat the walls of the balloon without raising the temperature of the crystal surface to a significant value. In the case of a plastic microballoons-sensitized emulsion explosive, I would think that the breakage of the microballoon by the initial shock, say, from a cap, is necessary for efficient sensitization.

## DISCUSSION

**M. M. SAMIRANT**  
French German Research Institute  
(ISL)  
St. Louis, France

In your experiments you see a large influence of the  $\gamma$  of the gas contained within collapsing bubbles. Do you mean that hot spots energy comes from adiabatic compression?

## REPLY BY M. M. CHAUDHRI

Yes, I do think that the thermal energy in the hot spots in my experiments comes from the rapid compression of the gas contained within the bubbles. By knowing the volume change (from high-speed photographs), we

have worked out the total heat generated within a collapsed bubble. In Reference 27, we have shown that a sufficient amount of heat is transferred to the crystal surface to give rise to an initiation of fast reaction in a time of the order of 1 microsecond or less.

## DISCUSSION

**P. KATSABANIS**  
Queen's University

We have observed sensitization of explosives when mixed with higher density solids (example: emulsions with sand). What is the mechanism if shock interactions are not important?

Similarly, sensitization is observed in low density explosive systems with microballoons. Jetting is quite difficult with the very low pressures involved. Are shock interactions not important?

## REPLY BY M. M. CHAUDHRI

In the case of low strength (1-2 kbar) initial shocks, a direct comparison of the sensitization efficiency of a bubble and a high density solid particle can be found in Figure 7 of Reference 27. You will see that the initiation occurs at the bubble and not at the solid particle. In some cases, such as the one you mentioned and that reported by Engleke (*Physics of Fluids*, Vol. 22, 1979, pp. 1623-1630), the hot spots are likely to form by frictional heating at the interface of the colliding sand and silica particles.

In the case of your low-density explosive systems containing glass microballoons, I would expect the sensitization to be observed only if the microballoons collapse, thus, producing jetting and causing heating of the contained gas. If the initial shock is unable to collapse the balloons, I would not expect any sensitization.

I do believe that shock interactions, which give rise to hot spots away from the discontinuity, are only important under very extreme conditions.

**CHARACTERIZATION OF DEFECT MICROSTRUCTURE IN HIGH  
EXPLOSIVES SINGLE CRYSTALS BY SYNCHROTRON X-RAY  
TOMOGRAPHY**

**W. C. Tao and J. H. Kinney  
Lawrence Livermore National Laboratory  
Livermore, California 94550**

This paper was presented at the Ninth  
Symposium (International) on Detonation.  
However, it is not published here because the

authors have submitted it for publication (late  
1990) in the *Journal of Chemical Physics*.

# CAVITY COLLAPSE IN A HETEROGENEOUS COMMERCIAL EXPLOSIVE

N. K. Bourne and J. E. Field  
Cavendish Laboratory  
University of Cambridge, Madingley Road  
Cambridge, CB3 0HE UNITED KINGDOM

*The collapse of large (1-12 mm) cavities formed within inert gelatine slabs and sheets of an emulsion explosive has been studied using high-speed framing photography and employing a schlieren technique. The cavities were punched, and in some cases solid particles were cast, into sheets that were then sandwiched between transparent blocks. This allowed processes occurring within and around the cavity to be recorded. Shocks were introduced by impact from a metal flier-plate or directly from an explosive plane wave generator. The asymmetric collapse of circular cavities was observed; a high-speed liquid jet crossed the cavity and impacted on the downstream wall. Perturbations to the direction of jet travel and to the convection of the collapse site in the flow were caused by adjacent solid particles. Regions of high temperature within the collapsing cavity appeared as areas of gas luminescence. The development of reaction sites around collapsing bubbles in an emulsion explosive was photographed.*

## INTRODUCTION

The voidage present in many classes of explosive has long been recognized as a sensitizing agent to ignition by shock or compression waves. This has prompted the addition of artificial cavities to insensitive energetic materials, particularly ammonium nitrate (AN), in commercial applications. The role of bubble collapse in initiation was first systematically investigated by Bowden and Yoffe.<sup>1</sup> They considered collapses occurring over times of the order 100  $\mu$ s to 1 ms and ascribed the thermal initiation of the reactive material surrounding the bubble to adiabatic heating of trapped gas within the cavity during collapse. Johansson<sup>2</sup> calculated the increase in temperature around a gas cavity due to heating by conduction from the compressed gas, and showed it to be insufficient to cause ignition in the surrounding explosive. He hypothesized that the reaction of droplets spalled into the hot gas from the cavity wall during collapse would be sufficient to raise temperature to the point where ignition of the surrounding explosive might occur. Chaudhri and Field<sup>3</sup>

and Starckenberg<sup>4</sup> found that in situations where large cavities collapsed relatively slowly gas phase heating was the dominant ignition mechanism.

Meanwhile the features of bubble collapse in water were being considered by workers in connection with the cavitation erosion of propellers and hydraulic machinery. Kornfeld and Suvorov<sup>5</sup> had suggested as early as 1944 that a bubble might collapse asymmetrically forming a high-speed liquid jet. Benjamin and Ellis<sup>6</sup> obtained photographic evidence of such a collapse, and Plesset and Chapman<sup>7</sup> produced a numerical simulation of a bubble collapsing in the asymmetric pressure field due to the presence of a solid boundary; a liquid microjet formed which was directed towards the solid surface. In the work presented here, such a steady but asymmetric pressure field is replaced by the transient pressure discontinuity of a shock wave.

A description of such asymmetric collapses in terms of the conservation of fluid momentum (the Kelvin impulse) has been

advanced by several authors.<sup>6,8</sup> It can be shown that the cavity surface must deform to become multiply connected so that a vortex system results that conserves the original Kelvin impulse. Vortex generation has been observed in the interaction of acoustic shocks in air with various gas-filled spherical and cylindrical cavities<sup>9,10</sup> and with solid cylinders.<sup>11</sup> The presence of vorticity in the flows studied in this work considerably enhances mass and thermal diffusivity.

The gas shock induced by the passage of the incident liquid shock over the cavity and subsequently trapped within the cavity during its collapse, determines an inhomogeneous temperature field within the gas. The gas temperature along the shock front during its first pass across a cavity has been modelled<sup>12</sup> and shows variations. However, the higher ignition temperatures are not realized until much later during the final stages of collapse. Our work suggests that the positions of high transient temperature within the cavity occur at temporally distinct times, and influence the initial shape of the reaction site.

Many studies in the past have highlighted the role of mechanisms other than gas compression in concentrating shock energy at points at which rapid reaction might commence. Amongst these mechanisms must be mentioned viscous heating in the matrix material and the heating produced by compression of material downstream of the cavity on impact of the liquid jet. Mader and Kershner<sup>13</sup> have reported the initiation of sensitive and insensitive HEs in a hydrodynamic model. Chaudhri et al.<sup>14</sup> reported the initiation of fresh emulsion explosive by the jet impact from a glass sphere collapsed by a 2 GPa shock in water. Frey<sup>15</sup> has noted that viscoplastic work is the most efficient mechanism for production of high temperature and that only for small cavities (of size  $< 1\mu\text{m}$ ) will heat conduction away from the hot spot be significant. In our work, where the cavity size is large, gas compression, viscosity, and jet impact will be the major factors in hot spot formation.

## EXPERIMENTAL

Our experiments have been carried out using a two-dimensional geometry originally suggested by Brunton and Camus<sup>16,17,18</sup> for studying drop impact and cavity collapse in water. The technique was further developed by Dear and Field<sup>19,20</sup> who used gelatine layers; this is the approach used here. The advantage of using such a method is that details of processes occurring within the cavity may be followed without the refraction problems associated with viewing through a three-dimensional curved wall.

A 12 percent by weight mix of gelatine in water at 330K (to give a gel density,  $\rho_{\text{gel}} = 970 \pm 50 \text{ kg m}^{-3}$ ) was cast into a sheet of thickness 3 mm. Chosen cavity distributions were then created in the sheet by application of a suitable punch. Solid particles were cast into the sheet as required. The prepared sample was then sandwiched between glass or polymethylmethacrylate (PMMA) blocks, and PMMA spacers were butted against the remaining free gelatine surfaces to prevent rarefactions relieving shock pressure from the sides. Alternatively, the sample was sandwiched between two further sheets of gelatine and the entire block was placed in a water-filled aquarium. Sample sheets of emulsion explosive of the same thickness were similarly prepared with chosen cavity distributions and placed between PMMA blocks as above.

Plane shock waves were introduced into the sheets by firing a rectangular, phosphor-bronze flier-plate (of weight 5.5 g) so that it impacted the surface of the gelatine or by using an explosive plane wave generator with shock pressure controlled by a PMMA gap. Blocks or aquaria could be bonded directly onto the surface of the attenuator (Figure 1). The gelatine underwent a phase change under the shock overpressures introduced and lost all of its viscoelastic properties. A disadvantage of using a large aquarium to contain the gelatine sandwich was that viewing the event through the slightly curved shock front masked some of the details of events occurring within the

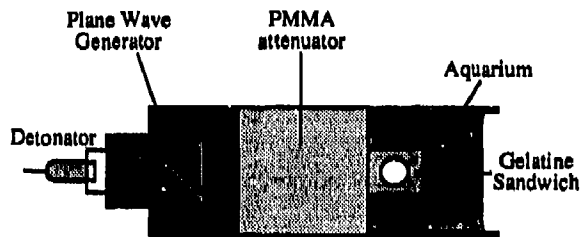


Figure 1. Plane Wave Generator with Aquarium. Alternatively PMMA blocks containing a sheet of emulsion explosive were cemented onto the PMMA gap.

cavity, although effects due to an impedance mismatch at the gel/block interface were eliminated.

The interaction of the incident shock with the cavities and solids was photographed using a high-speed camera, the Imacon 790, at rates ranging from  $2 \times 10^5$  to  $5 \times 10^6$  frames per second. When gelatine was used as a matrix, shocks were visualized using a schlieren method. The arrangement was of the two mirror Z configuration (Figure 2).

The flash source employed was a Xenon Mullard FA5 tube. When emulsions were photographed, no external lighting was used and only emitted light was recorded.

The flash source employed was a Xenon Mullard FA5 tube. When emulsions were photographed, no external lighting was used and only emitted light was recorded.

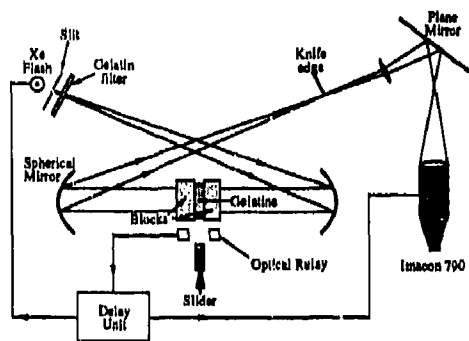


Figure 2. Two Mirror Z Configuration Constructed Around the Two-Dimensional Experiment. The mirrors are of focal length 1.2m and are 0.1m in diameter.

## RESULTS

### Single Cavity Collapse and the Formation of High-speed Jets

The collapse and initial stage of rebound of a 12 mm cavity in gelatine and containing air is shown in Figure 3. The incident shock introduced by the slider impact was of overpressure 0.26 GPa and it is just visible in frame 1 marked S. The initial shock is gone by frame 2 and an air shock, A, runs within the cavity at close to its acoustic velocity, flattening as it approaches reflection in frame 4. The shock is just apparent in frames 5 and 6 (at the base of the arrows) where it appears as a dark line as a result of a phase change on reflection, and can be followed throughout the remaining frames bouncing within the closing cavity and thus strengthening.



Figure 3. A 12 mm Cavity Containing Air Collapses in Gelatine. The sequence is a composite constructed from several experiments. Instability starts in frames 3 and 4. A jet appears in frame 6 and impacts in frame 11. Interframe time 10  $\mu$ s.

The onset of jetting starts as an instability of sinusoidal form in frames 2 and 3, and a well-formed jet appears in frame 6, impacting in frame 11. The jet tip travels at a constant velocity of 130 m s<sup>-1</sup> throughout its flight. Two lobes of gas, L, are isolated in frame 12. Jet penetration produces a vortex pair, V, after collapse.

The violence of the collapse when the bubble is subjected to higher incident shock pressures from a plane-wave generator is apparent in the reduced collapse times and increased jet velocities. If the jet hits the downstream wall with velocity  $v$ , then a transient pressure,  $P_{\text{Impact}}$ , of magnitude

$$P_{\text{Impact}} = \frac{\rho c v}{2}, \quad (1)$$

will be created in a liquid of density  $\rho$  for a time  $\tau$  given by

$$\tau = \frac{r}{c}, \quad (2)$$

where  $r$  is the radius of the jet tip and  $c$  is the liquid shock velocity. The radius of the jets is of the order of 0.1 mm giving  $\tau = 100$  ns. Table 1 shows the recorded jet velocities and times to collapse,  $t$  (defined here to be the time from which the shock passes the rear wall to the moment of impact of the jet tip), for several cavity diameters and shock pressures. Velocities are measured directly from photographic sequences, while impact pressures are calculated from Equation (1).

In other work<sup>14,19</sup> it was found that bubbles placed side by side and close together collapsed such that their jets diverged from one another. In the case of three bubbles placed in a line parallel to the shock front it was found that the central of the three jetted in a direction perpendicular to this front, whereas the jets of the outer two diverged away from the central cavity. If separations were very small, multiple jets were observed. When cavities were placed in a column, the rebound shock from the first collapse triggered collapse in the next cavity downstream. Similarly, the incident shock interacting with a square array was shielded from all but the first row of the array and subsequent cavity collapse was by the rebound shocks from this row.

Table 1. Variation of  $t$ ,  $v$ , and  $P$  for 3, 6, and 12 mm Cavities. The designations A, B, and C refer to the geometries of Figure 4. The shock pressures are those recorded exiting the PMMA attenuator except for † where the pressure in the gelatine is known.

Shock Pressure, P (GPa)	Cavity Diameter (mm)	Collapse Time, t (μs)	$P_{\text{Impact}}$ (GPa)	Jet Velocity, (m s <sup>-1</sup> )
0.26†	3A	15 ± 1	0.14	190 ± 5
0.26†	3B	10 ± 1	0.23	300 ± 5
0.26†	3C	20 ± 1	0.11	150 ± 5
1	3	2 ± 1	1.1	1000-3000
3	3	1.0 ± 0.2	2.3	3000 ± 600
0.26†	6	40 ± 1	0.11	150 ± 5
1	6	4 ± 1	1.1	1500 ± 400
3	6	1.8 ± 0.2	3.8	5000 ± 300
5	6	2 ± 1	2.3-4.5	3000-6000
0.26†	12	96 ± 1	0.1	130 ± 5
1	12	7 ± 1	1.3	1700 ± 250

### The Collapse of Cavities in the Presence of Solid Particles

Cavity/solid interaction is only important when an inhomogeneity is placed sufficiently close that an acoustic perturbation travels from its source to the collapse site before the collapse is complete. Cavity and particle density are thus major variables determining the effects due to adjacent inhomogeneities. This limits useful work to the investigation of the interactions of inhomogeneities up to five cavity diameters apart.

In these experiments the particles were 3 mm diameter lead or nylon discs cast into the gelatine sheet. Five geometries have been studied and are illustrated schematically in Figure 4(a). The cavity collapse times and jet velocities measured for the geometries A, B, and C have appeared already in Table 1 with the same labeling. The interacting compressive shocks, C, and tensile shocks, T, due to reflection of the incident shock at solid particles and cavity boundaries are marked in on the schematics, and can be followed in the collapse sequences. Note also areas of lower

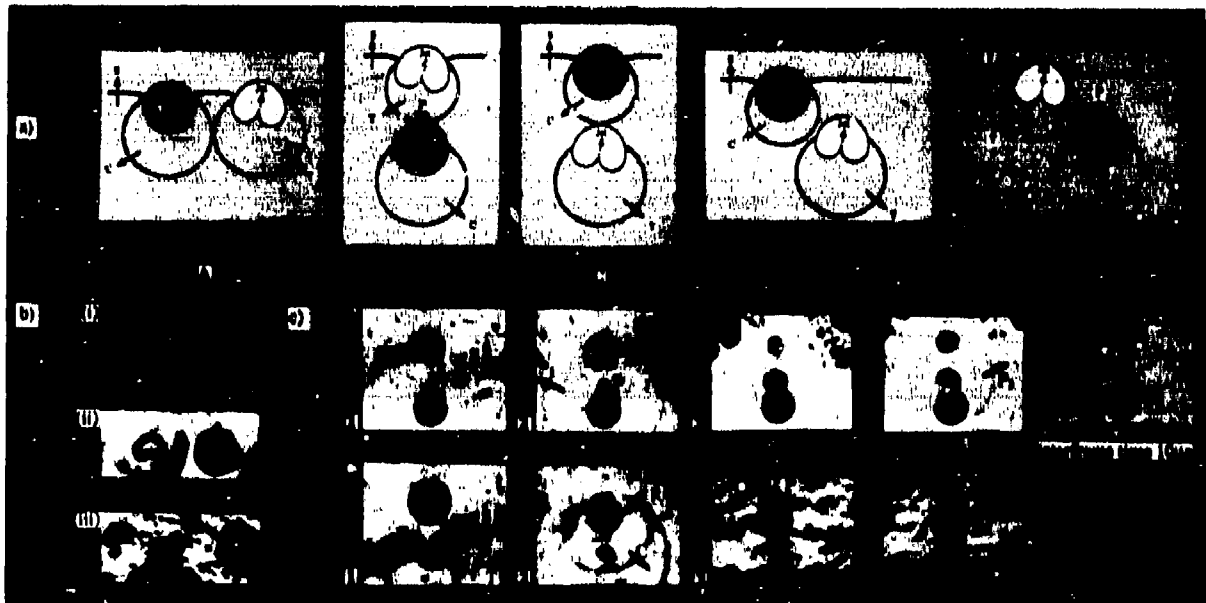


**Figure 4. (a) Schematic of Configurations Used (b) Collapse of 3 mm Cavities in Presence of Solid Particles. Note jet deviation as separation is varied. (c) Sequences Showing Collapse Geometries B and C. Note incident shock, S; tensile shock, T; rebound shock, R; and surface waves, P<sub>1</sub> and P<sub>2</sub>.**

pressure, P, that appear at the downstream stagnation points of the cylinders in the flow.

In Figure 4(b) frames from sequences taken from the collapse of cavities adjacent to lead and nylon discs (geometry A) are shown. The initial cavity wall motion is perpendicular to the incident shock and can only deviate from this direction after arrival of the compressive reflection from the particle. Jet deviation away from both lead and nylon particles is observed if the cavity/particle separation is greater than a cavity diameter,  $d$ , for lead particles, and greater than  $1.5d$  for nylon particles [Figure 4(b) iii]. Interestingly, when cavity and particle are within a diameter of one another the jet moves towards the particle [Figure 4(b) i]. Similar effects are observed when a particle is placed up or downstream of cavities as in geometries D or E.

When cavity and particle are placed on an axis perpendicular to the shock front, no jet deviation is observed. However, this configuration alters the collapse times according to the geometry. Figure 4(c) C shows the interaction of the incident shock with a cavity placed directly in front of a particle. The cavity collapse time of  $10 \mu\text{s}$  is marginally faster than would be expected for a single cavity alone. The release wave from the cavity, T, and the

rebound shock, R, are apparent. Later frames show the convection of the collapse site downstream at  $10 \text{ m s}^{-1}$  where it parts to flow around the particle, which is held stationary by its inertia.

In the alternative geometry in which the cavity is placed in the diffraction zone of the particle, the violence of the collapse is markedly reduced to  $t \approx 20 \mu\text{s}$ . The incident shock, S, is clearly seen in frame 1 of 4(c) B. As the stagnation area, P, begins to form behind the particle (frame 2) a wave, P<sub>1</sub>, centered on the rear of the cylinder is seen to begin propagating at a velocity of some  $1400 \text{ m s}^{-1}$ . It is believed to be a surface wave propagating at the glass/fluid interface. As the area is shed in frame 4 a further surface wave P<sub>2</sub> is emitted. Finally, the area shed from behind the cavity, and the collapse site are convected downstream with the flow (frame 5)

#### **Areas of High Temperature in Gas Contained Within Collapsing Cavities**

Measurements of the temperatures reached by gas under compression within collapsing cavities have yielded values between 600 and 1600K.<sup>1,23</sup> Dear et al.<sup>20</sup> used an image intensifier to observe the collapse of a 3 mm cavity in gelatine by a 0.26 GPa shock and

observed two lobed-shaped regions on the back cavity wall in which luminescence occurred. In other work reported in Reference 20, 10 mg of silver nitrotetrazole was embedded in the material downstream of the cavity. An incident shock of strength 0.26 GPa passed upwards and a jet started to form. Ignition occurred at a site to the left of the point of jet impact, adjacent to one of the lobes isolated in collapse. In a further experiment, the gas confinement was removed by placing the primary ahead of a semicircular cavity in air. The jet impingement alone was insufficient to cause ignition.

In Figure 5(a) a sequence is shown of a 6 mm cavity collapsing in gelatine with an incident shock pressure leaving the PMMA attenuator of a PWG of 3 GPa. The experiment was carried out in an aquarium. Collapse has begun by frame 2 and proceeds to jet impact between frames 2 and 3. The rebound shock R is visible in frame 4 between the shock and the reaction products. Although the finite curvature of the shock front obscures the cavity, two flashes of luminescence, L, are observed in frame 3. These correspond in position to the luminescence observed in Reference 20. Figure 5(b) shows the luminescence of the above collapse at the same incident shock pressure observed at a higher framing rate. Frame 1 shows the appearance of a flash J, which has disappeared by frame 2 where only a faint spot is seen. In frame 3, however, the two lobes L, are observed as in the sequence of Figure 5(a). Note that the initial flash appears in an axial position, while those later appear to the right and left of this area. The duration of the high temperatures giving rise to this luminescence is less than 1  $\mu$ s.

#### The Initiation of Sites Within an Unsensitized Emulsion Explosive

In this section we present results showing the collapse of 1, 2, and 5 mm cavities punched into a 3 mm sheet of an emulsion explosive (ammonium nitrate, oil, and water). The sheet was held between PMMA blocks of thickness 25 mm and an incident shock (leaving the PMMA gap) of 8 GPa was introduced. The emulsion was not sensitized with microballoons.

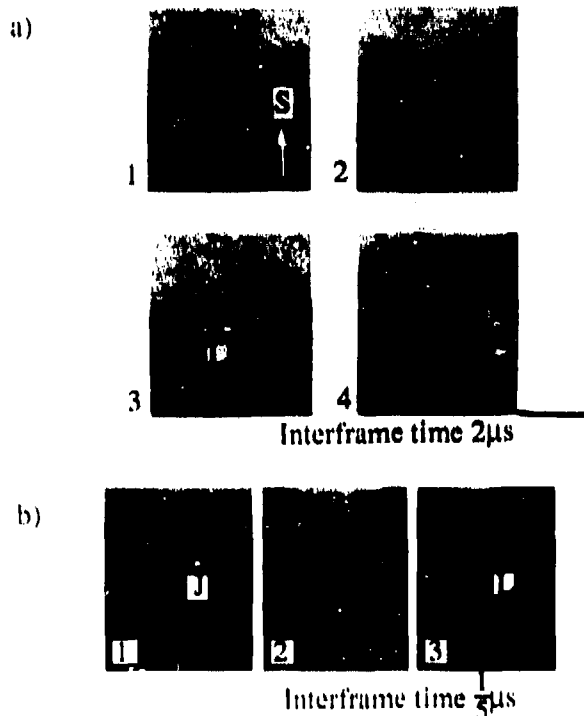


Figure 5. (a) Collapse of a Single 3 mm Cavity in an Aquarium. The shock pressure leaving the PWG is 3 GPa. Luminescence, L, is seen in frame 3. The rebound shock is visible in frame 4. (b) At higher framing rate a single flash, J, is observed followed by lobes, L.

Figure 6(a) shows the collapse of a hexagonal array of 1 mm cavities and 6(b), a rectangular array of 2 mm cavities. The light emitted corresponds well with the position of cavities in the emulsion. Linear areas of flame at the right and left hand edges of the frames correspond to the reaction of emulsion fragments smeared onto the PMMA spacers at either side and sensitized by trapped air. The areas of emitted light have been transferred to a time-integrated frame to the right of each sequence. The hexagonal array is much better defined than the rectangular array, even though the cavities are larger in the latter.

Figure 7 shows the collapse of a rectangular array of 5 mm cavities in the same emulsion. The incident shock starts collapse of the first cavity row in frame 1 and jet impact occurs between frames 1 and 2. The material

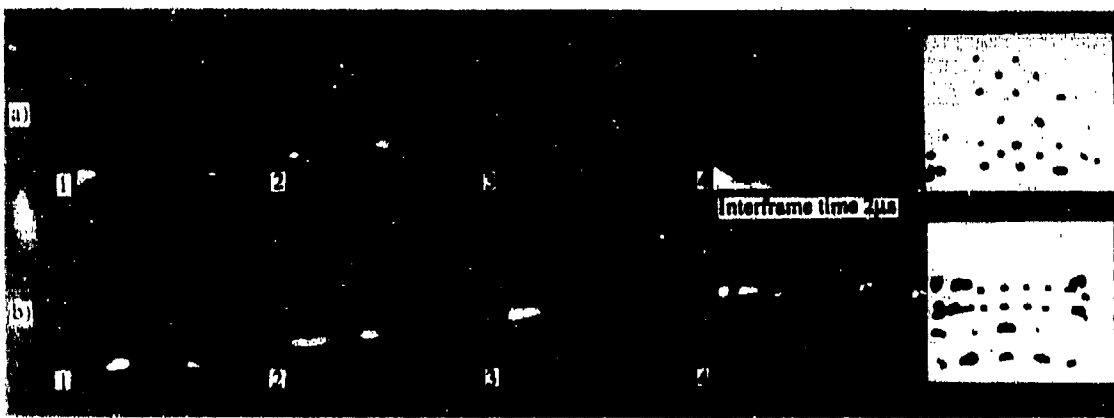


Figure 6. A Hexagonal Array of 1 mm Cavities (a), and a Square Array of 2 mm Cavities, (b) Collapse in an Emulsion. The interframes time is 2  $\mu$ s. The areas of burning are transferred to frames on the right.

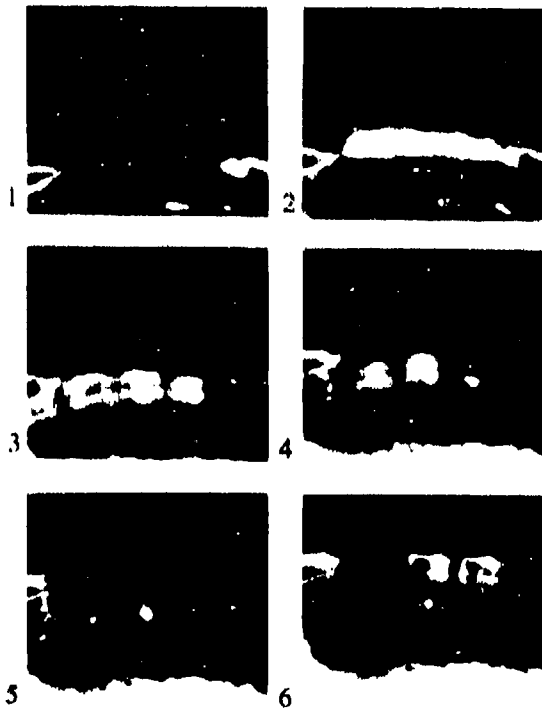


Figure 7. A Square Array of 5 mm Cavities Collapses in Emulsion. The shock pressure leaving the PMMA is 8 GPa. Note the sequential collapse of each row and reaction occurring in the material ahead of the rear cavity wall.

downstream of the first row ignites in frame 2 and these sites persist for 3-4  $\mu$ s, convecting in the flow behind the shock up to frame 6. The second row collapses in frame 5 where ignition at a point at the jet tip of the central cavity is observed. The shape of the reaction sites

corresponds with that of the collapse sites seen earlier. When a corresponding close-packed hexagonal array is created, sites form *between* adjacent cavities in the downstream row and the reaction site is of shorter duration.

## DISCUSSION AND CONCLUSIONS

Analysis of the collapse of a circular cavity under shock has been attempted analytically in two dimensions by Lesser.<sup>19</sup> He allows each particle of the free rear surface of the cavity to move with a resolved part of the velocity of the incident shock. The model qualitatively predicts the form assumed by the back wall, but underestimates the measured jet velocities.

It seems that the collapse should more correctly be regarded as a process comprising three different regimes. In the first, the free cavity surface is accelerated into the gas within the cavity. The surface might be expected to form a shock induced Rayleigh-Taylor<sup>21</sup> instability sometimes called the Richtmeyer-Meshkov instability.<sup>10</sup> Such an instability is seen to arise in the early stages of Figure 3, developing as the amplitude of the disturbance becomes large into the constant velocity jet characteristic of the second regime of collapse. The final regime begins with the jet impact upon the downstream wall, and includes the formation of two vortices ahead of the collapse site as the jet penetrates. The compression of the gas trapped in the remnants of the cavity completes the collapse.

The transition from the linear acoustic regimes of the flier-plate impact experiments to strong-shock collapses by explosively-driven shocks does not qualitatively appear to introduce any new features due to non-linear effects. However, the jet impact pressures are of significant magnitude and generate a rebound shock capable of inducing further collapse in adjacent cavity layers.

The interactions of cavities with other cavities and particles within a fluid is a complex, time-varying function of pressure and particle velocity around the collapse site. The important features of the collapse are the direction of jet travel within the cavity, the compressive and tensile reflections from inhomogeneities in the fluid, and the production of areas of high vorticity and mixing within the flow.

The direction of jetting may be explained in terms of the pressures acting around the back boundary of the cavity during collapse. The compressive reflections of the incident shock by solid particles act to divert the direction of jetting in adjacent cavities away from the particle. This is sufficient to explain the observed results for situations in which bubble and particle are separated by more than a bubble diameter. At closer separations the jet directs itself toward the particle, an example of the Bjerknes effect which will decrease in strength with distance away from the particle. In the case where an inclusion is axially downstream from the cavity, the collapse time may be reduced by the acceleration of the downstream cavity wall towards the inverting upstream wall.

The areas of lower pressure that develop behind the particle are believed to be stagnation points similar to those produced in steady flow around cylinders. Associated vortices are then shed downstream. A vortex pair is also present in the collapse site after the jet has penetrated the downstream wall. The flow thus contains significant regions of mixing which are distributed through the flow by convection of sites around solid particles (see Figure 4(c)). Leiper et al.<sup>22</sup> attributed the rate increase in an air-sensitized commercial explosive (AN, water, oil) with increased voidage to the higher mass and thermal diffusivity resulting from the chaotic motion arising from complex shock

interactions with the voidage. Such cavity interactions may be seen here explicitly giving rise to the chaotic motion inferred by Leiper et al. These sites of high vorticity are also those associated with the initiation of burning in an unsensitized emulsion of the type used in Reference 22.

Dear et al.<sup>20</sup> estimated a temperature within their luminescing cavity in excess of 750 K by assuming adiabatic compression of the gas within the cavity, consistent with luminescence arising from free-radical creation and radiative recombination. The experiments with the primary explosive indicate the importance of gas confinement when dealing with regimes in which cavity size is large and shock pressures are relatively low.

Lesser and Finnström<sup>12</sup> explained the results of Reference 20 in terms of temperature gradients existing along the front of the induced gas shock running inside the cavity. However, their model put the high temperature areas, giving rise to luminescence, in the first pass of the gas shock across the cavity, in contradiction to the sequence of Figure 5 which shows luminescence occurring in the final stages of collapse. It seems that the creation of these transient high temperatures is a multi-stage process. The strengthening gas shock bouncing within the cavity (see Figure 3) will give rise to an inhomogeneous and rapidly varying temperature field. This culminates in a flash of light associated with the jet impacting, followed some 0.4  $\mu$ s later by further luminescence associated with gas compression in the two lobes of gas isolated by the jet impact. This implies that there are two temporally distinct positions on the downstream cavity wall at which thermal initiation might occur. The first, near the jet tip is associated on impact some nanoseconds later with high transient pressures. The second, to the left and right of this area, experiences high temperatures for a more extended time.

The above observations of collapse in an inert medium may be used to describe ignition at cavity collapse sites in an AN, oil, water emulsion explosive. The general features of such collapses are ignition at the point of jet impact followed directly by ignition of the material ahead of the original downstream

cavity wall (as observed in the simulations of Reference 13). There is no ignition before cavity collapse has completed. With the geometry used in this work, no propagating reaction front was generated. However, reaction sites were present convecting in the flow for 3-5  $\mu$ s before extinguishing. For lower void densities collapse proceeded row by row with the most violent collapses observed for the hexagonal geometry where the penetration of the incident shock into the array was most efficient. Closer spacing of cavities in downstream rows appears to quench the burning, by pressure release and restriction of the material available for reaction.

The sequences show that ignition in the case of large cavities in a matrix of low viscosity is largely a result of the temperature at the downstream cavity wall created by gas compression. The development of the reaction site is consistent with ignition of an area of high mixing caused by linear vortices created by jet penetration of the downstream wall. It is likely that gas temperatures within a cavity in the final stages of collapse are inhomogeneous due to complex shock reflections within, and higher than those predicted by an adiabatic compression model.

## ACKNOWLEDGEMENTS

The authors acknowledge financial support from the SERC and the EGTC of ICI. Thanks to Messrs. G. A. Leiper and A. Hackett of ICI for practical help and comments.

## REFERENCES

1. Bowden, F. P. and Yoffe, A. D., *Initiation and Growth of Explosion in Liquids and Solids*, 1958, reprinted CUP, 1985.
2. Johansson, C. H., *Proc. Roy. Soc. Lond. A.*, Vol. 340, 1974, pp. 231-244.
3. Chaudhri, M. M. and Field, J. E., *Proc. Roy. Soc. Lond. A.*, Vol. 340, 1958, pp. 113-128.
4. Starkenberg, J., in *Seventh Symposium (International) on Detonation*, Naval Surface Weapons Center, White Oak, MD, NSWC MP 82-334, 16-19 Jul 1981, pp. 3-16.

5. Kornfeld, M. and Suvorov, L., *J. Applied Phys.*, Vol. 15, 1944, pp. 409-425.
6. Benjamin, T. B. and Ellis, A. T., *Phil. Trans. Roy. Soc. A.*, Vol. 260, 1966, pp. 221-240.
7. Plesset, M. S. and Chapman, R. B., *J. Fluid Mech.*, Vol. 7, 1972, pp. 283-290.
8. Blake, J. R. and Gibson, D. C., *Ann. Rev. Fluid Mech.*, Vol. 19, 1987, pp. 99-123.
9. Rudinger, G. and Somers, L. M., *J. Fluid Mech.*, Vol. 7, 1960, pp. 161-176.
10. Haas J-F. and Sturtevant B., *J. Fluid Mech.*, Vol. 181, 1987, pp. 41-76.
11. Bryson, A. E. and Gross R. W. F., *J. Fluid Mech.*, Vol. 10, 1961, pp. 1-16.
12. Lesser, M. B. and Finnström, M., *Proc. 7th Conf. on "Erosion by Liquid and Solid Impact,"* Cavendish Lab, Cambridge, United Kingdom, 1987, Paper 23, pp. 23-1 to 23-7.
13. Mader, C. L. and Kershner, J. D., *Eighth Symposium (International) on Detonation*, Albuquerque, New Mexico, 15-19 July 1985, pp. 42-51.
14. Chaudhri, M. M.; Almgren L-A; and Persson A., *Proceedings of 15th Int. Conf. on High Speed Photography and Photonics*, SPIE, Vol. 348, pp. 388-394.
15. Frey, R. B., *Eighth Symposium (International) on Detonation*, Albuquerque, NM, 15-19 July 1985, pp. 68-80.
16. Brunton, J. H., *Int. Conf. on Rain Erosion*, Eds. Fyall, A. A. and King, R. B., R. A. E. Farnborough, United Kingdom, 1967, p. 821.
17. Brunton, J. H. and Camus, J-J, *Proc. Int. Conf. on High Speed Photography*, Eds. Hyzes, W. G. and Chase, W. G., SMPTE, New York, 1970, p. 444.
18. Camus, J-J, *High Speed Flow in Impact and its Effect on Solid Surfaces*, Ph.D. Thesis, University of Cambridge, 1971.
19. Lesser, M. B.; Dear, J. P.; and Field, J. E., *J. Fluid Mech.*, Vol. 190, 1988, pp. 409-425.

20. Dear, J. P.; Field, J. E.; and Walton, A. J., *Nature*, Vol. 332, No. 6164, 1988, pp. 505-508.
21. Taylor, G. I., *Proc. Roy. Soc. Lond. A.*, Vol. 201, 1950, p. 192.
22. Leiper, G. A.; Kirby, I. J.; Hackett, A., *Eighth Symposium (International) on Detonation*, Albuquerque, New Mexico, 15-19 July 1985, pp. 187-195.
23. Von Holle, W. G. and Tarver, C. M., *Seventh Symposium (International) on Detonation*, Naval Surface Weapons Center, White Oak, MD, NSWC MP 82-334, 16-19 July 1981, pp. 993-1003.

## DISCUSSION

**J. ROTH, Consultant**  
Portola Valley, CA

Have you tried different gases in your collapsing cavities?

### REPLY BY N. K. BOURNE

The only gas introduced into the cavities was air at ambient pressure and temperature. It would be interesting to vary the ratio of specific heats of the cavity contents and/or the initial gas pressure in order to quantitatively assess the importance of jet impact versus adiabatic heating as an ignition mechanism.

## DISCUSSION

**H. GRYTING, Gryting Energetics**  
Sciences Company, San Antonio, TX

Do you have (semi-) quantitative information concerning the relative importance (as related to ignition to detonation) of the heating of the gas by adiabatic compression during hot spot formation upon shock wave impingement, and the simultaneous attack upon the explosive at the far hot spot sphere wall from fragmented explosive particles flung inward from the shock that causes the hot spot to collapse?

### REPLY BY N. K. BOURNE

The sequences I have taken suggest that in the explosive system presented in this work it is the hydrodynamic heating resulting from the jet impact that is the primary ignition mechanism. The adiabatically compressed gas does have an influence on the ignitions observed, but at a temporally distinct time after a site has begun to develop centered on the point of jet impact. The spatial extent of the site is thus influenced by the ignition from the hot gas. In a few cases, ignition of vapor within the cavities has been tentatively identified. These sequences will appear in a future paper. I must stress that our system is one in which viscosity is low and cavities are large so that visco-plastic work contributes negligibly to temperature rises. This is not generally the case in many systems of interest.

# RESPONSE OF COMPOSITE PROPELLANTS TO SHOCK LOADING

Bai Chunhua and Ding Jing\*  
Beijing Institute of Technology  
Department of Engineering Mechanics  
P. O. Box 327, Beijing 100081, PEOPLE'S REPUBLIC OF CHINA

*The response of two composite propellants, FT-1 and FT-2, to two shock loadings, 2.0 GPa and 10.0 GPa, has been studied. In the shock initiation process produced by a 2.0 GPa shock wave, there are two peaks behind the shock front in histories of particle velocity, pressure, reaction rate, and others. The reaction proceeds with three stages. In a detonation process under 10.0 GPa shock loading, the reaction zone extends for more than 1.0  $\mu$ s and the detonation is non-ideal. Analyses using the Lagrangian technique show that the two peaks are produced by the physical and chemical interaction of the ammonium perchlorate and the binder, HTPB or thiokol.*

## INTRODUCTION

During the development of propellants, the shock wave sensitivity must be considered. In manufacturing, machining, stockpiling, transporting, and during use, propellants are often acted on by shock waves. On the other hand, in a process of deflagration to detonation transition (DDT), the shock to detonation transition (SDT) is the final stage.<sup>1,2</sup> For a long time the shock wave sensitivity of solid propellants was evaluated by Gap Test,<sup>3,4</sup> the behavior of propellants under shock loading has been widely studied. Later, the Modified Gap Test<sup>5,6</sup> was developed. Using this test, two thresholds can be obtained. One is the reaction threshold and the other is the detonation threshold. Probe and wedge experiments<sup>7,8</sup> were used to get the locus of the shock front. Some researchers<sup>9</sup> studied qualitatively the interaction of components using numerical modeling.

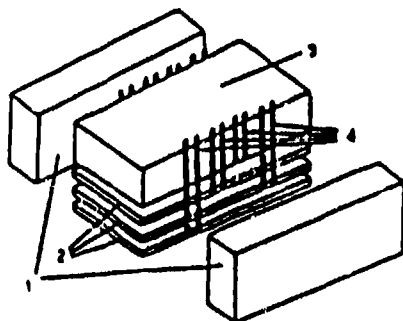
In this work, two composite propellants are studied which are named FT-1 and FT-2. The main formulation for FT-1 is 21/8/65 wt percent thiokol/aluminum powder

(Al)/ammonium perchlorate (AP), and that for FT-2 is 11/18/68 wt percent hydroxy-terminated polybutadiene (HTPB)/Al/AP. First, by using Lagrange gauges and Lagrangian analysis, histories of particle velocity, pressure, specific volume, and internal energy are obtained. Then, based on these results, reaction characteristics are calculated which are composed of reaction extent, reaction rate, energy-release rates, and instantaneous heat of reaction. Finally, the reaction process is analyzed with the help of component experiments.

## METHODS

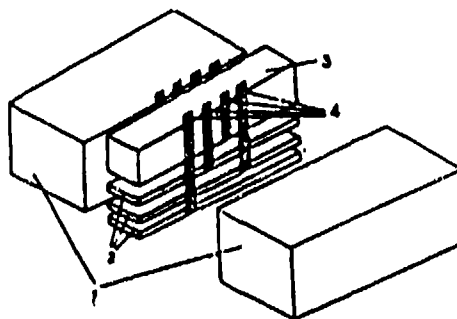
The shock wave system consists of a 100-mm diameter plane wave generator, a 10-mm thick Baratol pad, and a gap used to adjust pressure. Using EMV gauges and managanin pressure gauges, a set of particle velocities and pressure histories are measured. The assemblies of the two kinds of gauges are shown in Figure 1. When using EMV gauge, the influence of detonation product conductivity on the results of measurement was studied. The results show the error is less than 4 percent.<sup>10</sup> The magnetic field, which is produced by a Helmholtz coil in a 160 mm diameter sphere, is  $1,000 \pm 5$  Gauss.

\* Currently on sabbatical leave at CETR, New Mexico Tech, Socorro, New Mexico 87801



*Pressure History Measurement*

- 1- 80 x 25 x 30 mm
- 2- 80 x 30 x 3 mm
- 3- 80 x 30 x 20 mm
- 4- H type manganin gauge



*Particle Velocity History Measurement*

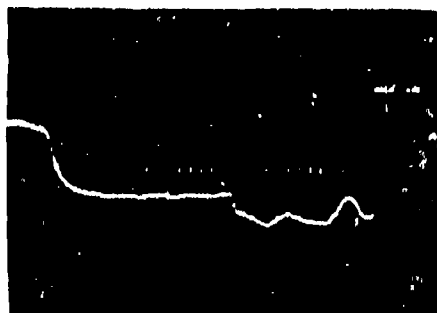
- 1- 80 x 25 x 30 mm
- 2- 80 x 30 x 3 mm
- 3- 80 x 30 x 20 mm
- 4- U type EMVG



a.



b.



c.



d.

*Experimental records of particle velocity histories (a,b) and pressure histories (c,d)*

*a,c- FT-1 Propellant*

*b,d- FT-2 Propellant*

*Figure 1. Assemblies of a set of (a) EMV gauges and (b) manganin pressure gauges*

Based on the experimental results for particle velocity and pressure, specific volume and specific internal energy are evaluated from the following equations:

$$V(h,t) = V(h,\tau) + \frac{1}{\rho_0} \int_{\tau}^t \left( \frac{\partial U}{\partial h} \right)_t dt \quad (1)$$

$$E(h,t) = E(h,\tau) - \frac{1}{\rho_0} \int_{\tau}^t P \left( \frac{\partial U}{\partial h} \right)_t dt \quad (2)$$

Here,  $U$ ,  $P$ ,  $V$ , and  $E$  are particle velocity, pressure, specific volume, and specific internal energy, respectively.  $h$  and  $t$  are Lagrangian coordinates,  $\tau$  is the time of shock front arrival, subscript 0 expresses initial state and

$$\left( \frac{\partial U}{\partial h} \right)_t$$

is determined by the pathline technique.<sup>11</sup> The state of shocked propellants is described by Equations (3) to (9). Reaction extent,  $\lambda$ , is obtained through substituting the results of Lagrangian measurements and Lagrangian analysis to these equations.

$$P_u = c_0^2(\rho_u - \rho_0) + (\gamma - 1)\rho_u E_u \quad (3)$$

$$\gamma = 4s - 2 \left( 1 - \frac{\rho_0}{\rho_u} \right) s^2 - 1 \quad (4)$$

$$E_p = P_p / [\rho_p (k - 1)] \quad (5)$$

$$P = P_u = P_p \quad (6)$$

$$V = \lambda V_p + (1 - \lambda) V_u \quad (7)$$

$$E = \lambda E_p + (1 - \lambda) E_u + \lambda Q \quad (8)$$

$$P = \frac{1}{V} \quad (9)$$

Here  $Q$  is the heat of reaction;  $c_0$  and  $s$  are the coefficients in the Hugoniot relation  $D = c_0 + sU$ , and are determined by experiment; and  $k$  is the ratio of specific heat of the products. Subscripts  $u$  and  $p$  indicate unreacted propellants and reaction products. Other reaction characteristics—reaction rate  $r$ , volumetric energy-release rate  $\dot{p}$ , chemical energy release rate<sup>12</sup>  $\sigma$ , and instantaneous heat of reaction<sup>13</sup>  $\tilde{Q}$ —can be calculated based on the results of Lagrangian measurements and Lagrangian analysis.

$$r = \left( \frac{\partial \lambda}{\partial t} \right)_h \quad (10)$$

$$\dot{p} = \left( \frac{\partial P}{\partial t} \right)_h + \left( \frac{c}{V} \right)^2 \left( \frac{\partial V}{\partial t} \right)_h \quad (11)$$

$$\sigma = \frac{\dot{p}}{\rho c^2} \quad (12)$$

$$\tilde{Q} = \frac{\dot{p}}{\Gamma \rho r} \quad (13)$$

Here  $c$  is the frozen sound speed,  $\Gamma$  the Grüneisen parameter, and  $\sigma$  the thermicity coefficient.

## SHOCK INITIATION

The shock initiation process of FT-1 and FT-2 produced by a shock wave with a front pressure of 2.0 GPa was studied. Histories of particle velocity and pressure were measured at four profiles using Lagrangian gauges. Specific volume and specific internal energy were calculated using Lagrangian analysis. Reaction extent, reaction rate, energy-release rates, and instantaneous heat were also calculated. FT-1 and FT-2 have similar behavior. Some results of FT-2 are shown in Figure 2.

From the experimental and calculated results, two peaks behind the shock front are

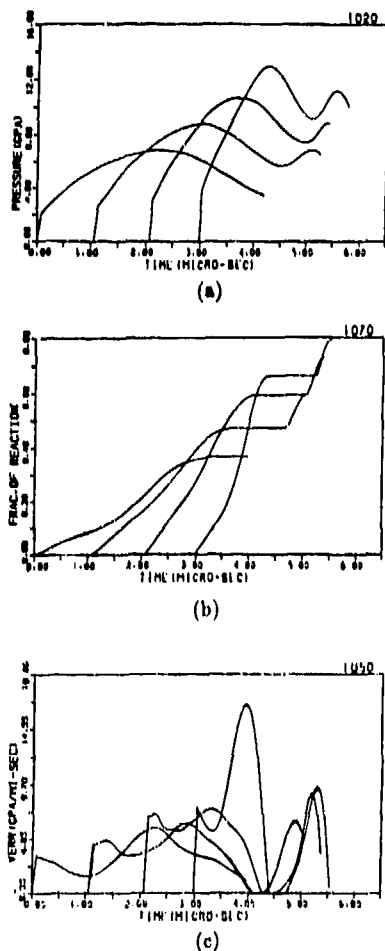


Figure 2. Histories of (a) Pressure, (b) Reaction Extent, and (c) Volumetric Energy Release Rate of FT-2

found in the histories of particle velocity, pressure, reaction rate, and others. The history of reaction extent is composed of three stages with the middle one being a reactionless stage. Comparison of the first and last stages shows that in the last stage the reaction develops more quickly.

## DETONATION

When a shock wave with front pressure 10.0 GPa acts on FT-1 and FT-2, Lagrangian gauges record the detonation process. In particle velocity and pressure histories there is one peak behind the shock front. In Figure 3a are the pressure histories of FT-2. Based on the results of Lagrangian gauges, specific

volume, and specific internal energy, other reaction characteristics are calculated. Figure 3b is the results of volumetric energy-release rate of FT-2. From these results it is found under detonation the reaction continues for about 1.0  $\mu$ s and the width of the reaction zone is more than 5.0 mm.

Experimental detonation parameters were obtained from Lagrangian gauge measurements and ideal detonation parameters were calculated using BKW code.<sup>14</sup> Some results are shown in Table 1. Comparison of the experimental and calculated results shows the detonation of composite propellants is non-ideal.

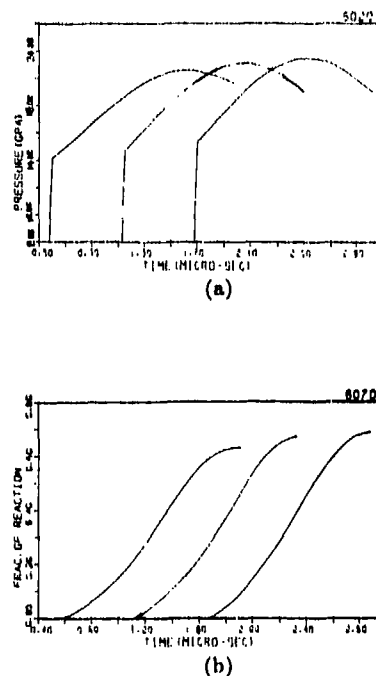


Figure 3. Histories of (a) Pressure and (b) Reaction Extent of FT-2 Under Detonation

Table 1. Experimental and Calculated Detonation Velocity  $D$  and Detonation Pressure  $P$

Propellant	$D_{\text{exp}}$ (km/s)	$D_{\text{calc}}$ (km/s)	$P_{\text{exp}}$ (GPa)	$P_{\text{calc}}$ (GPa)
FT-1	6.10	7.03	14.5	23.9
FT-2	6.45	7.70	16.0	28.7

## ANALYSIS

In order to help analyze the complicated process of shock initiation and detonation of composite propellants, manganin pressure gauges were used to measure the pressure histories individually for the following six kinds of compositions:

- (1) AP
- (2) HTPB and thiokol
- (3) mixture of AP + Al
- (4) mixtures of AP + HTPB and AP + thiokol
- (5) mixtures of Al + HTPB and Al + thiokol
- (6) FT-1 and FT-2

Some results are shown in Figure 4.

The result of binder alone (Figure 4c), HTPB or thiokol, shows that under 6.0 GPa shock loading the reaction of the binder continues near the front so that the pressure of front is about 8.0 GPa, which agrees with the result of numerical simulation.<sup>15</sup> The reaction of AP starts at the shock front, but occurs mostly behind the front (Figure 4a).

From the results of AP + Al (Figure 4b), it is found that Al starts to react before the reaction of AP stops. In the mixtures of AP + binder there are two peaks similar to those in FT-1 and FT-2 (Figure 4d). This indicates the double peaks are the result of interaction of AP and binder, HTPB or thiokol.

Comparison of the results of AP and the mixture of AP + binder shows the first

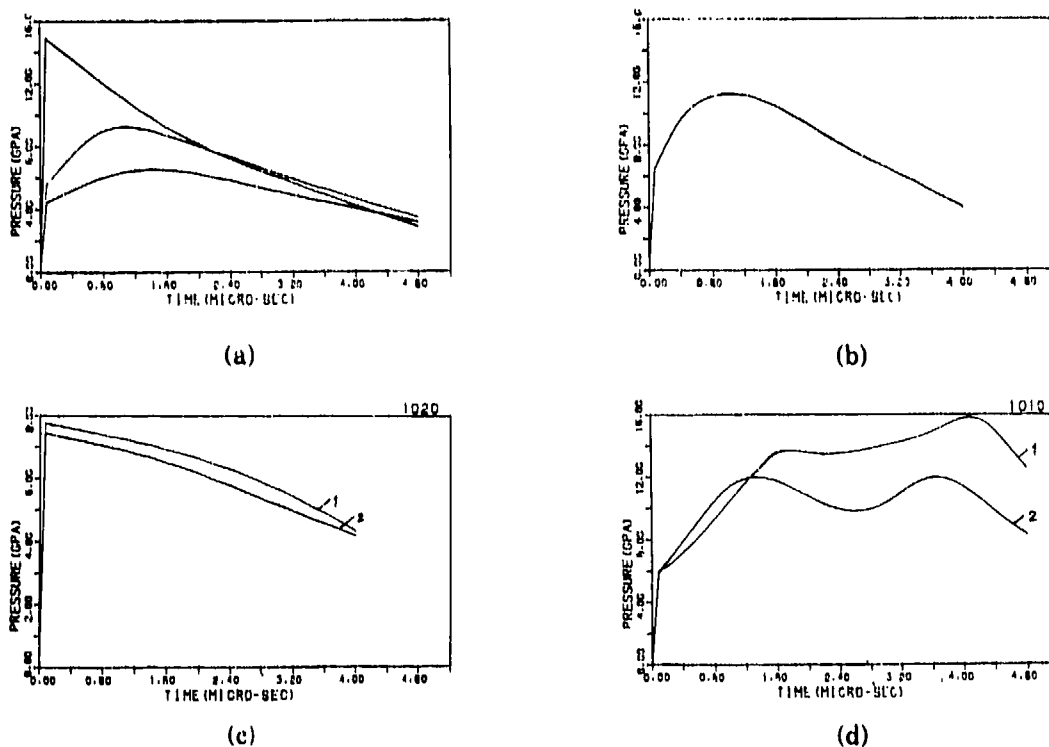


Figure 4. Pressure Histories of Single Component and Mixtures of Two Components System.

a - AP under different shock loadings.

b - Mixture of AP and Al under 6 GPa shock loading.

c - HTPB alone (curve 1) mixture of HTPB and Al (curve 2).

d - AP + HTPB (curve 2) in comparison with FT-2 (curve 1).

peak of the mixture is higher than the peak of the AP alone (Figure 4a and 4d). This means the products of AP can react with those of the binder because the binder reacts near the shock front. Comparing the results of the mixture of AP + binder with that of the composite propellants, it is found that the two peaks of the propellants are higher than those of the mixtures (Figure 4d). This shows the reaction of Al with oxidants strengthens the two peaks.

## CONCLUSION

The behavior of two commercial propellants—binders of which are thiokol and HTPB, respectively—differs greatly with that of double-base and high energy modified double-base propellants. For these composite propellants, there are two peaks behind the shock wave front in the histories of particle velocity, pressure, and others. The formation of hot spots and the ignition of composite propellants have been modeled numerically.<sup>15</sup>

The reaction process of composite propellants under shock loading proceeds with three stages. In the first stage, binder and AP react independently. Binders and AP-air react very fast and they will all react within about 0.1  $\mu$ s in a ball of diameter within the range 0.05 - 0.1 mm. The products of AP also react with that of binders and aluminum powder. In the first stage, the chemical reaction does not have its highest rate at the shock front, but grows up gradually. This means that the reaction taking place beyond the shock front is very important for composite propellants. At the end of the first stage, under the high shock pressure, the binder becomes a viscous liquid which partially covers the AP crystal surface. The same conclusion was reached by W. Xu et al.<sup>16</sup> For this reason a short reactionless stage intervened. After a time delay of about 1-2 microseconds for transport processes, reactions resume and the third stage proceeds. At the last stage, particle velocity, pressure, and reaction extent go up again until the end.

With a better physical model, a better approach to evaluating the hazardous properties of composite propellants under shock loading is possible, and the prevention of their disastrous accidents shall be within sight.

## ACKNOWLEDGMENT

We would like to express our appreciation to Hou Zhulin, Huang Zhenping, Zhao Hengyang, and Chen Renmin for their kind assistance.

## REFERENCE

1. Cowperthwaite, M., "Phenomenology of the Deflagration to Detonation Transition in Propellants and Explosives," *Proceedings of the Seventh Symposium (International) on Detonation*, Annapolis, MD, 16 Jun 1981, pp. 225-233.
2. Krier, H.; Cudak, C. A.; Stewart, J. R.; and Butler, P. B., "A Model for Shock Initiation of Porous Propellants by Ramp-Induced Compression Processes," *Proceedings of the Eighth Symposium (International) on Detonation*, Albuquerque, NM, 15 Jul 1985, pp. 962-971.
3. Price, D., "Shock Sensitivity, A Property of Many Aspects," *Proceedings Fifth Symposium (International) on Detonation*, Pasadena, CA, 18 Aug 1970, pp. 207-217.
4. Price, D.; Clairmont, A. R., Jr.; and Erkman, J. O., "The NOL Large Scale Gap Test," NOLTR 74-40, 1974.
5. Liddiard, T. P. and Forbes, J. W., "Initiation of Burning and Detonation in Cast H-6 and Cast PBX W-109," *Proceedings of the Fifth Symposium (International) on Detonation*, Annapolis, MD, 16 Jun 1981, pp. 308-315.
6. Tasker, D. G., "Shock Initiation and Subsequent Growth of Reaction in Explosives and Propellants: the Low Amplitude Initiation Test, LASI," *Proceedings of the Seventh Symposium (International) on Detonation*, Annapolis, MD, 16 Jun 1981, pp. 285-298.
7. Dick, J. J., "Nonideal Detonation and Initiation Behavior of a Composite Solid Rocket Propellant," *ibid*, pp. 620-623.
8. Dick, J. J., "Detonation Initiation and Behavior of Some HMX/AP/Al Propellants," *Combustion and Flame*, Vol. 37, 1980, pp. 95-99.

9. Westmoreland, C. and Lee, E. L., "Modeling Studies of the Performance Characteristics of Composite Solid Propellants," *Proceedings of the Seventh Symposium (International) on Detonation*, Annapolis, MD, 16 Jun 1981, pp. 517-522.
10. Bai Chunhua, "Response of Solid Propellants to Shock Waves," Ph.D. dissertation, Beijing Institute of Technology, Jun 1988.
11. Grady, D. E., "Experimental Analysis of Spherical Wave Propagation," *J. Geophys. Res.*, Vol. 78, 1973, p. 1249.
12. Fickett, W. and Davis, W. C., *Detonation*, University of California Press, Berkeley, 1979, pp. 78.
13. Huan, S.; Xue, H.; and Ding, J., "Lagrange Gauge Analysis for Evaluating Reaction Characteristics in Shocked Explosives," *Proceedings of the International Symposium on Intensive Dynamic Loading and its Effects*, Beijing, China, 3 Jun 1983, pp. 144-149.
14. Mader, C. L., *Numerical Modeling of Detonation*, University of California Press, Berkeley, 1979, pp. 412-418.
15. Bai Chunhua and Ding Jing, "A Numerical Study of Hot Spot Formation and Ignition of Composite Propellants Under Shock Loading," to be published in *Shock Waves in Condensed Matter*, 1989.
16. Xu Wengan, Li Junli, Li Baoxuan, and Wang Kexiu, "Covering of the Molten Binder over the Oxidizer Surface,"

*Combustion and Detonation Phenomena*, 19th International Annual Conference of ICT 1988, Karlsruhe, FRG, pp. 66-1 to 66-13.

## DISCUSSION

**PIER K. TANG**  
 Los Alamos National Laboratory  
 Los Alamos, NM

I am not surprised by the pressure of the second stage. The decomposition products from the first stage have to mix together before they can react further. The mixing process involves migration of various components and the rate is very slow. In this stage, the energy production is practically zero. The binder before melting acts as a barrier for the mixing process. Can you comment on this scenario?

## REPLY BY DING JING

The scenario given in this paper is quite complicated. The existence of a reactionless or a very slow reaction stage has been shown by the analysis of experimental results. However, the detailed mechanism of such a stage is not very clear so far. There might be a stage of slow reaction in the condensed phase. It has been investigated by Xu Wengan et al.<sup>16</sup> on the covering of molten binder (HTPB) over AP using X-ray photo electron spectroscopy. The average covering amounts 10.9 percent of the total surface for HTPB composite propellant under an average pressure of 40.8 kg/cm<sup>2</sup>. They also confirmed by their experimental results that the condensed-phase reaction of AP actually exists in the burning process of AP-based composite propellants.

# DEFORMATION AND EXPLOSIVE PROPERTIES OF HMX POWDERS AND POLYMER BONDED EXPLOSIVES

J. E. Field, M. A. Parry\*, S. J. P. Palmer, and J. M. Huntley  
Cavendish Laboratory, University of Cambridge,  
Madingley Road, Cambridge CB3 0HE, UNITED KINGDOM

*Techniques have been developed for studying the behavior of explosives when impacted for recording their strength, failure, and ignition properties. They include a drop-weight facility with transparent anvils, an instrumented drop-weight machine, a miniaturized Hopkinson bar system for high strain rate property measurement, laser speckle for studying the deformation and fracture of PBXs, an automated system for analyzing speckle patterns, and heat sensitive film for recording the positions and temperatures of "hot spots." Polishing and staining methods have been developed to observe the microstructure of PBXs and failure during quasi-static loading. Further evidence is given of shear banding in PETN, and the effect of particle size on the behavior of HMX during impact is described. The quasi-static strengths of PBX samples were measured using the Brazilian test with the strains recorded using laser speckle photography. Data is given for five PBX compositions.*

## INTRODUCTION

This paper describes the response of explosives to stress and impact. Samples in the form of powder layers, pressed pellets, and polymer bonded explosives (PBXs) have been studied. It is important with all of these systems to understand the factors which affect their mechanical and thermal properties since these influence the mechanisms of "hot spot" formation and the explosives' "sensitiveness" and "explosiveness."

## EXPERIMENTAL

### High Speed Photography; Transparent Anvil Drop-Weight Apparatus

Advances in the understanding of explosive phenomena have been greatly assisted by direct observation of events using high-speed

photography. The ability to obtain both temporal and spatial resolutions during impact has been particularly valuable in establishing the sequence of events. The arrangement used in the present work (Figure 1) was originally employed by Blackwood and Bowden<sup>1</sup> and has more recently been extensively used by Heavens, Field, Swallowe, and others.<sup>2-9</sup> Typically, 25 mg samples of material, in the form of powders, pressed discs, or PBX samples, are compressed between toughened glass anvils with an impact velocity of typically  $4.5 \text{ m s}^{-1}$ . The drop weight (mass 5 kg) which carries the upper anvil is dropped from a height of up to 1.5 m and is guided by three rods to ensure a planar impact. Shortly before contact, the mirror within the weight comes into alignment to complete the optical path from the xenon flash light source, through to the high-speed camera. The AWRE C4 rotating mirror camera, is of the continuous access variety so that synchronization is not required. The full length of film (140 frames) is scanned in approximately 1 ms so that the duration of the flash also functions as a shutter.

\*Now at Materials Research Laboratory, Ascot Vale, Victoria 3032, Australia.

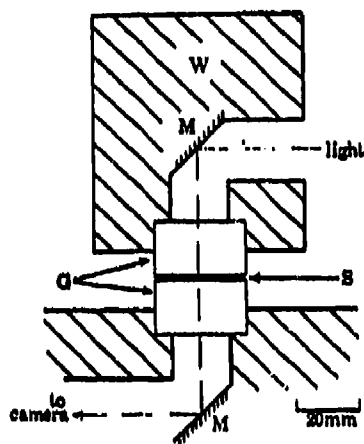


Figure 1. A Cross Section of the C4 Drop-Weight System. *W* is the weight, *M* a mirror, and *G* the toughened glass anvils with *S* the specimen.

Field et al.<sup>6,7</sup> determined that the initiation of explosive samples usually occurs after rapid radial flow (greater than ca.  $100 \text{ m s}^{-1}$ ) unless sensitizing grits are present. Valuable data which can be extracted from the photographs is, therefore, the radius as a function of time and, thereby, the velocity as a function of time. Rapid flow can occur as a result of mechanical failure of the sample but while this may be true in some cases, it is not a necessary precursor. If the material is sufficiently weak that it generates negligible retardation to the falling weight and deforms at constant volume, then high radial velocities are a natural outcome. In addition to the bulk plastic behavior, other physical processes such as fracture, jetting, bulk plastic flow, localized adiabatic shear, melting, and elastic recovery can be observed under favorable conditions. Explosive reaction is visible since it is self-luminous. Although photographs present a large amount of information, they cannot usually tell the whole story without corroborative evidence from other sources such as dynamic stress measurement.

### Instrumented Drop-Weight Apparatus

A second drop-weight machine is available with instrumented steel anvils (Figure 2). The system rests on a large blacksmith's anvil, which provides an almost ideal rigid support for a small load cell which measures the impact

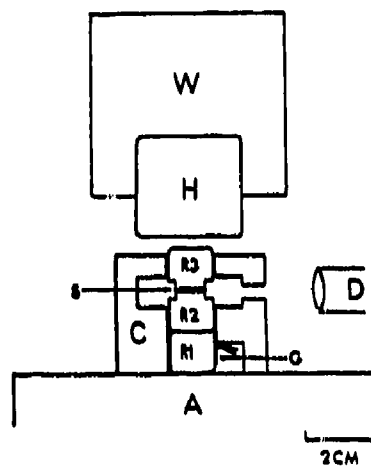


Figure 2. Instrumented Drop Weight. *W* is the weight; *A* the anvil; *R*<sub>1</sub>, *R*<sub>2</sub>, and *R*<sub>3</sub> the steel rollers, the lowest being the load cell having strain gauges *G*; and *D* the light detector.

force. The cell is of in-house design being made from a 12.7 mm x 12.7 mm steel bearing roller with two pairs of strain gauges fixed axially on opposite sides of the roller which has four flats machined on it. An impact cell is formed by two further rollers stacked on top of the load cell, and samples are placed between this pair, the whole arrangement being impacted by a weight of 2.5, or 4.7 kg.

The dynamics of the system have been described in detail earlier,<sup>2,3</sup> but a comparison with the behavior of a direct impact Hopkinson bar (next subsection) is illuminating. Unlike the Hopkinson bar, the dynamics of the drop weight system do not require explicit account to be taken of stress wave propagation. The pressure bar in the smallest of our miniaturized Hopkinson apparatuses is made deliberately long at 150 mm, so that a stress wave can be observed without interference from reflections. The drop-weight load cell is much shorter, being 25 mm including the protective roller on top of it, but the timescale over which it operates is 400  $\mu\text{s}$  compared with 16  $\mu\text{s}$  for the pressure bar. Consequently, there are many stress wave reflections in the load cell and its behavior is therefore quasi-static.

A further facility which is used with 25 mg samples when initiation is expected is the detection of electrical conductivity between the anvils. This can detect ionized gas and pinpoint the initiation of explosion. Alternatively,

ignition is detected by monitoring light output with a photo-cell.

### Miniaturized Hopkinson Bar

In a conventional Hopkinson bar system (see, for example, Reference 10), the specimen is placed between two long, cylindrical rods. A stress pulse is then sent down the input bar, and gauges record incident, reflected, and transmitted waves. From these records, it is possible to obtain stress/strain behavior of the specimen at strain rates of ca.  $10^3 \text{ s}^{-1}$ . A few years ago, Gorham<sup>11</sup> developed a direct impact (no input bar) miniaturized system. Initially, a high-speed camera was used to measure strains, but this is not essential and stress strain curves can be obtained from the gauge records on the output bar following an analysis given by Pope and Field.<sup>12</sup> The advantages of the new apparatus are that strain rates up to ca.  $10^5 \text{ s}^{-1}$  can be achieved and high strength specimens investigated. Results on a range of PBXs were presented at the last Detonation Symposium.<sup>9</sup>

### Brazilian Test and Laser Speckle for Tensile Strengths and Strains to Failure

The Brazilian test geometry (Figure 3) and laser speckle photography have been used to study the tensile strengths and rupture strains of a variety of PBX compositions at strain rates of ca.  $10^{-4} \text{ s}^{-1}$ .

The compression induces tensile stresses normal to the loading axis which are sensibly constant over a region about the center of a specimen. The tensile strength of the material is then calculated from

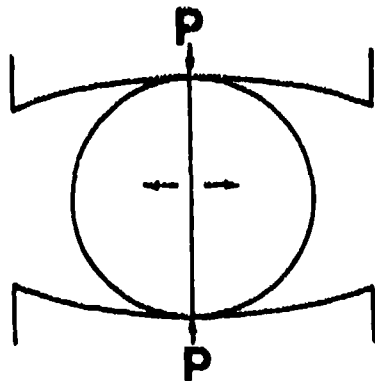


Figure 3. Loading Arrangement Used in Brazilian Test

$$\sigma_t = 2P / \pi Dt, \quad (1)$$

in which  $P$  is the failure load, and  $D$  and  $t$  the diameter and thickness of the specimen, respectively. The validity of Equation 1 is based on the assumptions that failure occurs at the point of maximum tensile stress (i.e., at the center), and that the compressive stress has no influence on the failure. In practice, the use of plane anvils can produce very high contact stresses at the loading points, and lead to the collapse of the contact edge. Awaji and Sato<sup>13</sup> have shown that by using curved anvils, collapse of the edge can be avoided, and shear stresses under the points of loading may be substantially reduced. If the ratio of the contact half-width,  $b$ , to the disc radius,  $R$ , is larger than approximately 0.27, the maximum principal stresses near the contact area are compressive. Then the tensile stress at the center is given by

$$\sigma_t^* = \{1 - (b/R)^2\} \sigma_t. \quad (2)$$

Other workers<sup>14-16</sup> using the Brazilian test geometry have employed displacement transducers to measure the average tensile strain across a diameter. However, the use of a relatively simple optical technique called "speckle photography" allows in-plane displacements to be measured to an accuracy of ca.  $0.1 \mu\text{m}$  at different positions on the sample surface, and thereby determine the strain field at any point.<sup>17,18</sup> There is the added advantage that it is a remote sensing technique which does not involve attaching gauges to the sample. For displacement and strain measurements, a double exposure is photographically recorded before and after deformation. Displacement information can be extracted by allowing an unexpanded laser beam to pass through the negative. If, at the point illuminated the "speckles" have been displaced between exposures, the displacement vector is manifested by a Young's fringe pattern observed at the far-field Fraunhofer diffraction plane. The displacement vector is perpendicular to the fringe orientation with magnitude inversely proportional to the fringe spacing. Complete analysis involves many measurements, and becomes tedious when performed manually. For this reason, a fully automatic

electro-optical system for measuring the displacement field from a double exposure speckle photograph has been constructed.<sup>19</sup> With the present system the computation time per fringe pattern is under 10 s, giving a total analysis time per photograph of typically 30-40 minutes.

### Heat Sensitive Film Technique

The technique used in this work was first suggested by Coffey and Jacobs.<sup>20</sup> It is based on the use of an acetate sheet coated with a sensitive layer which darkens on exposure to heat. For very short duration heat pulses ( $<10^{-4}$  s) the film color is yellowish-brown rather than black, and the degree of darkening increases as the contact time is increased, until the film is fully blackened. The coloration is believed to be due to the reaction in the sensitive layer being unable to go to completion in the time available. Film darkening is a function of both temperature and time, so to use the film to estimate the temperature achieved during deformation, one must know the time over which the deformation occurred, and then refer to a set of calibration curves (darkening as a function of time and temperature) for the film. Details of how the film has been calibrated can be found in Reference 21.

To use the calibration to obtain a temperature in an impact experiment, it was necessary to measure the time during which the darkening took place. These measurements were made by using the transparent anvil arrangement described above. Experiments were carried out by placing the film on the glass anvils with the sensitive side in contact with the sample. Results giving the temperatures achieved during the deformation, shear banding, and fracture of a range of polymers can be found in Reference 21.

### Microstructure and Fracture Paths in PBXs

Polishing and staining techniques have recently been developed to study the relationship between the microstructure of polymer-bonded explosives and their fracture routes when broken in the Brazilian test under quasi-static conditions. A post-failure examination

of the fracture route through the microstructure provides a valuable insight into the fracture mechanisms. It is not, however, usually possible to determine where failures initiated, or the order in which events occur during crack propagation. A technique has therefore been developed using a computer operated camera (Olympus OM2 with motor drive), attached to a microscope stage to record photographic sequences of the microstructure at the center of a sample during a Brazilian test.

## RESULTS

### Drop-Weight Impact on PETN; Further Evidence for Ignition by Adiabatic Shear

Drop-weight impact, using the transparent anvil, and instrumented apparatus (Figures 1 and 2) was first used by Heavens and Field in the early 1970s.<sup>2,3</sup> They showed that thin layers exhibited fracture, compaction, sintering, plastic flow at high velocities, jetting, melting, and ignition in the glass anvil apparatus. Banded structures which became visible in some sequences, with both PETN and RDX, were interpreted, we now think wrongly, as ripples caused by jetting. The evidence on this point was re-interpreted by Field et al.<sup>6</sup> and evidence was presented to show that the features were shear bands; a mechanism for hot-spot production and ignition which had been suggested by Winter and Field for other explosives in 1975.<sup>22</sup> At the last Detonation Symposium, photographic evidence was presented of adiabatic banding in PBXs and PETN.<sup>9</sup>

Figure 4 shows the result of an experiment when the heat sensitive film was used. The original is in color, but the black and white reproduction shows the key features. Where there has been fast reaction the products have removed much of the heat-sensitive layer, but at the top of the picture where the film remains, it is a deep orange-brown. In the lower part of the film there is a great arc of banding, and where the heat sensitive layer remains attached, it varies from light brown to almost black, all indicative of high temperatures. The ignition also clearly starts from the region where the bands are located. Figure 5

Table 1

Type	Comments	Particle size range/ $\mu\text{m}$	Median particle size/ $\mu\text{m}$
A	Granular powder produced by recrystallization from cyclohexanol.	100 to 1000	480
B	Fine powder produced by colloid milling of type A. Bimodal distribution.	2 to 130	28.5
TC/14	Micronized by fluid energy milling of type A.	2 to 180	20
TC/13	"	2 to 36	10
TC/12	"	2 to 29	6.4



Figure 4. Heat Sensitive Film Record of an Impact on PETN. Original in color. Clear evidence of shear banding and associated ignition.

#### Drop-weight Impact on HMX of Different Particle Sizes

The HMX was provided by AWRE and Table 1 gives details.

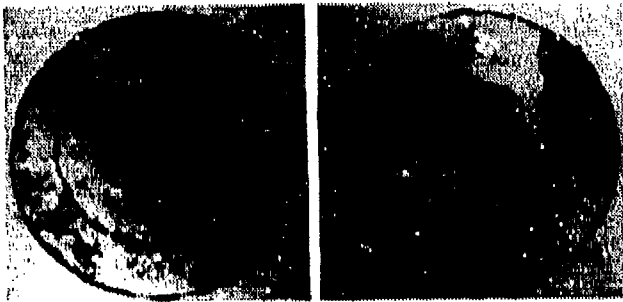
**Experiments with Heat-Sensitive Film.** The HMX samples were impacted using 12 mm discs of heat-sensitive film (HSF) on the lower roller of the steel anvil apparatus, with the emulsion side of the film against the explosive. A range of drop-heights were used, and the  $H_{50}$ 's determined for the HMX samples in the presence of HSF. These  $H_{50}$ 's were in fact *higher* than the  $H_{50}$ 's with bare anvils. The desensitizing effect of the HSF is thought to be due to the increased friction which decreases the velocity and extent of rapid flow.

Figure 6 shows two HSF discs viewed in silhouette, and also the extent of flow of the HMX (dashed line). The sample originally occupied an area similar to that of the discolored region. The extent of radial flow of the sample with HSF was less than when bare metal anvils were used. Presumably this was due to increased friction between the explosive and the HSF. The band-like character of the heat output during the impact experiment is



Figure 5. Shear Banding in PETN After Impact, Where Ignition Failed to Occur

shows an impact from a subcritical height onto a PETN layer. It shows the families of shear bands particularly well in part of the unexploded layer.



**Figure 6.** *Two Recovered Discs of Heat-Sensitive Film (HSF). The explosive has been removed: (a) The area that the HMX occupied after impact is indicated. The discoloration of the HSF appears as a pattern of both radial and parallel lines. The sample originally covered an area similar to the discolored area. (b) Partial reaction has occurred and part of the HSF disc has been consumed, but the band-like pattern is still apparent near the center of the disc.*

evident in Figure 6a, and can still be detected in Figure 6b, even though partial ignition and propagation of the explosive had occurred.

Figure 7 is an HSF disc viewed by reflected light. Note, the original photograph was in color! The patterns on the recovered HSF disc consists of families of approximately parallel lines, some of which bifurcate, and which are characteristic of shear bands. The figure shows that black (very hot) areas also occur at the junction of some lines (labeled C). Figure 8 shows failure patterns in HMX which has remained on the steel rollers after impacts from sub-critical heights. Figure 8a shows the HMX after a test with HSF and reveals the close resemblance between lines on the HSF and failure in the explosive. This type of failure pattern was also observed during impact of HMX with bare metal rollers. Figure 8b is a clear example of shear bands in an impacted layer of HMX. The conclusion is that HMX fails by shear banding in these experiments and that these shear bands are the hot-spot sites which cause ignition.

**High Speed Photography.** Heavens and Field<sup>2,3</sup> showed that HMX compacted, jetted, flowed plastically, and ignited, but unlike PETN and RDX did not sinter and melt. Although the propagation rate in HMX was high, combustion was invariably incomplete in

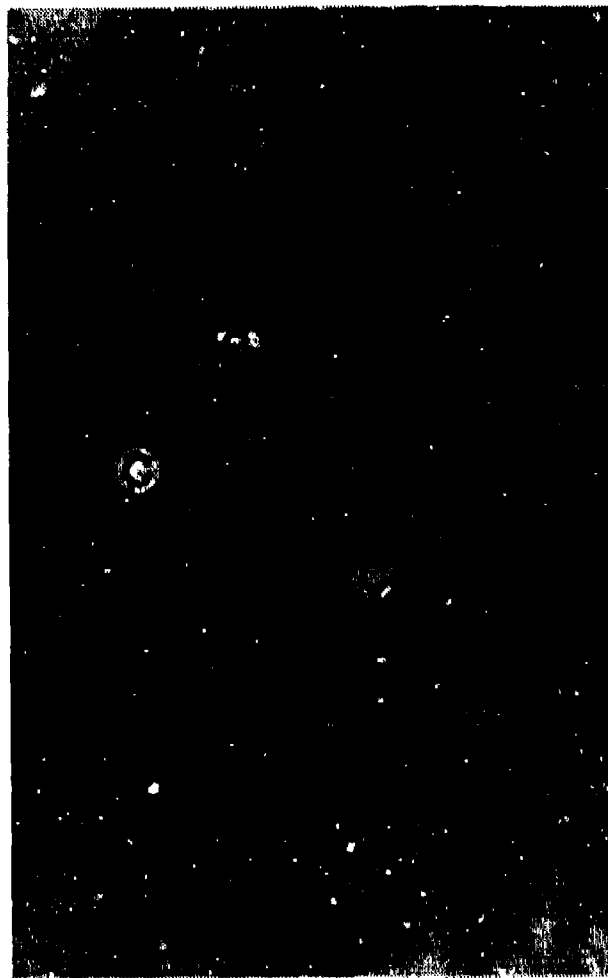


**Figure 7.** *HSF Recovered after Impact of HMX Showing Branching of the Shear Bands and Discoloration Where Branching Occurs. Original in color.*

the drop-weight experiments. This type of behavior was found in the present work, with the residue varying considerably. All the experiments were from a 1 m drop-height onto 25 mg powdered layers.

Figure 9 is for type A HMX and is typical of all impacts on this coarse material (Table 1) where ignition took place. The small, slightly darker region which is just visible near the center in most of the frames is due to overwriting as the camera mirror comes into position again. All the stages listed above are clearly shown. Ignition occurred on rebound after a short plateau region and is a perfect example of what we classify as a "widespread" ignition from a multitude of sites. The finer



Figure 8. Photographs of Explosive Remaining on Hardened Steel Rollers after Impact. (a) is from a test with HSF. Notice the lines in the disc resemble the failure pattern in the explosive. (b) was obtained during impacts with bare metal rollers and shows a band-like failure pattern.

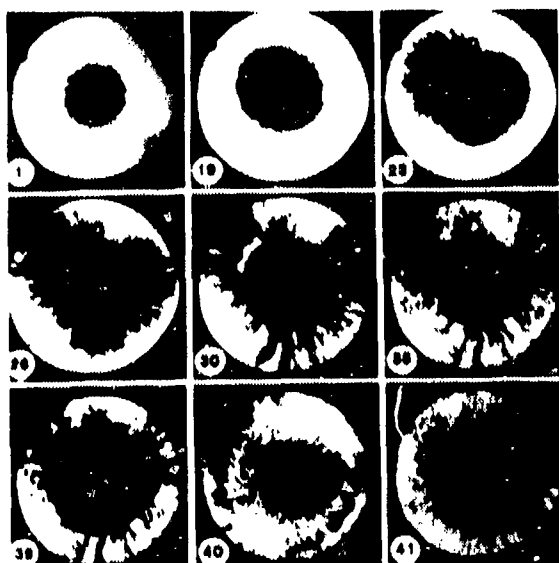


Figure 9. Impact on Type A HMX, Widespread Ignition With Rapid Flow (Maximum Velocity  $240 \text{ m s}^{-1}$ ). Framing intervals  $6.5 \mu\text{s}$ , field of view  $20 \text{ mm}$ .

grain samples all exhibited "local" ignitions. Figure 10 is an example for TC/12 HMX (Table 1) where it took place during the initial rapid flow stage. The initial propagation in frame 42 is very similar to the patterns found on the heat-sensitive film (Figures 6-8). Figure 11 is for type B HMX (Table 1) and contains some interesting extra features. Local ignition occurs during the rapid flow

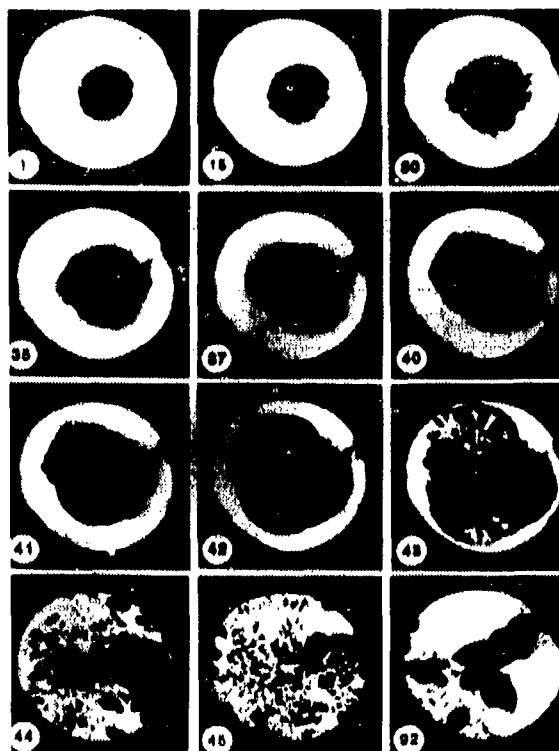


Figure 10. Impact on Fine Grain HMX (TC/12). Local ignition during rapid flow (maximum velocity  $240 \text{ m s}^{-1}$ ), framing interval  $7 \mu\text{s}$ , field of view  $20 \text{ mm}$ .

stage at a group of small sites (three white dots) in frame 48. But these fade and extinguish (frames 48-54). Local ignition at a new site eventually takes over. Enlarged views of frames 48, 49, and 54 are shown in Figure 12. Note that the structure of the main hot spot is reminiscent of the patterns on the HSF. Finally, the banded structure which influences the propagation so strongly in frame 57 also suggests the presence of shear bands in the deforming HMX.

**Explosiveness, Propagation; Dependence on Particle Size.** Damage to the surface of the glass anvils after impact depended on the particle size of HMX used, and only occurred when there was an explosive reaction. The area of damage for coarse HMX was larger than for fine HMX, although there was overlap. The high-speed photographic records also showed that the propagation of reaction was higher in coarser material. This fits in

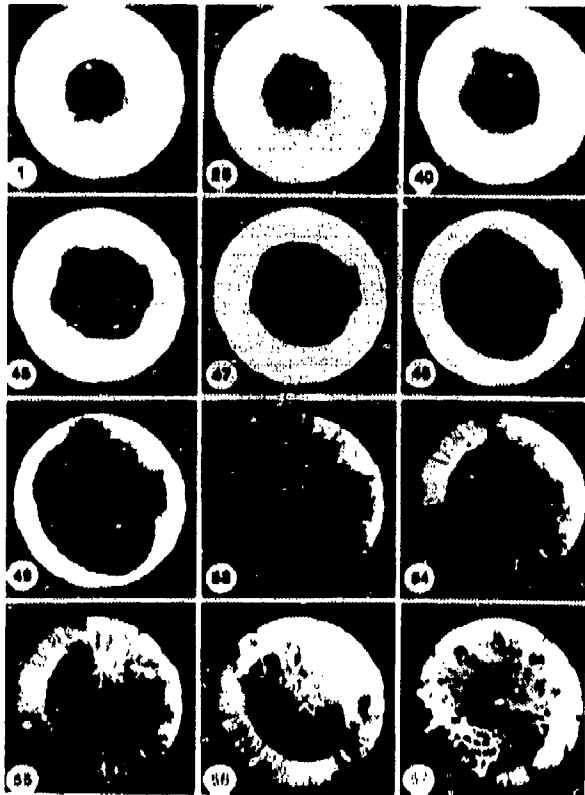


Figure 11. Type B HMX. Maximum velocity of  $185 \text{ m s}^{-1}$ . The first local ignition seen in frame 48 fades. A local ignition which propagates starts in frame 54. Note the banded appearance in frame 57. Framing interval  $7 \mu\text{s}$ , field of view  $20 \text{ mm}$ .

with LABSET data (the AWE test for "explosiveness") on the PBXs that we have tested. The LABSET figure is usually higher if it contains coarser material compared to micronized crystals.

Cross sections of impacted layers which did not ignite show a denser compacted material with fine powders and an open structure with coarser material. The burning front clearly propagates more readily through a compacted layer of coarser material. See, for example, Figure 9 with its "widespread" ignition and propagation. For finer material (see, for example, Figures 10 and 11) there is propagation from "local" sites along a few channels. A second factor which assists more rapid propagation through a compacted layer with larger particles is the higher heat conduction. The more frequent grain boundaries with compacted fine-grain crystals lower

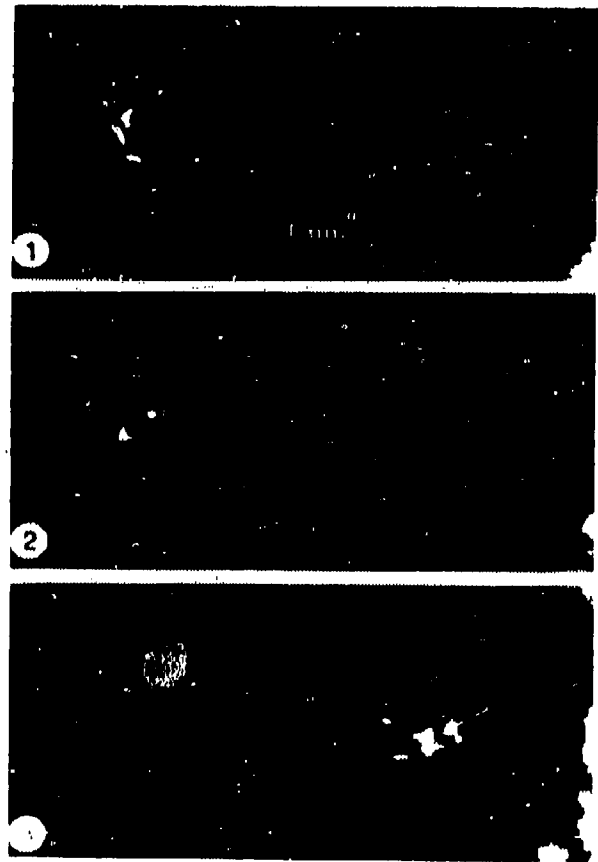


Figure 12. Enlarged View of Frames 48, 49, and 54 of Figure 11. Frame 1 is  $337 \mu\text{s}$  after first contact.

the bulk conductivity. We have measured the thermal conductivity of pressed powdered layers; the value for coarse HMX was twice that of micronized HMX.

#### Quasi-Static Strengths and Strains to Failure of Some PBXs

Samples from five different PBX compositions in the form of discs  $6.35 \text{ mm}$  in diameter by  $2.0 \text{ mm}$  thick (Table 2) were used to measure the quasi-static strengths and strains to failure, at a strain rate of  $10^{-4} \text{ s}^{-1}$ , with the laser speckle technique.

Typically ten samples were tested for each material. There is only space to illustrate one set of data (Figure 13) and to discuss the results briefly.

**Stress Versus Time Plot.** Of the five materials tested, compositions PBX 0298 and

Table 2. Details of PBX Compositions

Composition	Constituent	Weight %	Tensile strength /MPa	Fracture Strain /millistrain
PBX 9501	HMX	95.0	0.78 ± 0.1	3.92
	ESTANE	2.50		
	BDNPA	1.25		
	BDNPF	1.25		
PBX 9502	TATB	95.0	3.23 ± 0.1	2.91
	KEL-F	5.0		
PBX 0298	HMX	97.50	1.06 ± 0.1	11.20
	Kraton	1.125		
	Oil	1.375		
PBX 0407	TATB	69.8	4.12 ± 0.3	3.03
	PETN	25.0		
	KEL-F	5.0		
	Dye	0.20		
PBX 0344	TATB	71.25	4.17 ± 0.4	1.70
	HMX	23.75		
	KEL-F	5.0		

STRESS STRAIN PBX 0344

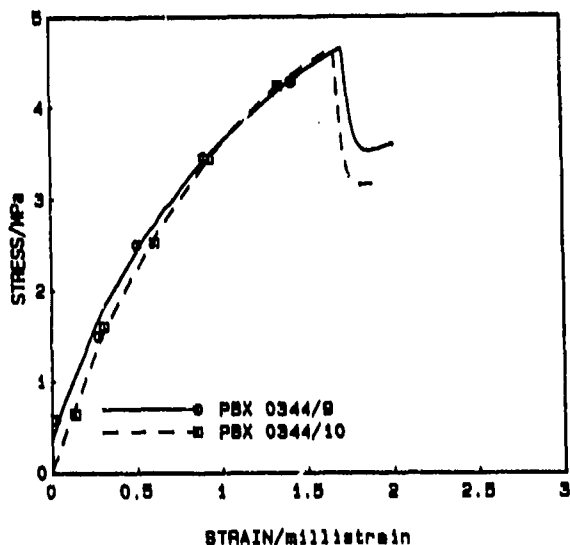


Figure 13. Results for PBX 0344

9501 showed the lowest tensile strengths, failing at a stress of 1 MPa or less. Both materials behaved in a rather ductile manner. However, the strains to failure were very different since PBX 0298 fails at about 1 percent strain, while PBX 9501 failed at less

than half this value. The remaining three materials, PBX 0344, 0407, and 9502, exhibited very similar tensile strengths, particularly 0407 and 0344. The stress-strain curves for these materials (an example is given in Figure 13) show a much more brittle behavior. Although the tensile strengths of 0344 and 0407 are very close, the failure strain of 0344 is significantly smaller than 0407. If the tensile strengths of 0407 and 9502 are compared, together with their compositions, it appears that the replacement of TATB (IHE) by a TATB/PETN mixture, significantly increases the tensile strength of the composite without affecting its strain to failure. Replacing TATB by a TATB/HMX mixture (as in 0344) also increases the tensile strength by a similar amount, although the strain to failure is reduced. This may be due to the HMX component, as this is a weaker and more brittle crystal than PETN, and may be more susceptible to fracture as a result of deformation twinning.<sup>23</sup> Since neither of the two weakest materials contained the KEL-F binder, it is not possible to ascertain the influence of the binder on the mechanical properties of the composites. Consequently, it may be the large volume fractions of HMX, or the replacement binders, that are responsible for the low tensile strengths of 0298 and 9501.

**Fracture Paths.** Figure 14 is an example of a fracture path in PBX 9501. The sample was stressed in the Brazilian geometry (Figure 3). In this case there is little or no evidence of crystal fracture except at the bottom left of the picture. The most striking feature is the amount of interfacial failure with the fracture path predominantly following the boundaries of crystals.

An example of time lapse photography is given in Figure 15 for PBX X-0298 again loaded in the Brazilian test. This sample failed at a load of 1.64 kgf corresponding to a tensile stress of 1.28 MPa at a time of 167 s after start of loading ( $\dot{\epsilon} \approx 10^{-4} \text{ s}^{-1}$ ). The frames were recorded at 8 s intervals. Failure started at three separate sites (arrowed in frame (a)). Note that the upper failure propagated through two crystals while the lower failures propagated along crystal boundaries and through the matrix. By frame (d) a continuous fracture



**Figure 14. The Fracture Path in PBX 9501**

path had developed. The value of the time-lapse photography is that it shows that multiple nucleation sites can be involved and that tears in the binder can initiate interfacial debonding, as well as crystal fracture.

### **ACKNOWLEDGEMENTS**

This work was supported by grants from MOD (Procurement Executive) and the U.S. European Office on contract DAJA45-85-C-0052.

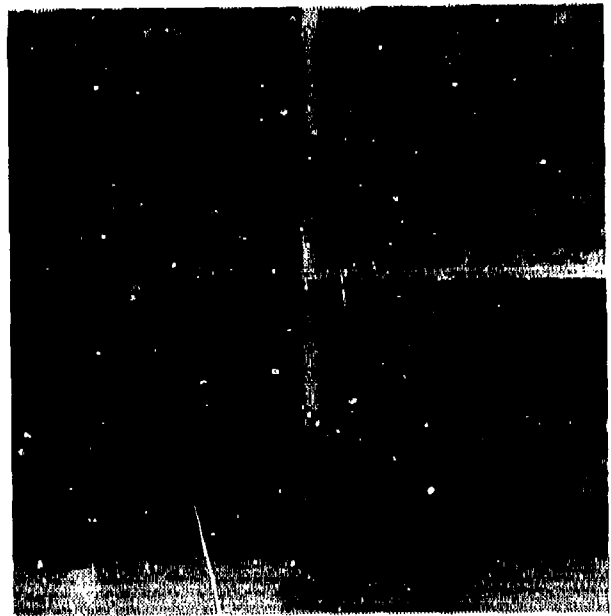


**Figure 15. A Time Lapse Photographic Sequence for PBX X-0298**

### **REFERENCES**

1. Blackwood, J. D. and Bowden, F. P., *Proceedings of the Royal Society of London*, Vol. A 213, 1952, p. 285.
2. Heavens, S. N., PhD Thesis, University of Cambridge, 1973.
3. Heavens, S. N. and Field, J. E., *Proceedings of the Royal Society of London*, Vol. A 338, 1974, p. 77.
4. Swallowe, G. M., PhD Thesis, University of Cambridge, 1979.
5. Swallowe, G. M. and Field, J. E., *Proceedings of the Royal Society of London*, Vol. A 379, 1982, p. 389.
6. Field, J. E.; Swallowe, G. M.; and Heavens, S. N., *Proceedings of the Royal Society of London*, Vol. A 382, 1982, p. 231.
7. Krishna Mohan, V. and Field, J. E., *Combustion and Flame*, Vol. 56, 1984, p. 269.
8. Krishna Mohan, V.; Field, J. E.; and Swallowe, G. M., *Combustion Sci. and Tech.*, Vol. 44, 1984, p. 269.

9. Field, J. E.; Palmer, S. J. P.; Pope, P. H.; Sundarajan, R.; and Swallow, G. M., *Proceedings of the Eighth Symposium (International) on Detonation*, Albuquerque, NM, 1985.
10. Kolsky, H., *Stress Waves in Solids*, Dover, NY, 1963.
11. Gorham, D. A., *Inst. Phys. Conf. Ser.*, Vol. 47, 1979, p. 16.
12. Pope, P. H. and Field, J. E., *J. Phys. E.*, Vol. 17, 1984, p. 817.
13. Awaji, H. and Sato, S., *J. Eng. Mater. and Tech.*, Vol. 101, 1979, p. 140.
14. Johnson, H. D., MH SMP-78-08, Amarillo, TX, 1979.
15. Johnson, H. D., MH SMP-79-26, Amarillo, TX, 1979.
16. Johnson, H. D., MH SMP-81-22, Amarillo, TX, 1981.
17. Chiang, F. P., *Opt. Eng.*, Vol. 21, 1982, p. 379.
18. Ennos, A. E., *Laser Speckle and Related Phenomena*, edited by J. C. Dainty, Springer, Heidelberg, 1975, pp. 203-253.
19. Huntley, J. M., *J. Phys. E.*, Vol. 19, 1986, p. 43.
20. Coffey, C. S. and Jacobs, S. J., *J. Appl. Phys.*, Vol. 52, 1981, p. 6991.
21. Swallowe, G. M.; Field, J. E.; and Horn, L. A., *J. Mater. Sci.*, Vol. 21, 1986, p. 4089.
22. Winter, R. E. and Field, J. E., *Proceedings of the Royal Society of London*, Vol. A 343, 1975, p. 399.
23. Palmer, S. J. P. and Field, J. E., *Proceedings of the Royal Society of London*, Vol. A 383, 1982, p. 399.

# PHYSICAL AND CHEMICAL NATURE OF HOT SPOTS IN TATB AND HMX

J. Sharma, B. C. Beard, J. Forbes, and C. S. Coffey  
Naval Surface Warfare Center  
10801 New Hampshire Avenue  
Silver Spring, Maryland 20903-5000

and

V. M. Boyle  
U.S. Army Ballistic Research Laboratory  
Aberdeen Proving Ground  
Aberdeen, Maryland

*The physical and chemical response of TATB, HMX, and AP to underwater shock, impact, high rate shear, and beam irradiation have been investigated. The initiating stimulus was held to sub-ignition levels to assure the maximum effect without consuming the sample. The products observed were identical to those observed by thermal decomposition and were independent of the extent decomposition. New products in the solid residue of damaged AP and nitramines have been detected. Physical evidence of extinguished hot spots, surrounded by partial decomposition products of increased sensitivity, has been observed in shocked explosives.*

## INTRODUCTION

Our report in the last detonation symposium discussed the initial reaction products observed for several materials.<sup>1</sup> The current report will concentrate specifically on TATB, the nitramines HMX and RDX, and the oxidizer Ammonium Perchlorate, (AP). The driving force of our investigations is a fundamental understanding of the initial chemical and physical response of energetic materials to stimuli leading to sustained detonation.

For this study, TATB, the nitramines HMX and RDX, and the oxidizer AP were driven close to the threshold of ignition by different stimuli such as shock, impact, high rate shear, or irradiation. The recovered samples were analyzed by x-ray photoelectron spectroscopy (XPS), and scanning electron microscopy (SEM). The surface specific chemical information obtained from XPS gives an advantage of at least a thousand compared

to bulk analytical techniques (i.e., chromatography).<sup>1</sup> We attribute much of this advantage to the fact that reactions seem to be localized on the surfaces of the particles where friction and heating are concentrated.

The importance of this work goes well beyond fundamental curiosity. In most cases the reaction products which result from partial decomposition of energetic materials are more sensitive to impact or shock initiation than the parent material.<sup>1</sup> Even though the concentrations of these products are very small ( $10^{-2}$  -  $10^{-3}$  percent)<sup>2</sup> their existence poses a safety hazard. In addition, identification of the first steps of reaction will answer such questions as which bond is the first to break, and whether the first reaction is inter- or intramolecular.

## EXPERIMENTAL

For studying the effects of shock, the aquarium test of Liddiard<sup>3</sup> was used, where a

shock of 4-10 kbars with the duration of a few microseconds was given to the explosive. The surviving samples were recovered and analyzed. For the study of impact, a 10 Kg drop test machine<sup>4</sup> was used, in which the sample was sandwiched between sheets of heat sensitive film. When necessary, the effects of friction are augmented by adding sand to the explosive. The effect of high rate shear was studied by using an actuator, which pushes a plug of polyethylene at a pressure of about 10 kbars through a layer of explosive at 60 m/sec. The effect of irradiation was studied by soft x-ray (15 KV, 12 ma) and pulsed particle beams.

X-ray photoelectron spectroscopic study of the recovered samples was carried out in a Kratos ES-300 instrument described earlier.<sup>1</sup> Fine particulate debris from the recovered samples was mounted on Duco cement then decorated with gold for analysis in an AMR 1000A scanning electron microscope.

## RESULTS

### TATB

As has been reported earlier,<sup>5</sup> the initial reaction products of TATB are furoxan and furazan derivatives of TATB. The physical nature of such decomposition products was determined by SEM. Figure 1 shows the formation of spherical deposits close to the edges of the crystallographic planes of TATB. In many cases, the damage was characterized by small holes ( $\sim 0.5 \times 10^{-6}$  m) in the crystal planes, with products deposited all around. The new products appear as beady deposits on the planar structure of the parent TATB. The interpretation is that a hot spot initiated, but reaction died out prior to consumption of the bulk material. TATB pyrolyzed by beam irradiation showed products with morphological structure (Figure 2) and chemical composition similar to those observed in the shocked or impacted samples.

### Nitramines HMX and RDX

For the first time, reaction products in the solid residue of shocked HMX have been detected. Recent experiments with HMX and RDX have generated samples, subjected to shock



Figure 1. Spherical Deposits of TATB Decomposition Products Located About Quenched Hot Spots



Figure 2. Residue of Pyrolyzed TATB Shows Similar Morphology and Chemistry as the Products Developed in Shocked TATB

and rapid beam heating, that demonstrate the presence of partial decomposition products.

**Underwater Shock.** HMX recovered from underwater shock of 4.1 kbar suffered nitro group loss observed as a decrease in intensity from the nitro peak in the XPS N(1s) spectrum (Figure 3). Nitroso and triazine-like nitrogen chemistries were also observed in the N(1s) XPS spectra of shocked HMX. These chemical states of nitrogen were identified by comparison with N(1s) binding energies obtained from trinitroso RDX and  $\beta$ -Triazine. Nitroso groups appear 1.4 eV above the peak from the amines in HMX while triazine appeared 1.8 eV below this same peak.

Electron microscopic analysis of the shocked HMX demonstrated a significant change in the morphology when compared to the starting pressed pellet (Figure 4). The micrographs of the pressed pellet indicate a large degree of included porosity presumably from residual voids. Following the passage of the shock wave through the material the porosity is lost. The exact mechanism involved in this transformation is uncertain.

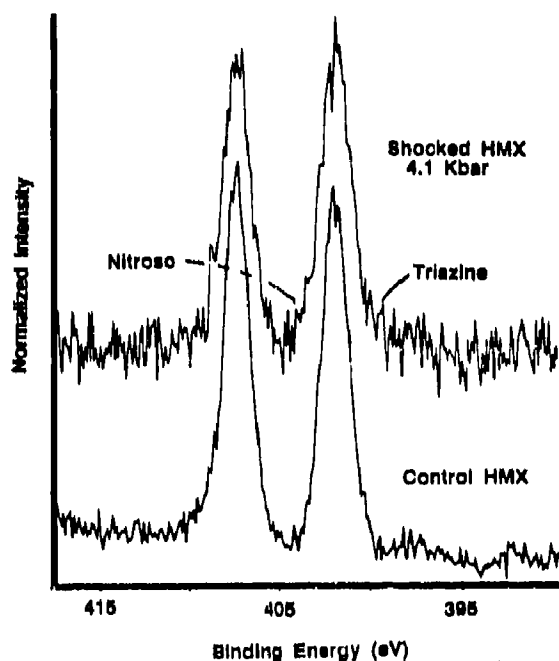


Figure 3. Comparison of N(1s) XPS Spectra from Shocked and Control HMX. Shocked HMX has lost intensity from the nitro peak (407.3 eV) and shows the development of new nitrogen chemistries.

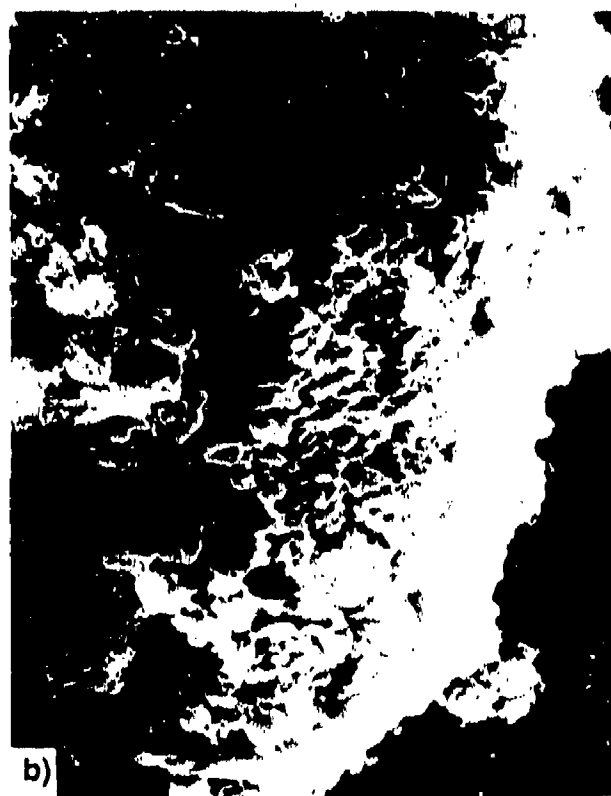
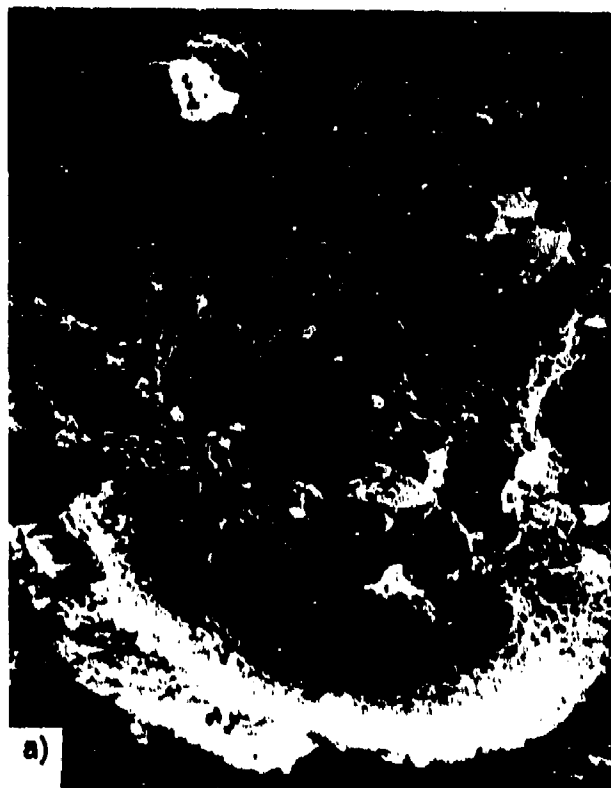


Figure 4. Electron Micrographs of a) Pressed HMX Before Shock, (2000 x); and b) Pressed HMX After 4.1 kbar Underwater Shock, (5000 x).

The relatively long duration of the underwater shock may favor such a transformation while not depositing enough instantaneous energy to initiate detonation.

**Beam Irradiation Pyrolysis.** Rapid heating of HMX by beam irradiation produced a fused mass of material filled with bubbles. The HMX began as pellets which flowed and consolidated during heating without initiating (Figure 5). X-ray diffraction analysis of the pyrolyzed sample indicated that the material had been completely converted to the  $\delta$ -phase.<sup>6</sup> This result indicates that the temperature during irradiation was at least 167-183°C, the temperature of the  $\beta \rightarrow \delta$  phase change.<sup>7</sup> Consolidation of the pellets suggests that the temperature was even higher approaching the melting point of 275°C. The highly porous nature of the resulting material is presumably due to gas generation by decomposition. XPS analysis of these samples



Figure 5. Mass of HMX Resulting From Liquefaction During Beam Heating. Bubbles in the material suggest development of gaseous reaction products.

found significant losses in intensity from the nitro peak and the emergence of intensity attributed to nitrogens in a triazine-like chemical state. The peak for nitroso was not observed in these samples indicating high temperature instability of the nitroso product. Washing the pyrolyzed HMX with water generated a solution which, when dried, left a residue that yielded an XPS N(1s) spectrum comprised almost exclusively of the triazine-like nitrogen. Figure 6 is a comparison of N(1s) spectra from the wash solution residue, the pyrolyzed HMX and control HMX.

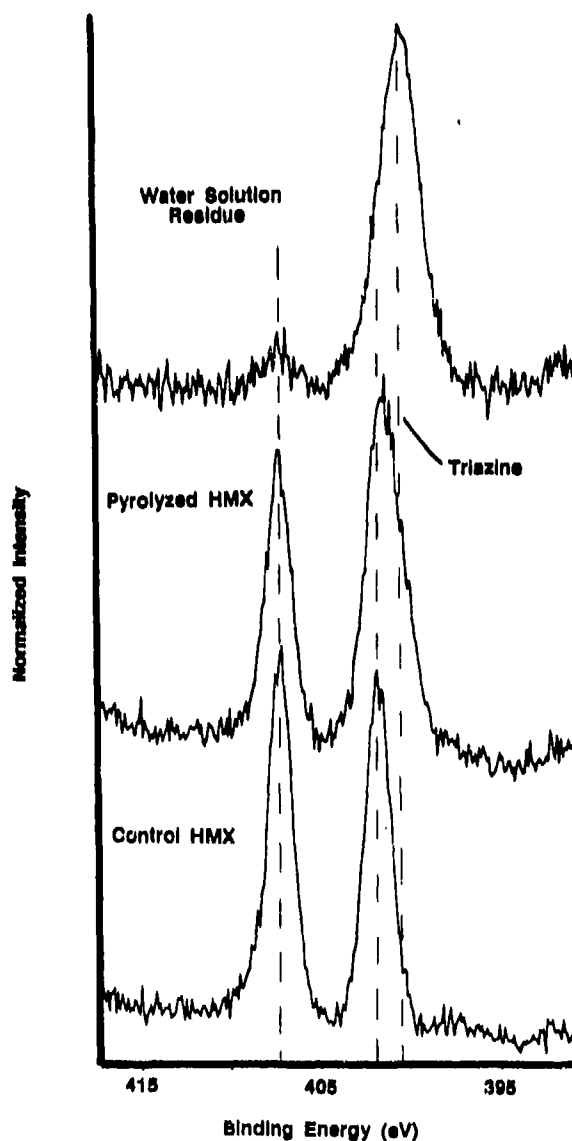


Figure 6. Comparison of N(1s) XPS Spectra From Control, Pyrolyzed, and Water Wash Solution Residue, HMX Samples

Recent studies of the degradation of RDX under soft x-ray irradiation in the XPS instrument have provided new insights into the initial reactions of nitramines. Slow radiation degradation by the XPS x-ray source is a controllable method for damaging a material while continuously monitoring its chemistry. Data collected at room temperature demonstrate the slow development of the same nitroso and triazine products as in the shock, impact, and pyrolyzed samples. By cooling the RDX to  $-50^{\circ}\text{C}$  during irradiation, additional products are observed. Shown in Figure 7 are the N(1s) peak positions from low and room temperature x-ray damaged RDX samples, compared with standards. The detection of the nitrite ester is a new discovery that suggests several reaction steps in the initial decomposition of nitramines. Upon warming, the nitrite ester and some nitroso and triazine-like nitrogen XPS peak intensity is lost, demonstrating the intermediate role of these products under combustion or explosion conditions.

**High Rate Shear.** Most of the reaction was observed on the surface that was created by the plug and was found not to penetrate the

bulk explosive. In Composition B, surface loss of TNT was evident; however, where Composition B was impacted with a steel plate, it caused preferential decomposition of RDX, giving triazine-like products, as discussed above.

### Ammonium Perchlorate

Studies of the initial reactions of AP in response to shock have recently begun in our laboratory. The application of XPS to the study of AP has great advantage due to the large shift in binding energy between all of the oxychloride anions, ( $\text{ClO}_x$ ,  $x = 0 - 4$ ). Previously reported results demonstrated the effect of impact on AP,<sup>1</sup> tentatively identifying the products as chlorite, hypochlorite, and chloride. Compilation of reference spectra from the alkali salt of each oxychloride available provided support to definitively identify the decomposition products. These Cl(2p) XPS spectra clearly demonstrate the shift between each of the oxychloride anions. Using the standard spectra for comparison, the product peaks developed are attributed to hypochlorite, and chloride. Figure 8 shows the Cl(2p) XPS binding energy position from

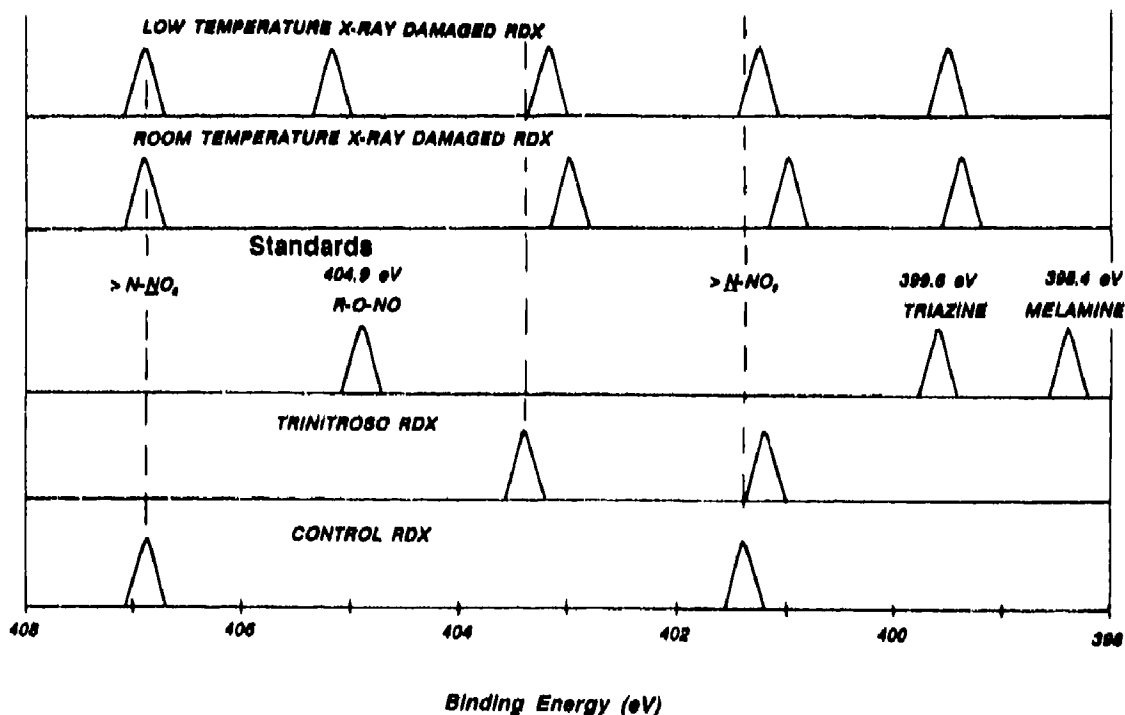


Figure 7. XPS N(1s) Peak Position of the Products Formed by X-ray Radiation Damaged in RDX Compared With Standards

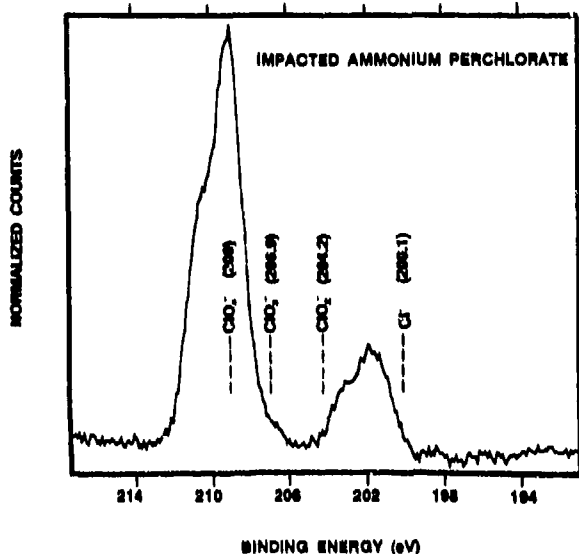


Figure 8. Composite Figure Demonstrating the Cl(2p) Binding Energy Positions of Four Oxychloride Anion Salts Superposed on a Spectrum from Impacted AP

perchlorate, chlorate, chlorite, and chloride chemical states of chlorine compared with a spectrum from impacted AP. The observation of the hypo-chlorite product is very confusing as this compound is not known. At this time, we do not offer a mechanism for the formation or stabilization of this material. If the hypo-chlorite is indeed the major product, its instability is of great concern with regard for the safety of damaged AP.

Data currently in hand demonstrate that the hypochlorite product formation is greatly reduced in the case of high temperature decomposition of AP. This result supports the notion of instability of the hypochlorite salt while indicating chloride as the favored high temperature product.

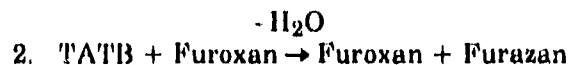
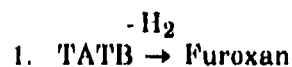
## DISCUSSION

The results presented for the response of TATB to shock or impact demonstrate that the reaction begins at microscopic sites. Observation of these initial reaction sites is highly encouraging for the application of similar experiments to other energetic

molecules. The size of these sites ranges from tenths to tens of microns, agreeing with the suggestion of Bowden and Yoffe.<sup>8</sup> The location of the reaction centers at the exterior of the crystalline planes of shocked TATB suggests that the accumulation of crystalline defects involving dislocations and molecular disruptions at the plane edges may lead to the initiation of reaction. Impact initiation favors interparticle friction developed as the material rapidly flows away from the high pressure of the striker.

The size of the reaction sites and the extent of decomposition have been found to be governed by the nature of the stimulus. For example, more extensive decomposition is observed when the effects of impact are augmented by friction from added particles of sand. Extensive damage to the planes themselves was also evident, indicating that the shock induced compression and friction were concentrated at the exposed crystal planes of the particle.

Furoxans and furazans have been identified as the product species that develop around the reaction site. Furoxans are the result of the first endothermic step and furazans are created by the exothermic release of a water molecule from TATB, providing energy to propagate the reaction. The trend indicated by our data is that the furoxan product is always present at low concentrations. The concentration of the furazan, however, increases as damage becomes more severe. The furoxan product, therefore, appears to be an intermediate which reacts further to produce furazan. It is suggested that furoxan actually promotes the formation of furazan by reaction with TATB to form furazan and another molecule of furoxan. The reaction steps could be summarized as:



The result of such a reaction scheme would be the consumption of TATB with the formation of the stable partial decomposition product furazan. Furoxan concentration levels would

remain small and essentially constant until all TATB is reacted.

Furoxans are far more sensitive than TATB having a drop height comparable to that of TNT.<sup>9</sup> (Amino dinitrofuroxan has a drop weight impact sensitivity of 56 cm; TNT sensitivity is 54 cm, compared to 185 cm for TATB.) The presence of furoxan compounds in a quenched hot spot creates a site for sensitization of the TATB, due to its inherent sensitivity and physical proximity to the defect site. We have chosen to refer to such sites as "sensitization centers."<sup>10</sup>

For the first time, condensed phase partial decomposition products from the nitramines HMX and RDX have been detected. The predominant products observed in the N(1s) XPS spectrum from underwater shocked HMX were a nitroso compound and triazine compound. Nitroso compounds are well-known products in the decomposition of nitramines,<sup>11</sup> and are stable under typical ambient conditions. Triazine is known to be highly susceptible to hydrolysis. The observed triazine-like product, however, is water stable as indicated by its recovery from water solution. The stability of the product molecule to water indicates that the triazine nitrogen is somehow stabilized. Certainly the product molecule has enhanced water solubility relative to HMX as indicated by the relative concentration of the products observed by XPS from the water solution residue.

Unlike the results from the shocked TATB, shocked HMX does not show the existence of reaction centers. Probably the unique layered structure of TATB facilitated the observation of new products. Changes of the pressed HMX powder did occur; however, these were limited to the removal of included porosity left from pressing. Transformation of the HMX from  $\beta$  to  $\delta$  phase has been found to occur readily in the presence of RDX.<sup>6</sup> The HMX pressed into pellets for the beam experiments was of a production grade and therefore contained traces of RDX which would favor the  $\beta \rightarrow \delta$  transformation.

The low temperature radiation damage of RDX has detected for the first time the presence of a nitrite ester intermediate. The

anticipated mechanism for the formation of this intermediate is by the rearrangement of the  $-N-NO_2$  to  $-N-O-NO$ . Quantum chemical calculations of this rearrangement have shown it to be a lower energy pathway in the decomposition of nitromethane.<sup>12</sup> Evidence for the existence of this intermediate was first observed by Wodtke et al. in molecular beam experiments, again with nitromethane.<sup>13</sup> Loss of the nitrite ester upon warming the damaged sample to room temperature is not a surprise based on the bond energies and free energies of reaction involved. Nitrite ester would decompose via  $-N-O-NO \rightarrow >N-O + NO$ . The surprising result observed from warming the low temperature damaged sample to room temperature was the loss of significant intensity from the peaks attributed to nitroso and triazine nitrogen chemistries. Further warming of damaged nitramine, as in the case of the pyrolyzed HMX, produced a sample demonstrating the presence of little if any nitroso. These results provide very interesting information about the solid state reactions and relative stability of partial decomposition products that occur during the evolution of gaseous products (i.e., NO).

It has been a general observation for the materials studied to date that under all forms of stimulation the same products appeared no matter what the extent of decomposition observed. Therefore, the same reactions are in play during the onset of decomposition as at the exhaustion of the parent material. The condensed phase products observed then are truly stable intermediates representing early stages of the decomposition mechanism. Our method of examination has the advantage of observing such products, in that those molecules that completely decompose lead to the formation of small gaseous products which cannot be seen by XPS, (unless somehow trapped in the lattice).

An important question concerning the effects of different stimuli on materials is how do the products formed compare with those from slow thermal decomposition. Our results, so far, indicate that the principal products are similar to those of thermal decomposition, although minor reaction products are not observed. This is not

surprising, because the amount of decomposition seen is not very large and so to date only the principal products have been identified.

## SUMMARY

The damage inflicted by various stimuli on energetic materials manifests itself in chemical and physical changes. The physical changes are dependent upon the physical properties of the materials themselves, (i.e., melting point, crystallinity). Chemical changes are always toward a more reduced product molecule, reflecting the redox nature of the reactions involved in energetic materials consumption. Typically, at least one of the partial decomposition products is more sensitive than the parent molecule. Clear examples can be listed from the materials discussed above: furoxans from TATB, nitrite esters in nitramines, and hypochlorite in AP. The observed decrease in stability of these products may stem solely from their chemistry or be aggravated by the physical structure in which they are produced, (e.g., holes at the plane edges of TATB).

## ACKNOWLEDGEMENTS

The authors are thankful to Dr. M. Norr for the SEM micrographs. This work was carried out under support from the Independent Research Program at NSWC.

## REFERENCES

1. Sharma, J.; Hoffsommer, J. C.; Glover, D. J.; Coffey, C. S.; Forbes, J. W.; Liddiard, T. P.; Elban, W. L.; and Santiago, F., "Sub-Ignition Reactions at Molecular Levels in Explosives Subjected to Impact and Underwater Shock," *Proceedings of the Eighth International Detonation Symposium*, Albuquerque, NM, 15-19 Jul 1985, p. 725.
2. Fox, P. G. and Soria-Ruiz, J., "Fracture-Induced Thermal Decomposition in Brittle Crystalline Solids," *Proc. Roy. Soc. Lond.*, Vol. A, 317, 1970, p. 79.
3. Liddiard, T. P., *Proceedings of the Fourth (International) Detonation Symposium*, Naval Ordnance Laboratory, White Oak, MD, U.S. Government Printing Office, Washington, D.C., 1965, p. 487.
4. Coffey, C. S. and Jacobs, S. J., *J. Appl. Phys.*, Vol. 52, 1981, p. 6991.
5. Sharma, J.; Hoffsommer, J. C.; Glover, D. J.; Coffey, C. S.; Santiago, F.; Stolovy, A.; and Yasuda, S., *Shock Waves in Condensed Matter—1983*, J. R. Asay, R. A. Graham, G. K. Straub, Eds, Elsevier Science Publishers B.V., 1984, p. 543.
6. Cady, H. H. and Smith, L. C., *Studies of the Polymorphs of HMX*, LAMS-2652, Los Alamos Scientific Laboratory, Los Alamos, NM, 3 May 1962.
7. Meyer, R., *Explosives*, Second Edition, Verlag Chemie, Deerfield Beach, FL, 1981, p. 249.
8. Bowden, F. P. and Yoffe, A. D., *Initiation and Growth of Explosions in Liquids and Solids*, Cambridge University Press, Cambridge, 1952.
9. Hollins, R., NWC, China Lake, private communication.
10. Sharma, J.; Forbes, J. W.; Coffey, C. S.; and Liddiard, T. P., "The Physical and Chemical Nature of Sensitization Centers Left from Hot Spots Caused in Triamino-trinitrobenzene by Shock or Impact," *J. Phys. Chem.*, Vol. 91, 1987, p. 5139.
11. Hoffsommer, J. C.; Glover, D. J.; and Elban, W. L., "Quantitative Evidence for Nitroso Compound Formation in Drop-Weight Impacted RDX Crystals," *J. Energet. Mat.*, Vol. 3, 1985, p. 149.
12. Dewar, J. S.; Ritchie, J. P.; and Alster, J., "Thermolysis of Molecules Containing NO<sub>2</sub> Groups," *J. Org. Chem.*, Vol. 50, 1985, p. 1031.
13. Wodtke, A. M.; Hints, E. J.; and Lee, Y. T., "The Observation of CH<sub>3</sub>O in the Collision Free Multiphoton Dissociation of CH<sub>3</sub>NO<sub>2</sub>," *J. Chem. Phys.*, Vol. 84, No. 2, 1986, p. 1044.

## **DISCUSSION**

**PER-ANDERS PERSSON**  
CETR/New Mexico Tech  
Socorro, NM

Where on the samples were these electron micrographs taken?

### **REPLY BY BRUCE C. BEARD**

SEM micrographs are shown for both impacted and shocked TATB. The material used for the micrographs were recovered from

the damaged sample. Mounting was performed by sprinkling the material onto a Duco cement covered microscope stub. There was no attempt to maintain any account of the position of specific particles; the samples were powders that were completely randomized during recovery. The mounted particles were decorated with gold at a very slow rate to eliminate any possible heating effects. Areas of imaging were chosen at random; however, the greatest effect of the shock or impact appeared at the edges of crystallographic planes.

# HOT SPOT FORMATION IN A COLLAPSING VOID OF CONDENSED-PHASE, ENERGETIC MATERIAL

P. B. Butler and J. Kang  
The University of Iowa  
Iowa City, Iowa 52240

and

M. R. Baer  
Fluid and Thermal Sciences Department  
Sandia National Laboratories  
Albuquerque, New Mexico 87185

*In this work a hollow-sphere configuration is used in modeling the dynamics of hot spot formation in porous, condensed-phase, reactive materials. In addition to treating the mechanics of pore motion, thermal processes such as viscoplastic heating, finite-rate chemical effects, and heat exchange between the pore gas and surrounding material are evaluated. The analysis considers chemical decomposition at the pore interface and in the gas phase. Two proposed reaction mechanisms are used to investigate the role of gas-phase chemistry on hot spot growth in RDX. In preliminary calculations, the gas-phase chemistry is modeled using a finite-rate, single-step process. Following a discussion of the preliminary results, the simple gas-phase chemistry is replaced with a more detailed reaction scheme involving 167 elementary reactions and 43 chemical species. Both studies incorporate a real gas version of the CHEMKIN chemical kinetics package to assemble the gas-phase thermodynamic properties and chemical production rates.*

## INTRODUCTION

The work discussed here addresses the issue of hot spot initiation in porous, energetic materials. Carroll and Holt's original pore collapse formulation<sup>1-4</sup> is extended in this work to model the dynamic behavior of a hollow sphere subjected to an externally applied hydrostatic stress. The hollow sphere model is used to simulate a void present in a field of condensed-phase, reactive material. In addition to treating pore dynamics, the hot spot model includes energy balances for the pore gas and surrounding material. Important thermal processes such as viscoplastic heating, finite-rate chemical effects, and heat exchange between the pore gas and surrounding material are evaluated.

In brief, the dynamic pore collapse analysis described in Reference 1 is extended in the present study to include condensed-phase material viscosity and pore gas pressure in the integrated form of the radial momentum equation. In addition, first law analyses for the condensed-phase material and pore gas are introduced in order to track temporal variations of interface and gas temperatures. Material decomposition at the pore interface is also considered, whereby a portion of the condensed-phase material reacts exothermically at the interface, and the remainder of mass flux into the pore is through equilibrium vaporization. In some instances, gaseous species generated at the interface further contribute to the net energy

release by undergoing exothermic, gas-phase reactions.

A principal objective of this work is to study the role of gas-phase chemistry on hot spot formation. Two different gas-phase reaction mechanisms are investigated here. In the preliminary calculations performed in Part I, the gas-phase chemistry is modeled using a finite-rate, single-step process.<sup>5</sup> In Part II, the simple gas-phase chemistry is replaced with a more detailed reaction scheme<sup>6</sup> involving 167 elementary reactions and 43 chemical species. Both Parts I and II incorporate a real gas version of the CHEMKIN chemical kinetics package<sup>7-8</sup> to assemble the gas-phase thermodynamic properties and chemical production rates.

## HOT SPOT MODEL

Figure 1 shows a hollow sphere of condensed-phase, energetic material. This simple configuration is used to model the dynamic and thermodynamic interactions between a material void and its immediate surroundings when a constant hydrostatic stress,  $P_\infty$ , is exerted on the system. The pore has an initial radius,  $a_0$ , and contains a nonreactive gas mixture at initial pressure,  $P_{g0}$ , and temperature,  $T_{g0}$ . Initially, the incompressible solid material surrounding the

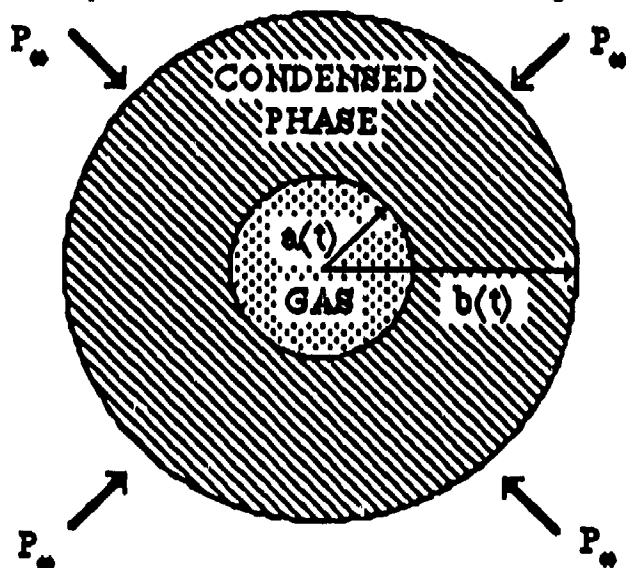


Figure 1. Illustration of Hollow-Sphere Configuration Used to Model Hot Spot Formation in Porous, Energetic Material (RDX)

void has uniform temperature and is in thermal equilibrium with the pore gas ( $T_{s0} = T_{g0}$ ).

The initial external radius of the sphere  $b_0$  together with  $a_0$  prescribe the initial sphere porosity:

$$\phi_0 = \frac{V_{g0}}{V_{g0} + V_{s0}} = a_0^3/b_0^3 \quad (1)$$

In Equation (1),  $V_{g0}$  represents the initial pore volume and  $V_{s0}$  is the volume occupied by the solid. Following the earlier work of Carroll et al.,<sup>1-3</sup> the initial pore radius and sphere porosity are taken to be descriptive of the average pore size and porosity of a much larger material sample.

Although the hollow-sphere hot spot formulation treats just one pore and its immediate surroundings, it can easily be extended to analyze pore-pore interactions in a matrix of pores. In the latter configuration, the quantity  $2(b_0 - a_0)$  represents the approximate distance between adjacent pores when the material is in the relaxed state.

## GOVERNING EQUATIONS

### Pore Radial Motion

Formulation of the governing equations for this model begins with an expression for conservation of radial momentum for the one-dimensional pore geometry shown in Figure 1. Here it is assumed the gas-phase thermodynamic properties are time-varying and spatially uniform within the pore. It is further assumed the solid density,  $\rho_s$ , and material viscosity,  $\mu_s$ , are constant. Under these conditions, the radial motion of a spherically symmetric pore in an incompressible, viscous medium with internal pore pressure can be expressed as:<sup>1</sup>

$$\rho_s a \dot{a} C_1 + \frac{3}{2} \rho_s \dot{a}^2 C_2 = -P_t - 4\mu_s \frac{\dot{a}}{a} (1 - \phi) \quad (2)$$

where

$$P_t = P_\infty - P_g + \text{sign}(\dot{a})\beta_s, \quad (3a)$$

$$C_1 = 1 - \phi^{1/3}, \quad (3b)$$

and

$$C_2 = 1 - \left( \frac{4-\phi}{3} \right) \phi^{1/3}. \quad (3c)$$

The porosity-dependent variables,  $C_1$  and  $C_2$ , appearing in Equation (2) result from the finite-volume assumption ( $b_0 \neq \infty$ ,  $\phi_0 \neq 0$ ). For the ideal configuration of a pore in an infinite medium ( $b_0 = \infty$ ,  $\phi_0 = 0$ ),  $C_1 = C_2 = 1$  and Equation (2) reduces to a form of the Rayleigh bubble equation.<sup>9</sup>

In the equation of motion, (Equation (2)), the term  $P_\infty$  represents the hydrostatic stress applied at the external radius of the sphere ( $r = b$ ),  $P_g$  is the instantaneous gas pressure in the pore, and  $\beta_s$  is the deviatoric component of stress. For the conditions considered in this work,  $\beta_s$  is expressed for a material undergoing plastic deformation<sup>1</sup> with a yield stress  $Y$ :

$$\beta_s = \frac{2}{3} Y \ln(1/\phi). \quad (4)$$

The contribution  $\beta_s$  has on interface motion depends on its magnitude and the sign of  $\dot{a}$ . For example, during pore collapse  $P_\infty$  can be considered an inward driving potential that is resisted by the combination of stresses  $P_g + \beta_s$ . Under conditions of pore expansion, however,  $P_g$  acts as an outward driving potential and  $P_\infty$  and  $\beta_s$  resist the motion.

### Energy - Condensed Phase

An important aspect of this modeling effort is the treatment of transport phenomena at the pore/solid interface. In order to properly address these issues, the thermal field in the solid material must be examined. More specifically, an evaluation of the temporal variation of interface temperature is required.

In general, an expression for energy conservation in the solid material surrounding the pore can be written as:

$$\frac{DT_s}{Dt} = \frac{\alpha}{r} \frac{\partial^2(rT_s)}{\partial r^2} + \frac{2}{\rho_s C_s} \left[ 6\mu_s \frac{\dot{a}^2 a^4}{r^6} + Y \frac{|\dot{a}| a^2}{r^3} \right]. \quad (5)$$

The three terms on the right-hand side of the equation represent energy contributions due to heat conduction in the radial direction, viscous dissipation, and plastic work, respectively. It is apparent from the form of Equation (5) that both the viscous and plastic work contributions to condensed-phase heating decay rapidly for  $r > a$ . In addition, it should be noted the plastic work term in the energy equation is written here with the absolute value of interface velocity  $|\dot{a}|$  in order to model plastic work during pore collapse ( $\dot{a} > 0$ ) and expansion ( $\dot{a} < 0$ ).

Rather than solve the complete thermal field over the domain  $a \leq r \leq b$ , an approximate solution for the interface temperature,  $T_i$ , can be developed by applying an integral approximation to the energy balance. This technique simplifies the problem at hand by reducing the energy equation from its partial differential equation form, to an ordinary differential equation for  $T_i$ . Correctly tracking the interface temperature is important to this modeling effort since  $T_i$  governs the transport of mass and energy across the pore boundary.

Consistent with the classical integral approximation method for a hollow sphere with time-varying heat flux at  $r = a$ , the following functional form of the thermal profile in the solid phase is assumed:

$$T_s(r,t) - T_\infty = \left[ T_i - T_\infty + \frac{2atQ}{C_3 a} \right] \exp\left(-\frac{(r-a)^2}{4at}\right) - \frac{2atQ}{C_3 a} \exp\left(-C_3 \frac{r^2 - a^2}{4at}\right). \quad (6)$$

Equation (6) is a reasonable candidate for the thermal profile since it exhibits the exponential-type behavior that is characteristic of many spherical conduction solutions.<sup>10</sup> Also, Equation (6) satisfies the proper initial and boundary conditions:  $T(r,0) = T_\infty$ , for  $a \leq r \leq \infty$ ;  $T(a,t) = T_i$  and  $\partial T/\partial r(a,t) = Q$ , for  $t > 0$ ;  $T(\infty,t) = T_\infty$  and  $\partial T/\partial r(\infty,t) = 0$  for  $t > 0$ . The term  $C_3$  is a pure constant that is included in the thermal profile (6) to correct for the time-varying heat flux at  $r = a$ .

Given the differential form of the energy balance (5) and an assumed form of the thermal profile (6), a differential expression for  $T_1$  can be developed by performing Leibnitz's rule,

$$\frac{d}{dt} \int_{r_1(t)}^{r_2(t)} f(r,t) dr = \int_{r_1(t)}^{r_2(t)} \frac{\partial f}{\partial t} dr + \left( f(r_2,t) \frac{dr_2}{dt} - f(r_1,t) \frac{dr_1}{dt} \right), \quad (7)$$

with

$$f(r,t) = r(T_g(r,t) - T_\infty). \quad (8)$$

The integration in Equation (7) is evaluated over the limits  $r_1 = a$  to  $r_2 = b$ . In practice, the upper limit ( $r_2 = b$ ) can be replaced with  $r_2 = \infty$  since the thermal layer diffusing into the solid from the pore interface typically has a thickness much less than  $b$ . The physical significance of this substitution is that the hot spots are thermally isolated from their nearest neighbors during the preheat period.

### Interface Boundary Conditions

The energy boundary condition at the solid/gas interface is given as:

$$-k_s \left( \frac{\partial T}{\partial r} \right)_{r=a} = \dot{q}_g - \dot{m}_s q_{s1}. \quad (9)$$

In Equation (9) the term  $q_g$  represents the effective heat exchange with the pore gas:

$$\dot{q}_g = \frac{k}{a} (T_g - T_1) + \epsilon_g \sigma (T_g^4 - T_1^4). \quad (10)$$

Also appearing in Equation (9) is the product of effective heat release,  $q_w$ , and the surface mass flux,  $\dot{m}_s$ . The term  $q_w$  combines thermal contributions from two processes, exothermic surface reaction,  $q_c$ , and the latent heat of phase change,  $L$ . The effective heat release is:

$$q_w = LG - (1-G)q_c. \quad (11)$$

In Equation (11), the quantity  $G$  represents the mass flux fraction of energetic material entering the vapor phase from the

condensed phase.<sup>5</sup> Consequently, the quantity  $(1-G)$  is the mass flux fraction that reacts exothermically at the surface to produce product gases. A value of  $G = 0$  implies complete condensed-phase decomposition, whereas,  $G = 1$  implies complete vaporization at the surface. In a study on nitramine deflagration waves, Mitani and Williams<sup>6</sup> report  $G \approx 0.70$  for HMX ( $C_4H_8N_8O_8$ ) over the range  $0.01 < P_g(\text{MPa}) < 100$ . Melius<sup>6</sup> has indicated that  $G \approx 0.90$  is more characteristic of RDX ( $C_3H_6N_6O_6$ ) deflagration waves.

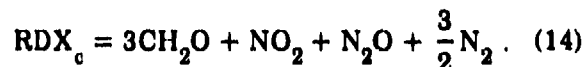
An approximation to the instantaneous mass flux at  $r = a$  is obtained through an activation energy asymptotic solution for steady state deflagration waves.<sup>5</sup> The resulting expression used in this model is:

$$\dot{m}_s = \sqrt{\frac{p_g \lambda_s T_1}{q_c \delta} \left\{ \frac{RT_1}{E_s} \right\} \frac{A_s \exp(-E_s/RT_1)}{[\delta(1-G) + (1-\delta)\ln(1/G)]}}. \quad (12)$$

In Equation (12), the term  $\delta$  represents a nondimensional heat release in the condensed phase:

$$\delta = q_c / \int_{T_0}^{T_s} C_s dT. \quad (13)$$

In both Parts I and II of this work, it is assumed the condensed-phase nitramine surface reaction is irreversible and produces four product species ( $CH_2O$ ,  $NO_2$ ,  $N_2O$ , and  $N_2$ ). For decomposition of condensed-phase RDX ( $RDX_c$ ), the chemically balanced reaction is thus:



Equation (14) has a heat release of  $Q_c = 360$  cal/gm (1.51 MJ/kg), a reaction rate pre-exponent of  $A_s = 5 \times 10^{15} \text{ s}^{-1}$ , and activation energy of  $E_s = 46.1$  kcal/mole (193 MJ/mole).

### Continuity - Gas Phase

As stated previously, the gas mixture contained within the pore is assumed to have time-varying, but spatially uniform thermodynamic properties. Thus, the time rate of

change of gas density for the spherical void with surface mass flux and nonconstant volume is:

$$\frac{d\rho_g}{dt} = -\frac{3\rho_g \dot{a}}{a} + \frac{3\dot{m}_s}{a} \quad (15)$$

The first term on the right hand side of Equation (15) treats density variations due to pore volume changes, whereas the second term reflects the increase in gas density due to surface mass flux.

### Energy - Gas Phase

From classical thermodynamics, the energy balance for a spatially uniform reactive gas mixture takes the form:

$$\rho_g C_{vg} \frac{dT_g}{dt} = -\sum (u_k \dot{\omega}_k) - \frac{3}{a} P_g \dot{a} + \frac{3}{a} \dot{q}_g + \frac{3}{a} \left[ \dot{m}_s \sum Y_{ks} \{h_k(T_s) - u_k(T_g)\} \right] \quad (16)$$

Equation (16) is written specifically for a spherical system with nonconstant volume and energy/mass flux at the surface. Under the same constraints, species conservation within the spherical pore yields the equation:

$$\rho_g \frac{dY_k}{dt} = W_k \dot{\omega}_k + \frac{3}{a} \dot{m}_{sk} (Y_{ks} - Y_k) \quad (17)$$

In Equations (16) and (17),  $W_k$  is molecular weight and  $\dot{\omega}_k$  is the molar production rate of the  $k$ -th species in the gas. Also,  $Y_{ks}$  represents the mass fraction of the  $k$ -th species created at the interface:

$$Y_{ks} = \dot{m}_{sk} / \dot{m}_s \quad (18)$$

### Equation Of State

For both Parts I and II of this work a constant-covolume equation of state<sup>8</sup> was used:

$$P_g = \frac{\rho_g RT_g}{1 - \eta \rho_g} \quad (19)$$

In the limit of low gas density, Equation (19) approaches perfect gas behavior, whereas at highly compressed states the covolume correction term  $(1 - \eta \rho_g)$  corrects for nonideal thermodynamic states.

## GAS-PHASE KINETICS

### Part I - Single Reaction

In Part I of this work, it is assumed the nitramine present in the vapor phase ( $RDX_g$ ) undergoes a single, finite-rate, gas-phase reaction. The product gas is assumed to have the same composition as the final product of a constant-volume explosion of  $RDX_g$  (i.e., major species:  $N_2$ ,  $CO$ ,  $CO_2$ ,  $H_2$ ,  $H_2O$ ,  $H$ ,  $OH$ ,  $O$ ,  $O_2$ ,  $NO$ ). Also, the gas-phase reaction for Part I proceeds irreversibly and has a molar production rate given by:

$$\dot{\omega}_{RDX-g} = -\frac{1}{W_k} P_g^n A_g \exp(-E_g/RT_g) \quad (20)$$

The coefficients (i.e.,  $A_g$ ,  $E_g$ ,  $n$ ) appearing in Equation (20) are based on estimates developed in a previous study of steady-state nitramine deflagration at pressures up to 100 MPa.<sup>5</sup>

### Part II - Multiple Reactions

For Part II of this work, the decomposition of gas-phase RDX is modeled using a set of 167 elementary reactions involving 43 chemical species.<sup>6-7</sup> Table 1 presents a list of the gaseous species considered in this work, including intermediate species. Some of the CHNO species appearing in Table 1 are given abbreviations in parentheses. For example,  $RDXR$  represents  $C_3H_8N_5O_4$ , the radical formed when a nitro group is removed from RDX.

The decomposition of  $RDX_c$  was modeled by Equation (14). This is the same as the condensed-phase reaction law used in Part I. However, in Part II the four species produced by the surface reaction ( $CH_2O$ ,  $N_2O$ ,  $NO_2$ ,  $N_2$ ) were allowed to react with other species present in the pore.

Table 1. List of Species: Part II

C <sub>3</sub> H <sub>6</sub> N <sub>6</sub> O <sub>6</sub> (RDX)	H	CO <sub>2</sub>	H <sub>2</sub> CNH
C <sub>3</sub> H <sub>6</sub> N <sub>5</sub> O <sub>4</sub> (RDXR)	O	CO	H <sub>2</sub> CNO
C <sub>3</sub> H <sub>6</sub> N <sub>5</sub> O <sub>4</sub> (RDXRO)	N	HCNO	H <sub>2</sub> CNNO <sub>2</sub>
C <sub>3</sub> H <sub>6</sub> N <sub>6</sub> O <sub>5</sub> (MRDX)	H <sub>2</sub> O	HOCN	H <sub>2</sub> CNCH <sub>2</sub>
C <sub>3</sub> H <sub>6</sub> N <sub>5</sub> O <sub>3</sub> (MRDXR)	OH	NNH	H <sub>2</sub> CNNO
C <sub>3</sub> H <sub>7</sub> N <sub>5</sub> O <sub>4</sub> (RDXH)	HO <sub>2</sub>	CNO	H <sub>2</sub> CN
C <sub>3</sub> H <sub>7</sub> N <sub>4</sub> O <sub>2</sub> (RDXHR)	NO <sub>2</sub>	N <sub>2</sub> O	C <sub>2</sub> N <sub>2</sub>
CH <sub>2</sub> O	NO	HNO	HONO
H <sub>2</sub>	NH	NH <sub>2</sub>	NH <sub>3</sub>
O <sub>2</sub>	CN	HCN	HCO
N <sub>2</sub>	NCO	HNCO	

## RESULTS

### Part I - Single Reaction

Input parameters and initial conditions for a series of test cases are presented in Table 2. In all cases, the energetic material surrounding the pore was the nitramine explosive RDX. Two initial porosities (0.05, 0.10) and a range of applied external stresses were examined. The applied stress at  $r = b$  was a constant with  $P = P_{\infty}$  for all time. For consistency with the results presented in Part II, the chemical kinetics FORTRAN package CHEMKIN<sup>7-8</sup> was used to assemble the thermodynamic properties and molar production rates of all gaseous species.

Figures 2-5 show some of the trends predicted by the version of the hot spot model that incorporates simple gas-phase kinetics (Part I). Here, the applied stress is 300 MPa and the initial porosity is 0.05. During the time interval  $0 < t (\mu\text{s}) < 0.34$ , the pore collapses from the initial radius of  $a_0 = 5 \mu\text{m}$  to a minimum value of  $a = 4.5 \mu\text{m}$  (see Figure 2). Pore collapse ( $\dot{a} < 0$ ) occurs during this period since the total resistive stress ( $P_g + \beta_g$ ) is less than the external hydrostatic stress  $P_{\infty}$ .

As the pore collapses, several different heating mechanisms contribute to an increase in interface surface temperature  $T_i$  (see Figure 4). An examination of the individual terms in Equation (5) indicates the primary source of surface heating during pore collapse is from plastic work. Since this

Table 2. Input Parameters for RDX

Variable [units]	Value
$\rho_R$ [kg/m <sup>3</sup> ]	1806
$T_{\infty} = T_{\infty} = T_{g0}$ [K]	300
$P_{g0}$ [MPa]	0.10
$a_0$ [ $\mu\text{m}$ ]	5.0
$\dot{a}_0$ [m/s]	0
$e_g$	1.0
$C_3$	100
$\mu_g$ [poise]	500
$A_g$ [s <sup>-1</sup> ]	$5 \times 10^{15}$
$E_g$ [MJ/mole]	193
$A_g$ [s <sup>-1</sup> ]	34785
$E_g$ [MJ/mole]	136
G	0.90
Y [MPa]	110
L [MJ/kg]	0.392
$k_g$ [W/m-k]	0.0833
$k_g$ [W/m-k]	0.2093
$q_c$ [MJ/kg]	1.51
n	1.22
$\eta$ [m <sup>3</sup> /kg]	0.001
$C_p$ [J/kg-K]	1485
$\Phi_0$	0.10, 0.05
$P_{\infty}$ [MPa]	200 - 800

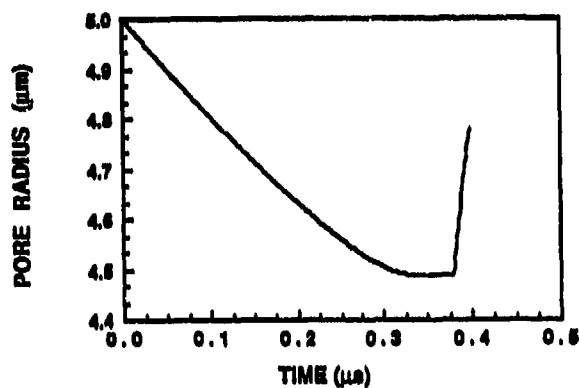


Figure 2. Pore Radius Profile for Part I,  $P_{\infty} = 300$  MPa and  $\phi_0 = 0.05$ . Initial pore collapse is followed by a brief induction period at minimum volume state and eventual pore explosion.

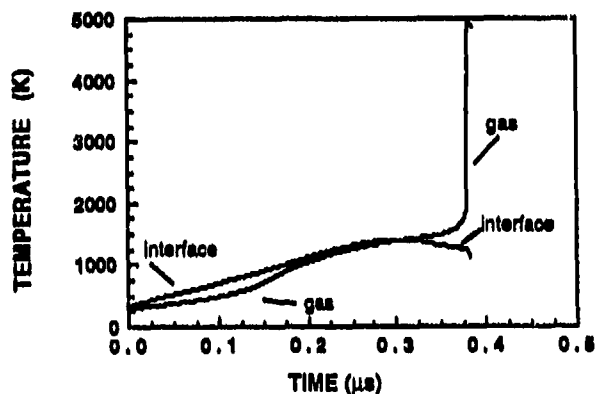


Figure 4. Temperature Profiles for Part I,  $P_{\infty} = 300$  MPa and  $\phi_0 = 0.05$ . Runaway gas-phase reaction occurs at  $t \approx 0.38$   $\mu$ s.

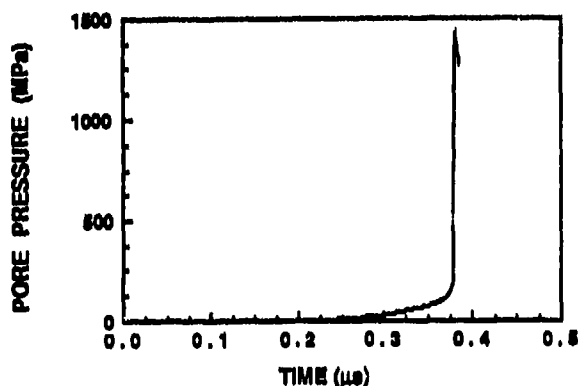


Figure 3. Gas Pressure Profile for Part I,  $P_{\infty} = 300$  MPa and  $\phi_0 = 0.05$ . Initial increase in  $P_g$  is primarily due to gas compression. Rapid increase in  $P_g$  after delay is associated with pore explosion.

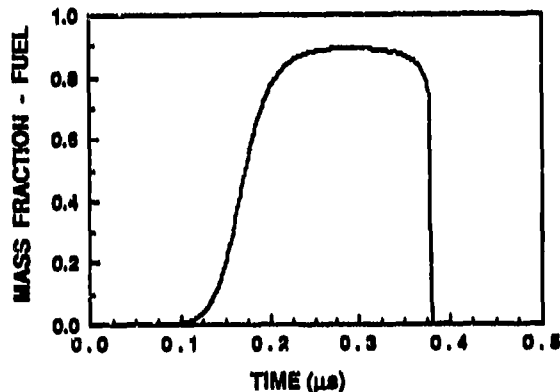


Figure 5. Fuel Mass Fraction Profile for Part I,  $P_{\infty} = 300$  MPa and  $\phi_0 = 0.05$ . Initial production of  $RDX_g$  is from decomposition at pore interface. Rapid decrease in  $Y$  at  $t \approx 0.38$   $\mu$ s is from runaway gas-phase reaction.

contributes through the yield term in the energy equation (i.e.,  $Y |a| a^2/r^3$ ), the heating rate decays rapidly ( $\sim 1/r^3$ ) for radii much greater than  $r = a$ . Thus, the heating due to plastic work is effectively confined to the pore surface and adjacent material. Compared with the yield term in the energy equation, the viscous work contribution is very small (yield term: viscous term  $\sim 3.3$ ). Similar to plastic work, the viscous contribution to heating also decays rapidly for  $r > a$ .

The presence of mass transfer at the gas/solid interface is apparent from the thermodynamic profiles displayed in Figures 3 - 5.

The reaction model used in both Parts I and II assumes the gases evolving from the surface are composed of 90 percent unreacted nitramine vapor ( $RDX_g$ ) and 10 percent reaction products ( $3CH_2O + NO_2 + N_2O + (3/2)N_2$ ). The 90 percent of mass flux undergoing phase change from  $RDX_c$  to  $RDX_g$  requires energy (latent heat). The remaining 10 percent of mass flux that reacts from  $RDX_c$  to gaseous products releases heat at the surface.

Since the net surface mass flux is dependent on interface temperature,  $T_i$ , the rate of gas production increases steadily over the pore collapse time frame ( $t < 0.34$   $\mu$ s).

Figure 5 shows a steadily increasing mass fraction of unreacted  $RDX_g$  in the pore prior to  $t = 0.34 \mu s$ . Also,  $T_1 > T_g$  during most of this time frame and heat transfer occurs from the solid interface to the pore gas. The pore gas pressure increases during this time as a result of two different processes, pore volume decrease and mass flux into the pore.

By  $t = 0.34 \mu s$  the gas temperature has increased to approximately  $T_g = 1500$  K and a reaction initiates in the gas phase. Over the next  $0.04 \mu s$ ,  $T_g$  steadily increases from 1500 K to approximately 2000 K and the gas-phase composition changes from 90 percent unreacted vapors and 10 percent products, to almost 100 percent products. Because of the magnitude of  $T_1$ , the rate of nitramine vapors being produced at the pore surface is very high. During this gas-phase thermal induction period  $T_g > T_1$  and the flow of heat is from gas to solid.

While the system is at rest in the state of minimum pore volume,  $P_g$  must overcome the total resistive pressure ( $\beta_s + P_\infty$ ) in order to initiate motion in the outward direction. Over the time interval  $0.34 < t (\mu s) < 0.38$  the pore pressure increases, but  $\dot{a} = 0$  since  $P_g < \beta_s + P_\infty$ . At approximately  $t = 0.38 \mu s$ ,  $P_g$  exceeds the resistive pressures and pore expansion takes place ( $\dot{a} > 0$ ). Due to the high rate of increase in pore pressure, pore expansion is very rapid (see Figure 2).

This example is characteristic of a situation where the applied pressure is large enough to result in pore collapse, decomposition of the energetic material, and rapid pore explosion. However, not all cases result in the type of behavior exemplified in Figures 2 - 5. The pore dynamics and thermodynamics predicted by this model depend, of course, on the initial conditions and material properties. To examine the influence of initial conditions on hot spot formation, a parametric study was made on the effects of  $P_\infty$  and  $\phi_0$  on maximum pore pressure. Figure 6 highlights the results of this study.

For a given initial pore configuration, there are two characteristic states of hot spot formation. The first state is identified in Figure 6 as the point of first ignition and the

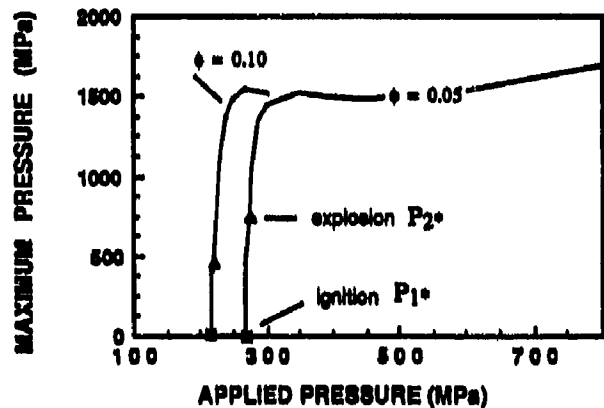


Figure 6. Maximum Pore Pressures for Several Porosities and Range of Applied Stresses

corresponding applied stress is referred to as  $P_{1*}$ . For cases where the applied stress is less than  $P_{1*}$ , the pore generally undergoes a slow rate of collapse and exhibits minimal heating at the interface. The increase in  $T_1$  is not enough to initiate significant surface decomposition and gas-phase reaction.

For applied pressures in the range  $P_{1*} < P_\infty < P_{2*}$ , interface heating is sufficient to cause some gas-phase decomposition, but the rate of gas production is insufficient to result in pore explosion. In brief, energy is being conducted away from the interface faster than it is accumulating in the pore. When the applied stress exceeds  $P_{2*}$  the rate of energy accumulation in the pore far exceeds the rate at which it is transported away and the result is pore explosion. Figure 7 shows the threshold of explosion ( $P_{2*}$ ) for a range of initial porosities.

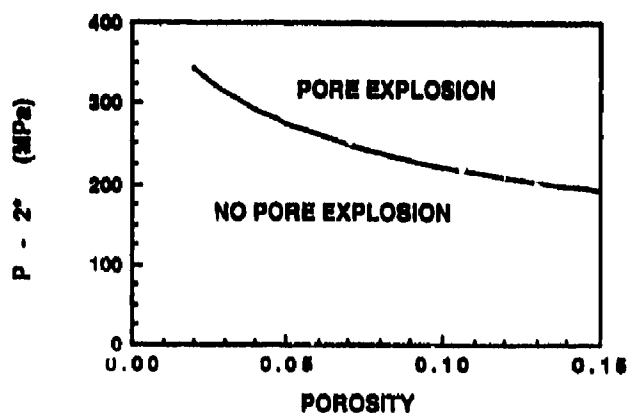


Figure 7. Critical Applied Stress  $P_{2*}$  for Range of Material Porosities ( $a_0 = 5 \mu m$ )

## Part II - Multiple Reactions

The single gas-phase reaction used in Part I of this work was replaced in Part II with the lengthy set of elementary reactions discussed previously. Input parameters and initial conditions for Part II were the same as those cited for the previous cases (Table 2). For comparison with the result shown in Figures 2 - 5, the applied stress and initial porosity for this case were again,  $P_\infty = 300$  MPa and  $\phi_0 = 0.05$ .

Figure 8 shows the pore pressure profile. Similar to the pressure history shown in Figure 3, there is a slow initial increase in pressure followed by a rapid increase at approximately  $t = 0.40 \mu\text{s}$ . Unlike Figure 3, however, Figure 8 displays a second distinct increase in pressure after a short delay time. The pore gas temperature profile shown in Figure 9 reflects this same behavior. Selected species profiles help explain the observed two-tier pressure and temperature profiles (see Figures 10 - 14).

During the initial pore collapse and interface heating phase ( $t < 0.40 \mu\text{s}$ ), the gaseous species  $\text{RDX}_g$ ,  $\text{CH}_2\text{O}$ ,  $\text{NO}_2$ ,  $\text{N}_2\text{O}$ , and  $\text{N}_2$  are produced at the pore surface. Because 90 percent of the mass flux into the gas phase is unreacted  $\text{RDX}_g$ , the net exothermicity and rate of  $T_g$  increase are very low. During this period, the event is essentially identical to the

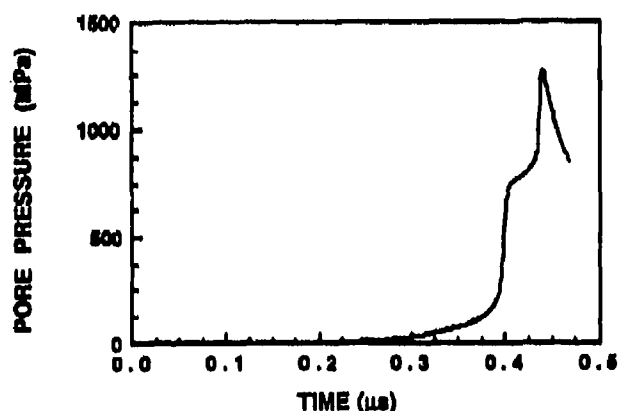


Figure 8. Gas Pressure Profile for Part II,  $P_\infty = 300$  MPa and  $\phi_0 = 0.05$ . Multiple gas-phase reactions are evaluated (compare with Figure 3).

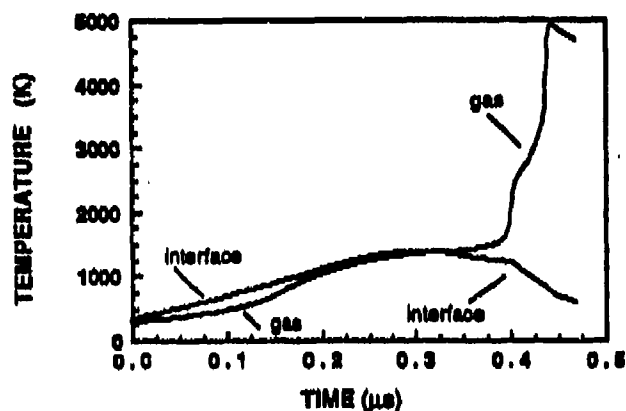


Figure 9. Temperature profiles for Part II,  $P_\infty = 300$  MPa and  $\phi_0 = 0.05$  (compare with Figure 4)

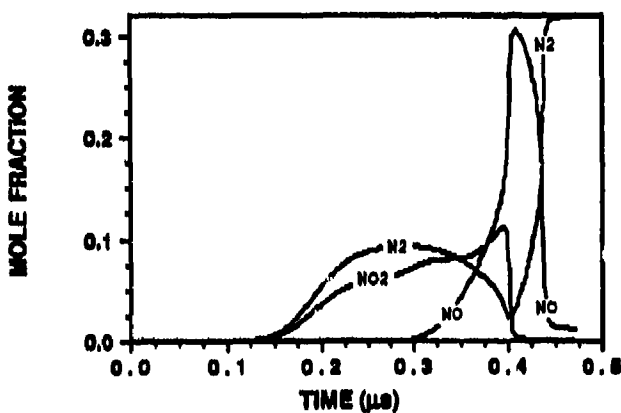


Figure 10.  $\text{NO}_2$ ,  $\text{N}_2$ , and  $\text{NO}$  Species Profiles for Part II,  $P_\infty = 300$  MPa and  $\phi_0 = 0.05$

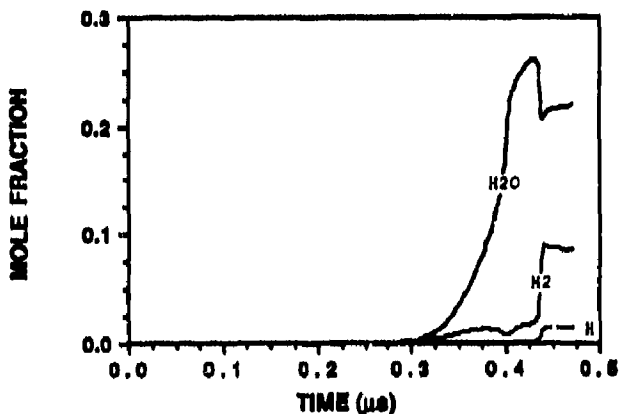


Figure 11.  $\text{H}_2\text{O}$  and  $\text{H}_2$  Species Profiles for Part II,  $P_\infty = 300$  MPa and  $\phi_0 = 0.05$

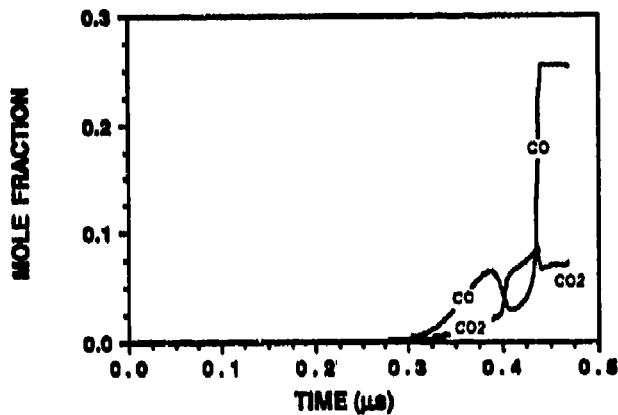


Figure 12.  $CO_2$  and  $CO$  Species Profiles for Part II,  $P_\infty = 300 \text{ MPa}$  and  $\phi_0 = 0.05$

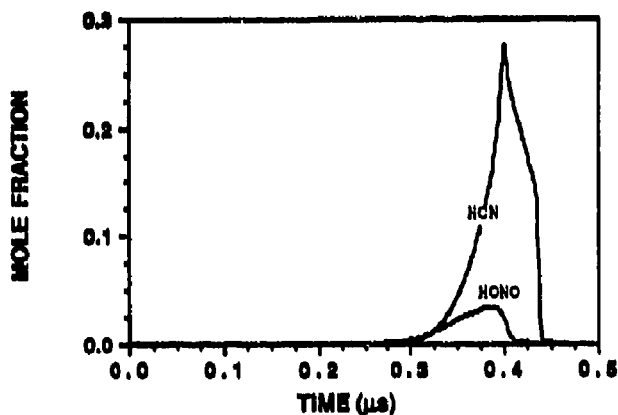


Figure 13.  $HCN$  and  $HONO$  Species Profiles for Part II,  $P_\infty = 300 \text{ MPa}$  and  $\phi_0 = 0.05$

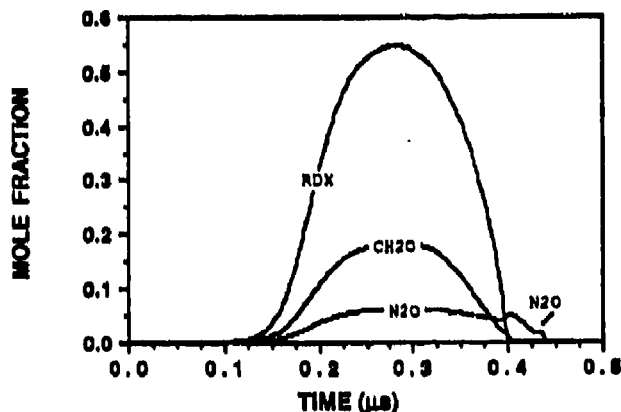


Figure 14.  $RDX_g$ ,  $N_2O$ , and  $CH_2O$  Species Profiles for Part II,  $P_\infty = 300 \text{ MPa}$  and  $\phi_0 = 0.05$

case examined in Part I (Figures 2 - 5). Once the gas temperature increases after the first delay period,  $RDX_g$  and the other species react to form additional intermediate species such as  $HONO$ ,  $HCN$ ,  $NO$ ,  $H_2O$ , etc. Recall in Part I, the reaction went directly from  $RDX_g$  to final products. The delay time associated with the first energy release is not a true "thermal induction time" since a portion of the gas heating is from other mechanisms (e.g., compression, etc.) besides self-heating.

Following a second induction time delay, the intermediate species further react causing the second-tier increases in  $T_g$  and  $P_g$ . The gaseous chemical composition after the second energy release is similar to the equilibrium composition for a constant-volume explosion process involving  $RDX_g$ . Table 3 compares the mole fractions of major species predicted by the pore collapse model with the composition predicted by an equilibrium calculation for constant-volume explosion.

Table 3. List of Species at Final State

Species (Partial List)	Mole Fractions	
	Hot-Spot (Final State)	Equilibrium Calculation
$N_2$	0.913	0.309
$CO$	0.253	0.255
$H_2O$	0.212	0.186
$H_2$	0.087	0.093
$CO_2$	0.067	0.060
$OH$	0.027	0.038
$NO$	0.016	0.012
$H$	0.013	0.034
$O_2$	0.002	0.008
$O$	0.002	0.008
$NO_2$	0.000	0.000
$N_2O$	0.000	0.000
$CH_2O$	0.000	0.000
$HONO$	0.000	0.000

## SUMMARY

Under certain initial conditions, the model presented here predicts a well-defined sequence of events leading to hot spot formation in porous, energetic materials. After a constant hydrostatic stress,  $P_0$ , is applied to the porous material, a time-dependent pore collapse commences. Heat generation due to plastic work and exothermic reaction, and heat transfer at the solid/gas interface, result in an increasing interface temperature. As the interface temperature increases, thermal diffusion within the solid phase generates a growing thermal layer that extends into the solid from the pore interface. Nitramine vapors produced at the pore interface react in the gas phase while simultaneously being compressed by the collapsing pore. Both mechanisms contribute to an increase in pore gas pressure and under certain conditions, the pore pressure overcomes the inertia of the collapsing solid and the pore explodes rapidly outward.

Two different gas-phase reaction mechanisms were investigated in this work. In the preliminary calculations performed in Part I, the gas-phase decomposition was modeled as a finite rate, single-step process. In Part II, a more detailed reaction scheme involving 167 elementary reactions and 43 chemical species was incorporated into the hot spot model. Although the overall trends were similar for both parts, the multiple gas-phase reactions treated in Part II demonstrated a two-tier induction stage prior to pore explosion. This was a direct result of the production and ultimate destruction of intermediate species in the pore gas mixture.

## REFERENCES

1. Carroll, M. M. and Holt, A. C., "Static and Dynamic Pore-Collapse Relations for Ductile Porous Materials," *J. Appl. Phys.*, Vol. 43, No. 4, 1972.
2. Butcher, B. M.; Carroll, M. M.; and Holt, A. C., "Shock Wave Compaction of Porous Aluminum," *J. Appl. Phys.*, Vol. 45, No. 9, 1974.
3. Carroll, M. M.; Kim, K. T.; and Nesterenko, V. F., "The Effect of

Temperature on Viscoplastic Pore-Collapse," *J. Appl. Phys.*, Vol. 59, No. 6, 1986.

4. Maiden, D. E. and Nutt, G. L., "A Hot Spot Model for Calculating the Threshold for Shock Initiation of Pyrotechnic Mixtures," *Proceedings of the Eleventh International Pyrotechnics Seminar*, Vail, Colorado, 7-11 Jul 1986.
5. Mitani, T. and Williams, F. A., *A Model for the Deflagration of Nitramines*, Sandia National Laboratories Report, SAND 86-8230, 1986.
6. Personal communication with C. F. Melius, Sandia National Laboratories, Livermore, CA, 1989.
7. Kee, R. J.; Miller, J. A.; and Jefferson, T. H., *CHEMKIN: A General-Purpose, Problem-Independent, Transportable, FORTRAN Chemical Kinetics Code Package*, Sandia National Laboratories Report, SAND80-8009, 1980.
8. Butler, P. B., *Real Gas Equations of State for CHEMKIN*, Sandia National Laboratories Report, SAND80-3118, 1989.
9. Plesset, M. S. and Prosperetti, A., "Bubble Dynamics and Cavitation," *Ann. Rev. Fluid Mech.*, Vol. 9, 1977.
10. Carslaw, H. S. and Jaeger, J. C., *Conduction of Heat in Solids*, Second Edition, Oxford University Press, London, 1959.

## DISCUSSION

DAVID F. ALDIS  
Lawrence Livermore National Lab.  
Livermore, CA

Your model assumptions include spherical symmetry that may not be realistic at some shock strengths. Over what shock pressure range do you think this would be appropriate?

## REPLY BY P. B. BUTLER

It is difficult to identify the shock strength at which the pore no longer exhibits spherical symmetry since it depends on many factors, including the material properties of

the condensed phase. This value would then have to be compared to the minimum shock strength required for ignition. If it exceeds the minimum ignition criterion, the spherical symmetry assumption is valid since ignition would occur prior to pore deformation.

### DISCUSSION

**DENNIS HAYES**  
Sandia National Laboratories  
Albuquerque, NM

A shock in a porous bed will broaden until the rise time of the shock is approximately equal to the pore collapse time. Thus, instead of a step function in pressure, each

pore sees a ramp in pressure, terminating at pore closure time. This kind of pressure boundary history will greatly influence inner wall motion and thus problem solution.

### REPLY BY P. B. BUTLER

Our hot spot model is formulated such that any  $P(t)$  profile can be specified as the exterior ( $r = b$ ) boundary condition. Finite rise time shock waves are of interest, and we intend to study this problem in the near future. However, it should also be mentioned there are circumstances where a condensed-phase energetic material can experience a very short rise time shock input.

# BROAD BANDWIDTH STUDY OF THE TOPOGRAPHY OF THE FRACTURE SURFACES OF EXPLOSIVES

M. Yvonne D. Lanzerotti and James J. Pinto  
U.S. Army ARDEC  
Picatinny Arsenal, New Jersey 07806-5000

and

Allan Wolfe  
Department of Physics  
New York City Technical College  
Brooklyn, New York 11021

*The Z,X coordinates of the fracture surfaces of TNT and Composition B have been measured with a stylus profilometer. The fracture surfaces of the material under study are obtained by accelerating prepared samples in an ultracentrifuge. When the tensile or shear strength is exceeded, a fracture surface is obtained. Using diamond and sapphire styli the topography of the fracture surface has been studied from a wavelength of 1.0 micron to nearly 1.0 centimeter. The power spectra have been calculated from the data using a prolate spheroidal data window in the horizontal space domain prior to the employment of the fast Fourier transform algorithm. The power spectra are found to decrease with increasing spatial frequency. Peaks are observed in the low frequency region of the TNT power spectra and indicate that much of the fracture is occurring at grain boundaries. Peaks corresponding to the RDX particle size are observed in the Composition B power spectra and indicate that the fracture is occurring between the RDX and TNT grains.*

## INTRODUCTION

In this work power spectral techniques have been used to study the topography of the fracture surfaces of energetic materials.<sup>1-4</sup> The slopes of the log-log power spectra are studied, and the slopes are used to determine if the surface topography can be characterized by a fractal dimension. The fractal dimension is a parameter describing the scaling properties of surface topography. That is, how topography or roughness varies with surface dimension. The mechanical properties of two surfaces in contact depend strongly on the topography of the contacting surfaces. Therefore, knowledge of the fractal dimension is potentially important for determining the scaling of surface topography,

mechanical properties of contacting surfaces,<sup>5</sup> and the understanding of mechanical sensitivity tests including friction and impact.

Spectral analysis techniques are also useful tools to understand the fundamental physics of the fracture processes of energetic materials and to make quantitative comparisons between different materials. Since the fractal dimension provides concise quantitative descriptions of the fracture surfaces of energetic materials, it might be expected that such descriptions will lead to improvements in cast and composition. Such quantitative descriptions are not presently available by any other method. Improved knowledge of energetic materials has resulted from this approach.

## EXPERIMENT

A Beckman preparative ultracentrifuge model I.8-80 with a swinging bucket rotor model SW 60 Ti is used to rotate the sample under study up to 60,000 rpm. The distance of the specimen from the axis of rotation can be chosen as a variable between 6 and 12 cm.<sup>6-9</sup>

Samples are prepared as follows. Cylindrical polycrystalline plugs of explosive are prepared by pouring about one-half gram of the material into 9-mm internal diameter (i.d.) polycarbonate tubes and allowing the material to crystallize. The open-ended sample tube is then joined to a short, closed-end polycarbonate centrifuge tube. The as-cast surface of the explosive faces away from the axis of rotation. The sample experiences a time rate of change of the acceleration up to a maximum acceleration. The sample then decelerates smoothly to zero acceleration. The initial maximum acceleration is less than the fracture acceleration for the material. The maximum acceleration for the sample is then increased systematically in each successive run. Particles break loose from the surface exposed to the acceleration and transfer to the closed-end tube when the strength of the material is exceeded. A hemispherical fracture surface is formed.

The Z,X coordinates of the concave fracture surfaces are measured with a stylus profilometer. Two types of styli were used to measure the Z,X coordinates. One stylus is a diamond tipped, 90° included angle truncated pyramid with a 1.3- $\mu$ m edge in the direction of motion. The other stylus is a sapphire ball with 397- $\mu$ m radius. The Form Talysurf instrument is capable of recording profile lengths from 0.5 mm to 120 cm. The diamond stylus height range is 4.0 mm with 10 nm resolution. The sapphire stylus height range is 8.0 mm with 20 nm resolution. The largest wavelength is the length of the profile. The smallest wavelength is twice the horizontal measurement spacing corresponding to the Nyquist cutoff frequency.<sup>5</sup> In addition, the finite dimension of the stylus imposes a cutoff wavelength equal to the tip radius,<sup>10</sup> 397  $\mu$ m for the sapphire stylus. The truncated pyramid diamond stylus cannot resolve a wavelength shorter than twice the length of

the edge in the direction of motion, 2.6  $\mu$ m for the diamond stylus.<sup>11</sup>

## RESULTS

### TNT

The sample of melt-cast TNT has been found to fracture at 41,000 g at 25°C. Crystallites are visually seen to protrude from the surface and range in size from approximately 100 to 500  $\mu$ m. The topography of the fracture surface of TNT has been studied from wavelengths of 1.0  $\mu$ m to 8 mm using a stylus profilometer.

An 8-mm surface height profile of one trace across the fracture surface of TNT is shown in Figure 1. The Z,X coordinates of this profile have been measured with the diamond stylus at a horizontal spacing (mean sampling interval) of 0.006 mm. The vertical displacement is plotted as a function of horizontal displacement.

The spectrum analyses are performed by using a prolate spheroidal data window<sup>12,13</sup> in the horizontal space domain prior to the employment of a fast Fourier transform algorithm to compute the power spectral density.<sup>14</sup> The prolate spheroidal window is used because it is superior to more commonly used windows in analyses of short series.<sup>13</sup> The spatial power spectrum of the fracture surface profile of the TNT sample of Figure 1 is shown in Figure 2. The power spectral density is

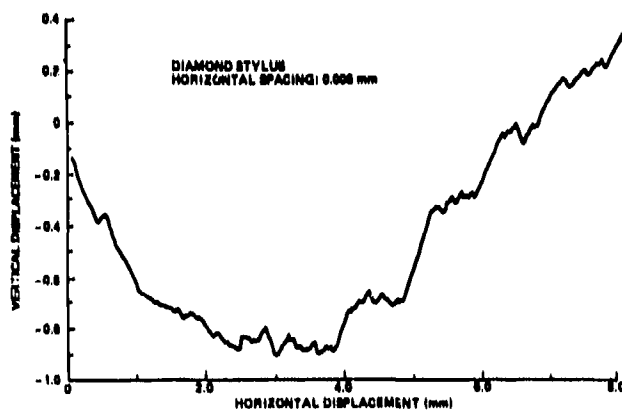


Figure 1. Surface Height Profile of the Fracture Surface of TNT

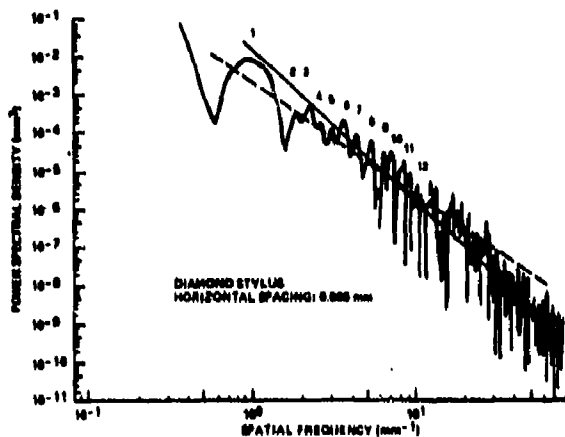


Figure 2. Spatial Power Spectrum of the Fracture Surface Profile of TNT

plotted as a function of spatial frequency on a log-log plot. The power spectral density decreases with increasing spatial frequency. At low spatial frequencies the slope (dashed line) of the spectrum is about -3. At high spatial frequencies the slope (solid line) of the spectrum is about -4. The location of the change in slope corresponds approximately to the smallest grain size observed in the fracture surface (0.1 mm).

The relationship of the spectral slope,  $s$ , to the fractal dimension,  $D$ , is given<sup>5,16,17</sup> for a profile by

$$s = -(5-2D).$$

This is the relationship used<sup>5,17</sup> to interpret the power spectra of a profile with a self-affine fractal model.<sup>16</sup> The slope must lie in the range  $-3 < s \leq -2$  in order to yield interpretable results. Therefore, at low spatial frequencies the fractal dimension is found to be about 1. At high spatial frequencies, the slope is about -4. For spectral slopes steeper than -3, the relationship between spectral slope and fractal dimension does not hold.<sup>5</sup> In this case, the dimension is exactly equal to 1, the topological dimension. Therefore, at spatial frequencies greater than  $10 \text{ mm}^{-1}$  the fracture surface is non-fractal. Apparently these fracture surfaces are not fractal at wavelengths smaller than the grain size when the profilometer stylus traverses smooth crystal cleavage surfaces.

Peaks are observed in the low frequency region of the power spectrum and correspond roughly to the size of the crystals in the sample. These peaks indicate that much of the fracture is occurring at crystal boundaries. The power spectral peaks are listed as a function of spatial frequency in Table 1. The power spectral peaks appear to be quasi-periodic over the range measured.

The spatial power spectrum has also been calculated from the Z,X coordinates of an independent fracture surface profile of TNT measured with the sapphire stylus. Similar results are obtained. The power spectral density decreases with increasing spatial frequency. At low spatial frequencies the slope of the spectrum is about -3. At high spatial frequencies the slope of the spectrum is about -4. Again the change in slope corresponds approximately to the smallest grain size observed in the fracture surface. Peaks are also observed in the low frequency region of the power spectrum and correspond to the size of the crystals in the sample. The power spectral peaks in this power spectrum are also listed as a function of spatial frequency in Table 1. These spectral peaks also appear to be quasi-periodic. In addition, many peaks in both spectra from the two individual samples are at approximately similar frequencies.

Peaks have also been observed in the Fourier spectra of fracture profiles of metals.<sup>18,19</sup> The periodicities observed for these peaks have been ascribed to a fundamental fracture unit which has a triangular shape.<sup>18</sup>

The root-mean-square (rms) roughness,  $R$ , has been calculated for the fracture surface profile of TNT shown in Figure 1. The roughness has been obtained from data measured by the diamond stylus. The determination has also been made for thirty-two separate subprofiles chosen at random from this profile. A straight line has been fit to the points by the method of least squares. The equation of the line is:

$$\log R = (0.83 \pm 0.10) \log L - (0.64 \pm 0.22),$$

where  $L$  is the profile length. The best line fit has a linear correlation coefficient equal

**Table 1. Power Spectral Peaks as a Function of Spatial Frequency for TNT Profiles**

Diamond Stylus Horizontal Spacing = 0.006 mm		Sapphire Stylus Horizontal Spacing = 0.005 mm	
Peak No.	Spatial Frequency (mm <sup>-1</sup> )	Spatial Frequency (mm <sup>-1</sup> )	Peak No.
1	0.9	0.8	1
2	1.7	1.5	2
3	2.1	2.1	3
4	2.5	---	---
5	2.9	2.8	4
6	3.4	3.5	5
7	4.2	4.0	6
8	5.2	4.7	7
9	6.3	---	---
10	7.1	6.7	8
11	8.1	8.3	9
12	8.8	---	---

to 0.83. This is beyond the 99.9 percent significance level for the thirty-two data points.<sup>20</sup> The log of the rms roughness increases linearly with the log of the profile length. Nevertheless, each specific value of rms roughness is valid only for the particular subprofile from which it is obtained.<sup>6,21</sup> These rms roughness values are plotted as a function of profile length on a log-log plot in Figure 3.

#### Composition B

The topography of the fracture surface of Composition B has been studied from wavelengths of 1.0  $\mu\text{m}$  to 5 mm using the diamond stylus. Composition B is a formulation containing 59 percent cyclotrimethylenetrinitramine (RDX), 40 percent TNT, and 1 percent wax. The sample of melt-cast Composition B has been found to fracture at 41,000 g at 25°C. The crystals are seen visually to protrude from the surface; they appear to be approximately 0.1 mm in size. The logarithmic normal crystal size distribution of RDX as specified by military specification Class 1<sup>22</sup> is shown in Figure 4.

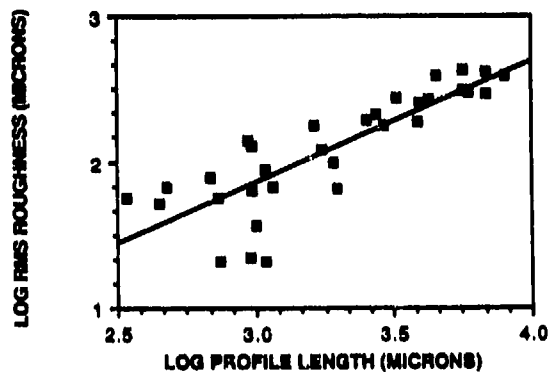


*Figure 3. Log of the Root-mean-square Roughness of TNT as a Function of the Log of the Profile Length*

The distribution for an actual RDX sample, Holston lot 21-40, is also shown. The geometric means of the particle sizes (50 percent point on the graph) are 189  $\mu\text{m}$  and 123  $\mu\text{m}$ , respectively. The geometric

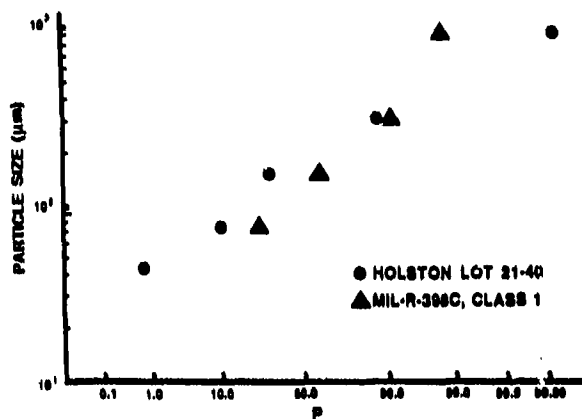


Figure 4. RDX Particle Size Distribution.  $P$  is the cumulative percentage of measurements equal to or less than the particle size.

mean particle size corresponds approximately to the size of the crystallites observed in the fracture surface.

Five-mm and 5- $\mu$ m surface height profiles of two traces across the fracture surface of Composition B have been studied. The  $Z, X$  coordinates of these profiles have been measured with the diamond stylus at a horizontal spacing (mean sampling interval) of 0.006 mm and 0.0006 mm, respectively. The spatial power spectra of these fracture surface profiles are shown in Figures 5 and 6, respectively. The power spectral density decreases with increasing spatial frequency. The spectral slopes vary from -3.3 to -3.9 and indicate that the fracture surface is non-fractal.

As in the case of the TNT sample, peaks are observed in the power spectra of Composition B. These peaks indicate that much of the fracture is occurring between RDX and TNT grains. The power spectral peaks are listed as a function of spatial frequency in Table 2. The peaks appear to be quasi-periodic over the range measured. The quasi-harmonic peaks correspond roughly to the size of the RDX crystals in the sample.

## CONCLUSIONS

The results presented here of the power spectra of profilometer traces across TNT and

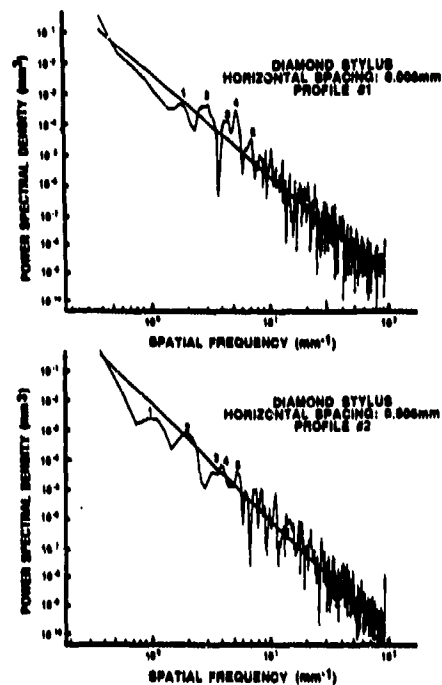


Figure 5. Spatial Power Spectra of Fracture Surface Profiles of Composition B. The slope of Profile #1 is -3.3; the slope of Profile #2 is -3.9.

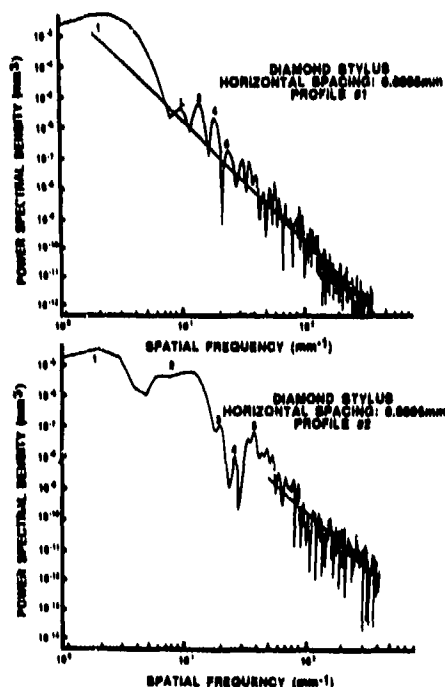


Figure 6. Spatial Power Spectra of Fracture Surface Profiles of Composition B. The slope of Profile #1 is -3.8; the slope of Profile #2 is -3.4.

Table 2. Power Spectral Peaks as a Function of Spatial Frequency for Composition B Profiles

DIAMOND STYLUS							
Horizontal Spacing = 0.006 mm				Horizontal Spacing = 0.0005 mm			
Profile #1		Profile #2		Profile #1		Profile #2	
Peak No.	Spatial Frequency (mm <sup>-1</sup> )	Spatial Frequency (mm <sup>-1</sup> )	Peak No.	Peak No.	Spatial Frequency (mm <sup>-1</sup> )	Spatial Frequency (mm <sup>-1</sup> )	Peak No.
---	---	1.0	1	1	2.2	1.8	1
1	1.8	1.9	2	2	10.0	8.6	2
2	2.9	3.2	3	3	14.2	---	---
3	4.4	3.9	4	4	19.4	19.4	3
4	5.3	5.2	5	5	25.5	26.5	4
5	6.9	---	---	---	---	33.5	5

Composition B fracture surfaces show that the spectral slopes change with spatial frequency. At the lower frequencies, the slopes for the 'TNT' spectra, interpreted in terms of the self-affine fractal model, yield a fractal dimension of approximately 1. At the higher frequencies, for both 'TNT' and Composition B, the slopes are  $< -3$ , and therefore, the spatial scaling is non-fractal. Such band-limited fractal dimensions and non-fractal behavior have been reported by Brown and Scholz<sup>5</sup> in studies of natural rock surfaces.

Understanding of the fracture and rupture of energetic materials subjected to high acceleration is a key to better practical designs in several fields, including ordnance, the extraction industry, and space propulsion. In such applications the materials can often be subjected to high, fluctuating, and/or sustained accelerations. We have presented experimental data on the studies of the fracture of energetic materials under high accelerations and have introduced the use of fractal geometry techniques to characterize the fracture surfaces. We have shown that the fractal and other statistical measures provide new ways to parameterize the fracture surfaces and also provide new insights into the fracture process. The results also suggest that at certain spatial wavelengths the fracture statistically occurs at grain boundaries. We believe the

experimental and analysis techniques used here have wide applicability in future studies of energetic materials.

## ACKNOWLEDGEMENT

We would like to thank Dr. Stephen R. Brown, Geomechanics Division, Sandia National Laboratories, Albuquerque, NM, for helpful discussions, and Mr. Steve Pollaine and Mr. Ken Blaidel, Lawrence Livermore National Laboratory, for a BASIC program to transfer data from the Form 'Talsurf to a PC formatted diskette.

## REFERENCES

1. Lanzerotti, M. Y. D. and Pinto, J., "Fractal Dimension of Fracture Surfaces of Energetic Materials," *Fractal Aspects of Materials II*, Schaefer, D. W.; Laibowitz, R. B.; Mandelbrot, B. B.; and Liu, S. H., Eds., Materials Research Society, Pittsburgh, PA, 1986, pp. 133-134.
2. Lanzerotti, M. Y. D. and Pinto, J., *Bull. Am. Phys. Soc.*, Vol. 32, 1987, p. 937.
3. Lanzerotti, M. Y. D.; Pinto, J.; and Wolfe, A., "Fractal Characteristics of Fracture Surfaces of Energetic Materials," *Fractal Aspects of Materials: Disordered Systems*, EA-13, Hurd, A. J.; Weitz, D. A.; and Mandelbrot, B. B., Eds.,

- Materials Research Society, Pittsburgh, PA, 1987, p. 30.
4. Lanzerotti, M. Y. D.; Pinto, J.; and Wolfe, A., "Fractal Properties of Fracture Surfaces of Energetic Materials," 1988 Army Science Conference, Fort Monroe, VA.
  5. Brown, S. R. and Scholz, C. H., *J. Geophys. Res.*, Vol. 90, 1985, p. 12,575.
  6. Lanzerotti, M. Y. D. and Sharma, J., "Brittle Behavior of Explosives During High Acceleration," *Appl. Phys. Lett.*, Vol. 39, 1981, p. 455.
  7. Lanzerotti, M. Y. D., "Fracture Phenomena of Energetic Materials During High Acceleration," *Proc. Symposium on Thermomechanical Properties of Energetic Materials and Their Effects on Munitions Survivability*, Vol. 2, Naval Weapons Center, China Lake, CA, Mar 1985, pp. 1-43.
  8. Lanzerotti, M. Y. D., "Mechanical Behavior of Gun Propellant During High Acceleration," *Proc. 21st JANNAF Combustion Meeting*, Vol. 1, Johns Hopkins University, Laurel, MD, 1984, pp. 275-280.
  9. Lanzerotti, M. Y. D. and Pinto, J., "Chemical Reaction of Energetic Materials During High Acceleration," *Shock Waves in Condensed Matter*, Gupta, Y. M., Ed., Plenum Publishing Corp., NY, 1986, pp. 909-916.
  10. Hunter, A. G. M. and Smith, E. A., *Wear*, Vol. 59, 1980, p. 383.
  11. Thomas, T. R., "Stylus Instruments," *Rough Surfaces*, Thomas, T. R., Ed., Longman, London, 1982, p.16.
  12. Thomson, D. J., "Spectral Analysis of Short Series," Ph. D. Dissertation, Department of Electrical Engineering, Polytechnic Institute of Brooklyn, Brooklyn, NY, 1971.
  13. Thomson, D. J., *Proc. IEEE*, Vol. 70, 1982, p. 1055.
  14. Thomson, D. J.; Robbins, M. F.; MacLennan, C. F.; and Lanzerotti, L. J., *Physics of the Earth and Planetary Interiors*, Vol. 12, 1976, p. 217.
  15. Mandelbrot, B. B., *The Fractal Geometry of Nature*, Freeman, NY, 1983; also *Fractals*, Freeman, NY, 1977.
  16. Mandelbrot, B. B., *Physica Scripta*, Vol. 32, 1985, pp. 257-260.
  17. Jordan, D. L.; Hollins, R. C.; and Jakeman, E., *Appl. Phys.*, Vol. B31, 1983, pp. 179-186.
  18. Passoja, D. E. and Amborski, D. J., *Microstructural Science*, Vol. 6, 1978, p. 143.
  19. Passoja, D. E. and Psioda, J. A., "Fourier Transform Techniques - Fracture and Fatigue," *Fractography and Materials Science*, ASTM STP 733, Gilbertson, L. N. and Zipp, R. D., Eds., American Society for Testing and Materials, Philadelphia, PA, 1981, pp. 355-386.
  20. Bevington, P. R., *Data Reduction and Error Analysis for the Physical Sciences*, McGraw-Hill, NY, 1969, p. 310.
  21. Sayles, R. S. and Thomas, T. R., *Nature*, Vol. 271, 1978, p. 431.
  22. RDX, MIL-R-398C, 22 Aug 1962, and INT AMENDMENT 5, 1 May 1978.

# EFFECTS OF MICROBALLOON CONCENTRATION ON THE DETONATION CHARACTERISTICS OF NITROMETHANE - PMMA MIXTURES

H. N. Presles, J. Campos\*, O. Heuzé, and P. Bauer

Laboratoire d'Energétique et de Détonique, E.N.S.M.A., 86034 Poitiers, FRANCE

\*Faculty of Sciences and Technology - University of Coimbra 3000 Coimbra, PORTUGAL

*The detonation velocity and pressure of mixtures of nitromethane (NM) - PMMA and glass microballoons (GMB) were measured with respect to the GMB concentration. These results show the detonation characteristics of NM can be changed in a drastic way when high concentrations of GMB are used.*

*The detonation of these mixtures is far from ideal, so there exists a large discrepancy between the experimental and calculated values.*

## INTRODUCTION

Glass microballoons (GMB) are generally used to sensitize emulsion explosives. This kind of explosive is very important today, from an industrial view point. In order not to decrease their detonation characteristics too much, these explosives contain only a few percent of GMB. The initiation sensitivity, detonation characteristics, and critical diameters depend upon the concentration of GMB.<sup>1,2,3</sup> Nevertheless, one may wonder about the effective role of GMB in these complex heterogeneous explosives.

Nitromethane (NM) is a homogeneous explosive, and likely to be the best known among all explosives. Like emulsions, its sensitivity is very poor. Therefore, mixtures of NM and GMB could be very useful to understanding the specific role of GMB. Furthermore, these mixtures are very easy to prepare, and could allow the study of the influence of several parameters such as concentration, size, and nature of microballoons. Thus, they could contribute to a better knowledge of hot spots.

But, first of all, it is necessary to investigate whether, if any and under which conditions, a self-sustained detonation would propagate in these mixtures. In such a case, the determination of its detonation character-

istics, with respect to the GMB concentration, would be a key parameter.

## INITIAL STATE OF THE MIXTURES

Because of the large discrepancy between the NM density (1.135) and GMB density, (0.132) it is not possible to obtain a homogeneous mixture without increasing the NM viscosity. Such requirement was met by adding PMMA.<sup>4</sup> Thus, a 3 percent mass fraction of PMMA in a NM/PMMA mixture was used in each composition. Each NM-PMMA/GMB composition that is presented hereafter is defined by the mass fraction  $X$  of GMB in the mixture. The size of GMB is 5 to 170  $\mu\text{m}$ . The initial density  $\rho_0$  of mixtures up to  $X = 40$  percent was measured (Table 1), since a steady detonation can propagate in any of them.

Three comments must be made:

1) when  $X > 15$  percent, there is not enough NM in the mixture to fill the gap between the GMB, which leads to extra voids.

2) the density of mixtures with  $X > 15$  percent is less than the density which could be expected from that resulting from each component.

Table 1. Density of NM-PMMA/GMB Mixtures

X (%)	Volume Fraction of NM-PMMA (%)	$\rho_0$
0	100	1.14
10	61.6	0.78
20	40.3	0.575
30	24	0.39
40	13.6	0.258

3) when  $X > 15$  percent, each GMB is covered with a layer of NM-PMMA.

## DETONATION CHARACTERISTICS

A previous study led to experimental detonation characteristics of mixtures with  $15 \geq X \geq 0$  confined in brass tubes.<sup>5</sup> As soon as  $X > 20$  percent, a steady detonation cannot propagate in this kind of confinement. This can be explained by the detonation velocity that becomes less than the sound speed of brass. For this reason experimental data reported in this paper, in the case where  $40 \geq X \geq 10$  percent, were obtained using PVC confinements.

Detonation velocity and pressure were measured and compared to calculated values provided by the QUATUOR Code,<sup>6</sup> using the BKW equation of state.<sup>7</sup>

## DETONATION VELOCITY

The detonation velocity of  $X = 10, 20,$  and  $30$  percent mixtures was measured with respect to the diameter  $\phi$  of the load ( $44 \geq \phi \geq 14$  mm) (Figure 1) in order to extrapolate to the infinite diameter detonation velocity ( $D_\infty$ ) (Table 2). These values are reported in Figure 2, as well as the corresponding value obtained in the mixture defined by  $X = 10$  percent confined in brass tubes. This result is 5 percent greater than that obtained in a weak confinement, and is correctly predicted by the BKW equation of state.

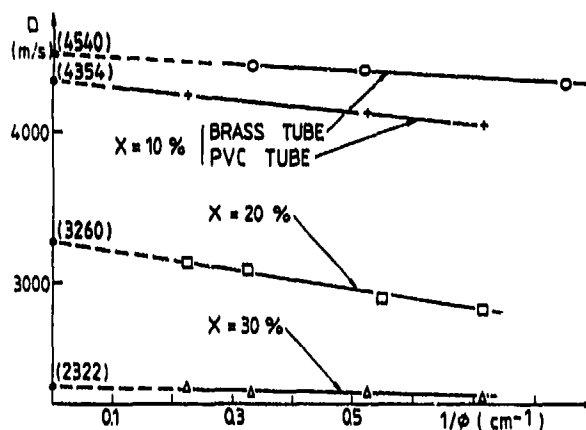


Figure 1. Detonation Velocity of NM-PMMA/GMB Mixtures Versus The Inverse Diameter of the Charge

Table 2. Measured and Calculated Detonation Characteristics

X	$D_\infty$ Brass tube (m/s)	$D_\infty$ PVC Tube (m/s)	D(BKW) m/s	P(exp) kbar	P(BKW) kbar
10	4540	4354	4557	37.4* 43	48
20		3260	3575	15	
30		2322	2769	6	10.7
40			2152	4	4.5

\*Configuration Figure 3a.

Hence, only experimental values obtained in mixtures where  $X \leq 15$  percent and shot in strong confinements may be compared to calculated values.

As  $X$  increases, the discrepancy between experimental and calculated values increases, reaching 16 percent at  $X = 30$  percent. Obviously, the behavior of these mixtures is far from ideal.

## DETONATION PRESSURE

Detonation pressures of the mixtures were measured by means of the electromagnetic gauge technique, which consists in recording the potential generated by a metallic foil dragged by the detonation products inside a magnetic field.

Up to  $X = 15$  percent, two configurations of the metallic foil were used, namely, with the foil located (i) inside the explosive and (ii) at the interface between the explosive and the PMMA plate at the end of the detonation tube (Figure 3). All of the results are shown in Figure 4. First, one can observe that both configurations lead to similar values (within an experimental error of about 8 percent).

As the GMB concentration increases, the detonation pressure decreases reaching 4 kbar at  $X = 40$  percent. These results show that the NM detonation characteristics can be changed to a large extent by addition of a large amount of GMB, since neat NM detonation pressure is 120 kbar or so.

As we already mentioned, the detonation pressure experiments were performed using 30 mm, i.d., PVC confinement. In this case the detonation velocity is much less than ideal, which explains why the experimental values of the detonation pressure are less than the ideal ones.

The fact that experimental and calculated values are nearly the same when  $X = 40$  percent has no significant physical meaning.

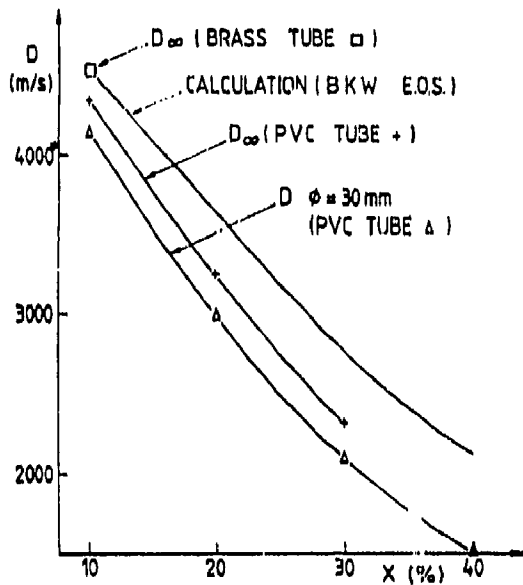


Figure 2. Detonation Velocity of NM-PMMA/GMB Mixtures Versus GMB Concentration

The critical diameter of these mixtures was not studied but is likely to be very small, since, regardless of the composition, all the values in Figure 1 (even for  $\phi = 14$  mm) fall on the same line.

One must recall that the critical diameter of NM confined in PVC tube is close to 15 mm.<sup>8</sup> This shows the very efficient role of GMB in the detonation propagation mechanism.

The detonation velocity of the mixtures confined in 30 mm i.d. PVC tubes is reported in Figure 2, as are detonation pressure measurements which were conducted using the same confinement. A detonation velocity as low as 1500 m/s is obtained with  $X = 40$  percent. This value is nearly 40 percent lower than the calculated one. Experimental values are far from ideal and, therefore, cannot be predicted by an a priori calculation derived from classical thermochemical codes.

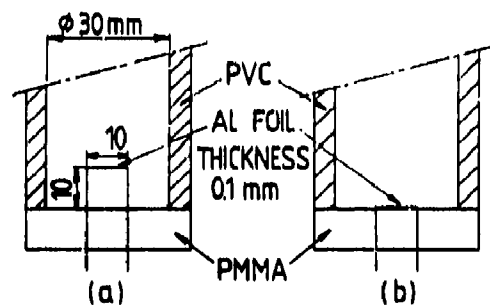


Figure 3. Different Gauge Locations Inside the Detonation Tube for Particle Velocity Measurements

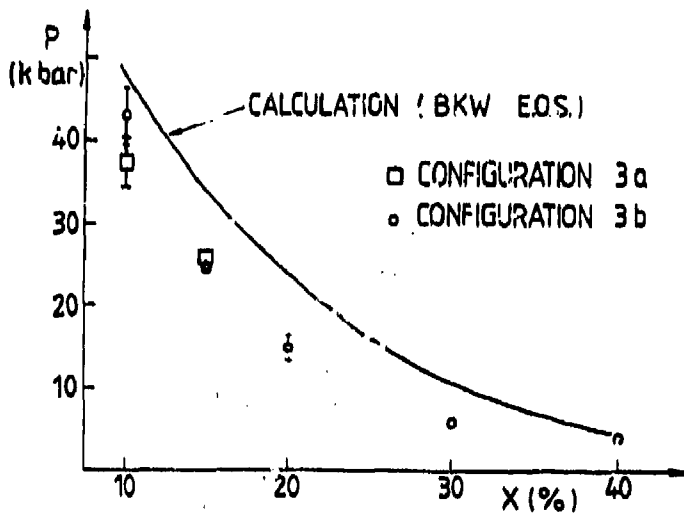


Figure 4. Detonation Pressure of NM-PMMA/GMB Mixtures Versus GMB Concentration

## CONCLUSIONS

Experimental measurements of the detonation velocities and pressures in NM-PMMA/GMB mixtures show that it is possible to change the NM detonation characteristics over a large scale, reaching very low values when high GMB concentrations are involved.

These results show the key role of GMB on the detonation propagation mechanism. The volume fraction of NM inside the mixture defined with  $X = 40$  percent is less than 15 percent. Nevertheless, a self-sustained detonation can propagate in these mixtures.

This study is the preliminary step of a work in progress aimed at the understanding of hot spot generation.

## ACKNOWLEDGEMENTS

The authors are very grateful to Y. Sarrazin and I. Hamada for their participation in the experiments.

## REFERENCES

1. Yoshida, M.; Iida, M.; Tanaka, K.; Fujiwara, S.; Kusakabe, M.; and Shiino, K., "Detonation Behavior of Emulsion Explosives Containing Glass Microballoons," *Proceedings of the Eighth Sym-*

*posium (International) on Detonation*, Naval Surface Weapons Center, Albuquerque, NM, 15-19 Jul 1985, pp. 993-1000.

2. Okamoto, T.; Sato, S.; and Sunagawa, T., "High Performance Water Gel Explosives," *Proceedings of the International Symposium on Pyrotechnics and Explosives*, China Academic Publishers, Beijing, 12-15 Oct 1987, pp. 313-317.
3. Tanaka, K.; Yoshida, M.; Iida, M.; and Fujiwara, S., "Detonation Properties of Water Gels," *Proceedings of the International Symposium on Pyrotechnics and Explosives*, China Academic Publishers, Beijing, 12-15 Oct 1987, pp. 328-332.
4. Kato, Y. and Brochet, C., "Cellular Structure of Detonation in Nitromethane Containing Aluminum Particles," *Proceedings of the Sixth Symposium (International) on Detonation*, Office of Naval Research, White Oak, 24-27 Aug 1976, pp. 124-132.
5. Presles, H. N.; Canpos, J.; Houzé, O.; and Bauer, P., "Détonation de Mélanges Nitrométhane-PMMA. Billes de Verre Creuses," *Proceedings of the Third Symposium on Behaviour of Dense Media under High Dynamic Pressures*, La Grande Motte, France, 1989.
6. Houzé, O.; Presles, H. N.; and Bauer, P., "Quatuor: A Thermochemical Code for Computing Thermodynamic Properties of Detonation and Combustion Products," *Proceedings of the Congrès International de Pyrotechnie Spatiale*, Association Française de Pyrotechnie, Juan-les-Pins, France, 8-12 Jun 1987, pp. 91-96.
7. Mader, C. L., *Detonation Properties of Condensed Explosives Computed Using the BKW Equation of State*, LA 2900, Los Alamos, NM, 1963.
8. Presles, H. N., *Etude de la Détonation de Systèmes Explosifs Binaires à base de Nitrométhane*, Thesis, Poitiers, France, 1978.

## DISCUSSION

**P. KATSABANIS, Queen's University  
Kingston, Ontario, Canada**

What calibration parameters were used for the calculations with the BKW EOS and do these parameters reliably predict performance of low density explosives?

### REPLY BY H. N. PRESLES

We used the parameter set fitting TNT. We know from related studies that with the detonation of compressed gaseous explosives these parameters lead to an overestimation of the performances of low density explosives and so, with our mixtures, to an increasing discrepancy when increasing the glass microballoon concentration.

## DISCUSSION

**A. VAN DER STEEN  
TNO Prins Maurits Laboratory  
The Netherlands**

Did you measure the shock sensitivity as a function of the microballoon concentration?

### REPLY BY H. N. PRESLES

Such experiments are planned in the near future. Right now we can say that the mixture most concentrated with microballoons ( $X = 40$  percent) upon which we performed experiments is very shock sensitive, since with a detonation pressure of about 4 kbar the ZND pic pressure is about 10 kbar.

**SESSION ON**  
**DETONATION PRODUCTS**

**Cochairmen: Anita Renlund**  
**Sandia National Laboratories**

**Gert Bjarnholt**  
**Swedish Defense Research Establishment**

# DETONATION CHARACTERISTICS OF DENSE GASEOUS EXPLOSIVE MIXTURES

P. Bauer, M. Dunand, H. N. Presles, and O. Heuzé  
Laboratoire d'Energétique et de Détonique  
E.N.S.M.A., 86034 Poitiers, FRANCE

*A new experimental technique is described. It allows the measurement of detonation velocities of gaseous explosives at an initial pressure of 100 bar to 500 bar. The detonation is initiated by means of a solid explosive generating an overdriven detonation in the gaseous mixture. The velocities are measured on eight successive sets of ionization probes located along 2 m long tubes. Their inside diameter varies. The detonation is rapidly steady except at the upper limit of the pressure range where side effects occur. They are probably due to the proximity of the critical point of the hydrocarbon, which could lead to some heterogeneity in the mixture. It appears that the Percus Yevick EOS is no longer valid, and one must use the JCZ3 EOS instead. These calculated results were obtained by QUATUOR Code involving the Redlich Kwong EOS to describe the initial state of the mixtures.*

## INTRODUCTION

In order to provide data on the detonation properties of dense gaseous explosive mixtures, an experimental investigation was undertaken. During the last decade<sup>1</sup> hydrocarbon-oxygen-nitrogen mixtures in various concentrations were studied at an initial pressure of 100 bar. Simultaneously a thermochemical code (QUATUOR Code<sup>2,3</sup>) was developed. This code is based on several equations of state (EOS). The Boltzmann EOS together with the Percus Yevick EOS turn out to yield detonation velocities that are in good agreement with experimental ones. However, the purpose of the work in progress is to check whether the validity of these EOS can be stretched to a higher range of density. In other words, more compressed gaseous explosives are more likely to substantiate such a range of validity. Moreover, one has to fill a gap between the gaseous explosives at ambient pressure and the high explosives. Such a goal was that of the present study which deals with gaseous explosive mixtures at an initial pressure ranging from 100 to 500 bar. These mixtures yield detonation pressures on the order of 10 to

15 kbar, which may be regarded as a gateway to the field of high explosives.

Previous experiments were performed in two different tubes: (1) 2 m long and 20 mm i.d. and (2) 4.5 m long and 55 mm i.d. They could only withstand a pressure of 7 kbar and 3 kbar, respectively; therefore, a new technique had to be created. The mixtures were confined in tubes that could only contain them at the initial pressures but were torn after each shot. In addition, detonator #8 turned out to be inoperative when located in an ambient pressure beyond 150 bar; therefore, a new ignition device had to be designed.

## EXPERIMENTAL FACILITIES

Several i.d. tubes were used: 12 mm, 16 mm, 21 mm, and 26 mm. They were 2 m long with 8 consecutive sets of measurements 20 cm in length (Figure 1). This allowed a check of the stability of the detonation wave. Ionization pickups, which had to be carefully adjusted to avoid any leakage, were installed for this purpose. The first set was located at a distance of 40 cm from the ignition point. Each

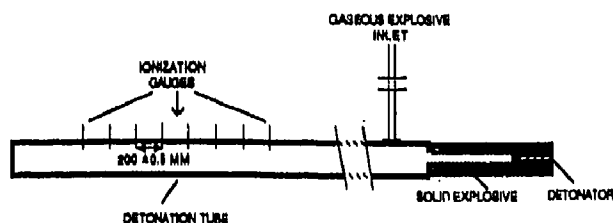


Figure 1. Sketch of the Detonation Tube

gauge consisted of a central pin stuck in a 2 mm cylindrical glass piece inserted and glued into the tube wall.

The difficulty encountered previously, concerning the inability of the ignition device beyond  $p_0 = 150$  bar, led to operation in such a way that the triggering of the detonation would be from outside of the tube. For this purpose, a 1 cm thick layer of solid explosive was pasted around one end of the tube over a length of approximately 10 cm. This technique was used previously by Sellam et al.<sup>4</sup> to generate overdriven detonations. The detonation in the outer explosive leads to the formation of a Mach stem in the inner core and an overdriven detonation takes place in the central gaseous explosive.

As will be discussed later, the opening of the confinement leads rapidly to a steady state, at least beyond the first 40 cm of propagation.

Three different mixtures of slightly rich ethylene-air were studied in a range of initial pressures varying from 100 to 500 bar. The mixtures were prepared in storage vessels using a weighing system<sup>1</sup> and the composition was checked by a gas chromatography analysis.

A preliminary study<sup>5</sup> has shown the feasibility of the whole experimental technique at an initial pressure of up to 320 bar. However, several particular problems had to be solved, namely, the effect, if any, of the tube diameter and, moreover, to what extent a much higher initial pressure could be reached experimentally. A pressure of 500 bar was the very highest that could be expected since the installation was only designed to operate safely to this limit.

## EXPERIMENTAL RESULTS

Despite the strong ignition device, values recorded over the different sets of measurements were quite close -- less than 1 percent -- at least within the experimental uncertainty, showing the CJ self-sustained state of the detonation. This can be explained by the rapid opening of the confinement that occurs within the first 40 cm of the tube, prior to the first set of measurements. Depending upon the tube diameter, that is, upon its strength, one could observe in the lower range of initial pressure some fluctuations in the velocity on the order of 1 percent. However, the average velocity can be regarded as reliable. Therefore, shorter tubes may be used in the future.

Measured detonation velocities are reported on Figure 2 as a function of the initial pressure. All sets of values fall along the same line, and the light change in the equivalence ratio does not lead to any significant discrepancy. All sets of data may be regarded as reliable up to an initial pressure of 300 bar or so. Beyond this value, the velocity exhibits

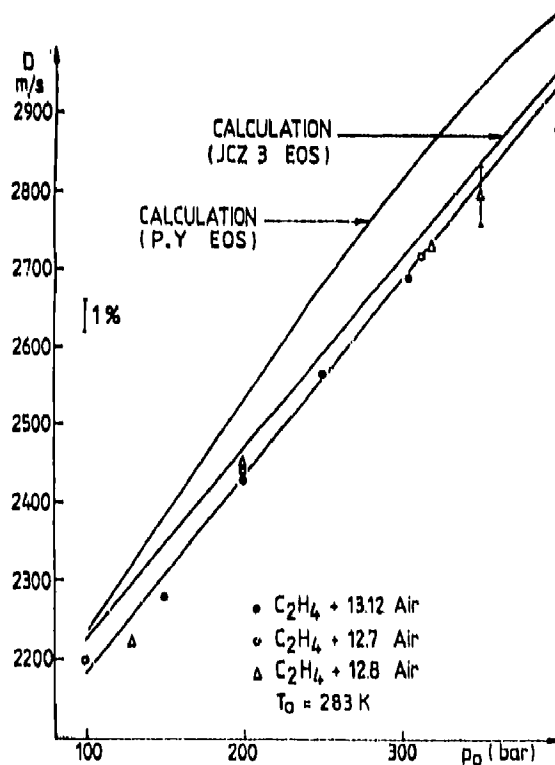


Figure 2. Detonation Velocity Vs. Initial Pressure

large fluctuations; the uncertainty attached to its value is far from what can usually be expected, i.e., less than 1 percent. For instance, the values corresponding to  $p_0 = 350$  bar and  $p_0 = 400$  bar were exhibiting fluctuations on the order of 3 percent. Although they have been reported on the plot, one must be very cautious as to the reliability of such data. Results obtained at a pressure of 500 bar were not reported in this paper since all shots provided values that were unlikely to be realistic, i.e.,  $D = 3000 \pm 200$  m/s. This can be explained by the proximity of the critical conditions with regard to the initial state of ethylene prior to each experiment. Some heating of the mixture at a temperature of 300 to 310 K would presumably help avoid this critical state and favor a more homogeneous mixture. Another side effect is that of the precursor wall waves with associated rarefactions. This phenomenon, as described by Watson,<sup>6</sup> may locally act in such a way that the hydrocarbon would undergo a change of state. Anyhow, this upper range of initial pressure cannot yet yield reliable results, at least with this type of hydrocarbon.

In order to check the eventual role of the diameter of the tube, experiments were performed at a pressure  $p_0 = 200$  bar in several i.d. tubes. No significant discrepancy between the measured values was observed, at least within the range of uncertainty. This result leads to the conclusion that the reaction zone thickness is very small compared to the detonation wave curvature. This is supported by a previous investigation on the influence of pressure on the cell size of the detonation front.<sup>7</sup> It shows that an extremely thin structure of the detonation front can be expected.

## COMPARISON WITH A PRIORI CALCULATION

Together with these experimental values, calculated values are reported on the same plot. They were obtained by means of QUATUOR Code<sup>8</sup> running with Percus Yevick EOS as well as with JCZ3 EOS.<sup>9</sup> This former EOS was very satisfying since it predicted the detonation properties of most hydrocarbon-oxygen-nitrogen mixtures at initial pressures up to 100 bar.<sup>10</sup> A more simple one, Boltzmann

EOS, was also very efficient. However, as the plot shows, the Percus Yevick EOS is no longer valid -- either in terms of profile or deviation with experimental data -- in a higher range of initial pressure, unless its parameters are thoroughly adjusted. But then it would not fit the previous range of initial pressures. The JCZ3 must be used instead, since it yields results in good agreement with experimental data. This EOS was designed in order to describe the behavior of detonation products of high explosives; therefore, its validity in the present case is not totally surprising, although the detonation pressure is one order of magnitude less than that of high explosives. As a reference, the calculation providing detonation pressure as a function of initial pressure is presented in Figure 3 for the present mixtures.

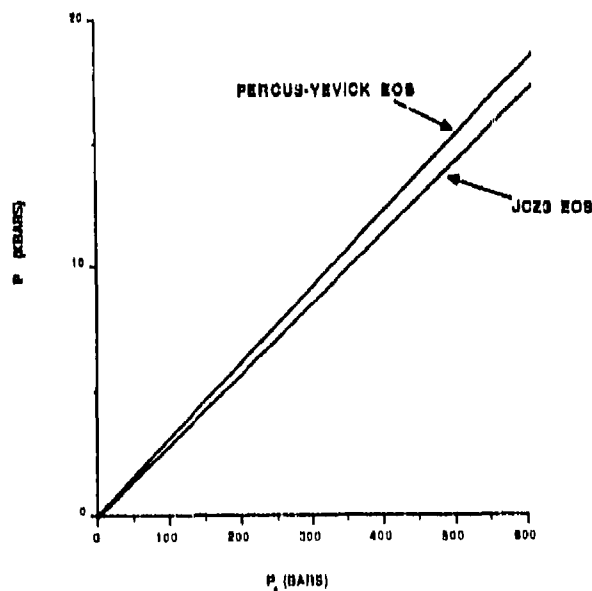


Figure 3. Computed CJ Pressure Vs. Initial Pressure

Thermodynamic data used in the calculations of the detonation velocities were those provided by Gordon and McBride polynomial forms, which have been extensively detailed in previous papers.<sup>1,2,3,8</sup>

The calculation was performed considering fresh mixtures at a temperature of 283 K. Moreover, the initial state of the mixture was calculated using a real gas EOS, that of Redlich Kwong. It is fairly suited for mixtures

at pressures less than 1000 bar; moreover, its formulation is quite simple and the required data are solely the critical pressure and temperature of each pure component. We used a combination rule to obtain these critical parameters with regard to the mixture. This rule has been detailed in a previous paper<sup>12</sup> and leads to satisfying results. It appears that a calculation ignoring this real gas behavior of the fresh mixture would be unrealistic and would not allow any reliable comparison of both calculated and experimental values. This was a key point in the buildup of the thermochemical code. The calculated results presented in this paper were based on the assumption that detonation products only yield gaseous species. A different statement led to a greater discrepancy between both sets of data.

## SUMMARY AND CONCLUSION

Detonation velocities were measured in dense gaseous explosive mixtures at a pressure in the range from  $p_0 = 100$  bar to  $p_0 = 500$  bar in various slightly rich ethylene-air mixtures. Their equivalence ratios were very close to one another, which provided some check on the repeatability of the measurements. These mixtures were detonated in the same way as high explosives, that is, using a weak confinement that could merely withstand the initial pressure. They were ignited by means of solid explosive generating an overdriven detonation. It was observed that the detonation, once propagating over a few tens of cm, slowed down to a steady CJ state. This was checked through eight successive sets of measurements. Data obtained at the highest levels of pressure -- i.e.,  $p_0 = 400$  bar and, more particularly,  $p_0 = 500$  bar, may be regarded as less reliable, since one has to be cautious about the homogeneity of such mixtures where the hydrocarbon is likely to be in a state close to the critical one.

Nevertheless, a reliable comparison could be made on the basis of calculated values provided by QUATUOR Code running with both Percus Yevick and JCZ3 EOS. The latter turns out to yield a satisfactory agreement with experimental values. Its validity can, therefore, be stated in a range of pressure -- from 10 to 15 kbar, one order of magnitude less than that for which it had been designed. The

results show the feasibility of this new setup and, presumably, should provide new data in the near future. It may, therefore, be regarded as a reliable technique to generate detonation pressures on the order of those obtained by means of inhibited high explosives.<sup>13</sup> This would make a continuum in the knowledge of both gaseous explosives at atmospheric pressure and high explosives.

## ACKNOWLEDGEMENTS

The authors are indebted to Y. Sarrazin and H. Simonnet for their technical assistance, as well as to J. J. Denis for his advice in designing the probes system, to D. Falaise who carried out all the gas analysis, and to F. G. Marsh for literary corrections.

## REFERENCES

1. Bauer, P., *Contribution à l'Etude de la Détonation de Mélanges Explosifs Gazeux à Pression Initiale Elevée*, Thèse de Doctorat ès Sciences, University of Poitiers, France, Jun 1985.
2. Heuzé, O., *Contribution au Calcul des Caractéristiques de Détonation de Substances Explosives Gazeuses ou Condensées*, Thèse de Doctorat d'Université, University of Poitiers, France, Jun 1985.
3. Heuzé, O.; Bauer, P.; Presles, H. N.; and Brochet, C., "Equations of State for Detonation Products and Their Incorporation into the QUATUOR Code," *Proceedings of the Eighth Symposium on Detonation*, Albuquerque, NM, 15-19 Jul 1985, pp. 762-769.
4. Sellam, M.; Presles, H. N.; Brochet, C.; and Chéret, R., "Characterization of Strong Detonation Waves in Nitromethane," *Proceedings of the Eighth Symposium on Detonation*, Albuquerque, NM, 15-19 Jul 1985, pp. 425-428.
5. Bauer, P.; Presles, H. N.; and Dunand, M., "Premières Etudes Expérimentales sur la Détonation dans les Mélanges Explosifs Gazeux à Pression Initiale Supérieure à 100 Bar," *C.R.A.S.*, Paris, Vol. 308, 1989, pp. 1405-1408.

6. Watson, R. W.; Summers, C. R.; Gibson, F. C.; and Dolah, Van R. W., "Detonation in Liquid Explosives: The Low Velocity Regime," *Proceedings of the Fourth Symposium on Detonation*, Office of Naval Research, MD, 12-15 Oct 1965, pp. 117-124.
7. Bauer, P.; Presles, H. N.; Heuzé, O.; and Brochet, C., "Measurement of Cell Lengths in the Detonation Front of Hydrocarbon -- Oxygen and Nitrogen Mixtures at Elevated Initial Pressures," *Comb. and Flame*, 6, 1986, pp. 112-123.
8. Heuzé, O.; Presles, H. N.; and Bauer, P., "QUATUOR: A Thermochemical Code for Computing Thermodynamic Properties of Detonation and Combustion Products," *Proceedings of the Twelfth International Pyrotechnics Seminar*, Ed. SERIEP, Paris, Juan-les-Pins, France, 8-12 Jun 1987, pp. 91-96.
9. Cowperthwaite, M. and Zwisler, W. H., "The JCZ Equations of State for Detonation Products and Their Incorporation into the TIGER Code," *Proceedings of the Sixth Symposium on Detonation*, Office of Naval Research, MD, 24-27 Aug 1976, pp. 162-172.
10. Bauer, P.; Brochet, C.; and Presles, H. N., "Detonation Study of Gaseous Mixtures at Initial Pressures Reaching 10 MPa," *Archivum Combustionis*, Vol. 4, N°3, 1984, pp. 191-195.
11. Austing, J. and Selman, J. R., "Part I: Equations of State, and Thermodynamic, and Hugoniot Relationships," *Proceedings of the Eleventh International Pyrotechnics Seminar*, Vail, CO, 7-11 Jul 1986, pp. 631-632.
12. Bauer, P.; Vidal, P.; and Manson, N., "Applicability of the Inverse Method for the Determination of CJ Parameters for Gaseous Mixtures at Elevated Pressures," *AIAA Progress in Astronautics and Aeronautics*, Vol. 114, 1988, pp. 64-76.
13. Presles, H. N.; Campos, J.; Heuzé, O.; and Bauer, P., "Effects of Microballoons Concentration on the Detonation Characteristics of Nitromethane -- PMMA

Mixtures," *Proceedings of the Ninth International Symposium on Detonation*, Portland, OR, 28 Aug - 1 Sep 1989.

## DISCUSSION

J. KURY, Lawrence Livermore  
National Laboratory, Livermore, CA

Additional information on EOS could easily be obtained by measuring the wall velocity of the confining tube with a technique similar to that used in the cylinder test for solid explosives.

## REPLY BY P. BAUER

This type of information would indeed be interesting to collect. However, since it would require the observation of the wall velocity, we could not perform these experiments in the present range of initial pressures. The opening of the confinement started to be compared to that of a solid explosive at initial pressures beyond 300 bar. In the lower range of initial pressures, we sometimes observed a partially torn tube. However, we do believe that such experiments could be conducted in the future for higher values of the initial pressure.

## DISCUSSION

J. ROTH, Consultant  
Portola Valley, CA

Did you calculate initial gas densities using realistic equations of state? Also, were there any  $P_{CJ}$  measurements made?

## REPLY BY P. BAUER

The calculation of initial gas densities is part of the thermochemical code QUATUOR. It is a key point in the code since the compressibility effects start to play a prominent role beyond an initial pressure of the order of few tens of bar. The equation of state used for this purpose is that of Redlich and Kwong (refer to Kemp, M. K. et al., *J. Chem. Educ.*, 52(12), 1975, pp. 802-803).

We have not performed any reliable CJ measurements. However, the CJ detonation pressure has been calculated on the basis of the

inverse method. A detailed description of this method is provided in the following reference: P. A. Bauer et al., *A.I.A.A. Progress in Astronautics and Aeronautics*, Vol. 114, 1988, pp. 64-76.

## DISCUSSION

**H. GRYTING**, Gryting Energetics  
Sciences Company, San Antonio, TX

Have you determined any detonation limits for ethylene in air? What other fuels have you studied?

## REPLY BY P. BAUER

We did not observe any detonation limit in ethylene-air mixtures. The only problem was the detonation velocity fluctuations in the higher range of initial pressures, as mentioned in the paper. We believe that such limit is unlikely to occur, due to particularly small size of the cells in that case. This is the reason why the diameter effect is not anymore noticeable at initial pressures higher than 10 bar.

We performed a great number of experiments in various hydrocarbon oxygen mixtures more or less diluted in nitrogen. These were  $\text{CH}_4$ ,  $\text{C}_2\text{H}_4$ ,  $\text{C}_2\text{H}_6$ ,  $\text{C}_3\text{H}_8$ ,  $\text{H}_2$ , as well as various compositions of  $\text{CH}_4 - \text{C}_2\text{H}_6$  and  $\text{CH}_4 - \text{C}_3\text{H}_8$  (supposed to exhibit the same behavior as natural gas) and  $\text{CH}_4 - \text{C}_2\text{H}_6 - \text{H}_2$ .

## DISCUSSION

**W. BYERS BROWN**, University of  
Manchester, Dept. of Chemistry  
Manchester, United Kingdom

I would like to ask Dr. Bauer how the various intermolecular potential parameters

appearing in the various equations of state used in the theoretical comparisons with experiment were chosen.

## REPLY BY P. BAUER

Most of the equations of state (EOS) we used in the code are based on a virial development, either in a straightforward form, like in Boltzmann EOS, or in form of a summation, like in Percus Yevick EOS. Concerning the description of the molecular interactions, two different approaches were made: either a simple one where only like molecules interactions are considered, or a more sophisticated one like that involved in JCZ3 EOS, for instance. In any case, we used data that are available in the literature either for the intermolecular potential exponent regarding the molecular interaction distance or energy involved in the reduced temperature. In order to fit experimental data, a degree of freedom was kept using an adjustable parameter in the average interaction distance as suggested by Edwards, J. C. and Chaiken, R. F.; *Comb. and Flame*, Vol. 22, 1974, p. 269.

In the case where extremely high pressures are concerned, namely beyond 100 kbars, the Morse potential is supposed to give a good description of the interaction phenomenon. However, due to the lower range of pressure with which we are confronted, we did not use this form. We kept the form suggested by the authors from whom we chose the EOS. One may find a thorough description of these parameters in References 1 and 2 of the present paper.

# DETONATION TEMPERATURE OF SOME LIQUID AND SOLID EXPLOSIVES

Y. Kato, N. Mori, and H. Sakai  
Chemicals and Explosives Laboratory  
Nippon Oil and Fats Co., Ltd.  
Taketoyo, Aichi 470-23, JAPAN

and

T. Sakurai and T. Hikita  
Fukui Institute of Technology  
Gakuen, Fukui 910, JAPAN

*Detonation temperature of liquid explosives containing Hydrazine Nitrate and solid explosives at various initial densities was investigated with a four-color pyrometer. The liquid explosives containing Hydrazine Nitrate were chosen as representative of H-N-O composition. The experimental results show that the detonation products of H-N-O composition radiate like a blackbody. It was shown that the measured detonation front temperatures of solid explosives are almost constant within an experimental error, in the range of initial density investigated. The measured detonation front temperatures of solid explosives were compared with CJ temperatures calculated using various types of equations of state. Good agreement was obtained between the measured and calculated values.*

## INTRODUCTION

It is important to know the detonation characteristics of high explosives from both a practical and a theoretical point of view. Detonation temperature may be the most important parameter for understanding chemical kinetics in the reaction zone and the thermodynamic state of detonation products.

At present, for various applications, the detonation characteristics can be predicted using thermo-hydrodynamic computer codes with various types of equations of state for detonation products. It is well known that the detonation velocity and pressure are less dependent on the type of equation of state. Measurements of detonation temperature are very important as criteria to check the validity of equation of state.

Recently, it has been proven that temperature measurements by optical techniques are

very useful tools in detonation study; significant contributions have been made by Urtiew,<sup>1</sup> Burton et al.,<sup>2</sup> and Kato et al.<sup>3-5</sup> In a previous paper,<sup>5</sup> it was shown that optical techniques can be used to measure the temperature of detonation products of solid explosives. In this study, we applied the temperature measurements by optical pyrometer to liquid explosives containing Hydrazine Nitrate and solid explosives at different initial density. The measured detonation temperatures were compared with CJ temperatures calculated using various types of equations of state. Good agreement was obtained between the measured and calculated detonation temperatures.

## EXPERIMENT

Temperature measurements were obtained using a four-color pyrometer shown in Figure 1. The four-color pyrometer consists of

**Table 1. Properties of HN/H<sub>2</sub>O and HN/HH Solutions**

Explosive	Composition (wt.%)	Fudge Point (°C)	Initial Temp. (°C)
HN/H <sub>2</sub> O	95/5	60	65-70
	90/10	50	55-60
	85/15	40	45-50
	80/20	30	35-40
HN/HH	75/25	-	20-25
	70/25	-	20-25
	65/35	-	20-25
	60/40	-	20-25
	55/45	-	20-25

HN: Hydrazine Nitrate - N<sub>2</sub>H<sub>4</sub> · HNO<sub>3</sub>  
 HH: Hydrazine Hydrate - N<sub>2</sub>H<sub>4</sub> · H<sub>2</sub>O

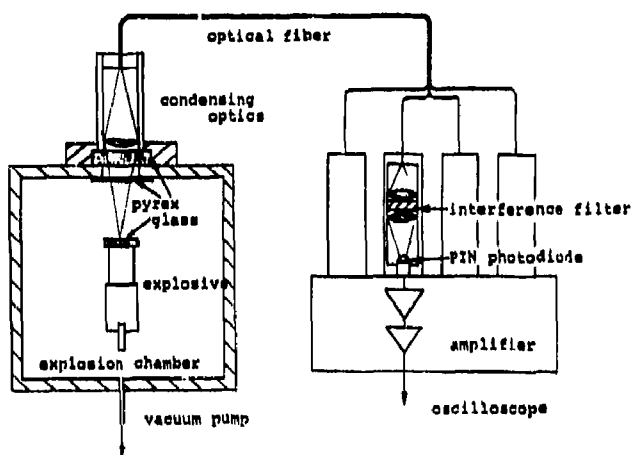


**Figure 1. Experimental Setup**

condensing optics, optical fibers, interferential filters (center wavelength  $\lambda = 0.65, 0.75, 0.85,$  and  $0.95 \mu\text{m}$ ; band width at half peak transmission  $\Delta\lambda = 0.01$  and  $0.07 \mu\text{m}$ ), PIN photodiodes, and an amplifier. Radiation, emitted from the area of 1 mm in diameter on the advancing detonation front or detonation products, was focused on one end of the optical fibers by a condensing lens. The output of the amplifier was recorded by digital recorder (Sony-Tektronix 390 AD) via coaxial cables and 50 ohm load resistors. The rise time of the overall system was measured to be less than 10 nsec. The calibration of the four-color pyrometer was performed with a tungsten ribbon lamp and a carbon arc.

Liquid explosives studied were Hydrazine Nitrate (HN)/Water (H<sub>2</sub>O) and HN/Hydrazine Hydrate (HH) solutions. Composition of the liquid explosives is presented in Table 1. These liquid explosives were chosen as representative of the H-N-O composition. Liquid explosives were contained in glass tubes to avoid contact with metal (Figure 2). The initial temperature of liquid explosives was maintained at a temperature 5-10°C higher than its fudge point (Table 1).

Solid explosives studied were TNT, Tetryl, and RDX which were loaded in PVC tube (50 mm long, 20 mm in diameter) by hand press to the desired initial density. The properties of solid explosives are presented in

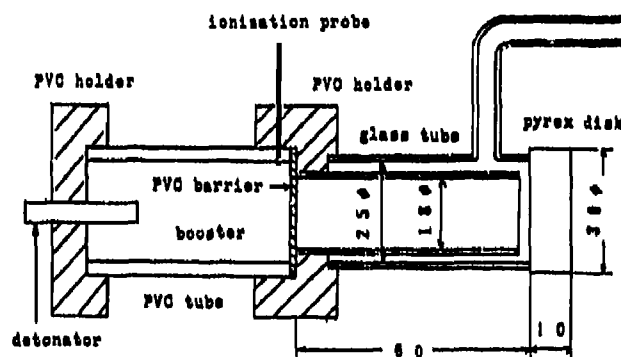


**Figure 2. Detonation Tube**

Table 2. The PVC tube had a 10-mm thick transparent anvil (pyrex glass) at one end and a booster charge at the other. The transparent anvil was pressed to the end surface of the solid explosives to avoid voids at the interface between explosive and anvil. The detonation tube was placed in an explosion chamber where the internal pressure was reduced to 20-30 mm Hg for each shot.

## RESULTS AND DISCUSSION

### Detonation Temperature of HN/H<sub>2</sub>O and HN/HH Solutions

Figure 3 shows a typical record of temperature measurements of the HN/HH solution

Table 2. Properties of Solid Explosives

Explosive	Formula	Initial Density
TNT 2,4,6 Trinitrotoluen	$C_7H_5N_3O_6$	$1.0 \pm 0.02$ ( $g/cm^3$ ) $1.2 \pm 0.02$ $1.4 \pm 0.02$ $1.51 \pm 0.01$
Tetryl N-Methyl-N,2,4,6-tetranitroaniline	$C_7H_5N_5O_8$	$1.0 \pm 0.02$ $1.2 \pm 0.02$ $1.4 \pm 0.02$ $1.61 \pm 0.01$ (cont. 1.0 wt.% graphite)
RDX Cyclotrimethylene trinitramine	$C_3H_6N_6O_6$	$1.0 \pm 0.02$ $1.2 \pm 0.02$ $1.4 \pm 0.02$ $1.66 \pm 0.01$ (cont. 5.4 wt.% wax)

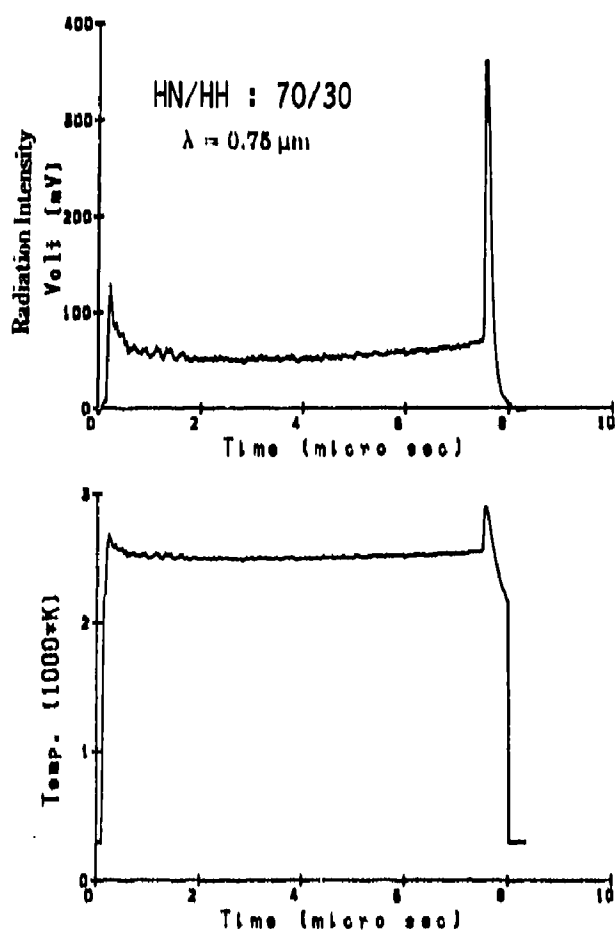


Figure 3. Typical Record of Temperature Measurements of Detonation in HN/HH Solution (HN/HH Mass Ratio: 70/30)

(HN/HH mass ratio: 70/30). It is shown that during the first 1  $\mu$ sec, the detonation wave was in an overdriven state, and afterward it propagated at a steady state (detonation velocity  $\sim 8200$  m/s). The detonation front interacted with the transparent anvil at about 7.5  $\mu$ s after initiation. The measured detonation front temperatures were  $2590 \pm 100$  K for four wavelengths. In the case of HN/HH solutions, very stable detonation waves were obtained in the HN mass ratio range of 55-75 percent. Figure 4 presents a typical record of temperature measurements of the HN/H<sub>2</sub>O solution (HN/H<sub>2</sub>O mass ratio: 85/15). After initiation, a steady detonation wave propagated, although localized failure waves were produced. These localized failure waves were observed in all HN/H<sub>2</sub>O solutions studied. Detonation failure occurred when the HN mass ratio became less than 75 percent in the case of HN/H<sub>2</sub>O solutions. For all HN/H<sub>2</sub>O and HN/HH solutions investigated, the measured detonation front temperatures showed no particular wavelength dependence within the accuracy of the measurements. The results indicate that the detonation products of H-N-O compositions provide high optical thickness and radiate as a blackbody.

The measured detonation front temperatures of HN/H<sub>2</sub>O and HN/HH solutions are summarized in Figure 5, and compared with CJ

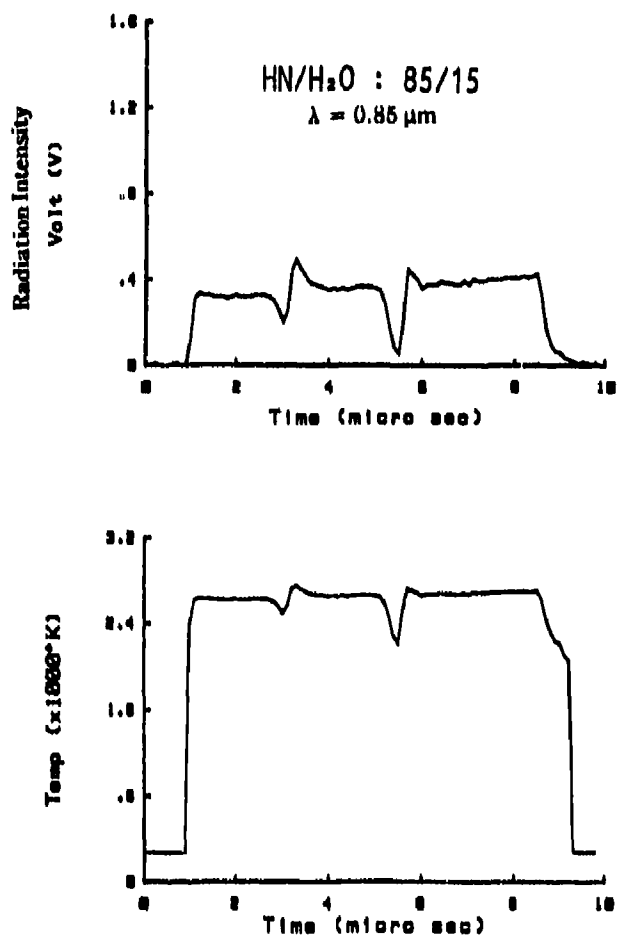


Figure 4. Typical Record of Temperature Measurements of Detonation in HN/H<sub>2</sub>O Solution (HN/H<sub>2</sub>O Mass Ratio: 85/15)

temperatures calculated using KHT equation of state. It is shown that the measured detonation front temperatures decrease linearly with the decrease of HN mass ratio. Good agreement between the measured detonation front temperatures and calculated CJ temperatures was obtained in the case of HN/HH solutions. However, a discrepancy of more than 1000 K was observed between the measured and calculated results in the case of HN/H<sub>2</sub>O solutions.

After the detonation front arrived at the transparent anvil, a reflected shock or rarefaction wave propagated into detonation products, due to the difference of shock impedance between the detonation products and the transparent anvil. For HN/H<sub>2</sub>O and HN/HH solutions investigated, the shock impedance of the detonation products is very

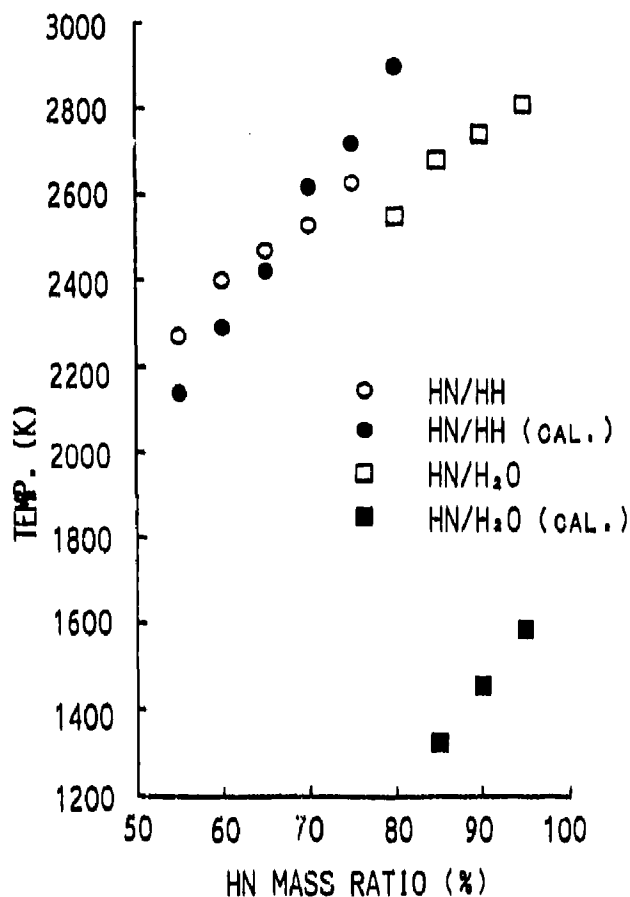


Figure 5. Summary of Measured and Calculated Detonation Front Temperatures of HN/H<sub>2</sub>O and HN/HH Solutions

close to that of pyrex glass.<sup>6</sup> In the case of HN/HH solutions, a temperature increase of more than 300 K was observed at all wavelengths after the interaction between detonation front and transparent anvil. It is impossible to explain such a high temperature increase by the effects of difference of shock impedance.

#### Detonation Temperature of TNT, Tetryl, and RDX

Figure 6 shows a typical record of temperature measurements of TNT (initial density 1.2 and 1.51 g/cm<sup>3</sup>). Because solid explosives are opaque, the four-color pyrometer begins to record the radiation emitted from the detonation wave when the detonation front approaches the transparent anvil. During the

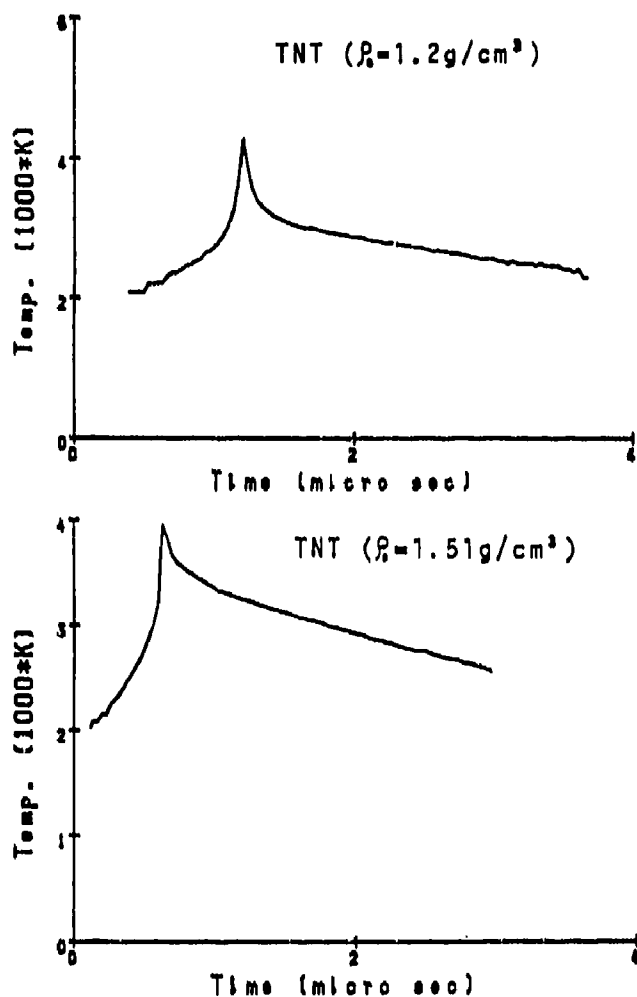


Figure 6. Typical Record of Temperature Measurements of TNT Detonation

first 0.2 - 0.5  $\mu$ s, radiation intensity increases exponentially with the decrease of radiation absorption by the unreacted explosive, and it attains its maximum when the detonation front interacts with the transparent anvil. The duration of this peak is less than 0.2  $\mu$ s. It is erroneous to deduce the detonation front temperature from this peak because of possible effects of voids contained in the heterogeneous solid explosives. After the interaction between detonation front and transparent anvil, the temperature of detonation products at the interface is measured, and it decreases gradually because of a Taylor wave behind the detonation front.

In the previous paper,<sup>5</sup> it was shown that the time variation of measured temperatures of detonation products of solid explosives

agrees with the results of numerical simulation by the 2DL hydrodynamic code using the KHT equation of state. From the comparison between the measured and calculated time variation of detonation products' temperatures, the detonation front temperature of solid explosives was evaluated. In this study, a similar procedure was applied to TNT, Tetryl, and RDX at different initial densities.

The time variations of measured detonation products' temperature of TNT are shown in Figure 7. Time variations of measured detonation products' temperature are very similar in the range of initial density investigated. For TNT at an initial density of 1.51 g/cm<sup>3</sup>, the measured temperature of detonation products are compared with calculated values. Good agreement was obtained between the measured and calculated results. The temperature of detonation products is slightly increased by reflected shock, because the shock impedance of pyrex glass is higher than that of detonation products of TNT. To verify the influences of the transparent anvil material, temperature measurements were obtained using pyrex glass, sapphire, and lithium fluoride (LiF) as an anvil, in the case of the Nitromethane. In the case of the sapphire and LiF anvil, a higher temperature increase by reflected shock was observed because of the higher shock impedance of these materials. However, the effect on the time variation of detonation products' temperature was negligibly small. From the time variation of measured detonation products' temperature, detonation front temperatures of TNT are determined. They are summarized in Figure 8. The measured detonation front temperatures of TNT decrease slightly with the decrease of initial density in the range of the initial density investigated. They are compared with CJ temperatures calculated using various types of equations of state (Figure 8). Good agreement was obtained between the measured detonation front temperatures and calculated CJ temperatures.

The time variations of measured detonation products' temperature of Tetryl and RDX are very similar to those of TNT. The measured detonation front temperatures of Tetryl and RDX are summarized in Figures 9 and 10.

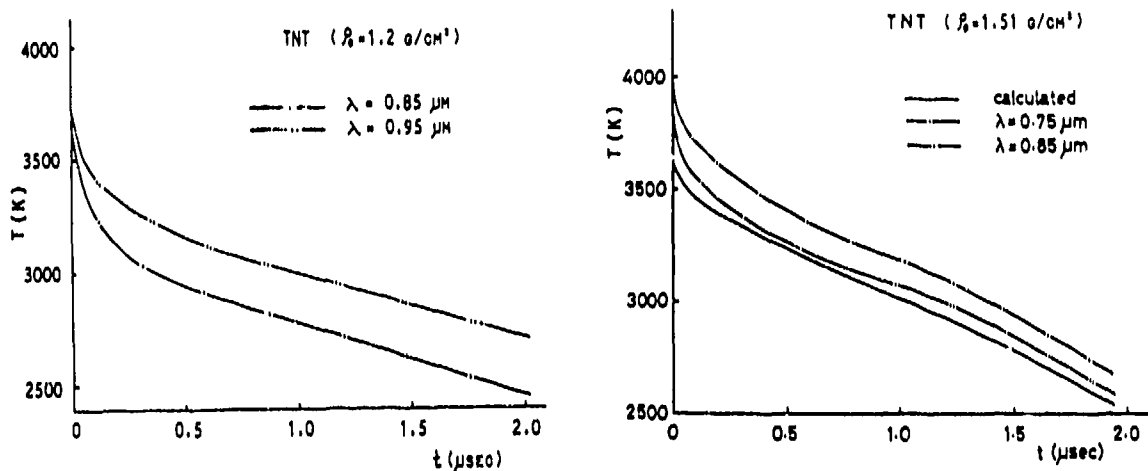


Figure 7. Time Variation of Detonation Products Temperature of TNT

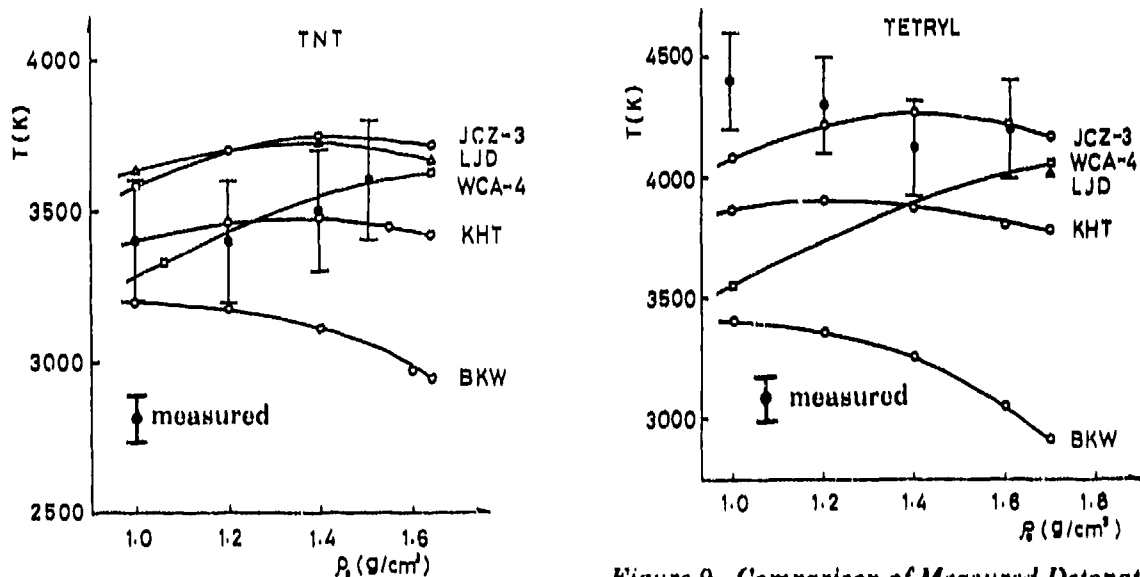


Figure 9. Comparison of Measured Detonation Front Temperatures and Calculated CJ Temperatures of Tetryl

Figure 8. Comparison of Measured Detonation Front Temperatures and Calculated CJ Temperatures of TNT

They are compared with CJ temperatures calculated using various types of equations of state (Figures 9 and 10). Good agreement was obtained between the measured detonation front temperatures and calculated CJ temperatures.

## CONCLUSIONS

Detonation front temperatures of HN/H<sub>2</sub>O and HN/HH solutions were measured

with a four-color pyrometer. The measured detonation front temperatures present no particular wavelength dependence within the accuracy of measurements. The results indicate that the detonation products of H-N-O composition radiate as a blackbody. Good agreement between the measured detonation front temperatures and CJ temperatures calculated using the KHT equation of state was obtained in the case of HN/HH solutions. However, a discrepancy of more than 1000 K was observed between the measured and

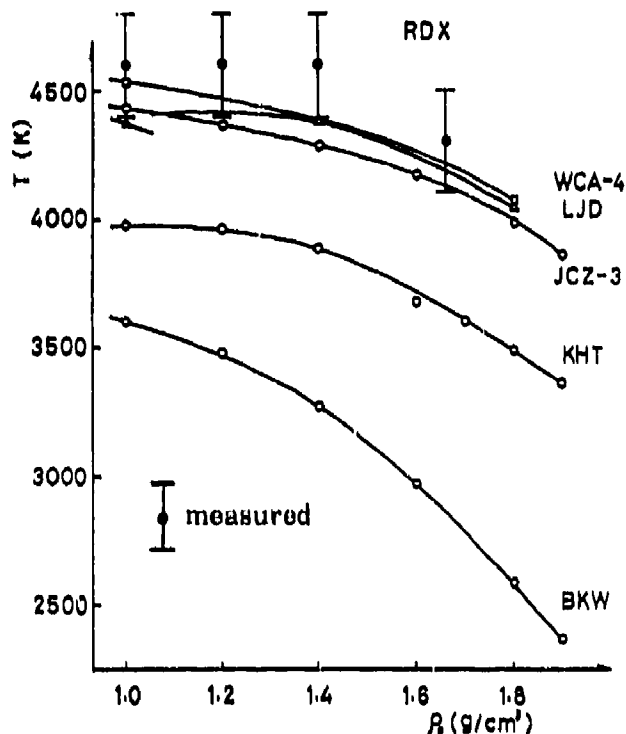


Figure 10. Comparison of Measured Detonation Front Temperatures and Calculated CJ Temperatures of RDX

calculated results in the case of HN/H<sub>2</sub>O solutions.

Detonation front temperatures of TNT, Tetryl, and RDX at various initial densities were measured with a four-color pyrometer. The measured detonation front temperatures of these solid explosives are almost constant within the accuracy of measurements, in the range of initial density investigated. The measured detonation front temperatures present good agreement with CJ temperatures calculated using various types of equations of state. The results indicate the capability of the optical technique to measure the detonation temperature of heterogeneous solid explosives at low initial density.

## REFERENCES

1. Urtiew, P. A., "Brightness Temperature of Detonation Wave in Liquid Explosives," *Acta Astronautica*, Vol. 3, 1976, pp. 555-566.

2. Burton, J. T. A.; Hawkins, S. J.; and Hooper, G., "Detonation Temperature of Some Liquid Explosives," *Proceedings of the Seventh Symposium (International) on Detonation*, NSWC, White Oak, MD, 1981, pp. 759-767.
3. Kato, Y.; Bouriannes, R.; and Brochet, C., "Mesure de Température de Luminance des Détonations d'Explosifs Transparents et Opaques," *Proceedings of H.D.P. Symposium*, CEA, Paris, 1978, pp. 439-449.
4. Kato, Y. and Brochet, C., "Detonation Temperatures of Nitromethane Aluminum Gels," *Dynamics of Shock Waves, Explosion and Detonations, Progress in Astronautics and Aeronautics*, 1985, pp. 416-426.
5. Kato, Y.; Mori, N.; Sakai, H.; Tanaka, J.; Sakurai, T.; and Hikita, T., "Detonation Temperature of Nitromethane and Some Solid High Explosives," *Proceedings of the Eighth Symposium (International) on Detonation*, NSWC, White Oak, MD, 1985, pp. 558-566.
6. LASL Shock Hugoniot Data, University of California Press, CA, 1983.

## DISCUSSION

J. A. MORGAN  
Los Alamos National Laboratory  
Los Alamos, NM

SiO<sub>2</sub> end window problem --

1. The anomalously high temperature seen at the end of the temperature measurement on transparent explosives may be due to emission of light from the pyrex end window. SiO<sub>2</sub> collapses into coesite and stishovite on compression. The volume change and, hence, the PΔV on compression is quite large. The accompanying temperature changes in the pyrex window may have become brighter than the temperature of the reflected shock in the detonation products, thus explaining the anomaly.
2. The graph showing temperature of detonation products in solid explosives

indicates different temperatures at different wavelengths. One possible explanation of this observation is that the optical density of the detonation products varies with wavelength, and their measurement is looking at differing regions of the reshocked detonation products.

### REPLY BY Y. KATO

1. CJ pressures of HN/HH and HN/H<sub>2</sub>O solutions are in the range of 16-25 GPa, and CJ states of these solutions are very close to shock Hugoniot of pyrex glass.<sup>1</sup> Pressure of shock compressed pyrex glass is estimated to be in the range of 16-25 GPa. According to reference 1, shock Hugoniot of pyrex glass is practically identical to that of fused quartz. Recently, shock properties of fused quartz, particularly radiation properties of shock compressed fused quartz were studied by several authors.<sup>2,3,4,5</sup> Calculated shock temperature and measured brightness temperature of fused quartz compressed to the pressure range of 16-25 GPa were respectively less than 2100K and 1800K,<sup>2,3,4</sup> and were much lower than measured detonation front temperatures of HN/HH and HN/H<sub>2</sub>O solutions. At the pressure below 25 GPa, radiation intensity from shock compressed fused quartz increases very gradually with time, which is characteristic of radiation from partially transparent materials.<sup>2,4</sup> The anomalously high temperature at the end of the temperature measurement was observed only in the case of HN/HH solutions, and it was not observed in the case of HN/H<sub>2</sub>O solutions. It is difficult to consider

that light emission from shock compressed pyrex glass is the cause of the anomalously high temperature seen at the end of the temperature measurement.

2. The precision of calibration of our pyrometer is  $\pm 100\text{K}$  at  $\sim 3400\text{K}$ . The measured temperatures do not present particular wavelength dependence. It is difficult to refer the observed temperature difference at different wavelength to the nature of the detonation products.

### REFERENCES TO REPLY

1. *LASA Shock Hugoniot Data*, University of California Press, CA, 1983.
2. Sugiura, H.; Kondo, K.; and Sawaoka, A., "Shock Temperatures in Fused Silica Measured by Optical Technique," *J. Appl. Phys.*, 53(6), Jun 1982, pp. 4512-4514.
3. Kondo, K. and Sawaoka, A., "Electrical Measurements on Fused Quartz under Shock Compression," *J. Appl. Phys.*, 52(8), Aug 1981, pp. 5084-5089.
4. Kondo, K.; Ahrens, T. J.; and Sawaoka, A., "Shock-Induced Radiation Spectra of Fused Quartz," *J. Appl. Phys.*, 54(8), Aug 1983, pp. 4382-4385.
5. Brannon, P. J.; Konrad, C. H.; Morris, R. W.; Jones, E. D.; and Asay, J. R., "Spectral and Spatial Studies of Shock-Induced Luminescence from Quartz," Sandia Report SAND82-2469, 1983.

# THE STUDYING OF DETONATION TEMPERATURES OF SOLID HIGH EXPLOSIVES

Shi Huisheng, Han Chengbang, Kang Shufang, and Huang Lihong  
Xian Modern Chemistry Research Institute  
Xian, CHINA

*Detonation temperatures of solid high explosives (TNT, Tetryl, PETN, RDX and HMX) have been determined. In order to estimate the accuracy of the results, the effects of density, impedance matching, and void gas on the temperature measurements were studied. The measured temperatures were compared with the calculated results using various types of equations of state.*

## INTRODUCTION

It is important to know the detonation temperature of solid high explosives in the study of high explosives. In practical applications, the knowledge of detonation temperature is helpful for us to predict and control the performance of explosives.

Currently, it is well-known that detonation characteristics can be predicted by using thermo-hydrodynamic computer codes with various types of equations of state for detonation products in practical applications. Detonation velocity and pressure are less dependent on the type of equation of state. Measurement of detonation temperature is very important; it can be taken as criteria to check the validity of equations of state. Unfortunately, there are few measured data on detonation temperature and no measurements of detonation temperature for many high explosives.

Recently, it has been proven that the measurements of detonation temperature by optical technique are a very useful means in detonation study. Initial attempts to measure detonation temperature of high explosives were made by Gibson et al<sup>1</sup> followed by several investigators.<sup>2-8</sup> However, in these studies the measurements were mainly limited to transparent liquid explosives or explosive mixtures, and the measured detonation front temperatures were referred to C-J

temperature according to the physical consideration.

Measurement of detonation temperature of solid explosives, which are essentially opaque and granular, is very difficult. In this study, the detonation temperatures of solid high explosives (TNT, Tetryl, PETN, RDX, and HMX) were determined using the optical technique. In addition, the effects of the charge density, impedance matching, and void gas on the temperature measurements were studied. In the end, the measured temperatures were compared to the calculated results using several equations of state.

## EXPERIMENT

Detonation temperature of solid high explosives was measured with a two-color pyrometer similar to that described in the previous work.<sup>9</sup>

The explosives we studied in the experiment were TNT, Tetryl, PETN, RDX, and HMX. The properties of these explosives are presented in Table 1. The pressed charges were made in two sizes: one was 20 mm in diameter by 20 mm length, and the other 30 mm in diameter by 30 mm length. Two or three pieces of these charges were assembled in a plastic tube 80 mm long, 20 mm (or 30 mm) in diameter, and 3 mm thick. Covering over samples with transparent

**Table 1. Properties of Solid High Explosives Studied**

Name	Formal	Composition
TNT	$C_7H_5N_3O_6$	
Tetryl	$C_7H_5N_5O_8$	
PETN	$C_5H_8N_4O_{12}$	
RDX	$C_3H_6N_6O_6$	5 wt. % wax
HMX	$C_4H_8N_8O_8$	5 wt. % wax

medium not only eliminated the influence of luminescence of airshock waves on the results, but also improved the impedance matching.

### RESULTS

Figure 1 presents typical records of temperature measurement of RDX. Because solid explosives are opaque, the two-color pyrometer begins to record the radiation emitted from the detonation wave when the detonation front approaches the transparent medium. During the first 0.2  $\mu$ sec., radiation intensity increases exponentially as radiation absorption by unreacted explosives decreases, and radiation attains its maximum. The duration of this peak is less than 0.1  $\mu$ sec. Thus the time history of measured temperature of detonation products is recorded.



10 mv/div      10 mv/div  
 0.1  $\mu$ s/div    0.1  $\mu$ s/div  
 6940 Å          4880 Å

**Figure 1. Typical Record of Temperature Measurement of RDX Detonation**

### EFFECT OF CHARGE DENSITY ON THE TEMPERATURE MEASUREMENT

The detonation temperatures of several densities of explosives in Table 1 have been determined. Figure 2 shows the results of different densities of PETN. In the experiment, we prepared PETN charges with densities of  $\rho_1 = 1.62 \pm 0.01$  g/cm<sup>3</sup>,  $\rho_2 = 1.66 \pm 0.01$  g/cm<sup>3</sup>,  $\rho_3 = 1.71 \pm 0.01$  g/cm<sup>3</sup>, and  $\rho_4 = 1.78$  g/cm<sup>3</sup>, respectively. We observed the time histories of measured temperature of detonation products. In Figure 2, curves 1, 2, 3, and 4 represent the relations between temperature and time at different densities of  $\rho_1$ ,  $\rho_2$ ,  $\rho_3$ , and crystal density.

In Figure 2, it is also shown that with the increase in density, there is a drop in temperature, approaching the detonation temperature of the crystal.

### THE EFFECT OF IMPEDANCE MATCHING ON THE TEMPERATURE MEASUREMENT

Because most solid explosives are not transparent, we can only determine the brightness of radiant light at the moment it radiates out from the end of the detonating charge. Thus, the reflection of a detonation wave at an interface will change the pressure of detonation product, causing the temperature determined not to correspond to the

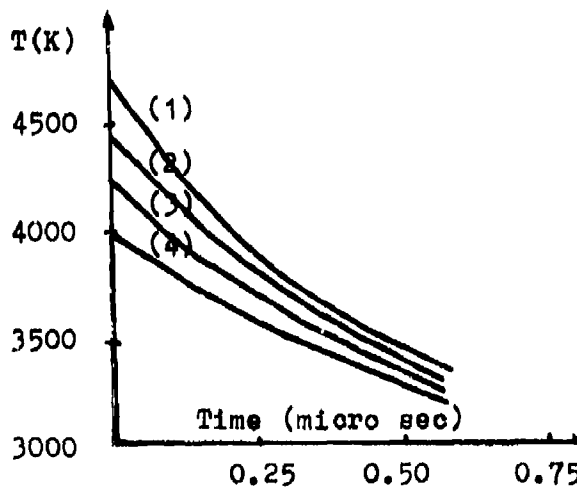


**Figure 2. Time History of Measured Temperature of Detonation Products of PETN**

true detonation temperature. In order to evaluate the effect, we have tested different transparent mediums of different impedance, such as water and bromoform, etc. With a density of  $\rho_0 = 1.64 \pm 0.01$  g/cm, the impedance matching of Tetryl is equal to that of bromoform ( $\rho_m = 2.89$  g/cm<sup>3</sup>):

$$\eta = \frac{\rho_0 D}{\rho_m U} = 1 \pm 0.01 \quad (1)$$

where,  $\rho_0 D$  is the density and detonation velocity of Tetryl, and  $\rho_m U$  is the density and shock velocity of bromoform. The results are shown in Figure 3.

In addition, with HMX of the density of  $\rho_0 = 1.70 \pm 0.01$  g/cm, water, glass, and plexiglass have been tested. The results are shown in Table 2.

In Figure 3 and Table 2, it is shown that if the voidage in an adjacent charge is less, there is no apparent effect on the measured detonation temperature, the data variation being within experimental error. For convenience, from then on, we only used water as the charge closing medium.

### THE EFFECT OF VOID GASES ON THE TEMPERATURE MEASUREMENT

The experimental work had been finished by our pioneer He Xianchu et al.<sup>9</sup>

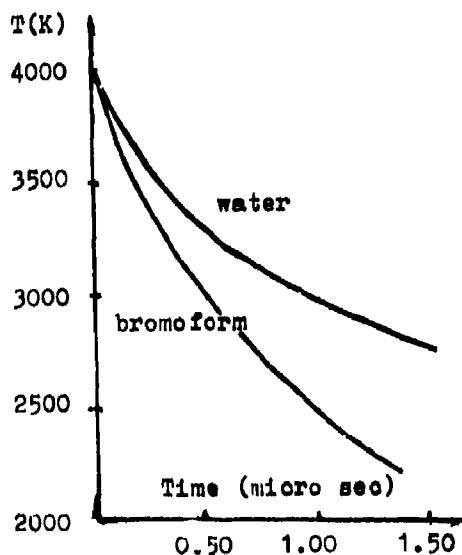


Figure 3. Time History of Measured Temperature of Tetryl

Table 2. The Detonation Front Temperature of HMX ( $\rho_0 = 1.70 + 0.01$  g/cm) in Contact with Different Transparent Medium

Charge Number	Medium	Front Temperature (K)	Average (K)
0927-3	Glass	2670	2700
0927-4	Glass	2660	
0929-1	Glass	2780	
1007-1	water	2550	2560
0929-5	water	2560	
1011-2	Plexiglass	2750	2690
1011-3	Plexiglass	2800	
0927-1	Plexiglass	2720	
0927-2	Plexiglass	2690	

Through treating these experimental results, the measured temperatures of detonation products of a TNT charge with density of  $\rho_0 = 1.61 \pm 0.01$  g/cm<sup>3</sup> and Tetryl with density of  $\rho_0 = 1.70 \pm 0.01$  g/cm<sup>3</sup> are shown in Figures 4 and 5.

In these figures, it is shown that if the voidage in the charge is less—in other words, the charge density is higher—the results are less different than each other in the low density.<sup>9</sup> It is also shown that while high density charges of TNT and Tetryl treated by vacuumization are detonating, the fluctuation of measured temperature of detonation products can be observed. This fluctuation

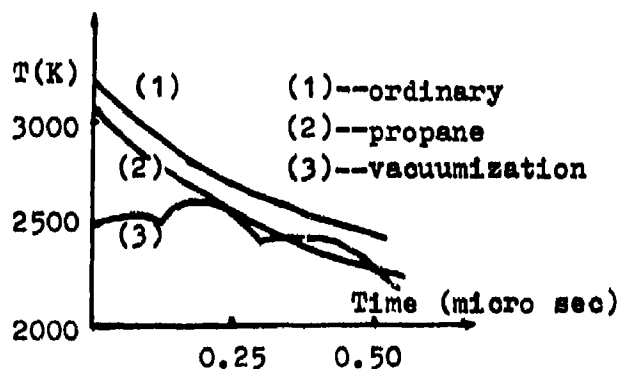


Figure 4. Time History of Measured Temperature of Detonation Products of TNT Treated with Different Methods

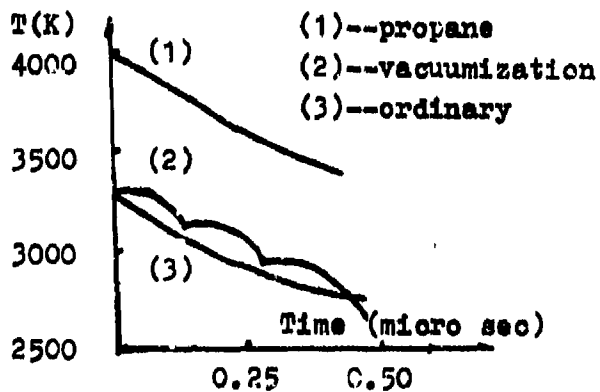


Figure 5. Time History of Measured Temperature of Detonation Products of Tetryl Treated with Different Methods

disappeared gradually as the charge densities decreased.

#### Compared Measured Temperature with the Calculated Result<sup>10,11</sup>

The temperature of detonation products of some solid high explosives (TNT, Tetryl, PETN, RDX, and HMX) was measured with a two-color pyrometer. Through treating these experimental results, detonation front temperatures of TNT charges with densities of  $\rho_1 = 1.50 \pm 0.01 \text{ g/cm}^3$ ,  $\rho_2 = 1.56 \pm 0.01 \text{ g/cm}^3$ , and  $\rho_3 = 1.61 \pm 0.01 \text{ g/cm}^3$ , were determined to be  $3700 \pm 100 \text{ K}$ ,  $3400 \pm 100 \text{ K}$ , and  $3000 \pm 100 \text{ K}$ , respectively. They are compared with the C-J temperatures calculated using various types of equations of state in Figure 6. The difference between these results and the results in Reference 9 were within 5 percent.

From the history of time of the measured temperature of detonation products, detonation front temperatures of Tetryl charges with densities of  $\rho_1 = 1.55 \pm 0.01 \text{ g/cm}^3$ ,  $\rho_2 = 1.62 \pm 0.01 \text{ g/cm}^3$ , and  $\rho_3 = 1.69 \pm 0.01 \text{ g/cm}^3$ , are determined to be  $4200 \pm 150 \text{ K}$ ,  $4000 \pm 150 \text{ K}$ , and  $3200 \pm 100 \text{ K}$ , respectively. They are compared with the C-J temperatures calculated with various types of equations of state in Figure 7.

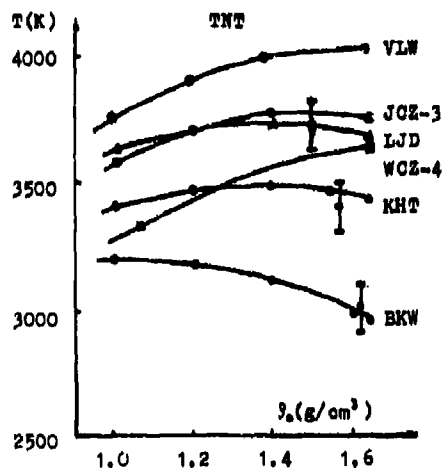


Figure 6. Comparison of Measured Detonation Front Temperature and Calculated C-J Temperature of TNT

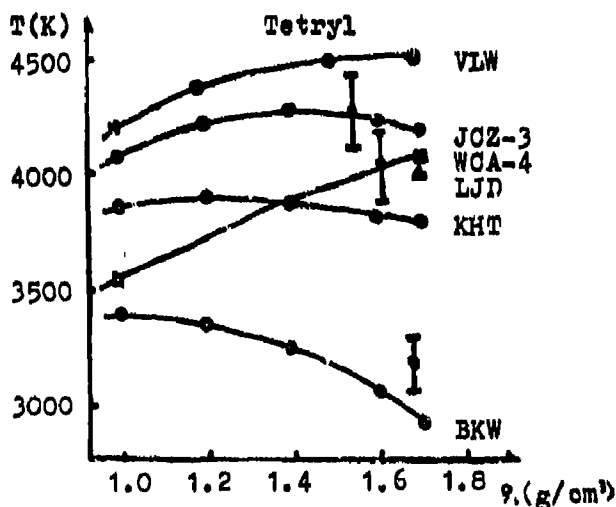


Figure 7. Comparison of Measured Detonation Front Temperature of Tetryl and Calculated C-J Temperature of Tetryl

Similarly, detonation front temperatures of PETN, RDX, and HMX have been determined. These results are compared with the C-J temperatures calculated using various types of equations of state in Figures 8, 9, and 10, respectively.

## SUMMARY

The detonation temperatures of some solid high explosives have been determined with a transient optical electrical two-color pyrometer. In order to estimate the accuracy

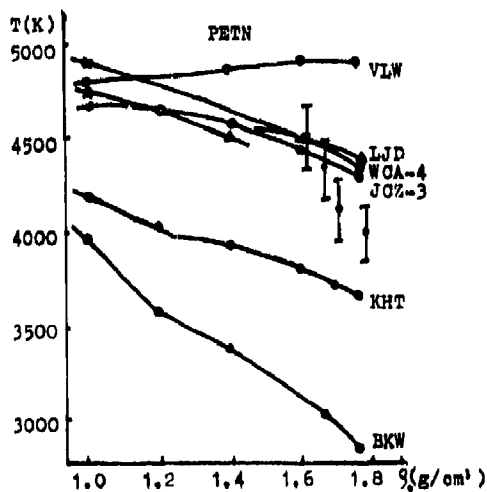


Figure 8. Comparison of Measured Detonation Front Temperature and Calculated C-J Temperature of PETN

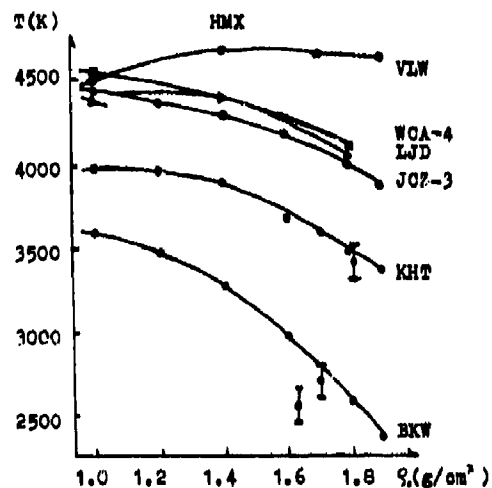


Figure 10. Comparison of Measured Detonation Front Temperature and Calculated C-J Temperature of HMX

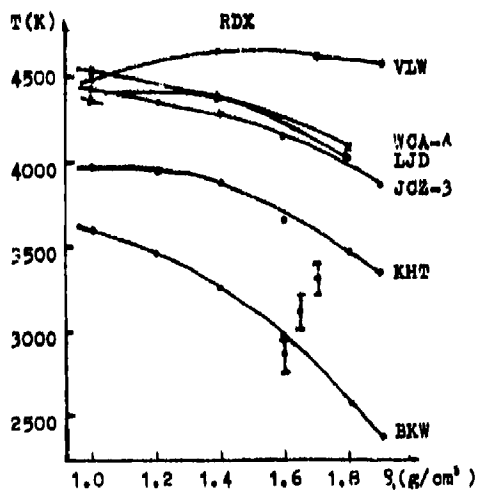


Figure 9. Comparison of Measured Detonation Front Temperature and Calculated C-J Temperature of RDX

of results, the effects of density, impedance matching, and void gas on the temperature measurements were studied.

Because of the influence of void gases, effect of materials at the explosive end face on the measured temperature, and other factors, it was difficult to measure front temperature of explosive products accurately. There were many experimental errors in our work. Currently, we are still facing some questions. First, does the radiant nature of the detonation front of solid explosives conform to

that of a black body or a grey body? Secondly, being under high density and shock pressure, how much does the change of transparent medium characteristics at the front of the shock wave affect the reception and conduction of the radiant light of high explosives detonation? Thirdly, does the method of end measurement truly reflect the detonation temperature of solid high explosives? These questions should be further studied.

## REFERENCES

1. Gibson, F. C.; Bowser, C. R.; Summers, C. R.; Scott, F. H.; and Mason, C. M., "Use of an Electro-optical Method to Determine Detonation Temperatures in High Explosives," *J. Appl. Phys.*, Vol. 29, No. 4, 1958, pp. 628-632.
2. Voskoboynikov, I. M. and Apin, A. Y., "Measurement of Detonation Front Temperature for Explosives," *Dokl. Akad. Nauk USSR*, Vol. 130, No. 4, 1960, pp. 804-806.
3. Davis, W. C. and Mader, C. L., Los Alamos Sci. Lab. Report LA-2712, 1962.
4. Dremin, A. N. and Savrov, S. D., "Emission Spectrum of a Detonation Wave in Nitromethane," *Z.P.M.T.F.*, No. 1, 1965, pp. 103-105.

5. Trofimov, V. S. and Trojan, A. V., "Detonation Luminescence Spectrum of Nitromethane," *Fiz. Gor. I. Vary.*, Vol. 5, No. 2, 1969, pp. 280-282.
6. Burton, J. G. A.; Hawkins, S. J.; and Hooper, G., "Detonation Temperature of Some Liquid Explosives," *Proceedings of the Seventh Symposium (International) on Detonation*, NSWC, White Oak, MD, 1983, pp. 759-767.
7. Urtiew, P. A., "Brightness Temperature of Detonation Waves in Liquid Explosives," *Acta Astronautica*, Vol. 3, 1976, pp. 555-566.
8. Kato, Y.; Bauer, P.; Brochet, C.; and Bourianne, "Brightness Temperature of Detonation Waves in Nitromethane-Tetranitromethane Mixtures and in Gaseous Mixtures at High Initial Pressure," *Proceedings of the Seventh Symposium (International) on Detonation*, NSWC, White Oak, MD, 1983, pp. 768-774.
9. He Xianchu, Han Chengbang, and Kang Shufang, "The Measurement of Detonation Temperature of Condensed Explosives with Two-color Optical Fibre Pyrometer," *Proceedings of the Eighth Symposium (International) on Detonation*, 1985, pp. 322-329.
10. Kato, Y.; Mori, N.; Sakai, H.; Tanaka, K.; Sakurai, T.; and Hikita, T., "Detonation Temperature of Nitromethane and Some Solid High Explosives," *Proceedings of the Eighth Symposium (International) on Detonation*, 1985, pp. 314-321.
11. Wu Xiong, Modern Chemistry Research Institute, Xian, China, private communication, Jul, 1988.

# FREE-EXPANSION EXPERIMENTS AND MODELING IN DETONATION: CHEMISTRY AND HYDRODYNAMICS ON A LABORATORY SCALE

N. Roy Greiner and Normand Blais  
Chemical and Laser Sciences Division  
Los Alamos National Laboratory  
Los Alamos, New Mexico 87545

*Laboratory-scale (25-50 mg) detonations of PETN, RDX, HNS, and TNT have been carried out in a high-vacuum chamber, and collisionless molecular beams of the freely expanding detonation products have been analyzed as a function of time with a mass spectrometer. Concurrently, time-sequenced schlieren and shadowgraph images of the initial expansion of the product plume are recorded using a pulsed laser for illumination. These data tie the chemistry and hydrodynamics of the detonation event together. The results, interpreted with the aid of a computer model, suggest that this experiment freezes the chemical reactions of detonation by rapid adiabatic cooling and provides a continuum of samples in the molecular beam, representing the sequence of reactions in the detonating charge. With a suitable model of the expansion hydrodynamics, the hydrodynamic histories of a sequence of volume elements can be associated with their frozen chemistries. We expect experiments like this to provide a test for molecular models of detonation.*

## INTRODUCTION

Chemical reactions drive detonation through several measurable processes. Among these are shock (hot-spot) initiation, run-to-detonation, reaction zone chemistry, and reactions during product expansion. Insofar as these processes are measurable, they deviate from the assumption of instant equilibrium and affect the process of detonation. Yet, we know almost no details of these important chemical processes, which, with hydrodynamics, form the basis of detonation science and engineering. Although molecular quantum mechanics is making contributions to low-pressure combustion science, it does not assist effectively in understanding detonation because the molecular detail necessary to test and challenge theory under detonation conditions (up to  $10^6$  atm and 5000 K) is lacking from detonation experiments. The work we describe here provides a look at detonation processes in the molecular detail necessary to

link molecular quantum mechanics to detonation science. Further development and modeling of these experiments appear to have potential as a laboratory-scale test for high explosives that simultaneously measures several aspects of sensitivity, performance, and chemistry. Numerous publications of this work have already appeared.<sup>1-6</sup> This paper will be an overview of the main features of the progress made to date.

## EXPERIMENTAL RESULTS AND DISCUSSION

We have reported some experimental data identifying the major reaction products of some common solid explosives, such as HNS,<sup>1</sup> PETN,<sup>4</sup> and RDX.<sup>5</sup> Here we report additional data on these explosives and new data on TNT. Almost all of the studies were conducted with laboratory-scale explosive charges of 25-50 mg, and all were reasonably "pure" detonator-grade explosives without plastic binders. They

were detonated in a vacuum chamber using only slappers, except for TNT, which required a PETN booster charge of about 10 mg. The apparatus used to make the measurements has been described previously in some detail,<sup>1,4</sup> but briefly can be described as a vacuum chamber with dimensions and operating conditions that permit the free expansion of the detonation products to occur without any collisions other than intermolecular collisions between the products themselves. That is, this method samples the detonation products without reshock. A skimmer admits a collisionless molecular beam of the expanding products to a mass spectrometer where the abundance of a chosen molecular mass is measured as a function of time. By interpreting our experimental

data with computer models, we find that some of the products we observe represent conditions that occurred less than a fraction of a microsecond after the detonation wave passed through the explosive charge. For some explosives such as TNT and HNS, these products are probably characteristic of the reaction zone conditions.

Figure 1 shows composite time-integrated spectra from the explosives PETN, RDX, HNS, and TNT. The most striking characteristic of these spectra is that, in all four cases, they differ enormously from the spectra expected from complete reaction of the explosive. For example, Figure 2 shows the reconstructed spectra of the products observed in a detonation calorimeter from these same explosives.<sup>7</sup>

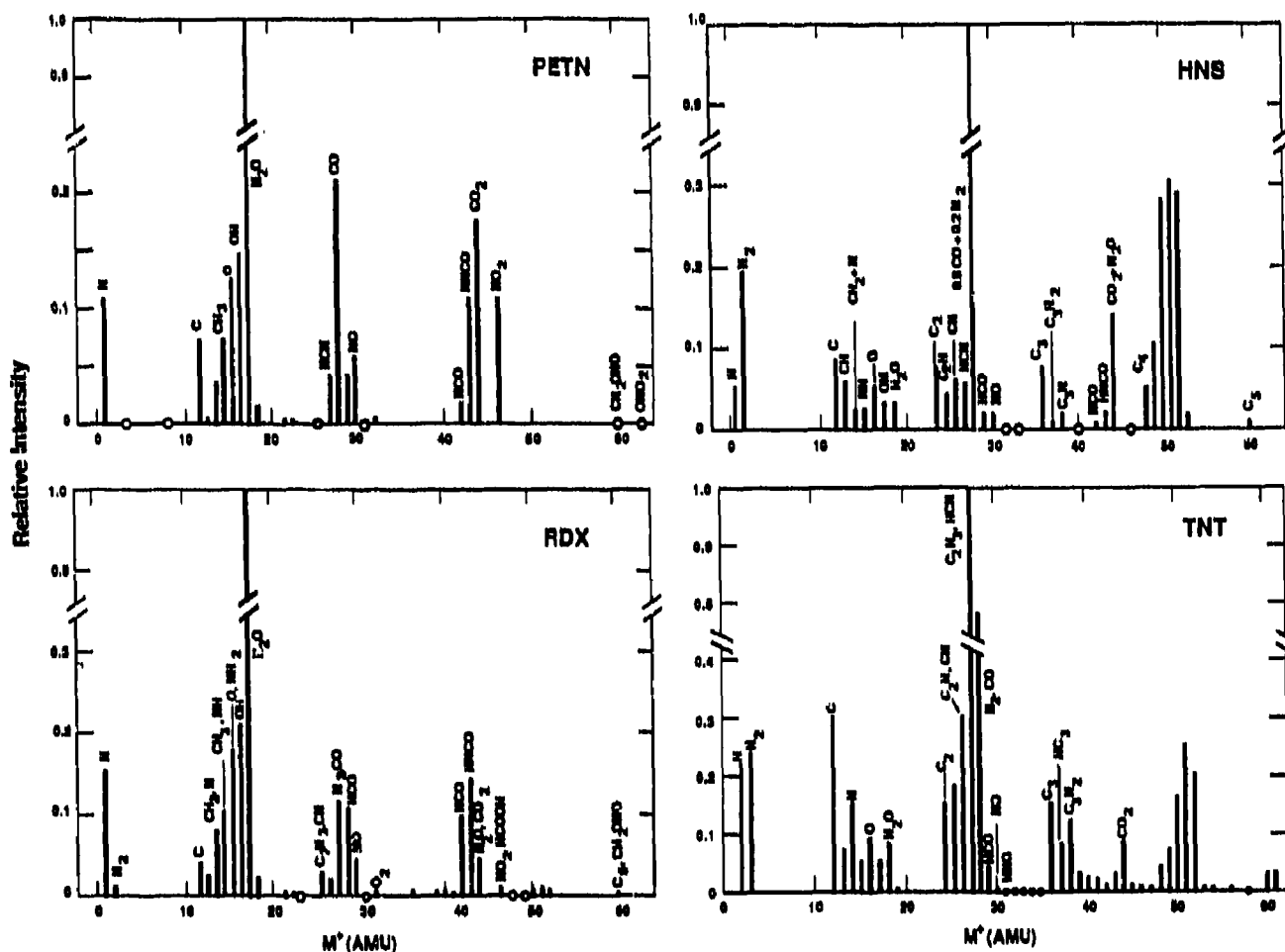


Figure 1. The Time-Integrated Spectrum from the Freely Expanding Detonation Products of PETN, RDX, HNS, and TNT. In each spectrum mass peaks are labeled with possible parent or fragment ions. These spectra from rapidly quenched detonations can be compared to those expected from slowly quenched detonations shown in Figure 2.

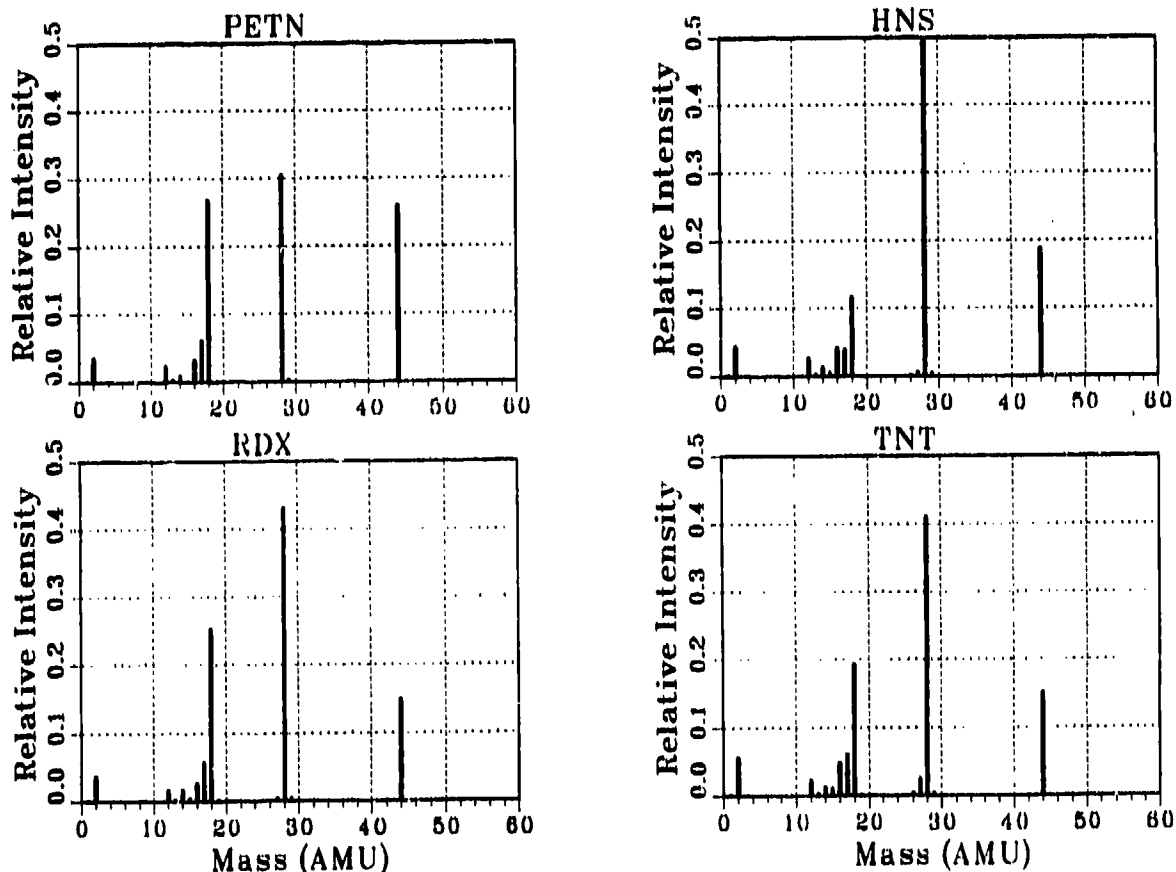


Figure 2. Reconstructed Spectra of the Detonation Products Observed from Slow Quenching in a Detonation Calorimeter.<sup>7</sup> The products are approximately the distribution expected from the BKW equation of state and a freeze-out temperature of 2000-2500 K.

The calorimeter detonations were confined inside a gold pipe, so those products expanded slowly, and are believed to represent typical detonation products quenched by freeze-out in the vicinity of 2300 K. On the other hand, the free-expansion spectra presented here show many more components and a markedly different distribution of the expected equilibrium products,  $H_2O$ ,  $CO_2$ ,  $CO$ , and  $H_2$ . A possible explanation is that the free expansions are much more rapid (see Modeling), freezing out a variety of reaction intermediates from incomplete reactions. These intermediates might be stable molecules or even free radicals. It is startling to note that the explosives appear to detonate, but the products observed are not the expected final products. If this is true, a process closely resembling detonation can

occur without the expected complete reaction! Mechanisms of detonation at the molecular level will have to take into account results like these.

Other comparisons are also interesting. HNS and TNT are oxygen-poor explosives that produce lots of soot in the products,<sup>7,8</sup> whereas PETN and RDX have a higher oxygen balance. It is evident that the oxygen-poor explosives have spectra that are similar to each other. Similarly, RDX and PETN have spectra that are much alike but differ considerably from the two oxygen-poor explosives. There were no significant product intensities at masses larger than 60 mass units, where some effort was made to find larger clusters of soot or mass peaks of unburned explosives.

Time-resolved schlieren and shadowgraph images of the first 35 mm of the detonation product expansion have been recorded for several of the explosives. These data give a useful view of the initial stages of the expansion dynamics, such as profiles of expansion-front velocity and density, which can be compared with schlieren images derived from our computer model described below.<sup>3,9</sup> These time-resolved images are closely related to the product equation of state, the detonation velocity, and the progression of the detonation front through the explosive pellet. Some information about slow chemical processes, such as soot formation, may be obtainable by comparing simultaneous schlieren and shadowgraph images of the expanding charge.

## MODELING

A common question is whether the small charges we study, particularly of the less sensitive explosives, are really detonating. The schlieren and shadowgraph photography and the modeling of the early expansion now give us independent information to assess whether they are detonating or not. The images for PETN, RDX, and HNS indicate that the early rapid acceleration of the products, the product velocities, and the product density profiles are as expected from detonations, and the experimental images agree with images computed with the KIVA code using the equation of state (BKW) of the expected detonation products.<sup>3</sup> The expansion-front velocity profiles computed by KIVA also match the velocities observed experimentally. Under free-expansion conditions, the expansion front is expected to have a velocity equal to the local particle velocity plus the sound velocity in the medium if gamma is equal to 3, as it is, approximately, for many explosives of interest. The expansion front velocity under these conditions is also equal to the detonation velocity, a fundamental performance parameter for an explosive. Further work on this result is being done to extend this concept to conditions where gamma may differ from 3.

The molecular density as a function of arrival time measured at the mass filter also agrees quite well in several respects with KIVA computations. A density-vs-time curve

is recorded for each mass, then a time-resolved spectrum is obtained by plotting density-vs-mass for each 10  $\mu$ s time interval (Figures 3 and 4). The composition recorded for each 10- $\mu$ s time period corresponds to a particular volume element on the axis of the charge, identifiable by the hydrodynamic model and the equation of state used in the KIVA calculation. A mass spectrum of the material coming from each volume element can then be constructed by assembling the mass filter data for the corresponding time period from individual shots with the filter tuned for each mass in the spectrum. A hydrodynamic history (density, temperature, and other properties vs time, Figure 5) can be computed for each volume element sampled (approximately 0.02 mm in the charge corresponds to the 10- $\mu$ s sampling time at the mass spectrometer) so that the time-sequenced chemical analyses associated with that volume element can be interpreted kinetically. The chemical data (Figures 3 and 4) can then be used to test reaction mechanisms and rate parameters derived from quantum mechanical reaction dynamics calculations.

In addition to the quenching process, the free expansion affords another valuable advantage. Material in a layer 0.020 mm thick in the detonating charge experiences the passage of the detonation wave (moving at 8 km/s) in 2.5 ns. Detailed results from our model<sup>10</sup> show that after expansion this same layer will take about 10 microseconds to transit the sampling point in the mass spectrometer. Thus, the technique affords us a "time lever," so that the characterization of events that differ in time during the detonation process only by a few nanoseconds can be accomplished at the mass spectrometer during the leisurely time period of ten microseconds. Material deeper below the charge surface experiences the detonation wave earlier and therefore has a longer time to react before the expansion wave reaches it and quenching begins. Its quenching history also lasts longer, because it expands more slowly while it pushes material nearer the surface out of the way. The expansion model allows us to map progressively later arrival times at the mass spectrometer to correspondingly deeper layers in the charge, so we have a series of

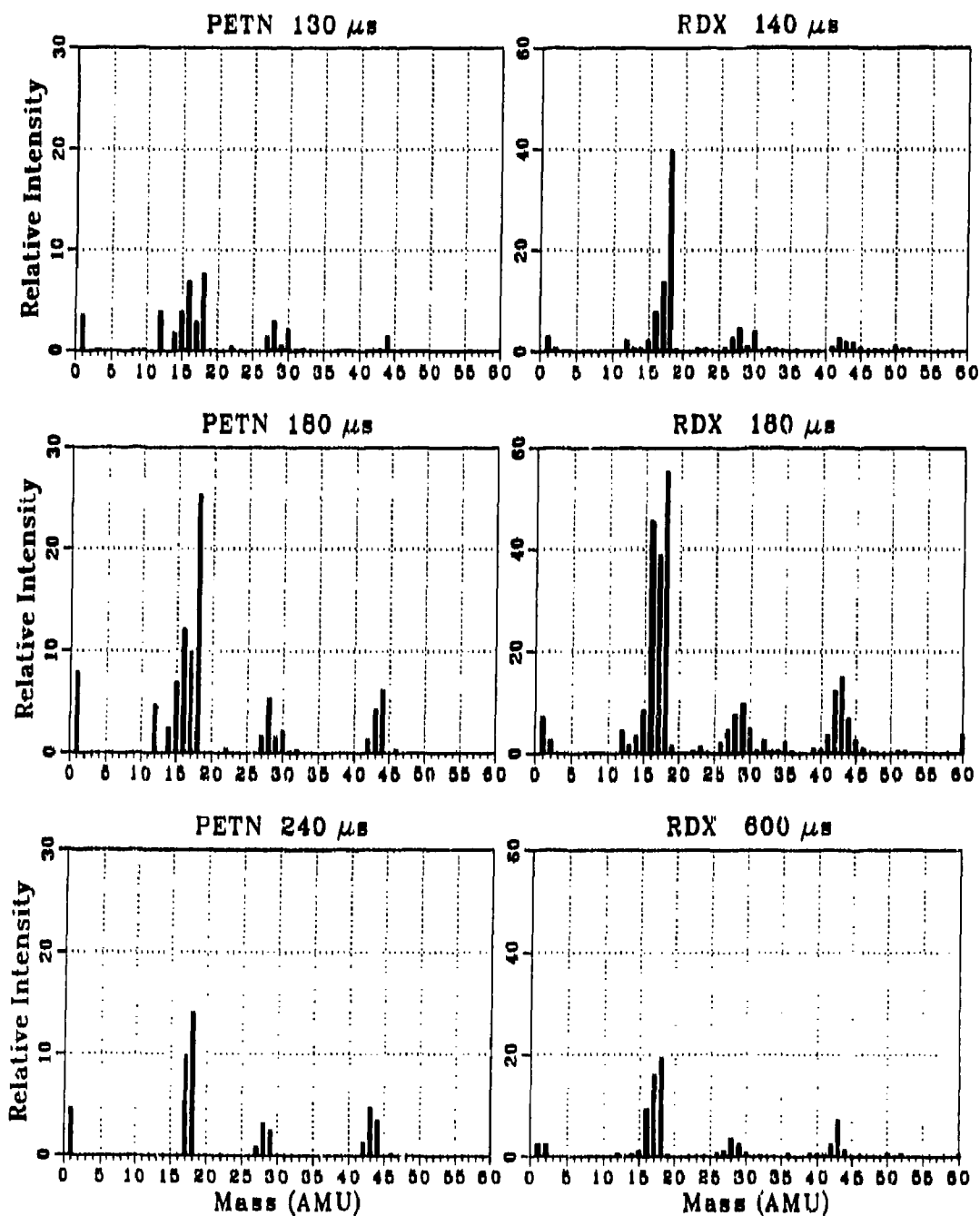


Figure 3. Time-Resolved Spectra of the Expanding Products from the Detonation of PETN and RDX in a High Vacuum. For example, with PETN the indicated times of arrival at the mass spectrometer can be mapped approximately to corresponding depths in the initial charge (measured from the charge surface nearest the spectrometer) as follows: 130  $\mu$ s (0.04 mm), 180  $\mu$ s (0.10 mm), and 240  $\mu$ s (0.20 mm). The 10- $\mu$ s time resolution of the mass spectra corresponds to 0.02 mm in the charge, and this number divided by the detonation velocity of 8 mm/ $\mu$ s gives a time resolution of 2.5 ns in the detonating charge. The PETN product wave arriving at the mass spectrometer peaks at 165  $\mu$ s and that of RDX at 200  $\mu$ s. These peaking times are shorter than those of HNS and TNT in Figure 4.

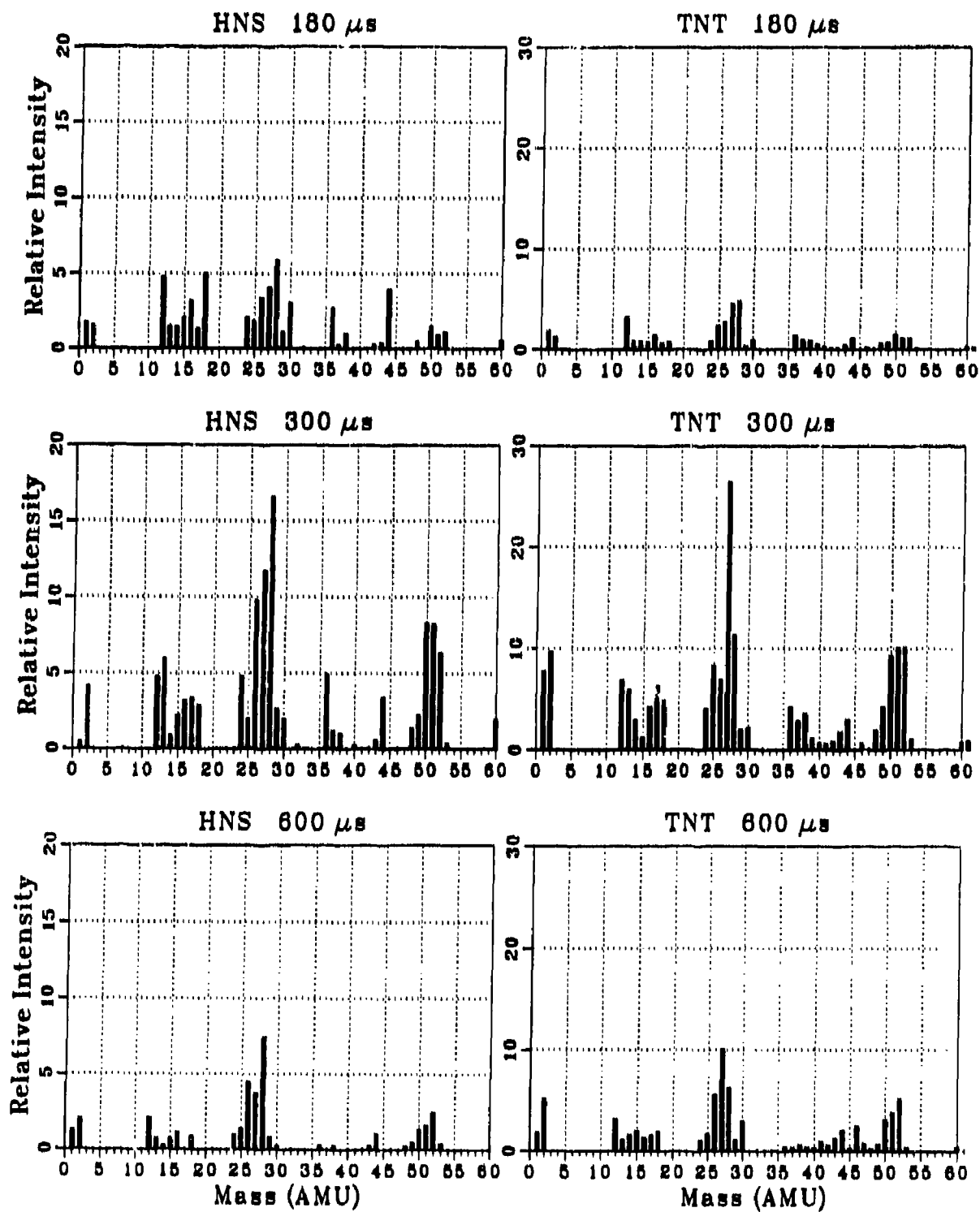


Figure 4. Time-Resolved Spectra of the Expanding Products from the Detonation of HNS and TNT in a High Vacuum. The arrival time of the peak for the products from HNS is 300  $\mu\text{s}$ , and that of TNT is 325  $\mu\text{s}$ .

### CYLW03 CELL(I= 1,K=20)

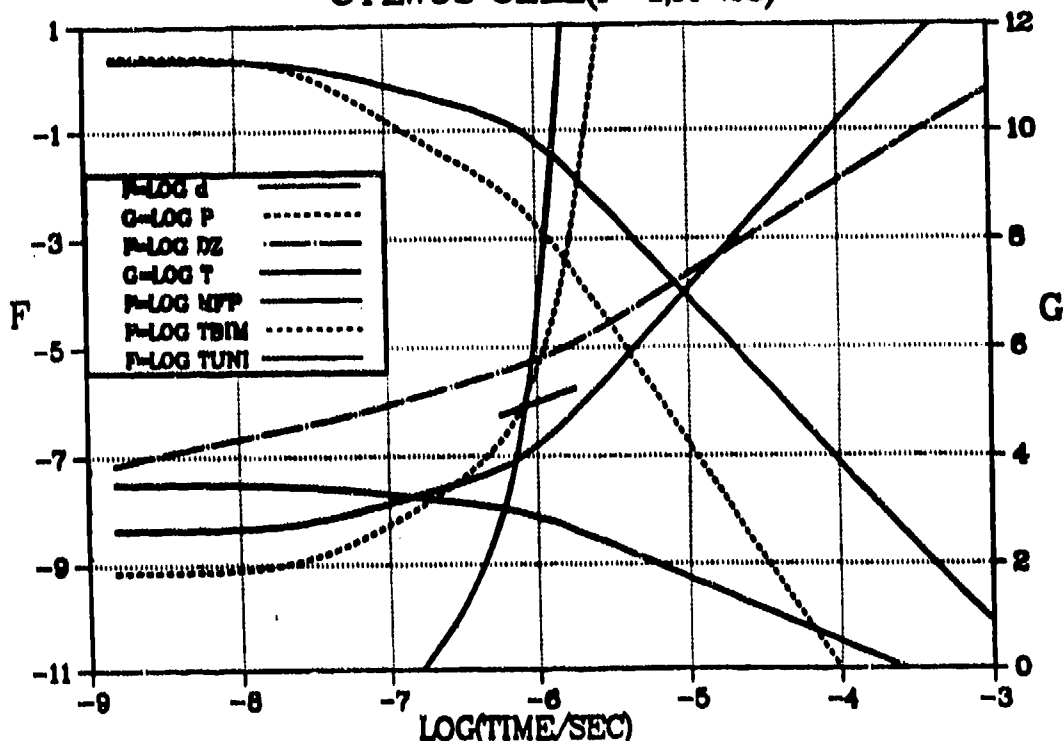


Figure 5. Hydrodynamic History Calculated by KIVA for Cell (1,20) of a 3-mm-diam x 3-mm-high Charge of PETN with an Initial Density of  $1.67 \text{ g/cm}^3$ . This cell is on the charge-skimmer axis and is the first layer (0.15 mm thick) to expand into the vacuum. Units of the parameters are cm-g-sec-k units.  $D$  = density,  $P$  = pressure,  $DZ$  = mean diffusion distance,  $T$  = temperature,  $MFP$  = mean free path,  $TBIM$  = reaction time for a bimolecular reaction ( $A = 10^{12} \text{ cm}^3 \text{ mol}^{-1} \text{ S}^{-1}$  and  $E = 10\,000 \text{ cal mol}^{-1}$ ),  $TUNI$  = reaction time for a unimolecular reaction ( $A = 10^{16} \text{ S}^{-1}$  and  $E = 40\,000 \text{ cal mol}^{-1}$ ). The partial line cutting the last two curves indicates the point of quenching.

mass spectra that are assignable to contiguous volume elements, each experiencing the arrival of the detonation wave at times progressively later by only 2.5 nanoseconds. Deeper volume elements experience the detonation wave earlier, so they cook longer before quenching and expansion. The latest arrival time recorded in these experiments (1000 microseconds) corresponds to a layer 0.65 mm deep in the charge and 0.006 mm thick, which experienced the detonation wave about 180 ns before the release wave reached it and quenching began. This depth encompasses typical reaction zones and part of the Taylor wave. Characterization of slower chemical events far behind the detonation wave would

require larger charges or greater confinement than we report here.

We expect that, as the detonation wave reaches the outer surface of the explosive, small jets form between the particles of the pressed powder making up the charge. The jets come from the collapse of void volumes exposed directly to the vacuum, and they would be of lower density, higher velocity, and higher temperature compared to the bulk material. These are conditions that might favor ion formation and longer molecular mean-free-paths (see  $MFP$  in the bulk material, Figure 5), possibly resulting in some mass differentiation, as reported by Lundborg<sup>12</sup> and Hay, et al.,<sup>11</sup> who

visualize this region as "a lamina of infinitesimal thickness." We picture the collapsing void volumes (similar to hot spots deeper inside the charge) as being about a particle diameter deep with an area exposed to the vacuum amounting to a small fraction of the bulk surface area, depending on the void fraction in the explosive charge. We sometimes observe, prior to the rapidly rising front of our product wave, a precursor (barely detectable by our mass spectrometer) that may correspond to the high-velocity material reported by Lundborg<sup>12</sup> and Hay et al.<sup>11</sup> However, the material that we identify with layers of the reaction zone, and which arrives just after the precursor, appears to be undifferentiated by mass in our experiments.

Another process under investigation is solid-phase carbon formation. The Shaw-Johnson (SJ) diffusion model<sup>13</sup> can be incorporated into KIVA to give estimates of the progress of that process as a function of time and position in the charge. The schlieren and shadowgraph images recorded for HNS detonations appear to give evidence for solid particle formation early in the product expansion. After a small amount of expansion, PETN and RDX become and remain transparent to the laser light used to record the shadowgraph images, but, in the case of HNS, within about a microsecond the product plume again becomes opaque, suggesting the formation of light-scattering material in the products. The KIVA code is being modified to compute particle-growth kinetics from the SJ model and light scattering by the resulting particles for comparison with the time-sequenced experimental images.

In addition to the interpretation of experimental results, the modeling with KIVA is being used to refine experimental configurations and to design improved apparatus and instrumentation.

## CONCLUSIONS

These results are revealing the details of a new chemical dimension in detonation science. Experiments with real, not surrogate, explosives are providing provocative new data on the basic chemical processes underlying sensitivity and reactivity in high explosives. It

is expected that this database will provide a robust test for molecular quantum mechanical models of bonding and reaction dynamics in explosives. Additionally, these experiments hold promise for elucidating the interaction of chemical and physical effects, such as in the tribochemical processes believed to be the basis of hot-spot initiation of detonation by shock and impact. Finally, these experiments and the associated modeling appear to give us a prototype laboratory-scale test that links quenched detonation chemistry with shock sensitivity and a rudimentary measure of detonation performance.

## ACKNOWLEDGEMENTS

Peter O'Rourke and Tony Amsden assisted greatly in adapting the KIVA code for this work. Jim Ritchie provided BKW calculations. Scott Murray assisted in making the mass spectra data base, running the KIVA code, and interpreting the output. Wilbur Fernandez assisted in running the experiments and in maintaining and modifying the apparatus. Discussions with Wildon Fickett and Jack Jacobson concerning modeling of detonation have been most helpful.

## REFERENCES

1. Blais, N. C., "Real-time Analysis of HNS Detonation Products: Carbon Clusters," *Journal of Energetic Materials*, Vol. 5, 1987, p. 57.
2. Greiner, N. R. and Blais, N. C., "Real-time Analysis of the Chemical Products from Shocked Nitric Oxide," *Seventeenth International Annual Conference of ICT--Analysis of Propellants and Explosives*, Fraunhofer Institut für Treib- und Explosivstoffe (ICT), Karlsruhe, Federal Republic of Germany, 25-27 Jun 1986, pp. 33-1 to 33-10.
3. Greiner, N. R., "Freely Expanding Detonation Products: Scaling of Rate Processes," *Nineteenth International Annual Conference of ICT--Combustion and Detonation Phenomena*, Fraunhofer Institut für Chemische Technologie, Karlsruhe, Federal Republic of Germany, 29 Jun - 1 Jul 1988, pp. 36-1 to 36-13.

4. Blais, N. C. and Valentini, J. J., "Real Time Analysis of PETN Detonation Products," *Proceedings of the Eighth Symposium (International) on Detonation*, Albuquerque, NM, 15-19 Jul 1985, pp. 701-709.
5. Blais, N. C., "Real-Time Analysis of the Detonation Products of RDX," *Journal of Energetic Materials*, to be published.
6. Blais, N. C. and Greiner, N. R., "Real-Time Analysis of the Reaction Products of Shocked Nitric Oxide," *Journal of Energetic Materials*, Vol. 6, 1988, pp. 255-281.
7. Ornellas, D. L., *Calorimetric Determination of Heat and Products of Detonation for Explosives: October 1961 to April 1982*, UCRL-52821, Apr 1982, Lawrence Livermore National Laboratory, Livermore, CA.
8. Greiner, N. R.; Phillips, D. S.; Johnson, J. D.; and Volk, F., "Diamonds in Detonation Soot," *Nature*, Vol. 333, 1988, pp. 440-442.
9. Ansdan, A. A.; Ramshaw, J. D.; O'Rourke, P. J.; and Dukowicz, J. K., *KIVA: A Computer Program for Two- and Three-Dimensional Fluid Flows with Chemical Reactions and Fuel Sprays*, LA-10245-MS, Feb 1985, Los Alamos National Laboratory, Los Alamos, NM.
10. Greiner, N. R., "KIVA Reactive Hydrodynamics Code Applied to Detonations in High Vacuum," *Proceedings of the NATO Advanced Study Institute on Chemistry and Physics of the Molecular Processes in Energetic Materials*, Sicily, Italy, 3-15 Sep 1989, Kluwer Academic Publishers, Dordrecht, the Netherlands (in Press).
11. Hay, J. E.; Peters, W. C.; and Watson, R. W., "Observations of Detonation in a High Vacuum," *Proceedings of the Fifth Symposium (International) on Detonation*, Pasadena, California, 18-21 Aug 1970, pp. 559-565.
12. Lundborg, N., "Front and Mass Velocity at Detonation in Evacuated Chambers," *Proceedings of the Fourth Symposium (International) on Detonation*, White Oak, MD, 12-15 Oct 1985, pp. 176-178.
13. Shaw, M. S. and Johnson, J. D., "Carbon Clustering in Detonations," *Journal of Applied Physics*, Vol. 62, 1987, pp. 2080-2085.

## DISCUSSION

**HAROLD GRYTING**  
Gryting Energetics Sciences Company  
San Antonio, TX

What is the standard deviation of your mass detectibility? Can you readily differentiate HCN from CO?

## REPLY BY N. ROY GREINER

If I understand the question correctly, the answer is yes, we can readily differentiate HCN which has a mass of 27 from CO which has a mass of 28.

# DETONATION PRODUCTS OF LESS SENSITIVE HIGH EXPLOSIVES FORMED UNDER DIFFERENT PRESSURES OF ARGON AND IN VACUUM

F. Volk and F. Schedlbauer  
Fraunhofer-Institut für Chemische  
Technologie, ICT, 7507 Pfinztal, FRG

*Less sensitive high explosive charges of TNT/nitroguanidine (NQ) and PBX charges with polybutadiene (PB) and Cariflex binder containing RDX with and without NQ and Al were detonated in a stainless steel chamber of 1.5 m<sup>3</sup> in vacuum and under different ambient argon pressures up to 0.3 MPa. Gaseous and solid reaction products were analyzed and enthalpy of detonation calculated from the products and the components of the charge. It was found that the products were highly dependent on the ambient pressure of argon. The most important changes of the reaction products were found between vacuum and atmospheric pressure of argon (0.1 MPa). With increasing pressure, H<sub>2</sub> and CO decrease and CO<sub>2</sub>, H<sub>2</sub>O, C<sub>s</sub>, NH<sub>3</sub>, HCN, CH<sub>4</sub>, and C<sub>2</sub>H<sub>2</sub> increase. In the same way enthalpy of detonation increases up to 50 percent.*

## INTRODUCTION

The energy output released during the detonation reaction of high explosives (HE) depends on the following parameters:

- energy content of the charge
- oxygen balance
- grain size of the components
- degree of confinement
- completeness of the reaction of metals, such as Al, with the reaction products of the high explosive.

Confinement influences the reaction in so far as it adds resistance to the expansion of the gaseous detonation products, and maintains high pressure and high temperature for a longer period of time before lateral rarefactions from the side quench it.<sup>1</sup>

By using a confinement, the Boudouard-Equilibrium



is influenced to form higher concentrations of CO<sub>2</sub> and C<sub>s</sub>. Additionally, the amount of H<sub>2</sub>O increases, whereas H<sub>2</sub> and CO decrease.<sup>2</sup>

Both reactions increase the heat of detonation of confined charges.

Earlier investigations have shown that less sensitive high explosive charges consisting of TNT and nitroguanidine produced very different detonation products when initiated in vacuum, compared with those under one atmosphere of argon.<sup>3</sup> In this case, argon behaves as a confining medium.

In order to learn more about prepressurization, we also studied other high explosive charges, such as PBXs based on RDX and nitroguanidine, with and without additional aluminum in our stainless steel chamber. By varying the argon pressure from vacuum up to 0.3 MPa, the detonation products were analyzed with regard to the gas and soot formation. Additionally, the heat output of detonation was evaluated.

## EXPERIMENTS

For the experiments, a container of stainless steel which could be evacuated, with a volume of 1.5 m<sup>3</sup> was used.

The high explosive charges had a diameter of 50 mm and a length between 85 and 95 mm. The mass was approximately 300 g without boosters. For the initiation, a detonator cap No. 8 of Dynamit Nobel AG, together with a 10 g RDX booster, were used. Because of the corner effect, a second booster of about 18 g having the same diameter as the main charge was glued onto the charge.<sup>4</sup>

After hanging the explosive charge horizontally inside the chamber, the vacuum pump was started in order to provide a detonation in vacuum or under different pressures of argon. After firing, gas samples were taken for the measurement of NO in a chemiluminescence analyzer and the mass spectrometric analysis of the detonation gas. Then the chamber was opened in order to collect the solid residue as completely as possible by the use of vacuum cleaner. The residue was analyzed for carbon, hydrogen and nitrogen. The unreacted aluminum was determined after reaction with HCl by measuring the volume of hydrogen.

In some cases, soot was examined in more detail at the Los Alamos National Laboratory by using X-ray diffraction and convergent-beam electron diffraction. Previous investigations have shown that X-ray diffraction powder patterns exhibited the same diamond spacings, matching the pattern from an authentic diamond sample.<sup>5</sup>

### Manufacturing of the Explosive Charges

**TNT-Charges.** The charges containing TNT were manufactured by heating TNT above its melting point, and by the addition of ingredients such as spherical nitroguanidine (NQ), Al, and others. Cylindrical high explosive charges of 50 mm in diameter and 80 to 90 mm in length were cast in order to obtain charges of about 300 g. With regard to nitroguanidine, a distribution of spherules of 28 percent with 150-200  $\mu\text{m}$  and 72 percent with 500-1000  $\mu\text{m}$  was used.

**Charges with Polybutadiene (PB) Binder.** The pre-mix consisting of the pre-polymer R 45 M and the ingredients RDX, NQ, Al, etc., was treated in a horizontal mixer. Later, the curing agent Isophorondiisocyanate

(IDPI) was added. After mixing a short time, the explosive mass was cast into a cylindrical form. The following mean particle size distributions were used:

RDX Class C;  $X_{50} \approx 225 \mu\text{m}$

RDX ground;  $X_{50} \approx 10 \mu\text{m}$

Al Alcan;  $X_{50} \approx 5 \mu\text{m}$

### Charges with Thermoplastic Binders.

For the preparation of high explosive charges containing a thermoplastic elastomer binder, the triblock copolymer Cariflex 1107 was used. A granular mix consisting of 85 percent RDX and 15 percent binder was used. The granulated material was heated in a double piston press to 80°C, and pressed at 25 MPa under vacuum.

### High Explosives Investigated

The following high explosives were investigated:

Composition	Density [g/cm <sup>3</sup> ]	Detonation Velocity [m/s]
TNT	1.64	6900
45% TNT/55% NQ	1.63	7224
45% TNT/55% NQ (Glass confinement)	1.63	7224
HX 72: 80% RDX (10 $\mu\text{m}$ )/20% PB	1.48	7750
HX 76: 55% NQ/30% RDX (10 $\mu\text{m}$ )/ 15% PB	1.51	7420
PHX 31: 85% RDX (10 $\mu\text{m}$ )/15% Cariflex 1107	1.57	7960
HXA 123: 56% RDX Class C/14% RDX (10 $\mu\text{m}$ ) 15% PB/15% Al Alcan 400	1.62	7350

### Evaluation of Results

Most of the gaseous reaction products such as H<sub>2</sub>, N<sub>2</sub>, NO, N<sub>2</sub>O, CO, CO<sub>2</sub>, HCN, CH<sub>4</sub>, and C<sub>2</sub>H<sub>4</sub> can be analyzed quantitatively by mass spectrometry.

In order to determine the amount of H<sub>2</sub>O vapor, we calculated it as the difference of the hydrogen balance which was evaluated between the total hydrogen content and the analyzed content. The same was also done for evaluating the amount of free carbon, which was formed as soot during the detonation reaction.

On the other hand, the amount of unreacted aluminum (Al) was analyzed by measuring the hydrogen content of the reaction



Also, the soot was analyzed for determining the amount of C, H, and N using elemental analysis based on the complete combustion to CO<sub>2</sub>, H<sub>2</sub>O, and N<sub>2</sub>.

If we have analyzed

- a) the gaseous reaction products by mass spectrometry: H<sub>2</sub>, N<sub>2</sub>, NO, N<sub>2</sub>O, CO, CO<sub>2</sub>, HCN, CH<sub>4</sub>, C<sub>2</sub>H<sub>4</sub>, and C<sub>2</sub>H<sub>2</sub>,
- b) the composition of the soot: % C, % H, and % N, and
- c) and the amount of the unreacted Al,

we are able to calculate the amounts of water vapor and of solid carbon.

For this calculation a computer program was written. Input parameters of this program are: the above mentioned analytical results (a, b, c) and, additionally, the stoichiometric composition of the complete explosive charge, including both boosters. By comparing the mass balance, it is possible to get a complete composition of the reaction products. Beyond that, we calculated the heats of formation of the products and the unreacted explosive charge. Additionally, the freezing-out temperature of the components of the water gas reaction products is evaluated by calculating the equilibrium constant, using the partial pressures according to:

$$K_p(T) = \frac{P_{\text{CO}} \times P_{\text{H}_2\text{O}}}{P_{\text{CO}_2} \times P_{\text{H}_2}}$$

Finally, the computer program provides us with the following results, as seen in Table 1:

1. Mass of the explosive charge
2. Mass of the boosters
3. Composition of the charge
4. Heat of formation of the charge
5. O<sub>2</sub>-balance
6. Sum formula of the explosive charge included the boosters
7. Sum formula of the soot
8. Amount of unreacted aluminum
9. Mass spectrometric analysis of the reaction gas without water vapor
10. Complete reaction products including water vapor, solid carbon, Al and Al<sub>2</sub>O<sub>3</sub> in Mol percent, and reaction products per kilogram high explosive charge (mol/kg)
11. Enthalpy of detonation (-H<sub>det</sub>)
12. Water gas equilibrium constant K<sub>p</sub>(T)
13. Amount of carbon in residue (percent of total C or in grams)
14. Amount of unreacted Al in percent
15. Gas formation in Mol/kg
16. Comparison of theoretical and experimental mass balance, with and without ammonia (NH<sub>3</sub>)

## RESULTS

### Reaction Products of TNT

The reaction products of a charge consisting of 300 g TNT and 29 g booster without confinement were compared with those published by D. Ornellas<sup>2</sup> which have been formed in a detonation calorimeter; see Table 2.

Two samples of D. Ornellas were tested under confinement: one in a cylinder of gold, the other of alumina (Al<sub>2</sub>O<sub>3</sub>). The third sample (26 g) was without a confinement.

It is interesting to see that our unconfined large TNT charge (300 g TNT + 29 g booster) exhibits nearly the same reaction products as the small charge (22 g) with the gold confinement, but is very different from the unconfined

**Table 1. Example for the Evaluation of the Complete Detonation Products and the Heat of Detonation of Composition B**

9. R. 909		No. 2470		COMPOSITION B	
EXPLOSIVE MASS:	301.0 (G)				
EXPLOSIVE FOIL:	17.5 (G)				
RDX BOOSTER:	10.0 (G)				
TOTAL MASS:	328.5 (G)				
57.58% HEXOGEN		59.50%			
0.91% PARAFFINE		1.00%			
36.19% 2,4,6-TNT		39.50%			
5.32% EXPLOSIVE FOIL		0.00%			
Heat of formation:	-8.5 KCal/Kg = -39.5 KJ/Kg				
Oxygen balance:	-45.63%				
Sum formula:	C	O	N	H	
	2.0519	2.0977	2.1083	2.6409	
Scale:	1.0000	0.0000	0.0533	0.0713	
(MOL%)	ANALYSIS WITH H <sub>2</sub> O and SOOT		(MOL/KG)		
H <sub>2</sub>	12.05	7.38	3.35		
CH <sub>4</sub>	0.38	0.17	0.08		
CO	33.49	30.51	9.99		
CO <sub>2</sub>	15.18	9.89	4.08		
N <sub>2</sub>	26.55	25.00	10.35		
N <sub>2</sub> O	0.00	0.00	0.00		
NO	0.09	0.00	0.02		
HCN	0.37	0.33	0.10		
H <sub>2</sub> O		21.87	9.59		
SOOT		16.90	7.41		
Kp(T) Watergas:	6.540				
Δ H <sub>det</sub> (KJ/KG):	5008.3				
MOL/KG:	TOTAL: 42.41	GAZ: 30.44	COND: 7.41		
Comparison of mass balance:	Theory	Experiment			
N/C	1.0275	1.0275			
N/H	0.7983	0.7983			
N/O	0.7815	0.7830			
Theor. amount of carbon in residue: 29.0 (G) = 35.8% of carbon					

small TNT charge (26 g). This leads to the conclusion that for a large charge with a diameter of about 50 mm, argon atmosphere behaves as a confining medium.

### Charges With 45 Percent TNT/55 Percent NQ

In order to determine the influence of different argon pressures on the detonation products of cast high explosive charges consisting of 45 percent TNT and 55 percent spherical nitroguanidine (NQ), experiments have been conducted in the detonation container described. In each case, the detonation products of three shots were analyzed: one in the evacuated container, the other under 0.05 MPa, and the third under 0.1 MPa of argon (Ar); see Table 3.

**Table 2. Heats and Products of Detonation of TNT Under Varying Conditions: Comparisons Between ICT and LLNL**

Sample	ICT 28/30	Detonation Calorimeter D. Ornellas, LLNL		
		no	Gold	Al203 no
Confinement				
Charge:				
Density (g/cm)	?	1.533	1.533	1.000
Diameter (mm)	50	12.7	12.7	12.7
Weight TNT (g)	300	22	22	26
Booster	(g)	29	?	?
Products, (Mol %)				
H <sub>2</sub>	3.4	4.3	4.1	20.4
CH <sub>4</sub>	0.2	0.9	1.0	0.1
CO	17.2	18.5	18.9	53.9
CO <sub>2</sub>	9.9	11.7	12.5	0.3
N <sub>2</sub>	13.5	12.3	12.6	11.9
NO	0.07		0.01	0.01
HCN	0.8	1.9	0.5	0.3
NH <sub>3</sub>	?	1.8	1.8	0.9
H <sub>2</sub> O	19.6	14.9	13.3	3.4
C <sub>s</sub>	35.4	234.0	35.2	8.8
Δ H <sub>det</sub> (KJ/Kg):				
Experimental		4576	4480	2437
Calc. from products	4320	4744	4091	2977

**Table 3. Charges of 45 Percent TNT/55 Percent NQ in Different Ar Pressures**

Sample No.	1450/1c	1450/2c	1450/3c
	Ar pressure, MPa		
Composition	45% TNT/ 55% NQ		
02-Balance, %	-47.6		
Charge Weight, g	331	332	331
Δ H <sub>p</sub> KJ/Kg	-661	-662	-657
Products, Mol%:			
H <sub>2</sub>	20.7	8.3	5.0
CH <sub>4</sub>	0.04	0.1	0.24
CO	32.1	17.9	14.3
CO <sub>2</sub>	3.7	7.9	10.3
N <sub>2</sub>	27.5	26.1	25.6
NO	0.1	0.1	0.13
HCN	0.3	3.2	3.6
NH <sub>3</sub>	0.5	3.0	4.9
C <sub>2</sub> H <sub>2</sub>	0.02	0.03	0.1
H <sub>2</sub> O	10.7	19.6	20.0
C <sub>s</sub>	4.4	13.8	15.9
Δ H <sub>det</sub> , KJ/Kg	2999	3653	3763
C in Residue (% of total C)	10.8	32.2	35.7
Gas formation (mol/Kg)	44.5	37.9	35.7

Additionally, three charges of the same mass and the same composition but in a glass confinement with a thickness of 9 mm were

investigated, also in vacuum, under 0.05 and 0.1 MPa argon. The results are listed in Table 4.

**Table 4. Charges of 45 Percent TNT/55 Percent NQ in Glass Confinement and Different Ar Pressures**

Sample No.	1451/1	1451/2	1451/3
Ar pressure, MPa	Vac.	0.05	0.1
Composition	45% TNT/ 55% NQ		
O2-Balance, %		-47.6	
Charge Weight, g	332	335	332
$\Delta H_f$ , KJ/Kg	-656	-658	-658
<b>Products, Mol%:</b>			
H <sub>2</sub>	8.7	4.2	3.1
CH <sub>4</sub>	0.2	0.4	0.44
CO	15.9	10.2	9.3
CO <sub>2</sub>	7.9	11.9	12.7
N <sub>2</sub>	27.3	26.0	25.6
NO	0.06	0.05	0.14
HCN	1.36	2.4	1.1
NH <sub>3</sub>	1.15	4.7	5.3
C <sub>2</sub> H <sub>2</sub>	0.07	0.1	0.13
H <sub>2</sub> O	20.5	20.7	21.0
C <sub>s</sub>	16.8	19.2	21.3
$\Delta H_{det}$ , KJ/Kg	3779	3960	4003
C in Residue [% of total C]	39.8	43.3	47.2
Gas formation [mol/Kg]	37.1	34.4	33.0

The results of the unconfined shots in Table 3 show that the products formed under an evacuated condition are very different from those produced under 0.5 bar (0.05 MPa) and one bar (0.1 MPa).

With increased pressure we see a distinct decrease of H<sub>2</sub> and CO on one side and a strong increase of CO<sub>2</sub>, H<sub>2</sub>O, and solid carbon (C<sub>s</sub>) on the other.

In the same direction the enthalpy of detonation ( $\Delta H_{det}$ ) increases markedly from vacuum to 0.05 MPa of argon, but only slightly from 0.05 MPa to 0.1 MPa of Ar. The highest value of the gas formation is obtained in vacuum.

It is also interesting to see how the concentrations of ammonia (NH<sub>3</sub>) and hydrocyanic acid (HCN) increase with a higher pressure of argon; the same holds also for methane (CH<sub>4</sub>) and acetylene.

It seems as if argon behaves as a confinement. It leads to a distinct increase in the heat of detonation because of the increase in the

species representative of a lower-temperature isentrope such as CO<sub>2</sub>, H<sub>2</sub>O, and solid carbon (C<sub>s</sub>), and a corresponding decrease in the species representative of a higher-temperature isentrope: CO and H<sub>2</sub>.<sup>2</sup>

From vacuum to 0.1 MPa argon, enthalpy of detonation increases from 2999 to 3763 kJ/kg by 20.6 percent. On the other hand, the glass confined charge exhibits at 0.1 MPa argon a value of 4003 kJ/kg, which corresponds to an increase of only 6.4 percent, compared with the unconfined charge at the same pressure (see Tables 3 and 4).

Because of the effectivity of argon, we tried to analyze also the detonation products formed under higher argon pressures such as 0.2 and 0.3 MPa. The results are listed in Table 5.

**Table 5. Charges of 45 Percent TNT/55 Percent NQ in Ar Pressures of 0.1 to 0.3 MPa**

Sample No.	1450/3c	1450/2b	1450/3b
Ar pressure, MPa	0.1	0.2	0.3
Composition	45% TNT/ 55% NQ		
O2-Balance, %		-47.6	
Charge Weight, g	331	328	327
$\Delta H_f$ , KJ/Kg	-657	-648	-646
<b>Products, Mol%:</b>			
H <sub>2</sub>	5.0	4.2	4.4
CH <sub>4</sub>	0.2	0.3	0.35
CO	14.3	11.4	11.4
CO <sub>2</sub>	10.3	10.7	11.3
N <sub>2</sub>	25.6	25.2	24.8
NO	0.13	0.22	0.3
HCN		0.5	0.8
NH <sub>3</sub>	3.6	1.4	1.0
C <sub>2</sub> H <sub>2</sub>	0.1	0.1	0.1
H <sub>2</sub> O	20.0	21.7	20.8
C <sub>s</sub>	15.9	20.8	21.2
$\Delta H_{det}$ , KJ/Kg	3763	3790	3706
C in Residue [% of total C]	35.7	46.4	46.6
Gas formation [mol/Kg]	35.7	33.4	32.8

As we see, an additional atmosphere of Ar (0.2 MPa) increases the heat of detonation only by 27 kJ, and a further pre-pressurization to 0.3 MPa exhibits no additional improvement of the heat output.

#### Analysis of Soot

After each shot, the residue was collected, dried, and analyzed for carbon, hydrogen, and

nitrogen by combustion analysis. For comparison, carbon residue is also calculated from the mass balance.

In Table 6, we have listed the elemental analysis of the soot, as well as the analyzed and calculated amounts of carbon. We clearly see how the carbon content increases when going from vacuum to 0.05, 0.1, and 0.2 MPa of argon.

**Table 6. Analysis of the Residual Soot of the Charges 45 Percent TNT/55 Percent NQ**

Sample No.	Ar Pressure [MPa]	C %	H %	N %	Total Carbon [g]	
					Analyzed	Calculated
1450/1c	Vacuum	87.3	1.0	10.4	5.9	8.1
1450/2c	0.05	86.9	1.1	12.0	20.9	24.2
1450/3c	0.1	85.4	1.3	13.3	31.6	26.6
1450/1b	0.1	82.4	1.7	15.9	31.7	36.6
1450/2b	0.2	73.1	2.4	24.5	36.1	34.6
1450/3b	0.3	68.9	2.8	28.2	35.8	34.8

The elemental analyses have shown that the nitrogen content increases, too, when argon pressure is raised. We assume that the formation of organic substances containing nitrogen increase in the same manner as HCN and NH<sub>3</sub>.<sup>6</sup>

We suspect that the formation of diamonds will also be favored under stronger confinement.<sup>8</sup>

#### Reaction Products of PBX-Charges in Different Argon Pressures

In addition to the TNT/nitroguanidine cast high explosive, some PBX charges were investigated which exhibited different RDX and binder contents. Also, charges containing aluminum (Al) were included.

The detonation products of charges consisting of 80 percent RDX, with a mean grain size of 10 μm and 20 percent of a polybutadiene binder, are shown in Table 7.

Comparing the results of the evacuated container with those of 0.05 and 0.1 MPa of argon, we see the same behavior as discussed before: a decrease of H<sub>2</sub> and CO, and an increase of CO<sub>2</sub>, H<sub>2</sub>O, C<sub>s</sub>, NH<sub>3</sub>, HCN, C<sub>2</sub>H<sub>2</sub>, and CII<sub>4</sub>.

**Table 7. PBX Charges with 80 Percent RDX/20 Percent PB**

Sample No.	HX 72/1	HX 72/2	HX 72/3
Ar pressure, MPa	Vacuum	0.05	0.1
Composition	20% PB/80% RDX (10 μm)		
O <sub>2</sub> -Balance, %	-73.3		
Charge Weight, g	329	328	330
Δ H <sub>r</sub> , KJ/Kg	-94	-90	-95
Products, Mol%:			
H <sub>2</sub>	33.5	15.0	12.3
CH <sub>4</sub>	0.1	0.7	2.9
CO	34.4	17.3	13.1
CO <sub>2</sub>	1.2	3.5	6.8
N <sub>2</sub>	18.8	18.0	18.8
NO	0.05	0.03	0.02
HCN	0.1	0.8	0.9
NH <sub>3</sub>	0.5	2.9	2.8
C <sub>2</sub> H <sub>2</sub>	-	0.06	0.5
H <sub>2</sub> O	4.8	19.6	19.9
C <sub>s</sub>	6.8	22.2	22.2
Δ H <sub>det</sub> , KJ/Kg	2949	4214	4440
C in Residue [% of total C]	15.7	49.9	47.3
Gas formation [mol/Kg]	52.1	42.0	39.7

There is also an increase in the enthalpy of detonation, and a decrease in the gas formation. It is notable that the very high formation of H<sub>2</sub> in the vacuum shot is due to the high amount of PB binder, which leads to an extreme negative oxygen balance of -73.3 percent. But, nevertheless, the heat of detonation is much higher than that of 45 TNT/55 NQ. The reason for this is that the enthalpy of formation is much less negative for the RDX containing charge (-94.0 kJ/kg) than that of 45 TNT/55 NQ with a value of -646 kJ/kg. From vacuum to one bar argon, heat of detonation increases by 50.6 percent from 2949 to 4440 kJ/kg.

#### PBX - Charges Containing RDX and Spherical Nitroguanidine (NQ)

On the basis of the more negative enthalpy of formation of nitroguanidine, we understand that the detonation decreases by replacing RDX with nitroguanidine (NQ). In Table 8, the detonation products of charges with 15 percent PB binder, 55 percent NQ, and 30 percent RDX are listed.

The most important difference between here and the RDX containing charges in Table 7 is to be seen in the formation of HCN

**Table 8. Charges Containing RDX and Spherical Nitroguanidine (NQ)**

Sample No.	HX 76/1	HX 76/2	HX 76/3
Ar pressure, MPa	Vacuum	0.05	0.1
Composition	15% PB/55% NQ/30% RDX (10 μm)		
O <sub>2</sub> -Balance, %		-64.8	
Charge Weight, g	330	330	331
ΔH <sub>f</sub> , KJ/Kg	-625	-626	-629
<b>Products, Mol%:</b>			
H <sub>2</sub>	23.2	9.2	5.9
CH <sub>4</sub>	0.7	1.7	2.9
CO	22.4	10.7	7.7
CO <sub>2</sub>	3.5	7.5	9.6
N <sub>2</sub>	23.4	22.9	24.0
NO	0.06	0.07	0.1
HCN	5.1	6.0	3.4
NH <sub>3</sub>	4.0	8.8	9.3
C <sub>2</sub> H <sub>2</sub>	0.1	0.7	0.8
C <sub>2</sub> H <sub>4</sub>	-	0.1	0.5
H <sub>2</sub> O	11.3	18.6	19.0
C <sub>s</sub>	6.2	13.9	16.8
ΔH <sub>det</sub> , KJ/Kg	2575	3274	3530
C in Residue [% of total C]	16.4	33.5	39.0
Gas formation (mol/Kg)	47.2	39.8	37.1

and NH<sub>3</sub>: nitroguanidine is responsible for concentrations up to 6.0 Mol percent HCN and 9.3 Mol percent NH<sub>3</sub>. This behavior may be explained by the fact that NH<sub>3</sub> and HCN are decomposition products of nitroguanidine. Because of the positive heat of formation of HCN, the enthalpy of detonation is decreased distinctly.

We assume that the relatively high HCN concentration of detonation gases produced from nitroguanidine containing high explosives, is responsible for discrepancies between calculated and measured detonation velocities. The calculated velocities will be marked lower when taking into account the heat loss for which HCN, with its positive heat of formation, is responsible:



#### Charges With 85 Percent RDX (10 μm) and a Cariflex Thermoplastic Elastomer Binder

It is the special merits of thermoplastic binders that the manufacturing process of high explosives is more flexible. Using 15 percent of a Cariflex binder and 85 percent RDX, an oxygen balance of -64.5 percent can be obtained for

the charge, including both boosters. Besides a high gas formation, a considerable heat output was also determined by analyzing the detonation products, as is shown in Table 9.

**Table 9. Charges With 85 Percent RDX (10 μm) and a Thermoplastic Cariflex Binder**

Sample No.	PHX 31/1	PHX 31/2	PHX 31/3
Ar pressure, MPa	Vacuum	0.05	0.1
Composition	15% Cariflex / 85% RDX (10 μm)		
O <sub>2</sub> -Balance, %		-64.5	
Charge Weight, g	328	329	329
ΔH <sub>f</sub> , KJ/Kg	-78	-80	-81
<b>Products, Mol%:</b>			
H <sub>2</sub>	28.8	17.6	11.7
CH <sub>4</sub>	-	0.5	1.7
CO	34.1	20.4	14.5
CO <sub>2</sub>	1.4	3.5	6.2
N <sub>2</sub>	20.7	20.8	20.8
NO	0.06	0.03	0.02
HCN	0.8	0.8	1.05
NH <sub>3</sub>	0.9	1.1	2.4
C <sub>2</sub> H <sub>2</sub>	-	0.1	0.4
C <sub>2</sub> H <sub>4</sub>	-	0.06	0.1
H <sub>2</sub> O	8.1	18.4	21.2
C <sub>s</sub>	5.4	16.9	20.0
ΔH <sub>det</sub> , KJ/Kg	3428	4323	4676
C in Residue [% of total C]	13.0	40.1	45.1
Gas formation (mol/Kg)	49.8	42.9	39.5

The concentration of NH<sub>3</sub> and HCN is much smaller than in the case of NQ containing charges.

From vacuum to atmospheric pressure of argon, the enthalpy of detonation increases from 3428 to 4676 kJ/kg (36.4 percent).

#### PBX Charges With RDX and Aluminum

The aim of the following investigations was to find out the influence of different argon pressures on the detonation products of Al-containing PBXs.

In the container, a high explosive consisting of 56 percent RDX Class C, 14 percent RDX (10 μm), 15 percent Al Alcan 400, and 15 percent polybutadiene binder was detonated in vacuum and in argon atmosphere (0.1 MPa). The results are listed in Table 10.

It is shown that the shot in vacuum produced detonation products which were

Table 10. PBX Charges with RDX and Al Alcan 400

Sample No.	HXA 123/1	HXA 123/3
Ar pressure, MPa	Vacuum	0.1
Composition	15% PB/ 15% Al Alcan 400 56% RDX Class C/ 14% RDX (10 µm)	
O <sub>2</sub> -Balance, %		-69.3
Charge Weight, g	331	331
ΔH <sub>f</sub> , KJ/Kg	-73	-71
Products, Mol%:		
	H <sub>2</sub> 29.5	25.8
	CH <sub>4</sub> 0.04	1.1
	CO 26.1	20.1
	CO <sub>2</sub> 0.01	2.7
	N <sub>2</sub> 16.9	18.1
	NO 0.07	0.05
	HCN 0.1	2.35
	NH <sub>3</sub> 2.2	0.9
	C <sub>2</sub> H <sub>2</sub> 0.04	0.3
	C <sub>2</sub> H <sub>4</sub> 0.03	0.2
	H <sub>2</sub> O 4.2	7.2
	Al <sub>2</sub> O <sub>3</sub> 4.6	3.9
	Al 1.6	3.0
	C <sub>s</sub> 14.6	14.3
K <sub>p</sub> (T)	?	2,018
Freeze out Temp. (K)		1365
ΔH <sub>det</sub> , KJ/Kg	5143	5066
C in Residue [% of total C]	35.6	34.5
Unreacted Al, %	15.0	28.0
Gas formation (mol/Kg)	38.6	37.0

much more similar to those of 0.1 MPa argon than were obtained in all earlier shots by using charges without aluminum.

This means that the influence of argon as a confining medium is reduced by using Al containing high explosives. This behavior can also be derived from the values of the enthalpies of detonation, which only exhibit a difference of 1.5 percent between the detonation in vacuum and atmospheric pressure of argon.

The results have also shown that an amount of unreacted Al of 15 percent for vacuum and 28.0 percent for 0.1 MPa of argon related to the whole Al content was analyzed.

Comparing the freeze-out temperature of the water gas reaction, we see that it is very

high for the shot in vacuum, whereas it has a realistic value of 1365K under 0.1 MPa of argon.

## CONCLUSIONS

We have presented results demonstrating the usefulness of analyzing detonation products in a stainless steel container of about 1.5 m<sup>3</sup>.

By using less sensitive high explosive charges of more than 300 g, the influence of different ambient pressures of argon on the detonation products was determined.

Charges containing TNT/nitroguanidino, PBX charges with polybutadien binders containing RDX/nitroguanidino, and RDX/Al and thermoplastic binders with RDX were detonated in vacuum in 0.05 MPa and 0.1 MPa of argon pressure. We have shown that the detonation products were highly dependent on the pressure. At atmospheric pressure of argon, enthalpy of detonation was up to 50 percent higher than under vacuum. With increased pressure, we found a distinct decrease of H<sub>2</sub> and CO and a strong increase of CO<sub>2</sub>, H<sub>2</sub>O, solid carbon, NH<sub>3</sub>, HCN, CH<sub>4</sub>, and C<sub>2</sub>H<sub>2</sub>.

On the other hand, Al containing PBX charges exhibited only a small effect under different pre-pressurization.

## REFERENCES

1. Price, D. and Zerilli, F. J., Notes from lectures on detonation physics, Naval Surface Weapons Center, White Oak, MD, NSWC MP 81-399, Oct 1981.
2. Ornellas, D. L., "Calorimetric Determinations of the Heat and Products of Detonation for Explosives: Oct 1961 to Apr 1982" MCRL - 52821, Lawrence Livermore National Laboratory, Apr 5 1982.
3. Volk, F., "Detonation Gases and Residues of Composite Explosives," *J. Energetic Materials*, No. 4, 1983, pp. 93-113.
4. Held, M., "Corner Turning Distance and Detonation Radius," *Prop. Expl. Pyrot.*, 1989, in press.

5. Greiner, R. N.;<sup>\*</sup> Phillips, D. S.;<sup>\*</sup> Johnson, J. D.;<sup>\*</sup> and Volk, F.,<sup>\*\*</sup> "Diamonds in Detonation Soot," *Nature* 333, 1988, pp. 440-442.
6. Greiner, R. N.,<sup>\*</sup> "Chemistry of Detonation Soot," DEA-A-76-G-1218, *Energetic Materials for Munitions*, Fraunhofer Institut für Chemische Technologie, Pfinztal, FRG, Jun 20-23, 1988.

## DISCUSSION

**HAROLD GRYTING**  
Gryting Energetics Sciences Company  
San Antonio, California

In Table 3 for composition 45 percent TNT/55 percent NQ, is the increased pressure of argon primarily responsible for the increase in H<sub>2</sub>O from 10.7 mole percent to 19.6 mole percent from vacuum to 0.05 MPa argon pressure in the predetonation condition?

If so, how do you account for the almost negligible increase in H<sub>2</sub>O when the argon pressure is doubled (increasing from 0.05 to 0.1 MPa) with H<sub>2</sub>O only increasing from 19.6 to 20.0 mole percent for about the same charge weights? Tables 4 and 5 do not show these anomalies.

## REPLY BY F. VOLK

In all cases we found that the reaction gases changed strongly between vacuum and 0.05 MPa argon.

From 0.05 to 0.1, 0.2, and 0.3 MPa only a little change of the products was analyzed, see Table 5.

Tables 4 and 5 do not show these changes because Table 4 deals with a glass confined charge and glass confinement behaves like a high argon pressure. Table 5 shows that there is nearly no changing between 0.1 MPa and 0.3 MPa of argon.

<sup>\*</sup> Los Alamos National Laboratory, Los Alamos, NM

<sup>\*\*</sup> Fraunhofer Institut für Chemische Technologie, D 7507 Pfinztal, FRG

## DISCUSSION

**JOHN KURY**  
Lawrence Livermore National  
Laboratory  
Livermore, California

The product composition differences seen between experiments with confinement and those in vacuum are primarily due to reshocking of the products to well above freeze out temperatures for the vacuum experiments (see Ornellas' paper).

## REPLY BY F. VOLK

Yes, I agree. Reshocking means that the freeze out temperature of the water gas equilibrium shifts to a higher temperature and that carbon formation and detonation heat is reduced.

In our case, it is shown that the unconfined charge under argon pressure leads to detonation products which are nearly the same as from the confined charge: a high concentration of CO<sub>2</sub>, H<sub>2</sub>O, and C. In this case, reshocking must be negligible. However, under vacuum conditions, products have been analyzed which are very similar to reshocked conditions: a high content of H<sub>2</sub> and CO, a low heat of detonation, and a high freeze-out temperature of the water gas equilibrium.

## DISCUSSION

**PER ANDERS PERSSON**  
CETR/New Mexico Tech  
Socorro, New Mexico

For a 300 g charge of these relatively insensitive explosives, one would expect the detonation at the surface of the charge when in a vacuum to be a great deal less ideal than at the center of the charge. The confinement and increased Ar pressure would presumably decrease this difference. Do you feel that the glass-confined 300 g charges produce reaction products representative of those from a large charge of the same explosive, say a 300 kg charge?

## REPLY BY F. VOLK

The critical diameter of the charge compositions we have analyzed is between 30 and 40 mm. Our charges that we investigated in the detonation chamber exhibited diameters of 50 mm. So we can assume that by increasing the diameter we will not have a distinct change of the detonation products compared with a glass-confined charge.

## DISCUSSION

GREGORY A. BUNTAIN  
Los Alamos National Laboratory  
Los Alamos, New Mexico

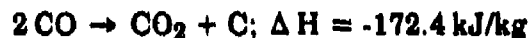
I wonder what affect the argon flash in your chamber will have on product decomposition.

Could some of the changes in product distribution in the presence of argon be a result of secondary photolytic reactions?

## REPLY BY F. VOLK

I do not know if photolytic reactions are responsible for the reactions in the chamber.

We suppose that the interaction of the early detonation products during the expansion process with the argon atoms promote reactions which are pressure dependent such as:



We will have the same behavior when using nitrogen as inert atmosphere.

## DISCUSSION

I. B. AKST  
Los Alamos National Laboratory  
Los Alamos, New Mexico

Regarding re-equilibrium by shock at container walls, a calculation at LLNL some time ago showed that products would not reach the walls of a container of your size (~1 meter diameter) in significant quantities if there was 150 mm Hg pressure of a noble gas in the sphere.

## REPLY BY F. VOLK

Thank you for this comment.

# EXPLOSIVE POTENTIAL OF CARBOHYDRATE-METAL COMPOSITES

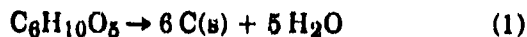
A. J. Tullis, J. L. Austing, W. K. Sumida, D. E. Baker, and D. J. Hrdina  
IIT Research Institute  
Chicago, Illinois 60616

*Chemical equilibrium computer calculations establish that typical carbohydrates, such as starch or sugar, would provide about half as much energy as TNT if they could detonate. Similar computations using metal additives to these carbohydrates indicate that they would provide about 50 percent greater energy in detonation than TNT. Because of the anticipated difficulty in achieving detonation in carbohydrate-metal composites, experiments were conducted using small amounts of high explosive additives to these composites. In particular, use was made of 10 weight percent nitroglycerine in  $\beta$ -lactose, a commercially available pharmaceutical formulation. Adding 10 percent aluminum powder to this composition caused it to become detonable in 25.4-mm steel tubes at 2500-m/s detonation velocity, and about 1.2-GPa detonation pressure at a density of about 1.0 Mg/m<sup>3</sup>. A 4.54-kg charge of this same composition was detonated, and the blast output was monitored. It was established that the blast output was just slightly less than that for TNT, both in terms of blast pressures and impulses. A further experiment, in which 40 weight percent ammonium perchlorate was added to this composition, resulted in a blast output more than twice as great as that from an equal amount of TNT.*

## INTRODUCTION

Organic high explosives (e.g., TNT, RDX, and PETN) are metastable molecular compounds composed of carbon, hydrogen, nitrogen, and oxygen atoms; i.e., CHNO compounds. The nitrogen plays a key role in bonding the oxygen atoms (e.g., as  $-\text{NO}_2$  or  $-\text{O}-\text{NO}_2$ ), but when yielded as a product such as NO or HCN, does not appreciably contribute to the exothermicity of the detonation. It does provide energy, in that its bonding in the metastable CHNO explosives provides energy release even when it is released as elemental nitrogen. This is the energy release mechanism in the detonation of the azides, such as lead azide, which decomposes to the metal and  $\text{N}_2$ . Nevertheless, the lack of nitrogen in carbohydrates is not considered a disadvantage, because exothermic species such as  $\text{H}_2\text{O}$ , CO, and  $\text{CO}_2$  are the major product species that provide the energy in decomposition, or in detonation. Let us now consider the carbohydrates; i.e., CHO compounds.

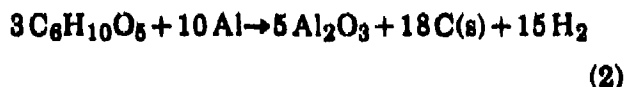
The potential of energy release in the explosion of carbohydrates, such as starch and sugar, are legend. Of course, in these instances these materials are fuels, and lead to catastrophic explosions only upon dispersal and combustion in air. However, these materials are also known to undergo autocatalytic decomposition, even under anaerobic conditions, with considerable exothermic energy release. Consider a typical unit molecule of starch, and assume decomposition as follows:



Under this ideal, optimum chemistry, the net energy yield would be 0.53 kcal/g starch. This is about half the energy release in the detonation of TNT. The carbon remains unreacted.

Because of the many devious decomposition paths of starch, as well as of most carbohydrates, it is most unlikely that they would detonate. Next, consider the addition of

a metal fuel, such as aluminum, to this typical unit molecule of starch:



Even though neither the carbon or the hydrogen are combusted in this simplified chemistry, the net yield would be 1.83 kcal/g starch and aluminum reactants. This is far superior to most high explosives.

Initially, the intent in studying these carbohydrate-metal composites was to consider them as energetic fuels for use in fuel-air explosive applications, which objective is presently under investigation. However, they have also been investigated in the work being reported here as candidates for a new, very novel approach to the development of powerful, yet extremely safe, insensitive explosives.

## BACKGROUND

Although both starch (or other carbohydrate) and aluminum (or other metal) are both extremely energetic when combusted, they manifest their energy release in different ways. In considering these materials as fuels for fuel-air explosives, thermochemical computer codes were implemented to assess their potential Chapman-Jouguet (CJ) characteristics, if they were to detonate as dispersions in air at various concentrations.<sup>1</sup> The CJ temperatures for the two pure components are extremely different, with starch about 2600 K and aluminum about 4200 K at their optimum concentrations in air. Mixtures of starch and aluminum fall at intermediate levels of temperature between these two extremes. In regard to the amount of gas output for the two pure components, starch provides the highest amount of gas per unit weight of material, about 46 mol/kg, while aluminum provides substantially less, about 30 mol/kg at very low concentrations to about 23 mol/kg near stoichiometric conditions. This is as expected, as the aluminum forms condensed species, whereas the starch forms gases. Again, mixtures of starch and aluminum fall intermediate between these two extremes.

However, when the CJ pressures are considered for the two pure components and their

mixtures as a function of concentration, it is evident why mixtures of the two would be advantageous; i.e., both starch and aluminum alone provide relatively low values, just over 2 MPa for starch and about 2.4 MPa for aluminum, whereas mixtures of the two components provide CJ pressures greater than either alone. This is due to the fact that the compromise between the very high temperatures in the case of the aluminum, and the very high amount of gas in the case of the starch, results in heating of the gases to achieve much higher pressure. Of particular interest is the 80/20 weight\* percent starch/aluminum mixture, for which the pressure increases monotonically with increasing concentration. Computations were extended to 1 Mg/m<sup>3</sup>, which is about bulk density of these materials. For comparative purposes, a similar computation was conducted for TNT. Figure 1 illustrates the results of these computations over four orders of magnitude of concentration; i.e., from an aerosol in air to essentially bulk compositions exclusive of air. At the lower concentrations, the higher values of pressure are attributed to the influence of

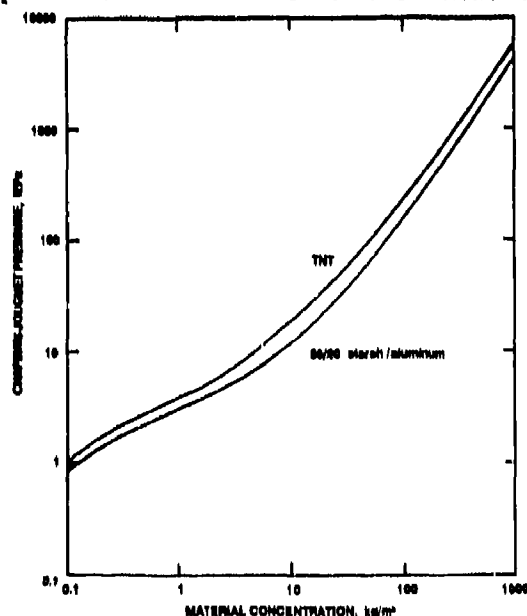


Figure 1. TIGER Code Computed Chapman-Jouguet Pressures for a Specific Mixture of Starch and Aluminum and for TNT as a Function of Concentration in Air from an Aerosol to Bulk Densities of 1 Mg/m<sup>3</sup>

\* All percent values will be on a weight basis, unless stated to the contrary.

air on both TNT and the starch/aluminum mixture. TNT is very fuel-rich, so that at low concentrations<sup>2</sup> oxygen in air provides improved performance. However, the main purpose of this illustration is to demonstrate that an 80/20 percent starch/aluminum mixture at concentrations approaching, and achieving, bulk densities, provides CJ pressures almost comparable to those of TNT!

Hence, additional computations were conducted and effort was expended into investigation of carbohydrate-metal compositions as explosives, in particular, as insensitive explosives. Of course, analytical thermochemical computations for CJ conditions only provide CJ characteristics that could be expected if the investigated material/composition were to detonate. As will be shown later, even starch by itself provides relatively good CJ characteristics, if it should detonate.

Several mixtures of starch and aluminum powder were prepared and tested, and although very energetic outputs were obtained, they did

not detonate under the conditions of the tests; i.e., confined in 25.4-mm diameter steel tubes. Hence, to sensitize these compositions so as to possibly achieve detonation, small amounts of explosive powders were added. This technique was based on previous work involving the detonability of very poorly detonable explosives, such as ammonium perchlorate (AP), which were sensitized to achieve stable detonation in tubes of about 6-mm diameter, using as little as 2 or 3 percent nitroguanidine (NQ).<sup>3</sup>

## ANALYTICAL COMPUTATIONS

Before these experiments were conducted, thermochemical computer computations were conducted to assess the influence of some molecular explosive additives upon CJ characteristics of the starch/aluminum compositions. Tables 1 and 2 illustrate the influence of various amounts of NQ and PETN additives; e.g., from 9 to 33 percent, for a 67/33 percent starch/aluminum composition.

*Table 1. Computed Chapman-Jouguet Detonation Characteristics for 67/33 Weight Ratio Starch/Aluminum Alone and with Various Amounts of Nitroguanidine Additive at a Density of 1.0 Mg/m<sup>3</sup>*

<u>Composition Percent</u> Starch/Al/NQ	<u>Temperature</u> K	<u>Pressure</u> GPa	<u>Velocity</u> km/s	<u>Gas Volume</u> mol/kg
67/33/00	3463	3.09	3.49	17.3
61/30/09	3343	3.73	3.78	20.4
55/28/17	3272	4.25	4.01	22.7
52/25/23	3296	4.40	4.05	23.4
45/22/33	3093	5.05	4.40	27.7

*Table 2. Computed Chapman-Jouguet Detonation Characteristics for 67/33 Weight Ratio Starch/Aluminum Alone and with Various Amounts of PETN Additive at a Density of 1.0 Mg/m<sup>3</sup>*

<u>Composition Percent</u> Starch/Al/PETN	<u>Temperature</u> K	<u>Pressure</u> GPa	<u>Velocity</u> km/s	<u>Gas Volume</u> mol/kg
67/33/00	3463	3.09	3.49	17.3
61/30/09	3427	3.85	3.84	20.5
55/28/17	3418	4.44	4.07	23.0
52/25/23	3403	4.89	4.25	25.1
45/22/33	3529	5.04	4.41	28.1

In both cases all of the CJ characteristics improved; i.e., detonation temperature, pressure, velocity, and amount of gas, except in the case of NQ where the temperature decreased with increased amounts of NQ. Figures 2 and 3 illustrate the influence on detonation product species as a function of explosive additive. It is evident, that the slightly oxidizer-rich PETN explosive causes much quicker combustion of carbon to CO than does the fuel-rich NQ. Hence, the addition of explosives to the carbohydrate-metal compositions causes improvement in oxygen balance by providing oxygen to the uncombusted carbon and hydrogen; preferentially for

the carbon to CO first, and then for the hydrogen to H<sub>2</sub>O next, especially in the case of the PETN. Species below 3 mole percent were not included in these figures. Even at the highest levels of explosive addition; i.e., 50 percent, there is insufficient oxygen to combust the hydrogen, much less to combust the CO to CO<sub>2</sub>.

For experimental purposes, use was made of commercial nitroglycerine (NG) as available in the pharmaceutical product absorbed on β-lactose (LAC). Therefore, thermochemical computations were conducted on this formulation with various amounts of aluminum

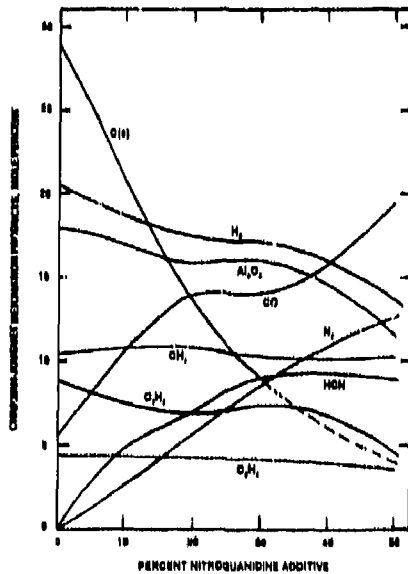


Figure 2. TIGER Code Computations of the Influence of Nitroguanidine Additive on a Typical Mixture of Starch and Aluminum at 1.0 Mg/m<sup>3</sup> Regarding the Chapman-Jouguet Product Species

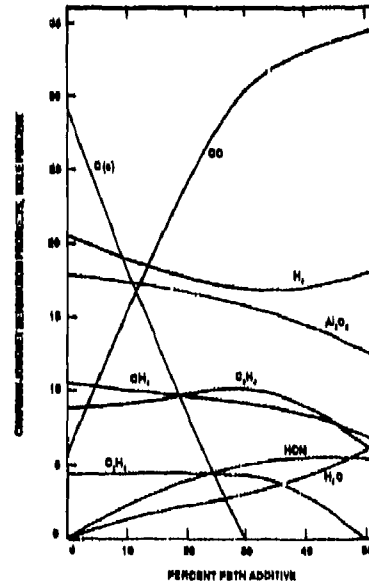


Figure 3. TIGER Code Computations of the Influence of PETN Additive on a Typical Mixture of Starch and Aluminum at 1.0 Mg/m<sup>3</sup> Regarding the Chapman-Jouguet Product Species

Table 3. Chapman-Jouguet State Computations for LAC/NG/Al Compositions at a Density of 1.0 Mg/m<sup>3</sup> Using the Tiger Code

Composition Percent LAC/NG/Al	Temperature K	Pressure MPa	Detonation Velocity m/s
100.0/00.0/00.0	1703	3948	4087
90.0/10.0/00.0	1806	4955	4563
85.5/09.5/05.0	1890	5710	4771
81.0/09.0/10.0	1870	5684	4655
76.5/08.5/15.0	2321	5668	4619
72.0/08.0/20.0	2660	5396	4427
67.5/07.5/25.0	3022	5073	4199

additive. Table 3 illustrates the results of these computations, from the carbohydrate alone to 75 percent of the 10/90 percent NG/LAC and 25 percent aluminum.

As was indicated earlier, note that the carbohydrate alone is theoretically (thermodynamically) capable of detonation. For the aluminum additive, it appears that CJ pressures and velocities become optimized at about 5 percent, degrading considerably beyond about 15 percent. The temperature, of course, continues to increase with increase in aluminum, as would be expected, due to continued increase in the formation of highly exothermic  $Al_2O_3$ .

Hence, computations indicated that about 5 percent aluminum and no more than 15 percent was optimum for the aluminum additive, whereas explosive additive improved without such optimum level, to the extent investigated at 50 percent explosive. Since it was desired that the amount of explosive additive be minimized, eventually no explosive additive would be desired based on the critical conditions for achieving detonation in carbohydrate-metal compositions. Later, in carbohydrate-metal-oxidizer compositions, the least amount of explosive that would provide sufficient sensitization of the composition to achieve detonation was desired. However, the influence of various explosive additives on the computed CJ characteristics had to be considered. Therefore, computations were conducted using glucose as a typical carbohydrate with various explosive additives; e.g., NQ, NG, PETN, RDX, and HMX. The results indicated essentially very little variance in detonation characteristics in regard to the type of explosive. In all cases, the temperature continued to increase in the region investigated; i.e., up to 25 percent explosive, whereas both pressures and velocities appeared to peak in the neighborhood of 10 to 15 percent explosive additive. This was especially fortuitous, since the experimental composition that was to be used in this investigation was 10 percent NG. Nevertheless, it was of interest to assess the amount of NG as a variable with the amount of aluminum to be added. Figures 4 through 6 illustrate the results of these computations. The amount of NG provides improvement across the whole region, except at the higher levels of

aluminum, wherein the amount of NG makes little difference. In Figure 4, at 10 percent NG and 10 percent aluminum, a near optimum condition for detonation velocity is achieved. In Figure 5 temperature, as usual, increases, although here it maximizes at about 40 percent for all levels of NG additive. Figure 6, which illustrates the most important characteristic, indicates a maximum of 10 percent aluminum with no substantial improvement with increased amount of NG. This further confirmed that the 10/90 percent NG/LAC was near optimum, and that 10 percent aluminum would also be near optimum. These computations provided the basis for the subsequent experimental investigation.

## EXPERIMENTAL INVESTIGATION

The experimental investigation was conducted using two types of experiments: (1) confined "pipe" tests to assess the detonability of the compositions in terms of go/no-go of detonation, as well as establishing detonation velocities and pressures; and (2) large-scale blast-pad experiments, wherein blast outputs were monitored to establish relative outputs of the compositions in comparison to standard explosives, such as TNT.

### Confined Diagnostic Pipe Tests

Figure 7 illustrates the "pipe" apparatus that was used to evaluate the detonability of candidate explosives, as well as to measure both detonation velocities and pressures at multiple incremental stations over an extended distance; i.e., 304.8 mm. This experimental technique, which was developed and described many years ago by IITRI,<sup>4</sup> is an excellent diagnostic device for evaluating the detonation, as well as deflagration, characteristics of explosives and pyrotechnics. The size of the device is made sufficiently long to establish steady-state propagation velocities, if they exist, and the diameter can be varied to evaluate critical diameter effects. Typically, the device is 25.4 mm in diameter and 304.8 mm long. The collocated fiber-optic light-detector probes and carbon-resistor shock arrival-time/pressure gauges are located at multiple stations along the length of the tube,

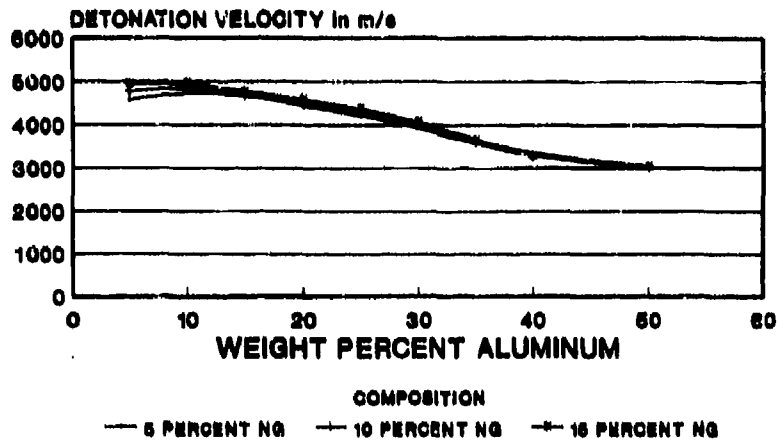


Figure 4. TIGER Code Computations of Chapman-Jouguet Detonation Velocity for Glucose at Several Amounts of NG Additive as a Function of Aluminum Additive at a Density of  $1.0 \text{ Mg/m}^3$

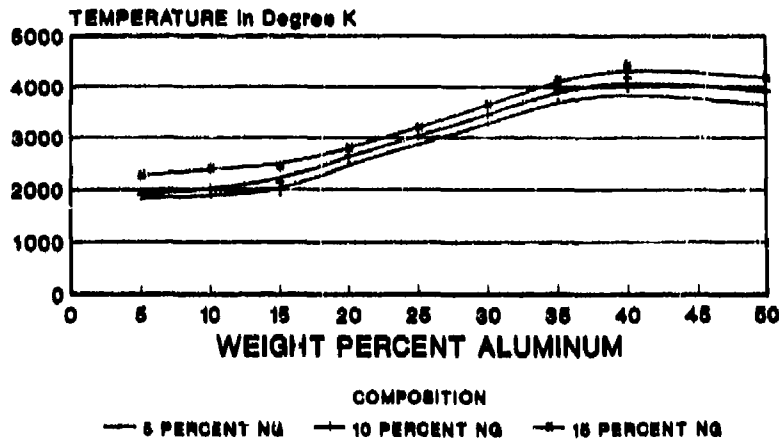


Figure 5. TIGER Code Computations of Chapman-Jouguet Detonation Temperature for Glucose at Several Amounts of NG Additive as a Function of Aluminum Additive at a Density of  $1.0 \text{ Mg/m}^3$

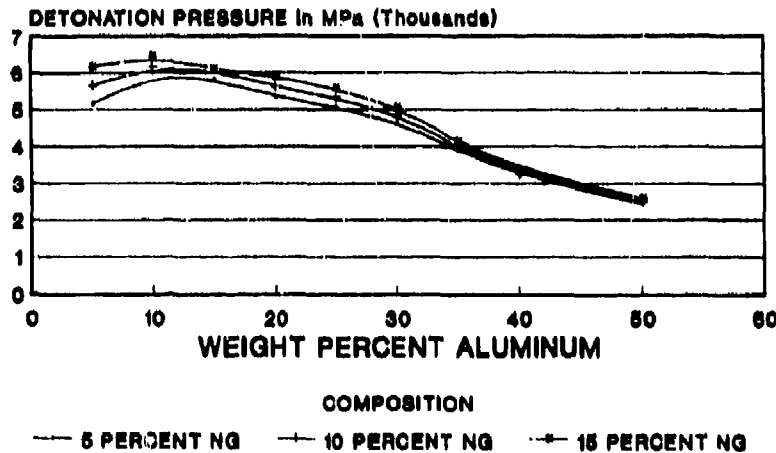
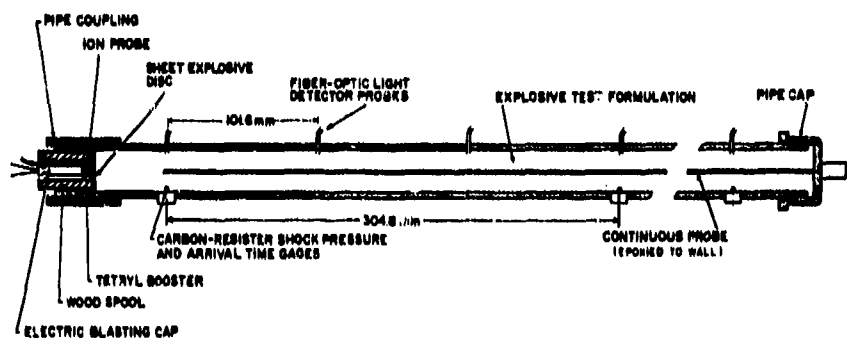


Figure 6. TIGER Code Computations of Chapman-Jouguet Detonation Pressure for Glucose at Several Amounts of NG Additive as a Function of Aluminum Additive at a Density of  $1.0 \text{ Mg/m}^3$



*Figure 7. Schematic of the IITRI-Developed Apparatus for Characterization of Detonation or Deflagration in Explosive and Pyrotechnic Compositions with Emphasis Upon the Reaction Flame and Shock Fronts*

and provide information regarding the detonation/deflagration velocity, induction time, pressure, and presence of instability or transition of the reaction process; or steady propagation velocity, as the case might be. The light-detector sensors respond to the flame front (and reaction duration) of the reaction, while the pressure gauges respond to the shock/pressure front. Since the flame- and pressure-front sensors are collocated, induction times between the two fronts can be assessed. An extended reaction zone, generally quite luminous, is also observed when present but may complicate the resolution unless the monitoring stations are sufficiently separated or are monitored on individual channels. In the experiments discussed here, the light-detector stations were 101.6 mm apart, and their responses were monitored on two channels; i.e., the odd-numbered stations were monitored on one channel, and the even-numbered stations on the other channel. Hence, on each channel the distance between consecutive stations was 203.2 mm.

The use of the carbon-resistor gauges to determine detonation pressures has been previously described,<sup>5</sup> but considerable present effort is being conducted to better quantify the responses, as well as to develop better utilization of these gauges for high pressure output explosives. Their present use for the work described here is based on calibration procedures using Composition C4, RDX, and NQ, and will be published in the near future.

Although illustrated in the figure of this apparatus, the continuous-velocity probe was not used in the present work. Initiation of detonation is generally attempted using conventional detonator and booster pellets, but further augmented by using one or more sheet explosive discs of Detasheet®, as needed, of the same diameter as the I.D. of the tube. Overdrive or underdrive is readily identified from the light-detector signals.

As discussed earlier, for expediency the pharmaceutical formulation 10/90 percent NG/LAC was used as is, and additives, therefore, caused the amount of NG to vary accordingly; i.e., the ratio of NG to the LAC always remained unchanged. Hence, by adding 10 percent flaked aluminum powder to this material, the overall percentages became as follows: aluminum, 10; NG, 9; and LAC, 81. This composition was tested in the apparatus described here, and detonated with stable velocity of about 2500 m/s. Figure 8 illustrates the light-detector output signals obtained using the fiber-optic probes, which are then plotted incrementally in Figure 9. It appears that the detonation was initially underdriven, and accelerated to a stable velocity.

In another test, a composition containing a 5-percent additive of aluminum was similarly tested. Figure 10 illustrates the stable detonation velocity observed in this case. It became quite stable at about 2000 m/s, and appeared to be initially slightly overdriven by the initiation charge. In this test, the actual

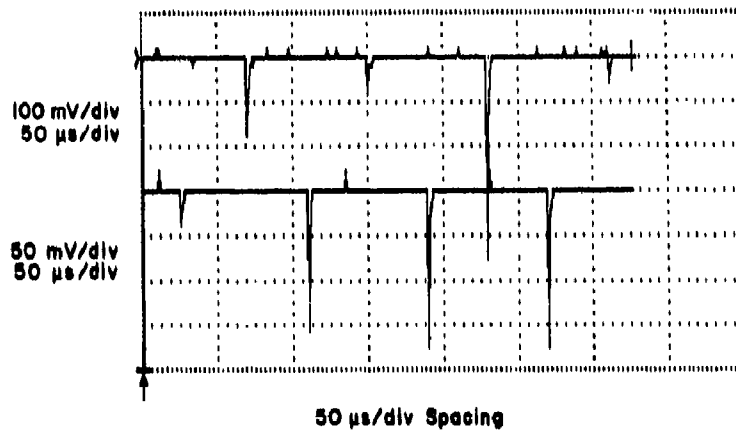


Figure 8. Example of Fiber-Optic Light-Detector Probe Signals Obtained in the Detonation of 10/90 Percent NG/LAC with 10 Percent Aluminum Powder Additive in the Detonation/Deflagration Tube Apparatus Illustrated in Figure 7

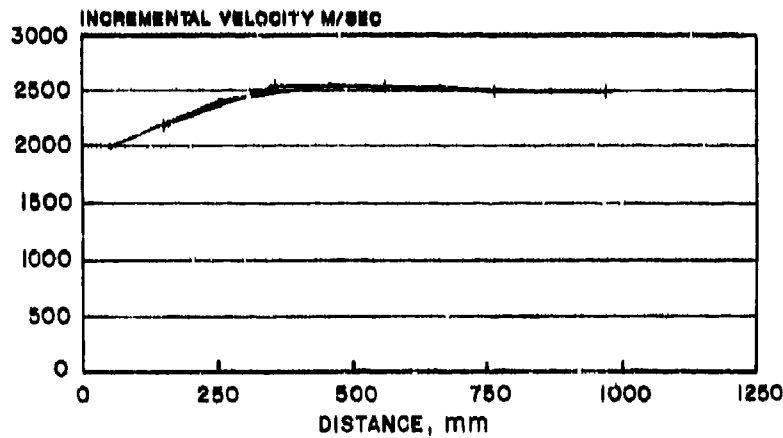


Figure 9. Incremental Velocities Obtained from the Fiber-Optic Light-Detector Probes for the Detonation of 10/90 Percent NG/LAC with 10 Percent Aluminum Powder Additive at a Density of  $1.0 \text{ Mg/m}^3$  Tested in the Tube Apparatus Illustrated in Figure 7

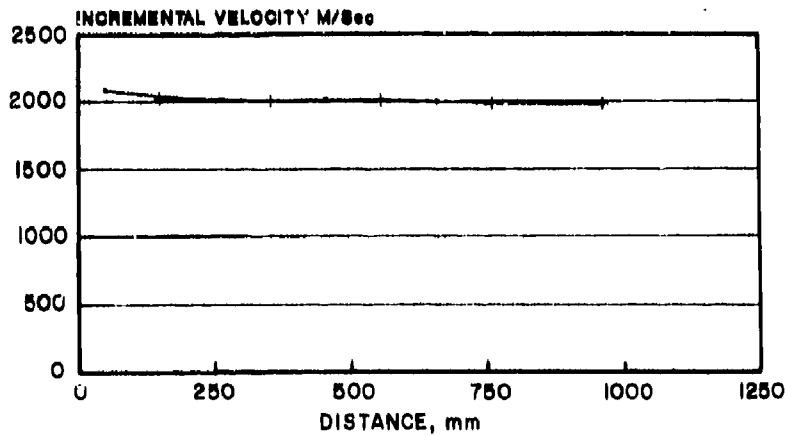


Figure 10. Incremental Velocities Obtained from the Fiber-Optic Light-Detector Probes for the Detonation of 10/90 Percent NG/LAC with 5 Percent Aluminum Powder Additive at a Density of  $1.0 \text{ Mg/m}^3$  Tested in the Tube Apparatus Illustrated in Figure 7

composition percentages were: aluminum, 5; NG, 9.5; and LAC, 85.5. A composition containing 15 percent aluminum failed to detonate. Hence, another test was conducted with a composition that contained 12.5 percent aluminum. In this case, an incipient detonation occurred, but failed by the third monitoring station.

Chemical equilibrium TIGER code computations for the 10 percent aluminum, 10/90 percent NG/LAC composition at  $1 \text{ Mg/m}^3$  predicted a detonation velocity of 4655 m/s, which is about double the value obtained experimentally. It is highly probable that the test condition of only 25.4-mm diameter was subcritical, and although a stable detonation velocity was obtained, it was not the CJ condition. Further studies in larger tubes will be required to resolve this.

Nevertheless, detonation was obtained in both the compositions containing 5 and 10 percent aluminum additive. The composition containing 10 percent aluminum provided superior velocity and pressure. It is quite possible that, although the finest aluminum powder, i.e., flaked aluminum at 3 to 4  $\text{m}^2/\text{g}$  surface-to-mass ratio, was used (which would be equivalent to spherical aluminum particles of less than a micron diameter for the same surface-to-mass ratio), all of the aluminum powder was not available to the detonation regime. This will also require further study.

### Large-Scale Blast-Pad Test

Although detonation of the carbohydrate-metal composition was achieved, albeit sensitized with NG additive, it was not known how much energy was in fact released or to what extent the carbohydrate-metal components were involved. Therefore, a large-scale unconfined blast-pad test was conducted, using 4.165 kg of the same composition of 10 percent aluminum and 90 percent NG/LAC. The composition was placed in a cardboard cylindrical canister of 177.8-mm I.D. and about the same height. Implosive initiation was achieved using two wraps of C1 Detasheet®, in turn initiated with a wagon-wheel Detasheet® on the top of the charge. Hence, the total weight of the initiation charge was 371 g. Although this is a considerable amount of initiation charge, it was believed that such amount and

an implosion method of initiation might be necessary because of the anticipated insensitivity of this composition, especially in the unconfined condition.

A high-speed 16-mm color film Photec camera was used to monitor the results, in addition to the blast pressure, impulse, and arrival times obtained from the piezoelectric PCB pressure transducers located in the blast-pad facility. The composition did detonate, generating a spall from the center of the 25.4-mm thick steel plate upon which the charge had been placed. Such spall could only occur if the total composition detonated; i.e., not simply the outside wrap of Detasheet®. However, it was also evident that considerable energy release occurred after the detonation, as a huge orange fireball appeared. This is consistent with the analytical predictions, and indicative of the vast amount of hot carbon generated.

The blast data from this test are plotted in Figures 11 and 12, and compared to those of a TNT hemisphere, as functions of scaled distance. It is apparent that the blast pressures were comparable to those of the TNT, especially close-in to the charge, but that the scaled impulses were well below those of the TNT. Nevertheless, these results are very

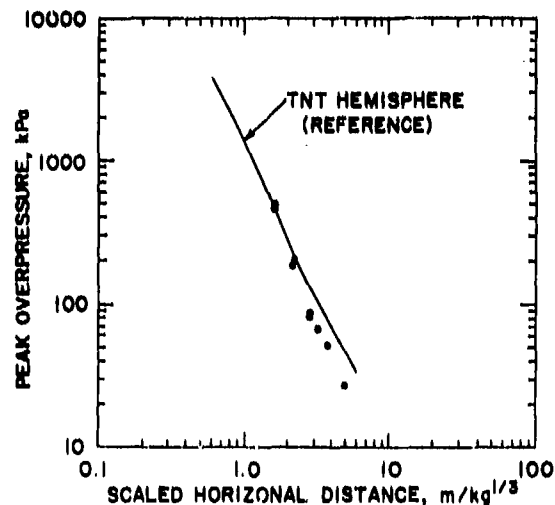


Figure 11. Blast Pressure Comparison for the Detonation of 10/90 Percent NG/LAC with 10 Percent Aluminum Powder Additive at a Density of  $1.0 \text{ Mg/m}^3$  and Cast TNT

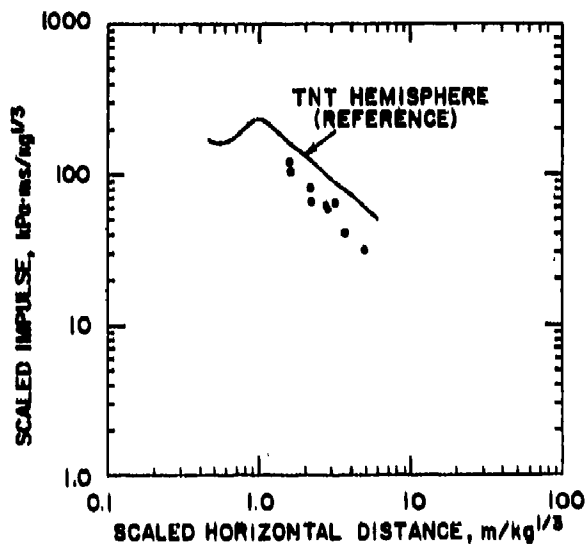


Figure 12. Blast Scaled Impulse Comparison for the Detonation of 10/90 Percent NG/LAC with 10 Percent Aluminum Powder Additive at a Density of 1.0 Mg/m<sup>3</sup> and Cust TNT

encouraging, especially since no effort was made to compensate for the extremely fuel-rich condition of this composition. Such effort is presently underway, and some preliminary information on these studies is included here.

#### Improved Stoichiometry Using Ammonium Perchlorate

Although it was established that, under the compromise of sensitizing with a small amount of explosive powder, the carbohydrate-metal compositions were capable of detonation, both components are indeed excellent fuels. Therefore, in order to assess the potential of these compositions as ingredients to insensitive explosives, some experiments were conducted using various amounts of AP additive. This work is currently in progress, and results will be published at a future date. However, some preliminary results are included here.

Several tests were conducted with the standard NG/LAC/Al with percentages of 9/81/10, respectively, to which 15, 30, and 45 percent AP was added. These compositions were nominally at a density of 1.0 Mg/m<sup>3</sup>, and achieved detonation velocities between 3500

and 4000 m/s with accompanying detonation pressures of nominally 10 to 20 GPa.

A large-scale test was also conducted, using 4.165 kg of the standard NG/LAC/Al composition, to which 40 percent AP was added. This test was also conducted upon the blast-pad to monitor blast output. The test was conducted in an identical manner as the previously described large-scale test without the AP. The output of this detonation, as expected, was substantially greater than in the case of the test without the AP. Figures 13 and 14 provide a comparison of this test with the former test. Figure 13 illustrates the blast pressures that were obtained for both tests, and Figure 14 illustrates the scaled impulse for both tests; plotted as functions of scaled distance in both cases. As these are logarithmic plots, it is evident that the composition with the AP provides very substantial improvement in both blast pressure and impulse. In fact, the improvement of the composition with the AP is better than twice the effective equivalence for TNT.

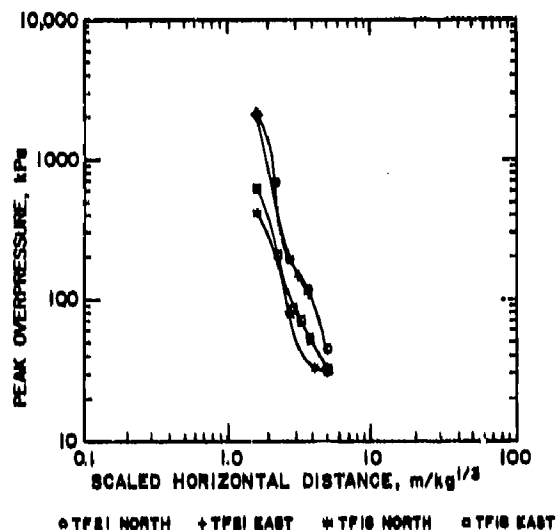


Figure 13. Blast Pressure Comparison for the Detonation of 10/90 Percent NG/LAC with 10 Percent Aluminum Powder Additive (TF18) and the Same Composition at 60 Percent with 40 Percent AP Additive (TF21), Both at Nominally 1.0 Mg/m<sup>3</sup>

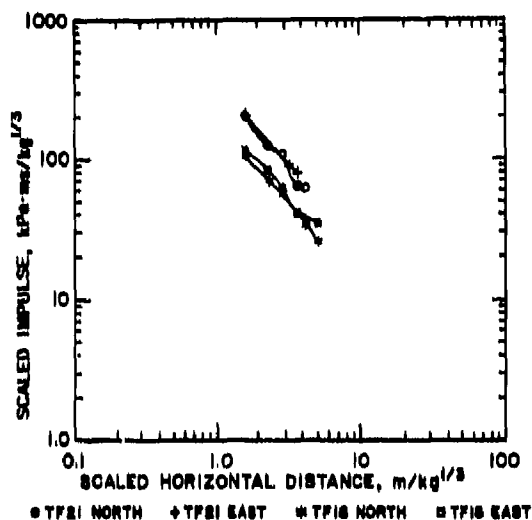


Figure 14. Blast Scaled Impulse Comparison for the Detonation of 10/90 Percent NG/LAC with 10 Percent Powder Aluminum Additive (TF18) and the Same Composition at 60 Percent with 40 Percent AP Additive (TF21), Both at Nominally  $1.0 \text{ Mg/m}^3$

## DISCUSSION

The detonation of carbohydrates with metal additives appears to be feasible, and was achieved in this work by sensitizing the compositions with a small amount of explosive (for expediency NQ, although it is believed that comparable results would be obtained with most molecular  $\text{CHNO}$  explosives). Both NQ and PETN have been previously used to sensitize pyrotechnics, such as aluminum-potassium perchlorate and Teflon<sup>®</sup>-aluminum, to achieve detonation in confined pipe tests similar to those described in this work.<sup>6</sup> Hence, although these carbohydrate-metal compositions have the potential to be useful as insensitive explosives, or as components of insensitive explosives, they no doubt have very large critical diameters and require very high thresholds for stimuli to achieve detonation. Furthermore, starches and sugars may not be the most advantageous candidates in the vast domain of carbohydrates, and factors such as stability and particle size must be considered. Particle size has not been emphasized here, but it is probably the major factor that influences the potential detonability of the compositions

discussed in this work, as well as in typical fuel/oxidizer composite explosives.<sup>7</sup>

Further work is required, and is, at present, underway. The carbohydrate-metal compositions, alone and with oxidizer additive to improve the fuel/oxidizer balance, are expected to form the basis for novel categories of insensitive explosives, with perhaps an added advantage of more powerful explosives. However, the bulk densities of these compositions are presently too low to provide the anticipated performance that would be obtained at densities comparable to typical high explosives, such as RDX and TNT.

## ACKNOWLEDGEMENT

The work reported here was conducted at IITRI under Internal Research and Development (IR&D) effort, and is considered proprietary. The authors express their appreciation to IITRI for the opportunity to conduct this work.

## REFERENCES

1. Tulis, A. J. and Sumida, W. K., "Computations of Chapman-Jouguet Characteristics for Fuel and Reactive Powder Mixtures in the Dispersed and Condensed States," *Eighteenth Annual ICT Conference, Karlsruhe, West Germany, 1987*, pp. 4711-4713.
2. Tulis, A. J.; Austing, J. L.; and Heberlein, D. C., "Detonation Tube Studies of Reactive Particles in Two-Phase Detonations," *Fourteenth (International) Symposium on Shock Tubes and Waves, Sydney, Australia, 1983*.
3. Tulis, A. J., "Sympathetic Detonation of Ammonium Perchlorate by Small Amounts of Nitroguanidine," *Sixth (International) Symposium on Detonation, San Diego, CA, ONR ACR-221, 1976*, pp. 173-182.
4. Tulis, A. J. and Selman, J. R., "Characterization of Shock and Reaction Fronts in Detonations," *Rev. Sci. Instrum.*, 53(10), 1982, pp. 1586-1591.
5. Austing, J. L.; Tulis, A. J.; and Johnson, C. D., "Detonation Characteristics of Very Low Density Explosive Systems," *Fifth*

*(International) Symposium on Detonation*, Pasadena, CA, ONR ACR-184, 1970, pp. 47-57.

6. Tulis, A. J., "Detonation of Pyrotechnics with Explosive Additives," *Fourth (International) Conf. of Group de Travail de Pyrotechnie*, LaGrande-Motte, France, 1989.
7. Tulis, A. J., "Influence of Multi-Modal Particle Size Distributions on Detonation Stoichiometry of Fuel Oxidizer Powders," *Symposium (International) on Pyrotechnics and Explosives*, Beijing, China, ISPE, China Academic Publishers, 1987, pp. 119-124.

## DISCUSSION

**H. GRYTING, Gryting Energetics  
Sciences Company, San Antonio, TX**

Can you indicate the reliability of detonation of sucrose and aluminum mixtures with and without ammonium perchlorate present? Have you established any detonation limits for such mixtures? Have you established the amount of oxide coating on the aluminum you use?

## REPLY BY A. J. TULIS

We have not, to date, obtained sustained detonation in sucrose and aluminum mixtures without sensitizing with small amounts of explosive powder, probably due to the tremendous insensitivity (and associated critical diameters) of these mixtures. With the presence of ammonium perchlorate, we have qualitatively achieved detonation, but it is not known to what extent the detonation was driven by the aluminum and ammonium perchlorate irrespective of the presence of the carbohydrate.

Detonation limits for fuel and oxidizer powders are not specific, being functions of particle size, for instance, and particle size distributions. Our studies to date have been concerned with the feasibility of achieving detonation and the parameters that are most critical, such as particle size in relation to homogeneity and stoichiometry. We do not anticipate determining specific detonation limits except as established in this work for the case of aluminum additive to the NG/LAC composition, and this was dependent upon the apparatus, particle size/geometry of the aluminum powder, and confinement and pipe diameter. Furthermore, the influence of density has not been investigated.

The manufacturer of the flaked aluminum used in this work quotes a 3 percent by weight aluminum oxide coating. The thickness of the aluminum oxide coating, of course, degrades the probability of detonation as well as degrading performance.

## DISCUSSION

**D. F. ALDIS, Lawrence Livermore  
National Laboratory, Livermore, CA**

Do you have any experimental results with aluminum and starch?

## REPLY BY A. J. TULIS

We do not have any detonation results with aluminum and starch; in 25.4 mm diameter steel pipes such compositions deflagrated violently. At present, we are experimenting with aluminum and starch sensitized with PETN, RDX, and nitroguanidine powder. The problem rests with obtaining starch of sufficiently small particle size.

**SESSIONS ON**  
**CHEMISTRY AND COMPOSITION**

**Cochairmen: Tom Larson**  
**Los Alamos National Laboratory**

**Fritz Schedlbauer**  
**Fraunhofer Institut für Chemische**

**and**

**Horst Adolph**  
**Naval Surface Warfare Center**

**Fred Volk**  
**Fraunhofer Institut für Chemische**

# A REVIEW OF PARAMAGNETIC RESONANCE PRODUCTS IN CONDENSED PHASE ENERGETIC MATERIALS

M. D. Pace  
Code 6120

Naval Research Laboratory  
Washington, D. C. 20375-5000

*Since 1980 studies of free radical formation in condensed phase explosives and propellants have expanded. As a result, free radicals have been detected in most well-known energetic materials including RDX, HMX, TATB, tetryl, TNT, and nitroguanidine. Researchers at F. J. Seiler Research Laboratory (FJSRL), the Army Armament Research and Development Center, and the Naval Research Laboratory (NRL) have contributed to much of the current literature. Reports of work by these Laboratories have appeared in prior Proceedings of the Symposium (International) on Detonation. Many additional reports by these and other researchers have been published in the scientific literature. In this review, the detection and identification of free radicals in energetic materials is summarized and discussed.*

## INTRODUCTION

This review covers papers from 1971 to 1988 describing the analysis of free radical products in condensed phase energetic materials. Free radicals are paramagnetic having an electron spin quantum number of  $S \geq 1/2$ . Most studies of free radicals in the condensed phase (including crystals, powders, and solutions) have detected free radicals by using cw electron paramagnetic resonance spectroscopy (EPR). The spectra derived from cw EPR are used to determine a free radical's structure. Dynamics of the electron spin system require time-resolved pulsed experiments yet to be performed.

Free radicals may be produced in condensed phases by electron transfer reactions or by fragmentation of parent molecules during photolytic, thermal, or shock initiation. This review is divided into these three categories of initiation. This review is not comprehensive. In particular, the vast amount of material of photolysis of nitroaromatics in solution is not covered. Instead, selected papers are included whose references lead to most other literature on this subject. Some references are included

in the section entitled Shock Initiation, which do not report experimental detection of free radicals, but allude to their formation. Tables 1 and 2 show structures of the molecular and free radical products which are referenced by Roman numerals.

## PHOTOLYTIC INITIATION

The number of papers on free radicals in energetic materials has increased since 1980; however, several key papers were published in the period from 1970-1980. Early studies recognized that photochemical decomposition of RDX produces free radicals. In studies by Stals and co-workers,<sup>1</sup> powder samples of RDX were irradiated with  $\gamma$ -radiation or by 254-nm light yielding evidence of paramagnetic  $\text{NO}_2$  and other unidentified free radicals. The EPR spectra generated at 77K were invariant to added amounts of  $\text{NO}$ ,  $\text{NO}_2$ , and  $\text{O}_2$  during the photolysis. Mechanisms of decomposition were suggested from these results. However, in these studies only paramagnetic  $\text{NO}_2$  was specifically identified. During the same period two additional papers appeared which reported similar findings for other nitramines. Bodnar and Rowell<sup>2</sup> give one of the first reports of

nitroxyl free radicals formed in nitramines as a result of uv photolysis. In this study, nitroxyl radicals were produced for a series of cyclic nitramines including N-nitropyrrolidine, nitropiperidines, N-nitromorpholine, and cyclic di-, tri-, and tetra-nitramines including RDX and HMX. Their study found that at room temperature uv-irradiation of single crystals produced detectable free radicals in these compounds *except* in RDX and HMX where irradiation led to degradation of the crystals, but no detectable EPR signals. Ultraviolet irradiation of solution phases produced nitroxyl radicals at room temperature for RDX (I), but not for HMX.

Another paper by Darnez and Paviot<sup>3</sup> reported results for uv photolysis of RDX and HMX in acetonitrile solution. These researchers used <sup>15</sup>N-labeled and deuterium substituted RDX and HMX to deduce the structures of the nitroxyl radicals. They also reported that the irradiation of RDX solutions produced three successive paramagnetic species whose appearance and decay depends upon temperature. The radicals are assigned as a cyclic nitroxyl radical (I), an unidentified radical with a spectrum similar to that observed for thermal decomposition of neat RDX near 200°C, and a third radical (IX). HMX was found to produce only a nitroxyl radical (III and IV) providing evidence of different decomposition pathways of these two nitramines. Researchers at FJSRL showed that uv-photolysis of RDX and HMX in dioxane solution produces identical nitroxyl radicals to those reported in Reference 3.<sup>8</sup> Photolysis of N,N'-dimethyl-dinitroxamide produced the radical with structure X in Table 1. Photolysis of dimethylnitramine in acetonitrile was found to produce (CH<sub>3</sub>)NO· radicals. A study of photolyzed single crystals of dimethylnitramine was later reported by Owens and Vogel in 1976.<sup>4</sup>

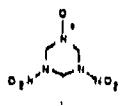
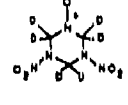
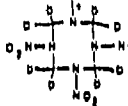
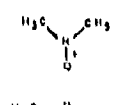
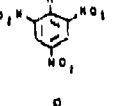
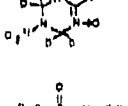
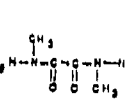
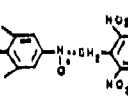
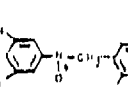
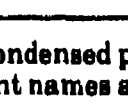
The initial findings of Stals that NO<sub>2</sub> is produced in photolyzed RDX powder at low temperatures was further investigated by researchers at NRL. Single crystals of RDX and HMX photolyzed with broadband uv-light at 77K are shown to have ordered orientations of NO<sub>2</sub> in these crystal lattices. Different sites corresponding to loss of both axial and

equatorial NO<sub>2</sub> groups were assigned to the RDX results.<sup>15</sup> HMX has higher molecular symmetry and loss of NO<sub>2</sub> due to dissociation of the N(3)-N(4) bond was assigned.<sup>35</sup> NO<sub>2</sub> production was further investigated in solution. RDX, HMX, and Nitroguanidine dissolved in DMSO and DMSO-d<sub>6</sub> were shown to undergo a complex uv-initiated decomposition reaction to form an adduct radical with the deuterated solvent (VIII).<sup>20</sup> A different free radical was observed from RDX uv-irradiated in DMSO (II). HMX and nitroguanidine did not produce detectable EPR signals in DMSO during uv-photolysis.

There are several energetic materials in which stabilized free radicals are observed at room temperature. Salt crystals of nitroguanidine yield detectable levels of NO<sub>2</sub> and a second radical (XIV) when irradiated with x-radiation at room temperature. These structures were correlated with the reported crystal structures.<sup>26</sup> A crystalline phase matrix isolated radical (VI) is observed by uv-irradiation of tetryl.<sup>31</sup> This radical is stable at room temperature, but has a complicated set of single-crystal EPR spectra. In further studies of tetryl at NRL, we have observed that crystals of tetryl exposed to visible light for several months also contain the same radical, stable at room temperature. An attempt to analyze the complicated EPR spectra is in progress.

The photochemical decomposition of TNT and related compounds has been studied by FJSRL.<sup>11</sup> Photolysis of TNT in dioxane produced three types of radicals: a radical anion (XVII), a hydrogen-adduct radical (XVI), and a solvent-adduct radical (XV). The radical anion was produced immediately upon irradiation. The formation of XVII was attributed to decay of the hydrogen-adduct species which was observed by the photolysis of TNT in diethyl ether. Photolysis of the related compounds nitrobenzene and p-nitrotoluene yielded solvent adduct radicals. Owens<sup>23</sup> later investigated the formation of uv-induced radicals in TNT and DNT powders. The complicated powder spectrum and a five-line solution phase spectrum of the radical extracted into benzene led to assignment of a nitroso anion radical species (XVIII).<sup>20</sup> Similar studies of TATB

**Table 1. Nitroxyl Radicals of Energetic Materials**

Designation in Text	Structure	Parent Compound	Means of Initiation	Phase <sup>a</sup>	Temperature <sup>b</sup>	References
I		RDX	uv thermal	sulfolane acetonitrile	RT 170°C	2, 3, 20, 21, 29
II		RDX-d <sub>6</sub>	uv	DMSO-d <sub>6</sub>	RT	3, 21
III		HMX	uv thermal	DMSO sulfolane	RT 190°C	2, 3, 24
IV		HMX-d <sub>6</sub>	uv	crystal DMSO-d <sub>6</sub>	RT	3
V		Dimethyl Nitramine	uv	DMSO	RT	3
VI		Tetryl	uv	crystal	RT	3, 31
VII		RDX-d <sub>6</sub>	thermal	sulfolane	190°C	28
VIII		RDX/DMSO-d <sub>6</sub>	uv	DMSO-d <sub>6</sub>	RT	20
IX		RDX	uv	acetonitrile	RT	3
X		N-N'-dimethyl dinitroxamide	uv	acetonitrile	RT	3
XI		TNT	thermal	kieselguhr <sup>c</sup>	240°C	32
XII		TNT/TNE	thermal	kieselguhr	240°C	32

<sup>a</sup> The condensed phases are indicated as the medium in which the free radicals are detected. Solvent names are indicated for solutions, and crystal or powder for solids.

<sup>b</sup> Temperatures at which free radicals were observed are listed.

<sup>c</sup> Kieselguhr is an inert powder.

Table 2. Other Free Radicals of Energetic Materials

Designation in Text	Structure	Parent Compound	Means of Initiation	Phase <sup>a</sup>	Temperature <sup>b</sup>	References
XIII		RDX, HMX TNT, NQ <sup>+</sup> Cl <sup>-</sup>	uv	crystal powder	RT, < RT	1, 6, 7, 9, 13, 15, 28
XIV		NQ <sup>+</sup> Cl <sup>-</sup>	x-ray	crystal	RT	28
XV		nitrobenzene dinitrobenzene	uv	dioxane	RT	11
XVI		TATB	uv-vis	DMSO	RT	10
XVII		TNT	uv	dioxane	RT	11
XVIII		TNT	uv	benzene	< 5°C	23
XIX		p-nitro- phenylacetate	uv	H <sub>2</sub> O	RT	33
XX	$\text{Cu}(\text{NH}_3)_2^{2+}$	$\text{Cu}(\text{NH}_3)_4(\text{NO}_3)_2$	thermal	powder	160°C	16, 17

<sup>a</sup>The condensed phases are indicated as the medium in which the free radicals are detected. Solvent names are indicated for solutions, and crystal or powder for solids.

<sup>b</sup>Temperatures at which free radicals were observed are listed.

have shown the formation of a hydrogen adduct radical in uv-irradiated powders (XVI).<sup>10</sup> In related studies p-nitrophenyl acetic acid, which

contains a single nitro group, has been shown to produce an anion radical in uv photolyzed solutions (XIX).<sup>33</sup>

Some general observations are that RDX and HMX undergo different photolysis decomposition mechanisms as shown, for example, by References 2 and 16. Another significant point is that different EPR spectra are observed in the solution phase photolysis studies of TNT versus the spectra observed by thermal decomposition of TNT. However, the nitroxyl radical originally postulated by Stals as occurring near the melting point of RDX has been observed in thermal decomposition studies as described in the next section.

## THERMAL INITIATION

Two of the most widely studied energetic materials are RDX and HMX. Past studies have investigated the end products of pyrolysis or thermal decomposition pathways. Some initial pyrolysis studies of HMX used matrix isolation to detect condensed  $\text{NO}_2$  as a by-product of the pyrolysis.<sup>7</sup> The procedure used by these researchers consisted of heating HMX slowly in a constant temperature sandbath or heating HMX rapidly with a flame or quartz iodine lamp and then condensing the gaseous products in a frozen argon matrix at 15K where spectra were recorded. Their results detected  $\text{NO}_2$  and  $(\text{NO}_2)_2$  as products of the rapid heating by the flame and  $\text{NO}_2$  and  $\text{CH}_2\text{N}\cdot$  as products of the slow heating. These findings were significant, but only gaseous products from thermal decomposition of HMX were detected.

Since 1980, research has addressed real-time condensed phase thermal decomposition mechanisms. In three separate studies, free radicals in RDX have been shown to correlate with temperature as RDX was heated from room temperature to 200°C. These studies include neat RDX, RDX in solution, and RDX in molten TNT. The first report was by researchers at FJSRL.<sup>8</sup> Thermal decomposition of neat RDX was found to produce a free radical spectrum from the molten phase near 200°C. A steady-state concentration of the free radicals can be detected for several hours from a single 100 mg sample at a constant temperature of 195°C. At NRI, this result was reproduced and experiments of RDX in solution with sulfolane, a viscous high boiling point solvent, provided additional results.

Dilution of RDX in this viscous solvent reduces the diffusion rate of the molecules. At 170°C, a signal was detected which corresponded to the identical nitroxyl radical observed in solution photolysis studies (I).<sup>21</sup> The radical is consistent with loss of NO from the parent RDX molecule. At 190°C the nitroxyl radical decayed and a free radical identical to that reported by FJSRL in neat RDX near 200°C was observed.<sup>21</sup> Experiments were repeated with the same conditions using isotopically labeled RDX- $d_6$  and RDX- $^{15}\text{NO}_2$  in sulfolane.<sup>28</sup> The results were consistent with assignment of the radical spectrum at 190°C to a nitronyl nitroxyl radical (VII). This assignment requires further work to be conclusive.

The observation of RDX free radicals has been reported using different experimental conditions. RDX in molten TNT is observed to form 3 different free radicals when heated at a constant temperature of 145°C.<sup>12,13</sup> The first radical formed within seconds of heating and was assigned hyperfine couplings of  $a_N = .98\text{mT}$  and  $a_H = .3\text{mT}$  with four equivalent proton couplings. A second free radical species having a spectrum identical to that in molten RDX at 195°C appeared after 50 minutes at 145°C. A third radical was assigned as  $\text{NO}_2$ . The third radical's formation was found to correlate with the decay of the second species suggesting that  $\text{NO}_2$  is derived from the decomposition of the second species. The overall experimental evidence suggests that the RDX molecule thermally decomposes by a stepwise process with the molecular rings intact up to 200°C.

Similar thermal studies of HMX reveal a different behavior. When neat HMX is heated to its decomposition, only one free radical EPR signal is detected.<sup>8</sup> When HMX is heated in solution with sulfolane, a nitroxyl radical (III) spectrum similar to that observed in photolysis studies is observed.<sup>24</sup> The significant difference, as compared to RDX, is that no secondary free radical was observed.

Attempts have been made to use the spin trapping technique to identify the free radicals observed during thermal decomposition of RDX. In a study using four different spin traps, adduct radicals were detected at temperatures well below the decomposition

temperatures of RDX (110°C-150°C), but no assignment was made due to linebroadening.<sup>27</sup>

In more recent studies of TNT thermal decomposition, adduct radicals have been shown for the first time to form by intermolecular coupling.<sup>32</sup> This study by McKinney, Warren, Goldberg, and Swanson shows that neat TNT or TNT in the presence of hydrogen donors (such as hexamethylbenzene) forms intermolecular nitroxyl radicals (XI and XII). The TNT or TNT/H-donor mixtures had to be dissolved into a matrix of kieselguhr in order to observe the signals. The mechanism suggested by their findings correlates closely with the mechanism of photolytic decomposition of nitramines which undergo proton transfer.

## SHOCK INITIATION

Shock or impact studies of energetic materials provide information of the origin of hot spots, the propagation of hot spots, and the sensitization of energetic materials during handling. Field and co-workers<sup>18</sup> have described how viscous heating, frictional heating due to mechanical shear, and adiabatic compression mechanisms of energetic materials during impact can create hot spots. Studies of Kamlet and Adolph<sup>5</sup> have shown that impact sensitization of organic high explosives correlates with the thermal decomposition processes generated by impact. In support of this, recent progress has been made toward identifying diamagnetic reaction products formed near hot spot remnants of impacted TATB.<sup>34</sup> These are furoxan derivatives of TATB which are more shock sensitive than TATB. As discussed in Reference 34, the discovery of furoxan derivatives provides additional evidence that thermal processes are significant in impacted explosives since furoxans are observed during slow thermal decomposition of TATB. Paramagnetic products of impacted TATB have also been detected.<sup>6</sup> In this study, formation of NO<sub>2</sub> was observed from samples of shocked TATB. In other studies, TATB was found to form free radicals by mechanical grinding and by shock initiation. Studies of Miles, Gustavson, and DeVries in 1983 showed that mechanical grinding and impact of TATB at room temperature produces a

significant increase in the free radical EPR signal of TATB.<sup>22</sup> Evidence of shock damage in RDX, TNT, and ammonium nitrate was also detected. When subjected to shocks of 20-40 kbars paramagnetic products in TNT and RDX were observed at room temperature.<sup>9</sup> These results provide direct evidence that a shock less than necessary to cause detonation can break or alter internal molecular bonds.

Explosives may also be desensitized by shock. Impact formation of nitroso-derivatives of RDX have been reported.<sup>30</sup> The trinitroso-derivative of RDX has been shown to be less shock sensitive than RDX.<sup>19</sup> In unpublished thermal decomposition studies at NRL, we have observed that the trinitroso-derivative of RDX does not form nitroxyl radicals under the same decomposition conditions as RDX. This may help to explain the absence of an NO<sub>2</sub> EPR signal from RDX samples subjected to shock pressures less than 4 kbar since formation of nitroso-derivatives leaves the N-N bonds intact.<sup>14</sup> (Shock pressures of 40 kbar do produce EPR signals in RDX.<sup>9</sup>) In shock studies of inorganic explosives, Owens<sup>16,17</sup> has shown that copper tetramine nitrate converted completely into copper diamine nitrate during shock loading.

## SUMMARY

In general, nitramines are found to form free radicals by fragmentation pathways, whereas nitroaromatics tend to form adduct radicals. Detection of free radical products produced by shock has not been as extensively studied as photolytic or thermal initiation of free radicals in energetic materials.

## REFERENCES

1. Stals, J.; Buchanan, A. S.; and Barraclough, C. G., "Chemistry of Aliphatic Unconjugated Nitramines Part 5. Primary Photochemical Processes in Polycrystalline RDX," *Trans. Faraday Soc.*, Vol. 67, 1971, p. 1749.
2. Bodnar, J. W. and Rowell, C. F., "ESR Studies of Unsubstituted Cyclic Nitroxides in Solids," *J. Chem. Phys.*, Vol. 56, 1972, p. 707.

3. Darnez, C. and Paviot, J., "Mise En Evidence Par R.P.E. D'Espèces Inter-médiaires Radicalaires Intervenant Dans La Décomposition De Quelques Nitramines Irradiées," *Int. J. Radiat. Phys. Chem.*, Vol. 4, 1972, p. 11.
4. Owens, F. J. and Vogel, V. L., "Paramagnetic Resonance Study of Photolyzed Crystals of Dimethylnitramine," *J. Chem. Phys.*, Vol. 64, 1976, p. 851.
5. Kamlet, M. J. and Adolph, H. G., "The Relationship of Impact Sensitivity with Structure of Organic High Explosives II. Polynitroaromatic Explosives," *Propellants and Explosives*, Vol. 4, 1979, p. 30.
6. Sharma, J. and Owens, F. J., "XPS Study of UV and Shock Decomposed Triamino-Trinitrobenzene," *Chem. Phys. Letters*, Vol. 61, 1979, p. 280.
7. Morgan, C. U. and Beyer, R. A., "Electron Spin Resonance Studies of HMX Pyrolysis Products," *Combustion and Flame*, Vol. 36, 1979, p. 99.
8. Dorey, R. C., et al., *Progress Report On Research Into Chemical Structure/Bonding Decomposition Relationships for Energetic Materials*, FJSRL-80-0026, Dec 1980, AFSL, USAF Academy, CO.
9. Owens, F. J. and Sharma, J., "X-ray Photoelectron Spectroscopy and Paramagnetic Resonance Evidence for Shock-induced Intramolecular Bond Breaking in Some Energetic Solids," *J. Appl. Phys.*, Vol. 51, 1980, p. 1494.
10. Britt, A. D.; Moniz, W. B.; Chingas, G. C.; Moore, D. W.; Heller, C. A.; and Ko, C. L., "Free Radicals of TATB," *Propellants and Explosives*, Vol. 6, 1981, p. 94.
11. Davis, L. P.; Wilkes, J. S.; Turner, A. G.; and Dorey, R. C., "Photochemical Decomposition of TNT: Radical Identification and Theoretical Studies," *J. Phys. Chem.*, Vol. 85, 1981, p. 3505.
12. Davis, L. P., et al., *Thermochemical Decomposition of TNT: Radical Identification and Theoretical Studies*, FJSRL-TR-81-0002, AFSL, USAF Academy, CO, Apr 1981.
13. Davis, L. P.; Wilkes, J. S.; Carper, W. R.; and Dorey, R. C., "Thermal Decomposition of RDX Below the Melting Point," *Proceedings of the Seventh Symposium (International) on Detonation*, U.S. Naval Academy, Annapolis, MD, 16 Jun 1981, pp. 75-83.
14. Miles, M. H.; DeVries, K. L.; Britt, A. D.; and Moniz, W. B., "Generation of Free Radicals in RDX and HMX Compositions," *Propellants, Explosives, and Pyrotechnics*, Vol. 7, 1982, p. 100.
15. Pace, M. D. and Moniz, W. B., "EPR Spectra of NO<sub>2</sub> Radicals Produced by UV Photolysis of RDX Single Crystals," *J. Magn. Reson.*, Vol. 47, 1982, p. 510.
16. Owens, F. J., "EPR Study of Shock and Thermally Induced Reaction in Solid Copper Tetramine Nitrate," *J. Chem. Phys.*, Vol. 77, 1982, p. 5549.
17. Owens, F. J., "EPR Study of the Role of CuO Additives in Altering Phase Transition Behavior of Ammonium Nitrate," *J. Appl. Phys.*, Vol. 53, 1982, p. 368.
18. Field, J. E.; Swallowe, G. M.; and Heavens, S. N., "Ignition Mechanisms of Explosives During Mechanical Deformation," *Proc. Roy. Soc. Lond.*, Vol. A 382, 1982, p. 231.
19. Iyer, S., "Explosive Desensitization Studies via Chemical Group Modification of Nitroso-derivatives of RDX and 3-Amino-trinitrotoluene," *Propellants, Explosives, and Pyrotechnics*, Vol. 7, 1982, p. 37.
20. Pace, M. D. and Holmes, B. S., "Spin Trapping of NO<sub>2</sub> Radicals Produced by UV Photolysis of RDX, HMX, and Nitroguanidine," *J. Magn. Reson.*, Vol. 52, 1983, p. 143.
21. Pace, M. D., et al., EPR Spectroscopy of Thermally Initiated Free Radicals in RDX, NRL Memorandum Report 5212, NRL, Washington, D. C., Oct 1983.
22. Miles, H. M.; Gustavson, D.; and DeVries, K. L., "Stress Induced Radical Generation in TATB," *J. Mat. Sci.*, Vol. 18, 1983, p. 3243.

23. Owens, F. J., "Paramagnetic Resonance Studies of UV and Thermally Induced Radicals in Trinitrotoluene and Dinitrotoluene," *Mol. Cryst. Liq. Cryst.*, Vol. 101, 1983, p. 235.
24. Britt, A. D.; Pace, M. D.; and Moniz, W. B., "EPR Investigations of Thermal Decomposition of Nitramines II. Primary Nitroxide Radicals from HMX," *J. Energetic Mat.*, Vol. 1, 1983, p. 367.
25. Elban, W., et al., Microstructural Origins of Hot Spots in RDX Explosive and Several Reference Inert Materials, NSWC MP 84-358, NSWC, Silver Spring, MD, Nov 1984.
26. Pace, M. D. and Flippen-Anderson, J. L., "Crystal Structures and EPR Spectra of Nitroguanidine Chloride and Nitroguanidine Nitrate," *J. Energetic Mat.*, Vol. 2, 1984, p. 43.
27. Pace, M. D.; Britt, A. D.; Moniz, W. B.; and Stec D., "Paramagnetic Decomposition Products from Energetic Materials," *Proceedings of the Eighth Symposium (International) on Detonation*, Albuquerque, NM, 15 Jul 1985, pp. 734-741.
28. Pace, M. D., "Thermal Decomposition of RDX: Evidence of a Nitronyl Nitroxyl Free Radical Intermediate," *J. Energetic Mat.*, Vol. 3, 1985, p. 279.
29. Owens, F. J., "Paramagnetic Resonance of Radicals in Decomposed Trinitroaromatics," *Proceedings of the Eighth Symposium (International) on Detonation*, Albuquerque, NM, 15 Jul 1985, pp. 742-746.
30. Hoffsommer, J. C.; Glover, D. J.; and Elban, W. L., "Quantitative Evidence for Nitroso Compound Formation in Drop-Weight Impacted RDX Crystals," *J. Energetic Mat.*, Vol. 3, 1985, p. 149.
31. Owens, F. J., "Paramagnetic Resonance of Radicals in Decomposed Solid N-Methyl-N-2,4,6-Nitroindazole," *Mol. Cryst. Liq. Cryst.*, Vol. 126, 1985, p. 379.
32. McKinney, T. M.; Warren, L. F.; and Goldberg, I. B., "EPR Observation of Nitroxide Free Radicals During Thermal Decomposition of 2,4,6-Trinitrotoluene and Related Compounds," *J. Phys. Chem.*, Vol. 90, 1986, p. 1008.
33. Craig, B. B. and Pace, M. D., "UV-visible and ESR Probing of the Reactions of Photogenerated p-Nitrobenzyl Anion in Aqueous Media," *J. Chem. Soc.*, 1987, p. 1144.
34. Sharma, J.; Forbes, J. W.; Coffey, C. S.; and Liddiard, T. P., "The Physical and Chemical Nature of Sensitization Centers Left from Hot Spots Caused in Triaminotrinitrobenzene by Shock and Impact," *J. Phys. Chem.*, Vol. 91, 1987, p. 5139.
35. Pace, M. D., "EPR of UV Irradiated HMX Single Crystals," *Mol. Cryst. Inc. Nonlin. Opt.*, Vol. 156, 1988, p. 167.

## DISCUSSION

**JACQUES BOILEAU**  
SNPE, Paris, France

Is it interesting, in order to understand some mechanisms, to use oligomers free radicals, such as disclosed in the German Symposium in Freiburg/Breisgau, FRG in March 1988?

## REPLY BY M. D. PACE

Dimerization-like mechanisms have recently been shown to be important in radical formation during thermal decomposition of TNT mixtures. Higher order oligomer formation may also be important; however, I was not aware of findings of the Freiburg Symposium.

# PROPERTIES OF BIS (2, 2, 2, - TRINITROETHYL-N-NITRO) ETHYLENEDIAMINE AND FORMULATIONS THEREOF

Dong Haishan

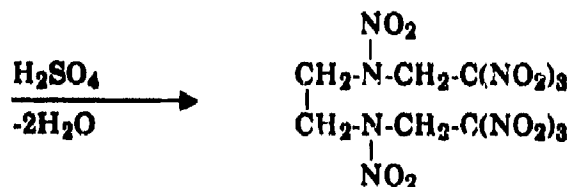
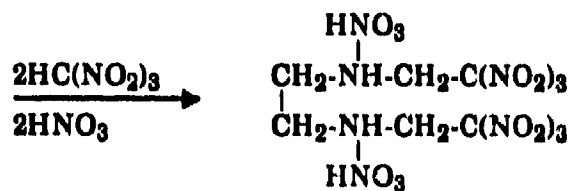
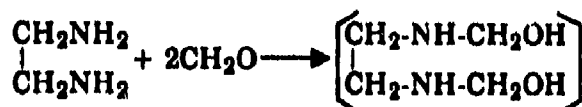
Southwest Institute of Chemical Material and Technology  
P. O. Box 518, Chengdu, Sichuan, CHINA

*Bis (2, 2, 2-Trinitroethyl-N-nitroethylenediamine is a zero oxygen balance explosive (ZOX) with crystal density 1.87 g/cm<sup>3</sup>, detonation velocity 8970 M/S (ρ<sub>0</sub> = 1.842 g/cm<sup>3</sup>). ZOX is characterized by its small critical diameter, sensitivity to shock and exploding bridewire initiation. It can be used in EBW detonators, explosive trains, and some other special applications.*

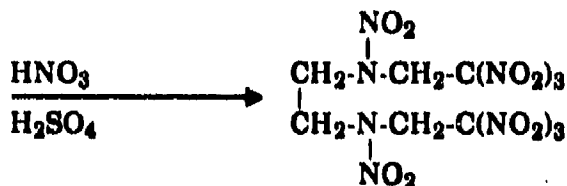
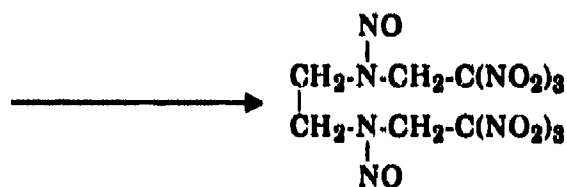
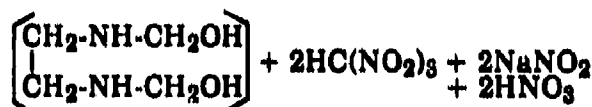
## THE SYNTHESIS OF ZOX<sup>1</sup>

ZOX being an outstanding representative of explosives based on nitroform (NF) was synthesized first in 1952 by Avakyan in the USSR. (The yield is 58 percent on NF). According to Avakyan's procedure we synthesized ZOX in 1962 and designate it as 2# (Number 2 Explosive). Then we studied the synthetic process carefully and developed two new procedures:

• Adding ethylenediamine/formaldehyde condensation product to a solution of NF in diluted nitric acid (NA), followed to nitrate it by sulfuric/nitric acid mixture. The yield is 78 percent.<sup>1</sup>



• Adding ethylenediamine/formaldehyde condensation product and sodium nitrite simultaneously to acetylene nitration solution composed of NF, NA, and a little mercury nitrate as a nitration catalyst:



Filtrating the precipitated Bis (2, 2, 2-trinitroethyl-N-nitroso) ethylenediamine and nitrating it to ZOX.

ZOX was put into production in 1969 in China.

## PHYSICAL PROPERTIES OF ZOX<sup>2,3</sup>

ZOX is monoclinic. Its cell parameters are given in Table 1.

Table 1. Cell Parameters of ZOX

Length of unit cell edge	Å
a	5.9767
b	12.0146
c	11.8436
Angle $\beta$	97.171°
Molecules per unit cell	2

The data of its bond length and angles are given in Figure 1 and Table 2.

The crystal density is 1.87 g/cm<sup>3</sup> by direct measurement. X-ray determination gives a value of 1.88 g/cm.<sup>3</sup>

Its melting point is 179.2-181.5°C with decomposition.

### CHEMICAL PROPERTIES OF ZOX

ZOX is relatively stable in acids, but sensitive to alkalis. Reacting with NaOH solution, ZOX decomposes to ethylene dinitramine, nitroform sodium and formaldehyde:

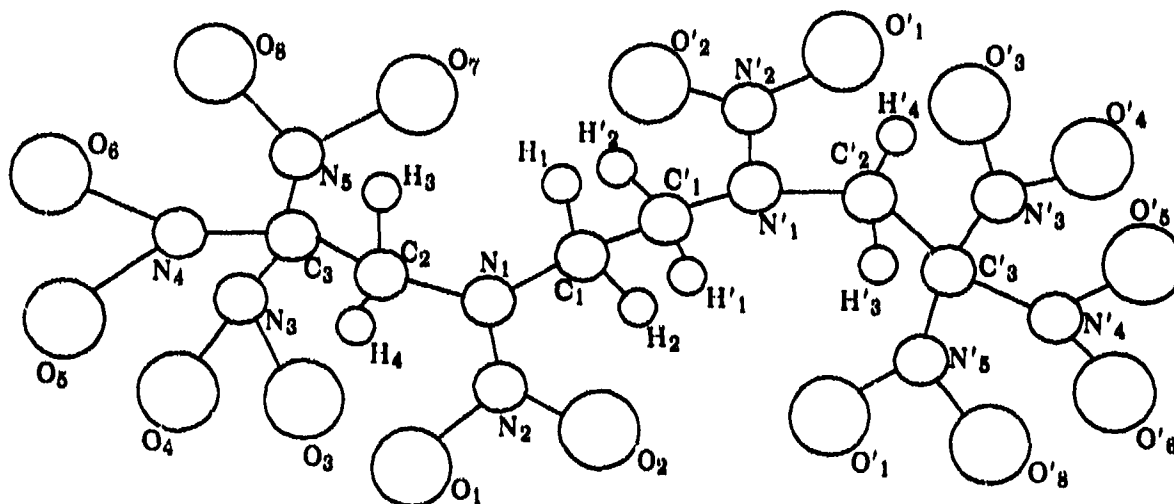
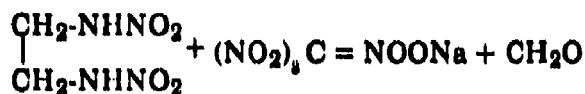
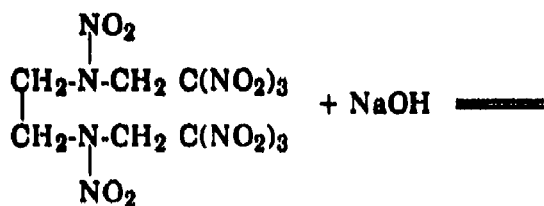


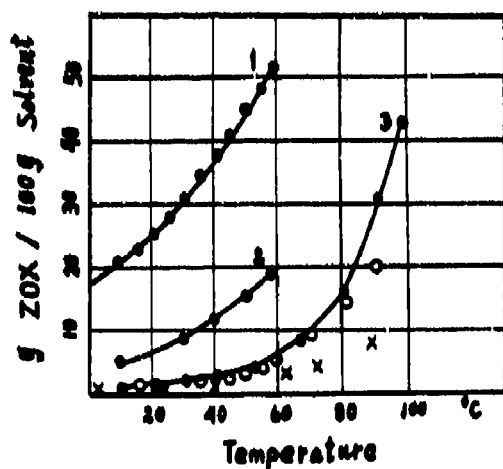
Figure 1. Molecule Constitution of ZOX

Table 2. Bond Length and Angle Data of ZOX

Bond Length (Å)				Bond angle (degree)			
C <sub>1</sub> -C <sub>1</sub> '	1.543	N <sub>2</sub> -O <sub>1</sub>	1.239	∠C <sub>1</sub> -N <sub>1</sub> -N <sub>2</sub>	114.9	∠O <sub>2</sub> -N <sub>2</sub> -N <sub>1</sub>	118.1
C <sub>1</sub> -N <sub>1</sub>	1.482	N <sub>2</sub> -O <sub>2</sub>	1.219	∠C <sub>1</sub> -N <sub>1</sub> -C <sub>2</sub>	121.9	∠O <sub>3</sub> -N <sub>3</sub> -O <sub>4</sub>	128.3
N <sub>1</sub> -N <sub>2</sub>	1.379	N <sub>3</sub> -O <sub>3</sub>	1.205	∠N <sub>1</sub> -C <sub>2</sub> -C <sub>3</sub>	114.6	∠O <sub>3</sub> -N <sub>3</sub> -C <sub>3</sub>	116.1
N <sub>1</sub> -C <sub>2</sub>	1.432	N <sub>3</sub> -O <sub>4</sub>	1.206	∠C <sub>2</sub> -C <sub>3</sub> -N <sub>3</sub>	111.9	∠O <sub>4</sub> -N <sub>3</sub> -C <sub>3</sub>	115.4
C <sub>2</sub> -C <sub>3</sub>	1.531	N <sub>4</sub> -O <sub>5</sub>	1.212	∠C <sub>2</sub> -C <sub>3</sub> -N <sub>4</sub>	110.5	∠O <sub>5</sub> -N <sub>4</sub> -O <sub>5</sub>	127.1
C <sub>3</sub> -N <sub>3</sub>	1.523	N <sub>4</sub> -O <sub>6</sub>	1.196	∠C <sub>2</sub> -C <sub>3</sub> -N <sub>5</sub>	112.5	∠C <sub>3</sub> -N <sub>4</sub> -O <sub>5</sub>	115.8
C <sub>3</sub> -N <sub>4</sub>	1.529	N <sub>5</sub> -O <sub>7</sub>	1.195	∠N <sub>3</sub> -C <sub>3</sub> -N <sub>5</sub>	107.7	∠C <sub>3</sub> -N <sub>4</sub> -O <sub>6</sub>	117.2
C <sub>3</sub> -N <sub>5</sub>	1.522	N <sub>5</sub> -O <sub>8</sub>	1.217	∠N <sub>4</sub> -C <sub>3</sub> -N <sub>5</sub>	108.8	∠O <sub>7</sub> -N <sub>5</sub> -O <sub>4</sub>	125.5
--	--	--	--	∠O <sub>1</sub> -N <sub>2</sub> -O <sub>2</sub>	124.8	∠O <sub>7</sub> -N <sub>5</sub> -C <sub>3</sub>	117.7
--	--	--	--	∠O <sub>1</sub> -N <sub>2</sub> -N <sub>1</sub>	117.1	∠O <sub>8</sub> -N <sub>5</sub> -C <sub>3</sub>	116.7



ZOX is soluble in acetone, not NA and dioxane, methyl and ethyl acetate; slightly soluble in methanol, ethanol and acetic anhydride; insoluble in water, ether, benzene, toluene, chloroform, tetrachloromethane, and dichloroethane. It can be purified from ethylacetate, nitromethane, NA, and dioxane. The ZOX solutions in solvents containing carboxyl radical become yellow when heated for a long time. The solubilities of ZOX in some solvents are shown in Figure 2.



1. Acetone
  2. Methyl acetate
  3. nitromethane
- O-dioxane  
X-N A (98.7 percent)

Figure 2. Solubility of ZOX

The combustion heat of ZOX is 7.25 MJ/Kg (1732 Kcal/Kg) and its formation heat is 53.5 KJ/mole (12.79 Kcal/ mole).

## DETONATION PROPERTIES OF ZOX<sup>3</sup>

Owing to ZOX's zero oxygen balance composition, it has a high detonation heat. The calculated detonation heat is 1704 Kcal/Kg and the measured is 1542 Kcal/Kg (6.456 MJ/Kg) with a specific volume of its detonation products 0.712 M<sup>3</sup>/Kg.

The detonation velocity of ZOX is 8970 M/S ( $\rho_0 = 1.842 \text{ g/cm}^3$ , charge diameter 10 mm).

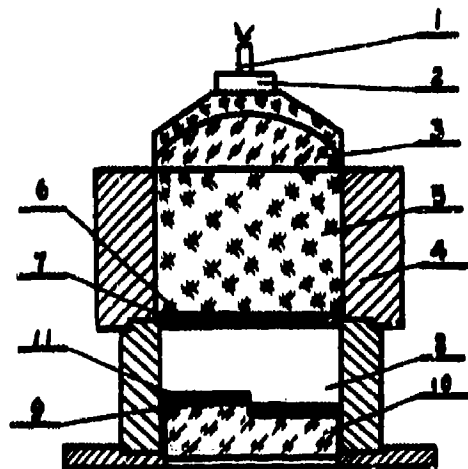
Its detonation pressure was determined by aluminium free-surface velocity measurement with  $\phi 100 \times 80$ -mm charges initiated by a plane wave lens. In view of the hazards involved in the process of pressing 100-mm diameter billets of pure ZOX, we formulated a mixture of ZOX with the additives which are the same as those of PB-HMX-9159 to measure its  $P_{CJ}$ . The experimental data are shown in Table 3.

Standard cylinder tests and plate push tests were performed to evaluate the ability of ZOX to accelerate metal. In the plate push test a 100-mm diameter 80-mm-thick explosive charge is initiated by a 100-mm diameter Comp B/Baratol plane wave lens to push a 96-mm diameter, 2-mm-thick steel plate. The plate velocities  $U$ , at 45 mm displacement are measured with a streak camera technique (see Figure 3). Comparative results of three formulations in cylinder test and plate push test are given in Table 4. Thus the increase in energy of ZOX over HMX is about 5 percent.

ZOX is characterized by its small critical diameter. A formulation of ZOX/silicon resin (80/20) was tested. Its critical diameter

Table 3. Detonation Parameters of PB-ZOX

Explosive	$\rho_0(\text{g/cm}^3)$	D(M/S)	$P_{CJ}(\text{GPa})$	K
PB-ZOX-9159(95%ZOX)	1.840	8816 ± 6	37.8 ± 0.3	2.79 ± 0.03
PB-HMX-9159(95%HMX)	1.860	8862 ± 17	36.8 ± 0.2	2.97 ± 0.02



1. Detonator
2. Booster
3. Lens
4. Steel Case
5. Explosive
6. Plexiglass
7. Steel Plate
8. Cavity
9. Barium Nitrate
10. Plexiglass
11. Al Foil

Figure 3. Setup of Plate Push Test

Table 4. The Energy Output of PB-ZOX

Cylinder Test					Plate Push Test		
Explosive	TMD (g/cm <sup>3</sup> )	$\rho_0$ (g/cm <sup>3</sup> )	$\rho_0$ /TMD (%)	E (19 mm) (KJ/g)	$\rho_0$ (g/cm <sup>3</sup> )	$U_f$ (M/S)	$1/2 U_f^2$ (KJ/g)
PB-ZOX-9159	1.855	1.802	97.1	1.722	1.840	4632 ± 22	10.73
PB-HMX-9159	1.889	1.863	98.6	1.651	1.860	4557 ± 19	10.38
PBX-9404	1.865	1.841	98.7	1.620	1.840	4519 ± 31	10.21

in open channels of Al plate is 0.2 mm. ZOX used in the formulation was prepared by adding its acetone solution to cool water with rapid agitation. But thermostability of so obtained ZOX is exceedingly decreased (see next paragraph). In order to obtain the explosive mixture with qualified thermal stability, normal ZOX (recrystallized from ethyl acetate, NA or NM) must be used; under this circumstance the critical diameter of the formulation is 0.7 mm.

### THERMAL STABILITY AND COMPATIBILITY OF ZOX

ZOX is the most stable of high explosives based on NF. However, the compounds containing the NF radical generally are less stable than common nitrocompounds—which are more closely related to the longer C-N bond in the NF radical (1.523, 1.529, 1.522 Å) than to that of normal C-N (1.47 Å).

Song Quancai et al. studied thermal decomposition of ZOX (double recrystallized from NM) with Bourdon glass barometer. They found that the activation energy for 0.01 percent sample decomposition in the temperature range 70-130°C is 35.8 Kcal/mole and the times needed for 0.01 percent decomposition ( $t_{0.01\%}$ ) in 70-130°C are as listed in Table 5. The data of initial decomposition velocity ( $W_0$ ) and half life ( $t_{0.5}$ ) in a higher temperature range (130-170°C) are shown in Table 6 where the data of PETN (double recrystallized from acetone) are given for comparison.<sup>4</sup>

Table 5. Thermal Decomposition of ZOX

Temperature (°C)	70	85	100	115	130
$t_{0.01\%}$ (min)	65760	7428	1212	567	28.2

**Table 6. Initial Decomposition Velocity  $W_0$  (ml/min. gramm) and Halflife  $\tau_{0.5}$  (min.) of ZOX and PETN**

T(°C)	130		140	145	150		155	160		165	170	
	$W_0$	$\tau_{0.5}$	$\tau_{0.5}$	$W_0$	$W_0$	$\tau_{0.5}$	$W_0$	$W_0$	$\tau_{0.5}$	$W_0$	$W_0$	$\tau_{0.5}$
ZOX	0.001	9540	--	--	0.032	449.5	--	0.090	110.3	--	0.30	26.0
PETN	--	--	--	0.58	1.1	--	2.0	3.5	--	6.2	--	--

**Table 7. Experimental Data of ZOX, PETN, Tetryl in VST, BGET, CRT and TG**

Explosive	VST 120° C, 48 hrs., ml/5g	BGET 120° C, 48 hrs., ml/1g	CRT 150° C, 2 hrs., ml/1g	TG 100° C, 48 hrs., %
ZOX (Indust. grade)	3.7	1.861	3.9	0.06
PETN (Indust. grade)	>20	28.2	98.2	0.23
Tetryl (Indust. grade)	1.12	--	36.3	0.09

**Table 8. Effect of Recrystallization Process on Thermal Stability of ZOX**

Sample No.	Process of Recrystallization	VST 100° C, 48 hrs., ml/g	
1	ZOX recrystallized from ethyl acetate-benzene	0.09,	0.24.
2	ZOX precipitated by pouring acetone solution of sample No. 1 to cool water with agitation	8.7	
3	PETN precipitated by pouring its acetone solution to cool water with agitation	0.642	

The experimental results of ZOX, PETN and Tetryl in VST, Gas Evolved Test in Bourdon glass (BGET), CRT and TG are shown in Table 7.

Therefore, the recrystallized ZOX is more stable than recrystallized PETN. However, ZOX precipitated by pouring its acetone solution to cool water with agitation owing to its crystal defect is remarkably less stable than PETN as shown in Table 8.

The compatibility of ZOX with related materials is poor. Experimental data in VST, CRT, BGET and DT-GC show that only a few of binders and phlegmatizers, like silicon rubber, fluororubber, and fluorographite (FG) are

compatible with ZOX. Some VST data are given in Table 9.

### SENSITIVITY OF ZOX

The results in the Drop weight impact test and Kazlov friction test show that ZOX is more sensitive to mechanical stimulus than common explosives of interest. The comparative results are given in Table 10.

It is very difficult to reduce the sensitivity of ZOX to low value. The sensitivity of ZOX formulations to impact and friction can be reduced enormously when composite phlegmatizers are used and some appropriate amount of HMX is added. The sensitivity data of such a

**Table 9. Compatibility Data of ZOX in VST (120°C, 48 hrs.)**

Material	m/5g	Mixture (1:1)	m/5g
ZOX	3.70	ZOX/nylon	explode
F <sub>2314</sub>	1.15	ZOX/F <sub>2314</sub>	4.15
Polyisobutylene	0.25	ZOX/PIB	96.35
Silicon resin	2.65	ZOX/Silicon resin	2.60
Wax	0.55	ZOX/Wax	87.45

**Table 10. Sensitivity of ZOX, HMX, RDX, PETN to Impact and Friction**

			ZOX	RDX	HMX	PETN
Friction test (Percent of Explosion)	Pendular angle	90°	88%	4%	28%	32%
	Gage pressure	25 Kg/cm <sup>2</sup>				
	Pendular angle	90°	100%	76%	100%	92%
	Gage pressure	40 Kg/cm <sup>2</sup>				
Impact test (Percent of Explosion)	Hammer weight	10 Kg	100%	80%	100%	100%
	Drop height	25 cm				

formulation B-01 (ZOX/HMX TATB/F<sub>2311</sub> /Pg/Graphite/Wax = 70/22/ 4/ 2/0.5/0.5/ 1) are shown below:<sup>5</sup>

Impact test 10 Kg, 25 cm	Friction test 90°, 40 Kg/cm <sup>2</sup>	H <sub>5</sub> O cm
0 - 4%	4 - 16%	78

ZOX is more sensitive to mechanical stimulus than common explosives of interest. The comparative results are given in Table 10.

ZOX is more easily initiated by shock wave and bridgewire than PETN and its detonation builds up faster than that of the latter.

Explosion temperature data (at 5 second duration time) of ZOX and some other explosives are given as follows:

Explosive	ZOX	PETN	RDX
Explosion Temperature °C	232	225	230

## ACKNOWLEDGEMENTS

The author wishes to thank Chu Shijin, Zhang Xiaoyi, Li Guanglai, Hua Pinhuan, Han Dunxin, Lu Xueguo, and Chen Qizhen for measuring thermal stability data and detonation parameters. The author also wishes to thank Ye Huatang, Tang Yepeng, et al. for their participation in formulation work.

## REFERENCES

1. Dong Haishan, Li Changquin, Xiao Yangang, et al., "The Research on Bis (2, 2, 2-Trinitroethyl-N-nitro) Ethylenediamine," 1962, 1963, 1964.
2. Cai, Zhinhua et al., private communication.
3. Dong Haishan and Zhou Fenfen, et al., *Properties of High Explosives and Related Materials* will be issued, Aug 1989, Beijing.
4. Song Quancai, et al., private communication, 1964.
5. Li Bingren, *Explosion and Shock Waves*, Vol.8, No. 3, 1988.

# NTO DEVELOPMENT AT LOS ALAMOS

Lonnie B. Chapman  
Los Alamos National Laboratory  
Los Alamos, New Mexico 87545

*NTO is an explosive with calculated performance near that of RDX but with sensitivity approaching that of TATB. Possible uses for NTO would be as an alternative to RDX in formulations where a lower sensitivity is desired or as an alternative to TATB where more performance is required without a large increase in sensitivity. Efforts have been concentrated on producing NTO and in testing the performance and sensitivity of NTO and NTO formulations. Two-hundred pounds of NTO have been produced and some performance and sensitivity data have been obtained. Work is being done to determine the diameter effect for large-crystal-size NTO. Additional work is being done to improve the small-charge diameter performance of NTO by adding small amounts of RDX or by changing the crystal size and/or crystal habit of the NTO.*

## INTRODUCTION

A new molecule, 3-nitro-1,2,4-triazole-5-one (NTO), was found in the literature<sup>1</sup> without reference to its energetic properties. NTO was first recognized as a potential explosive molecule and then synthesized by K. Y. Lee and M. D. Coburn<sup>2</sup> at Los Alamos. Small-scale sensitivity and thermal tests indicated that NTO was a very impact insensitive and thermally stable molecule. Preliminary performance calculations also indicated that the performance of NTO would be near that of RDX. Based upon this preliminary information, NTO was synthesized and tested in small scale at Los Alamos. The performance of NTO in these small-scale tests was not as good as the preliminary calculations indicated it should be, therefore, larger quantities were required for more extensive performance and sensitivity tests as well as for development of NTO formulations that might be useful in both DOE and DoD applications.

## NTO SCALE-UP AND PRODUCTION

NTO production begins by producing the intermediate, 1,2,4-triazole-5-one (TO). TO is made by reacting semicarbazide HCl with

90 percent formic acid at 90 to 100°C as is shown in Figure 1. NMR studies by Don Ott<sup>3</sup> have shown that the reaction to TO is essentially complete when the HCl gas evolution stops and there is no need for extended reaction times. It was also determined that some HCl is needed to complete the reaction and that semicarbazide alone without the HCl stabilizer does not produce ring closure to form TO. TO batch production has been scaled up to a 30-gal reactor with recovered product weight of 16.62 kg at a 73.8 percent yield.

The nitration of TO to NTO is shown in Figure 2. NTO reaction yield has averaged 76 percent when a mixture of nitric and sulfuric acid is used to nitrate TO. The highest yield (87.5 percent) was obtained when the acid mixture was first added to the reactor and brought to 60-70°C. The acid mixture contains an 85:15 ratio of nitric to sulfuric acid (the nitric acid concentration used is 70 percent while the sulfuric acid is 96 percent). TO was then added slowly, after the acid reached reaction temperature.

NTO was produced in 5-kg batches with a total recrystallized production of 47.7 kg (104.9 lb). Three 15-kg batches have also been produced but have not been recrystallized.

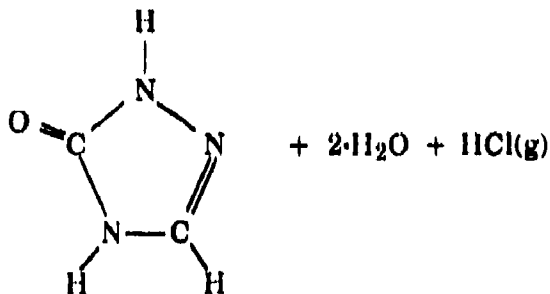
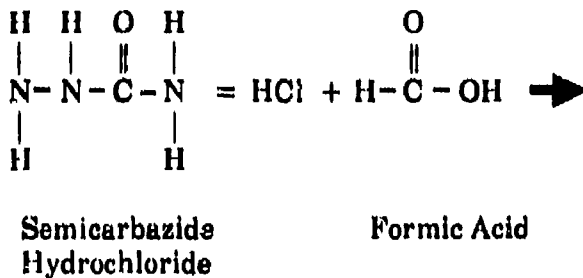


Figure 1. TO Synthesis Reaction

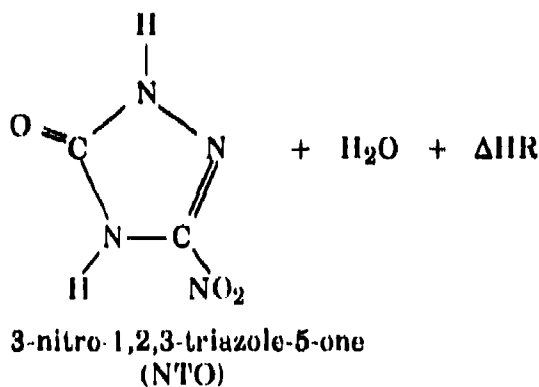
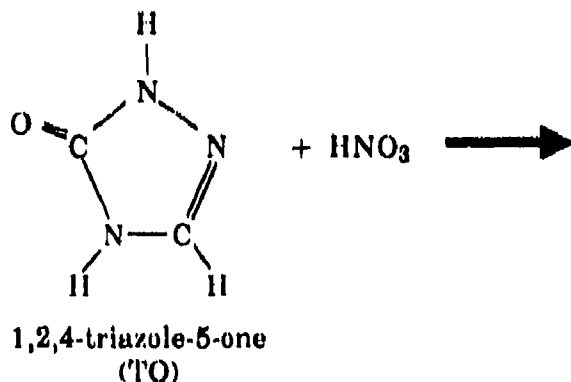


Figure 2. TO Nitration Reaction

## TOXICOLOGICAL STUDIES ON NTO AND TO

Toxicological studies have been done for both NTO<sup>4</sup> and the production intermediate TO.<sup>5</sup> Results of the tests indicate that neither NTO nor TO present concerns of acute toxicity, skin irritation, skin sensitization, or eye irritation. In fact, the acute oral LD 50 for both NTO and TO is greater than 5 g/kg in rats and mice, which is considered only mildly or non-toxic in both species.

## DEPARTMENT OF TRANSPORTATION CLASSIFICATION TESTS

Thermal stability and sensitivity tests were done at Los Alamos in order to apply for a D.O.T. shipping hazard classification. A heating test was conducted for 48 hours at 75°C and produced no evidence of decomposition or discoloration. Two ignition and unconfined burns were done with a single sample 2 x 2 x 2 inches and another was done with four samples end to end. There was no detonation and burn times exceeded 300 seconds. Impact sensitivity for large-particle-size NTO is much less than RDX and near the height limits of the Los Alamos drop-weight impact machine. The shock sensitivity was tested by a confined-gap test and results were comparable to PBX 9502 in the same test. A sample of bulk NTO was detonated with a number-6 blasting cap.

Based upon the results of these tests, NTO fits the criteria for a Class A explosive. NTO has not received a permanent D.O.T. classification at this time.

## HIGH-SPEED-MACHINING TEST

Pure, pressed NTO and NTO cast with 50 weight percent TNT have undergone high-speed-machining tests. The standard test is performed by drilling 40 0.250-inch diameter holes into an explosive charge. The drill speed is 2260 RPM and the penetration rate is 0.025 inch per revolution. NTO is soluble in water and was, therefore, machined dry. Both samples produced no reaction during testing and were approved for remote-control machining operations.

## NTO PERFORMANCE

### NTO Cylinder Tests

Two-inch diameter NTO charges were pressed at 1.855, 1.825, and 1.800 g/cm<sup>3</sup>. The diameters were machined to fit into 2-inch diameter copper cylinders for cylinder-expansion tests. Two of the three charges were fired successfully indicating NTO has a performance greater than TATB.

### Confined NTO Plate-Dent/Detonation Velocities

Several plate-dent tests were made with explosives of known performance to try and calibrate a confined plate-dent test. The explosives were confined in schedule 80 steel pipe with an inner diameter machined to accept 1-5/8-inch pressed charges. NTO was also tested in the same manner to determine if confinement would improve its performance in smaller diameters. The preliminary measured velocities are shown in Table 1 along with calculated values. Additional tests were done with NTO pressed to 97% TMD (1.871 g/cm<sup>3</sup>) in both confined and unconfined modes for comparison. The detonation velocities are obtained from piezoelectric pins in contact with the HE surface and are for screening only. These results indicate that there is a diameter effect present in NTO fired in 1-5/8-inch diameter at high densities.

### NTO Failure Diameter and Diameter Effect

Experiments were performed by Ray Engelke<sup>8</sup> to determine diameter effects and failure diameter of large-crystal-size NTO (Blend 87-10). The first NTO charges were pressed to 1.868 g/cm<sup>3</sup> (96.8% TMD) and machined down to 36 mm diameter. A 36 mm diameter rate stick was fired and propagated at 8.176 ± 0.001 km/s. A second rate stick was fired that included three different diameters; 32.5, 28.9, and 25.35 mm. A third rate stick was set up with 25.1, 19.1, and 16.7 mm diameter NTO charges arranged from large to small diameter following the booster. This failed in the 25.4 mm diameter section.

Table 1. Performance Comparisons

Density (g/cm <sup>3</sup> )	Calculated (unconfined)		Measured Det. Vel. (km/s)
	Pres. (kbar)	Vel. (km/s)	
1.93 (100% TMD)	340	8.67	---
1.871 (97% TMD)	---	---	8.22 confined
1.871 (97% TMD)	---	---	8.12 unconfined
1.855 (96.1% TMD)	306	8.34	8.20 confined
1.825 (94.6% TMD)	294	8.21	8.09 confined
1.800 (93.3% TMD)	283	8.11	8.02 confined

Rate sticks are normally initiated using an RP-1 detonator with a 1/2 inch diameter by 1/2 inch high PBX 9407 booster pellet. This booster pellet then initiates a PBX 9404 charge that is at least as large in diameter as the largest diameter test charge. A fourth NTO rate stick was assembled with an NTO charge 25.76 mm diameter, using a booster consisting of a P22 plane-wave lens followed by a 0.25 inch thick by 2 inch diameter PBX 9404 charge. This rate stick propagated its entire length with a steady velocity. Detonation velocity results are shown in Table 2. These results indicate the failure diameter of large-crystal-size NTO at this density is near one inch.

### NTO/Binder Formulations

NTO/binder formulations in 95/5 weight percent concentrations were tested in 5-g slurry batch sizes to determine compatibility before further scale-up. FPC-461, Viton-A, Kel-F 800, Estane, and Kraton G were evaluated for possible binders. None of the NTO/binder combinations showed evidence of incompatibility. All of the binders produced a formulation that was less impact sensitive than the pure NTO. Ethyl acetate was chosen over MIBK as a solvent because it produced a

better attraction between the lacquer and the explosive. Because NTO is soluble in hot water, a saturated NTO solution at 55°C was used as the carrier instead of pure water. NTO was mixed with the lacquer to provide intimate contact and wetting of the NTO crystals before the water was added. Based upon high binder density and the higher bulk densities obtained in the initial 5-g scale work, four binders were chosen for scale-up to 50-g batches. Kraton G did not produce an acceptable formulation. As was found in the 5-g scale batches, FPC-461 produced the best agglomerates with a bulk density of 0.7 - 0.75 g/cm<sup>3</sup>. Based upon small-scale results, FPC 461 was used to make a 1-kg batch of X-0483\* by the water-slurry method.

Table 2. NTO Blend 87-10 Detonation Velocity

Diameter (mm)	Det. Vel. (km/s)	Density (g/cm <sup>3</sup> )
36.00	8.176 ± 0.001	1.868
32.51	8.160 ± 0.001	1.870
28.91	8.169 ± 0.004	1.869
25.35	8.144 ± 0.001	1.867
25.40	Failed	1.868
25.76	8.142 ± 0.005	1.870

## NTO/TNT CASTINGS

X-0489\*\* was cast in one 4-inch diameter by 6-inch high cylinder and in eight 1-5/8-inch diameter by 4-inch high cylinders. All the charges were radiographed and showed minimal shrinkage and bubbles. Vacuum was not applied to the melt but the castings were cooled from the bottom to the top. A casting sample was taken for thermal-stability and impact-sensitivity testing and a release has been issued for this batch. The 4-inch diameter by 6-inch high cylinder was used for a high-speed machining test. After the material passed the machining test, the casting risers were removed from the 1-5/8-inch charges, which were then fired in a combination plate dent/rate stick to

\* X-0483 - 95/5 wt% NTO/FPC-461

\*\* X-0489 - 50/50 wt% NTO/TNT

determine the performance of the X-0489. The results are shown in Table 3, along with a calculated performance for comparison.

Table 3. Performance of X-0489 Castings

Stick Number	Density (g/cm <sup>3</sup> )	Pressure (kbar)	Det. Vel. (km/s)
1	1.733	240	no data
2	1.717	241	7.226 ± 0.011
3	1.720	242	7.225 ± 0.008
Calculated	1.720	246	7.56

## NTO RECRYSTALLIZATION

### Introduction

Normally NTO is recrystallized from hot water after initial production to remove entrapped nitric acid. A mean particle size of 250 microns, shown in Figure 3, is obtained by the normal recrystallization method of cooling the entire vessel and contents from 90 to 5°C over a 30-minute period. A smaller particle size was desired for PBX formulations work and to determine the effect of smaller particles on performance, sensitivity, and failure diameter. Preliminary results indicate that impact sensitivity and performance do change with particle/crystal-size distribution.



Figure 3. NTO Recrystallized Slowly From Water

## NTO Recrystallization From Water

Work was done to reduce NTO particle size by crash precipitating a saturated NTO/water solution at 93°C into ice water. The melting ice maintained the recrystallization temperature between 0 and 5°C. Particle size in this batch (LBC-III-7B) averaged about 40 microns. SEM photographs in Figure 4 show that the NTO clumps are made up of 5 to 25 micron crystals. These clumps are smaller and more randomly arranged than previous precipitations done at 5 to 20°C.

## NTO Batch Recrystallization From NMP

Particle/crystal size were reduced further by dissolving NTO into N-methyl pyrrolidone (NMP) in a 65 g/100 g concentration at 90°C. This solution was poured into ice water with agitation and with ice being added to maintain the temperature below 5°C. Batch LBC-III-6C, shown in Figure 5, was made using this procedure. This SEM photograph shows 50 to 100 micron "clumps" that contain many 2 to 10 micron crystals, but the crystals are randomly packed and look like they contain a large amount of voids.

NTO dissolved in NMP and crashed into ice water can produce spherical crystal growth that is similar to spherical NQ produced at Los Alamos. The crystal size produced with a 3:1 ratio of H<sub>2</sub>O:NMP, shown in Figure 6, is very small (i.e., 1-5 microns) and is in spheres ranging from 10 to 30 microns in diameter. Individual crystal size can be controlled by changing the ratio of ice water to NMP:NTO solution. Agglomerates containing a random arrangement of small crystals can be obtained by adding additional NMP:NTO solution to the combined solutions after crystal formation has begun.

Small-crystal-size (i.e., 1-10 micron) spherical NTO produced by batch recrystallization from NMP was pressed into 1/2 inch diameter pellets for plate dent comparison with previously produced NTO. Plate-dent results for Batch-III-222, shown in Figure 7, were 263 kbar at 1.764 g/cm<sup>3</sup> (91.4% TMD) and 257 kbar at 1.827 g/cm<sup>3</sup> (94.7% TMD). Drop-weight-impact sensitivity is about 200 cm for



Figure 4. NTO Crash Precipitated From Water

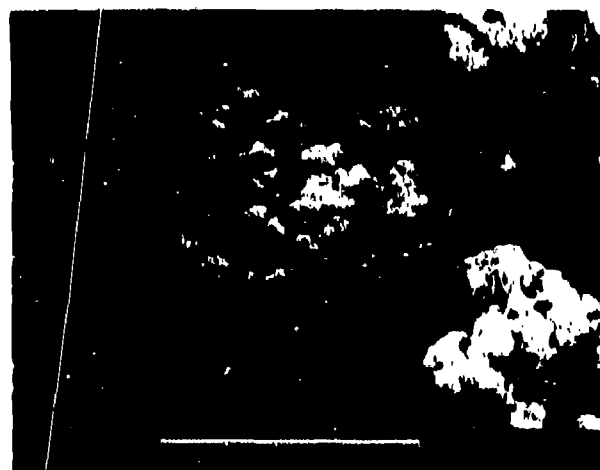


Figure 5. NTO Recrystallized From NMP, Random Growth

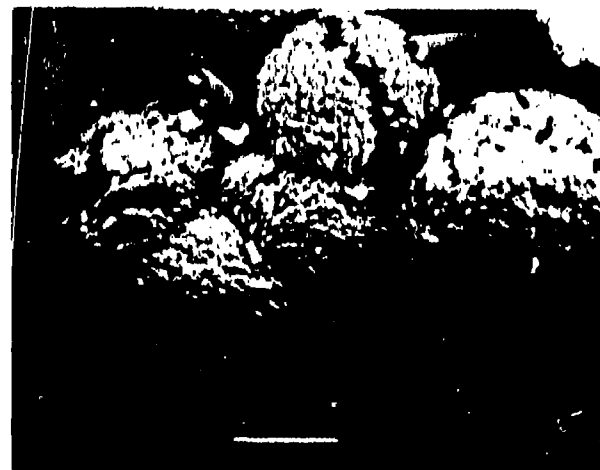


Figure 6. NTO Crystallized From NMP, Spherical Growth

this small-crystal-size material. These results are not significantly different from other small-crystal-size NTO, which indicates that spherical crystal habit does not seem to be as important as individual crystal size in reducing failure diameter.

Plate-dent results, shown in Figure 7, indicate the performance of Batch LBC-III-6C (designated 6C) is close to the BKW prediction while the other small-particle-size batches (designated 7a and 222) perform better than the large-particle-size NTO at the same density. Previous unconfined plate dents using large-particle-size NTO in 1/2- and 1-inch diameter failed to propagate at densities greater than 1.79 g/cm<sup>3</sup>. Also 1/2-inch diameter plate dents using NTO Blend 87-10 failed to propagate at 1.78 g/cm<sup>3</sup>. Unconfined 1-5/8 inch diameter plate dents using large-particle-size NTO have propagated at densities up to 1.872 g/cm<sup>3</sup> but the performance, shown in Figure 7, is lower than expected and begins to drop with increasing density at 1.855 g/cm<sup>3</sup>. These results show that smaller particle sizes can improve NTO performance in small diameters and might perform close to BKW predictions at higher densities in larger diameters.

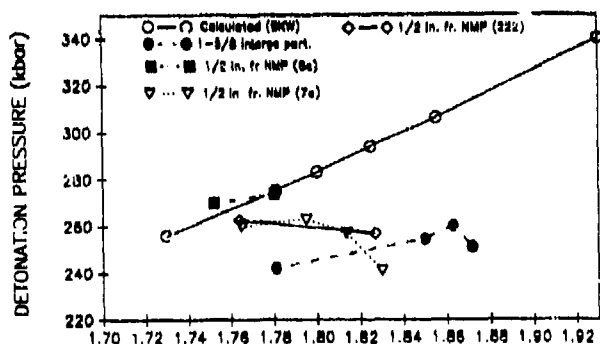


Figure 7. Charge Density (g/cm<sup>3</sup>)

### NTO Continuous Recrystallization From NMP

Equipment for continuous, single-vessel recrystallization was tested at a rate that would produce 800 g/h of NTO at 90 percent yield. The NTO/NMP solution is first cooled to room temperature before mixing with the water to reduce the amount of heat exchange required. NTO/NMP remains a stable solution for several hours at room temperature in the concentration used. The coolant temperature

was increased from -12 to -5°C and a distilled water flush was installed to reduce heat exchanger plugging.

A new recrystallization vessel is being made to allow flow patterns approaching plug-flow and to provide capacity for increased flow rates. The new vessel is jacketed to provide cooling to replace the double-pipe heat exchanger that is currently causing plugging problems.

### NTO/RDX/BINDER FORMULATIONS

PBXs using mixtures of NTO and RDX are being prepared in an attempt to reduce the failure diameter of NTO formulations. The failure diameter as a function of RDX content will be investigated. PBXs containing both NTO and RDX were successfully made with good agglomerate size and strength. Impact sensitivity and thermal analysis data for these PBXs indicate there is no incompatibility between NTO, RDX, and these binders.

### REFERENCES

1. Chipen, G. I.; Bokalder, R. P.; and Crishten, V. Ya. "1,2,4-Triazol-3-one and Its Nitro and Amino Derivatives," *Khim. Getero. Soed.*, Vol. 2, No. 1, 1966, pp. 110-166.
2. Lee, K.-Y. and Coburn, M. D., *3-Nitro-1,2,4-triazole-5-one a Less Sensitive Explosive*, Los Alamos National Laboratory Report No. LA-10302-MS, Feb 1985.
3. Ott, D. G., Los Alamos National Laboratory, 1986, unpublished data.
4. London, J. E. and Smith, D. M., *A Toxicological Study of NTO*, Los Alamos National Laboratory Report No. LA-10533-MS, Sep 1985.
5. London, J. E., *A Toxicological Study of 1,2,4-Triazole-5-one*, Los Alamos National Laboratory Report No. LA-11461-MS, Dec 1988.
6. Engelke, R. P., *NTO Diameter-Effect Curve and Failure Diameter*, Los Alamos National Laboratory, Dec 1988, unpublished report.

## DISCUSSION

**I. B. MISHRA**  
Kanan Associates, Inc.  
Churchville, MD

I am worried at how easily you get spherical NTO, and its significantly reduced impact data and yet contradictory other data. You also show voids (more) in spherical NTO. Is it possible you have solvent sticking to it? Have you analyzed this?

## REPLY BY L. CHAPMAN

The spherical NTO has been analyzed for residual solvent by NMR and there is no significant amount evident.

## DISCUSSION

**F. VOLK**  
Franhoffer Institute  
Pfinztal, FRG

Can you say something about the melting and decomposition behavior of NTO?

## REPLY BY L. CHAPMAN

NTO shows no endotherm or exotherm in our standard DTA until decomposition takes place at about 260°C.

## DISCUSSION

**H. SHUBERT**  
Franhoffer Institute  
Pfinztal, FRG

Do you find other liquid in the cubic NTO?

## REPLY BY L. CHAPMAN

Recrystallization from water removes the residual nitric acid that is trapped in the cubic crystals during the nitration reaction.

## DISCUSSION

**C. D. HUTCHINSON**  
Atomic Weapons Establishment  
Reading, UK

Have you any information on the hazard properties of NTO or its formulations?

## REPLY BY L. CHAPMAN

The above paper contains all the information the author has on the hazard properties of NTO and its formulations.

## DISCUSSION

**L. ROTHSTEIN**, Consultant  
Newport News, VA

Nitration in an inert solvent may solve the problem of impurity formation, is easier to control nitration temperature, and if chosen well, will precipitate a pure material by precipitation that should not require recrystallization.

# USE OF OXYNITROTRIAZOLE TO PREPARE AN INSENSITIVE HIGH EXPLOSIVE

A. Becuwe and A. Delclos  
S.N.P.E.  
Centre de Recherches du Bouchet  
91710 VERT-LE-PETIT  
FRANCE

*A comparison between experimental data concerning performances and sensitivity on different high explosives is presented.*

*High explosives involved are:*

- *an industrial French PBX named ORA 86 filled with 86 percent of HMX,*
- *a pilot-plant-scaled French PBX named B 2214 filled with a mixture of 12 percent of HMX and 72 percent of NTO.*

*In some cases comparison includes comp. B (hexol 60/40). The decrease of the sensitivity obtained with the NTO based PBX indicates that B 2214 is an Insensitive High Explosive belonging to the 1.6 class and has a very good behavior versus sympathetic detonation.*

## INTRODUCTION

For several years, SNPE has been working to prepare high explosives compositions with a low sensitivity level intended for low vulnerability ammunitions (LOVA). In the past, SNPE has shown the interest of using either Triamino Trinitro Benzene (TATB) or Oxynitrotriazole (ONTA or NTO) as insensitive molecules to decrease the sensitivity of HMX based PBX.<sup>1,2,3</sup> The purpose of our present work is to actually prove that a cast-cured PBX containing a high content of NTO can be an Insensitive High Explosive (IHE) belonging to the 1.6 class, and having a very good behavior versus sympathetic detonation. A set of sensitivity tests is used to compare an industrial cast-cured PBX "ORA 86," filled only with HMX, and a pilot-plant-scaled cast-cured PBX "B 2214," filled with a mixture of HMX and NTO. For some tests, the comparison includes data concerning a melt cast explosive "hexol 60/40," to have a more precise idea of the improvement on a well-known melt cast explosive. Detonation

velocity of the NTO based PBX in confined and unconfined has also been measured.

## COMPOSITIONS

ORA 86 is an industrial composition used in a French missile warhead. B 2214 is a composition prepared at pilot-plant-scale by 50 kg-batches. Composition of both PBX are shown in Table 1.

*Table 1. Composition of PBX*

% Mass	Name	ORA 86	B2214
	% inert binder	14	16
	% HMX	86	12
	% NTO	0	72
	Density	1.71	1.63

Both compositions have been formulated with a classical process to prepare cast-cured PBX. Paste viscosity of B 2214 was optimized by using available classes of NTO particle size

manufactured by SNPE. Samples for evaluation are obtained directly by casting and curing, or by machining after curing.

## DETONATION VELOCITY

For ORA 86, the detonation velocity is given versus charge diameter in an unconfined configuration. For B 2214, the detonation velocity was measured versus charge diameter either in an unconfined or confined (10 mm of steel) configuration. All samples were ignited by a plane wave generator. The results are shown in Table 2.

Table 2. Detonation Velocity

Charge Diameter (mm)	ORA 86 Unconfined (m/s)	B 2214	
		Unconfined (m/s)	Confined (m/s)
15	8250	.	.
20	8280	.	.
30	8310	.	SD
40	.	.	7100
50	8380	ND	7360
63	.	ND	7320
70	.	8770	.
75	.	.	7540
80	.	7410	7440
90	.	7440	.

ND: No Detonation  
SD: Stop Detonation

For B 2214, the detonation velocity progression is illustrated in Figure 1 for the confined and unconfined tests. The failure diameters are respectively 35 or 65 mm with or without confinement.

## FAST COOK OFF

The fast cook off test is used to assess the explosive behavior of PBXs confined in a bomb, and subjected to fuel fire type thermal environments. The bomb consists of a steel pipe [40 mm internal diameter, 4 mm thickness, 200 mm length] enclosed with two plugs. The calculated static rupture pressure of this pipe is around 75 MPa. The bomb is set horizontally 20 cm above a fire pan filled with 1.5 liter of fuel. The fire temperature is about

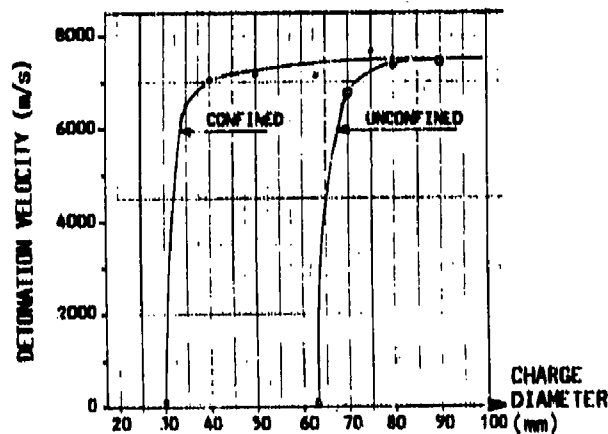


FIGURE 1

Figure 1. Det. Vel. Vs. Charge Diameter B 2214: (72 percent NTO - 12 percent HMX)

800°C. For both compositions, ORA 86 and B 2214, there is no detonation, but only a pneumatic burst of the confinement after 2 minutes.

## BULLET IMPACT TEST

This test is performed on a small-scale warhead with a 125 mm diameter, 90 mm length-sample confined by 20 mm steel (rupture pressure 140 MPa). 12.7 AP bullets are shot by a gun with increasing velocities from 740 to 1140 m/s.

The results obtained for the highest velocity (1140 m/s) are as follows:

- Hexol 60/40: detonation
- ORA 86: no detonation - Burning and opening of the confinement
- B 2214: no detonation - Burning without opening of the confinement

An illustration of the final state of the confinement is given by Figure 2.

## LARGE-SCALE GAP TEST

The gap test is used to determine the threshold of the propagation of detonation in a solid substance. An inert barrier (.19 mm thick cellulose acetate cards) is placed between an initiating booster [hexo wax 95/5 - 40 mm diameter] and a sample of explosive to be tested [40 mm diameter - 200 mm length]



Figure 2a. No Reaction. Bullet velocity 1140 m/s. Composition B 2214. Smooth burning without violent pyrotechnic event.



Figure 2b. Pneumatic Burst. Bullet velocity 1140 m/s. Composition ORA 86. Burning with pneumatic burst.



Figure 2c. Detonation. Bullet velocity 1140 m/s. Hexol 60/40. Detonation.

confined in a 4 mm thick steel pipe. A reference booster in contact with the lower end of the sample and a steel witness plate permit verification, if detonation of the sample has occurred or not. The result is given in number of cards needed to avoid the detonation of the sample. It can also be expressed in thickness of barrier or in shock pressure for the ignition. The detail of the apparatus is shown in Figure 3 below.

The results obtained with hexol 60/40, ORA 86, and B 2214 are given in Table 3. When taking hexol as a reference, it can be seen that the needed pressure to ignite the high explosive sample is 1.6 times higher for ORA 86 and 4.3 times higher for B 2214.

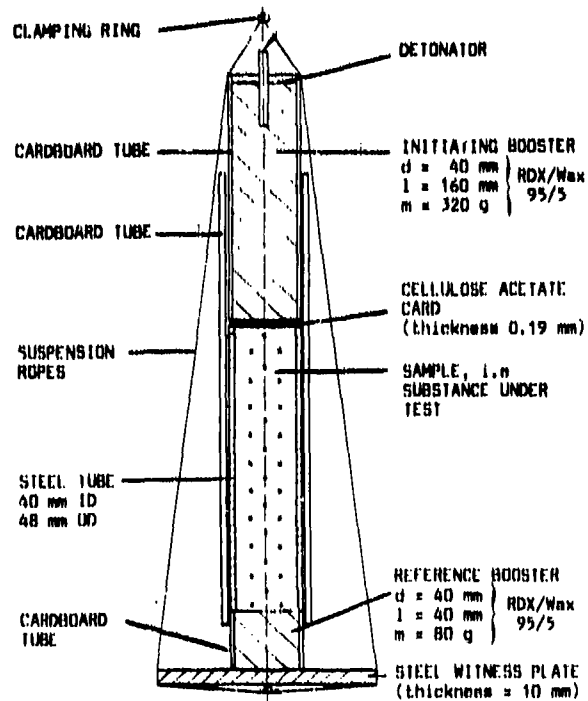


Figure 3. Gap Test for Solids.

Table 3. Gap Test Results

Compositions	Card Gap Test		
	Number of Cards	Thickness (mm)	Pressure (kbar)
Hexol 60/40	200	38	30
ORA 86	160	30	50
B 2214	25	4,7	145

## FLYER PLATE TEST

This test is not only a sensitivity test, but it is much more representative of the level of energy needed to ignite a high explosive by a pure shock wave. The shock wave is generated by impacting a sample of the high explosive (80 mm length - 63 mm diameter) confined by 10 mm steel with a metallic plate. The pressure and the duration of the shockwave can be calibrated by varying the impact velocity and the thickness of the impacting plate. The crude result of the test is detonation or no detonation. After performing the test around ten times, a curve of sensitivity can be drawn in the pressure-time plane. Results obtained for ORA 86 and B 2214 are shown in Figure 4.

To compare high explosives in this kind of test, it is convenient to look only at the pressure and the surface energy for a shock duration of 1.5  $\mu$ s. These values are given in Table 4 for Hexol 60/40, ORA 86, and B 2214. If Hexol 60/40 is taken as a reference, it can be seen that the ignition pressure is 1.7 times higher for ORA 86 and 6.5 times higher for B 2214. The ignition energy is 2.6 times higher for ORA 86 and 21 times higher for B 2214.

## SENSITIVITY TO HEAVY FRAGMENT IMPACT

This test, usually performed in France, is a good way to simulate the impact of a sea-to-sea missile fragment. The impact test is carried out using a steel ball (39.5 mm diameter - 252 g weight) shot by a gun. The velocity can be increased up to 2300 m/s. The high explosive sample is a cylinder [123 mm diameter - 240 mm length] confined by a 10 mm thick shell. For each velocity the result is detonation or no detonation, and the final result of the test is expressed as the maximum impact velocity avoiding detonation of the explosive sample. This result can also be expressed in terms of initial shock pressure. The results obtained with Hexol 60/40, ORA 86, and B 2214 are summarized in Table 5. It should be noticed that for the maximum velocity which can be reached in this test, it was not possible to make the B 2214 detonate.

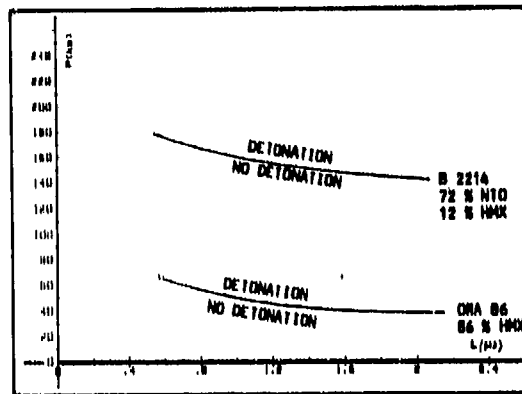


Figure 4. Flyer Plate Test

Table 4. Flyer Plate Test Results

Composition	Ignition Threshold at 1.5 $\mu$ s	
	Pressure (kbar)	Energy ( $J/cm^3$ )
Hexol 60/40	23	150
ORA 86	40	400
B 2214	150	3200

Table 5. Heavy Fragment Impact - Maximum Velocity Without Detonation

Composition	Heavy Fragment	
	Velocity (m/s)	Pressure (kbar)
Hexol 60/40	1350	25
ORA 86	1910	60
B 2214	>2270	>90

When taking Hexol 60/40 as a reference, the maximum pressure avoiding detonation is multiplied by 2.4 for ORA 86 and more than 4.4 for B 2214.

## SENSITIVITY TO A SHAPED-CHARGE SHOT

Both PBX involved in this work (i.e., ORA 86 and B 2214) have been subjected to

the impact of a 90 mm caliber shaped-charge jet. This shaped-charge was filled with a 91 percent PETN containing PBX. The sample of high explosive tested are 90 mm diameter - 320 mm height cylinders. The "stand-off" was one caliber. The following results were obtained:

- ORA 86: Detonation
- B 2214: No detonation

## SENSITIVITY TO SYMPATHETIC DETONATION

This test is performed to evaluate the behavior of an explosive submitted to a detonation (blast, fragments, and heat). The experimental setting is shown in Figure 5. The sample of high explosive to be tested is a 75 mm diameter - 280 mm height cylinder confined by 12 mm steel. The donor has the same size. Its composition is Hexol 60/40. The distance between donor and receptor is 25 or 500 mm. Reactions obtained with Hexol 60/40, ORA 86, and B 2214 are summarized in Table 6.

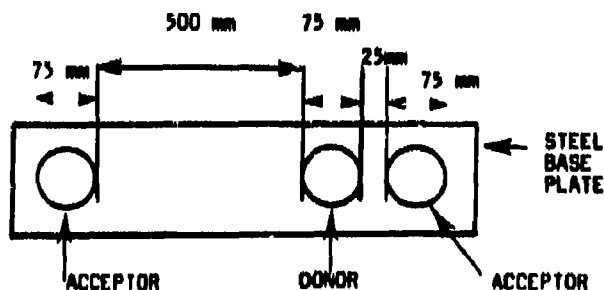


Figure 5. Sensitivity to Sympathetic Detonation- Experimental Setting

Table 6. Behavior Vs. Sympathetic Detonation

Composition	Behavior at a Distance of'	
	2, 5 cm	50 cm
Hexol 60/40	Detonation	Detonation
ORA 86	Deflagration	Deflagration
B 2214	No reaction	No reaction

## CONCLUSIONS

The studies performed by SNPE in the field of synthesis and recrystallization of NTO,

then its use as an insensitive high explosive in PBX, have permitted us to perfect at the pilot-plant scale (50 kg batches) an inert binder based PBX (B 2214) filled with 12 percent HMX and 72 percent NTO.

The characterization in terms of:

- sensitivity to fuel fire and bullet impact,
- sensitivity to ignition by a shock wave,
- sensitivity to shaped-charge jet, and
- sensitivity to sympathetic detonation

shows that B 2214 is clearly less sensitive than Hexol 60/40 or ORA 86; a 86 percent HMX PBX. The studies made by SNPE were mainly to show it was possible by using an insensitive filler, such as NTO, to obtain 1.6 classed PBX; insensitive to sympathetic detonation. Of course, performances of B 2214, in terms of detonation, velocity, and pressure, are a little weak but can be improved by increasing the filler content, increasing the HMX ratio in the mixture NTO-HMX, or by adding various ingredients like aluminum or ammonium perchlorate to obtain special effects (blast, bubble, etc.).

## REFERENCES

1. Deneuille, P.; Gaudin, C.; de Longueville, Y.; and Mala, J., "Comparison of TATB and DINGU Explosive Properties," *Proceedings of the 7th International Symposium on Detonation*, Annapolis, 16-19 Jun 1981.
2. Becuwe, A. and Delclos, A., "L'oxynitrotriazole et Son Utilisation en Tant Qu'explosif Insensible," *Proceedings of 18th International Annual Conference of ICT*, Karlsruhe (FRG), 1-3 Jul 1987.
3. Becuwe, A. and Delclos, A., "Use of Oxynitrotriazole as a Low Sensitivity Explosive," *Proceedings of the International Symposium on Pyrotechnics and Explosives*, Beijing, China, 12-15 Oct 1987.

This work has been performed under the auspices of the French Ministry of Defense (STPE).

## **DISCUSSION**

**INDU B. MISHRA**  
Kanan Associates, Inc.  
Churchville, Maryland

In your NTO formulation for insensitive HE, you have taken NTO-HMX of 84 percent and 16 percent binder (by weight) where as your HMX composition had 86 percent RDX and the rest binder. Is it not possible to formulate, with 14 percent binder, your NTO-based HE? What was your volumetric loading for HMX-HE and NTO-HMX-HE (by comparison)?

### **REPLY BY A. BECUWE**

When the B2214 PBX binder was formulated, the particle sizes of available NTO

did not permit us to obtain an acceptable feasibility with more than 84 percent filler content. Volumetric loading for HMX-HE was 76.5 percent and for NTO-HMX-HE, 71.5 percent.

**HILTMAR SCHUBERT**  
Fraunhofer Institut  
West Germany

Which particle size do you use in your NTO composition?

### **REPLY BY A. BECUWE**

It is a mixture of three different particle sizes: a fine one around 10 $\mu$ , a medium one around 200 $\mu$ , and a coarse one around 700 $\mu$ .

# EFFECTS OF BINDER CONCENTRATION ON THE PROPERTIES OF PLASTIC-BONDED EXPLOSIVES

Raymond D. Steele, Lawrence A. Stretz, Gene W. Taylor, and Thomas Rivera  
Los Alamos National Laboratory  
Los Alamos, New Mexico 87545

*A series of plastic-bonded explosives (PBX) has been formulated with more binder than is normally contained in high-energy formulations. Adding a relatively small amount of binder to a material such as PBX 9501 [95/2.5/1.25/1.25 wt percent HMX/Estane/BDNPA/BDNPF (the BDNPA and BDNPF form a eutectic that is frequently called simply the eutectic)] was found to decrease the shock sensitivity while not decreasing the energy of the explosive. The best compromise for a PBX 9501-type material contains about 92 wt percent HMX. Adding additional binder does not continue to decrease the gap sensitivity of the formulation; however, the energy of the PBX decreases as expected. The higher-binder formulations are of potential use because of the possibility of formulating a PBX with energy similar to TATB formulations, such as PBX 9502 (95/5 wt percent TATB/Kel-F 800), and with a higher strain to failure.*

## INTRODUCTION

This study was initiated to determine the effects of binder concentration on the properties of a PBX. The sensitivity of the Estane/eutectic system used for PBX 9501 was not known as a function of concentration. The sensitivity of the system was of special interest when the energy was matched to PBX 9502. The behavior of PBX 9502-like systems is interesting because their unique mechanical properties, such as high strain to failure, might be designed into a useful formulation usable as a substitute for PBX 9502.

Desensitizing high-energy PBXs was another reason for undertaking this work. One of the most important mechanisms for the initiation of explosives is believed to be hot spots caused by voids or other density discontinuities. High-energy PBXs, such as PBX 9501, typically can be pressed to 98 percent of theoretical density (TMD). This means that the explosive composites have about 2 volume percent voids that may serve as hot spot locations. It appears that removal of

the voids is the logical starting place to desensitize a PBX.

## EXPERIMENTAL

The experiments used in this study were the large scale gap test and the plate dent test described by Gibbs and Popolato.<sup>1</sup> The plate dent test is a measure of the energy delivered by an explosive to a calibrated steel plate. It has been found experimentally that this delivered energy can be closely related to the Chapman-Jouquet (CJ) pressure of the explosive being tested. A theoretical basis may be found for this relationship in such works as Fickett and Davis.<sup>2</sup> For this reason it is customary to calibrate the plate dent test to accepted CJ pressures and to report the results as CJ pressure. Because this pressure is a measure of the delivered energy, we will refer to the results of the plate dent test as the energy of the explosive.

A low-void material was formulated to investigate the effect of the removal of voids from a PBX. The material to be tested was a

formulation with HMX and the Estane/eutectic binder used in PBX 9501 (X-0242-92-01-04 - 92/8 wt percent HMX/binder).

This formulation was chosen to provide more than ample binder to fill all the voids in the composite. To assure elimination of all voids, the PBX was pressed at an unusually high pressure (30,000 psi), at a maximum permissible temperature (100°C), with maximum vacuum on the powder before pressing, and with five intensifications. The resulting PBX had a density of 99.7% TMD. The CJ pressure and gap sensitivity were measured for this material; the results were CJ pressure of 366 kbar and a gap sensitivity of 47 mm. This compares with values of 360 kbar and 55.6 mm for PBX 9501.<sup>1</sup> These data are included in Table 1. It is possible to formulate a PBX with less sensitivity than PBX 9501 at no loss in energy, and perhaps even a small gain.

*Table 1. Performance and Sensitivity of High-Binder PBXs*

<u>Material</u>	<u>Composition</u>	<u>Gap (mm)</u>	<u>CJ (kbar)</u>	<u>TMD</u>
PBX 9501	95/2.5/2.5 HMX/Estane/eutectic	55.6	360	98.0
X-0242-94-01-03	94/3/3 HMX/Estane/eutectic	55.1	363	99.1
X-0242-93-01-03.5	93/3.3/3.5 HMX/Estane/eutectic	50.3	364	99.4
X-0242-92-01-04	92/4/4 HMX/Estane/eutectic	47.68	366	99.7
X-0242-91-01-04.5	91/4.5/4.5 HMX/Estane/eutectic	48.46	360	99.8
X-0242-90-01-05	90/5/5 HMX/Estane/eutectic	48.08	355	99.8
X-0444	88/6/6 HMX/Estane/eutectic	46	340	99.8
X-0438	80.5/9.5/9.5/0.5 HMX/Estane/eutectic/stearate	47.3	284	95.3
X-0430	88/6/6 HMX/Kraton/Tuffin Oil	46	283	99.6

The pressing conditions used to obtain the void-free samples of X-0242-92-01-04 were rather extreme. A pressing evaluation was conducted to evaluate which of the measures

used in processing this PBX were responsible for the improved performance. All the variables used in the processing of X-0242-92-01-04 were varied from normal to extreme in an experimental design, and the density of the sample at these conditions was measured. The concentration of the binder and, to a lesser extent, the number of pressing intensifications were found to be the only variables that significantly influenced the densities of the pressed samples. The CJ pressure and the gap sensitivity were redetermined for one sample of X-0242-92-01-04 pressed under nominal pressing conditions. The results reproduced those of the formulation pressed under more extreme conditions. Decreased sensitivity in a PBX can be obtained by simply increasing the fraction of binder in the composite while using three intensifications.

To investigate in detail the behavior of the HMX/Estane/eutectic system, a number of formulations were made with HMX compositions varying from 80.5 to 94 wt percent. These materials were pressed, the detonation pressures were determined with plate-dent experiments, and the gap sensitivity was measured. These data are listed in Table 1, with the literature values for PBX 9501 included for reference.

All the HMX/Estane/eutectic materials listed in Table 1 made satisfactory pressings with the exception of the 80.5 wt percent formulation. This material was extremely "gummy" and tended to extrude around the seals in the press. We were not able to obtain the desired density for this formulation. The properties of this material are interesting even though they are not directly comparable with the other formulations.

The first observation made from the data in Table 1 is that the gap sensitivity falls off dramatically as the HMX in the formulation is decreased, reaching a plateau at about 46 or 47 mm (Figure 1). The second observation is that the energy of the system remains relatively constant as the HMX in the formulation is decreased until the mixture is approximately 92 wt percent HMX (Figure 2). This result does not seem too surprising, if one realizes that voids of zero energy are being replaced with an energetic binder. Looking at

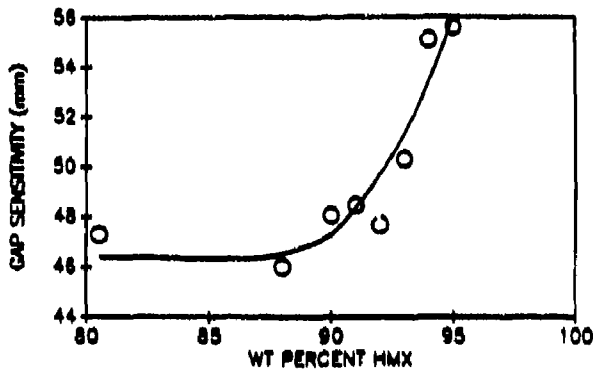


Figure 1. Gap Sensitivity as a Function of HMX Concentration

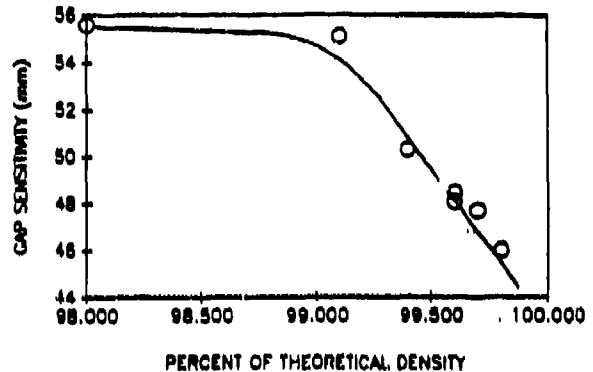


Figure 4. Gap Sensitivity as a Function of Percent of Theoretical Density

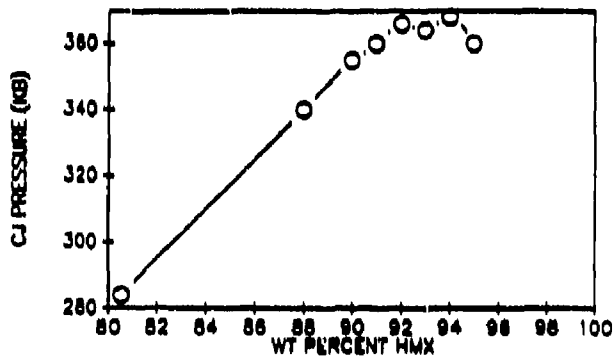


Figure 2. CJ Pressure as a Function of HMX Concentration

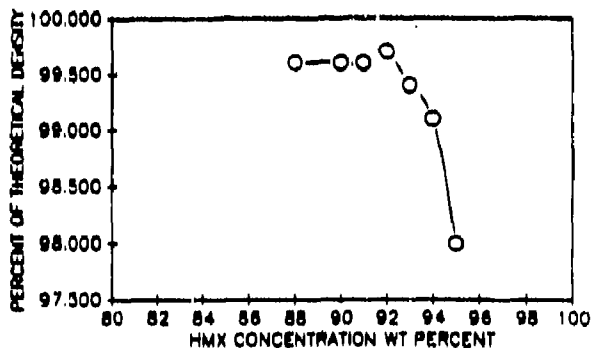


Figure 3. Percent of Theoretical Density as a Function of HMX Concentration

the results presented in Figures 1 and 2, one concludes that an improved version of PBX 9501 can be obtained by decreasing the HMX content to 92 wt percent. The gap sensitivity will be decreased while the energy will remain constant.

Additional insight into the behavior of the HMX/Estane/eutectic system can be obtained by examining the data in Table 1. The percent TMD is seen to be a function of the binder loading in the system, with the percent TMD decreasing rapidly as the HMX fraction is increased (Figure 3). There does, however, appear to be a reasonable amount of scatter in the system, which indicates that variables other than binder loading are probably important when trying to reach very high percent TMDs. The importance of reaching very high percent TMDs is seen in Figure 4, where the gap sensitivity is plotted as a function of percent TMD. It is apparent that a PBX should be at the maximum possible percent TMD. To obtain the best sensitivity in a HMX/Estane/eutectic formulation, it will be necessary to determine what controls the relatively small differences in pressing densities.

When Figures 1 through 4 are examined, it appears that PBX 9501 may be anomalous. The PBX 9501 data were taken from the literature and may not be consistent with the other data in Table 1. Additional experiments

are planned to verify the behavior of PBX 9501.

The behavior of binder systems other than the Estane/eutectic is also of interest. A PBX with 88 wt percent HMX, 6 wt percent Kraton, and 6 wt percent Tufflo Oil was formulated (X-0430) for this reason. Its gap sensitivity and CJ pressure were determined and are reported in Table 1. Interestingly, the gap sensitivity is the same as for the high-binder Estane/eutectic formulations. Based on very limited evidence, the gap sensitivity of a high-binder formulation does not appear extremely dependent on the binder material.

One of the purposes for this study was to investigate the properties of HMX-based PBXs with energies similar to PBX 9502s. Two of the formulations discussed above, X-0430 and X-0438, were designed to have the energy of PBX 9502. The energy of these two formulations was indeed very near to that of PBX 9502. The X-0430 performed very much as expected; the HMX coated well and no major problems were encountered in pressing. The X-0438, however, was another problem because the Estane/eutectic is a very soft, rubbery material that flows much too easily and sticks to the metal parts in the press. Excessive amounts of this binder make the samples very hard to press and creates problems in uniformity of material, and produces a pressing that is not dimensionally stable. Additional experiments are planned to investigate the properties of Estane/eutectic binder formulations with decreased amounts of the eutectic. This will provide a stiffer material and perhaps overcome some of the problems of X-0438. The amount of HMX will need to be increased in these experiments to maintain the desired energy level.

## CONCLUSIONS

In conclusion, a series of PBXs has been formulated with more binder than is normally used in high-energy explosives. It was determined that adding a relatively small amount of binder to a material such as PBX 9501 will improve the gap sensitivity without degrading the energy of the explosive. It appears that the best compromise for a PBX 9501-type material

is about 92 wt percent HMX. Adding additional binder does not continue to improve the gap sensitivity of the formulation. However, the energy of the PBX decreases as expected. The high-binder formulations are of potential use because of the possibility of formulating a PBX with energy similar to PBX 9502s, but with a much higher strain to failure and other desirable advantages.

## REFERENCES

1. Gibbs, T. and Popolato, A., *LASL Explosives Data*, University of California Press, Berkeley, 1980, pp. 105-119, 280, 425.
2. Fickett, W. and Davis, W., *Detonation*, University of California Press, Berkeley, 1979.

## DISCUSSION

I. B. MISHRA  
Kanan Associates, Inc.  
Churchville, MD

1. It is perhaps risky to say that binders had "no" effect toward sensitivity at the 8 percent level. In our work we find binder playing a significant role in PBX in contributing to or altering sensitivity. We have even found energetic binders reducing sensitivity.
2. It is interesting that you find a 92 percent formulation a somewhat "ideal" one. Not knowing your results we have been formulating 91-92 percent solids loaded HE and insensitive HE.

## REPLY BY R. D. STEELE

1. We do not claim that the different binders do not have an effect on sensitivity. In fact, we know that different binders have extreme effects on different types of sensitivities. Two important formulations, PBX 9404 and PBX 9501, differ principally in their binders. When the two materials are subjected to a drop skid test, they have a drop height of 4 and 26 feet, respectively. We did, however, observe that two different binders did not seem to have an effect on a gap test. We cannot make any general conclusions on these limited data. However, at least for our limited sample, it

appears that shock initiation is not affected by the nature of the binder. Since in shock imitation we have probably exceeded any of the limiting mechanical properties of the binder, this observation may have wider applicability than the limited data might suggest.

2. We would like to add a note of caution that this optimization was for one binder with one particle size distribution of HMX. Should one change the binder, the particle size distribution, or the explosive, then 8 percent binder would probably no longer represent an optimal formulation.

## DISCUSSION

**H. GRYTING**  
Gryting Energetics Sciences Company  
San Antonio, TX

Is the eutectic just the usual combination of energetic plasticizers? Does either of these also form a simple binary or a ternary eutectic with HMX?

## REPLY BY R. D. STEELE

The eutectic is a 50-50 percent mixture by weight of bis(2,2-dinitropropyl)-acetal (BDNPA) with bis(2,2-dinitropropyl)formal (BDNPF). This is our normal plasticizer used to soften Estane for use in PBX 9501. The BDNPA/BDNPF mixture provides an energetic contribution to the formulation. As the terminology eutectic suggests, the mixture forms a minimum freezing point eutectic at 50-50 percent by weight. This property is important because it prevents the plasticizer from freezing and stiffing the binder.

# CHEMISTRY OF NITROMETHANE AT VERY HIGH PRESSURE

Stephen F. Agnew and Basil I. Swanson  
Los Alamos National Laboratory  
Isotope and Nuclear Chemistry Division  
Group INC-4, Mail Stop C346  
Los Alamos, New Mexico 87545

and

John Kenney and Inga Kenney  
Department of Physical Sciences  
Eastern New Mexico University  
Portales, New Mexico 88130

*Decomposition of nitromethane is reported over the range of 115-180°C and 0.6-8.5 GPa. About 5 µg of nitromethane is compressed with a diamond-anvil cell, heated to the point that reaction occurs, and held typically 10-20 minutes at the reaction temperature. The cell is cooled and the volatile contents of the cell are frozen as a thin layer in vacuo and an infrared absorption spectrum is recorded. The three volatile products observed are N<sub>2</sub>O, CO<sub>2</sub>, and water, with N<sub>2</sub>O production peaking at 1.5 GPa, 135°C, and 35 percent of NME; CO<sub>2</sub> production peaking at 3.5 GPa, 135°C, and 65 percent of NME, and water yields at 20-50 percent of NME at the highest pressure measured, 8.5 GPa and 175°C. Water yields were difficult to quantify due to background contamination. Results indicate three different reactions for solid NME dependent primarily on the pressure of the reaction, and that fluid NME does not decompose at 0.6 GPa and 175°C, although the solid decomposes readily at 1.1 GPa and 120°C. The authors conclude that, while various decomposition mechanisms are possible, the initial step  $\text{CH}_3\text{NO}_2 \rightarrow \cdot\text{CH}_3 + \cdot\text{NO}_2$  is very unlikely.*

## INTRODUCTION

The tendency for energetic materials, both high explosives and propellants, to undergo inadvertent detonation is a serious and not well understood problem. Detonations can be thought of as self-driven shock waves and are initiated by a variety of stimuli or insults. The initial chemistry that drives the deflagration (or fast burning) to detonation transition is of primary importance to understanding the initiation event, and a good amount of activity is occurring with regards to trying to understand the reactions that are important for this chemistry.

In order to obtain a better understanding of the kinds of chemistry that might be important for initiation events, we are studying reactions of simple energetic materials, e.g., nitromethane, under conditions of confinement at very high pressure. We have chosen these conditions for two reasons: 1) The reactions that are expected to be important in deflagration to detonation transitions are, under low pressure conditions, solid to gas reactions. These reactions drive the energetic decomposition that leads to detonation and are reactions that produce small, stable, and hot molecules. Since these reactions are both fast and not diffusion limited, they will probably

involve many concerted steps. Performing measurements at high pressure allows us to choose the phase of the products, which, since we can choose the pressure, can be either fluid or solid. This allows a control over diffusion and mixing that is impossible by any other method. 2) We expect the initiation reactions to be extremely pressure dependent. The very notion of a detonation wave is one that involves pressure- and temperature-induced chemical events that lead to further pressure and temperature increase until finally a dissipative process limits the energy release rate and a steady state is reached.

The concept of an activation energy for a given reaction and the role of temperature in surmounting it is well understood and the traditional Arrhenius activation is normally assumed to be valid even at very high density. Pressure-induced reactivity, on the other hand, does not involve overcoming the activation barrier in a dynamical sense. It is more subtle and involves actually *changing* the activation energy, now more properly considered the activation enthalpy. It is then reasonable to expect that we must, from the very start, consider the activation enthalpy instead of only the activation energy,  $E_a$ . The activation enthalpy will be a natural function of pressure as  $\Delta H^\ddagger = \Delta E^\ddagger + P\Delta V^\ddagger$ , and pressure-induced reactivity should really, by all rights, be called "pressure-catalyzed" reactivity. This emphasizes the very different role that pressure has compared to temperature and the critical parameter in describing the pressure dependence of the reaction rate or branching ratios then becomes the activation volume,  $\Delta V^\ddagger$ .

An initial reaction or transition state with a substantial volume *decrease* ( $-\Delta V$  or  $-\Delta V^\ddagger$ ), increases the reaction rate and the presumption is that with energetic materials, the initial reactions do possess  $-\Delta V^\ddagger$ . Otherwise, increasing pressure would not increase the reaction rate, and may actually decrease it. While the initial reaction must involve  $-\Delta V$ , the overall reaction must, on the other hand, have a  $+\Delta V$  in order to sustain the detonation. Thus, we expect to find (and must look for) reactions that have these two important characteristics.

Studying the reactions of energetic materials at high density allows us to probe chemistry that is slow or even nonexistent at low pressure. In particular, concerted intermolecular reactions should become very important at high density, whereas at low pressure one often sees volatilization of the material prior to any actual chemistry. With the aid of pressure, then, we can hold molecules in their lattice to much higher temperature than would otherwise be possible. Another important factor in condensed phase reactions is that of the solvent cage and its effect on reaction rates. Cage effects are extremely important in solution reactions and they certainly will be even more important at high density. Furthermore, reactions of energetic materials ultimately will have more in common with solid state chemistry than with solution chemistry. Thus, for energetic materials the solid-state chemical notion of *reactive cages* and also concerted intermolecular reactions will be very important.

We are trying to understand the very complicated reactions at high density for an energetic material undergoing deflagration or detonation. We must find ways of understanding these reactions, despite their complicated natures, in order to predict and possibly control such properties as sensitivity, performance, and burn rate. The obvious limitations of performing experiments on such materials while they are reacting and the small amount of information that is obtained from those experiments means that we will always have to resort to some kind of approximation in order to understand the chemistry associated with initiation. With this work, we hope to establish at the very least, some general principles for the kind of chemistry that is associated with detonation initiation.

## EXPERIMENT

We have used diamond-anvil cells of the Merrill-Bassett design<sup>1</sup> to compress nitromethane and have used the position of the C-N stretch infrared absorption, calibrated versus the ruby fluorescence standard, as a measure of pressure. Optical microscopy was used to observe the onset of reaction while the cell was

heated with an external heater. For many of the samples, infrared absorption microscopy was used to determine the extent of reaction and also to determine the reaction products that accumulated within the cell. The release apparatus, shown in Figure 1, allowed the release and freezing of the contents of the diamond-anvil cell onto a CsBr window mounted on an Air Products closed cycle helium refrigerator (a displax) and held at 20°K. Following deposition, the cryotip was rotated 90° within its shroud and an absorption spectrum was recorded at 2 cm<sup>-1</sup> resolution and 256 scans. Such a procedure allowed the determination of absorption peaks on the order of 0.005 Å, although this apparatus had a large water background due to outgassing. Water also did not evaporate readily from the cell when the cell pressure was released and, as a consequence, only very qualitative data was obtained on the amount of water that evolved from the experiment.

A Digilab FTS-40 spectrometer was used for the thin layer experiments with a Bio-Rad infrared microscope installed in an auxiliary sample compartment to record the spectrum of nitromethane and/or products while under compression within the diamond-anvil cell.

## RESULTS

At pressures less than 0.8 GPa, the nitromethane melted about 80°C and showed very little reaction up to 175°C for over two hours. However, at 1.1 GPa, the NME did not

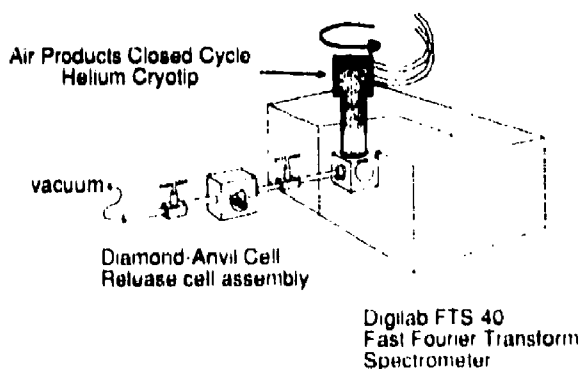


Figure 1. Diagram of the Release Apparatus

melt on increasing temperature, but began to react at 120°C as evidenced by the nucleation and growth of bubbles. Infrared spectra in Figure 2 show the spectra of the nitromethane within the diamond-anvil cell before reaction, after four hours, and after six hours at the temperature and pressure indicated. As the sample reacted, the infrared signal became progressively weaker, but new features are evident: 1) a broad, saturated absorption at 3200-3400 cm<sup>-1</sup>; 2) a broad, saturated band for the -NO<sub>2</sub> group symmetric and antisymmetric stretches in place of the two features that were evident before reaction; and 3) two absorption bands at 2220 and 2250 cm<sup>-1</sup> that are partially obscured by the diamond second-order absorption. Little spectral information is available for the reacting sample, implying that the products are absorbing completely at the nucleation sites. Eventually, as the reaction proceeds to completion, the infrared signal completely disappears.

When we release the contents of the diamond-anvil cell following reaction, freeze the volatiles in a thin layer, and measure the infrared absorption of that thin layer (Figure 3), we find that N<sub>2</sub>O, CO<sub>2</sub>, and water are the dominant volatile products. Their relative amounts depend on the particular temperature and pressure at which the reaction was performed as shown in Figure 4. One can see that these volatile products are substantial fractions of the starting material. We know that water is present in significant amounts among

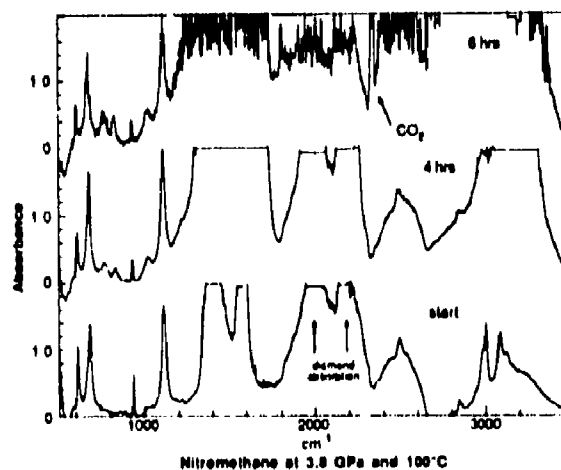


Figure 2. Nitromethane Before and During Reaction Within Diamond-Anvil Cell

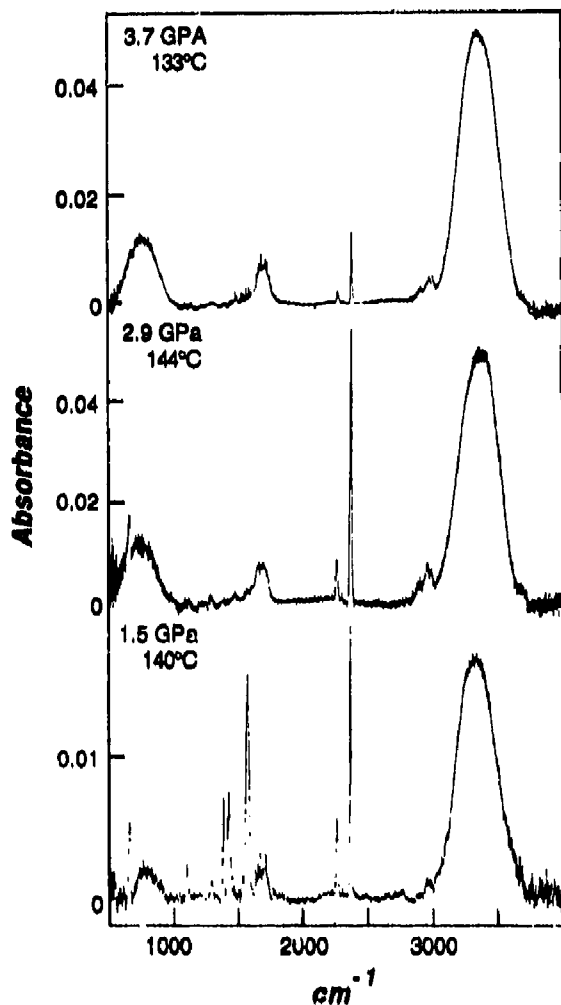


Figure 3. Infrared Absorption Spectra of Thin Layer of NME Reaction Products at Various Pressures and Temperatures

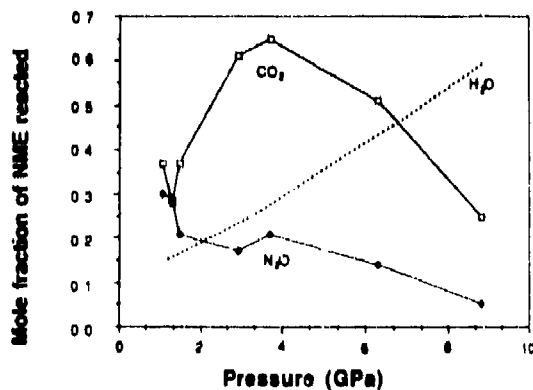


Figure 4. Reaction Yields of CO<sub>2</sub>, N<sub>2</sub>O, and Water for NME Decomposition as a Function of Pressure and Temperature of Onset of Reaction

the products, but have been unable to quantify it very well. (Evidently, water escapes from the cell upon release in variable amounts, since our results with releasing pure water from a diamond cell under identical conditions were subject to a large error.) Whenever NME melts before the temperature reaches ~120°C, no appreciable reaction occurs up to 175°C. We conclude, then that fluid nitromethane does not react appreciably over a period of 30 minutes at the pressure and temperature noted on the diagram. A P-T reaction diagram is shown in Figure 5 and shows that between 1.0 and 2.5 GPa (reaction regime A), nitromethane is solid at 120°C, while the N<sub>2</sub>O and CO<sub>2</sub> products are fluid, and nucleation and growth centers can be readily observed in the solid nitromethane involving these fluid products. Thus, the reaction is assisted by topochemical control of the crystal lattice (i.e., the relative orientations of the NME molecules in the solid). There is time for subsequent dissolution of some NME into these reaction product bubbles, but we feel that any reaction that takes place subsequently in the solution may follow a different pathway, since fluid NME itself shows no reaction at this temperature and slightly lower pressure.

Between 2.5 and 5.0 GPa (reaction regime B), CO<sub>2</sub> becomes the dominant product, consuming nearly 65 mole percent of the NME

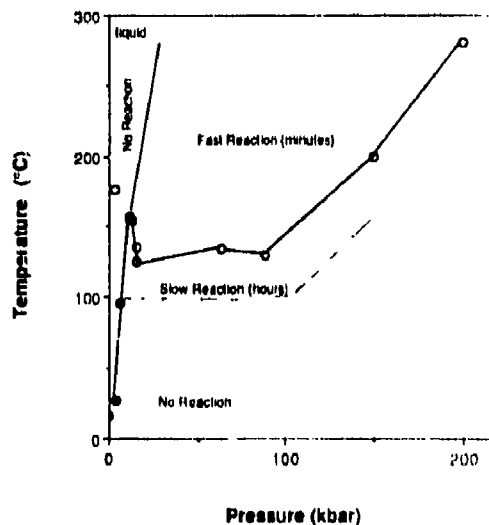


Figure 5. Pressure-Temperature Reaction Diagram for NME Decomposition Showing the Temperature for the Onset of Reaction at Various Pressures

at 3.5 GPa, and then decreasing with increasing pressure. In both regimes B and C, we expect that  $N_2O$  and  $CO_2$  will be solid, and we do not observe the bubble growth that was so pronounced at lower pressure. The temperature at which the reaction begins is increasing with increasing pressure, indicating that very high pressure suppresses all NME chemistry. At pressures  $> 5.0$  GPa (reaction regime C), both  $N_2O$  and  $CO_2$  become much less pronounced and water is the primary volatile product, and we have qualitatively determined that with pressure in excess of 20 GPa, NME is stable to  $300^\circ C$ . The solid residue that remains following chemistry at all of these pressures and temperatures qualitatively reflects the trends noted with the volatile products. In reaction regimes A and B with the highest yields of  $CO_2$  and  $N_2O$ , there is very little residue, and that which remains has an oily nature. On the other hand, at the highest pressure that we have measured, reaction regime C, a solid residue fills our gasket completely and there is much less  $CO_2$  and no  $N_2O$ .

## DISCUSSION

There have been many different kinds of studies of NME decomposition including studies under conditions of photolysis,<sup>2,3</sup> pyrolysis,<sup>4</sup> and high pressure.<sup>5,6,7</sup> We believe that the decomposition chemistry in compressed nitromethane found for reaction regime A is different from any that has been previously reported for this molecule. This chemistry, therefore, does not involve radical production,  $CH_3NO_2 \rightarrow \cdot CH_3 + \cdot NO_2$ , which is typical of most of nitromethane's pyrolytic and photochemical reactions. Although we have not yet determined our limits of detectivity for methane, ethane, or  $NO_2$ , we do not observe any of these products and their absence would mean that the radical reaction is not the dominant decomposition pathway.

The three basic reaction regimes that we observe can be categorized as the nitrogen coupling regime (A), carbon oxidation regime (B), and dehydration regime (C). We suggest that the nitrogen coupling reaction necessary for  $N_2O$  production (regime A) involves either an N-nitroso or an N-nitrate intermediate, but

we have no information yet to confirm that. The relatively small amount of residue would then be a polymer, possibly similar to polyvinyl alcohol (PVA). Regime B involves oxidation of the carbon and presumably, simultaneous reduction of the nitrogen to amine. Direct attack of the oxygen on the carbon and then hydrogen transfer to the nitrogen site is a plausible route to produce hydroxyamine formate, a likely precursor to  $CO_2$  evolution. It is notable that even under conditions that produce the largest amounts of  $CO_2$ , neither formaldehyde (as a volatile) nor paraformaldehyde (detected in the residue) are observed among the products.

Finally, in regime C a notable amount of orange colored solid remains after the reaction, with water as the only volatile detected. This dehydration product could be related to the methazonate polymer that is known to result following further reaction of the aci-ion. On the other hand, there are reports<sup>5,6,8</sup> that this solid is largely either ammonium formate or ammonium oxalate, with the orange color then due to small amounts of other minor products.

These results are consistent with the hypothesis that, for nitromethane initiation, reactions that produce small, stable molecules are going to be important. These reactions will release the large amount of compressive energy that is necessary to drive subsequent chemistry. Therefore, we consider both reactions A and B to be important in the initiation process. Reaction C, however, largely results in solid products and should consume compressive energy due to its  $-\Delta V$ , thereby quenching any initiation chemistry that might occur.

These reactions occur in the solid state and are therefore quite complicated, but one must study these types of neat phase reactions if a better understanding of the chemistry of initiation is to follow. We feel that even a crude understanding of many of the reactions is preferable to no understanding of the neat, condensed phase reactions at all. It is obvious that extreme caution must be used, for example, if one wishes to relate these condensed phase reactions to gas phase pyrolytic chemistry or photochemistry. The implication is that concerted reactions will more often than not

dominate over the bond-breaking reactions that dominate at low density in the gas phase.

Both HMX(cyclo tetramethylene tetranitramine) and RDX(cyclo trimethylene trinitramine), which are very important military high explosives, produce  $N_2O$  in their thermal decomposition at low pressure.<sup>9</sup> It has been shown<sup>10</sup> that RDX, under isolated molecule pyrolysis, undergoes a concerted ring breaking step to first produce methylene nitramine, subsequently decomposing to formaldehyde and  $N_2O$  as  $1/3RDX \rightarrow CH_2 = N-NO_2 \rightarrow N_2O + CH_2O$ . Ammonium nitrate, the primary component of industrial high explosives, also produces  $N_2O$  upon decomposition.<sup>11</sup> This latter  $N_2O$  production has been explained as due to the initial dehydration to produce nitramine as  $(NH_4)(NO_3) \rightarrow H_2N-NO_2 + H_2O$ , followed by further dehydration of nitramine with an HNO dimer intermediate as  $H_2N-NO_2 \rightarrow (HNO)_2 \rightarrow N_2O + H_2O$ . Key in both of these schemes is the nitramine intermediate, and we suggest that nitromethane decomposition most likely involves a dimerization or reaction between the nitrogens of adjacent nitromethanes. This could be due to unimolecular rearrangement of NME to hydroxylamine formate,  $HCOO-NH_2$ , with subsequent attack on another nitromethane to produce  $H_2COOCH_3 + NH_2-NO_2$ , simultaneous isomerizations of adjacent NMEs to methyl nitrite with a coupling reaction to produce  $CH_3OCH_3$  and  $N_2O$ , or unimolecular formation of an  $(H_2CO)(HNO)$  intermediate for adjacent NMEs with reaction of two HNOs to form  $N_2O$  and water as shown above. All of these mechanisms must in turn be controlled by the solid state phase that we know is important for the reaction to proceed.

Another possible initial reaction is the isomerization to the nitrite form,  $CH_3-NO_2 \rightarrow CH_3-O-NO$ , with subsequent reaction to produce the observed products. This reaction would presumably result in  $N_2O$  and  $CO_2$  production through an intermolecular coupling reaction, although one expects significant amounts of methanol or perhaps formaldehyde to result. A recent report<sup>12</sup> on supercritical nitromethane pyrolysis also suggests this reaction is a first step under those conditions. However, we have independently found that

formaldehyde polymerizes readily under these conditions to form paraformaldehyde, which is directly characterizable in the infrared. Since we find no evidence for either formaldehyde, formalyn, or paraformaldehyde among the reaction products of nitromethane, the suggestion is that there is another pathway to both  $N_2O$  and  $CO_2$ . Also, there is no reason to expect the isomerization to be inhibited in the fluid phase, at slightly lower pressure. The fact that we do not observe significant NME decomposition in the fluid then implies that the nitrite isomerization is not the initial reaction leading to decomposition.

Much previous work has been performed<sup>13</sup> on the role of the aci-ion of nitromethane in the sensitization of nitromethane to shock initiation. We therefore consider the activation of nitromethane by means of either water or hydroxide ion to be a logical first reaction step. Since it is well established that the aci-ion dimerizes readily under ambient conditions to form the methazonate ion, it is hard to believe that the aci-ion itself would lead to the chemistry that we observe, since subsequent reaction of the methazonate produces an ill-defined colored polymer. That is, the aci-ion form evidently activates the carbon center for further reaction. In order to produce  $N_2O$ , we must have a nitrogen activation.

The exact nature of this nitrogen coupling reaction will have to wait for further experiments. We are currently working to improve our apparatus by increasing the heating rate and decreasing the contamination level of water. Such an improved apparatus should allow us to improve our measurements significantly.

## CONCLUSION

Very different decomposition reactions occur for solid nitromethane at high pressure as compared with ambient or low pressure conditions. These reactions are evidently concerted intermolecular reactions, and three very different reaction regimes occur as a function of pressure and temperature. We suggest that the first two reaction regimes, those that produce  $N_2O$  and  $CO_2$ , are most closely related to the chemistry of initiation. Moreover, we expect that, in general, reactions

in energetic materials that very quickly produce small, stable molecules (i.e.,  $+\Delta V$  overall), but are nevertheless associated with  $-\Delta V^\ddagger$  (a decrease in volume for the activated complex), will be most important for determining the initiation of the material.

## REFERENCES

1. Merrill, L. and Bassett, W. A., *Rev. Sci. Instrum.*, Vol. 45, 1974, p. 290.
2. Brown, H. W. and Pimental, G. C., *J. Chem. Phys.*, Vol. 29, 1958, p. 883.
3. Jacox, M. E., *J. Phys. Chem.*, Vol. 88, 1984, p. 3373-9.
4. Crawford, C. G. and Waddington, D. J., *J. Phys. Chem.*, Vol. 74, 1970, p. 2793.
5. Makovsky, A. and Gruenwald, T. B., *Trans. Faraday Soc.*, Vol. 5, 1959, p. 952.
6. Lee, E. L.; Sanbord, R. H.; and Stromberg, H. D., *Fifth Symposium (International) on Detonation*, Jacobs, S. J., Ed.; Office of Naval Research, Washington, D.C., 1970, pp. 331-337.
7. Brasch, J. W., *J. Phys. Chem.*, Vol. 84, 1980, p. 2084.
8. Engelke, R.; Earl, W. L.; and Rohlfing, C. M., *J. Chem. Phys.*, Vol. 84, 1986, pp. 142-146.
9. Piermarini, G. J.; Block, S.; and Miller, P. J., *J. Chem. Phys.*, Vol. 93, 1989, pp. 457-462.
10. Behrens, R., Office of Naval Research Workshop on Energetic Material Initiation Fundamentals, Combustion Research Facility, Sandia National Laboratories, Livermore, CA, 5-9 Dec 1988.
11. Wodtke, A. M.; Hintsa, E. J.; and Lee, Y. T., *J. Phys. Chem.*, 1986, Vol. 90, p. 3549.
12. Szabo, Z. G.; Tompler, J.; Hollos, E.; and Zapp, E. E., *Proceedings of the First European Symposium on Thermal Analysis*, Dollimore, D., Ed., University of Salford, U.K., 20-24 Sep 1976, pp. 272-277.
13. Brower, K. R., *J. Organic Chem.*, 1988, Vol. 53, pp. 3776-3779.
14. Engelke, R.; Earl, W. L.; and Rohlfing, C. M., *J. Chem. Phys.*, submitted.

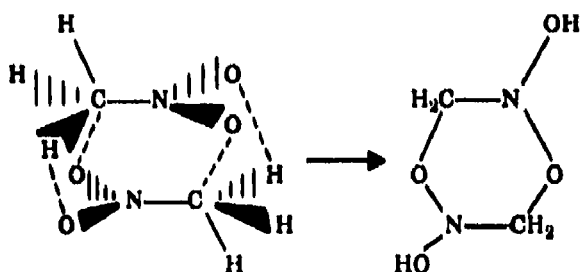
## DISCUSSION

CHARLES DICKINSON, NSWC/WO  
Silver Spring, MD

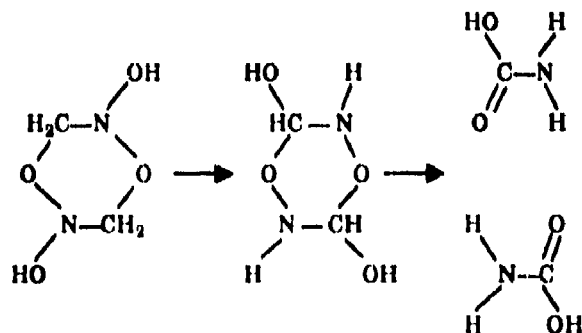
Is there a reasonable chemical pathway to obtain the ammonium formate reported as a product from nitromethane?

## REPLY BY STEPHEN F. AGNEW

I have a mechanism for formation of formyl amine, which is an isomer of nitromethane, as opposed to ammonium formate. (The analyses that have been performed on the product would not differentiate between ammonium formate and formyl amine.) First, there is a dimerization involving insertion of oxygen into the C-H bond, with concomitant migration of the hydrogen to the other oxygen of the  $\text{NO}_2$ .

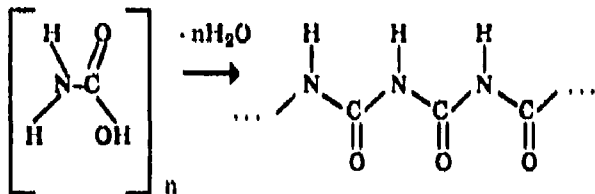


I show it here as a concerted pathway, but it could very well be multi-step. Next, the carbon must be further oxidized, and I suggest that one possible mechanism is one in which the carbon is again oxidized, while the nitrogen is reduced to an amine.



Thus, we end up with the mass-balanced isomerization of nitromethane to formyl amine.

This process will be thermodynamically favored, since the carbon oxidation and nitrogen reduction are the driving forces for nitromethane's decomposition. This molecule is not, however, known to be stable. It would be the simplest amino acid if it were. I suggest that a condensation polymerization that forms various oligomers is very likely as



## DISCUSSION

**STEVEN F. RICE**  
Lawrence Livermore National  
Laboratory  
Livermore, CA 94550

I have noticed in experiments similar to yours, without nearly your detail, that

continued heating of nitromethane eventually produces a colored reddish and then black deposit. Have you observed this and could you comment as to what may be happening here?

## REPLY BY STEPHEN F. AGNEW

As I noted in my talk, there are at least three very different product distributions, which I attribute to at least three separate pathways. The one that I believe that you are referring to involves the formation of formyl amine and its condensation analogs. I have observed reddish and black products, and believe that the reddish color is due in part to the nitroxalates that are formed upon attack of the oxygen on the carbon. I also expect that there will be significant nitronate formation (i.e., reduction of the carbon) to form  $\text{Y}_2\text{C}=\text{NOO}^-$ , species of which are known to polymerize. The corresponding oligomers should range from red to black.

# DECOMPOSITION MECHANISMS AND CHEMICAL SENSITIZATION IN NITRO, NITRAMINE, AND NITRATE EXPLOSIVES

M. D. Cook and P. J. Haskins

Royal Armament Research and Development Establishment  
Fort Halstead, Sevenoaks, Kent TN14 7BP, UNITED KINGDOM

*In this paper we report the results of ab-initio molecular orbital calculations on C-N bond scission in nitromethane, and on the influence of an ammonia molecule on this mode of decomposition. Similar, but more preliminary, results are given for methyl nitramine and methyl nitrate. These calculations are discussed in conjunction with the results of some recent experiments, and a new mechanism for the amine sensitization of nitro compounds is proposed.*

## INTRODUCTION

The chemistry involved in initiation and detonation of energetic materials has become a rapidly growing field of interest over the last few years. A number of decomposition schemes have been suggested for some explosives, but conclusive evidence to support these predictions has not been forthcoming to date. This is not surprising in view of the considerable experimental obstacles to studying such fast and complex reactions. Theoretical treatments are also difficult due to the complex nature of the reactants and the large number of reaction pathways that need to be considered. It is therefore necessary to proceed cautiously using all available experimental evidence to guide the theoretical predictions. In the work reported here we have adopted a joint theoretical/experimental approach in an attempt to elucidate the rate controlling step in the decomposition of a number of energetic materials. Our studies have encompassed a number of nitro, nitramine and nitrate ester explosives, with the major effort to date directed at nitro compounds (some preliminary results are given in References 1 and 2).

This study has concentrated upon the effect some compounds have on the sensitivity of various explosives. For example, nitromethane is strongly sensitized by amines. Engelke was probably the first to study such systems and recognize their significance in

understanding detonation chemistry. He realized that the sensitization of nitromethane by amines implied one of two things: either new faster chemical pathways are afforded by the action of the amines, or the pathways already in effect without the amine present are enhanced, for example, by the production of a higher concentration of a rate controlling species. Engelke<sup>3,4,5</sup> has written a number of papers in which he has reported spectroscopic and chemical studies on the sensitization of nitromethane by amines. He has attempted to explain his results in terms of the production of a new chemical species; the "aci-ion." In this paper we present new experimental and theoretical evidence to support an alternative mechanism.

## POTENTIAL ENERGY CALCULATIONS

Our theoretical studies have been based on ab-initio molecular orbital calculations performed using the Gaussian 86 code and its predecessor Gaussian 82.<sup>6</sup> All computations were carried out on a Cray 1S computer. The majority of the calculations have been carried out using a modest sized (6-31G split-valence) basis set in order to save computational time, and to ease problems of SCF convergence which were experienced with Gaussian 82. Convergence problems were negligible with Gaussian 86 and some of the more recent

calculations have been carried out using a larger (6-311G\*\*) basis set. Additional calculations have been carried out at post SCF levels using Moller-Plesset MBPT to either second (MP2) or fourth order (MP4). The MP4 calculations include single, double, triple, and quadruple excitations.

### Nitromethane

At the last conference in this series,<sup>7</sup> we reported details of some Hartree Fock calculations of the potential energy surface for unimolecular  $\text{CH}_3\text{-NO}_2$  bond scission. However, the HF approach to this problem suffers from two major defects. Firstly, the single determinant wavefunction gives a poor representation of the ground state (and distorted species on the potential surface) due to the significant singlet bi-radical character of nitro compounds.<sup>8</sup> Secondly, HF calculations are generally very poor at predicting the energetics of reactions involving rupture or formation of electron-pair bonds. It is generally found that HF dissociation energies will be too low, sometimes by as much as 50 kcal/mol.<sup>9</sup> It is also worth noting that a HF study of the potential energy surface for this reaction (obtained by systematically increasing the C-N bond and re-optimizing the remainder of the geometry) would suggest  $\text{CH}_3^+$  and  $\text{NO}_2^-$  as the products instead of the (lower energy) neutral radicals which are formed. However, the bond dissociation energy can be obtained from HF calculations by carrying out UHF calculations on the separated product radicals. If one also makes the reasonable assumption that there will be no significant barrier to the radical back reaction then the bond dissociation and activation energies are identical. The results of such HF calculations are shown in Figure 1, the bond dissociation energy obtained being 46 kcal/mol.

Clearly the HF approach is inadequate, and it is well-known that corrections for electron correlation are necessary to satisfactorily describe systems of this type. We have therefore repeated our early calculations on the unimolecular  $\text{CH}_3\text{-NO}_2$  decomposition at both the MP2 and MP4 levels of accuracy using the HF optimized geometry and a 6-311G\*\* basis set. The potential energy

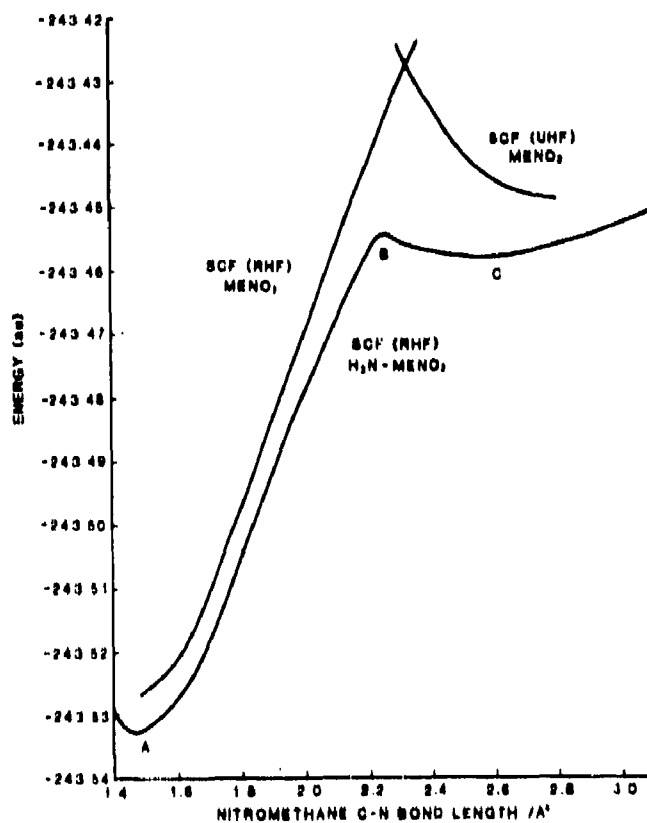


Figure 1. HF Calculations on Nitromethane and an Ammonia - Nitromethane Complex

surfaces derived by both methods are shown in Figure 2. The MP4 surface is a smooth curve from the ground state of the molecule to the final radical products  $\cdot\text{CH}_3$  and  $\cdot\text{NO}_2$ , and even predicts a small Van der Waals attraction between the radicals at around 3.2 Å. The bond dissociation energy obtained from the MP4 calculation is 65.6 kcal/mol which compares reasonably well with the experimental value of 60.3 kcal/mol, particularly when one considers that the geometries were optimized at the HF (as opposed to MP4) level to reduce computational time. The MP2 calculations give a very similar bond dissociation energy (67.1 kcal/mol) but like the HF approach predict an incorrect dissociation to  $\text{CH}_3^+$  and  $\text{NO}_2^-$ .

To ascertain if a smaller basis set would still give reasonable dissociation energies, the ground state and radical product energies were recalculated at the MP4 and MP2 levels with a 6-31G basis. Those yielded dissociation energies of 68.1 and 66.7 kcal/mol for the MP2 and

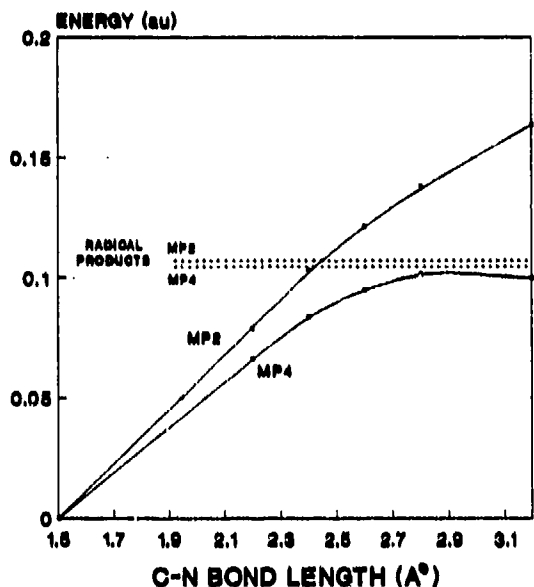


Figure 2. MP2 and MP4 Calculations on Nitromethane

MP4 calculations respectively. On the basis of these satisfactory values it was decided to carry out the calculations, reported later, on the ammonia/nitromethane complex with a 6-31G basis. In addition, we have carried out full MP2/6-31G optimizations of the ground state and final products. This more refined approach lowered the dissociation energy to 57 kcal/mol.

#### Amine/Nitromethane Calculations

We have recently described<sup>1</sup> some preliminary calculations on the interaction of an ammonia molecule with a nitromethane molecule. This work was carried out in order to study the sensitization effect that amines have on nitromethane, and hopefully, aid us in understanding the decomposition of pure nitromethane. In our calculations an ammonia molecule was used as a model amine to reduce computational time. Full geometry optimizations were carried out on a number of orientations. These included structures where the ammonia nitrogen atom was aligned along the C-H and C-N bonds of the nitromethane molecule. In addition a ring structure was studied in which the ammonia nitrogen atom was adjacent to a hydrogen atom on the

nitromethane methyl group, while a hydrogen atom on the ammonia molecule was adjacent to an oxygen atom. The interaction of the ammonia hydrogens with the nitromethane oxygen atoms was also examined. Full geometry optimizations on these structures at the RHF/6-31G level indicated that the ammonia was hydrogen bonded to the nitromethane molecule in all cases. The interaction energies ranged from 4.7 kcal/mol for the ring structure to 1.0 kcal/mol for the interaction of the ammonia hydrogens with the nitromethane oxygens. The ring structure was the most energetically favored arrangement, although only by a small margin.

In a previous publication<sup>1</sup> we described HF studies of the potential energy surface for C-H bond scission of nitromethane. Identical calculations have also been performed with an ammonia molecule aligned along the nitromethane C-H bond. The results of these calculations showed that the C-H bond breaking process was not affected, the activation energies calculated, with and without an ammonia molecule present, being identical.

Recently we have carried out potential surface calculations on C-N bond scission in nitromethane with an ammonia molecule aligned along the nitromethane C-N bond. The initial calculations were at the HF/6-31G level and these gave the potential surface shown in Figure 1. The surface was generated by incrementing the C-N bond and fully optimizing the geometry at each point. It can be seen that it is markedly different from that for an isolated nitromethane molecule, which is shown in the same figure. The potential energy surface for C-N bond scission of the ammonia/nitromethane complex shows some interesting features. Firstly, the HF calculations appear to behave sensibly as the C-N bond is stretched, rising in energy initially, reaching a peak at B, then dipping to a local minimum before rising again. The regions labeled A, B, C correspond to the structures shown in Figure 3. Structure A corresponds to the ground state of the ammonia/nitromethane hydrogen bonded complex. Structure B represents the transition state, while C corresponds to the interacting species  $\{\text{CH}_3\text{NH}_3\}^+ + \text{NO}_2^-$ . The activation energy for C-N scission

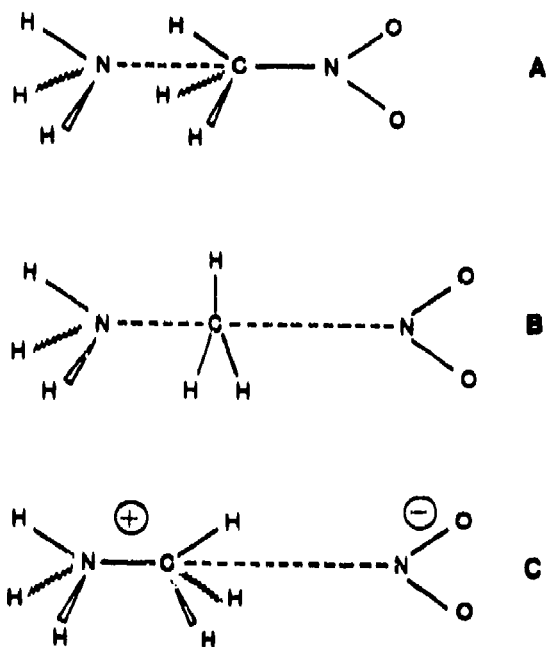


Figure 3. Illustration of Structures on the Potential Surface for an Ammonia-Nitromethane Complex

in the hydrogen bonded complex was calculated to be 50 kcal/mol.

The potential surface for C-N bond scission in the ammonia/nitromethane complex was recalculated using full geometry optimization at the MP2/6-31G level. Further

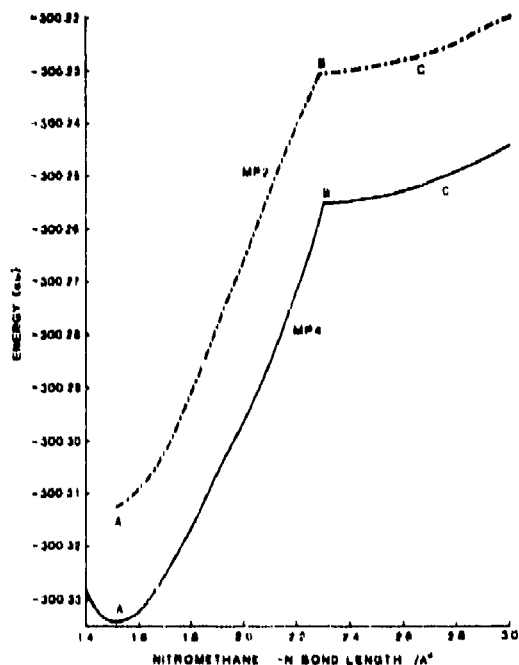


Figure 4. MP2 and MP4 Calculations on an Ammonia-Nitromethane Complex

calculations were also carried out at the MP4/6-31G level using SCF optimized geometries. Results from both these calculations are shown in Figure 4. It can be seen that although neither of these surfaces show a local minimum, they are in all other respects similar to the SCF surface shown in Figure 1. The dissociation energies are also very similar (MP2 gave 51 kcal/mol and MP4 49 kcal/mol).

Examination of the optimized geometries shows that when the C-N bond length is increased from 2.26 Å to 2.3 Å there is a sudden drop in the optimum ammonia nitrogen/nitromethane carbon distance from 2.7 Å to 1.77 Å. The methyl group inverts at the same C-N spacing. This represents the point at which the NO<sub>2</sub> group is effectively no longer bonded to the methyl group. The calculations therefore suggest that the C-N bond scission occurs abruptly at around 2.3 Å, but a well-defined transition state has not been identified to-date.

These calculations show that the presence of an ammonia molecule provides a considerably lower energy pathway for C-N bond scission in nitromethane. The MP4/6-31G calculations show a reduction in activation energy of ca. 17.7 kcal/mol. Clearly if C-N bond scission is the rate determining step in the shock decomposition of nitromethane then these calculations provide an explanation for the large increase in sensitivity upon addition of amines.

The similarity of the HF results to those at MP2 and MP4 levels for the ammonia/nitromethane complex is interesting in view of the significant differences for nitromethane alone. The different behavior of the HF solutions is probably largely due to the fact that in the complex, unlike the isolated nitromethane, the number of electron pair bonds is conserved throughout the reaction.

#### Methyl Nitrate and Methyl Nitramine

The majority of our computational effort to-date has been concentrated on nitromethane. We are, however, interested in other classes of energetic materials, the most important of these being nitramines and nitrate esters. For studies on these systems we

have chosen methyl nitramine and methyl nitrate as model compounds. We have computed potential energy surfaces for the unimolecular bond scission process leading to loss of a nitro group for both of these molecules as a comparison with the work on nitromethane. Initial calculations were again carried out at the HF/6-31G level using the same procedure as described in the section entitled "Nitromethane." The calculated bond dissociation energies were 30 and 31 kcal/mol for methyl nitrate and nitramine, respectively. We have refined these results by recalculating the energies of the ground states and the products at the MP4/6-31G level (using SCF optimized geometries). The MP4 estimates for the bond dissociation energies being 47 kcal/mol for methyl nitramine and 38 kcal/mol for methyl nitrate. These results taken with those for nitromethane are, as expected, in the order nitro > nitramine > nitrate. This ordering is consistent with the well-known trends in stability and sensitivity for these families of energetic materials.

The calculations on the interaction of ammonia with nitromethane (section "Amine/Nitromethane Calculations") suggested that ammonia (and presumably amines) sensitize nitromethane by providing a low energy pathway for C-N bond scission. To further explore this possible sensitization mechanism on explosives, some preliminary HF calculations were performed on methyl nitramine and methyl nitrate, with an ammonia molecule placed by the methyl group and aligned along the C-X bond of each molecule. The results of these calculations indicated that while these compounds formed hydrogen bonded complexes with amines the X-NO<sub>2</sub> bond strength was not affected. Consequently, provided it is assumed that X-NO<sub>2</sub> bond scission is the rate determining step in the decomposition, these preliminary results suggest that methyl nitramine and nitrate should not be sensitized by amines.

## EXPERIMENTAL STUDIES ON SENSITIZATION EFFECTS

In order to test our theoretical predictions we have carried out a number of initiation experiments using both a modified version of

the NOI large-scale gap test and also the Rotter drop weight impact test. The experimental details of these tests have been described in a previous publication.<sup>2</sup>

Using the gap test we have examined the sensitization effect of diethylene triamine on a series of nitroalkanes having progressively less readily abstractable  $\alpha$ -hydrogens. These nitroalkanes were nitromethane, nitroethane, 2-nitropropane, and 2-methyl-2-nitropropane. Gap test experiments showed that the pure nitroalkanes were all very insensitive, and with the exception of nitromethane all failed to detonate even with the donor charge in direct contact. Further gap test experiments on nitroalkane/diethylene triamine (5 percent v/v) mixtures have shown that it is increasingly difficult to sensitize them along the series. A mixture of 2-methyl-2-nitropropane and 5 percent diethylene triamine failed to detonate even with the donor charge in direct contact. It should be noted that while both nitroethane and 2-nitropropane were sensitized their shock sensitivity is still considerably less than nitromethane.

Addition of diethylene triamine to both nitromethane and nitroethane gave straw-yellow solutions; addition of the same amine to 2-nitropropane gave a thick white precipitate which, if left, evaporated. No precipitate or color change was noted when ethylene diamine was added to 2-methyl-nitropropane, and the mixture remained colorless.

In order to examine the effect of amines on a greater variety of explosives we have used the Rotter drop weight impact test which is a faster technique than the gap test, and has the added advantage of only requiring a few grams of the explosive. This test is an impact sensitiveness test, as compared with the gap test which measures the shock sensitivity of an explosive. With nitromethane the results from this test correlate well with those from the gap test experiments even to the extent that the test correctly predicts that ethylene diamine has a greater sensitization effect than diethylene triamine. Unfortunately the other nitroalkanes failed to initiate at the highest drop heights available in the Rotter machine. This is a result of the low sensitivity of these materials (even when

sensitized) combined with a relatively low maximum available drop height.

Recently we have used the Rotter test to assess the sensitizing effect of diethylene triamine on a number of crystalline explosives. The detailed results of these tests have been reported elsewhere,<sup>10</sup> but we summarize the main points here as they provide additional support for our proposed sensitization mechanism. The first crystalline explosive we studied in the Rotter test was 2,4,6-trinitrotoluene (TNT). This showed a marked sensitization effect on addition of ca. 5 percent diethylene triamine. The TNT was also observed to change color from pale yellow to dark purple on addition of the amine. This is indicative of a charge transfer or Meisenheimer type complex.

In view of Engelke's hypothesis<sup>3,4,5</sup> that the aci-ion is the important species in the sensitization of nitro compounds by amines we decided to use the Rotter test to investigate sensitization in 1,3,5-trinitrobenzene (TNB). TNB cannot form a resonance stabilized aci-quinone form (as TNT can), hence the aci-ion theory would not predict a sensitization effect in TNB. The results of the Rotter sensitization experiment on the TNB showed not only that it was indeed sensitized, but that the sensitization was of the same magnitude as with TNT. TNB also underwent the same color change as TNT on addition of the amine.

We have also carried out Rotter tests on RDX and PETN, both pure and with 5 percent diethylene triamine. For both these explosives no sensitization effect was observed. This is consistent with our tentative hypothesis concerning nitramines and nitrates (section "Methyl Nitrate and Methyl Nitramine").

## DISCUSSION AND CONCLUSIONS

The results presented in the section entitled "Nitromethane" on the unimolecular C-N bond scission in nitromethane are a good illustration of the inadequacy of HF calculations to realistically model such reactions. Although this has been remarked upon by other workers it is probably less well-known that MP2 calculations also fail to predict the correct dissociation. MP2 does, however, give a

good estimate of the dissociation energy. MP4 on the other hand, appears to adequately describe the whole potential surface and gives similar dissociation energies with both 6-31G and 6-311G\*\* basis sets.

Comparison of the activation energy required for C-N bond scission in an isolated nitromethane molecule and in the ammonia/nitromethane complex shows a dramatic difference. The MP4/6-31G calculations show that the presence of the ammonia molecule appears to lower the activation energy by ca. 27 percent. This new low energy pathway is primarily the result of a bimolecular process in which a new bond is created, to form a protonated methylamine molecule, as the nitromethane C-N bond is broken. To date we have only examined this reaction in a geometry where the ammonia nitrogen is aligned along the nitromethane C-N bond. It is quite possible that other geometries, particularly the ring type (mentioned in the section entitled "Amine/Nitromethane Calculations"), may provide even lower energy pathways.

The chemistry that occurs in the ammonia/nitromethane reaction after the nitromethane C-N bond is essentially broken (i.e., greater than 2.3 Å°) has not yet been investigated. De-protonation of the  $(\text{CH}_3\text{NH}_2)^+$  species may well occur at an early stage and may even be part of a concerted reaction in some orientations. The potential surfaces beyond 2.3 Å°, shown in Figures 1 and 4, reflect certain geometry constraints which were imposed. These constraints were convenient for studying the initial reaction but prevent us drawing any firm conclusions as to the subsequent chemistry. It is our intention to investigate further reactions in the near future.

The hydrogen bonding between the ammonia and the nitromethane may be significant in two contexts. Firstly, it might, in the bulk material, help to ensure a favorable orientation for the subsequent bimolecular reaction. Secondly, it is possible that the hydrogen bonding has a direct influence on the strength of the nitromethane C-N bond. In a recent paper Fliszar et al<sup>11</sup> gave a theoretical basis for weak interactions involving the "exterior" of a molecule (e.g. hydrogen bonds)

having a marked effect on "interior" bonds in a molecule. They note that although the former bonds may be relatively weak, any charge imbalance resulting from their formation is capable of inducing significant modifications in the "interior" of the bonded partners and thus can affect their reactivity. This is possible because for a reaction involving a bond scission process the product radicals will be electro-neutral whereas the same individual moieties in the reactant will probably not be. Thus to describe the dissociation energy, a term which accounts for the neutralization of one fragment (e.g.,  $\text{CH}_3$ ) by the other ( $\text{NO}_2$ ) must be included. Examination of the calculated charges in nitromethane and in the nitromethane/ammonia complex shows that the polarity of the C-N bond is reduced upon formation of the complex. It might therefore be argued that the interaction will have weakened the C-N bond. How important this aspect is relative to the bimolecular reaction discussed above is not yet clear.

The theory that we have proposed regarding the sensitization of nitromethane would also be expected to apply to other alkyl nitro compounds. It is also conceivable that aromatic nitro compounds may be sensitized by a similar mechanism. To back up our theoretical predictions we have performed a number of experiments to study the sensitization effects of amines on a variety of explosives. Rotter drop weight impact experiments on sensitized nitromethane were found to be in accordance with gap test sensitization experiments. Further experiments on sensitized TNT and TNB showed that these compounds were not only sensitized, but to the same extent. The TNB result is very significant since, while it can be argued that an aci-quinone form could be responsible for the sensitization of TNT, the same reasoning cannot be applied to TNB. This is because, unlike TNT, TNB has no alkyl groups and it is energetically unfavorable for a ring hydrogen to be abstracted to form an aci-ion type structure. The only explanation for the observed experimental results is for both TNT and TNB to be sensitized by the same mechanism, which negates the aci-ion theory for aromatics. In view of the color change which takes place when amines are added to these

nitroaromatics it seems likely that a complex may be formed. We intend to address the structure of these aromatic complexes in the near future.

Calculations on two model explosives suggested that neither nitramines nor nitrate esters should be sensitized by amines since the X- $\text{NO}_2$  bonds are not weakened by the interaction. This is of course true only if it is assumed that the first step involves cleavage of the X- $\text{NO}_2$  bond. The results from Rotter experiments appear to be consistent with this hypothesis although only one nitramine and one nitrate have been tested to date.

The calculations that we have presented in this paper suggest a new mechanism for the chemical sensitization of nitro compounds by amines. The mechanism proposed is consistent with the evidence from sensitization experiments. Considerably more work is needed to understand the details of the reactions suggested here, particularly for the nitroaromatics.

## REFERENCES

1. Cook, M. D. and Haskins, P. J., "Decomposition of Nitromethane: A Critical Study of the Initial Steps," *12th International Pyrotechnic Seminar*, Juan-Les Pins, 1987, pp. 43-48.
2. Cook, M. D. and Haskins, P. J., "Chemical Sensitization of Nitro Compounds," *19th International Annual Conference of ICT*, Karlsruhe, FRG, 1988, pp. 85.1-85.8.
3. Engelke, R.; Earl, W. L.; and Rohlfsing, C. M., "Production of the Nitromethane Aci-Ion by UV Irradiation: Its Effect on Detonation Sensitivity," *J. Phys. Chem.*, 90, (4), 1986, p. 545.
4. Engelke, R.; Earl, W. L.; and Rohlfsing, C. M., "The Importance of Enolate Anions in the High Pressure Kinetics of Nitroalkanes and Nitroaromatics," *Int. J. Chem. Kinet.*, 18, 1986, p. 1205.
5. Engelke, R.; Earl, W. L.; and Rohlfsing, C. M., "Microscopic Evidence that the Nitromethane Aci-Ion is a Rate Controlling Species in the Detonation of

Liquid Nitromethane," *J. Chem. Phys.*, 84, (1), 1986, p. 142.

6. *Gaussian 86*, Carnegie-Mellon Quantum Chemistry Publishing Unit, Pittsburgh, PA, 1984.
7. Haskins, P. J. and Cook, M. D., "Quantum Chemical Studies of Energetic Materials," *Proceedings of the Eighth Symposium (International) on Detonation*, Albuquerque, NM, USA, 1985, pp. 827-838.
8. Kleier, D. A. and Lipton, M. A., "The Electronic Structure of Nitro Compounds," *J. Mol. Struct.*, Vol. 109, 1984, p. 39.
9. Pople, J. A.; Binkley, J. S.; and Seeger, R., "Theoretical Models Incorporating Electron Correlation," *Int. J. Quantum Chem.*, Vol. 10, 1976, p. 1.
10. Cook, M. D. and Haskins, P. J., "Chemical Sensitization of Secondary Explosives," *Fourth International Conference of the Groupe de Travail de Pyrotechnie*, in press, 1989.
11. Fliszar, S. and Minchino, C., "Bond Energies and Bond Dissociation Energies," *Approches Microscopique et Macroscopique des Detonations, Megeve Palais des Congres (France)*, *Journal De Physique*, 48, (C4), 1987, pp. 367-375.

©Controller HMSO, London, 1989.

## DISCUSSION

HORST ADOLPH  
Naval Surface Warfare Center  
Silver Spring, MD

1. It may be true that the addition of ammonia does not affect  $E_{Act}$  for C-H bond breaking, but it should affect the equilibrium concentration of aci-anion and this could be the cause of sensitization.
2. What is the evidence for charge transfer when diethylenetriamine is added

to TNT? I believe the TNT anion is colored also, and so are Meisenheimer complexes. TNB can react differently with amines than TNT. Just because there is a similar color change does not mean that there is the same reaction; that is not sufficient evidence.

3. There is substantial literature on amine interactions with nitroaromatics. It might be helpful to consult this literature.

## REPLY BY MALCOLM COOK

1. Addition of ammonia will increase the concentration of aci-ions that is not disputed. However, no one yet has explained how the aci-ions could actually cause sensitization of nitromethane, whereas the alternative explanation outlined in the paper does.
2. It is true that the TNT anion, as well as the Meisenheimer complexes, are colored. The term charge transfer complex was used as a general term to cover a range of possibilities. The actual form of the complex is not known. The important point which was highlighted in the paper was that both TNT and TNB have been shown to exhibit identical sensitization effects as measured in the Rotter Drop Weight Impact Test. The conclusion that both are sensitized by the same mechanism is, therefore, not based on the color change alone. Indeed, the very fact that TNB can be sensitized by amines, yet cannot form any significant quantity of aci-ions (as it has no easily abstractable hydrogens) implies that the formation of aci-ions are not important to the sensitization effect.
3. The authors are well aware and have consulted the substantial literature on the interactions of amines with nitroaromatics.

## DISCUSSION

P. R. BOLDUC  
USAF/MSD/AFATL/MNE  
Eglin AFB, FL 32542-5434

Nitronate ions are often implicated as the "bad actors" in nitroalkanes sensitivity. It seems to me that an acid-base reaction of the ammonia with the nitronic acid (aka aci) form (which is some 6 pk units or so more acidic than the nitro form) would be a more straight forward explanation. Couldn't the amine sensitization be just a special case of general base catalysis?

### REPLY BY MALCOLM COOK

I refer back to my answer given to the last question. I do not dispute that addition of ammonia will increase the concentration of aci-ions, but the question arises how the aci-ions could actually cause sensitization of nitromethane. This has not been explained. Furthermore, if aci-ions were responsible for the sensitization effect increasing amine concentration should lead to further sensitization whereas, 5% v/v amine/nitromethane appears to give the maximum effect. However, probably the most important experimental evidence against the aci-ion theory is that both TNT and TNB have been shown to exhibit identical sensitization effects as measured in the Rotter Drop Weight Impact Test. The very fact that TNB can be sensitized by amines yet cannot form any significant quantity of aci-ions (as it has no easily abstractable hydrogens) implies that the formation of aci-ions are not important to the sensitization effect.

## DISCUSSION

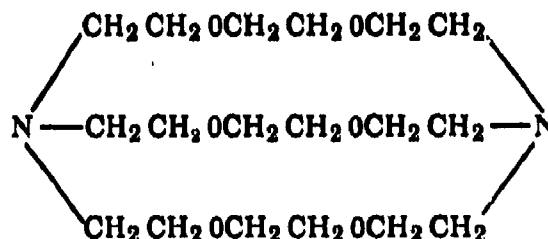
JAEQUES BOILEAU  
SNPE  
Paris, France

1. I had prepared a complex TNT-ammonia through a reaction in totally anhydrous medium, but I did not have the apparatus to

study the structure-description in Memorial des Loudres in the year 1950.

2. How do you explain through a cycle the sensitization of  $\text{CH}_3\text{NO}_2$  by a tertiary amine such as  $\text{NE} + \text{s}$ ?

3. It would be interesting to verify if crystals can sensitize nitromethane: formula of cryptand 2-2-2



(The cage has a known geometrical form and can trap the cations.) Is the nitromethane desensitized by cryptand 2-2-2 after sensitization by NaOH by trapping  $\text{Na}^+$ , the cation  $\text{CH}_2\text{NO}_2$  complexed by the 2-2-2 cryptand?

### REPLY BY MALCOLM COOK

The sensitization of amines by tertiary amines (e.g., triethylamine) has been observed, although I have not personally verified this. The sensitization effect can be explained in exactly the same way as with ammonia. Although I described a cyclic complex structure for nitromethane/ammonia, linear and non-linear structures are similar in energy. The important interaction occurs through the amine nitrogen and the nitromethane methyl group.

As far as cryptand 2-2-2 as a sensitizing agent for nitromethane is concerned, I would have thought that it would indeed sensitize nitromethane provided that it was soluble enough. We have not carried out any experiments with cryptand 2-2-2, but if desensitization were to occur following sensitization by NaOH it could be explained simply by a competition between formation of the nitromethane cryptand 2-2-2 complex and reaction of NaOH with the cryptand 2-2-2.

## DISCUSSION

**C. P. CONSTANTINOU**  
Cavendish Physics Laboratory  
Cambridge, England

In some of your NM experiments you are getting sensitization with NaOH - a smaller effect than with amines but nevertheless there. Would you say that an acid-based sensitization mechanism is also operative but less effectively?

## REPLY BY MALCOLM COOK

It is always possible that an acid-base sensitization leading to a more reactive species is responsible, but less effective. However, addition of H<sub>2</sub>O to nitromethane is an exothermic reaction probably due to the presence of water. Thus the nitromethane was hotter in these experiments than usual and this could increase the likelihood of physical processes playing a part.

# DECOMPOSITION OF ENERGETIC MATERIALS ON THE DROP-WEIGHT-IMPACT MACHINE

Gregory A. Buntain, Theodore L. McKinney,  
Thomas Rivera, and Gene W. Taylor  
Los Alamos National Laboratory, University of California  
Los Alamos, New Mexico 87545

*The drop-weight-impact test is heavily relied upon for initial characterization of limited amounts of new energetic materials. The mechanisms for reaction of energetic materials on the drop-weight machine are largely unknown. Partly as a consequence of this lack of understanding, results obtained on the drop-weight machine are often misleading and inconsistent. We are investigating decomposition of explosives on the drop-weight machine using radiometric and spectroscopic methods. Initial radiometric results reveal consistent, sequential emissions for specific impacted explosives that may correspond to time-resolved chemical reactions. A method to quantify the extent of an impact-induced reaction using radiography is discussed. Limited results have also been obtained using time-resolved spectroscopy.*

## INTRODUCTION

The drop-weight-impact test is one of the cornerstones of explosive sensitivity testing. Despite widespread use, however, numerous problems detract from the reliability of the test. These problems have inspired work at this Laboratory directed towards better understanding the principles of the drop-weight-impact test as well as the decomposition chemistry of impacted explosives. Work in this vein is being conducted by radiometric and spectroscopic examination of impacted energetic materials.

The drop-weight-impact test is one of the methods most relied upon for initial characterization of high-explosives (HE) sensitivity. This does not bespeak of superior results provided by the impact test but, rather a lack of better results obtained by other methods with limited amounts of materials and a limited investment of time and effort. Other preliminary sensitivity tests include the minimum-priming, friction, spark, and small- and large-scale gap tests.<sup>1</sup> Subsequent large-scale tests include the Susan, spigot, skid,

bullet, high-speed machining, and heavily confined heating tests.<sup>2</sup> While all of these tests provide valuable information regarding explosive sensitivity, all require far greater amounts of material and effort than does the impact test. Because of the pivotal role the drop-weight-impact test plays in explosive sensitivity testing, one might expect the test to be well characterized and defined. Unfortunately, this is not the case. For a given set of explosives, the ranking of sensitivity predicted by the impact test is often different from that predicted by other tests.<sup>1</sup> Indeed, even correlation between different drop-weight-impact machines seems to be the exception rather than the rule. For example, Table 1 lists H<sub>50</sub> values (that height from which a falling weight causes explosive reaction 50 percent of the time) for some common explosives tested at Lawrence Livermore National Laboratory (LLNL) and Los Alamos National Laboratory (LANL). The use of a 5-kg weight at LLNL compared to a 2.5-kg weight used at LANL should dictate drop height ratios of approximately 1:2. Obviously, this is not the case. The British impact-sensitivity test, or Rotter Test,

*Table 1. Comparison of  $H_{50}$  Values (CM)  
Published at LANL and LLNL*

	LLNL (5.0 kg)	LANL (2.5 kg)	Ratio
FEFO	28	60	2.1
TNT	80	148	1.9
PETN	11	14	1.3
Baratol	95	110	1.2
PBX 9501	44	48	1.1
RDX	28	28	1.0
HMX	33	32	0.97
Octol	41	38	0.93
DIPAM	95	85	0.89

gives yet a different set of results.<sup>3</sup> Problems of reproducibility are further aggravated by a lack of protocol for sample preparation at different laboratories. Particle size, percent voids, sample handling, etc. are all variables that profoundly affect explosive sensitivity yet are not addressed when reporting  $H_{50}$  values. This degree of uncertainty in a test as crucial as the drop-weight-impact test is disturbing. Thus, efforts have been made in this Laboratory and others<sup>4,5,6,7</sup> to better understand the chemistry occurring on the impact machine. While some progress has been made, the problem is far from resolved.

## CURRENT RESEARCH

Efforts at Los Alamos have centered on utilizing light emission from impacted energetic materials in an attempt to better understand the decomposition chemistry occurring on the drop-weight-impact machine. These efforts can be divided into two parts: time-resolved radiometry and time-resolved emission spectroscopy.

## RADIOMETRY

### Equipment

In the course of radiometric work conducted with the drop-weight-impact machine, the relationship between drop height and temporally resolved light emission was examined. The experimental apparatus for

this study (Figure 1) consists of a modified drop-weight machine with a specially designed anvil (Figure 2) to allow light transmission via a fiber-optic bundle to an RCA 8850 photomultiplier tube (PMT). The PMT signal is amplified by an Ortec 9301 fast preamplifier and an Ortec 9302 amplifier/discriminator. The amplified analog signal is stored and processed on a Nicolet 4562 oscilloscope. Signal plotting is accomplished with an Apple Macintosh computer, while integration is done with a Hewlett Packard 3390A recorder/integrator.

In a typical experiment, 30-mg samples of explosive powder are placed on the sapphire window of the anvil. The weight is dropped from varying heights and the resulting light signal recorded on the oscilloscope. The duration of light emission is typically between 70 and 90 microseconds. Representative signal traces are shown in Figure 3.

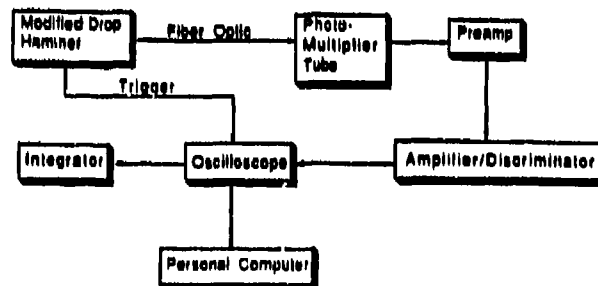


*Figure 1. Experimental Apparatus for Radiometry*

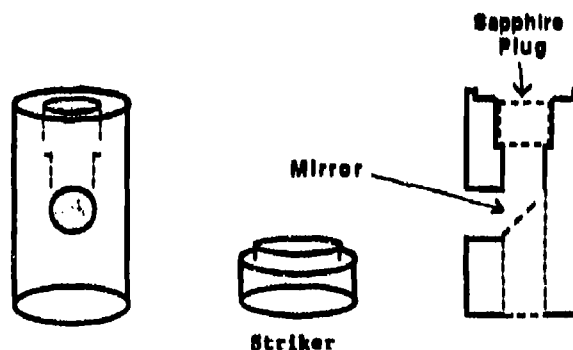


*Figure 2. Modified Experimental Anvil*

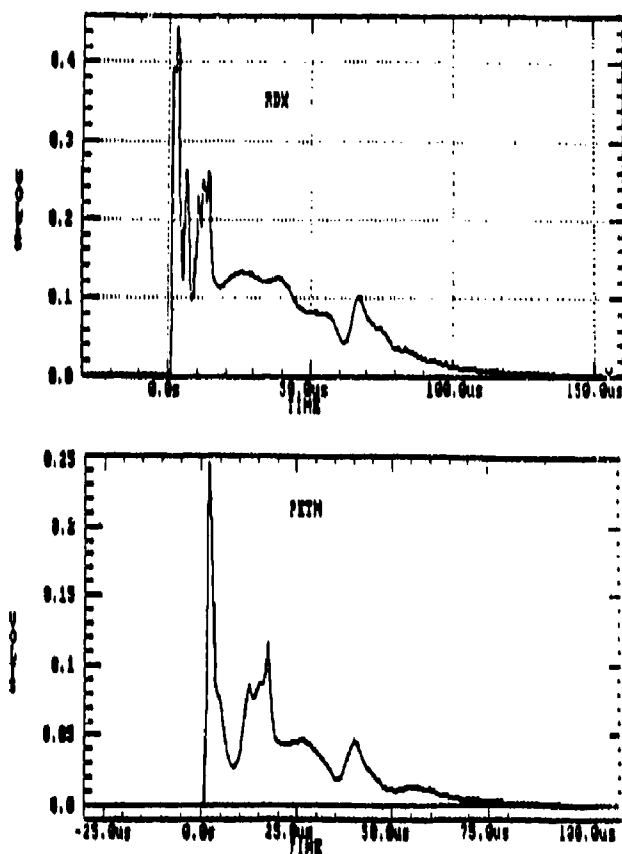


Figure 3. Time Resolved Emission from Impacted Explosives

### Results

In the case of full "goes," a consistently shaped light trace was obtained for each explosive examined to date. The fact that light emissions from different explosives show characteristic and consistent features implies that unique, sequential chemical reactions are occurring and are being resolved temporally. Using filters, this light can be broken down into ultraviolet (UV), visible (VIS), and infrared (IR) components. UV light occurs early and is of short duration, while visible and IR components are present throughout the emission. Occasionally, duplicate, yet virtually identical traces are obtained, indicating perhaps that two separate hot spots are forming displaced in time and propagating independently. The consistency in emission characteristics fails when samples are only partially consumed and essentially no light is generated by "no-goes."

Early radiometry results indicated the quantity of light produced by an impacted explosive varied as a function of impact height. Thus, total emission seems to be an intrinsic indicator of the extent of chemical decomposition. A set of explosives extensively used at Los Alamos was subjected to impact from a 3-kg weight on a modified drop-weight-impact machine and the total integrated light emission recorded. A plot of averaged total light emission for PETN, in arbitrary units, versus drop height is shown in Figure 4. At least five drops were made at each height. "No-goes" were obtained along with "goes" at the lowest drop heights. In these cases a value of zero light emission was averaged into the emission obtained from "goes." Apparently, drop heights above some threshold value provide sufficient energy for propagation of the decomposition reaction and are characterized by a more-or-less consistent amount of emission. At lower drop heights, a break occurs where light produced by the explosive begins to drop off rapidly with decreasing drop height. This is probably indicative of insufficient impact energy to guarantee propagation of the decomposition reaction to the point of sample consumption. Eventually a point is reached where no sample reaction occurs and no light signal is obtained within the number of experimental trials performed. Statistically, if the number of drops from very low heights were increased, a reaction with accompanying light would eventually be obtained, but experimental practicality limits the number of drops that are reasonable.

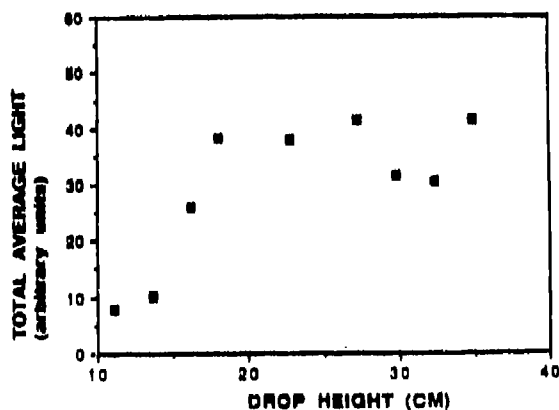


Figure 4. Plot of Drop Height Vs. Average of Total Integrated Light from Impacted PETN

These results are consistent with high-speed photography work done by J. E. Field where it is possible to see hot spots form and die out in impacted secondary explosives.<sup>4</sup> At low drop heights, hot spots quickly die out, thus decreasing the amount of light signal detected.

## Conclusion

We believe that light emission from energetic materials might offer an alternative method for quantifying sample decomposition on the drop-weight machine. While this method is probably not practically suited to replace the electronic ear now used, it does offer supplemental information regarding explosive behavior on the drop-weight machine and does not suffer from some of the limitations imposed by the current method. For example, this method would be far less sensitive to operator and equipment-related inconsistencies associated with the electronic ear. In the radiometric method, long-term equipment fluctuations such as a loss of sensitivity in the PMT, would be characterized by shifts of the integrated light curve up and down without affecting the point where the curve breaks. Long-term fluctuations in the sensitivity of the electronic ear currently in use can allow misleading  $H_{50}$  values to be published. Furthermore, impact characterization of propellants, which occasionally do not "pop" on the impact machine because of their slow rate of reaction, might be improved. Before conclusions can be drawn regarding the practicality of this method of characterization; however, more work must be done to assure test predictions are in agreement with historical knowledge regarding sensitivities of common energetic materials.

## SPECTROSCOPY

In addition to examining radiometry from impacted explosives, attempts were made to identify the molecular species responsible for emission. Previous work in this area involved examination of IR emission, but few questions were resolved.<sup>5</sup> The mechanism whereby an impacted explosive goes from reactant to products is largely unknown. The light emitted during that process offers one of the

few practical means of exploring this chemical discontinuity. Radiometry work has suggested that emissions from sequential chemical reactions occurring during explosive impact can be temporally resolved. This suggests that emission spectra obtained at different times after impact might permit identification of unique chemical species associated with different stages of decomposition. If time-resolved chemical emissions can be identified, some mechanistic insight regarding impact-induced decomposition might be obtained.

## Equipment

The experimental apparatus used in this study is described in Figure 5. A bifurcated, fused-silica fiber-optic bundle is used to connect the drop-hammer apparatus with a 0.25-m Jarrel Ash spectrometer and a PMT. The PMT-amplifier/discriminator section, already described, is used to provide a trigger for a Tracor Northern TN6500 optical multi-channel analyzer (OMA) and TN6143 vidicon-array detector. By utilizing a TN6130-1 pulse amplifier/driver, it is possible to gate the detector on and off to obtain spectra down to 150 nanoseconds pulse width. By varying the delay between first emission and fast spectrum acquisition, it is possible to obtain time-resolved emission spectra.

A large variety of explosives were examined on the drop hammer, including HMX, RDX, TATB, NTO, TNT, tetryl, HNS, 4-nitro-1-picryl-1,2,3-triazole, sulfur nitride, and PETN. Less sensitive explosives that would

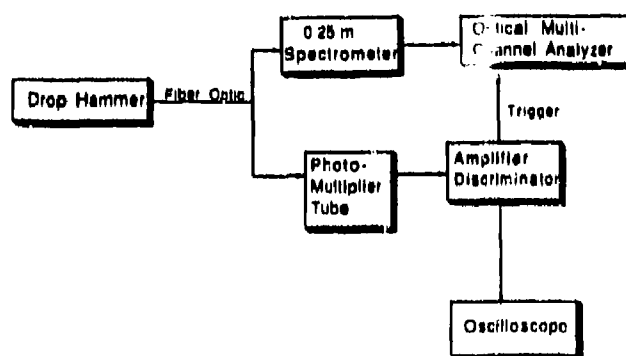


Figure 5. Experimental Apparatus for Spectroscopy

not react on the experimental drop hammer under normal conditions were initiated using a slapper accessory in conjunction with the modified anvil already described. This slapper accessory consists of a hardened steel piece that attaches to the anvil and locates a 2-mm hole directly over the sapphire window. A flyer from a Kapton sheet placed over the hole is driven into the explosive under investigation by the primary explosive sulfur nitride that is resting on top of the Kapton and initiated by impact. Barrel length is approximately 5-mm.

## Results

Attempts to obtain emission spectra from impacted explosives have met with limited success. The light obtained from all the explosives examined is largely black body in nature with a few areas of exception.

Most of the explosives investigated exhibit a strong emission in the vicinity of 5899Å (Figure 6). Sodium emission has been identified frequently by other workers examining light from detonating explosives and, consequently, this feature was initially attributed to the strong sodium lines occurring at 5890Å and 5896Å.<sup>8</sup> Further experimentation, however, indicated sodium an unlikely source for this emission feature.

Spectra obtained from a sodium source show a sharp, unresolved doublet with a

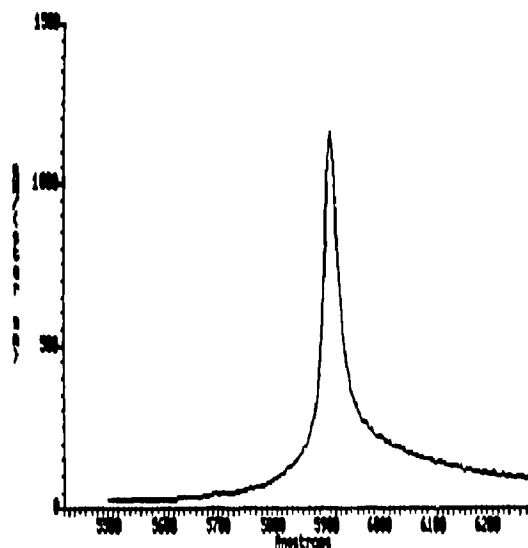


Figure 6. Emission from Impacted PETN

maximum consistently at 5890 ± 1Å. The emission from impacted explosives samples maximized between 5896Å and 5970Å although 5899Å was typical. The shape and intensity of this peak proved to be a function of time after impact. For example, impacted PETN samples first exhibit the 5899Å band 40 microseconds after first light, with maximum intensity occurring after 70 microseconds. All the samples exhibiting a 5899Å emission did so at late time relative to first light. When the samples were slapper initiated, however, prompt initiation eradicated time dependence of the 5899Å emission.

Only carbon containing explosives show emission at 5899Å, although not every carbon containing explosive emits in this region (for example, 4-nitro-1-picryl-1,2,3-triazole). The non-carbon containing explosive, sulfur nitride, does not emit in this region even when doped with sodium salts. Furthermore, intimate mixing of strong oxidizers such as  $\text{KMnO}_4$  or Oxone<sup>TM</sup> (Aldrich) drastically reduce or eliminate the peak in question. NTO emits strongly at 5899Å, yet the sodium and potassium salts of NTO show no emission above black body in this area.

Thus, the source of emission in the 5899Å region in impacted explosives is probably not sodium. Positive identification of the emission source from the present data is impossible. The peak position does correspond closely with a high pressure  $\text{C}_2^*$  (6,8) emission attributed to carbon radical recombination, e.g.,  $[\text{C}(\text{}^3\text{P}) + \text{C}(\text{}^3\text{P}) \rightarrow \text{C}_2^*(\text{d}^3\text{ng})]$ . If the emission source were  $\text{C}_2^*$ , this would help explain the effect of strong oxidizers on the peak intensity. Other investigators have identified  $\text{C}_2^*$  emission from detonating explosives, but have identified numerous peaks in a band system rather than a single emission.<sup>9,10</sup> Why, in this instance, only the  $\text{C}_2^*$  (6,8) emission would occur is not known, but others have observed this phenomenon.<sup>11</sup>

No other molecular emissions were consistently identified. Nitramines occasionally showed a strong OH band at 3064Å, but no pattern for appearance was discerned. TNT exhibited a shoulder at 4315Å above black body radiation. A strong CH system begins at 4315Å, but no other peaks in the system were

observed, thus definitive assignment is impossible.

Emission for all the explosives examined consists of UV, VIS, and IR components. UV light is of short duration, occurring early, while VIS and IR components persist throughout the emission. In PETN, for example, UV light is detectable for the first 40 microseconds of emission, while VIS and IR light linger the entire 90 microseconds of emission.

Limited results using powdered and pelletized explosive samples promoted usage of very thin, optically transparent explosive samples. Unfortunately, this did not alter the experimental results in any positive way. It was concluded, therefore, that definitive identification of discrete molecular emissions from impacted explosives was not practically feasible.

## CONCLUSION

A thorough understanding of the chemistry occurring on the drop-weight-impact machine remains elusive. Results from this work imply that reproducible sequential chemical reactions unique to a given explosive are probably initiated by impact. Furthermore, the amount of light emitted by an impacted explosive may be used as an intrinsic indicator for extent of impact-induced reaction. Identification of specific molecular species along the reaction pathway for impact-induced explosive decomposition has not proven possible by this method. Further mechanistic work in this area is certainly warranted. At this Laboratory, research examining emission from explosives subjected to laser induced decomposition is underway in conjunction with other projects.

## REFERENCES

1. Urizar, M. J.; Peterson, S. W.; Smith, L. C., *Detonation Sensitivity Tests*, LA-7193-MS, Los Alamos National Laboratory, Los Alamos, NM, Apr 1978.
2. Dobratz, B. M. and Crawford, P. C., *LLNL Explosives Handbook, Properties of Chemical Explosives and Explosive*

*Simulants*, UCRL 52997, Lawrence Livermore National Laboratory, Livermore, CA, Jan 31, 1985, p. 9-1.

3. Smith, L. C., *Los Alamos National Laboratory Explosives Orientation Course*, LA-11010-MS, Los Alamos National Laboratory, Los Alamos, NM, Jul 1987.
4. Field, J. E.; Swallowe, G. M.; Heavens, S. N., "Ignition Mechanisms of Explosives During Mechanical Deformation," *Proc. R. Soc. Lond.*, 1982, Vol. A382, pp. 231-244.
5. Miller, P. J.; Coffey, C. S.; De Vost, V. F., *Infrared Emission Study of Deformation and Ignition of Energetic Materials*, NSWC TR 85-452, Naval Surface Weapons Center, White Oak, MD, 1985.
6. Elban, W. L.; Hoffsommer, J. C.; Coffey, C. S.; Yoo, K. C.; Rosemeier, R. G., *Microstructure Origins of Hot Spots in RDX Explosive and a Reference Inert Material*, NSWC MP 84-200, Naval Surface Weapons Center, White Oak, MD, 1984.
7. Mullay, J., "Relationships Between Impact Sensitivity and Molecular Electronic Structure," *Propellants, Explosives, Pyrotechnics*, 1987, Vol. 12, pp. 121-124.
8. Renlund, A. M. and Trott, W. M., *Spectra of Visible Emission from Detonating PETN and PBX 9407*, Sand-83-2168, Sandia National Laboratories, Albuquerque, NM, Feb 1984.
9. Dossier, L. R., Mound National Laboratory, personal communication, 1987.
10. Renlund, A. M. and Trott, W. M., "Time-Resolved Spectroscopic Studies of Detonating Heterogeneous Explosives," in *Proceedings 8th Symposium (International) on Detonation*, Jul, 15-18, 1985, pp. 691-700.
11. Davis, W. C., LLNL, personal communication, 1988.

## DISCUSSION

**STEPHEN F. AGNEW**, Los Alamos National Laboratory, Los Alamos, NM

Did you see  $N_2$  emission at 314 nm? What was the line width of the 5899Å line?

### REPLY BY G. A. BUNTAIN

No, I did not see any sign of  $N_2$  emission at 3140Å. The shape of the 5899Å emission varied as a function of detector head gate delay. Generally, the FWHM was about 500Å.

## DISCUSSION

**BARRY T. NEYEN**  
EG&G Mound Applied Tech  
Miamisburg, OH

1. How does the radiometric measurement look for explosives that do not detonate?
2. It looks like the ratio of drop weight energies for explosive initiation for the LLNL and LANL testers is closer to 1 than 2, indicating that sensitivity is a function of velocity rather than energy. Any comment on this?

### REPLY BY G. A. BUNTAIN

1. The radiometric traces for impacted explosives that did not decompose to completion were not at all reproducible. These traces tended to be characterized by isolated, free-standing light spikes as if the sample lit, but did not react to completion.

2. The ratios of published impact sensitivities between LANL (2.5 kg weight) and LLNL (5 kg weight) are indeed closer to 1 than 2. Furthermore, this holds for quite a few explosives other than those listed in Figure 1. This implies velocity may be more significant than mass in determining impact numbers. On the other hand, there is unpublished data from work done by Larry Hantel at Los Alamos, where drop-weight mass was varied while other conditions were held constant, indicating that mass has a very significant effect on impact numbers. I do not understand this inconsistency, and feel further work in the area could be productive.

## DISCUSSION

**HOWARD SHEINFELD**  
U.S. Army Foreign Science &  
Technology Center  
Charlottesville, VA

To what specific transition do you attribute the brief emission of UV in some of your tests?

### REPLY BY G. A. BUNTAIN

All of the impacted explosives give a broad, short-lived UV emission. We do not attribute this to a specific transition, but rather to a multitude of electronic transitions that cannot be discretely identified.

**SESSIONS ON**  
**SPECIAL INITIATION**

**Cochairmen: Pai Lu**  
**Army Research, Development, and Engineering**  
**Center**

**Christopher Hutchinson**  
**Atomic Weapons Establishment**

**and**

**Edward Lee**  
**Lawrence Livermore National Laboratory**

**Krishna Mohan**  
**IDL Chemicals Limited**

# BEHAVIOR OF AN UNREACTED COMPOSITE EXPLOSIVE ON LOW VELOCITY IMPACT

C. Loupiau and A. Fanget  
C. E. G. 46500 Gramat - FRANCE

*This paper demonstrates the behavior of a composite unreacted explosive under aggression by a small caliber projectile. The CEG has studied the dynamic behavior of the composite explosive: octorane 86A (composition: 16 percent Pu, 84 percent HMX). Hopkinson bar and plate impact tests were carried out on this material to fit a viscoelastic-plastic model obtained with an inert composite. This behavior model was then validated by testing its capacity to reproduce the propagation of a plane wave produced by plate impact. The range of application of this model is [0., 0.5 GPa] pressure and [ $10^2$ ,  $5 \cdot 10^4$  s<sup>-1</sup>] strain rate.*

## INTRODUCTION

Vulnerability of explosives against low velocity impact is an important part of the general vulnerability problem. To understand how an explosive can react under this kind of loading, the first step is to be able to simulate the mechanical behavior of the unreacted explosive in the appropriate range of pressure and strain rate. This problem is complicated by the composite nature of many of the explosives used. This composite nature with a large amount of polymer, usually about 10 percent, requires sophisticated behavior models. The aim of this work is to present a behavior adapted to vulnerability studies of composite explosives.

### Range of Investigations

Two-dimensional calculations were made to obtain pressure range at low velocity impact. A steel bullet with a velocity of 1000 m/s impacts the target. In this calculation, the explosive is treated as a nonreactive material with a simple Mie-Grunelisen equation of state. The Hull code was used for these calculations. Close to the axis, the maximum pressure can reach about 3 GPa. For off-axis locations, this maximum pressure drops strongly to a few GPa when the distance from the axis is greater than two or three times the diameter of the bullet. Therefore, most of the

material is submitted to pressure of a few GPa. To describe the mechanical behavior of an inert material, the study starts by making quasi-static experiments in order to obtain some basic parameters (elastic modulus, bulk modulus, etc.) and to get an idea of the form to be used (viscoelastic, viscoplastic, etc.). However, most of these experiments are not possible with an energetic material, and we have therefore been obliged to develop an inert material with the same characteristics as the explosive we are interested in. Both materials are compared in Table 1.

The inert material was used to get quasi-static information, and dynamic experiments were conducted with the explosive.

## INFORMATION FROM EXPERIMENTS ON THE INERT MATERIAL

A behavior model was first developed for the inert material of Table 1. This work was

*Table 1. Characteristics of the Two Composite Materials*

Material	Polymer	Grain	% Polymer
Explosive	PU	HMX	16
Inert	PU	KCl-Mg <sub>2</sub> SiO <sub>4</sub>	19

presented by J. Cagnoux at the DYMAT Congress in Ajaccio (September 1988). Static, quasi-static, and dynamic experiments were performed. They allowed the determination of a model adapted to these kinds of materials. The basic features of the model are:

1) A viscoelastic response expressed by:

$$\begin{aligned} \sigma'_{ij} &= 2\mu' \epsilon'_{ij} \\ \sigma'_{ij} &= \text{stress deviator} \\ \epsilon'_{ij} &= \text{strain deviator} \\ \mu' &= \text{apparent shear modulus} \end{aligned}$$

and

$$\mu' = \mu_\infty [1 + \Lambda_\mu (\bar{\epsilon})^\ell] [1 + C_\mu P]$$

with  $\mu_\infty$ ,  $\Lambda_\mu$ ,  $C_\mu$ , and  $\ell$  as material parameters, and  $\bar{\epsilon}$  as the equivalent strain rate:

$$\bar{\epsilon} = \sqrt{\frac{2}{3} \dot{\epsilon}_{ij} \dot{\epsilon}_{ij}}$$

2) A sensitivity of the yield stress  $Y$  to pressure, strain-rate, and equivalent plastic strain. This was expressed by assuming the existence of a plastic potential:

$$F = \tilde{F}(\sigma'_{ij}, \bar{\epsilon}'^P, \bar{\epsilon}, P)$$

$$\bar{\epsilon}'^P = \text{equivalent plastic strain}$$

$$\bar{\epsilon}'^P = \sqrt{\frac{2}{3} \dot{\epsilon}'^P_{ij} \dot{\epsilon}'^P_{ij}}$$

and

$$F = -\sqrt{3 J'_2} + Y_0 [1 + B \bar{\epsilon}'^P] [1 + A_y (\bar{\epsilon})^m] [1 + C_y P]$$

$Y_0$ ,  $A_y$ ,  $B$ ,  $C_y$ , and  $m$  are material parameters,  $J'_2$  is the second invariant of the stress deviator.

3) A pressure-volume relation of the form:

Loading:

$$P = K_1 \left( \frac{V_0 - V}{V} \right) + K_2 \left( \frac{V_0 - V}{V} \right)^2$$

$$+ K_3 \left( \frac{V_0 - V}{V} \right)^3$$

Unloading:

$$P = K_d \left( \frac{V_0 - V}{V} \right)$$

where  $K_1$ ,  $K_2$ ,  $K_3$ , and  $K_d$  are material parameters.

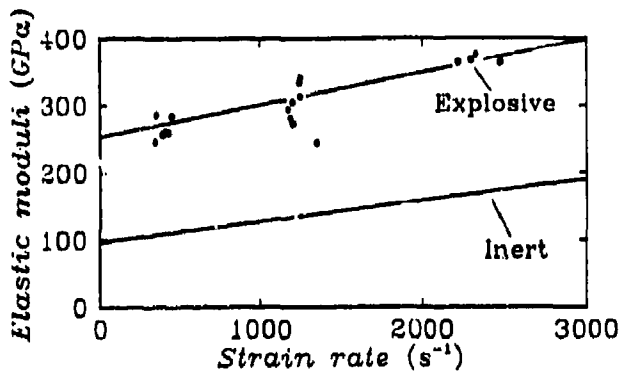
The experiments gave the value of the material parameters. The parameters obtained from static or quasi-static experiments were then used for the explosive.

## DYNAMIC EXPERIMENTS ON THE ENERGETIC MATERIAL

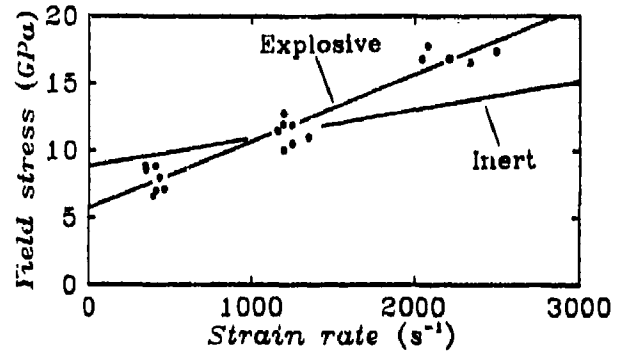
Dynamic experiments were performed in dynamic uniaxial compression (Hopkinson bar) and dynamic uniaxial strain (plate impact) on the energetic material.

For dynamic uniaxial compression using a Hopkinson bar, the results also revealed an increase in the elastic moduli and in the yield stress in relation to the strain rate (Figures 1a and 1b). As expected, the two materials of Table 1 have a similar behavior. For dynamic uniaxial strain, experiments consisted of the projection of plates onto a flat target using a compressed gas gun. A pyrex glass impactor was used to provoke instant unloading of the composite material. The signal of the dilatational wave produced by the impact was measured at the PMMA-Window interface, using a visar velocity interferometer. The particle velocity diagrams (Figures 2a and 2b) show a 33 m/s intensity precursor for shot 1031 and 21 m/s for shot 1038. The targets had a diameter of 80 mm and a thickness of 5 or 10 mm according to the test. The dynamic experiments allowed us to get specific parameters for the explosive. All parameters for the model of the explosive are given in Table 2.

The model was introduced into the Hull code and a numerical simulation was made of the dynamic uniaxial strain experiments. Comparison with the experiments is given in Figures 3a and 3b.

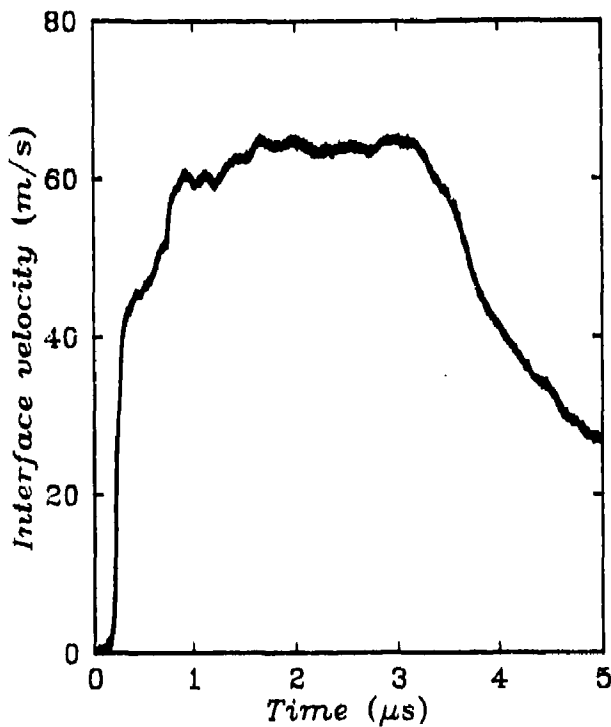


a) Apparent Elastic Moduli Vs. Strain Rate

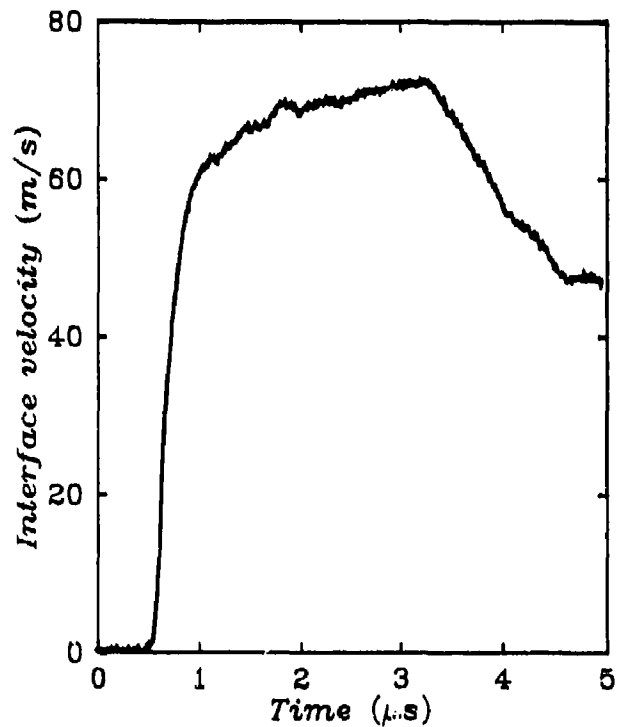


b) Linearity Limit Vs. Strain Rate

Figure 1. Yield Stress Vs. Strain Rate (Hopkinson Test)



a) Shot N° 1038,  $V_p = 78$  M/S



b) Shot N° 1031,  $V_p = 93$  M/S

Figure 2. Visar Results of Two Experiments

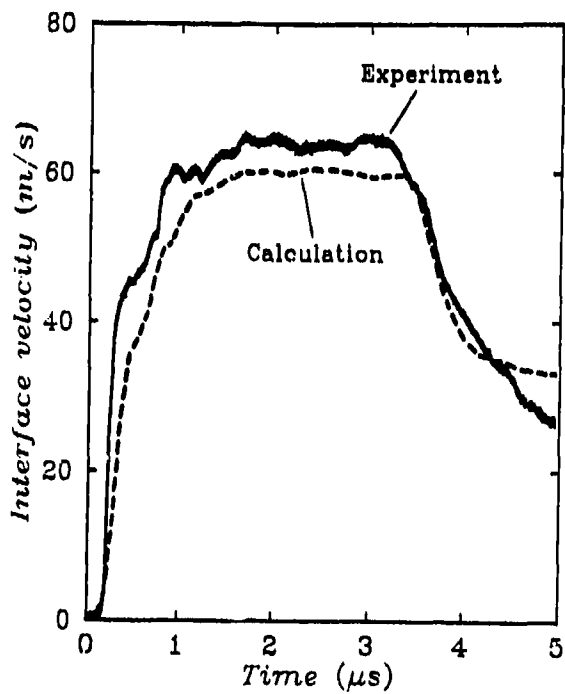
## CONCLUSIONS

We have developed a model adapted to low vulnerability problems involving composite explosives. This model is able to describe the mechanical behavior of the unreacted explosive. The extension of validity

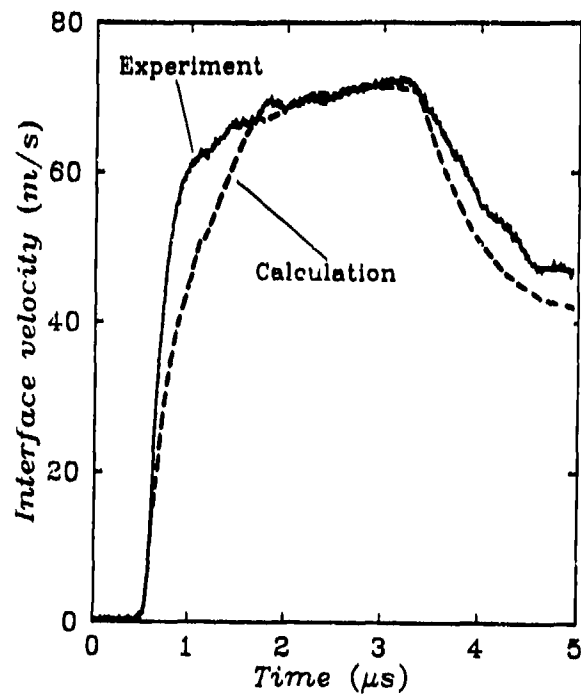
range of pressure will allow us to study its capacity to reproduce two-dimensional experiments (Figures 4a and 4b). A study of the damage (Figures 5a and 5b) to these kinds of materials has also been undertaken. We hope that this research will lead us to a better comprehension of an explosive's response to a low

Table 2. Parameters Used for the Explosive

Parameter	Value	Experiment used for calculation
$K_1$	53.3 kbar	hydrostatic compression (inert)
$K_2$	-278 kbar	hydrostatic compression (inert)
$K_3$	$1.27 \cdot 10^4$ kbar	hydrostatic compression (inert)
$K_d$	100 kbar	hydrostatic compression (inert)
$\mu_\infty$	0.838 kbar	quasi-static uniaxial compression (inert)
$A_\mu$	$1.6 \cdot 10^{-4}$	dynamic experiments (explosive)
$l$	1.006	dynamic experiments (explosive)
$C_\mu$	$1.5 \text{ kbar}^{-1}$	same as $C_y$ by hypothesis
$Y_0$	17	quasi-static uniaxial compression (inert)
$A_y$	1.077	dynamic experiments (explosive)
$m$	0.238	quasi-static uniaxial compression (inert)
$C_y$	$1.5 \text{ kbar}^{-1}$	quasi-static triaxial compression (inert)
$B$	50	quasi-static triaxial compression (inert)



a) Shot N° 1038



b) Shot N° 1031

Figure 3. Experiment-Calculation Comparison

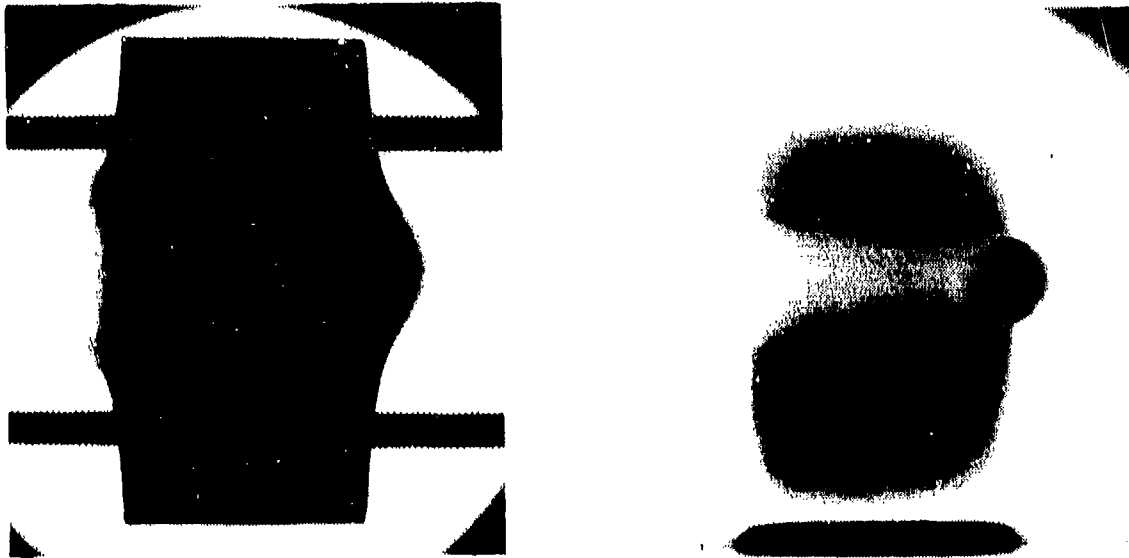
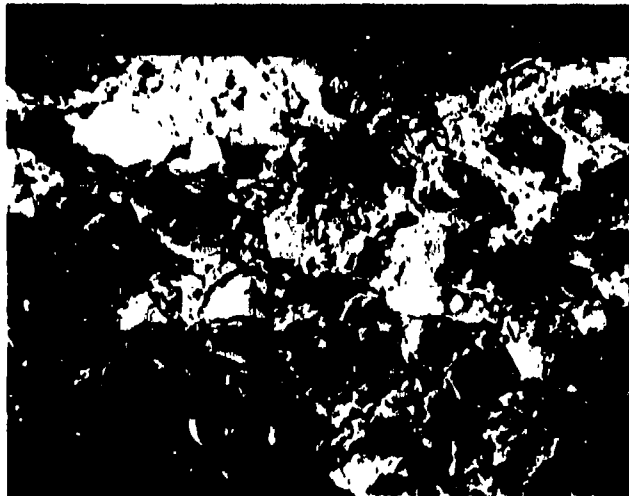


*Figure 4. Two-Dimensional Experiment*



*a) Explosive Sample Before Loading*



*b) Explosive Sample After Loading*

*Figure 5. Micrographics Views Before and After Loading*

velocity impact and to determine the conditions of initiation.

## REFERENCES

1. Société Nationale des Poudres et Explosifs, Private communication.
2. Cagnoux, J., "Dynamic Behavior of a Filled Polymer," *Proceedings of Dymat '88*, AJACCIO France, 1988.

# RESPONSE OF ROCKET PROPELLANTS TO PROJECTILE IMPACT

S. Y. Ho

Weapons Systems Research Laboratory  
Defence Science and Technology Organisation  
P.O. Box 1700, Salisbury, South Australia, 5108, AUSTRALIA

*Two high strain-rate impact tests (modified Hopkinson Bar and Shotgun tests) have been developed to measure the fracture and ignition properties of energetic materials. These tests are useful in determining the impact and ignition sensitivity of energetic materials and also give an insight into the impact ignition mechanism. Photographic evidence of the events prior to and during ignition and initial burning were obtained by microflash photography.*

## INTRODUCTION

There are generally two response modes to impact leading to detonation of energetic materials: (1) prompt initiation to detonation which is induced by strong shock transmitted into the sample, and (2) delayed initiation where detonation is produced by weak shock or conditions/reactions that first cause ignition followed by deflagration to detonation transition (DDT). It is widely accepted that the prompt initiation mechanism is reasonably well understood. However, the mechanisms in the delayed reaction mode are more complex as the time scales are longer, and the events before DDT are less clear. This paper presents results from two high strain-rate impact tests. These results give some insight into the sequence of events in the pre-ignition and initial burning regimes, and may perhaps be relevant in the DDT threshold process in the delayed initiation mode.

The modified Hopkinson Bar (used in conjunction with light detectors and blast pressure gauges) and the Shotgun tests<sup>1,2</sup> have been developed at WSRL to determine the high strain-rate fracture and ignition properties of a variety of composite and cast double base propellants. Both tests are high strain-rate ( $10^3$  to  $10^4$  s<sup>-1</sup>) impact tests measuring the sensitivity of a propellant to high velocity impact, and can be used to investigate the

fracture, ignition, and initial burning events. Detonation does not occur in these tests because the propellants were unconfined and the sample sizes were small.

The modified Hopkinson Bar test consists of a moving input bar (projectile) which is fired at a specimen fixed to a stationary output bar (Figure 1). A fast response photodetector and a blast pressure pencil gauge are used in conjunction with the Hopkinson Bar test apparatus. High strain-rate mechanical properties of the propellant, ignition time, and light output and blast pressure (as a result of ignition and/or initial burning) can be measured using this technique.<sup>2</sup>

The major components of the Shotgun test are a shotgun, a target assembly (consisting of a target plate in an instrumented tube), a velocity measuring system, light detectors, a blast pressure pencil gauge, and strain gauges to measure applied stresses (Figure 2). The test sample is fired from the shotgun and impinges on the target plate. The light output and blast pressure, as a result of ignition and/or burning, and work done on the propellant prior to ignition are measured.

The two techniques used are based on slightly different concepts. In the Hopkinson bar test the deformation of the sample is by

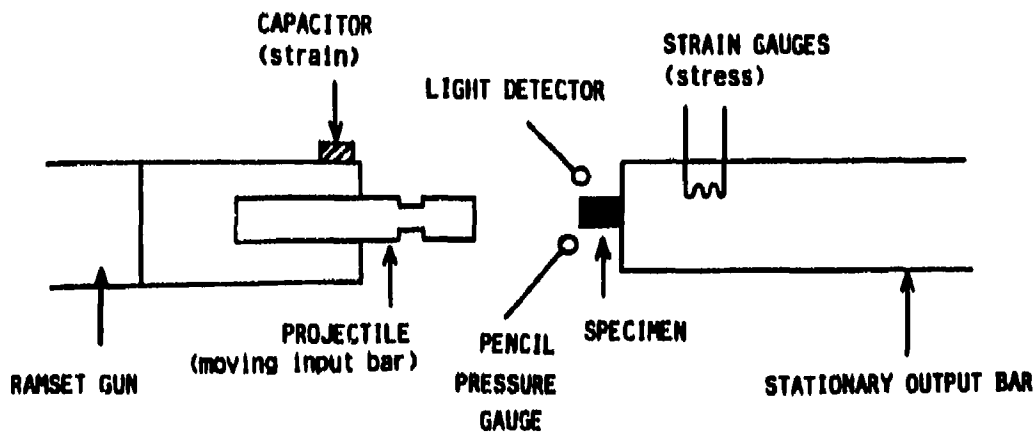


Figure 1. Schematic Diagram of Modified Hopkinson Bar Test

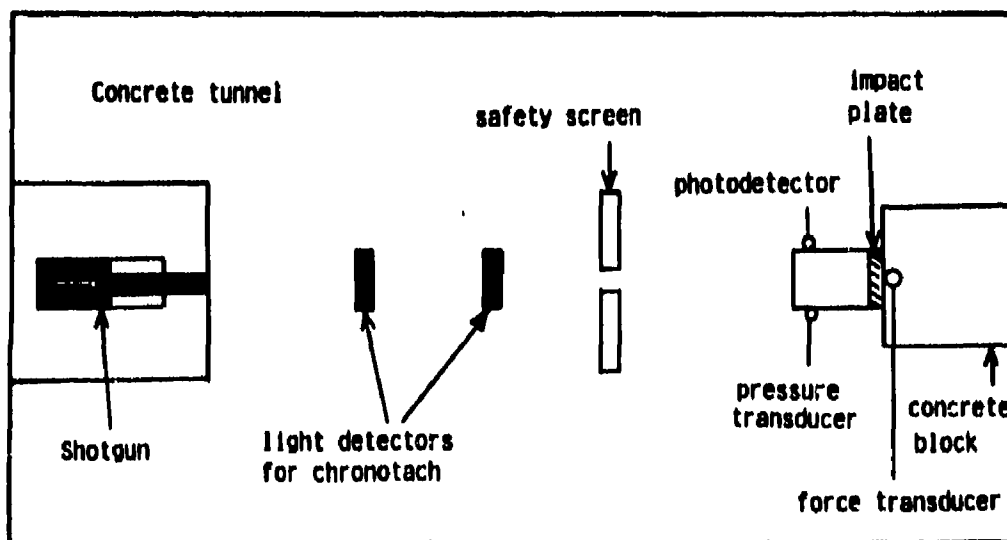


Figure 2. Schematic Diagram of Shotgun Test

compression and shear, whereas in the Shotgun test the deformation is mainly by shear. Also, the impact velocity used in the Shotgun test is approximately ten times higher than that used in the Hopkinson Bar test. However, the kinetic energy transferred to the propellant on

impact in the Hopkinson Bar test is only 2-3 times lower than that for the Shotgun test because of the mass of the projectile used to impact the propellant. Hence, assuming that the rate of energy transfer and the distribution between heat and kinetic energy are similar

for the two tests, and the amount of energy that is delivered to the propellant on impact is the important factor in the ignition process, the impact ignition mechanisms for the two tests would not be expected to be very different.

This study presents the results from two high strain-rate impact tests that provide some insight into the impact ignition mechanism. Microflash photographic studies of the impact event were also conducted to obtain further information on the fracture, ignition, and burning processes.

## EXPERIMENTAL

### Materials

The composite propellants and cast double base propellants were made by standard processing techniques, as described previously.<sup>3,4</sup> The processed propellants were machined into 8 mm diameter x 8 mm cylindrical pellets for the Hopkinson Bar test, and 17 mm diameter x 20 mm pellets for the Shotgun test.

### Measurements

**Hopkinson Bar Test.** For the Hopkinson Bar test, the specimens were fixed to the output stationary bar (connected to strain gauges to measure applied loads) by grease. A moving input bar (projectile) was then fired (using a ramset gun) at the specimen which was compressed between the two bars. A high sensitivity photodetector (5  $\mu$ s response time) and a blast pressure pencil gauge were used in conjunction with the Hopkinson Bar to measure the ignition and explosive properties of the propellants. The light and pressure resulting from sample ignition and/or burning and the stress-strain data were collected using a NICOLET 4094 four-channel digital oscilloscope and a HP 9826 computer, and the results analysed as previously described.<sup>3,4</sup> About 8-10 specimens were tested at a given impact velocity at ambient temperature. Impact velocities were varied from 6 to 30  $\text{ms}^{-1}$ .

During impact it was possible to conduct single photographs of the compressed specimens using microflash photography. Thus, it is necessary to impact a number of specimens (under identical impact conditions) to photograph, at

various times during the load-time measurements, the sequence of events leading to fracture and ignition. The experimental arrangement for photographing the impact event is illustrated in Figure 3. Photographic records were obtained by using a standard 35 mm camera operated in the open flash mode in a darkened environment; the event being manually triggered during a 1 second camera exposure. The flash gun was a multiple head short pulse (flash duration of 0.5  $\mu$ s) photoflash system, designed for ballistic photography, and equipped with a variable trigger delay of 4-1000  $\mu$ s. Flash delay intervals of 50  $\mu$ s were used to obtain photographs at various times during the load-time measurements. Delay times varied from 400  $\mu$ s to 1 ms. A detailed description of the microflash photographic experiments is given in another paper.<sup>5</sup>

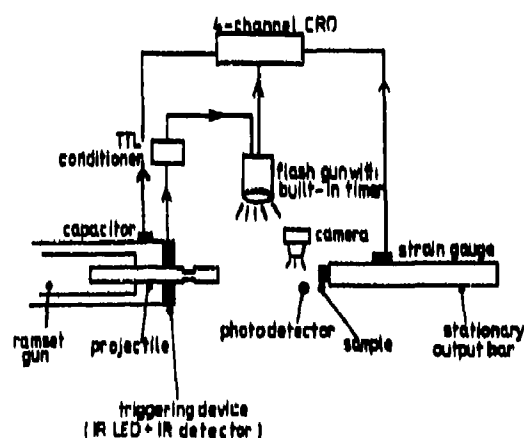


Figure 3. Experimental Arrangement for Microflash Photography During Hopkinson Bar Test

**Shotgun Test.** For the Shotgun test, a 12-gauge shotgun was used to fire pellets of propellants against a target plate in a tube instrumented with two light detectors. A blast pressure pencil gauge is mounted on a lead block and placed at a fixed distance from the target assembly. About 50 specimens were fired over a velocity range of 120-600  $\text{ms}^{-1}$ , at ambient temperature. Projectile velocities were varied by varying the amount of Red Dot smokeless gunpowder in the shotgun shell, prior to firing. A Chronotach was used to calculate the projectile velocity. Light intensity and blast overpressure, produced by ignition and/or

burning, were collected using a NICOLET 4094 four-channel digital oscilloscope.

## RESULTS AND DISCUSSION

### Hopkinson Bar Test

The load-time, visible emission ( $\lambda = 350\text{--}1100\text{ nm}$  with a maximum response at  $800\text{ nm}$ ), intensity-time, and blast pressure-time profiles (load, light, and pressure triggered simultaneously on the oscilloscope) of a typical propellant are shown in Figure 4(a). Interpretation of the fracture processes that occur in the different regions of the stress-strain curves (Figure 4(b)) and of the ignition data, has been discussed in detail in previous papers.<sup>1,4</sup> This is confirmed by recent microflash photographic studies<sup>5</sup> of the impact ignition event. Figures 5(a) to (g) show the photographs for a typical composite propellant taken at various times during the load-time measurements. The vertical line on the corresponding load-time Figure 5 (h) curve indicates when the photograph was taken. The diameter of the specimens ( $10\text{ mm}$ ) used for this study was bigger than that for the standard size ( $8\text{ mm}$ ), to obtain clearer photographs.

Figure 5(a) was taken in the initial linear "elastic" region of the stress-strain curve, and shows compression of the specimen on impact by the moving input bar (projectile). The initial linear region of the stress-strain curve is only a pseudo elastic phenomenon, since there is good evidence from SEM examinations that small cracks do occur in the sample during this portion of the stress-strain curve.<sup>3</sup>

Figure 5(b) shows further compression of the specimen. This occurs in the post-yield "ductile" region of the stress-strain curve. Viscoelastic/plastic deformation, further crack propagation, and other secondary deformation mechanisms contribute to this portion of the curve.<sup>3</sup> The specimen is still intact in this region, as indicated by the photograph.

Figure 5(c) shows extensive crushing and bulging of the propellant. Big cracks and some plastic flow are also visible.

Figure 5(d) shows the propellant undergoing further compression, crushing, and plastic flow. Some fragmentation of the propellant is also visible. The first signs of ignition

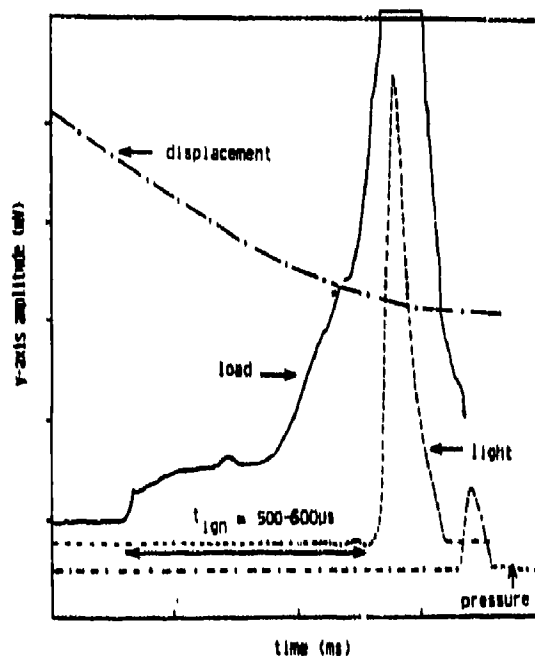


Figure 4(a). Hopkinson Bar Test - Simultaneous Load-Time, Displacement-Time, Light Intensity-Time, and Pressure-Time Profiles for a Typical Propellant at the Impact Velocity  $18\text{ ms}^{-1}$

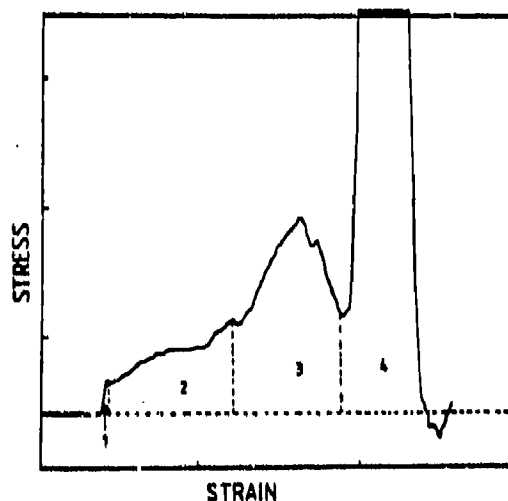
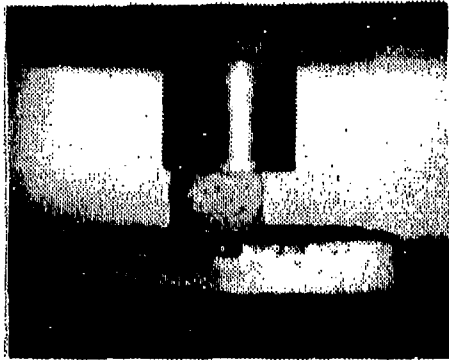
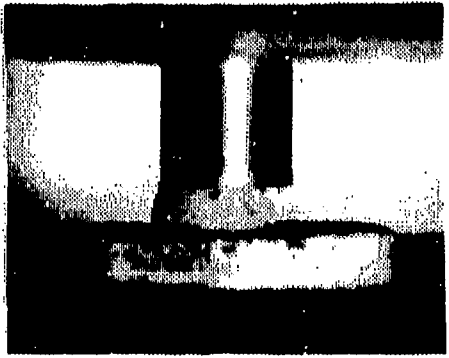


Figure 4(b). Schematic Stress-Strain Curve, at Impact Velocity  $20\text{ ms}^{-1}$ , Defining the Regions Where the Various Fracture Processes Occur

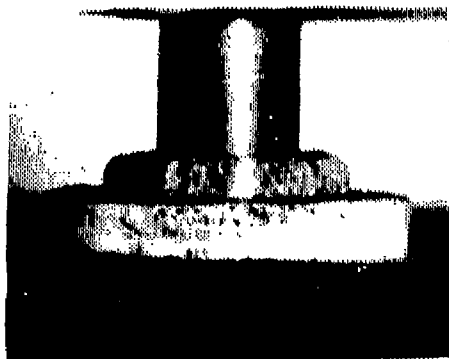
are observed around cracks and at the specimen-projectile interface (region of maximum shear). Plastic deformation and flow is a possible mechanism for hot spot formation and subsequent ignition. It is widely believed<sup>6,7</sup> that the heat dissipated by plastic deformation/flow is



(a)



(b)



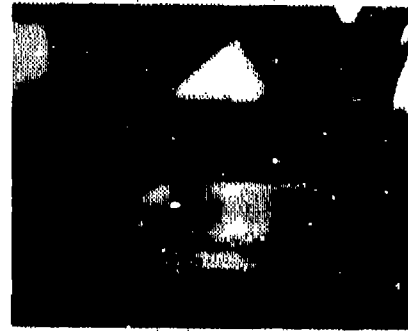
(c)



(d)



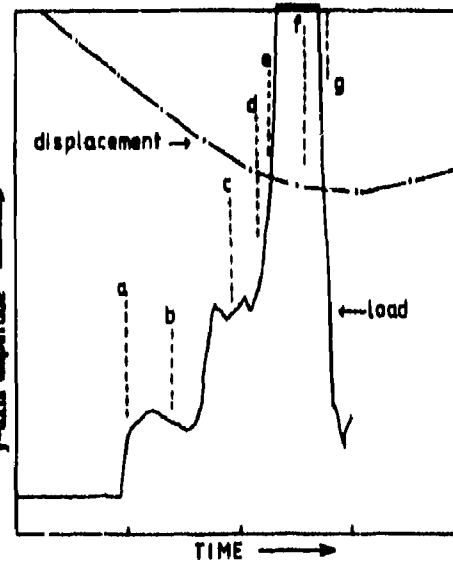
(e)



(f)



(g)



(h)

Figure 5. Photographs Taken at Various Times During the Load-Time Measurements. The vertical line on the load-time curve indicates when the photograph was taken.

localized in shear bands because only a small temperature rise would be produced if the deformation energy was uniformly distributed, as the energy is dissipated over a relatively large volume of material during plastic flow. In the present work, it was not possible to observe whether or not shear bands had formed in the impacted propellant samples, because they were fragmented after impact.

Figure 5(e) shows further crushing of the remaining fragment to a thin layer, plastic flow, sample breakup, and further ignition and burning of the propellant.

Figure 5(f) shows a low order deflagration or burning and the structural collapse of the remaining fragment under compressive stress (i.e., mechanical failure of the specimen where the stress rapidly drops to zero with increasing strain). The structural collapse of the sample is not associated with explosion of the propellant, as structural collapse is also observed in inert propellants where explosion does not occur. At this stage, the remaining propellant appears as a very viscous liquid and viscous flow is visible.

Figure 5(g) is attributed to an explosion, and a corresponding increase in blast pressure is noted. The light emitted in an explosion appears to be more intense and of shorter wavelength than that emitted in ignition and burning, where a more reddish color emission is observed.

The results clearly show that ignition occurs at a much later time in relation to fracture, i.e., after viscoelastic/plastic deformation, extensive crushing, and fragmentation of the propellant. For relatively ductile materials, such as the composite propellants, the photographs provide clear evidence that plastic flow occurs before ignition (which is first detected in regions of maximum shear, i.e., the specimen-projectile interface). These results support the theory that plastic deformation and shear induced flow, and the probable localization of energy in shear bands in the crystalline oxidizer particles, is the main mechanism for hot spot formation. Cracks and voids (formed by dewetting of the crystalline oxidizer particles from the polymer matrix) may also act as sites for hot spot formation. For propellants

which exhibit brittle fracture under impact loading at high strain-rates, e.g., cast double base (NC/NG) propellants, preliminary photographic sequences indicate that these samples showed comparatively little tendency to undergo plastic flow. Processes involving friction, such as pinching or grinding of the sample, may play a more important role in ignition in brittle propellants than in ductile propellants. A comparison of the mechanism of impact ignition of brittle propellants with that of ductile propellants will be described in greater detail elsewhere.<sup>5</sup>

Fracture toughness of the propellants in the initial linear "elastic" and post yield "ductile" regions can be obtained from the area under regions 1 and 2 of the stress-strain curve (Figure 4(b)). The stress-strain curves up to region 2 are reproducible to within  $\pm 30\%$ . The results from the Hopkinson Bar test can be used to obtain the threshold velocity for ignition (this gives an indication of the ease with which the propellant is ignited) and the extent of the reaction, once ignition has occurred (slope of the light intensity vs. impact velocity plot).<sup>1,2</sup> Previous studies<sup>1,2</sup> highlighted the importance of mechanical properties in impact ignition. The ease with which the propellant is ignited by impact is determined to a large extent by its fracture toughness. However, the extent to which propellant burning develops, once ignition has taken place and releases enough energy to cause ignition to continue, is governed by several interrelated propellant properties such as energy content, burning rate, thermal decomposition and kinetics, etc.<sup>1</sup>

### Shotgun Test

The visible emission intensity-time and pressure-time profiles of a typical propellant at low projectile velocity are shown in Figure 6(a). The small light peak in the visible emission intensity-time profile corresponds to a flash or a spark (due to ignition) observed visually. As the impact velocity is increased, other reactions (large flash, burning, explosion, and violent explosion) are noted. The visible emission intensity-time profile changes from a single peak to a peak and a broad region of high light intensity [Figure 6(b)]. At very high velocities

the small peak and the broad light signal merge into one broad region of high light intensity [Figure 6(c)]. The observed light signals are assigned to (1) ignition and initial burning, and (2) sustained "steady-state" burning or deflagration [Figure 7(a)]. The assignment of the broad light signal to sustained "steady-state" burning is supported by the visual observation of intense burning whenever the broad light signal is recorded. At very high velocities, the time between ignition and sustained burning is very short and the two light signals merge [Figure 7(b)]. A marked increase in blast pressure is also observed and explosion is noted. When an explosion occurs, the reaction is very rapid (~45 ms compared to 650 ms for sustained burning) and the measured light intensity is much lower than when there is ignition and sustained burning. The low level of light intensity that was measured during an explosion may be explained by a shift in the spectrum of the emitted light to shorter wavelengths; i.e., most of the emitted light from an explosion is not detected because it is outside the range of the photodetector used in this study. Some evidence for this blue shift of the emission spectrum comes from experiments where a blue pass filter was used to cut off light in the

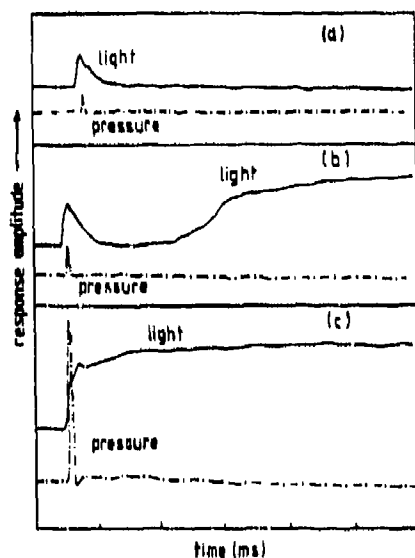


Figure 6. Shotgun Test - Simultaneous Light-Time and Pressure-Time Profiles for a Typical Propellant at Various Projectile Velocities (40 ms Time Interval). (a)  $180 \text{ ms}^{-1}$ , (b)  $260 \text{ ms}^{-1}$ , (c)  $370 \text{ ms}^{-1}$ .

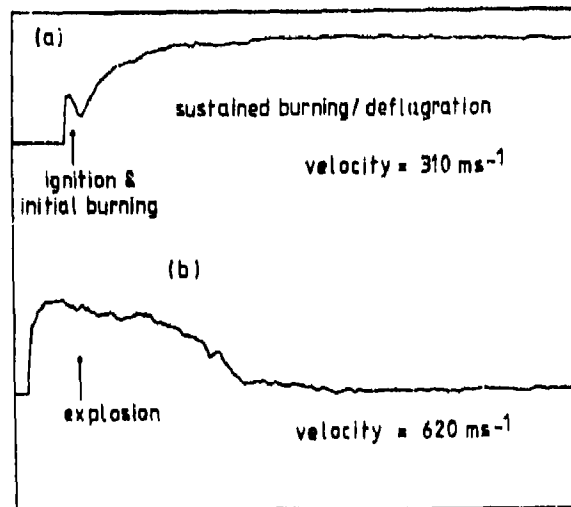


Figure 7. Shotgun Test - Schematic Diagrams of Light Output vs. Time, at Various Velocities, Defining the Regions Where Ignition, Initial Burning, Sustained Burning/Deflagration, and Explosion Occur (100 ms Time Interval)

red/near IR region of the emission spectrum. When the filter was used, the light intensity for ignition and sustained burning decreased by a factor of 2-3 whereas that for explosion remained almost the same, suggesting that the emitted light from explosion is of shorter wavelengths than that from ignition and sustained burning.

A detailed discussion of analysis and interpretation of the results has been given in a previous paper.<sup>2</sup> A typical plot of total area of light output vs. impact velocity is shown in Figure 8. Results for impact velocities where there is an explosion are not included in these plots. The total area of light output vs. impact velocity plot shows that the light output increases almost linearly with impact velocity, and then increases very rapidly above a certain velocity,  $CV_1$ . The velocity where the sudden increase in light output occurs corresponds to the velocity where the broad light signal starts to appear, i.e., where the mechanism changes from ignition and initial burning to sustained burning or deflagration.

Impact ignition characteristics that can be obtained from the Shotgun test include:

- (1) The critical impact velocity for ignition and initial burning ( $CV_1$ ) and slope<sub>1</sub> from Figure 8, and

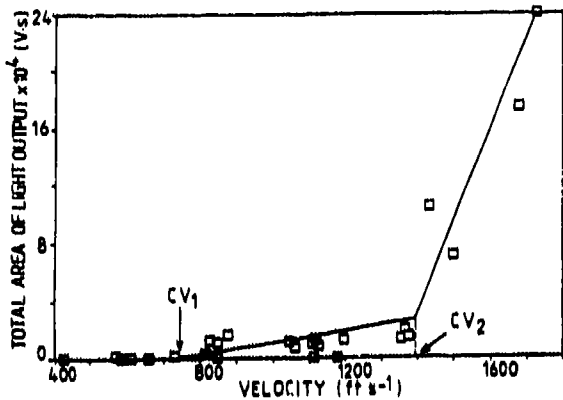


Figure 8. Shotgun Test - Total Area of Light Output vs. Impact Velocity

- (2) The critical impact velocity for sustained burning/deflagration ( $CV_2$ ) and slope<sub>2</sub> from Figure 8.

The critical impact velocity for ignition and initial burning,  $CV_1$ , can be used to rank propellants according to their sensitiveness to impact ignition. The results generally show the same trends as the Hopkinson Bar test, i.e.,  $CV_1$  is related mainly to the mechanical properties of the propellant.<sup>2</sup>

The critical impact velocity for sustained burning/deflagration,  $CV_2$ , appears to be related to several factors. These include (1) type of oxidizer, (2) oxidizer loading, (3) mechanical properties, and (4) energy content of the propellant. The extent of the influence of these various factors on  $CV_2$  is not clear.

Similar trends are observed for slope<sub>1</sub> and slope<sub>2</sub> of the total area of light output vs. impact velocity plot. They give an indication of the extent to which propellant burning develops at velocities above the critical value. These values appear to be related primarily to the energy content (oxidizer loading, oxidizer type, binder type, and NG content) and burning rate (surface area available for burning, etc.) of the propellant.<sup>1</sup>

## CONCLUSION

The impact ignition sensitivities obtained from the Hopkinson Bar and Shotgun tests are generally comparable, except for very "soft"

samples, e.g., a HTPB/AP propellant containing plasticizer. This may be explained by the slightly different deformation mechanisms. In the Hopkinson Bar test, cracks tend to close up during compression and the specimens appear tougher than what they would be under shear deformation. Samples subjected to the Hopkinson Bar test appear to behave more viscoelastically than those subjected to the Shotgun test and are, therefore, more sensitive to the effects of temperature and strain-rate. The propellant appears more brittle in the Shotgun test because of the higher strain-rate.

Microflash photography has been used to follow the sequence of events leading to fracture, ignition and burning in energetic materials during impact at high strain-rate. It gave further insight into the mechanism of impact ignition. For ductile composite propellants, fracture and plastic deformation/flow were observed before ignition (which was first detected at the propellant-projectile interface, i.e., where shear was maximum). These experiments also gave clear evidence that ignition and reaction buildup are separate processes in energetic materials during impact.

## REFERENCES

1. Ho, S. Y. and Fong, C. W., *Combustion and Flame*, 75, 139, 1989.
2. Ho, S. Y.; Fong, C. W.; and Hamshere, B. L., *Combustion and Flame*, Vol. 77, 1990, p. 395.
3. Ho, S. Y. and Fong, C. W., *Polymer*, Vol. 28, 739, 1987.
4. Ho, S. Y. and Fong, C. W., *J. Mater. Sci.*, Vol. 22, 3023, 1987.
5. Ho, S. Y.; Hammond, R. T.; Schebella, K. J.; and Wilson, A. G., *WSRI Report WSRI-000-000*, in press, 1989.
6. Winter, R. E. and Field, J. E., *Proc. R. Soc. Lond. A.*, Vol. 343, 399, 1975.
7. Swallowe, G. M. and Field, J. E., *Proc. Roy. Soc. Lond.*, Vol. A 379, 389, 1982.

# CHARACTERIZATION OF BOOSTER-ROCKET PROPELLANTS AND THEIR SIMULANTS

L. J. Weirick  
Sandia National Laboratories  
Albuquerque, New Mexico

*A series of shock-loading experiments on a composite and an energetic propellant and their simulants was conducted on a light-gas gun. The initial objectives were to obtain Hugoniot data, to investigate the pressure threshold at which a reaction occurs, and to measure spall threshold at various impact velocities. The Hugoniot data measured for the propellants fit the Hugoniot curves provided by the manufacturer of the propellants extremely well, and the Hugoniot curves developed for the simulants matched those of the propellants. Threshold pressures to initiate reactions in the composite and energetic propellants were found to be 40 and 3 kbars, respectively. In spall tests, the composite propellant and its simulant exhibited spall strengths around 0.25 and 0.18 kbar, respectively. The energetic propellant and its simulant were somewhat stronger with spall strengths just above 0.33 and 0.22 kbar.*

## INTRODUCTION

This investigation was begun to aid in the studies of the vulnerability and lethality of solid propellant booster stages. The materials of interest are a composite and an energetic propellant and their simulants.

The shock Hugoniot of a material is determined when the relationship between the shock and particle velocities is known. This relationship can be experimentally determined from planar, gun-impact experiments and can generally be approximated by a linear fit:

$$U_s = C_0 + S U_p \quad (1)$$

where  $U_s$  is the shock velocity,  $C_0$  is the initial bulk sound velocity,  $S$  is a constant, and  $U_p$  is the particle velocity.

The detonability of composite propellants has been studied since their inception. A recent study was done at Lawrence Livermore National Laboratory (LLNL)<sup>1</sup> on the detonability of a composite propellant. Delayed

explosions were observed in the impact-damaged propellant at impact pressures above 30 kbar.

The sensitivity and power of energetic propellants was studied in the 1970's at LLNL.<sup>2</sup> This work, together with investigations by SRI International and others, was summarized in a report from the High Energy Propellant Safety (HEPS) Committee.<sup>3</sup> More recently a study was done at LLNL on the detonability of energetic propellants.<sup>4</sup> They found a delayed detonation threshold of 6.2 kbar and a shock detonation threshold of 13.2 kbar for the most energetic of these propellants.

The process of spallation has been studied in a number of laboratories with a view to obtaining the criteria for dynamic fracture at high stress rate. Tension is induced within a sample by allowing a stress wave to reflect as a rarefaction from a free surface. The tension increases by interaction of the rarefaction wave with the primary wave until a critical value is reached and fracture occurs. The fact that the free-surface velocity stops dropping

and then rises ("spall rebound or pullback") is due to the generation of compressive waves at the spall plane that increase the pressure. The clearly defined onset of fracture at a specific value of pullback suggests a characteristic material strength which corresponds to a damage threshold tension. This material property is referred to as the incipient fracture strength or spall strength,  $\sigma$ . The value of  $\sigma$  may be approximately related to the observed pullback by considering the interaction of the reflected wave with the primary wave assuming a perfect reflection at the free surface.<sup>5</sup> The resultant expression is:

$$\sigma = 1/2 C_0 \rho_0 \Delta\mu \quad (2)$$

where  $C_0$  is the initial bulk sound velocity,  $\rho_0$  is the material density and  $\Delta\mu$  is the measured pullback. The incipient fracture is understood in material terms as the macroscopic yield stress necessary for the growth of internal voids into a free surface or spall plane. One method of observing the details of the complete fracture history has been free-surface

velocity measurements using a laser interferometer. SRI International performed dynamic fracture experiments on energetic propellants.<sup>6</sup> They observed no damage for impact stresses up to 1.4 kbar. At an impact stress of 1.58 kbar, the recovered specimen was fragmented, and at 6.3 kbar, the propellant burned.

The initial objectives of this study are to obtain Hugoniot data, to investigate the pressure threshold at which a reaction occurs, and to measure spall damage at various impact velocities.

## EXPERIMENTAL PROCEDURE

One propellant, TP-H1207C, and its simulant, H-19, are of composite formulation and the other propellant, WAK-2, and its simulant, UGS, are based upon energetic formulations, as given in Tables 1 and 2.<sup>7</sup> None of the materials have any significant porosity. The H-19 contains large, rectangular crystals of potassium chloride and small, spherically-shaped particles of metallic

Table 1. Composite Formulations and Mechanical Properties

	TP-H1207C	H-19	
Composition		(weight %)	
-Fuel	Aluminum	Al	31.75
-Oxidizer	Ammonium Perchlorate	AP	5.0
-Inerts		KCl	51.5
-Polymers	Hydroxy-Terminated Polybutadiene	HTPB	8.8
-Curatives		IPDI	0.7
-Plasticizer		DOA	2.0
-Bonding Agent		Tepanol	0.2
-Processing Aid		ODI	0.04
-Cure Catalyst		TPB	0.02
<b>Mechanical Properties</b>			
-Density (g/cc)	1.84		1.89
-Tensile Strength (psi/kbar)	140.0/0.01		114.0/0.008
-Maximum Elong. (%)	45.3		32.0
-Tensile Modulus (psi)	637.0		450.0

**Table 2. Composite Formulations and Mechanical Properties**

	WAK-2	UGS
<b>Composition</b>		(weight %)
-Fuel	Double-base Propellant Aluminum	DBP 19.7 Al 5.0
-Oxidizer	HMX Ammonium Perchlorate	HMX 0.0 AP 0.0
-Inerts		Na <sub>2</sub> SO <sub>4</sub> 65.3
-Polymers		HDAP 9.0
-Curatives		N100 1.0
-Processing Aid		HDI 0.04
<b>Mechanical Properties</b>		
-Density (g/cc)	1.85	1.85
-Tensile Strength (psi/kbar)	100.0/0.007	158.0/0.011
-Maximum Elong. (%)	250.0	50.0
-Tensile Modulus (psi)	450.0	490.0

aluminum. The matrix which binds these constituents together is a hydroxy-terminated, polybutadiene-polyurethane polymer, HTPB. The TP-H1207C propellant formulation is based upon ammonium perchlorate with aluminum additions and bound together with the HTPB.

The WAK-2 propellant formulation is based upon a double-base mix of nitrocellulose and nitroglycerin. It also contains aluminum and HMX. The UGS simulant contains large, rectangular crystals of sodium sulphate and small, spherically-shaped particles of aluminum. The matrix which binds these constituents together is a mix of diallyl phthalate, HDAP, and the double-base propellant. The "static" mechanical properties of these materials are also given in Tables 1 and 2. The tensile strengths of these materials are very low (near 0.01 kbar) with moderate elongations (50 percent). Densities near 1.85 g/cc are typical of solid rocket booster propellants.

The light-gas gun system used is described in detail in Reference 8. Briefly, the barrel is 9 meters long, with an inside diameter of 63.4 mm. The breech is of a quick-acting,

quick-change design with two inserts; one termed a "wraparound" for low-velocity shots utilizing nitrogen (below 0.5 km/s) and a second called a "dual-diaphragm" for higher-velocity shots using helium (up to 1.5 km/s for projectiles with weights below 0.2 kg).

One modern technique used for measurement of shock phenomena is the Velocity Interferometer System for Any Reflector (VISAR).<sup>9</sup> A "Push-Pull" VISAR method developed by Hemsing<sup>10</sup> and used in these experiments results in effective cancellation of self-light from a reaction. An important variation on the Push-Pull VISAR is a system which has an extended (that is 166 cm long) air-delay leg in place of the quartz-delay leg. This replacement allows the accurate measurement of particle velocity in a very-low velocity regime, that is below 0.1 km/s.

#### **Projectiles/Targets for Hugoniot/Reaction Threshold Set-up**

A 5-cm diameter by 1.2-cm-thick disc (50 g) of propellant/simulant is epoxied to the front end of a lightweight (200 g) nylon/foam projectile. The target consists of a 6.2-cm

diameter by 1.2-cm-thick disc of quartz or lithium fluoride with an evaporated layer of aluminum on the front covered by a 0.5-mm-thick quartz (Dynasil 1000) buffer plate. The laser beam comes in from the back of the target and is reflected off the back surface of the mirror. The buffer plate smooths the spatial non-uniformities in the wavefront generated at the impact interface and generates some initial fringes which simplify the VISAR data reduction.

### Projectiles/Targets for Spall Set-up

A 5-cm diameter by either 0.75-cm or 1.25-cm thick disc of propellant/simulant is bonded to an aluminum ring holder on the target mount. A 0.01-mm-thick piece of aluminum foil is epoxied with urethane cement to the back side of the propellant/simulant disc to function as a reflecting mirror for the laser beam. This mirror is considered a "free surface." The projectiles are designed for maximum weight (3.5 kg) by using aluminum cylindrical shells to contain a lead-shot/epoxy mix. A 0.32-cm-thick PMMA disc (low-impedance impactor) is attached to a 6-mm long, aluminum standoff ring at the front of the projectile. By using heavy projectiles and pressurizing the breech with nitrogen, the best control for very-low projectile velocities (0.01 km/sec) can be attained.

## RESULTS

### Hugoniot Curves

**TP-H1207C Propellant and H19 Simulant.** Propellant discs were impacted at velocities ranging from 1.0 to 1.44 km/s (impact pressures from 41 to 66 kbars) and the resultant particle velocities were determined. Plotting the particle velocities versus the stress (impact pressure) gives the Hugoniot curve for this propellant as shown in Figure 1. The solid curve is the Hugoniot calculated from the Hugoniot parameters provided by the manufacturer of the propellant, Morton-Thiokol. Simulant discs were impacted at velocities ranging from 0.51 to 1.37 km/s (impact pressures from 20 to 58 kbars) and the resultant particle velocities were determined.

The Hugoniot curve determined for H-19 is also shown in Figure 1.

**WAK-2 Propellant and UGS Simulant.** Propellant discs were impacted at velocities ranging from 0.15 to 0.53 km/s (impact pressures from 5.2 to 22.0 kbars) and the resultant particle velocities were determined. The Hugoniot curve for this propellant is shown in Figure 2. The solid curve is the Hugoniot calculated from the Hugoniot parameters provided by the manufacturer of the propellant, Morton-Thiokol. Simulant discs were impacted at velocities ranging from 0.25 to 1.00 km/s (impact pressures from 9.1 to 43.8 kbars) and the resultant particle

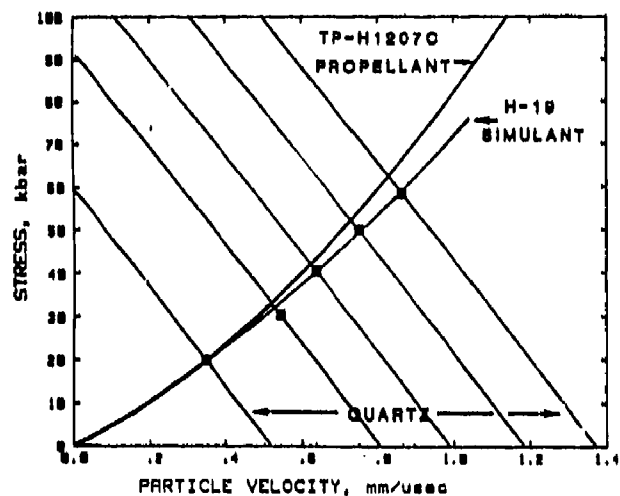


Figure 1. Hugoniot curves for TP-H1207C and H-19

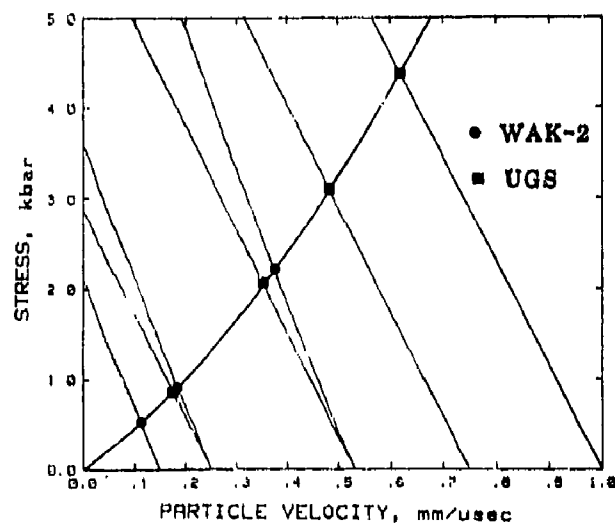


Figure 2. Hugoniot curves for WAK-2 and UGS

velocities were determined. The Hugoniot curve for UGS simulant was found to be the same as that for the propellant WAK-2.

### Reaction Thresholds

When a material which does not subsequently react—such as a simulant—is impacted, the velocity record should show a jump at impact to the equilibrium particle velocity and then remain constant with time until release waves from side walls or rear surfaces reach the observation point. Figure 3 gives the particle velocity versus time record for UGS impacting quartz at 0.53 mm/ $\mu$ sec (20.4 kbar impact pressure). The particle velocity record for lithium fluoride upon being impacted by WAK-2 at 0.53 mm/ $\mu$ sec (22.0 kbar impact pressure) is also shown in Figure 3. At impact, the particle velocity of the quartz jumped to approximately 0.156 mm/ $\mu$ sec and remained essentially constant for 3.5  $\mu$ sec. At 3.5  $\mu$ sec after impact, the velocity begins to steadily increase, indicating the initiation of a reaction within the WAK-2 propellant. Post-test observation of the test hardware indicated that a violent reaction had occurred. The propellant had completely reacted and no remnant traces were recovered.

Figure 3 also shows the particle velocity versus time record for WAK-2 impacting lithium fluoride at 9.1 and 5.3 kbar, respectively. Post-test observation of the test at 9.1 kbar confirmed that a reaction had

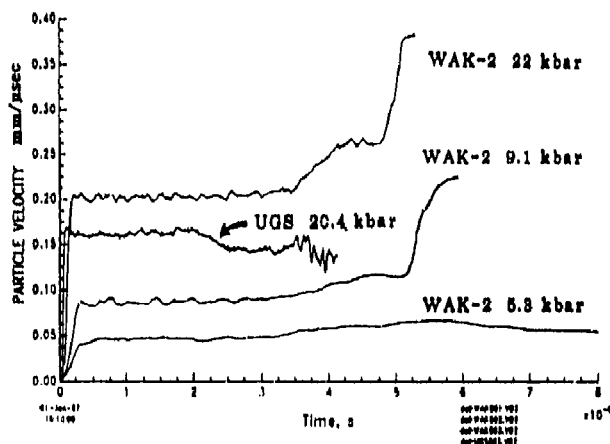


Figure 3. Reaction Profiles for WAK-2 and UGS

occurred. The target holder and associated hardware were fragmented and no remnants of propellant remained. The test at an impact pressure of 5.2 kbar produced an interesting result, also shown in Figure 3. The particle velocity jumped to 0.037 mm/ $\mu$ sec and remained constant for 3.3  $\mu$ sec, at which time a reaction began and the particle velocity increased, a pattern analogous to the other WAK-2 tests. However, after 3.3  $\mu$ sec of reaction time, the reaction ceased. Post-test observation of the test hardware gave no evidence of a reaction in that the target holder and focusing lens were found intact and the propellant was found to be mechanically damaged but unreacted.

Figure 4 gives the particle velocity versus time record for H-19 impacting quartz at 40 kbar impact pressure, a typical record for a non-reacting material. The particle velocity record for quartz upon being impacted by TP-H1207C at 41 kbar impact pressure is also shown in Figure 4. At impact, the particle velocity of the quartz jumped to approximately 0.36 mm/ $\mu$ sec and remained essentially constant for 2.0  $\mu$ sec. At 2.0  $\mu$ sec after impact, the velocity begins to steadily increase, indicating the initiation of a reaction within the TP-H1207C propellant. A violent reaction was not observed for this test, in that the target holder and focusing lens were recovered in an intact condition. However, the propellant had completely reacted and no remnant traces were recovered. Similar

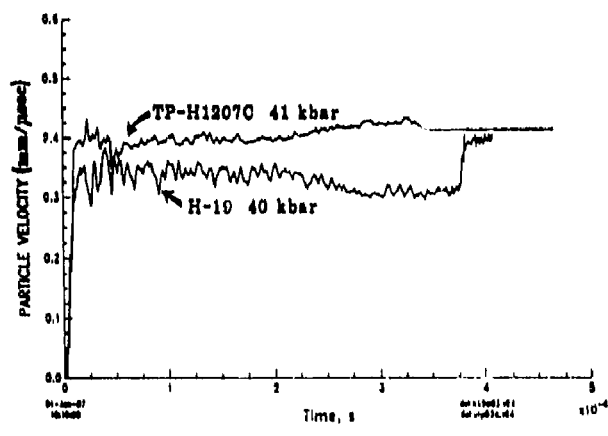


Figure 4. Reaction Profiles for TP-H1207C and H-19

results were found for shots at higher impact stresses, but with more violent reactions observed, particularly at impact pressures above 50 kbar.

### Spall Strength

**H-19.** Spall shots were done on H-19 at impact pressures from 0.18 to 2.75 kbars, with projectile velocities of 10 to 147 m/sec, respectively. An example of the resultant particle velocity versus time plot for H-19 impacted by PMMA is shown in Figure 5. This example is for an impact pressure of 1.6 kbar, corresponding to a projectile velocity of 88 m/sec. The spall strength for H-19 calculated for this shot using Equation (2) with velocity pullback of 0.008 mm/ $\mu$ sec, density of 1.89 g/cc, and sound velocity of 2.25 mm/ $\mu$ sec, producing a spall strength of 0.175 kbar (2540 psi). The results for this set of spall tests on H-19 are tabulated in Table 3.

Figure 6 shows the H-19 samples after the spall shots. The spall planes are readily visible in most of the samples. However, the samples impacted at 10 m/sec (0.18 kbar) and 36 m/sec (0.65 kbar), respectively, do not show obvious spall planes. The sample impacted at 10 m/sec did not spall, according to the VISAR record, which agrees with the visual evidence. The VISAR record for the sample impacted at 36 m/sec indicated that the sample had spalled. The photograph does not show a spall plane. However, an SEM analysis at higher magnification (150X) done in the center of the

Table 3. Spall Results for H-19 Simulant

Projectile Velocity Measured (m/sec)	Impact Stress Calculated (kbar)	Spall Strength Measured (kbar)
10	0.178	No Spall
36	0.646	0.180
88	1.609	0.175
101	1.856	0.132
110	2.028	0.154
147	2.745	0.132

impacted sample showed a discontinuous cracking along the potential spall plane.

**TP-H1207C.** Spall shots were done on TP-H1207C at impact pressures from 0.63 to 2.7 kbars. These results are given in Table 4. A representative value for spall strength for TP-H1207C is 0.22 kbar.

**UGS and WAK-2.** Spall shots were done on UGS at impact pressures from 1.1 to 3.1 kbars and on WAK-2 at impact pressures from 1.36 to 3.03 kbars, respectively. The results for these sets of spall tests are tabulated in Tables 5 and 6. The data in Table 6

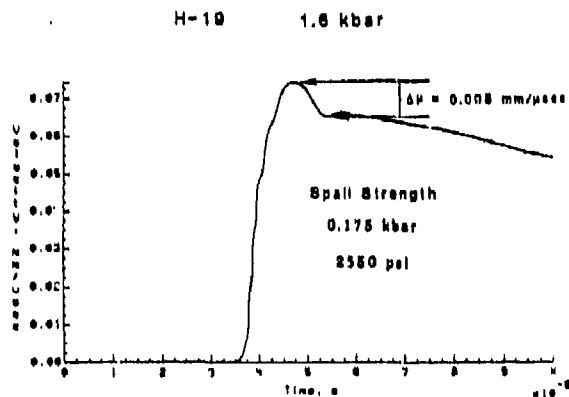


Figure 5. Spall Profile for H-19



Figure 6. H-19 Spall Samples

**Table 4. Spall Results for TP-H1207C Propellant**

Projectile Velocity Measured (m/sec)	Impact Stress Calculated (kbar)	Spall Strength Measured (kbar)
35	0.63	0.165
61	1.11	0.209
72	1.31	0.247
108	1.99	0.083*
144	2.69	0.209

\* Post spall curve loaded up, not unloaded; bad shot?

**Table 5. Spall Results for UGS Simulant**

Projectile Velocity Measured (m/sec)	Impact Stress Calculated*	Spall Strength Measured (kbar)
62	1.11	0.224
132	2.42	0.214
167	3.10	0.305#

\* WAK-2:PMMA

# best estimate

**Table 6. Spall Results for WAK-2 Propellant**

Projectile Velocity Measured (m/sec)	Impact Stress Calculated*	Spall Strength Measured (kbar)
76	1.36	0.346
115	2.10	0.315
163	3.03	Reacted#

\* WAK-2:PMMA

# trigger pin malfunctioned

also indicates that a WAK-2 sample reacted upon being impacted by PMMA at 3 kbar. This result is to be compared with the result obtained in the reaction threshold tests where a WAK-2 sample impacted at the same velocity (0.15 mm/ $\mu$ sec), but onto lithium fluoride, to produce a higher impact stress (5.2 kbar), reacted briefly, and then stopped.

## DISCUSSION

### Hugoniot Measurements

The impact shots of TP-H1207C propellant resulted in Hugoniot data which agreed very well with that supplied by the manufacturer, Morton-Thiokol. Using the values for density  $\rho = 1.84$  g/cc and initial bulk sound velocity  $C_0 = 2.3$  mm/ $\mu$ sec, the coefficient S can be calculated from the Hugoniot curve and Equation (1). The value of S for TP-H1207C was calculated to be 2.16. The impact shots of H-19 simulant resulted in Hugoniot data which were close to that of TP-H1207C, particularly at low impact pressures. The values for the H-19 simulant were 1.89 g/cc, 2.25 mm/ $\mu$ sec, and 1.5, respectively. Thus, the H-19 is acting as a good simulant for TP-H1207C propellant with respect to shock properties, particularly at lower input pressures.

The impact shots of WAK-2 propellant resulted in Hugoniot data which agreed very well with that supplied by the manufacturer, Morton-Thiokol. Using the values for density  $\rho = 1.85$  g/cc, initial bulk sound velocity  $C_0 = 2.2$  mm/ $\mu$ sec, and coefficient  $S = 2.66$ , provides an accurate Hugoniot relation for this material for modeling. The impact shots of UGS simulant resulted in Hugoniot data which was the same as that of WAK-2 for the range of pressures investigated. Thus, the UGS is acting as a good simulant for WAK-2 propellant with respect to shock properties, particularly at lower input pressures.

### Reaction Threshold Measurements

The reaction threshold pressure for WAK-2 propellant was found to be approximately 3 kbar, for the material dimensions and physical constraints of these tests. This reaction threshold pressure is in agreement in

magnitude with values reported in the literature for energetic propellants. The study done at SRI International<sup>6</sup> on VRA propellant found that an impact pressure of 6.3 kbar caused the propellant to burn. The sample size was 50.8-mm diameter by 6.4-mm-thick. Thus, a threshold value for WAK-2 of 3 kbar, particularly for the larger size (50.8-mm diameter by 12.7-mm-thick), is in good agreement with results from SRI experiments.

Experiments done at LLNL<sup>4</sup> on VXV, an energetic propellant analogous to WAK-2, found that for samples of dimensions 152-mm diameter by 102-mm long an impact of 8.4 kbar produced a mild reaction and an impact of 8.6 kbar caused a detonation after a 201  $\mu$ s delay. Smaller samples (76-mm diameter by 76-mm long) needed higher-pressure impacts to produce reactions and detonations. The sample hit at 10.1 kbar burned at a moderate rate whereas the one impacted at 10.2 kbar detonated. Since the objective of the LLNL study was primarily to determine the impact pressure at which a delayed detonation occurred, they did not investigate the lowest pressure at which a reaction was initiated. However, their findings that impact at 8 and 10 kbars produce reactions and detonations that agree with the results from this study, where a 9 kbar impact produced a complete sample burn and a 22 kbar impact produced a violent reaction (detonation?).

The reaction threshold pressure for TP-H1207C propellant was found to be approximately 40 kbar for the material dimensions and physical constraints of these tests. Increasing the impact pressure above this threshold decreased the reaction delay time and increased the reaction rate or reaction intensity. These reaction threshold pressures agree in magnitude with values reported in the literature for composite propellants, those being near 50 kbar. Experiments done at LLNL<sup>1</sup> on TPII-1123, a composite propellant analogous to TP-H1207C, found that for samples of dimensions 152-mm diameter by 102-mm long an impact of 17 kbar produced mild burning and an impact of 35 kbar caused a moderate burn. Larger samples (152-mm diameter by 366-mm long) reacted more vigorously at lower-pressure

impacts. The sample hit at 24 kbar burned at a moderate rate whereas the one impacted at 33 kbar reacted violently. Thus, a threshold value for TP-H1207C of 40 kbar, particularly for the smaller size (50.8-mm diameter by 12.7-mm long), is in good agreement with results from past experiments.

Although these reaction threshold pressures measured in the two studies agree in magnitude for the various sample sizes, there is a disagreement on when the reaction occurs. The study done at LLNL indicated that a reaction did not begin upon passage of the shock wave through the propellant, but a latter explosion occurred upon impact of the shock-damaged propellant. VISAR data taken during the presently discussed study showed the beginning of a reaction within two microseconds after the shock jump. Additional study of this phenomenon is necessary to address this difference.

### Spall Strength Measurements

The spall strengths of most materials (plastics, metals, ceramics, and explosives) increase with increasing strain rate. Typically, the spall strength of a material increases from twofold to tenfold with an increase in strain rate from "static" ( $10^{-3} \text{ s}^{-1}$ ) to "dynamic," greater than  $10^{+3} \text{ s}^{-1}$ . The spall strength of the H-19 simulant in this study increased from a static value of just above 0.008 kbar (114 psi) to about 0.175 kbar (2540 psi) under shock loading. The strengths of the individual constituents of H-19 are all above those of the H-19 composite. Therefore, the resultant strength of H-19 is not an average of the strengths of the individual constituents proportional to their percentage within the composite. The magnitude of the relative strength values suggest that the strength of H-19 is a result of fracture of one or more materials in the composite and separation between boundaries of other constituents of the composite along the fracture plane. One possibility for fracture takes into account the very weak bonding between the urethane binder and potassium chloride and aluminum particles. In this fracture hypothesis, the crack propagates along the KCl-urethane and Al-urethane boundaries causing a separation at

these locations and then propagates across the urethane along the fracture plane. This phenomenon is called "dewetting" and occurs in all composite solid propellants to some extent when a load is applied.<sup>11</sup> The relative motion of particles embedded in the matrix produces sufficiently high stresses near the binder-filler interfaces to cause rupture, and the binder-filler bonds may be pulled loose. As dewetting takes place, the reinforcing effects of the filler are reduced, and a decreasing modulus of elasticity results. Any continued deformation, such as tearing, is sustained by the binder until the sample breaks or spalls.

Examination of a fracture in H-19 confirmed this second hypothesis. The fracture runs alongside of the KCl crystals and Al spheres, thus at the bond planes between them and the urethane, and through the connecting urethane. The fracture strength is reflected in the stress needed to fracture the proportion of urethane binder between solid fillers, the KCl crystals and Al particles. This "line density" for urethane is approximately equal to the volume percentage of urethane in the composite, approximately 18.7 percent. Multiplying this percentage, 0.187, times the measured spall strength of urethane, 0.91 kbar (13110 psi), results in a value of 0.17 kbar (2465 psi) which is in very good agreement with the spall strength measured for H-19, 0.175 kbar (2540 psi).

Similar results have been found for the TP-H1207C propellant. The tensile strength was reported to be near 0.01 kbar (140 psi).<sup>7</sup> The spall strength was found to be 0.25 kbar (3625 psi). The same arguments can be used for the fracture of TP-H1207C as were used for the fracture of H-19. The spall strength is a result of the fracture of the HTPB urethane and the strength is approximately proportional to the volume percentage of binder material in the propellant.

Lee et al.<sup>12</sup> reported spall data for the propellant ANB-3600. ANB-3600 is an ammonium perchlorate-based, composite propellant. They found that it took an impact of 1.8 kbar to see incipient spall and 2.0 kbar for detachment. These values agree very well with those reported for this work in Table 3 for TP-H1207C and Table 4 for H-19. Impact

stresses over 1.3 kbar were needed to observe the spall fracture. However, this work has shown that spall strengths inferred in this manner are an order of magnitude too high. First, incipient spall can be seen in samples impacted at low pressures if a microscope (100X) is used for observation. Second, if a free-surface velocity measurement is done to obtain the value for pullback, a value for spall strength is obtained which is an order of magnitude lower than that obtained by visual observation of spall detachment. Also, these values of spall calculated from the pullback measurements are closer to values estimated from static tensile strengths. In addition, the impact stress is not the same as the tensile stress experienced at the location of spall, which is the cause of failure. The pullback signal is a true measure of this tensile stress. Therefore, incipient spall strengths of these composite propellants and their simulants in the range of 0.175 to 0.25 kbar are good values to use in numerical modeling.

The spall strength of the UGS simulant in this study increased from a static value of just above 0.011 kbar (158 psi) to about 0.22 kbar (3200 psi) under shock loading. The fracture in UGS is similar to that discussed in H-19. The fracture runs alongside of the  $\text{NaSO}_4$  crystals and Al spheres, thus at the bond planes between them and the polymers, and through the connecting polymers. The fracture strength is reflected in the stress needed to fracture the proportion of polymer binder between solid fillers, the  $\text{NaSO}_4$  crystals and Al particles. Similar results have been found for the WAK-2 propellant. The tensile strength was reported to be near 0.007 kbar (100 psi).<sup>7</sup> The spall strength was found to be 0.33 kbar (4785). The spall strength is a result of the fracture of the double-base propellant and the strength is approximately proportional to the volume percentage of polymer material in the propellant.

In addition, it was found at SRI on studies of VRA<sup>6</sup> that the dynamic tensile strength was near 0.1 kbar (1500 psi), a factor of fifteen higher than the static tensile strength. Therefore, a spall strength of 0.33 kbar measured on a similar propellant is in good agreement with these tensile strength values.

Results from the SRI study also indicated that an impact stress of near 1.6 kbar was necessary to produce a visible spall plane in a sample. This result agrees with results from this study. However, this study has demonstrated that a spall plane may form in the sample at lower impact stresses, but that it is necessary to use a microscope at 100X to see the fracture. In addition, the value of spall strength is more properly calculated from "pullback" measurements, and these values are at least a factor of five lower than the values obtained from visible fracture at threshold impact stresses.

Finally, observations on the fracture morphology of VRA propellant at SRI<sup>6</sup> showed that fracture was initiating both within HMX grains and at the HMX-matrix interface and then propagating across the double-base propellant matrix. This result agrees with the observations of this study. The spall strength is primarily a result of fracture across the double-base propellant matrix.

The spall strengths measured for the energetic propellant, WAK-2, and its simulant, UGS, in this study, 0.33 and 0.22 kbar, respectively, are somewhat higher than those found for the composite propellant, TP-H1207C, and its simulant, H-19, 0.25, and 0.18 kbar, respectively, in the previous study. All of the materials had similar fracture characteristics and the spall strengths were in the same strength range.

## REFERENCES

1. Green, L. R.; James, E.; and Lee, E., *The Detonability of Composite Propellants*, UCRL-94174, LLNL, Livermore, CA, Feb 1986.
2. Green, L. R.; James, E.; Lee, E.; Nidick, E.; and Chambers, E., *Air Force Propellant Study*, UCID 19041, May 1981, LLNL, Livermore, CA.
3. Urtiew, P.; James, E.; and Scribner, K., *High Energy Propellant Safety (HEPS) Program, Highlights, Volume 1*, UCID 17272-79-3, 1979, LLNL, Livermore, CA.
4. Green, L. R.; Chambers, E.; James, E.; Lee, E.; and Weston, A., *Summary Report on Experimental Work Using the 155-mm Gun*, UCID 19424, Jne 1982, LLNL, Livermore, CA.
5. Speight, C. S., *Observation of Spallation and Attenuation Effects in Aluminum from Free-Surface Velocity Measurements*, FDN 4/71, AWRE, Aldermaston, England, 1971.
6. Murri, W. J.; Horie, Y.; and Curran, D. R., *Dynamic Fracture Experiments on VRA Propellant*, UCRL-15550, LLNL, Livermore, CA, Jun 1977.
7. Morton-Thiokol Inc., Wasatch Operations Memorandum, Subj: Extended Ambient Cure of H-19 Propellant, Brigham City, Utah, 12 Oct 1987.
8. Sheffield, S. A. and Dugan, D. W., "Description of a New 63-mm Diameter Gas Gun Facility," *Shock Waves in Condensed Matter*, ed. Gupta, Y. M., Plenum Press, 1986.
9. Barker, L. M. and Hollenbach, R. E., "Laser Interferometer for Measuring High Velocities of Any Reflecting Surface," *J. Appl. Phys.*, Vol. 43, No. 11, Nov 1972.
10. Hemsing, W. F., "Velocity Sensing Interferometer (VISAR) Modification," *Rev. Sci. Instrum.*, Vol. 50, No. 1, Jan 1979.
11. Kelly, F. N., "Solid Propellant Mechanical Property Testing, Failure Criteria, and Aging," *Propellants Manufacture, Hazards, and Testing*, eds. Boyers, C. and Klager, K., American Chemical Society, Washington, D.C., 1969.
12. Lee, L. M.; Jenrette, B. D.; Fogelson, D. J.; and Newcomb, C. G., *MX Stage II Impact Test Program Volume II: Equation-of-State Data for Composites, Rubber, Cork, Metal, and Propellant*, AFWL-TR-82-35, Vol. II of II, K-Tech Corporation, Albuquerque, NM, Jun 1982.

# EXPERIMENTAL STUDY AND NUMERICAL MODELING OF THERMAL IGNITION AND COMBUSTION OF HIGH HETEROGENEOUS EXPLOSIVES

C. Castille, D. Bainville, P. Reynier, and R. Beinaes  
Commissariat a L'Energie Atomique  
Centre D'Etudes de Vaujours, Moronvilliers  
BP n°7 - 77181 Courtry, FRANCE

*The study of thermal ignition and combustion propagation is one of the main topics involved in explosive safety. We present the experimental studies performed in our laboratories to examine this kind of phenomena. These thermal tests allow us to develop models and codes which can be applied to the analysis of the safety of explosive structures submitted to thermal loading.*

## INTRODUCTION

The experimental investigation and numerical simulation of the thermal ignition of the explosives and subsequent phenomena are necessary in the assessment of the hazard and vulnerability of munitions.

When submitted to thermal loading, low sensitivity explosives like TATB based, or mixed HMX-TATB compositions can exhibit slow rate decomposition reactions characteristic of the combustion process.

The analysis of this reactional scheme needs to take into account two phenomena:

- thermal ignition,
- combustion propagation.

All compositions mentioned in this paper are about 95 percent explosive and 5 percent inert binder in volume.

## EXPERIMENTAL STUDY

### Thermal Ignition

The One-Dimensional Time to Explosion (ODTX) test developed at the Lawrence Livermore National Laboratory is of great interest.<sup>1</sup> A detailed description of our experimental setup is given in Reference 2.

A spherical explosive sample is heavily confined between two steel anvils regulated to the test temperature (see Figure 1). What is measured is the time to obtain a significant reaction, (typically the breakup of the assembly) and the evolution of the decomposition gases pressure.

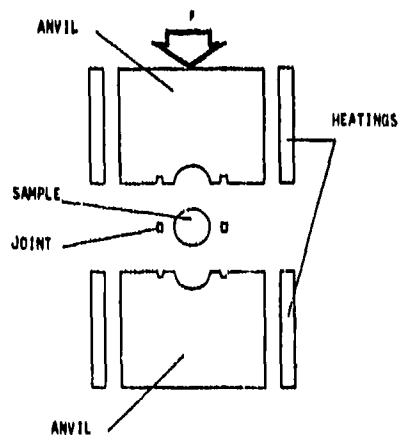


Figure 1. ODTX Test--Experimental Setup

For a given explosive or composition, the ODTX test allows the determination of the following:

- The relationship between the time to explosion ( $t$ ) and the test temperature ( $T$ ).

- The critical temperature below which no reaction occurs.

As an example, the results obtained with a TATB (T2) and a mixed TATB-HMX (TX1) explosive compositions are presented in Figure 2.

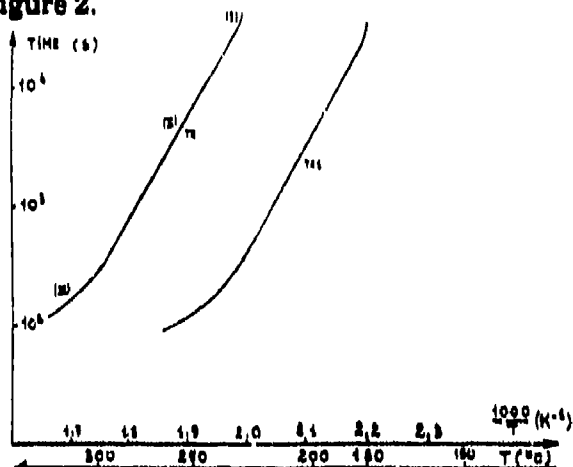


Figure 2. ODTX Experimental Results

This plot exhibits the following results:

1. The mixed composition is much more sensitive than the TATB one. In fact, we verified that a pure HMX composition would give essentially the same results as the mixed one from which we can infer that HMX determines the step at which the reaction begins. However, HMX compositions develop more violent and damaging reactions than mixed compositions, which shows the interest of these for explosive safety.

2. The  $\log(t) = f(1/T)$  curves are composed of three parts (I, II, III):

- (I) The test temperature is closed to the critical temperature and time to explosion becomes very long.
- (II) At these intermediate temperatures, the explosive samples reach thermal equilibrium and the reaction develops at the center of the sphere according to a cook off phenomenon (as shown by computations--see the Thermal Ignition section under "Numerical Simulations and Comparisons to Experimental Results").
- (III) The temperatures are high. The samples do not reach thermal equilibrium

and the reaction develops on the sphere boundary.

These different (and somewhat complex) behaviors between high and low test temperatures show that kinetics parameters cannot be deduced simply from these plots. Especially, activation energy for zeroth order Arrhenius kinetics cannot be directly determined from the linear part of the curves because conduction effects are of great importance in this range of test temperatures.

3. The critical temperature is about 230°C for the TATB composition and about 180°C for the mixed one.

However, these results are useful to compare the thermal sensitivity of different explosives and to test the validity of the kinetics of decomposition used in the numerical simulations. This latter point is one of the main interests of the ODTX test.

In order to analyze the behavior of explosives when submitted to dynamic thermal loading, we have modified the ODTX apparatus to perform another kind of experiment where the temperature rises with time all along the test at a given rate.

Another dynamic thermal loading experiment is the induction test where a cylindrical explosive sample is brought into contact with a heating plate, the temperature of which rises linearly with time (see Figure 3). Intermediate materials can be put between the heating plate and the explosive sample to simulate pyrotechnic structures. We measure the time to explosion and the temperature as a function of time at different depths in the explosive sample.

These tests are useful for explosive safety studies and for the validation of the kinetics of decomposition used in numerical simulations by comparing experimental results and computations.

The temperature rise rate can be adjusted to simulate accidental environmental conditions (e.g., wild-fires, etc.) and to study the behavior of the explosive under these conditions.

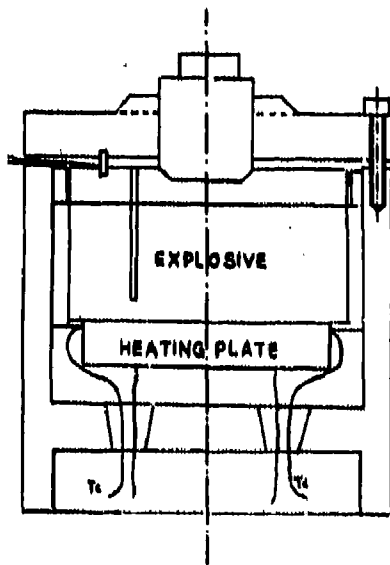


Figure 3. Induction Time Test Experimental Setup

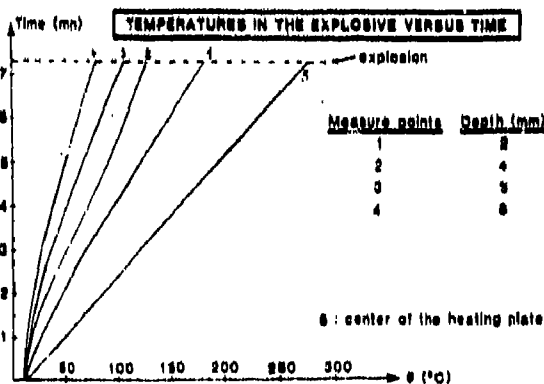


Figure 4. Induction Test--Experimental Results

The results obtained for an HMX composition X1 and a temperature rise rate of  $0.5^{\circ}\text{C}/\text{s}$  are presented in Figure 4. A strong reaction is obtained at about 7 minutes. Because of a little imperfection in the contact between the plate and the sample, the temperature in the explosive at the interface is slightly lower (about  $250^{\circ}\text{C}$ ) than the temperature at the center of the heating plate.

Nevertheless, the explosive temperature is greater than the critical value measured in the ODTX test, which is presently due to dynamic thermal loading. This fact offers a

very good point of comparison with numerical simulations.

### Combustion Process

A cylindrical explosive sample is initiated by a hot plate regulated in a furnace at the test temperature (see Figure 5). What is measured is:

- The time at which the combustion reaction begins.
- The temperature at different points of the explosive.

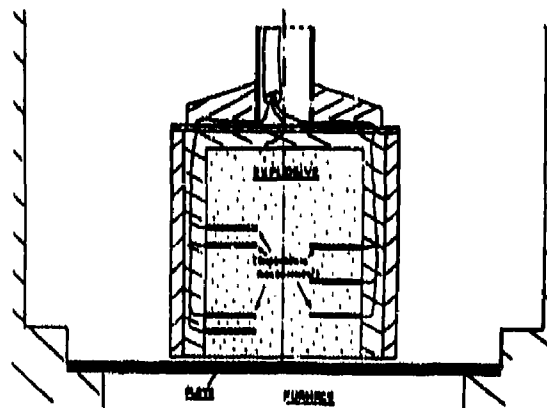


Figure 5. Combustion Test Setup

As an example of results, the temperature records obtained for composition T2 are given in Figure 6.

These measurements allow us to determine, for a given composition:

- The maximum combustion temperature ( $1100^{\circ}\text{C} \pm 50^{\circ}\text{C}$  for composition T2).
- The rate at which the combustion front propagates through the explosive ( $\sim 3.5$  mm/minute for composition T2).
- The temperature rise time when the combustion wave passes through. This kind of test is very convenient to determine physical parameters necessary for the combustion models used in numerical simulations. Similar phenomena can be obtained with TX1 composition.

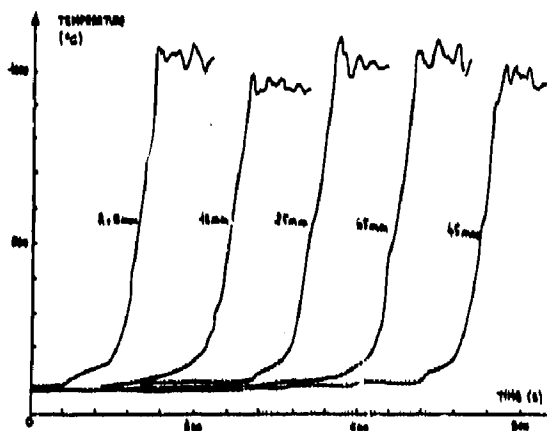


Figure 6. Combustion Test Experimental Results

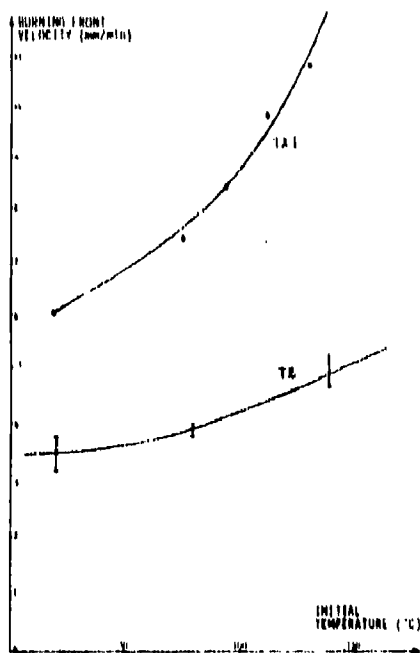


Figure 7. Influence of Initial Temperature on Burning Front Velocity

The sample can be preheated to a given temperature before the beginning of the test to study the influence of initial temperature distribution on combustion process.

An example of this influence is given in Figure 7 where we can see the increase of the burning rate as a function of the initial temperature.

This increase is greater for the mixed composition TX1 than for the TATB one, T2, and this is an important point for explosive safety.

What is important to notice too is that, for mixed compositions, the burning front velocity can be simply evaluated from the following formula (neglecting the small percentage of binder).

$$\frac{V_{\text{HMX}} + V_{\text{TATB}}}{C_M} = \frac{V_{\text{HMX}}}{C_{\text{HMX}}} + \frac{V_{\text{TATB}}}{C_{\text{TATB}}}$$

where:  $C_M$ ,  $C_{\text{HMX}}$ ,  $C_{\text{TATB}}$ , are the burning front velocities for mixed composition, and pure HMX and TATB;  $V_{\text{HMX}}$  and  $V_{\text{TATB}}$  are the volume percentages of the two explosives in the mixed composition.

This indicates that, inside this kind of composition, the HMX and TATB grains burn alternatively, which shows how TATB moderates the reaction intensity in the mixed explosives.

## NUMERICAL SIMULATIONS AND COMPARISONS TO EXPERIMENTAL RESULTS

### Thermal Ignition

We have developed a finite element code (named CAT) for the calculations of thermal ignition phenomena.

It is based on the numerical treatment of the classical heat transfer equation to which is added a special term ( $Q$ ) to take into account the exothermic decomposition of the explosive.

$$\int_V \text{div } \lambda \text{ grad } \theta \, dV + \int_V Q \, dV +$$

$$\int_S \phi \, dS = \int_V C \cdot \frac{d\theta}{dt} \cdot dV$$

- $\theta$  = temperature
- $\lambda$  = thermal conductivity
- $C$  = heat capacity
- $\phi$  = surface (S) fluxes

V = element volume  
t = time

The main capabilities of this code are:

- Two dimensional plane or axisymmetric geometries.
- Nonlinear calculations (materials conductivity and heat capacity vary with the computed temperature).
- Convection and radiation fluxes in cavities of the studied structure or in the surrounding medium.

The Q-term form depends on the kinetic chosen to describe the thermal decomposition of the studied explosives.

We used multi-staged kinetics of the same type as those developed at the LLNL,<sup>3</sup> but different in the details.

A plot of the time to explosion as a function of inverse temperature for the ODTX test is given in Figure 8 for compositions T2 and TX1.

The kinetic parameters are scaled in order to obtain a good agreement between experimental results and numerical simulations performed with CAT. The validity of the kinetics is controlled by comparisons of computations to other experimental results.

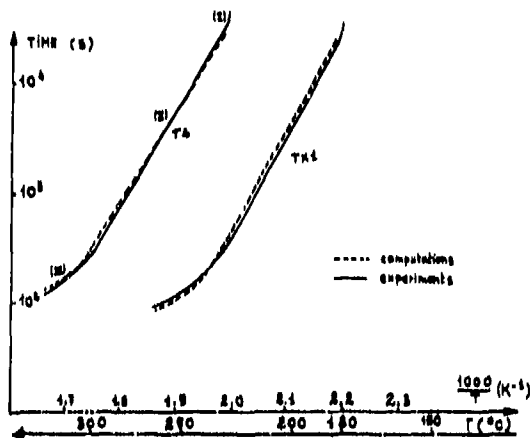


Figure 8. ODTX--Comparison Between Experiments and Computations

A plot of the temperature at various points of the explosive sample as a function of time is presented in Figure 9 in the case of the thermal induction test applied to composition X1.

We obtain a good agreement between measurements and calculations for the time to explosion and the temperature values.

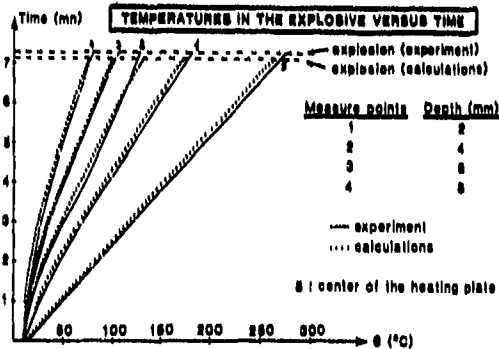


Figure 9. Induction--Comparison Between Experiments and Computations

### Combustion Process

We have modified the CAT code to implement a combustion model based on experimental observations and measurements.

The flame front velocity is fixed to its experimental value depending on temperature before the front. When it is attained by this front, an element burns, giving a heat flux  $q$  during a time  $t$  which is a function of the temperature of this element just before the front arrival. This simple model allows the use of coarse meshes which reduces time computations.

All the parameters necessary for this model are deduced from the one-dimensional combustion tests previously described.

A good agreement between computed and measured temperatures at various points of the explosive sample is obtained as shown in Figure 10, for composition T2. The little discrepancy between calculations and measurements for  $h = 15$  mm is due to an experimental imperfection (involuntary cooling of the sample).

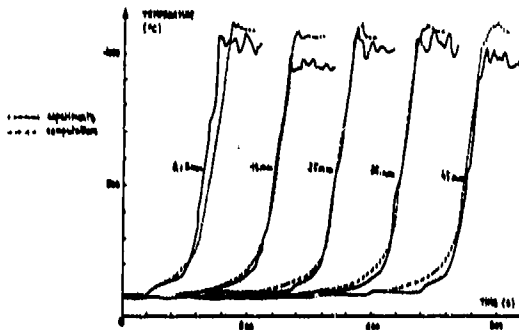


Figure 10. Combustion--Comparison Between Experiments and Computations

## CONCLUSION

We have performed experiments and developed a code, CAT, in order to analyze and simulate thermal ignition and combustion phenomena, particularly of interest in the case of low sensitivity compositions, including TATB.

The good agreement between measurements and computed results confirms the validity of the CAT code as an efficient numerical simulation tool for experimental results analysis and studies of explosive safety.

## REFERENCES

1. Catalano, E. et al., "The Thermal Decomposition and Reaction of Confined Explosive," *Sixth Symposium (International) on Detonation*, Coronado, 1976.
2. Coulonnier, G. and Reynier, P., "Essai d'induction thermique monodimensionnel sous confinement," *Congrès International de Pyrotechnie Spatiale*. Juan-les-Pins, France, 1987.
3. McGuire, R. R. and Tarver, C. M., "Chemical Decomposition Models for the Thermal Explosion of Confined HMX, TATB, RDX, and TNT Explosives," *Seventh Symposium (International) on Detonation*, Annapolis, MD, 1981.

# ELECTROSTATIC SENSITIVITY TESTING OF EXPLOSIVES AT LOS ALAMOS

Thomas E. Larson, P. Dimas, and C. E. Hannaford  
Los Alamos National Laboratory, University of California  
Los Alamos, New Mexico 87545

*An electrostatic sensitivity test for determining the handling hazards associated with both new and established explosives has been developed at Los Alamos and is now in routine use. The apparatus is a moving electrode device similar to that described by Kusler and Brown.<sup>1</sup> The energy stored in selected capacitors of a capacitor bank is discharged through the sample of explosive. A unique system of confining the samples with lead foil allows one to measure various degrees of sample response to changes in the electrostatic stimulus. Varying the foil thickness provides information about both the "sensitiveness" and the "explosiveness" of the sample. The lead-foil-confinement technique eliminates the subjective description of the response of a secondary explosive to a marginal stimulus as is common in many explosives tests on secondaries. Variables studied included: particle size, sample weight, electrode material, series resistance, temperature, voltage, sample volume, and degree of confinement.*

## INTRODUCTION

In any organization engaged in research and development on explosives, energetic materials, propellants, etc., it is necessary to develop small-scale sensitivity tests to evaluate their hazards and establish safe handling conditions to ensure personnel safety. These small-scale tests do not necessarily provide exact scientific values, but rather relative ones that depend upon the testing conditions employed. We must rely on knowledgeable, experienced personnel to interpret even the relative values in any safety assessment.

It is important in any sensitivity test, especially small scale, to avoid the temptation to attribute a greater scientific content to the results than is really present.

Most of these small tests will not scale to either larger circumstances or slightly different stimuli, so their results must be used with caution. For example, the ERL drop-weight-impact machine does not distinguish between PBX 9404 and PBX 9501. Yet, in a large-scale

skid test, the PBX 9404 has a 50 percent drop height of 1.5 m, while the value for PBX 9501 is 8 m. It required an accident in the UK to bring about development of the skid test.

Even the well-characterized gap test, which determines shock sensitivities of explosives, can have faults. If one tests explosives with very short duration shocks, one observes differences and details that cannot be found in gap-test results.<sup>2</sup>

Another problem with sensitivity tests is the demand for standardization. Standardization can result in many problems, accidents, blind acceptance of numbers, and neglect of important parameters, especially if one standardizes on the "wrong" test.

To further complicate matters, secondary explosives are more difficult to test for sensitivity characteristics than are primary explosives. The primary explosives give clear-cut responses to low-level stimuli. (Yes, they explode or No, they don't.) With secondary explosives, the response is proportional to the

stimulus up to a point where the reaction becomes self-sustaining. For example, if one hits a small sample of PETN with a hammer, it goes "bang;" if hit harder, it goes "bang" louder. Thus, in the sensitivity testing of secondary explosives, one is forced to make a decision as to what level of response is significant.

## RECENT ESD IGNITION CONCERNS

The Pershing accident in January 1985, clearly illustrates that small-scale ESD tests either do not scale or that they neglect some important parameters. The accident has been officially attributed to an ignition of the rocket propellant by an electrostatic discharge.<sup>3</sup> This propellant did not show any adverse behavior in the small-scale ESD tests used by propellant manufacturers. The French<sup>4</sup> had shown in the late 1970s that some types of propellants could be ignited by electrostatic discharges in a particular large-scale test. As a result of the Pershing accident and subsequent events, there has been a considerable effort among the propellant community to develop large-scale ESD tests. Covino and Graham<sup>5</sup> of the Naval Weapons Center have duplicated the French test and Drietzler<sup>6</sup> of the Army Missile Command has developed another large-scale ESD test. Losee<sup>7</sup> of Hercules has carried out an ESD test on a 500-pound segment of a rocket propellant under the auspices of Lockheed and the Navy. An Electrostatic Discharge Panel was formed in the JANNAF Propulsion Systems Hazard Subcommittee in 1985, and has met regularly since that time. The progress in testing, modeling, and interpretation can be found in the Proceedings of these meetings.<sup>8</sup> The French<sup>9</sup> have not observed reactions in explosive formulations using their test unless the formulations contained metal particles. We have had two DOE explosives, 9501 and 9502, subjected to the French test at the Naval Weapon Center facilities at China Lake. No reactions or ignitions occurred.<sup>10</sup>

## DESCRIPTION OF APPARATUS AND TEST VARIABLES

The method used to determine the sensitivity of an explosive to spark initiation is, in

general, to subject it to a single discharge from a condenser that has been charged to a high voltage. The energy of the discharge is varied, and by an up-and-down procedure, the energy producing initiation of the sample in 50 percent of the trials is estimated. (Bruceton method.)<sup>11</sup>

A variable (0-15 kV) power supply is used to charge the selected condensers in a condenser bank.<sup>12</sup> Any total value of capacitance from  $2 \times 10^{-4}$  to  $3 \mu\text{F}$  may be obtained by a switching arrangement that allows one to connect any of the 18 condensers in the bank in parallel.<sup>12</sup> The condenser output, in turn, is connected to a moving electrode device, similar to that of Brown, Kusler, and Gibson.<sup>13</sup> It may be described as a spring-loaded phonograph needle chuck or, perhaps more simply, as a single-stroke sewing machine. The apparatus is cocked, and a metal phonograph needle placed in the chuck. When the spring is released, the needle moves downward 31.75 mm (1- $\frac{1}{4}$  inches) and returns. The duration of this stroke is approximately 0.04 s. In all tests carried out so far, the needle has been positively charged, and the spark produced passes through the explosive sample to ground. By keeping the needle positive, corona losses are avoided.

The spark energy is taken to be the energy stored in the selected condensers,  $E = \frac{1}{2} CV^2$ , where E is the spark energy, C the capacitance, and V the applied voltage. Fifty tests were performed in which the voltage on the condensers was measured immediately after spark discharge. The voltage was found to be anywhere from less than 10 to 390 V. The condensers had originally been charged to 5000 V in the tests. Therefore, less than 0.6 percent of the energy remains after discharge.

## Sample Holders and Degree of Reaction

During preliminary experiments using this apparatus, it became evident that it was very difficult to describe the results of subjecting secondary explosives to low-energy discharges in any quantitative fashion. Therefore, special sample holders were

designed that would allow the reproducible detection of a limited amount of reaction in the sample.

Such a sample holder is shown in Figure 1. A polystyrene sleeve is cemented around a steel dowel pin, leaving a space 4.76-mm diam x 6.35-mm (3/16-inch diam x 1/4-inch) high to contain the sample. A circular piece of lead foil is placed over this opening to confine the sample. The polystyrene clamping ring, which holds the foil by the outer edges, is then clamped down over the polystyrene sleeve.

In using these sample holders, the needle punctures the lead foil and a spark is discharged through the explosive sample. A "Go" (positive event) is indicated by a ruptured foil, while a "No-Go" is evidenced by a punctured, but otherwise intact foil. The

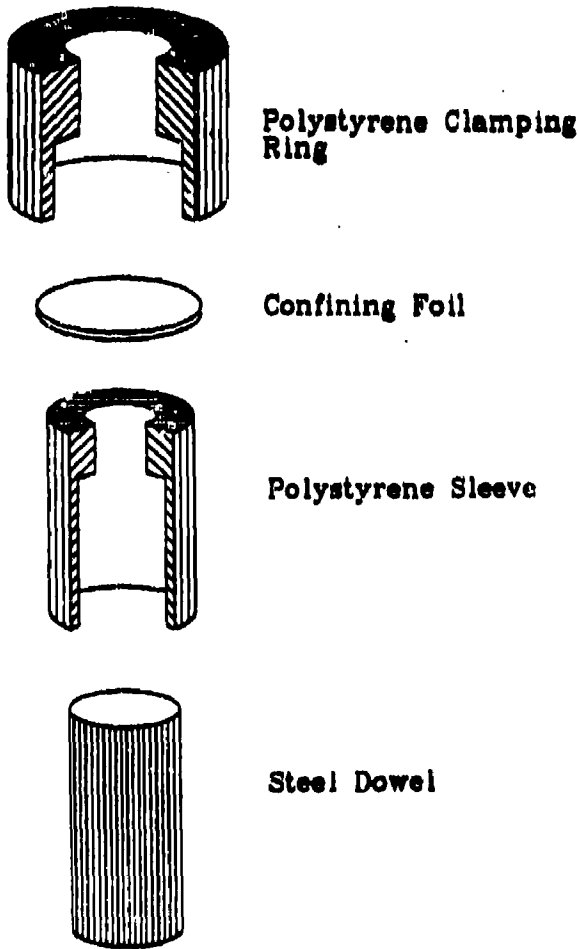


Figure 1. Exploded View of Sample Holder

degree of reaction can be changed by changing the foil thickness because as one increases the confining lead foil thickness, it should take a greater degree of reaction to provide sufficient pressure build-up to rupture the foil.

PETN was chosen as the material to study the variables involved in this test. Figure 2 shows the results of a number of experiments with several types of PETN and several degrees of confinement.

These results suggest that two types of reactions may be occurring:

- a. In the low-energy region, the amount of reaction appears to be proportional to the energy.

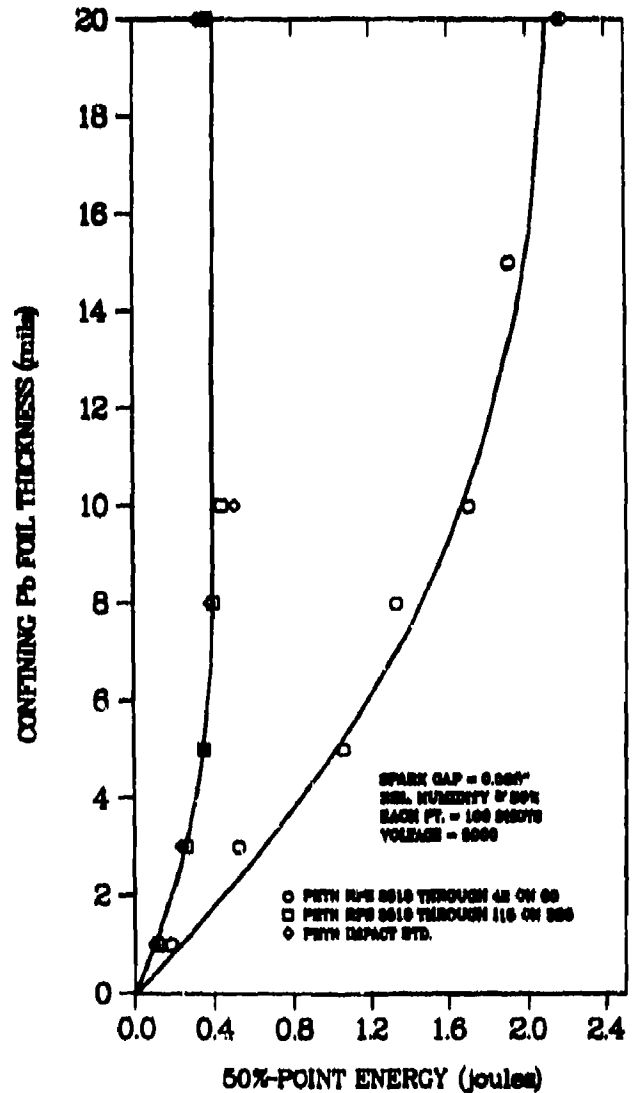


Figure 2

- b. As the energy is increased beyond a certain value, the amount of reaction is no longer proportional to the energy because a self-sustaining reaction occurs. The pressure from this reaction is sufficient to rupture the thickest foils tested. In fact, many of these reactions destroy the plastic part of the sample holder. Sample destruction is tabulated as percent explosions (% Expl.).

It can also be seen that while the fine PETN is only slightly more sensitive to a spark in the minimum reaction region, it is very much more sensitive than the coarse PETN in the violent region.

### Particle-Size Effects

In preliminary experiments, it appeared that the fines in a sample governed its sensitivity. To study this effect of the particle size of the sample in greater detail, one lot of PETN was sieved, and each fraction was tested. Table 1 shows that, as the particle size decreases, the sensitivity increases. It is interesting to note that for the minimum reaction region, the sensitivity has only increased about 1.5 times, but for the more violent reactions, the sensitivity has increased about ten fold as the particle size was decreased.

Table 1. PETN: Particle Size Effects

Sample Particle Size <sup>a</sup>	50%-Point Energy (joules)		
	1-mil Foil	10-mil Foil	% Expl.
On 35	0.162	4.0φ	0
Through 35 on 42	0.150	2.42	0
Through 42 on 60	0.165	1.83	0
Through 60 on 80	0.138	1.23	0
Through 80 on 115	0.135	1.00	15
Through 115 on 325	0.098	0.408	33

<sup>a</sup>U.S. Standard Sieve Series  
tested with steel phonograph needles

Detonator-grade PETN having a large surface area appears to be slightly less sensitive than fine crystalline PETN. A possible

explanation is that detonator material forms a kind of mat, and the spark is forced to take a longer, more circuitous path through the material that results in a lower energy density in the spark.

### Series Resistance

Other investigators<sup>14</sup> have reported that increasing the series resistance in the circuit resulted in an increase in the sensitivity of the explosives. Their studies were carried out using only primary explosives.

A series of tests was carried out using the following explosives: PETN, RDX, HMX, Pentolite, Tetryl, and TNT. Resistances of 0.1, 0.51, 1.0, 5.1, 10, 51, and 100 kΩ have been used individually in series with the spark gap. Each of the listed explosives was tested at energies of 1, 5, and 10 J. PETN, the most sensitive explosive, was also tested at 25 J. All samples were confined with a 3-mil Pb foil. In no case did a "Go" occur. When using resistances of 51 and 100 kΩ (long RC times), an examination of the PETN samples after the spark discharge clearly indicated that the samples were fused and that some melting had taken place.

The 50 percent point energies for the above materials with no added resistance range from 0.19 to 0.54 J. Thus, secondary explosives behave opposite to primary explosives in that adding resistances to the discharge circuit decreases the secondaries' sensitivities very markedly.

### Sample Weight

A series of experiments was performed with samples of PETN that weighed 30, 40, 50, 60, 75, 100, and 110 mg. The samples were confined with 1- and 10-mil Pb foils. The sensitivity of the minimum reaction samples decreased by a factor of 2, while the severe reaction samples' sensitivity increased by a factor of ~3.5. These results were explained on the basis of two competing effects of increasing the sample weight; namely, the decrease in free volume of the container, and the greater inertia of the material over the site of the ignition. The first was presumed to predominate with the thicker foil, the second

with the thin foil. This explanation was at least partially confirmed by fabricating special sample holders in which a free volume of 0.086 cm<sup>3</sup> was maintained above the bulk sample at each sample weight (lengthening the polystyrene sleeve). The same sample weights mentioned above were tested with the modified sample holders. The variation of the results with sample weight were reduced considerably in these tests, indicating that our explanations were confirmed, and that a constant free volume in the loaded sample holder was desirable. As a result of this set of experiments, we chose to standardize on constant-volume samples.

## STANDARDIZATION AND RESULTS

As a result of our studies, we chose a set of conditions that were used as a routine version of the spark-sensitivity test. These conditions are listed below:

- a. Tests would be run using two different foil thicknesses, a thin foil (3 mils) and a thicker foil (10 mils). The data from the thin foil confinement would be used for the evaluation of hazards, while the test using the thicker foil confinement would provide information about the severity of the reaction.
- b. Brass pins would be used as the upper electrode rather than steel phonograph needles. Experiments showed that the variation in the sensitivity of PETN with sample weight is less when brass pins are used as the upper electrode.
- c. Experiments with PETN have shown that its spark sensitivity is very dependent upon the particle size of the sample. Therefore, it may be necessary to specify particle size when comparing a series of explosives. On the other hand, in evaluating a material for hazards it should be tested "as received," because it is handled in this form.
- d. Samples are scooped to a constant volume rather than weighed. Results

in the last section indicate that maintaining a constant free volume in the sample holder results in less dependence of the sensitivity upon the sample weight.

- e. A voltage of 5,000 is standard. Energy is taken as  $\frac{1}{2} CV^2$  and is changed by varying the capacitance. Limited studies on PETN showed that energy, not voltage, was the important quantity.

We have tested our "impact standard" explosives over the years in our routine version of the test. Table 2 gives typical results.

At Los Alamos, we use many molding powders that are pressed into large pieces. Electrostatic discharges have been thought to be less of a hazard with consolidated charges than with powdered explosives. (This may no longer be valid in view of the past few year's experience with propellants.) Therefore, we prefer to test an explosive in the most sensitive form in which it is handled. In the case of many molding powders, the agglomerates or pellets are too large to fit into our sample holders. Therefore, we decided to test these materials in the form of chips and turnings from machined charges. This is actually a commonly occurring condition, since there are still facilities where these materials are machined dry. The materials were tested under our standard conditions, previously out-lined. Samples were scooped to a constant volume, where volume,

Table 2. Common Explosives

Material	50% Point Energy (joules)		% Expl.
	3-mil Foil	10-mil Foil	
PETN (DuPont)	0.19	0.75	8
RDX (Impact Std)	0.21	0.96	0
HMX (Impact Std)	0.23	1.42	23
Tetryl (Impact Std)	0.54	3.79	42
TNT (Impact Std)	0.46	3.75	0
PYX	1.18	9.00	0
DATB (Lot 11426)	1.48	10.79	0
TATB (X-398)	4.25	18.14	0
max. human static charge % 0.015 joules <sup>1</sup>			

where possible, and yielded samples weighing 27-30 mg. Otherwise, 30-mg samples were weighed and loaded. These results are given in Table 3.

**Table 3. Molding Powders  
(Machined Turnings)**

Material	50% Point Energy (joules)		% Expl.
	3-mil Foil	10-mil Foil	
Pentolite	0.32	1.96	15
75/25 Cyclotol	0.38	3.29	23
PBX 9404	0.42	3.13	0
PBX 9205	0.55	1.37	42
Comp A	0.63	4.38	0
PBX 9407	0.77	1.50	50
PBX 9010	0.79	1.53	54
Octol	0.82	4.63	17
PBX 9501	0.84	2.52	78
LX-04	1.04	2.58	38
PBX 9011	1.09	2.77	33

The materials are listed in order of decreasing sensitivity as determined by the rupture of a 3-mil Pb foil. This is a minimum type of reaction. If the 10-mil Pb foil results were used, an entirely different order would result, with the RDX-based explosives being the most sensitive materials.

### Heated Samples

In some cases, it is desirable to test materials at temperatures above room temperature. This allows one to evaluate hazards that may exist during the processing of these materials (for example, molding powders at their preheat temperatures). In this variation of the test, each sample holder is fitted with a heat reservoir, which consists of a steel block 25.4-mm diam x 19.1-mm (1-inch diam x 3/4 inch) high drilled to receive the dowel pin of the standard sample holder. The sample-holder/heat-reservoir assembly is heated to the desired temperature in an oven, then rapidly transferred to the firing chamber and tested. It was found that when the sample-holder/heat-reservoir assembly was removed from an oven at 160°C, the temperature dropped at a rate of ~0.2°C/s for the first several

minutes. The average time from removal from the oven to firing is about 15 s. In elevated temperature testing, the polystyrene sample holders are replaced by identical Teflon holders.

Tables 4 and 5 show the results obtained when testing several common military explosives and typical DOE molding powders as a function of increasing temperature. It can be seen that the sensitivity increases somewhat as a function of temperature. The major effect appears to be the severity of the reaction when confined with a 10-mil Pb foil. The percent explosion increases, and the degree of reaction to shatter a Teflon holder is considerably greater than that required for destruction of one fabricated from polystyrene.

**Table 4. Heated Explosives**

Temperature (°C)	50%-Point Energy (joules)		% Expl.
	3-mil Foil	10-mil Foil	
<b>PETN (Trojan Barrel No. 1)</b>			
22	0.25	0.70	50 <sup>a</sup>
50	0.24	0.78	42 <sup>b</sup>
75	0.21	0.70	15 <sup>b</sup>
100	0.18	0.60	42 <sup>b</sup>
125	0.26	0.79	40 <sup>b</sup>
<b>RDX (Wabash Ground)</b>			
22	0.27	1.88	8.3 <sup>a</sup>
75	0.18	1.05	7.7 <sup>b</sup>
125	0.18	0.93	23.0 <sup>b</sup>
175	0.10	0.37	92.0 <sup>b</sup>
<b>HMX (88-63)</b>			
22	0.26	1.12	75 <sup>a</sup>
75	0.26	1.03	0 <sup>b</sup>
125	0.19	0.80	0 <sup>b</sup>
175	0.12	0.52	25 <sup>b</sup>
200	0.125	0.36	54 <sup>b</sup>

<sup>a</sup>Polystyrene holders  
<sup>b</sup>Teflon holders

### Materials Exhibiting Anomalous Behavior

Since testing was begun at Los Alamos, we have found a number of materials that behave somewhat differently than our usual

explosives and molding powders. Some of these are listed in Table 6.

Cedesol 10 is a double cesium nitrate salt of decaborane. It always exploded at the lowest energies we could supply from

Table 5. Heated Molding Powders

Temperature (°C)	50%-Point Energy (joules)		% Expl.
	3-mil Foil	10-mil Foil	
<b>Composition A</b>			
22	0.63	4.38	0 <sup>a</sup>
50	0.42	4.75	0 <sup>b</sup>
75	0.51	6.75	0 <sup>b</sup>
125	0.58	5.25	0 <sup>b</sup>
<b>9404 (94/3/3 - HMX/NC/CEF)</b>			
22	0.42	3.13	0 <sup>a</sup>
75	0.33	3.25	0 <sup>b</sup>
125	0.30	2.50	0 <sup>b</sup>
175	0.24	1.92	25 <sup>b</sup>
<b>LX-04 (85/15 - HMX/Viton)</b>			
22	1.04	2.58	38 <sup>a</sup>
75	0.78	2.35	0 <sup>b</sup>
125	0.73	2.10	42 <sup>b</sup>
175	0.65	2.15	31 <sup>b</sup>
<b>9407 (94/6 - RDX/Exon)</b>			
22	0.77	1.50	50 <sup>a</sup>
75	0.53	1.14	0 <sup>b</sup>
125	0.45	1.01	35 <sup>b</sup>
175	0.43	1.02	31 <sup>b</sup>

<sup>a</sup>Polystyrene holders  
<sup>b</sup>Teflon holders

Table 6. Anomalous Materials

Material	50% Point Energy (joules)		% Expl.
	3-mil Foil	10-mil Foil	
Cedesol 10	(same value for 0 and 1 mil)		0.0025 ---
Heat Powder 88/12	0.018	0.019	---
TVB	0.02	(same value unconfined)	---
B/KNO <sub>3</sub>	0.23	0.32	---
ZPCP	0.31 (17% Expl)	0.40	100
BTF (HNB)	0.14	0.19	85.7
Pentanitroaniline	0.21	0.31	75
4-Nitro-1-picryl-1,2,3,1H-triazole	0.24	0.23	100
KHND	0.51	0.43	67
K Picrate	0.73	0.54	100

our equipment. The value of 0.0025 J is ~1/6 of the energy that can be built up on a human. In fact, we set the material off by sliding out of a chair. It also had an impact sensitivity of 4-7 cm drop height. The material behaves like a primary explosive in these two tests. It is believed to be an ingredient of Hivelite, which has been implicated in several accidents.

The next three materials are best classed as pyrotechnics. One of their characteristics is that once a reaction starts, the entire sample is consumed. Both the heat powder and Ti/B igniter have sensitivity values similar to human electrostatic energies.

ZPCP, BTF, and pentanitroaniline all transform into very vigorous reactions with only a slight increase of energy. This behavior is more typical of the behavior of a primary explosive and care should be exercised with these materials. The latter two materials, BTF and pentanitroaniline, have threshold sensitivities similar to that of PETN.

KHND, potassium picrate, and the triazole are anomalous in that they require less energy to cause a reaction under heavier confinement. These reactions are also much more severe than those with light confinement, as shown by the sample holder destruction. While none of three materials are unduly sensitive, one would predict that in an accident, propagation would occur that could lead to serious results.

## GLOSSARY AND COMPOSITIONS

B/KNO <sub>3</sub>	18/82 wt%
BTF	benzotrifuroxan
Cedesol 10	B <sub>10</sub> H <sub>12</sub> (CsNO <sub>3</sub> ) <sub>2</sub>
Comp A	RDX/Wax 91/9 wt%
75/25 Cyclotol	RDX/TNT 75/25 wt%
Heat Powder	Fe/KClO <sub>4</sub> 88/12 wt%
KHND	potassium salt of hexanitrodiphenylamine
LX-04	HMX/Viton A 85/15 wt%
Octol	HMX/TNT 75/25 wt%
PBX 9010	RDX/Kel-F 90/10 wt%

PBX 9011 HMX/Estane 90/10 wt%  
 PBX 9205 RDX/polystyrene/dioctyl-  
 thalate 92/6/2 wt%  
 PBX 9404 HMX/nitrocellulose/  
 chloroethyl-phosphate  
 94/3/3 wt%  
 PBX 9407 RDX/Exon 461 94/6 wt%  
 PBX 9501 HMX/dinitropropyl acetal -  
 formal/Estane 95/2.5/2/5  
 wt%  
 PYX 2,6-bis(picrylamino)-3,5-  
 dinitropyridine  
 T/B 68/32 wt%  
 ZPCP azidopentamine cobalt  
 (III) perchlorate

## REFERENCES

1. Brown, F. W.; Kusler, D. J.; and Gibson, F. C., Bureau of Mines, RI 5002.
2. Rabie, R. L., Los Alamos National Laboratory, private communication, Jun 1982.
3. Pershing II Accident Report - white sheet handed out in Germany, 23 Apr 1985, and at the Pentagon, 24 Apr 1985.
4. Kent, R. and Rat, R., SNPE, "Static Electricity Phenomena in the Manufacture of Solid Propellants," 20th Explosive Seminar, AD-A124 400, 26 Aug 1982.
5. Covino, J. and Graham, K. J., "Methodology and Apparatus for ESD Sensitivity Testing of Solid Rocket Propellants at the Naval Weapons Center," NWC TP 8716, Aug 1986.
6. Mellor, T. M. and Drietzler, D., "Hazards Initiation in Solid Rocket and Gun Propellants and Explosives Progress," *Energy and Combustion Science*, Vol. 14, No. 3, 1988.
7. Losee, L., private communication, 1989.
8. Chemical Propulsion Information Agency, The John Hopkins University, Applied Physics Laboratory, Laurel, MD.

9. Kent, R. (France), private communication, Oct 1985.
10. Contract between Los Alamos and the Naval Weapon Center, DE-A1 32-87AL 43224.
11. Dixon, W. J. and Mood, A. M., *J. American Stat. Assoc.*, Vol. 43, 1948, p. 109.
12. Los Alamos Drawing Numbers 4Y 40403, 4Y-40410 D-11.
13. Los Alamos Drawing Number 27Y-81341 D-1-E.
14. Wyatt, R. M. H.; Moore, P. W. J.; Adams, G. K.; and Sumner, J. F., *Proc. Roy. Soc., Series A*, No. 1245, Jul 1958, p. 189.

## DISCUSSION

HAUS J. PASURAX, PML-TMO, NL  
 Rijswijk, Holland

Did you vary and optimize the duration of the spark? I ask this because you made the comparison with the potential energy the human body can produce and it is known that, e.g., for combustible dust materials, it makes much difference whether you have a short or longer duration spark.

## REPLY BY T. E. LARSON

This is discussed in the "Series Resistance" section of the paper.

## DISCUSSION

HAROLD GRYPING,  
 Gryping Energetics Sciences Co.  
 San Antonio, TX

How do these tests order common explosives and propellants compared to the more usual electrostatic tests? Are there any order reversals?

## REPLY BY T. E. LARSON

We have not compared the results from our test with other electrostatic tests. The results from other tests may be found in the *Proceedings of JANNAF Hazards Subcommittee* and other explosives literature.

# MOLECULE-SURFACE COLLISION-INDUCED EXCITATION AND DISSOCIATION: $n,i$ - $C_3F_7NO$ , $C_6F_5NO$ , 2-METHYL,5-VINYLTETRAZOLE AND $C(NO_2)_4$ WITH $MgO(100)$ SURFACES AT $E_{incident} \leq 7.5$ eV

E. Kolodney, P. S. Powers, L. Iwata, H. Reisler, and C. Wittig  
Department of Chemistry  
University of Southern California  
Los Angeles, California 90089-0482

and

I. B. Mishra  
Kanan Associates  
2925 Churchville Road  
Churchville, Maryland 21028

and

C. Capellos  
ARDEC  
Picatinny Arsenal, New Jersey 07849

*A technique is described in which neutral polyatomic molecules are accelerated aerodynamically to velocities  $\sim 3 \times 10^5$  cm s<sup>-1</sup>, corresponding to lab kinetic energies up to 7.5 eV, using 300 K H<sub>2</sub> or He carriers. Collisions with MgO(100) surfaces then excite a sizable fraction of the incident molecules to energies above  $D_0$ , and subsequent decomposition is monitored state selectively using laser photoionization. Processes examined include excitation, dissociation via simple bond fission, and dissociation via nitro  $\rightarrow$  nitrite rearrangement followed by bond fission. It appears that reactions occur via low energy pathways, thus providing a valuable diagnostic, and a rough statistical model is in qualitative agreement with the initial results.*

## INTRODUCTION

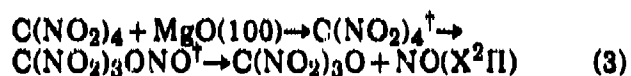
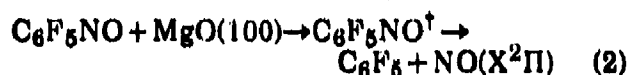
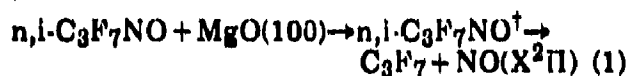
Collisional energy transfer between gaseous species during binary encounters is of both scientific and technological importance, spanning a wide range of energies and touching areas as diverse as laser development and mass spectroscopy. With center-of-mass (c.m.) collision energies below  $\sim 100$  eV, the exchange of translational and internal energies has been shown to be very efficient in collisions of polyatomic ions with small neutrals [e.g.,  $C_3H_5X^+ + N_2(Ar)$ ],<sup>1</sup> with observed thresholds corresponding to known reaction endoergies, rapidly-increasing reaction cross sections above threshold, and saturation of the reaction cross sections at close to the hard sphere values.<sup>2</sup> Although it is thought that perhaps not all of the degrees of freedom are randomized in the collision, the subsequent fragmentation of the energized molecular ions can be described as

statistical unimolecular decomposition, following the rules of RRKM/QET models.<sup>3</sup> In retrospect, it is not surprising that T $\rightarrow$ V transfer is efficient at collision energies of at least several eV, since distortion of the molecular frame is necessarily severe, and the requirements for elasticity carry the burden of entropic deficiency. High energy collisions ( $> 1$  keV), on the other hand, have relatively low reaction cross sections, which can be attributed to electronic excitation followed by internal conversion and unimolecular decomposition.<sup>4</sup> Key issues that remain in the low-energy ion-molecule collisions are the fraction of the collision energy lost per event, how it varies with collision energy, and how it depends on the nature of the collision partner.

In molecule-surface collisions at incident energies as high as 7.5 eV (i.e., those used in the present study), many of the above issues

and questions remain valid. One cannot overlook the obvious fact that serious distortions of the molecular and crystal structures can result from such encounters, and that this can lead to efficient conversion of molecular translational motion in the laboratory system into lattice phonons and molecular V,R excitation in the rebounding molecule.

The efficacious promotion of molecular vibrational excitation in inelastically scattered species can thus be anticipated, based on similarities to the previously-studied gas-phase systems and the mechanical principles common to both systems. It is with this background and perspective that we present here the first examples of molecule-surface collision-induced dissociation (CID) experiments in which state-resolved reaction product excitations are observed under UHV conditions using well-characterized, chemically-inert MgO(100) surfaces:



A schematic drawing that indicates the molecule-surface collision for the case of  $n-C_3F_7NO$  is given in Figure 1. In each case,

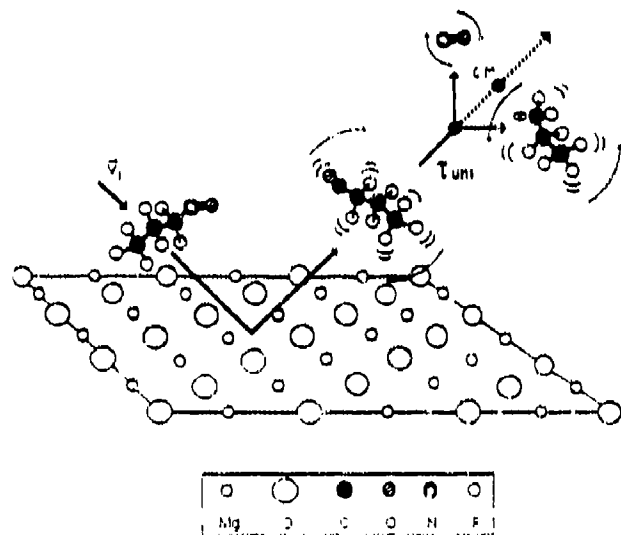


Figure 1. A Polyatomic Molecule, in this Case  $n-C_3F_7NO$ , Moves Toward the Surface with High Incident Kinetic Energy, Undergoes a Collision with the Surface that Leaves the Molecule Internally Excited, and Subsequently Decomposes

we observe the  $NO(X^2\Pi)$  product with full state resolution following high-energy impact, using 2-frequency, 2-photon laser ionization, and assign its parentage to the decomposition of excited parent molecules that have scattered inelastically from the surface. Signals increase sharply with collision energy, and reaction probabilities as high as several percent are reported. Several possible mechanisms may participate in CID under the present experimental conditions. A model is described in which inelastically scattered parent species obtain substantial vibrational excitation from the impulsive molecule-surface collision, with conversion of a large fraction of the incident translational energy to molecular and crystal excitations. This excitation is assumed to be randomized amongst the molecular and some of the crystal vibrations, in accord with the rapid intramolecular vibrational redistribution (IVR) that is common to large molecules. Although qualitative and empirically-based, the model agrees with the observed rapid increase of the signal with collision energy and the nearly-statistical NO internal state distributions. It predicts that the technique may be a generally applicable and useful means of energizing large polyatomics under well-characterized conditions in order to study decomposition pathways, mechanisms and kinetics.

In the material that follows, we first give a detailed description of the experimental arrangement and procedures, as this has not been done previously. CID results are then presented for  $C_3F_7NO$  and  $C_6F_5NO$ , where simple bond fission occurs. Next, tetranitromethane decomposition involving nitro→nitrite rearrangement is shown to occur, underscoring the viability of the method for perusing the low-energy decomposition channels. MVT, a polymeric binder, is then shown to undergo dramatic excitation (possibly dissociation) at a collision energy of only 3.6 eV. Next, detailed photodissociation results are presented for the case of  $C_3F_7NO$ . These can be invaluable in helping assign a mechanism(s) for the CID process. Finally, a simple model is presented, and future work is discussed.

## EXPERIMENTAL ARRANGEMENTS

### Molecule-Surface Collision-Induced Dissociation

The CID experimental arrangement involves a pulsed, seeded ( $H_2$  or He carrier),

supersonic molecular beam source that is mated via a differentially-pumped region to a UHV chamber containing the MgO(100) crystal. The central and UHV regions are bakable to 200°C and can be isolated from the source region. Schematic drawings of the overall arrangement are shown in Figures 2 through 4, and Figure 5 depicts the most salient features of the experiment—namely, the incident and scattered molecular beams and the laser detection regions (darkened circles). The source region is pumped by a standard diffusion pump (VHS-6), while the main scattering chamber is pumped by a *very carefully* LN<sub>2</sub> trapped and isolated Alcatel 150 diffusion pump, which is backed by another diffusion pump, in order to increase the compression

ratio for pumping light gases, and several vapor traps. This allows all molecular beam constituents, including the light He and H<sub>2</sub> carriers, to be efficiently removed between pulses. The base pressure is  $\sim 2 \times 10^{-10}$  Torr, and after two years, there are still no signs of pump oil in the mass spectra. A small ion pump (Perkin Elmer 25) maintains UHV when the system is not in use. The central region between the source and UHV chambers has laser beam ports and an ion detector for molecular beam diagnostics.

The pulsed, piezoelectrically-driven valve (Laser Technics, 0.5 mm diameter) is operated in a choked-flow regime (effective diameter = 0.2 mm) because of the small plunger movement ( $\sim 30 \mu\text{m}$ ). Temporal pulse widths were typically 100-150  $\mu\text{s}$ . These long pulse

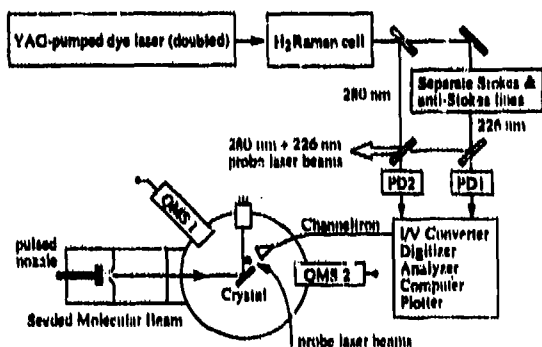


Figure 2. Schematic Drawing of the Overall Experimental Arrangement for Molecule-Surface CID Studies

#### UHV Surface Scattering Apparatus

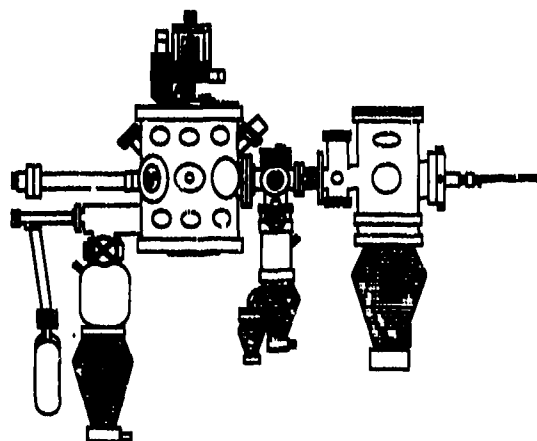


Figure 3. Sketch of the Collision Chamber Arrangement Shown Schematically in Figure 2 (Side View). The probe laser beams (not shown) enter from the bottom of the UHV Portion. The nozzle-surface distance is 43 cm.

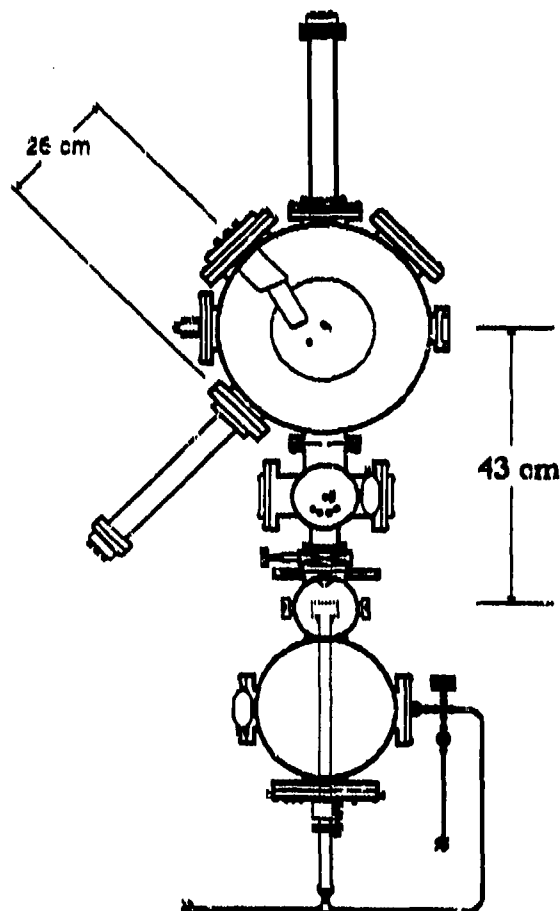
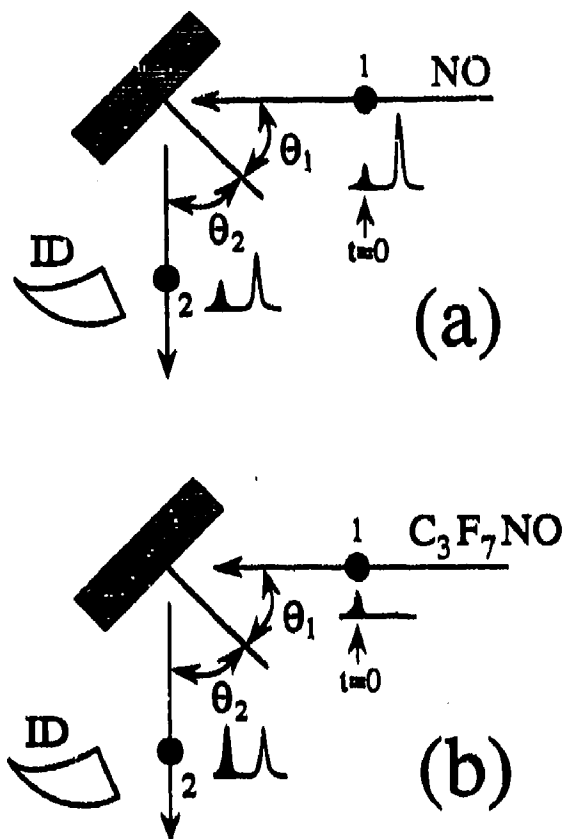


Figure 4. Sketch of the Collision Chamber Arrangement Shown Schematically in Figure 2 (Top View)



**Figure 5. Schematic Drawing Showing Probe/Surface Configurations for (a) Detecting Scattered NO from an Incident Beam of Known Composition and (b) Detecting NO Following CID of  $C_3F_7NO$ ,  $C(NO_2)_4$ , etc. (ID = channeltron). The  $t = 0$  pulse (darkened) appears concomitantly with the firing of the probe beams, and is probably due to photons striking the channeltron. These arrangements are used to estimate the CID efficiency.**

durations, as well as velocity inhomogeneities in the leading and trailing edges of the beam, precluded meaningful velocity analyses of the scattered beam. In order to quantify the velocity distribution of the incident beam, NO was seeded in a light carrier (e.g., 1 percent in He) and detected state selectively (see below) at two points spaced 20 cm apart along the beam axis, i.e., in the center of the buffer chamber and 10 mm from the surface in the scattering chamber. By recording the NO density profiles at these points, the velocity distribution could be obtained quite accurately, and leading and trailing-edge effects were seen to be minor. In addition, the steep dependence of the CID probability on  $E_{\text{incident}}$  discriminates against

the lower velocities in the incoming beam. We conclude that contributions from velocity inhomogeneities in the beam pulse are within the experimental uncertainty of the  $E_{\text{incident}}$  measurements, as discussed below.

The valve was mounted on an XYZ translation stage and could be resistively heated to  $120^\circ\text{C}$  continuously under normal operating conditions, and heated intermittently to  $160^\circ\text{C}$  using differential heating. The main problem encountered at high temperatures was failure of the glue that holds the plunger to the piezoelectric disc. The expansion was skimmed using thin nickel electroformed skimmers (Beam Dynamics, 0.8-1.5 mm orifices), and the optimal nozzle-skimmer distance (typically 12-15 mm) depended on the skimmer orifice and the nozzle throughput. The skimmed beam was further collimated by a 1.2 mm x 4.0 mm slit as it entered the main scattering chamber.

The incident molecular beam was scattered from a cleaved, single-crystal  $MgO(100)$  surface (Atomergic, 10 mm x 10 mm x 1 mm). The beam was scattered from the center of the surface and its dimension at the surface was 1.6 mm x 6.0 mm. The crystal was x-ray analyzed in order to determine the plane and azimuthal directions prior to mounting. Once inside the UHV chamber, the crystal was annealed at 1100-1200 K for several hours, and fast Ar-atom bombardment (Ion Tech) was sometimes used to clean the surface before thermal annealing. The crystal holder, which was made of tantalum and molybdenum, provided for resistive heating of the crystal up to 1600 K.

This arrangement and cleaning procedure resulted in reliable He diffraction patterns and a sharp, background-free Xe scattering angular distribution ( $8^\circ$  FWHM at  $E_{\text{incident}} = 2.1$  eV), as shown in Figure 6. Although He diffraction was characterized by a substantial amount of incoherent elastic background, as expected for cleaved surfaces,<sup>6</sup> Xe scattering was essentially background-free, indicative of an atomically clean surface, as seen by the physically large and heavy collider. In order to ensure surface cleanliness (adsorbate-free and direct scattering conditions), the surface temperature,  $T_s$ , was maintained at 600 K during all experiments, except those in which  $T_s$ -dependences were investigated. None of the results reported here depended strongly on temperature in the range 400-600 K, reflecting the impulsive nature of the scattering process,

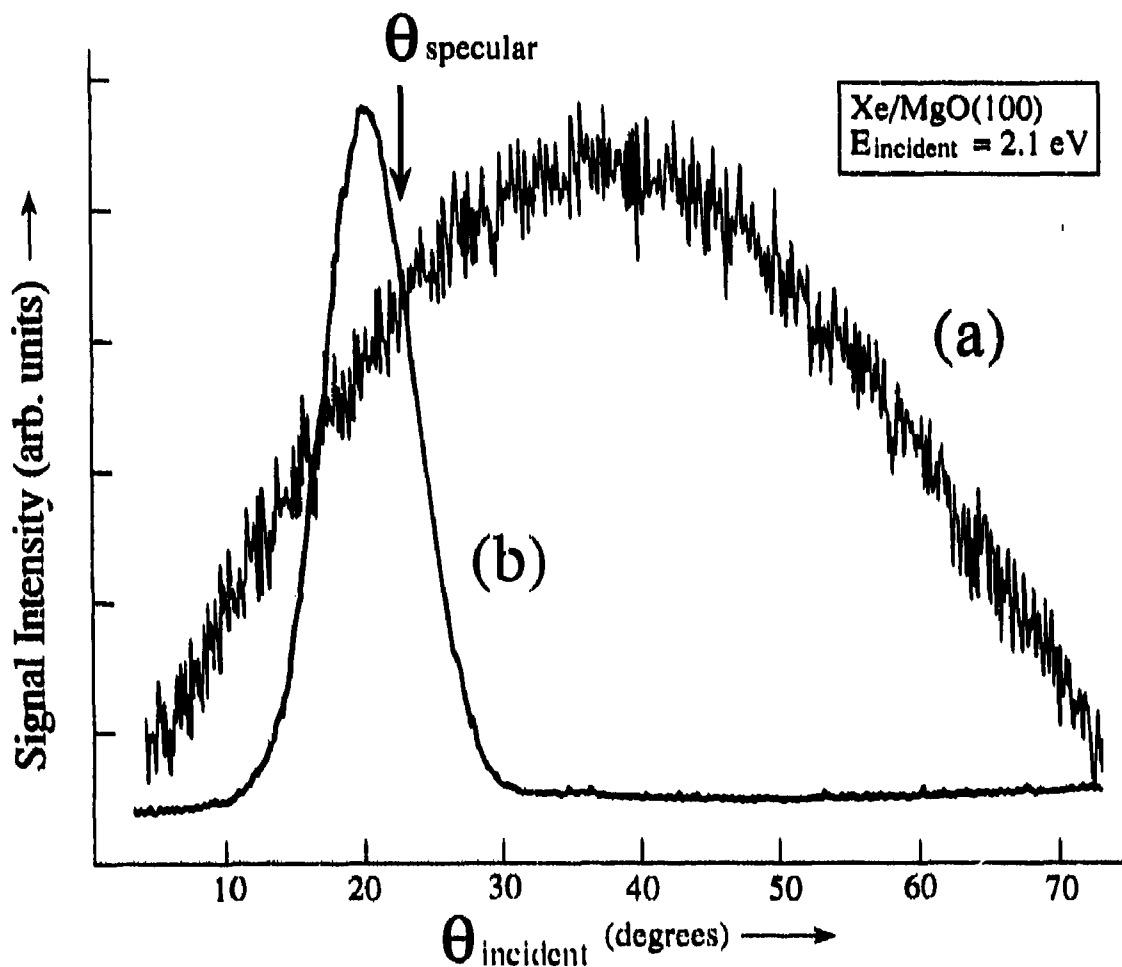


Figure 6. Scattering of Xe with  $E = 2.1$  eV from (a) a Dirty Surface and (b) a Clean Surface

although preliminary measurements in our laboratory indicate that dissociation efficiency increases with  $T_s$ , particularly above 700 K.<sup>6</sup>

The beam was scattered from the surface center, and as mentioned above, the geometries of the skimmer and slit resulted in a beam shape at the surface which could be approximated by a 1.6 mm x 6.0 mm rectangle—meaningfully smaller than the effective (weighted by a cosine projection factor) surface dimensions (7.5 mm x 10 mm). The rectangular beam offers several advantages over a circular one: (a) the rectangular shape matches the shape and area of the rotating square surface, while scattering from the surface holder in the slit lateral plane (scattering plane) is avoided; (b) increasing the beam size in the slit longitudinal direction provides larger signals, while not degrading the in-plane angular resolution;

(c) the rectangular density profile approximately matches the effective ionization zone, since the probe laser is mildly focused (150 cm focal length), resulting in an increased depth of field.

### Xe Scattering

We found that Xe scattering at  $E_{\text{incident}}$  values of 1-5 eV was quite useful for characterizing surface conditions for collisions of heavy molecules with the surface. The angular scattering width narrows with increasing  $E_{\text{incident}}$  (e.g., 8° FWHM at 2.1 eV vs. 6° FWHM at 3.6 eV) without any background contribution. At such energies, no surface damage was observed, as opposed to fast atom bombardment with  $E_{\text{incident}} \geq 10$  eV.<sup>7</sup> We also studied the scattering of lower energy Xe atoms ( $E_{\text{incident}} = 2.1$  eV) from partially contaminated

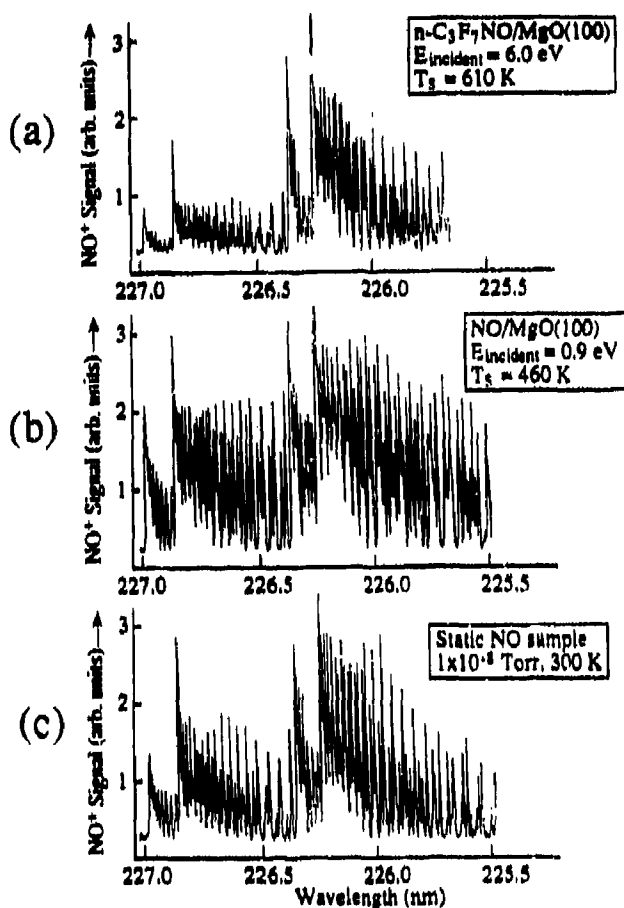


Figure 7.  $\text{NO } A^2\Sigma \leftarrow X^2\Pi$  2-Photon, 2-Frequency Photolization Spectra. (a) NO is detected 12 mm from the 610 K surface using  $\text{C}_3\text{F}_7\text{NO}$  at  $E_{\text{incident}} = 6 \text{ eV}$ . (b) NO is scattered inelastically from the 460 K surface at  $E_{\text{incident}} = 0.9 \text{ eV}$ . (c) A room-temperature, static NO sample can be used for calibrations.

300 K NO, which is always good to have on hand for calibration and comparisons.

It should be pointed out that the inadvertent detection of NO as a photodissociation product (i.e.,  $\text{RNO} + h\nu(226 \text{ nm}) \rightarrow \text{R} + \text{NO}(X^2\Pi)$ , followed by  $\text{NO}(X^2\Pi) + h\nu(226 \text{ nm}) \rightarrow \text{NO}(A^2\Sigma)$ ;  $\text{NO}(A^2\Sigma) + h\nu(280 \text{ nm}) \rightarrow \text{NO}^+ + e$ ) is a 3-photon process, requiring two 226 nm photons, and its probability is, therefore, negligible under the present experimental conditions. An experimental verification of this is given in the Experimental Results section. In the present experiments, 2-photon photoionization with two 226 nm photons was < 1 percent as efficient as 2-photon 226 + 280 nm photoionization.

The probe beams entered the main scattering chamber from the bottom through a 6 cm diameter sapphire window, crossing the

scattering plane at right angles, for an in-plane angular resolution of approximately  $8^\circ$  and full integration out of plane (i.e., along the long dimension of the rectangular scattered beam profile). For increased angular resolution, the laser beams were moved as much as 4 cm from the surface. Both probe beams were either collimated or mildly focused using a 150 cm focal length lens. Ions were collected with a channeltron (Galileo) whose output was amplified, digitized, and sent to the computer system.

### Controlling and Varying $E_{\text{incident}}$

$E_{\text{incident}}$  values for the heavy molecules were varied using aerodynamic acceleration in seeded beams ( $\text{H}_2$  or He carriers) with small amounts of Ar used for deceleration. Typical dilution ratios in  $\text{H}_2$  or He were 1:300 to 1:600. Nozzle heating was limited to about  $75^\circ\text{C}$  because of  $\text{C}_3\text{F}_7\text{NO}$  thermal decomposition; 10 percent dissociation at  $95^\circ\text{C}$  was observed. Thus, all  $E_{\text{incident}}$  values up to 6 eV were obtained with the nozzle at room temperature. Beam velocities were determined using the TOF technique, measuring the time delay between the valve's electrical trigger and the peak of the gas pulse arriving at the QMS ionizer, located 76 cm downstream from the nozzle orifice. Reliable measurements were essential due to the existence of considerable velocity slip in seeded beams with mass ratios as high as 100.<sup>10</sup> The main problem arising in accurate TOF measurements using the Laser Technics pulsed valve was estimating the electromechanical response time. Since it was found that this delay depends on plunger amplitude and backing pressure, each TOF measurement was preceded by a set of calibration measurements with neat He and Ar beams, for which the terminal supersonic velocities for 300 K expansions are known. The ion TOF in the QMS was calculated iteratively and subtracted from the measured delay. We have also compared the kinetic energies determined using this procedure with the more accurate laser-TOF measurements, where the beam contour was obtained using NO photoionization vs. the valve-laser delay at points along the beam path 20 cm apart, as described above. Good agreement between the two methods was found when compared for different  $\text{H}_2/\text{NO}$  mixtures.

### Photodissociation of Expansion-Cooled $\text{C}_3\text{F}_7\text{NO}$

The experimental arrangement that was used to study the collision-free 1-photon

photolysis of expansion-cooled  $C_3F_7NO$  has been described previously,<sup>11</sup> and only those aspects germane to the present measurements are given here. A schematic drawing is given in Figure 8. A pulsed nozzle (Laser Technics, 0.5 mm diameter) was used to expand HE: $C_3F_7NO$  samples (typically 100:1) into the LIF chamber, which was maintained at  $\sim 10^{-4}$  Torr. Care was taken to purify samples immediately prior to use, in order to minimize NO contamination. A standard pump-probe configuration allowed nascent  $NO(X^2\Pi)$  to be detected at variable delays following photolysis throughout the visible/near-IR  $n^* \leftarrow n$  system using the output from a tunable dye laser. NO was detected via 1-photon laser-induced fluorescence (LIF) using the  $A^2\Sigma \leftarrow X^2\Pi$ -system. The probe laser energies were maintained below  $40 \mu J \text{ pulse}^{-1}$  to avoid saturation of the transition and dissociation of  $C_3F_7NO$  by 226 nm radiation. Photofragment yield spectra were obtained by positioning the probe laser at the  $P_{11}$  bandhead and scanning the photolysis laser. Room temperature absorption spectra were taken with a Shimadzu UV-visible spectrophotometer.

The  $n^* \leftarrow n$  systems of both  $n\text{-}C_3F_7NO$  and  $i\text{-}C_3F_7NO$  extend from the visible to the near-IR. It is known that  $S_1$  decays non-radiatively in these systems, and following the extensive work done with similar systems,<sup>12</sup> unimolecular decomposition on  $T_1$  and/or  $S_0$  is anticipated.

### Sample Handling and Purification

For the CID experiments,  $C_3F_7NO$  was used as supplied by Fluorochem, without further purification. Checks were made periodically for NO contamination by probing the incident molecular beam. For the photodisso-

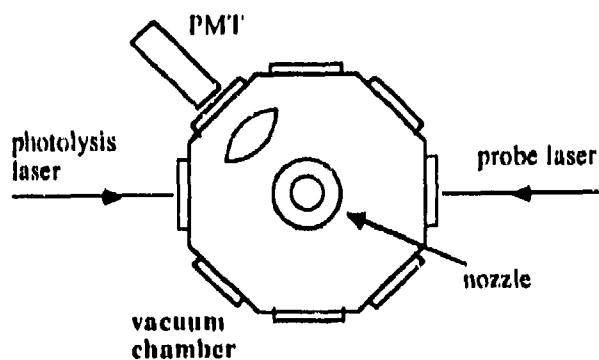


Figure 8. Schematic Drawing of the Pump-Probe Experimental Arrangement Used in the Collision-Free, 1-Photon  $C_3F_7NO$  Photolysis Experiments.

ciation experiments, samples of  $\leq 1$  percent  $C_3F_7NO$  seeded in  $\sim 500$  Torr He were prepared daily in a blackened glass bulb.  $C_3F_7NO$  was stored at 77 K and was purified by trap-to-trap distillation to minimize NO contamination. Although NO could not be completely eliminated, expansion-cooled NO is limited to a few states (i.e.,  $X^2\Pi_{1/2}$ ,  $J'' \leq 4.5$ ). Care was taken to avoid this region of the spectrum.

$C_6F_5NO$  was used as supplied by PCR and refrigerated when not in use.  $H_2$  carrier was flowed through the nozzle, which contained a piece of the solid material. The seed ratio could be controlled by changing the carrier backing pressure or heating the sample to increase its vapor pressure. The measured 300 K vapor pressure was  $\sim 2$  Torr.

TNM (98 percent) was used as supplied by Aldrich and refrigerated when not in use. Approximately 0.5 ml was placed in a stainless steel liquid vessel through which the carrier gas was flowed. As with  $C_6F_5NO$ , the seed ratio could be controlled by changing the carrier backing pressure. The 300 K vapor pressure is approximately 12 Torr.

## EXPERIMENTAL RESULTS

### Collision-Induced Excitation and Dissociation

The high S/N shown in Figure 7(a) was typical of results obtained in the CID experiments, and therefore it was straightforward to obtain  $NO(X^2\Pi)$  V,R and spin-orbit distributions under a variety of conditions. No marked  $\Lambda$ -doublet propensities (Hund's case (b) regime,  $J'' \geq 15.5$ ) were observed, so this matter was not pursued. For the case of  $C_3F_7NO$ , where our data base is most complete, both normal and iso conformers were used, yielding similar results, in accord with the small difference in  $D_0$  values (40.8 and 39.4 kcal mol<sup>-1</sup>, respectively). Thus, no attempt was made to explore differences between  $n\text{-}C_3F_7NO$  and  $i\text{-}C_3F_7NO$  in the CID experiments.

It should be emphasized that all measurements are of relative NO state densities. These measured populations are not the same as the relative rates of  $C_3F_7NO^+$  decomposition into the different product-state channels. The latter is a fundamental quantity in the  $C_3F_7NO$  c.m. system, while all measurements are done in the lab system. Namely, the CID measurements detect those species having small lab speeds more efficiently than their faster counterparts,

since the slower fragments accumulate higher densities. Therefore, we expect the nascent NO internal state distributions that derive from reaction (1) to be somewhat hotter than the measured populations reported below.



The measured NO( $X^2\Pi$ ) internal state distribution associated with the spectrum shown in Figure 7(a) is presented in Figure 9, along with distributions obtained at two additional  $E_{\text{incident}}$  values, 3 and 5 eV. Although NO rotational excitation rises slightly, it is hardly a marked effect. More striking is the change in dissociation probability that occurs over this range. Figure 10 summarizes data obtained over a 6-month period, using both *n*- $\text{C}_3\text{F}_7\text{NO}$  and *i*- $\text{C}_3\text{F}_7\text{NO}$ , and the technique described in Section II and shown in Figure 5 for obtaining relative NO( $X^2\Pi$ ) densities at different  $E_{\text{incident}}$  values. The sharp rise in dissociation probability is striking, as are the rather high values—up to 9 percent, albeit with an uncertainty of as much as a factor of 2 in the absolute percentages.

There was little, if any, dependence of the measured NO internal state distributions on  $T_s$ , as shown in Figure 11. This is not surprising in light of the weak  $E_{\text{incident}}$ -dependence shown in Figure 9. After all, at the classical turning point of the molecule-surface interaction, vibrational kinetic and potential energies

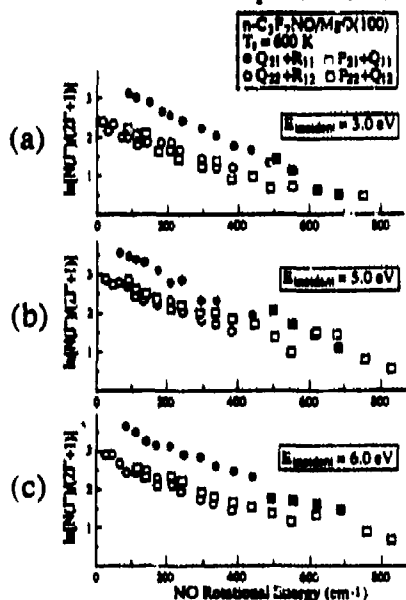


Figure 9. CID of *n*- $\text{C}_3\text{F}_7\text{NO}$  at  $E_{\text{incident}}$  Values of 3, 5, and 6 eV ( $T_s = 600$  K). Relative (a), (b), and (c) populations are not given; i.e., the vertical axes are offset from one another arbitrarily.

of the incident molecules and a number of adjacent atoms of the lattice are coupled. Thus, from Figures 9 and 10, one anticipates that NO populations will display a weak  $T_s$ -dependence, but that the dissociation probability will show a quite measurable dependence, particularly near threshold, as is observed experimentally.<sup>8</sup>

Finally, there is the possibility of photodissociation of molecules that are vibrationally excited following inelastic scattering from the surface. To test this experimentally, the product  $I_{226-280}$  was varied, where  $I_{226(280)}$  is the probe fluence at 226(280) nm. The linear variation shown in Figure 12 indicates that only two photons are involved in producing  $\text{NO}^+$ , thus eliminating the possibility of unwanted  $\text{C}_3\text{F}_7\text{NO}$  photodissociation with either of the probe beams.



For the sake of brevity, these results are summarized succinctly as follows: (i) Dissociation was observed and nascent NO( $X^2\Pi$ ) was detected, just as with  $\text{C}_3\text{F}_7\text{NO}$ . (ii) The CID efficiency was much smaller than for the case of  $\text{C}_3\text{F}_7\text{NO}$  at all values of  $E_{\text{incident}}$ . This was expected; the aromatic skeleton is much stiffer than that of  $\text{C}_3\text{F}_7\text{NO}$ . (iii) NO state distributions were similar to those shown in Figures 9 and 11. (iv) A large number of ions were produced by the impulsive impact—at least a

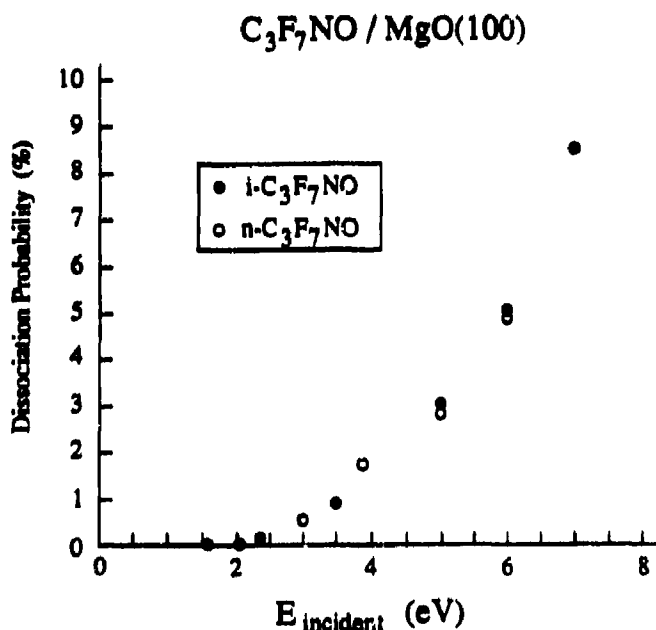


Figure 10. Dissociation Probability Vs.  $E_{\text{incident}}$  for both *n*- $\text{C}_3\text{F}_7\text{NO}$  and *i*- $\text{C}_3\text{F}_7\text{NO}$ ;  $D_0 = 1.71$  and  $1.87$  eV, Respectively

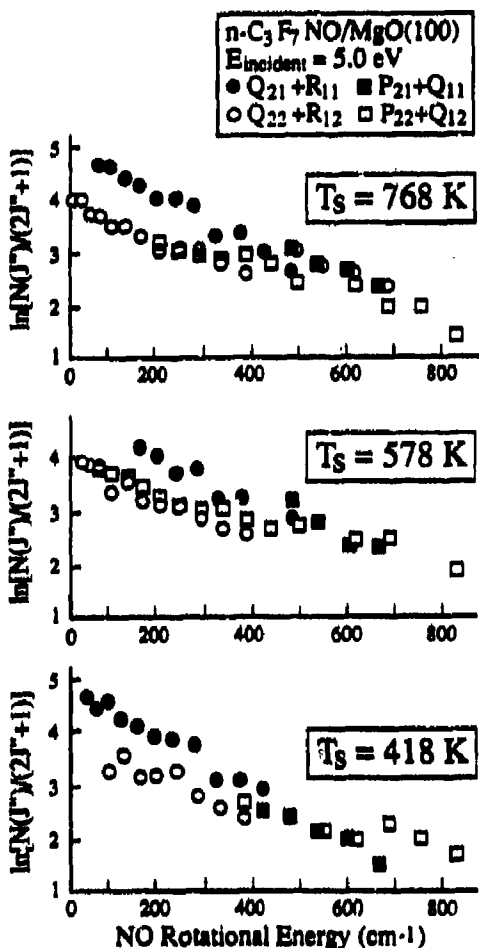


Figure 11. CID of  $n\text{-C}_3\text{F}_7\text{NO}$  at  $T_s$  Values of  $K$  ( $E_{\text{incident}} = 5.0$  eV). Relative (a), (b), and (c) populations are not given; i.e. the vertical axes are offset from one another arbitrarily.

hundredfold more than with  $\text{C}_3\text{F}_7\text{NO}$  at the same value of  $E_{\text{incident}}$ . However, even with the relatively smaller dissociation probabilities and large ion yields,  $[\text{ions}] \ll [\text{neutral fragments}]$  for the case of  $\text{C}_8\text{F}_5\text{NO}$ .



Tetranitromethane has been studied in the gas phase by Capellos and co-workers, who showed that UV excitation near 248 nm results in the formation of electronically excited  $\text{NO}_2(^2\text{B}_2)$  as a nascent product.<sup>13</sup> In this case, the full 5 eV photon energy is implanted as initial TNM excitation, and the observation of vibrationally-excited  $\text{NO}_2(^2\text{B}_2)$  is attributed to initial excitation remaining localized at an  $\text{NO}_2$  moiety during the rapid ensuing frag-

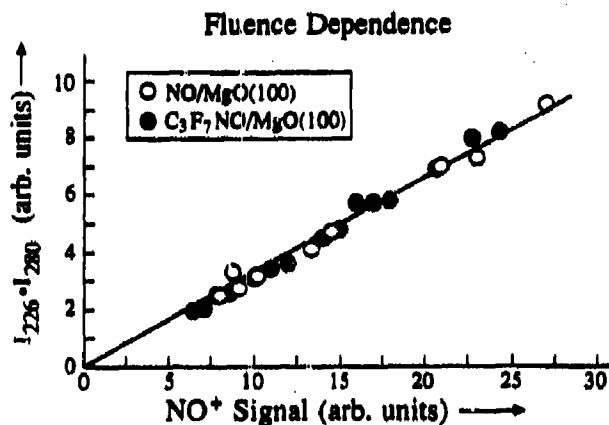


Figure 12. The Linearity of the  $\text{NO}^+$  Vs.  $I_{226} \cdot I_{280}$  Plot Indicates that  $\text{NO}$  is not Produced Photolytically

mentation. In contrast, the present experiments probe lower energies, namely, those just above  $D_0$ . Here, on the ground PES, one must consider the possibility of isomerization, as is well-known for nitroalkanes.<sup>14</sup> This can be followed by simple bond fission, in this case producing  $\text{C}(\text{NO}_2)_3\text{O} + \text{NO}$ , which is favored energetically over the  $\text{C}(\text{NO}_2)_3 + \text{NO}_2$  channel.

Indeed, we have observed nascent  $\text{NO}$  following CID of TNM at several  $E_{\text{incident}}$  values. A representative spectrum and the corresponding  $\text{NO}$  state distribution are shown in Figure 13. Although we have not yet collected as many data as with  $\text{C}_3\text{F}_7\text{NO}$ , the S/Ns are comparable and the observed channel is clearly a major reaction pathway, although possibly not the only one. This result further underscores the generality of the method and the efficacy of energy exchange in the hyperthermal energy regime. Although we have not yet ensured (as in Figure 12) that  $\text{NO}^+$  derives solely from a 2-photon process, the 280 nm absorption is rather weak (see Figure 14), and if  $\text{NO}$  were deriving from  $\text{NO}_2$  photodissociation, the resulting dissociation efficiencies would be unrealistically large.

### 2-Methyl,5-Vinyl Tetrazole: A Somewhat Energetic Polymeric Binder

In its polymeric form, MVT is somewhat more energetic than other hydrocarbon binders used in gun propellants and explosives. It was first synthesized by Henery,<sup>15</sup> and Mishra et al.<sup>16</sup> discovered that an energetic binder polymer blend composed of poly-2-methyl-5-vinyl tetrazole and polyethylene glycol selectively

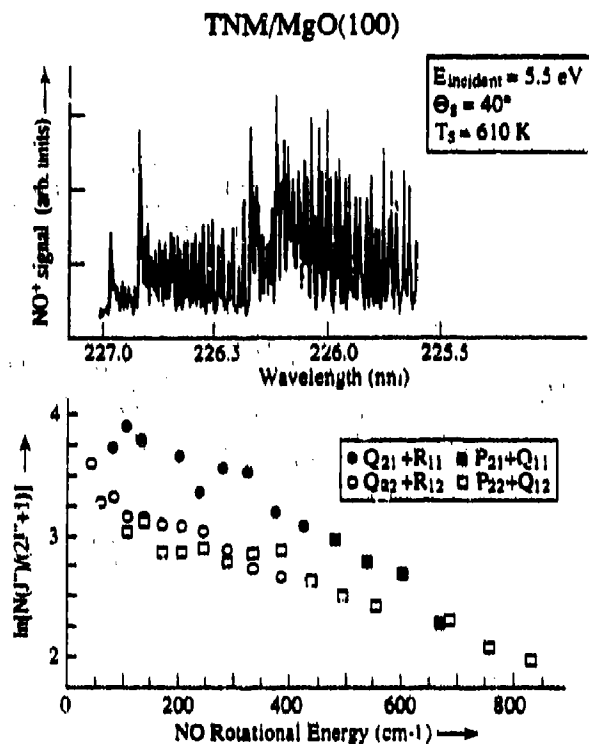


Figure 13. (Upper) NO Spectrum from the CID of TNM; (Lower) Corresponding Rotational State Distribution

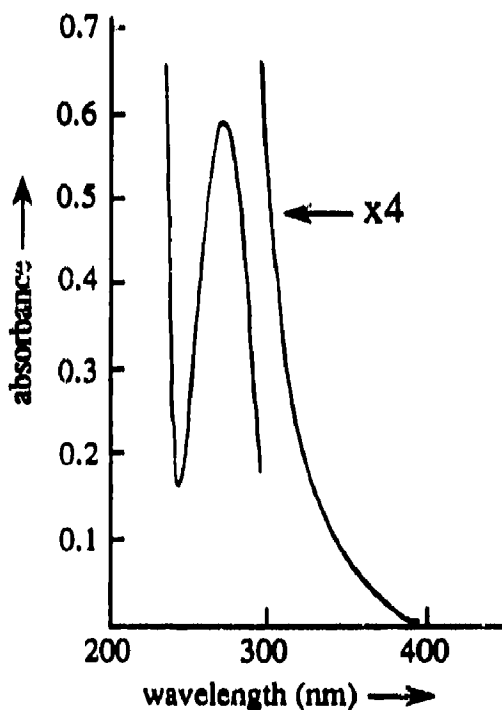


Figure 14. UV Absorption Spectra of TNM (from Reference 13)

desensitized explosives containing nitramines and was less violent to shaped charge jet attack upon a LOVA gun propellant.<sup>17</sup> These results led Mishra et al. to look for hitherto unknown modes of rapid energy dissipation and storage in these binders.

MVT molecules were accelerated to a maximum kinetic energy of 3.6 eV, and mass spectra and fragment intensities were measured for both direct and scattered beams, for surface temperatures between 500 and 725°C. Since NO is not a product of MVT decomposition, it was necessary to carry out all product analyses using mass spectroscopy. In comparing fragmentation in the direct beam with that in the scattered beam, one needs to account for small differences between the similar QMS probes. In order to eliminate these differences, we used the same probe for both the direct and scattered beam measurements.

Mass spectra for the direct molecular beam differed from those obtained under 100-200°C bulk conditions. The bulk spectra were taken with a similar QMS working at the same electron energies (30, 50, and 70 eV) and mass resolution. The main differences between the molecular beam and bulk spectra are for the mass ratio  $M(82)/M(54)$ , which is lower by a factor of  $\sim 4$  with the molecular beam. Temperature effects were also observed in the bulk mass spectra over the range 100-200°C, and all such variations are tentatively attributed to the influence of parent vibrational energy on mass spectrometer cracking patterns. Such dependences are to be expected for large energetic species like MVT, and need to be understood before evaluating the relative roles of collision-induced vibrational excitation and dissociation.

The scattered beam angular distribution was nearly specular, indicative of an impulsive molecule-surface interaction (i.e., no sticking). This was superimposed on a weak, diffuse background. Mass spectra were scanned at the specular angle (22.5°). The main findings from the scattered beam mass spectra can be summarized as follows: (a) The molecular peak at 110 amu disappeared completely (within the detection limits) in the scattered beam mass spectra, as shown in Figures 15 and 16. In order to quantify this, we compared the signals at 82 and 110 for both the direct and scattered beams. For the direct beam,  $M(82)/M(110) \sim 10$ , while for the scattered beam,  $M(82)/M(110) > 1000$ , i.e.,  $M(110)$  is essentially undetectable. The temperature required to produce so large a

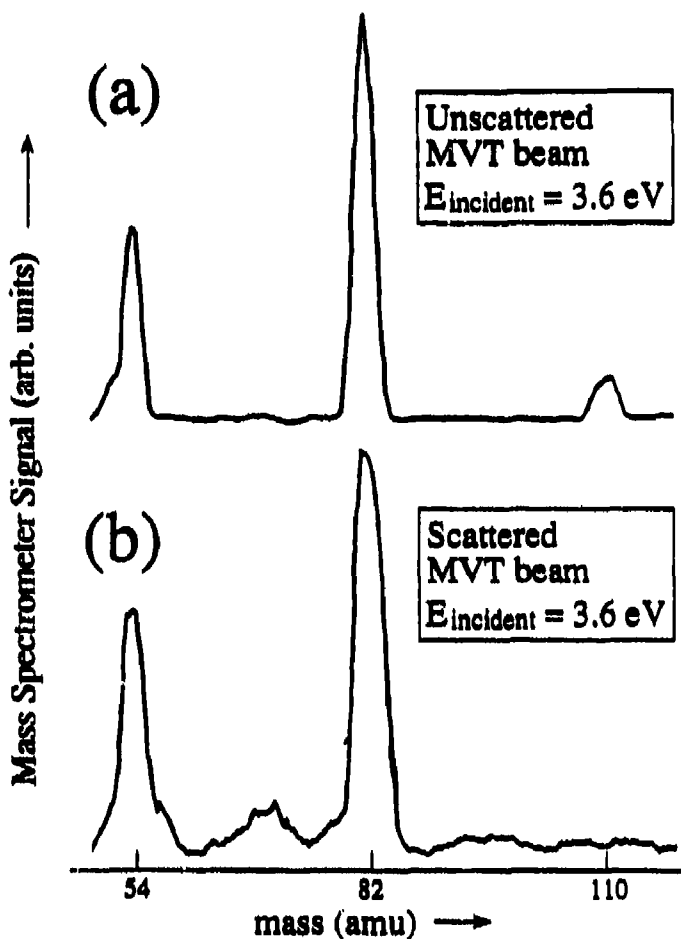


Figure 15. Mass Spectrometer Signals Showing the Unscattered and Scattered MVT Beams. Note in (b) that the peak corresponding to the parent is absent.

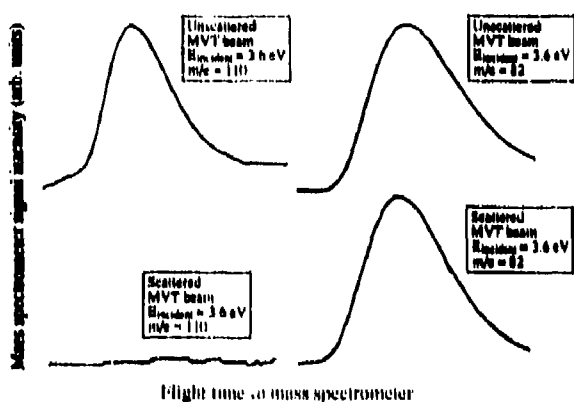
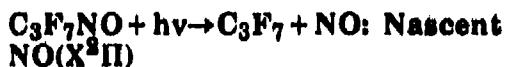


Figure 16. Time-Resolved Mass Spectrometer Signals Showing Parent (110) and Daughter (82) Peaks. Note the almost complete loss of the signal at 110 amu.

ratio would probably exceed 1000 K. (b) The ratio of signals  $M(82)/M(54)$  varies with surface temperature, from  $\sim 1.5$  at  $500^\circ\text{C}$  to  $\sim 5$  at  $725^\circ\text{C}$ .



Both *n*- $\text{C}_3\text{F}_7\text{NO}$  and *i*- $\text{C}_3\text{F}_7\text{NO}$  display the usual prominent visible/near-IR  $n^* \leftarrow n$  absorptions characteristic of RNO species. Room temperature absorption spectra ( $\epsilon_{\text{max}} = 22.7$ ) showing barely resolvable structure are presented in Figure 17, where NO fragment yield spectra obtained using expansion-cooled samples are seen to sharpen this structure for the case of *i*- $\text{C}_3\text{F}_7\text{NO}$ . With *i*- $\text{C}_3\text{F}_7\text{NO}$ , the yield spectrum seems to follow the small bumps in the 300 K absorption profile, turning on near 680 nm, at the rising edge of the  $n^* \leftarrow n$  system. The lowest accessible  $E^\ddagger$  values are  $\sim 1500 \text{ cm}^{-1}$ , limited most probably by the  $n^* \leftarrow n$  absorption strength. In all cases, measured reaction lifetimes are  $< 200 \text{ ns}$ , dropping slightly with increasing  $E^\ddagger$  to values  $\sim 100 \text{ ns}$  near  $E^\ddagger$  values of  $4500 \text{ cm}^{-1}$ . These short lifetimes lead us to believe that dissociation takes place from  $T_1$ . This is consistent with RRKM calculations.

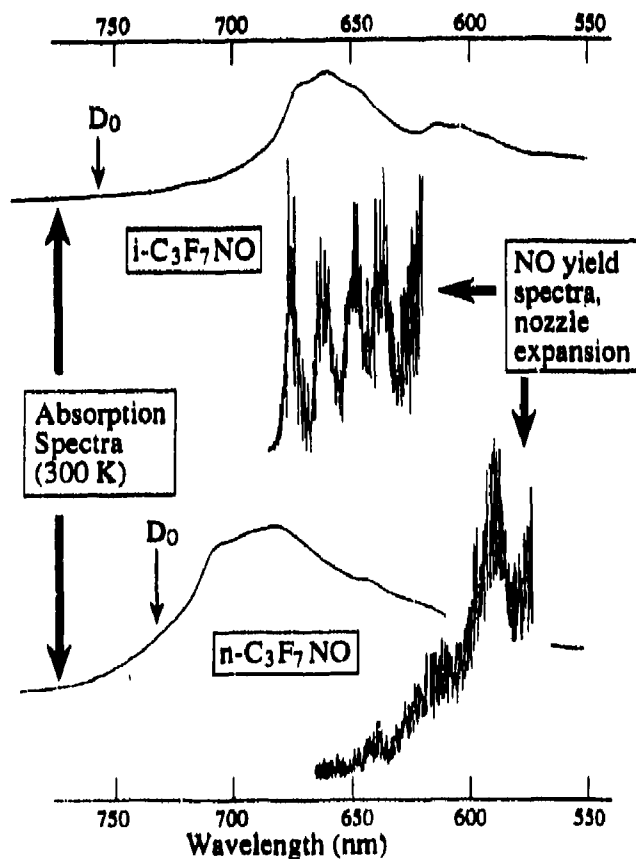


Figure 17. 300 K Absorption Spectra and NO Yield Spectra for *i*- $\text{C}_3\text{F}_7\text{NO}$  and *n*- $\text{C}_3\text{F}_7\text{NO}$

In contrast, yield spectra obtained using  $n\text{-C}_3\text{F}_7\text{NO}$  show a marked increase in signal with decreasing photolysis wavelength, in a part of the spectrum where the room temperature absorption is decreasing with decreasing photolysis wavelength. Unlike  $i\text{-C}_3\text{F}_7\text{NO}$ , the NO yield is negligible where the  $n^*\leftarrow n$  absorption is strongest, rising sharply only on the high energy side of the peak of the room temperature absorption spectrum. Since  $S_1$  decays non-radiatively (i.e., there is essentially no parent LIF), this indicates that  $n\text{-C}_3\text{F}_7\text{NO}$  molecules just above  $D_0$  do not dissociate within the time frame of the pump-probe delays used in these measurements,  $\leq 1 \mu\text{s}$ . This is consistent with  $n\text{-C}_3\text{F}_7\text{NO}$  existing on  $S_0$ , where the long unimolecular decay times (i.e., estimated using RRKM theory) preclude the possibility of reaction on a  $\leq 1 \mu\text{s}$  time scale. Therefore, dissociation on  $S_0$  is a dark channel in the photodissociation experiments.

The observed rise in the  $n\text{-C}_3\text{F}_7\text{NO}$  NO yield spectrum can be rationalized in several ways. One explanation involves a competition between dissociation on  $T_1$  (which may or may not have a small exit channel barrier) and intersystem crossing (ISC) from  $T_1$  to  $S_0$ . If, with increasing  $E^\dagger$ , the  $T_1$  reaction rate increases faster than the ISC rate, dissociation via  $T_1$  will rise with  $E^\dagger$ . Since slow dissociation on  $S_0$  is a dark channel, only products reacting on  $T_1$  will be observed. In this case, the rise in the yield spectrum, despite the fall in the room temperature absorption spectrum, reflects the ratio of the two rates out of  $T_1$ .

Another possible explanation for the rise in the product yield spectrum is a competition between reactions that transpire via the zeroth-order  $S_0$  and  $T_1$  surfaces. Namely, just above  $D_0$  a barrier on  $T_1$  blocks this channel, as has been seen previously for the case of  $t\text{-BuNO}$ .<sup>12</sup> Thus, reactions occur solely on  $S_0$ , and the corresponding small unimolecular decomposition rates render this channel 'dark' in the present experiments. Above the  $T_1$  barrier, there is competition between the two channels:  $T_1 \rightarrow \text{products}$ , and  $T_1 \rightarrow S_0$ , with dissociation via  $T_1$  increasing with  $E^\dagger$ .

In either of the above cases, we note that calculated reaction rates for  $T_1$  are much larger than those for  $S_0$  at the same energies relative to the respective exit channel barriers. Thus, we conclude that the observed NO fragments are due to dissociation via  $T_1$ .

NO internal state distributions were obtained at several values of  $E^\dagger$  for both  $n\text{-C}_3\text{F}_7\text{NO}$  and  $i\text{-C}_3\text{F}_7\text{NO}$ , as shown in Figures 18 and 19. The NO is produced predominantly in  $v'' = 0$  ( $< 1$  percent  $v'' = 1$ ). The solid lines correspond to calculated statistical distributions (priors) of product excitations at fixed  $E^\dagger$  values.<sup>18</sup> Details of the calculations will be published elsewhere. For the prior distributions, each spin-orbit state is separately normalized to the data and the true relative spin orbit populations are as shown in the figures (i.e., the populations of each of the spin orbit states are statistical, but the spin-orbit ratio is non-statistical). The remarkably good fit, with the

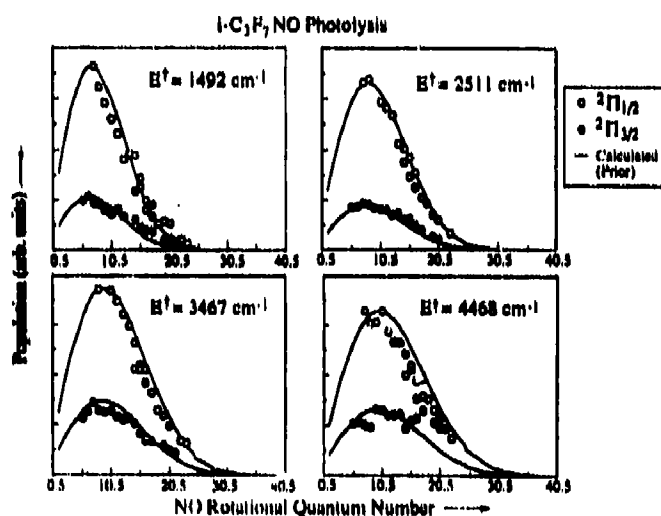


Figure 18. For the Case of  $i\text{-C}_3\text{F}_7\text{NO}$  Photodissociation, All of the Measured NO State Distributions Obtained at Different  $E^\dagger$  Fit the Corresponding Prior Distributions.

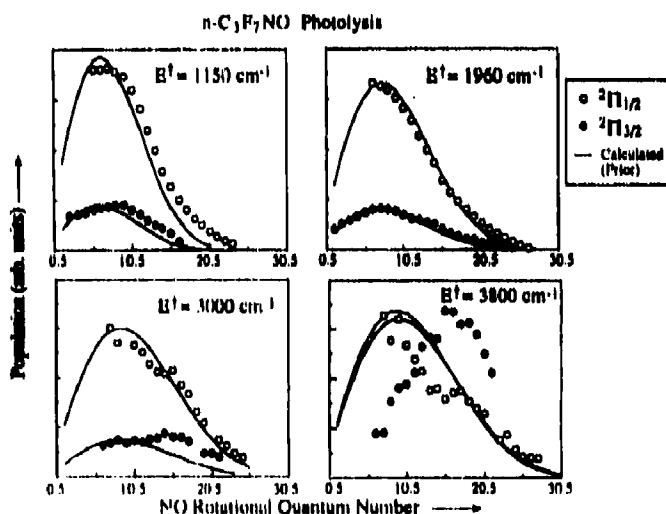


Figure 19. For  $n\text{-C}_3\text{F}_7\text{NO}$ , the NO Rotational Distribution Obtained at the Highest  $E^\dagger$  Does Not Fit a Prior Distribution.

exception of the higher excess energies, is consistent with previous results, in which  $S_0$  and/or  $T_1$  were implicated as the reactive surfaces, following radiationless decay of  $S_1$ .<sup>12</sup> One possible explanation for the nonstatistical behavior at higher  $E^\ddagger$  (i.e.,  $n\text{-C}_3\text{F}_7\text{NO}$  at  $3800\text{ cm}^{-1}$ ) is direct dissociation from  $S_1$  over a barrier. Since the rotational distributions at lower  $E^\ddagger$  were statistical, by fitting the lower energy prior distributions to the best fit of  $E^\ddagger$ ,  $D_0$  could be obtained. For  $i\text{-C}_3\text{F}_7\text{NO}$ ,  $D_0 = 13200 \pm 100\text{ cm}^{-1}$  and for  $n\text{-C}_3\text{F}_7\text{NO}$ ,  $D_0 = 13670 \pm 100\text{ cm}^{-1}$ .

The correspondence between the CID and photolysis results is shown in Figure 20, where one sees that the CID distributions are not far from those observed at low  $E^\ddagger$  in the photolysis experiments. Since the latter react via a long-lived intermediate—at least at low  $E^\ddagger$ —it is clear that the CID results are consistent with a unimolecular decomposition mechanism, in this case probably via  $T_1$ , with little or no exit channel barrier. However, it is very difficult to make a direct comparison between the two experiments. The photodissociation experiments are done at a specific  $E^\ddagger$  and the CID experiments are done at a distribution of  $E^\ddagger$  values, the incident kinetic energy being an upper limit.

## DISCUSSION AND CONCLUSIONS

The main features of the work reported here are purely experimental—direct observations of molecule-surface CID, variations of measured NO internal state distributions with  $E_{\text{incident}}$  and  $T_{\text{m}}$ , variations of the dissociation probability with  $E_{\text{incident}}$  and  $T_{\text{m}}$ , observation of the isomerization pathway in the case of TNM, excitation and possible dissociation in MVT, etc. It appears that the method is general, dissociation can be efficient, and that low-energy pathways are followed. Thus, we envisage a technique that can be applied to the study of a number of reactive processes in medium/large polyatomic molecules, with particular applicability to energetic molecules with their characteristically low  $D_0$  values.

### A Model for Molecule-Surface CID Processes

In discussing possible models that can rationalize the present experimental observations, we are less inclined to invoke entrance channel charge transfer mechanisms<sup>19</sup> than

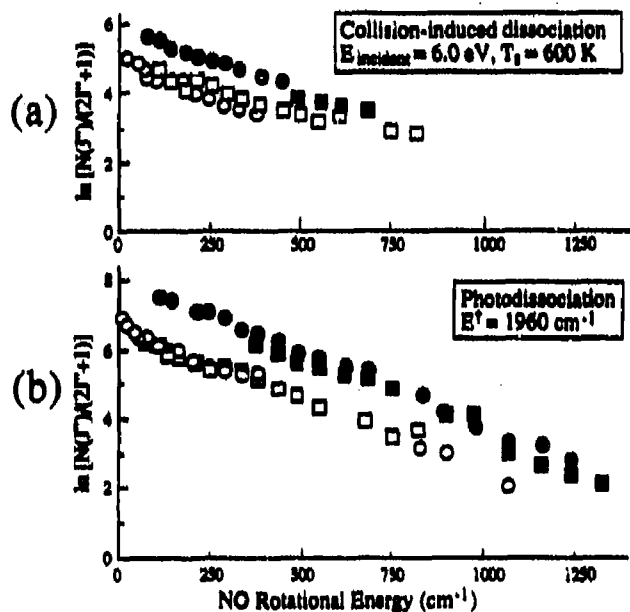


Figure 20. Comparison Between NO Distributions Obtained Using (a) CID and (b) Photodissociation at  $E^\ddagger = 1960\text{ cm}^{-1}$ .

consequences of the molecular catastrophe brought about by abruptly converting  $E_{\text{incident}}$  into vibrational kinetic and potential energies at the classical turning point of the molecule-surface collision. Certainly the situation can be different for metals and semiconductors, but for an insulator such as MgO, we envision a purely repulsive molecule-surface interaction at the high  $E_{\text{incident}}$  values reported here. Although MgO itself has no electronic states below  $\sim 6\text{ eV}$ , RNO does, and low-lying  $S_1$  and  $T_1$  PESs are energetically accessible via intramolecular conversion. However, as mentioned above and documented thoroughly in the literature for a number of RNO species,<sup>12</sup> the zeroth-order  $S_1$  state is strongly mixed with  $T_1$  and/or  $S_0$ :  $\Psi = a\Psi_{S_1} + b\Psi_{S_0} + c\Psi_{T_1}$ , as evidenced by the very low fluorescence quantum yield. Thus,  $S_1$  has no legitimate separate identity, and we limit our considerations to  $T_1$  and  $S_0$ , both of which react via unimolecular decomposition mechanisms, the former with possibly a small exit-channel barrier and the latter with no such barrier.

From the photodissociation results presented in the last section, where we tentatively concluded that the observed NO product derived from  $T_1$ , it is clear that  $T_1$  may also be implicated in the CID results, since the nascent NO distributions are similar. In the photodissociation experiments, the NO quantum yield was very low (compared to that of  $\text{CF}_3\text{NO}$ , for example), while the CID

efficiencies are not so low at all. However, in the CID experiments products can accrue near the surface over 10s of  $\mu$ s, while in the photodissociation experiments observation was limited to  $\leq 1 \mu$ s after initiation. Thus,  $S_0$  may participate to a greater extent in CID than photodissociation, and the similar nascent product state distributions anticipated for both  $T_1$  and  $S_0$  channels preclude differentiation on this basis. Also, as pointed out above, state distributions from photodissociation and CID experiments cannot be compared directly, since the former represent the microscopic product state branching ratios, while the latter are laboratory densities that include effects of c.m. transformations, backscattered NO-surface collisions,  $k_{uni}$  and its space/time variation in the lab, etc. While these effects may not markedly affect conclusions, they should be taken into account in any detailed analysis of the process.

We conclude that NO deriving from molecule-surface CID has the signature of statistical unimolecular decomposition and that this probably implicates the low-lying  $T_1$  and  $S_0$  PESs. Their respective roles are unclear, but what is clear is that a significant number of incident molecules are excited above  $D_0$ , and that serious contortions of the molecular frame occur during impact.

Space does not permit a detailed discussion of the model whose applicability we are presently exploring, but a few summary comments are in order. First, we assume that the relevant degrees of freedom are those of the incident and rebounding molecule (e.g.,  $C_3F_7NO$ ) and some 'effective number' of lattice vibrational degrees of freedom, say 15-30. The total energy available in this microcosm, which we treat as a microcanonical ensemble, is taken to be  $E_{total} = E_{incident} + \langle E_{vib}(MgO) \rangle$ , where the latter quantity is the thermally-averaged energy of the 15-30 effective MgO vibrations available during the collision. Thus, for a given  $E_{incident}$ , the energy in the rebounding molecule,  $E_{mol}$ , is  $T_s$ -dependent.

The simplest statistical treatment gives the formula:

$$P(E_{mol}) = \rho_{mol}(E_{mol}) \cdot \rho_{MgO}(E_{total} - E_{mol}) \quad (4)$$

where  $P(E_{mol})$  is the probability of the rebounding molecule having energy  $E_{mol}$ , and the  $\rho$ s are densities of states. At this point, the number of MgO lattice vibrations put into the calculation of  $\rho_{MgO}$  is an 'adjustable parameter', while  $\rho_{mol}$  is calculated fairly well using a direct-

count procedure and good molecular vibrational frequencies. This formula for  $P(E_{mol})$  predicts (i) a fairly steep increase in the variation of the dissociation probability with  $E_{inc}$ , as observed experimentally; (ii) increasing dissociation probability with  $T_s$ , more pronounced at threshold than high  $E_{inc}$ , as observed experimentally; and (iii) relatively little dependence of the measured NO internal state distributions on  $T_s$ , again confirmed experimentally. Thus, we think we are on the right track. Details will be published separately.

### Possibilities for Future Work

Clearly, there are a number of twists and variations that can and will be tried in the future. For example, species can be adsorbed on the surface and subjected to high energy impact, so that binary encounters can be explored (e.g., MVT on the surface with TNM incident, RDX on the surface, Xe or  $I_2$  'hammers', etc.). Furthermore, beams of free radicals ( $NH_2$ ,  $(CH_3)_2N$ , etc.) can attack adsorbed species, where the radicals can be either expansion-cooled or prepared state-selectively. Such experiments address issues of initiation, shock, initial chemical steps, etc., and we hope they will enlighten us about energetic material decomposition and sensitivity.

### ACKNOWLEDGEMENT

This research was supported by the U.S. Army Research Office under the auspices of the Center for the Study of Fast Transient Processes, and the U.S. Air Force Office of Scientific Research.

### REFERENCES

1. Yost, R. A. and Enke, C. G., *J. Am. Chem. Soc.*, 100, 1978, p. 2274. Yost, R. A. and Enke, C. G., *Anal. Chem.*, 51, 1979, p. 1251.
2. Douglas, D. J., *J. Phys. Chem.*, 86, 1982, p. 185.
3. Forst, W., *Theory of Unimolecular Reactions*, Academic, 1973.
4. Boyd, R. K. and Beynon, J. H., *Advances in Mass Spectrometry*, R. Daly, ed., Heyden, London, 1978, and references cited therein.
5. Reider, K. H., *Surface Sci.*, 118, 1982, p. 57. Kolodney, E. and Amirav, A., *Surface Sci.*, 155, 1985, p. 715.

6. Powers, P. S.; Kolodney, E.; Iwata, L.; Reisler, H.; and Wittig, C., unpublished.
7. Metiu, H. and DePristo, A. E., *J. Chem. Phys.*, 91, 1989, p. 2735.
8. Qian, C. X. W.; Nobel, M.; Nadler, I.; Reisler, H.; and Wittig, C., *J. Chem. Phys.*, 83, 1985, p. 5573.
9. Kolodney, E.; Baugh, D.; Powers, P. S.; Reisler, H.; and Wittig, C., *Chem. Phys. Lett.* 145, 1988, p. 177.
10. Kolodney, E. and Amirav, A., *Chem. Phys.*, 82, 1983, p. 269.
11. Nobel, M.; Qian, C. X. W.; Reisler, H.; and Wittig, C., *J. Chem. Phys.*, 85, 1986, p. 5763.
12. Reisler, H.; Noble, M.; and Wittig, C., *Molecular Photodissociation Dynamics*, J. Bagott and M. N. R. Ashfold, eds., Royal Society of Chemistry, London, 1987. Nobel, M.; Qian, C. X. W.; Reisler, H.; and Wittig, C., *J. Chem. Phys.*, 85, 1986, p. 5763.
13. Capellos, C.; Iyer, S.; Liang, Y.; and Gamms, I. A., *J. Chem. Soc., Faraday Trans.* 282, 1986, p. 2195.
14. Wodtke, A. M.; Hints, E. J.; and Lee, Y. T., *J. Phys. Chem.*, 90, 1986, p. 3549.
15. Henery, R. A. and Finnegan, W., NWC Report, AD314-300, 1959, available from NTIS.
16. Mishra, I. B.; Vande Kieft, L. J.; and Vander Hart, D., *Proceedings, Society of Plastics Engineers*, ANTEC Meeting, Atlanta, 1988, p. 1229.
17. Mishra, I. B. and Vande Kieft, L. J., *Proc. Intl. Conf. Fraunhofer Institute of Chem. Tech.*, Karlsruhe, FRG, Jun 29 - Jul 1, 1988.
18. Levine, R. D. and Bernstein, R. B., *Molecular Reaction Dynamics*, Oxford, 1987.
19. Gadzuk, J. W. and Holloway, S., *J. Chem. Phys.*, 84, 1986, p. 3502. Gadzuk, J. W. and Holloway, S., *Chem. Phys. Lett.* 114, 1985, p. 314.

## DISCUSSION

**S. F. RICE**  
 POB 808 L-282, Livermore, CA 94550

Do you see yourself being able to ultimately shoot RDX molecules at an RDX surface? Can you get enough RDX in your beam?

## REPLY BY C. WITTIG

Yes, we envision shooting RDX monomers at the surface, although this is not the very next step in our plans. First, we are going to put molecules on a cold (100 K) MgO surface and collide Xe or I<sub>2</sub> at lab energies up to at least 10 eV. We will also photoinitiate reactions in surface-bound molecules. This avoids inherent difficulties in making molecular beams of low vapor pressure, not-too-stable materials. On the other hand, we can study very interesting binary interactions such as RDX (surface) with incident TNM or free radical beams.

MgO(100) surfaces, i.e., left overnight at  $3 \times 10^{-8}$  Torr, mainly water contamination. The combined effect of partial surface cleaning by Xe-atom bombardment and the chemical inertness of the MgO(100) surface resulted in quite similar angular scattering distributions, i.e., slightly broader and with some background.

### Detectors

Throughout the experiments, we used a probe laser as the main detector, providing state-selective scattering distributions in the energy, time, and space domains. In addition, two quadrupole mass spectrometers (QMSs) were used for measuring angular scattering distributions and time-of-flight (TOF) spectra, and also served as residual gas analyzers (RGAs). A channeled ionization gauge (CVC IG28) was used as a flux detector for the He diffraction measurements. The scattering/detection arrangement is that of fixed detectors and a rotating crystal. One QMS was oriented at  $45^\circ$  relative to the incident molecular beam, 26 cm from the surface, and was equipped with a collimator to give  $1.1^\circ$  resolution both in and out of the scattering plane. A second QMS was placed in-line with the molecular beam for beam diagnostics, and incident kinetic energy measurements using the TOF technique. The channeled ionization gauge was mounted at  $90^\circ$  relative to the beam direction. Its entrance aperture was a rectangular duct with dimensions 15 mm x 2.6 mm (sides) and 12 mm length, providing high signal/flux detection (beam trapping) with an inherent response time of 17 ns, both measured and calculated. Under these conditions, operating the pulsed valve at 40 Hz resulted in a periodic exponential signal having a duty cycle of  $\sim 1/2$  and high intensity in the first harmonic, thus giving a nice diffraction signal using a lock-in amplifier (PAR HR-8).

### Laser Detection

NO was detected state-selectively using 2-photon, 2-frequency ionization via the  $A^2\Sigma \leftarrow X^2\Pi$ -system; several  $\mu\text{J}$  of radiation near 226 nm and  $\sim 1$  mJ of ionizing radiation near 280 nm resulted in a sensitivity of approximately  $10^{-12}$  Torr per quantum state when using a 300 K static sample. The output from a Nd:YAG-laser-pumped dye laser (Quanta-Ray) was doubled to give approximately 5 mJ of tunable radiation near 280 nm. Part of this output was converted to  $\sim 226$  nm (second anti-Stokes line from a high pressure  $\text{H}_2$  cell), and

$\sim 1$  mJ of the 280 nm radiation was overlapped with the 226 nm radiation, thus providing 2-frequency excitation. Both beams travelled similar pathlengths between splitting and recombination. Temporal overlap was better than  $\pm 0.3$  ns when using  $\sim 4$   $\mu\text{J}$  (in  $1$   $\text{mm}^2$ ) to excite  $\gamma(0-0)$  rotational transitions, and  $\sim 1$  mJ near 280 nm to pump the ionizing transition. High S/N was achieved without even partially saturating the  $\gamma$ -bands.

There are two distinct advantages to this 2-frequency photoionization scheme, as opposed to using two 226 nm photons. Both are associated with the low intensities of the 226 nm radiation used: (a) there was a very low level of stray photoions caused by scattered 226 nm photons hitting the channeltron. The 280 nm radiation generates almost no photoions—less than 1 percent yield relative to 226 nm photons, despite the markedly different intensities; and (b) no dissociation of the parent molecule is detected, i.e., less than 2 percent of the scattered signal. This is mainly due to the fact that the 226 nm  $n^+ \leftarrow n$  RNO absorption cross section is larger, by at least a factor of 50, than that at 280 nm.

$\text{NO}^+$  ions are collected with the multipliers labelled ID in Figure 5, and spectra were analyzed according to previously reported procedures.<sup>8</sup> Using this system, we demonstrated  $1^\circ$  angular resolution 4 cm from the surface when scattering NO from MgO(100),<sup>9</sup> which is better resolution than required by the physics of the processes of concern. Since it is possible to use a trade-off between angular resolution and sensitivity, it seems reasonable that a sensitivity of  $10^{-13}$  Torr per quantum state can be ultimately achieved with  $5$ - $10^\circ$  angular resolution, without challenging the theoretical limit. This corresponds to extracting ions efficiently from a volume of  $\sim 0.1$   $\text{cm}^3$ . From our experiences with higher pressure environments, such high sensitivities are possible with UHV mainly because of little or no background.

With the overlapped, co-propagating probe beams located approximately 12 mm from the point where the incident molecular beam strikes the surface, NO fragments were readily detected over a wide range of conditions. Figure 7(a) shows the NO spectrum obtained with  $T_s = 610$  K,  $\theta_1 = \theta_2 = 45^\circ$ , and  $E_{\text{incident}} = 6.0$  eV, for the case of  $n\text{-C}_3\text{F}_7\text{NO}$ . For comparison, the spectrum of inelastically scattered NO [see Figure 5(a)] is shown in Figure 7(b). Figure 7(c) shows a spectrum of

# INITIATION AND PROPAGATION IN PRIMARY EXPLOSIVES

P. M. Dickson, M. A. Parry,\* J. E. Field  
Cavendish Laboratory, University of Cambridge  
Madingley Road, Cambridge CB3 0HE, UNITED KINGDOM

*The initiation and propagation of deflagration and detonation in mercury fulminate, lead azide, mercuric-5-nitrotetrazole, and silver-5-nitrotetrazole has been studied using various techniques. Streak and framing high-speed photography were used to observe these events directly. The main objective has been to investigate the factors which affect DDT and the related phenomenon of dead-pressing, which may be regarded as a failure of the DDT process at high pressed densities. These factors include the variable properties of pressed density, grain size distribution, void structure, confinement and charge dimension and geometry, and also fixed properties (for a given explosive) such as shock and thermal sensitivities, heat of explosion, and the quantity and state of the reaction products. The nature and strength of the initiating stimulus also has a major effect on the subsequent reaction.*

## INTRODUCTION

The main difference between a primary explosive and a secondary explosive is the ease of ignition of the former. The two main requirements of a primary explosive are that first, it must reliably detonate upon receipt of a low energy stimulus, either thermal, electrical, or mechanical; and second, it must detonate strongly enough to initiate the next element of the explosive train. Additionally, it should not be so sensitive that it might detonate accidentally under expected operating conditions, and it should be chemically stable in its operating environment. Relatively few materials have a combination of properties which perform this role satisfactorily.

Mercuric bisfulminate was described by Howard in 1800,<sup>1</sup> but it was not until the mid 1800s that Alfred Nobel patented its use in detonators. Mercury fulminate was replaced because it had poor stability, unreliable performance, and it exhibited dead-pressing (DDT failure at high pressed densities).

Lead azide was used from the early 1900s and seemed to be the ideal detonant; it detonated reliably at high pressing loads, smaller amounts were needed to reliably detonate an adjacent explosive, and it had much better thermal stability. Lead azide is used extensively in modern commercial and military detonators, but is now the subject of a replacement program because of problems associated with hydrolytic instability and incompatibility with copper.<sup>2</sup>

Bates and Jenkins<sup>3</sup> examined a range of possible replacements for lead azide and concluded that silver-5-nitrotetrazole and mercuric-5-nitrotetrazole were two promising materials which deserved further study. Silver-5-nitrotetrazole was reported to exist in more than one polymorphic form, to exhibit dead-pressing at varying densities, and also to have a lower output than lead azide.<sup>4</sup> Only one polymorphic form of mercuric-5-nitrotetrazole was found, giving a performance superior to lead azide when tested in a small detonator. However, the purity of the chemical intermediate used in the preparation of mercuric-5-nitrotetrazole, sodium-5-nitrotetrazolate, affected the properties of the mercuric salt. The temperature of ignition and the

\* Now at Materials Research Lab., Ascot Vale, Victoria 3032, Australia.

loading pressure at which dead-pressing of mercuric-5-nitrotetrazole occurred increased with the purity of the intermediate. When the intermediate was recrystallized, dead-pressing of the mercuric-5-nitrotetrazole did not occur with pressing loads to 28 MPa (the maximum tested). Since silver-5-nitrotetrazole had been found to dead-press, further work has mainly concentrated on the mercuric salt; its manufacture has been scaled-up<sup>5</sup> and it has been proposed for use in a number of single-component detonators.<sup>6-8</sup> Silver-5-nitrotetrazole and mercuric-5-nitrotetrazole have since been prepared via a new chemical intermediate, bis(ethylenediamine)-copper(II) nitrotetrazolate, and Parry<sup>9</sup> found that mercuric-5-nitrotetrazole prepared in this way did not exhibit dead-pressing at pressing loads up to 69 MPa. The nitrotetrazoles used in this study were also prepared by this route.

DDT has been studied fairly extensively, particularly in secondary explosives, for several decades, but less work has been directed at primary explosives where the process is more difficult to observe and there is a less clearly defined burning region. We have used high-speed photography to try to observe dead-pressing and to obtain information on DDT in primary explosives under a variety of different conditions. Differential scanning calorimetry and thermogravimetric analysis have been used to measure heats of explosion and ignition temperatures where these values were not already known. Grain sizes before and after pressing were estimated by optical microscopy.

## DEFLAGRATION TO DETONATION TRANSITION

The precise mechanism by which a deflagration at the surface of a pressed granular explosive makes the transition to detonation is not well understood, but it is generally believed to pass through a number of distinct stages: conductive burning, convective burning, compressive burning leading to the formation of shock waves of increasing strength, and, when the critical shock initiation pressure of the explosive is exceeded, detonation. It is the mechanism by which the shock waves are first formed and then strengthened which is least easily explained. Most of the work in this field

has been concerned with secondary explosives and propellants, and so the existing theories are not based on observation of primaries. Relatively few instrumented studies of DDT in primary explosives have been made.

Thermal ignition at the surface of the explosive gives rise to laminar conductive burning which proceeds relatively slowly into the explosive bed. Intrusion of hot gaseous products into the bed ahead of the burning front leads to convective burning and a build-up of pressure due to confinement of the products, causing the burning rate, which is usually observed to be roughly proportional to the pressure, to increase. Burning speeds of up to  $1 \text{ mm } \mu\text{s}^{-1}$  may be achieved by this means. Some workers<sup>10</sup> have suggested that under suitable confinement, which may include inertial confinement by the explosive, this convective burning can lead to shock wave formation when the rate of energy release becomes great enough. It has also been suggested<sup>11</sup> that under suitable conditions the compression waves from the burning zone may reinforce and steepen into a shock wave, causing compressive heating, possibly with hot-spot formation due to pore collapse, adiabatic shear, and other effects.

An alternative explanation<sup>12</sup> is that as the pressure continues to rise, and with sufficient confinement, bed compaction begins to occur, decreasing its permeability and leading to the formation of a non-porous plug of unreacted material in front of the burning zone which is driven into the unreacted explosive by the high-pressure combustion products. The compaction wave caused by the plug is reinforced by the increasingly strong compression waves which overtake it, and it steepens into a shock wave at some point ahead of the burning zone, leading to detonation forwards and the occasionally observed retonation back towards the burning zone.

Ermolaev et al.<sup>13</sup> suggest that there are two distinct forms of DDT: one through shock wave formation ahead of the reaction zone, and the other involving the formation of a secondary compressive wave behind the reaction zone which subsequently overtakes it.

## DEAD-PRESSING

Dead-pressing is a problem associated with compacted granular primary explosives. It manifests itself as a failure of the charge to undergo satisfactory detonation, either by failing to detonate at all or by exhibiting a large induction time and/or a long run-to-detonation length. If the detonation occurs, it is usually of reduced strength, i.e., lower detonation pressure and lower VOD. Dead-pressing is now generally accepted to be due to inadequate propagation of the initial deflagration into the bulk of the explosive, so that prompt DDT does not occur. Most of the possible mechanisms for DDT are strongly dependent on the porosity of the explosive bed, and so this may be due to high compaction in pressing, or the formation of a non-porous plug in the initial stages of the reaction without the necessary conditions for this to lead to the production of strengthening shock waves. If the deflagration does not propagate into the bulk of the explosive, then there will be no significant build-up of pressure, no shock wave formation, and no run to detonation.

Swallows and Field<sup>14</sup> investigated dead-pressing in samples of mercury fulminate using high-speed photography, pressure measurements, and scanning electron microscopy. They found that detonation performance after impact initiation, as measured by detonation pressure, decreased considerably when the mercury fulminate was pressed to densities exceeding  $4 \text{ g cm}^{-3}$ , and they noticed distinct differences between the void structures in the two samples. They described the void structure in the dead-pressed samples as essentially uni-directional, whereas the non-dead-pressed samples had a network of inter-connecting voids. If the propagation of the reaction front in the early stages depends on the intrusion of hot gaseous reaction products into unreacted explosive, then the relatively closed void structure in a highly compacted sample could be expected to hinder this process more than the branched void structure in a less dense sample. Kistiakowsky<sup>15</sup> suggested that dead-pressing in mercury fulminate at high pressing loads was due to its soft consistency, leading to the formation of a non-porous mass into which the

deflagration products could not penetrate, and Muraour et al.<sup>16,17</sup> advanced similar theories.

Chaudhri et al.<sup>18</sup> used high-speed photography to look at the propagation velocity in single crystals of lead azide after ignition by an exploding wire, and found that small crystals deflagrated but large crystals detonated with a VOD of about  $8 \text{ mm } \mu\text{s}^{-1}$ . Single crystals represent the limit of high density, and clearly have a negligible void structure by comparison with compacts. Either DDT or SDT is occurring here in the absence of void structure.

However, dead-pressing has been reported by Kistiakowsky<sup>15</sup> in samples of lead azide, and so there are clearly other factors to be taken into consideration. In particular, the method of initiation may play an important role in determining whether or not dead-pressing manifests itself in a sample. The same sample might detonate normally when initiated by a powerful stimulus such as an exploding wire, and yet appear to be dead-pressed when a more gentle stimulus is used. This is of great practical importance since most detonator systems employ much lower energy ignition methods than exploding wires. In this study, the following indications have been taken to suggest that dead-pressing has occurred: (i) non-linearity in the plot of VOD against density at higher densities; (ii) an increase in the induction times, i.e., the time from initiation to visible propagation.

Bowden and Yoffe<sup>19</sup> reported that primary explosives fall into two classes with respect to their behavior on initiation. The first, which includes lead styphnate and mercury fulminate, resembles secondary explosives in that it shows an accelerated burning to detonation. The second, including lead azide, shows no clear burning zone, with the detonation starting close to the point of initiation.

## EXPERIMENTAL

The photographic study of the explosives involved streak and framing photography, in order to observe the structure of the reaction as well as measure the reaction rate. Streak photography was used extensively since it allowed accurate measurements of VOD, to within a few percent, and was performed using

an Imacon 790 with a variable streak unit. Both the Imacon 790 and a Beckman and Whitley 189 framing camera were used to take framing sequences.

The explosives were pressed into a variety of polycarbonate test pieces. Figure 1(a) depicts two polycarbonate blocks bolted together, with the channel milled into one of the blocks. In Figure 1(b) the channel is cut into a brass plate between the blocks, which complicates the nature of the confinement but acts as a useful witness plate for determining run-to-detonation lengths. The design in Figure 1(c) allowed the explosive to be pressed in a single increment, with the direction of the pressing load perpendicular to the direction of propagation of the reaction. This allowed us to investigate whether the direction of the pressing load affected the void structure sufficiently to modify the response of the explosive. Figure 2 shows a simple circular channel drilled into a polycarbonate rod, an arrangement which replaced the version in Figure 1(a) in all the later work, being easier to produce and fill, and more closely representing the 2-D situation. This was produced with 2-mm and 3-mm diameter channels. In each of these cases, the explosive was incrementally pressed into the channels at various pressing loads, the height of the increments being less than the diameter of the channel to ensure as uniform a pressed density as possible.

The channel dimensions were chosen so that the mass of explosive fired in each shot was small enough ( $< 0.5$  g) to permit the tests to be conducted in the laboratory without using an elaborate test cell, while keeping well above the critical diameter of the primaries. The pressed density was estimated from the volume of the channels and a knowledge of the mass of explosive used in each pressing.

For the purpose of framing photography with the Beckman and Whitley 189 camera and some of the streak shots, initiation was achieved by passing a fast 5 kV, 16 J electrical pulse through a 6-mm long, V-shaped, 100- $\mu$ m gold bridge-wire held in contact with the surface of the explosive. This produced a prompt and reproducible stimulus which was necessary to achieve satisfactory synchronization with the rotating mirror framing camera.

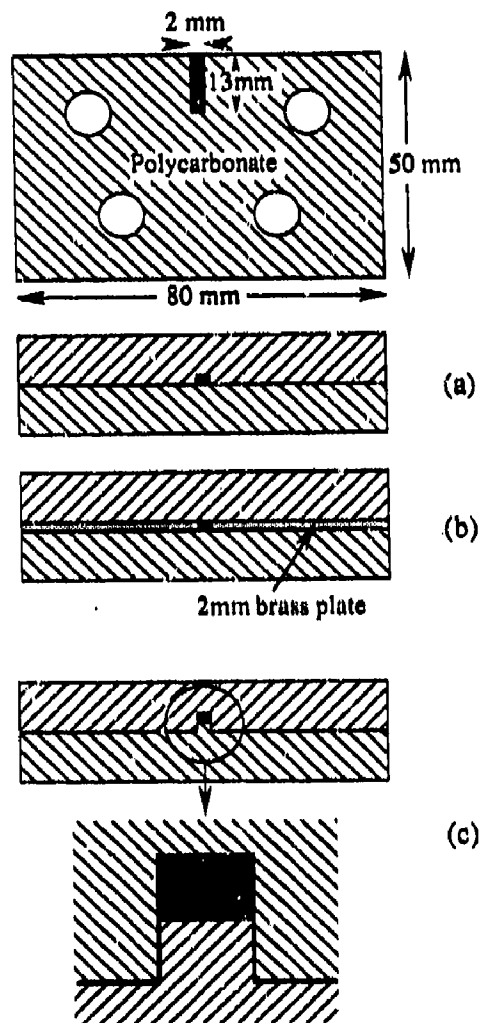


Figure 1. Schematic Diagram of Polycarbonate Sandwich Test Pieces

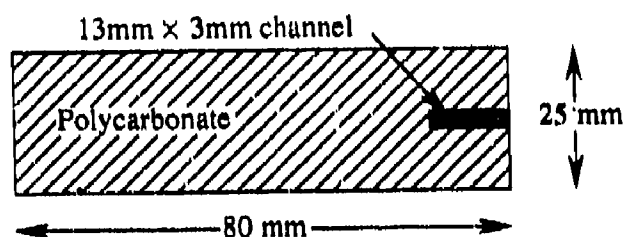


Figure 2. Schematic Diagram of Cylindrical Polycarbonate Test Piece

Other initiation methods, ranging from hot-wire to a No. 8 commercial detonator, were also tested to determine to what extent the nature and magnitude of the stimulus affected the DDT process.

Table 1 gives some data for the explosives studied: crystal density ( $\rho$ ), heat of decomposition ( $\Delta H_D$ ), temperature of ignition ( $T_I$ ),

Table 1. Physical and Thermodynamic Data

	$\rho$ (g cm <sup>-3</sup> )	$-\Delta H_D$ (kJ mol <sup>-1</sup> )	$-\Delta H_D$ (kJ g <sup>-1</sup> )	$T_i$ (K)	F of I
Mercuric-5-nitrotetrazole	3.20	890 ± 40 <sup>20</sup>	2.07 ± 0.09	510	~20
Silver-5-nitrotetrazole	2.85	430 ± 20 <sup>20</sup>	1.94 ± 0.10	538	~10
Lead azide (RD1333)	4.66	448 <sup>21</sup>	1.54	603	30
Mercury fulminate	4.42	430 ± 10 <sup>20</sup>	1.52 ± 0.03	483	10

and figure of insensitivity for impact (F of I). Table 2 shows the range of pressing loads and pressed densities.

## RESULTS

Our results suggest that the explosives tested may be usefully split into two groups from the point of view of initiation by a thermal stimulus. Lead azide, silver-5-nitrotetrazole, and mercuric-5-nitrotetrazole detonate promptly even at high pressed densities, and show little or no evidence of a well-defined burning zone. Mercury fulminate, in contrast, does not detonate reliably at high pressed densities and even at lower densities, when detonation does occur, it is characterized by long induction times and run-to-detonation lengths.

### Lead Azide/Silver-5-Nitrotetrazole/ Mercuric-5-Nitrotetrazole

These materials are characterized by prompt detonation over the range of pressed

Table 2. Pressing Loads and Densities Tested

	Pressing Loads (MPa)	Range of Densities (g cm <sup>-3</sup> )
Mercuric-5-nitrotetrazole	34.5 - 103.5	2.25 - 2.92
Silver-5-nitrotetrazole	6.9 - 103.5	1.18 - 2.72
Lead azide (RD1333)	86.3	3.05 - 3.31
Mercury fulminate	6.9 - 103.5	2.00 - 3.88

densities tested and with a variety of strengths of stimuli. No evidence of dead-pressing has been found, and streak records do not reveal the presence of a distinct burning zone before transition to detonation. The measured VOD for these primaries was found to increase steadily with pressing load.

Figure 3 shows a typical streak record from one of these materials, in this case silver-5-nitrotetrazole pressed at 69 MPa to a density of ~2.7 g cm<sup>-3</sup>, initiated by an exploding gold wire. DDT is not apparent, and the detonation propagates uniformly at 5.2 mm  $\mu$ s<sup>-1</sup>. The light output at the beginning of the trace is from the wire. Figure 4 is a section through a cylindrical test-piece showing the damage caused by mercuric-5-nitrotetrazole pressed to 69 MPa. Initiation was by hot-wire, and prompt detonation appears to have taken place. Figure 5 is a selection of frames from a sequence taken on the Beckman and Whitley 189 camera of a detonation propagating in a column of mercuric-5-nitrotetrazole pressed at 103.5 MPa to a density of 3.08 g cm<sup>-3</sup>, and initiated by an exploding gold wire. The column was front-illuminated using an argon flash tube. The reaction is seen to pick up and run very soon after the wire explosion. The VOD was estimated from these frames to be about 7 mm  $\mu$ s<sup>-1</sup>. The large apparent thickness of the reaction zone in sequences such as this is caused by the finite exposure time, which is approximately one fifth of the interframe time for this camera.

This sample was pressed into one of the polycarbonate sandwich test pieces, and it is interesting that there is also light emitted from the polycarbonate to the side of the explosive column, which is clearly coupled to the

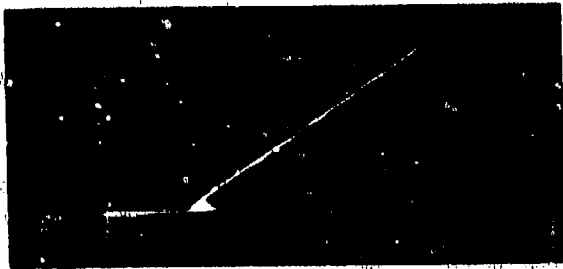


**Figure 3.** *Streak Record of Detonation in Silver-5-Nitrotetrazole Pressed at 69 MPa. Ignition by exploding gold wire. Streak speed  $98 \text{ ns mm}^{-1}$ .*



**Figure 4.** *Section Through Polycarbonate Test Piece After Detonation of Mercuric-5-Nitrotetrazole Pressed at 69 MPa. Ignition by hot-wire.*

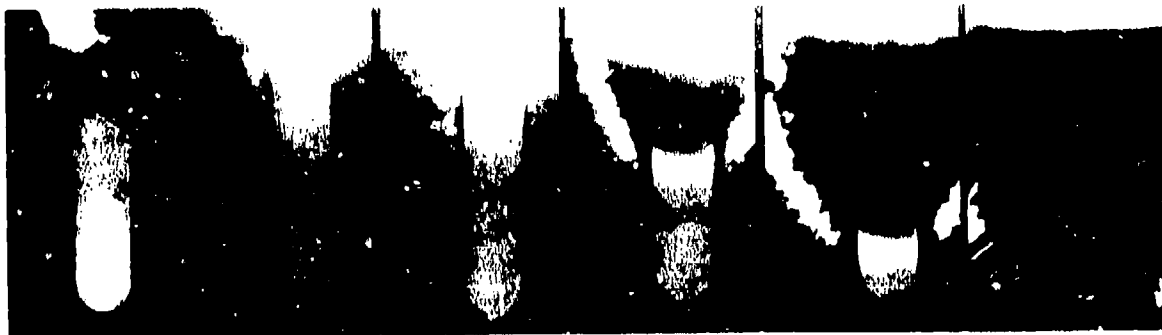


**Figure 5.** *Mercuric-5-Nitrotetrazole Pressed at 103.5 MPa.  $1 \mu\text{s}$  interframe time. Ignition by exploding gold wire.*

detonation front and appears to coincide with the position of the shock wave in the polycarbonate. Tests have shown that this is not caused by triboluminescence of the polycarbonate but is due to adiabatic gas compression in the small gap between the two blocks. The measured shock velocity in the confinement can be used to estimate the shock pressure from the detonating explosive.

In order to obtain a better view of the reaction zone, the Imacon 790 was operated in streak mode with the time axis parallel to the direction of propagation of the detonation wave. Figure 6 shows the reaction zone of a detonation wave in mercuric-5-nitrotetrazole pressed at 69 MPa to a density of  $2.85 \text{ g cm}^{-3}$ . The streak speed was set to twice the expected VOD in order to obtain an expanded image.

### Mercury Fulminate

Mercury fulminate has been found to dead-press with normal pressing methods at pressing loads of 69 MPa and above to the extent that on initiation with an exploding gold wire, the samples did not achieve detonation within the 13-mm length of the channel. Virtually all the samples reacted completely, but the deflagration was accompanied by relatively little damage to the test piece and, in some cases, was slow enough to be audible as a whistle. All the samples displayed long and variable induction times before propagation. As a result of these induction times,



**Figure 6. Streak Optical Image of Detonation Wave Running in a 3 mm Column of Mercuric-5-Nitrotetrazole Pressed at 69 MPa**

DDT in the less dense samples was not recorded on the streak records, but is in evidence on examination of the brass plates in those samples which included them. Figure 7 shows the result of DDT occurring towards the bottom of one of these brass channels containing mercury fulminate pressed to 6.9 MPa. Figure 8 is a selection of frames from a sequence from the Beckman and Whitley 189 camera of mercury fulminate pressed at 69 MPa to a density of  $3.9 \text{ g cm}^{-3}$ . No propagation is evident down the column from the top surface. The three frames given here were taken about 17  $\mu\text{s}$  after the wire explosion, and show reaction down the side of the column, presumably where the pressing operation had left loose powder in the gap between the blocks. The entire sample was eventually consumed, but did not detonate.

In contrast to these findings, those samples which were pressed in one increment, with the direction of the pressing being perpendicular to the direction of propagation of the reaction, did not exhibit dead-pressing up to 69 MPa, which was the maximum tested, but detonated strongly when initiated by an exploding gold wire. Relatively long induction times were still found, but the damage to the test-pieces indicated that the run-to-detonation length was small. This suggests that the void structure within the pressed compact may be somewhat anisotropic with the voids being more interconnected in a direction perpendicular to the pressing load, which is consistent with the findings of Swallowe and Field<sup>14</sup> and directly supports the view that the intrusion of the hot gaseous reaction products into the compact in the very early stages of the



**Figure 7. Brass Witness Plate Showing Evidence of DDT Near the Bottom of the Channel. Mercury fulminate pressed at 6.9 MPa.**



**Figure 8. Mercury Fulminate Pressed at 69 MPa. 1  $\mu\text{s}$  interframe time. Ignition by exploding gold wire.**

reaction is vital to achieving the necessary pressure build-up for DDT to occur.

Mercury fulminate samples pressed conventionally to 69 MPa and 103.5 MPa were also initiated by shock from a flat ended No. 8 detonator fired through brass shims of varying thicknesses to establish that they were capable of sustaining a stable detonation wave and to measure the VOD at higher densities. The No. 8 detonator contains a main charge of about 400 mg PETN and produces a shock pressure of about 100 kbar. All the samples initiated in this way detonated promptly, as would be expected, producing linear streak

records. Figure 9 shows one of these for mercury fulminate pressed at 69 MPa to a density of  $3.75 \text{ g cm}^{-3}$ , indicating a VOD of  $5.0 \text{ mm } \mu\text{s}^{-1}$ . This technique is being extended to measure the relative shock sensitivities of the primaries.

### Velocity of Detonation

These were calculated from the streak results, and the values obtained for mercuric-5-nitrotetrazole and silver-5-nitrotetrazole are presented graphically in Figures 10 and 11. The time axis on the streak pictures was calibrated with a certified 1 MHz signal, and the spatial axis by photographing the test-pieces in framing mode before firing. The results from the present study are compared, together with earlier results<sup>21,22</sup> for mercury fulminate and lead azide, in Figure 12.



Figure 9. Streak Record of Detonation in Mercury Fulminate Pressed at 69 MPa. Ignition by no. 8 detonator. Streak speed  $98 \text{ ns mm}^{-1}$ .

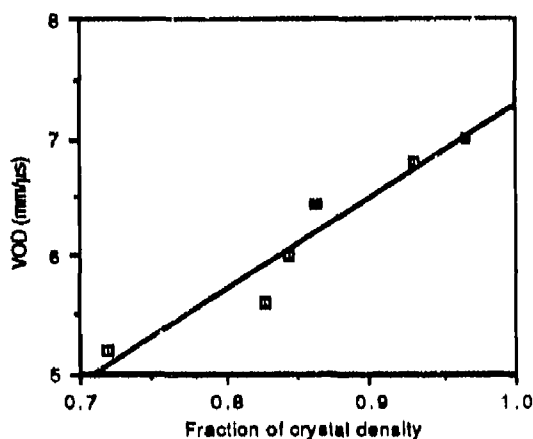


Figure 10. VOD Versus Fraction of Crystal Density for Mercuric-5-Nitrotetrazole

## CONCLUSIONS

Of the explosives studied, only mercury fulminate exhibited dead-pressing, indicated by failure to detonate, long run-to-detonation lengths, and/or long induction times ( $> 100 \mu\text{s}$ ) in heavily pressed samples. However, the dead-pressing was found to be dependent on the direction of pressing, being far less evident in samples pressed at right angles to the direction of propagation of the reaction. Neither of the nitrotetrazoles nor lead azide

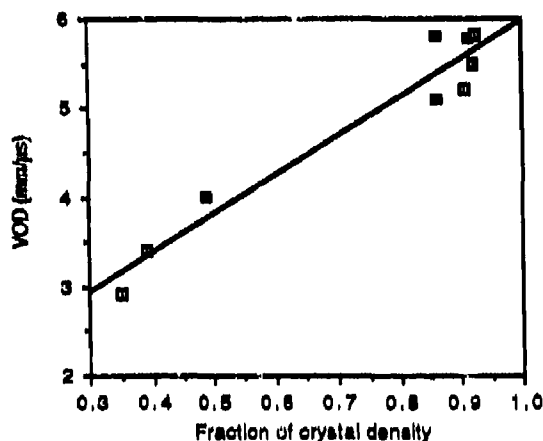


Figure 11. VOD Versus Fraction of Crystal Density for Silver-5-Nitrotetrazole

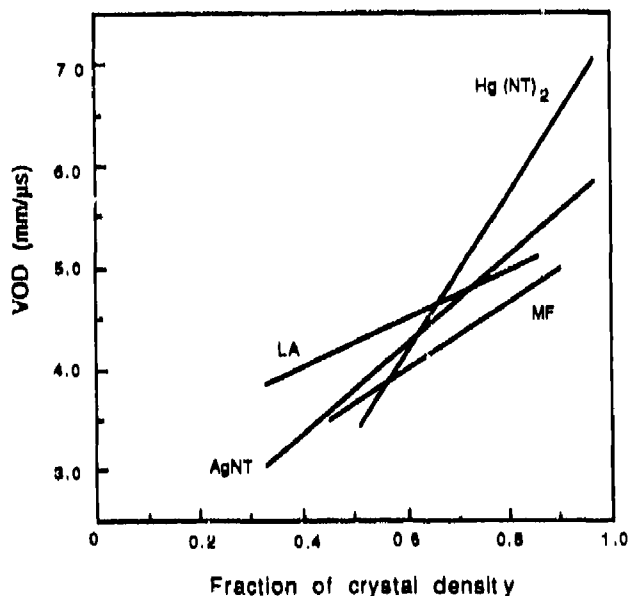


Figure 12. Comparison of VODs For Mercuric-5-Nitrotetrazole, Silver-5-Nitrotetrazole, Lead Azide, and Mercury Fulminate

exhibited dead-pressing over the range of loads studied, up to 103 MPa. The earlier reports of dead-pressing of silver-5-nitrotetrazole were not confirmed by our tests on samples prepared via the intermediate bis(ethylenediamine)-copper(II) nitrotetrazolate, possibly due to the higher purity of the latter than of the sodium salt used previously. Muraour<sup>16,17</sup> has suggested that the lack of gas penetration into the bulk is a major factor in explaining dead-pressing. Earlier studies in this laboratory<sup>14</sup> of the microstructure of pressed mercury fulminate have given clear evidence that heavily pressed samples have uni-directional voiding (across the column) while lightly-pressed samples have a network of branched voids. The problems of dead-pressing shown by mercury fulminate, when ignition was by exploding wire, were not found when samples were shock initiated. Our findings support these ideas, but do not explain why only mercury fulminate of those tested is susceptible. This may be due to the crystalline properties of the materials, which determine the amount and character of the grain fracture under compacting forces, and hence the resulting void structure.

## ACKNOWLEDGEMENTS

We thank RARDE for the provision of samples and the MoD Proc. Exec. for a grant to the laboratory. MAP wishes to thank the Australian Department of Defence for financial support in the form of a Postgraduate Study Award.

## REFERENCES

- Howard, E., *Phil. Trans. Roy. Soc. Lond.*, 1800, p. 204.
- Pollock, B. D.; Fisco, W. J.; Kramer, H.; and Forsyth, A. C., *Energetic Materials*, H. D. Fair and R. F. Walker, Eds., Plenum Press, New York, Vol. 2, Chap. 3, 1977, pp. 91-96.
- Bates, L. R. and Jenkins, J. M., *Proceedings of the International Conference on Research in Primary Explosives*, J. M. Jenkins and J. R. White, Eds., MoD, Waltham Abbey, England, Paper 14, 1975.
- White, J. R. and Williams, R. J., *ibid*, Paper 16, 1975.
- Farncomb, R. E.; Chang, M.; and Piscane, F. J., NSW/WOL TR 77-82, 1976.
- Scott, C. L. and Leopold, H. S., U.S. Patent 3,965,951, 1976.
- Scott, C. L. and Leopold, H. S., U.S. Patent 4,024,818, 1977.
- Baudler, B. and Simpson, B., NSW TR 82-484, 1983.
- Parry, M.; Field, J. E.; and Chaudhri, M. M., Annual Report (RARDE Agreement No. 2029/197), 1985.
- Taylor, J. W., *Trans. Faraday Soc.*, Vol. 58, 1982, pp. 561-568.
- Macek, A., *J. Chem. Phys.*, Vol. 31, 1959, pp. 162-167.
- Campbell, A. W., *Deflagration-to-Detonation Transition in Granular HMX*, LA-UR 80-2016.
- Ermolaev, B. S.; Sulimov, A. A.; Okunev, V. A.; and Khrapvoskii, V. E., *Fiz. Goreniya Vzryva*, Vol. 24, No. 1, 1988, pp. 65-68.
- Swallowe, G. M. and Field, J. E., *Proceedings of the 15th International Conference on High Speed Photography*, San Diego, 1982, p. 484.
- Kistiakowsky, G. B., *Proceedings of the Third International Symposium on Combustion and Flame and Explosion Phenomena*, Williams and Wilkins, Baltimore, 1949, p. 560.
- Maraour, H., *Mem. Artill. France*, Vol. 18, 1939, p. 8954.
- Muraour, H. and Demays, A., *Chim. and Ind.*, Paris, Vol. 56, 1946, p. 463.
- Chaudhri, M. M.; Garrett, W. L.; Sandus, O.; and Slagg, N., *Propellants and Explosives*, Vol. 2, 1977, p. 91.
- Bowden, F. P. and Yoffe, A. D., *Initiation and Growth of Explosion in Liquids and Solids*, Cambridge University Press, Chap. 5, 1958.

20. Brown, M. E. and Swallowe, G. M., *Thermochemica Acta*, Vol. 49, 1981, pp. 333-349.
21. Dobratz, B. M., *LLNL Explosives Handbook*, UCRL-52997, 1985.
22. *Properties of Explosives of Military Interest*, U.S. Army Material Command Pamphlet 706-177, Alexandria, VA, 1971.

### DISCUSSION

J. ROTH, Consultant  
Portola Valley, CA

Lead styphnate is easy to dead-press. However, at loading pressures at which it will

not initiate with a hot bridge wire, it can be readily detonated by a detonating fuse. This behavior is thus similar to what you observed with mercuric fulminate.

### REPLY BY P. M. DICKSON

This observation is quite correct and this type of behavior is probably even more marked in the case of lead styphnate because it is more difficult to initiate (i.e., less sensitive) than mercury fulminate anyway.

# PROMPT DETONATION OF SECONDARY EXPLOSIVES BY LASER

Dennis L. Paisley  
Los Alamos National Laboratory  
Los Alamos, New Mexico 87545

*Secondary high explosives have been promptly detonated by directing a laser beam of various wavelengths from 266 nanometers to 1.06 micron on the surface of the explosives. For this paper "prompt" means the excess transit time through an explosive charge is ~250 nanoseconds (or less) less than the accepted full detonation velocity time. Timing between laser pulse, explosive initiation and detonation velocity and function time have been recorded. The laser parameters studied include: wavelength, pulse length, energy and power density, and beam diameter (spot size). Explosives evaluated include: PETN, HNS, HMX, and graphited PETN, HNS, and HMX. Explosive parameters that have been correlated with optical parameters include: density, surface area, critical diameter (spot size), spectral characteristics, and graphite as an additive to alter spectral characteristics and enhance absorption. Some explosives have been promptly detonated over the entire range of wavelengths, possibly by two competing initiating mechanisms. Other explosives could not be detonated at any of the wavelengths or power densities tested.*

## INTRODUCTION

Numerous experimenters since the mid-1960s have used lasers of various wavelengths (usually 694 nm and 1.06 micron) to initiate primary and secondary explosives.<sup>1,2,3</sup> Initiation can be accomplished by three methods: 1) ablating a metal film in contact with the explosive (EBW-mode), 2) ablating a metal film to launch a high velocity flyer plate to impact the explosive, and 3) directing a laser beam on the confined (or unconfined) explosive surface. This paper covers experimental results for the third case of direct laser initiation of explosives. Direct laser initiation incorporates knowledge of optical properties of the lasers and explosives, and optical coupling efficiency. Literature<sup>4,5</sup> and explosives chemists suggest the UV end of the spectrum is better absorbed by most crystalline explosives and the higher energy photons (248 nm = 5 eV) could break molecular bonds. Spectral transmission studies indicate that most secondary explosives are about an order of

magnitude more absorbing at 250 nanometers than from 550 nanometers to 1.06 micron. Therefore we decided to begin our experiments at UV wavelengths. We will present the functional performance of several explosives to various wavelength laser pulses, correlate traditional explosive and spectral parameters with performance results, and offer several possible hypotheses as to the mechanisms of initiation and transition to prompt detonation.

## EXPLOSIVE PROPERTIES

### Chemical and Physical

The explosives tested include PETN, HNS, HMX, and 5 and 10 percent graphite mixtures of each explosive. Surface area, batch number to identify processing method, and other characteristics were recorded for each explosive sample. For ease of handling and experimentation, all explosives were pressed in small aluminum cups. Except for special tests, all explosive column lengths were

3.5-mm and 7.5-mm in diameter. Explosives powders under test were pressed to densities ranging 0.9 - 1.5 g/cm<sup>3</sup> over a 1.6-g/cm<sup>3</sup> PBX-9407 output charge 3.00 mm long (Figure 1).

### Optical

Optical extinction coefficients at various wavelengths for most explosives of interest have been determined.<sup>1,2</sup> H. H. Cady, Los Alamos, made additional measurements on large single crystals of PETN (Figure 2). Most optical measurements are made in solutions, suspensions, or single crystal transmissions. Since our experiments involved compacted explosive powders, it seemed appropriate to measure reflection (R) from the surfaces of compacted powder samples and determine absorption by (1-R) assuming no transmission. W. Fleming, Unidynamics-Phoenix (UPX), used a Varian Carey 2300 spectrophotometer to record the spectral reflection from samples of PETN, HMX, HNS, and graphited PETN, HMX, and HNS. Typical data are reported (Figure 3). These data are not absolute values but are relative to one another. Different particle size and density explosives were tested by UPX with a fixed solid angle for collection of reflected light. To evaluate the affect of angle dependence and wavelength on optical scattering from compacted explosive powder surfaces, John Stephens, Los Alamos, made reflection optical measurements that were angle and wavelength dependent (Figure 4). These data correspond to UPX data, H. H. Cady's single crystal PETN and published optical data.<sup>4,5</sup>

### EXPERIMENTAL TECHNIQUE

Initial testing was begun using a XeCl Excimer laser (308 nm) with a 20 ns pulse

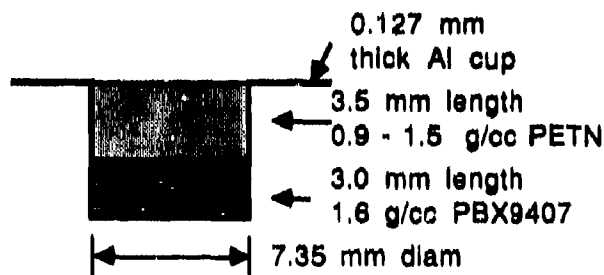


Figure 1. Explosive Test Sample for Laser Initiation (UV-Quartz Window, Optional)

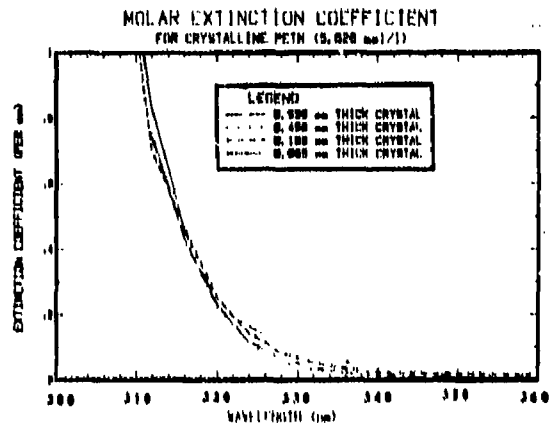


Figure 2. Molar Extinction Coefficient for Single Crystals of PETN

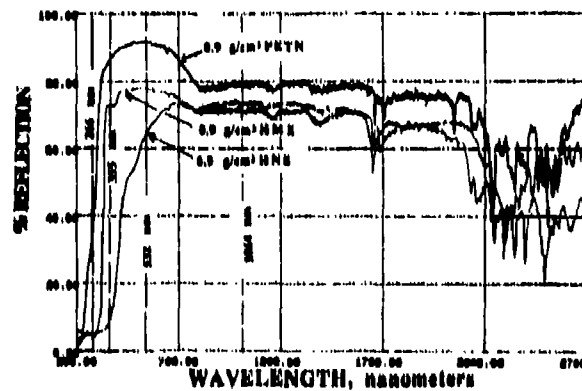


Figure 3. Reflection of PETN, HMX, and HNS Surfaces

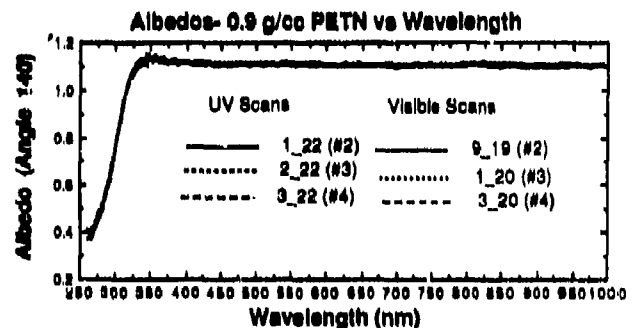


Figure 4a. Wavelength Vs. Reflection

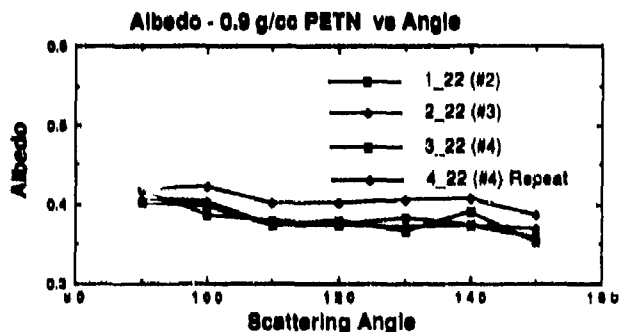


Figure 4b. Scattering Angle Vs. Reflection

length and up to 180 mJ on target. Most tests were conducted with a Quanta-Ray Nd:YAG laser operating at 1.06 micron, 355 nm, or 266 nm. The Nd:YAG pulse length was 10 ns with a pseudo-annular ring beam profile resulting from the diffraction coupled resonator (DCR). The experimental set-up and technique (Figure 5) involve operating the laser at near maximum output and attenuating the beam for the desired energy on target. The laser beam was focused through a barricade window and on the surface to the explosive sample. The lens used was a 250-mm focal length lens with  $f/28$  and large depth offield. The explosive surface to be initiated was either unconfined or confined with a UV-quartz window. Care was taken to assure that dielectric breakdown did not occur in the air or UV-quartz window before the beam reached the explosive surface. All tests were performed at ambient atmospheric conditions for Los Alamos. No gap existed between the window and the explosive surface. Each sample was aligned to the laser beam using an autocollimator/alignment telescope. In all tests, 8 percent of the beam was split off and sent to an energy meter and recorded. Extensive testing was performed to assure correlation between on-target energy and energy measurement readings were accurate. A fast (500-ps risetime) biplanar photodiode detected the laser pulse for a time zero ( $t_0$ ) to be used for explosive timing purposes. A conventional electrical pin switch was placed on the output side of the aluminum cup opposite the  $1.8 \text{ g/cm}^3$  PBX-9407 explosive for measuring function time ( $t_f$ ). Both signals were recorded on a digital oscilloscope and digital time interval counter. Since we are interested in prompt detonation, function timing is essential to distinguish between prompt detonation and deflagration-to-detonation transition (DDT). Many previous experimenters apparently did not have the need to record function time, making their data essentially unrelatable to our work where we must distinguish prompt detonation from DDT. The initiation process cannot be understood without timing considerations. Midway in our testing, we acquired and installed a Beamcode<sup>®</sup> CID two-dimensional beam profiler (200 nm - 1100 nm) to record beam profile for each individual test.

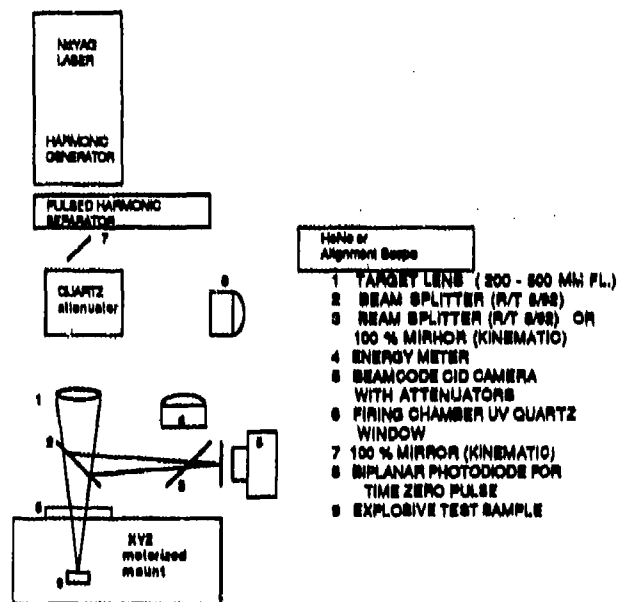


Figure 5. Optical Test Set-up for Laser Initiation of Explosives

Each test data includes: explosive parameters (particle size, batch number, density, physical dimensions), laser parameters (energy, power, energy/power density, pulse length, beam profile), and function time of the explosive. Special tests were performed to evaluate explosive run distance to full detonation and induction time (time from laser pulse to onset of chemical reaction).

## EXPERIMENTAL DATA AND RESULTS

PETN and HMX were promptly detonated at 308 nanometers at power densities that relate to explosive type and density (Figure 6). These data represent approximately 30 tests at each density. The threshold value and error bars were determined by the ASENT<sup>®</sup> computer code. HNS could not be detonated at any power density up to the laser's maximum of  $\sim 5 \text{ GW/cm}^2$ . The reason is uncertain, since the optical reflection data for all three of the explosives is not significantly different.

Approximately 400 PETN and 100 HMX total tests were performed at 1.06 micron, 355 nm, and 266 nm at explosive densities  $0.9 - 1.3 \text{ g/cm}^3$ . The explosive function times ( $t_f$ )

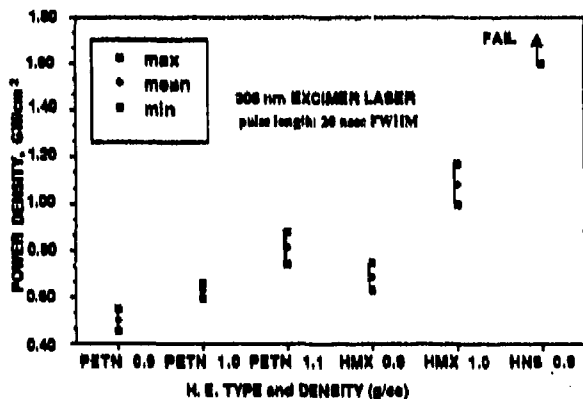


Figure 6. Threshold for Initiation of PETN, HMX, and HNS at 308 nm

were measured from the time the laser beam impacted the explosive surface ( $t_0$ ) to the time of pin switch closure at the output side of the explosive sample (Figures 7, 8, and 9). In all tests as the stimulus increased the function time decreased to an asymptotic limit of ~100 - 150 nanoseconds longer than the full detonation velocity through the sample would predict. As the stimulus was decreased to near threshold, the function time would increase by ~300 nanoseconds and at lower stimulus fail. The mixed region stimulus between fire/fail was usually small (~0.05 GW/cm<sup>2</sup>).

Since power densities (> 0.7 GW/cm<sup>2</sup>) resulted in an excess function time of ~100 - 300 nanoseconds, we conducted experiments to evaluate the explosive surface during the imparting of the laser energy at various power densities from threshold to well above threshold. We added to our experimental set-up (Figure 10) to include the ability to view the surface of the explosive with an electronic streak camera synchronized with the laser pulse. Streak records were recorded from below threshold (0.7 GW/cm<sup>2</sup>) to 1.62 GW/cm<sup>2</sup> (Figures 11 a-f). These streak records show the plasma from the laser pulse interacting with the explosive, the time delay between laser pulse and initiation, and the detonation front expanding out radially at the explosive/window interface. One can see the slope (detonation velocity) increase and then continue at a constant detonation velocity. These data have been quantified (Figure 12) and compared with full detonation velocity for 0.9 g/cm<sup>3</sup> PETN. The measured function time

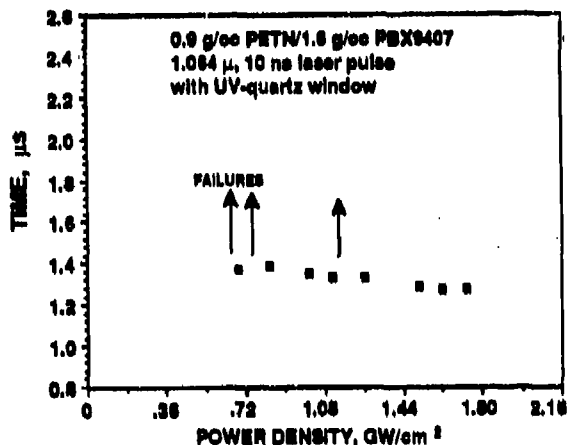


Figure 7. Power Density Vs. Function Time and Threshold for PETN at 1.06 Micron

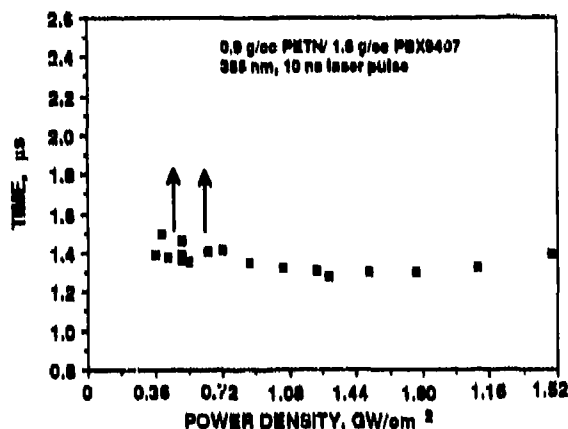


Figure 8. Power Density Vs. Function Time and Threshold for PETN at 355 nm

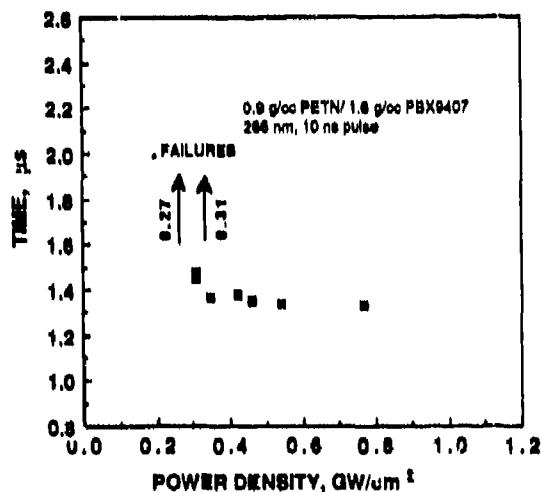


Figure 9. Detonation of 0.9 g/cc PETN at 266 nm, 10 ns Laser Pulse with Window

( $t_f$ ) less the inherent delay time from laser pulse to initiation should result in the full

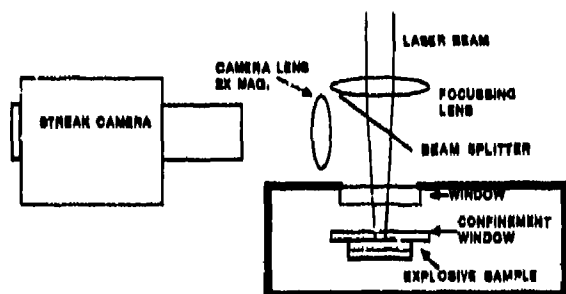


Figure 10. Streak Camera Technique for Induction Time Measurement

detonation velocity. The streak record in Figure 11c was tested near threshold ( $0.75 \text{ GW/cm}^2$ ) and exhibits an unusual initiation profile. The explosive, initiated along the periphery of the laser pulse, propagates radially outward, but not inward, at least on the surface of the PETN.

## DISCUSSION OF EXPERIMENTAL RESULTS

XeCl (308 nm) Excimer beam diameters were measured by laser burn patterns on laser burn paper. The CID beam profiler was incorporated early in the Nd:YAG test data. The beam envelope on target was essentially the same on all Nd:YAG tests, but energy/power distribution in the envelope did vary. However, we have not been able to attribute any unpredictable performance because of energy distribution within the envelope.

Prompt laser initiation of PETN is easier than HMX at wavelengths 1.06 micron, 355 nm, and 266 nm. HNS ( $0.9 \text{ g/cm}^3$ ) cannot be initiated at power densities as high as  $5.0 \text{ GW/cm}^2$  at any of the wavelengths tested even though spectral data would suggest otherwise. The addition of graphite (5-10 percent) does not decrease the power threshold. Streak camera records of laser/explosive surface interaction show how the lower optical power density input affects the initiation and builds to full detonation velocity. The lower power densities result in longer times between laser pulse and first reaction of the explosive. This phenomenon is similar to streak records for initiating PETN by exploding bridgewires.<sup>7</sup>

Streak records can help interpret earlier timing data. One particular test (Figure 11c), fired at near threshold condition, exhibits an unusual initiation begun on the periphery of the laser pulse. We originally thought this streak record to be an anomaly, however, review of earlier theoretical calculations<sup>8</sup> suggest periphery initiation is possible. R. J. Harrach, Lawrence Livermore National Laboratory, has calculated a thermal initiation model indicating that under certain circumstances the center of a beam could ablate the explosive surface and initiate on the beam edge. This is exactly what we observed under slightly different, but similar conditions, and thus adds credence to a thermal initiation mechanism at 1.06 micron. At UV wavelengths, confinement of the initiating surface is not as significant as with 1.06 micron. Since an order of magnitude increase in optical absorption in the UV and confinement at UV wavelengths has no appreciable effect on initiation, one can speculate that different mechanisms might be taking place at 1.06 micron and 266 nanometer (possibly thermal and photodissociation, respectively).

## CONCLUSIONS

The longer wavelengths (i.e. 1.06 micron) appear to cause initiation by thermal hot spots that grow to detonation, whereas the shorter wavelengths (266 - 308 nanometers) may possibly initiate by bond-breaking (or at least energy deposited inside crystals, Table I). These hypotheses are partly supported by the fact that for longer wavelengths, the laser pulse/explosive surface must be confined by an optically transmitting window in order for prompt detonation to occur, but short wavelengths can promptly detonate the same explosive at lower energy and power densities with or without physical confinement of the interface.

## ACKNOWLEDGEMENTS

We greatly appreciate the technical assistance of N. Montoya and D. Stahl, and J. Meier in conducting tests and collecting data. We also thank H. H. Cady, J. Stephens, and W. Fleming for their discussions and optical measurements on explosive samples.

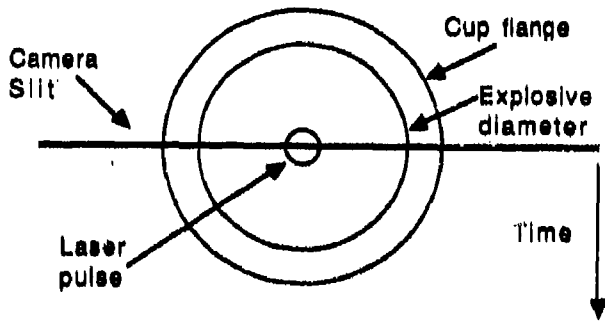


**Figure 11a. Streak Camera View of Explosive/Laser Pulse Interaction Surface Through a UV-Quartz Window**

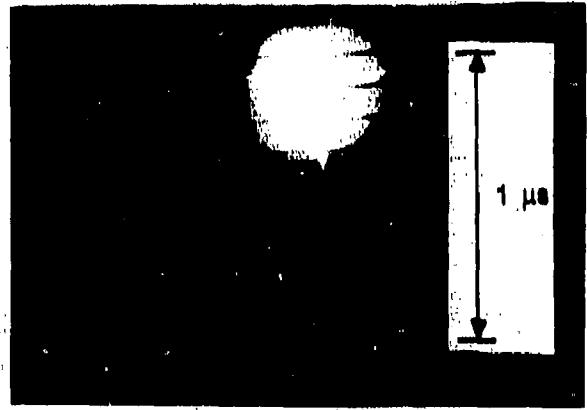


**Figure 11b. Fired at 0.62 GW/cm<sup>2</sup>; Laser Plasma Only**

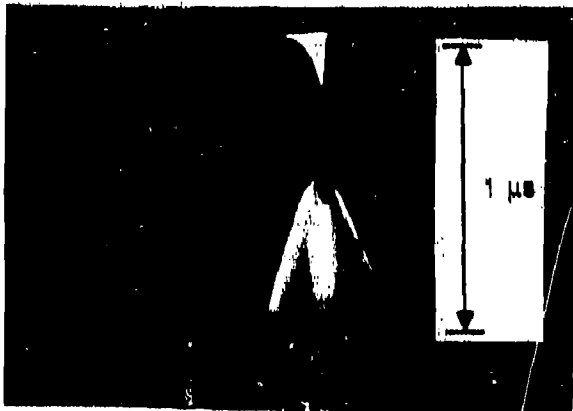


**Figure 11c. Fired at 0.67 GW/cm<sup>2</sup>; Laser Plasma and Detonation Front Recorded**

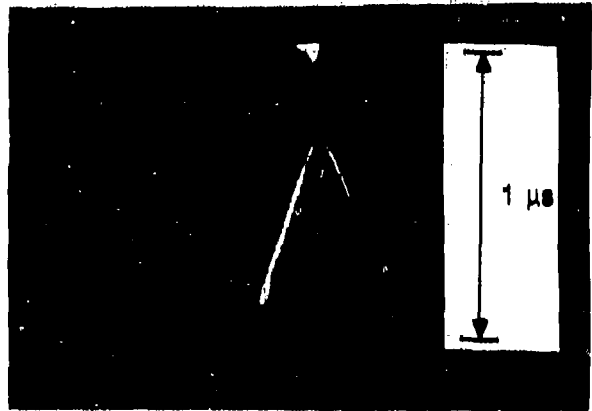


**Figure 11d. Fired at 0.73 GW/cm<sup>2</sup>; Laser Plasma and Detonation Front Recorded**

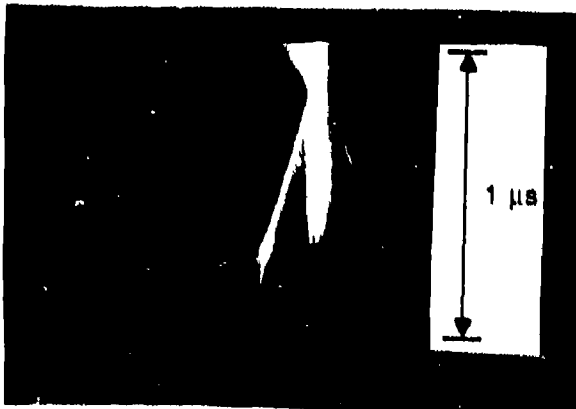


**Figure 11e. Fired at 1.13 GW/cm<sup>2</sup>; Laser Plasma and Detonation Front Recorded**

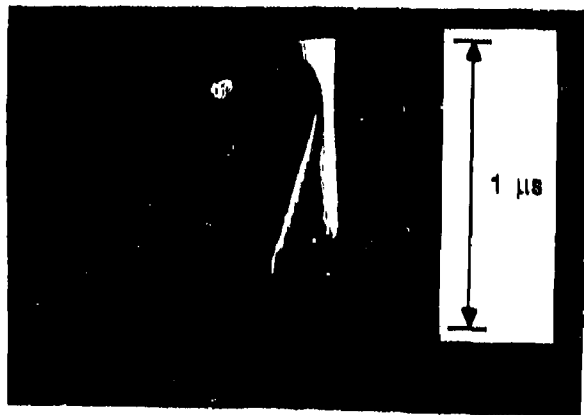


**Figure 11f. Fired at 1.60 GW/cm<sup>2</sup>; Laser Plasma and Detonation Front Recorded**

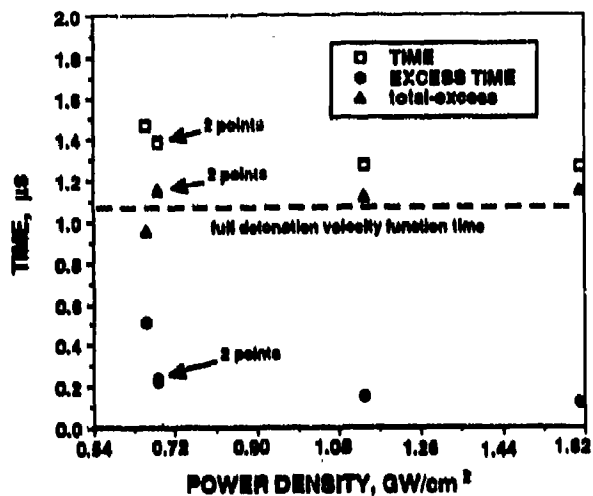


Figure 12. Quantified Data from Figure 11; Excess Times, Function Times, and Difference in Times Compared to Full Detonation Velocity

## REFERENCES

1. Jia Baoren et al., "Experimental Studies on PETN Detonators Initiated by Laser Radiation," *Proceedings of the International Symposium on Pyrotechnics and Explosives*, Beijing, China, 12-15 Oct 1987, pp. 49-56.
2. Bochier, M., "A Contribution to the Study of Laser-Based Ignition of Pyrotechnical Substances," *Proceedings of the Nineteenth International Annual Conference of I.C.T.*, Karlsruhe, FRG, Jun 1988.
3. Yang, L. C. and Minechelli, V. J., "Laser Initiation of Insensitive High Explosives," *Proceedings of the Sixth Symposium (International) on Detonation*, San Diego, Aug 1975.
4. Urbanski, T., *Chemistry and Technology of Explosives*, Vol. II, Pergamon Press, Oxford, 1965, p. 177.
5. Mullen, P. A. and Orloff, M. K., "Ultra-violet Absorption Spectrum of Pentaerythritol Tetranitrate," *Journal of Physical Chemistry*, Vol. 77, No. 7, 1973, p. 910.
6. ASENT Computer Program, Report SAND80-8216, original by Sandia Corp., Livermore, CA, 1980, with modifications by R. J. Yactor, Los Alamos National Laboratory, M-7, Los Alamos, NM 87545, 1989.
7. Blackburn, J. H. and Reithel, R. J., "Exploding Wire Detonators: Sweeping-Image Photographs of the Exploding Bridgewire Initiation of PETN," *Exploding Wires*, Vol. 3, 1964, Plenum Press, New York.
8. Harrach, R. J., "Estimates on the Ignition of High-Explosives by Laser Pulses," *Journal of Applied Physics*, Vol. 47, No. 6, June 1976.

Table 1. PETN Data Summary

Wavelength (nm)	Detonation Power Density Threshold with UV-Quartz Confinement (GW/cm <sup>2</sup> )	Detonation Power Density Threshold without UV-Quartz Confinement (GW/cm <sup>2</sup> )
1064	0.71	> 5.00
355	0.50	2.50
308	0.50	0.70
266	0.25	0.50

## DISCUSSION

**BARRY T. NEYER**  
EG&G Mound Applied Technology  
P.O. Box 3000  
Miamisburg, Ohio 45343

Have you noticed any changes in the velocity at threshold as a function of flyer thickness?

### REPLY BY DENNIS PAISLEY

No, I have not noticed any changes in the thickness of the plates that we tested. Thinner plates have a higher velocity. We have not performed detailed tests that would allow me

to directly answer to your question; however, the thinnest plates tested did initiate high density secondary explosives.

## DISCUSSION

**MANFRED HELD**  
Messerschmitt-Bolkow-Blohm  
8898 Schrobenhausen, West Germany

What was the diameter of the laser spot?

### REPLY BY DENNIS PAISLEY

The diameter of the laser spot was about 1 millimeter.

# LASER INITIATION OF SECONDARY EXPLOSIVES

Anita M. Renlund, Phillip L. Stanton, and Wayne M. Trott  
Sandia National Laboratories  
Albuquerque, New Mexico 87185

*We have performed several experiments to investigate the effects of explosive material parameters on energy thresholds for direct laser initiation of secondary explosives. Laser energy requirements for initiation of pentaerythritol tetranitrate (PETN) were decreased for small particle size powder and low density pressings. Promptness of detonation, however, was aided by higher densities. Initiation of PETN was achieved at energies at or below 10 mJ (power densities  $\sim 0.2 \text{ GW cm}^{-2}$ ) at laser wavelengths of 1.06  $\mu\text{m}$ , 532 nm, and 355 nm and strong confinement of the explosive sample assisted buildup to detonation. At 355 and 308 nm, PETN could be initiated by irradiation on the bare explosive surface. Hexahydro-1,3,5-trinitro-s-triazine (RDX) was initiated at 308 nm, but not at 1.06  $\mu\text{m}$ . We were unable to initiate hexanitrostilbene (HNS) by direct irradiation at any of these wavelengths. The results suggest that if sufficient energy is deposited, a fast deflagration or convective burn is achieved and that this grows to detonation via a conventional deflagration-to-detonation transition (DDT).*

## INTRODUCTION

Experimental and theoretical studies on prompt initiation of energetic materials began in the 1960s, shortly after the advent of the laser. This continues to be an active research field driven, in part, by improvements in miniaturization of high-power lasers.<sup>1-7</sup> Survey of much of the literature reveals that in several cases these studies of laser initiation have not documented important experimental parameters. In particular, description of the high explosive (HE) material (e.g., microstructural properties, dopants, etc.) has generally been inadequate. Thus, while feasibility of laser initiation of HEs is well established, there remains little understanding of controlling mechanisms or material parameters which affect initiation thresholds.

Laser radiation has been used in two distinct approaches to lead to prompt initiation of an HE. Acceleration of a thin flyer plate by a laser-generated plasma and subsequent impact of the flyer onto the HE causes

initiation via a shock mechanism.<sup>5</sup> Further characterization of this initiation scheme is needed; however, the important HE parameters are expected to be very similar to those associated with electrically-driven flyer initiation. Another approach to prompt HE initiation relies on direct interaction of the laser output or the laser-generated plasma with the explosive material.<sup>3,6</sup> The experiments described in this paper focus on the effects of both laser and explosive material parameters on these "direct" initiation processes. In addition, we consider initiation of only secondary HEs.

Pentaerythritol tetranitrate (PETN) has been our explosive of choice for this study, in part because recent work showed that it could be initiated at modest laser energies.<sup>6,7</sup> Other HE materials which we have attempted to initiate include hexanitrostilbene (HNS) and hexahydro-1,3,5-trinitro-s-triazine (RDX). The sheer number of material and laser parameters which may influence initiation and detonation behavior make this ongoing study

complex and time consuming. The variables over which we have exercised some control include the HE particle size and density, the confining window materials, dopants added to enhance absorption of the laser energy, coatings on the window to enhance plasma generation, and laser wavelength, pulse duration and spot size. Our aim has been to observe the effects of these variables on both the energy threshold and promptness of initiation. In addition we have employed optical diagnostics that might aid in elucidating the initiation mechanism.

## EXPERIMENTAL

### Sample Preparation

PETN powder was obtained from several sources. Table 1 lists some of the powders we tested, their sources and lot numbers, and particle size information where available. Since particle size measurements based on the Fisher sieve size and BET are not directly comparable, we obtained scanning electron microscopy photographs of samples of the first four materials listed. These showed that the Mound ER17119 (HSSA) was in fact smaller in particle size than the Pantex 7119-304M-01 (Micronized) and the listing in the table is in order of apparent particle size.

For the initiation tests described here, the powders were pressed into cylindrical fixtures

that confined the HE radially in an aluminum ring and on the faces with optical windows. The powder was pressed to the desired density (linear mechanical pressing) into the ring against the optical window through which the laser radiation was later admitted. For reference purposes, this will be called the front or initiation face. To obtain different confinement conditions we used windows of different shock impedances, namely sapphire, fused silica (FS), and lucite. In some experiments we used windows onto which 500-A thick aluminum had been vapor deposited. The aluminum was used to enhance plasma formation at the window/HE interface. After pressing, a lucite window was affixed to the back of the aluminum ring to complete confinement of the HE powder column. Nominal densities of PETN ranged from 0.9 to 1.4 g cm<sup>-3</sup> (51 percent to 79 percent theoretical maximum density) and the charge dimensions were 3.18 mm in diameter by 6.35 mm long.

### Initiation Tests

The experimental arrangement is shown schematically in Figure 1. For most of these tests we used a Q-switched Nd:YAG laser (Quanta-Ray DCR 2A) operating at 1.064  $\mu$ m. At full power, the temporal profile of the output consisted of several high intensity mode spikes in an envelope of  $\sim 10$  ns (FWHM). The pulse width could be lengthened to 35 ns by adjusting the bank voltages to the oscillator

Table 1. PETN Powders for Laser Initiation Studies

Source <sup>a</sup>	Lot #	Sp. Surf. Area m <sup>2</sup> g <sup>-1</sup>	Comments
Mound	ER17119	2.1 (Fisher)	"High Spec. Surf. Area" (HSSA)
Mound	UK 1-150	0.6 (Fisher)	UK fine
Pantex	7119-304M-01	3.0 (BET)	Micronized
Pantex	1076-0211-195	0.4 (BET)	XTX grade
LANL	Type 12	1.3	Type 12
UPI	EL-82493	NA	XTX grade
UPI	EL-82494	NA	3% Zr-doped XTX grade

<sup>a</sup> Samples obtained from R. Thorpe of EG&G Mound Laboratories, A. Duncan of Mason & Hanger Pantex Plant, D. Paisley of Los Alamos National Laboratory (LANL), and J. Fronabarger of Unidynamics Phoenix, Inc. (UPI).

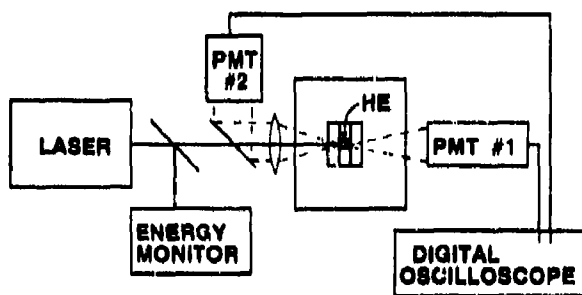


Figure 1. Schematic Drawing of Experimental Arrangement for Laser Initiation Tests

and amplifier lamps. Most of the tests were carried out with a pulse width of 20 ns. The energy was attenuated to the desired level using optical filters. The spatial profile of the output was not uniform over the output spot but was in the familiar "donut" mode.

Simple lenses (12- to 15-cm focal lengths) were used to focus the laser energy onto the HE. In order to avoid air breakdown due to the high optical power density near the focal plane, the sample fixture was mounted in a vacuum chamber which was evacuated to  $<0.1$  Torr prior to firing. The fixture was positioned so that the laser output was brought to a focus at the window/HE interface; some defocussing in the window, however, limited the spot size to  $\sim 0.5$ -mm diameter on the HE surface. The sample position was adjusted as needed to account for the different refractive indices of the window materials. Spot sizes were estimated from energy measured through a pinhole scanned in contact with the rear surface of a window. A 10 percent beamsplitter was used to direct a portion of each laser pulse to an energy probe. This was calibrated to the actual energy delivered to the HE sample. All laser energies cited here are those calculated to be seen by the HE. In addition to the energy monitor, a phototube (not shown) viewed the laser pulse to give an initial time marker.

A photomultiplier tube (PMT #1) monitoring light output at the back surface of the HE charge was used to determine function time. In previous experiments we have observed that care must be exercised when using detonation emission as a timing marker since first light observed from the back of the

charge is often due to emission shining through unreacted material.<sup>8</sup> Fortunately, the light coincident with detonation wave "break-out" at the back surface can be distinguished from "shine through" light by direct comparison of the temporal and spatial properties of the emission. Accordingly, we have verified the timing by simultaneously measuring the output of the PMT and recording the emission on a fast-framing electronic image-converter camera (Hadland Photonics Ltd., Imacon 675).

A limited number of initiation tests were made using wavelengths other than  $1.06 \mu\text{m}$ . Both the second and third harmonics of the Nd:YAG laser were used in experimental configurations much the same as that described above. The only substantive change concomitant with doubling and tripling the laser frequency was in the pulse width. For conditions yielding a 20 ns pulse width at  $1.06 \mu\text{m}$ , the pulse widths at 532 nm and 355 nm were 15 ns and 12 ns, respectively. In addition to the Nd:YAG laser we used an excimer laser (Lambda Physik, EMG200) at 308 nm in some tests. Its pulse width was 24 ns (FWHM). The temporal profile of this laser lacked the intense mode spikes of the Nd:YAG laser. Its beam size at the focus was  $\sim 1 \times 2$  mm.

Optical diagnostics were used to study reactions at the initiation face of the HE. In the simplest configuration (see Figure 1) PMT #2 viewed light from the front surface to observe the time at which substantial reaction occurred. We also analyzed that emission spectroscopically. Single-pulse Raman spectroscopy was employed to monitor reaction progress at the front face. This required a second laser pulse (a dye laser at 527 nm) delayed relative to the initiation laser with the Raman signal collected and analyzed as described in Reference 9.

## RESULTS

### Initiation Thresholds

At the present stage of this study, we have been unable to fire enough identical explosive devices to establish the initiation threshold values at a high statistical confidence level. Generally only five identical

samples were fired at different laser energy levels (all other conditions, i.e., laser spot size, wavelength and pulse width being unchanged) to establish go/no go levels. Threshold values cited here are the lowest energies at which detonation was achieved. A practical upper limit on laser energy was reached at  $\sim 250$  mJ ( $>1$  GW  $\text{cm}^{-2}$ ) due to damage and energy dissipation in the windows. Two types of explosive events were observed. In a few cases, buildup to detonation did not occur and the PETN only deflagrated. At somewhat higher laser energies, detonation was usually achieved in similar samples. Clear differences were observed between the deflagrating and detonating samples, both in the device function times and in the damage to the explosive fixture. Table 2 lists results from several test conditions for initiation of PETN using 1.06- $\mu\text{m}$  radiation. In separate tests we observed no significant difference in initiation thresholds for laser pulse widths between 10 and 25 ns, but slightly higher laser energies were required at longer pulse widths.

### Function Times

Figure 2 shows typical data traces from which we derived the device function times. The upper trace is from the phototube viewing the laser pulse, the lower trace is from PMT #1 viewing the end of the PETN column. Figure 3 is a fast-framing photograph of the detonation event as seen from the back of the fixture. The early frames show the shine-through of detonation light from within the sample. The two bright frames (frames 5 and 6) are of light generated when the detonation wave interacted with the rear lucite window. These are coincident in time with the sharp rise and narrow peak of the PMT #1 signal shown in Figure 2. The function time of the device was therefore the interval between the laser pulse and the sharp rise observed on the back PMT signal. Our measure of promptness was the excess function time, i.e., the time measured in excess of that of a steady detonation wave traveling through the 6.35-mm long column of PETN, at the given density. In all cases, we observed an increase in function time as the laser energy was reduced to the threshold value. At sufficiently high energy, the excess

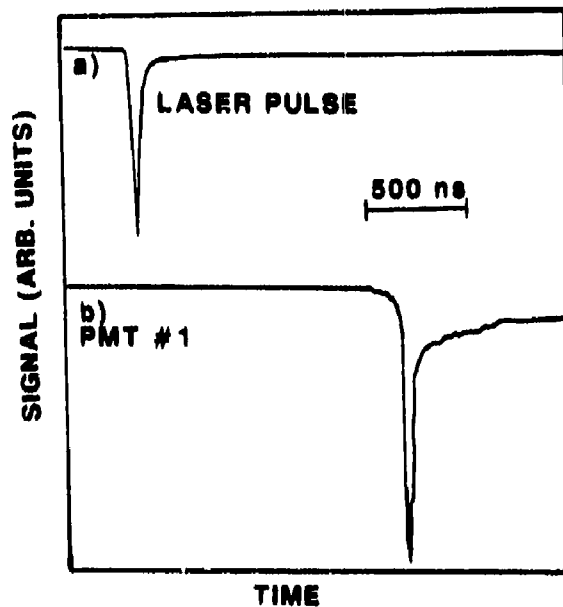


Figure 2. PMT Traces from Which We Derive Device Function Time. a) Laser initiation pulse. b) Temporal profile of emission observed at the end of the detonating PETN column. (Compare to spatial profile of emission shown in Figure 3.) The function time for this device (HSSA,  $\rho = 1.0$  g  $\text{cm}^{-3}$ ) was 1.35  $\mu\text{s}$ , the excess transit time was 200 ns.

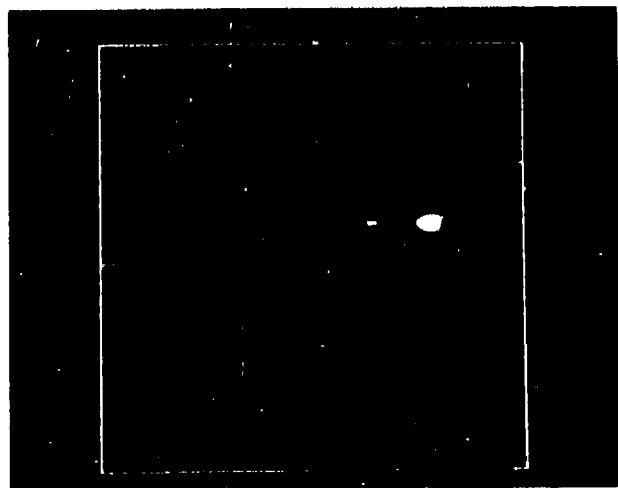


Figure 3. Fast-framing Photograph of Emission Viewed at the End of the Detonating PETN Column. (Compare to temporal profile shown in Figure 2b.)

transit time approached a limiting value which depended on the HE sample and its confinement. We include in Table 2 the shortest

Table 2. Initiation Test Data Summary

A. Effect of powder (FS window, $1.2 \text{ g cm}^{-3}$ , 0.7-mm spot size)			
Powder	Threshold	Min $t_{ex}$	Energy at min $t_{ex}$
HSSA	47 mJ	60 ns	53 mJ
Micronized	43	150	72
UK Fine	52	300	54
LANI-12	59	50	72
XTX	165	>5000--Defl	195
XTX/Zr	100	700	105
B. Effect of density (FS window, HSSA, 0.6-mm spot size)			
Density	Threshold	Min $t_{ex}$	Energy at min $t_{ex}$
$0.9 \text{ g cm}^{-3}$	20 mJ	120 ns	41 mJ
1.0	18	110	44
1.2	39	50	50
1.4	59	40	86
C. Effect of window (UK fine, $1.2 \text{ g cm}^{-3}$ , 0.7-mm spot size)			
Window	Threshold	Min $t_{ex}$	Energy at min $t_{ex}$
Lucite	64 mJ	400 ns	73 mJ
FS	52	300	54
Sapphire	46	100	70
D. Effect of Al on window (HSSA, $1.2 \text{ g cm}^{-3}$ , 0.5-mm spot size)			
Window	Threshold	Min $t_{ex}$	Energy at min $t_{ex}$
FS	36 mJ	50 ns	52 mJ
FS with Al	22	15	36

excess transit times (min  $t_{ex}$ ) we measured for a given test series. The laser energies at which these min  $t_{ex}$ 's were measured are also given in Table 2. In some cases, the min  $t_{ex}$  may not represent the true limiting values which can require a laser energy twice the threshold energy.

### Wavelength Dependence

We performed some initiation tests at wavelengths other than the Nd: YAG fundamental to see if there was any wavelength specificity to the initiation process. For HSSA PETN at a density of  $1.0 \text{ g cm}^{-3}$ , confined by a fused silica window, we observed no significant changes in laser energy thresholds or function times in going to 532 or 355 nm. For both wavelengths, we achieved initiation at 7 mJ

with excess transit times of 200 ns. Under similar conditions the lowest energy at which PETN was initiated at  $1.06 \mu\text{m}$  was 10 mJ. The corresponding power densities were all  $\sim 0.2 \text{ GW cm}^{-2}$ . Experiments at 308 nm used an excimer laser operating on XeCl. The spot size was larger and the pulse length longer with this laser. Initiation thresholds were  $\sim 75 \text{ mJ}$  (power density  $\sim 0.15 \text{ GW cm}^{-2}$ ). The excess transit times were generally  $< 100 \text{ ns}$ .

One marked difference was observed in initiation of the PETN at the shorter wavelengths. The need for confinement was not as great. In fact, the PETN was easily initiated at 308 nm without window confinement. We observed roughly the same initiation thresholds with and without windows at this wavelength; those samples with windows

functioned, on average, about 50 ns faster than those without windows. At 355 nm there was a more marked difference in thresholds with and without a window; three times greater energy was required to initiate unconfined PETN. At both 532 nm and 1.06  $\mu\text{m}$  we were unable to initiate PETN without window confinement at energies up to 200 mJ.

### Optical Diagnostics

These preliminary studies were aimed at giving us information on the mechanism of the initiation process. In the simplest case, we looked at the time when light was emitted from the front face of the detonating HE sample. Data from such experiments are shown in Figure 4. The first peak in the emission profile is due to the laser and the laser-generated plasma. Emission from the plasma was observed in all experiments including initiation failures. The second emission feature varied in time depending on initiation parameters. It was usually delayed by less than 400 ns relative to the laser pulse for those samples which detonated fairly promptly ( $< 200$  ns excess transit time). In slow functioning devices, however, it was occasionally delayed so that it appeared after the light was viewed at the rear surface. Experiments that resolved this emission spectrally showed that the light was broad and unstructured.

Raman experiments on the front surface were difficult. The Raman signal was viewed on top of an emission continuum from either the laser-generated plasma or the detonation light. Also, there were some lines that arose from the interactions of the driving laser with the confining window. A typical spectrum is shown in Figure 5. In general, we were unable to see anything but bright plasma emission at early times and only detonation light at late times. In between, we observed mostly a decrease in the intensity of the PETN signal with time, but observed no significant new species. The parent PETN signal persisted until it was swamped by the detonation light.

### RDX and HNS

RDX was successfully initiated at 308 nm, but not at 1.06  $\mu\text{m}$ . The RDX powder has not been fully characterized at this time.

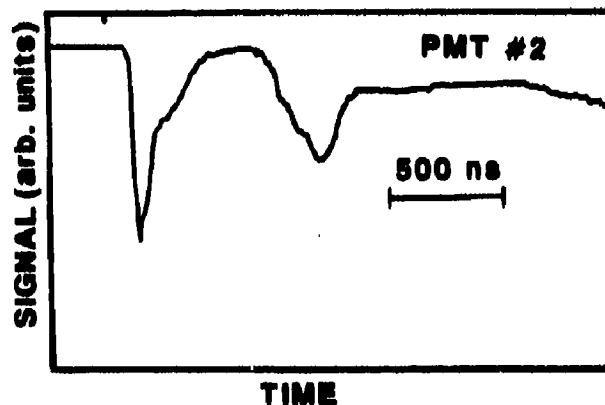


Figure 4. Temporal Profile of Emission Viewed at the Initiation Face of the PETN. The first peak is due to the laser pulse. It is broadened relative to that in Figure 2a because of emission from the laser-generated plasma, which was characteristic of all experiments including those samples that failed to initiate. The function time for this device (HSSA,  $\rho = 1.0 \text{ g cm}^{-3}$ ) was 1.44  $\mu\text{s}$ , the excess transit time was 290 ns.

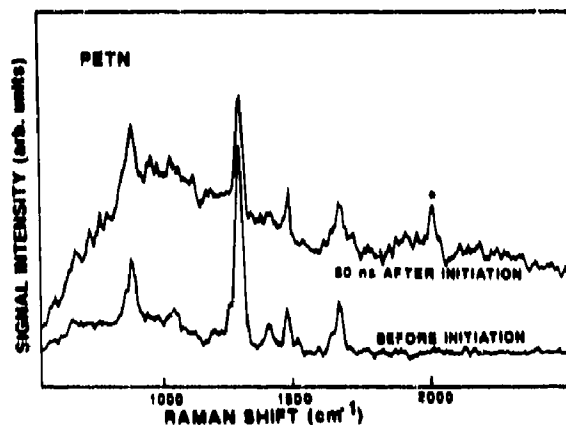


Figure 5. Single-pulse Raman Spectra of the Front Face of the PETN Before and 80 ns After Initiating Laser Pulse. The peak marked with an asterisk (\*) is emission at 580 nm from Na impurity in the PETN. The Raman laser excitation wavelength was 527 nm.

The laser energy threshold was similar to that for HSSA PETN, but the excess function time was considerably longer at  $> 300$  ns. We were unable to initiate fine particle HNS (specific surface areas of 6  $\text{m}^2 \text{ g}^{-1}$  and 13  $\text{m}^2 \text{ g}^{-1}$ ) at densities from 1.2 to 1.6  $\text{g cm}^{-3}$  by direct laser

irradiation at energy levels to 250 mJ (power density  $> 1 \text{ GW cm}^{-2}$ ). We did see significant charring of the HNS pellet, but reaction did not grow to sustained deflagration or detonation. In separate experiments, however, HNS was initiated by a laser-accelerated flyer at laser energies  $< 100 \text{ mJ}$ .

## DISCUSSION

Examination of the results presented above shows that specific design choices can be made to optimize the initiation of PETN at  $1.06 \mu\text{m}$ . At these densities it is clearly advantageous to use fine particle PETN; this leads to a decreased energy threshold for initiation at no cost to detonation performance. By contrast, while decreasing the density of the PETN in this range also leads to lower threshold energies, the excess transit time generally increases. Moreover, timing reliability is compromised, i.e., the jitter in the function time increases. Whether the observed uncertainty in timing is due solely to the device reproducibility in this study or to some fundamental difficulty in the physical and chemical processes leading to detonation cannot be inferred from the limited data base.

While we have not yet employed extensive diagnostics to determine the details of the initiation mechanism, we do have sufficient data to explore how the absorption of optical radiation can lead to detonation. In particular, we are interested in understanding the processes that give rise to the excess transit times measured in these experiments. For applications of laser initiation it may be vital to control the excess transit time as this will govern the function time precision of an optically-driven detonator.

A simplified distance-time ( $x-t$ ) diagram is shown in Figure 6, which illustrates two possible causes of the excess time. Point #1 in the figure is the measured function time of the device. The slope of the line approaching point #1 is determined by the known detonation velocity,  $D^*$ , for PETN at the given density. Extrapolation of this line to  $x = 0$  describes a process where an induction time is needed at the front surface to generate the pressure and temperature conditions to promote detonation.

Detonation would then proceed from this surface at the usual detonation velocity. The excess transit time would thus be a measure of this induction or delay time. An alternative description of the initiation process views detonation as reached after transition from a slower process (deflagration or reactive shock propagation) generated by the laser pulse. In this case, there is a transition to the steady detonation wave after some induction length,  $l$ , within the bulk of the HE. The excess transit time is then a measure of the velocity of the slow process and how far it travels prior to transition to detonation.

Our results lead us to believe that it is the second mechanism, involving a transition to detonation, either deflagration-to-detonation transition (DDT), or shock-to-detonation transition (SDT), that dominates in these laser initiation experiments. One indication of this is obtained from the observation of light generated at the front face of the explosive at some delay after the laser pulse (see Figure 4). If the first mechanism controlled initiation, one would expect the emission observed at the front face to occur at a time indicative of the excess transit time, but we usually observe light from 0.1 to  $1 \mu\text{s}$  later. Instead, if this emission results from the interaction of a detonation wave at the front surface of the explosive, the time at which we observed the

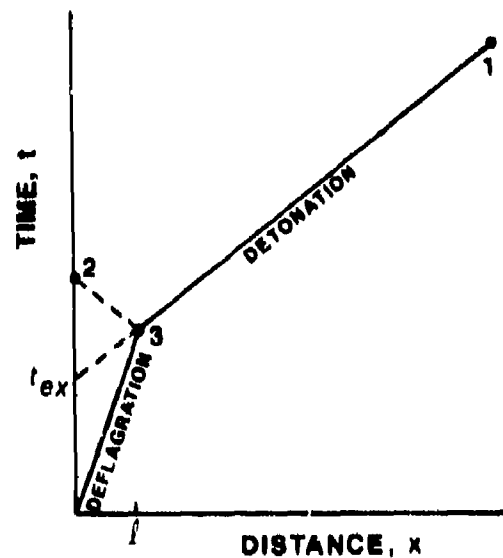


Figure 6. Simplified Distance-Time Diagram Describing Laser-Initiation Mechanisms

light corresponds to point #2 on the x-t plot of Figure 6. Assuming the retonation velocity equals that of the detonation, point #2 would be reached along a line which intersects the detonation at point #3. From this intersection we can obtain the induction distance,  $\ell$ , and the average deflagration or reactive shock velocity,  $v$ . For most of our experiments this analysis leads to values of  $\ell$  from 0.4 to 2.5 mm and  $v$  in the range of 1.5 to 3 mm  $\mu\text{s}^{-1}$ .

The actual DDT process is more complex than the description above. The compressive nature of the deflagration or shock wave leads to two main differences from the simplified analysis. First, retonation is generally faster than detonation since the wave propagates through higher density material. Second, point #2 probably is displaced from  $x = 0$ . Another complication arises from the multi-dimensional wave profile; as the laser pulse impinges on the small area of the surface the compressive wave leaves a concave dent in the HE and the ensuing waves are decidedly non-planar. The arrival of the retonation at the emitting surface therefore occurs first at the deepest point on the emitting surface, i.e., the spot where the laser beam impinged. The retonation wave will then continue to propagate to the sides of the charge, which were originally compressed only slightly. This should lead to an emission temporal profile longer than if the interaction had been with a flat surface. This was indeed what we saw when we compared emission at the front and back surfaces. These effects combine such that the real value of  $\ell$  is less than predicted from the simplified analysis and that the deflagration velocity,  $v$ , should be larger than the earlier estimate.

Discriminating between SDT and DDT is difficult, and further experiments are necessary to determine unambiguously which is active in these initiation processes. A main difference is the need for gas permeability in DDT. Many of the trends observed in these tests indicate that DDT is quite likely. Conventional descriptions of DDT in low-density PETN contain three distinct regions: layer-by-layer deflagration which is slow, a fast convective burn, and the steady-state detonation.<sup>10</sup> If there is sufficient initial

pressure, the slow process may be absent. In agreement with the above analysis based on the emission, the trends in threshold energy and function time as a function of density and particle size within the ranges of this study are consistent with conventional DDT models.<sup>10,11</sup>

The primary role of the laser in prompt initiation appears to be generation of sufficient pressure and chemical energy release to sustain the fast convective burn. Confinement is usually necessary to allow buildup to the needed pressure, hence the beneficial effect of high impedance window materials we observed. Below the initiation threshold, not only is there insufficient energy for DDT to occur but the fast convective burn is itself dissipated. The ease of DDT is governed by the material parameters. In this density range, coarse particle PETN is less likely to undergo DDT than the fine particle material.<sup>11</sup> Also, buildup of a convective burn in RDX is less facile than in PETN and is extremely difficult in fine particle HNS due to its poor gas permeability.<sup>12</sup>

While the details of laser interaction with these materials are not well understood, we expect facile plasma formation during the laser pulse at the power densities used in these experiments. The evidence strongly suggests that the generation of the plasma is enhanced by the aluminum coating we used in some of the experiments and which led to reduced laser energy requirements. This effect has also been observed by others.<sup>2,3</sup>

While much of the laser absorption is done by the plasma, it appears that the material absorptivity has specific consequences. It is most probable that initiation of the Zr-doped PETN was assisted by improved absorption of the laser radiation, although doping may also alter the DDT characteristics of the HE. Similarly, RDX, with its uv absorption band beginning between 320 and 340 nm\*, was initiated at 308 nm, but not at the longer wavelengths. The most striking consequence of the material absorptivity was

\*Absorption spectra were measured using a Cary 2300 uv-vis-nir spectrophotometer by J. Fronabarger of Unidynamics Phoenix, Inc.

seen in the initiation requirement of confinement as a function of laser wavelength. The red edge of the absorption band for PETN is between 300 and 320 nm.\* In general, strong photochemical effects, such as photoablation<sup>13</sup> occur at shorter wavelengths. It is not necessary to invoke an alternative initiation mechanism to explain how PETN can be initiated without front-surface confinement at 308 nm. We hypothesize that the depth of laser penetration into the HE is significantly less at shorter wavelengths as the absorption band of PETN is approached. In selected wavelength regions, the pressed HE surface may act as its own confinement until the required pressure is reached to sustain the convective burn. This explanation is consistent with the observation that the laser energy threshold at 308 nm was not significantly affected by window confinement, but the excess transit time, or the time to DDT, was decreased by the presence of the window.

## CONCLUSIONS

We have demonstrated that various material parameters can affect performance of HE initiation by laser radiation. We believe several design variables can be optimized to reduce laser energy requirements while maintaining fast function times. We have shown that PETN can be initiated at laser energies < 10 mJ or with excess function times as low as 20 ns at higher energies, but the test conditions in which we obtained these results were not fully optimized. Our preliminary results suggest that absorption of the laser radiation by the HE leads to a fast convective burn which may then transit to detonation. In future experiments we will attempt to monitor the fast deflagration and the buildup to detonation using velocity interferometry and other optical diagnostics on HE samples of various thicknesses.

## ACKNOWLEDGEMENTS

This work was performed at Sandia National Laboratories, Albuquerque, NM, supported by the U.S. Department of Energy under contract number DE-AC04-76DP00789. We wish to acknowledge with thanks the excellent technical assistance of J. C. Miller,

W. P. Brigham, and H. C. Richardson. We also thank C. E. Haynes for his help in preparing the explosive test devices. We have benefited from helpful discussions with M. R. Baer and R. E. Setchell of Sandia National Laboratories and with D.L. Paisley of Los Alamos National Laboratory.

## REFERENCES

1. Brish, A. A.; Galeev, I. A.; Zaitsev, B. N.; Sbitner, E. A.; and Tatarintsev, L. V., *Combustion Explosion and Shock Waves*, Vol. 2, 1966, p. 81.
2. Yang, L. C. and Menichelli, V. J., *Appl. Phys. Lett.*, Vol. 19, 1971, p. 473.
3. Yang, L. C. and Menichelli, V. J., in *Proceedings of the Sixth Symposium (International) on Detonation*, Coronado, CA, 1976, p. 612.
4. Bykhalo, A. I.; Zhuzhukalo, E. V.; Koval'skii, N. G.; Kolomiiskii, A. N.; Korobov, V. V.; Rozhkov, A. D.; and Yudin, A. I., *Combustion, Explosion and Shock Waves*, Vol. 21, 1985, p. 481.
5. Sheffield, S. A.; Rogers, J. W.; and Castanoda, J. N., in *Proceedings of the American Physical Society Topical Conference on Shock Waves in Condensed Matter*, Spokane, WA, 1985, p. 541.
6. Jia, B.; Chen, D.; Wang, Z.; Li, Y.; Zhang, K.; Liu, X.; and Lian, Y., "Experimental Studies of PETN Detonators Initiated by Laser Radiation," *Proceedings of the International Symposium on Pyrotechnics and Explosives*, Beijing, China, 1987, p. 49.
7. Paisley, D. L., Los Alamos National Laboratory, private communication.
8. Trott, W. M. and Renlund, A. M., in *Proceedings of the Eighth Symposium (International) on Detonation*, Albuquerque, NM, 1985, p. 691.
9. Trott, W. M. and Renlund, A. M., *Appl. Opt.* 24, 1985, p. 1520.
10. Belyaev, A. F.; Boblev, V. K.; Korotkov, A. I.; Sulinov, A. A.; and Chuiko, S. V., *Transition from Deflagration to*

*Detonation in Condensed Phases*, Israel Program for Scientific Translations, Jerusalem, 1976.

11. Baer, M. R. and Nunziato, J. W., *Int. J. Multiphase Flow*, Vol. 12, 1986, p. 861.
12. Shepherd, J. E. and Begeal, D. R., "Transient Compressible Flow in Porous Materials," Sandia National Laboratories Report SAND83-1788, 1988.
13. Srinivasan, R., in *Laser Processing Diagnostics*, D. Bauerle, Ed., Springer-Verlag, New York, 1984, p. 343.

## DISCUSSION

**DOUGLAS E. KOOKER**  
U.S. Army Ballistic Research  
Laboratory  
Aberdeen Proving Ground, MD

I am intrigued by your results, although I know nothing about laser initiation. Evidently your data suggest that the transition region is characterized by an effective wave speed of 1.5 to 3 mm/ $\mu$ s. Since wave speeds in this range often imply a reactive shock wave, I was curious about your reference to a "fast convective burn" and use of the term DDT. Would it be possible that the laser-induced reaction is strong enough to begin driving a reactive shock wave into the granular material, and the transition process is more like an SDT?

## REPLY BY ANITA M. RENLUND

With the diagnostics employed in these tests, it is indeed difficult to discriminate between a fast convective burn and a reactive shock wave. At this point, we note that the trends for initiation thresholds and function

times with particle size and density of PETN are consistent with a DDT model. This description is, however, not unique. Further experiments are planned where we will monitor wave growth and buildup to detonation. These tests should more clearly elucidate the initiation mechanism.

## DISCUSSION

**HAROLD GRYPING**  
Gryting Energetics Sciences Company  
San Antonio, TX

Have you considered correlating input energies from lasers with that from impact, friction, or electrostatic sensitivity methods?

## REPLY

Currently, we do not have sufficient data to make a meaningful correlation with other initiation mechanisms.

## DISCUSSION

**BARRY NEYER**  
EG&G Mound Applied Technology  
Miamisburg, OH 45343

It is possible, even with sample sizes of 5 to 10, to determine precise threshold values if an efficient threshold test and proper analysis techniques are used.

## REPLY

No reply from the authors.

## **POSTER PAPERS**

**Organizer and Chairman: Robert Frey**  
**Army Ballistic Research Laboratory**

**Cochairmen: Harold Sandusky**  
**Naval Surface Warfare Center**

**John Kury**  
**Lawrence Livermore National Laboratory**

**Philip Stanton**  
**Sandia National Laboratories**

**Allan Anderson**  
**Los Alamos National Laboratory**

**Michel Samirant**  
**Institut Saint-Louis (ISL)**

**Thomas Boggs**  
**Naval Weapons Center**

# INTENSE ELECTRON BEAM DETONATION OF TATB EXPLOSIVES

Dave Demske  
Naval Surface Warfare Center  
Silver Spring, Maryland 20903-5000

Nick Brazell, W. Edwin Farley, Steve Miller  
Lawrence Livermore National Laboratory  
Livermore, California 94550

and

Richard Warnes  
Los Alamos National Laboratory  
Los Alamos, New Mexico 87545

*Initiation threshold experiments have been conducted employing submicrosecond pulses of high current relativistic electrons. Pulsed electron beam detonation of a highly insensitive explosive was demonstrated and the initiating beam energy fluence parameters measured. In these experiments, exposures were made at a series of beam fluence levels by aperturing the size of the incident beam current. Electron energy distribution spectrum and radiation exposure time (i.e., current pulse-duration) were accelerator-defined "fixed" parameters. Nanosecond resolved measurements of the electron charge distribution were obtained, both at the surface and through the depth of the explosive sample. Fabry-Perot interferometry and shock velocity pins were employed to assess levels of explosive response and the initiation-onset over a wide range of incident beam current densities. In this paper, we present the experimental criteria and techniques used in studying fast transient electron beam-explosive interactions. The diagnostic methods successfully employed to achieve our experimental goals are described in some detail. We endeavor to discuss some of the observed explosion-detonation phenomena which are unique to electron beam induced detonations.*

## INTRODUCTION

In a series of experiments performed with the ECTOR accelerator, a pulsed relativistic electron beam was used to produce in-depth, sudden (adiabatic) heating and molecular decomposition (radiolysis) of an insensitive explosive. In these experiments, a high fluence electron pulse of 110 nanosecond duration was nonuniformly deposited 7-9 mm into cylindrical TATB samples to induce relatively constant volume (isochoric) explosion. For sufficiently high electron depositions, evidence

of "nearly-instantaneous," detonation-like behavior was observed. Using interferometer data, the event onset was inferred to occur about 127 nanoseconds after the beam front penetrated the incident surface of the explosive.

The explosive selected for study is the TATB-based composite, PBX 9502. In addition to having a well-established explosive data base, PBX 9502 is known for its inherently high thermal insensitivity, making it a well-suited candidate for e-beam "worst-case"

vulnerability studies.<sup>1</sup> Whereas TATB is conventionally surface-area shock initiated via explosive-to-explosive (e.g., booster) coupling, we have evidence of bulk-volume thermal explosion and thermogenerated shock initiation by prompt electron charge deposition.

Experiments and computer simulations indicate these initiation events to be dependent upon deposition rate, confinement, and charge size. In these experiments, the explosive samples were laterally confined in open-ended cylinders; about half the exposures were made on samples confined in heavy-walled, steel witness cylinders.

Our experimental goal was to reliably measure the electron beam threshold for detonation. A secondary purpose was to gain a better physical insight into the initiation mechanisms with the hope of adjusting beam parameters which would ultimately enable us to further lower threshold requirements. Within the experimental constraints imposed by the accelerator "machine parameters" (i.e., pulse width, beam emittance, and energy spectrum), we were able to measure the critical beam parameters establishing the fluence levels required for the onset of detonation.

ECTOR is nominally a 3.5 MeV diode accelerator, generally configured to perform pulsed radiography tests. In these experiments, it was reconfigured to e-beam mode to produce a beam current of tens of kiloamperes, in a half cycle sinusoid waveform of 110 nanoseconds, full pulsewidth. This current pulse was collimated and apertured down to a critical level where detonation was observed to quench out from insufficient beam initiation energy. Above this level, *sustained* detonation was found to occur; below this level, the initiation was overdriven and varying degrees of explosion ensued.

Traditionally, four e-beam generated initiation mechanisms have been proposed: compressive shock; thermogenerated shock; thermal activation (e.g., pyrolysis, deflagration, thermal explosion); and spark discharge. Generally, not all four of these exist independently. Depending on the current pulse-waveform and radiolysis rates, some interactive combination of these modes will

synergetically activate a high level explosion. Moreover, two of these modes, namely thermogenerated shocks and spark discharges, will be somewhat radiation dose rate dependent. Although not investigated here, multipulse interactions may induce yet other possible mechanisms, either through presensitization or by predischARGE space-charge reconfiguration. At this time, the optimal initiation mechanism is still unknown, and the noted mechanisms are not well understood.

### Initial Condition Specifications

In assessing explosive sensitivity, the quantities of interest are incident beam fluence, absorbed dose, and dose rate. The electron energy spectrum and the primary current are sufficient to characterize initial conditions. For threshold studies, the physical quantity expressly minimized is the beam fluence or time-integrated beam power density (i.e., the electron energy-current density product) delivered to the target. In practice, to achieve the characteristic threshold level, a given beam energy distribution is specified, the beam current is incrementally attenuated, and exposure-time (i.e., the pulse-width) is shortened. For these experiments, the primary beam current was "stopped-down" by using a conically tapered carbon collimator with a thin brass aperture behind it. The current was monitored at the target surface, downstream of the collimator assembly. Our diagnostic approach provided a direct measurement of the primary beam current impinging the sample; it circumvented the return plasma current complications generally plaguing such measurements. The beam energy distribution was determined from coincident measurements of the accelerator diode voltage waveform, taken at the diode gap. In this series of experiments, exposure times could not be varied (e.g., by pulse-width "clipping").

### Interaction Parameters

Primary beam parameters alone do not provide adequate insight on how dose rate and dose distribution can be adjusted to influence various explosive reaction mechanisms.<sup>2</sup> For instance, the primary beam current does not account for the multiplicity of secondary

charged particles produced in its passage through the sample. In fact, experimental evidence indicates that a substantial fraction of the initiating chemical decomposition is known to result from the lower energy, secondary electrons. Moreover, as the electrons are slowed down to expend more of their impulse time in the vicinity of an absorber, the density of multiple ionizations increases.<sup>3</sup> Specifically, the average energy loss to molecular excitation varies inversely with electron velocity. Local hot spots become closer-spaced as particle energies are reduced to thermal levels by molecular collisions where the subelectronic (i.e., vibrational, rotational, and translational) states are excited. In these experiments, we monitored the net electron

distribution deposited through the explosive sample, by employing an array of electron charge-viewing detectors down the length of the sample.

## RADIOLYSIS-STIMULATED DETONATION

### Geometric Criticality Conditions

Figure 1 schematically illustrates a sequence of events in response to a collimated incident beam, of a diameter which is significantly less than the explosive lateral dimensions, but larger than some minimum dimension required for a critical strength stimulus initiating detonation.<sup>1</sup> An electron-generated priming volume can be specified as a

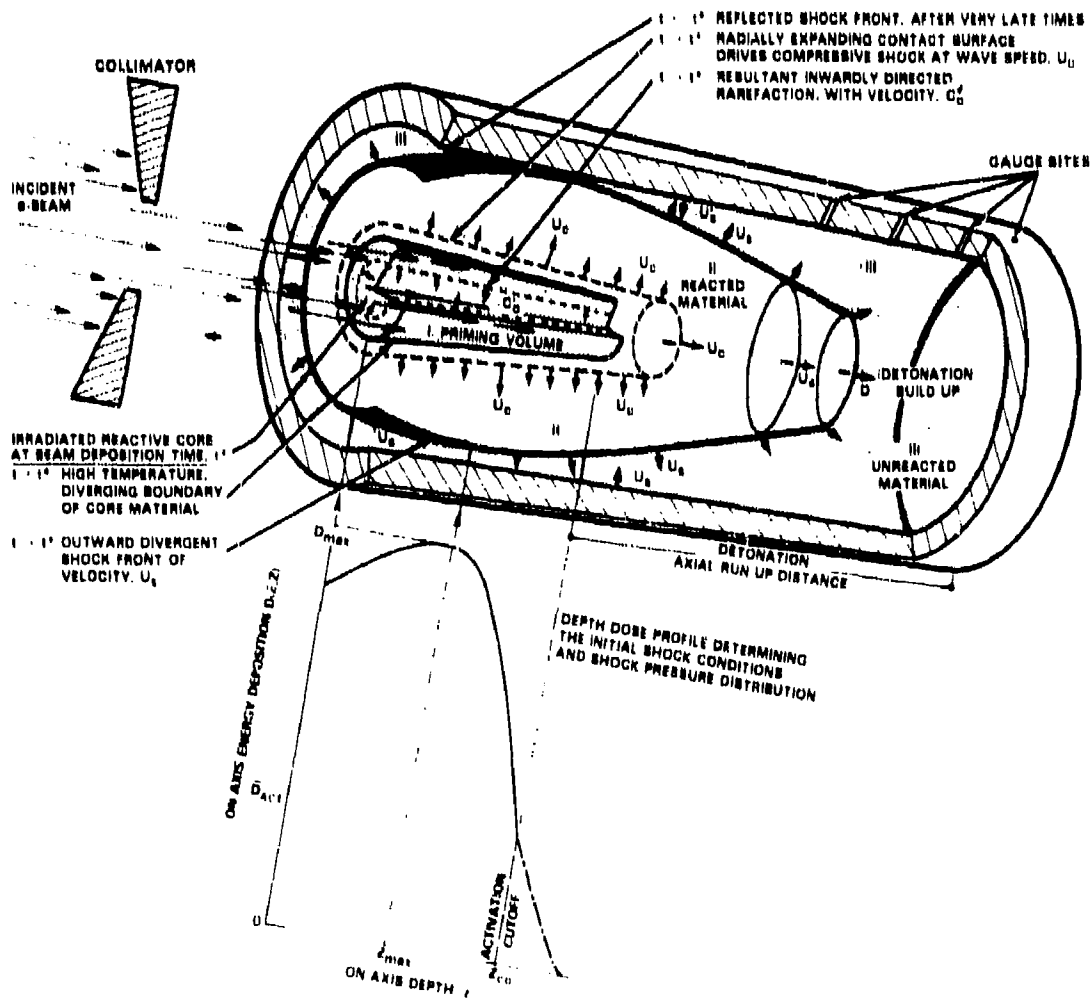


Figure 1. Time Evolution of Thermoshock Front as a Function of the Beam Deposition Profile

truncated interaction cone which effectively "cuts off" at some depth ( $Z_{co}$ ) predetermined by the incident beam fluence and explosive's constituent dissociation energy. The level of exothermic effects from electron deposition,  $D(E, Z_{co})$ , beyond this depth is negligible compared to secondary radiation energy losses. Electrons are designated as "stopped" when their energy approaches this chemical activating "cut-off." If the priming volume is above the critical size where the reaction can provide sufficient reactive buildup, the explosion ultimately transitions from a shock with velocity  $U_s$  to detonation  $D_s$ .

### Deposition Profile Effects

Since a portion of the primary beam energy is extracted in the production of secondaries, the explosive initiation threshold depends on how effectively the interaction energy is absorbed (specifically, on the molecular structure's sensitivity to electron radiolysis).

The energy integrated, weighted-fluence distribution through successive layers of priming volume determines the deposition distribution,  $D(E, Z)$ . For a pulse of normal incident electrons of energy  $E$  (typically, a few MeV), the specific beam power transferred to the explosive can be reasonably estimated in the "thin stopping" limit by

$$P_s(Z) = (S(E)/\rho)_c J(Z, t).$$

$P_s(Z)$  is the effective specific power deposited at various depths through a stacked array of thin scattering layers of absorber. Its time integral is the specific energy deposited by the pulse.  $(S(E)/\rho)_c$  is the collision-dominated specific energy loss per electron in an absorber of density  $\rho$ .  $J(Z, t)$ , the current density, is the rate of charge concentration at position  $Z$  crossing some priming volume area,  $A(Z)$ . Ample evidence indicates that if beam spread (i.e., the emergent emittance) is too excessive—thereby promoting subcritical current densities—thermal loss to the cooler, adjacent material will result in too diffuse a localized hot spot concentration for stimulating initiation. This imposes restrictions on the allowable minimum current density.

Figure 1 depicts the effects of the electron deposition profile in the early evolutionary

stages of a shock front advancing with velocity  $U_s$ . The priming volume begins interaction with the unexposed explosive by expanding with reactive flow at some velocity  $U_c$ , sending a rarefaction release wave of velocity  $C_0$  back into the heated deposition region. Thereafter, the expanding wave auto-accelerates by virtue of its own chemical self-release energy to velocity  $U_s$ . A two-dimensional hydrodynamics code, DYNA2D, indicates that the extensive tapering of this divergent shock front results from the electron deposition profile characteristics.<sup>4</sup> Using the profile as input, DYNA2D forecasts how the wavefront evolves from central core ignition to later-time reactive flow past the shock velocity gauge sites.

### Deposition Duration Time Effects

Past attempts to initiate confined TATB samples using "long duration" (multisecond) exposures failed to achieve sustained detonation. Our "short duration" pulse exposures of 45-mm long samples were successful when adequate lateral confinement was provided.

For a given explosive, explosive morphology, density, and specified confinement conditions, different reaction levels of explosion will be found for different energy deposition rates. Specifically, the reaction processes generally depend on the pulse-profile.<sup>2</sup> The initiating chemical effects ultimately depend upon the relative times required for various competitive reaction processes to occur; not all will necessarily transition to a stable detonation.<sup>2,3</sup>

Exposure duration times are distinguished as "long" or "short" on the basis of the beam current duration. Figure 1 depicts a well-collimated beam incident on a reactive target sample to create a priming volume of radius  $r$  and length  $Z_{co}$ . The exposed region is portrayed with a material having a dilatational sound speed  $C_0$ , which is temperature dependent. For a beam of current pulse width  $t^*$ , which is short compared to  $r/C_0$  (the thermo-mechanical relaxation time), deposition heating will be so rapid that there is no time for significant priming volume expansion to occur. The thermogenerated shock essentially exists because of the significant temperature gradient across the boundary separating the

exposed from the unexposed material. For the ECTOR exposure,  $t/C_0 \approx 1.1$  microseconds. Consequently, the priming volume was regarded as inertially self-confined during the 110 nanosecond pulse duration. For such fast deposition exposures, nearly isochoric conditions exist, and the peak pressure  $p(r,z)$  can be regarded as the cumulative response to the specific energy deposited and the radiolysis "heat of reaction"  $e(r,z)$ . On these time scales, relatively little thermal energy will be transferred out of the irradiated region; Bremsstrahlung losses are low, and since energy is supplied in a time shorter than the shortest significant thermal energy-loss time, conditions are also adiabatic. The physical significance is that for short pulse exposures, i.e., where  $t^*(r/C_0)^{-1} < 1$ , a threshold characteristic can be readily specified in terms of measurable quantities by the isochoric energy-pressure coupling coefficient  $(\partial p(r,z)/\partial e(r,z))_v$ , an experimental determinant. Consequently, the priming volume pressure response is conveyed in terms of the net energy deposition. (This response is noted later in Table 1 for the two priming volume experiments.) The condition may not necessarily reflect the minimum threshold. A lower beam fluence level might be achieved by readjusting the beam pulse-profile, for instance, by shortening the deposition duration, thereby lowering the total beam energy delivered to the target.

As the exposure time durations become  $t^*(r/C_0)^{-1} > 1$ , the thermoshock effect is severely mitigated, and compressive-reactive flow becomes the dominant effect. Progressively longer duration exposures produce pyrolysis, culminating in accelerated burning, which under sustained confinement, may transit to a high level thermal explosion, such as that typically observed in long pulse duration experiments.

## EXPERIMENT

### Diagnostic Arrangement

In these experiments, a series of shots at various fluences were made by adjusting the incident beam aperture. The experimental arrangement, illustrated in Figure 2, shows the high explosive sample concentrically positioned

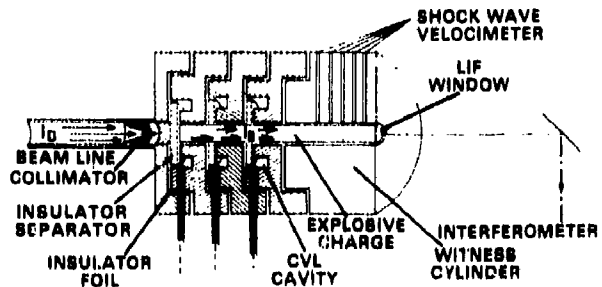


Figure 2. Experimental Arrangement

in the diagnostic assembly. The entire explosive assembly is bolted to the downstream end of the accelerator's electron transport tube.

Experiments were performed with two explosive sample lengths: 45-mm long samples were used to verify explosion-detonation events; shorter, 9-mm samples were selected for priming volume and coupling coefficient studies.<sup>2</sup> The short sample length was selected on the basis of electron penetration range for the peak accelerator energy. It was predetermined from electron transport code calculations using a TATB simulant.

In Figure 2, the long sample is shown coaxially enclosed in an array of three in-line stages of current-viewing monitors. In each stage, four orthogonally positioned, active elements were positioned cylindrically about the outer surface of the irradiated sample interaction region. In the actual experimental setup, the sample extended some 34 mm further beyond a fourth current sensor, and through a steel witness cylinder into which seven pressure-activated sensor pins were imbedded. The current sensors are low inductance, cavity-type, current-viewing inductors (CVL) with nanosecond response. The cavity configuration is designed to serve as a series of radial transmission lines for signals generated in response to magnetic flux changes of the beam current. The sensors were spatially interleaved to resolve the localized charge distribution to within 3-mm thick sections, down the sample length.

Electrically-biased, coax shorting pins and fiber optic microballoon sensors were positioned beyond the beam penetration zone to monitor the shock wave velocity propagating perpendicular to the sensors. An Argon ion laser was reflected from the rear surface of a lithium

fluoride covered sample into a Fabry-Perot interferometer. The interferometer provided a record of the particle velocity to accuracies of better than 2 percent. Using known Hugoniot data on lithium fluoride, the shock velocity was determined. The results, in turn, provided information to infer the total energy and pressure.

An attempt was made to obtain CVL sensor current data at various points along the irradiated portion of the explosive. Used in conjunction with the "thin-stopping power" relation ( $P_s(z)$  in the "Deposition Profile Effects" section) and the interferometer results, the depth-deposition profile could be deduced. Interferometer data also allowed us to infer the beam-generated shock pressures. Subsequently, the energy-pressure coupling coefficient was determinable.

### Diagnostic Observations and Results

Nine shots were conducted in this series of experiments. An initial, nonexplosive baseline shot was made to provide correction for collimator aberrations, and to account for electron scattering (hence, current density changes) on beam passage through the sample. Microdensitometer records of exposed radiochronic film disks, which were positioned at various thicknesses through the sample, indicated that the effects were somewhat marginal for these experiments.

Coaxial electric pin data provided consistently reliable shock velocity records on the long sample charges. Of the eight explosive shots, velocity records indicated that two culminated in detonation; the electric pin data showed one of these was unstable and ultimately quenched. Adequate sample confinement appeared to be an important factor in these shots.

All diagnostics were triggered or time-referenced to ECTOR accelerator trigger time. The interferometer was set to begin monitoring prior to ECTOR trigger, allowing for the possible capture of events early in the 110 ns beam current pulse. Interferometer sensitivity was adjusted to resolve 20-40 ns, with a velocity accuracy of about 2 percent. With this time-resolution, unresolvably abrupt

"ramp-up" to velocities ranging 1.4 to 1.6 km/s were observed at the 9-mm sample-lithium fluoride interface. The arrival times at the interface were about 124-127 ns relative to commencement of the diode beam current pulse. As observed from pin data, further aperturing resulted in lower level explosions.

Voltage-current waveforms were obtained. Figure 3 shows a typical profile. The collimated incident current-time profile shown here came from the CVL sensor positioned at the front of the sample surface. The beam fluence was determined by numerically integrating the product of the accelerator voltage (i.e., electron energy) and the corresponding beam current (time-correlated to that voltage) over the entire voltage waveform. This quantity was considered the excitation level responsible for producing a given explosive event.

Time-profile characteristics of the pulse is also physically informative. In particular, since the depth to which electrons penetrate increases with their energy, the thickness of the thermally-affected region will increase during the first 28 ns.

An endeavor was made to obtain charge deposition data from the two subsequent in-line sensors, but broadband Bremsstrahlung radiation strongly interfered with the attempts on the early shots. On later experiments, the deposition data showed large, extremely fast-rise oscillations in the current profiles (i.e., pronounced  $dI/dt$ ). These characteristics strongly indicated internal arc-discharge patterns were developing during the first 45-50 ns.

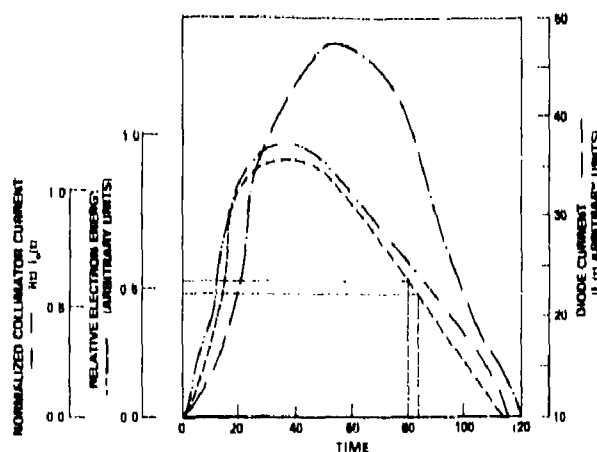


Figure 3. Incident Beam Characteristics

Similar waveform characteristics were obtained on pre-test shots at the Naval Laboratory facility, where transparent Lexan rods replaced the explosive as target samples. The irradiated rods provided explicit evidence of internal dielectric breakdown.

Figure 4 shows a cutaway cross section of a steel witness cylinder, comparing conventional and e-beam initiation. The e-beam initiated explosive resulted in the witness cylinder showing spall off the back surface, and excessive explosive residue on the inner cylinder wall. Hardness tests were made before and after the events, but no significant results were found.

## CONCLUSIONS

Table 1 gives a qualitative summary of observed explosion events. Quantitative data, incorporating the beam fluence threshold levels and dosages for these events, have been previously presented elsewhere. Some features peculiar to pulsed, high current, e-beam initiation are noteworthy.

1. Results obtained from a laser interferometer, monitoring the back surface of the

deposition (irradiated) volume, indicate energy depositions generating reactive thermal shocks in excess of 260 kbars (i.e., TATB detonation pressure) within buildup times of tens of nano-seconds. Such extremely short buildup times are not generally observed in conventional initiation processes.

2. The beam interaction, or "minimum priming" volume dimensions, are smaller than what has been observed for the TATB-based explosives, ranging from 0.20 to 0.27 cm<sup>3</sup>. However, the condition is very confinement dependent. Our attempts to initiate inadequately confined 45-mm long TATB samples resulted in high-order explosion which ultimately quenched, leaving TATB fragments behind. These effects are also noted two-dimensional reactive hydrodynamic code results showing the radial effect of the priming volume on detonation.<sup>5</sup>

3. Electric self-discharge of the injected electron space-charge in the priming volume is noted from the downstream CVL sensor current waveform data. There is evidence of internal spark discharge occurring in the interior of the priming volume, about 40-50 ns after beam commencement.

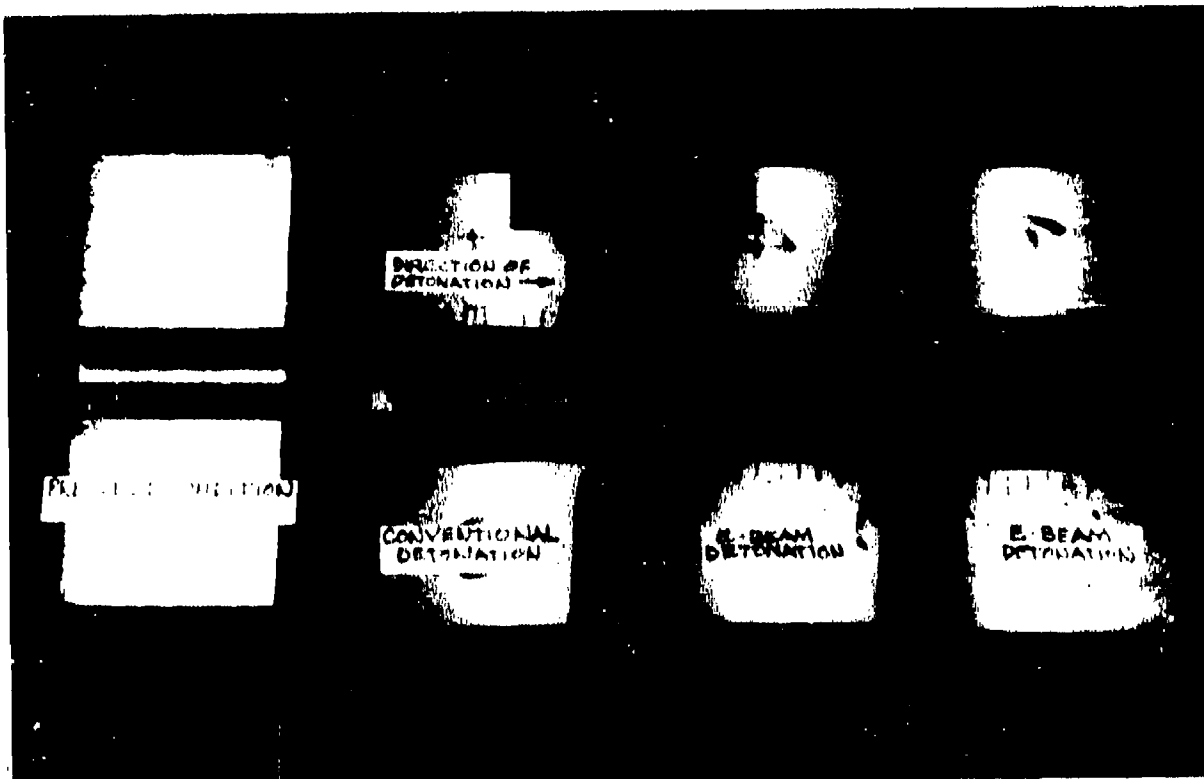


Figure 4. Cutaway Cross Section of a Steel Witness Cylinder

Table 1. Summary of Results

Observed Events		
Extent of Reaction	Measured	Results
Low Level Explosion	(1) 3.19 Km/s	Explosion Quenched Out.
High Level Explosion	(1) 8.95→4.499 Km/s	Sample is Heavily Confined. Reaction Quenches.
Stable Detonation	(1) 7.76 Km/s	Sample is Heavily Confined.
High Level Explosion	(1) 6.66 Km/s	Sample is Heavily Confined. Explosion Buildup.
Initiation Effect	(2) 6.46 Km/s 264 Kbar	Minimum Priming Volume. Short Charge.
Initiation Effect	(2) 6.65 Km/s 319 Kbar	Minimum Priming Volume. Short Charge.
Low Level Explosion	(1,3) 2.31 Km/s	Double Collimator: Upstream 6.5 mm; Downstream 20 mm.

(1) Electric, coaxial shorting pin data on 45 mm sample.

(2) Inferred from laser interferometer data.

(3) Double collimator effect.

4. Since the ECTOR current and voltage waveform were observed to be basically sinusoidal, we were able to use the waveform peaks ( $V_p$ ,  $I_p$ ) to assess the specific fluence of a beam collimated to area  $A$ :

$$\begin{aligned} \text{FLUENCE} &= \frac{V_p I_p}{A} \int_0^{t^*} \sin^2\left(\frac{\pi t'}{t^*}\right) dt' \\ &= \frac{V_p I_p}{2A} t^*. \end{aligned}$$

Unfortunately, we could not shorten  $t^*$  in these experiments because it was a "machine-fixed" parameter.

Both interferometer and crush-pin data strongly suggests that the ECTOR initiated detonations are not overdriven since lower

beam currents result in velocities below detonation velocity. For the 110 ns primary beam duration and subsequent submicrosecond response, we concluded ("Deposition Duration Time Effects" section) that near-constant volume (isochoric) explosion (in the priming volume) is evident. In the early initiation stages ( $t < t^*$ ), the initial state does not fall on a Hugoniot. At later times ( $t > t^*$ ), as the priming volume expands and compression of the surrounding (unexposed) explosive occurs, we ultimately reside on a final reactive Hugoniot state. These initiation conditions are derived from the fact that the bulk-volume energy deposition is very rapid relative to the thermomechanical relaxation characteristics of explosive.

To corroborate these results and better understand their mechanisms, ongoing efforts

at more fundamental levels are still being undertaken.

## ACKNOWLEDGEMENTS

We would like to thank G. Whittemore (LANL) for performing the Fabry-Perot measurements, C. Frost (Sandia) for his current monitor design, M. Ralieggh (now at G. T. Devices) for his fast response integrator and the diligent calibration and help on pre-test checkout of the CVL sensors at the NRL Pulsad facility, B. Freeman (NSWC) for the precision machining of the CVL cavities, D. Bussell and J. Armstrong (LANL) for their assistance with running the accelerator, and A. Ridore (NSWC) for patiently preparing this manuscript.

## REFERENCES

1. Dobratz, B. M., et al., *The Sensitivity of Triaminotrinitrobenzene (TATB) and TATB Formulations: Summary Report*, UCID-17808, 15 Sep 1978, pp. 3-1 to 3-10.
2. Demske, D. L.; Brazell, N.; Farley, W. E.; Pogue, E.; and Warnes, R., "Intense Electron Beam Detonation of Insensitive Energetic Materials," *Proceedings of the 1987 APS Topical Conference of Shock Wave Physics In Condensed Matter*, Jul 1987.
3. Newton, A. S., *Radiation Effects in Organic Materials*, B. O. Bolt and J. G. Carroll, Eds., Academic Press, New York and London, 1963, pp. 7-32.
4. Hallquist, J., *Users Manual for DYNA2D —An Explicit Two-Dimensional Hydrodynamic Finite Element Code with Interacting Resonance*, UCID-18756 Rev. 2, 1984.
5. Private communication with Steve Miller, LLNL.

# TIME-RESOLVED MASS SPECTROMETRY TECHNIQUE FOR STUDYING FAST TRANSIENT CHNO EXPLOSIVE DECOMPOSITION KINETICS

R. D. Skocypec and K. L. Erickson  
Fluid and Thermal Sciences Department  
Sandia National Laboratories  
Albuquerque, New Mexico 87185

*An experimental system is being developed to study the fast transient kinetics governing solid-phase decomposition and subsequent interaction with decomposition products. The first phase of this work addresses the decomposition step. The experiment integrates a thin-film sample configuration with two chemical diagnostic techniques, time-of-flight mass spectrometry and time-resolved infrared spectral photography, and a pulsed-laser heat source. The experiment has microsecond temporal resolution to examine both condensed-phase mechanisms and concurrent gas-phase species evolution from samples at temperatures up to 1000°C. Experiments are underway to demonstrate and assess the use of thin-film samples with the experimental system. Results of these experiments, the diagnostic capabilities of the experimental system, and the advantages, preparation and characterization of thin-film samples are presented.*

## INTRODUCTION

The ignition, deflagration, and detonation of energetic materials are controlled by coupled thermal, chemical and mechanical phenomena. Ignition, as well as related cook-off events, are particularly sensitive to chemical reaction kinetics. Development of reliable models requires detailed understanding of three general reaction mechanisms: (1) initial solid-phase decomposition, (2) subsequent interaction of decomposition products with the remaining solid phase, and (3) gas-phase reaction of decomposition products to form the ultimate reaction products. The former two mechanisms are the least understood and most difficult to study.

There is a general lack of experimental chemical data having microsecond temporal resolution for samples at ignition temperatures. Information is especially limited on condensed-phase reactions, which are believed to play a significant role in high-melting point nitramines,<sup>1</sup> particularly advanced polycyclic

nitramines for which substantial decomposition occurs in the condensed phase. One experimental technique to obtain chemical data pertinent to ignition is to rapidly heat the sample, maintain isothermal conditions, and observe transient species formation and destruction. The temporal resolution of this type of experiment includes both the resolution of equipment (diagnostic and data acquisition) and the minimum time required for the sample to reach isothermal conditions so that the focus can be on reaction chemistry. The second requirement has not been generally satisfied at temperature levels appropriate for ignition. Thus, we believe the lack of data is due to the difficulty in: (1) probing condensed-phase chemistry, and (2) producing samples that can attain ignition temperatures and be isothermal within the microsecond time scales appropriate for ignition events.

We are developing an experimental system, based on time-of-flight mass spectrometry (TOFMS) and time-resolved infrared spectral photography (TRISP), having microsecond

temporal resolution to examine both condensed-phase mechanisms and concurrent gas-phase species evolution from samples at temperatures up to 1000°C. TRISP is currently a single-shot technique for sub-millisecond experiments, so multiple experiments are necessary to temporally resolve condensed-phase mechanisms. The first phase of this work focuses on the initial solid-phase decomposition step. Our approach to solve the problems of probing the condensed phase and obtaining, within microseconds, isothermal samples at ignition temperatures is to use a pulsed laser to heat and decompose thin-film samples of energetic material deposited on inert substrates. Since the films are optically thin, condensed-phase reactions can be monitored using TRISP. The system is designed to study a variety of energetic materials. This paper will describe some significant capabilities that are being developed, including the ability to: examine concurrently both condensed-phase mechanisms and gas-phase species evolution, obtain data with microsecond temporal resolution, rapidly heat samples (up to  $10^8$  K/s), obtain high sample temperatures (up to 1000°C), have well-characterized samples with uniform temperature, utilize small samples to permit evaluation of new materials, and evaluate any macroscopic physical response.

Experiments are underway to demonstrate and assess the use of thin-film samples with the experimental system. Results of these experiments, the diagnostic capabilities of the experimental system, and the advantages, preparation and characterization of the thin-film samples are presented.

## EXPERIMENTAL SYSTEM

The experiment is configured with the thin-film sample located inside the vacuum chamber of the TOFMS. The sample is laser-heated, either indirectly by irradiating the opposite side of the substrate, or directly by irradiating the material. As the explosive decomposes into the vacuum, the gas-phase reaction products and their evolution rates are measured, and an infrared spectrum of the condensed phase is obtained with TRISP. The vacuum environment inhibits reaction

of the gaseous decomposition products. The regression rate of the film is monitored *in situ* with a high-speed ellipsometer. The substrate temperature is measured with an infrared linear detector array.

The experimental equipment consists of five major systems: (1) physical vapor deposition system for preparing thin-film samples, (2) TOFMS and high-speed ellipsometer, (3) TRISP, (4) laser heating system and infrared linear detector array, and (5) high-speed data acquisition system. The next section describes the sample configuration and heating, followed by a description of the experimental diagnostics, thin-film sample development and results from preliminary experiments.

## Sample Configuration and Heating

The basic sample configuration, shown schematically in Figure 1, is a thin film (0.03 to 0.3  $\mu\text{m}$  thick) of energetic material deposited on one surface of an inert substrate. The thin film has two primary advantages relative to bulk granular samples: (1) rapid thermal equilibration to produce an isothermal sample within 1  $\mu\text{s}$  or less following a temperature change at the substrate-film interface, and (2) optical access for techniques such as TRISP to examine directly the chemistry occurring in the condensed phase. Additionally, thin-film samples can be well-characterized relative to

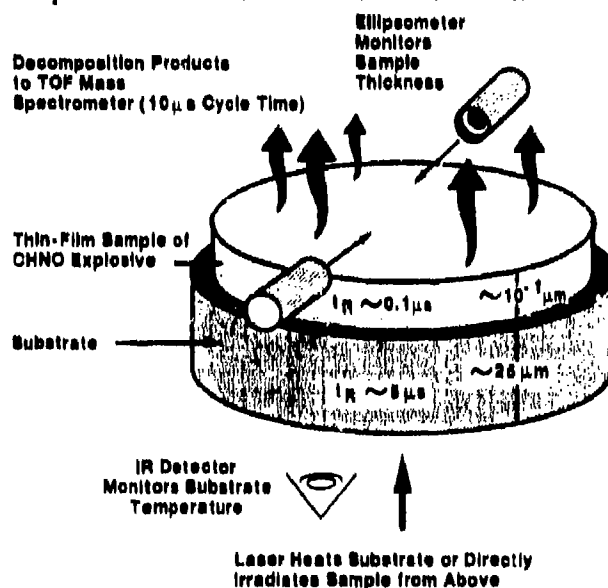


Figure 1. Schematic of Thin-film Sample Configuration

granular samples, and complex heat and mass transfer effects are minimized so that decomposition chemistry can be examined directly.

The minimum sample film thickness that provides sufficient material for mass spectrometry is  $\sim 0.03$  to  $0.3 \mu\text{m}$  (for a typical  $1 \text{ cm}^2$  cross-sectional area). The thin-film sample thermal response to the laser pulse is dictated by substrate characteristics. The relaxation time  $t_r$  for a temperature gradient in a thin film having thickness  $l$  can be estimated from the expression  $t_r = l^2/\alpha$ , where  $\alpha$  is the thermal diffusivity of the film material. For explosives such as HMX and RDX,  $\alpha$  is on the order<sup>2</sup> of  $2 \times 10^{-3} \text{ cm}^2/\text{s}$  and consequently, values for the film relaxation time  $t_r$  are on the order of  $0.5 \mu\text{s}$  or less.

Predictions of the two-dimensional transient temperature history of a  $25\text{-}\mu\text{m}$ -thick tungsten substrate have been made using a finite element heat transfer code<sup>3</sup> for various incident energy levels assuming both uniform and Gaussian laser beam profiles. The substrate was assumed to have a temperature-varying thermal conductivity,<sup>4</sup> absorb 50 percent of the incident energy (a conservative estimate as discussed below) and radiate energy (emissivity of 0.7) to the room-temperature environment. The predicted temperature responses for a Gaussian incident flux profile containing 10 J of energy within a  $2.5 \mu\text{s}$  pulse and a uniform flux profile containing 15 J of energy within a  $2.5 \mu\text{s}$  pulse are shown in Figures 2 and 3. For these plots, "front" refers to the illuminated side of the substrate, "back" refers to the substrate/film interface,  $r$  is the radial location and  $R$  is the substrate radius. The maximum substrate temperature occurs at  $2.5 \mu\text{s}$ . In neither case does the peak temperature exceed the melting point of tungsten ( $3410^\circ\text{C}$ ) and in both cases the temperature of the substrate is virtually isothermal across its thickness within  $10 \mu\text{s}$  after the beginning of the laser pulse. For the Gaussian profile, a radial gradient exists, governed by the radial distribution of the laser beam. The assumed Gaussian laser beam profile is a worst-case scenario since the actual beam is delivered through an optical fiber, which can produce a spatially uniform beam profile. The film interface temperature for the

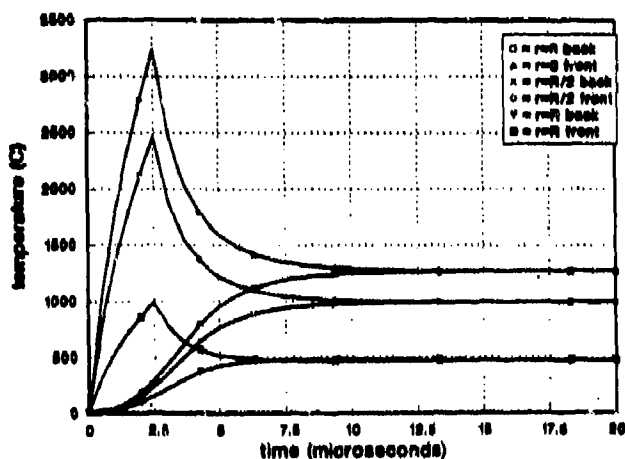


Figure 2. Predicted Tungsten Substrate Thermal Response to Gaussian Laser Flux Profile, 10 J within  $2.5 \mu\text{s}$  Pulse. "Front" indicates illuminated side, "back" indicates substrate/film interface,  $R$  is radius.

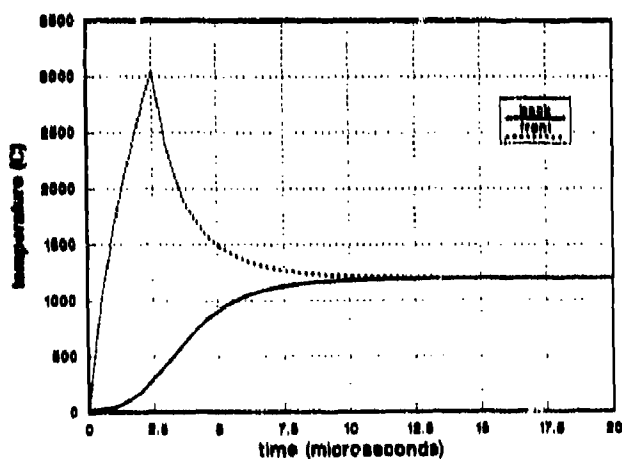


Figure 3. Predicted Tungsten Substrate Thermal Response to Uniform Laser Flux Profile, 15 J within  $2.5 \mu\text{s}$  Pulse. "Front" indicates illuminated side, "back" indicates substrate/film interface.

uniform 15 J pulse attains local equilibrium above  $1000^\circ\text{C}$  within  $10 \mu\text{s}$ . This implies that for experiments having a duration greater than about  $10 \mu\text{s}$ , the rate of temperature equilibration across the thickness of the substrate and film is fast enough so that the film is isothermal and has a temperature equal to

that of the substrate-film interface within the relaxation time. The film temperature can be inferred by observing the illuminated surface of the substrate with the infrared array.

The substrate material should be chemically inert, have a high melting point, have high strength (so that the substrate remains flat while minimally supported), and be amenable to surface preparation to promote uniform sample film growth. Tungsten has been chosen as the primary substrate material because it has the desired physical properties and minimum surface preparation has been required to obtain good quality sample films. Typical substrates are 25- $\mu\text{m}$  or 50- $\mu\text{m}$ -thick (1- or 2-mil) foil discs (1.40 cm diameter), one side of which is roughened and oxidized to provide maximum absorption (>94 percent) of the incident laser energy. The other side is polished and solvent-cleaned for film deposition. To maintain planarity, the substrates are vacuum annealed (reducing inherent strain).

The energetic material is heated by laser-illuminating the substrate surface opposite the film. The laser heating technique can deposit large amounts of energy in a short time period, vary input power levels (and therefore sample temperature) relatively easily, and be used to investigate direct film illumination effects. The laser system incorporates a flashlamp-pumped dye laser that can produce 20 J of energy within a 2.5  $\mu\text{s}$  pulse and a continuous wave Nd:YAG laser. The pulsed laser initially brings the substrate and sample to the desired temperature, and for long-duration experiments, the continuous wave laser maintains the temperature for the duration of the experiment. To ensure that the laser energy deposited in the substrate is repeatable and well-defined, both the pulsed and continuous-wave beams are monitored during the experiment for energy density and uniformity.

## Diagnostics

**Temperature.** Sample temperatures are obtained with an infrared linear detector array (Electro-Optical Systems, Inc., Mulvorn, PA). This diagnostic is nonintrusive, fast responding, flexible, and does not remove energy from the sample as a direct contact device does. The array is focused on the illuminated side of the

substrate foil. Data are acquired from the array at rates greater than 200 kHz using parallel output and digitization. Since the array is viewing a nonreactive surface, data reduction and interpretation to evaluate temperature is much less complex than if the reacting material was viewed directly. Multi-color techniques may be used, if necessary, to reduce emittance uncertainties. The array allows an estimate to be made of the spatial isothermality of the substrate.

**Gas-Phase Species Evolution.** The temporal history of the decomposition products is determined with the time-of-flight mass spectrometer (TOFMS). Repetitive operation of the spectrometer is fast. All ions are simultaneously accelerated from the ion source, and a complete mass spectrum is produced each cycle, which can be as short as  $\sim 10 \mu\text{s}$ . To utilize the full capabilities of the TOFMS,<sup>5,6</sup> the mass spectrum signal is digitized and recorded by a 200 MHz, 10-bit transient waveform recorder and is temporarily stored in a 4 megaword memory module. The spectrum is then downloaded for post-test data processing and analysis.

**Dynamic Sample Mass Loss.** Sample mass loss is determined by pre- and post-test weighings using an ultra-micro balance. An estimate of the dynamic mass loss during decomposition is obtained using the high-speed ellipsometer. Ellipsometry provides simultaneous, but indirect, measurement of the thickness and refractive index of thin films on a reflecting surface. The ellipsometer measures the optical reflectivities and phase shifts of each of the two polarization vectors for a monochromatic beam of light obliquely reflected from the surface. Thickness and index are then calculated using standard relationships.

A limitation of standard ellipsometric devices has been the slow data sampling rate. This limitation has been overcome by the development of Photo-Elastic Modulator (PEM) Ellipsometers, which have significantly increased system bandwidths, permitting both a greater number of sampling points as well as greater signal sensitivity. An ultra-fast (500 kHz) in-situ ellipsometry research system is being developed with GRQ Instruments to

resolve dynamically thicknesses of thin films undergoing rapid decomposition. In many other (non-ellipsometric) optical film thickness measurement techniques, the film index must be known *a priori*, and the measurement accuracy is highly dependent on the accuracy to which the index is known. A major advantage of ellipsometry is that both parameters are obtained simultaneously. For the dynamic measurement of rapidly decomposing thin films, this is essential since the index may vary significantly due to density variations occurring during heatup and decomposition.

### Thin-Film Samples

Several energetic materials have been selected for thin-film sample development. These include RDX, HMX, TATB, PETN, HNS, NC, CP, AP, KP, and a polycyclic nitramine (PCN). Two general sample preparation techniques are being pursued: (1) physical vapor deposition and (2) deposition from solution. Physical vapor deposition provides reasonably precise control of film properties. The technique can be used with any material that has a sufficient vapor pressure at temperatures low enough so that decomposition of the material is negligible, which is the case for RDX, HMX, TATB, PETN, HNS, and PCN. However, polymeric materials such as NC or ionic materials such as CP, AP, and KP do not have a sufficient vapor pressure. Deposition of these materials from solution is the simplest alternative. However, deposition from solution does not permit as precise control of film properties or film uniformity.

Good quality samples of RDX, HMX, TATB, and HNS have been prepared by physical vapor deposition on a variety of substrates that include tungsten, aluminum, pyrex, and barium fluoride. (The latter three are not used for laser-heated experiments.) Preliminary work with PCN deposited on tungsten also has been encouraging. The film thicknesses were varied between about 0.04 and 10  $\mu\text{m}$ . Examination of the samples with optical and scanning electron microscopes (SEM) indicated that the films were relatively uniform, flat, and nearly fully dense. Figure 4 is an SEM micrograph of the surface of a 2- $\mu\text{m}$  film deposited on polished tungsten. X-ray

diffraction patterns obtained from the samples exhibited very narrow peaks, which indicated that the films were well-crystallized. The pattern for a 10- $\mu\text{m}$ -thick RDX film deposited on pyrex is shown in Figure 5. The patterns from thinner films showed equally narrow peaks, but due to low signal intensity only the most prominent peaks were distinguishable from noise.

Uniform, relatively flat samples of RDX as thin as 0.04  $\mu\text{m}$  have been prepared on

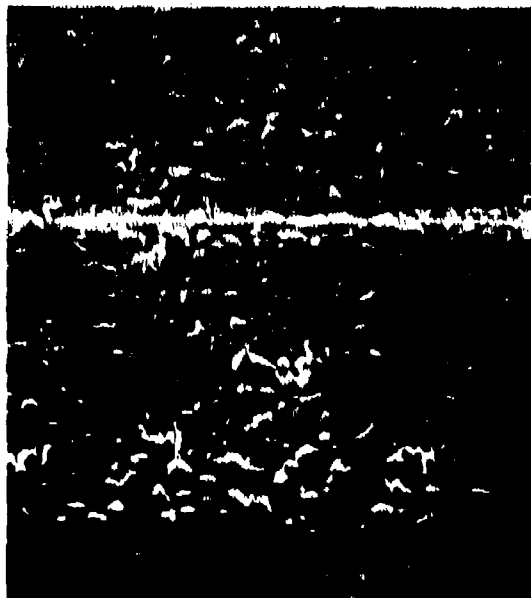


Figure 4. Scanning Electron Micrograph of 2- $\mu\text{m}$  Thick RDX Film Vapor-Deposited on Polished Tungsten Substrate

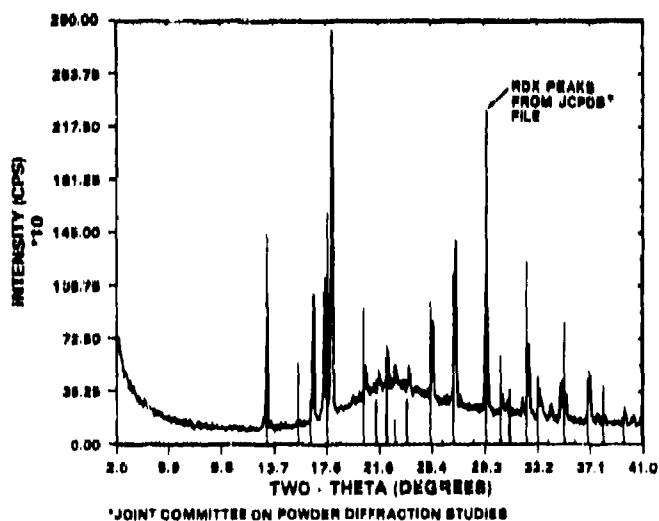


Figure 5. X-ray Diffraction Pattern for 10- $\mu\text{m}$ -thick RDX Film Vapor-Deposited on Pyrex

tungsten substrates. Currently, techniques are being developed to examine such thin samples using the transmission electron microscope (TEM) to obtain electron diffraction patterns for crystal structure analysis.

Good quality samples of NC have been deposited from solution. Films about 5  $\mu\text{m}$  thick have been prepared by evaporation of an acetone solution containing 1 percent NC by weight. Currently, procedures are being developed for preparing thinner samples of NC and samples of CP, AP, and KP. In general, substantially different procedures are required for each material deposited from solution.

In addition to having short thermal relaxation times and providing optical access to the condensed phase, thin-film samples also have the advantage of requiring small amounts of the energetic material. This is particularly advantageous for preliminary or "screening" experiments with newly developed materials, which are generally available in limited amounts. For example, only about 20 mg of material were required for preparation of each sample that was made by physical vapor deposition.

## PRELIMINARY EXPERIMENTS

Initially, some questions must be addressed regarding the use of thin film samples and the applicability of chemical behavior to bulk material. These include: (1) the effect (such as catalysis) of the substrate on decomposition mechanisms, (2) assumptions regarding film characteristics that are used in the analytical ellipsometric models, (3) film/substrate stability, and (4) macroscopic physical behavior of the thin-film sample.

The effects of the substrate on decomposition are to be examined by comparing the mass spectra obtained from slow thermal decomposition of thin films with those obtained from thick films or granular material. The effects of the assumptions in the analytical ellipsometric models can be evaluated at temperature in slow thermal decomposition experiments. Preliminary experiments are being conducted to evaluate film/substrate stability, macroscopic physical behavior and

the feasibility of applying TRISP to thin-film samples.

## Film/Substrate Stability

Substrate processing, film deposition techniques, film thickness and heating rate can all affect the physical stability of energetic thin films undergoing thermal decomposition. Substrate warpage is minimized by the small sample size, by allowing unconstrained radial expansion of the substrate, and by a vacuum annealing process to reduce inherent strain in the substrate. The geometrical configuration (planar, horizontal) of the sample is less sensitive to "blowoff" (separation of the film from the substrate prior to decomposition) than other configurations such as coated wires. Sample and substrate preparation, however, is critical. The substrate must be absolutely dry prior to film deposition or steam expansion from the substrate-film interface can blow off the film. The substrates are dried by heating under vacuum prior to film deposition. The thermal expansion coefficient mismatch between the film and substrate (the energetic film will expand more than the substrate) may be overcome, if necessary, by "expansion joints" (regions of no deposition) in the film.

To determine if energetic films will remain in contact with substrates under rapid heating conditions in vacuum, a simple light-scattering detection experiment is being conducted with RDX films. As depicted in Figure 6, a HeNe laser is directed over the top of the thin-film sample. Any material that is ejected off the substrate is monitored by detecting forward-scattered laser light. The lens focuses the volume directly above the sample within which the HeNe laser beam passes onto a photomultiplier tube (PMT) detector. A HeNe notch filter is used to eliminate any PMT response to luminous sources within the scattering volume other than the scattered laser light. The detection limit and response was calibrated by placing a known concentration and size of aerosol particulate in the scattering volume. Using an aerosol atomizer/analyzer (TSI 3076/3071) with monodisperse polystyrene latex spheres (Duke Scientific), it was verified that particles

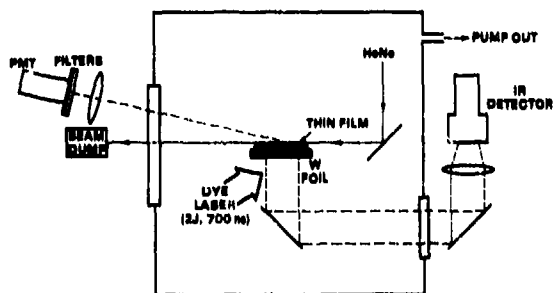


Figure 6. Schematic of Thin Film Physical Stability Test Assembly

greater than  $0.3 \mu\text{m}$  can be detected as discrete scattering events. The thin-film sample is heated with a flashlamp-pumped dye laser delivering 2 J of energy within 700 ns (see Figure 7 for the pulse power curve). The laser uniformly illuminates the substrate via an optical fiber. The substrate temperature (from which the film temperature is determined as discussed above) is obtained with the infrared detector. To obtain an appropriate heating rate with this lower laser energy, the sample size for these tests was reduced to an area of  $0.25 \text{ cm}^2$ . The predicted film/substrate interface temperature response is shown in Figure 8. Slow-heating experiments were conducted to compare with the rapid-heating response. The slow heating ( $\sim 10 \text{ K/s}$ ) experiments were conducted using an electric button heater and thermocouple instead of the dye laser and infrared detector, respectively.

The observed light-scattered signals are expected to vary with heating rate and RDX film thickness. Slow heating ( $\sim 10 \text{ K/s}$ ) does not produce discrete scattering events, but produces a small continuous signal as material sublimates into vacuum, indicating no significant solid material is ejected. Experiments rapidly heating ( $\sim 10^8 \text{ K/s}$ ) thick ( $10 \mu\text{m}$ ) and thin ( $\sim 0.1 \mu\text{m}$ ) films are currently underway.

#### Effect of Film Thickness on Physical Behavior

Published results from experiments with granular nitramines (such as HMX) and bulk

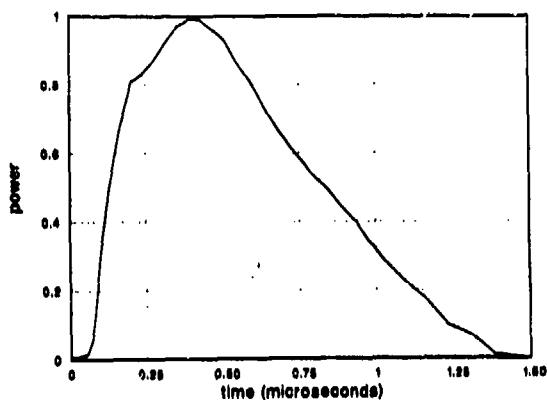


Figure 7. Laser-pulse Power Curve Used in Thin Film Physical Stability Tests

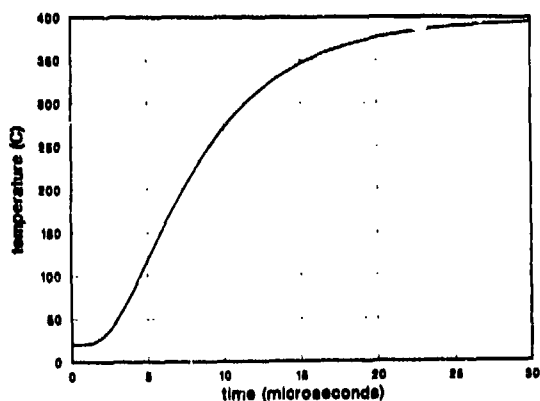


Figure 8. Predicted Film/Substrate Interface Temperature Response for Thin Film Physical Stability Tests

propellants have shown complicated physical effects involving liquefaction and bubble formation in the condensed phase.<sup>8-10</sup> Preliminary experiments employing slow heating rates were conducted to examine these effects in thin-film samples of RDX. The experiments were performed with the film confined between the tungsten substrate and a quartz or pyrex window. The confinement prevented the film from evaporating prior to attaining decomposition temperatures in the slow-heating experiments. Video imaging of samples that were 2 to  $3 \mu\text{m}$  thick indicated partial liquefaction and (or) bubble formation at

temperatures between about 440 and 525 K. The bubbles initially were relatively evenly dispersed and subsequently grew and coalesced until the RDX was consumed. At similar temperatures, samples that were about 0.05  $\mu\text{m}$  thick exhibited a uniform solid-to-gas transition, without any liquefaction or bubble formation.

The results from the confined experiments provide a limited indication that for sufficiently thin samples, decomposition will occur faster than the rate at which macroscopic effects such as bubble formation will occur. This would permit chemical reaction mechanisms and kinetics to be studied in the absence of complicated physical effects and multi-phase interactions. Thicker films could then be used to study the onset and effects of complicated physical interactions that are believed to be present in bulk material.

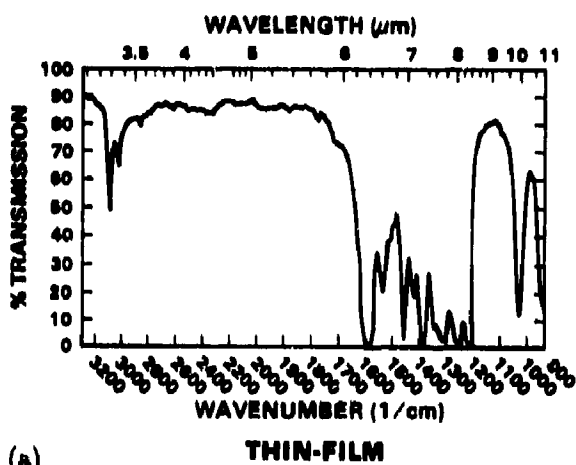
### Feasibility of TRISP

Published experimental studies of the pyrolysis of nitramines (such as HMX) have indicated that the overall rate of pyrolysis may be significantly affected by condensed-phase phenomena.<sup>10,11</sup> However, the nature of these condensed-phase mechanisms is unclear. Observed pyrolysis rates suggest an overall reaction scheme with an autocatalytic step.<sup>8,9,12,13</sup> That is, the formation of a reaction product acts as a catalyst for further reaction. This autocatalytic step may involve the condensed-phase interaction of decomposition products with nitramines. For example, work by Behrens<sup>10,11</sup> indicates that some  $\text{CH}_2\text{O}$  formed during slow thermal decomposition of HMX may have significant residence time in the condensed phase before being liberated to the gas phase. The retention of  $\text{CH}_2\text{O}$  in the condensed phase could contribute to an autocatalytic effect since, under certain conditions, the presence of  $\text{CH}_2\text{O}$  has been shown to increase RDX decomposition rates.<sup>8,9</sup>

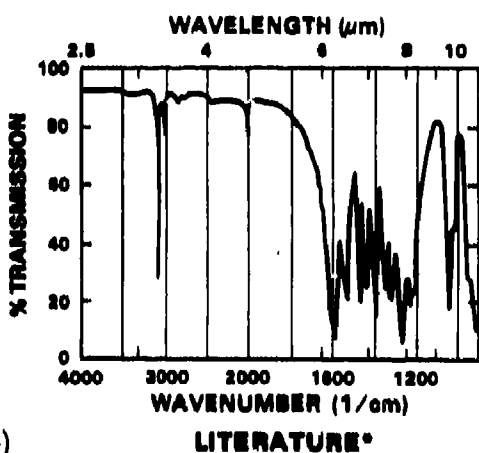
To understand the important condensed-phase phenomena occurring during thermal decomposition of nitramines and other  $\text{CHNO}$  explosives, a diagnostic tool is needed for direct observation of condensed-phase reaction mechanisms and kinetics. Time-resolved infrared spectral photography (TRISP) shows promise

for obtaining this condensed-phase information. TRISP was originally developed by Sorokin and co-workers at IBM to examine gas-phase photochemistry.<sup>14</sup> Subsequently, Renlund and Trott at Sandia National Laboratories showed that TRISP could be applied to condensed-phase samples.<sup>15,16</sup> A cooperative effort between Trott, Renlund, and the authors was established to determine the feasibility of using TRISP to examine condensed-phase reaction mechanisms occurring in the thin-film samples developed for use with the TOFMS discussed above. Essentially, TRISP can provide 5-ns "snap shots" of the IR spectra of the decomposing film. These can provide information about bond cleavage, the accumulation of decomposition products in the condensed phase, and ultimately, a direct measure of condensed-phase reaction kinetics. An overall description for the decomposition kinetics can then be developed by combining the condensed-phase reaction results with data for the gas-phase decomposition products that are observed with the TOFMS. A current limitation of TRISP is that for sub-millisecond experiments, it is essentially a single-shot technique. Time-delayed TRISP diagnostics on multiple similar shots will be employed to evaluate condensed-phase mechanisms of interest.

Preliminary experiments with a conventional infrared spectrometer were conducted to: (1) compare thin-film spectra with literature data, and (2) determine the film thickness required to produce a useful TRISP response. Conventional spectra were obtained from RDX, TATB, and HNS thin films, 2 to 5  $\mu\text{m}$  thick, and agreed with the corresponding published spectra. As an example, results for RDX are shown in Figures 9 a,b. The conventional infrared spectra indicated that the optimum path length for a transmitted signal is about 1 to 3  $\mu\text{m}$ . Using a reflected signal, it appears that TRISP can be used with samples as thin as 0.5  $\mu\text{m}$ , and if a multipass arrangement is employed (5 or 6 passes being reasonable), useful TRISP spectra should be obtained from samples as thin as about 0.1  $\mu\text{m}$ . The film thicknesses required to use TRISP with HMX, PETN, and NC are currently being investigated.



(a)



(b)

\*LASL Explosive Property Data, T.R. Gibbs, A. Popolisto, Eds.

Figure 9. Conventional RDX Infrared Spectra: (a) 2- $\mu$ m-thick Film on Barium Fluoride Substrate, (b) Literature

Based on the above conventional infrared results, preliminary experiments were performed to evaluate the use of TRISP with thin-film samples. TRISP spectra were obtained from room-temperature samples (about 2  $\mu$ m thick) of RDX, HNS, and TATB and agreed with conventional infrared spectra. TRISP spectra were then obtained from unconfined samples of RDX and TATB (about 2  $\mu$ m thick) that were slowly heated in air at atmospheric pressure. Examination of the RDX spectra shown in Figure 10 indicates the broad spectral range captured in a single shot. The weakening of the RDX absorption bands near

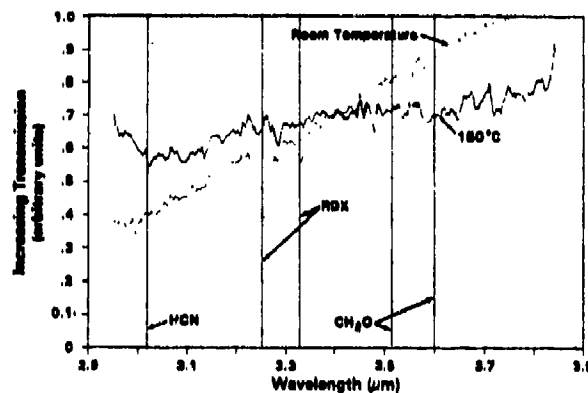


Figure 10. Preliminary TRISP Spectra from 2- $\mu$ m RDX Film on Tungsten Heated Slowly in Atmosphere

3.3  $\mu$ m from room temperature to  $\sim 150^\circ\text{C}$  indicates the disappearance of the RDX molecule. The spectral locations of the absorption bands for HCN and  $\text{CH}_2\text{O}$  are shown for comparison to the observed spectra. Preliminary RDX data suggest that in this configuration the concentration of decomposition products HCN and  $\text{CH}_2\text{O}$  were at or below the detection limit. Higher concentrations may be present under confinement and/or during rapid heating. Additional experiments are underway to examine the presence of HCN and  $\text{CH}_2\text{O}$  in the condensed phase during decomposition of confined RDX thin films.

The above results are encouraging. In future experiments with rapidly heated samples, TRISP initially will be applied to separate samples subjected to the same experimental conditions as similar samples heated in the TOFMS. Ultimately, experiments would be configured to employ simultaneously both TOFMS and TRISP with the same sample.

## SUMMARY

An experimental system is being developed to study the fast kinetics governing solid-phase decomposition under ignition conditions. Thin-film samples of a variety of energetic materials have been prepared. Characterization indicates they are uniform and well-crystallized. Sample preparation and

deposition techniques have been presented. Preliminary experiments have been conducted to demonstrate and assess the use of thin-film samples with the experimental system. Encouraging results have been obtained. Thin-film samples remain in contact with substrates during slow heating. TRISP spectra have been obtained for decomposing RDX, demonstrating the feasibility to obtain condensed-phase chemical information. Thicker films (~5  $\mu\text{m}$ ) can exhibit macroscopic responses (bubble formation and growth, etc.) during decomposition, whereas thin films (~0.05  $\mu\text{m}$ ) have not exhibited macroscopic inhomogeneities.

## ACKNOWLEDGEMENTS

This work performed at Sandia National Laboratories supported by the U.S. Department of Energy under Contract DE-AC04-76DP00789. We would like to acknowledge the following individuals for their continuing assistance in this effort: Mel Baer, Barry Boughton, Frank Chavez, Tom Headley, John Lewin, Rod Mahoney, Jill Miller, Steve Ohrt, Dan Rader, Hampton Richardson (all of Sandia National Laboratories, Albuquerque, NM); Rich Behrens (Sandia National Laboratories, Livermore, CA); and Jack Cheng (GRQ Instruments, Livermore, CA).

## REFERENCES

- Alexander, M. H., et al., "Nitramine Propellant Ignition and Combustion Research: New Tools and New Directions," Army Research Office Technical Report, Feb 1989, Research Triangle Park, NC.
- Dobratz, B. M., "Properties of Chemical Explosives and Explosive Simulants," UCRL-51319 Rev. 1, Lawrence Livermore National Laboratory, Livermore, CA, 31 Jul 1974.
- "PATRAN Plus User's Manual," PATRAN, Division of PDA Engineering, Costa Mesa, CA, 1987.
- Touloukian, Y. S., Ed., *Thermophysical Properties of Matter*, Vol. 1, 1970.
- Howarth, S. B.; Lippiatt, J. H.; Price, D.; Ward, G. B.; and Meyer, P., *Int. J. Mass Spectrom. Ion Phys.*, Vol. 9, 1972, p. 95.
- Lincoln, K. A., "Data Acquisition Techniques for Exploiting the Uniqueness of the Time-of-Flight Mass Spectrometer: Application to Sampling Pulsed Gas Systems," *Dynamic Mass Spectrometry*, Ch. 8, Vol. 6, D. Price and J. F. J. Todd, Eds., Heydon and Son, Philadelphia, PA, 1981.
- Cheng, J. C., "Polarization Scrambling Using a Photoelastic Modulator: Application to Linear Dichroism Measurement," *Rev. Sci. Instrum.*, Vol. 47, No. 6, 1976, p. 4.
- Boggs, T. L., "The Thermal Behavior of Cyclotrimethylenetrinitramine (RDX) and Cyclotetramethylenetetranitramine (HMX)," *Fundamentals of Solid-Propellant Combustion*, K. K. Kuo and M. Summerfield, Eds., *Prog. Astronautics and Aeronautics*, Vol. 90, 1984.
- Fifer, R. A., "Chemistry of Nitrate Ester and Nitramine Propellants," *Fundamentals of Solid-Propellant Combustion*, K. K. Kuo and M. Summerfield, Eds., *Prog. Astronautics and Aeronautics*, Vol. 90, 1984.
- Behrens, R., Jr., "Thermal Decomposition of RDX and HMX in the Condensed Phase," *Combustion of Energetic Materials, Semi-Annual Report April 1, 1988-September 30, 1988*, Sandia National Laboratories, SAND89-8002, 1989.
- Behrens, R., Jr., "Thermal Decomposition Mechanisms of RDX and HMX," *Combustion of Energetic Materials, Semi-Annual Report April - September 1987*, Sandia National Laboratories, SAND88-8001, 1988.
- Behrens, R., Jr., "Determination of the Rates of Formation of Gaseous Products from the Pyrolysis of Octahydro 1,3,5,7-tetranitro-1,3,5,7-tetrazocine (HMX) by Simultaneous Thermogravimetric Modulated Beam Mass Spectrometry," Sandia

National Laboratories, SAND89-8412, 1989.

13. Behrens, R., Jr., "Identification of Octahydro-1,3,5,7-tetranitro-1,3,5,7-tetrazocine (HMX) Pyrolysis Products by Simultaneous Modulated Beam Mass Spectrometry and Time-of-Flight Velocity-Spectra Measurements," Sandia National Laboratories, SAND89-8416, 1989.
14. Avouris, P.; Bethune, D. S.; Lankard, J. R.; Ors, J. A.; and Sorokin, P. P., "Time-Resolved Infrared Spectral Photography: Study of Laser-Initiated Explosions in  $\text{HN}_3$ ," *J. Chem. Phys.*, Vol. 74, No. 4, 1981, p. 2304.
15. Trott, W. M. and Renlund, A. M., "Optical Methods for the Study of Explosive Chemistry," *Topical Meeting on Lasers in Materials Diagnostics*, 11-12 Feb 1987, Albuquerque, NM, Paper WC4.
16. Renlund, A. M.; Sheffield, S. A.; and Trott, W. M., "Time-Resolved Infrared Spectral Photography Studies of Shock-Induced Chemistry in  $\text{CS}_2$ ," *Proc. 4th American Phys. Soc., Topical Conf. on Shock Waves in Condensed Matter*, Y. M. Gupta, Ed., 1986, p. 237.

# LASER IGNITION OF EXPLOSIVES: RAMAN SPECTROSCOPY OF THE IGNITION ZONE

Helena Nilsson and Henric Östmark  
Swedish Defence Research Establishment  
S-102 54 Stockholm, SWEDEN

*By combining a laser ignition technique with laser Raman spectroscopy we have developed a method for studying the gas phase reactions occurring in the ignition zone of a high explosive. The apparatus consists of a 300 W CO<sub>2</sub>-laser as ignition source and of a pulsed KrF-laser for the Raman Scattering. By using a variable time delay between the two lasers, it is possible to study the ignition processes pseudo time resolved. This technique used on the ignition zone of RDX enabled the detection of CH<sub>2</sub>O, NO<sub>2</sub>, N<sub>2</sub>, CO, and CN/HCN.*

## INTRODUCTION

The ignition of deflagration of explosives has proved to be a multi-phase reaction. This has created a need for fast methods for studying the gas phase reactions and the decompositions. Schultz et al.<sup>1</sup> divides the sequence in which RDX is shocked to detonation into four phases, each of which it is possible to make measurements on. Schultz et al. also point out the need to use techniques like Raman spectroscopy or Laser Induced Fluorescence (LIF) in the first phase when no light is emitted.

Fairchild et al.<sup>2</sup> have developed a laser pyrolysis/laser fluorescence technique for the real-time measurements of radicals/molecules in combustion processes. They use a CO<sub>2</sub>-laser and a Nd:YAG pumped dye-laser fired in sequence to monitor the reaction. The delay between the two lasers is controlled by two delay generators and can be varied.

The laser ignition method has in earlier studies of pyrotechnical mixtures proved to be very useful.<sup>3,4</sup> Studies of high explosives with this method have shown that the threshold ignition energy, to a high degree, is dependent on the pressure.<sup>3,5</sup> Leeuw et al.<sup>6</sup> used an excimer laser working at 248 nm to ignite primary explosives, and by using emission spectroscopy they studied the formation of decomposition products of lead styphnate and

mercury fulminate. Trott and Renlund<sup>7</sup> have used emission spectroscopy and Raman scattering for studying solid detonating high explosives (HE).

Earlier work has shown that Raman spectroscopy can be a powerful tool when investigating the ignition of explosives.<sup>7,8</sup> This paper will show how Raman spectroscopy can be used to study the ignition reaction zone, and how it is possible to follow the transition from a weak decomposition to a strong deflagration.

## EXPERIMENTAL

The laser ignition set-up described in earlier work<sup>3-5</sup> has been extended to suit our Raman experiments. A schematical representation of the set-up is given in Figure 1. About 300 mg of RDX is pressed to a pellet with a 10-mm diameter and a thickness of 2 mm. The density of the explosive is 95 percent of the theoretical maximum density for RDX. The pellet is fastened with double-adhesive tape to a sample holder in the explosive chamber. The sample holder is continuously rotated by an electrical motor, so that unreacted explosive during a period of time is exposed to the CO<sub>2</sub>-laser beam. The explosion chamber is constructed to withstand pressures up to 4.0 MPa and the experiments are carried out in a helium atmosphere to keep the explosive from reacting with air. The helium

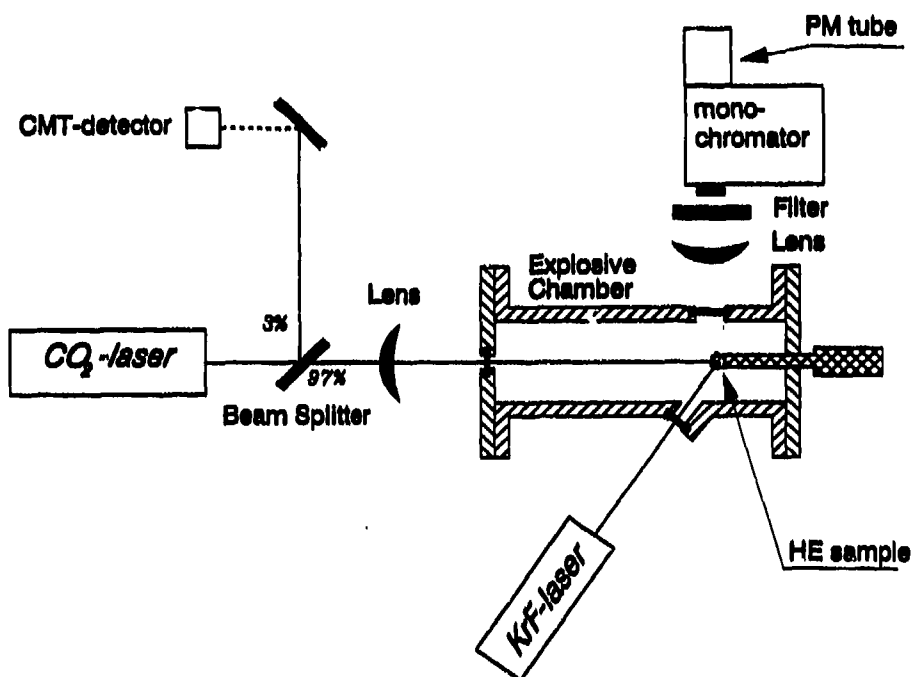


Figure 1. A Schematic View of the Experimental Setup

atmosphere also has a good effect on the signal-to-noise ratio due to the fact that it does not cause any Raman scattering.

The ignition pulse is delivered by a 300 W CW CO<sub>2</sub>-laser (Coherent CR 41) which is electrically pulsed and has a pulse width of 1 ms - CW. In the experiments presented here, the pulse width has been 2 ms. The measuring pulse is given by an excimer laser (Spectra Physics EMG 201E) using the KrF line at 248 nm and with a pulse width of 20 ns. The beam from the KrF-laser was focused into the gas phase 2 mm from the surface of the HE. The scattered light was analyzed with a Spex 500M monochromator with a Hamamatsu photomultiplier. The Raman scattering detected by the photomultiplier is preamplified 5-25 times and then connected to a gated boxcar integrator (Stanford Research System) which amplifies the signal 2-5 times and then averages 1-10 pulses. This averaged signal is then recorded.

The experiments included several tests with an Nd:YAG laser (Quantel YG581), working at the 532 nm line, as probe laser. This set-up created some problems with

increased background noise and a lower Raman cross section (see Table 1) leading to weaker Raman signals. Because of these problems, we decided to do these preliminary experiments with the excimer laser.

Table 1. Raman Cross-Sections at 248 nm and 532 nm<sup>9</sup>

Molecule	Vibrational frequency (cm <sup>-1</sup> )	$\left(\frac{d\sigma}{d\Omega}\right)_{\lambda=248\text{nm}}$ (10 <sup>-30</sup> cm <sup>2</sup> /sr)	$\left(\frac{d\sigma}{d\Omega}\right)_{\lambda=532\text{nm}}$ (10 <sup>-30</sup> cm <sup>2</sup> /sr)
NO	1877	5.5	0.2
NO <sub>2</sub>	$\nu_1$ 1320	182.8	7.37
	$\nu_2$ 754	84.3	3.63
N <sub>2</sub>	2331	13.1	0.46
H <sub>2</sub> O	3652	30.8	0.9
O <sub>2</sub>	1556	16.6	0.65
CO	2145	13.3	0.48
CO <sub>2</sub>	$\nu_1$ 1388	15.1	0.6
	$2\nu_2$ 1285	11.1	0.45

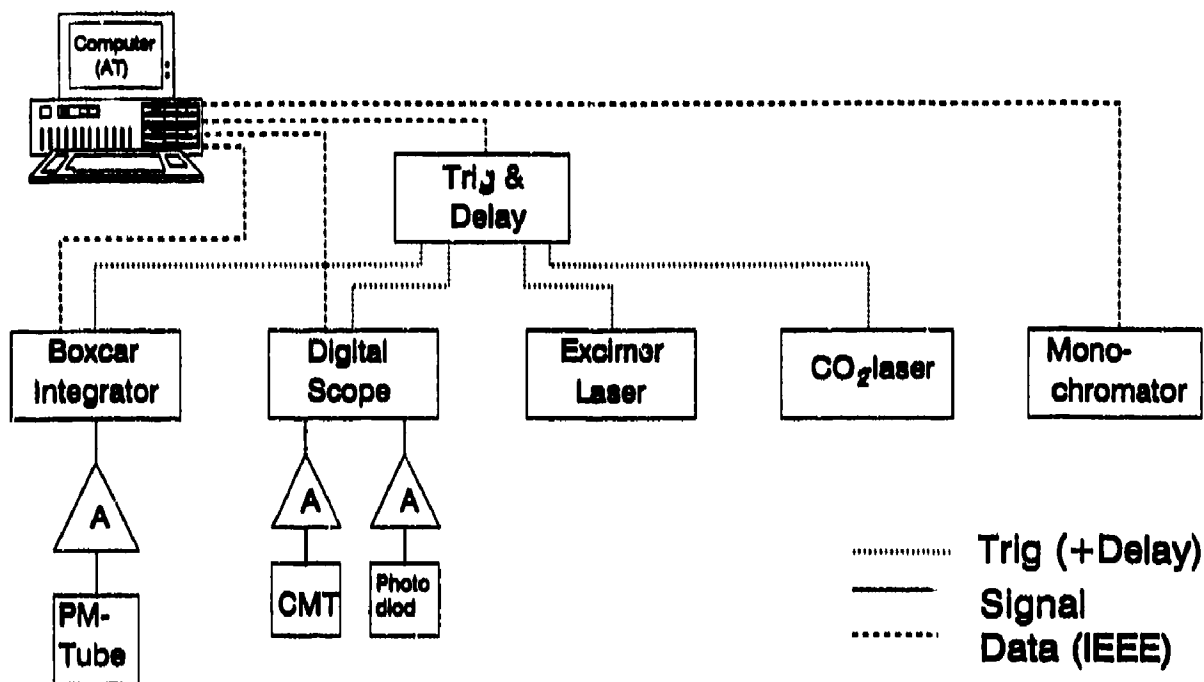


Figure 2. A Schematic View of the Electrical Setup

To make the two lasers and the gated boxcar integrator work simultaneously a trig and delay unit (Stanford Research Systems) is used. The setup also includes a digital scope (HP 54111D). The scope is mainly used to monitor the pulse width of the electrically pulsed CO<sub>2</sub>-laser with the help of a CMT detector. The digital scope also monitors the total emitted light from the explosive, and the delay between the CO<sub>2</sub>-laser and the probe laser. In this case, the delay between the CO<sub>2</sub>-laser pulse and the Raman pulse is varied between 0.2-5 ns. See Figure 2 for an overview of the electrical set-up.

## RESULTS

The results given in this paper are for RDX, due to the fact that a lot of work on RDX decomposition have been published,<sup>10,14</sup> which leads to an easy analysis of the experimental results. After evaluating the method, the test program also includes the following high explosives: HMX, Tetryl, PETN, TNT, TATB,

and NTO. These latter studies are still in progress.

Figure 3 shows two independent registrations of a Raman spectrum for RDX between 261 nm - 267 nm made with the excimer laser in helium atmosphere at a pressure of 0.4 MPa. The time delay between the two lasers was 1 ns. These are only two of several registrations showing that the method has a very good reproducibility. In the left spectrum (262 nm - 267 nm), the following peaks have been identified:<sup>9,15</sup> CH<sub>2</sub>O (266.3 nm), NO<sub>2</sub> (265.4 nm), N<sub>2</sub> (263.4 nm), and CO (262.1 nm). In the spectrum to the right, the following peaks have been identified:<sup>9,15</sup> NO<sub>2</sub> (265.4 nm), N<sub>2</sub> (263.4 nm), CO (262.1 nm), and HCN/CN (261.4 nm).

In connection with the Raman measurements, a couple of emission registrations were made. Two of these registrations are shown in Figure 4. Large amounts of radicals such as OH and CN are formed in the thermal ignition

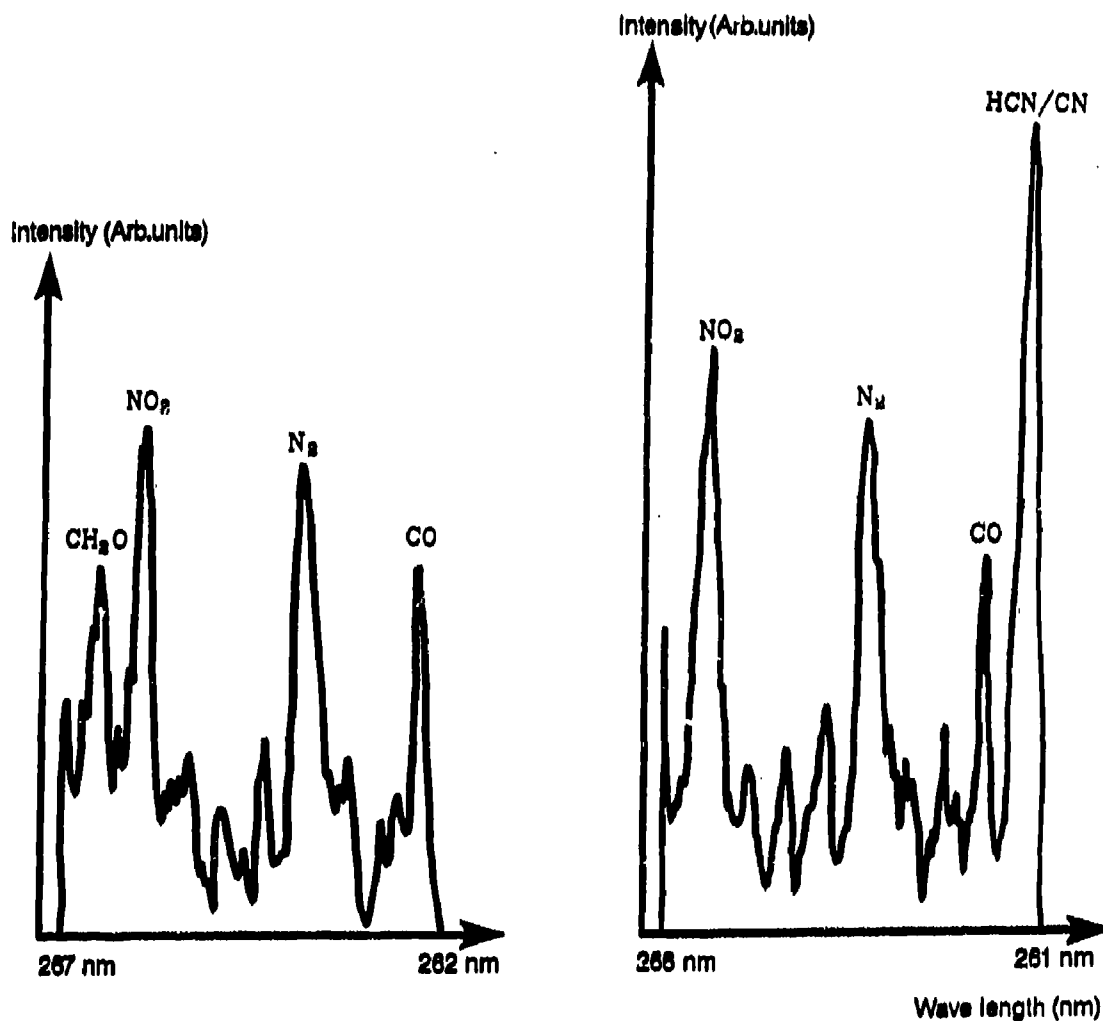


Figure 3. Raman Spectra of RDX in Helium at 0.4 MPa

zone. The fact that these radicals occur during the thermal ignition implies that a high temperature prevails in the reaction zone.

The results from the Raman and emission measurements correspond well with the results from a mass spectroscopic study performed in the same set-up.<sup>16</sup>

## DISCUSSION

The method described in this paper, combining laser ignition and Raman spectroscopy to study the ignition processes, differs from earlier studies<sup>6,7</sup> in the way that the measurements presented here take place in the thermal ignition zone. In Figure 5, one can see two

curves representing the laser pulse and the emitted light. From the emitted light curve one can distinguish two phases: a pre-ignition reaction and the self-sustaining ignition. Our Raman measurements take place in the pre-ignition or ignition zone. This leads to problems like high background noise, but it also gives a great advantage, namely that the measurement takes place before a significant amount of decomposition has occurred. The background noise is reduced by working in the inert helium atmosphere. This method approaches the possibility of measuring the steps in the decomposition chain which leads to ignition, and possibly also the initial steps in the thermal decomposition chain.

This jigsaw will be one of the keys to a correct decomposition chain and thereby the key to more accurate mathematical models for the decomposition and ignition of explosives.

One of the advantages of the laser ignition method is that there are no external chemical substances interfering with either the decomposition or the measurements. One drawback, though, is that one cannot neglect the fact that the laser pulse to some extent mechanically shocks the system, so it cannot be described as totally undisturbed.

Two different types of probe lasers were used, an Nd:YAG laser (Quantel YG581) working at 532 nm (doubled) and an excimer laser (Spectra Physics EMG 201E) using the KrF line at 248 nm. The band width of the Nd:YAG laser is  $0.7 \text{ cm}^{-1}$  while the band width of the excimer laser is 0.3 nm. Both lasers created laser breakthrough in air, but by using a lens with a long focal length (200 mm) to focus the excimer beam the problem was less evident, apparently due to the fact that the excimer beam is of a lower quality. During measurements in the explosive chamber in helium atmosphere, the problem reoccurred when "dust clouds" were created during imperfect decomposition in the pre-ignition zone.

When choosing the type of probe laser, the influence of the laser wavelength on the Raman cross sections of the molecules must be considered. P.J. Hargis<sup>17</sup> has pointed out the possibility of trace detection of small molecules when using an excimer laser working at 248 nm. In Table 1 the Raman cross sections for the two relevant wavelengths are listed for selected molecules.

The fact that the Raman cross section is so low at 532 nm compared with that at 248 nm (approximately 1:25), and the problems with breakthrough for the Nd:YAG laser makes it very difficult to use an Nd:YAG laser for Raman measurements in the ignition zone.

The method would be improved by using an OMA (Optical Multi-channel Analyzer) so that full advantage could be taken of the simultaneous multi-species detection possibility offered by Raman spectroscopy. The occurrence of several molecules could be

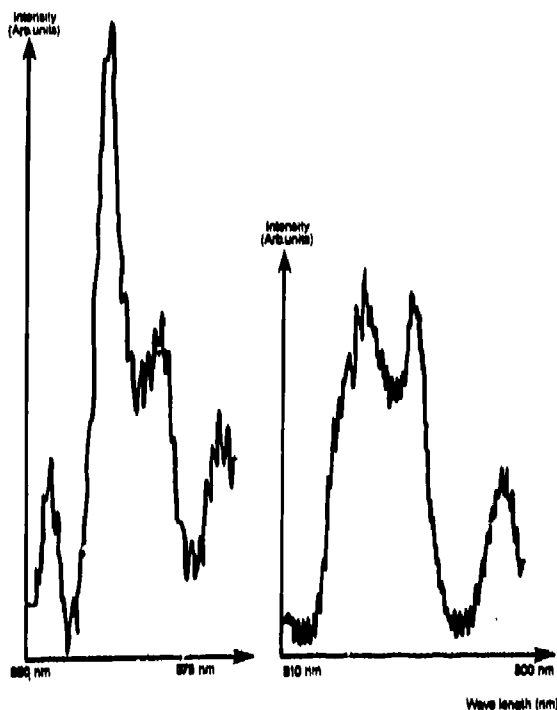


Figure 4. Emission Spectra of CN and OH Radicals

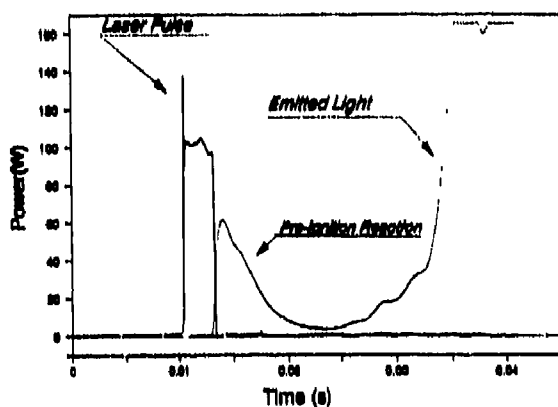


Figure 5. Example of Registrations at a Laser Ignition Experiment. In the figure is shown both the laser ignition pulse and the reaction light from the HE (PETN). (From [5].)

By monitoring a selected line time resolved during and after the ignition pulse, it is possible to study the time variation of a particular molecule (e.g.,  $\text{NO}_2$ ,  $\text{N}_2\text{O}$ , or  $\text{NO}$ ). By repeating these measurements for all possible molecules, a giant jigsaw is formed.

studied with one laser pulse and the problems connected with the produced dust would thus be avoided.

## CONCLUSIONS

The combined method of laser ignition/laser Raman spectroscopy has proved to be a powerful tool when investigating ignition of HE. The method has a couple of drawbacks, which also influence the results in this work: the band width of the excimer laser of 0.3 nm limits the resolution in the spectra, the laser pulse width limits the time resolution, and the Raman signals are very weak.

However, it is our belief that a great deal may be achieved by combining laser Raman spectroscopy with other spectroscopy methods.

## REFERENCES

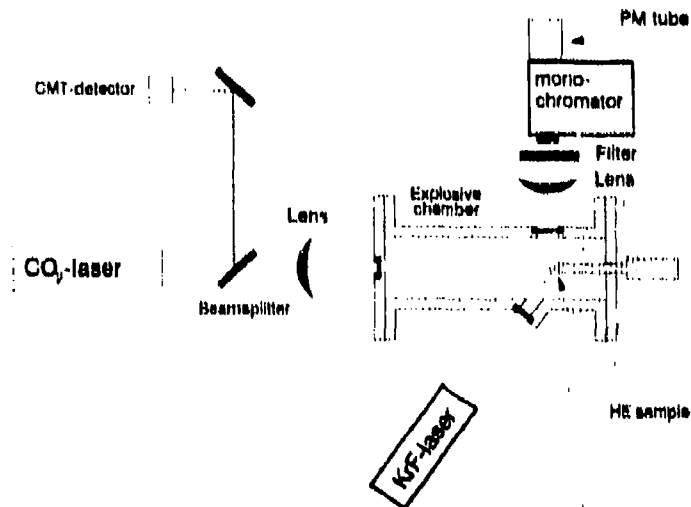
1. Schultz, C.; Lineares, B.; Cherville, J.; and Poulard, S., "Ultra-Fast Physico-Chemical Diagnoses of Detonation Initiation Mechanisms," *Proceedings of the Eighth Symposium on Explosives & Pyrotechnics*, 1974, pp. 49.1-49.11.
2. Fairchild, P. W.; Smith, G. P.; and Crosley, D. R., "A Laser Pyrolysis/Laser Fluorescence Technique for Combustion Chemical Kinetics," *Nineteenth Symposium (International) on Combustion*, 1982, pp. 107-116.
3. Östmark, H., "Laser as a Tool in Sensitivity Testing of Explosives," *Proceedings of the Eighth Symposium (International) on Detonation*, Naval Surface Weapons Center, NSWC 86-194, Albuquerque, NM, 15-19 Jul 1985, pp. 473-484.
4. Östmark, H., "Laser Ignition of Explosives: Ignition Energy Dependence on Particle Size," *3e Congrès International de Pyrotechnie Du Groupe de Travail de Pyrotechnie Spatial & 12th International Pyrotechnics Seminar*, Juan-les-Pins, France, Jun 1987, pp. 241-245.
5. Östmark, H. and Gräns, R., "Laser Ignition of Explosives: Effects of Gas Pressure on the Threshold Ignition Energy," submitted to *J. Energetic Materials*.
6. Leeuw, M. W.; Rooljers, A. J. Th.; and Van der Steen, A. C., "Fast Spectrographic Analysis of Laser Initiated Decomposition Reactions in Explosives," *Proceedings of the Eighth Symposium (International) on Detonation*, Naval Weapons Center, NSWC 86-194, Albuquerque, NM, 15-19 Jul 1985, pp. 710-714.
7. Trott, W. M. and Renlund, A. M., "Time-Resolved Spectroscopic Studies of Detonating Heterogeneous Explosives," *Proceedings of the Eighth Symposium (International) on Detonation*, Naval Weapons Center, NSWC 86-194, Albuquerque, NM, 15-19 Jul 1985, pp. 691-700.
8. Nilsson, H., *Laser raman spektroskopi: En litteratur studie*, FOA Report C 20753-2.3, Stockholm, Sweden, Apr 1989.
9. Eckbreth, A. C.; Bonczyk, P. A.; and Verdick, J. F., "Laser Raman and Fluorescence Techniques for Practical Combustion Diagnostics," *Applied Spectroscopy Reviews*, Vol. 13, No. 1, 1977, pp. 15-164.
10. Rauch, F. C. and Fanelli, A. J., "The Thermal Decomposition Kinetics of Hexahydro-1,3,5-trinitro-s-triazine above the Melting Point: Evidence for Both a Gas and Liquid Phase Decomposition," *J. Physical Chemistry*, Vol. 73, 1969, pp. 1604-1608.
11. Cosgrove, J. D. and Owen, A. J., "The Thermal Decomposition of 1,3,5 Trinitro Hexahydro 1.3.5 Triazine (RDX) - Part 1: The Products and Physical Parameters," *Combustion and Flame*, Vol. 22, 1974, pp. 13-18.
12. Bradley, J. N.; Butler, A. K.; Capey, W. D.; and Gilbert, J. R., "Mass Spectrometric Study of the Thermal Decomposition of 1,3,5-Trinitrohexahydro-1,3,5-triazine (RDX)," *J. Chem. Soc. Trans. Faraday I*, Vol. 73, 1977, pp. 1789-1795.

13. Oyumi, Y. and Brill, T. B., "Thermal Decomposition of Energetic Materials 3.\* A High-Rate, In Situ, FTIR Study of the Thermolysis of RDX and HMX with Pressure and Heating Rate as Variables," *Combustion and Flame*, Vol. 62, 1985, pp. 213-224.
14. Schroeder, M. A., "Critical Analysis of Nitramine Decomposition Data: Activation Energies and Frequency Factors for HMX and RDX Decomposition," U.S. Army Ballistic Research Laboratory Aberdeen Proving Ground, MD, Sep 1985.
15. Hertzberg, G., "Infrared and Raman Spectra of Polyatomic Molecules," *Molecular Spectra and Molecular Structure*, Vol. 2, D. Van Nostrand Company, Inc., Princeton, 1962.
16. Östmark, H. and Nilsson, H., "Laser Ignition of Explosives: A Mass Spectroscopic Study of the Pre-ignition Reaction Zone," *Proceedings of the Ninth Symposium (International) on Detonation*, Portland, OR, 28 Aug - 1 Sep 1989.
17. Hargis, Jr., P. J., "Trace Detection of Small Molecules by Pulsed-Ultraviolet (UV) Laser Raman Spectroscopy," *S.P.I.E.*, Vol. 286, 1981, pp. 139-145.

**LASER IGNITION OF EXPLOSIVES**  
**Raman spectroscopy of the ignition zone**

# Helena Nilsson • Henric Östmark

## Swedish Defence Research Establishment

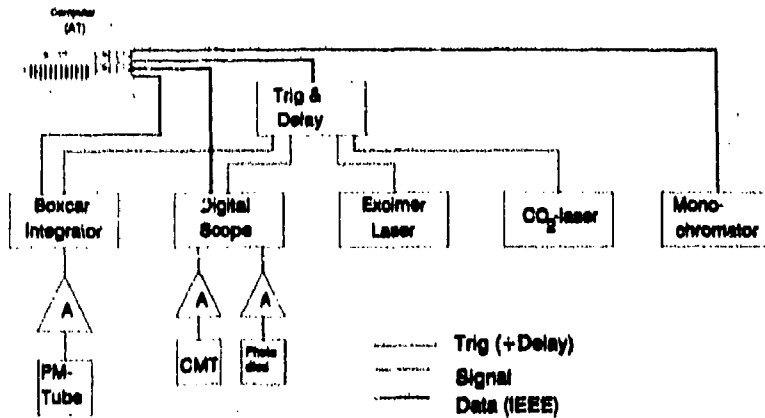


A schematical view of the experimental set-up. The CO<sub>2</sub>-laser is used to ignite the HE sample while the KrF-laser is used to induce the Raman scattering. To monitor the pulse width from the CO<sub>2</sub>-laser 3% of the laser beam is directed to a CMT-detector via a beamsplitter. The filter in front of the monochromator consists of butyl acetate.

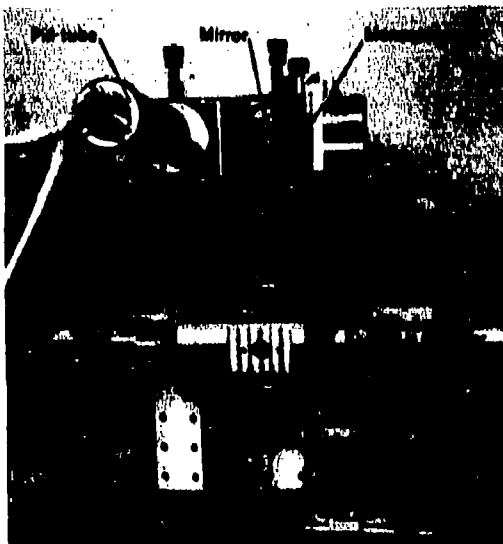
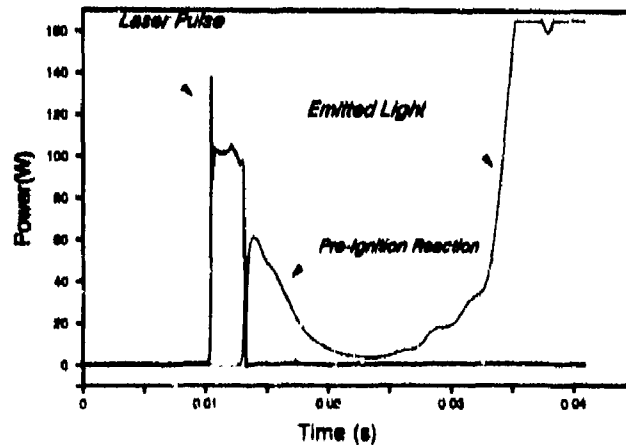




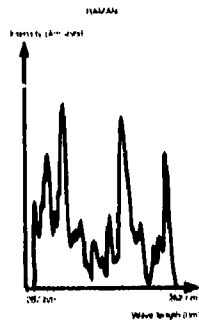
## Electrical Setup



In the figure one can see the laser pulse (blue line) and the emitted light (red line). From the emitted light curve one can distinguish two phases: a pre-ignition reaction and the ignition. The Raman measurements have taken place in the pre-ignition reaction phase.



The two photographs on the left show the experimental set-up. On fig. 1 one can see the mirror and the lens used to focus the laser beam on to the HE sample and the CMT-detector used to monitor the pulse width. On fig. 2 one can see the mirror that is used to focus the Raman signal into the monochromator, the PM-tube, the monochromator and the explosive chamber.



### RAMAN SPECTRA OF RDX

The pictures show two independent registrations. These registrations have proved to have a very good reproducibility. The peaks have been designated to  $\text{CH}_2$ ,  $\text{NO}_2$ ,  $\text{N}_2$ ,  $\text{CO}$  (left) and  $\text{NO}_2$ ,  $\text{N}_2$ ,  $\text{CO}$ ,  $\text{HON/ON}$  (right).



### EMISSION SPECTRA OF RDX

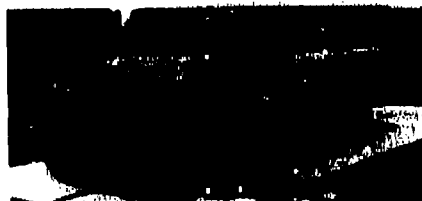
Selected wavelengths. To the left 300 - 310nm,  $\text{OH}$ -radical. To the right 375 - 390nm,  $\text{ON}$ -molecule.



# Summary



The excimer laser works at the KrF-line at 248nm and gives a laser energy of 0.5J. It has a bandwidth of 0.8nm. Raman cross-section is favourable to the excimer laser compared to the Nd-YAG laser (quotient of 2).



The Nd-YAG laser works at 633nm (doubled). It has a band width of 0.7  $\text{cm}^{-1}$  and gives a laser energy of 0.5J. The Raman cross-section given for the molecules by the Nd-YAG laser is a factor 10 better cross-section given by the excimer laser (quotient of 10).

### ADVANTAGES WITH THE RAMAN TECHNIQUE

- Simultaneous multiplex detection possible
- Fast measuring technique (10 - 20 ns)
- System not disturbed when measuring

### DISADVANTAGES WITH THE RAMAN TECHNIQUE

- The set-up is spatial sensitive
- Interference from the solid surface
- Weak signals

### POSSIBLE IMPROVEMENTS OF THE METHOD

- Using an OMA one can fully use the simultaneous multiplex detection possibility
- An OMA also makes it possible to take a complete scan with one H<sub>2</sub> sample

# THE EFFECT OF THE PENTAFLUOROTHIO ( $SF_5$ ) GROUP ON THE PROPERTIES OF EXPLOSIVE NITRO COMPOUNDS: NEW $SF_5$ EXPLOSIVES

M. E. Sitzmann  
Naval Surface Warfare Center  
Silver Spring, Maryland 20903-5000

and

D. L. Ornellas  
Lawrence Livermore National Laboratory  
Livermore, California 94550

*The effect of the pentafluorothio ( $SF_5$ ) group on the properties of explosive nitro compounds was investigated. During the initial part of this investigation, several polynitro  $SF_5$  model compounds were prepared and the best model compound (based on overall properties such as melting point, stability, ease of synthesis, etc.) was selected for in-depth physical evaluation. The evaluation included determination of impact sensitivity, thermal stability, and the heat and products of detonation. Based on the encouraging results from this model compound, additional  $SF_5$  explosives were prepared and studied, including candidate  $SF_5$  explosives for incorporation into a formulation for a cylinder test. The results from this investigation support the hypothesis that the  $SF_5$  group can provide nitro explosives with improved properties (increased density, decreased sensitivity, and good thermal stability) and produce energy in the detonation (due to formation of HF as a detonation product).*

## INTRODUCTION

Current and future Navy munitions require explosives that combine high performance with low vulnerability towards accidental detonation. To help satisfy this need for insensitive high-performance explosives, an investigation was initiated into the effect of the pentafluorothio ( $SF_5$ ) group on the properties of explosive nitro compounds. The investigation was based upon the following considerations: (a) the predicted energy release due to formation of HF in the detonation of  $SF_5$  explosives [compare the average S-F bond energy (79 kcal/mol) to that of H-F (135 kcal/mol)]; (b) the predicted energy release from  $SF_5$  compounds in metalized compositions (for example, compare the respective S-F and Al-F bond energies, 79 and 158 kcal/mol);

and (c) indications that the  $SF_5$  group can provide explosive nitro compounds with improved properties, i.e., increased density, decreased sensitivity, and good thermal stability (prior to our investigation, the only polynitro  $SF_5$  compound was fluoro-dinitroethyl pentafluorothioacetate which was described as a thermally stable, insensitive liquid with a density of 1.697 g/cc).<sup>1,2</sup>

The approach to  $SF_5$  explosives was to prepare several polynitro  $SF_5$  model compounds and choose the best (based on melting point, density, stability, ease of synthesis, etc.) for in-depth physical evaluation. This evaluation would include determination of the impact sensitivity and thermal stability as well as calorimetric determination of the heat and products of detonation. Seven  $SF_5$  explosives (model compounds) were prepared and the one

(model compounds) were prepared and the one selected for further evaluation gave sufficiently encouraging results to warrant an attempt to measure the performance of an SF<sub>5</sub> explosive in a cylinder test. The SF<sub>5</sub> explosive for the cylinder tests was to be part of a formulation containing HMX along with FEFO, bis(fluoro-dinitroethyl) formal, as plasticizer.<sup>3</sup> To minimize sample preparation problems, it was desirable to use an SF<sub>5</sub> explosive that has a low solubility (similar to that of HMX) in FEFO. In a search for such a material, a series of eight energetic SF<sub>5</sub> carbamates and dicarbamates were prepared and evaluated.

The initial SF<sub>5</sub> explosives prepared during the course of this investigation were straight chain polynitroaliphatic compounds. More recently, a cyclic polynitroaliphatic SF<sub>5</sub> compound as well as a polynitroaromatic compound containing an SF<sub>5</sub> substituent have been synthesized. Their properties were determined and compared with similar materials containing no SF<sub>5</sub> group.

## RESULTS

### Synthesis of Polynitro SF<sub>5</sub> Model Compounds

The SF<sub>5</sub> starting material for the preparation of the polynitro SF<sub>5</sub> model compounds was pentafluorothioacetyl chloride.<sup>4</sup> This material was hydrolyzed to pentafluorothioacetic acid<sup>4</sup> (F<sub>5</sub>SCH<sub>2</sub>CO<sub>2</sub>H) which was condensed with polynitroalcohols such as 2,2-dinitropropanol, 3-fluoro-3,3-dinitropropanol, and 3,3,3-trinitropropanol to give esters (compounds 1 - 3 in Table 1).

The low melting points (see Table 1) of the esters (1 - 3) made them unattractive as candidates for further evaluation (impact sensitivity and detonation calorimetry measurements are more convenient for solid samples). In a search for higher melting SF<sub>5</sub> explosives, the starting pentafluorothioacetyl chloride was first reduced to pentafluorothioethanol<sup>5</sup> (F<sub>5</sub>SCH<sub>2</sub>CH<sub>2</sub>OH) which was then treated with a variety of energetic intermediates including 2,2,2-trinitroethyl isocyanate,<sup>6</sup> N,N-bis(2-fluoro-2,2-dinitroethyl)carbonyl chloride,<sup>7</sup> 4,4,4-trinitrobutyric acid, and tris(2-fluoro-2,2-dinitroethyl)chloroorthoformate.<sup>8,9</sup> The prod-

ucts (compounds 4 - 7) had sufficiently high melting points to be attractive candidates for this study (see Table 2).

Table 1. Polynitroaliphatic Esters of Pentafluorothioacetic Acid

$\text{F}_5\text{SCH}_2\overset{\text{O}}{\parallel}\text{C}-\text{OR}$		
Compound	R	Melting Point, °C
1	-CH <sub>2</sub> C(NO <sub>2</sub> ) <sub>2</sub> CH <sub>3</sub>	22
2	-CH <sub>2</sub> CH <sub>2</sub> CF(NO <sub>2</sub> ) <sub>2</sub>	28
3	-CH <sub>2</sub> CH <sub>2</sub> C(NO <sub>2</sub> ) <sub>3</sub>	32

Table 2. SF<sub>5</sub> Explosives from Pentafluorothioethanol

$\text{ROCH}_2\text{CH}_2\text{SF}_5$			
Compound	R	mp °C	Density (g/cc)
4	(NO <sub>2</sub> ) <sub>3</sub> CCH <sub>2</sub> NHC- $\text{O}$ $\parallel$	81	1.82 <sup>a</sup>
5	[(NO <sub>2</sub> ) <sub>2</sub> FCCH <sub>2</sub> ] <sub>2</sub> NC- $\text{O}$ $\parallel$	61	-
6	(NO <sub>2</sub> ) <sub>3</sub> CCH <sub>2</sub> CH <sub>2</sub> C- $\text{O}$ $\parallel$	45	-
7	[(NO <sub>2</sub> ) <sub>2</sub> FCCH <sub>2</sub> O] <sub>3</sub> C-	96	1.81 <sup>a</sup>

<sup>a</sup> By gas pycnometer; Dr. Michael Chaykovsky, Naval Surface Warfare Center

### Polynitro SF<sub>5</sub> Model Compound Chosen for Further Evaluation: Model Compound with Best Overall Properties

The best polynitro SF<sub>5</sub> model compound, based mainly on melting point and ease of synthesis, was compound 7, tris(2-fluoro-2,2-dinitroethyl)-pentafluorothioethyl orthocarbonate. Approximately 75 grams of compound 7 was prepared to provide sufficient material for further evaluation. The properties of 7 (including impact sensitivity and thermal stability) are shown in Table 3 and are compared with those

Table 3. Properties of Orthocarbonates

[(NO <sub>2</sub> ) <sub>2</sub> FCCH <sub>2</sub> O] <sub>3</sub> COCH <sub>2</sub> R					
Compound	R	H <sub>50</sub> % (cm)	Density (g/cc)	Thermal Stab.	mp °C
7	-CH <sub>2</sub> SF <sub>5</sub>	61; RDX = 17 <sup>a</sup> 91; RDX = 28 <sup>b</sup>	1.81 <sup>d</sup>	0.04-0.05 <sup>f</sup>	96
8	-CH <sub>2</sub> NO <sub>2</sub>	41; RDX = 28 <sup>a</sup>	-	-	89
9	-CF(NO <sub>2</sub> ) <sub>2</sub>	26; RDX = 24 <sup>c</sup>	1.80 <sup>e</sup>	-	136

<sup>a</sup> Determined at NSWC; although it has been suggested by a reviewer that we normalize the data in this table, at NSWC we traditionally have reported the actual values of standard and test compounds measured on the same day. The values of standard RDX vary over time with different operators, test conditions, sandpaper, etc.

<sup>b</sup> Determined at LLNL; HMX = 32, TNT = 148

<sup>c</sup> Determined at NSWC<sup>10</sup>

<sup>d</sup> By gas pycnometer, Dr. Michael Chaykovsky, NSWC

<sup>e</sup> X-ray crystal density<sup>11</sup>

<sup>f</sup> Determined at LLNL; total gas from 0.25 g after 22h at 120°C; HMX: < 0.01, RDX: 0.02-0.025, TNT: 0.01-0.012

of tris(2-fluoro-2,2-dinitroethyl)-(2-nitroethyl) orthocarbonate (compound 7) and tetrakis (2-fluoro-2,2-dinitroethyl)orthocarbonate (compound 9). As expected, 7 has good thermal stability, but the most striking property of 7 is its appreciably lowered impact sensitivity relative to 8 and 9. This large reduction in impact sensitivity is a strong indication that the SF<sub>5</sub> group is effective in reducing the impact sensitivity of nitro explosives.

#### Heat and Products of Detonation for the Selected Polynitro SF<sub>5</sub> Model Compound (Compound 7)

The calorimetric determination of the heat and products of detonation for 7 was done at LLNL using a monel calorimeter bomb with a gold confining cylinder.<sup>12,13</sup> For the detonation calorimetry experiments, compound 7 was pressed into two 26 gram charges using a pressure of 230 MPa (34,000 psi) under a vacuum of less than 0.5 mm Hg at a temperature of 45°C to give average densities for the charges of 1.801 and 1.807 g/cc (99.5 and 99.8 percent of theoretical maximum density). The charges were initiated with a PETN booster and the heat of detonation was measured to be 1.085 ± 25 cal/g.

The detonation calorimetry experiments showed that the only fluorine containing detonation product was HF, and no CF<sub>4</sub>, SF<sub>4</sub>, SF<sub>6</sub>, etc., were detected. This was a desirable result since the conversion of S-F to HF in the detonation is an exothermic process (compare respective bond energies of 79 and 135 kcal/mol). Surprisingly, the main sulfur species (about 70 percent) recovered after the detonation was carbonyl sulfide (COS) and no significant amounts of SO<sub>2</sub>, SO<sub>3</sub>, or products derived therefrom were found. This is an important result since it indicates that incorporation of sulfur will not reduce the limited amount of oxygen available for hydrocarbon combustion. In fact, with the formation of COS, sulfur is not consuming oxygen in the detonation process but is behaving as an oxidant. Hydrogen sulfide (H<sub>2</sub>S) was identified as the other major sulfur detonation product, a product in which sulfur again behaves as an oxidant.

#### Energetic SF<sub>5</sub> Carbamates and Dicarbamates: Candidates for a Cylinder Test

A number of energetic SF<sub>5</sub> carbamates (compounds 10 - 13, see Table 4) were prepared

Table 4. Energetic SF<sub>5</sub> Carbamates

$\begin{array}{c} \text{H O} \\   \parallel \\ \text{F}_5\text{SN}-\text{C}-\text{OR} \end{array}$			
Compound	R	mp °C	Density (g/cc)
<u>10</u>	-CH <sub>2</sub> C(NO <sub>2</sub> ) <sub>2</sub> CH <sub>3</sub>	92	-
<u>11</u>	-CH <sub>2</sub> CH <sub>2</sub> C(NO <sub>2</sub> ) <sub>3</sub>	67	-
<u>12</u>	-CH <sub>2</sub> CF(NO <sub>2</sub> ) <sub>2</sub>	81	2.04 <sup>a</sup> at -40°C
<u>13</u>	-CH <sub>2</sub> C(NO <sub>2</sub> ) <sub>3</sub>	88	-

<sup>a</sup> X-ray crystal density by Dr. Richard Gilardi, Naval Research Laboratory, Washington, D.C.

by the addition of energetic alcohols (2,2-dinitropropanol, 3,3,3-trinitropropanol, 2-fluoro-2,2-dinitroethanol, and 2,2,2-trinitroethanol) to pentafluorosulfanyl isocyanate<sup>14</sup> (F<sub>5</sub>SN=C=O). It was initially hoped that the carbamates (10 - 13) would be useful as SF<sub>5</sub> explosives in a formulation for a cylinder test. Similar formulations, containing HMX with a binder and FEFO as plasticizer, had been tested and the plan was to replace part of the HMX with an SF<sub>5</sub> explosive.<sup>3</sup> Hence, one of the main criteria in the selection of a candidate SF<sub>5</sub> explosive for the new formulation was that the SF<sub>5</sub> explosive have low solubility (similar to that of HMX) in the plasticizer. Unfortunately, the SF<sub>5</sub> carbamates (10 - 13) were discovered to be too soluble in FEFO to be useful in such a formulation.

Energetic SF<sub>5</sub> dicarbamates, which should be less soluble in FEFO than the mono carbamates, were therefore investigated as candidates for the cylinder test. The dicarbamates (compounds 14 - 17, see Table 5) were prepared by reacting 2 moles of pentafluorosulfanyl isocyanate<sup>14</sup> with each of the following energetic diols: 2,2-dinitropropane-1,3-diol; 2,2,8,8-tetranitro-4,6-dioxanonane-1,9-diol; 3-nitrazo-5,5-dinitrooctane-1,8-diol; and 3,6-dinitrazooctane-1,8-diol. As anticipated, the SF<sub>5</sub> dicarbamates had lower solubilities in FEFO

with compound 17 being the least soluble. A mixture of 0.06 g of 17 and 2.1 g of FEFO at 50-52°C contains an appreciable amount of undissolved 17 and requires heating to 80°C to dissolve all material; holding overnight at 80°C gave no visible signs of decomposition and 17 reprecipitated upon cooling. Thus, based largely on its solubility in FEFO, 17 (impact sensitivity > 320 cm) was selected as the SF<sub>5</sub> explosive for the cylinder test.

A cylinder test has been recently conducted on a formulation containing compound 17, HMX, FEFO, and a binder. The data from the test are currently being analyzed and a definitive interpretation of the results has not yet been made. However, initial indications are that the energy contribution to the formulation by the SF<sub>5</sub> group will be no more than half that from a nitro group.<sup>3</sup>

## CYCLIC POLYNITROALIPHATIC SF<sub>5</sub> EXPLOSIVE

The cyclic SF<sub>5</sub> explosive, 1,3-dinitro-2-imidazolidone-N-pentafluorosulfanylimine (compound 18, Table 6), was prepared as follows: (a) N-pentafluorosulfanyl dichloroimine<sup>15</sup> (F<sub>5</sub>SN=CCl<sub>2</sub>) was treated with ethylenediamine to provide 2-imidazolidone-N-pentafluorosulfanylimine (compound 19); (b) nitration of

Table 5. Energetic SF<sub>5</sub> Dicarbamates

$\begin{array}{c} \text{H} \quad \text{O} \\   \quad    \\ (\text{F}_5\text{SN}-\text{C}-\text{O})_2\text{R} \end{array}$			
Compound	R	mp °C	Density (g/cc)
<u>14</u>	-CH <sub>2</sub> C(NO <sub>2</sub> ) <sub>2</sub> CH <sub>2</sub> -	160	1.99 <sup>a</sup>
<u>15</u>	$\begin{array}{c} -\text{CH}_2\text{C}(\text{NO}_2)_2\text{CH}_2\text{O} \\   \\ \text{CH}_2 \\   \\ -\text{CH}_2\text{C}(\text{NO}_2)_2\text{CH}_2\text{O} \end{array}$	135	-
<u>16</u>	$\begin{array}{c} \text{NO}_2 \\   \\ -\text{CH}_2\text{CH}_2\text{NCH}_2 \\   \\ \text{C}(\text{NO}_2)_2 \\   \\ -\text{CH}_2\text{CH}_2\text{CH}_2 \end{array}$	140	-
<u>17</u>	$\begin{array}{c} \text{NO}_2 \\   \\ -\text{CH}_2\text{CH}_2\text{NCH}_2 \\   \\ -\text{CH}_2\text{CH}_2\text{NCH}_2 \\   \\ \text{NO}_2 \end{array}$	144	1.90 <sup>a</sup>

<sup>a</sup> X-ray crystal density by Dr. Richard Gilardi, Naval Research Laboratory, Washington, D.C.

Table 6. 2-Imidazolidone Derivatives

$\begin{array}{c} \text{X} \\    \\ \text{R}_1-\text{N}-\text{C}-\text{N}-\text{R}_2 \\   \quad   \\ \text{CH}_2-\text{CH}_2 \end{array}$					
Compound	X	R <sub>1</sub>	R <sub>2</sub>	mp °C	Density (g/cc)
<u>19</u>	NSF <sub>5</sub>	H	H	147	-
<u>20</u>	NSF <sub>5</sub>	H	NO <sub>2</sub>	114	2.02 <sup>b</sup>
<u>18</u>	NSF <sub>5</sub>	NO <sub>2</sub>	NO <sub>2</sub>	41	2.03 <sup>c</sup>
<u>21</u>	O	NO <sub>2</sub>	NO <sub>2</sub>	210 <sup>a</sup>	1.79 <sup>b</sup>

<sup>a</sup> Reported in literature

<sup>b</sup> X-ray crystal density by Dr. Richard Gilardi, Naval Research Laboratory, Washington, D.C.

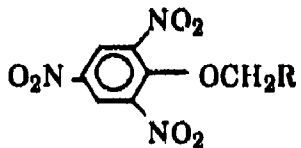
<sup>c</sup> Calculated<sup>11</sup>

19 with nitric-sulfuric acid yielded the mono nitro derivative (compound 20); and (c) 20 with trifluoroacetic anhydride-nitric acid produced the dinitro compound 18. Table 6 shows the large differences in the properties of 18 and the corresponding 1,3-dinitro-2-imidazolidone (compound 21). The melting point of 18 is remarkably lower than that of 21 and the calculated density for 18 is appreciably higher than the density of 21. The x-ray density for 18 has not yet been measured because of a lack of suitable crystals. Crystals of 18 could be grown from carbon tetrachloride but they were clusters, and crystals from benzene proved to be solvates containing 2 molecules of 18 per molecule of benzene.<sup>16</sup> However, from density data for SF<sub>5</sub> nitro compounds, a value of 51.39 cc/mole for the atomic volume of an SF<sub>5</sub> group was calculated<sup>17</sup> and this value was used to predict<sup>11</sup> the density of 18.

**POLYNITROAROMATIC EXPLOSIVE WITH SF<sub>5</sub> SUBSTITUENT. EFFECT OF C-H VS. C-SF<sub>5</sub> ON IMPACT SENSITIVITY.**

In Table 7, the properties of several picryl ethers (compounds **22** - **24**) are compared with those of picryl-(2-pentafluorothioethyl) ether (compound **25**). It was hoped that picryl-(2-nitroethyl)ether (R = -CH<sub>2</sub>NO<sub>2</sub>) could be included in the series but this compound has not been reported in the literature nor could it be prepared by the standard method from picryl chloride and 2-nitroethanol. The data in Table 7 again show the tendency of the SF<sub>5</sub> group to lower the melting points and increase the densities of nitro explosives. However, the main objective for the study of the picryl ether series was to obtain more data concerning the effect of the SF<sub>5</sub> group on the sensitivity of nitro explosives, especially the effect of replacing H with SF<sub>5</sub> (compounds **24** and **25**). Even though the SF<sub>5</sub> group will make **25** more energetic than **24**, it was anticipated that compound **25** could still have the lesser sensitivity. Unfortunately, a comparison of the sensitivities of **24** and **25** could not be made because both had impact sensitivities greater than the limits (320 cm) of the impact machine. Thus other series, containing more sensitive

Table 7. Picryl Ethers

				
Compound	R	mp °C	Density (g/cc)	H <sub>50</sub> % (cm)
<b>22</b>	-CH <sub>2</sub> ONO <sub>2</sub>	104 <sup>b</sup>	1.68 <sup>b</sup>	-
<b>23</b>	-CF <sub>3</sub>	104 <sup>b</sup>	1.78 <sup>c</sup>	-
<b>24</b>	-CH <sub>3</sub>	78 <sup>b</sup>	1.52 <sup>c</sup>	> 320
<b>25</b>	-CH <sub>2</sub> SF <sub>5</sub> <sup>a</sup>	78	1.83 <sup>c</sup>	> 320

<sup>a</sup> Compound **25** has good thermal stability (0.06 cc/g for 48 hr at 100°C)

<sup>b</sup> Reported in literature

<sup>c</sup> By gas pycnometer, Dr. Michael Chaykovsky, NSWC

materials, will be investigated to better determine the effect of SF<sub>5</sub> vs. H on sensitivity. Target compounds for one of these series include (NO<sub>2</sub>)<sub>3</sub>CCH<sub>2</sub>N(NO<sub>2</sub>)CH<sub>2</sub>CH<sub>2</sub>SF<sub>5</sub> and (NO<sub>2</sub>)<sub>3</sub>CCH<sub>2</sub>N(NO<sub>2</sub>)CH<sub>2</sub>CH<sub>3</sub>.

**IMPACT SENSITIVITY OF AN ENERGETIC SF<sub>5</sub> CARBAMATE. EFFECT OF N-H VS. N-SF<sub>5</sub> ON IMPACT SENSITIVITY.**

In Table 8, properties of (N-pentafluoro-sulfanyl)-3,3,3-trinitropropyl carbamate (compound **11**, see also Table 6) are compared with those of 3,3,3-trinitropropyl carbamate (compound **26**). The lower melting point of **11** relative to **26** is consistent with earlier observations that the SF<sub>5</sub> group tends to produce lower melting compounds. However, the most striking property of **11** is its greatly lowered impact sensitivity relative to **26**, providing additional support for the hypothesis that the SF<sub>5</sub> group will reduce the sensitivity of nitro explosives.

Table 8. Properties of Trinitropropyl Carbamates

			
Compound	R	H <sub>50</sub> % (cm)	mp °C
<b>11</b>	SF <sub>5</sub>	117 <sup>b</sup>	67
<b>26<sup>a</sup></b>	H	44 <sup>b</sup>	82

<sup>a</sup> Prepared by treating trinitropropyl chloroformate (from triphosgene<sup>16</sup> and 3,3,3-trinitropropanol) with ammonia

<sup>b</sup> RDX = 28

**SUMMARY AND CONCLUSIONS**

Several polynitro SF<sub>5</sub> model compounds were prepared and one was selected for in-depth physical evaluation. The SF<sub>5</sub> compound exhibited high density and good thermal stability but most significantly showed greatly reduced impact sensitivity relative to very similar compounds that contain no SF<sub>5</sub> group.

Detonation calorimetry for the model compound showed that the only fluorine containing detonation product was HF, a desirable result since conversion of S-F to HF in the detonation is exothermic (comparison of bond energies). The main sulfur species among the detonation products was COS, another beneficial result since sulfur did not consume any oxygen needed for hydrocarbon combustion. A number of energetic SF<sub>5</sub> carbamates and dicarbamates were prepared and representatives from this group were found to have crystal densities ranging from 1.90 to 2.04 g/cc. Cyclic SF<sub>5</sub> nitramines were also found to have densities greater than 2.0 g/cc. These initial results support the hypothesis that the SF<sub>5</sub> group can provide nitro explosives with improved properties (increased density, decreased sensitivity, good thermal stability) and produce energy in the detonation.

Also during the course of this investigation, it was observed that the SF<sub>5</sub> group exhibits a strong tendency to lower the melting points of nitro explosives. Therefore the SF<sub>5</sub> group should also prove advantageous for the preparation of low melting energetic plasticizers, an area that is currently being explored.

## ACKNOWLEDGEMENTS

This work was supported by the NSWC Independent Research Program. Gratitude is extended to Drs. H. G. Adolph and D. A. Cichra of NSWC for their support of this work and for helpful discussions.

## REFERENCES

1. Witucki, E. F. and Frankel, M. B., *Energetic Aliphatic Sulfur Pentafluoride Derivatives*, UCRL-13809, Rockwell International, Rocketdyne Division, Canoga Park, CA, Apr 1978.
2. Witucki, E. F. and Frankel, M. B., "Preparation and Properties of 2-Fluoro-2,2-dinitroethyl Pentafluorothioacetate," *Journal of Chemical and Engineering Data*, Vol. 24, No. 4, 1979, p. 382.
3. Adolph, H. G. and Cichra, D. A., Naval Surface Warfare Center, Silver Spring, MD, private communications, 1987-1988.
4. Coffman, D. D. and Tullock, C. W., "Carbonylic Compounds Containing the SF<sub>5</sub> Function," U.S. Patent No. 3102903, 3 Sep 1963. The pentafluorothioacetyl chloride for this investigation was supplied by Dr. M. B. Frankel of Rockwell International, Rocketdyne Division.
5. Wessel J.; Kleeman, G.; and Seppelt, K., "Sulfuranonium-Ionen, R-SF<sub>4</sub><sup>+</sup>, Darstellung, Nachweis and Stabilität," *Chemische Berichte*, Vol. 116, 1983, p. 2399.
6. Sitzmann, M. E. and Gilligan, W. H., "Novel Route from Thiocarbamate to Isocyanate: 2,2,2-Trinitroethyl Isocyanate," *Journal of Organic Chemistry*, Vol. 50, No. 26, 1985, p. 5879.
7. Gilligan, W. H. and Sitzmann, M. E., "Derivatives of a Weakly Basic Amine: N, N-Bis(2-fluoro-2,2-dinitroethyl)amine," *Journal of Chemical and Engineering Data*, Vol. 27, No. 1, 1982, p. 97.
8. Sitzmann, M. E. and Gilligan, W. H., "Novel Trialkoxymethyl Disulfides via Nucleophilic Addition to Thionocarbonates: Tris(2-fluoro-2,2-dinitroethoxy) methyl Trichloromethyl Disulfide and Related Products," *Journal of Organic Chemistry*, Vol. 48, No. 19, 1983, p. 3354.
9. Gilligan, W. H. and Sitzmann, M. E., "Synthesis of Mixed Polynitroorthocarbonates and Related Derivatives," *Journal of Energetic Materials*, Vol. 1, 1983, p. 95.
10. Kamlet, M. J. and Adolph, H. G., "Some Comments Regarding the Sensitivities, Thermal Stabilities, and Explosive Performance Characteristics of Fluorodinitromethyl Compounds," *Proceedings of Seventh Symposium (International) on Detonation*, U.S. Naval Academy, Annapolis, MD, 16-19 Jun 1981, pp. 84-92.
11. Cichra, D. A.; Holden, J. R.; and Dickinson, C., *Estimation of "Normal" Densities of Explosive Compounds from Empirical Atomic Volumes*, Naval Surface Warfare Center, NSWC TR 79-273, Silver Spring, MD, Feb 1980.

12. Ornellas, D. L., *Calorimetric Determination of the Heat and Products of Detonation for Explosives: October 1981 to April 1982*, UCRL-52821, Lawrence Livermore National Laboratory, Livermore, CA, Apr 1982.
13. Ornellas, D. L., "Calorimetric Determination of the Heat and Products of Detonation of an Unusual CHNOSF Explosive," *Propellants, Explosives and Pyrotechnics*, Vol. 14, 1989, p. 122.
14. Thrasher, J. S.; Howell, J. L.; and Clifford, A. F., "Reactions of Pentafluorosulfanyl Isocyanate and Isothiocyanate," *Chemische Berichte*, Vol. 117, 1984, p. 1707. The pentafluorosulfanyl isocyanate for this investigation was supplied by Dr. J. S. Thrasher, University of Alabama, Tuscaloosa, AL.
15. Thrasher, J. S. and Clifford, A. F., "Preparation and Characterization of N-Pentafluorosulfanylamine Derivatives," *Journal of Fluorine Chemistry*, Vol. 19, 1982, p. 411. The pentafluorosulfanyl-dichloroimine for this investigation was supplied by Dr. J. S. Thrasher, University of Alabama, Tuscaloosa, AL.
16. Gilardi, R., Naval Research Laboratory, Washington, D.C., private communication, 1988.
17. Holden, J. R., Naval Surface Warfare Center, Silver Spring, MD, private communication, 1988.
18. Eckert, H. and Forster, B., "Triphosgene, a Crystalline Phosgene Substitute," *Angewandte Chemie, International Edition in English*, Vol. 26, No. 9, 1987, p. 894.

# CHEMISTRY OF DETONATION SOOT: DIAMONDS, GRAPHITE, AND VOLATILES

N. Roy Greiner  
Los Alamos National Laboratory  
Chemical and Laser Sciences Division  
Los Alamos, New Mexico 87545

and

Robert Hermes  
Los Alamos National Laboratory  
Materials Science and Technology Division  
Los Alamos, New Mexico 87545

*Detonation of a number of pure and composite explosives in tanks filled with Ar gas have yielded solid carbonaceous products (soots) with a rich chemistry. Although there are similarities, the soot from each explosive has some uniqueness. The soots are composed of very small solid particles of graphite and often diamond, having characteristic dimensions of about 20 atomic diameters. This small size and the presence of a 25 wt % heat-labile component implies an important surface chemistry for these soots. The heat-labile compounds may give clues about the structure, the surface chemistry, and the mechanism of soot formation.*

## INTRODUCTION

Detailed knowledge of the chemical kinetics and equilibria of detonation have long been a desired, but elusive, goal. One focus of this chemistry is the coagulation of carbonaceous solid (soot) from carbon initially present as the skeletal atoms of small organic CHNO molecules. Current detonation models<sup>1</sup> predict that the oxygen reacts first to form H<sub>2</sub>O from the available hydrogen, then the remainder reacts with carbon to form CO<sub>2</sub>. Any carbon left over forms the soot. (The nitrogen forms N<sub>2</sub>.) The nature of this soot and the details of its formation have been the subject of much discussion.<sup>2</sup> The literature on non-detonation soots is extensive, and numerous soot types have been described.<sup>3-5</sup> However, reports on the chemical composition and structure of detonation soot are just beginning to appear.<sup>6,7</sup>

The characteristic dimensions of the basic soot particles observed,<sup>8</sup> both diamond and

graphite, are on the order of 20 interatomic bond lengths. These are smaller than the maximum size permitted by an agglomeration process limited only by diffusion in the dense detonation products.<sup>8</sup> The graphite particles are not balls of small polynuclear aromatic hydrocarbon (PAH) crystals, as in hydrocarbon combustion soot.<sup>3</sup> Instead, they are ribbons resembling carbon blacks graphitized at high temperature.<sup>3,5,9</sup> Because of this similarity to carbon blacks, it seems plausible that the growth processes may be similar. Furthermore, a rapidly quenched mixture containing these graphite ribbons might scavenge soot-growth intermediates<sup>10</sup> and other chemical species in the detonating explosive, including reaction intermediates and stable products which might give clues about the soot-formation chemistry. These considerations led us to investigate possible heat-labile surface components of the soots.

Earlier work on detonation products established that the soots contain some nitrogen,

hydrogen, and probably oxygen, in addition to the largest component, carbon.<sup>11,12</sup> From detonation calorimeter data one could deduce a positive heat of formation for the soot.<sup>12</sup> The bonding of the noncarbon atoms in the soot had not been established. Here we will review briefly pertinent previous data, report further work on soot diamond, and present new findings on a large variety of thermally labile molecules found in the soot. These results suggest possible chemical structures in the detonation soot, give support to a restricted diffusion model of solid carbonaceous cluster formation, and suggest a way to estimate the heat of formation of the soot from its components.

## EXPERIMENTAL

Some of the soot samples in this study came from explosive charges fired at the Fraunhofer-Institut für Chemische Technologie (ICT) in the Federal Republic of Germany, and others came from the Los Alamos National Laboratory.

The following came from ICT: Samples #27/30 and #28/30 were pure cast TNT. Composite explosives were cast from molten TNT mixed with 59.5 wt % powdered cyclotrimethylene-trinitramine (RDX) to make samples #27 and #34/30; 50 wt % powdered triaminotrinitrobenzene (TATB) to make sample #60; 50 wt % powdered nitroguanidine (NIGU) to make samples #63, #55/20, and #10/41; and 50 wt % powdered ammonium nitrate (AN) to make sample #36.

The charges were in the form of (nominally) 300-g cylinders 50 mm diam x 100 mm long. They were boosted by a 15-g pellet of RDX and were fired in a 1.5 m<sup>3</sup> tank filled with 1 atmosphere of Ar gas, except for sample #10/41, which was fired in vacuum. A few minutes after firing, the Ar was replaced with air and the soot was swept from the tank into sample bottles. Samples were dried at 105°C to constant weight. Elemental analyses<sup>11</sup> and initial results<sup>12</sup> from samples #27, #60, and #63 have been published.

The following samples were from Los Alamos: Sample #H1057 was pure TNT pressed to a density of 1.470 g/cm<sup>3</sup>, sample #H1017 was pure TNT pressed to a density of

1.630 g/cm<sup>3</sup>, sample #H1058 was pure TATB pressed to near crystal density, and sample #H1059 was pure RDX pressed to near crystal density. These charges were cylindrical, 50 mm diam x 100 mm long, and were boosted with a 15-g charge of RDX. The Los Alamos charges were fired in a steel sphere 6 feet (1.83 m) in diameter, with a volume of 3.0 m<sup>3</sup> filled with 760 torr (1 atm) of Ar gas. The soots were collected and dried as described above.

The micromorphologies of the soots were recorded by transmission electron microscopy (TEM), and crystal structures were determined by transmission electron microscope electron diffraction (TEMED).<sup>6</sup> The diamonds were isolated by oxidative removal of the other soot components with HNO<sub>3</sub> and HClO<sub>4</sub>.<sup>6</sup> Diamond in the residue was identified by x-ray diffraction (XRD) powder patterns. Measurements with an x-ray diffractometer determined the diameters of the recovered diamonds and confirmed the diamond lattice spacings. Thermally labile components in the soot were weighed by thermogravimetric analysis (TGA) and were identified with direct insertion probe (DIP) mass spectrometry.

## ANALYSIS OF RAW SOOTS

TEM examination of samples #27, #60, and #63 has shown that the soots are composed of graphite ribbons having a smallest dimension of 3 nm and diamonds having diameters of 3-7 nm (Figure 1 and Reference 6). The interplanar spacings measured by TEMED from a group of the diamonds in sample #27 agree well with the spacings of bulk diamond (Table 1 and Reference 6).

The detonation graphite appears as partially graphitized (turbostratic structure by TEMED) ribbons a few nm thick, not as aggregated smaller particles or crystals. This observation contrasts with the reported structures of graphitic soots from hydrocarbon flames, which are typically spheres 10-500 nm in diameter, composed of many small graphitic crystallites less than about 1 nm thick.<sup>3</sup> The detonation diamond appears to be almost perfect single crystals, rather than aggregates of smaller crystals. We have found no evidence for "rolled chickenwire" structures of the buckminsterfullerene family.<sup>13</sup> Furthermore, the sizes of



*Figure 1. TEM Micrograph of the Soot from Sample #27 (TNT/RDX). D denotes diamond structures and T, the turbostratic graphite ribbons. The bar scale shows 10 nm which is about 70 interatomic covalent bond lengths in diamond or graphite.*

Table 1. Diamond Structure

	TNT/ RDX #27	TNT/ TATB #60	TNT/ NIGU #63
Wt % in soot	16	24	24
Diameters, nm			
TEM image	7	3	5
XRD, diffractometer	4.5	2.8	2.8
Spacings (TEMED), nm			
(111)	0.2058		
(220)	0.1266		
(311)	0.1075		
(400)	0.0884		
(440)	0.0636		
Spacings (XRD Diffractometer), nm			
(111)	0.206	0.206	0.206
(220)	0.126	0.126	0.126
(311)	0.108	0.108	0.108

the diamond and graphite particles observed in these detonations appear to be too small for unrestricted growth by aggregation.

A model for growth of detonation soot by diffusion-controlled aggregation has been developed by Shaw and Johnson (SJ).<sup>2</sup> We can apply the SJ model to these detonations with the aid of a hydrodynamic model for the expansion of the detonation products.<sup>14</sup> A large portion of the explosive charge is maintained near the detonation density for about  $3 \times 10^{-6}$  s, whereas the characteristic time for the unrestricted aggregation of solid carbon in the SJ model is  $2 \times 10^{-12}$  s. The growth time divided by the characteristic time gives the number of atoms in the most probable particle size, in our case  $1.5 \times 10^6$  atoms. A crystalline diamond sphere this size would be 26 nm in diameter, whereas we see a 7-nm maximum, too small in volume by a factor of 50.

The differences suggest that (1) particle growth has additional restrictions and (2) either aggregation progresses in increments closer in size to atoms than to small crystals or the final aggregates are annealed well enough to obscure component crystallites, but, in the case of graphite, not well enough to accomplish extensive graphitization. The small size of the diamonds

and the graphite ribbons raise the possibility that surface chemistry may influence their relative stabilities,<sup>15</sup> their heats of formation, and possibly their growth mechanism.

Gouy-balance measurements on the raw soot show evidence of unpaired electrons, a common feature of finely divided solid carbons. Elemental analysis of the dry soots shows the presence of a few atom % each of H, N, and O atoms in addition to C atoms, and TGA analysis shows that about 25% of the soot is heat-labile (Figure 2). The section below on volatiles lists some of the probable heat-labile components, which give an idea of the functional group chemistry of the soots.

## DIAMOND RESIDUES

Diamond structures were found in the TEM images,<sup>6</sup> and the presence of diamond was confirmed by strong x-ray powder patterns in the oxidation residues of samples #27, #60, and #63. The oxidation residue from sample #34/30 (60% RDX/40% TNT, the same as sample #27) also shows a strong powder pattern of 5-nm-diam diamond. However, the soots from the pure explosives from both ICT and Los Alamos yield only small amounts of residue after oxidation, and the residues show only weak diamond x-ray powder patterns. This result agrees with Soviet results, where they find that a 50/50 mixture of TNT and RDX produces more diamond than pure TNT.<sup>7</sup>

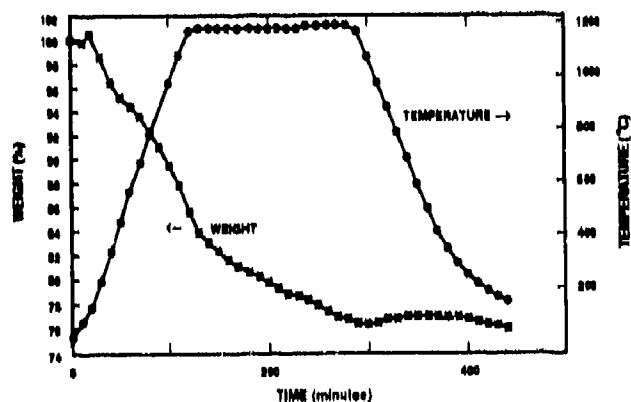


Figure 2. TGA of Raw Soot Sample #27/30 (Pure TNT) in 1 atm of HE Gas. There is about 5% weight loss at 350°C, the upper limit of the dip gas analyses, and about 25% at the termination of the run at 1200°C after 300 min.

The diameters of the diamonds in the oxidation residues showing strong diamond powder patterns were determined by the widths of their diffraction lines measured on an x-ray diffractometer and, in all three cases, they are nearly equal to the diameter of the diamonds observed in the TEM images (Table 1), implying that the diamonds are single crystals.

No measurable residue was obtained from sample #10/41 (TNT/NIGU), which was fired in a vacuum. This result can be compared to that of sample #63 (also TNT/NIGU, but fired in 1 atm of Ar), where diamond residue is 24 wt % of the soot. Sample #10/41 obviously underwent reshock at the vessel wall; evidently, the diamonds do not survive this process. The residue from sample #36 (TNT/AN) also contained no diamonds.

Auger/ESCA analysis shows that the diamond residue from sample #63 has some O and N atoms, which are probably on the surface because they are largely removed by surface sputtering.

## VOLATILES

DIP mass spectrometry of raw soots (with the temperature ramped at 20°C/min up to 350°C) typically shows the sequence H<sub>2</sub>O, CO, CO<sub>2</sub>, NH<sub>3</sub>, HNCO, HCN, and HCl as major volatiles. Patterns attributable to a variety of organics generally start at ca. 150°C. A prominent peak at 60 atomic mass units (AMU) suggests the presence of urea. In the case of sample #10/41 (TNT/NIGU), the pattern of (undecomposed) NIGU is present. Sample #55/20 (TNT/NIGU) releases a short burst of gas at about 240°C that fits the empirical formula (HNO)<sub>x</sub>. The DIP results from sample #27/30 (pure TNT) show clearly a number of peaks consistent with a sequence of fused aromatic ring compounds, similar to soot precursors in other chemical systems,<sup>4</sup> but here with occasional -CN group substitution (Figure 3). Identifications were aided by comparison with known samples run in the DIP and with published spectra.<sup>16,17</sup>

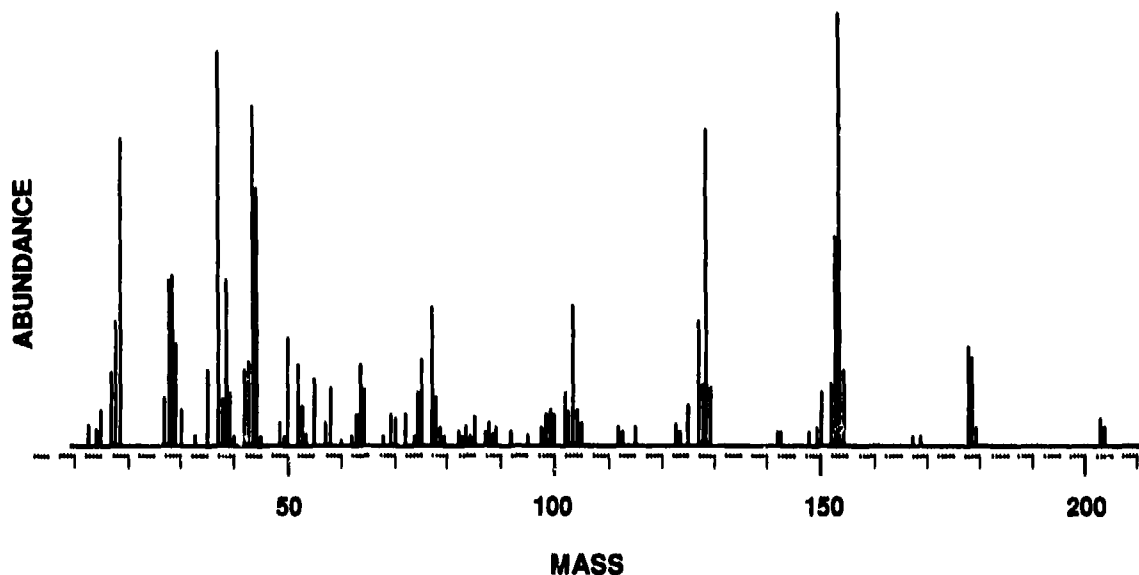


Figure 3. DIP Mass Spectrum from Sample #27/30 (Pure TNT). The time evolution of the major peaks seen in this spectrum (AMU of principal peaks in parentheses) are consistent with the presence of NH<sub>3</sub> (17,16), H<sub>2</sub>O (18), HCN (27), CO (28), NO (30), HCl (36), HNCO (43), CO<sub>2</sub> (44), Benzonitrile (103), Naphthalene/Benzenedicarbonitrile (128), Acenaphthalene/Biphenylene (152), Naphthalenecarbonitrile (153), Phenanthrene/Anthracene (178), Pyrene/Fluoranthene (202), and Anthracenecarbonitrile (203).

Diamond isolated from sample #83 gives off H<sub>2</sub>O at low temperatures and a CO<sub>2</sub>-CO mixture starting at ca. 300°C, which suggests that the diamond recovered by acid oxidation may have a carboxylated surface. No significant nitrogen-containing species were driven off.

## CONCLUSIONS

These results show that the soot has a rich chemistry involving heteroatoms. Heat-labile components, containing a variety of chemical species, have been found in quantities comparable to the number of surface atoms on the solids. The results from the possible soot precursors suggest that -CN groups may be present as surface terminators.

These initial investigations suggest a way to characterize the chemical structure of detonation soot, which might permit estimates of the heat of soot formation and give important clues about possible mechanisms of soot formation. If the various methods outlined above can be made sufficiently quantitative, bounds can be put on the heat of soot formation. The interiors of the diamonds are crystallographically the same as bulk diamond, the graphite appears to be a recognized form, and the volatiles are all known molecules. The principal unknowns are the surface contributions of the diamond and graphite, which could be considerable because of the large specific areas. Further challenges are understanding the kinetics of the soot formation and the binding of the adsorbed species to the surfaces.

## ACKNOWLEDGEMENTS

It is a pleasure to acknowledge the assistance of Larry Stretz and Carl Vecere with firing the charges, John O'Rourke and Brad Roof with the x-ray diffraction measurements, Yvonne Rogers and Dorothy Hoard with the oxidations, Doug Farr with the Auger/ESCA analyses, Al Sattleberger with the Gouy-balance measurements, Liz Foltyn with the TGA, and Dale Spall with the analysis of the soot volatiles. Chuck Mader and J. D. Johnson offered much support, shared many insights, and provided information on the Soviet work. We thank Fred Volk and the Fraunhofer-

Institut für Chemische Technologie for samples of detonation soot.

## REFERENCES

1. Mader, C. L., *Numerical Modeling of Detonations*, University of California Press, Berkeley, California, 1979.
2. Shaw, M. S. and Johnson, J. D., "Carbon Clustering in Detonations," *Journal of Applied Physics*, Vol. 62, 1987, pp. 2080-2085.
3. Lahayo, J. and Prado, G., "Morphology and Internal Structure of Soot and Carbon Blacks," *Particulate Carbon Formation During Combustion*, Siegl, D. C. and Smith, G. W., Eds., Plenum Press, New York, 1981, pp. 33-55.
4. Bittner, J. D. and Howard, J. B., "Pre-Particle Chemistry in Soot Formation," in *Particulate Carbon Formation During Combustion*, Siegl, D. C. and Smith, G. W., Eds., Plenum Press, New York, 1981, pp. 109-142.
5. Jenkins, G. M. and Kawamura, K., *Polymeric Carbons-Carbon Fibre, Glass and Char*, Cambridge University Press, Cambridge, England, 1976, pp. 70-71.
6. Greiner, N. R.; Phillips, D. S.; Johnson, J. D.; and Volk, F., "Diamonds in Detonation Soot," *Nature*, Vol. 333, 1988, pp. 440-442.
7. Llamkin, A. I.; Petrov, E. A.; Ershov, A. P.; Sakovich, G. V.; Staver, A. M.; and Titov, V. M., "Production of Diamonds from Explosives," *Doklady Akademii Nauk USSR*, Vol. 302, No. 3, 1988, pp. 611-613 (Russian).
8. Greiner, N. R., "Diamonds in the Chemical Products of Detonation," *Proceedings of the Fuel Chemistry Division of the American Chemical Society*, Dallas, Texas, 9-14 Apr 1989 (in press).
9. Oberlin, A.; Bonnamy, S.; Bourrat, X.; Monthieux, M.; and Rouzaud, J. N., "Electron Microscopic Observations on Carbonization and Graphitization," *Petroleum-Derived Carbons*, ACS Symposium Series, Vol. 303, American

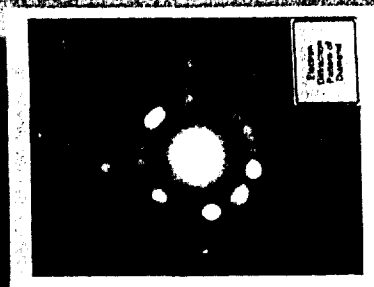
- Chemical Society, Washington, DC, 1986, pp. 85-98.
10. Lee, M. L. and Bartle, K. D., "The Chemical Analysis of Particulate Carbon," *Particulate Carbon Formation During Combustion*, Siegl, D. C. and Smith, G. S., Eds., Plenum Press, New York, 1981, pp. 91-106.
  11. Volk, F.; Bathelt, H.; Schedlbauer, F.; and Wagner, J., "Detonation Products of Insensitive Cast High Explosives," *Eighth Symposium (International) on Detonation*, Albuquerque, New Mexico, 1985, pp. 577-586.
  12. Ornellas, D. L., *Calorimetric Determination of Heat and Products of Detonation for Explosives: October 1961 to April 1982*, UCRL-52821, Lawrence Livermore National Laboratory, Livermore, California, Apr 1982.
  13. Kroto, H., "Space, Stars,  $C_{60}$ , and Soot," *Science*, Vol. 242, 1988, pp. 1139-1145.
  14. Greiner, N. R., "Freely Expanding Detonation Products: Scaling of Rate Processes," in *19th International Annual Conference of ICT--Combustion and Detonation Phenomena*, Fraunhofer Institut Für Chemische Technologie, Karlsruhe, Federal Republic of Germany, 29 Jun - 1 Jul 1988, pp. 36-1 to 36-13.
  15. Badziag, P.; Verwoerd, W. S.; Ellis, W. P.; and Greiner, N. R., "Nanometre-Sized Diamonds Are More Stable than Graphite," *Nature*, Vol. 343, 1990, pp. 244-245.
  16. Belson, D. J. and Strachan, A. N., "Preparation and Properties of Isocyanic Acid," *Chemical Society Reviews*, Vol. 11, 1982, pp. 41-56.
  17. Bogan, D. J. and Hand, C. W., "Mass Spectrum of Isocyanic Acid," *Journal of Physical Chemistry*, Vol. 75, 1971, pp. 1532-1536.

# CHEMISTRY OF DETONATION SOOT: DIAMONDS, GRAPHITE, AND VOLATILES - PART I

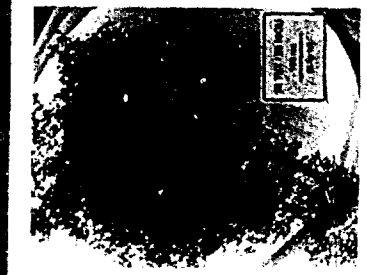
Sponsors: U.S. DOE and U.S. Army  
N. Roy Greiner, Chemical and Laser Sciences Division  
Robert Hermes, Materials Science and Technology Division



## ELECTRON MICROSCOPY SHOWS COLLOIDAL STRUCTURE OF DETONATION SOOT



## ELECTRON DIFFRACTION IDENTIFIES CRYSTAL STRUCTURES



## CHEMISTRY OF DETONATION SOOT

### COLLABORATORS

Fred Volk  
J. D. Johnson  
Dave Phillips  
Yvonne Rogers  
Dorothy Hoard  
Brad Roof  
John O'Rourke  
Dale Spall  
Robert Hermes

Doug Farr  
Dave Schiferl  
Friedeman Freund  
David Blake  
Dieter Heymann  
Liz Foltyn  
Carl Vecere  
Joe Sandoval

Los Alamos  
CL-80-776

## WHY STUDY CARBON?

### Questions:

- Isolated explosive molecules contain only a few carbon atoms
- These must polymerize to form solid carbon (soot)
- Polymerization may tie up energy and release it slowly

### Benefits:

- Better understanding
- Better modeling
- Better explosives designs

Los Alamos  
CL-80-808

## SUMMARY OF RESULTS

- Detonation soot can contain graphite, diamond, and a variety of volatiles
- Diamonds are 3 to 4.5 nm (20 to 30 atoms) in diameter, 10<sup>4</sup> atoms/crystal -- *macromolecules!*
- Graphite ribbons are 2 to 3 nm thick
- Volatiles can be 30 wt% of the soot
- 30% of the diamond or graphite atoms are surface atoms
- Pure explosives produce less diamond than TNT composites
- Each soot has a unique volatile "fingerprint"

Los Alamos  
CL-80-776A

## BIBLIOGRAPHY OF RECENT PAPERS

1. Greiner, N. R., Phillips, D. S., Johnson, J. D., and Volk, F., "Diamonds in Detonation Soot," Nature, Vol. 333, 1988, pp. 440-442.
2. Liankin, A. I., Petrov, E. A., Ershov, A. P., Sakovich, G. V., Staver, A. M., and Tilor, V. M., "Production of Diamonds from Explosives," Doklady Akademi Nauk USSR, Vol. 302, No. 3, 1988, pp. 611-613 (Russian).
3. Tilor, V. M., Anisichkin, V. F., Mal'kov, I. Yu., "Synthesis of Ultrafine Diamonds in Detonation Waves," Ninth Symposium (International) on Detonation, Preprints, Vol. 1, 1989, pp. 175-183.
4. Johnson, J. D., "Carbon in Detonations," ibid., pp. 184-189.
5. Blake, D., Freund, F., Bauch, T., Chang, S., Tleless, A., and Greiner, N. R., "A Comparison of Alkane Diamond with Diamond from Detonation Soot," Proc. of the Lunar and Planetary Science Conference, Vol. 19, 1988, pp. 94-95.
6. Greiner, N. R., "Diamonds in the Chemical Products of Detonation," in Proceedings of the Fuel Chemistry Division of the American Chemical Society, Dallas, Texas, April 9-14, 1989 (in press), pp. 527-534.
7. Badzige, P., Verwoerd, W. S., Ellis, W. P., and Greiner, N. R., "Binding Energies of Tetrahedral Versus Hexagonal Hydrocarbon Molecular Clusters," (in preparation).
8. Shaw, M. S., and Johnson, J. D., "Carbon Clustering in Detonations," Journal of Applied Physics, Vol. 62, 1987, pp. 2080-2085.

Los Alamos  
CL-80-782A

John Sandoval Emission Containment Ball



Carl Vecere (left) and Joe Sandoval position chamber



### SOURCES OF DETONATION SOOTS

FRAUNHOFER-INSTITUT (ICT)

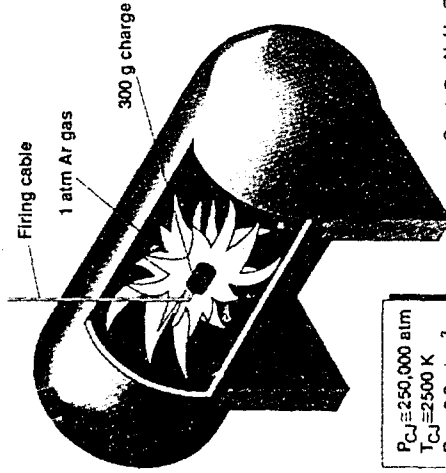
LOS ALAMOS

TNT (ICT)  
TNT (DIEHL)  
Comp B (DIEHL)  
60RDX/40TNT  
50NIGU/50TNT  
50TATB/50TNT

TNT (d = 1.63 g/cm<sup>3</sup>)  
TNT (d = 1.47 g/cm<sup>3</sup>)  
RDX  
TATB  
...  
HMX  
HNS  
NIGU  
NTO  
Comp B

Los Alamos  
CLS-88-4008

### Schießkessel (Fraunhofer Institut)

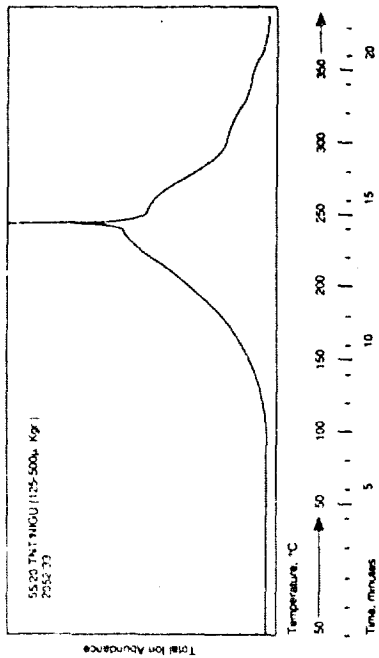


$P_{CJ} \approx 250,000 \text{ atm}$   
 $T_{CJ} \approx 2500 \text{ K}$   
 $P_{CJ} \approx 2.3 \text{ g/cm}^3$

Soot:  $C_{10}N_4H_{10}O_7$

Los Alamos  
CLS-88-4008

Direct insertion probe (DIP)  
mass spectrometry  
generates chemical  
fingerprint of soot  
volatiles



## SOOT VOLATILES

- Contribute to Thermochemistry
- Contain Heteroatoms: N, H, and O
- May Contain Remnants of Cluster Growth

### DIRECT-INSERTION-PROBE MASS SPECTROMETRY SHOWS

#### PERMANENT GASES:

$H_2O$ ,  $NH_3$ ,  $CO$ ,  $CO_2$ ,  $HCN$ ,  $C_2H_4$

#### ORGANICS:

$H-N-C=O$

$H_2N$

$H_2N$

$C=O$

#### SUBSTITUTIONS:

$(-C_2Cl)_n$

$(-NH_2)_n$

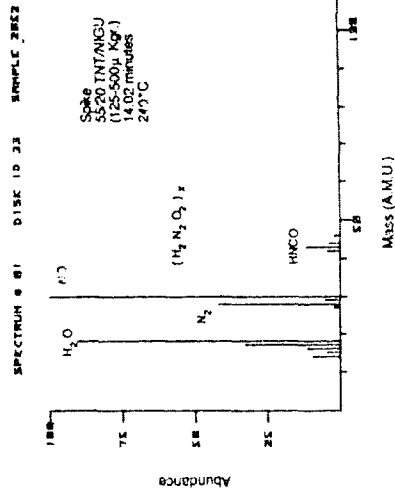
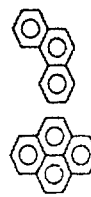
$(-CN)_n$

$(-CH_3)_n$

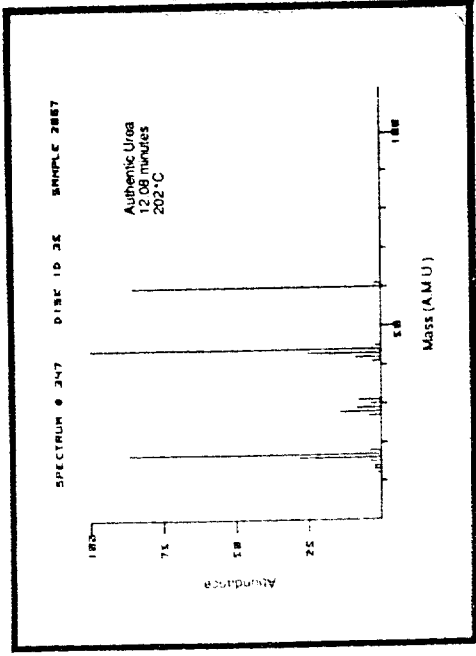
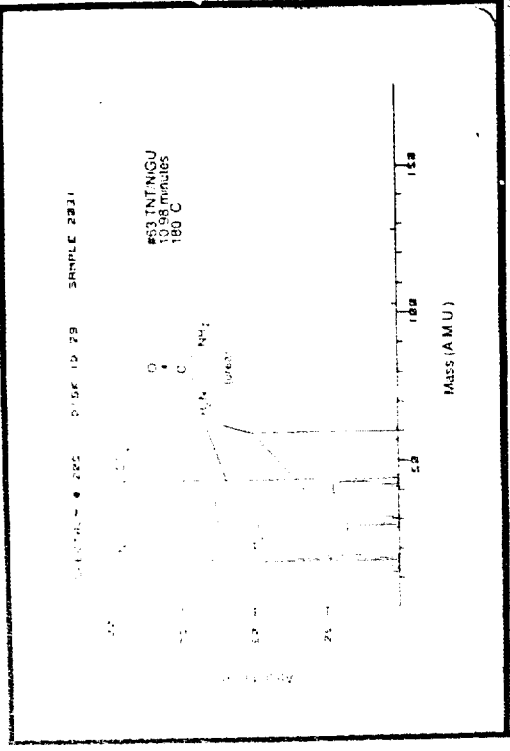
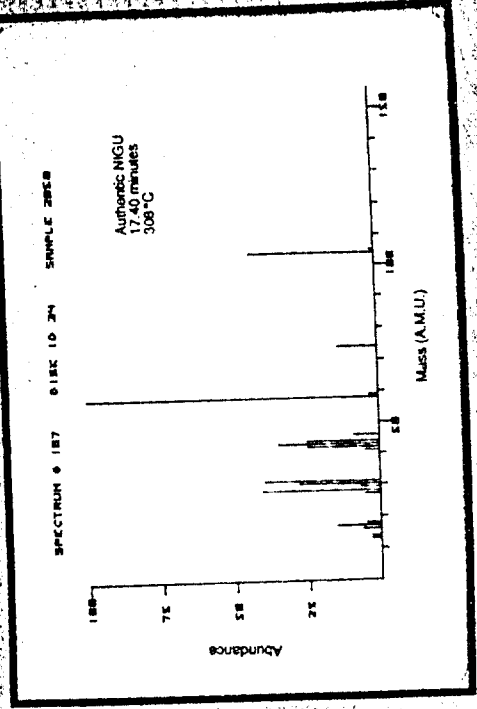
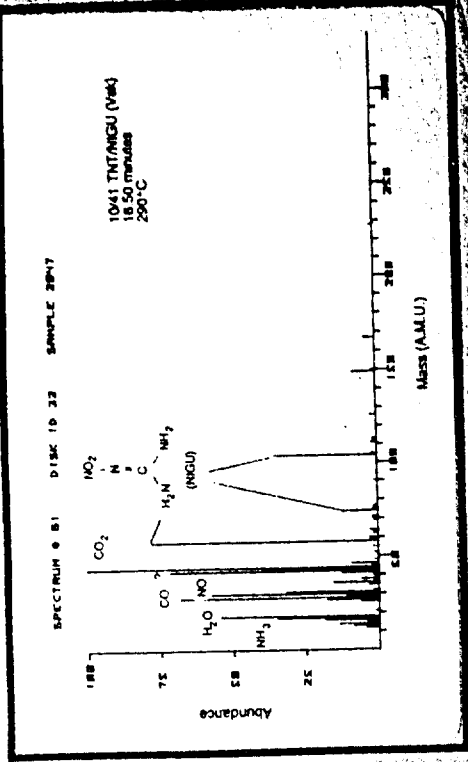
ALKANES:  $(C_{15}-C_{18}, \text{etc.})$  Proto-diamond (?)

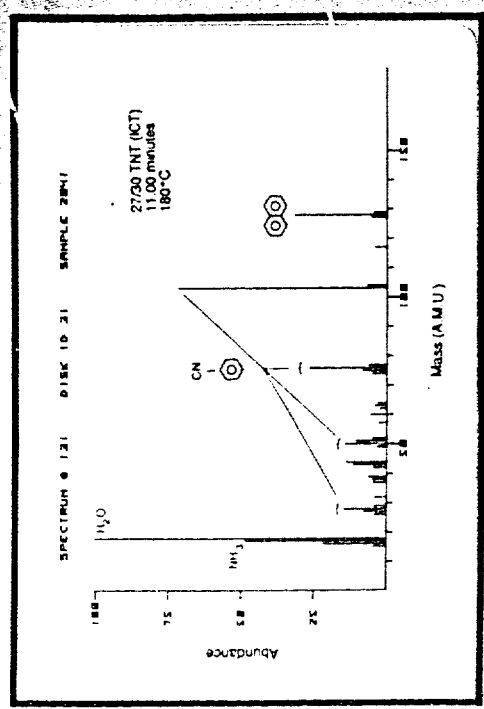
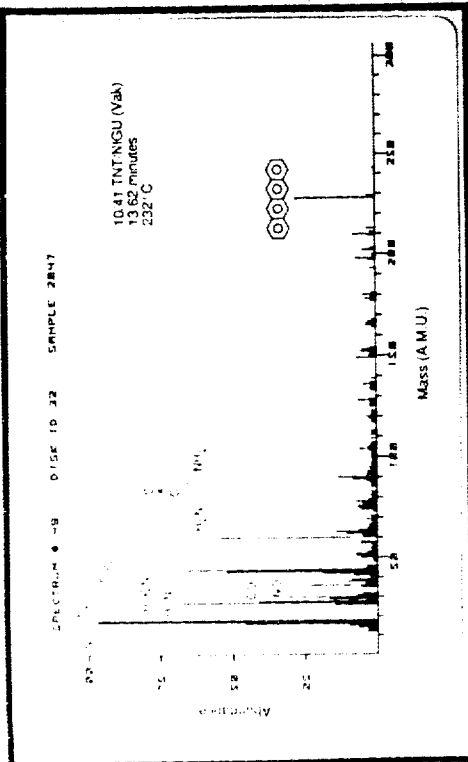
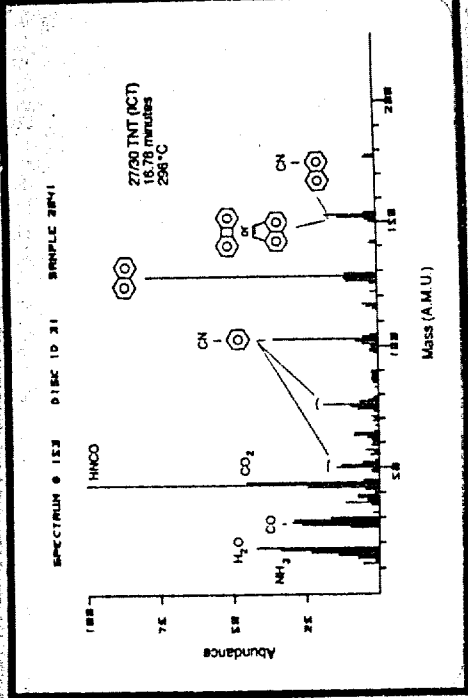
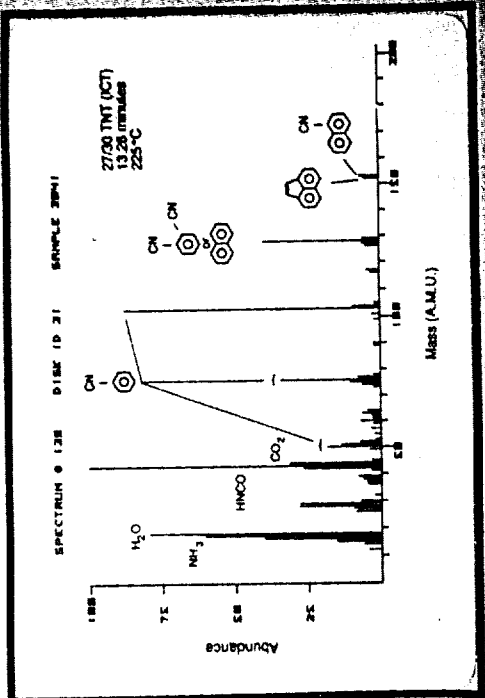
#### AROMATICS:

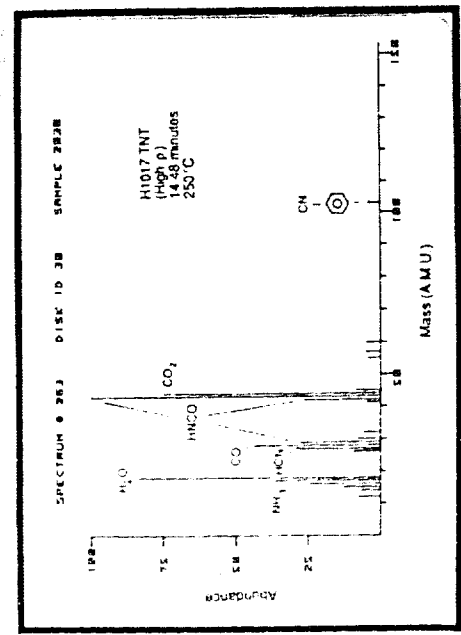
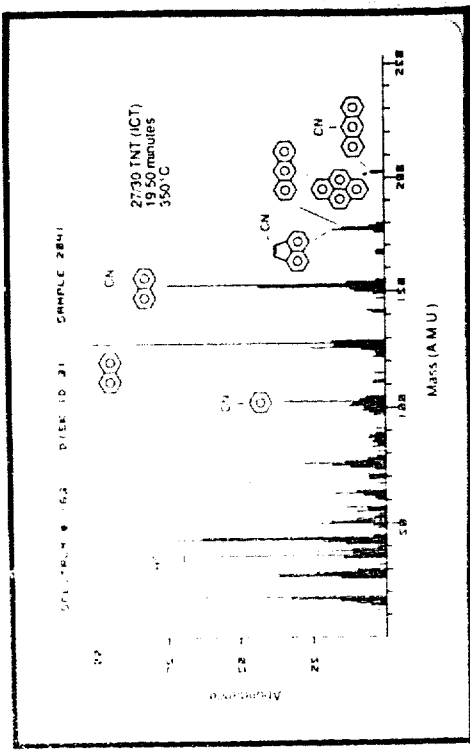
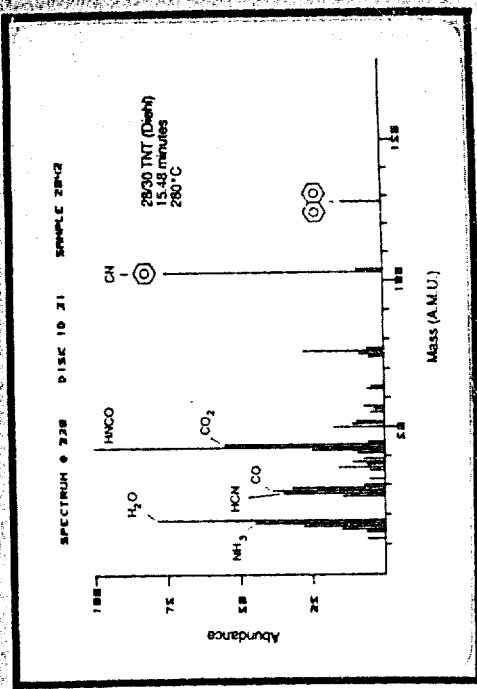
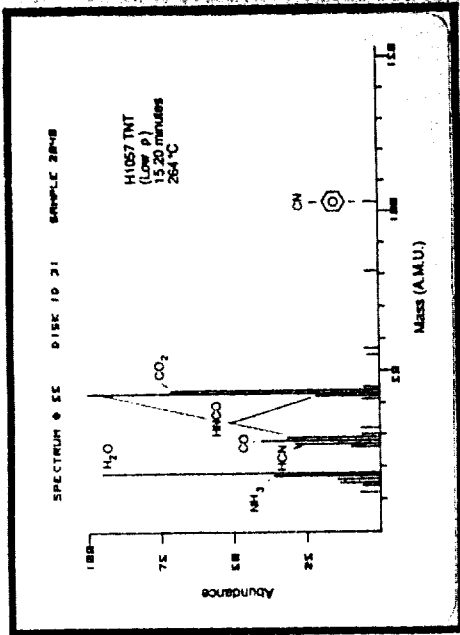
Proto-graphite (?)



Lot Alamos  
GM-28-370W







## LOOSE ENDS

- How representative of detonation conditions are the observed soot features?
- What is the surface chemistry of soot diamond and graphite?
- Is the graphite made up of identifiable polycyclic aromatic components?
- Are other identifiable compounds such as "fullerenes" present in the soot?
- When in the detonation process are diamonds, graphite, and volatiles formed?
- What factors determine diamond and graphite growth kinetics?
- What are the energetics of soot formation?

Los Alamos  
CLS-89-7789

## PLANS

- Pyrolysis/GC/MS analysis (ongoing)
- Analysis of soots from pure HNS, HMX, NTO, NIGU, and Comp B (ongoing)
- Super critical fluid GC/MS analysis (being evaluated)
- Look for carbonaceous clusters in freely expanding detonation products

Los Alamos  
CLS-89-7890

## CONCLUSIONS

- Surface chemistry is important in soot-forming detonations
- Soot graphite resembles high-surface area carbon blacks
- Some soot volatiles resemble carbon-black precursors (polycyclic aromatics) with -CN substitution
- Some soot volatiles appear to be detonation gases ( $H_2O$ ,  $CO_2$ ,  $CO$ ,  $H_2N$ , and  $NH_3$ ) adsorbed on the soot
- The presence of HNCN and urea in soot suggests the presence of "intermediate-size" molecules in detonation products
- Soot diamonds resemble diamonds in meteorites
- About half of the soot has familiar chemistry

Los Alamos  
CLS-89-7788A

# MOLECULAR MODELS FOR EXPLOSIVES: APPLICATIONS TO NTO

James P. Ritchie and Edward M. Kober  
Mail Stop B214  
Los Alamos National Laboratory  
Los Alamos, New Mexico 87545

*We calculated structures and energies for several isomers of 3-nitro-1,2,4-triazol-5-one (NTO), using molecular orbital theory. The 1H,4H isomer was found to be lowest in energy. We predict the existence of an additional low-lying form that may either be directly observable or have its existence inferred in experiments. We also calculated some possible forms of the conjugate base of NTO. Finally, we have applied a new method of calculation to predict the geometry of the diaminoguanidinium salt of NTO.*

## INTRODUCTION

Advances in computer technology and computational algorithms have enabled accurate molecular orbital calculations to be performed for molecules the size of some common IIEs. These calculations provide fundamental molecular properties and can serve as a useful adjunct to experiment in trying to understand the behavior of explosives. Our long-term goal is to determine the relationships between the fundamental properties of explosives and their observed behavior. This paper reports some of our results for the explosive 3-nitro-1,2,4-triazol-5-one (NTO).<sup>1</sup> Our results demonstrate what levels of theory are required to obtain accurate predictions.

Among the properties that one would like to know are: molecular structure, energy, and spectroscopic constants; reactivity, and intermolecular interactions. The molecular structure, energy, and spectroscopic constants are useful for determining the thermodynamic properties and establishing the identity of a proposed compound or reactive intermediate. These quantities are becoming increasingly important as spectroscopic investigations are performed with the intention of determining decomposition mechanisms in energetic materials. Thus, comparison of observed spectra with calculated spectra for specific

species can help to identify reactive intermediates. Reactions and reactivity of explosives are obviously of great concern. Likewise, intermolecular interactions are important in determining crystal structures.

## METHODS

Quantum mechanical calculations reported in this paper were performed with the GAUSSIAN82 computer program.<sup>2</sup> Standard basis sets were used throughout.<sup>3</sup>

## RESULTS

Figure 1 shows the structure usually drawn for NTO as I; however, hydrogens on amide nitrogens are frequently quite labile and mobile. Various tautomers of NTO that are difficult to distinguish experimentally from one another and from NTO may thus be formed by possibly facile rearrangements of hydrogens. Other possible tautomers are shown as II-IV in Figure 1. With the available experimental data, it is difficult to establish with certainty that the explosive we commonly refer to as NTO has, in fact, structure I. Although X-ray data has been obtained<sup>4</sup> and may strongly support structure I, the definitive neutron structure has not yet been obtained. Consequently, ab initio molecular orbital calculations were performed to determine the

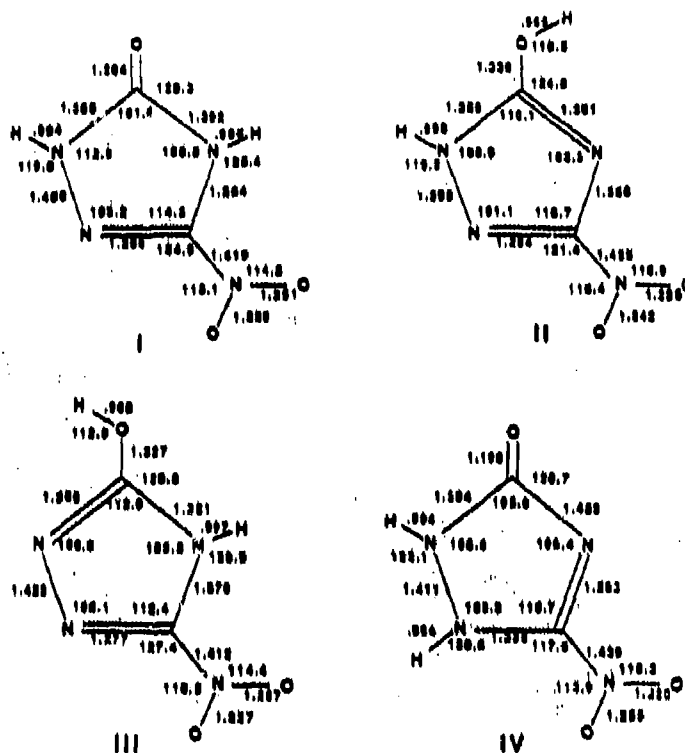


Figure 1. Optimized Geometries Obtained From 3-21G Calculations

structures and relative energies of NTO and its tautomers.

Table 1 shows the energies calculated for I-IV at the various levels of theory employed. Energies obtained from the AM1 method,<sup>5</sup> which is superior to MINDO/3 in some regards, are also included for comparison. These energies are seen to wildly disagree.

Our best calculations, at 6-31G\*\*/3-21G, indicate that I is the correct structure of NTO. II-IV lie somewhat higher in energy, but conceivably could play a role in solution because they may be energetically accessible. In addition, II-IV have a larger dipole moment than does I and polar solvents may preferentially stabilize II-IV due to solvation differences.

A heat of formation of NTO can be estimated using the calculated energies and atom equivalents of Ibrahim and Schleyer developed for this purpose.<sup>6</sup> Table 2 shows the result of this calculation. The 6-31G\*\*/3-21G calculations are our best and yield a  $H_f(g) = 3.2$  kcal.

The heat of formation obtained by this method is appropriate for the gas phase.

Measurements are, however, commonly made in the solid phase. These quantities can be related using the ad hoc correlation we have previously devised.<sup>7</sup> The relationship is shown in Equation 1.

$$H_f(c) = 1.13 * H_f(g) - 23.03$$

$$N = 23, r = 0.987, SD = 4.4 \text{ kcal}, \quad (1)$$

quantities in kcal

Use of Equation 1 with the 6-31G\*\*/3-21G  $H_f(g)$  yields a  $H_f(c)$  of -26.7 kcal, our preferred result.

#### Calculated Structures and Energies for the Conjugate Bases of NTO

Initial calculations were performed with the 3-21G basis set,<sup>3</sup> geometries were completely optimized assuming the molecules to be planar. Because anions are better described with diffuse functions, additional calculations were also performed using the 6-31G+ basis set<sup>4</sup> at the 3-21G geometry. The two sets of

Table 1. Calculated Energies of NTO and Its Tautomers From Various Levels of Theory

Method	I	II	III	IV
MINDO/3 (kcal)	-91.4	-88.1	-92.6	-72.5
AM1 (kcal)	43.8	52.2	45.8	69.9
3-21G//3-21G (au)	-516.17789	-516.12835	-516.14608	-516.13727
6-31G*//3-21G (au)	-519.12631	-519.10175	-519.10217	-519.08916
Dipole (D)	1.25	8.6	5.4	6.3

Table 2. Atom Equivalents and Calculated Heat of Formation of NTO

Atom Type and Number	3-21G Equivalent	6-31G* Equivalent
O <sub>d</sub> -(C)	-74.36505	-74.79644
2 C <sub>d</sub> -(C <sub>d</sub> )(C) <sub>2</sub>	2(-37.66998)	2(-37.88371)
2 N-(H) <sub>2</sub> (CO)	2(-54.17266)	2(-54.46869)
N <sub>d</sub> -(H)(C <sub>d</sub> )	-54.13350	-54.45209
N <sub>d</sub> -(C)(O <sub>d</sub> )(O <sub>w</sub> )	-54.09780	-54.44017
O <sub>w</sub> -(N)	-74.38389	-74.79848
O <sub>d</sub> -(N)	-74.36505	-74.79644
2 H-(N)	2(-00.56322)	2(-00.56636)
SUM	-516.15701	-519.12114
Calc. E	-516.17781	-519.12631
H <sub>f</sub> (g) in kcal	-13.1	-3.2
H <sub>f</sub> (c) in kcal from Eq. 1	-37.8	-26.7

calculations are then conveniently denoted as: 3-21G//3-21G and 6-31G+//3-21G, respectively.

The structures and energies of the three forms of the conjugate base of NTO were obtained and are shown in Figure 2. Table 3 shows the calculated total energies for V-VII and the energy of I for comparison. The calculated energies of V-VII show V to be the

most stable form. The preference for V is quite small, however, at the 6-31+G//3-21G level.

The calculations agree with the recent crystal structure of the ethylene diamine salt of NTO, which shows deprotonation at the 4 position. Table 4 compares the calculated structure of V with that observed for the ethylene diamine salt of NTO. In general, considering the possible effects of crystal

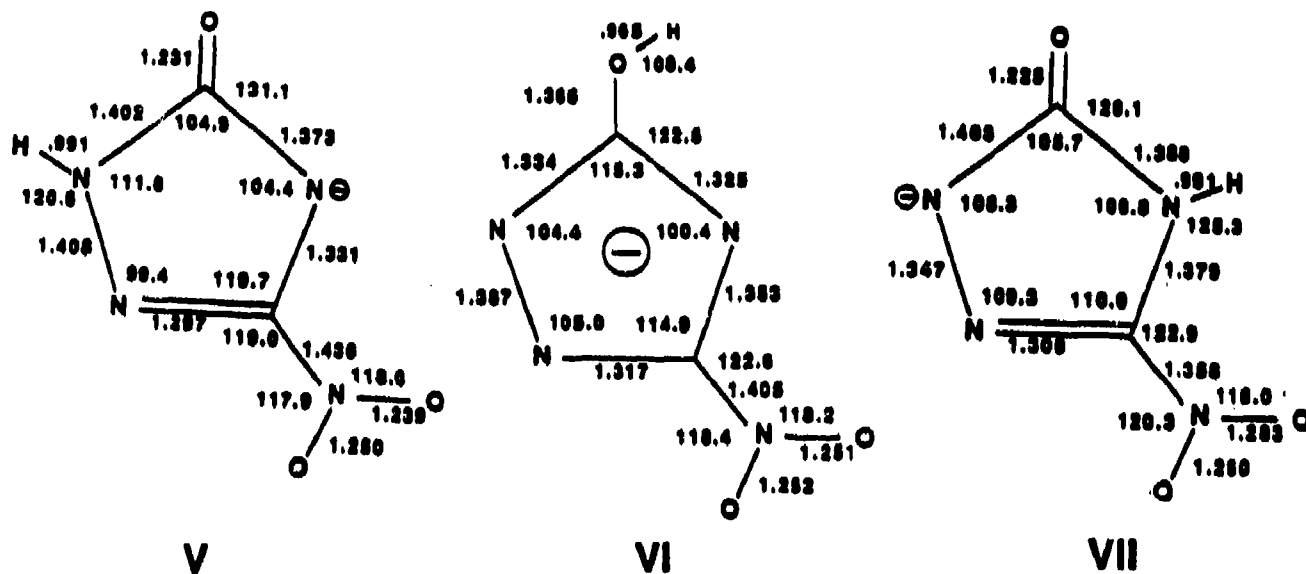


Figure 2. Optimized Geometries Obtained From 3-21G Calculations

Table 3. Calculated Relative Energies (in Au) for NTO (I) and its Conjugate Bases (V-VII) from Two Theoretical Models

Model	I	V	VI	VII
3-21G//3-21G	-516.17789	-515.61923	-515.61544	-515.60387
6-31G+//3-21G	-518.86806	-518.33579	-518.33510	-518.32235

Table 4. Comparison of Calculated Bond Lengths in V and Those Observed in the Ethylene Diamine Salt of NTO

Bond	Obs. (avg.)			Calc.	Error	
C <sub>5</sub> -O	1.276,	1.257,	1.260	(1.264)	1.231	-0.033
N <sub>1</sub> -N <sub>2</sub>	1.370,	1.359,	1.363	(1.364)	1.406	+0.044
N <sub>2</sub> -C <sub>3</sub>	1.304,	1.307,	1.307	(1.306)	1.297	-0.009
C <sub>3</sub> -N <sub>4</sub>	1.337,	1.333,	1.338	(1.336)	1.331	-0.005
N <sub>4</sub> -C <sub>5</sub>	1.356,	1.357,	1.354	(1.356)	1.373	+0.017
C <sub>5</sub> -N <sub>1</sub>	1.358,	1.364,	1.362	(1.361)	1.402	+0.041
C <sub>3</sub> -NO <sub>2</sub>	1.451,	1.450,	1.449	(1.450)	1.436	-0.014
N-O	1.228,	1.216,	1.220	(1.221)	1.250	+0.029
N-O	1.219,	1.237,	1.222	(1.226)	1.239	+0.013

environment and limitations of the theory, the agreement is about as good as can be expected, the maximum deviations being +0.044 and -0.033 Å. The average unsigned error in bond length is 0.023 Å, which is typical for calculations at this level.

#### Electrostatic Models for Intermolecular Interactions

As shown above, we can obtain reasonably accurate predictions for molecules the size of NTO. Another quantity available from these calculations is the total molecular

electron density distribution. We believe that this information can be used to approximate the electrostatic component of intermolecular interactions. Since accurate *ab initio* calculations are still out of reach for systems including two or three or more molecules the size of NTO, we are exploring ways in which the information from a high quality calculation on a single molecule might be used to improve empirical methods for calculating intermolecular interactions among several, possibly up to hundreds, of molecules.

We have previously devised a means of apportioning the total electron density in a molecule among the constituent atoms.<sup>9</sup> The electronic charge distribution associated with an atom in a molecule may then be described by a multipole expansion. Collected together these atom-centered multipole expansions (ACMEs) describe the total molecular charge distribution in a convenient and compact form. In addition, these ACMEs can be used to calculate electrostatic interactions between molecules.<sup>10</sup> Once the ACMEs have been obtained, calculation of the electrostatic energy can be done very quickly.<sup>11</sup>

Other workers have shown that electrostatic considerations play a significant role in determining the total energy of intermolecular interactions.<sup>12</sup> This has been especially well-studied in hydrogen-bonded systems. What is found is that inductive attractions and overlap repulsions nearly balance one another. The electrostatic energy then remains and closely parallels the total energy of interaction.

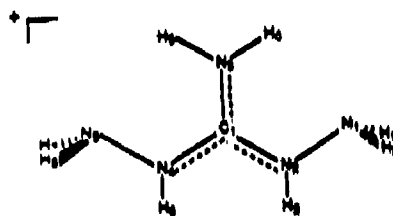
Despite the recognized importance of electrostatics in determining intermolecular interactions, computer programs used to calculate molecular crystal structures either ignore this effect entirely or include only very rough estimates for it. The techniques we have developed might ultimately be incorporated into crystal structure calculations as a means of using the information available from molecular orbital calculations. Such an approach would provide a means by which the effects of the molecular environment upon a constituent atom might be taken into account.

NTO readily reacts with amine bases to produce salts. The diaminoguanidinium salt of

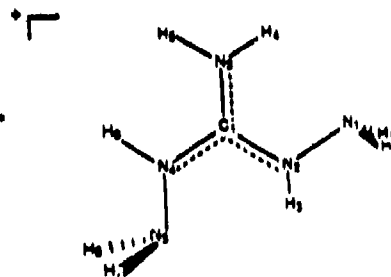
NTO has been produced in this fashion at Los Alamos.<sup>13</sup> X-ray structure analysis<sup>14</sup> reveals that the diaminoguanidinium ion of this salt appears in the A configuration indicated below; we denote this geometry as DAGA. Interestingly, X-ray structure analysis of the diaminoguanidinium salt of nitric acid shows another form of the cation,<sup>15</sup> indicated as B, below, which we denote DAGB.

The results of molecular orbital calculations for both forms of the diaminoguanidinium ion are summarized in Table 5. They show that DAGA, as found in the NTO salt, is higher in energy than DAGB, as found in the nitric acid salt. The question to be answered then is why does the conjugate base of NTO selectively bind DAGA when another lower energy form is available?

To answer this question ACMEs were obtained for the conjugate base of NTO and both forms of the diaminoguanidinium cation. The electrostatic energy of interaction of the anion with DAGA and DAGB was then calculated for different geometries. The geometries of the anion and cation fragments were fixed at those found in the original MO calculations. Intermolecular distances and angles were varied however to optimize the electrostatic interactions. The complexes were prevented



A,  $C_{2v}$  Symmetry



B,  $C_{2v}$  Symmetry

Table 5. Optimized Geometrical Parameters and Energies for the A and B Forms of Diaminoguanidium Ion (See text)

	A		B	
	3-21G	6-31G*	3-21G	6-31G*
$E_{tot}(au)$	-312.78369	-314.51739	-312.78528	-314.51830
$E_{rel}(kcal)$	0.0	0.0	-1.0	-0.6
$R(C_1-N_2)$	1.304	1.307	1.316	1.317
$R(C_1-N_3)$	1.334	1.331	1.322	1.321
$R(C_1-N_4)$	"	"	1.333	1.331
$R(N_3-N_5)$	1.421	1.388	1.421	1.388
$R(N_4-N_6)$	"	"	1.422	1.387
$R(N_2-H_7)$	1.001	0.997	0.998	0.995
$R(N_2-H_8)$	"	"	1.003	0.998
$R(N_3-H_9)$	1.000	0.998	1.002	0.999
$R(N_4-H_{10})$	"	"	1.000	0.998
$R(N_5-H_{11})$	1.005	1.001	1.006	1.001

from collapsing by surrounding each atom with a hard sphere, the diameter of which was taken from Bondi.<sup>16</sup>

Figure 3 shows the minimum energy configurations found for NTO/DAGA and NTO/DAGB. Many other structures were investigated, but these are the lowest energy forms found. The two structures are very similar in their hydrogen-bonding interactions with two N-H moieties of DAG directed toward the carbonyl oxygen and the 4-nitrogen of NTO. These two atoms are the most highly negatively charged of NTO and present the most favorable sites for hydrogen-bonding. In both cases, the DAG molecules are skewed toward the oxygen of the nitro group, which is also highly negatively charged. Both complexes were found to be planar, although they were not constrained to be so.

The NTO/DAGA complex was found to be 3.4 kcal/mol more stable than the NTO/DAGB complex. The C-NH<sub>2</sub> nitrogen of DAG is found to be more negatively charged than the C-NH-NH<sub>2</sub> nitrogens, and should therefore form a weaker hydrogen-bond. This appears to

be the major reason that DAGA interacts more strongly with NTO than DAGB. A comparison between our calculated structure for the NTO/DAGA complex and the asymmetric unit determined by X-ray crystallography is shown in Figure 4. The electrostatic model is seen to reproduce the observed structure at least qualitatively. Since the difference in energy between the two complexes is larger than the difference in energy of the isolated molecules, as shown in Table 5, it is the electrostatic energy which selectively allows the conjugate base of NTO to bind DAGA.

## CONCLUSIONS

We have demonstrated that MO calculations provide useful information about the structure, energy, and reactivity of NTO. Many of these calculations were performed before the corresponding experiments were performed, indicating that reliable predictions can be made, provided that the molecule is not so large as to preclude the use of large basis sets and other means for performing accurate calculations.

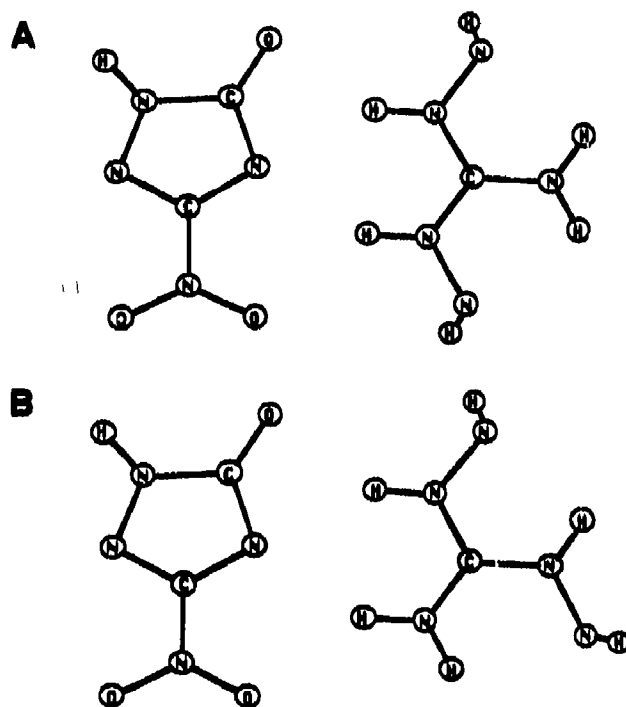


**Figure 3. Lowest Electrostatic Energy Forms for NTO/DAGA (A) and NTO/DAGB (B) Anion-Cation Pairs**

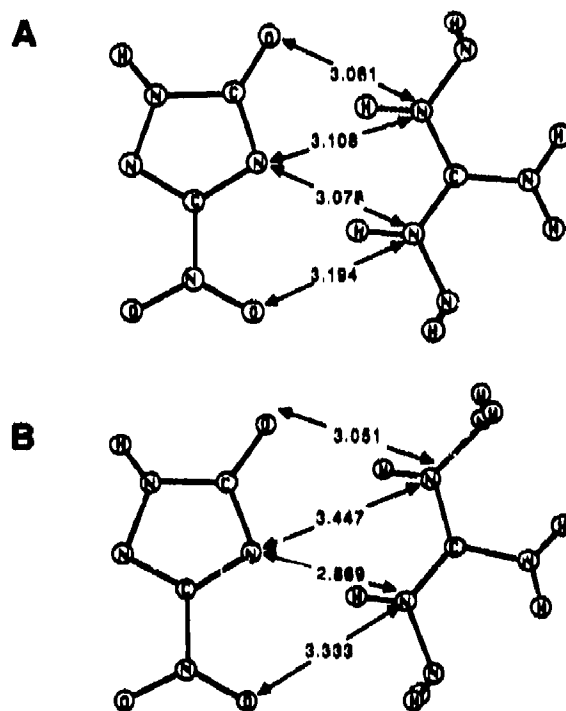


**Figure 4. Comparison of Some Intermolecular Distances for the Calculated NTO/DAGA Pair (A) and Those Found Experimentally for the Asymmetric Unit of the Diaminoguanidinium Salt of NTO (B)**

## REFERENCES

1. a) Lee, K. -Y. and Coburn, M. D., *3-Nitro-1,2,4-Triazol-5-One, A Less Sensitive Explosive*, LA-10302-MS, 1985. b) Lee, K. -Y.; Chapman, L. B.; and Coburn, M. D., *J. Energetic Mat.*, Vol. 5, 1987, p. 27.
2. Binkely, J. S.; Frisch, M. J.; DeFrees, D. J.; Ragavachari, K.; Whiteside, R. A.; Schlegel, H. B.; Fluder, E. M.; and Pople, J. A., Carnegie-Mellon University. The CTSS version was implemented by Dr. R. Martin, Los Alamos.
3. 3-21G: Binkley, J. S.; Pople, J. A.; and Hehre, W. J., "3-21G," *J. Am. Chem. Soc.*, Vol. 102, 1980, p. 939. Clark, T.; Chandrasekhar, J.; Spitznagel, G. W.; and Schleyer, P. v. R., "6-31G+," *J. Computational Chem.*, Vol. 4, 1983, p. 294. Hariharan, P. C. and Pople, J. A., "6-31G+," *Theoret. Chim. Acta (Berl.)*, Vol. 28, 1973, p. 213.
4. Cromer, D. T. and Ryan, R. R., Los Alamos, unpublished results.
5. Dewar, M. J. S.; Zoebisch, E. G.; Healy, E. F.; and Stewart, J. J. P., *J. Am. Chem. Soc.*, Vol. 107, 1985, p. 3902.
6. Ibrahim, M. R. and Schleyer, P. v. R., *J. Comput. Chem.*, Vol. 6, 1985, p. 157.
7. Ritchie, J. P. and Bachrach, S. M., *Journal de Physique*, Vol. C4, 1987, p. 377.
8. Lee, K. Y.; Cromer, D. T.; and Ryan, R. R., *Acta Cryst. C*, submitted.
9. Ritchie, J. P., *J. Am. Chem. Soc.*, Vol. 107, 1985, p. 1829.
10. Ritchie, J. P. and Bachrach, S. M., *J. Comput. Chem.*, Vol. 8, 1987, p. 499.
11. Ritchie, J. P.; Kober, E. M.; and Lee, D., to be submitted.
12. Umeyama, H. and Morokuma, K., *J. Am. Chem. Soc.*, Vol. 99, 1977, p. 1316.
13. Lee, K. -Y., unpublished results.
14. Lee, K. -Y.; Cromer, D. T.; and Ryan, R. R., *Acta Cryst. C*, submitted.
15. Lee, K. -Y.; Cromer, D. T.; and Ryan, R. R., to be submitted.
16. Bondi, A., *J. Phys. Chem.*, Vol. 68, 1964, p. 441.

# REACTION AND DIFFUSION IN DETONATION

N. J. B. Green, M. J. Pilling, and S. H. Robertson  
Physical Chemistry Laboratory, South Parks Rd., Oxford,  
OX1 3QZ, UNITED KINGDOM

*The role of diffusion in two aspects of detonation chemistry is examined. In the first, the early time evolution of a modal hot spot is investigated using two techniques, a diffusion-reaction equation and a stochastic simulation. It is shown that for small hot spots containing few reactive particles stochastic effects are important and may lead to the quenching of the hot spot. In the second, we present a theoretical framework to describe the transition between diffusion and activation-controlled kinetics. A diffusion equation for a pair distribution function is set up and solved in the steady state using a radiation boundary condition in terms of the potential of mean force. Application of the solution requires a knowledge of the diffusion coefficient over a range of temperatures and densities. These are calculated using molecular dynamics.*

## INTRODUCTION

The detailed modelling of detonation requires an understanding of complex, interacting kinetic and hydrodynamic processes. This paper is concerned primarily with the former and with the specific considerations which need to be made at the high temperatures and pressures involved. In particular, we address the interaction between diffusion of molecular and radical species and their reaction on encounter. Two aspects are considered: (a) the early stage of the initiation process and its development into a detonation, and (b) the post-detonation kinetics, where the system relaxes from the Chapman-Jouguet point.

## INITIATION

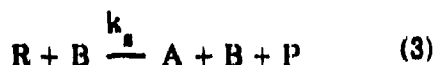
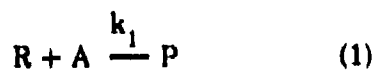
There is a great deal of interest in the mechanism of shock initiation of energetic materials. Treatments tend to be concerned with the full development of the detonation wave and generally include oversimplified, and often unrealistic chemical kinetic processes. There are some exceptions but such treatments impose spatial simplifications often involving homogeneous kinetics.<sup>1</sup> The aim of this work is to model the initial stages of a

detonation from a microscopic chemical kinetic viewpoint.

Hot spots, produced as a result of the passage of a shock front are central to most theories of initiation.<sup>2</sup> In a polycrystalline solid hot spots are formed by friction between grain boundaries, cavity collapse, or impurities; in a pure liquid they are generated either by bubble collapse or by instabilities in the shock front.<sup>3</sup> From a chemical kinetic viewpoint, hot spots are regions of high temperature in which locally high concentrations of active species, such as radicals, are produced.

The development of a detonation might be considered to occur in two stages. Initially, individual hot spots develop with time; chemical reaction occurs; heat is liberated, increasing the pressure; and the hot spot expands by diffusion and convection. In the second stage, initially separate hot spots interact to produce a self-sustaining reaction wave. In this section we are interested in the former process, in which the important aspects are the requirements for reaction initiated at the hot spot to be sustained, and for the reaction zone to expand.

As a first step, it is necessary to choose a simplified, though not wholly unrealistic, chemical kinetic mechanism for a detonation.



In this mechanism R is a fuel molecule, A is an active intermediate (radical, etc.), P is a product molecule, and B is a branching species which is involved in the autocatalytic step (3).

The mechanism was examined in two ways. The first method employs a conventional deterministic approach, in which coupled kinetic rate equations and diffusion equations for the above species are numerically integrated. For species A, this equation is of the form

$$\frac{\partial C_A}{\partial t} = D_A \nabla^2 C_A + k_3 C_R C_B - k_1 C_R C_A - k_2 C_A C_P \quad (4)$$

where  $C_i$  is the concentration and  $D_i$  the diffusion coefficient of species  $i$ , and the irreversible rate coefficients are denoted  $k$ . These equations, subject to suitable boundary conditions, were integrated using finite difference methods. Two geometries were considered: linear and spherical. For the linear case the single dimension was divided into 50 cells, each associated with initial concentrations for every species. The total concentration for each cell corresponds roughly to a compressed fluid and the small initial concentration of A molecules in the first cell models an incipient hot spot. The same analysis was applied to the spherical case, except that the space was divided into 50 concentric spherical shells, and the diffusion equation was modified to take account of the spherical geometry. Results for the linear case are shown in Figure 1. The frames are spaced at 0.2 ns intervals. It can be seen that, after a small initial period, a definite reaction wave is formed which moves out with a speed of approximately 30 ms<sup>-1</sup>. This is, of course, substantially less than the normal

detonation speed, and is more consistent with a deflagration arising from diffusive transport. An increase of 10 ms<sup>-1</sup> was obtained when thermal conductivity was introduced into the model. The present mechanism includes only diffusion-controlled reactions with weak temperature dependencies; no reactive heat release was considered. The inclusion of heat release and of activation controlled reactions, which are more sensitive to increases in temperature, would provide a further mechanism for positive feedback (thermal explosion). Work is also in progress on the introduction of momentum transfer. All these effects can be included with only a modest increase in computing time. Our main concern here is to compare a deterministic model which is, admittedly, crude with a stochastic model.

The above macroscopic analysis is acceptable for large hot spots, where the discrete nature of the reactive species may justifiably be neglected. However, when the hot spots are small, then small numbers of reactive species are involved and a stochastic approach may be more appropriate. Initially, an approach based on a master equation was investigated. A master equation is a set of coupled differential equations describing the time evolution of the distribution of state probabilities. For example, in the simple one-dimensional model outlined above the state of each cell is determined by the number of molecules of each type. A probability distribution function (p.d.f.) can be defined for each cell  $p_j(a,b,p,r,t)$ , such that there are  $a$  molecules of type A,  $b$  molecules of type B, etc., in the  $j$ th cell at time  $t$ . The evolution of the p.d.f. with time is dictated by a master equation. Even for a modest system, the number of coupled equations may be in excess of 10,000 which makes the direct solution of the master equation computationally prohibitive.

It was, therefore, decided to simulate the process instead. The state of the system at a given time is defined by the integer values of  $a, b, p$ , and  $r$ . The various types of reactive (e.g., A + R) and diffusive (e.g., transport from cell  $j$  to cell  $j + 1$ ) events form competing Poisson processes in the sense that each process occurs with a characteristic, first order rate, which depends on the number of relevant particles in

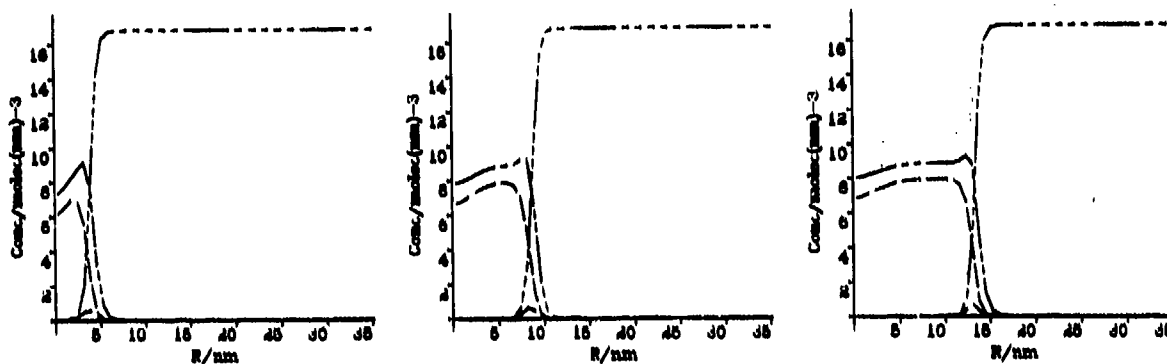


Figure 1. Species Distributions for Diffusion-Reaction Model at 0.2, 0.4, and 0.6 ns. Initial distribution of  $C_A = 5.6$ ,  $C_B = 0$ ,  $C_P = 0$ , and  $C_R = 11.2$  molec/nm<sup>3</sup> in first cell, and  $C_R = 16.8$  molec/nm<sup>3</sup> in remainder. --- A, ---- B, - - - - P, and - · - · - R.

the cell. These first order rates are used to generate exponentially distributed event times for each cell. The minimum such time is taken to correspond to the first event, which modifies the state. New characteristic rates are then calculated and now event times generated for those cells which have been modified. The outline of this procedure is shown in the flow diagram in Figure 2. A similar method has been used with considerable success in studies of radiation chemistry.<sup>4,5</sup>

The results are shown in Figure 3. As can be seen, the distributions are very different from the deterministic case. This difference arises because, in the simulation, both of the initial A molecules present can react independently with R molecules to produce P molecules, thus precluding reaction (2) and the production of the catalytic B molecule. This leads to the quenching of the hot spot. The effect is absent from the deterministic case. As a check that the two methods approach the same limit for large  $a$ , runs were conducted with an excess of A molecules in the first two grains and agreement found, within statistical error, between the two models. A diff reaction wave is now generated in the stochastic model and, although somewhat broadened by statistical effects, it propagates at approximately the same speed as that found in the deterministic model.

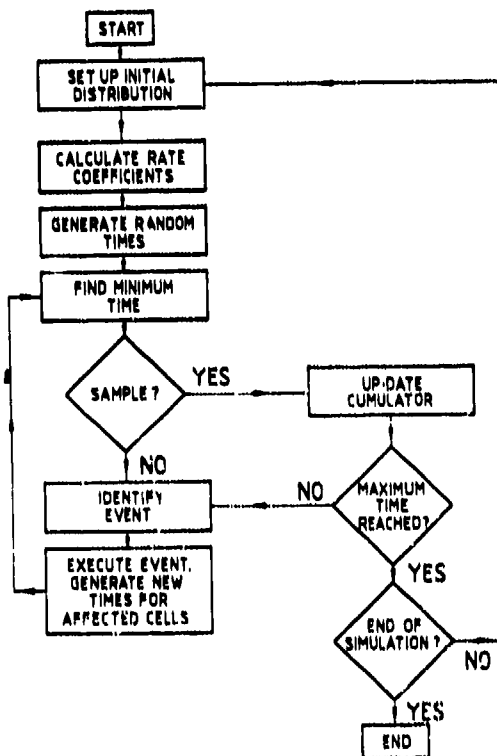


Figure 2. Flow Diagram for Stochastic Model

This stochastic model is crude and requires improvement. For example, at present there is no limit to the number of molecules that can occupy a given cell, which is clearly unrealistic. The model has no facility to deal

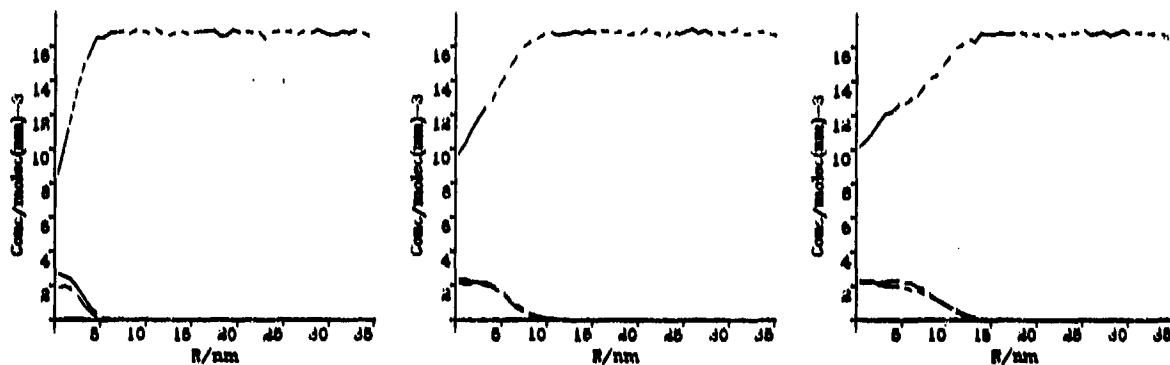


Figure 3. Species Distributions for Stochastic Model at 0.2, 0.4, and 0.6 ns. Same initial distributions and markings as Figure 1.

with thermal conductivity. Finally, and in common with the deterministic model, no account is taken of momentum transfer.

This is not the first time a stochastic technique has been applied to detonations,<sup>6</sup> but the spatial dependence has not been treated. For this particular model, we have demonstrated that stochastic effects are significant under the conditions where a deterministic description would lead to propagation, and can lead to the quenching of the hot spot. This in turn means that, if a reaction wave is to be propagated and if the individual hot spots are small, then their number density must be higher than is required in a deterministic treatment.

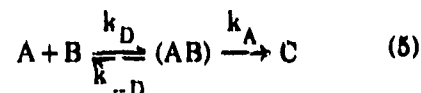
## FUME CHEMISTRY

Much effort in commercial explosives research is expended in designing explosives whose products are neither combustible nor toxic. Such explosives are designed for use in confined spaces or where there is a risk of further combustion, e.g., coal mines. In designing such explosives, a detailed survey of the elementary reactions that occur in the post-detonation fume is required. Data from such surveys are then incorporated into large kinetic models based on standard rate theory.

There are a number of weaknesses in this procedure, not least of which is that the kinetic

data used in such models are often obtained from low gas density experiments. Many bimolecular reactions, and especially the important class of metathesis reactions, show well characterized simple Arrhenius or curved Arrhenius behavior at the temperatures and pressures studied in the laboratory. The reactants have to overcome activation barriers before forming products and the reactions are termed "activation-controlled." At the high temperatures and pressures encountered in detonation where diffusion is comparatively slow many of the reactions, and especially those with small or moderate activation barriers, become diffusion-controlled with rates determined by the diffusive approach of reactants. A technique is required, therefore, for describing the transition from activation to diffusion control, and for determining rate constants in the transitional regime.

The transition between diffusion and activation control may be illustrated by the simplified scheme<sup>7</sup>



where  $k_D$  is the (second order) rate coefficient for diffusive approach,  $k_{-D}$  is the rate coefficient for diffusive loss of encountered pairs (AB), and  $k_A$  the rate coefficient for the activated step to form the product C. Pairs must encounter

before reaction. Application of the steady state approximation for (AB) gives a second order rate coefficient for reaction of

$$k_2 = \frac{k_D k_A}{k_{-D} + k_A} = \frac{k_D}{1 + \frac{k_{-D}}{k_A}} \quad (6)$$

In the activation-controlled limit  $k_A \ll k_D$  and in consequence  $k_2 \rightarrow k_A k_D / k_{-D}$ , showing that (AB) is in equilibrium with A and B; in the diffusion-controlled limit  $k_A \gg k_D$  and  $k_2 \rightarrow k_D$ .

This picture is a useful illustration, but in order to make any quantitative predictions, we need to have a theory which allows us to calculate  $k_D$ ,  $k_{-D}$ , and  $k_A$  more rigorously. Diffusion theory is a suitable framework, as it enables the model to be based on concentration gradients or pair distribution functions. The pair distribution function for A about B,  $g(r)$ , obeys the diffusion equation<sup>8</sup>

$$\nabla \cdot D \cdot [\nabla g + g \nabla(\beta U)] = \frac{\partial g}{\partial t} \quad (7)$$

where  $U$  is the potential of mean force and  $\beta = 1/kT$ .  $g(r)$  is related to the radial distribution functions given by

$$\rho(r) = 4\pi r^2 g(r) \quad (8)$$

To calculate a steady-state rate coefficient, we need the reactive flux from the steady-state radial distribution which, for an isotropic system, obeys the equation

$$\frac{\partial}{\partial r} \left[ D \left( \frac{\partial \rho}{\partial r} + \rho \left( \frac{\alpha(\beta U)}{\partial r} - \frac{2}{r} \right) \right) \right] = 0 \quad (9)$$

$\rho(r)$  is the solution of this equation subject to appropriate boundary conditions. A reactive boundary condition which has a broad range of validity is the radiation boundary condition<sup>9</sup>

$$D \left[ \frac{\partial \rho}{\partial r} + \rho \left( \frac{\alpha(\beta U)}{\partial r} - \frac{2}{r} \right) \right] \Big|_R = v \rho(R) \quad (10)$$

The term on the right can be thought of as a flux through a sphere of radius  $R$ , with a characteristic "boundary velocity"  $v$ , corresponding to the activated step to form products. The outer boundary condition is a natural boundary, such that

$$\rho(r) \rightarrow 4\pi r^2 \text{ as } r \rightarrow \infty \quad (11)$$

The solution of these equations gives the radial distribution function modified by reaction, and is given by

$$\left[ \begin{array}{l} \rho(r) = 4\pi r^2 e^{-\beta U} \\ \frac{D e^{\beta U}}{v R^2} + \int_R^r r^{-2} e^{\beta U} dr \\ \frac{D e^{\beta U}}{v R^2} + \int_R^\infty r^{-2} e^{\beta U} dr \end{array} \right] \quad (12)$$

Now in the limit that  $v \rightarrow 0$ , there is no reaction, and we obtain

$$\rho(r) = 4\pi r^2 e^{-\beta U} = 4\pi r^2 g_0(r) = \rho_0(r) \quad (13)$$

which is the equilibrium distribution, as might be simulated by molecular dynamics, or calculated from the potential of mean force.

The general solution for  $k_{ss}$  (the steady state rate coefficient) with non-zero boundary velocity is, according to the radiation boundary condition,  $v\rho(r)$ , which can be expressed in terms of  $\rho_0(r)$  (the equilibrium radial distribution function with no reaction),

$$k_{ss} = \frac{D}{\left[ \int_R^\infty \rho_0^{-1} dr + \frac{D}{v \rho_0(R)} \right]} \quad (14)$$

In the diffusion controlled limit  $v \rightarrow \infty$  and

$$k_{ss} = \frac{D}{\int_R^\infty \rho_0^{-1} dr} \quad (15)$$

which is a modification of the usual formula, to account for the effects of solvent structure through  $\rho_0(r)$ . The usual formula ignores this effect, setting  $g_0(r) = 1$ .

Thus, to obtain values for  $k_{ss}$ , the diffusion coefficient  $D$  and  $\rho_0(r)$  (or the potential of mean force) are required. Both are amenable to simulation. The diffusion coefficient, for example, can be determined using molecular dynamics. To do this, a standard molecular dynamics code<sup>10</sup> using a Lennard-Jones 12-6

potential was modified to calculate the diffusion coefficient via the Einstein-Smoluchowski relation, i.e.

$$\langle r^2 \rangle = 6Dt, \quad (16)$$

averaging over 108 particles and 300 time origins. After an initial transient period the diffusion coefficient may be calculated from the linear dependence for  $\langle r^2 \rangle$  on  $t$ . Simulations were performed at a number of temperatures and densities. The temperature dependence of the diffusion coefficient is illustrated in Figure 4 for  $N_2$ , with a molar volume of  $4.5 \times 10^{-6} \text{ m}^3$  giving pressures typically in the region of 100 MPa. Further work is in progress.

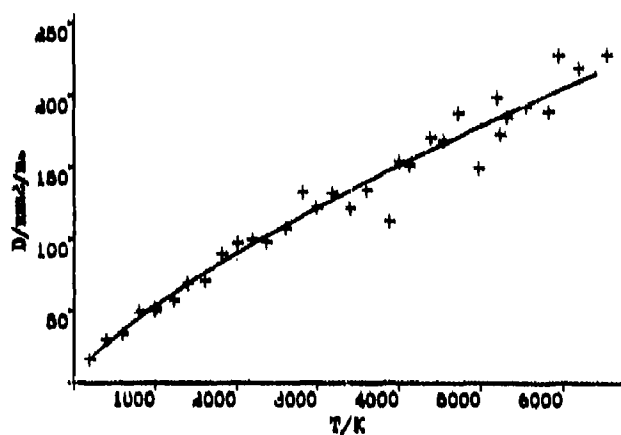


Figure 4. Temperature Dependence of Diffusion Coefficient for  $N_2$  with a Molar Volume  $4.5 \times 10^{-6} \text{ m}^3$

## ACKNOWLEDGEMENTS

We are grateful to Martin Braithwaite and Graeme Leiper for helpful and stimulating discussions. SHR thanks SERC and ICI Explosives Group Technical Centre for the award of a research studentship.

## REFERENCES

1. Frank-Kamenetskii, D. A, *Acta Phys. Chim, URSS*, Vol. 10, No. 3, 1939, p. 729.
2. Bowden, F. P. and Yoffe, Y. D., *Initiation and Growth of Explosion in Liquids and Solids*, Cambridge University Press, Cambridge, U. K., 1985.
3. Johnson, J. N.; Tang, P. K.; and Forest, C. A., "Shock Wave Initiation of Heterogeneous Reactive Solids," *Journal of Applied Physics*, Vol. 57, No. 9, 1985, p. 4323.
4. Clifford, P.; Green, N. J. B.; and Pilling, M. J., "Statistical Models of Chemical Kinetics in Liquids," *Journal of the Royal Statistical Society B*, Vol. 49, No. 3, 1987, p. 266.
5. Green, N. J. B.; Pilling, M. J.; Pimblott, S. M.; and Clifford, P., "Stochastic Models of Short-Time Kinetics in Irradiated Liquids," *Radiation Physics and Chemistry*, In press.
6. Gorecki, J. and Gryko, J., "The Adiabatic Thermal Explosion in a Small System-Comparison of the Stochastic Approach with the Molecular Dynamics Simulation," *International Atomic Energy Agency Report IC/85/221*, 1985.
7. Pilling, M. J., *Reaction Kinetics*, Oxford University Press, Oxford, U. K., 1975, pp. 69-71.
8. Debye, P., "Reactions in Ionic Solutions," *Journal of the Electrochemical Society*, Vol. 82, 1942, p. 265.
9. Collins, F. C. and Kimball, G. E., "Diffusion Controlled Reaction Rates," *Journal of Colloid Science*, Vol. 4, 1949, p. 425.
10. MDATOM Computer Program, Department of Chemistry, Royal Holloway College, U. K., 1980.

# A THERMOCHEMICAL MODEL FOR SHOCK-INDUCED CHEMICAL REACTIONS IN POROUS SOLIDS: ANALOGS AND CONTRASTS TO DETONATION

M. B. Boslough  
Sandia National Laboratories  
Albuquerque, New Mexico 87185-5800

*There is a class of non-explosive energetic materials that undergo rapid shock-induced chemical reactions, but whose products contain no vapor that can undergo a rapid expansion upon pressure release. The present paper presents a thermochemical model describing such reactions in terms analogous to detonation. By contrast, however, the chemical energy is converted mostly to heat rather than work by the shock wave, and an unsupported reaction wave will decay. In the absence of volatiles, there are no large increases in pressure, specific volume, or particle velocity associated with such reactions. Thus, experimental methods normally applied to high explosives are insensitive, and time-resolved temperature measurements are the most appropriate. The pressure-volume-velocity relationships are strongly dependent on small amounts of volatiles (such as water) when present, but the shock temperature is not. Thermochemically, the possibility of a sustained detonation in a volatile-bearing reactive powder cannot be precluded. By the same arguments, geochemical detonations in volatile-saturated, supercooled magmas are thermochemically possible.*

## INTRODUCTION

There have been a number of efforts to study the problem of shock-initiation of chemical reactions in non-explosive porous solids. Graham<sup>1</sup> has recently pointed out that such reactions are fundamentally different from either high explosive detonations or pyrotechnic reactions. The controlling features seem to be shock-induced mixing, shock activation, configuration change, and heating.<sup>2</sup>

The experimental work to date has been dominated by studies aimed at understanding shock-induced chemical synthesis by examination of samples recovered from exposure to explosive loading.<sup>3-4</sup> Such recovery experiments have provided evidence for the uniqueness of the shock environment in its ability to mix and activate substituents, initiating reactions at a rate commensurate with that of shock wave propagation.

Hugoniot measurements on lead nitrate/aluminum,<sup>5</sup> and tin/sulfur mixtures,<sup>6</sup> have demonstrated that shock-initiated reactions occur at a rapid enough rate to affect the pressure-volume state behind the shock wave in those mixtures. However, those experiments have the drawback that they are relatively insensitive to the amount of reaction, and are highly sensitive to small quantities of volatile impurities, as will be shown in this paper.

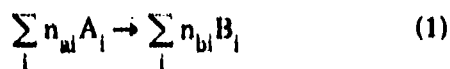
Radiation pyrometry has been used to measure the shock temperatures of nickel/aluminum<sup>7</sup> and iron oxide/aluminum (thermite) mixtures,<sup>8</sup> providing evidence that shock-induced exothermic reactions occur in less than 100 ns in those materials. However, there is some ambiguity as to whether the high temperatures measured in those experiments were due to chemical reactions or heterogeneous deposition of irreversible work.

More recent experiments<sup>9</sup> have removed the ambiguity by comparing the shock temperatures for reactive nickel/aluminum to those for inert pure nickel in fine-grained powders that rapidly achieved thermal equilibrium. The model presented here will demonstrate that, in contrast to Hugoniot measurements, shock temperatures are very sensitive to chemical reactions and insensitive to volatile impurities.

There have been several efforts at modeling shock-initiated chemical reactions in non-explosive energetic materials.<sup>10-13</sup> These models have all considered the kinetics of the reactions, making various assumptions as to the controlling factors. The model presented here is an attempt to develop a description based only on thermochemistry and shock wave physics, ignoring kinetic aspects entirely. The present model assumes only that the reaction proceeds rapidly enough that an equilibrium state can be defined behind the shock wave—a possibility suggested by the experiments mentioned above. It is intended to provide a conceptual framework to which the more advanced models can be related; an approach similar to the early descriptions of detonations without regard for chemical mechanisms.

## MIXING MODEL

If we consider a heterogeneous mixture of reactants  $A_i$  and products  $B_i$ , we can write an equation for a shock-induced chemical reaction as:



where  $n_{ai}$  and  $n_{bi}$  are the number of moles of reactant  $i$  and product  $i$ , respectively. The specific volume of a multi-component system with a uniform stress distribution is given by:

$$V = \sum_i n_i M_i V_i \quad (2)$$

where  $M_i$  and  $V_i$  are the relative molecular mass and specific volume of component  $i$ , respectively.

To determine the specific volume dependence on isentropic pressure ( $P_S$ ), we can use Bridgman's quadratic equation:<sup>14</sup>

$$V/V_0 = 1 - (P_S/K_{OS}) + \frac{1}{2} (1 + K'_{OS}) (P_S/K_{OS})^2 \quad (3)$$

where  $V_0$  is the specific volume at standard conditions,  $K_{OS}$  is the isentropic bulk modulus, and  $K'_{OS}$  is its first pressure derivative. This quadratic equation is only accurate for pressures at which the strain is very small (less than a few percent), so the present calculations are limited to pressures of less than 10 GPa. A higher-order finite strain theory can be used to describe isentropes at higher pressures, but would introduce unnecessary complications into the mixture theory at the pressures of interest here.

Summing Equation (3) for a multi-component system in Equation (2) results in a Reuss average composite bulk modulus and its pressure derivative in terms of those parameters for the individual components:

$$K_{OS} = \left[ \sum_i (v_i/K_{OSi}) \right]^{-1} \quad (4)$$

$$K'_{OS} = K_{OS}^2 \left\{ \sum_i \left[ v_i (1 + K'_{OSi}) / K_{OSi}^2 \right] \right\} - 1 \quad (5)$$

where  $v_i$  is the initial volume fraction of component  $i$ .

## HUGONIOT CALCULATIONS

For a porous, reactive material, the Rankine-Hugoniot equation relating the specific internal energy on the Hugoniot ( $E_H$ ) to that of the initial state ( $E_0$ ) can be written:

$$E_H - E_0 = -Q + \frac{1}{2} P_H (V_{00} - V) \quad (6)$$

where  $V_{00}$  is the initial (porous) volume,  $(P_H, V)$  is the pressure-volume state on the Hugoniot, and  $Q$  is the heat of reaction. The energy along the principal isentrope of a porous zero-strength solid is given by

$$E_s - E_0 = - \int_{V_0}^V P_S dV \quad (7)$$

Combining Equations (6) and (7) together with the Mie-Grüneisen approximation

$$E_H - E_S = (V/\gamma) (P_H - P_S) \quad (8)$$

gives an equation for the Hugoniot:

$$P_H(V) = \left( Q + \int_{V_0}^V P_S dV + \left[ \frac{V}{V_0} \right] P_S \right) / \left( \left[ \frac{V}{V_0} \right] - \frac{1}{2} (V_{00} - V) \right) \quad (9)$$

The theoretical Hugoniot of the reactants can be determined by setting  $Q$  to zero and inverting Equation (3) with parameters taken from Equations (4) and (5) from the known material properties of the components, and inserting that into Equation (9). The product Hugoniot is determined in the same way, with  $Q$  equal to the appropriate heat of reaction.

## THERMITE HUGONIOTS

For thermite, Equation (1) can be written:



The elastic constants have been calculated<sup>15</sup> using Equations (4) and (5) with ultrasonic data for hematite, aluminum, and alumina, and shock wave data for liquid iron (since the products are in the liquid state). A Grüneisen parameter was also determined for each mixture from a mass-fraction-weighted average of the experimental values for the components.<sup>15</sup> This method has been shown to be inaccurate,<sup>16</sup> but is a reasonable approximation for the present calculations. These calculated parameters for the thermite reactants and products are listed in Table 1.

Table 1. Thermite Equation of State Parameters

Parameter	Reactants	Products
Initial Density ( $\rho_0$ , g/cm <sup>3</sup> )	4.249	4.154
Initial Specific Volume ( $V_0$ , cm <sup>3</sup> /g)	0.2353	0.241
Zero Pressure Bulk Modulus ( $K_{0S}$ , GPa)	122	197
Pressure Derivative of $K_{0S}$ ( $K'_{0S}$ )	6.65	5.2
Zero Press. ) Grüneisen Parameter ( $\gamma_0$ )	2.08	1.7

Because the thermite product Hugoniot is at high temperature, the reference isentrope  $P_S$  used in Equation (9) was centered on the liquid side of the melting point of alumina at 1 atmosphere and 2312 K. This requires that the heat of reaction used in Equation (9) be reduced by the enthalpy required to heat the product mixture from standard conditions to 2312 K, including melting and other phase transformations. This calculation results in  $Q = -1.9 \times 10^6$  J/kg.<sup>15</sup> The calculated isentropes and families of porous Hugoniots for thermite reactants and products are plotted in Figures 1 and 2, respectively. The "anomalous Hugoniot" (positive P-V slope) for 50 percent porous reactant is due to large thermal pressure, as described by Zel'dovich and Raizer.<sup>17</sup>

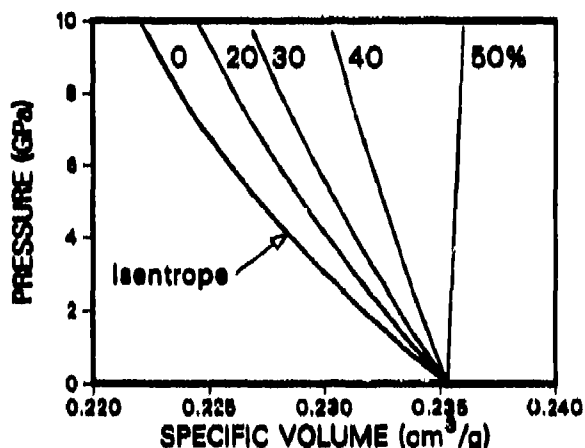


Figure 1. Calculated Reactant Isentrope and Family of Calculated Reactant Hugoniots for Porous Thermite Centered on Standard Conditions, Labeled With Respective Porosities.

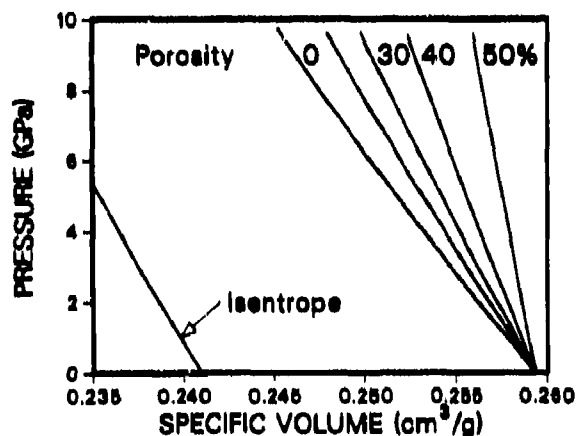


Figure 2. Calculated Product Reference Isentrope and Family of Calculated Product Hugoniots for Porous Thermite Centered on Standard Conditions Plus Heat of Reaction

To make comparisons to experimental shock wave data, a more useful way to represent the Hugoniot is in the pressure-particle velocity plane. The Rankine-Hugoniot equations can be used to write the particle velocity ( $u$ ) in terms of  $P$  and  $V$ :

$$u = \sqrt{P(V_0 - V)} \quad (11)$$

This equation was used to transform the reactant and product Hugoniot for 50 percent porous thermitite to the  $P$ - $u$  plane. Figure 3 shows that the pressure on the product Hugoniot is about 10 percent greater than that on the reactant Hugoniot at a given particle velocity. Similarly, the particle velocity is about 5 percent greater on the reactant Hugoniot compared to that on the product Hugoniot at the same shock pressure. This observation implies that experimental attempts to measure the reaction by performing Hugoniot measurements are bound to be complicated by the large uncertainties that are inherent for porous solids. Similarly, the time-resolved particle velocity measurements often applied to high explosives will also be insensitive to shock-initiated reactions in non-explosive solids.

### "HEAT DETONATIONS"

For reaction rates that are finite, but rapid enough to go to completion, the shock wave will first achieve a state on the reactant Hugoniot. After the reaction goes to completion

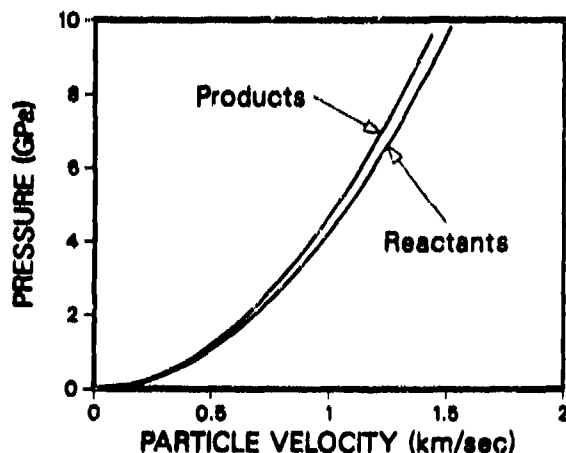


Figure 3. Calculated Reactant and Product Hugoniot for 50 Percent Porous Thermitite

the state behind the shock wave must lie on the product Hugoniot. It is well known<sup>18</sup> that a steady wave can only reach states intersected by the Rayleigh line, as illustrated in Figure 4 for a shock wave propagating into 50 percent porous thermitite. Since the product Hugoniot is steeper than the Rayleigh line at all possible points of intersection, an unsupported reaction wave will always decay.<sup>18</sup>

Such shock-induced reactions are not detonations in the conventional sense, because the products are not in the vapor phase and high pressures cannot be sustained upon expansion. However, examination of Figure 4 demonstrates that this type of reaction is the thermochemical equivalent of an overdriven detonation. The term "heat detonation" can be used to make the important distinction between these shock-initiated reactions, which rely on processes proceeding at the rate of the shock wave, and gasless combustion, which is controlled by the thermal and mass transport properties of the reacting material.<sup>19</sup>

### HEATING EFFICIENCY

One way to make a comparison between heat detonations and explosive detonations is to define a quantity called the "heating efficiency." The work efficiency has been used to describe the net amount of energy that can ideally be converted to work from the heat of reaction of a detonating explosive.<sup>20</sup> If  $Q$  is the

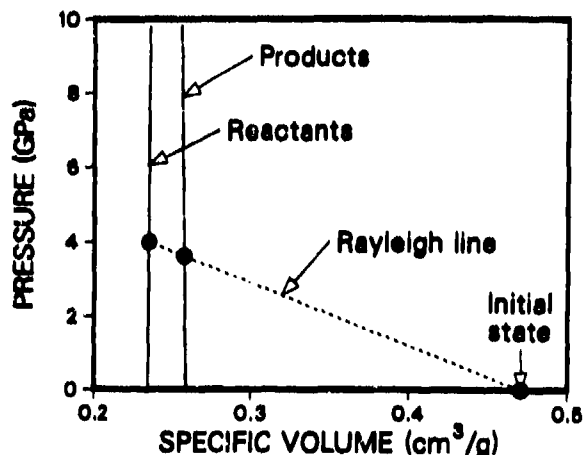


Figure 4. Calculated Reactant and Product Hugoniot for 50 Percent Porous Thermitite and Rayleigh Line Which Defines States Connected by Steady Reaction

heat of reaction, and  $V_f$  is the final specific volume of the reaction products after complete isentropic release, then the work efficiency is defined as

$$w = \left( \int_V^{V_f} P_S dv - \frac{1}{2} u^2 \right) / |Q| \quad (12)$$

By analogy, we can define the heating efficiency as the fraction of the heat of reaction that ideally remains in the reactants after they have isentropically released to zero pressure ( $h=1-w$ ). In Table 2, the calculated work and heat efficiencies for two explosives<sup>20</sup> are compared to those for 50 percent porous thermite shocked to 10 GPa. The >100 percent heat efficiency for the thermite indicates that some of the work associated with shock compression is converted to heat along with all of the chemical energy.

Table 2. Work and Heat Efficiencies

	RDX <sup>20</sup>	2Al/NH <sub>4</sub> NO <sub>3</sub> <sup>20</sup>	2Al/Fe <sub>2</sub> O <sub>3</sub>
Work Efficiency (%)	98	75	-29
Heat Efficiency (%)	2	25	129
Postshock Temperature (K)	374	1694	4600

## SHOCK TEMPERATURES

The temperatures along an isentrope are determined by integrating the differential equation obtained by substituting Maxwell's relations and the definition of the heat capacity  $C_V$  into the total differential of  $S(T, V)$ :

$$T dS = C_V dT + \left( \frac{\partial P}{\partial T} \right)_V T dV \quad (13)$$

with  $dS=0$ . For an isentrope centered on a reference state with temperature  $T_{ref}$  and volume  $V_{ref}$ , the temperature is

$$T_S = T_{ref} \exp \left[ \int_V^{V_{ref}} \frac{\gamma}{V} dv \right] \quad (14)$$

The temperature on the Hugoniot can be found by integrating Equation (13) and  $dE = T dS = P dV$ , setting  $dv=0$ :

$$\int_{T_S}^{T_H} C_V dT = \frac{V}{\gamma} (P_H - P_S) \quad (15)$$

These equations can be solved in simple form for the shock temperature if  $C_V$  and  $\gamma/V$  are both assumed to be constant:

$$T_H = \frac{1}{C_V} \frac{V_0}{\gamma_0} (P_H - P_S) + T_{ref} \exp \left[ \frac{\gamma_0}{V_0} (V_{ref} - V) \right] \quad (16)$$

Post-shock temperatures can be determined from the equation:

$$T_f = T_H \exp \left[ \frac{\gamma_0}{V_0} (V - V_f) \right] \quad (17)$$

Figure 5 depicts calculated temperatures for both reactant and product of 50 percent porous thermite.

Time-resolved shock temperature measurements have recently been performed on porous thermite mixtures.<sup>15</sup> The results for

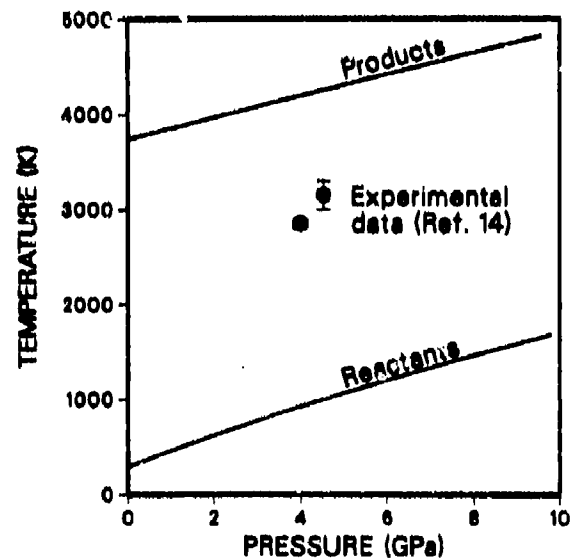


Figure 5. Calculated Temperatures for Reactant and Product Hugoniot of 50 Percent Porous Thermite

**Table 3. Shock Temperatures in Porous Thermite**

Experiment #	2274	2279
Porosity (%)	48	49
P <sub>H</sub> (GPa)	4.4-4.7	3.9-4.1
Measured T <sub>H</sub> (K)	3000-3300	2800-2900
Reactant T <sub>H</sub> (K)	980	910
Product T <sub>H</sub> (K)	4270	4200
Percent Reacted (%)	61-70	58-61

two experiments are listed in Table 3. The measured temperatures are much higher than those calculated for the reactants, but are also significantly less than those calculated for the products, implying that the reaction was not complete. A first-order estimate of the amount of reaction can be made by linearly interpolating between the two temperature calculations. A more accurate determination of the amount of reaction would require that phase transitions and variable specific heats are taken into account, an effort beyond the scope of the present paper.

### EFFECT OF VOLATILES

Thus far, all calculations have been based on the assumption that there are no volatile impurities in the mixed powders. Since many of the reactive powders that have been examined experimentally have small grain sizes (approximately 1 μm), and consequently large specific surface areas (about 10<sup>4</sup> cm<sup>2</sup>/g for smooth spherical particles), the possibility of a significant amount of surface-adsorbed water and other volatile impurities cannot be ignored. A monolayer of water adsorbed on such a powder (about 10<sup>15</sup> molecules/cm<sup>2</sup>) amounts to about 0.1 percent of the mass. Significant surface roughness or grain aspect ratios will give rise to even greater surface areas and amounts of impurities.

When the mass of a volatile impurity is a small fraction of the total mass, the resulting Hugoniot can be calculated by determining a

first-order correction to the Hugoniot of the pure powder. The family of equations of state of the mixture for various impurity mass fractions (*m*) can be expressed as the specific volume as a function of the intrinsic variables and of *m*:

$$V(P, T, m) = V^0(P, T) + m[V'(P, T) - V^0(P, T)] \quad (18)$$

where *V*<sup>0</sup> and *V*' are the specific volumes of the pure phase and the impurity, respectively. The family of Hugoniot can be written similarly:

$$V_H(P, m) = V^0(P, T_H) + m[V'(P, T_H) - V^0(P, T_H)] \quad (19)$$

where the shock temperature depends on *m*. The partial derivative can be written as

$$\left(\frac{\partial V}{\partial m}\right)_P = \left(\frac{\partial V^0}{\partial T_H}\right)_P \left(\frac{\partial T_H}{\partial m}\right)_P + V'(P, T_H) - V^0(P, T_H) \quad (20)$$

plus terms of order (*m*). This derivative can be inserted into the first order expansion

$$V_H(P, m) = V^0(P) + m\left(\frac{\partial V}{\partial m}\right)_P \quad (21)$$

to get the correction to the mixed Hugoniot. The following approximation can be made:

$$m\left(\frac{\partial T_H}{\partial m}\right)_P \approx T_H^0 - T_H = \Delta H/C_V \approx mQ/C_V \quad (22)$$

where *T*<sub>H</sub><sup>0</sup> is the shock temperature of the pure mixture, *Q* is the heat of reaction, and *C*<sub>V</sub> is the specific heat of the total mixture (including the impurity), which can be approximated by that for the pure mixture for small *m*. Implicit in these calculations is the assumption that the volatile component is chemically inert. If any significant reaction takes place between the volatile component and the thermite products, additional terms are required.

We can also make the approximation:

$$\left(\frac{\partial V^0}{\partial T_H}\right)_P = V\alpha = \gamma C_V / K_T \approx \gamma C_V / K_S$$

$$\approx \gamma C_V / (K_{OS} + PK'_{OS}) \quad (23)$$

and for  $V' \gg V^0$  we can write

$$V_H(P, m) \approx (1 - m)V_H^0(P)$$

$$+ m [Q_Y / (K_{OS} + PK'_{OS}) + V'(P, T_H)] \quad (24)$$

Equation (24) can be solved for water-bearing thermite by using the previously-determined thermite Hugoniot for  $V_H^0(P)$  and the Bakanova, et al.<sup>21</sup> equation of state of water for  $V'(P, T_H)$ , which is a fit to porous ice Hugoniot data with final (P, T) states in the same range as those of interest here. The resulting family of Hugoniot is plotted in Figures 6 and 7.

From Figure 6 it can be seen that, for certain combinations of initial porosity and volatile mass fraction, a Rayleigh line can be found that is tangent to the product Hugoniot. This fact indicates that a sustained detonation is thermochemically possible under those circumstances. As shown earlier for porous dry thermite, the shock-induced reaction can be described as an overdriven detonation that will decay when unsupported, because the product Hugoniot is always steeper than the Rayleigh line. By contrast, the Rayleigh line is steeper than the water-bearing thermite product Hugoniot below a given pressure. If this pressure is greater than that required for rapid shock-induced release of chemical energy, the sustained detonation will take place.

The purpose of Figure 7 is to show that measurements in the P-u plane are highly sensitive to volatile content, and attempts to determine amounts of reaction from pressure or particle velocity measurements are subject to very large errors unless the volatile content is precisely known. On the other hand, the temperature is influenced by the impurity, to first order, only to the extent that the heat of reaction is reduced by an amount proportional to the mass fraction, as noted in Equation (22). Thus, only shock temperature measurements

can provide an accurate determination of the amount of reaction that takes place under shock loading.

## GEOCHEMICAL DETONATIONS

The observation of rapid shock-induced chemical reactions in solids, combined with the fact that small amounts of water or other volatiles can control the ability of a reactive mixture to detonate, has important implications for earth science. Kuznetsov<sup>22</sup> outlined a set of criteria required for a detonation to take place due to a single-component phase transformation. These same criteria are met by a supercooled, volatile-saturated magma. One example of such metastable melts is described by Burnham and Davis.<sup>23-24</sup>

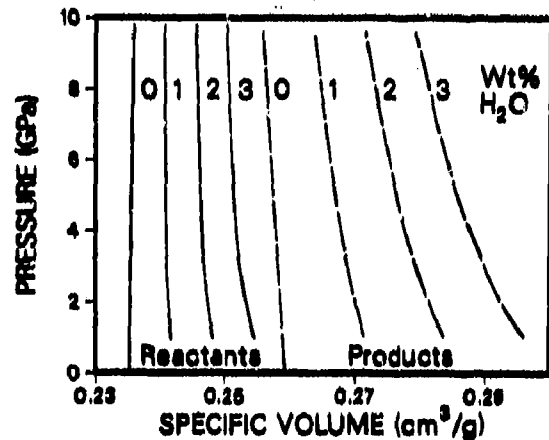


Figure 6. Family of Hugoniot for 50 Percent Porous Thermite Containing Various Amounts of Water

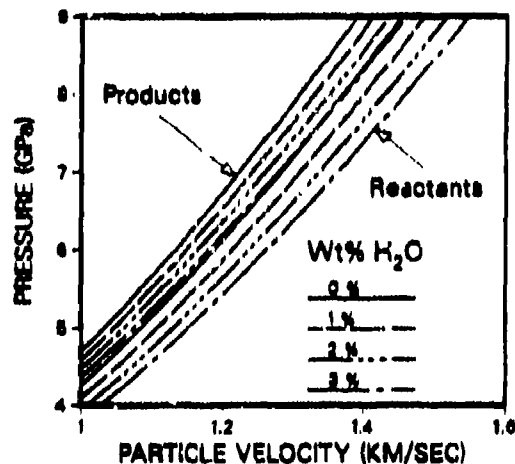


Figure 7. Pressure-Particle Velocity Diagram for Water-Bearing Thermite Hugoniot in Figure 6

The existence of phenomena akin to volcanic detonations has been invoked throughout history to explain structures now known to be impact craters.<sup>25</sup> Once the importance of hypervelocity impact was recognized, arguments involving natural detonations were dismissed, and volcanic eruptions are now considered to be decompression events in all cases. However, there is still significant controversy surrounding the origin of certain cryptoexplosion structures, which are geologic features suggestive of rapid, catastrophic (explosive) formation. Explanations based on internally-generated shock waves remain in the literature. For example, the Vredefort ring structure in South Africa contains rocks that appear to have experienced two separate events of shock deformation.<sup>26</sup> The improbability of two impacts at the same location has led to the hypothesis of an internal shock source for this formation. This hypothesis is supported by the observation of anomalous orientations of shatter cones at the site.<sup>27</sup>

The most famous debate between impact versus internal sources of shock waves concerns the 65 million year-old boundary between the Cretaceous and Tertiary geologic periods. The mass extinctions that took place at that time were attributed by Alvarez and others<sup>28</sup> to the hypervelocity impact of a large extraterrestrial body which left measurable traces of iridium and other rare elements in the boundary clays. This hypothesis gained strong support after the discovery of shocked quartz grains at the same boundary.<sup>29</sup> However, there are still a small number of workers who believe that shock features in quartz can be volcanically generated,<sup>30</sup> and that the Cretaceous-Tertiary event can be attributed to volcanic eruptions.

It has even been suggested that the May 18, 1980 eruption of Mt. St. Helens was triggered by some type of natural detonation.<sup>31</sup> This idea was based on seismic features that resemble those generated by an explosion at depth. However, because of timing uncertainties and lack of complete seismic coverage, there are other interpretations that are consistent with these data.<sup>32</sup>

Hypotheses that have invoked internally-generated shock waves have largely been ignored because a reasonable physico-chemical mechanism for volcanically-generated shock waves has never been proposed. To determine whether such a detonation is thermochemically possible, the product Hugoniot for a supercooled, water-saturated magma was calculated in a manner similar to that for the thermite. For simplicity, the magma was taken to consist of pure albite ( $\text{NaAlSi}_3\text{O}_8$ ). The extensive thermodynamic data on the albite-water system at high temperatures and pressures were used.<sup>23-24</sup> The product Hugoniot for water-saturated albite melt initially at  $P = 0.1$  GPa and  $T = 873$  K is plotted in Figure 8. If a Chapman-Jouguet detonation takes place, the C-J pressure is only about 0.6 GPa, which is very much lower than pressures normally achieved by a detonating high explosive. Since the product Hugoniot is dominated by the equation of state of water, it is unlikely that significantly higher shock pressures could be attained with more realistic melt compositions. The calculated detonation pressure is also not a strong function of the initial state. Moreover, when the shock pressure exceeds some value well below 10 GPa the equilibrium Hugoniot corresponds to the liquid, and the thermochemical possibility of detonation is lost.

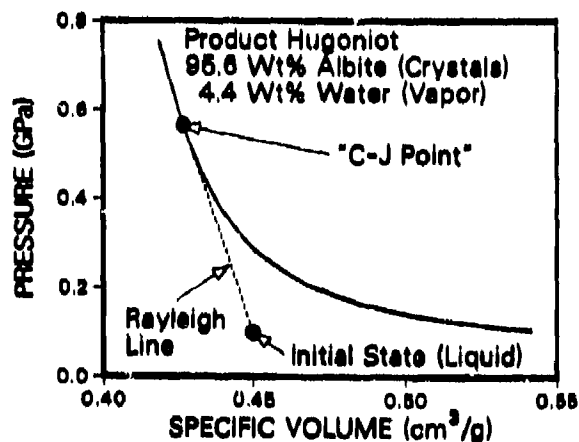


Figure 8. Calculated Hugoniots for Reactant and Product of Water-Saturated Undercooled Albite Melt. Rayleigh line indicates steady Chapman-Jouguet detonation.

According to these calculations, the pressures required to generate planar features diagnostic of shock deformation in quartz (10 GPa)<sup>34</sup> cannot be reached in a geochemical detonation, so an internal cause for the Cretaceous-Tertiary event can be eliminated. On the other hand, such detonations cannot be precluded on the basis of thermochemistry, and the implications for cryptoexplosion structures and explosive volcanism cannot immediately be dismissed.

While geochemical detonations are thermochemically allowed, there are serious questions as to whether they are kinetically possible. Since the concurrent crystallization and volatile exsolution required for geochemical detonations cannot occur without extremely rapid chemical transport, normal diffusion is out of the question. Instead, high strain-rate shock-induced shear transport, as described by Dremin and Breusov,<sup>35</sup> is necessary. The fact that significant reaction takes place in less than a microsecond in reactive powder mixtures implies that such transport can and does take place under some conditions. Whether or not a water-saturated supercooled silicate melt meets the requirements can only be determined experimentally.

## SUMMARY

A thermochemical model has been applied to shock-induced chemical reactions in porous solids. When the products consist of condensed phases only, the reaction front is thermochemically identical to an overdriven detonation. To distinguish this type of reaction from a conventional explosive detonation, the term "heat detonation" has been applied. This term is also descriptive in the sense that the chemical energy is converted mostly to heat rather than work, as is the case for detonations in explosives. The "heat efficiency" was defined by analogy to work efficiency in an attempt to quantify this difference.

Conventional Hugoniot, pressure, and particle velocity measurements are insensitive to shock-induced chemical reactions when the products do not include vapor phases. The experimental technique most sensitive to such reactions is the measurement of shock temperature. The addition of a volatile impurity

has a disproportionately large effect on the Hugoniot, but a small effect on the temperature, so Hugoniot, pressure, and particle velocity measurements are subject to impurity-induced errors, whereas temperature measurements are not. Moreover, a sustained detonation can become thermochemically possible when reactive powders contain a volatile component. The same type of mixing model that can determine the conditions required for detonations in volatile-bearing reactive powders predicts the possibility of geochemical detonations in volatile-saturated supercooled silicate melts. This latter possibility has significant implications in earth science.

## ACKNOWLEDGEMENTS

This work was performed at Sandia National Laboratories, supported by the United States Department of Energy under Contract # DE-AC04-76P00789. The helpful review by B. W. Dodson is gratefully acknowledged.

## REFERENCES

1. Graham, R. A., personal communication, 1989.
2. Graham, R. A., "Shock Compression of Solids as a Physical-Chemical-Mechanical Process," *Shock Waves in Condensed Matter -- 1987*, Monterey, CA, 20-23 Jul 1987, pp. 11-18.
3. Graham, R. A.; Morosin B.; Venturini, E. L.; Boslough, M. E.; Carr, M. J.; and Williamson, D. L., "Chemical Synthesis Under High Pressure Shock Loading," *Shock Waves in Condensed Matter*, Spokane, WA, 22-25 Jul 1985, pp. 693-711.
4. Graham, R. A.; Morosin, B.; Venturini, E. L.; and Carr, M. J., "Materials Modification and Synthesis under High Pressure Shock Compression," *Ann. Rev. Mater. Sci.*, Vol. 16, 1986, p. 315.
5. Kovalenko, A. N. and Ivanov, "Physico-chemical Transformations of Lead Nitrate in Mixtures with Aluminum Under the Effect of Shocks," *Combustion, Explosion, and Shock Waves*, Vol. 19, 1981, p. 481.

6. Batsanov, S. S.; Doronin, G. S.; Klochdov, S. V.; and Teut, A. I., "Synthesis Reactions Behind Shock Fronts," *Combustion, Explosion and Shock Waves*, Vol. 22, 1986, p. 765.
7. Boslough, M. B. and Graham, R. A., "Submicrosecond Shock-Induced Chemical Reactions in Solids: First Real-Time Observations," *Chem. Phys. Lett.*, Vol. 121, Nos. 4 and 5, 1985, p. 446.
8. Hornig, H.; Kury, J.; Simpson, R.; Helm, F.; and von Holle, W., "Shock Ignition of Pyrotechnic Heat Powders," *Proceedings of the Eleventh International Pyrotechnics Seminar*, Vail, CO, 7-11 Jul 1986, pp. 699-719.
9. Boslough, M. B., "Shock-Induced Chemical Reactions in Nickel-Aluminum Powder Mixtures: Radiation Pyrometer Measurements," *Chem. Phys. Lett.*, Vol. 160, Nos. 5 and 6, 1989, p. 618.
10. Maiden, D. E. and Nutt, G. L., "A Hot-Spot Model for Calculating the Threshold for Shock Initiation of Pyrotechnic Mixtures," *Proceedings of the Eleventh International Pyrotechnics Seminar*, Vail, CO, 7-11 Jul 1986, pp. 813-826.
11. Enikolopyan, N. S.; Khzardzhyan, A. A.; Gasparyan, E. E.; and Vol'eva, V. B., "Kinetics of Explosive Chemical Reactions in Solids," *Academy Nauk, USSR, Procs. Phys. Chem.*, Vol. 294, 1987, p. 567.
12. Horie, Y. and Kipp, M. E., "Modeling of Shock-Induced Chemical Reactions in Powder Mixtures," *J. Appl. Phys.*, Vol. 63, 1988, p. 5718.
13. Taylor, P. A.; Boslough, M. B.; and Horie, Y., "Modeling of Shock-Induced Chemistry in Nickel-Aluminum Systems," *Shock Waves in Condensed Matter--1987*, Monterey, CA, 20-23 Jul 1987, pp. 395-398.
14. Anderson O. L., "The Use of Ultrasonic Measurements Under Modest Pressure to Estimate Compression at High Pressure," *J. Phys. Chem. Solids*, Vol. 27, 1966, p. 547.
15. Boslough, M. B., "A Thermochemical Model for Shock-Induced Reactions (Heat Detonations) in Solids," *J. Chem. Phys.*, 1989, Vol. 92, No. 3, 1990, p. 1839.
16. Duvall, G. E. and Taylor, S. M., "Shock Parameters in a Two Component Mixture," *J. Composite Materials*, Vol. 5, 1971, p. 130.
17. Zel'dovich, Ya. B. and Raizer, Yu. P., *Physics of Shock Waves and High-Temperature Hydrodynamic Phenomena*, Academic Press, NY, 1967, pp. 685-784.
18. Courant, R. and Friedrichs, K. O., *Supersonic Flow and Shock Waves*, Springer-Verlog, New York, NY, 1976, pp. 204-232.
19. Merzhanov, A., "Theory of Gasless Combustion," *Archives of Combustion Processes*, Vol. 5, 1974.
20. Fickett, W. and Davis, W. C., *Detonation*, University of California Press, Berkeley, CA, 1979, pp. 35-39.
21. Bakanova, A. A.; Zubarev, V. N.; Sutulov, Yu. N.; and Trunin, R. I., "Thermodynamic Properties of Water at High Pressures and Temperatures," *Sov. Phys.--JETP*, Vol. 41, 1976, p. 544.
22. Kuznetsov, N. M., "Detonation and Gas-Dynamic Discontinuities in Phase Transitions of Metastable Substances," *Sov. Phys.--JETP*, Vol. 22, 1966, p. 1047.
23. Burnham, C. W. and Davis, N. F., "The Role of H<sub>2</sub>O in Silicate Melts I. P-V-T Relations in the System NaAlSi<sub>3</sub>O<sub>8</sub>-H<sub>2</sub>O to 10 Kilobars and 1000°C," *Am. J. Sci.*, Vol. 270, 1971, p. 54.
24. Burnham, C. W. and Davis, N. F., "The Role of H<sub>2</sub>O in Silicate Melts II. Thermodynamic and Phase Relations in the System NaAlSi<sub>3</sub>O<sub>8</sub>-H<sub>2</sub>O to 10 Kilobars, 700° to 1100°C," *Am. J. Sci.*, Vol. 274, 1974, p. 902.
25. Melosh, H. J., *Impact Cratering a Geologic Process*, Oxford University Press, New York, NY, 1989, pp. 3-13.

26. Lilly, P. A., "Shock Metamorphism in the Vredefort Collar: Evidence for Internal Shock Sources," *J. Geophys. Res.*, Vol. 86, No. B11, 1981, p. 10689.
27. Simpson, C., "Occurrence and Orientation of Shatter Cones in Pretoria Group Quartzites in the Collar of the Vredefort 'Dome': Impact Origin Precluded," *J. Geophys. Res.*, Vol. 86, No. B11, 1981, p. 10701.
28. Alvarez, L. W.; Alvarez, W.; Asaro, F.; and Michel, H. V., "Extraterrestrial Cause for the Cretaceous-Tertiary Extinction," *Science*, Vol. 208, No. 4448, 1980, p. 1095.
29. Bohor, B. F.; Foord, E. E.; and Modreski, P. J., "Mineralogic Evidence for an Impact Event at the Cretaceous-Tertiary Boundary," *Science*, Vol. 224, No. 4651, 1984, p. 867.
30. Carter, N. L.; Officer, C. B.; Chesner, C. A.; and Rose, W. I., "Dynamic Deformation of Volcanic Ejecta from the Toba Caldera: Possible Relevance to Cretaceous/Tertiary Boundary Phenomena," *Geology*, Vol. 14, 1986, p. 380.
31. Rice, A., "Shocked Minerals at the K/T Boundary: Explosive Volcanism as a Source," *Phys. Earth Planet. Interiors*, Vol. 48, 1987, p. 167.
32. Kanamori, H.; Given, J. W.; and Lay, T., "Analysis of Seismic Body Waves Excited by the Mount St. Helens Eruption of May 18, 1980," *J. Geophys. Res.*, Vol. 89, No. B3, 1984, p. 1856.
33. Burnham, C. W.; Holloway, J. R.; and Davis, N. F., *Thermodynamic Properties of Water to 1,000°C and 10,000 Bars*, Geological Society of America, Boulder, CO, 1969, p. 96.
34. Hürz, F., "Statistical Measurements of Deformation Structures and Refractive Indices in Experimentally Shock Loaded Quartz," *Shock Metamorphism of Natural Materials*, Mono Book Corp., Baltimore, MD, 1968, pp. 243-253.
35. Dremin A. N. and Breusov, O. N., "Processes Occurring in Solids Under the Action of Powerful Shock Waves," *Russian Chemical Reviews*, Vol. 37, No. 5, 1968, p. 392.

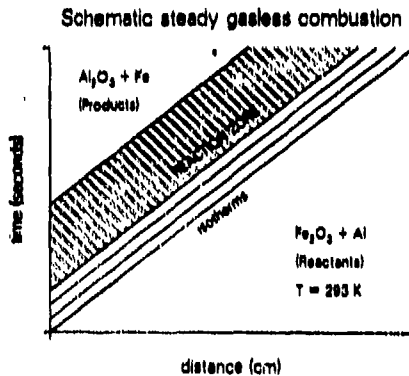
# A Thermochemical Model for Shock-Induced Chemical Reactions in Solids: Analogs and Contrasts to Detonation

M.B. Boslough  
Sandia National Laboratories  
Albuquerque, New Mexico

Ninth Symposium (International) on Detonation  
Portland, Oregon  
August 28 - September 1, 1989

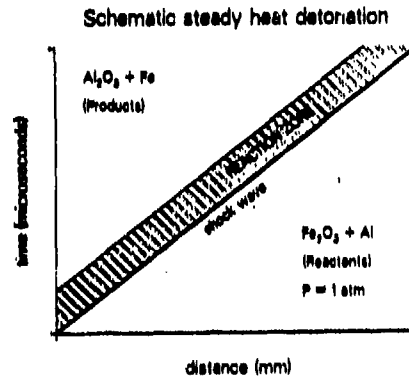
## GASLESS COMBUSTION

When a mixture of fine iron oxide and aluminum is ignited, it reacts to form aluminum oxide and iron, producing enough heat in the process to ignite adjacent layers and propagate a reaction front. This front moves very slowly (around 1 cm/sec), and is limited by heat flow and chemical diffusion rates. This process is analogous to deflagration, and is sometimes called "gasless combustion".



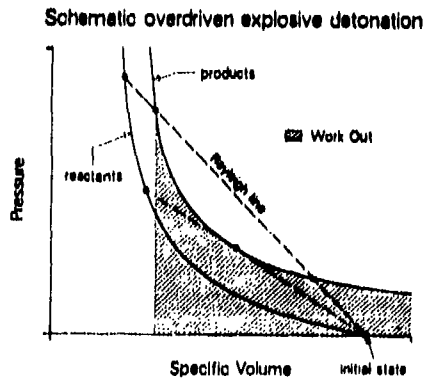
## HEAT DETONATION

When the same mixture is subjected to a sufficiently strong shock wave, the reaction can take place without heat or chemical diffusion. The temperature increases by shock heating, and the chemical substituents are brought together by high strain-rate shear deformation. The resulting reaction front moves at the shock velocity, and is analogous to a detonation. To distinguish this type of reaction from an explosive detonation, it can be called a "heat detonation".



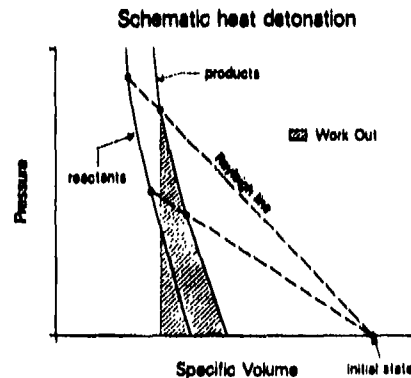
## EXPLOSIVE DETONATION

An overdriven steady detonation wave in an explosive is drawn with a Rayleigh line that crosses the product Hugoniot twice, because the products contain no vapor and expand to a volume much greater than that of the initial state. The work done by the products on the surroundings is proportional to the area under the product curve. When unsupported, the detonation will decay until the Chapman-Jouguet conditions are met.



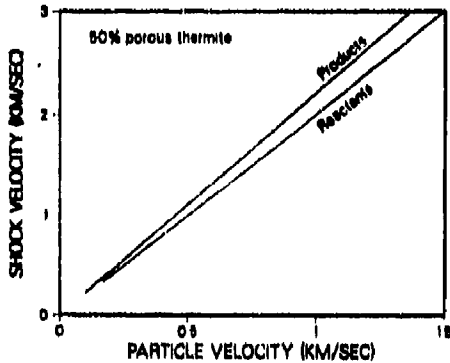
## HEAT DETONATION

The Rayleigh line for a heat detonation in a porous solid only intersects the product Hugoniot at one point, because the products contain no vapor and they expand to a volume less than that of the initial state. The work done on the surroundings is less than the work from the shock wave into the system, so all of the heat of reaction is retained by the products. An unsupported wave will continue to decay; Chapman-Jouguet conditions are never met.



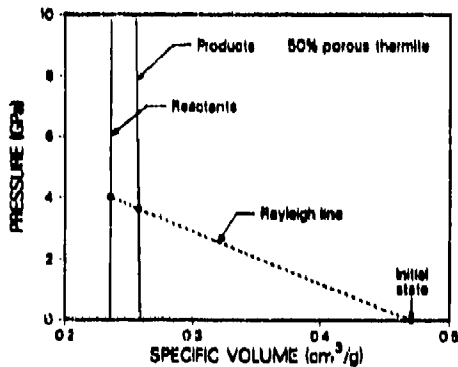
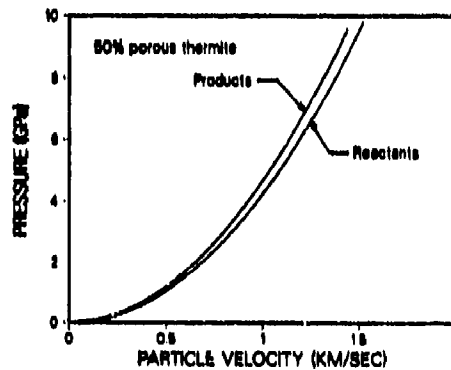
Shock temperature measurements  
are the most appropriate.

To determine which experimental approach is the most useful, the calculated reactant and product Hugoniot for 50% porous thermite are plotted in various planes. The variable that is by far the most sensitive to the reaction is the temperature.



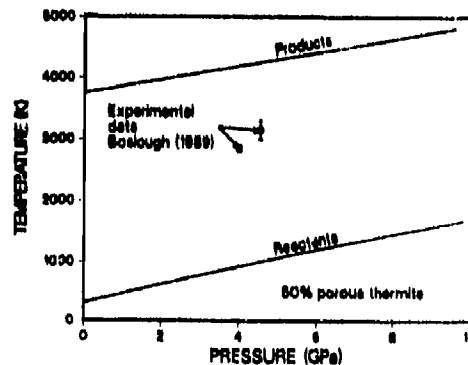
Experimental precisions are not good enough to confidently determine the amount of thermite reaction from data in the shock/particle velocity plane.

At a given pressure, the particle velocity associated with the product Hugoniot is 5% lower. Current experimental techniques cannot resolve the difference with acceptable precision.



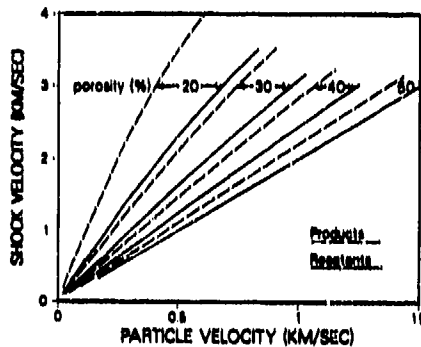
The difference in volume between the two Hugoniot is 10% of the total volume change upon compression. The amount of reaction would be difficult to resolve from data plotted in this plane.

A three hundred degree uncertainty in the measured shock temperature corresponds to only 10% of the difference between the two calculated Hugoniot. These radiation pyrometer data demonstrate that 60-70% of the thermite reacted when shocked to about 4 GPa.



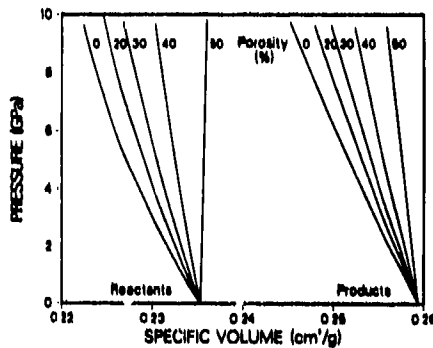
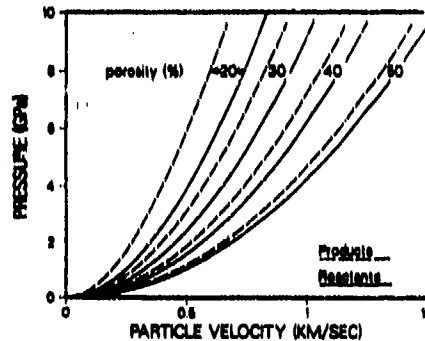
The effect of porosity  
on the calculated Hugoniot is large.  
Shock temperature measurements are best.

The thermite reactant and product  
Hugoniot were recalculated for various  
initial porosities to determine how  
porosity affects the ability of different  
measurement techniques to resolve the  
reaction. Temperature measurements are  
least sensitive to porosity.



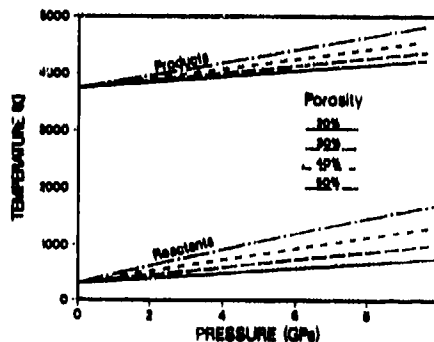
A 10% difference in porosity shifts  
shock/particle velocity Hugoniot  
more than a complete chemical  
reaction does.

The shock impedance of thermite is  
a much stronger function of porosity  
than of the amount of reaction.



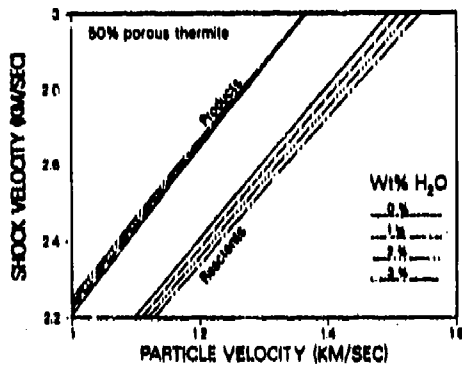
Pressure/volume Hugoniot are  
strongly affected by porosity.

Below 10 GPa, shock temperature  
measurements are relatively  
insensitive to porosity.



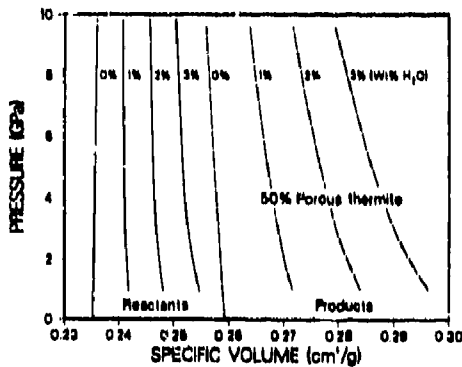
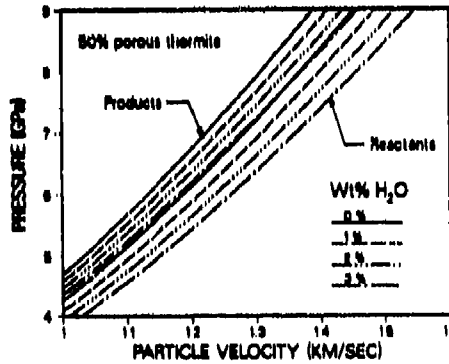
The role of volatile impurities on the Hugoniot is disproportionate. Shock temperatures are least affected.

Hugoniot were also recalculated for thermite containing up to 3% of water (by weight). Only shock temperature measurements remain a good option for observing the reaction in real time.



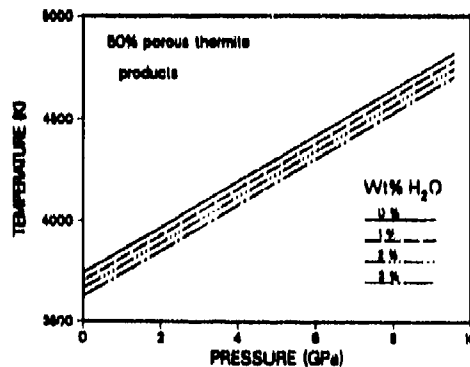
Volatiles have a small effect on shock/particle velocity Hugoniot, but the curves are too close together for good resolution.

A 3% amount of water translates the pressure/particle velocity Hugoniot as much as a complete reaction does.



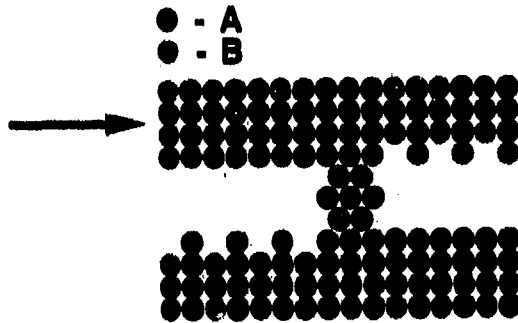
Specific volumes are greatly increased for water-bearing thermite, particularly at low shock pressures.

The effect of small amounts of water on shock temperatures is negligible.



## Volatile-controlled detonations

The addition of a volatile component gives rise to a reaction product in the vapor phase, and allows the possibility of an explosive detonation controlled by rapid shock-induced solid state chemical reactions.

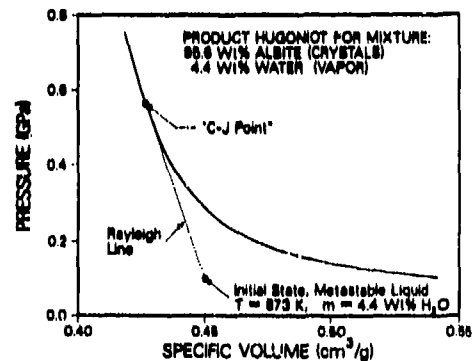


High strain-rate shear transport takes the place of diffusion. Nucleation and growth of phases can occur on sub-microsecond time scales (Dremin and Breusov, 1968).

## Geochemical detonations

The detonation of a supercooled, water-saturated silicate melt is thermochemically equivalent to that of a porous reactive solid with a water impurity. The shock-induced crystallization and steam exsolution require the same kind of high strain-rate shear transport that controls the heat detonations.

When water-saturated albite ( $\text{NaAlSi}_3\text{O}_8$ ) melt at 873 K and 0.1 GPa is shocked, and the state achieved is in chemical equilibrium (albite crystals and steam), a Chapman-Jouguet detonation can take place. The detonation pressure is dominated by the water equation of state, so pressures reached by detonations in other silicate melts will be similar.



## Implications of geochemical detonations

Explosive volcanic activity caused by a rapid pressure rise due to a sudden release of chemical energy has been suggested in attempts to explain a number of observations in earth science.

Calculations based on conventional detonation theory provide upper bounds to pressures and rates associated with the release of chemical energy.

### CRYPTOEXPLOSION STRUCTURES

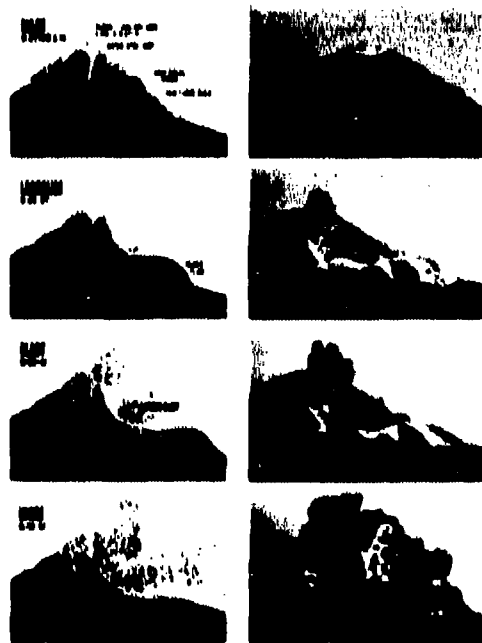
Most "cryptoexplosion structures" are attributed to meteorite impact. However, rocks from the Vredefort structure in South Africa show evidence of having experienced two separate shock events (Lilly, 1981). The low probability of two impacts at the same location points toward an internally-generated shock.

### EXPLOSIVE VOLCANISM

The magnitude 5.0 earthquake that triggered the massive landslide leading to the 8:32 am May 18, 1980 eruption of Mt. St. Helens had seismic features suggesting an underground explosion: the lack of azimuthal dependence on P-wave polarity, positive first motion, and a very weak S wave (Kanamori et al., 1984).



"You're kidding! ... I was struck twice by lightning, too!"



## CRETACEOUS/TERTIARY EVENT

Shock features in quartz grains from the Cretaceous/Tertiary boundary have provided the most convincing evidence for an impact as the cause for mass extinctions 65 million years ago. A shock wave from a geochemical detonation would be too weak to generate these features, which require 10 GPa (Horz, 1968).

Etched quartz grain recovered from explosive loading to 16 GPa by Cygan and Boslough (1989).

---



## REFERENCES

---

1. Boslough, M.B., *J. Chem. Phys.* (submitted, 1989).
2. Cygan, R.T. and Boslough, M.B. (unpublished, 1989).
3. Dremin, A.N. and Breusov, O.N., *Russian Chemical Reviews* 37 (1968).
4. Horz, F., in "Shock Metamorphism of Natural Materials", edited by French, B.M. and Short, N.M., Mono, Baltimore, 1968.
5. Kanamori, H., Given, J.W. and Lay, T. *J. Geophys. Res.* 87, 1856, (1984).
6. Lilly, P.A., *J. Geophys. Res.* 86, 10689, (1981).

# REACTIVE MODELING IN SHOCK INITIATION OF HETEROGENEOUS EXPLOSIVES

M. Quidot and J. Groux  
Societe Nationale des Poudres et Explosifs  
Centre de Recherches du Bouchet  
91710 Vert-Le-Petit, FRANCE

*As part of a program on the shock initiation of explosives, wedge test experiments and in situ pressure measurements in Lagrangian analysis have been investigated for design applications in explosive systems and safety/vulnerability evaluations. The reaction rate derived from these experiments for an HMX based cast cured PBX was used to compute two-dimensional diverging and converging detonations. Comparisons with experimental data are discussed.*

## INTRODUCTION

Reactive modeling in shock initiation of high explosives can be used for design applications in explosive systems and for safety vulnerability evaluations. The former case involves relative high pressures, short time durations and run distances to detonation. On the contrary, the later is generally characterized by low shock pressures long times and distances to detonation. Wedge-test experiments and in situ pressure measurements have been investigated with respect to these applications. Wedge-test experiments give a space-time diagram of shock and detonation wave and times and run distances to detonation. In a study of impact obliquity effect in this experiment we find that space time diagrams are relatively inaccurate, but transition points are quite well defined. So we think that reaction rates based on "pop-plot" are quite sufficient for buildup to detonation modeling in design applications. However, it is insufficient for safety vulnerability analysis and it must be completed with pressure measurements at low shock pressures to evaluate the hot spots ignition and early low pressure reaction growth.

In this study, wedge-test experiments and Lagrangian analysis of pressure measurements have been performed on an HMX-based cast-cured PBX. A reaction rate equation

derived from these experiments has been used in DYNA 2D code (Reference 1) in order to compare two-dimensional calculations with diverging and converging experiments.

## PROPERTIES OF THE PBX STUDIED

The high explosive composition used in this study is an HMX-based cast-cured PBX—86 percent HMX, 14 percent polyurethane binder, density  $1.71 \text{ g/cm}^3$  with detonation velocity 8380 m/s and CJ pressure 30 GPa. The equation of state for detonation products is determined by a cylinder test experiment and HUGONIOT for the unreacted material is derived from light gas gun impact experiments with pressure measurements. The coefficients for JWL equations of state are listed in Table 1.

Table 1. JWL Coefficients

	UNREACTED	PRODUCTS
A (Mbar)	49.30	6.96
B (Mbar)	-1.66	0.025
$R_1$	7.44	4.4
$R_2$	3.72	0.94
$\omega$	1.2	0.43
$E_0$ (Mbar)	0.00938	0.088

## LAGRANGIAN ANALYSIS OF PRESSURE MEASUREMENTS

A Lagrangian analysis of pressure measurements has been performed at a low shock pressure and is described in Reference 2. A 90 mm light gas gun is used to generate a planar sustained shock at 4.1 GPa. Pressure profiles were recorded with embedded manganin - constantan gauges at five Lagrangian locations: 0, 3.17, 6.17, 12.2, and 15.2 mm. Numerical integrations of conservation laws along path lines allow the calculation of other state variables. The degree of reaction and reaction rate can be calculated with classical assumptions on mixing rules for solid and gas phases and equations of state for the detonation products and unreacted explosive. Reaction rates are about  $0.1 \mu\text{s}^{-1}$  at impact plane and  $.55 \mu\text{s}^{-1}$  at the distance of 15 mm. We find a low pressure dependence on reaction rate. Reaction rate at high pressure (CJ pressure) may be about 10 to 100 times greater and then cannot be reasonably obtained from extrapolation of these values. Such results have been shown in Reference 3. So reaction rates deduced from these experiments may be used for low shock pressure, but pressure dependence must be modified for high shock pressure.

## WEDGE TEST EXPERIMENTS

The experimental arrangement shown in Figure 1 is very similar to the wedge test described in References 4 and 5. A 10 mm thick aluminum plate is propelled on a 6 mm thick aluminum plate which supports a double

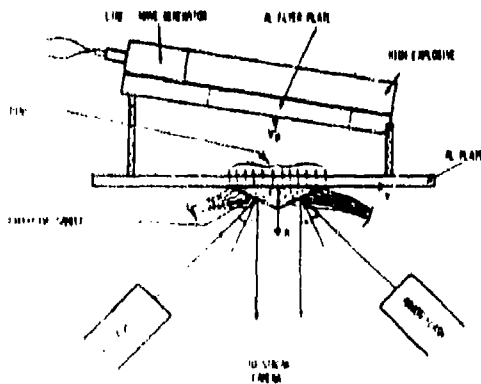


Figure 1. Wedge Test Arrangement

wedge ( $20^\circ$  wedge angle) sample to be tested. Two rows of six pins are used to measure flyer plate velocities and control planar shock. The shock front moving along the two slant faces is recorded. These two faces are covered with a 0.05 mm thin aluminized film. Light from pyrotechnic flash is reflected into a streak camera until the shock wave arrival occurs. Film records are digitalized and space time diagrams of the shock propagation are obtained. Experiments were performed in the range of 5-10 GPa.

## NUMERICAL EVALUATION OF ERRORS IN WEDGE TEST

Results from wedge test experiments are very sensitive to non-plane impact due to wedge angle  $\beta$  which is small to ensure 1D flow in the direction of impact. Two dimensional reactive calculations have been performed in order to evaluate experimental errors in this test. Four cases with constant obliquity  $\epsilon = \pm 5$  mrd (calculations a, a'),  $\epsilon = \pm 15$  mrd (b, b') and two cases with obliquity varying linearly from  $\epsilon = 0$  to  $\epsilon = 10$  mrd (c) and from  $\epsilon = -10$  mrd to  $\epsilon = 0$  (c') along the impact plane have been realized. These values are somewhat high, but ensure good numerical evaluations of errors. The flyer plate velocity is  $V_p = 1600$  m/s. To allow an objective and fine definition for the transition point, the space time diagram of the shock propagation is fitted by a least-squares 4th B-splines with three optimized knots (e.g., see Reference 6) corresponding to the acceleration, transition and steady detonation regions. Following the definition by Dick in Reference 7, the transition point is defined as the point where the acceleration is maximum and then is equal to the second optimized knot. Results of calculations are summarized in Table 2. Space time diagrams and shock velocity vs. distance from the impact plane calculated on the slant face of the wedge are shown in Figures 2 and 3. Results point out that the run distance to detonation is not modified by non-plane shock, but that the time to detonation and the shock (and steady detonation) velocity depends on obliquity.

Assuming a 1D propagation shock wave, errors on shock velocity can be evaluated.

**Table 2. Distance to Detonation  $x$ , Time to Detonation  $t$  and Initial Shock Velocity  $U_0$  Dependence on Non-Uniformity in Wedge Test**

	$x$ (mm)	error (%)	$t$ ( $\mu$ s)	error (%)	$U_0$ (mm/ $\mu$ s)	error (%)
0(ref.)	6.51		1.274		4.820	
a	6.35	-2.5	1.193	-6.3	5.030	4.3
a'	6.50	-0.2	1.323	3.9	4.640	-3.7
b	6.50	-0.1	1.107	-13.1	5.440	12.8
b'	6.58	1.1	1.452	14.0	4.370	-9.4
c	6.41	-1.6	1.075	-15.6	5.690	18.1
c'	6.56	-0.8	1.451	13.9	4.190	-13.0

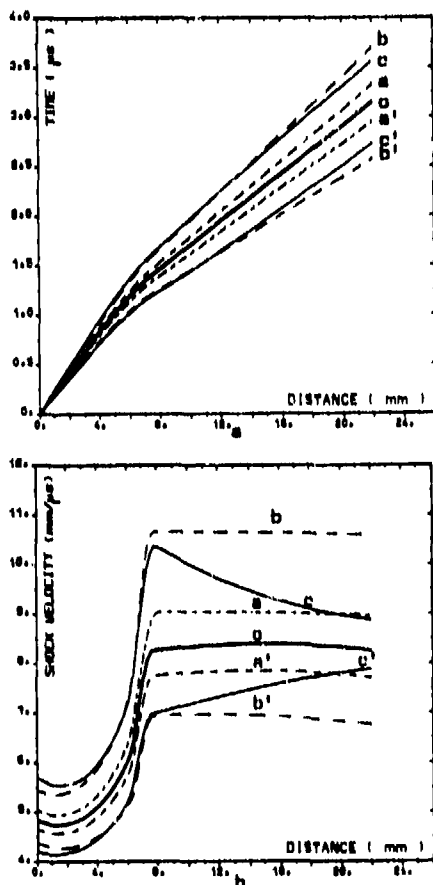


**Figure 2. Non-Uniformity Initiation Effects on Space Time Diagram (a) and Shock Velocity vs. Distance (b)**

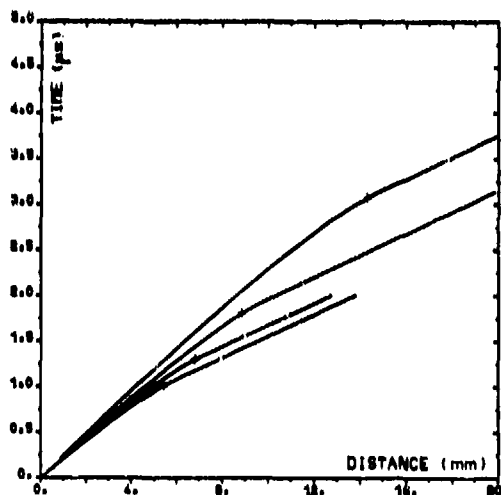


**Figure 3. Space Time Diagrams**

With this assumption, arrival time on the slant face of the wedge at a distance  $x$  from the impact face is:

$$t = \int_0^x \frac{dx}{U(x)} + \Delta t \quad (y = (X-x)/tg\beta) \\ - \Delta t \quad (y = X/tg\beta) \quad (1)$$

where  $U(x)$  denotes the shock velocity function,  $\Delta t(y)$  is the isochronic defect along the impact face (see Figure 1) and  $X$  ( $= 25$  mm in the calculations) is the depth of the wedge sample.

Derivation of Equation (1) leads to apparent shock wave (and steady detonation)  $U^*(x)$  as measured on the slant face function of real shock wave velocity  $U(x)$  and isochronic defect:

$$U^*(x) = \frac{U(x)}{1 - U(x) \frac{d\Delta t}{dy} / \tan \beta} \quad (2)$$

The equation shows the non-symmetric effect of non-plane impact and that common experimental case  $d\Delta t/dy > 0$  leads to apparent overshoot. Shock and steady detonation velocity found by 2D calculations compare well—within 1 percent to Equation (2)—and demonstrate the validity of 1D flow assumption. Our conclusions from this study are that shock velocity—and shock pressure if deduced from initial shock velocity—and time to detonation are sensitive to non-plane shock impact, but that run distance to detonation, if objectively and finely defined, is independent of non-uniform initiation.

### WEDGE TEST RESULTS

The run distance to detonation (mm) - pressure (GPa) data are expressed by  $x = 268 p^{-1.75}$ . The shock pressure is calculated with shock HUGONIOT from light gas gun impact experiments (Table 1) on account of previous discussion and also early reactions in the shock front. A Lee and Tarver<sup>8</sup> model,

$$\frac{dF}{dt} = 100 (25 - F) (\rho/\rho_0 - 1)^4 + 1000 (1 - F)^{101} F^{371} \rho^3,$$

with the geometric function deduced from Lagrangian analysis can fit reasonably well these results. Space time diagrams and shock velocities vs. distance back to the transition point for 5.3, 7.1, 8.3, and 9.4 GPa shock pressure are shown in Figures 3 and 4.

### DIVERGING DETONATION

A mushroom-shaped sample as described in Reference 9 has been used to study diverging detonation. The sample shown in

Figure 5 consists of a cylinder of diameter  $d$  (mushroom stalk: initiator) which detonates in a hemisphere of diameter  $\Phi$  (mushroom head: target). This detonation wave emergence on the hemisphere surface is recorded by a streak camera. Experiments with  $d = 10$  mm ( $\Phi = 20, 30, \dots, 60$  mm),  $d = 20$  mm ( $\Phi = 30, \dots, 60$  mm) and  $d = 30$  mm ( $\Phi = 40, 60$  mm) have been performed. For each stalk diameter, the detonation wave arrival times can be plotted as a function of the angular location  $\alpha$  or the distance  $x$  from the initiated plane as shown in Figure 5.

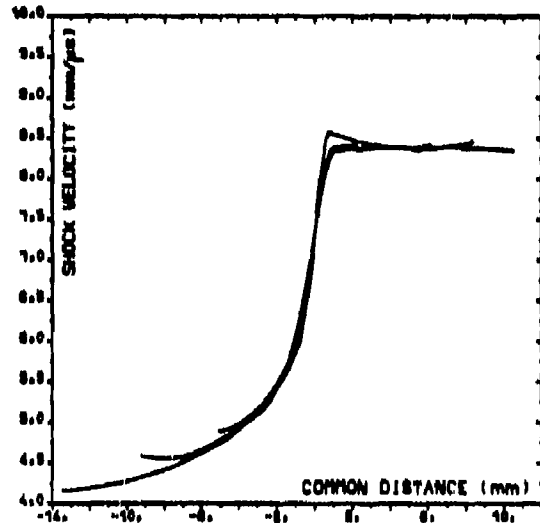


Figure 4. Shock Velocity vs. Common Distance

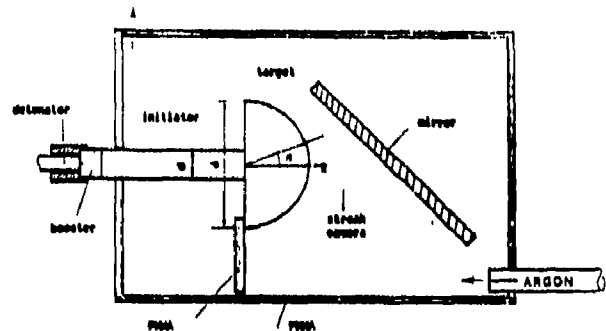
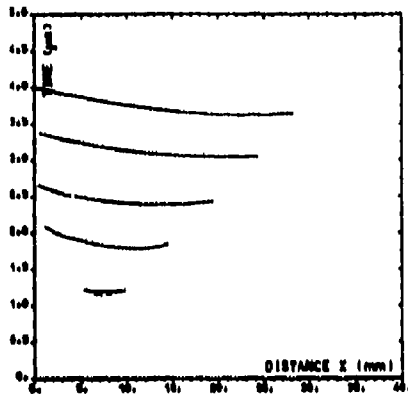
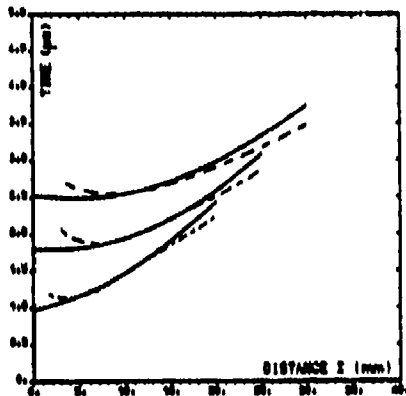


Figure 5. Experimental Arrangement for Diverging Detonation

For a 30 mm diameter initiator detonation expands radially (Figure 7) and numerical results are in good agreement with experimental measurements as shown in Figure 6. For a 10 mm diameter initiation detonation



a



b

Figure 6. Diverging Detonation - Experiment - Calculation --- for  $d = 10$  mm,  $\varnothing = 20$  mm, ...,  $\varnothing = 60$  mm (a) and  $d = 30$  mm,  $\varnothing = 40$ , ...,  $\varnothing = 60$  mm (b)

fails initially to expand radially as shown in Figure 8. Numerical results and experimental measurements indicate both a non-detonating region  $\alpha \geq 60^\circ$  for the 20 mm diameter target (Figure 6a). For the others, target diameters experiments indicate that the extent of non-detonating region decreases, but numerical results do not reproduce that because the reaction law is likely too sensitive to rarefaction waves.

## CONVERGING DETONATION

The experimental arrangement used for converging detonation has been described previously in References 10 and 11 and is shown in Figure 9.

The outer driving explosive ( $D_r = 8750$  m/s,  $P_{c_j} = 36.6$  GPa,  $\rho_0 = 1.83$  g/cm<sup>3</sup>) induces an overdriven detonation in the inner

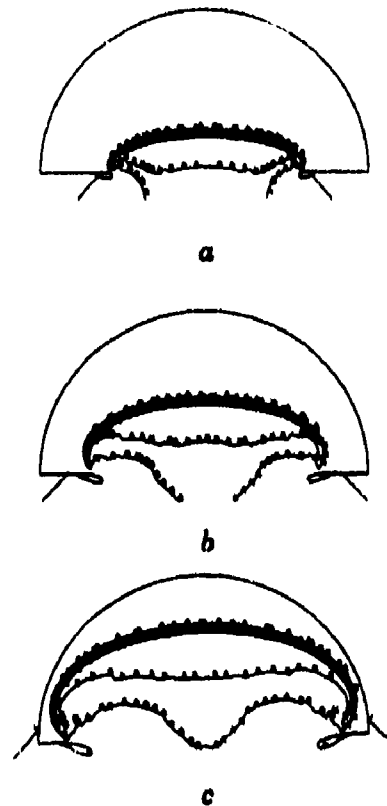


Figure 7. Diverging Detonation,  $d = 30$  mm,  $\varnothing = 60$  mm - Contours of Pressure (5, 10, 25 GPa) at Time  $0.6 \mu\text{s}$  (a),  $1.4 \mu\text{s}$  (b),  $2.25 \mu\text{s}$  (c)

explosive which is observed for different run distance with a streak camera. Both calculations and experiments indicate a quasi-steady flow beyond a distance of about 100 mm. Figure 10 shows experimental detonation profiles for 52.3 mm distances and calculated and experimental profiles for 52.3 mm are compared in Figure 10b. Calculations and experiments are also in agreement for greater distances if the mesh size is fine enough. The calculated pressure contours in Figure 10c shows a high pressure region  $P > 1.3 P_{c_j}$  in the inner explosive.

## DISCUSSION AND CONCLUSIONS

From this study, we conclude that "Pop" plot diagrams from wedge-test experiments are useful to calibrate global reaction rate in spite of non-uniformity in initiation. However, complex mechanisms of

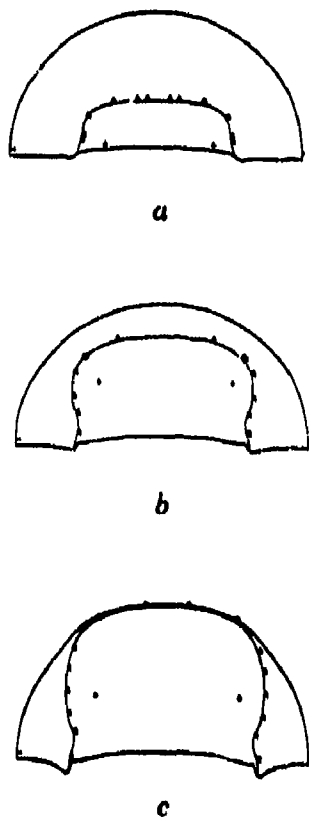


Figure 8. Diverging Detonation,  $d = 10$  mm,  $\varnothing = 20$  mm - Reactive Front at  $0.5 \mu\text{s}$  (a),  $1 \mu\text{s}$  (b),  $1.4 \mu\text{s}$  (c)

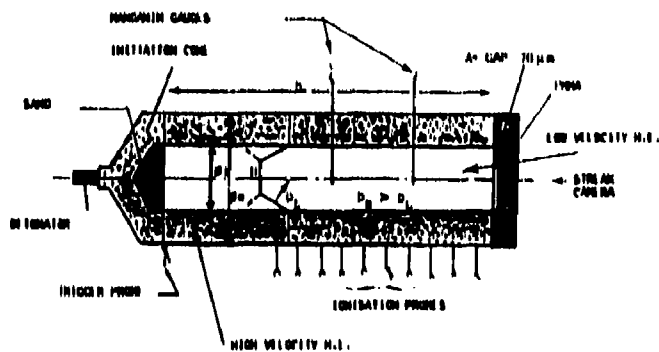


Figure 9. Experimental Setup for Converging Detonation

shock initiation of high explosive cannot be modeled only with these kinds of results. We have not yet time to expand a complete reaction rate law as a function of pressure to reproduce all the experiments described in this paper, but it is not perhaps the best way and

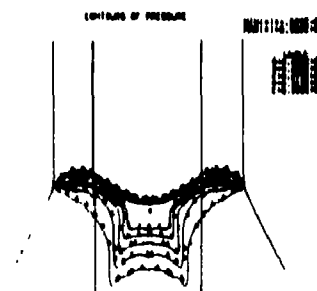
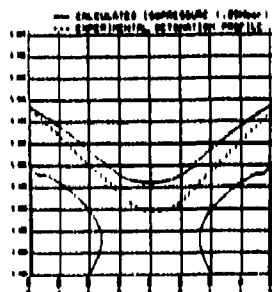


Figure 10. Converging Detonation. Experimental Detonation Profile (a), Calculated and Experimental Profile (b), Pressure Contours (c) for a 52.3 mm Distance

we rather plan to use these experiments, including Lagrangian analysis of pressure measurements, wedge test and diverging and converging detonation on an HMX-based cast cured PBX, to improve a more physically-based model.

## REFERENCES

1. Hallquist, J. O., *User's Manual for DYNA2D*, LLNL 18756, Jan 1984.
2. Kayser, V. and Bonthoux, F., "Use of Lagrangian Analysis to Determine Reaction Rate Laws for Hydrocode," *Proceedings of the International Symposium on Pyrotechnics and Explosives*, Beijing, China, 12-15 Oct 1987, pp. 556-563.
3. Vorthmann, J.; Andrews, G.; and Wackele, J., "Reaction Rate from Electromagnetic Gauges Data," *Proceedings of the Eighth International Symposium on Detonation*, Albuquerque, 15-19 Jul 1985, pp. 99-110.
4. Campbell, A. W.; Davis, W. C.; Ramsay, J. R.; and Travis, J. R., "Shock Initiation of Solid Explosives," *Phys. Fluids*, Vol. 4, No. 4, 1961, pp. 511-521.
5. Droux, R. and Mouchel, C., in *Proceedings of Symposium HPD*, Paris, 27-31 Aug 1978, p. 103.
6. IMSL, Fortran Subroutines of Mathematics and Statistics.
7. Dick, J. J., "Buildup to Detonation in Solid High Explosives During Plane Shock Initiation: Some Comparisons," in *Proceedings of the Eighteenth Symposium on Combustion*, 1981, pp. 1623-1629.
8. Lee, E. L. and Tarver, C. M., *Phys. Fluids*, Vol. 23, No. 12, 1980, p. 2362.
9. Bonthoux, F.; Deneuille, P.; and De Longueville, Y., "Diverging Detonation in RDX and PETN Based Cast-Cured PBX," *Proceedings of the Seventh Symposium on Detonation*, MD, 16-19 Jun 1981, pp. 408-415.
10. Souletis, J. and Groux, J., "Continuous, Observation of Mach Bridge and Mach Phenomena," *Proceedings of the Eighth Symposium on Detonation*, Albuquerque, 15-19 Jul 1985, pp. 431-439.
11. Souletis, J. and Nouguez, B., "Experiments and Numerical Simulation of Overdriven Detonation Waves," *Proceedings of the International Symposium on Pyrotechnics and Explosives*, Beijing, China, 12-15 Oct 1987.

This work has been performed under the auspices of the French Ministry of Defense (STPE).

# REACTIVE FLOW ANALYSIS AND ITS APPLICATIONS

Graeme A. Leiper  
Nobel's Explosives Company, Ltd.  
Stevenston, KA20 3LN, UNITED KINGDOM

and

David L. Kennedy  
ICI Australia Operations Pty Ltd.  
Newsom Street, Ascot Vale 3032, AUSTRALIA

*Finite element hydrocodes, the standard tools for hydrodynamic analysis of problems involving shocks and explosives, usually embody two means of modeling explosives, a simple prescribed geometric wave progression, and a reactive flow model in which the development of the detonation depends on the local flow parameters. In this paper one type of reactive flow model is described and assessed against a conventional Huygens wave propagation method. A reactive flow model based on a simple pressure dependent reaction rate was calibrated on the one-dimensional shock to detonation behavior of an RDX/wax composition at high voidage. The sensitivity of the parameterisation to mesh size was examined. The ability of the model to predict the effect of small changes in density was demonstrated. The model was used to investigate various aspects of explosive performance: corner-turning, Mach stem creation, lateral and axial metal pushing, and desensitization. Identical calculations were executed using the geometric wave approach. Two applications of the reactive flow model, one in fuse train design, the other in fragment impact on rocket motors were reported. The hydrocode DYNA2D was used for all simulations.*

## INTRODUCTION

The tremendous increase in computing power in recent years has greatly increased the scope of the explosives designer to predict accurately the performance of complex devices. Central to such work has been the hydrodynamic wave propagation code, or hydrocode: a numerical solution algorithm which can be used by the modeller to specify an arbitrarily complex problem in terms only of the initial geometry, material behavior, and boundary conditions. The code then predicts the time evolution of the solution given the relevant flow equations and constitutive relationships. The quality of such simulations is crucially dependent on the detail of the material models

within the code. In detonics problems, the results are only as reliable as the physical correctness of the detonation physics employed.

Two generic types of explosive models have been developed for use in hydrodynamic codes: a computationally cheap geometric method, and a more complex reactive flow technique. In the former, the behavior of the explosive is assumed to be that of an Ideal Chapman-Jouguet wave, moving through the mesh at a prescribed velocity in all directions simultaneously. The locus of the wave front is only dependent on the number and position of sites which are lit at the beginning of the calculation, and is thus invariant with

confinement, initiator effects, etc. This is often referred to as the Huygens construction. In the latter case, the behavior of the explosive is based on explicit shock induced chemical reaction in the energetic material. The explosive is treated as a chemically active medium in which conversion between the unreacted and reacted state is governed by a rate law dependent only on the local thermodynamic state of the material. The explosive is described by an unreacted equation of state, an equation of state for the reaction products, and a set of chemical reaction rate parameters. Compared to the Huygens technique, the complexity of the calculation is greatly increased, but no ad hoc assumptions are required on the structure or development of the detonation wave, which becomes a function of the local flow field. This is referred to as reactive flow analysis.

## REACTIVE FLOW MODELS

In virtually all commercial and military explosives, the chemical reaction can be modelled by a hot spot initiated grain burning mechanism. Hot spots are generated during shock compression, as small intensely heated areas. Typically these occur at slip planes, such as grain or crystal boundaries, and at density discontinuities such as voids or binder/filler interfaces. Any reaction which is initiated within these areas, then propagates a flame or mass explosion throughout the remainder of the explosive. The heat release rate therefore depends on the intrinsic chemical reactivity of the ingredients of the explosive, i.e. the thermal explosion time and burning velocity, and the geometrical distribution of initiation sites in the explosive. Two different classes of model can be identified, depending upon the treatment of the geometrical term in the rate law.

The first type of reactive flow models was those that lumped the effects of reaction geometry and specific chemical reaction rate together in a global expression. These sought only to reproduce the reaction rate of the particular explosive of interest without any physical interpretation of the functional form of the rate law. The simplest of these was Forest Fire,<sup>1</sup> which used a simple pressure dependent rate law,

$$\dot{\beta} = (1 - \beta) f(p)$$

where  $\beta$  was degree of chemical reaction,  $f(p)$  a polynomial in pressure and  $\dot{\phantom{x}}$  denoted time differentiation. Forest Fire reproduced the run to steady state detonation from a sustained shock impulse, but did not reproduce the reaction zone in the explosive.

Wackerle<sup>2</sup> used a modified Arrhenius reaction rate function to fit experimentally measured reaction rates from electromagnetic gauge data. Mader<sup>3</sup> used a similar rate law to resolve the reaction zone in military explosives. These models had an advantage in ease of calibration due to the small numbers of adjustable parameters present. As they did not explicitly model multi-phase, multi-component aspects of formulations, they were ineffective for practical application.

The next generation of rate laws sought to decouple the effects of intrinsic chemical reactivity and reaction geometry. The progenitor of all such work was the Ignition and Growth model,<sup>4</sup>

$$\dot{\beta} = I(1 - \beta)^x (v_0/v_e)^r + G(1 - \beta)^x \beta^y p^z$$

where  $v$  was specific volume, subscripts  $o, e$  referred to the porous unshocked and dense shocked states respectively, and  $I, G, r, x, y, z$  were fitting factors. Advantages were the relatively small number of adjustable parameters, the explicit voidage dependency, the use of the  $r$  exponent to model various hot-spot creation processes, e.g. plastic work, jetting, etc., and the use of the  $x$  and  $y$  parameters to describe the reaction geometry. Constraints were the implicit dependency on mesh size and bulk viscosity, and the inability of the model to reproduce sustained and sharp shock initiation data with one parameter set. Extensions to the model removed some drawbacks at the expense of increased numbers of adjustable parameters and ensuing parameterization problems.<sup>5</sup>

Other workers, notably Partoum,<sup>6</sup> and Johnson, Tang and Forest,<sup>7</sup> have used mixed pressure and temperature dependent laws to describe the shock initiation event. Johnson et al. have been successful in modeling the changes in shock initiation behavior with

changing density, and in modeling dynamic desensitization.

The model of shock initiation due to Kennedy,<sup>8</sup> was formulated after the work of Lee and Tarver and took the form of

$$\dot{\beta} = I\phi(\beta - \beta_h)(\beta - \beta_h)^{2/3}(v_0/v_0)^r +$$

$$G(1 - \beta)^{2/3}\beta^{2/3}pp_a^z$$

where  $\beta_h$  was the mass fraction of hot-spot phase, usually taken as the initial void volume,  $p_a$  the initial shock pressure, and  $\phi(\beta - \beta_h)$  a unitary step function. The rate law had only four adjustable parameters and had the capability of both precursor shock desensitization due to void closure, and of sharp shock/sustained shock initiation through the  $pp_a^z$  term in the growth function. There remained a sensitivity to mesh size and bulk viscosity but this was reduced by introduction of the  $\phi(\beta - \beta_h)$  term which eliminated the ignition term after the hot-spot had been consumed. Moreover, as  $\beta_h$  was a function of the initial voidage, the rate law could predict the effect of small changes in density on the shock initiation thresholds.

Kennedy has investigated the performance of this model in some depth. It has been shown to reproduce gross shock initiation data over large pressure ranges and to give realistic descriptions of wave growth within the explosive during shock initiation.<sup>8,9</sup> In this work the usefulness of the model in simulating various situations is assessed.

## ONE-DIMENSIONAL SUSTAINED SHOCK INITIATION

The explosive PBX 9407 was chosen because of the availability of 'Pop Plot' data in a non-linear region, and the usefulness of the material as a generic stemming composition at low density, and pressed fill at high density. An analytic one-dimensional shock initiation model was used to derive a reactive flow parameter set for the explosive at a density of 1.6 g/cc. Agreement with available experimental shock to detonation data<sup>10</sup> was obtained by manipulation of the four fitting parameters I, G, r, z in the rate law.

When these parameters were used in the model embedded in the hydrocode DYNA2D,<sup>11</sup> a mesh resolution of 100/mm reproduced the 'Pop Plot' over the pressure range 1.25 to 5 GPa. The predicted 'Pop Plot' was curved upwards concave as found experimentally. Below 1.25 GPa the run distance to detonation was underestimated by 10 percent, reflecting too little curvature in the computed 'Pop Plot.' The effect of cell size on these calculations was investigated by altering the resolution through the range 100/mm to 5/mm. Reducing the resolution of the mesh resulted in 'Pop Plots' which corresponded to significantly shorter runs to detonation than found experimentally. At 50/mm the run distance was between 20 and 50 percent too short at high and low pressures respectively; see Figure 1. The wave structure was still resolved. This error remained virtually constant with increasing mesh coarseness to below 10/mm, at which point the calculation ceased to have meaning due to the small number of cells in the analysis. Below 30/mm, the wave structure became severely degraded.

These results were contrasted to those published on Composition B3,<sup>9</sup> where decreasing mesh resolution gave longer run distances to detonation for any incident pressure. The anomaly in the two sets of results was resolved

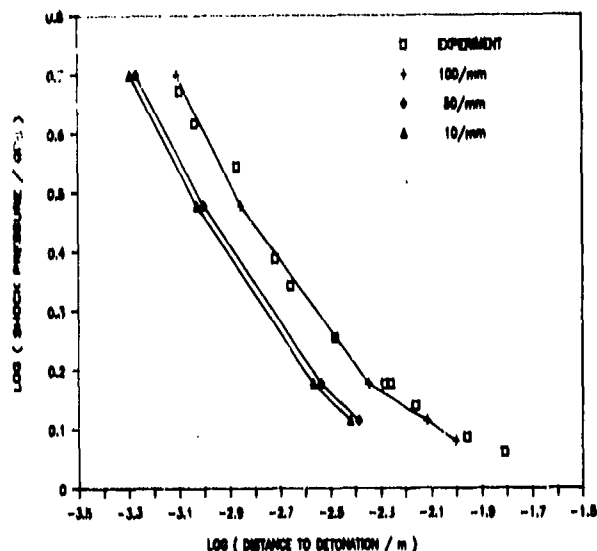


Figure 1. Effect of Mesh Size on Run to Detonation

by the major qualitative difference in the initiation behavior of PBX 9407 and Composition B3, as seen in the nature of the pressure distribution during buildup. In Composition B3 the pressure at the shock front was virtually constant during buildup, until the shock was engulfed by the pressure wave due to reaction. In PBX 9407 the shock pressure grew steadily throughout the buildup process. The different effects of mesh resolution on 'Pop Plot' predictions in the two cases reflected the different buildup behavior: for Composition B3, coarse meshing slowed the critical initiation event, the reaction wave traveling toward the front; but for PBX 9407, coarse meshing increased reaction at the shock front and hence accelerated buildup. Experimental evidence of both types of buildup has been found.<sup>4,12</sup>

## TEST PROBLEMS

The object in setting test problems was to contrast the behavior of the reactive flow model to a typical Huygens type model. Extensive experimental validation was not required, and the test meshes were designed to minimize computational problems.

The spatial resolution of the mesh was governed by the dimensions of the reaction zone in the explosive, typical zoning lay between twenty and two hundred zones per millimeter depending on the accuracy required of the analysis. In all cases time steps of the order of 1 ns were considered good. The models themselves were computationally expensive to use because of the complexities of the chemical reaction rate routines. Application of the technique was therefore limited by the size and speed of the computer facility being used. All test cases were physically small, and were represented in two dimensions.

In all cases the explosive used was PBX 9407 at a density of 1.767 g/cc. The cases were run using both the reactive flow model, parameterized as above, and a Huygens wave construction method. The reactive flow model was adjusted to the new density only by decreasing the mass of hot-spot material in line with the reduced voidage, and using the appropriate equations of state for the explosive

at the new density. Identical meshes were used for both techniques.

## Failure Thickness

The first test was to predict the failure thickness for PBX 9407 at 1.767 g/cc. Only the reactive flow model was used in this case. A 5° wedge running from 0.4 mm to 0.2 mm, initiated by a line generator of PBX 9407 was modelled as a half space in plane geometry. The detonation wave was seen to weaken as it progressed down wedge until edge rarefaction caused failure, i.e. the shock wave and reaction wave ceased to be coincident in space. The pressure and mass fraction contours at a position corresponding to a wedge thickness of 0.3 mm are shown in Figure 2. This was the computed critical thickness, and corresponded well with a measured value of 0.305 mm.<sup>10</sup> The structure apparent in the extent of reaction plot of Figure 2, was not a function of the spatial discretization used in the simulation, but reflected the effect of lateral rarefactions on the detonation process.

## Corner-Turning and Desensitization

The topics of corner-turning and desensitization are intimately linked. Corner-turning refers to the ability of the wave to overcome divergence in the flow field caused by an increase in area or change in direction of the detonation wave. Desensitization refers to a decrease in the shock sensitivity of an explosive due to passage of a low pressure shock wave, of insufficient strength to initiate significant chemical reaction, but of sufficient magnitude to physically activate the hot-spot forming mechanisms. Often both these phenomena occur simultaneously, wave divergence causing the shock to weaken such that it cannot promptly self-initiate the explosive.

A typical corner-turning event was modelled, with a small diameter cylinder of explosive initiating a larger cylinder, Figure 3. Two examples were investigated, one where the smaller diameter charge was encased in high density, low sound speed polymer, the other where aluminum was used as the case material.

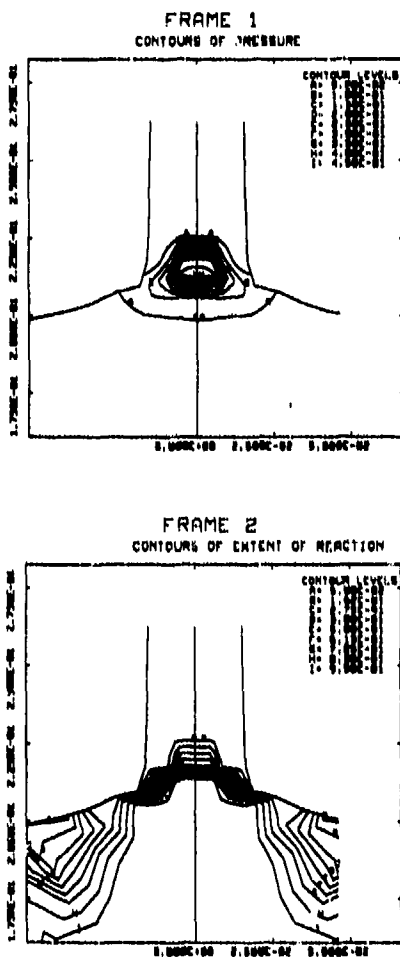


Figure 2. Pressure Contours for Wedge at Failure

The corner turning event was controlled by two phenomena: divergence of the detonation wave; and pre-shocking of the larger diameter charge by the shock traveling in the case material. The Huygens wave model and the reactive flow model predicted different results. The Huygens model gave a uniformly growing wave front. Immediately the wave passed over the corner, in frames 7 and 8. The reactive flow model predicted the effect of the divergence on the pressure field, and the effect of the lower shock pressure in the divergent shock on self-initiation in the explosive. This was evident from the highly curved wave forms predicted throughout the corner turning event, frames 1, 2, 3, and 4.

The effect of pre-shocking was also seen in the reactive flow analysis. When the polymer was used as the case material, a small area of desensitization, evidenced by an area of unreacted explosive, was seen midway along the case-explosive interface, in frame 5. This corresponded to the point where the shock transmitted through the polymer case to the explosive was not sufficiently strong to initiate the explosive before the detonation wave from the corner turning event arrived. The detonation wave had, however, to propagate through the pre-shocked region, which remained unreacted. When aluminum was used, the shock from the confinement was sufficient to initiate the explosive at all points along the interface, aiding the corner-turning process, in frame 6.

### Initiation Wave Interaction

The interaction of detonation waves emanating from multiple initiation sites is of interest. In this test the interaction of a toroidal detonation was studied as it coalesced along the charge axis. The mesh was of a metal-cased right cylindrical charge, peripherally initiated by a small slug of explosive; see Figure 4. During the early stages of coalescence, both the Huygens and reactive flow analysis gave similar results: frames 1 and 4. This corresponded to a region of massive overdrive of the detonation. However as the coalescence process progressed, the results of the two models diverged, frames 2 and 5. The reactive flow model predicted a flatter wave front and larger Mach disk—frames 3 and 6—due to the effect of the enhanced pressure field in the disk on the local chemical reaction rate.

### Acceleration of Metal

The ability of these models to predict correctly the acceleration of metal was tested by examining the axial and lateral velocity created by a charge detonating within a small diameter thick cylinder, capped at one end. The charges were plane wave initiated. The velocity time profiles of the wall and end cap were in good agreement for both models, reflecting the small effect that the reaction zone had in accelerating metal which was many times its own thickness. For very thin

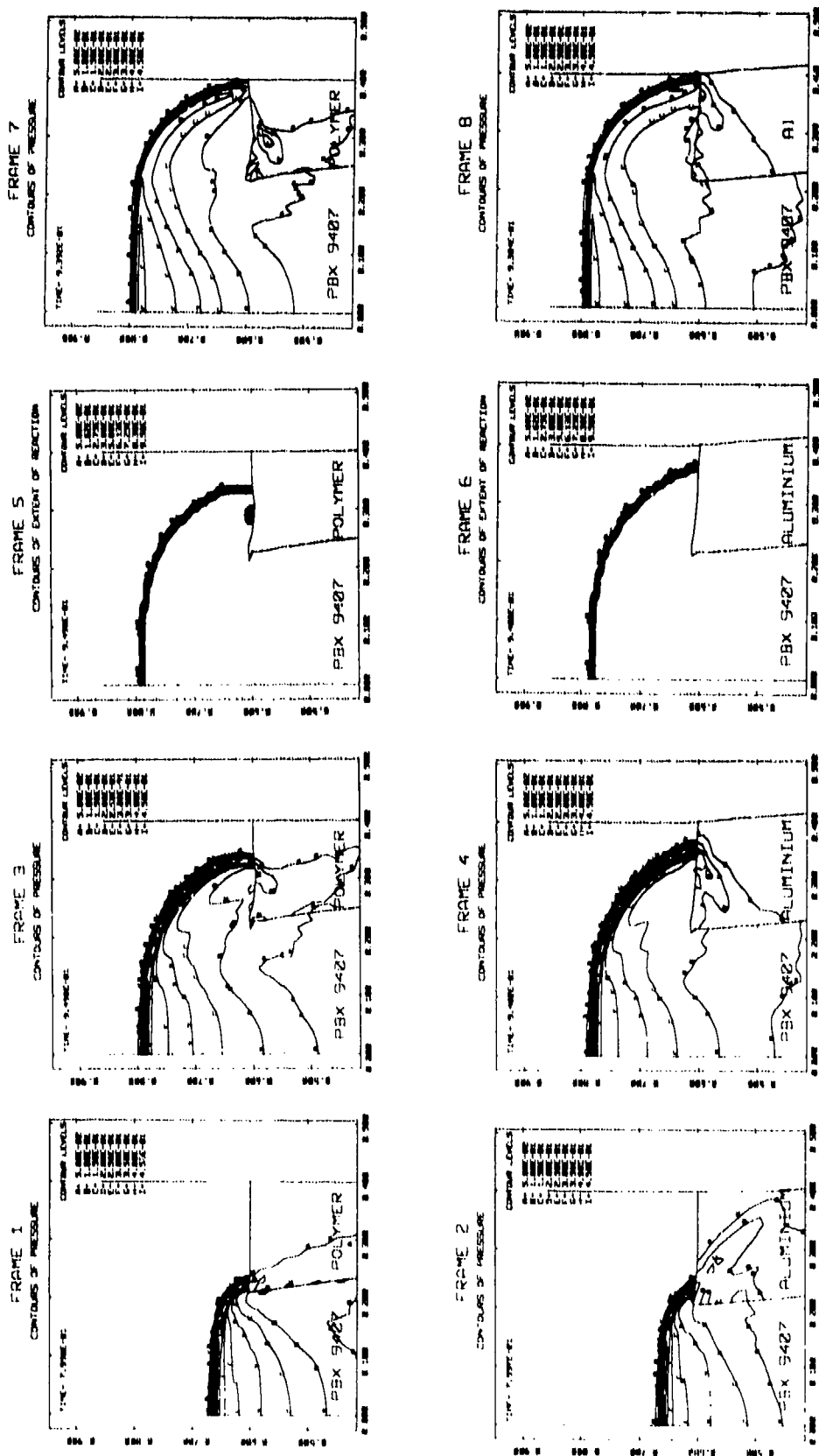


Figure 3. Corner-turning and Desensitization. The upper diagrams, Frames 1, 3, 5, 7, show the wave turning a polymer corner. The lower diagrams, Frames 2, 4, 6, 8 show the same simulation, but with the polymer replaced by aluminum. Frames 1 to 6 were generated using the reactive flow model: 1, 2 show pressure contours at 0.8 μs, Frames 2, 4 pressure contours at 0.94 μs; and 5, 6 the extent of reaction contours at 0.94 μs. Frames 7, 8 were generated using a Huygen's wave construction: they show the pressure contours at 0.94 μs.

metal there was a significant difference between the two results. This was in good agreement with experimental results.<sup>13</sup>

## TYPICAL APPLICATIONS

It has been demonstrated above that for regions close to initiation events, or for events which have a length scale comparable to the reaction zone in the explosive, reactive flow analysis yields a more precise simulation of the detonation event. Two classes of problems have been identified where such a technique could be of practical value.

## Initiation Train Analysis

Explosive fuse trains are used to convey and amplify a detonation from its point of initiation, the detonator, to its point of use. Reactive flow analysis can be used to improve the design in such applications by maximizing the robustness of the system whilst minimizing explosive mass. One such application involved a miniature electric detonator, initiating a low density explosive stemming and high density nitramine main charge; see Figure 5. The detonator was held in a clip, slightly above a shuttle which contained the stemming covered by an aluminum septum. Below the shuttle,

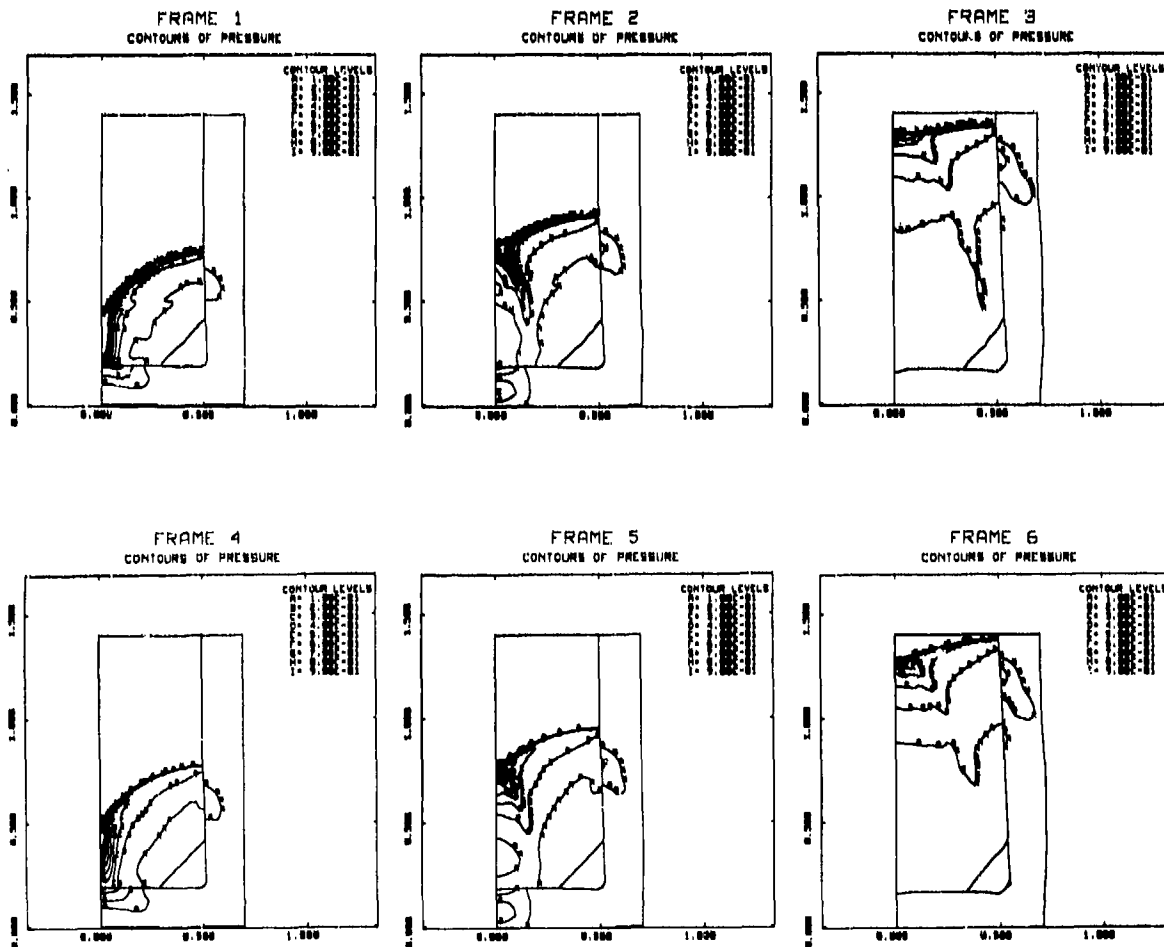


Figure 4. Initiation Site Interactions

separated by a small air gap was a pellet leading down to the main mass of explosive. In the simulation all explosives were modeled using a reactive flow model, except the azide in the detonator which was Huygens burned. In the simulation the detonator reacted to throw a small flyer across the air gap onto the septum: frame 1. The shock of the impact caused the stemming to detonate. The shock in the stemming was initially very curved: frame 2. The reacted stemming expanded across the air gap onto the pellet causing a detonation wave to propagate into the remaining explosive: frame 3. The wave had to corner-turn out of the pellet into the main charge. This was aided by the shock traveling in the material

confining the explosives: frame 4. The growth of the wave into the main charge was also aided by shock interaction at the interface between explosive and the casing in the top left corner: frame 5. The wave continued to move throughout the charge in a divergent fashion: frame 6. The high wave curvature even after a long run distance demonstrated the need for reactive flow analysis of the whole process.

### Hazard Analysis

Accidental initiation is a major hazard in the storage and application of all energetic materials. Two important topics in this field are sympathetic detonation where the shock

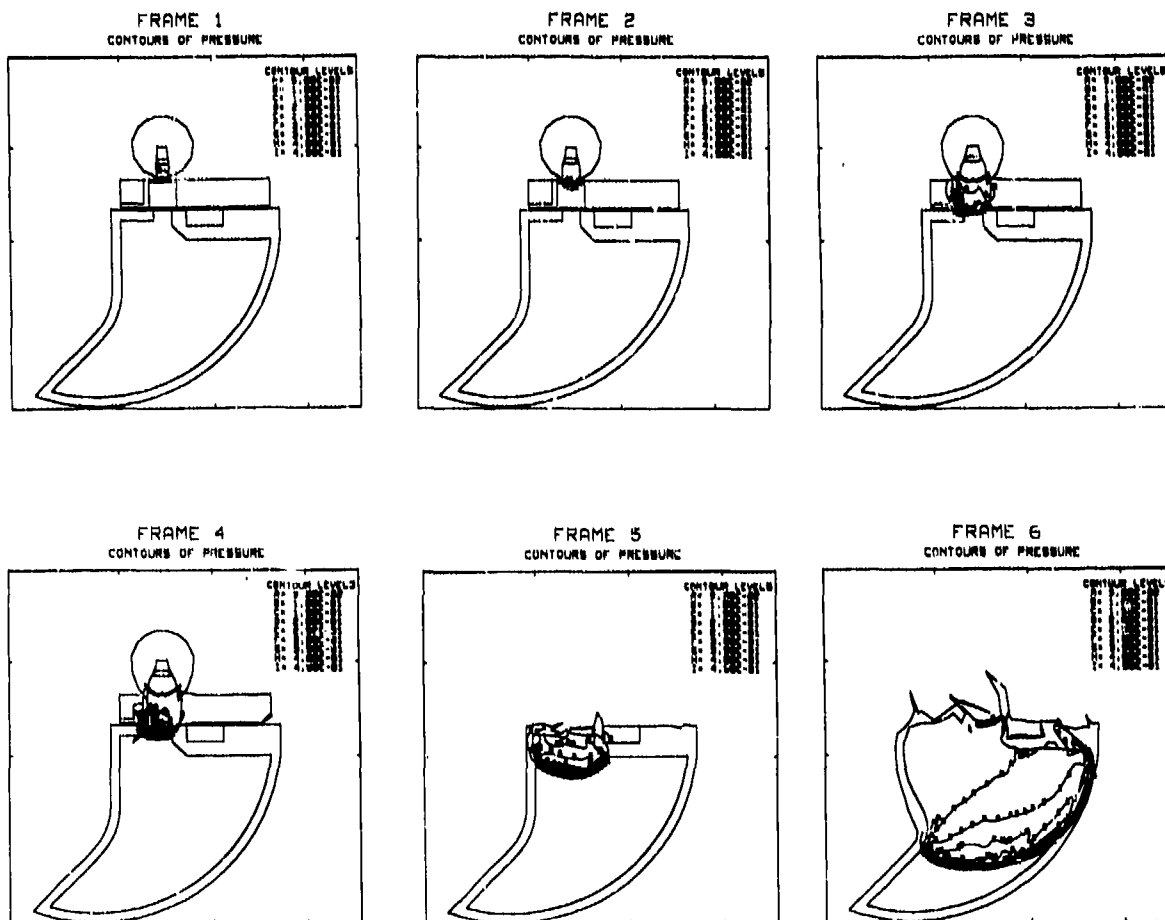


Figure 5. Typical Fuse Train Analysis

from one charge initiates a neighbor, and fragment impact where debris accelerated from a first event initiates a second. Examples of the use of reactive flow analysis in modeling sympathetic events have been published previously.<sup>9</sup>

A calculation was performed on the shock initiation of an aluminum cased rocket motor, filled with a typical Extruded Double Base propellant, by a flat nose steel projectile, Figure 6. The critical impact velocity for detonation was found to be between 800 m/s and 850 m/s. At 850 m/s the projectile initiated a highly divergent detonation—frame 1—which moved as a growing hemispherical cap through the propellant—frame 2—until it interacted

with the rocket motor walls: frame 3. At that point two waves occurred, a detonation moving forward, and a retonation moving rearward: frames 4 and 5. Small areas of desensitization on the periphery of the impact site were found, as seen in the mass fraction contours: frame 6. For an impact velocity of 800 m/s the shock in the propellant quickly died and little material reacted, in the time scale of the simulation (20  $\mu$ s).

## CONCLUSION

The efficacy of reactive flow analysis in modeling all classes of shock to detonation phenomena has been demonstrated. An overview of the various techniques used in

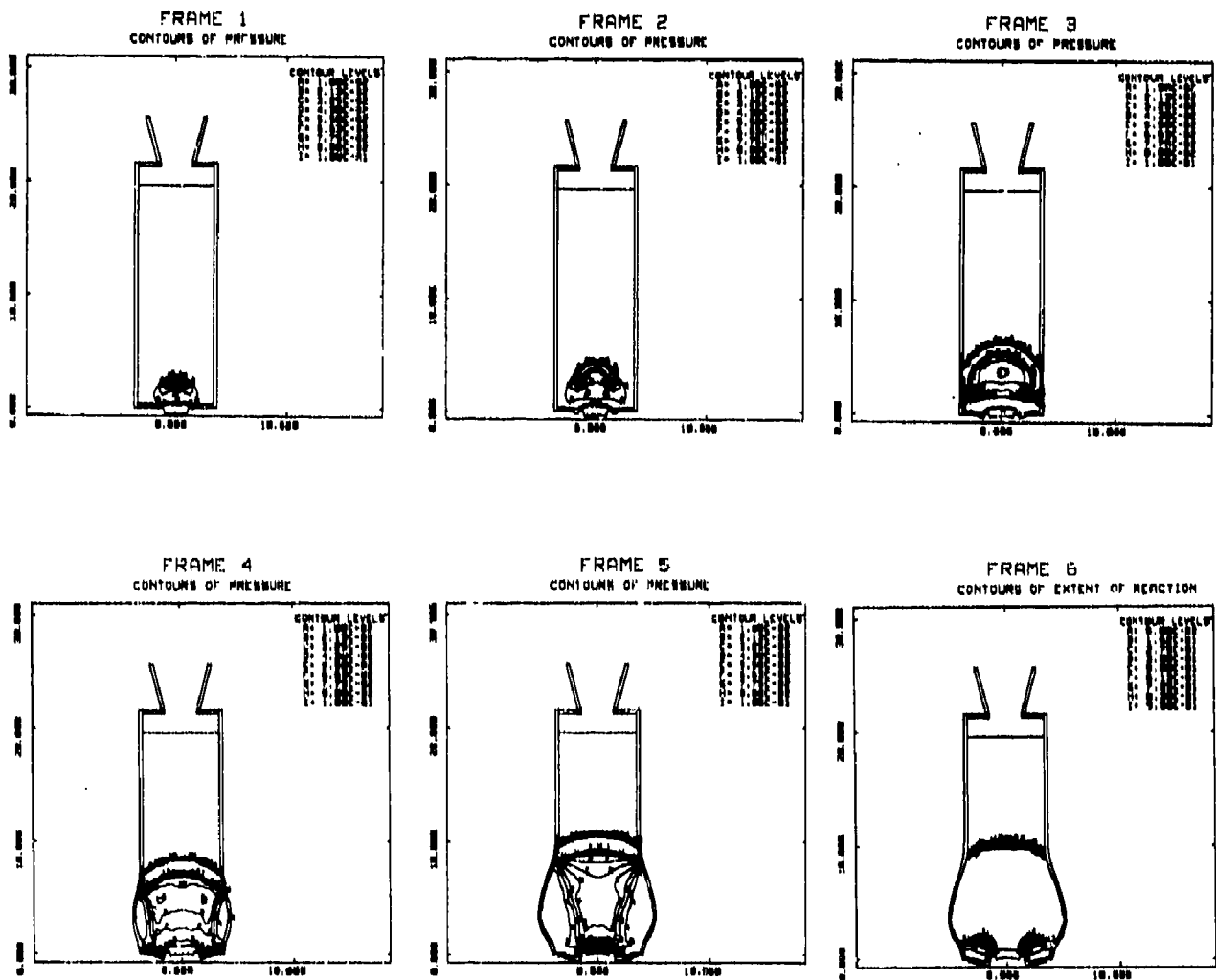


Figure 6. Fragment Attack on Rocket Motor

such computations has been given, and the strengths and weaknesses of the various methods assessed. The accuracy of the technique has been shown to be dependent on the calibration method, and on mesh sizing. A series of example calculations has been performed that illustrates the differences between reactive flow analysis and conventional Chapman-Jouguet wave techniques. Reactive flow analysis has been shown to differ significantly from C-J burn techniques when the scale of the event becomes close to that of the reaction zone in the explosive, or the explosive is undergoing transient wave phenomena such as initiation or failure.

## ACKNOWLEDGEMENTS

The authors acknowledge with thanks the permission of Nobel's Explosives Co. Ltd., and ICI Australia Operations Pty Ltd. to publish this work.

## REFERENCES

1. Mader, C. L. and Forest, C. A., *Two-Dimensional Homogeneous and Heterogeneous Detonation Wave Propagation*, LA 6259, 1976.
2. Wackerle, J.; Rabie, R. L.; and Ginsberg, M. J., *A Shock Initiation Study of PBX 9404*, *Proceedings of the Symposium on High Dynamic Pressures*, Paris, 1978, p. 127.
3. Mader, C. L., *Numerical Modeling of Detonation*, Univ. Cal., Berkeley, 1978.
4. Lee, E. and Tarver, C. M., "Phenomenological Model for the Shock Initiation of Heterogeneous Explosives," *Phys. Fluids*, Vol. 23, 1980, p. 2362.
5. Tarver, C. M. and Hallquist, J. O., *Proceedings of Eighth Symposium (International) on Detonation*, Albuquerque, NM, 1981.
6. Partoum Y., "A Void Collapse Model for Shock Initiation," *Proceedings of Seventh Symposium (International) on Detonation*, Annapolis, MD, 1981, NSWC MP 82-334.
7. Johnson, J. N.; Tang, P. K.; and Forest, C. A., "Shock Wave Initiation of Heterogeneous Reactive Solids," *J. App. Phys.*, Vol. 57, 1985, pp. 4323-4334.
8. Kennedy, D. L., "The Ignition and Growth Model of Shock Initiation," 4th MOD(PE) Detonics Working Group Seminar, Cavendish Lab., Cambridge, 1986.
9. Leiper, G. A. and Kennedy, D. L., "Applications of Reactive Flow Analysis in Explosives Technology," *Proceedings of 4th Symposium on High Dynamic Pressures*, La Grande Motte, France, Jun 1989.
10. Gibbs, T. R. and Poppelato, A., *LASL Explosives Property Data*, Univ. Cal., Berkeley, 1980.
11. Hallquist, J. O., *Users Manual for DYNA2D - An Explicit Two-Dimensional Hydrodynamic Finite Element Code With Interactive Rezoning*, UCID 18756 Rev. 2, 1984.
12. Dick, J. J., "Stress-Time Profiles in Low Density HMX," *Combustion and Flame*, Vol. 69, 1987, pp. 263-271.
13. Erikson, L. M. et al, *Free-Surface Velocity Measurements of Plates Driven By Reacting and Detonating RX-03-88 and PBX 9404*, First American Physical Society International Topical Conference on Shockwaves in Condensed Matter, Menlo Park, CA, 1981.

## DISCUSSION

J. BDZIL, Group M-9  
Los Alamos National Laboratory, NM

The Huygens construction that you showed is in error. The detonation shock in the shadow zone of the corner got there by

propagating along a single straight line from the initiation surface, *through* the polymer, and then back into the HE. Please fix this.

**REPLY BY GRAEME A. LEIPER  
AND DAVID L. KENNEDY**

We have modified our Huygen's algorithm in line with your comment, and Figure 3 has been updated in the final proceedings. There remains a significant difference in the wave profiles between the Huygen's construction and the reactive flow analysis. We believe that this difference will be magnified as the sensitivity of the explosive is reduced.

The diverse nature of methods proposed in the symposium for calculating the dynamic properties of detonation fronts highlights the need for further studies in the area. We believe the only logical fashion for attempting future work is to couple the chemical reaction closely to the hydrodynamic flow, as outlined by us and many previous authors. It is only in such a manner that the result of a simulation can be regarded as representative of the physics occurring in the detonating explosive, under all conditions of practical interest.

# PHYSICAL EVIDENCE OF DIFFERENT CHEMICAL REACTIONS IN EXPLOSIVES AS A FUNCTION OF STRESS

T. P. Liddiard and J. W. Forbes  
Naval Surface Warfare Center  
Silver Spring, Maryland 20903-5000

and

D. Price  
Advanced Technology and Research, Inc.  
Laurel, Maryland 20707

*This paper is concerned with an experimental study of the initiation of chemical reaction in high explosives by mechanical shocks of low to medium amplitudes (4-86 kbar). The results of this study establish a data base for ignition and initiation for 27 explosives, one of which is also a composite modified double base propellant. In addition, these results give clues to the nature of subdetonation reactions and may help to pave the way for future studies of such reactions using other experimental techniques.*

## INTRODUCTION

Discs of various explosives (acceptors) were subjected to shocks using two widely different donor/shock attenuator (gap) systems. One system, the Modified Gap Test (MGT),<sup>1,2</sup> is conducted in air and uses polymethyl methacrylate (PMMA) for the gap material. The other system, the Underwater Sensitivity Test (UST),<sup>1,2</sup> is conducted in water, using water as the gap material. In both systems the acceptors are 50.8 mm in diameter and usually 12.7 mm thick. Observations are made with high-speed framing cameras. MGT and UST first reaction thresholds of the explosives have been determined; MGT detonation thresholds have also been determined. Some of these data have been reported previously.<sup>2,3</sup> However, the shock systems have been recalibrated in recent years. A recent report<sup>1</sup> gives all the corrected data based on the latest and best calibrations of the shock producing (donor) systems. The "bulk burn" threshold in the previous report is now interpreted as the initial reaction threshold. This paper presents a summary of

the data, along with some new interpretations of the shapes of the response curves. The stress thresholds in the explosives were determined by impedance matching with the use of unreacted Hugoniot's of explosives reported in Reference 1.

The nominal densities and the tests conducted on the material are given in Table 1. In addition, whether the material was pressed, melt cast, or cast-cured is indicated. The major components, percentage by weight of ingredients, and initial particle size of the most energetic component are given in Table 2.

## MODIFIED GAP TEST

The configuration of the MGT is given in Figure 1. The donor/gap material/acceptor system is made up of contacting cylinders, all 50.8 mm in diameter. The donor/gap material system provides a quasi-triangular shaped shock pulse with a peak stress of 5-80 kbar, and a pulse width of 1-2  $\mu$ s at one half peak stress. From camera frame sequences, distance-time measurements are made of the

Table 1. Explosives Covered in this Report

EXPLOSIVE	MEAN DENSITY (g/cm <sup>3</sup> )	EXPERIMENTS PERFORMED	EXPLOSIVE	MEAN DENSITY (g/cm <sup>3</sup> )	EXPERIMENTS PERFORMED
TATS (P)	1.62	A	LX-04-0 (P)	1.66	A
TETRYL (P)	1.66	A, B	LX-04-1 (P)	1.66	A, B
TNT (P)	1.62	A, B	PBX 9404-03 (P)	1.64	A, B
TNT (G)	1.62	A	PBXC-121 (CC)	1.64	B
PENTOLITE (P)	1.67	A, B	PBXN-103 (CC)	1.64	B
PENTOLITE (G)	1.64	A	PBXC-117 (CC)	1.74	B
COMP B-3 (P)	1.72	A	PBXW-106 E (CC)	1.64	B
COMP B-3 (G)	1.71	A, B	AFX-108 E (CC)	1.49	B
60/40 CYCLOTOL (P)	1.70	A, B	PBXW-108 E (CC)	1.68	B
60/40 CYCLOTOL (G)	1.70	A	PBXW-108 I (CC)	1.67	B
25/75 CYCLOTOL (G)	1.66	B	PBXW-108 E (CC)	1.64	B
H-6 (G)	1.72	A, B	PBXW-108 I (CC)	1.66	A, B
HMX-1 (P)	1.76	A	PBXW-113 H (CC)	1.66	B
HMX-3 (P)	1.66	A, B	PBXW-114 H (CC)	1.71	B
B-2 (G)	1.66	A, B	EJC-90	1.79	A
LX-03-0 (P)	1.66	A			

(P) - PRESSURE (G) - GAST (P) - GAST (G) - GAST (CC) - GAST (CC)

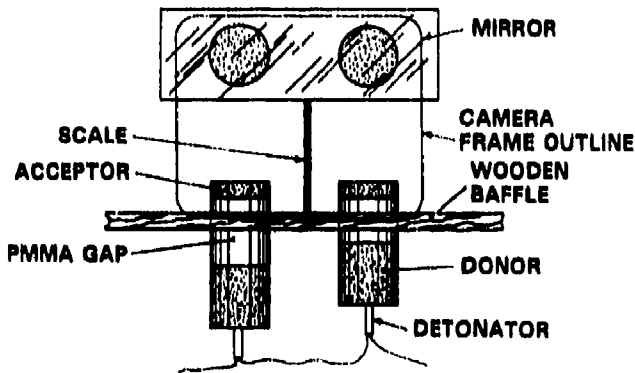


Figure 1. The MGT Arrangement

acceptor free surface motion. One velocity value for each input stress is obtained from each experiment. Typically, an abrupt rise in the acceptor free surface (blow off) velocity occurs with increasing stress when chemical reaction is present.

In using free surface velocity versus input stress as an indication of reaction, it is necessary to keep in mind that we are measuring a hydrodynamic phenomenon. Reaction does not specifically mean combustion (or ignition). It is generally agreed that combustion of solids requires formation of gases which can subsequently react to produce flame (radiation). In other words, the original solid materials must be heated until they form gases and possibly solid residue which can, in turn, burn. This heat decomposition (pyrolysis) can be considered an initiation phenomenon, leading to ignition and combustion. By contrast, we use the term "ignition" in the conventional sense of "sustained ignition (go/no go)" experimentally observed as a flame.<sup>4</sup>

Table 2. Explosives Compositions

EXPLOSIVE	INGREDIENTS	APPROXIMATE PERCENTAGE	FIRST HE PARTICLE SIZE (µm)
PENTOLITE	PETN/TNT*	49/51	149-210
COMP B-3	RDX/TNT*	60/40	85-80
60/40 CYCLOTOL	RDX/TNT*	60/40	149-210
25/75 CYCLOTOL	RDX/TNT	25/75	-
H-6	RDX/TNT/AI/D-2/O	44/20/20/5/2	120**
HMX-1***	RDX/TNT/AI/D-2	40/30/10/5	120**
HMX-3***	RDX/TNT/AI/D-2	30/20/30/5	120**
B-2	RDX/TNT/AI	63/22/15	85***
LX-03-0	HMX/DATS/VITON A	70/20/10	180**
LX-04-0	HMX/VITON A	25/15	20-30****
LX-04-1	HMX/VITON A	65/15	85-60****
PBX 9404-03	HMX/NO/TBP	34/3/3	150 & 45
PBXC-121	HMX/O	82/18	120**
PBXN-103	TT/AP/AI/O	23/40/27/10	N/A
PBXC-117	RDX/AI/O	71/17/12	520**
PBXW-106 E	RDX/BDNPA-F/O	75/14/7	100**
AFX-108 E	RDX/O	82/18	80**
PBXW-108 I	RDX/O	65/15	500**
PBXW-108 E	RDX/O	65/15	210**
PBXW-108 E	RDX/AI/O	64/20/16	120**
PBXW-108 I	RDX/AI/O	65/20/15	520**
PBXW-113 H	HMX/O	88/12	250***
PBXW-114 H	HMX/AI/O	78/10/12	200**
EJC-90	HMX/NO/NO/AP/AI/O	28/14/32/5/18/5	...

\*GAST VERSIONS OF THESE EXPLOSIVES HAD 0.2% NITROTOLENE ADDED.  
 \*\*APPROXIMATE MEDIAN PARTICLE SIZE (µm) CALCULATED FROM PERCENTAGE OF ALL MATERIAL PASSING THROUGH DIFFERENT SHIVE SIZES AS DEFINED BY THE PARTICLE SIZE CLASS SPECIFICATIONS OF THE EXPLOSIVE.  
 \*\*\*CALCIUM CHLORIDE AND CALCIUM SILICATE WERE NOT USED IN THESE HE AS THEY NORMALLY ARE.  
 \*\*\*\*MEASURED MPS.

AGRONYMS

AI: ALUMINUM  
 AP: AMMONIUM PERCHLORATE  
 BDNPA-F: 50% BDN (2, 2-DINITROPROPYL) FORMAL AND 50% BDN (2, 2-DINITROPROPYL) ACETAL  
 D-2: 84% DE WAX/14% NITROCELLULOSE/2% LEOTHIN  
 DATS: 1, 3-DIAMINO-2, 4, 6-TRINITROBENZENE  
 HMX: CYCLOTETRAMETHYLENE TETRANITRAMINE, OCTOGEN  
 NC: NITROCELLULOSE  
 NO: NITROGLYCERINE  
 PETN: PENTAERYTHRITOL TETRANITRATE, TEN  
 O: OTHER  
 RDX: CYCLOTETRAMETHYLENE TETRANITRAMINE, HEXOGEN  
 TATS: 1, 3, 5-TRIAMINO-2, 4, 6-TRINITROBENZENE  
 TBP: TRIS-BETA-CHLOROETHYL PHOSPHATE  
 TNT: 2, 4, 6-TRINITROTOLUENE, TRITOL  
 TT: TRIMETHYLETHANE TRINITRATE

The measured MGT free surface velocity minus the calculated free surface velocity for the unreacted material is plotted in Figure 2 against input stress. The stress where the surface velocity first exceeds the calculated velocity of the inert is taken as the first reaction threshold,  $P_e^R$ . The stress where the surface velocity reaches 4.5 mm/µs (indicated on Figure 2 as horizontal lines at the top of the curves) is chosen as the detonation threshold,  $P_e^D$ . This criterion is based on the observations of detonation light and the trend in instantaneous acceptor surface velocity.<sup>1</sup> The point of ignition ( $P_e^I$ ) is chosen as the end of any initial reaction and beginning of the main rapid reaction, as shown by the change in slope of the surface velocity-stress curve. The three thresholds are listed in Table 3 along with the theoretical maximum density (TMD).

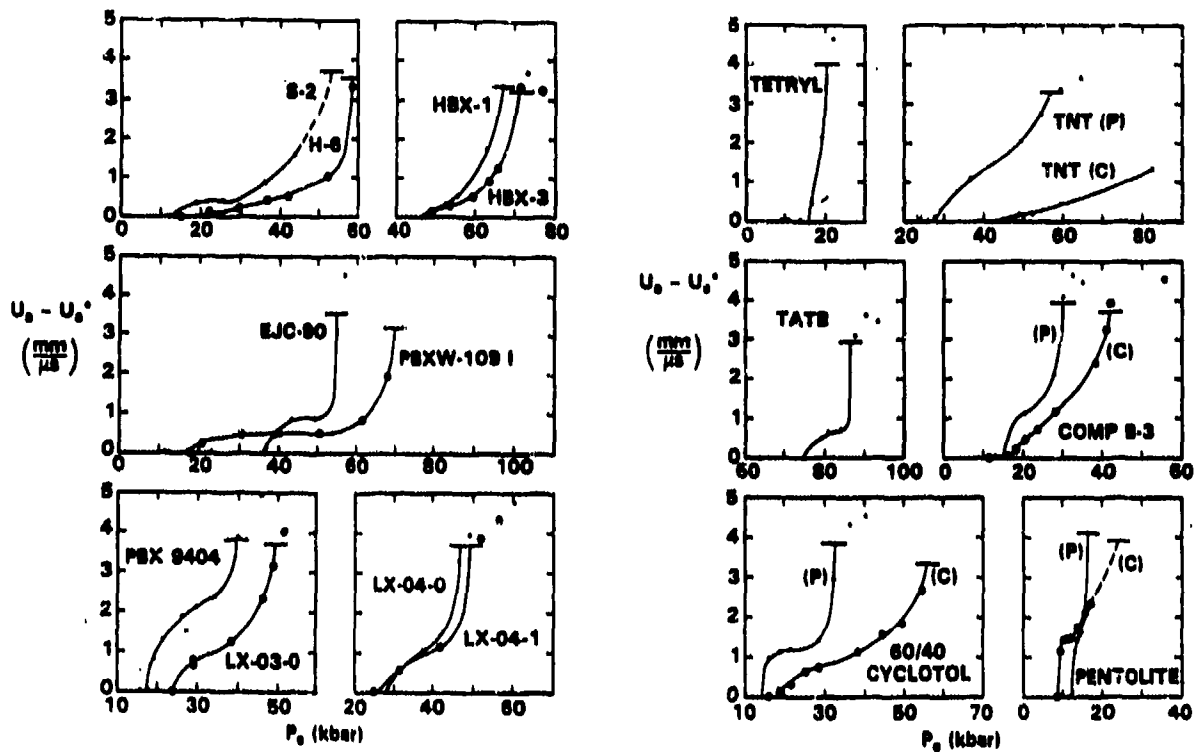


Figure 2. Excess Acceptor Velocity as a Function of Stress in the Explosive

Table 3. MGT First Reaction, Ignition and Detonation Threshold Data

EXPLOSIVE	% TMD	P <sub>0</sub> <sup>R</sup> (kbar)	P <sub>0</sub> <sup>I</sup> (kbar)	P <sub>0</sub> <sup>D</sup> (kbar)	% TMD	P <sub>0</sub> <sup>I</sup> (kbar)
PENTOLITE (C)	95.6	9	9	(24)	95.9	10
PENTOLITE (P)	97.2	12	12	16	97.1	12
S-2 (C)	—	13	29	(83) <sup>a</sup>	—	40
60/40 CYCLOTOL (P)	97.7	14	14	33	98.5	10 <sup>b,c</sup>
COMP B-3 (P)	99.6	15	15	30	98.5	16 <sup>b,c</sup>
TETRYL (P)	95.3	16	16	21	94.0	16
COMP B-3 (C)	98.4	17	25	42	98.6	22
PBX 9404-03 (P)	98.2	18	18	40	94.9	18
PBXW-109 I (CC)	(98.0) <sup>a</sup>	18	55	70	(98.0) <sup>a</sup>	63
H-8 (C)	(95.0) <sup>a</sup>	18	41	58	97.3	29 <sup>b,c</sup>
60/40 CYCLOTOL (C)	97.5	18	32	56	98.6	24 <sup>b,c</sup>
LX-03-0 (P)	98.5	24	32	50	98.0	29
LX-04-1 (P)	98.3	26	42	49	—	—
TNT (P)	97.9	28	28	57	98.1	28
LX-04-0 (P)	98.0	28	39	47	98.0	38
EJC-80	(95.0) <sup>a</sup>	36	49	58	(96.0) <sup>a</sup>	46
TNT (C)	97.6	41	55	(104)	98.1	56
HBX-1 (P)	98.2	46	52	67	—	—
HBX-3 (P)	98.4	46	56	71	—	—
TATB (P)	93.8	75	82	86	94.2	82

<sup>a</sup>VALUES IN PARENTHESES ARE LESS CERTAIN THAN THE OTHERS.  
<sup>b</sup>THIS VALUE IS FOR PRESSED COMP B.  
<sup>c</sup>THIS VALUE IS FOR CAST COMP B.

## DISCUSSION OF MGT RESULTS

A number of observations can be made from the MGT velocity versus stress curves of Figure 2. Comparison of the surface velocity curves of cast and pressed Comp B-3 and 60/40 cyclotol reveals that the cast materials require

very slightly higher stresses (to induce reaction) compared to the pressed materials, but the stress required to induce detonation is much higher for the cast materials.

The curves for pressed Comp B-3 and 60/40 cyclotol have much more structure than those of cast charges of the same high explosive (HE). In fact, their velocity curves have a distinct plateau that indicates the same reaction initiated over a range of pressures, or a lower temperature reaction different from that occurring at higher temperatures. In these two cases and five others the first interpretation was chosen because each explosive exhibiting a plateau contained appreciable amounts of RDX or HMX and, in one case, NG as well. Since these are very shock sensitive compounds, it is reasonable to assume that the plateau indicates the ignition of the most sensitive component; its reaction would, in turn, ignite the other components which are also ignited by higher initiating pressures beyond the plateau. The second possible interpretation (different reactions at different temperatures) probably applies to single component HE, such as TATB (P). In the case of other pressed explosives (TNT,

Comp B, cyclotol, and pentolite) consisting of one or two pure explosives, the velocity curves start at high angles and continue to increase in velocity. For these materials we have chosen  $P_e^I \approx P_e^R$ . The same materials in cast form and in composite explosives produce very different expansion curves from which the point of obvious acceleration of reaction is chosen as the sustained ignition threshold  $P_e^I$ . To determine whether this is the correct choice would require devising an experiment in which the reactions could be followed optically.

The effect of initial particle size on the shape of the curves for materials of the same composition is evident in the data for pressed Comp B-3 (finer RDX) and pressed 60/40 cyclotol. The reaction threshold for the charges with larger particles is slightly lower; in other words, it is slightly easier to ignite the charges with larger particles in agreement with the results reported in Reference 5. Of course, the particle size after pressing is unknown, as is the particle size in the cast charges. In this case, the detonation threshold is lower for the initially finer particles, but that can be reversed for different initiating pulses.<sup>5</sup> A similar small initial particle size effect is apparent for the results of LX-04-0 (finer HMX) and LX-04-1. Although Comp B-3 and 60/40 cyclotol have the same composition, their surface velocity curves are far from identical. This confirms the fact, already noted for cast versus pressed charges, that physical factors can overwhelm chemical ones.

Comparison of the pressed aluminized explosives HBX-1 and HBX-3 velocity curves reveals that detonation can be induced in HBX-1 at lower stresses than in HBX-3. HBX-1 has the same initial HE particle size distribution as HBX-3. Therefore, the sensitivity difference between these two explosives is consistent with higher RDX content and lower percentage of aluminum in HBX-1.

H-6 is aluminized 60/40 cyclotol. The addition of 20 percent aluminum and 5 percent wax to cast cyclotol has had very little effect on its sensitivity in our samples; the decrease in  $P_e^R$  and increase in  $P_e^D$  were, respectively, -1.1 and 3.6 percent. The other two cast, aluminized explosives are not directly related in composition to other tested materials.

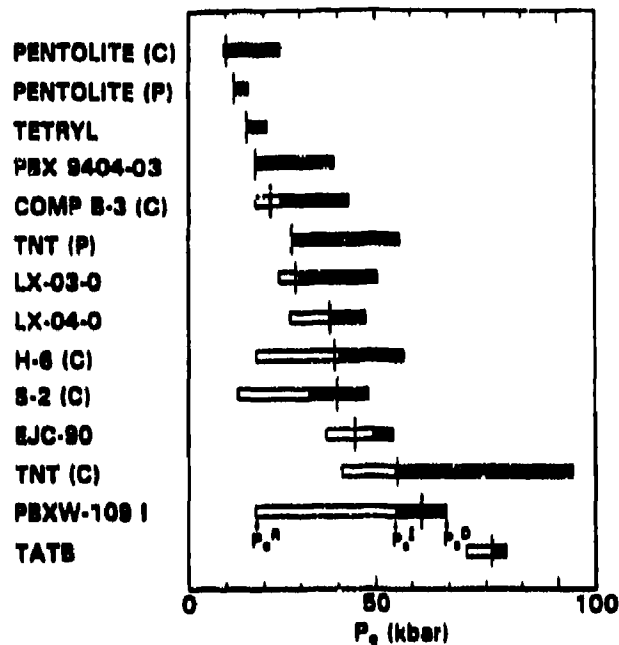
It is interesting that cast cured PBXW-109 has a  $P_e^R$  value of 18 kbar, i.e., close to that of cast 60/40 cyclotol and H-6, but a  $P_e^D$  of 70 kbar, about 25 percent higher. This is attributed to the effect of its rubbery binder, but the binder could also be considered as 15 percent inert or desensitizer. In contrast, S-2, with no inert but a larger amount of explosive and 25 percent less aluminum, has  $P_e^R$  and  $P_e^D$  of 13 and 53 kbar, respectively. It is easier to initiate to both first reaction and detonation, as might be expected.

In the MGT, stress thresholds for the first reactions ranged from 9 to 75 kbar. Stresses of 16 - 86 kbar are required to initiate detonation in the 12.7 mm thick secondary explosives. The MGT thresholds for first reaction, ignition, and detonation are summarized in Table 3. The MGT data are also plotted as a bar chart in Figure 3. The light area of the bar graph indicates the stress range of the first reactions, while the dark area of the bar graph gives the stress range for accelerated reactions. The beginning of the dark region on the bar graph is believed to be the value corresponding to the start of sustained ignition. This figure compares these data to the tabulated Large Scale Gap Test (LSGT) results,  $P_e^L$ , for the same materials.<sup>6</sup>

## UNDERWATER SENSITIVITY TEST

The configuration for the UST is given in Figure 4. The donor is an 82 mm diameter pentolite sphere which provides a quasi-triangular shaped pressure-time pulse with a peak pressure in water of 3-30 kbar and a pulse half-width of 10-50  $\mu$ s at one half peak stress. The induced shock pulse in the acceptor has a smaller pulse width (6-10  $\mu$ s) due to the size of the acceptor.

From camera frame sequences, the bulk expansion of the acceptor after the transit of the shock front is obtained as a function of time. The appropriate slope from the resulting curve yields a single expansion velocity value. The extrapolation of this curve to zero expansion is taken as the first reaction threshold. Detonation thresholds are not usually obtained from the UST because the higher stresses needed for detonation require placing the



NOTE: THE LARGE SCALE GAP TEST VALUE FOR DETONATION,  $P_e^D$ , IS INDICATED BY A CROSSBAR. CLEAR AREAS IN BARS INDICATE REGION OF LOW LEVEL REACTION.

Figure 3. Comparison of MGT Reaction Levels,  $P_e^R$ ,  $P_e^I$ , and  $P_e^D$ , with the LSGT Threshold,  $P_e^L$ .

acceptor at a distance from the donor where the peak stress calibration is uncertain.

## DISCUSSION OF UST RESULTS

The expansion velocity curves versus sample stress for materials studied in the UST are given in Figure 5. These sample expansion curves are not as revealing as those of the MGT. In part, this is due to the fact that the explosives are not stressed to the point of detonation in the UST. Ignition thresholds were not obtained in the UST due to the incompleteness of these curves. The stress thresholds for the initial reaction in the UST ranged from 4 to 9 kbar. These stress thresholds are summarized in Table 4.

The expansion curves for cast cured PBXW-113 and PBXW-114 show that at higher stresses the expansion is more rapid for PBXW-113 which has a higher IIMX content and no aluminum.

The expansion curve for cast H-6 has a plateau over a stress range of 19 to 29 kbar. The only other material displaying such a plateau was PBXW-108 I, again in the higher stress region.

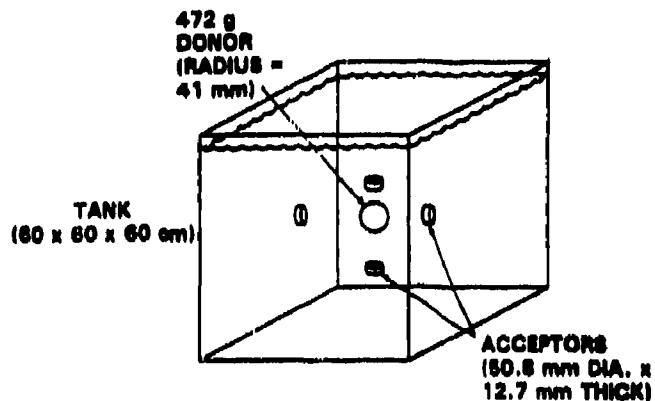


Figure 4. The UST Arrangement

It is interesting to note that the response curve of PBXW-106 E is very similar to that of PBXW-108 E. The RDX loading is lower in PBXW-106 E, but it does have an energetic binder containing BDNPA-F that appears to support the response curve as if the RDX had not been replaced.

PBXN-103 has an energetic binder consisting chiefly of nitrocellulose plasticized with trimethylolethane trinitrate. Although this explosive also contains appreciable amounts of ammonium perchlorate and aluminum, the binder produces a relatively homogeneous mixture with few or no voids. It is to this homogeneity that its relatively high reaction threshold is attributed.

PBXC-121 was the only explosive studied that had the consistency of paste. It had to be placed into plastic rings and covered with thin mylar to hold it in shape and position for the tests. It does have a very high reaction threshold compared to most explosives. The lack of rigidity of the binder appears to desensitize the material which contains 82 percent of RDX -- comparable to the content in the "108" composites.

## SUMMARY OF RESULTS

It is no surprise that the most dominant effect on sensitivity is the preparation of the material. In this study most materials were either cast or pressed to densities near voidless. Therefore, the major difference in material preparation was whether the

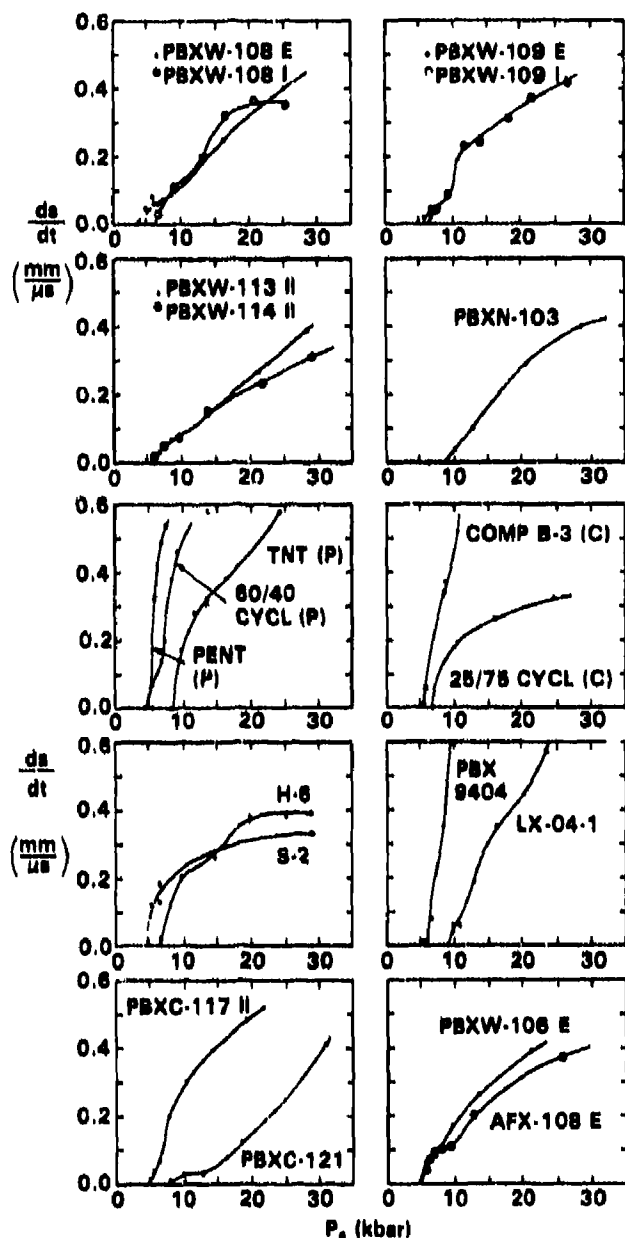


Figure 5. Expansion Velocity as a Function of Stress in the Explosive

material was cast or pressed. The cast materials have reaction thresholds slightly above those of pressed explosives with the same composition and same initial ingredient particle size. However, the detonation thresholds for cast materials are well above those of the pressed materials, i.e., require much larger stresses than do the pressed materials. Thus, the MGT confirmed the same large effect of preparation on sensitivity found with the LSGT. Other trends found to be the same in the two tests: addition of aluminum and/or wax to HE

Table 4. UST First Reaction Threshold Data

EXPLOSIVE	% TMD	$P_s^R$ (kbar)
PBXW-108 E (CC)	(98.0)*	(4.0)*
S-2 (C)	—	(4.8)*
PENTOLITE (P)	97.0	4.7
60/40 CYCLOTOL (P)	97.4	4.7
PBXW-106 E (CC)	(98.0)*	4.8
PBXC-117 (CC)	(98.0)*	5.1
AFX-108 E (CC)	(98.0)*	5.1
PBXW-114 II (CC)	(98.0)*	5.4
COMP B-3 (C)	98.6	5.5
PBXW-109 E (CC)	(98.0)*	5.6
PBXW-113 II (CC)	(98.0)*	5.9
PBX 9404-03 (P)	98.8	6.0
PBXW-108 I (CC)	(98.0)*	6.1
PBXW-108 I (CC)	(98.0)*	6.2
H-8 (C)	(96.0)*	6.4
28/78 CYCLOTOL (C)	98.1	6.7
PBXC-121 (CC)	(98.0)*	7.5
TNT (P)	97.5	8.7
PBXN-103 (CC)	(98.0)*	8.9
LX-04-1 (P)	98.3	9.0

\*VALUES IN PARENTHESES ARE LESS CERTAIN THAN THE OTHERS.

desensitizes it according to the amount added, and increasing the amount of HE in a composite causes a corresponding increase in sensitivity. Finally, on the few cases tested, the particle size effects also showed the same trends: the smaller particles were harder to ignite than the larger ones.

In many of the explosives tested in the MGT, particularly the cast explosives, the stress induced increase in surface velocity remains at a nearly constant low level for a wide range of input stresses. This low velocity plateau could be caused by the same reaction being activated over a broad range of stress (and hence of temperature). It could also occur for a material that has one reaction at a lower temperature, but a different reaction at a higher temperature (e.g., thermal decomposition of ammonium perchlorate, a component of EJC). A preignition reaction at the lower temperature might generate gases that affect the free surface velocity, but insufficient energy for a sustained ignition.

Pressed charges of Comp B-3 and 60/40 cyclotol each showed a stepped velocity-stress curve. These were interpreted as the ignition of RDX at the top (lower pressure range) followed by the ignition of the less sensitive TNT.

The first reaction thresholds ranged from 9 kbar to 75 kbar in the MGT and 4 kbar to 9 kbar in the UST. The ratio of these threshold stresses, MGT/UST is  $2.9 \pm 0.3$ ; this ratio is consistent with the durations of the respective

stresses. It follows that both tests are measuring the same initial reaction. Because of the direct proportionality, trends observed with the UST threshold stresses were the same as those found with the MGT. However, we could not interpret the UST expansion curves above that threshold; detonation could not be attained in the experimental design of this test.

The thresholds for sustained ignition were chosen as described in the text. The results are summarized in Figure 3. That figure omits six of the HE listed in Table 3 because the value for  $P_e^L$  was lacking or estimated. This bar graph shows reaction before ignition (open bar) and after ignition (solid bar). The tick marks are the LSGT value for that material. As the figure shows, the LSGT stress threshold for detonation was found to be essentially the same as the stress threshold for ignition in the MGT. This statement holds within experimental error for all explosives shown in Figure 3, except possibly S-2 and PBXW-109 I. For the six HE omitted from Figure 3, the incomplete data were consistent with  $P_e^I \approx P_e^L$  in every case but one.

In general, the LSGT measures ignition thresholds. Its test design is supercritical for most common explosives and for all reported here. If sustained ignition occurs in an explosive supercritical (i.e., detonable) in this test, detonation will also occur. It has been suggested a number of times in the past that the LSGT is an ignition test. Figure 3 confirms and reinforces that suggestion.

Future work should explore the sub-ignition reactions which occur between  $P_e^R$  and  $P_e^I$ . These seem most evident in cast and composite explosives.

## REFERENCES

1. Liddiard, T. P. and Forbes, J. W., "A Summary Report of the Modified Gap Test and the Underwater Sensitivity Test," NSWC TR 86-350, 12 Mar 1987.
2. Liddiard, T. P., Jr., "The Initiation of Burning in High Explosives by Shockwaves," *Fourth Symposium (International) on Detonation*, White Oak, MD, 12-15 Oct 1965, pp. 487-495.

3. Liddiard, T. P. and Forbes, J. W., "Initiation of Burning and Detonation in Cast H-6 and Cast PBXW-109," *Seventh Symposium (International) on Detonation*, Annapolis, MD, 16-19 Jun 1981, pp. 308-315.
4. Boggs, T. L.; Price, C. F.; Atwood, A. I.; Zurn, D. E.; Paar, T. P.; and Derr, R. L., *Proc. 19th JANNAF Comb. Mtg.*, CPIA Pub. 366, Vol. I, 1982, pp. 383-405.
5. Price, D., "Effect of Particle Size on the Shock Sensitivity of Porous HE," *J. Energetic Materials*, Vol. 6, 1988, pp. 283-317. Also NSWC TR 86-336, 1986.
6. Price, D.; Clairmont, A. R., Jr.; and Erkman, J. O., "The NOL Large Scale Gap Test. III. Compilation of Unclassified Data and Supplementary Information for Interpretation of Results," NOLTR 74-40, 8 Mar 1974.

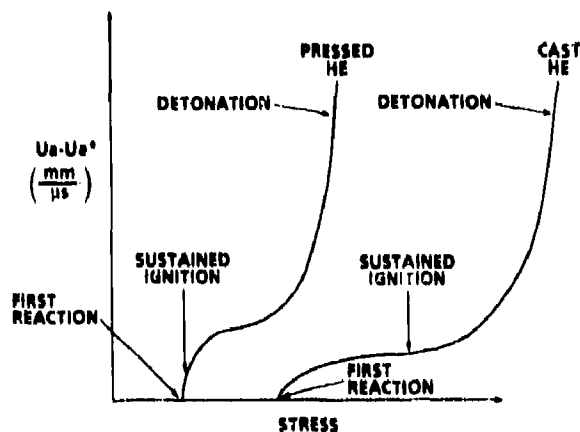
## DISCUSSION

R. FREY, U.S. Army Ballistic Research Laboratory, Aberdeen Proving Ground, MD

The manner of locating the point  $P_e^I$  on the second page is not clear. Could you show this point on some of the figures?

## REPLY BY J. FORBES

To understand how various thresholds are determined, look at the representative figure given below of surface velocity-stress. The



three thresholds (first reaction,  $P_e^R$ ; sustained ignition,  $P_e^I$ ; and detonation,  $P_e^D$ ) are shown for pressed and cast explosives.

### DISCUSSION

D. G. TASKER, Naval Surface Warfare Center, Silver Spring, MD

Your observation of the "first reaction" point is most interesting. To my surprise, I

have also found these points on my data (7th Detonation Symposium). I originally dismissed these points as being erroneous, but now . . . ? These points really deserve further study.

### REPLY BY J. FORBES

The authors agree with this comment and hope that further work in the first reaction region is pursued.

# TOWARDS DEVELOPING THE CAPABILITY TO PREDICT THE HAZARD RESPONSE OF ENERGETIC MATERIALS SUBJECTED TO IMPACT

C. S. Coffey, V. F. DeVost, and D. L. Woody  
Naval Surface Warfare Center  
Detonation Physics Branch  
Silver Spring, Maryland 20903-5000

*The problem of predicting the hazard response of energetic materials to impact has long defied an adequate solution. At least a part of this difficulty has been the lack of a clear, scientifically sound understanding of the impact ignition and reaction growth processes. Recently, enough of an understanding of these processes has been gained that, while still lacking in many details, indicates that it should be possible to predict the hazard response of an energetic material subjected to a wide range of different impacts on the basis of the response of the material to a few carefully chosen small-scale tests.*

*This paper presents three different drop weight impact tests that provide data that may make it possible to predict ignition behavior due to an arbitrary impact and establish the probable reaction violence. Further, they demonstrate that for most energetic solids the ignition process is a discontinuous one and that the ever present large fluctuations in the impact response are endemic to explosive materials.*

## INTRODUCTION

The inability to predict the hazard response of propellants or explosives to impact is a major and serious problem. This concern ranges over the entire spectrum of possible impact events, from the inevitable minor impacts incurred during routine handling through to much more violent accidental impacts and on ultimately to the response of these materials to bullet or fragment attack.

The wide range of possible impact stresses and the seemingly bewildering array of possible material responses to these impacts has proved to be extremely difficult to understand, analyze and predict. It has become prohibitively expensive to perform a sufficient number of large-scale impact tests to reliably establish the hazard risks associated with a particular propellant or explosive formulation. This same lack of understanding of the impact

ignition process has prevented a proper understanding of the small-scale laboratory type impact tests and has frustrated attempts to understand the results of the large-scale tests in terms of the results of small-scale tests.

For several years now at NSWC there has been an effort to understand the initiation and growth of reaction in explosives and propellants subjected to impact. A part of this effort has been devoted towards establishing the fundamental quantum mechanical basis for the energy localization/hot spot formation process that occurs during impact. Coupled with this has been an experimental effort to provide proof and direction to the theoretical effort, and to extend this fundamental understanding to predict the behavior of real energetic materials during impact. The purpose of this paper is to provide a summary of our

efforts to date to predict the behavior of explosives and propellants subjected to impact on the basis of results from small-scale tests. The results of the theoretical research are given elsewhere.<sup>1</sup> This theoretical understanding, however, provides the basis for understanding the experimental results and for establishing the approximations on which the predictive capability is founded. The two efforts are complementary and neither is adequate to stand by itself.

## **ENERGY LOCALIZATION AND HOT SPOT FORMATION**

It has long been recognized that during impact or shock ignition of energetic crystalline solids some form of energy localization must occur to focus the energy of the impact or shock into small regions of the sample material. This phenomenon, referred to as hot spots, is most easily shown in energy balance experiments where ignition can occur in impacted crystals at energy levels that are insufficient to raise the bulk temperature of the sample more than a few degrees K, which is far less than the bulk ignition temperature. A number of processes have been suggested as the cause of this energy localization.<sup>2,3</sup> The most well developed of these is that of adiabatic compression of gas within voids in the solid. This hypothesis is inadequate because during most impacts of interest the pressure is insufficient particularly at the moment of ignition, and the voids are either too small or nonexistent to achieve the temperature necessary for ignition. It has been demonstrated that shear is a controlling stimulus at low level impacts.<sup>4</sup> There is some evidence that shear is essential to shock ignition as well, certainly it is now clear that pressure has only an indirect role in shock ignition of crystalline explosives.<sup>5</sup> The most logical mechanism to account for the energy localization process is that of shear band formation that appears to occur in all crystalline solids, both inert and energetic, when they undergo rapid deformation.<sup>1</sup>

## **THE FAILURE OF THE CURRENT DROP WEIGHT IMPACT TESTS**

Perhaps the simplest impact test is that of the drop weight apparatus. To the authors'

knowledge the first such drop weight test was established in England about 1910 by Rotter.<sup>2</sup> Later, in the early 1940s, the Explosive Research Laboratory (ERL) at Bruceton developed what has since become the standard drop weight impact test used in the United States.<sup>6</sup>

While the general notion of a drop weight impact test appears quite simple, this simplicity is in appearances only. In actuality the test is quite complicated and these complications must be taken into account if the test is to be made to yield useful data. The major advantages of the test are that it requires only small quantities of sample material and that it can be easily and inexpensively made available in most laboratories.

As it is normally used, the drop weight test has a serious shortcoming. The standard drop weight impact test procedure seeks to establish a drop height at which ignition occurs in 50 percent of the impacts. Unfortunately, this procedure inextricably mixes the plastic energy required to deform and heat the sample to ignition with the elastic energy stored in the machine during impact. This stored elastic energy subsequently provides the energy to rebound the drop weight. It is easy to show by simultaneously monitoring both the light emitted during ignition and the deceleration of the drop weight that the 50 percent ignition level occurs at or near the point of maximum elastic energy stored in the anvil drop weight system. For most explosives and propellants the elastic energy at the 50 percent point substantially exceeds the plastic energy localized in hot spots required to heat the sample to ignition. Attempts to understand the 50 percent ignition drop weight impact test data in anything other than in a relative way will be fruitless unless this stored elastic energy is taken into account. Failure to do so means that the elastic properties of the particular impact machine will likely dominate any impact sensitivity measurements.

To overcome the shortcoming of the conventional drop weight impact tests in which the 50 percent go-no go drop height is measured, we have developed three different

but complimentary impact tests. These tests measure the energy required to initiate chemical reaction by the impact, the rate at which this chemical reaction occurs, and the amount of chemical energy released during the reaction.

After a great amount of searching for the proper impact test it became apparent that it was unlikely that any single laboratory impact test or even a series of impact tests will of themselves adequately predict the response of any energetic material to all of the kinds of impacts it could possibly encounter. The best that we are likely to be able to do is to generate a prediction of the impact response of an energetic compound based on data obtained from a few carefully chosen and carefully designed impact tests combined with a truly honest and correct theory of what is occurring in the material during impact. The less we accept in the way of adequate tests or a correct theory, the closer we move back towards the present impact test situation where the standard 50 percent point test reveals as much or more about the impact response of the particular impact machine as it does about the impact ignition response of the material being tested.

## THE NSWC IMPACT MACHINE

Over an interval of several years we have developed at NSWC a simple but very versatile impact machine shown in Figure 1. It is approximately 2 m high and 30 cm wide, Figure (1). It has two vertical guide rods to guide the impactor. Depending on the test, the mass of the drop weight can range from .4 to 10 kg. The free fall drop height is only 1.5 m, however impactor velocities of up to 40 m/s (80 m effective drop height) are easily achieved using elastic shock cords to accelerate the .4 kg impactor. The velocities are less for the higher mass impactors.

The NSWC machine is designed to accommodate many different anvil configurations and a variety of instrumentation. In what follows, two different anvil designs are employed: a simple flat anvil 3.175 cm in diameter for the energy to ignition test, and a cup-like anvil to achieve the confined volume

impact for the Ballistic Impact chamber (BIC) test.

The most convenient way to analyze this or any impact machine is to treat each component, the drop weight, the striker or drift (if used), and the anvil-base, as a mass spring-system. The interaction of these spring-mass components during impact lends itself to a straightforward analysis using Laplace transforms.<sup>7</sup> Summarizing this analysis briefly, the natural frequency of each element is just the square root of its spring constant,  $k$ , divided by its mass,  $m$ ,  $\omega = (k/m)^{1/2}$ . The natural period of the drop weight impactor determines the duration of the impact since after one half a period of oscillation the impactor begins to rebound and leaves the anvil. If a striker is used its mass is usually much less than that of the impactor so that its frequency of oscillation is usually much greater than that of the impactor, ( $\omega_{striker} \gg \omega_{impactor}$ ). Because of this the striker introduces a higher frequency of oscillation superimposed on the response of the impactor. The mass of the base-anvil system is typically much greater than that of the impactor,  $m_{anvil-base} \gg m_{impactor}$  so that  $\omega_{anvil-base} \ll \omega_{impactor}$ . For this reason usually the mass of the base-anvil system has

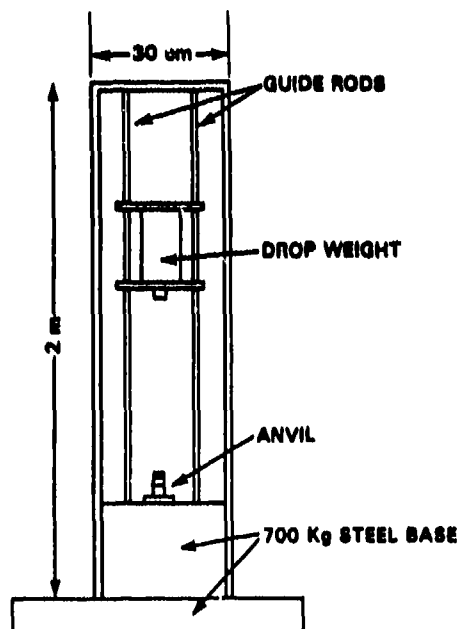


Figure 1. NSWC Impact Machine

little or no influence during the impact. (The standard ERL impact machine represents an enormous overkill in this regard since the mass of its base is so very much larger than the mass of the drop weight).

## ENERGY TO IGNITION

The energy to ignition test avoids the failure of the standard drop weight test by separating the elastic and plastic components of the impact energy. This is done by taking advantage of the energy flow during the impact process. Specifically, during the initial phase of the impact the kinetic energy of the impactor that is transferred to the sample and anvil system flows mostly into plastically deforming the sample and very little is stored as elastic energy in the anvil drop weight system. This is particularly the case for soft explosive or propellant materials. To take advantage of this partition of the transferred energy mainly into plastic deformation of the sample early during the impact, a high velocity impact must be chosen to cause ignition of the sample during the initial plastic deformation. The change in the velocity of the impactor,  $\Delta v$ , can be measured during the impact and this can be made to provide the change in the kinetic energy of the impactor at the moment of ignition. Let  $m$  be the mass of the impactor,  $V_0$  its velocity at the moment of impact and  $\Delta v$  the change in the velocity of the impactor at the moment of ignition. The change in the kinetic energy of the impactor up to the moment of ignition is just

$$\begin{aligned} \Delta E &= \frac{1}{2} m V_0^2 - \frac{1}{2} m (V_0 - \Delta v)^2 \\ &= m V_0 \Delta v - \frac{1}{2} m (\Delta v)^2 \end{aligned} \quad (1)$$

Since no striker is used in this test, this energy is divided between the energy required to plastically deform and heat the sample,  $E_{pl}$ , and the elastic energy stored in the drop weight-anvil system,  $E_{el}$ . By the above argument, during the very initial phase of the impact most of the energy transferred from the drop weight goes into plastically deforming the

sample,  $E_{pl} \gg E_{el}$ , so that early during the plastic deformation phase of the impact

$$E_{pl} \approx m V_0 \Delta v - \frac{1}{2} m (\Delta v)^2 \quad (2)$$

Typically, during this early phase of the impact  $\Delta v \ll V_0$ , so that Equation (2) simplifies further to

$$E_{pl} \approx m V_0 \Delta v \quad (3)$$

Figure 2 provides a schematic drawing of one of several impact schemes that we have used. Usually an accelerometer, strain gage, or a pressure gage was used to measure the deceleration of the impactor. The change in the impactor velocity,  $\Delta v$ , from the moment of first contact to the moment of ignition was obtained by integrating the acceleration time record. The moment of ignition was obtained by using three fast photo diodes arranged 120° apart around the outside of the anvil but level with the anvil surface. In a number of early experiments photo diodes sensitive to either infrared or visible emission were used to view the impact through a sapphire anvil. In both types of experiments the results were essentially identical. Table 1 lists the measured energy required to cause ignition for a variety of impacts on an impact sensitive propellant like-material containing ammonium perchlorate. Interestingly, these energy to ignition results appear to be almost independent of either the mass or the velocity of the impactor. In these early experiments the mass of the

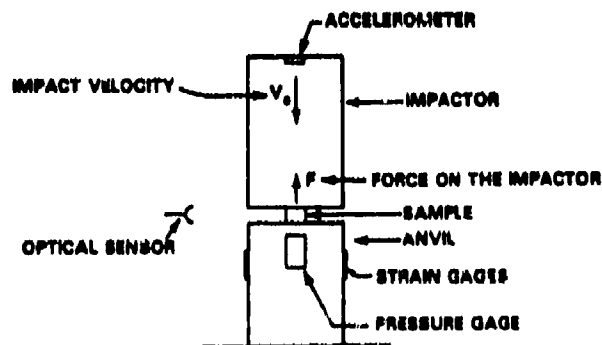


Figure 2. Energy to Ignition Test Apparatus

Table 1. Energy to Ignition of Propellant Like Material Pellet Samples (5 mm dia x 1 mm thick)

	$V_0$ (m/s) Velocity	$\Delta V$ (m/s) Change in Velocity	$\Delta E$ (J) Change in impact energy for ignition
Sapphire Anvil	1.4	.073	1.03
	1.4	.063	.88
	1.4	.065	.910
	1.4	.118	1.65
	2.8	.03	.84
	2.8	.053	1.47
	2.8	.0642	1.8
	4.43	.035	1.75
	4.43	.041	1.8
	5.37	.023	1.23
Steel Anvil (Rc 64)	3.13	.096	2.97
	3.13	.087	2.656
	3.13	.079	2.41
	3.13	.047	1.482
	3.13	.076	2.31
	3.13	.065	1.97
	3.13	.027	.84
	3.13	.039	1.215
	3.13	.041	1.265
	3.13	.082	2.56
	3.13	.085	2.62
	3.13	.085	2.62
	3.13	.072	2.24
	90.7	2.37	3.42
	167.4	1.63	4.37
	168.8	.48	1.30
	169.6	2.65	7.2
69.1	2.87	3.17	

are able to record the deceleration of the impactor up to the moment of ignition, they were always destroyed by the full force of the remaining impact. Thus while the energy to ignition was recorded early in the destruction of the force gages by the remainder of the impact load makes this a somewhat expensive and inconvenient test for insensitive materials. Typically, in these high velocity impacts the mass of the impactor was approximately .4 kg and the velocity of the impactor at the moment of impact was between 25 and 35 m/s. The maximum deceleration seen by the force gage regularly exceeded  $10^6$  g's. A number of techniques have been tried to limit this maximum deceleration or to use laser interferometer or velocimeter techniques in place of the force gages and while these are promising they are as yet unsatisfactory, particularly for a rapid turn around laboratory-use instrument. The problem is in achieving a 1 percent or better velocity measurement with an apparatus that can survive the full force of the impact.

Finally, while the ignition process is fundamentally an energy localization hot spot process, in practice any attempt to model ignition, especially in large systems, must to some degree involve a computer code calculation. Elsewhere we have attempted a first pass continuum calculation invoking an effective viscosity to calculate the energy to ignition.<sup>8</sup> The approach determines an effective viscosity coefficient from the energy to ignition data. This coefficient can be used to calculate ignition in more general impact situations.

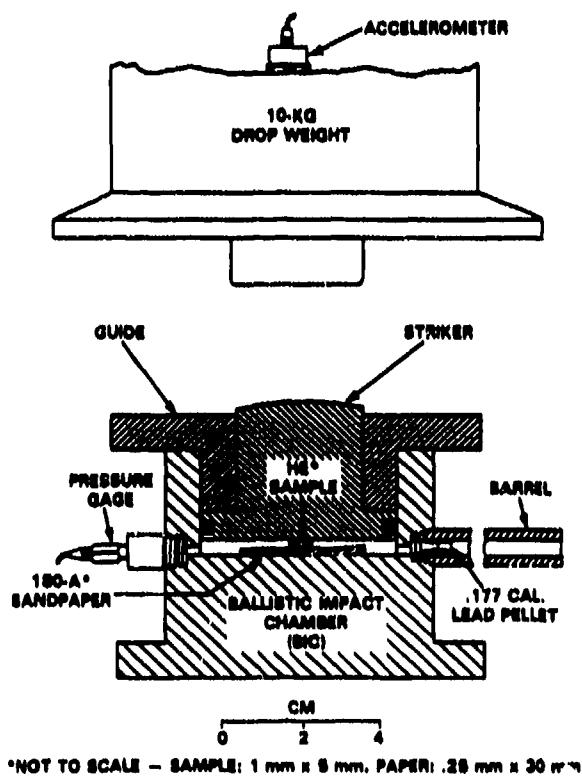
impactor was varied from 16 gm to 10 kg, and the impactor velocity from a few m/s to nearly 400 m/s. The changes that appear at the very high velocity impacts may be due to an inadequate response time of the gages. It seems likely that in its current form the energy to ignition test results are independent of the form of the test apparatus.

The technique has been applied to determine the energy to ignition of a number of impact insensitive explosives. Unfortunately, for these materials the initial impact energy must be so large to cause ignition early in the impact that, while the force measuring gages

## REACTION RATE AND ENERGY RELEASED: THE BIC TEST

To be able to predict the hazard response of an energetic material to impact it is insufficient to obtain just the energy required to cause ignition. Rather, in addition it is necessary to establish a measure of how violent the ensuing reaction will be. This is very similar to the concept of Explosiveness which was first developed by the British in their quest to determine hazard response. At NSW we have developed a closed volume impact test in which the pressure time history and the energy of reaction can be determined. These

provide a direct measure of the extent of reaction and the reaction buildup. A particular version of this test known as the Ballistic Impact Chamber or BIC test has received considerable attention and will be described here. The BIC test uses a closed volume impact chamber formed by a cup-like anvil, a guide sleeve insert, and a striker as shown in Figure 3. The space between the walls of the cup, the guide sleeve, and the striker are sealed with "O" rings. Cut in the walls of the cup are two ports. Attached to one is a 30 cm long .177 caliber gun barrel and to the other is attached a fast response pressure gage, (500,000 hz). The confined impact chamber acts as a breech from which the hot gases of the reacting sample can accelerate a .177 caliber pellet along the gun barrel. The work done on the pellet by the hot gases of the reaction gives a measure of the amount of energy released by the impacted explosive or propellant. The pressure gage measures the pressure time development of the reacting gases and the energy of the pellet as it exits the barrel.



\*NOT TO SCALE - SAMPLE: 1 mm x 5 mm. PAPER: .25 mm x 30 mm

Figure 3. BIC Test Impact Chamber

In order to minimize the amount of effort involved in a test series, it was decided to establish a standard impact of a ten kg mass released from a height of 1.5 m. A 180 grit sand or garrat paper was used to standardize and enhance the friction of the anvil surface. This combination of drop weight and drop height was found to always initiate even most of the insensitive TATB based materials. The so-called "Up-Down" method of varying the drop height was not considered because it has a dubious meaning as was pointed out earlier.

Our current goal is to develop a user-friendly test that provides a maximum of useful information with a minimum hassle to the user. As a result most of the instrumentation in the earlier test apparatus has been eliminated, and what has been retained is just the pressure gage and an occasional accelerometer. A conservative design has been selected which is sufficiently rugged to allow the machine to undergo several thousands of impacts sustaining little or no damage. As is always the case, these design goals have been achieved at the expense of some compromise in machine versatility and response.

## SOME RESULTS FROM THE BIC TEST

A substantial data base of results from the BIC test has been accumulated for a wide variety of explosives and propellants. In the interest of developing an efficient and meaningful test procedure we have found it necessary to conduct only ten impacts per sample type to obtain reasonable statistics. On occasion, when only a limited quantity of material was available, a reasonably complete data set was obtained with only five impacts per sample type. All of the BIC test results to be described here employed a uniform sample size in the form of a pellet 5 mm in diameter and approximately 1.25 mm thick, and having a mass of 40 to 45 mg.

Because it is a new test, employing instrumentation not previously used in explosive/propellant impact testing, the BIC test provided some new and unexpected insights into the behavior of energetic materials during impact induced ignition and

the subsequent reaction. The results presented here will focus mainly on these new observations.

Perhaps the most singular and most readily apparent result of the BIC test is that for the majority of explosives and propellants, impact-induced ignition is a discontinuous process. This is illustrated in Figure 4 displaying a series of pressure-time records taken from the standard BIC test for several different explosive and propellant materials. In all but the most insensitive TATB and NTO based materials the very initial reaction in the pressure-time records is a rapid, almost discontinuous pressure rise. Depending on the material, this pressure rise rate can range from .8 psi/ $\mu$ s to in excess of 2000 psi/ $\mu$ s. This discontinuous pressure jump is most likely due to the sudden ignition and reaction in a large explosive crystal or group of crystals located near the outer edge of the sample in the region of maximum shear and minimum pressure during the impact. The occurrence of multiple pressure spikes was frequently observed in

many samples. These are taken to be an indication of the presence of a number of large crystals located throughout the sample and which undergo sudden reaction due to the impact. Samples which were deliberately seeded with several large crystals separated by some distance showed a series of pressure spikes generally corresponding in number to the number of large crystals inserted into the sample. Ignition threshold experiments using heat sensitive film<sup>4</sup> confirmed this result by showing that the number of ignition sites on the heat sensitive film was the same as the number of pressure spikes in the pressure-time records.

The pressure-time data indicates that in addition to the sudden ignition in a single or at most a few crystals there also occurs a much slower burning-like reaction. This appears in the pressure-time records as a slower pressure rise on which is superimposed the much more rapid pressure spikes. For the very insensitive explosives frequently only the slower burning type reaction was observed. For most materials it is likely that the ignition of the burning reaction is due to the hot-spot-induced reaction spikes in the larger crystals or agglomerate of crystals.

In the course of these investigations we chose to focus on two components of the pressure-time data, the very initial rate of pressure rise,  $dp/dt$ , and the total area under the pressure-time curve, as having the most relevant physical significance. However, certainly other aspects of the data may be equally important. The initial rate of pressure increase must reflect the initial reaction rate. As such this data gives some information on the likelihood of a violent reaction occurring due to impact. The area under the pressure-time curve is a measure of the energy released during the reaction. Depending on the material, this energy can range from a few joules per gram of sample to in excess of several hundred joules per gram.

## THE FLUCTUATIONS

Ever present in the pressure-time data are large fluctuations. This should not be surprising since large fluctuations characterize all impact data from both large- and

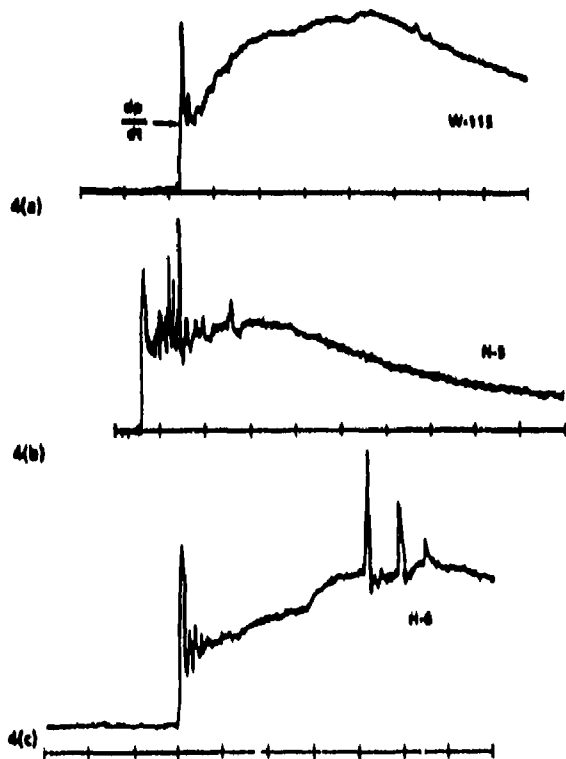


Figure 4. Typical Pressure-Time Records from BIC Test. Time scale is 20  $\mu$ s/division.

small-scale experiments. What is important is that these fluctuations provide an insight into the stability of these materials to undergo more violent reactions at higher energy impacts. Generally it is the case that the fluctuations can be made to yield valuable insights into the underlying physical processes, here the impact-induced reaction growth process.

Usually, most explosives are not totally consumed during the standard BIC impact-induced reaction. The fluctuations in energy released during the reaction reflect this as much of the explosive in the impact-initiated sample has to be scraped off the anvil and discarded after the impact. This is not the case for propellants which are designed to burn completely and usually leave little or no residue on the anvil. In a series of BIC impacts on five propellants, all with the same energy content but each with a different binder material, a total of 50 tests were made. The fluctuation in the energy released over these 50 impacts was less than 10 percent. From this data it can be inferred that not only was the total sample consumed during each of these impacts, but that the BIC test was able to faithfully record the energy released from each impacted sample while introducing little fluctuations of its own.

Invariably, the initial rate of reaction as reflected by the initial rate of pressure increase, always shows larger fluctuations than the energy released measurements. In part this is because the energy release measurements are averaged over a much longer time interval than the measurements of the initial pressure increase.

A recent theoretical analysis of the fluctuation in the impact or shock ignition process has taken the approach that for mild impacts the very first ignition occurs in the larger single crystals or cluster of crystals located in the regions of highest shear in the impacted sample.<sup>3</sup> This process is suggested in both the BIC initial reaction rate data as illustrated in Figure 4 and our earlier heat sensitive film experiments.<sup>4</sup> The correlated ignition fluctuations arise when there is a probability that one of these initially reacting particles can cause ignition in a similar

neighboring particle (or particle group). In this picture the interaction at mild impacts is mainly between particle pairs, while for higher energy impacts or shocks each particle may interact and stimulate reaction in more than just one other nearest neighbor particle. If the average reaction rate of the initial reaction is due to the ignition of a single particle, the maximum pair fluctuation occurs when the initial ignition stimulates ignition in a similar nearby neighboring particle. This maximum fluctuation occurs for interaction between pairs of particles with nearly the same energy for which the fluctuation in the reaction rate is 100 percent above the average reaction rate.

In Reference 9 it is shown that the fluctuation in the initial reaction rate can be written as

$$\frac{\Delta\left(\frac{dE}{dt}\right)}{\left\langle\frac{dE}{dt}\right\rangle} = \left\{ 2 \frac{V_0 - V_{In}}{V_0} \left[ \left( 1 + \frac{2h}{\ell} \right)^3 - 1 \right] \right\}^{1/2}, \quad (4)$$

Where  $V_{In}$  is the volume of the inert material and  $V_{In}/V_0$  is the volume fraction of inerts in the composition. The quantity  $\ell$  is the average crystal particle size while  $h$  is an interaction length, and also the maximum separation distance between two adjacent particles where if one particle reacts it will cause the other to react.

Figure 5 shows both the fluctuations as measured by the BIC test for a number of different explosives and propellants as a function of the volume fraction of inerts,  $V_{In}/V_0$  and the predicted fluctuation for Equation (4). The pair interaction hypothesis predicts that the maximum fluctuation is of the order of unity (100 percent) as  $V_{In} \rightarrow 0$ . On this basis the ratio  $h/\ell$  was determined to be  $h/\ell = .075$  which is not an unreasonable value. More importantly, the fluctuation data in Figure 5 is almost entirely less than unity which supports the hypothesis that for mild impact, such as the BIC test, only correlations between pairs of particles are important. If, however, for some reason the correlated interactions extend beyond nearest neighbor pairs to include

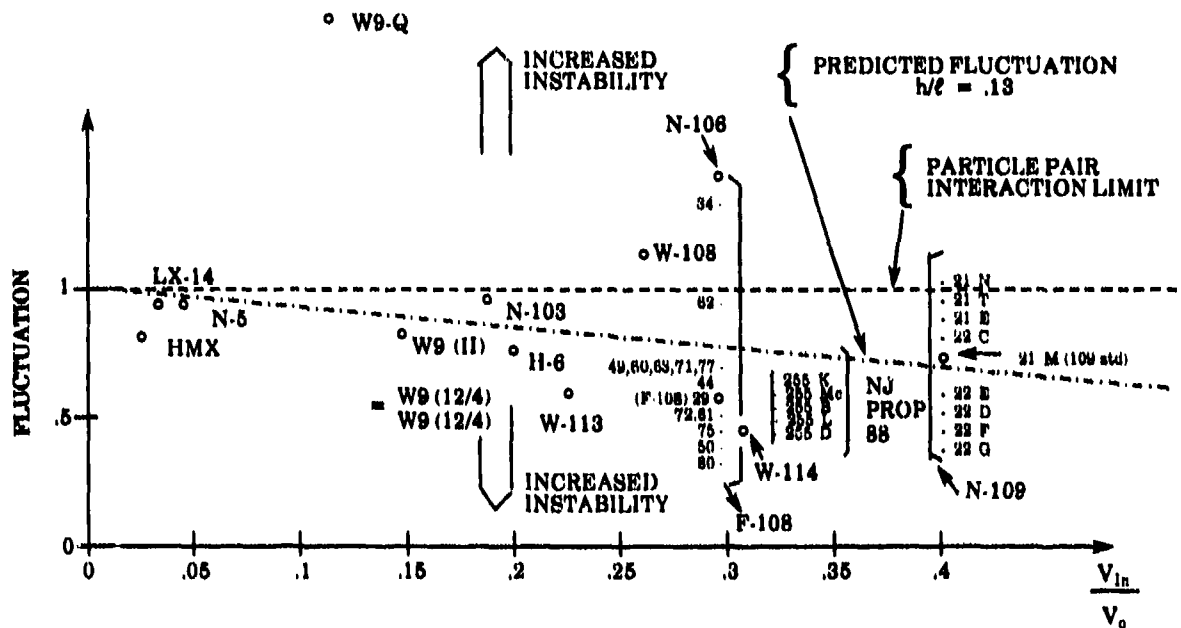


Figure 5. Fluctuations as a Function of Volume Fraction of Inerts for Some Representative Explosives. Each data point represents on average at least 10 test results.

additional particles, then the system becomes unstable because now a reacting particle will stimulate on average more than one additional particle causing it to react. Each of these particles can in turn stimulate two or more others so that a runaway reaction can develop. In Figure 5 only one set of data points labeled W9-Q has shown fluctuations significantly above unity. Material similar to this has been associated with violent pressure excursions on two of the three occasions in which it underwent a normally benign pressing operation at NSWC. In light of these relatively large fluctuations, the validity of the often-used Bruceton "up-down" method to obtain a 50 percent go-no go level needs to be reconsidered. Implicit in the "up-down" analysis is the assumption of a uniform response which is not the case. The go-no go problem is compounded by the fluctuation in the level of response that is accentuated at the 50 percent threshold level and this must be taken into account.

One of the advantages of this fluctuation approach is that it brings a step closer the ability to predict the response of a larger charge to

an arbitrary impact if the BIC data for the average initial reaction rate and its fluctuation are known. Reference 9 shows that the maximum reaction rate can be approximated as

$$\left. \frac{dE}{dt} \right|_{\text{Max}} \approx \left\langle \frac{dE}{dt} \right\rangle \left( 1 + \Delta \left( \frac{dE}{dt} \right) / \left\langle \frac{dE}{dt} \right\rangle \right), \quad (5)$$

where  $\Delta(dE/dt)/\langle dE/dt \rangle$  is given by Equation (4) and  $\langle dE/dt \rangle$  is the average initial reaction rate. The approximation given in Equation (5) is just the sum of the first few terms in a series summed over all of the reacting particles in the ignited material. Those first few terms give a reasonable estimate of the initial rate of the reaction due to impact initiation. A knowledge of the dependency of the interaction distance  $h$  on the energy and rate of application of the stimulus would allow an evaluation of these terms for an arbitrary impact and give an estimate of the rate of reaction buildup. The reaction rate of Equation (5) can be cast into a form that can directly utilize the small scale BIC test data by writing

$$\left. \frac{dE}{dt} \right|_{\text{Max}} = \left\langle \frac{dE}{dt} \right\rangle (1 + \delta), \quad (6)$$

where  $\delta$  is the experimentally measured fluctuation in the rate of reaction. Even with only the pair fluctuations of the mild impact of the BIC test, the BIC reaction rate data as reflected by the rate of pressure buildup when substituted into Equation (6) gives a good ranking of the relative hazards of a number of different explosives in bullet impact tests involving large explosive charges.

### SOME FUTURE PLANS

Much more work was done in developing these tests than was able to be presented here. Important portions of these results will be published elsewhere.<sup>8</sup> One ongoing effort deserves some further comments and that is our attempt to image with fast infrared arrays the development of hot spots during shock or impact. Hot spots have been a necessary part of the lore of shock and impact ignition of explosives since the 1930s but they have never been observed experimentally during their formation. We believe these hot spots are the shear bands that are frequently observed in crystalline solids that have been subjected to shock or impact.<sup>1</sup> At NSWC we are attempting to form real time images of these hot spots using fast linear (1 x 15) or rectangular (4 x 5) infrared arrays. The experimental apparatus has a response time of 30 ns limited by the response time of our multichannel analyzer. The objective of the current research is to establish with certainty the nature of the hot spots. Are they the shear bands? How fast do they grow in size and temperature? How far apart are they for a particular energetic crystal and how does the ignition reaction grow out of these hot regions?

### ACKNOWLEDGEMENTS

A number of individuals have contributed generally to this effort with their advice, support, and encouragement. These include Drs. C. Dickinson, L. Roslund, H. Haiss, S. J. Jacobs, and Ms. B. A. Yergey.

### REFERENCES

1. Coffey, C. S., "Initiation of Explosive Crystals by Shock or Impact," *Proceedings of the Ninth Symposium (International) on Detonation*, 1989.
2. Bowden, F. P. and Yoffe, A. D., *Fast Reactions in Solids*, Academic Press, New York, 1958.
3. Heavens, S. N. and Field, J. E., *Proc. of R. Soc. London*, See A 338 77 (1974).
4. Coffey, C. S.; Frankel, M. J.; Liddiard, T. P.; and Jacobs, S. J., *Proceedings of the Seventh Symposium (International) on Detonation* (NSWC MP 82-334), 1981.
5. Campbell, A. W. and Travis, J. R., *Proceedings of the 8th International Symposium on Detonation*, NSWC MP 86-194, 1986.
6. *Engineering Design Handbook/Principles of Explosive Behavior*, U.S. Army Material Command, AMCP-706-180 (1972).
7. Coffey, C. S. and DeVost, V. F., "Evaluation of Equipment Used to Impact Test Small-Scale Explosive and Propellant Samples," Appendix A, NSWC TR 81-215.
8. Coffey, C. S.; DeVost, V. F.; and Woody, D. L., *Proceedings of JANNAF Hazards Meeting March 1988*, also in NSWC Technical Report in preparation.
9. Coffey, C. S., to be submitted to the *Phys. Rev.*

# "FROZEN HOT SPOTS" IN SHOCKED EDC35, AN INSENSITIVE HIGH EXPLOSIVE

G. Eden, R. A. Belcher, M. I. Andrew, and W. R. Marlow  
MOD (PE), Atomic Weapons Establishment  
Aldermaston, Reading RG7 4PR  
Berkshire, ENGLAND

*An EDC35 donor charge, line initiated, was used to shock an acceptor charge through various inert barriers.*

*The system was confined by walls of polyethylene and mild steel, with a PMMA window bonded to the remote end of the receptor. It was illuminated by argon flash bombs and viewed by a framing camera. Piezoelectric probes also monitored wave arrival times.*

*Shots with a viewing window parallel to the barrier had acceptor charges 120 mm long. An angled acceptor charge of length 18 - 40 mm was used to monitor the development of shock effects.*

*During the run to detonation, small dark areas, postulated to be sites of local reaction, were seen in the wake of the shock. They did not grow significantly after the shock passed, but the increase in number and size is associated with increased wave velocity and pressure.*

*In these experiments, detonation, once started, did not propagate back through the pre-shocked, partially reacted part of the charge.*

## INTRODUCTION

This paper describes the direct time resolved observation of localized changes in an insensitive high explosive which, it is postulated, indicate the way in which isolated and short-lived reactions contribute to the general growth of the pressure amplitude as a shock in a heterogeneous explosive runs to detonation.

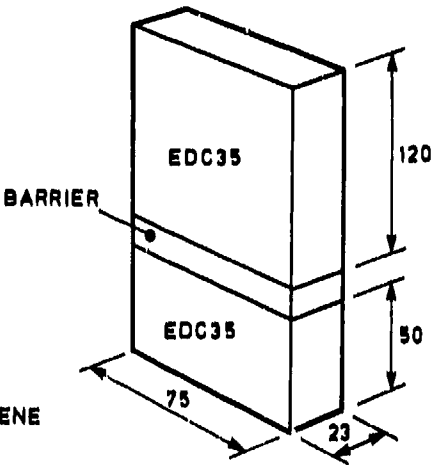
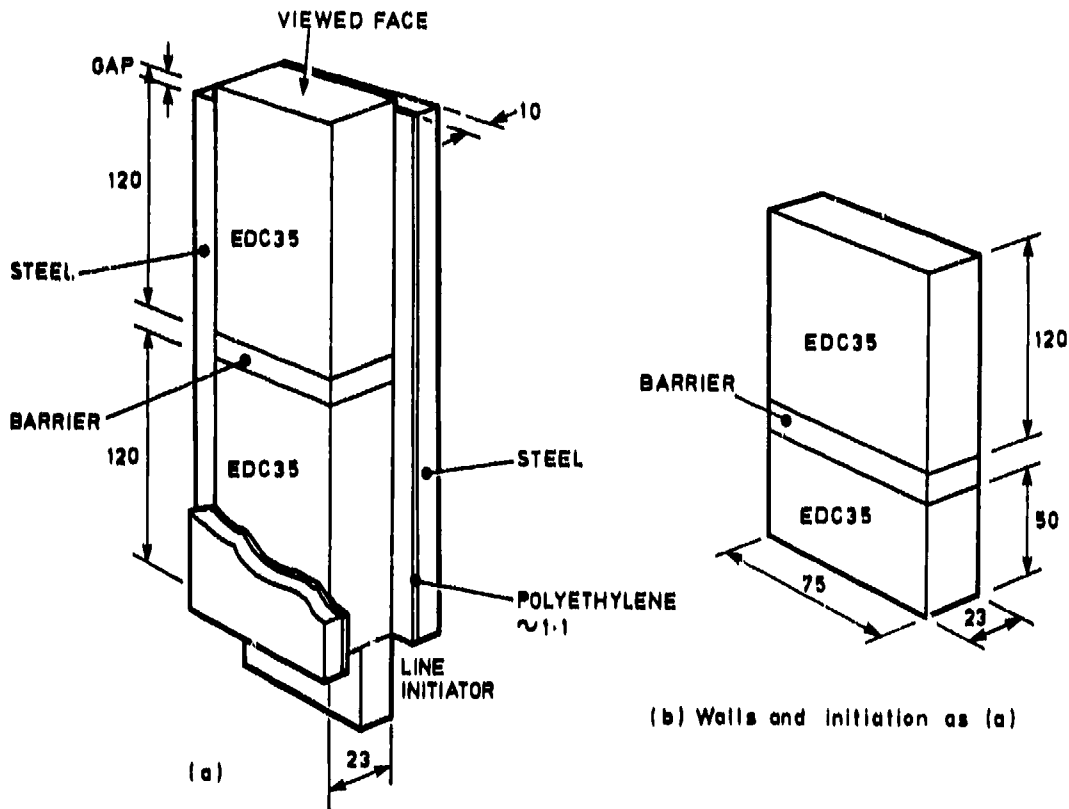
To study visual effects in shocked charges, an insensitive high explosive, EDC35, was chosen to provide a relatively expanded region between shock input face and the onset of full detonation. EDC35 contains 95 weight percent TATB and 5 percent Kelf, and the charge density was  $1.90 \text{ Mg/m}^3$ .

Gas gun impact is a most reliable method of generating characterized shocks, but it suffers from the limitation on bore size and area. The larger area available in explosively

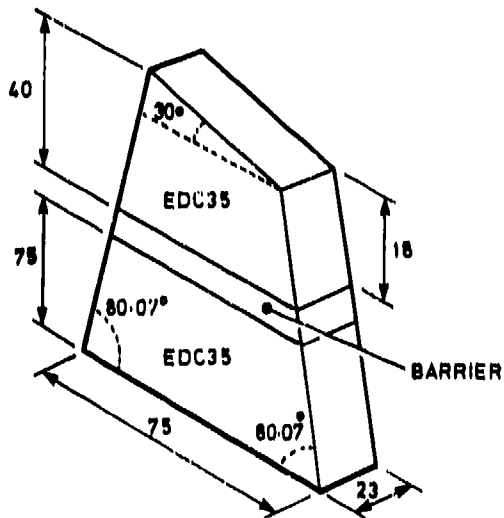
generated experiments was chosen as more appropriate for the anticipated large "run to detonation" (RTD) distance. The pressure pulse from detonation of one charge (the donor) was attenuated by an inert barrier, and passed into a second charge (the acceptor) in which the effects were to be studied.

## METHOD

In all experiments, an EDC35 donor charge was detonated at a 75 mm x 23 mm face by a line initiator of length 75 mm (see Figure 1). At the opposite end of the slab, an EDC35 acceptor charge, also 23 mm in thickness, was shocked by the wave transmitted from the donor to the acceptor via an inert barrier. The sides of the charges and barrier were confined by thin polyethylene and 10 mm thick mild steel plates, the polyethylene being



(b) Walls and initiation as (a)



BARRIER DETAIL IN FIGURE 2  
ALL DIMENSIONS IN MILLIMETRES

(c) Walls and initiation as for (a)

Figure 1. Charge and Barrier Systems

present to reduce possible atypical effects due to stronger shock reflections from the metal sides. Confinement stopped 5 mm short of the end of the acceptor, creating a gap to prevent direct shock transmission into an end viewing window. This was a sheet of PMMA 40 mm thick and optically transparent. To avoid self-luminous air shock interfering with observation, the PMMA was bonded to the charge surface with 0.1 mm of Sylgard. Illumination was by argon filled, explosively driven flash bombs.

The main diagnostic used was a Barr and Stroud C5 framing camera, capable of up to 115 frames with a framing interval of 0.14 microsecond, focussed on the face of the charge covered by the PMMA. The images were recorded on Fuji HR400 color film with standard processing. Piezoelectric probes were used to monitor wave arrival times, e.g., at the donor/barrier interface and at the acceptor/PMMA interface.

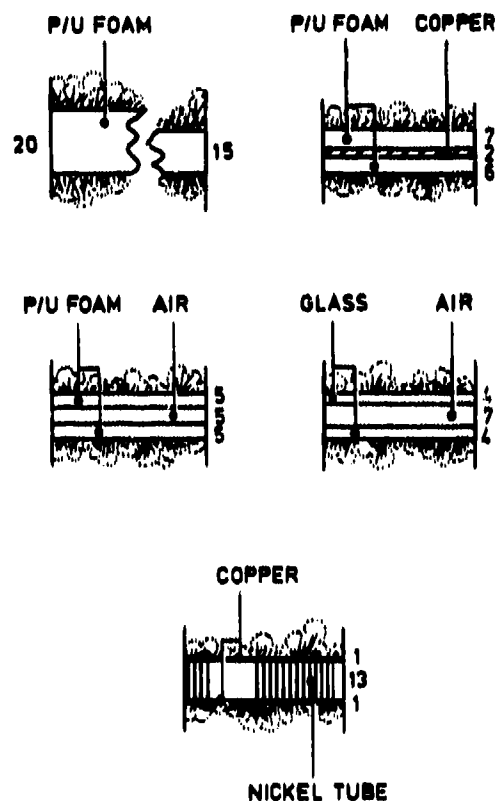
Shots 1015 and 1019 had an acceptor length of 120 mm with the PMMA window parallel to the barrier, as in Figure 1(a) and 1(b) respectively. The remaining shots had the "angled" design in which the acceptor face viewed by the camera was cut at an angle to the face in contact with the barrier, so that the progress of the shock could be followed from an acceptor thickness of 18 mm through to 40 mm.

A range of barrier designs (see Figure 2) was used to give a range of shock pressures in the acceptor and all experiments were at ambient temperatures, 15 to 20°C before firing.

## RESULTS

Each angled experiment yielded 20 or more Time vs. Distance points for the wave propagation through the acceptor charge (between 18 and 40 mm from the barrier). Superimposing all the plots in Figure 3, it can be seen that if we discount their non-linearity which is caused by curvature of the wavefront, their slopes alter in accord with the changes in appearance of the shocked acceptor charge, in the following order (see Figure 4):

(a) uniform color,



P/U = POLYURETHANE FOAM, DENSITY 0.1 g/cc.  
OVERALL DENSITY OF NICKEL TUBE  
BARRIER 4.7 g/cc

EXPLOSIVE  
ALL DIMENSIONS IN MILLIMETRES

Figure 2. Barriers

(b) a few discreet small areas of darkening, which do not grow significantly with time, i.e., are "frozen,"

(c) many and merging areas of darkening which do not grow significantly, and

(d) dark detonation products.

This general association of increased shock velocity with the proliferation of the small sites of darkening suggests that the latter are isolated, reacted Hot Spots whose growth has been arrested. Their isolation has allowed direct observation.

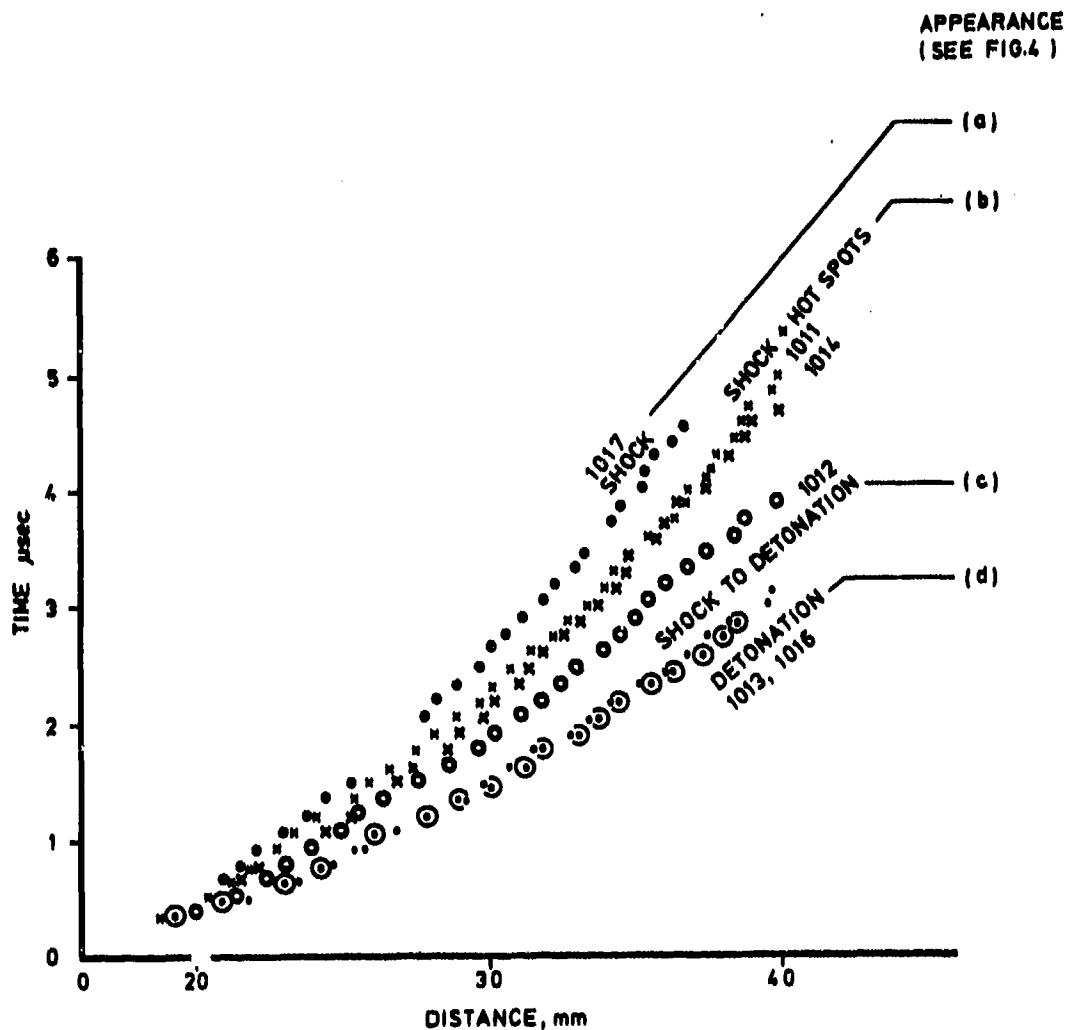


Figure 3. Wave Propagation in EDC35

From the middle part of each plot, shock velocities were derived and corresponding shock pressures calculated using Reference 1 reactions for PBX 9502 of initial density  $1.895 \text{ gcm}^{-3}$ :

$$U_s = 1.392 + 5.154u_p - 2.422u_p^2 + 0.5616u_p^3$$

( $0.5 < u_p < 1.2 \text{ mm} \cdot \mu\text{s}^{-1}$ )

$$U_s = 2.938 + 1.77u_p \quad (1.2 < u_p < 2.33 \text{ mm} \cdot \mu\text{s}^{-1})$$

( $U_s$  shock velocity,  $u_p$  particle velocity)

This is an approximation in the absence of unreacted shock Hugoniot data for EDC35 of density  $1.90 \text{ gcm}^{-3}$ .

Examples are listed in Table 1, in which "A" is a subjective estimate of the fractional

area of charge surface, which is darkened at the mean thickness (29 mm) of the angled charges, and "v" is the volume fraction of darkening, assuming

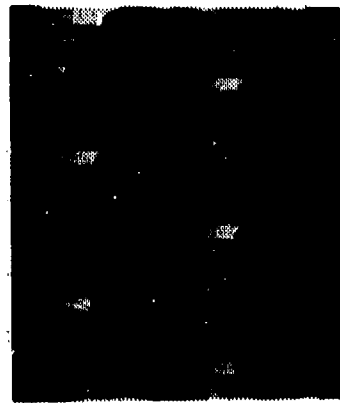
$$V = A^{1.5}$$

Both are expressed as percentages in Table 1.

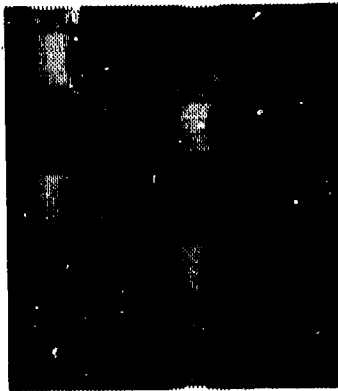
In Shot 1012, the shock, after generating multiple sites of local reaction, finally runs to detonation (at 35 mm from the barrier) which then propagates forward to the end of the wedge of acceptor, but which does not transmit backwards into the preshocked part of the charge. The shocked parts of the acceptor charge containing the "frozen" areas of



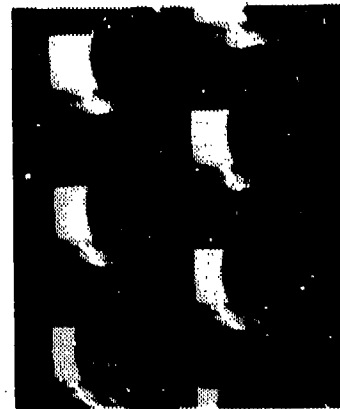
(a) No spots



(b) Discrete spots



(c) Merging spots



(d) Detonation

Figure 4. Types of Appearance of Shocked EDC35

Table 1. Shock Pressure vs. Reacted Volumes

SHOT	1017	1011	1014	1012	1013	1016
$U_s$ mm. $\mu$ s <sup>-1</sup>	3.7/4.0	4.1/4.5	4.6/5.0	5.3/5.8	6.6/8.0	6.6/8.1
$U_p$ mm. $\mu$ s <sup>-1</sup>	0.59/0.70	0.70/0.91	0.96/1.17	1.34/1.62	*	*!
P GPa	4.1/5.3	5.7/7.7	8.3/11.0	13.4/17.7	*	*
Appearance	(a)	(b)	(b)	(c)	(d)	(d)
A %	0	1.2	2.4	37	100	100
V %	0	0.1	0.4	22	100	100

\*Full detonation (unreacted Hugoniot not appropriate)

reaction are seen to survive virtually unchanged for at least another 10 microseconds after detonation starts.

There is some evidence that the appearance of the small areas of reaction may be an indicator of whether a shock will eventually run to detonation:

(i) In Shot 1017, no reacted sites are seen. In Shot 1019 which had an identical barrier, i.e., similar shock input but a much longer acceptor charge, 120 mm, the shock did not run to detonation.

(ii) In Shot 1014 (see Figure 4b), frozen areas of reaction occupy a few percent of the visible area. In Shot 1015, which had an identical barrier but a 120 mm acceptor charge, the shock ran to detonation, presumably somewhere between 40 and 120 mm.

(iii) Reference 2 suggests that "about 7.5 GPa" is the minimum shock pressure needed to shock initiate detonation in TATB, i.e., at about the level of Shot 1011 where a few isolated reaction sites are seen.

## CONCLUSIONS

The observations show clear evidence that small areas of local darkening are visible immediately after a shock of sufficient amplitude passes. These areas neither grow (at a significant rate) nor multiply with time at a given location in the charge, but as the shock pressure increases, more and larger areas are created. Greater profusion of these features is associated with increased wave velocity, and they are deduced to be areas of localized reaction in the explosive, or "Hot Spots" which fail to propagate ("freeze") before the RTD conditions are reached. There is also evidence that when detonation does start, the pre-shocked, partially reacted part of the charge does not support detonation, i.e., the detonation does not propagate in the reverse direction. This is in accord with many other such observations of shock desensitization; see for example the review and observations by Campbell and Travis in Reference 3.

## DISCUSSION

Proper correlation of the appearance of, or concentration of frozen Hot Spots with eventual run to detonation awaits further work, so the conclusions must be highly speculative, but this limited investigation has yielded an observation of what the authors currently believe to be the source of the energy which amplifies the pressure of a shock moving through a heterogeneous explosive during its run to detonation. That is, a direct observation of the number of the potential Hot Spots in the charge which react and feed energy to the shock front, but which individually fail to propagate further, leaving small areas of reaction products "frozen" in the body of the charge. More of the potential Hot Spots appear to react as the shock strength builds, although this is an average observation and anomalies are visible in the results where, for example in Shot 1012, there appear to be many and merging areas of reaction, followed by fewer areas, followed by full detonation.

Nevertheless, observations of this kind on a range of explosives, using better characterized shocks or compression waves, could assist construction and calibration of reaction models of detonation. They also make possible a study of the influence of artificial heterogeneities in a given explosive by introducing known concentrations of characterized cavities, defects, particles, etc., complementing the established Lagrangian gauge methods, which measure the average effects of the local reactions seen here.

## ACKNOWLEDGEMENTS

The authors gratefully acknowledge the support received from P. W. J. Moore and B. D. Lambourn, and they thank G. G. Dale and G. Reece for their invaluable assistance with the experiments.

## REFERENCES

1. Dick, J. J.; Forest, C. A.; Ramsay, J. B.; and Seirz, W. L., "The Hugoniot and Shock Sensitivity of a Plastic-bonded TATB Explosive PBX 9502," *Journal of Applied Physics*, **63**(10), 1988, p. 4881.

2. Simpson, A.L.; Urtiew, P. A.; and Erickson, L. M., "High Explosive Diagnostics," *LLNL Energy and Technology Review*, Jan/Feb 1988.
3. Campbell, A. W. and Travis, J. R., "The Shock Desensitization of PBX 9404 and Composition B-3," in *Proceedings of Eighth Symposium (International) on Detonation*, Albuquerque, NM, NSWC MP 86-194, pp. 1057-1068.

## DISCUSSION

**ALLAN ANDERSON**  
Los Alamos National Laboratory

Is it known that PMMA becomes opaque under shock loading (admitted at higher pressures)? The rate of this process is probably not known. Have you done the control experiment--Place an inert material such as aluminum beneath the PMMA; better yet, an

inert match to EDC35? This would demonstrate that the effect is, in fact, from EDC35.

## REPLY BY R. A. BELCHER

Although Chhabildas and Asay have reported loss of transparency between 23 and 25 GPa and our maximum pressure in the EDC35 was 13.2/16 GPa corresponding to PMMA pressure of around 12 GPa, we have much evidence in these rounds that transparency was unaffected. However, like you, we felt that a control experiment was necessary, but as a check that the thin layer Sylgard between the EDC35 and the PMMA was not itself reacting and producing the dark patches observed. In January and August 1989, we fired control experiments which subjected a Sylgard layer between slabs of PMMA to pressures of 10 to 20 GPa and no darkening was seen.

# DEFORMATION AND SHOCK LOADING STUDIES ON SINGLE CRYSTALS OF AMMONIUM PERCHLORATE RELATING TO HOT SPOTS

H. W. Sandusky, B. C. Glancy, and D. W. Carlson  
Naval Surface Warfare Center, White Oak  
Silver Spring, Maryland 20903-5000

and

W. L. Eiban  
Loyola College  
Baltimore, Maryland 21210

and

R. W. Armstrong  
University of Maryland  
College Park, Maryland 20742

*A microscopic-scale study of the role that crystal defects have in forming hot spots during shock loading has commenced for large, optical quality, pure single crystals of ammonium perchlorate (AP). The crystals were immersed in mineral oil at various distances from a detonator that provided the shock. The small explosive donor permitted recovery of the crystals for quantitative chemical analysis of decomposition and microindentation hardness testing. Hardness testing was also performed on an unshocked crystal to determine: (1) the slip systems associated with primary and secondary deformation in accommodating the indentation, and (2) the propagation directions at the surface, as well as into the crystal, of associated cracks. Slip and cracking systems identified by hardness testing were observed in high-speed photographs of the shock-loaded crystals. Some of the systems were luminous. In addition, when a crystal with a large indentation was shocked near its reaction threshold, significant light appeared in the vicinity of the indentation following shock passage. As such, preferred chemical reactivity in AP has been associated with its deformation systems and the presence of large strain centers.*

## INTRODUCTION

A number of years ago, the formation of "hot spots" was proposed and experimentally verified as occurring in energetic materials in response to mechanical forces, such as those from impact.<sup>1</sup> Circumstances where hot spots occur, suggest that their origin is closely connected to the microstructure and allied deformation properties of the energetic material. There is also experimental evidence

indicating that crystalline explosives have microstructural properties that influence their shock sensitivity. This was observed on a macroscopic scale by Green and James<sup>2</sup> in small-scale gap tests on cyclotetramethylene-tetranitramine (HMX) formulations made from crystals of differing quality. For pentaerythritoltetranitrate (PETN), Dick<sup>3</sup> determined that microscopic damage from gamma radiation enhanced the shock

sensitivity of single crystals over that of relatively defect-free crystals. In addition, the shock sensitivity of the latter crystals was a function of orientation, indicating that shock-induced defects depend on the lattice arrangement.<sup>4</sup> To date, however, no work has been reported that spatially relates sites of microstructural imperfection to enhanced chemical reactivity as an energetic material is impacted or shocked.

The present study is a beginning effort to determine the role of material microstructure in chemical reactivity and dynamic deformation of single crystals of energetic materials subjected to shock. The results of high-speed photographs are integrated with material property measurements and chemical analyses, both of which were performed before and after shocking the crystals. Ammonium perchlorate (AP) was chosen for this study, in part, because of its widespread use as an oxidizer ingredient in solid propellants and explosives. In addition, the thermal decomposition behavior is well understood, and the deformation behavior has been studied to some extent by other investigators,<sup>5,6</sup> providing valuable reference information for current deformation studies. In drop-weight impact tests reported by Heavens and Field,<sup>7</sup> AP ignited coincident with a sharp drop in the pressure-time curve, much like the result for cyclotrimethylene-trinitramine (RDX). Macek and Durfee<sup>8</sup> determined the threshold for shock-induced reaction in pressed AP with 13 percent porosity by measuring weight loss of sealed samples that had been impacted by a gun projectile (250 to 700 m/s). Relative to explosive crystals such as HMX, PETN, and RDX, local reaction sites in AP are more likely to quench without destroying the crystal. This suggests the feasibility of studying, perhaps on a microscopic scale, the role that crystal defects have in forming hot spots and in enhancing shock reactivity in AP.

## EXPERIMENTAL APPROACH

Large (> 1 cm), optical quality, pure single crystals of AP were provided by T. Boggs, Naval Weapons Center, China Lake, CA. AP has an orthorhombic unit cell with a crystal density of 1.95 g/cc. The drawing in Figure 1 is

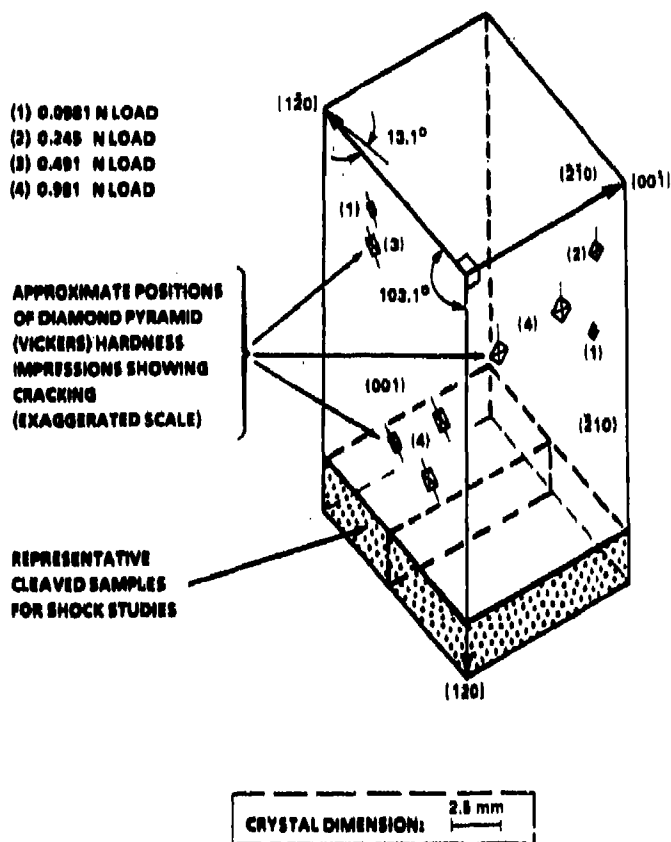


Figure 1. Scale Drawing of Cleaved AP Single Crystal Used in Microindentation Hardness Tests

for a typical cleaved crystal, showing size and shape along with cleavage surfaces and major crystallographic directions. The plastic deformation and fracture behaviors of AP were investigated by putting diamond pyramid (Vickers) microindentations into the  $(\bar{2}10)$  and  $(001)$  cleavage surfaces of the crystal, as shown in Figure 1.<sup>9</sup> Hardness results on the  $(001)$  surface will be emphasized in order to relate to shock loading observations obtained for the same surface.

Shock experiments<sup>9</sup> were conducted on relatively small crystals of AP (< 0.5 g) that were cleaved from a larger crystal, as indicated, for example, in Figure 1. Each crystal was immersed in mineral oil and shocked by a detonator (Reynolds RP-80) at a known separation distance. The Reynolds RP-80 uses an exploding bridgewire to initiate 78 mg of PETN, which in turn initiates 124 mg of RDX with binder. In the particular type of RP-80 that was used, the explosive components are in a Delrin sleeve which does not cover the output

end of the detonator; that end was sealed from the oil with a light coat of Duco cement. Thus, the detonator was much like a small donor charge with little confinement. The experiments were confined in a 0.9 liter steel chamber that has windows for photography and illumination (Figure 2). Both a rotating mirror streak camera and an Imacon electronic camera have been used with backlighting from an electronic flash. The crystal either rested on a piece of oil-soaked polyurethane foam or was supported above a piece of foam by tape (0.05 mm thickness). This arrangement allowed recovery of the crystal for subsequent chemical analysis and hardness testing, without obstructing the view of the camera. About 100 mg of most recovered samples were analyzed by liquid ion chromatography for the concentrations of  $\text{Cl}^-$ ,  $\text{ClO}_3^-$ ,  $\text{NO}_2^-$ , and  $\text{NO}_3^-$ .

The shock experiments were calibrated for peak pressure in the oil versus distance from the detonator (Figure 3). In a separate experiment, a rotating mirror streak camera was used to measure precisely shock position versus time, which was differentiated to obtain shock velocity. A Hugoniot for heavy mineral oil, density ( $\rho_0$ ) of 0.87 g/cc, was reported for the range of 15 to 150 kbar ( $U = 2.18 + 1.53 u$ ,

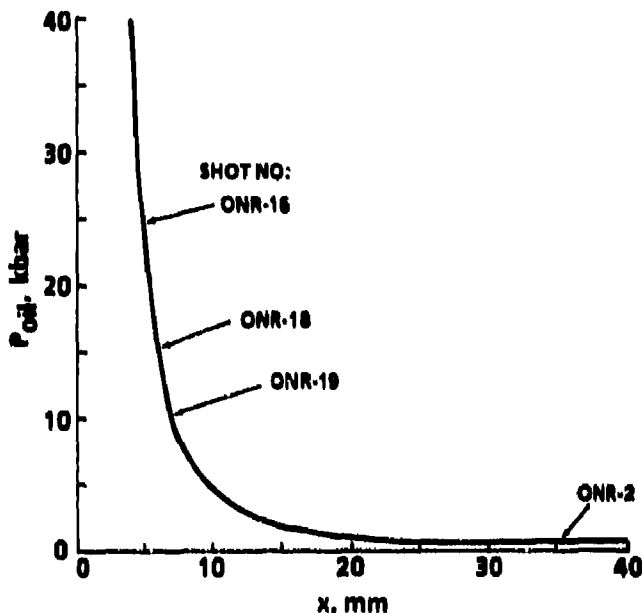


Figure 3. Calibration of Peak Shock Pressure in Mineral Oil Versus Distance from the Detonator

where "U" is the shock velocity and "u" is the particle velocity, both in units of  $\text{mm}/\mu\text{s}$ ).<sup>10</sup> Since pressures of less than 15 kbar were of interest, this Hugoniot was extrapolated to the 1.45  $\text{mm}/\mu\text{s}$  sound velocity ( $c_0$ ) for mineral oil with the equation

$$U/c_0 = 1.503 - 0.503 \exp(-5 u/c_0) + 1.53 u/c_0,$$

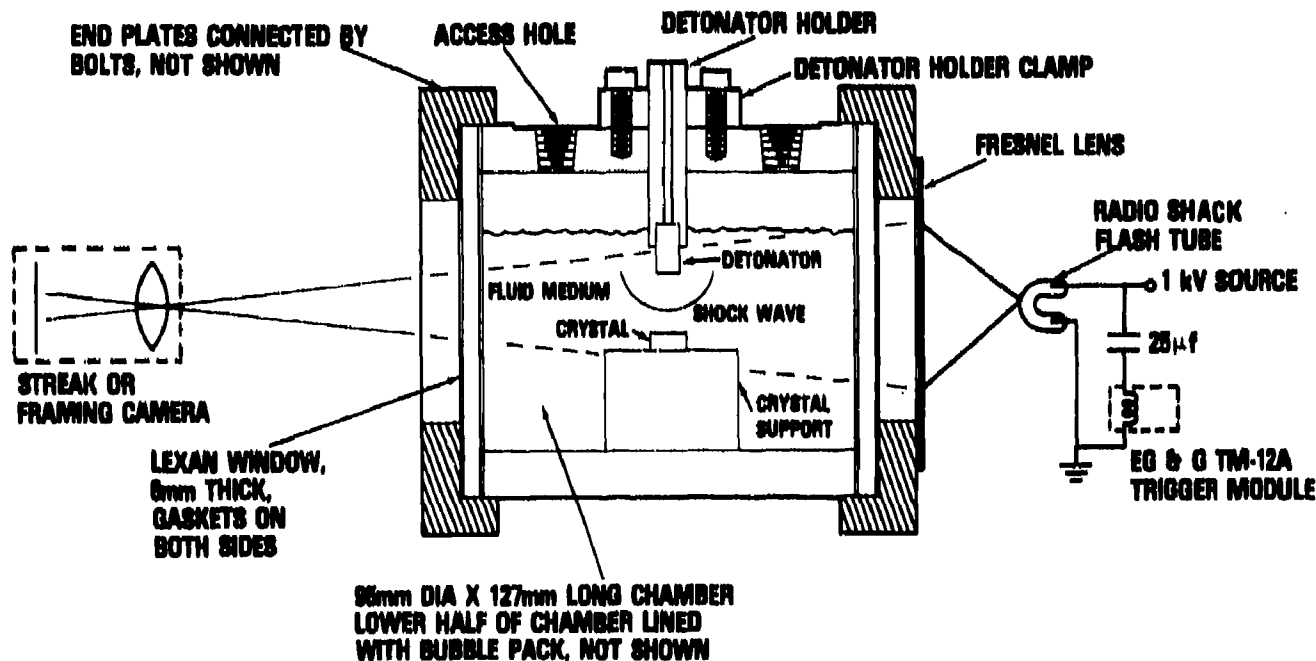


Figure 2. Closed Chamber for Photography of Shock Reaction in Small Samples

using an approach similar to that in Reference 11. With that modified Hugoniot and the experimental measurements of  $U$ , shock pressures in the oil were calculated using the jump equation,  $P_{o1}(kbar) = 10 \rho_o U u$ . The AP Hugoniot used for matching the shocks in the oil and the crystal was  $U = 2.84 + 1.6 u$ . A reported Hugoniot,  $U = 2.84 + 2 u$ ,<sup>12</sup> is consistent with a 2.84 mm/ $\mu$ s bulk sound speed in AP;<sup>13</sup> however, shock data for pressed AP (1.92 g/cc) at 155 and 178 kbars<sup>14</sup> was best fit with a slope of 1.6 in the  $U$  versus  $u$  relationship.

## MICROINDENTATION STUDIES (UNSHOCKED CRYSTAL)

Micrographs of a Vickers impression (100 gf = 0.981 N load) in the (001) surface appear in Figure 4. A Vickers hardness number (VHN) of 11 kgf/mm<sup>2</sup> (108 MPa) for that impression indicates that AP is soft, only 1/3 to 1/2 as hard as the molecular explosive RDX, using the results of various researchers as discussed in Reference 15. The transmitted light micrograph in Figure 4(A) shows that the four facets of the impression have a distorted 4-fold rotational symmetry. Large cracks emanate from two sides of the impression; beginning at a load of 500 gf (4.91 N), a second set of cracks in other indented AP crystals was observed with traces in the (001) surface approximately orthogonal to those in Figure 4. The indentation was viewed in polarized light, with the cross-polarizers oriented to provide maximum extinction (Figure 4(B)). The most obvious feature is a bright, sharply focused band of light near the impression at the tip of one of the cracks. This suggests that considerable strain energy is stored in the vicinity of this crack tip. Transmitted cross-polarized light was also observed close to the corners of the hardness impression. However, there was a surprising absence of transmitted light in the surrounding region away from the hardness impression. Rotating the AP crystal about the [001] direction between the cross-polarizers did not appear to alter this finding. This observation suggests that the strain energy around the residual impression is relatively localized, although plastic deformation has occurred around the impression. When the (001) impression was viewed in transmitted light that was partially obstructed before the light entered the crystal

(Figure 5), prominent troughs were observed to emanate from two facets of the impression.

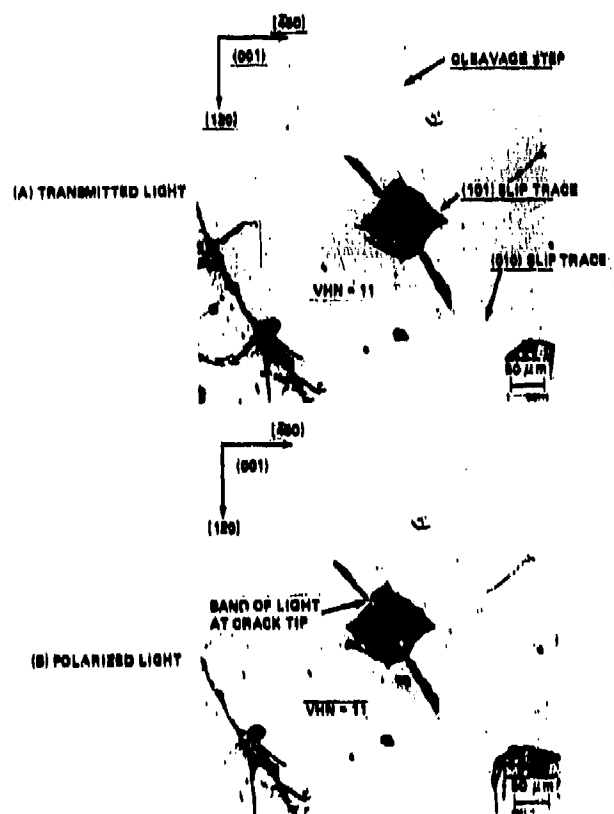


Figure 4. Diamond Pyramid (Vickers) Hardness Impression in (001) Surface of AP



Figure 5. Surface Relief at Vickers Hardness Impression in (001) Surface of AP

The indentation-forming (primary deformation) and volume-accommodating (secondary deformation) slip systems were identified for the (001) surface by performing a single-trace analysis utilizing, as much as possible, slip system information reported<sup>5,6</sup> previously. The results of the analysis are presented in the stereographic projection that appears in Figure 6. Subsequently, the results were confirmed by a two-trace analysis of slip lines, formed at a spherical indentation placed near to the edge of another crystal. The prominent troughs in Figure 5 along  $\pm[010]$  are attributed to primary deformation on the  $\pm(100)[001]$  slip system. As such, it is concluded that this slip system is the easiest operating system in AP. Secondary deformation slip traces, appearing twin-like, are crossing bands within the troughs. These bands are attributed to apparent  $\pm(010)[001]$  slip system activity orthogonal to the primary deformation system. Particularly noteworthy is the observation that initial cracking (i.e., at low loads) occurs (Figure 5) in the region of greatest plastic deformation for the impression. The occurrence of cracking in AP where the deformation is greatest has been confirmed for Vickers indentations put into a  $(\bar{2}10)$  surface.<sup>9</sup>

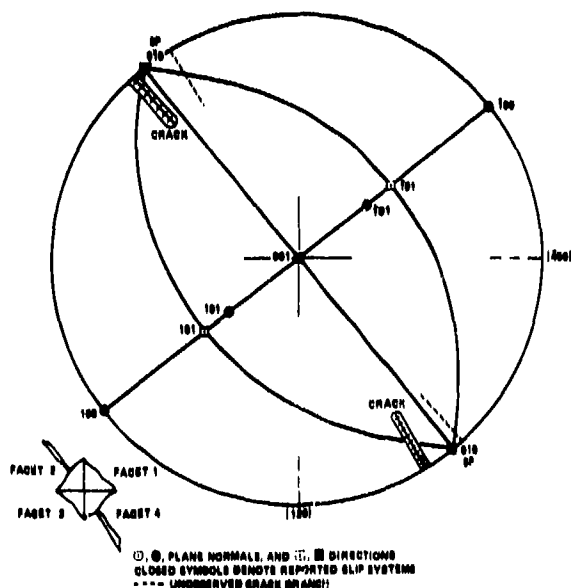


Figure 6. Deformation Systems for Vickers Hardness Impression in (001) Surface of AP

The effect of indenter force on indentation diagonal length for Vickers indentations put into the (001) surface has been determined for forces ranging from 10 gf to 1.5 kgf (0.0981 to 14.7 N) (Figure 7). Several additional crystals were studied, including some used in shock loading experiments to be described later. The diametral size of radial cracks emanating nearly along  $\pm[010]$  was also measured for some of the indentations. The hardness was observed to decrease with increasing force; an exponent of 1.87 was obtained for the power law dependence of indenter force on diagonal length. The exponent would be 2.0 for a constant value of hardness. The decrease in hardness is attributed to the occurrence of cracking. An exponent of a little less than 1.5 obtained for the force dependence on diametral

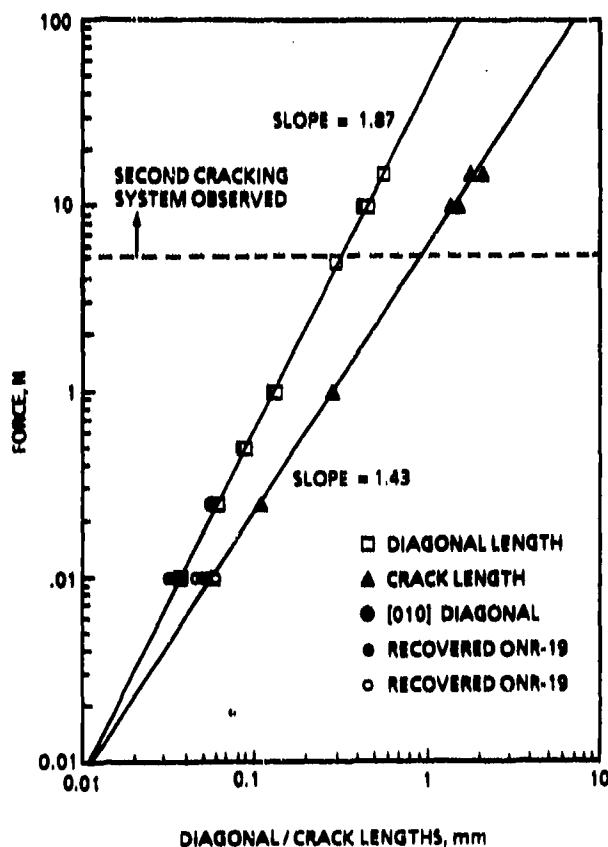


Figure 7. Force Versus Diagonal and Crack Lengths for Diamond Pyramid (Vickers) Impressions in (001) Surface of AP ( $[120]$  or  $[1\bar{2}0]$  Diagonal)

crack length correlates well with indentation fracture mechanics analyses developed by other researchers, as discussed in Reference 15. In this work, those indentations which exhibited the second cracking system were excluded from the least-squares analysis to determine the crack length exponent. The cracking apparently causes at least a partial strain energy release to occur, due to dislocations escaping at the crack surfaces, thus yielding the reduced hardness values.

A release of strain energy would explain the relative absence of transmitted light observed at hardness indentations in the (001) surface, when viewed using transmitted polarized light microscopy. The release of strain energy in AP, because of cracking, is also an important consideration in the shock reactivity work to be described below. A comparison of shock reactivity behavior has begun for AP crystals with and without Vickers indentations in the (001) cleavage surface. The desired enhanced shock reactivity at indentation sites would appear to be suppressed because of strain energy dissipation. With respect to hazards assessments, an initial comparison between AP and RDX was made of their ability to dissipate strain energy by cracking.<sup>16</sup>

## SHOCK LOADING STUDIES

The results of shock experiments over a range of 1 to 38 kbar are summarized in Table 1. Even at the highest shock pressures, most of each crystal was recovered for further analysis. The recovery of an intact crystal that was positioned only 7.0 mm from the detonator ( $P_{AP} = 16.7$  kbar, Shot ONR-19) can be contrasted with the pulverizing of another crystal that was not immersed in oil, but separated by the same distance from the detonator with a plastic (PMMA) gap. The chromatography measurements revealed a large increase in only the  $Cl^-$  concentration as shock pressure increased. Based on those measurements, the threshold of shock reaction for a relatively defect-free crystal in this arrangement was  $\sim 25$  kbar (shock pressure in the crystal ( $P_{AP}$ )). With the baseline established for the onset of reactivity in a "good" crystal, several experiments were performed on crystals with a macroscopic defect created at

the surface by the hardness indenter. High-speed framing camera records were obtained of the shock interaction with crystals in Shots ONR-16 through ONR-19; Shots ONR-18 and ONR-19 each had a 1000 gf (9.81 N) Vickers hardness impression in the (001) surface of the crystal.

At the highest shock pressure (Shot ONR-16), the photographs in Figure 8 show that the shock was still quite curved when entering the crystal and that the gas bubble from the expanding detonation products, which are opaque to the backlighting, reached the crystal shortly after the shock. Both the shock curvature and the additional gas bubble loading would have contributed to the breakup of the

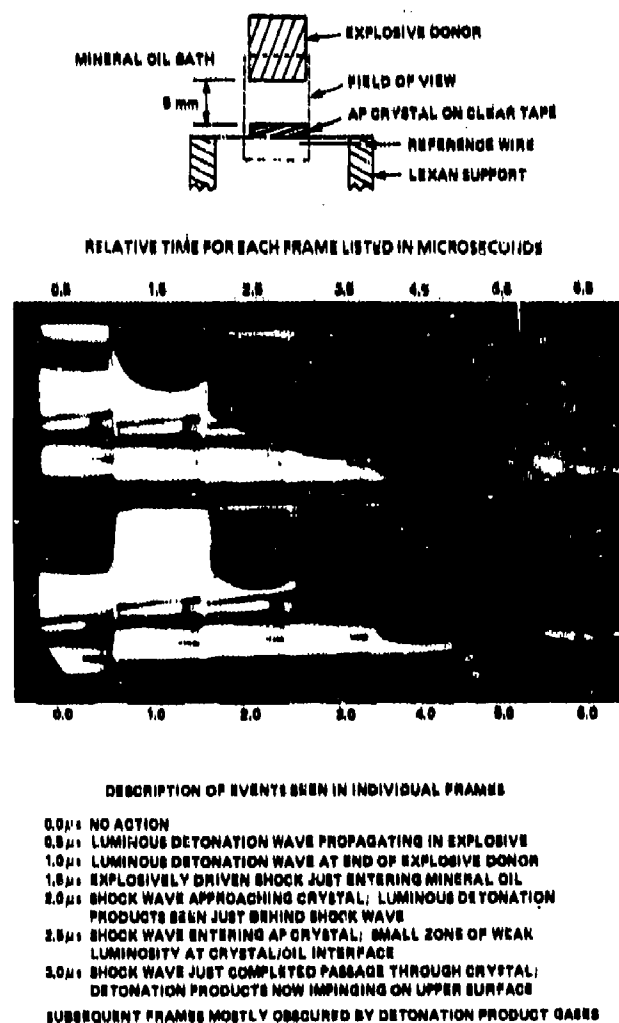


Figure 8. Backlit Framing Camera Record of an AP Crystal Being Shocked at 24 kbar (Shot ONR-16)

Table 1. Results from Shocking AP Crystals in Mineral Oil

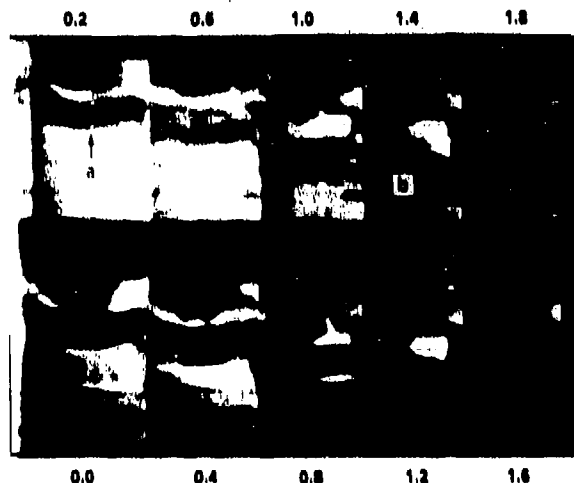
Shot ONR-	Mineral Oil		AP Crystal		AP Crystal Chemical Analysis (ppm)			
	Gap (mm)	P <sub>oil</sub> (kbar)	P <sub>AP</sub> (kbar)	Recovered Condition	Cl <sup>-</sup>	NO <sub>2</sub> <sup>-</sup>	NO <sub>3</sub> <sup>-</sup>	ClO <sub>3</sub> <sup>-</sup>
Not shocked, microhardness indentation					420	8	46	4
2	35	0.6	1.0	No damage	600	8	29	25
3	23	1.0	1.8	No damage	530	12	38	22
4	15	2.0	3.5	No damage	410	18	39	10
5	8.2	7.2	11.6	Broke into 5 pieces	520	20	45	20
19	7.0	10.5	16.7	Intact but cloudy (Figures 11-13)	Saved for hardness tests (Figure 7)			
[Vickers indentation High-speed photographs in Figure 10]								
17	6.0	15.5	24.4	Broke into 2 pieces	Two separate analyses:			
					1,400	6	60	-
					900	18	20	20
18	6.0	15.5	24.4	Broke into small pieces	(Analysis failed)			
[Vickers indentation High-speed photographs in Figure 9]								
16	5.0	24.8	38.5	Large pieces were 88% of original weight	11,000	8	46	4
[High-speed photographs in Figure 8]								

crystal. The shock fronts were luminous in the two crystals with P<sub>AP</sub> = 24.4 kbar (Shots ONR-17 and 18). In the second experiment (ONR-18), the top of the crystal was blackened with permanent ink to reduce any light originating from hot detonator products, in case that had contributed to the luminosity of the shock front. The crystal in Shot ONR-18 was located with the as-viewed (001) surface under the center of the detonator, whereas in other experiments, the crystal was centered under the detonator. The photographs in Figure 9 show the luminous front as well as a luminous band in the vicinity of the indentation. The luminous band first appeared in the 0.6 μs frame (approximately corresponding to the time interval required for the shock to pass the indentation) and then moved from right to

left across the crystal. The band was observed to be particularly intense and straight in the 1.4 μs frame. The linearity of the light band suggests that it is crystallographic in origin. The angle between the band and the [120] direction was measured to be 2° less than the analogous determination for the trace of the bottom crack at the hardness impression in Figures 4 and 5. This is the crack that extends from facet 4 of the impression as designated in the insert appearing in Figure 6. Even though the crack trace at the impression is wavy at the higher magnification in Figures 4 and 5, associating the band of light with this crack seems plausible because of its inclination to the (001) surface. It is important to note that the sense of the inclination requires that Figures 4 and 5 be rotated 180° about [001] in

6.0 mm GAP IN MINERAL OIL  
1000 gf VICKERS HARDNESS IMPRESSION IN (001) SURFACE  
AS-VIEW (001) SURFACE DIRECTLY UNDER DONOR

RELATIVE TIME FOR EACH FRAME LISTED IN MICROSECONDS



NOTE:

- a. LUMINOUS REGION BEHIND SHOCK FRONT (0.0 - 0.6  $\mu$ s)
- b. LUMINOUS BAND WHICH MOVES ACROSS THE CRYSTAL (0.6 - 1.8  $\mu$ s)

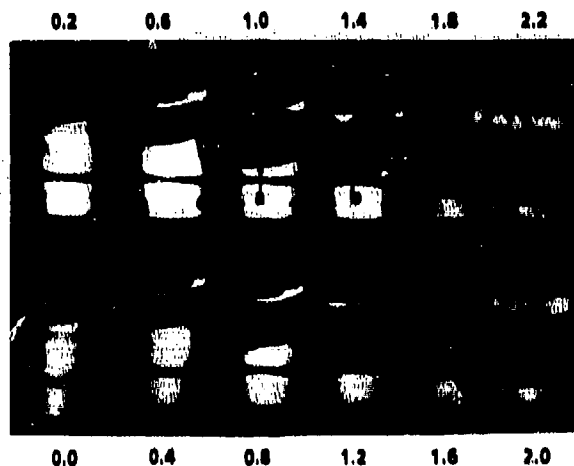
Figure 9. Backlit Framing Camera Record of an AP Crystal Being Shocked at 16 kbar (Shot ONR-18)

order that they properly correspond with Figure 9 as viewed. Then, the observed right-to-left movement of the light band would logically be attributed to this crack propagating away from the viewer more deeply into the crystal.

At the somewhat lower shock pressure ( $P_{AP} = 16.7$  kbar) in Shot ONR-19, the shock front in the crystal appeared as a distinct dark line (Figure 10). Thus, the luminous fronts in the previous experiments were probably a response of the crystal and not an optical effect from the backlighting. Between the shock front in Shot ONR-19 and the interaction of the shock with the as-viewed (001) surface, crystallographic-appearing diagonal lines in an otherwise clear region appeared, beginning in the 0.6  $\mu$ s frame. These diagonal lines occurred in only one basic direction and not in the normally expected complementary direction. Similar observations for Shots ONR-17 and 18 were probably obscured by the luminous shock fronts that were present. Further behind the shock front, most clearly seen in the

7.0 mm GAP IN MINERAL OIL  
1000 gf VICKERS HARDNESS IMPRESSION IN (001) SURFACE  
CRYSTAL CENTERED UNDER DONOR  
CRYSTAL RECOVERED INTACT

RELATIVE TIME FOR EACH FRAME LISTED IN MICROSECONDS



NOTE:

- a. DARK DIAGONAL BANDS BEHIND SHOCK FRONT (0.6 - 1.2  $\mu$ s)
- b. CLOSELY SPACED DIAGONAL BANDS FURTHER BEHIND SHOCK FRONT (1.4 - 1.8  $\mu$ s)
- c. LUMINOUS BAND (1.8  $\mu$ s)

Figure 10. Backlit Framing Camera Record of an AP Crystal Being Shocked at 13 kbar (Shot ONR-19)

1.4  $\mu$ s frame, there was a region of partial transmittance of the backlighting where many closely spaced diagonal lines appeared.

The angular relationships between various diagonal lines and the [120] direction were measured for Shot ONR-19 (Figure 10). Following shock passage, the prominent diagonal line in the 1.8  $\mu$ s frame was determined to coincide with an (010) trace to within 1°. During shock passage in the 1.0  $\mu$ s frame, the angular deviation from being an (010) trace varied from 4 to 15°. This deviation occurs in the correct rotational direction when attributed to shock compression. However, the magnitude of the rotation caused by uniaxial straining is estimated to be only 2°. Optical distortion in the shock to mineral oil is believed to be responsible for the remaining deviation. As such, the diagonal lines are believed to be associated with the (010)[001] slip system, the readily observable secondary (volume-accommodating) deformation system described earlier for the Vickers indentation.

Vickers microindentation hardness testing was performed on the crystal that had been recovered in Shot ONR-19 to determine changes in microstructure occurring as a result of shock loading. As indicated in Table 1, the sample in Shot ONR-19 was recovered intact after experiencing a significant shock loading (peak pressure in oil of 13 kbar). The recovered crystal was cloudy in appearance (Figure 11). Microscopic examination of the previously indented (001) surface revealed numerous straight lines, indicating that extensive slip trace formation had occurred (Figure 12). These traces were found to be orthogonal to one another and were identified as (010) and (100) slip planes (Figure 13). A series of 10 gf (0.0981 N) indentations were put into various areas of the (001) surface of the recovered crystal. The hardness and cracking properties changed depending on the location of the indentation, and the measurements are included in Figure 7. The largest increase in hardness (VHN = 19 versus 14 for an unshocked crystal) occurred in the region of the crystal that first experienced shock wave passage. A VHN of 17 was measured at the orthogonal intersection of slip traces near the 1000 gf indentation made prior to shock loading (Figures 12 and 13). The hardness in other regions of the crystal away from the 1000 gf indentation increased by ~7 percent. The accompanying radial crack extension was

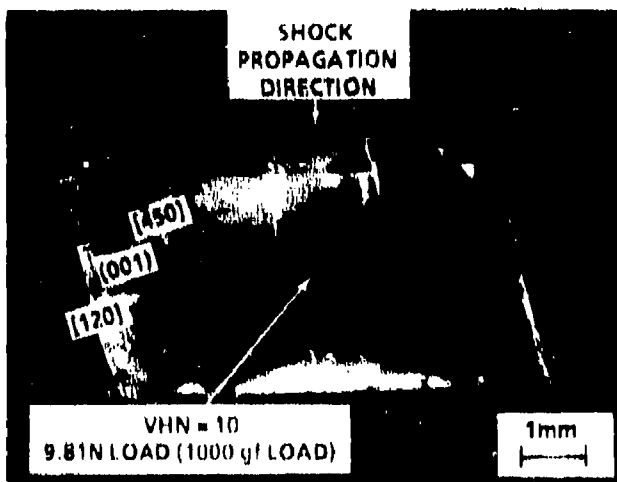


Figure 11. (001) Surface of Shocked AP Crystal from Shot ONR-19 Showing Large Hardness Impression

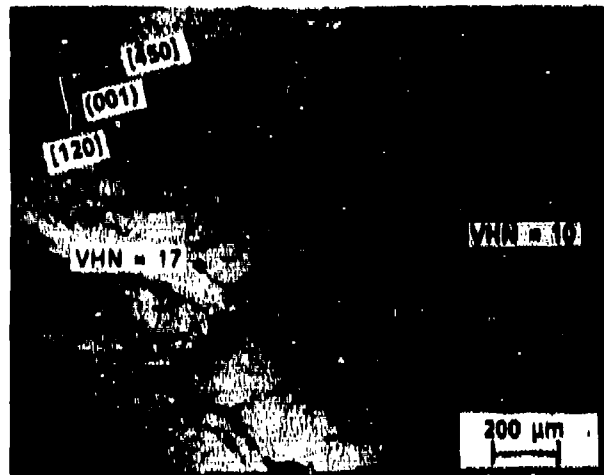


Figure 12. Reflected Light Photomicrograph of (001) Surface of Shocked AP Crystal (Shot ONR-19) Showing Original and Subsequent Vickers Hardness Impressions and Extensive Slip Trace Formation

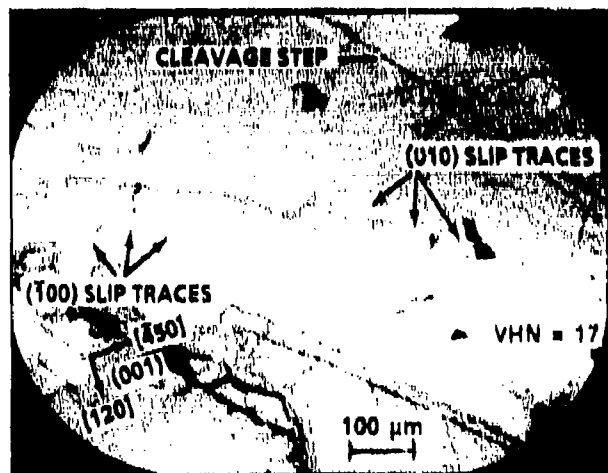


Figure 13. Reflected Light Photomicrograph of (001) Surface of Shocked AP Crystal (Shot ONR-19) Showing Numerous (100) and (010) Slip Traces

also measured for each of the 10 gf indentations. These measurements were compared to the average of two determinations obtained for 10 gf indentations put into the (001) cleavage surface of an unshocked crystal described in Reference 9. Crack extension in the shocked crystal was found to be reduced generally, with differences ranging from -18 to +5 percent.

## SUMMARY AND CONCLUSIONS

Initial results have been obtained for the roles that deformation, fracture, and material microstructure have on the shock reactivity of AP. Optical quality crystals of AP were shocked by a small explosive donor over a pressure range of 1 to 38.5 kbar, while immersed in mineral oil. Recovered pieces were chemically analyzed by liquid ion chromatography to determine an approximate reaction threshold of 25 kbar for relatively defect-free crystals. Over a pressure range of 16.7 to 38.5 kbar, high-speed photography was used to view the (001) surface of several crystals during shock loading. Two of the crystals had a large surface defect created by a diamond pyramid (Vickers) indenter. The high-speed photographs of the shocked crystals showed, although not in each experiment, a luminous shock front, distinct diagonal lines behind the front that appeared to be slip bands, a moving luminous band that appeared to be a propagating crack, and light in the vicinity of a surface indentation presumably due to chemical reaction. Near the reaction threshold, it appears that reaction in even a relatively defect-free crystal is inhomogeneous, being directly related to its material microstructure. Other investigators have recently observed what was probably reaction light when shocking RDX crystals of lesser quality, although at much higher pressures, ~100 kbar.<sup>17</sup>

Surface traces of slip planes and cracks associated with forming Vickers hardness impressions in the (210) and (001) cleavage surfaces of an unshocked crystal were crystallographically identified. Slip systems were determined, the easiest operative system being (100)[001]. Particularly noteworthy is the observation that cracking occurs in the region of greatest plastic deformation. The effect of indenter force on indentation and resultant crack sizes was investigated for Vickers indentations put into the (001) surface. The hardness was observed to decrease with increasing force, which was attributed to the occurrence of cracking.

## ACKNOWLEDGEMENTS

This work is supported by the Office of Naval Research under work request numbers N00014-87-K-0175 and N00014-85-WR-24103 as a cooperative effort between Loyola College, Baltimore, and the Naval Surface Warfare Center (NSWC), White Oak, including collaboration with the University of Maryland, College Park. Drs. Sigmund J. Jacobs and Richard R. Bernecker, NSWC, provided many helpful comments and guidance concerning the direction of the research. Dr. Donald A. Keefer, Loyola College, and Dr. Xian Jie Zhang, University of Maryland, College Park, helped with the micrographs in Figures 4 and 5. Dr. Paul J. Coyne, Jr., Loyola College, developed a computer program that generated the stereographic projection appearing in Figure 6. Dr. David S. Richards, Loyola College, helped with the analysis and preparation of Figure 7.

## REFERENCES

1. Bowden, F. P. and Yoffe, A. D., *Fast Reactions in Solids*, Butterworths Scientific Publications, London, 1958.
2. Green, L. G. and James, E., Jr., "Radius of Curvature Effect on Detonation Velocity," in *Fourth Symposium (International) on Detonation*, Office of Naval Research, Department of the Navy, Washington, DC, ACR-126, 1965, pp. 86-91.
3. Dick, J., "Plane Shock Initiation of Detonation in  $\gamma$ -Irradiated Pentaerythritol Tetranitrate," *Journal of Applied Physics*, Vol. 53, No. 9, 1982, pp. 6161-6167.
4. Dick, J., "Effect of Crystal Orientation on Shock Initiation Sensitivity of Pentaerythritol Tetranitrate Explosive," *Applied Physics Letters*, Vol. 44, No. 9, 1984, pp. 859-861.
5. Herley, P. J.; Jacobs, P. W. M.; and Levy, P. W., "Dislocations in Ammonium Perchlorate," *Journal of the Chemical Society, Section A*, No. 3, 1971, pp. 434-440.

6. Williams, J. O.; Thomas, J. M.; Savintsev, Y. P.; and Boldyrev, V. V., "Dislocations in Orthorhombic Ammonium Perchlorate," *Journal of the Chemical Society, Section A*, No. 11, 1971, pp. 1757-1760.
7. Heavens, S. N. and Field, J. E., "The Ignition of a Thin Layer of Explosive by Impact," *Proceedings of the Royal Society of London, Ser. A*, Vol. 338, No. 1612, pp. 77-93.
8. Macek, A. and Durfee, R. L., *A Study of Energy Release in Rocket Propellants by a Projectile Impact Method*, NASA Contractor Report No. 66395, Atlantic Research Corp., Alexandria, VA, Jun 1967.
9. Elban, W. L.; Coyne, P. J., Jr.; Sandusky, H. W.; Glancy, B. C.; Carlson, D. W.; and Armstrong, R. W., *Investigation of the Origin of Hot Spots in Deformed Crystals: Studies on Ammonium Perchlorate and Reference Inert Materials*, NSWC MP 88-178, Naval Surface Warfare Center, Silver Spring, MD, Apr 1988.
10. Netherwood, P. and Tauber, D., *The Shock Hugoniot of Mineral Oil*, BRL MR 2214, Ballistic Research Laboratories, Aberdeen, MD, Aug 1974.
11. Woolfolk, R. W.; Cowperthwaite, M.; and Shaw, R., "A 'Universal' Hugoniot for Liquids," *Thermochimica Acta*, Vol. 5, No. 4, 1973, pp. 409-414.
12. Martynyuk, V. F.; Khasainov, B. A.; Sulimov, A. A.; and Sukoyan, M. K., "Estimating Heat Production in the Detonation of Poured-Density Ammonium Perchlorate," *Combustion, Explosion, and Shock Waves*, Vol. 23, No. 1, 1987, pp. 58-60.
13. Dobratz, B. M. and Crawford, P. C., Eds., *LLNL Explosives Handbook*, UCRL-52997, Dec 1985, pp. 7-37.
14. Salzman, P. K.; Irwin, O. R.; and Andersen, W. H., "Theoretical Detonation Characteristics of Solid Composite Propellants," *AIAA Journal*, Vol. 3, No. 12, 1965, pp. 2230-2238.
15. Armstrong, R. W. and Elban, W. L., "Cracking at Hardness Microindentations in RDX Explosive and MgO Single Crystals," *Materials Science and Engineering*, Vol. A111, No. 1-2, 1988, pp. 35-43.
16. Elban, W. L.; Coyne, P. J., Jr.; Sandusky, H. W.; Glancy, B. C.; Carlson, D. W.; and Armstrong, R. W., "Microindentation and Shock Loading Studies on Single Crystals of Ammonium Perchlorate," in *Proceedings of the ONR Workshop on Energetic Material Initiation Fundamentals*, Vol. 1, CPIA Publ. 516, Dec 1988, pp. 608-637.
17. Forbes, J. W.; Tasker, D. G.; and Granholm, R. H., "Direct Observation of Shocked Explosive Crystals Immersed in Liquids," presented at *1989 APS Topical Conference on Shock Compression of Condensed Matter*, Albuquerque, NM, 14-17 Aug 1989.

# THE INFLUENCE OF GRAIN MORPHOLOGY ON THE BEHAVIOR OF EXPLOSIVES

S. Dufort, H. Cherin, and P. Gohar  
Commissariat à l'Énergie Atomique  
CER - BP n° 16 - 37260 Monts - FRANCE

*Many experimental observations have shown the influence of the granular form of an explosive on its behavior. Kinetic models describing the mechanisms of decomposition of the grains take into account the size and shape of the grains only in a very simplified way. In this study we describe a method of analysis allowing simulation of particle combustion mechanisms which makes use of optical microscopic images of the powder. The numerical treatment makes use of Mathematical Morphology theory applied to the real size and shape distribution of the grains. The results obtained reveal the importance of the morphological characteristics of the particles on their speed of combustion. Perspectives for the optimization of the kinetics of the decomposition by adjustment of the grain size parameters are presented.*

## INTRODUCTION

Study of the deflagration to detonation transition requires understanding of the mechanisms involved in the combustion of a heterogeneous explosive. The number of significant parameters involved is large; among these the morphological and grain size characteristics play a determinant role.<sup>1-4</sup>

A model including the influence of powder morphology on the decomposition kinetics is presented. The concepts of Mathematical Morphology developed on an image analyzer used as a simulation tool provided an original way of studying this problem. The decomposition of explosive particles is governed by combustion processes involving either the whole surface of the grain (homogeneous combustion) or which are initially localized at a few active centers (hot spots combustion). Examples of simulations of powder behavior based on each of these two processes are carried out using real granulometric distribution data (size and morphology). A study of the influence of the size distribution is made for some simple cases. An extension of these preliminary studies is proposed in the conclusion.

## GRAIN SIZE AND COMBUSTION

Particle size and porosity are recognized as important factors influencing explosive performance and shock sensitivity. The importance of grain size characteristics on the kinetics of decomposition remains unclear. Similarly, the influence of grain shape is almost totally neglected in the literature. Experiments carried out in our laboratories reveal, however, that two batches of RDX having the same granulometric characteristics, but different morphologies, have different exploding wire initiation thresholds.<sup>5</sup>

### Combustion Mechanisms

Two types of mechanisms may be involved in initiating the combustion of a particle:

1. The first involves the whole surface of the grain, which is uniformly consumed with a speed everywhere normal to the surface. At constant pressure, the speed of combustion is constant.
2. In the second mechanism the decomposition is initiated at reactive

centers at the surface and within the volume of the grains.

The first model (C. A. Forest: Reference (6)) expresses the speed of combustion of a particle in the form:

$$-\frac{1}{W} \frac{dW}{dt} = \frac{S(t)}{V(t)} CP^n \quad (1)$$

where  $CP^n = dx/dt =$  linear combustion speed normal to the surface,

$W =$  mass of undecomposed explosive,

$S(t) =$  surface of the particle at time  $t$ ,

$V(t) =$  volume of the particle at time  $t$ .

The morphological characteristics of the particle are involved through the ratio  $S(t)/V(t)$ . When a particle does not retain a simple geometry during its combustion, there is no simple analytical expression to describe the evolution of this term.

The induction of combustion from localized points ("hot spots") is the mechanism most commonly cited in the literature.<sup>7,8</sup> As regards the nature of the centers, the hypotheses are varied: to a first approximation, we may consider that the laws of germination-growth-coalescence describing the evolution of these zones are independent of their nature. It is easy to see that if the development of reactive centers occurs at the surface, the particle will be entirely covered by decomposition products after a certain period of decomposition. Thus, in the case of instantaneous germination, constant speed of growth and coalescence of the reactive centers, we can describe the case of circular, two dimensional germination nuclei by the equation:

$$\lambda = 1 - \exp(-Ct^3) \quad (2)$$

where  $C$  is constant and  $\lambda$  is the fraction of the surface covered by decomposition products at time  $t$ .

The spreading of surface nuclei results in a transition towards homogeneous combustion once the whole surface is covered. Note that homogeneous combustion from time zero is a very special case corresponding to the

formation of a large number of reactive centers whose growth on the surface of the grain is very rapid.

Using simple geometries (for example, spherical particles), it is possible to determine analytical curves representing the speed of combustion as a function of time for a population - possibly plurimodal - whose decomposition is governed by the germination-growth-coalescence process and homogeneous combustion. A description of grains of complex morphology cannot, however, be obtained using this approach.

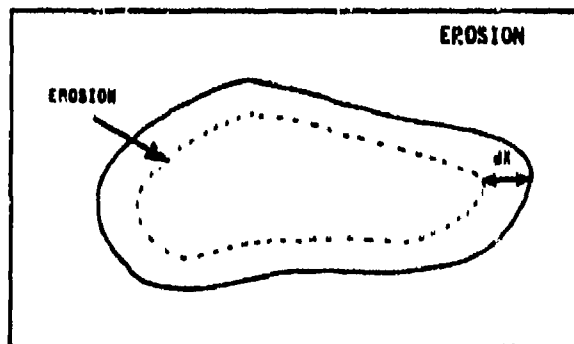
### Application of Mathematical Morphology to the Study of Combustion

**Homogeneous Combustion.** The process is based on the supposition of a combustion speed normal to the interface and having the same value at all points. Mathematical Morphology<sup>9</sup> allows this evolution to be simulated by a single morphological operation: erosion. In the rest of this article the image treatment is based on plane objects whose behavior in two dimensions reflects the changes in a real three-dimensional grain. In these conditions, Equation 1 may be written:

$$-\frac{1}{W} \frac{dW}{dt} = \frac{P(t)}{S(t)} CP^n \quad (3)$$

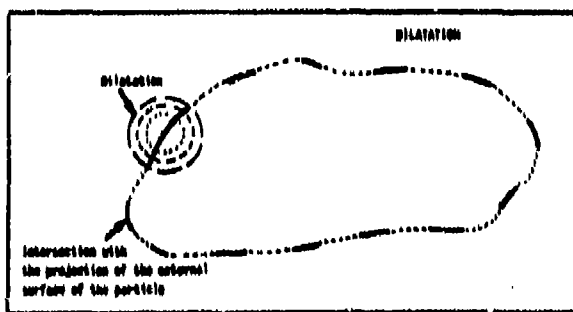
where  $P(t)$  is the length of the perimeter of the particle at time  $t$ .

The following schema represents the effects of an erosion operation equivalent to a combustion consuming a thickness  $dX$  of the particle in a time  $dt$ .



The perimeter and the surface of the particle are determined after each erosion operation. The speed of combustion  $1/W \cdot dW/dt$  is directly proportional to the ratio of these two granulometric characteristics. The last erosion, during which the particle disappears, ends the treatment.

**Combustion of Localized Zones.** Potential sites of germination are distributed at random along the perimeter of the particles. The germination mechanism is instantaneous; all the sites are active at time zero. The growth of the active zones is simulated by a succession of elementary Mathematical Morphology operations: dilatation followed by an intersection with the initial contour of the particle.



The speed of growth of the combustion centers is, therefore, determined by the number of dilatations-intersections carried out at each time step. When two zones interpenetrate each other, they become associated. The treatment simulating the growth-coalescence of the zones stops once they have reconstituted the whole of the initial perimeter.

The system then switches to a homogeneous combustion process. The time represented by the number of dilatations-intersections necessary to reach this transition point is the time of induction of the decomposition for each particle. It should be mentioned that the absence of germination sites on a particle implies homogeneous combustion right from time zero (this is commonly the case for small particles).

## RESULTS OF THE SIMULATION

The simulation is carried out on a projection plane, obtained by optical microscopy, of a population of explosive particles

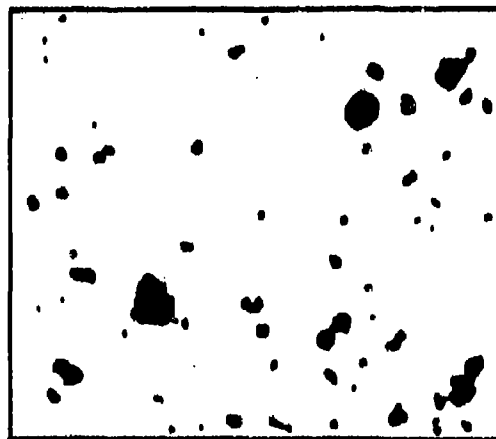


*Figure 1. Powder Sample Image*

shown in Figure 1. The grains comprising the sample have an average diameter of 30  $\mu\text{m}$ .

Figure 2 represents the speed of combustion as a function of time for two cases: homogeneous combustion of all the particles from time zero and germination-growth-coalescence of surface nuclei followed by homogeneous combustion.

The variation of the speed in the case of homogeneous combustion, right from the beginning, reveals fluctuations caused by the varying size and morphology of the particles. For comparison, the behavior of a single dispersed population of identical morphology is shown in this same figure. The last part of the curve corresponds to the disappearance of the last particles; the evolution is then that of the radio P/S as S tends to zero (cf. Equation (3)).

The speed of combustion in the case of a germination-growth-coalescence process reveals some remarkable features. Initially the combustion is rapid; the speed then decreases quickly to stabilize for a short period near the value determined by the homogeneous combustion curve. The last part corresponds to the evolution of speed in the homogeneous combustion process.

These simulations of real powders show the influence of the distribution of grain size and shape on the decomposition mechanism, whether homogeneous or localized, and thus make possible the systematic study of the

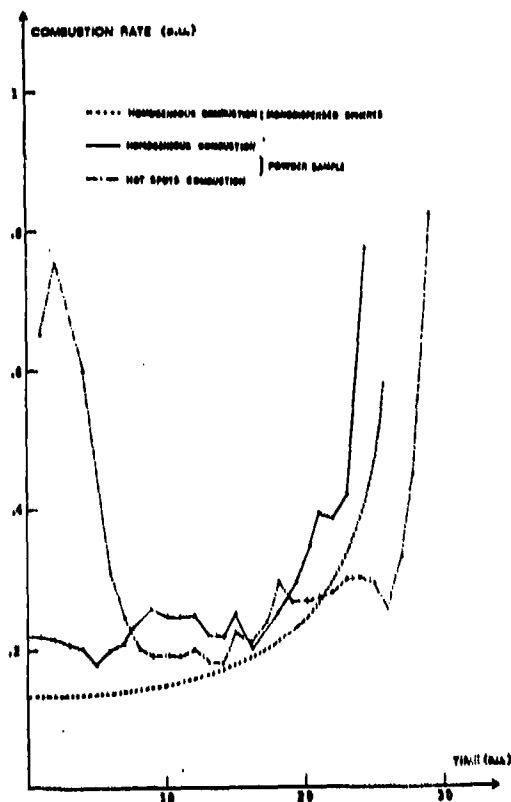


Figure 2. Combustion Rate of the Powder Sample Versus Time

relationship between combustion speed and morphological characteristics.

### EFFECT OF PARTICLE SIZE DISTRIBUTION

The simulation principles described above were applied to the different grain size populations shown in Figure 3. In order to separate, in an initial phase, the effect of the single parameter "grain size," the particles in these test samples are quasispherical. Figure 3 also shows the corresponding combustion speeds.

High initial combustion speeds are observed for the bimodal populations containing particles of small size whatever their proportion (SIMUL2 and SIMUL3). For a bimodal distribution where small particles are absent, this phenomenon disappears (SIMUL1) and the variation of combustion speed is analogous to that predicted in the case of homogeneous combustion. Simulation SIMUL3 shows

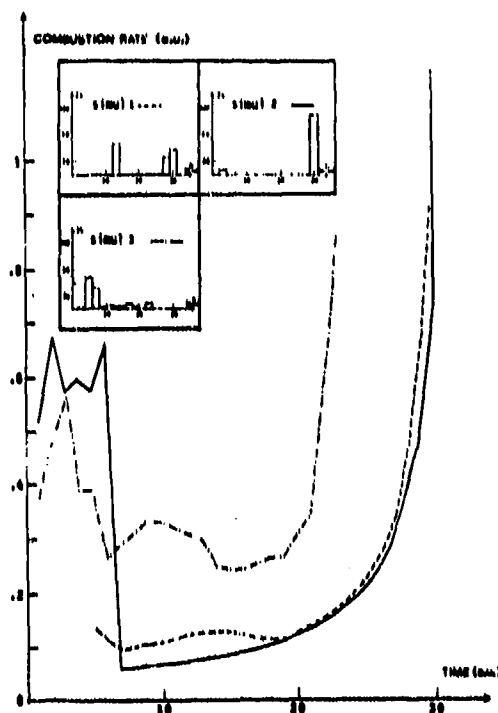


Figure 3. Combustion Rate Versus Time for the Three Tested Distribution

the interesting case of a rapid initial decomposition followed by an intermediate value of combustion speed significantly higher than for the other populations.

These preliminary results show that the decomposition kinetics based on a germination-growth-coalescence process are closely related to the particle size distribution of the population; knowledge of the average radius is in no case sufficient to indicate the behavior of the powder.

### CONCLUSION

Study of the microstructure of explosives constitutes the indispensable link between the intrinsic molecular properties and the hydrodynamic behavior at macroscopic level. The results of simulations carried out reveal the important influence of grain morphology on the decomposition regime of an explosive powder. Mathematical Morphology makes use of operators which transform images, allowing the action of different combustion mechanisms to be reproduced without any necessity of

making assumptions concerning grain shape. The evolution of the decomposition regimes obtained may be used directly in the kinetic equations describing the transition to detonation. It is therefore possible to optimize a priori the morphological characteristics of the powder (shape and size) so as to reduce the depth of initiation of the detonation.

## REFERENCES

1. Bernecker, R. R., *AIAA J.* 24 (1), 1986, pp. 8291.
2. Bernecker, R. R.; Sandusky, H. W.; and Clairmont, A. R., *The Seventh Symposium (International) on Detonation*, Annapolis, MD, 1981.
3. Lee, R.; Bloom, G.; Von Holle, W.; Weingart, R.; Erikson, L.; Sanders, S.; Slettevold, C.; and McGuire, R., *The Eighth Symposium (International) on Detonation*, Albuquerque, NM, 1985.
4. Taylor, P. A., *Shock Waves in Condensed Matter*, Azay, J. R.; Graham, R. A.; and Staub, G. X., Editors, Flavier, 1984, p. 597.
5. Dufort, S., *5ème Congrès International sur les méthodes de contrôle non destructif, (Bordeaux) France, Juin 1983*.
6. Forest, C. A., *The Seventh Symposium (International) on Detonation*, Annapolis, MD, 1981.
7. Partom, Y., *The Seventh Symposium (International) on Detonation*, Annapolis, MD, 1981.
8. Tarver, C. M.; Hallquist, J. O.; and Erickson, L. M., *The Eighth Symposium (International) on Detonation*, Albuquerque, NM, 1983.
9. Serra, J., *Image Analysis and Mathematical Morphology*, Academic Press, 1982.

# ROLE OF ADIABATIC SHEAR BANDS IN INITIATION OF EXPLOSIVES BY DROP-WEIGHT IMPACT

V. Krishna Mohan,\* V. C. Jyothi Bhasu,\* and J. E. Field  
Cavendish Laboratory  
University of Cambridge, United Kingdom, CB3 0HE

*Earlier work on the initiation mechanisms of energetic materials during impact has shown the existence/formation of localized hot spots. It has been postulated that local energy concentration occurs in shear bands and these bands eventually become ignition sites. A dislocation description of localized shear deformation occurring on a single slip plane has been reported. In this paper, we provide experimental evidence for the existence of localized dislocation zones in cyclotrimethylene trinitramine (RDX) and pentaerythritol tetranitrate (PETN). Single crystals of these explosives have been subjected to subcritical (for initiation) particle impact employing an explosive driver technique. Deformation characteristics were examined by carefully solvent etching the crystal surfaces. RDX crystals showed localized slip around the impact sites; two alignments of etch pits were noticeable. Similar results were obtained for PETN. Shear band formation in PETN, PBX-9503, and other high explosives during drop-weight impact has been observed. Calculated shear band spacings and widths using analytical expressions available in literature have been found to be in fair agreement with experimental values.*

## INTRODUCTION

It is well-known that for initiation to occur in crystalline explosives subjected to pressure-time histories typical of drop-weight impact conditions, the energy transferred must be localized within the explosive. In polycrystalline materials earlier researchers have established several mechanisms which could lead to ignition. These include adiabatic compression of the gases in the spaces between grains, frictional processes, and viscous flow.<sup>1-3</sup> Winter and Field,<sup>4</sup> based on their experiments on micro-particle high velocity impact on silver and lead azide crystals, have concluded that the heat generated by plastic deformation is also a viable mechanism. Using titanium as a model material, it has been

shown that within the plastic deformation zone surrounding an impact crater, the residual strains were highly localized in narrow bands characteristic of adiabatic shear deformation. They have examined the azide crystals under subcritical impact conditions and have shown that deformation is concentrated in narrow bands of material by adiabatic shear. It has been suggested that the temperature rise in these bands could become high enough for initiation.

Coffey and coworkers<sup>5,6</sup> have studied deformation-induced heating in several inorganic and organic, crystalline and polymeric materials. Their main observation has been that with appropriate modification, the same fundamental processes responsible for localized and adiabatic heating in metals are also responsible for the more pronounced localized heating effect in nonmetallic materials as they undergo rapid deformation. A dislocation

\*Present address: IDL-Nitro Nobel Basic Research Institute, Bangalore, India

description of localized shear deformation occurring on a single slip plane has been developed by Coffey and Armstrong<sup>5</sup> to indicate that appreciable heating can occur at a particular site where a dislocation pileup might be released suddenly in an avalanche configuration.

Studies on the characteristics of mechanically induced dislocations in organic energetic materials are limited in literature. The major work in this direction is that of Halfpenny et al.<sup>7</sup> who have characterized the primary dislocation slip systems in pentaerythritol tetranitrate (PETN) and cyclotrimethylene trinitramine (RDX) using a combination of dislocation etching and microhardness indentation techniques. The objective of the present work is to identify the nature of damage induced in single crystals of organic high explosives due to particle impact at subcritical velocities. The choice of an impact experiment in which the particle is small compared with a single crystal of explosive has been primarily based on the fact that it provides a controlled and well-defined impact situation. Post-impact examination of the deformation characteristics is easy under such conditions. This is particularly difficult to achieve under drop-weight impact conditions under which the entire crystal is involved in the deformation. Careful etching of the impacted crystal surfaces has been carried out to look at the emergent ends of dislocations. It is found that the dislocations generated upon impact are highly localized in rows. We have also carried out experiments wherein several high explosives have been subjected to subcritical impacts in the drop-weight impact equipment. Optical microscopic examination of the impacted samples shows the formation of shear bands. Finally, the experimental band spacings and widths for various explosives are compared with those computed using the analytical expressions derived by Grady and Kipp<sup>8</sup> for shear band spacing and width.

## EXPERIMENTAL

### Crystal Preparation

Crystals of PETN and RDX were grown from solution in acetone by slow evaporation at room temperature. The crystals of both solids

exhibited well-developed faceting. Laue photographs were recorded for these crystals and compared with published ones to verify proper crystal formation.

### Etching Studies

A number of solvents and mixtures of solvents were evaluated. It appeared that acetone and acetone/water mixture (1:1) gave good results and etching of "as grown" surfaces produced results similar to those reported by other workers.<sup>7,9</sup> These solvent systems were also used to examine the nature of damage produced on crystal surfaces by particle impact. It is well-known that a one-to-one correspondence exists between etchpits and the emergence of dislocation lines at crystal surfaces.

## PARTICLE IMPACT EXPERIMENTS

An explosive driver technique developed by Winter and Field<sup>4</sup> has been used in this work. PETN and RDX crystals were glued on a target plate (with a double-side gummed tape) and impacted by glass beads (100  $\mu\text{m}$  in size). The glass particles were placed on a 360  $\mu\text{m}$  phosphor-bronze plate below which a detonator was placed. The sheet was of sufficient thickness not to perforate when the detonator was fired. Previous work has shown that particle velocities are in the range of 150-200 m/s. Distance between the target plate and the glass particles was adjusted in such a way that upon impact the crystals did not disintegrate. Attenuators of varying thickness were also used to minimize damage. After impact the crystal surfaces were examined under an optical microscope. Microphotographs have been taken of the etchpits formed close to the impact sites.

### Drop-Weight Impact Tests

Experiments were carried out using a 5 kg weight dropped from different heights employing an apparatus described in Reference 3. The impacted samples have been examined under an optical microscope.

## RESULTS AND DISCUSSION

The principal forms for PETN and RDX crystals are as follows: PETN {110} and {101};

RDX {210} and {111}. All particle impact experiments have been carried out on well-formed crystal faces: {110} for PETN and {210} for RDX. Optical microscopy coupled with careful solvent etching has been used extensively to examine the nature of plastic deformation around the impact sites. Etching has been done with extreme care. Dislocation etch patterns on fresh crystals have been similar to those observed by Halpenny et al.<sup>7</sup> Figure 1 presents photographs of etchpits formed on RDX crystal surface by etching with acetone for 3-5 secs [Figure 1(a)] and the elongation of etchpits due to prolonged etching for 10 secs [Figure 1(b)]. Etching of PETN crystals with acetone has been found to be rapid and, hence, had to be carefully controlled. Acetone/water mixture in a 1:1 ratio was also tried. References 7 and 9 give a detailed description of the geometric shapes of the etchpits for the different crystallographic faces of these crystals. Thus, in the case of PETN, the etchpits on the {110} face were hexagonal in shape, while those on the {101} face were trapezoidal in shape. On the other hand, rectangular etch pits were formed on the {210} face of RDX. Figure 2 shows a series of photomicrographs taken before and after etching for both PETN and RDX crystals after impact. These photographs give a clear idea about the deformation around the impact sites and the density distribution of dislocations near such sites. The most important and unique observation made in the present work [Figures 2(b) and 2(c)] is that there is a very high concentration of dislocations within a microscopic region close to the impact zone. In fact, examination of the etchpit formation pattern in unimpacted crystals shows a uniform distribution of dislocations [see for example, Figure 1(a)]. Rows of etchpits are found only close to the impact sites, while farther away from these sites an increase in the density of dislocations is observed. These rows of etchpits we believe are indicative of the formation of piled up groups of dislocations in energetic materials upon dynamic loading. Then a final question which must be posed relates to the role played by such groups of dislocations in the initiation processes in these explosives. In fact, Halpenny et al.<sup>7</sup> have suggested that the greater sensitivity of PETN

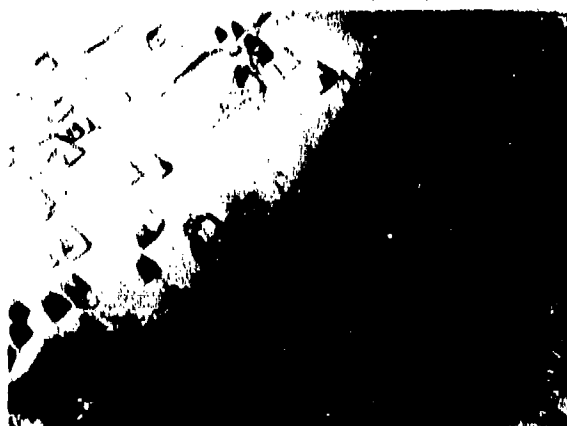


Figure 1(a). Etchpit Formation in RDX Crystal Produced by Acetone in 5 Secs, Magnification: 1 cm = 15  $\mu$ m

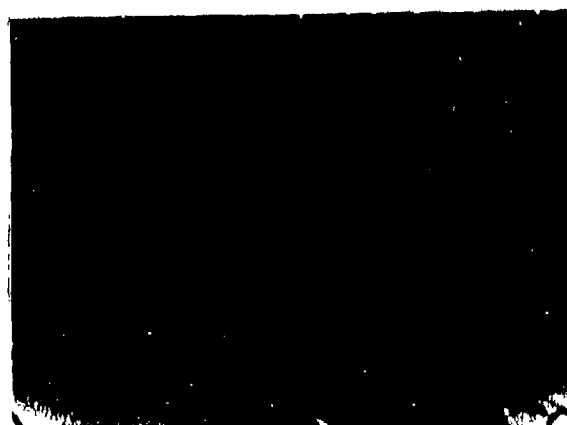


Figure 1(b). Elongation of Etchpits in RDX Crystal Due to Prolonged Etching for 10 Secs. (1 cm = 15  $\mu$ m)

to impact detonation, compared to RDX, could be due to the greater dislocation density around indentations and the confinement of the deformation zone to a smaller volume in the former explosive. Elban and Armstrong<sup>10</sup> have also observed that for RDX the etchpit arrays centered on each indentation are highly localized within the immediate vicinity of the residual hardness impressions. These authors suggested that such localized shear deformation should lead to hot spot formation under impact conditions. Theoretical calculations by Coffey and Armstrong<sup>5</sup> based on a catastrophic



**Figure 2(a).** *Impact site on a PETN Crystal Produced by a 100  $\mu\text{m}$  Particle (1 cm = 7  $\mu\text{m}$ )*



**Figure 2(b).** *Etchpit Formation in an Impacted PETN Crystal (1 cm = 20  $\mu\text{m}$ )*



**Figure 2(c).** *Magnified View of a Row of Etchpits in PETN Crystal (1 cm = 8  $\mu\text{m}$ )*



**Figure 2(d).** *Impact Site in a RDX Crystal Produced by a 100  $\mu\text{m}$  Glass Particle*

failure model of a dislocation pileup have shown that appreciable temperature rise leading to hot spot formation could take place in explosive molecular crystals. Winter and Field<sup>4</sup> have also shown that because of thermal softening, the deformation is concentrated in narrow bands of material by adiabatic shear and the temperature rise in these regions could become high enough for initiation.

Photographic evidence from particle impact experiments presented in Figure 2 has clearly demonstrated that the deformation in

PETN and RDX upon dynamic loading is localized in nature. We have also examined explosive materials subjected to subcritical impact in the drop-weight impact sensitivity test equipment. Several explosives, such as PETN, RDX, and PBX-9503 (a plastic bonded explosive), have been tested and the impacted samples examined under an optical microscope. Similar tests had been conducted earlier.<sup>3,71</sup> Evidence for localized shear in the explosive layer appears in recovered unexploded samples (Figure 3). It has also been found that ignition and propagation occur



Figure 2(e). Rows of Etchpits Near an Impact Site in RDX Crystal (1 cm = 15  $\mu$ m)



Figure 2(f). Magnified View of a Row of Etchpits in RDX Crystal (1 cm = 10  $\mu$ m)



Figure 3(a). Shear Band Formation in an Impacted PBX-9503 (1 cm = 20  $\mu$ m)



Figure 3(b). Shear Band Formation in an Impacted TATB/Ammonium Perchlorate Mixture (1 cm = 10  $\mu$ m)

preferentially in such shear bands.<sup>3</sup> Thus, even under drop-weight impact conditions localized deformation can occur as in the case of particle impact.

### SHEAR BAND MODEL. CALCULATIONS

Most model calculations have shown that if flow is uniform throughout the deforming region, very high strains are needed to produce temperatures high enough for initiation. On the other hand, if the deformation is localized, as in shear banding, significant temperature rise can occur. Several attempts have been

made in the past to assess the temperature rise in shear bands.<sup>12,13</sup> Grady and Kipp<sup>8</sup> have derived expressions for shear band spacing, width, and growth times based on a catastrophic growth model of unstable thermoplastic shear. Their expressions relate the shear band characteristics with the thermal properties of the material and the dynamic loading data. The expressions provided are as follows:

$$\text{Band width, } a_0 = \left( \frac{9\rho^3 c^2 k^3}{t_y^3 a^2 \dot{\gamma}} \right)^{1/4} \quad (1)$$

$$\text{Band spacing, } b_0 = 2 \left( \frac{9\rho c^2 k}{\tau_y \alpha^2 \dot{\gamma}^3} \right)^{1/4} \quad (2)$$

where  $\rho$  is the density,  $c$  is the specific heat,  $k$  is the thermal diffusivity ( $\lambda/\rho c$ ),  $\lambda$  is the thermal conductivity,  $\tau_y$  is the flow stress,  $\alpha$  is the thermal softening coefficient in the shear band, and  $\dot{\gamma}$  is the shearing strain rate. The thermal softening coefficient  $\alpha$ , is taken as  $2.0/T_m$  since the shear stress is assumed to fall to zero at half the melting point,  $T_m$ . The flow stress,  $\tau_y$ , is defined as  $\tau_y = 0.5Y$ , where  $Y$  is the uniaxial yield stress, which in turn is related to the Vickers Hardness value,  $H_v$ , by  $H_v = 3Y$ . The shear strain rate  $\dot{\gamma}$  is given by  $\sqrt{3} \dot{\epsilon}$  where  $\dot{\epsilon}$  is the longitudinal strain rate which is related to the radial velocity,  $V_r$ , by  $\dot{\epsilon} = 2V_r/r$ ,  $r$  being the radius of the sample.

Typical values for the various properties mentioned above for different explosives considered are given in Table 1. Calculated band spacings and widths and the corresponding experimental values for the former are listed in Table 2. Calculations have been done at two strain rates viz.  $2 \times 10^5$  and  $10^6/s$ , the former being a representative strain rate for drop-impact experiments.

It is evident from the results presented in Table 2 that a fair agreement exists between the calculated and experimental band spacings. It has to be pointed out here that the numbers given in the Table are only estimates and are meant to give an idea of the order of magnitude value for shear band spacings and

widths. Only calculated bandwidths are given in Table 2, since the experimental values could not be easily ascertained from the photographs. However, the latter are much higher than those predicted by Equation (2). Frey<sup>12</sup> has stated that the thickness of the shear region is typically less than one micron, while Howe et al.<sup>16</sup> have found shear cracks with widths in the range of 10-100  $\mu\text{m}$  in heavily confined explosive targets subjected to impact.

## CONCLUSIONS

If hot spots are to be produced in an impacted explosive, mechanisms must exist for localized dissipation of impact energy. In this paper experiments have been described in which single crystals of PETN and RDX were impacted by spherical particles and it was shown that deformation occurs in localized bands. Such shear bands have also been observed in explosives subjected to subcritical impacts in the drop-weight impact test. Calculated band spacings agree with the experimental values. Since substantial temperature rises have been predicted in shear bands, it is likely that they could serve as initiation sites in rapidly deforming explosives and experimental evidence (References 3, 4, 11) indeed confirms that adiabatic shear of the material is a plausible ignition mechanism.

## REFERENCES

1. Bowden, F. P. and Yoffe, A. D., *Initiation and Growth of Explosion in Liquids and Solids*, First Edition, Cambridge University Press, Cambridge, 1952.

Table 1. Physical Properties of Various Explosives

Explosive	$\rho$ g/cc	$\alpha$ ( $\times 10^3$ ) $K^{-1}$	$C$ J/kg.K	$\tau_y$ GPa	$\kappa$ ( $\times 10^8$ ) $m^2/s$
PETN	1.78	4.84	1092.0	0.050	12.96
RDX	1.81	4.18	1192.8	0.039	5.20
HMX	1.90	3.58	970.2	0.066	27.80
Tetryl	1.71	4.96	1058.4	0.050	15.80
Picric Acid	1.76	5.06	987.0	0.050	5.80

Values taken from References 14 and 15

Table 2. Shear Band Spacings and Widths for Different Explosives

Explosive	Band spacing ( $\mu\text{m}$ )				Band width ( $\mu\text{m}$ )	
	Calculated		Experimental		Calculated	
	$2 \times 10^5/\text{s}$	$10^6/\text{s}$	Drop Impact	Particle Impact	$2 \times 10^5/\text{s}$	$10^6/\text{s}$
PETN	255	76	250	75	0.12	0.08
RDX	237	71	-	50	0.08	0.05
HMX	321	96	400	-	0.20	0.14
Tetryl	260	77	-	-	0.13	0.09
Picric Acid	193	58	-	-	0.19	0.04

2. Mader, C. L., "Initiation of Detonation by the Interaction of Shock with Density Discontinuities," *Phys. Fluids*, Vol. 8, No. 10, 1965, p. 1811.
3. Field, J. E.; Swallowe, G. M.; and Heavens, S. M., "Ignition Mechanisms of Explosives During Mechanical Deformation," *Proc. R. Soc. Lond.*, Vol. A383, 1982, p. 231.
4. Winter, R. E. and Field, J. E., "The Role of Localized Plastic Flow in the Impact Initiation of Explosives," *Proc. R. Soc. Lond.* Vol. A343, 1975, p. 399.
5. Coffey, C. S. and Armstrong, R. W., "Shock Waves and High Strain Rate Phenomena in Metals: Concepts and Applications," Meyers, E. M. and Murr, E. L., Eds., Plenum, NY, 1981.
6. Coffey, C. S., "Phonon Generation and Energy Localization by Moving Edge Dislocations," *Phys. Rev.*, Vol. B24, No. 12, 1981, p. 6984.
7. Halfpenny, P. J.; Roberts, K. J.; and Sherwood, J. N., "Dislocations in Energetic Materials. 3. Etching and Microhardness Studies of Pentaerythritol Tetranitrate and Cyclotrimethylene Trinitramine," *J Mat. Sci.*, Vol. 19, 1984, p. 1629.
8. Grady, D. E. and Kipp, M. E., "The Growth of Unstable Thermoplastic Shear with Application to Steady-wave Shock Compression in Solids," *J. Mech. Phys. Solids*, Vol. 35, 1987, p. 95.
9. Connick, W. and May, F. G. J., "Dislocation Etching of Cyclotrimethylene Trinitramine Crystals," *J Cryst. Growth*, Vol. 5, 1969, p. 65.
10. Elban, W. L. and Armstrong, R. W., "Microhardness Study of RDX to Assess Localized Deformation and Its Role in Hot Spot Formation" *Proceedings of the Seventh Symposium (International) on Detonation*, Maryland, 16 Jun 1981, pp. 976-985.
11. Field, J. E.; Palmer, S. J. P.; Pope, J. H.; Sundararajan, R.; and Swallowe, G. M., "Mechanical Properties of PBXs and their Behavior During Drop-Weight Impact," *Proceedings of the Eighth Symposium (International) on Detonation*, Albuquerque, NM, 15 Jul 1985, pp. 635-644.
12. Frey, R. B., "The Initiation of Explosive Charges by Rapid Shear," *Proceedings of the Seventh Symposium (International) on Detonation*, MD, 16 Jun 1981, pp. 36-42.
13. Dienes, J. K., "On Reactive Shear Bands," *Phys. Letters A*, Vol. 118, No. 9, 1986, p. 433.
14. Dobratz, B. M., *LLNL Explosives Handbook*, UCRL 52997, Lawrence Livermore National Laboratory, 16 Mar 1981.

15. Palmer, S. J. P. and Field, J. E., "The Deformation and Fracture of HMX," *Proc. R. Soc. Lond.*, Vol. A383, 1982, p. 399.
16. Howe, P. M.; Gibbon, G.; and Wobber, P. E., "An Experimental Investigation of the Role of Shear in Initiation of Detonation by Impact," *Proceedings of the Eighth Symposium (International) on Detonation*, Albuquerque, NM, 15 Jul 1985, pp. 294-301.

# GAP TESTS AS A METHOD OF DISCRIMINATING SHOCK SENSITIVITY

Stephen A. Aubert, Gary H. Parsons, J. Gregory Glenn, and James L. Thoreen  
Air Force Armament Laboratory  
Energetic Materials Division  
Eglin AFB, Florida 32542

*The shock sensitivity of cast TNT-based explosives was determined using a modified Expanded Large Scale Gap Test (ELSGT). The modified test substituted cast Comp B for the pressed pentolite donors used originally. Piezoelectric pins were internally mounted in the acceptor charges to measure shock velocity, detonation velocity, and run to detonation distances. Cast TNT, Tritonal, Comp B, and AFX-1100 Mod II (66 percent TNT, 16 percent OD2 Wax, and 18 percent aluminum) were tested for Gap sensitivity. Pressed charges of PBX-9502 were also tested and used as a standard of comparison. The test was calibrated using shock time of arrival measurements to determine the shock velocity through the plexiglas gap. The plexiglas equation of state and conservation of momentum equation were used to derive the peak pressure profile in the plexiglas. The AFATL 8-inch diameter Gap test was also calibrated using this method. These results were then compared for correlation with existing data for the NOL LSGT and the AFATL 8-inch diameter Gap test. It was found that the apparent sensitivity to shock was strongly dependent on the diameter of the test charges. Tests at smaller diameters yielded higher gap peak pressures than tests of the same explosive at larger diameters. Less sensitive explosives like PBX-9502 and AFX-1100 showed little dependency between sensitivity and charge diameter, while TNT and Comp B showed a significant dependency between the two.*

## INTRODUCTION

Evaluation of the shock sensitivity characteristics of insensitive explosives by gap testing is complicated by their moderate to large failure diameters. Since steady state detonation cannot be sustained below an explosives failure diameter, standard gap tests such as the Small Scale Gap Test, the Naval Ordnance Lab (NOL) Large Scale Gap Test (LSGT), and the Los Alamos National Labs (LANL) Large Scale Gap Tests are of limited value, and can lead to erroneous estimates of the critical initiation pressure when large failure diameter materials are tested in these configurations.<sup>1</sup>

As part of a study to model sympathetic detonation of munitions and to account for diameter effects in testing, the Air Force Armament Laboratory (AFATL) developed an 8-inch diameter gap test.<sup>2</sup> The 8-inch diameter test geometry far exceeds the minimum failure diameter requirements of most materials. In addition, heavy confinement of donor and acceptor charges simulates the long duration shock pulses experienced by weapons in round to round propagation experiments. It has also been asserted and demonstrated that pulse duration as well as peak pressure is an important influence in explosive initiation.<sup>3,4</sup> The acceptor's 16-inch length allows adequate

time for transpiration of deflagration to detonation transitions, also important in round to round propagation. The large size of the test is a disadvantage when considering the need for the large number of tests necessary in the sensitivity screening and explosive characterization process.

The recently developed Expanded Large Scale Gap test (ELSGT) is a compromise between the smaller tests and the 8-inch test of AFATL.<sup>5</sup> The acceptor ID of 2.88 inches with 0.435 inch confinement is large enough to test most explosive materials accurately for shock sensitivity characteristics, yet small enough to meet the high throughput demands of composite explosive formulation and screening processes. A comparison of the geometry of various gap tests is found in Table 1.

The ELSGT has been modified by using cast Comp B boosters to replace the pressed pentolite donors used originally. Cast Comp B donors were preferred because of ease of processing and comparison with the 8-inch diameter gap test, which also uses cast Comp B donors. Ten piezoelectric pins were placed internal to the acceptors to obtain shock and detonation velocities, and run to detonation distances. The objective of this study was to obtain baseline data on cast TNT, Tritonal, Comp B, AFX-1100 II,<sup>6</sup> and PBX 9502, in a modified ELSGT configuration. In addition, it was desired to calibrate both the modified ELSGT and 8-inch diameter gap tests and compare and correlate the baseline data obtained here with existing data from the NOL LSGT and 8-inch diameter gap test.

## EXPERIMENTAL PROCEDURES

Calibration of the Modified ELSGT was accomplished by determination of the shock

velocity decay profile through the Polymethylmethacrylate (PMMA) gap. Piezoelectric pins were placed 1.75 inches into, and at 0.5 inch increments along the axis of wave propagation, of one continuous 3.75 inch diameter by 6 inch long cast PMMA rod. All machining tolerances were  $\pm 0.005$  inch. The test setup is depicted in Figure 1. Dynasen CA-1136 piezoelectric pins were used in all testing. Data was recorded on an HP 5180A digital waveform recorder with 50 nanosecond resolution. The resulting time-of-arrival signals were differentiated to determine the shock velocity at each station from 0.5 inch to 6 inches through the PMMA. Pins were radially spaced  $16^\circ$  and offset 0.125 inch from the center to reduce their intrusive effects on the response of downstream pins. Six tests with 11 stations each were conducted, three on the 0.5 inch at 0.5 inch increments and three on the 0.25 inch at 0.5 inch increments. A 0.25 inch shim disk was placed at the front of the 6-inch long rod to position the stations at the desired point from the Explosive PMMA interface in the second set of tests. The particle velocity in the PMMA was calculated using the plexiglas equation of state obtained by Jaffee et al.<sup>7</sup> (Equation (1)).

$$U_s = 1.52 u_p + 2.59 \quad (1)$$

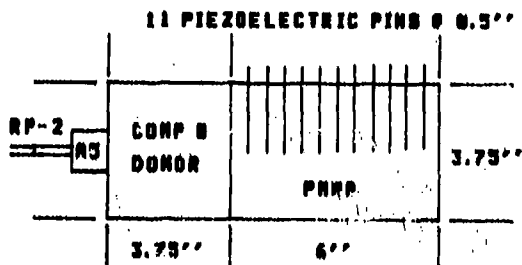
Where  $U_s$  is the shock velocity, and  $u_p$  is the particle velocity in the PMMA. The relation derived from the conservation of momentum equation (Equation (2)) was used to calculate the peak pressure.

$$P = p_0 U_s u_p \quad (2)$$

Where  $P$  is the peak pressure and  $p_0$  is the density of PMMA (1.185 g/cc).

Table 1. Gap Test Geometry Comparison

Test	Donor Dia (in) ID/OD/Casewall	Acceptor Dia (in) ID/OD/Casewall	Ex Wt. (lbs) Donor/Acceptor
NOL LSGT	0/2.00/0	1.44/1.87/0.217	0.25/0.5
ELSGT	0/3.75/0	2.88/3.75/0.435	2.5/4.5
8-Inch	7/8/0.5	7/8/0.5	20/33



PINS ARE RADIIALLY SPACED 16 DEGREES APART  
3 REPETITIONS AS SHOWN  
3 REPETITIONS WITH A 0.25 INCH THICK PMMA  
AT FRONT OF INSTRUMENTED ROD

Figure 1. Modified ELSGT Calibration Setup

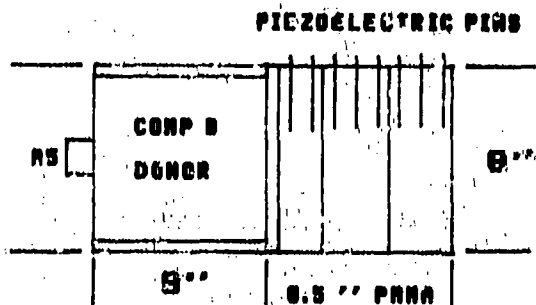
Treatment of data below  $U_a$  of 3.0 mm/us required use of an alternate Hugoniot due to the bend in the Hugoniot curve below this region, shown by Erkman.<sup>5</sup> However, to obtain the Hugoniot for this region, the Jaffee data was separately fit with a second linear equation for the points where  $U_a$  was less than 3.0 mm/us, resulting in Equation (3).

$$U_a = 2.16 u_p + 2.44 \quad (3)$$

This method was preferred over use of the Erkman<sup>5</sup> or Liddiard<sup>9</sup> equations because velocities as low as 2.702 mm/us were obtained in this work, a region to which these Hugoniot did not extend.

Calibration of the AFATL 8-Inch Gap test was conducted similarly to the modified ELSGT. The test setup is depicted in Figure 2. The piezoelectric pins were embedded only to 2.875 inches into the PMMA, as they were only 3 inches long, leaving the pin's sensor end 1.125 inches from the disk's center. The disks were fabricated from cast sheets of PMMA 2 or 3 inches thick, and machined to a tolerance of  $\pm 0.005$  inch, to facilitate assembly. A 0.5 inch or 1 inch thick shim disk was used to position the stations at the desired distances from the donor explosive/PMMA interface. Six tests, with 8 or 9 pin stations each were conducted. Three repetitions on the inch at 1 inch increments and three repetitions on the 0.5 inch at 1 inch increments were conducted.

The Modified ELSGT was conducted in accordance with methods established for the



PINS RADIIALLY SPACED 16 DEGREES APART  
3 REPETITIONS AS SHOWN  
3 REPETITIONS WITH A 1 INCH PMMA SPACER

Figure 2. Eight Inch Diameter Gap Test Calibration Setup

ELSGT by Liddiard & Price.<sup>5</sup> Cast composition B charges, 3.75 inches by 3.75 inches, were used as donors. Densities of donor charges averaged  $1.682 \pm 0.008$  grams/cc (98.94% TMD) as indicated in Table 2. A 1 by 1 inch A-5 pellet and RP2 electrical bridgewire detonator were used to initiate the donor charges. PMMA attenuators, fabricated from cast rod for 2 and 3 inch thick disks or cast sheet for 1 inch or less thick disks, resolved to one-sixteenth of an inch were used as the gap material. The surfaces of the PMMA disks were machined to a tolerance of  $\pm 0.005$  inch. The average densities of the PMMA disks were  $1.177 \pm 0.005$  grams/cc for disks from cast rods and  $1.184 \pm 0.008$  grams/cc for disks from cast sheet. The acceptor was placed 0.125 of an inch above a 0.75 inch thick 8 inch square cold rolled, mild steel witness plate. Ten piezoelectric pins were placed 1.44 inches into the charge to obtain shock and detonation velocities. A diagram of the test setup is shown in Figure 3. A modified Bruceton up/down method of testing was applied. Typically, however, only eight charges of each material were needed to resolve the gap distance within 0.062 of an inch of PMMA. Densities of all acceptor charges tested are listed in Table 2.

## RESULTS

The results of the modified ELSGT calibration, time of arrival (TOA), shock velocity ( $U_a$ ), and particle velocity ( $u_p$ ) data are tabulated in Table 3 and plotted in Figure 4. This data was then used to generate the

Table 2. Explosive Densities

Explosive	Charge	TMD (g/cc)	Density (g/cc)	% TMD	Standard Deviation (g/cc)
Comp B	Donor	1.73	1.682	96.94	0.008
TNT	Acceptor	1.65	1.586	96.14	0.009
Tritonal	Acceptor	1.79	1.711	95.57	0.002
Comp B	Acceptor	1.74	1.698	97.45	0.010
AFX-1100 II 000	Acceptor	1.59	1.521	95.66	0.006
AFX-1100 II 001	Acceptor	1.59	1.529	96.16	0.002
AFX-1100 II 002	Acceptor	1.59	1.530	96.20	0.020
PBX 9502	Acceptor	1.94	1.886	97.12	0.001

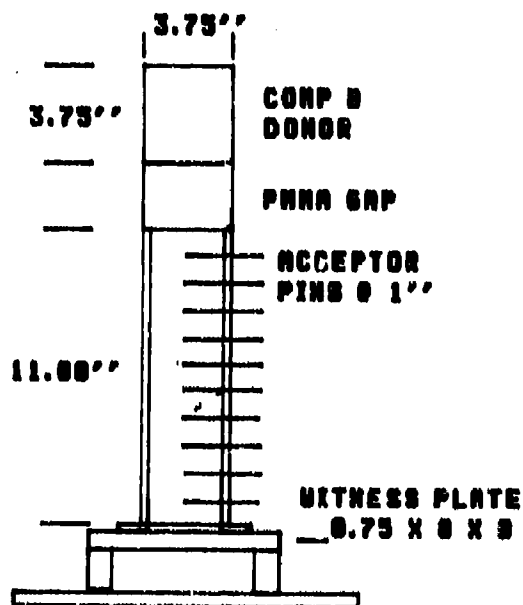


Figure 3. Modified ELSGT Setup

pressure versus distance data of Table 4 and plotted in Figure 5. The graphed data shows a characteristic bend in the curve at 1.75 inches. This corresponds proportionally to the bend seen in previous calibration of the NOL LSGT<sup>8</sup> which showed a bend in its pressure versus distance (P vs. X) curve at 1.38 inches. Pressures were calculated from  $U_s$ ,  $u_p$  data, using Equation (2) for each station of each test individually. The pressures for each station were then fit, using least squares method, with a double polynomial. The best fit of the data was obtained with a third and second order polynomial, for the left and right sides of the curves. The resulting equations were then

used in the final P versus X curve:

$$P(x) = \begin{cases} 12.29 + 28.38x - 42.76x^2 \\ \quad + 14.42x^3, \text{ for } x < 1.75 \\ 16.52 - 5.570x + 0.489x^2, \text{ for } x \geq 1.75 \end{cases}$$

The optimal joint is at 1.75 nonnormalized. The coefficient of multiple determination is equal to 0.9585. The curves were constrained to meet at the joint. The fitted data has been tabulated by AFATL/MNE.<sup>10</sup>

The data ( $TOA$ ,  $U_s$ ,  $u_p$ ) for the 8-Inch Diameter Gap Test Calibration is tabulated in Table 5 and plotted in Figure 6. At this diameter, the characteristic bend in the P vs. X curve occurred at 3.5 inches. The pressure versus distance (P vs. X) data is listed in Table 6 and plotted in Figure 7. Pressures were again calculated for each station and fit with a double polynomial, using a least squares method, to produce the final P vs. X curve, as was done with the modified ELSGT. Third and second order polynomials for the left and right sides of the curve, again produced the best fit of the data:

$$P(x) = \begin{cases} -17.49 + 41.91x - 18.42x^2 \\ \quad + 2.444x^3, \text{ for } x < 3.5 \\ 17.02 - 2.955x + 0.1391x^2, \text{ for } x \geq 3.5 \end{cases}$$

The optimal joint is 3.5 nonnormalized. The coefficients for multiple determination were equal to 0.9934. The calibration was not extended far into the low pressure region (below  $u_p < .5$ ), hence no special treatment of

Table 3. Modified ELSGT TOA, Shock, and Particle Velocity Data

X(in)	TOA usec	$U_s$ mm/usec	$u_p$ mm/usec	TOA usec	$U_s$ mm/usec	$u_p$ mm/usec	TOA usec	$U_s$ mm/usec	$u_p$ mm/usec
0.50	21.10	-	-	21.10	-	-	20.90	-	-
0.75	22.15	-	-	22.20	-	-	22.20	-	-
1.00	23.60	5.080	1.566	23.45	5.404	1.850	23.05	5.907	-
1.25	24.15	4.885	1.510	24.75	4.980	1.570	24.75	4.988	1.573
1.50	26.30	4.704	1.391	26.20	4.618	1.334	25.85	4.536	1.280
1.75	27.45	4.704	1.391	27.45	4.704	1.391	27.35	4.885	1.510
2.00	28.90	4.885	1.510	29.00	4.536	1.280	28.60	4.618	1.334
2.25	30.25	4.536	1.280	30.30	4.456	1.228	30.25	4.379	1.177
2.50	31.95	4.164	1.036	31.80	4.536	1.280	31.60	4.233	1.081
2.75	33.40	4.032	0.949	33.40	4.097	0.991	33.25	4.233	1.081
3.00	35.25	3.848	0.828	35.05	3.908	0.866	34.95	3.791	0.790
3.25	36.70	3.848	0.828	36.80	3.735	0.733	36.60	3.791	0.790
3.50	38.70	3.681	0.718	38.60	3.387	0.524	38.30	3.791	0.790
3.75	-	-	-	40.35	3.577	0.649	40.70	3.528	0.617
4.00	42.50	3.342	0.495	42.50	3.432	0.554	42.10	3.342	0.495
4.25	-	-	-	44.70	3.299	0.466	44.10	3.256	0.438
4.50	-	-	-	46.20	3.432	0.554	46.15	3.136	0.359
4.75	49.25	2.515	-	48.90	2.702	0.172	48.15	3.136	0.359
5.00	51.85	2.720	0.084	50.40	3.024	0.285	50.40	2.988	0.262
5.25	54.00	2.674	0.154	-	-	-	51.70	2.988	0.262
5.50	55.90	3.135	0.359	54.60	3.024	0.285	55.05	2.731	0.191
5.75	-	-	-	56.75	2.854	0.272	56.40	2.702	0.172

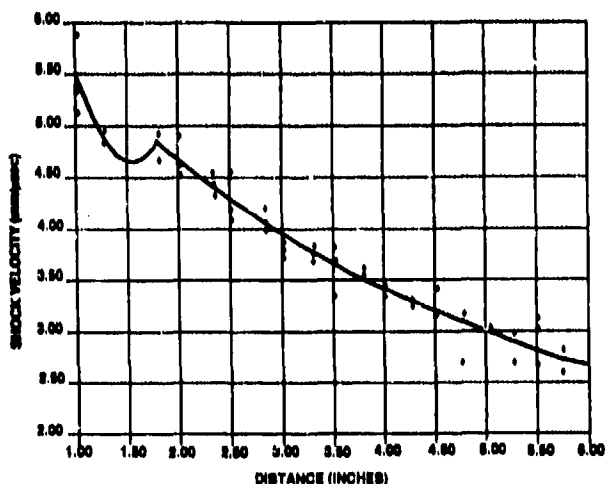


Figure 4. ELSGT  $U_s$  Vs. Distance Plot

low end data was required. The fitted data has been tabulated by AFATL/MNE.<sup>10</sup>

The results of the modified ELSGT series are listed in Table 7. TNT yielded a 50 percent gap thickness of between 438 (GO)

and 450 (NOGO) cards (.01 inch), or 17 to 16 kbar, while Tritonal yielded a value of between 408 (GO) and 412 (NOGO) cards, or 21 to 19 kbar. AFX-1100 MOD II showed some variability in the three different batches tested. This explosive yielded values between 256 and 263 cards (55-52 kbar) for charges with an average density of 1.521 g/cc and between 244 and 250 cards (59-56 kbar) for charges averaging 1.529 g/cc. Comp B gave a value of between 519 and 525 cards (10 to 9 kbar). PBX-9502 gave a value of between 200 and 206 cards (70-69 kbar). NOL LSQT data is also listed in Table 7. Data for TNT, Tritonal, and Comp B are averages of only the values derived using cast charges.<sup>11</sup> Pentolite donors were used in all NOL LSQTs.

## DISCUSSION

The calibration of both the modified ELSGT and 8-inch diameter gap test compared favorably with existing data for the NOL LSQT.<sup>8</sup> Pressures are sustained at higher

Table 4. Modified ELSGT Pressure Calibration Data

X(in)	P1(kbar)	P2(kbar)	P3(kbar)	P Avg (kbar)	Standard Deviation
1.00	94.3	118.65	-	106.50	12.15
1.25	87.48	92.87	92.81	91.05	3.09
1.50	77.60	73.06	-	75.30	2.54
1.75	77.59	77.59	57.88	71.02	11.38
2.00	-	68.87	73.02	70.94	2.08
2.25	68.87	64.88	61.07	64.94	3.90
2.50	51.14	68.87	54.22	58.08	9.47
2.75	45.36	48.17	54.22	49.25	4.53
3.00	37.77	40.15	35.49	37.80	2.33
3.25	37.77	33.36	35.49	35.54	2.20
3.50	31.34	21.06	35.49	29.29	4.29
3.75	-	28.76	25.80	27.28	1.48
4.00	29.61	22.55	19.59	23.92	5.15
4.25	-	18.25	16.90	17.58	1.68
4.50	-	22.55	13.35	18.02	4.67
4.75	-	-	13.35	13.35	-
5.00	-	10.22	9.27	9.74	0.48
5.25	-	-	9.27	9.27	-
5.50	-	10.22	6.20	8.21	2.01
5.75	-	9.22	5.52	7.37	1.85

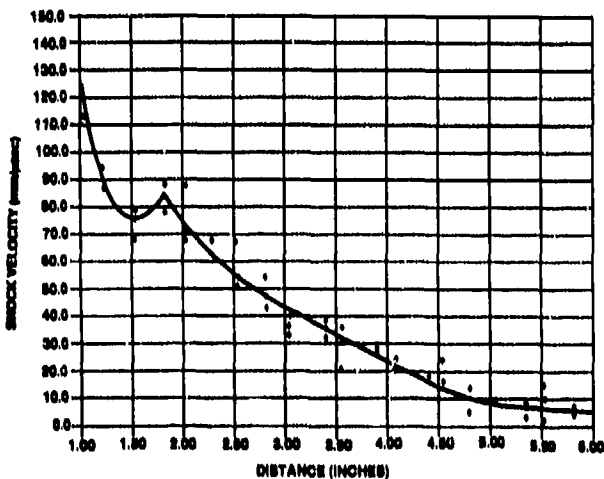


Figure 5. ELSGT PMMA Pressure Vs. Distance Profile

levels for longer distances as the test diameter is increased. This is due to the increase in the TOA for the lateral rarefaction wave with larger radius. Also of interest is the change in distance of the characteristic knee of each curve. The NOL LSGT's knee comes at 1.3 inches, the Modified ELSGT's is at 1.75 inches, and the 8-inch gap test's comes at 3.50 inches. This rough correlation of donor

diameter with curve knee position corresponds to the suggestion made by Price that the knee is due to shock rarefactions from the donor lateral side wall overtaking the lead shock wave.<sup>11</sup> The knee was also more pronounced than was expected for both size tests, and is presumably due to unequal radial TOA of the rarefaction, as a result of the off-centered pin sensor position.

Tests results for the cast TNT-based explosives revealed the Modified ELSGT test discriminated among the various explosives better than the standard NOL LSGT. TNT and Tritonal with gap peak pressures of 46.3 and 50.1 kbar, respectively, in the NOL LSGT gave results of 17 and 21 kbar in the modified ELSGT, a significant change in pressure. The insensitive PBX 9502 and AFX-1100 II showed little change in gap peak pressure from one test to the next. Values were 69.3 and 58.6 kbar, respectively, in the NOL LSGT and 69 and 56 kbar for the ELSGT test. The change indicates that the effect of diameter on the apparent sensitivity of an explosive can be strong and, further, that the effect changes from one explosive to the next. The general

Table 5. Eight-Inch Diameter Gap Test TOA, Shock, and Particle Velocity Data

X(in)	TOA usec	$U_s$ mm/usec	$u_p$ mm/usec	TOA usec	$U_s$ mm/usec	$u_p$ mm/usec	TOA usec	$U_s$ mm/usec	$u_p$ mm/usec
1.0	43.00	-	-	43.65	-	-	43.45	-	-
1.5	45.70	-	-	45.75	-	-	45.25	-	-
2.0	47.95	5.131	1.672	48.25	5.522	1.929	48.15	5.400	1.849
2.5	50.65	5.131	1.672	50.65	5.184	1.706	50.15	5.184	1.706
3.0	52.85	5.184	1.706	53.50	4.838	1.479	53.40	4.840	1.480
3.5	56.00	4.748	1.420	56.00	4.748	1.419	55.35	4.885	1.510
4.0	58.25	4.704	1.391	58.95	4.660	1.362	58.80	4.700	1.388
4.5	61.65	4.496	1.254	61.75	4.417	1.202	61.00	4.496	1.254
5.0	64.30	4.198	1.058	64.80	4.342	1.153	64.70	4.300	1.125
5.5	67.90	4.064	0.969	67.95	4.097	0.991	67.15	4.130	1.013
6.0	70.45	4.130	1.013	71.25	3.938	0.887	71.15	3.940	0.888
6.5	74.40	3.908	0.867	74.70	3.763	0.772	73.00	3.820	0.809
7.0	77.35	3.681	0.718	78.10	3.708	0.736	78.05	3.680	0.717
7.5	81.55	3.552	0.633	81.75	3.603	0.666	80.85	3.603	0.666
8.0	84.90	3.364	0.592	85.75	3.320	0.480	85.30	3.500	0.599
8.5	89.20	3.320	0.480	89.30	3.364	0.509	88.45	3.342	0.495
9.5	-	-	-	97.20	3.215	0.411	96.40	3.195	0.398

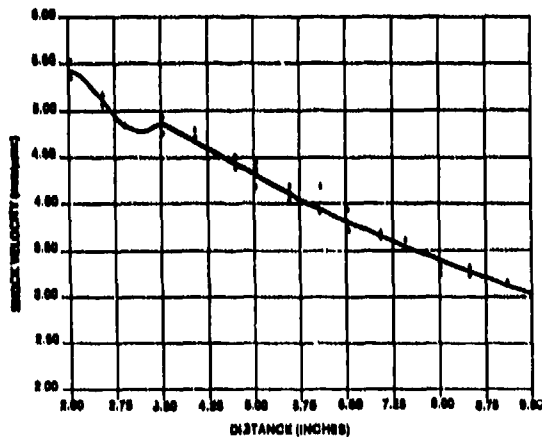


Figure 6. Eight-Inch Diameter Shock Velocity Profile

trend was for apparent sensitivities to be greater with greater test diameter.

The effect of diameter on apparent sensitivity is further evidenced by comparison with the data for the 8-inch diameter gap test, listed in Table 8 and Figure 8. All explosives tested showed decreasing gap peak pressures as test diameter was increased. TNT and Tritonal exhibited the most pronounced diameter effect. Their sensitivities changed from 46.3 and 50.1 kbar, respectively, at a diameter of 1.88 (OD), to 14 kbar each at a

diameter of 8 inches. The majority of sensitivity change occurred by the change to the ELSGT at 3.75 inch diameter geometry. It has been shown that the pulse duration of the applied shock in a gap test is lengthened with increased charge diameter.<sup>2,12</sup> The average pulse lengths at 50 percent of peak height from the regions of 30 to 70 kbar for the NOL LSGT and ELSGT are 3.2 and 6.05 usec, respectively.<sup>12</sup> The positive pulse duration for the 8-inch gap test varies from 26 to 33 usec in this same pressure region. A degree of uncertainty is unavoidable due to possible differences in pulse duration between Pentolite and Comp B. Any differences, however, are assumed to be small and insignificant compared with the effect of charge scale on pulse duration. Since pulse duration is proportional to charge diameter, the results of the TNT and Tritonal tests exhibit some correlation with the  $P^2t = \text{constant}$  relationship. Comp B showed a moderate diameter effect with apparent gap peak pressures changing from 18 to 9 kbar. Again, the majority of sensitivity change occurred before a diameter of 3.75 inches. PBX 9502 and AFX-1100 II showed somewhat different effects, although their apparent gap peak pressures decreased with increasing diameter, the effect was small and linear over

Table 6. Eight-Inch Gap Test Pressure Calibration Data

X(in)	P1(kbar)	P2(kbar)	P3(kbar)	P Avg (kbar)	Standard Deviation
1.5	134.48	134.48	163.18	144.05	16.57
2.0	118.40	101.75	126.22	115.46	12.50
2.5	101.75	104.92	104.91	103.86	1.83
3.0	84.97	104.88	84.95	91.60	11.50
3.5	79.94	79.93	87.48	82.45	4.36
4.0	77.38	77.60	75.27	76.75	1.29
4.5	66.86	62.98	66.87	65.57	2.24
5.0	57.37	52.68	59.19	56.41	3.36
5.5	46.74	48.16	49.63	48.18	1.44
6.0	41.50	49.62	41.49	44.20	4.69
6.5	40.19	31.04	36.64	37.09	2.90
7.0	26.39	31.29	29.81	29.16	2.51
7.5	26.66	28.47	28.48	27.87	1.05
8.0	24.85	20.19	18.19	21.32	1.20
8.5	18.91	20.32	19.61	19.61	0.70
9.5	-	15.68	15.08	15.38	0.42

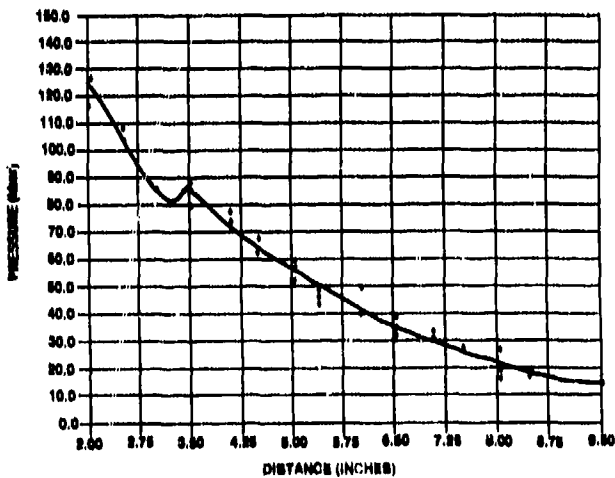


Figure 7. Eight Inch Diameter PMMA Pressure Vs. Distance Profile

the region of diameters tested. The results of the AFX-1100 II tests conflict with the  $P^2t = \text{constant}$  criterion as the effect of wax on Tritonal's sensitivity is much greater on the duration aspect than the peak pressure aspect. PBX 9502 showed virtually no change in gap peak pressure as the scale of the test was changed. This indicates it is not very pulse duration sensitive when tested in gap test and is in agreement with previous flyer plate

experiments.<sup>13</sup> Thus, it appears that truly insensitive materials such as PBX 9502 do not conform to the critical energy criterion  $E_{ci} = P^2t/p_0U_s$  for initiation.

## CONCLUSIONS AND RECOMMENDATIONS

The expanded large scale gap test adequately accounts for pulse duration effects on shock sensitivity, such that little change in apparent sensitivity occurs when gap tests are scaled to larger diameters. However, to get a true indication of the pressure time effect on explosive sensitivities, gap testing should be conducted at various geometries. Insensitive explosives such as PBX 9502 and AFX-1100 show little change in apparent sensitivity when tested in gap tests at various geometries (NOL LSGT, ELSGT, 8 inch diameter gap test). This characteristic should be used to distinguish insensitive munitions from sensitive ones.

## ACKNOWLEDGEMENTS

The authors wish to thank Dr. D. Price and Dr. R. Bernecker for their helpful advice on test preparation and data interpretation. George Lambert's assistance in testing proved valuable.

Table 7. Modified ELSGT Vs. LSGT Results

Explosive	MOD ELSGT				LSGT	
	Cards (.01 in)		(kbar)		Cards (.01 in)	(kbar)
	GO	NOGO	GO	NOGO		
TNT	438	450	17	16	131.7±8.3	46.3±2.4 <sup>11</sup>
Tritonal	406	412	21	19	120.7±6	50.1±1.8 <sup>11</sup>
Comp B	519	525	10	9	212.5±7.3	18.2±1.3 <sup>11</sup>
AFX-1100 II 000	256	263	55	52	96±1	58.6±0.4 <sup>6</sup>
AFX-1100 II 001	250	250	56	56	96±1	58.6±0.4 <sup>6</sup>
AFX-1100 II 002	244	250	59	56	96±1	58.6±0.4 <sup>6</sup>
PBX 9502	200	206	71	69	71±1	69.3±0.4 <sup>5</sup>

Table 8. Gap Test Comparison

Explosive	Gap Pressure (kbar)		
	NOL LSGT	Modified ELSGT	Eight-Inch Gap Test
TNT	46.3	17	14
Tritonal	50.1	19	14
Comp B	18.2	10	9
AFX-1100 II	58.6	56	50
PBX 9502	69.3	69	65

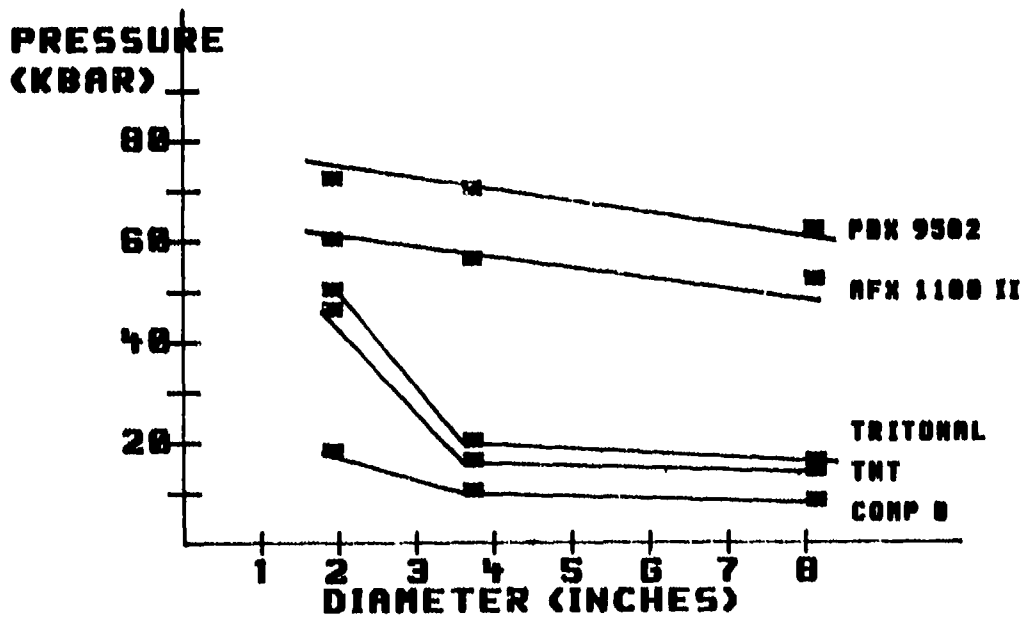


Figure 8. Gap Test Comparison of Pressure Vs. Diameter

## REFERENCES

1. Price, D., "Gap Tests and How They Grow," *DOD ESB Symposium*, Anaheim, CA, Aug 1986.
2. Foster, Jr., J. C.; Forbes, K. R.; and Gunger, M. E., "An Eight-Inch Diameter, Heavily Confined Card Gap Test," *8th Detonation Symposium*, Albuquerque, NM, 19 Jul 1985.
3. Price, D., *Critical Parameters for Detonation Propagation and Initiation of Solid Explosives*, NSWC TR 80-339, Naval Surface Weapons Center, Silver Spring, MD, 10 Sep 1981.
4. Walker, F. E. and Wasley, R. J., "Critical Energy for Shock Initiation of Heterogeneous Explosives," *Explosivstoffe*, Vol. 17 (1), 1969, p. 9.
5. Liddiard, T. P. and Price, D., *The Expanded Large Scale Gap Test*, NSWC-TR-86-32, Naval Surface Weapons Center, Silver Spring, MD, Mar 1987.
6. Aubert, S. A. et al., *Desensitization of Tritonal with Wax Emulsions*, AFATL-TR-88-32, Air Force Armament Laboratory, Eglin AFB, FL, Jul 1988.
7. Jaffee et al., *The Attenuation of Shock in Lucite*, NAVORD Report 6876, Naval Ordnance Laboratory, White Oak, MD, 27 May 1980.
8. Erkman, J. O. et al., *Calibration of the NOL Large Scale Gap Test; Hugoniot Data for Polymethyl Methacrylate*, White Oak, MD, 4 Apr 73.
9. Liddiard, Jr., T. P. and Price, D., *Recalibration of the Standard Card Gap Test*, NOL-TR-85-43, Naval Ordnance Lab, White Oak, MD, 20 Aug 1985.
10. Aubert, S. A. et al., *Calibration and Correlation of a Modified Expanded Large Scale Gap Test with the Large Scale Gap Test and the 8-Inch Gap Test*, AFATL-TR-89-46, Air Force Armament Laboratory, Eglin AFB, FL, Aug 1989.
11. Price, D. et al., *NOL Large Scale Gap Test III Compilation of Unclassified Data and Supplementary Information for Interpretation of Results*, NOL-TR-74-40, Naval Ordnance Laboratory, White Oak, MD, 8 Mar 1974.
12. Bernecker, R. R. and Clairmont, Jr., A. R., "Shock Initiation Studies of Cast Plastic-Bonded Explosives," *19th International Annual Conference of ICT 1988*, Karlsruhe, FDR, 29 Jun 88.
13. Honodel, C. A. et al., "Shock Initiation of TATB Formulations," *7th Detonation Symposium*, Annapolis, MD, 16-19 Jun 1981.

## DISCUSSION

DONNA PRICE  
ATR, Laurel, MD

Figure 8 of this paper shows the 50 percent point gap pressure ( $P_g$ ) plotted against the diameter of the test explosive (the acceptor). The data for the two larger diameters were obtained with gap tests using cast Comp B ( $1.68 \text{ g/cm}^3$ ) as the donor and from calibration curves of cast Comp B on PMMA gaps. The data for the tests of the smallest diameter (2 inches) were obtained with the NOL large scale gap test which was a pressed 50/50 pentolite donor ( $1.56 \text{ g/cm}^3$ ) and a calibration curve of pressed pentolite on PMMA.

Unfortunately, donors consisting of different explosives are seldom interchangeable in gap tests. In particular, pressed pentolite ( $1.56 \text{ g/cm}^3$ ) and cast Comp B ( $1.68 \text{ g/cm}^3$ ) have different C-J pressures and different pressure-time profiles at the same maximum pressure, e.g., at  $P_g$ . To obtain valid curves in Figure 8, it would be necessary to carry out the large scale gap test with a cast Comp B donor and to obtain a calibration curve for the cast Comp B donor on PMMA at this diameter (2 inches). If this were done, I suspect that the three curves of Figure 8 (Tritonal, TNT, and Comp B) would show a lower value for the  $P_g$  of 2-inch diameter charges and would no longer show a sharp upturn.

The 2-inch diameter value for PBX 9502 is also in some doubt, both for the above reasons and also because this explosive was reclaimed from a weapon and did not show a 95/5 TATB/Kel F composition by analysis.

For the reasons given above, I disagree with much of the Discussion section.

### REPLY BY STEPHEN A. AUBERT

Some uncertainty in the Gap pressures of the NOL tests points of Figure 8 is possible due to differences in the pulse duration and time loading in the PMMA produced by Comp B and Pentolite, respectively. However, for the sake of comparative purposes, these differences in pulse duration produced by Comp B and Pentolite are assumed to be small and insignificant in comparison with changes due to charge size. The justification for this assumption is found when comparing the results for PBX 9502 in this work using Comp B donors with the results for TATB/Kel F ( $93.7 \pm 0.3 / 8.3 \pm 0.3$ ) found in Reference 5. Although comparison with a known PBX 9502 would be preferred, this was the only testing at this size available and was considered suitable for this purpose. However, the charge densities were identical, at 1.886 g/cc (97.1 % TMD) in the two sets of tests.

In this work the result for PBX 9502 (95/5 TATB/Kel F), using Comp B donors, yielded a gap distance of 200-206 cards or 69 kbars. In the work of Reference 5 (using pentolite donors), TATB/Kel F (93.7/8.3) yielded a gap value of between 170 and 172 cards. Applying the calculated calibration curve provided to NSWC by Bowman of the LANL for the ELSGT with pressed pentolite donors at 1.56 g/cc, this corresponds to a pressure of 64-65 kbars. With a difference of 6 percent, these results are in fairly good agreement considering the different methods used to calibrate the two tests (measured for the modified ELSGT and calculated for the ELSGT), and the conditions of the test charges of Reference 5. Hence, the interchangeability of Comp B and Pentolite donors is supported by these results. Any differences in gap pressures for TNT and Tritonal in NOL Testing with Comp B donors would similarly be expected to be small. The comparison of these data suggest to us that the differences are small and Figure 8 is correct.

# SHOCK SENSITIVITY OF DAMAGED ENERGETIC MATERIALS

H. P. Richter, L. R. Boyer, K. J. Graham,\*  
A. H. Lepie, and N. G. Zwierschowski  
Research Department  
Naval Weapons Center  
China Lake, CA 93555-6001

*This paper presents the results of experimental studies conducted in the Research Department, Naval Weapons Center, China Lake, California. Specific topics discussed include: (1) a description of deformation induced internal damage in energetic materials, (2) techniques used in our laboratory to produce damage, (3) methods developed to characterize that damage, and (4) shock sensitivity increases with increasing damage levels. Significant increases in shock sensitivity were measured as a function of damage. The critical initiation pressure of explosives and propellants can be reduced by 50 percent with only 1 percent void volume created by the deformation of the energetic material.*

## INTRODUCTION

This paper is concerned with the influence of internal damage in the form of voids on the shock sensitivity of energetic materials: both plastic bonded explosives (PBXs) and solid rocket propellants.

The damage in the form of internal porosity can be induced through:

- Mechanical deformation ranging from low-rate tensile or shear straining to high-rate bullet/fragment impact or case failure in a rocket motor.
- Field storage of the energetic material at elevated temperature or moisture conditions such that voids or micro-cracking are produced.
- Poor processing conditions in the casting of the energetic material (e.g., insufficient vacuum or excess water reacting with isocyanate in polymer cure to produce voids).
- Thermally induced gassing such as in a cook-off environment or accelerated aging at elevated temperatures.

\*Now with the Atlantic Research Corporation, Gainesville, Virginia.

Research on the mechanisms, characterization, and effects of damage in energetic materials has been ongoing at the Naval Weapons Center (NWC) for years and is continuing.<sup>1</sup> Experimental techniques have been developed to measure changes in chemical, physical, and mechanical properties resulting from damage.

Damage is a critical concern when considering the probability of inadvertent explosion or detonation of both warheads and rocket motors. Previously, the effect of damage on energetic material hazards has been directed primarily to the study of porous materials. Porosity has been created by adding microballoons, using blowing agents during cure and by pressing to low density levels. Here our emphasis is on the production of well-characterized damage generated in a realistic manner for shock studies.

## DAMAGE DESCRIPTION

PBXs and solid propellants are highly filled polymers with up to 90+ weight percent solid filler content. Any finite deformation of such a material causes high stress fields around the filler particles and microstructural damage in the form of polymer chain scissions

and interfacial debonding. The debonding and chain scissions occur in close proximity to or on the surface of the filler particles; this is termed dewetting. The structural damage accumulates as a function of deformation and an increase in porosity occurs. Three types of porosity can be produced; closed cells, interconnected cells, and, after load has been removed, partially collapsed voids that represent permanent damage. Figure 1 illustrates a uniaxial tensile deformation where closed cell porosity develops initially next to embedded crystals. Further straining of the material stretches the voids into elliptical shapes and microcracking between them may occur, thus, developing an interconnected porosity with possible air penetration into the material. Upon removal of stress the voids collapse very rapidly, but a residual damage remains in the form of partially collapsed voids. These reopen easily on repeated deformation.

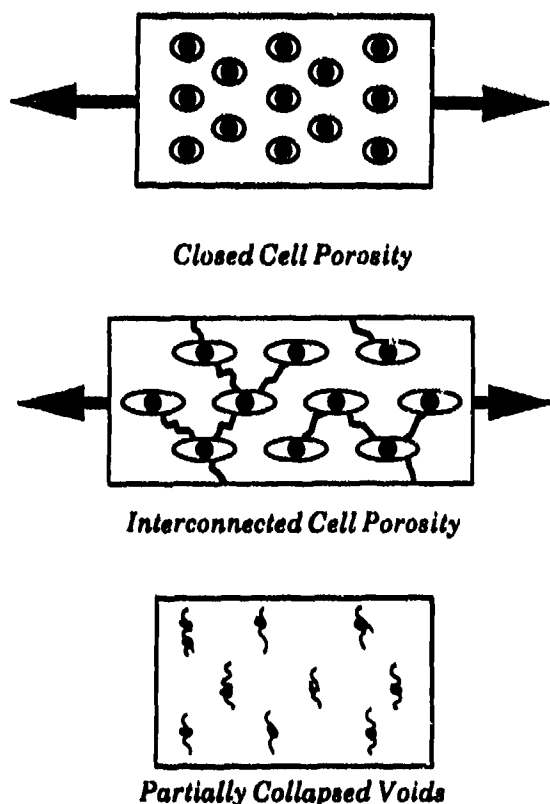


Figure 1. Damage Types Resulting from Deformation of Composite Energetic Materials

## DAMAGE PRODUCTION

Damage was produced by both uniaxial tensile deformation and high rate impact prior to shock sensitivity evaluation. In the tensile case, a "sister sample" approach was used: small uniaxial laboratory samples (7x1x1 cm) were tested in detailed damaged characterization studies while large specimens (10x4x4 cm) of the same material, from the same source, were damaged under the same conditions prior to shock testing.

The high rate impact approach of inducing damage is shown in Figure 2. Up to four large test specimens (8x4x4 cm) are held in a projectile such that the degree of confinement on the sides can be varied. The projectile is fired from a gas gun at velocities that can be varied from 20 to 100 m/sec. The impact of the projectile is followed by high speed photography and samples are recovered 30 minutes after damaging for shock testing. Generally, one of the test specimens was used to characterize the state of damage.

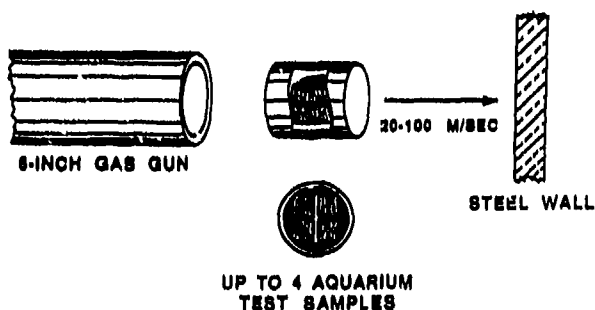


Figure 2. Gas Gun Damage Production Technique for Follow-on Aquarium GAP Testing

## DAMAGE CHARACTERIZATION

New experimental techniques have been developed at NWC to characterize porosity in energetic materials. The techniques deal with (1) initial voids of undamaged material, (2) real time measurement of voids produced during deformation, (3) the time-dependent collapse of voids following deformation where the stress load has been removed, and (4) the porosity of material at long times (minutes) after damaging.

Dilatometer is used to measure the onset of dewetting and the development of voids during mechanical deformation as well as the time-dependence of void collapse after the load is removed. Both uniaxial tensile and torsional shear dilatometers have been developed.<sup>2,3</sup>

The uniaxial tensile dilatometer is a new and relatively simple instrument which measures the stress-strain and void volume-strain properties simultaneously. The design, shown in Figure 3, uses the FC-43 Fluorinert Electronic Fluid (manufactured by the 3M Company, St. Paul, Minnesota) as the dilatometer fluid. This freon-like low-viscosity fluid is inert in terms of swelling or leaching of most energetic material compositions studied. The FC-43 Fluorinert liquid has a density of 1.86 g/cc, which is dense enough to carry the transducer float. The dilatometer housing is fabricated of Pyrex with an O-ring seal to the specimen supporting aluminum base. A water jacket is included for close temperature control which can be critical in very slow deformation rate studies. The load is transmitted to the specimen via a piano wire which passes through the precision-bore glass vent tube. The stress-strain behavior can thus be determined in a conventional manner with the Instron tester. A hollow glass float, to which a linear variable differential transformer (LVDT) core is attached, is then placed into the precision-bore glass sidearm. With the LVDT in position, volume changes of  $1 \times 10^{-2}$  cc can be reproducibly measured allowing for precise measurement of propellant volume changes. Void volumes up to 50 percent have been measured on energetic materials at break.

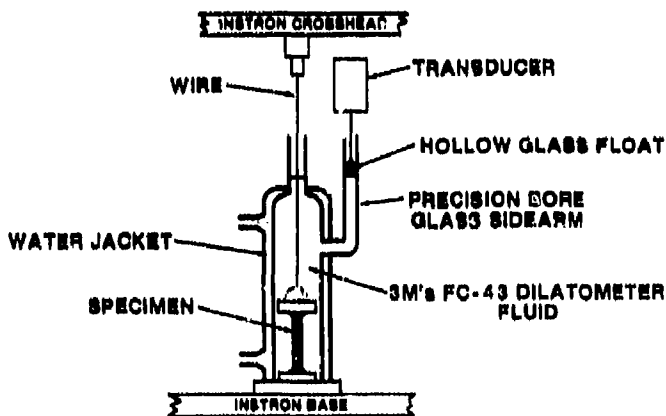


Figure 3. NWC Liquid Tensile Dilatometer

The shear dilatometer, as shown in Figure 4, measures stress-strain and void volume-strain properties simultaneously under torsional shear loading.<sup>2</sup> The instrument uses mercury as the dilatometer fluid and has been used to measure propellant volume changes in the range of  $1 \times 10^{-3}$  to 50 volume percent at shear strain rates from  $1 \times 10^{-2}$  to  $1 \times 10^{+3}$  min<sup>-1</sup>. Figure 5 shows the seven material properties that are routinely reported in tensile and shear dilatation studies.

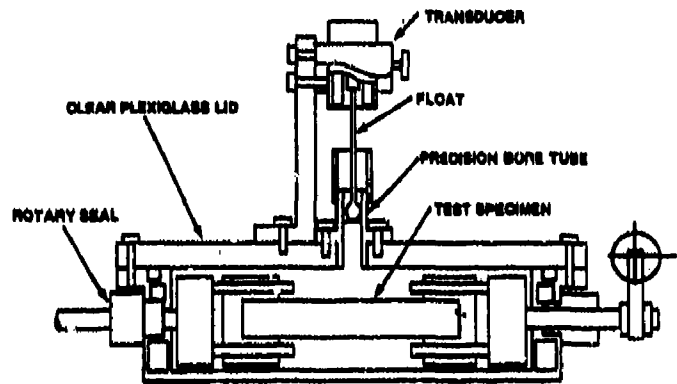


Figure 4. Torsional Shear Mercury Dilatometer

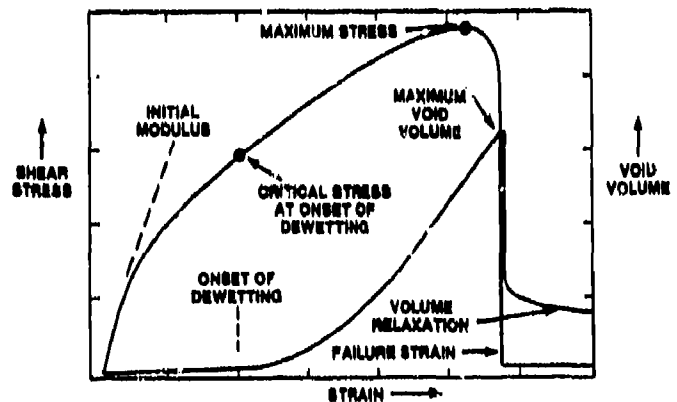


Figure 5. Propellant Properties Under Deformation

The void volume relaxation or collapse following deformation is a critical issue in terms of shock response. Our results to date suggest that the void volume at the time of shock initiation is the most critical factor in shock sensitivity, and not the maximum void volume that had been introduced during deformation. Thus, we find that measurements of the time-dependent void collapse are essential in understanding the effects of mechanical

damage. Figure 6 illustrates the deformation rate effects on both the void volume production and the void collapse after failure of a test specimen. At a high strain rate (approximately 100 times faster than slow) there is a pronounced increase in voids produced relative to the slow rate results. This is largely a function of the higher stresses produced around the largest particles at high rates. The void collapse after failure is very fast and is highly dependent on the strain rate. At high rates, the void volume produced is higher, but very rapid void collapse is seen. At lower rates, considerably less collapse is seen, such that at times greater than 1 second higher residual void volumes are seen. Again, it is the residual void volume that is critical to increases in shock sensitivity. The void collapse variation with rate is due to a viscous flow factor. As depicted in the spring and dashpot models in Figure 6, at high rates the spring deformation predominates and high snap-back occurs after failure. At slow rates, the deformation involves viscous flow of the dashpot and much less snap-back tensile force is generated.

A hydrostatic compression instrument<sup>4</sup> is used to measure the initial void content of baseline undamaged energetic materials, as well as the void volume remaining after mechanical deformation. As shown in Figure 7, two sample configurations can be applied. The first configuration uses three rectangular specimens immersed in FC-43 fluid which are compressed simultaneously. An LVDT transducer is used with each specimen to follow the uniaxial compression as a function of applied

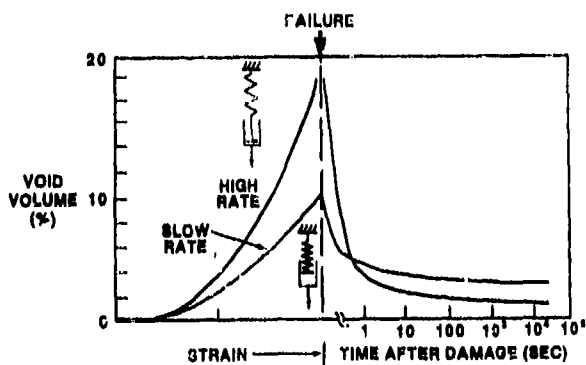


Figure 6. Void Volume Profile During and After Deformation

pressure. The second configuration uses a 2.5 cm cube of propellant where three LVDTs are used and the X, Y, Z directional compression properties are measured independently. In this case, any anisotropic behavior or voids produced in the direction of straining as compared to the lateral directions, for example, can be investigated. The damaged void volumes show this behavior; the linear compression in the strained direction may be 5 to 7 times greater than in either lateral directions. Void volumes in the range of  $5 \times 10^{-5}$  to 5 volume percent can be measured in selected pressure increments up to 1200 psi. With cast propellants or explosives that are undamaged, a compression of approximately 0.02 volume percent is seen at pressures from ambient up to 300 psi followed by a linear compression bulk modulus measurement. Bulk moduli of undamaged materials are typically  $1 \times 10^6$  psi (7 GPa). The void volume created by damaging an energetic material can be measured by straining a sample to failure in tension, followed by a volume collapse period prior to hydrostatic compression testing. Here an initial void compression ranging from 0.1 to 2.5 volume percent has been seen out to 300 psi with a typical bulk modulus reduced to  $5 \times 10^5$  psi (3.5 GPa).

Density changes before and after damage have also been used to determine volume damages and creation of voids. Densities are computed from sample weights in air and in silicone oil. A glass cube with a known volume is used as a standard, to compensate for temperature changes.

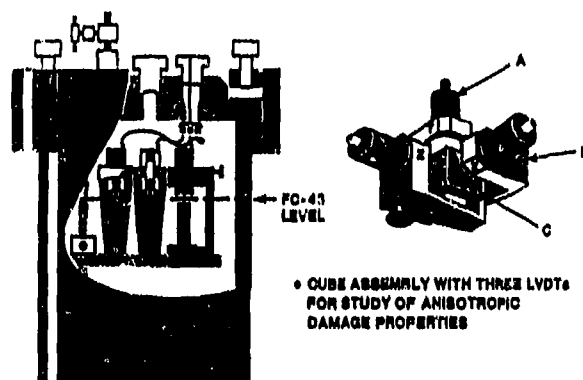


Figure 7. Hydrostatic Compression Chamber for Linear or Cube Specimen Studies up to 1200 psi

## SHOCK SENSITIVITY

In an effort to determine the shock sensitivity of energetic materials that have sustained various degrees of damage, three tests were considered: The NOL Large Scale Cap Test (LSGT); the Los Alamos National Laboratory (LANL) Wedge Test; and a variation of the Liddiard Aquarium Test. None of these established techniques lend themselves readily to studies of damaged material. The LSGT suffers from shockwave distortions due to the lateral unloading of the polymethylmethacrylate (PMMA) shock attenuator, and from the steel confinement tube. The LANL Wedge Test is expensive to run and wedge preparation with damaged material would be very difficult. The Aquarium Gap Test, suggested by Jacobs and Price,<sup>5</sup> has been implemented at NWC for this purpose. It uses water as the shock attenuator and has no steel confinement tube surrounding the specimen. Relatively long duration shocks (comparable to PMMA attenuation) in the pressure range of 0.5 - 8.0 GPa can be produced. Tests can be performed over the temperature range of 10 - 80°C on specimens typically 0.03 - 0.1 kg, and the specimens may be undamaged, predamaged or damaged in-situ. Shock sensitivity tests are run as a function of extent of damage and time from damage.

### AQUARIUM GAP TEST

Figure 8 shows the instrumented glass Aquarium Gap Test as developed at NWC. The acceptor test sample is supported on a steel witness plate a variable distance from the donor

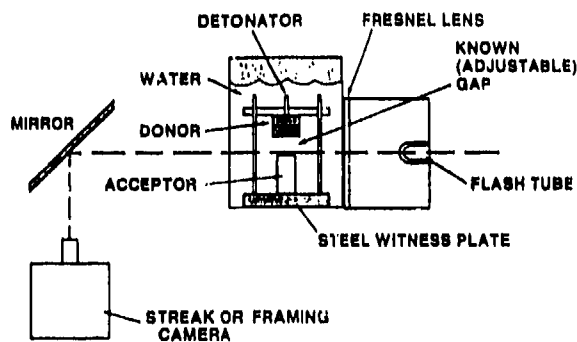


Figure 8. NWC Aquarium Gap Test Apparatus

charge (two standard Pentolite LSGT pellets). The aquarium is filled with water while avoiding air bubble accumulation on the surfaces. Instrumentation can include either a streak or framing camera recording of the flash bomb or flash tube illuminated arrangement as shown. Both front and back illumination has been used. A simplified "bucket" test arrangement is also used where only witness plate damage is used in evaluation of the acceptor response. A positive test for detonation includes punching of the witness plate. In both of the above tests, the measured gap is converted to input pressure in the material at the test conditions.

The shock sensitivity of a number of undamaged and damaged energetic materials was determined using one of the above test apparatus. Figure 9 shows typical results. The abscissa is percent void volume at time of shock test as determined using the dilatometer or hydrostatic compression results on an identical sample, while the ordinate gives ratio of critical initiation pressures necessary to cause shock to detonation transition (SDT) in the damaged and undamaged materials ( $P_{dam}/P_{undam}$ ). The plot shows that at 1 percent void volume the pressure required to detonate the damaged energetic material is approximately 50 percent of the pressure required to initiate the undamaged counterpart; or, that the damaged material is twice as sensitive.

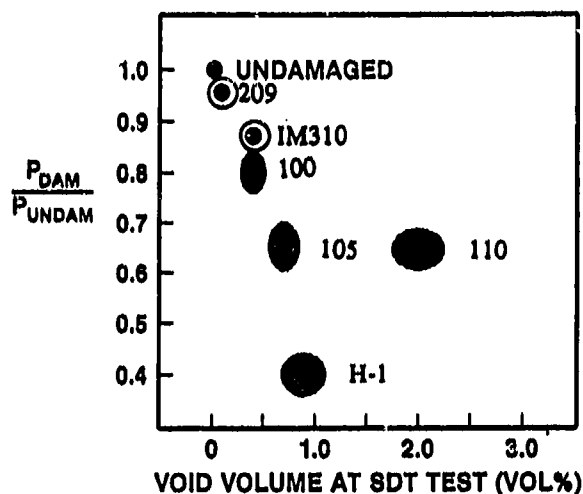


Figure 9. Normalized Critical Initiation Pressure as a Function of Void Volume

## CONCLUSIONS

This research has shown that damage, and voids that it creates, causes a very pronounced decrease in the critical shock initiation pressure of energetic materials. In the interest of minimizing the hazards of these materials, the void content must obviously be kept to a minimum. Voids introduced during manufacturing or aging are being studied. In energetic material processing, for example, the combined techniques of vacuum casting and pressure cure results in extremely low initial void content. The development of damage-resistant energetic material formulations holds the promise for materials which will withstand high rate deformation with minimum void formation.

Techniques to produce and characterize damage in energetic materials for shock studies have been developed. The extent and rate at which damage can be introduced can be varied so as to simulate slow rate aging up to high rate impact conditions.

## REFERENCES

1. Boggs, T. L.; Price, C. F.; Richter, H. P.; Atwood, A. I.; Lepie, A. H.; Zwierschowski, N. G.; and Boyer, L. R., "Detonation of Undamaged and Damaged Energetic Materials," *19th International Annual Conference of ICT*, Federal Republic of Germany, 1988.
2. Richter, H. P.; Lepie, A. H.; and Adicoff, A., "A New Shear Dilatometer for Filled Polymers," *1980 JANNAF Structures and Mechanical Behavior Subcommittee Meeting*, Redstone Arsenal, AL, CPIA Publication 331, 21-23 Oct 1980.
3. Lepie, A. H. and Adicoff A., "Advanced Physical Characterization Part I: Damaged, Volume Change and Dynamic Properties Under Strain," *1978 JANNAF Structures and Mechanical Behavior Subcommittee Meeting*, Monterey, CA, CPIA Publication 283, Feb 1977, pp. 51-61.
3. Lepie, A. H. and Moran, M. B., "A New Hydrostatic Compression Tester for Anisotropic Filled Polymers," *J. Appl. Polym. Sci*, 30, 1985, pp. 3153-3161.
5. Jacobs, S. J. and Price, D., "The NOL Gap Test: Past, Present, and Future," *1980 JANNAF Propulsion Systems Hazards Subcommittee Meeting*, Monterey, CA, CPIA Publication 330, Vol. 1, Oct 1980, pp. 257-265.

# SHOCK SENSITIVITY OF DAMAGED ENERGETIC MATERIALS

H. P. RICHTER, L. R. BOYER, K. J. GRAHAM,\*  
A. H. LEPIE, N. G. ZWIERZCHOWSKI

RESEARCH DEPARTMENT  
Naval Weapons Center  
China Lake, California



This paper presents the results of experimental studies conducted in the Research Department, Naval Weapons Center, China Lake, California. Specific topics discussed include (1) a description of deformation induced internal damage in energetic materials, (2) techniques used in our laboratory to produce damage, (3) methods developed to characterize that damage and (4) shock sensitivity increases with increasing damage levels. Significant increases in shock sensitivity were measured as a function of damage. The critical initiation pressure of explosives and propellants can be reduced by 50% with only 1% void volume created by the deformation of the energetic material.

\*Now with the Atlantic Research Corporation, Gainesville, Virginia.



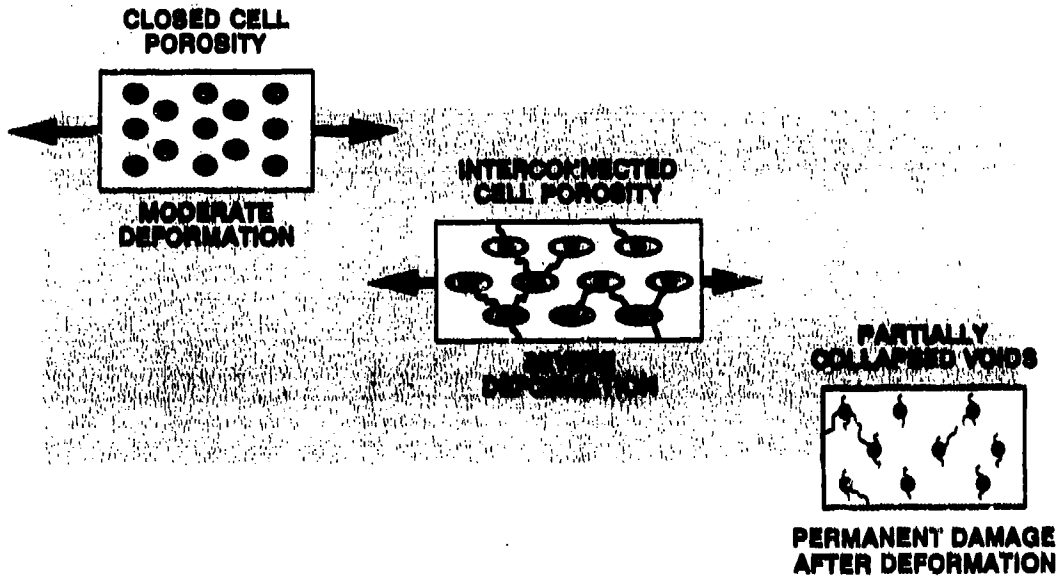
## DAMAGE PRODUCED BY DEFORMATION

---

- DAMAGE IS HIGHLY MATERIAL DEPENDENT
  - LOW SOLIDS LOADING MINIMIZES DAMAGE
  - SMALL PARTICLE SIZES SIGNIFICANT
  - TOUGH POLYMER NETWORK REQUIRED
- DAMAGE IS DEFORMATION RATE AND TIME DEPENDENT
  - HIGH RATES GENERATE HIGH DAMAGE LEVELS
    - BUT VOID COLLAPSE MORE PRONOUNCED
  - VOID VOLUME COLLAPSE AFTER UNLOADING IS FAST
    - 90% OF VOID VOLUME COLLAPSES IN 60 SECONDS
    - PERMANENT DAMAGE ALWAYS REMAINS

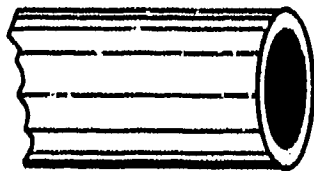


## DAMAGE TYPES RESULTING FROM DEFORMATION



## GAS GUN DAMAGE PRODUCTION TECHNIQUE FOR FOLLOW-ON AQUARIUM GAP TESTING

### HIGH RATE IMPACT DAMAGE PRODUCTION



6-INCH GAS GUN



20-100 M/SEC



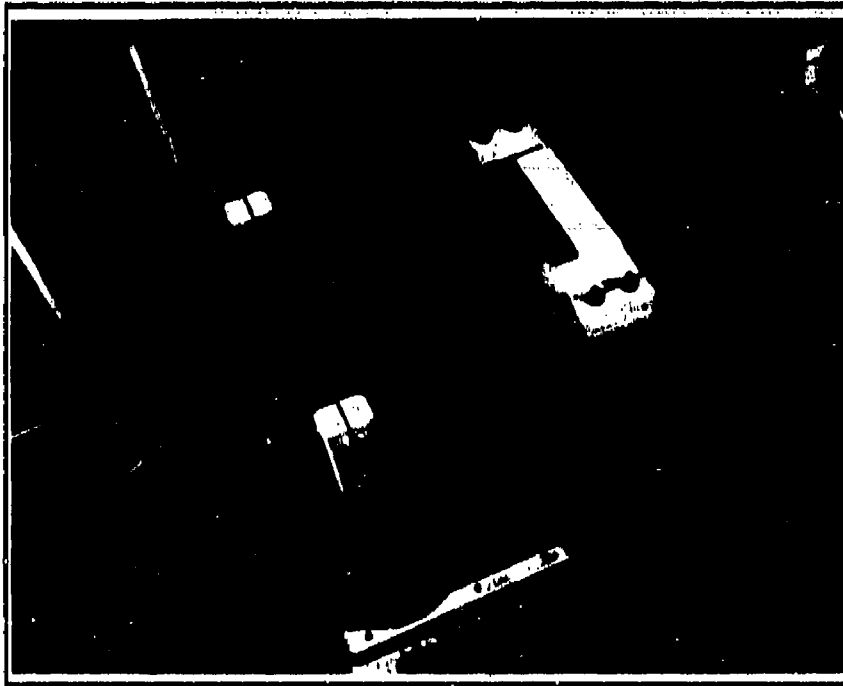
STEEL WALL



UP TO 4 AQUARIUM  
TEST SAMPLES  
VARIABLE CONFINEMENT



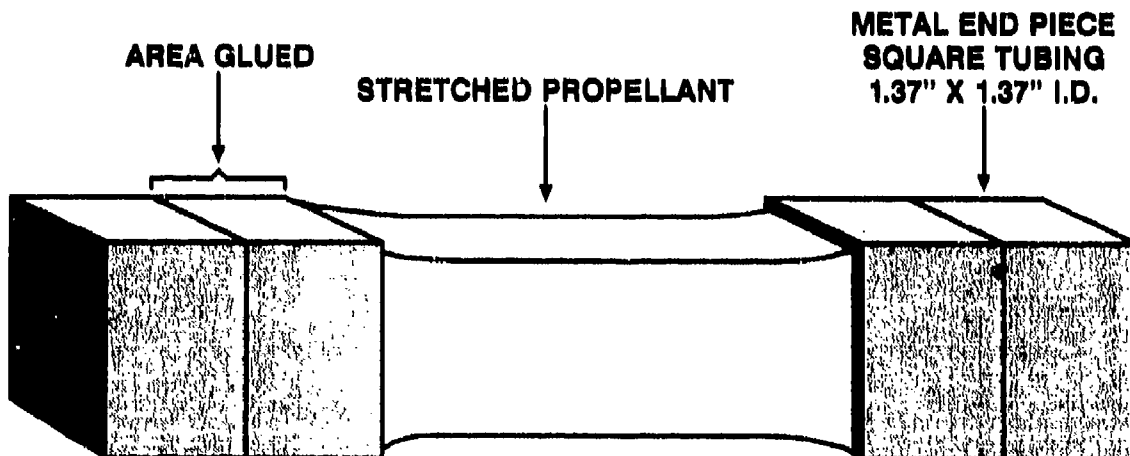
## DAMAGE PRODUCED BY LOW AND HIGH RATE TENSILE DEFORMATION



INSTRON TEST EQUIPMENT RATES FROM 0.01 TO 3 METERS PER SECOND

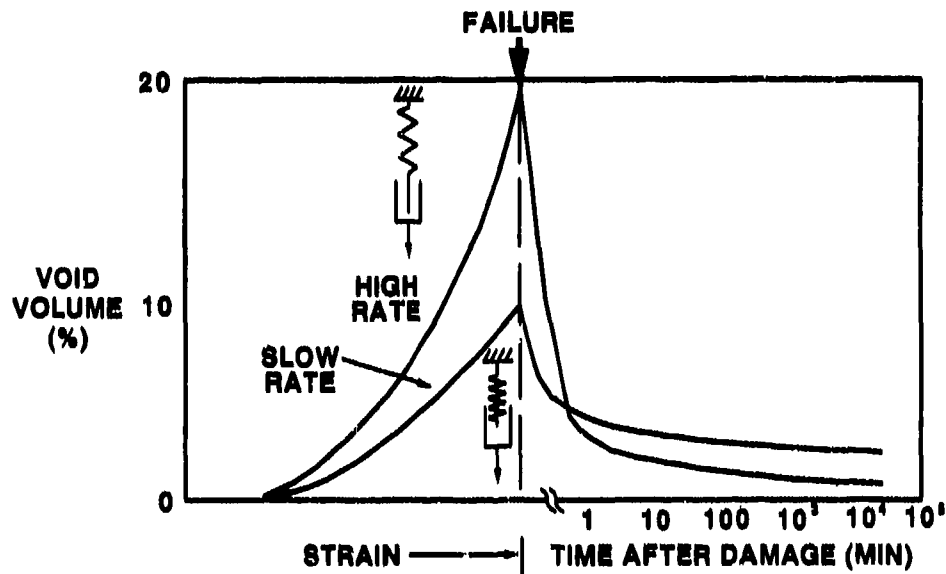


## SDT TEST SPECIMEN





## VOID VOLUME PROFILE DURING AND AFTER DEFORMATION

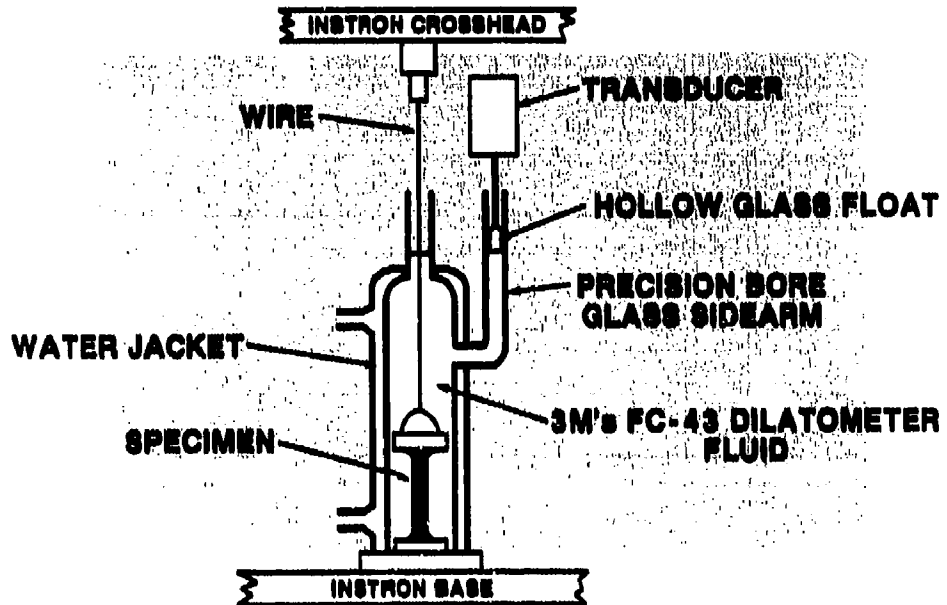


## DAMAGE IN PROPELLANTS AND EXPLOSIVES

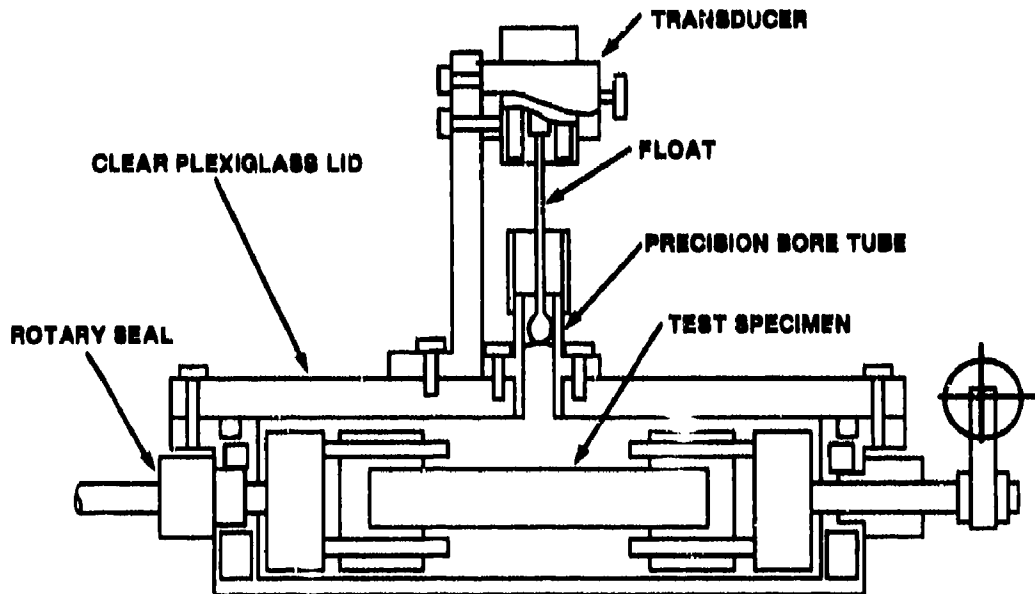
- INDUCED BY:
  - MECHANICAL DEFORMATION: LOW TO HIGH RATES
  - LONG TERM AGING
  - POOR PROCESSING OR CASTING CONDITIONS
  - THERMALLY INDUCED GASSING: COOKOFF CONDITIONS



## UNIAXIAL TENSILE DILATOMETER

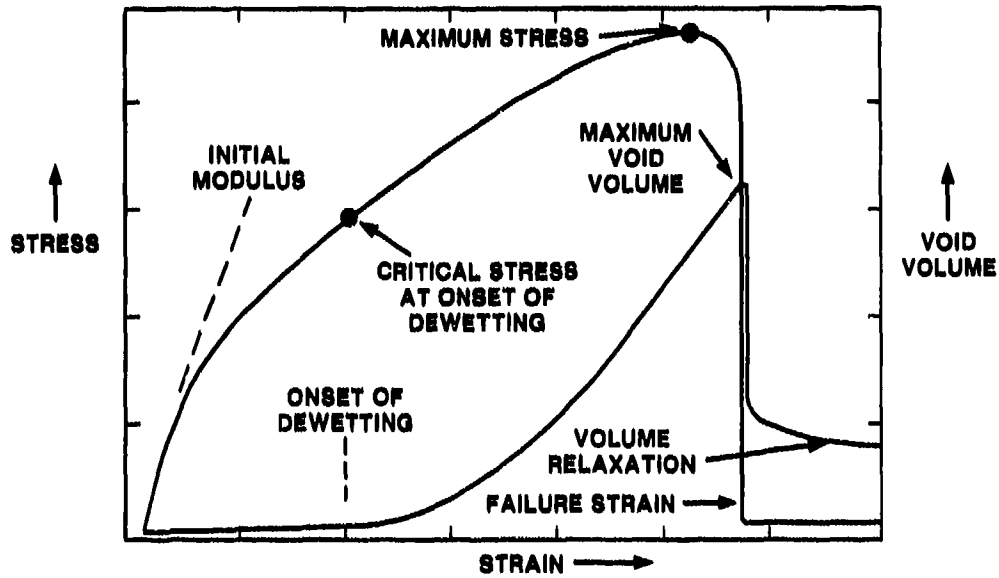


## TORSIONAL SHEAR MERCURY DILATOMETER

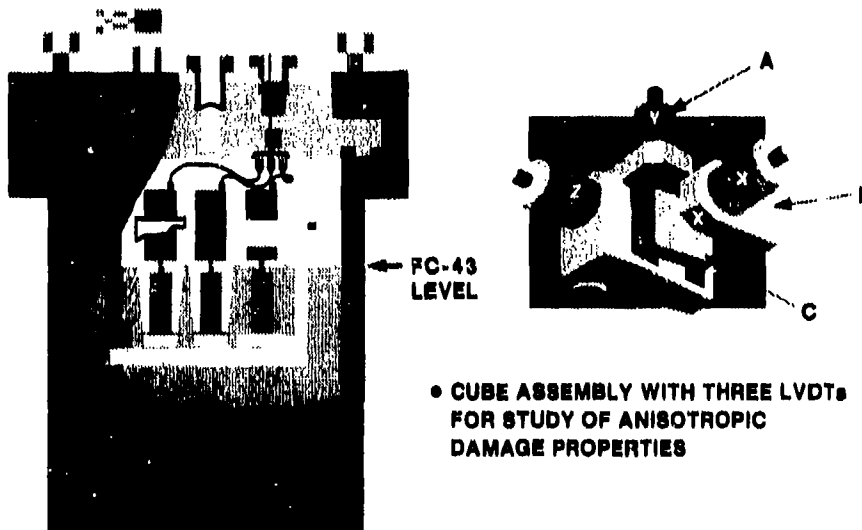




## MECHANICAL PROPERTIES OF A SOLID PROPELLANT

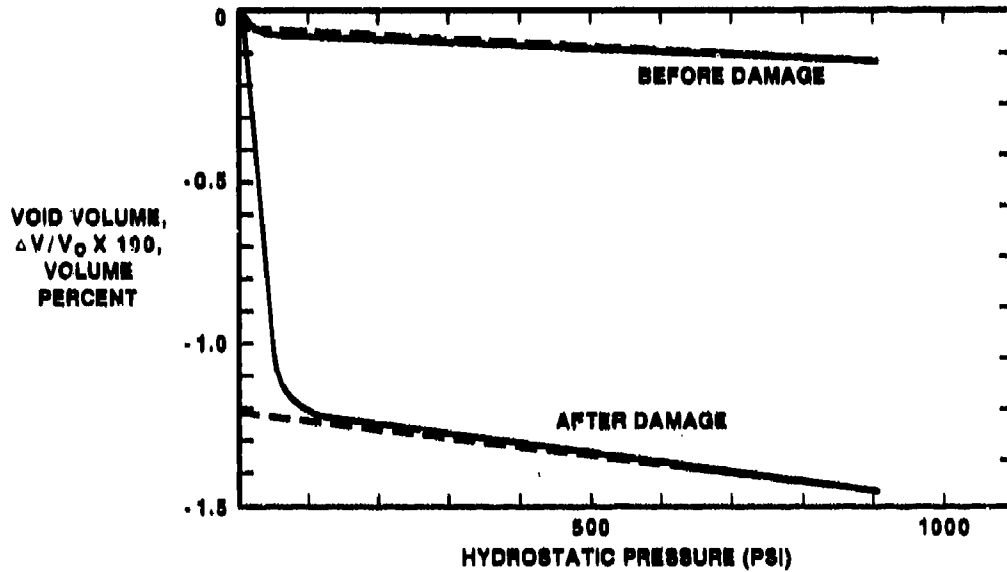


## HYDROSTATIC COMPRESSION CHAMBER

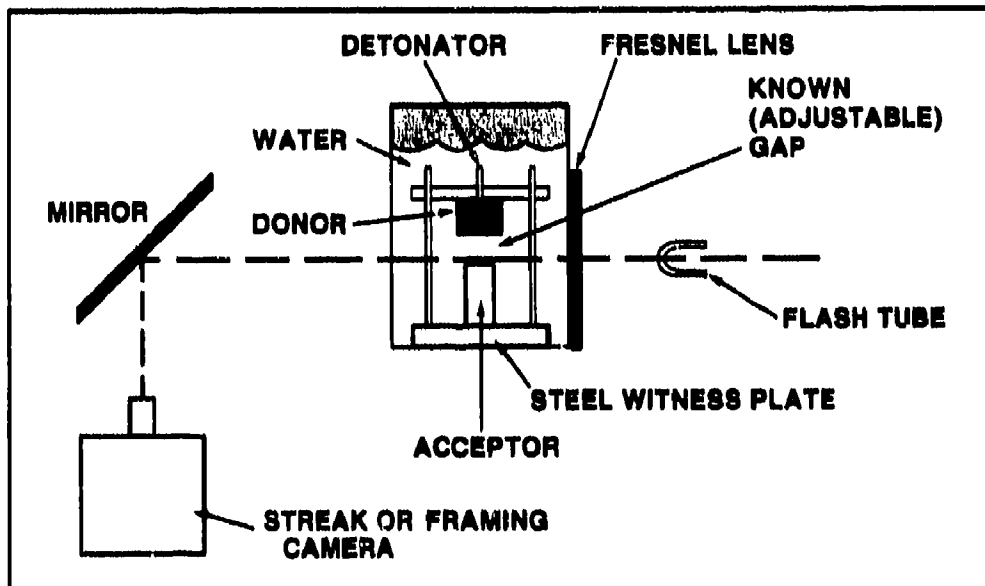




# HYDROSTATIC COMPRESSION PROPERTIES OF ENERGETIC MATERIALS

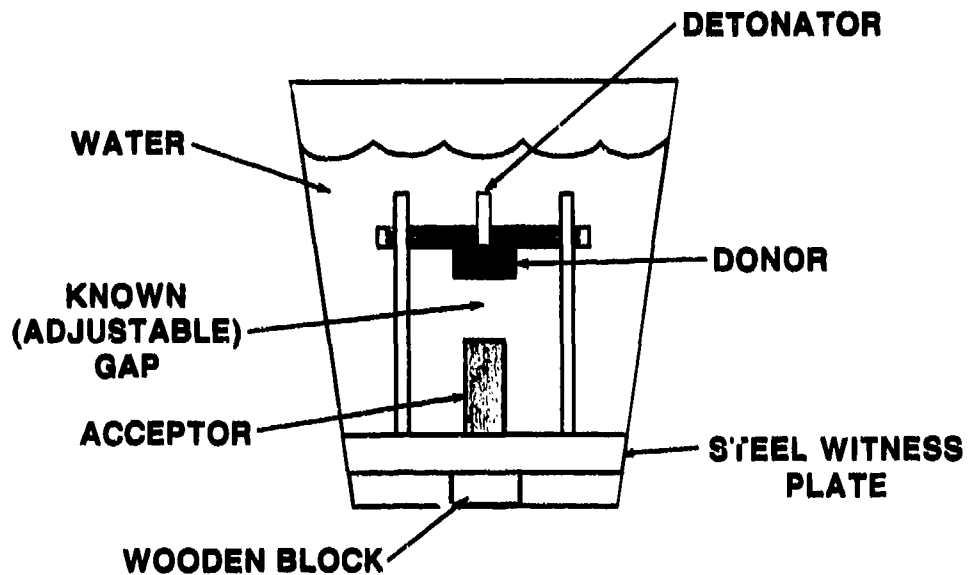


## NWC AQUARIUM GAP TEST APPARATUS



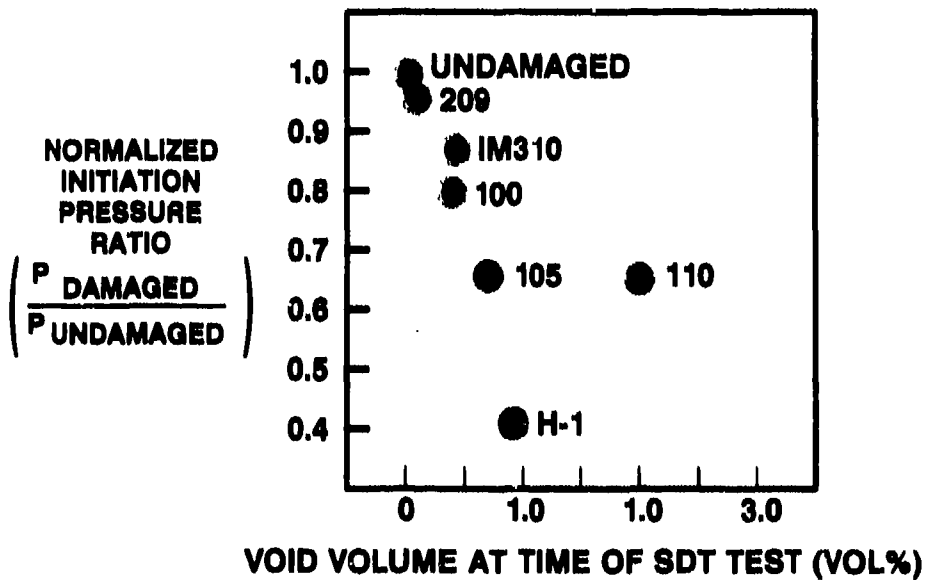


## BUCKET TEST VARIATION



## NORMALIZED CRITICAL INITIATION PRESSURE AS A FUNCTION OF VOID VOLUME

SDT TESTS AT 20-30 MINUTES AFTER DAMAGE INDUCED





## CONCLUSIONS

---

- **DAMAGE CAUSES A SENSITIVITY INCREASE IN ENERGETIC MATERIALS**
  - **CRITICAL INITIATION PRESSURE DECREASES TO 50% OF UNDAMAGED AT ONLY 1% VOIDS**
  - **TIME BETWEEN DAMAGE PRODUCTION AND SENSITIVITY TESTING IS SIGNIFICANT**
    - **MORE SENSITIVE AT SHORT TIMES**
- **TECHNIQUES DEVELOPED TO PRODUCE WELL CHARACTERIZED DAMAGE AND TO EVALUATE SHOCK SENSITIVITY CHANGE**
- **HAZARD REDUCTION REQUIRES DAMAGE RESISTANT ENERGETIC MATERIALS WITH VERY LOW INITIAL VOID VOLUMES**

# BURNING RATES OF TWO CAST NITRAMINE EXPLOSIVES USING A HYBRID CLOSED BOMB-STRAND BURNER

W. C. Tao, M. S. Costantino, and D. L. Ornellas  
Lawrence Livermore National Laboratory  
Livermore, California 94550

*The burn rate of two HMX-based cast explosives, RX-08-EL and RX-35-AP, is measured to pressures above 650 MPa using a hybrid closed bomb-strand burner. The hybrid design allows the simultaneous measurement of pressure and regression rate in each experiment over a large range of pressures. RX-08-EL is a high performance extrusion cast explosive with low sensitivity, and RX-35-AP is a cast-cured explosive with a mono-modal HMX particle size distribution. Up to 650 MPa, both explosives exhibit a planar burning mechanism with the regression rate obeying the classical  $aP^n$  formalism. Upon cycling to 400 MPa, unloading, and repressurizing, the RX-08-EL explosive exhibited a significant increase (an order of magnitude) in its burn rate.*

## INTRODUCTION

The ability to predict the combustion behavior and burning rate of energetic materials is of prime importance to many disciplines.<sup>1-5</sup> These range from the design of rocket motors and gun barrels, to hazards assessment of deflagration-to-detonation processes in propellants and explosives. For high performance rocket motors which require high thrust, short-burning solid-propellant grains, the burning rate has pronounced effects on the flame propagation, chamber pressurization processes, and the maximum motor pressure.<sup>1</sup> Sudden perturbation in the combustion rate due to cross-flow and pressure transients may cause significant degradation in the performance of the motor. Similarly, in the interior ballistic cycle of guns, a change of the burning phenomena from the design criteria adversely affects the range and accuracy of the projectile delivery.<sup>2</sup> Perhaps most important are the potential hazards involved in the use of detonable propellants under conditions where a deflagration-to-detonation transition may occur. An abrupt increase in pressure, from a shift of the burning rate, can trigger this transition.<sup>4,5</sup>

The burning mechanism of a condensed energetic material involves many chemical

and physical processes involving a change of phase and energy and mass transfer. Heat transfer from the flame zone to the material surface causes the propellant or explosive to pyrolyze, and the pyrolyzed gases to react close to the surface. The burning rate depends on a number of factors, such as the combustion pressure, initial temperature of the material, chemical composition of the fuel and oxidizer, particle size, presence of energetic or inert binders, and the morphology of the composite mixture. Since most applications involve burning at the relatively low pressures of rocket motors (10 MPa), or the somewhat higher pressures found in guns (400 MPa), efforts to understand the conversion of a condensed propellant or explosive to gaseous products have been limited to these pressure ranges. Additionally, even at low pressures, the basic physics and chemistry of burning energetic material are not well established, requiring empirical burning rate laws.

These empirical formalisms usually describe a mass regression rate,  $dm/dt$ ,

$$dm/dt = \rho Ar, \quad (1)$$

where  $\rho$  is the density of the condensed phase,  $A$  the surface area that is burning, and  $r$  the surface regression rate. Each term in this basic

equation is approximated in data reduction calculations. The density either is taken as a constant, equal to the density at 0.1 MPa (atmospheric pressure), or is calculated at high pressures using a scalar, pressure independent bulk modulus. Neither of these assumptions is correct, causing errors of as much as 10 percent in the mass generation rate at pressures greater than 400 MPa. Guesses about the surface area that happens to be burning at a particular instant are equally tenuous. In slow burning propellants, assumption of a regular, macroscopic burning surface probably introduces little error (in the absence of cracks and substantial connected porosity), while many of the commonly observed "slope breaks" in closed bomb burning data almost certainly are related to a change in the amount of surface area exposed to the flame.<sup>6</sup> The final term of Equation (1), the intrinsic burning rate, has some basis in theory, but generally is found experimentally to be

$$r = a_0 + a_1 P^n, \quad (2)$$

over specified pressure ranges. The parameter  $a_0$  usually is taken as zero, and other parameters are found by plotting strand burner or closed bomb data.

The change in the combustion surface area can be due to several mechanisms. For porous explosives, the transition from conductive to convective burning is due to the penetration of the hot gases into the pores ahead of the flame front. Fifer and Cole<sup>7</sup> have investigated the burning rate of HMX as a function of density, particle size, and confinement up to 350 MPa. They propose, for laterally confined low density charges, that a subsonic pressure wave crushes and deconsolidates the sample ahead of the flame. For unconfined charges, they observed a "progressive deconsolidation" mechanism in which the enhanced burning surface does not exist in the interior of the charge, but rather primarily in the two phase (gas-particle) zone extending a considerable distance from the sample. The extended flame zone is not related to gas phase chemistry, but rather is determined by the particle burnout distance, which in turn is dependent on the particle size and the intrinsic burning rate.

A third mechanism that changes the amount of burning surface is the shear fracture of the nitramine particles, creating a new particle distribution. This occurs if the details of the macroscopic applied stress, the as-formulated particle size distribution, and the amount and nature of the binder result in shear stresses at particle-particle contacts greater than the failure strength of the nitramine. The applied stress may result from a penetrating bullet or fragment, collision of a propellant grain with another grain or the breech wall in a gun, or a stress wave propagating ahead of the burning front. Costantino and Tao<sup>8</sup> investigated the change in particle size distribution of a nonconsolidated bed of HMX subjected to hydrostatic compression to 500 MPa. For a well-characterized 150-200  $\mu\text{m}$  distribution of Class C HMX, analysis with scanning electron micrograph and Coulter counter after pressure unloading shows a substantial shift to smaller particle sizes and multi-modal distribution. Figures 1 and 2 illustrate the SEM results for the HMX particles before and after hydrostatic compression, respectively.

The motivation for this work stems from two sources. First, we are interested in learning about the physics and chemistry of burning at high pressures (>500 MPa). Currently, we require something better in the computer models for hot spot ignition and growth in condensed explosives (such as those developed by Tarver et al.<sup>9</sup>) than the extrapolation of mass regression laws found at pressures an order of magnitude lower than the application pressure. Their model, shown in Equation (3), incorporates a similar  $aP^n$  mass regression factor in the ignition and growth terms. In practice, the quantities  $a$  and  $n$  are held constant at values found experimentally at low pressures, or are used as fitting parameters.

$$\frac{dF}{dt} = I[(1-F)^A(\rho/\rho_0-1)^B] + G_1[(1-F)^C F^D P^Y] + G_2[(1-F)^E F^F P^Z] \quad (3)$$

- F - fraction reacted
- I - fraction ignited as a  $F$  (shock strength)
- P - pressure
- $G_1$  - early growth rate constant
- $G_2$  - late growth rate constant
- $\rho$  - density



*Figure 1. Scanning Electron Micrograph of the Particle-Size Distribution of Class C HMX Prior to Hydrostatic Compression*

Second, we want to develop tests and diagnostics that can readily screen energetic materials for hazards and vulnerability associated with a sudden transition to higher regression rates. This requires an understanding of how "bench" formulations change when subjected to different levels of stress, and how that affects the combustion behavior.

The approach we have selected uses a hybrid closed bomb-strand burner, with diagnostics that provide estimates of the average burning rate over a pressure interval. This hybrid design allows the simultaneous measurements of regression rate and pressure, thereby generating information over a large pressure range in one experiment. We selected two non-porous HMX formulations, RX-08-EL and RX-35-AP, and measured their burning rates to 650 MPa. Both formulations have a similar HMX loading in a relatively compliant binder matrix. Of specific interest is the burning behavior of these explosives under different pressure loading and unloading conditions. Previous investigation<sup>10</sup> of a brittle



*Figure 2. Change in Particle-Size Distribution after 500 MPa Hydrostatic Compression as Revealed by SEM*

pressed formulation with a similar particle size loading and distribution (LX-14) yielded a burning behavior with several regions of uniformly increasing pressure, each with a higher slope than the previous one, with a sudden transition to even higher pressures at the end of the burn. It was found that large-scale breakup of the LX-14 strand contributed to a fast burning and premature ignition along the sides of the strand.

## EXPERIMENTAL APPROACH

### Material Preparation

The RX-08-EL is an extrusion cast explosive consisting of 72.93 wt% LX-04 grade HMX with a mean particle-size distribution of 60  $\mu\text{m}$ , 25.16 wt% FEFO, an energetic plasticizer, 1.04 wt% PCL 240, 0.58 wt% PVF 5/95, and 0.30 wt% Desmodur N-100 binder. The formulated material, with consistency like putty, is loaded into a deaerator mixer-loader to eliminate entrapped air and solvent. The loader portion is equipped with an extrusion

flange that can adapt to a variety of loading configurations. After deaeration, the formulation is extruded under vacuum into a break-apart mold, yielding cylindrical strands 6 mm in diameter and 4 cm in length at 100 percent TMD (1.804 g/cc).<sup>11</sup>

The RX-35-AP is a cast cured formulation consisting of 60 wt% HMX and 40 wt% NG/TA/PEG binder-plasticizer. The particle size of the HMX is a mono-modal screen-cut between 150-175  $\mu\text{m}$ . The formulated material is deaerated and cast into the break apart mold under vacuum. Upon curing, we obtain a rubbery strand with an approximately circular cross-section at 100 percent TMD.

### Hybrid Closed Bomb-Strand Burner

Since we are after the mass regression rate,  $dm/dt$  in Equation (1), and we measure the regression rate  $r$ , the experimental design should minimize uncertainties in  $A$  and  $\rho$ . The ideal sample and diagnostic configuration permits a continuous measurement of a burning surface with a well-defined area. At these burning rates, high speed photography of a cylindrical strand seems the best choice. Measurements by Boggs, et al.,<sup>12</sup> using a window bomb show that burning rates deduced from the closed bomb calculations, based on "infinitely fast" kinetics, are wrong. Interpretation of the results from high speed photography of burning strands of porous materials, demonstrates that workers must take care to distinguish between the surface regression rate of a material and the intrinsic burning rate of its components. Experiments by Boggs, et al.,<sup>6</sup> on pressed HMX strands did not show the "simple deconsolidation" seen in similar work by Fifer and Cole.<sup>7</sup> While optical pressure cells that can sustain 1-2 GPa are possible to build, one with an optical access to a strand 4 to 5 cm long presents a unique design problem.

At high pressures, both the closed bomb and strand burner methods of measuring the regression rate have significant disadvantages. The strand burner provides a direct measurement of the regression rate, within assumptions about the burning surface to volume relation and the value of the sample density at pressure, but must be carried out isobarically. This means that in a typical

experiment, you get only one data point on the  $P$  vs  $r$  curve and that the buffering volume used to minimize the pressure rise owing to the product gases must be very large. For extreme pressures, both the cost and the hazard of such a large volume are prohibitive.

The closed bomb method is used widely as a quantitative diagnostic and, within fairly serious assumptions, to calculate burning rate law coefficients. The method is attractive because the pressure vessel is small, and a large pressure range is available during a single experiment by adjusting the starting pressure and the loading density. However, there are no direct measurements of the surface regression rate, which must be calculated using assumptions about the shape of the burning surface and the thermochemistry.

Our approach is to make a hybrid strand burner-closed bomb experiment, in which a strand burns isochorically in a relatively small volume, causing an increase in pressure owing to the product gases, with the surface regression measured directly using strand-burner-type probes. Since the probes are located at discrete intervals along the strand, and the burning rate varies with the pressure as the flame moves between the probes, only an average burning rate between two probes can be calculated. Although there are techniques to make continuous measurements of the flame front, they either are unsuitable for extreme pressures (microwave and optical) or are too costly for production work (collapsing coils, potentiometric).

Figure 3 is an illustration of the apparatus, described in detail in Reference 10. In this work, we use a pressure vessel with a 3.05 cm diameter bore with 18 electrical feed-throughs in one sealing plug. A photograph of the sample assembly is in Figure 4. The surface of the sample is inhibited with a thin layer of 60 percent Epon 828/40 percent Ancamide 350A epoxy. The electrical feed through across the pressure seal is effected with a stainless steel ball-stem arrangement manufactured by numerical-controlled machining. Electrical insulation between the ball and the pressure vessel is accomplished with 75  $\mu\text{m}$  of mylar and 75  $\mu\text{m}$  of kapton. Thirteen of the leads are used for twelve signal

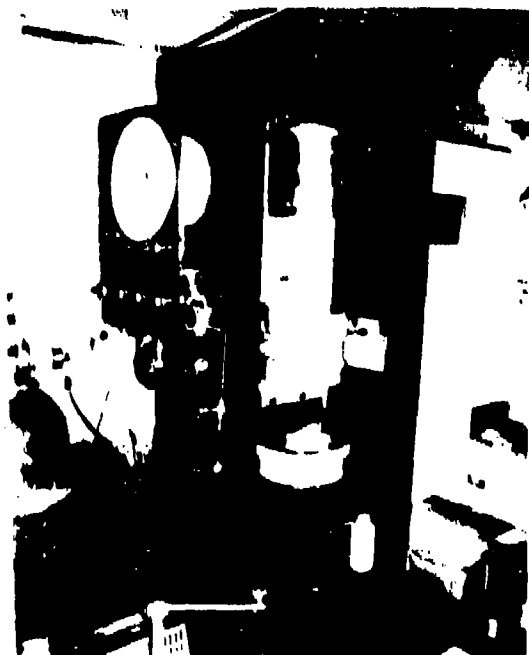


*Figure 3. Experimental Apparatus Consisting of Load Frame, 3.05 cm Diameter Bore Pressure Vessel, and Ullage Measuring Setup*

probes and one common return line. Another two leads are used to carry an ignition current across a nichrome heater of about 8 amps at 7.5 volts. All of the leads are terminated inside the vessel in a male plug that permits easy installation of the shot assembly.

The pressure generation system, shown in Figure 5, is a portable design using a chemically-clean diaphragm pump and a 1.2 GPa intensifier combination. The vessel is pressurized slowly with argon to the desired starting pressure and "frozen argon" valves are closed by immersing a length of high pressure tubing into liquid nitrogen. These valves are leak-free and are reliable to the bursting pressure of the tubing. We measure the pressure using a 1.3 MN load cell on top of the upper plug. At these burning rates (0.1-1.5 m/s), the pressure vessel-load frame is in mechanical equilibrium.

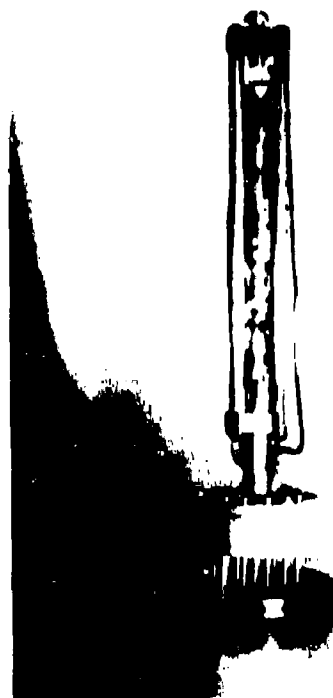


*Figure 4. Sample Assembly Exhibiting Copper Fuse Wires Embedded into an Epoxy Coated Strand of Explosive*

## EXPERIMENTAL RESULTS

Data for each shot consist of a pressure-time curve and the times at which the signal wires reported, correlated by a common trigger. We show in Figure 6 these data for a typical shot. Wires frequently would break during the initial pressurization or during the pressure rise on burning. Since the diameter of a wire is about half the diameter of the mean size of the largest particle fraction, we believe the breakage is a result of the relative motion of the nitramine particles as they move in the plastic binder. Nevertheless, there were adequate distance-time data in each shot not only to calculate burning rates, but to detect significant excursions from uniform burning down the length of the sample.

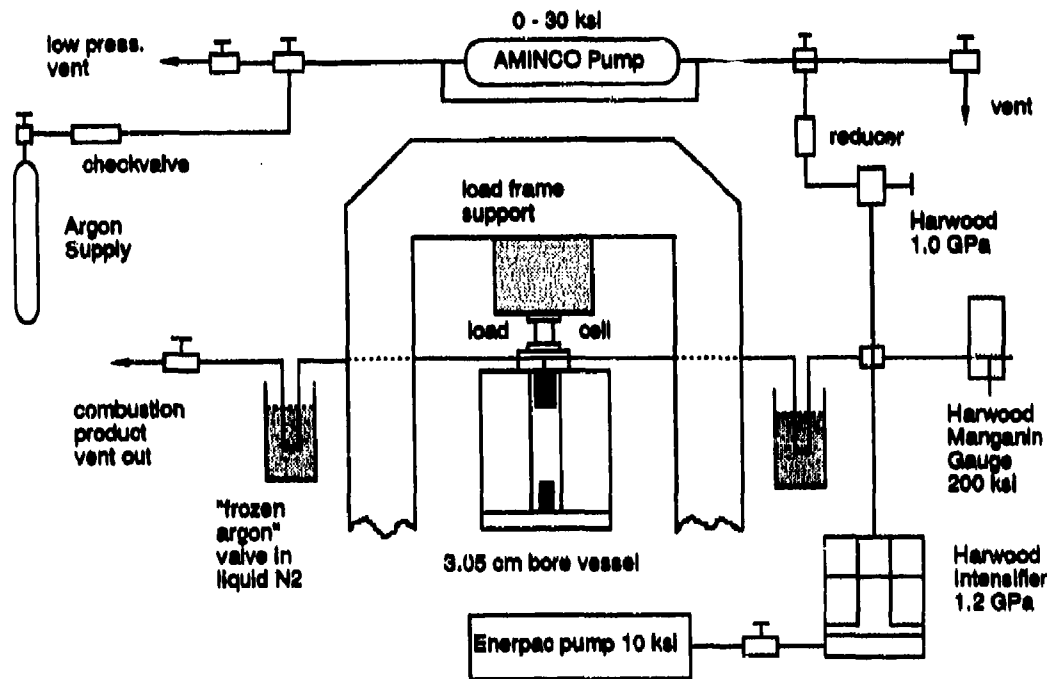


Figure 5. Portable 1.2 GPa Pressure Generation System. Note the Use of "Frozen Argon" Valves.

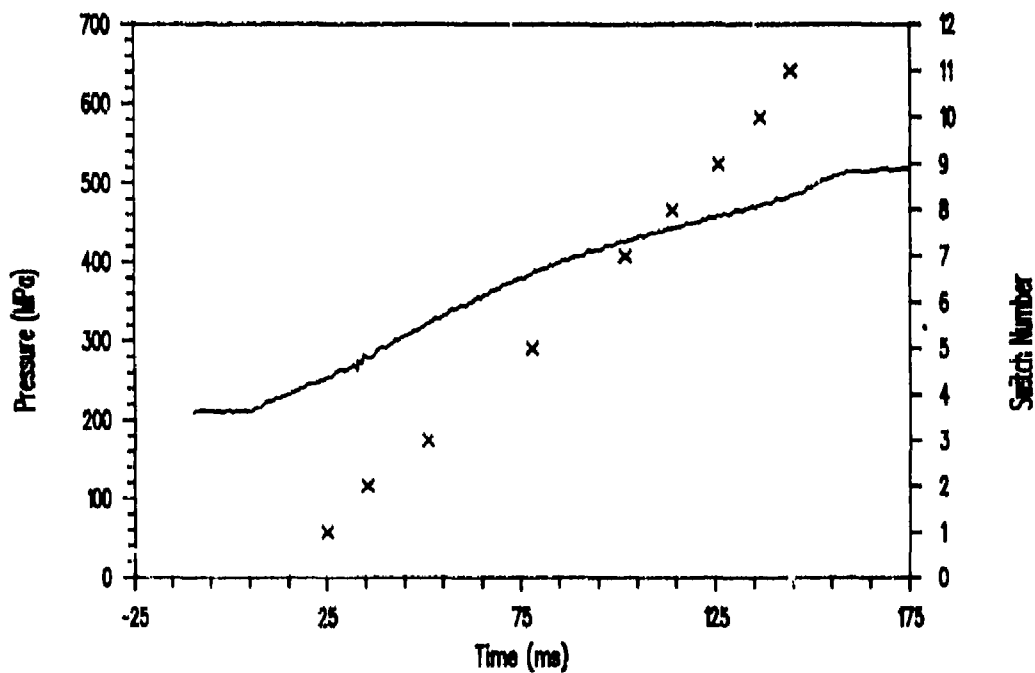


Figure 6. Synchronization Between Pressure and Time of Switch Reporting for a Typical Shot

Pressure-time curves for three RX-08-EL and one RX-35-AP shot fired at a starting pressure of 200 MPa are shown in Figure 7. We consider the curves for shot #85 and #86 to be "normal," based on the present data for RX-08-EL and previous work with RX-08-FO, another extrusion-cast explosive.<sup>10</sup> Shot #88 shows an abnormal pressure-time curve which can result from an increase in the macroscopic area,  $A$  in Equation (1), that is burning. This may happen when the inhibitor fails and the sides of the sample ahead of the planar burning front ignite, or when the sample breaks into large pieces. However, the wire reporting data for this shot indicated that the burning front moved uniformly along the length of the sample, and that the increase in pressure owed to an increase in the surface regression rate ( $r$  in Equation (1)).

Pressure-time curves for four RX-08-EL and one RX-35-AP shot fired at a 400 MPa

starting pressure are shown in Figure 8. Samples for shot #87 were cycled once between 400 MPa and 0.1 MPa before firing at 400 MPa. The pressure-time traces and burning speeds are significantly different than for shots #89 and #90, which were pressurized to 400 MPa and fired. After cycling, the sample surface had a blistered texture, with some areas showing "extruded" globules of explosive. Otherwise, the sample remained intact, without significant change in shape, fracturing, or deconsolidation. For both RX-08-EL and RX-35-AP, all of the pressure vs. time curves are quite smooth, indicative of a classical planar burning mechanism, with no deconsolidation or irregular ignition of macroscopic surfaces.

We fitted the entire P-t curve with a fourth order polynomial and used the fitted form to calculate  $dP/dt$  and to find the pressures at the times the switches reported.

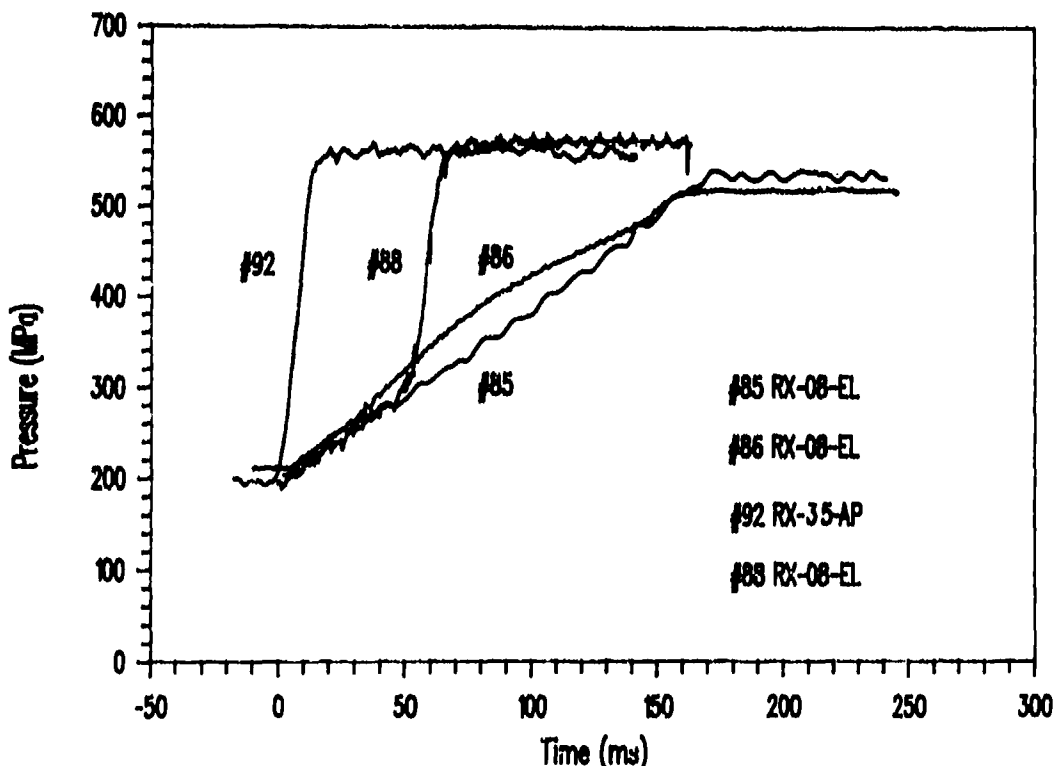


Figure 7. Pressure-Time Curves for RX-08-EL and RX-35-AP Fired at 200 MPa Starting Pressure

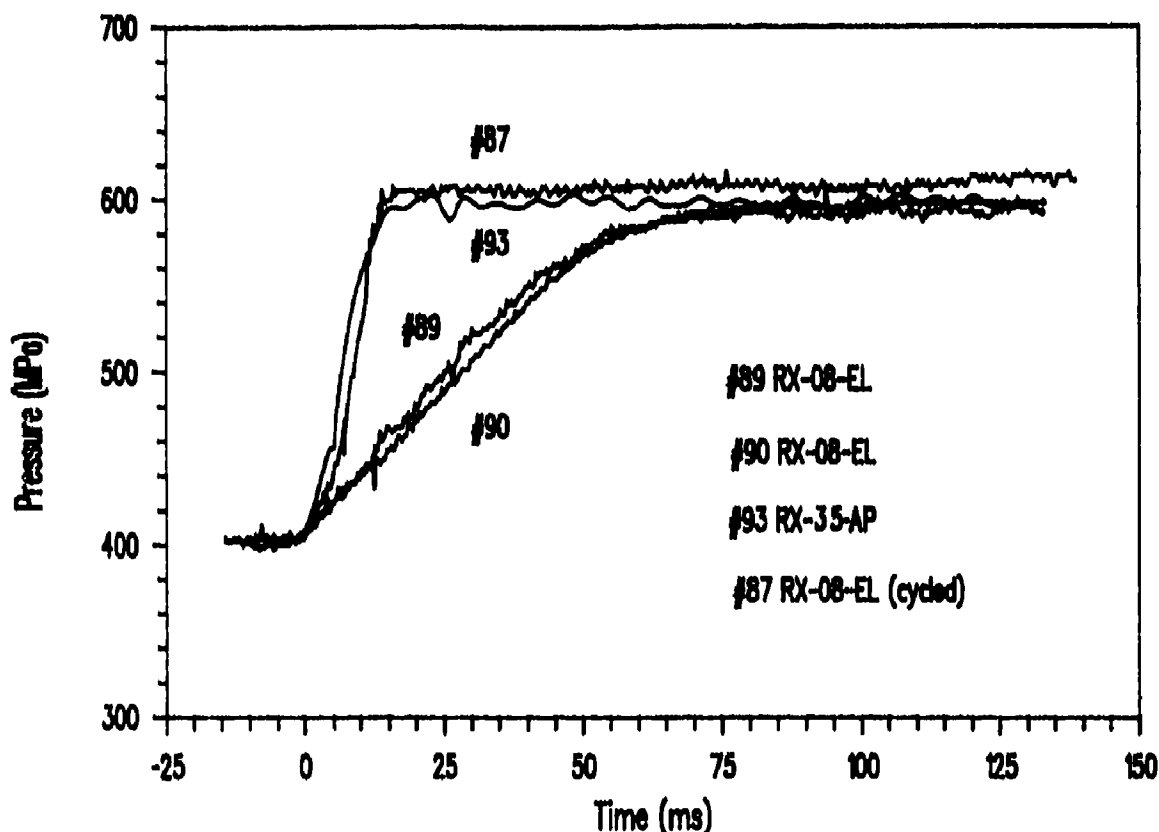


Figure 8. Pressure-Time Curves for RX-08-EL and RX-35-AP Fired at 400 MPa Starting Pressure

We then find the average surface regression rate between two switches using

$$r = (x_n - x_{n-1}) / (t_n - t_{n-1}),$$

where  $x_n$  is the distance of the  $n$ th switch from the ignition surface and  $t_n$  is the time the  $n$ th switch reported, at the average pressure  $(P(t_n) + P(t_{n-1})) / 2$ . Note that we do not correct for the change in density owing to the hydrostatic compression. This introduces an error of about 5 percent in the calculated speeds.<sup>13</sup>

## DISCUSSION

Over the past several years there have been attempts to measure burning rates of HMX and fast burning propellants. Fifer and Cole concluded that HMX strands of both small (<44 micron) and large (300 micron) particles having densities from 60 percent to 99 percent TMD do not burn with a uniform, planar flame.

Instead, they propose a "deconsolidation" mechanism, in which hot gases flow through the porosity ahead of the apparent flame front, loosening, heating, and igniting the HMX particles. These particles then become entrained in the flame and continue to burn. This means that the assumption of a uniform, plane flame, which separates the condensed and product phases, required in the strand burner does not hold, and the method can be used to measure only a surface regression rate and not the intrinsic burning rate. On the other hand, Boggs et al., using HMX compacts pressed to 99 percent TMD, showed a smooth burn, with no transition to a very fast burning rate.

### Intrinsic and Surface Regression Rates

According to Equation (1), the rate at which the condensed energetic phase is converted to gaseous products is a function of the

density of the condensed phase, the area of burning surface, and the surface regression rate. Although the density is important if the accuracy in  $dm/dt$  is to be better than 5 or 10 percent, we will ignore its variation with pressure in our discussion. The more difficult issue in interpretation of closed bomb, strand, or hybrid experiments is knowing what surface is burning. The simple assumption, that the thickness of the zone containing both unreacted condensed phase and products is small compared to the spatial resolution of the diagnostic used to detect the motion of the burning front, does not apply in most cases. An additional complication arises when, in experiments such as ours, the condensed phase is a mixture of nitramine component having a particular particle size distribution and a binder. In these situations, the product mass generation rate,  $dm/dt$ , requires not only a measurement of the surface regression rate,  $r$ , but also a knowledge of the particle morphology, size, and intrinsic burning rate.

For multi-component explosives, it is easy to see that the surface regression rate depends in detail on the connectivity and intrinsic burning rates of the components. For example, the surface regression rate of a formulation with a low loading density of nitramine in a binder having a low intrinsic burning rate will be close to the intrinsic burning rate of the binder. On the other hand, that for a formulation having a loading density of nitramine high enough so that the nitramine particle network is connected will have a surface regression rate nearer to the intrinsic nitramine rate, as the flame is propagated from particle to particle. Similarly, the component with the slower burning rate will continue to burn after the flame front passes. Our work in the cast and extrusion cast explosives is designed first to permit correct interpretation of surface regression rate measurements, then to use these data to predict the mass generation rate for proposed formulations.

The formulations used in this work differ in two important respects. The RX-08-EL uses a bi-modal HMX particle size distribution designed to provide high nitramine packing densities and an energetic binder that is both compliant and tough. The RX-35-AP

formulation has a monomodal HMX distribution, resulting in a somewhat lower packing density, and a binder that contains inert material (PEG). While we can estimate the intrinsic burning rate of the HMX using the data of Boggs, et al.,<sup>6</sup> we do not know the burning rates of the two binders. Following the arguments above, we might expect that the RX-08-EL would burn close to the rate of HMX, while the -AP formulation would burn faster or slower, depending on the intrinsic burning rate of the binder.

At elevated pressures, the response of the unburned explosive to the pressure may become important, owing to fracture of the HMX grains embedded in the compliant binder. As the pressure increases, the volume of the highly compressible binder decreases, permitting the relatively stiff nitramine particles to contact each other. At some point, the nitramine network carries a significant fraction of the applied load, and the particle-particle stresses are in excess of the failure surface, resulting in shear fracture. Thus, the original particle size distribution changes to one having a larger surface to volume ratio. We might expect, therefore, to see an increase in the surface regression speed in this pressure region. This effect can be enhanced by using a monomodal distribution, so that there is a minimum number of particle-particle contacts, as in the -AP formulation, and can be mitigated by using a multi-modal particle size distribution designed to fill the interstices, such as in the -EL formulation. Application of a non-monotonic external stress, as might occur in a shock-rarefaction or a subsonic "ringing," in which the condensed mixture is loaded and unloaded also changes the as-formulated particle size distribution and their relative orientation. In the latter case, porosity may be introduced as the particles separate from the binder as they translate and rotate in response to the applied stress.

#### Surface Regression Rates for RX-08-EL and RX-35-AP

Comparison of the pressure-time and wire reporting-time curves, indicates that there is no significant entrainment of still-burning condensed phase in the region behind the flame front. Extrapolation of the switch

number-time data in Figure 6, for example, to 0 and to 12 (the top and bottom of the sample, respectively) intersects the time axis at the point of first pressure rise and constant pressure at the end of the burn. Additionally, the slopes of the pressure-time curves are almost constant at the end of the burn. This means that the slope of the switch-time curve is an "intrinsic" regression rate for the nitramine-binder mixture. Further, as seen in Figures 9 and 10, the burning rate - pressure data can be fitted adequately with a power law of the form  $r = aP^n$ . Table 1 presents a summary of the fitting constants for RX-08-EL and RX-35-AP over the range 200 to 600 MPa.

Table 1. Summary of Fitting Constants for RX-08-EL and RX-35-AP

Cast Formulations	a	n
RX-08-EL (normal)	$3.13 (10^{-3})$	0.91
RX-08-EL (cycled)	$1.47 (10^{-6})$	2.35
RX-35-AP	$1.10 (10^{-1})$	0.61

The burning rate above 200 MPa for the RX-35-AP is significantly higher than for the -EL. In view of the arguments above, we might conclude that the intrinsic burning rate of the binder for -AP is greater than for the binder in the -EL, since the surface-to-volume ratio of the particle size distribution in the -EL is higher than that for the -AP and the area term in Equation (1) dominates. However, we made one shot for the -AP at a confining pressure of only 5 MPa. The measured burning rate at 5 MPa is substantially less than that found by extrapolation of the power law fitted to the -AP's  $r$  vs.  $P$  data for  $P > 200$  MPa. Thus, the possibility exists that the as-formulated particle size distribution of the -AP has changed significantly upon the application of pressure. Results of scanning electron microscope particle size characterization of these formulations before and after pressurization will be given in a subsequent publication.

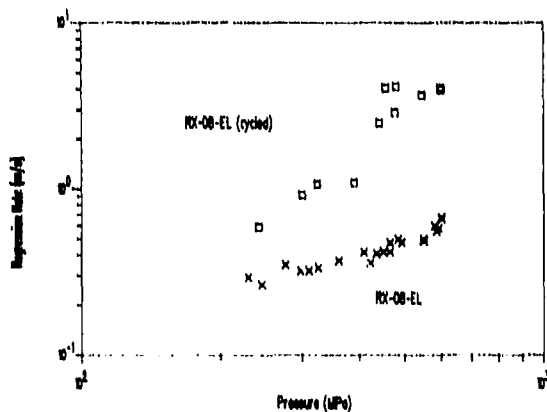


Figure 9. Burning Rate of RX-08-EL Up to 650 MPa. An increase in burning rate is observed for pressure cycled samples.

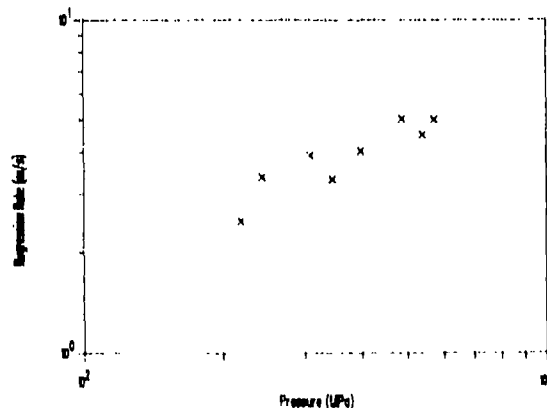


Figure 10. Burning Rate of RX-35-AP Up to 650 MPa

### The Effect of Pressure Cycling

All scenarios in which propellants or explosives are damaged prior to ignition involve stress loadings and unloadings. Sometimes the effect of the stress path results in "sensitization" of the material. The regression rate data for the RX-08-EL explosive cycled to 400 - 0.1 - 400 MPa and then ignited (shown in Figure 9), show that increases in the mass regression rate of as much as an order of magnitude can occur. Although we can suggest several mechanisms, such as (1) particle fracture and subsequent translation and rotation, resulting in debonding and creating porosity; (2) "thixotropic" separation of the binder and nitramine, causing the significantly greater fracture damage to the nitramine during the next loading cycle; and (3) microscopic damage to the nitramine crystals that increase its

intrinsic burning rate, etc., that might be irresponsible for this effect; we do not have adequate data to support a particular guess.

## SUMMARY

We have measured the surface regression rates of two highly compliant explosives using a hybrid closed bomb-strand burner apparatus to pressure greater than 800 MPa. The data indicate that the surface regression rate can be directly related to the intrinsic burning rate of the nitramine-binder mixture. The burning rates obey an  $aP^n$  law over the pressure range, using a single set of parameters. Cycling the explosive to 400 MPa once before pressurizing to 400 MPa and igniting results in an increase in burning rates by as much as an order of magnitude.

This work is a continuation of an on-going program to study the form of the mass regression law of energetic materials at high pressures. We believe that this is necessary not only to provide empirical data for the functional form and the parameters for the mass regression for use in explosive performance codes, but also to understand the effect of the stress history in vulnerability and hazards scenarios. Finally, we can easily imagine using the intrinsic mechanical properties of the components of the explosive, such as their failure strength, compressibility, etc., to tailor the mixture so that it has different properties under different stress fields. For example, using a large, monomodal particle size distribution for the nitramine in the as-formulated explosive, may result in a slow-burning, relatively safe explosive under normal stresses encountered in storage and handling. However, after exposure to a stress adequate to fracture the particles, it may have a desirably high burning rate in the application environment.

We have demonstrated the use of a hybrid strand burner-closed bomb apparatus to measure the surface regression rate of energetic materials to 0.6 GPa. We expect that peak pressures in excess of 2 GPa are possible. The method combines the relative simplicity of the strand burner in obtaining regression rates, with the very high pressure capability of the closed bomb. Our intent is to measure

regression rates at pressure well beyond those found in gun and rocket propellant studies. These empirical relations are required to deal with the problem found in deflagration to detonation transition, ignition and growth of reaction owing to particle impact, and abnormal burning in the interior ballistic cycle.

## ACKNOWLEDGEMENT

The authors would like to acknowledge Mr. Jack Bullock for his support of the experimental facility, and Mr. Ted Jessop for his help in preparing the samples.

## REFERENCES

1. Kubota, N., "Survey of Rocket Propellants and Their Combustion Characteristics," *Fundamentals of Solid-Propellant Combustion*, edited by K. Kuo and M. Summerfield, American Institute of Aeronautics and Astronautics, New York, NY, Vol. 90, 1984.
2. Serso, P. and Pierce, J., "Sensitivity of Ballistic Performance to Propellant Combustion Properties," *Interior Ballistics of Guns*, edited by H. Krier and M. Summerfield, American Institute of Aeronautics and Astronautics, New York, NY, Vol. 68, 1979.
3. Kumar, M. and Kuo, K., "Flame Spreading and Overall Ignition Transient," *Fundamentals of Solid-Propellant Combustion*, edited by K. Kuo and M. Summerfield, American Institute of Aeronautics and Astronautics, New York, NY, Vol. 90, 1984.
4. Price, C. F. and Boggs, T. L., "Modeling the Deflagration to Detonation Transition in Porous Beds of Propellant," *Proceedings of the Eighth Symposium (International) on Detonation*, NSWC, Albuquerque, NM, 1985, p. 934.
5. Kim, K. and Sohn, C. H., "Modeling of Reaction Buildup Processes in Shocked Porous Explosives," *Proceedings of the Eighth Symposium (International) on Detonation*, NSWC, Albuquerque, NM, 1985, p. 926.

6. Boggs, T. L.; Price, C. F.; Atwood, A. I.; Zurn, D. E.; and Eisel, J. L., "The Combustion of HMX," *Proceedings of the 17th JANNAF Combustion Meeting*, CPIA Publication 329, Vol. II, p. 431.
7. Fifer, R. A. and Cole, J. E., "Transitions from Laminar Burning for Porous Crystalline Explosives," *Proceedings of the Seventh Symposium (International) on Detonation*, U.S. Naval Academy, Annapolis, MD, 1981, p. 164.
8. Costantino, M. and Tao, W., "Compaction of Non-Consolidated HMX Beds," *Proceedings of the JANNAF Propulsion Systems Hazards Meeting*, Marshall Space Flight Center, Huntsville, AL, 1987.
9. Tarver, C. M.; Hallquist, J. O.; and Erickson, L. M., "Modeling Short Pulse Duration Shock Initiation of Solid Explosives," *Proceedings of the Eighth Symposium (International) on Detonation*, NSWC, Albuquerque, NM, 1985, p. 951.
10. Costantino, M. and Ornellas, D., "A Hybrid Closed Bomb-Strand Burner for Very High Pressure Burning Rate Measurements," *Proceedings of the 23rd JANNAF Combustion Meeting*, CPIA Publication 329.
11. Scribner, K. J.; von Holtz, E.; and Simpson, R. L., "High-Performance, Extrusion Cast Explosives with Low Sensitivity," *UCRL - 53890 Report*, Lawrence Livermore National Lab, Livermore, CA, 1989.
12. Boggs, T. L.; Price, C. F.; Zurn, D. E.; Derr, R. L.; and Dibble, E. J., "The Self-Deflagration of HMX," *13th Propulsion Conference*, AIAA Paper 77-859, 1977.
13. Costantino, M.; Tao, W.; Ornellas, D.; and Clements, R., "Compression of Two Extrusion-Cast Explosives to 500 MPa," *UCRL - 53827 Report*, Lawrence Livermore National Lab, Livermore, CA, 1987.

# EXPLOSIVENESS AND SHOCK-INDUCED DEFLAGRATION STUDIES OF LARGE CONFINED EXPLOSIVE CHARGES\*

P. J. Hubbard and R. Tomlinson  
Royal Armament Research and Development Establishment  
Ministry of Defence, PE, Fort Halstead  
Nr Sevenoaks, Kent, UNITED KINGDOM, TN14 7BP

*The effect of confinement has been examined on the violence of deflagrative events in a range of ordnance from 105 mm shells to 1,000 lb (454 kg) General Purpose (GP) bombs. Experiments have shown that the secondary explosives used as the main filling in these munitions burn without explosion or transiting to detonation if the deflagration is started at a large enough free air surface. However, explosions and detonations have been produced when initiatory explosives, intermediate explosives used as boosters, and certain age-deteriorated charges have been included in the burning process. Other experiments have demonstrated that the detonation of sheet explosive donors on the outside of shells reliably produces deflagrations in the explosive fillings. Similar donor charges applied to GP bombs sometimes produce deflagrations, but can also cause detonations. Weakening the bomb case with an explosive cutting charge before firing the donor can prevent the transition to detonation. The reproducibility of the deflagrative events and their low damage signatures suggests that these techniques may have a role in the demilitarization of ordnance.*

## INTRODUCTION

An RARDE paper presented at the Seventh Detonation Symposium<sup>1</sup> described studies on the explosiveness of explosives commonly used as munition fillings. The paper proposed that the hazard associated with a munition involved in an accident should be assessed both on the likelihood of initiation occurring (the sensitiveness of the explosive) and on the nature or violence of any event initiated (the explosiveness of the system). RARDE investigations into many different types of accidents involving munitions have demonstrated that most events not directly attributable to fuse failure have been caused by ignition of the main secondary high explosive filling. The violence of the event that ensued has been a function of the explosiveness of that system, which has been itself dependent on the deflagrative properties of the

the explosive and the level of confinement it has experienced.

A further RARDE paper presented at the Eighth Detonation Symposium<sup>2</sup> described how an initial deflagration in one munition could induce similar or more violent events in adjacent explosive filled stores. The possible extremes of consequence were failure to propagate or transfer of the deflagrative event to mass detonation.

The first paper based its conclusions on both small and large scaled model charges containing approximately 350 g and 10 kg, respectively. The second paper concentrated on deflagrations in artillery projectiles containing a maximum of 11.5 kg of explosive. This paper describes experiments on a wider range of munitions up to and including 1,000 lb (454 kg) General Purpose (GP) bombs. Deflagrative events have been purposely induced in the munitions by direct thermal

\*Copyright © Controller HMSO London 1989

means and, additionally, by explosively generated shocks.

## **INDUCED DEFLAGRATIONS BY DIRECT THERMAL MEANS**

### **Experiments on Shell and Small Rocket Warheads**

An experiment has been described previously<sup>2</sup> which used 155 mm shells filled with 11.5 kg of CW3, an analog of RDX/TNT 60/40. These shells were arranged in a row with their fuses and booster pellets removed. A small thermite charge was then introduced at the base of each fuse cavity and this was ignited remotely. All five shells experimented upon burned out completely, taking between a half to one hour. The deflagration of the explosive was non-disruptive, but did produce vigorous reactions with flames jetting from the shell noses for up to a meter. All the explosive was consumed leaving the shell bodies intact.

Subsequent experiments involving many 105 mm, 4.5 inch, and 155 mm shells filled with RDX/TNT or close analogs, have all shown identical characteristics. Provided the initial ignition site is at a free air surface, the subsequent deflagration remains as a relatively steady, non-disruptive burning.

Other experiments have been conducted with M107 155 mm shells filled with TNT. Again, the fuse and booster pellets had been removed and an electrically initiated thermite igniter was introduced into the fuse cavity. An initial burning reaction attributed to the thermite was quickly choked by black clouds of combustion products. Subsequent examination showed that little of the TNT had been consumed. It seemed that the 50 mm apertures at the nose of these 155 mm shells is insufficient to allow combustion to continue.

A further experiment was conducted on a TNT-filled rocket warhead. After some disassembly, this had a free air surface at one end, 210 mm in diameter. When a thermite charge was ignited at this point, the TNT charge burnt out completely.

Other experiments were conducted on the remains of 30 M107 155 mm TNT filled shells which had been broken open by a shock-induced

deflagration technique (qv). These still contained between 20 and 50 percent of the filling. All burnt out completely without causing an explosion.

Finally, 700 8 inch M106 shells that had been similarly opened up by a shock-induced deflagration, were burnt out completely without causing explosions.

### **Experiments with Large Rocket Warheads**

The experiments described in the previous section concerned explosive charges in the range 2.5 kg to 20 kg, generally associated with steel confinement, but all ignited at a free air surface of the explosive. A further series of experiments has been conducted against 130 kg charges of fiber-reinforced RDX/TNT 60/40 inside a light aluminum alloy casing a few millimeters thick. Initially the charges were totally confined, but without fusing or booster pellets. A circumferential charge of a lead sheathed linear cutting charge, Charge Linear Cutting (CLC), was positioned 57 mm from one end of the cylindrical charge. The CLC was stood away from the warhead by placing a 50 mm wide strip of 6.35 mm thick expanded polythene foam around the warhead between the CLC and the warhead case. This was designed to prevent shock initiation of the explosive filling.

When the cutting charge was detonated, the entire end plate of the warhead was severed. The action of the cutting jet also ignited the explosive and projected the end plate for several tens of meters. The 130 kg warheads then burnt vigorously without explosion. After 30 minutes, the reaction had consumed all the explosive and, in some cases, part of the aluminum alloy casing. The experiment was conducted more than 300 times without producing either an initial detonation on severing the end plate, or an explosion or detonation when the explosive burnt.

### **Experiments with General Purpose Bombs**

One thousand pound GP bombs in UK service contain up to 186 kg of either RDX/TNT/Aluminum or RDX/Wax/Aluminum. Access to the main explosive content of the bomb cannot be obtained through the fuse

pockets. In consequence, a technique had to be devised to remove the base plate explosively. Once the main filling was exposed, then a small electrically ignited thermitic incendiary charge was introduced into the cavity left by the expelled exploder tube.

The burning process was very vigorous and lasted between 30 and 40 minutes. Initial experiments were conducted on 15 bombs filled with Torpex 4A (RDX/TNT/Al, 20/55/25 with 3 percent Paraffin Wax and 2.5 percent Carbon Black) and 15 bombs filled with RDX/Wax/Al, (71/9/20). On no occasion did an explosion or detonation occur, although on one occasion a bomb filled with Torpex burnt slowly for five minutes then took off like a rocket. It travelled 100 meters by which time all the HE had been consumed leaving the bomb case intact. The other reactions have, however, been so vigorous that sufficient heat has sometimes been generated to melt and consume part of the steel of the bomb case. Similar experiments have now been conducted on a further 36 bombs with similar results.

## SHOCK-INDUCED DEFLAGRATIONS

### The Technique for Shells

An alternative means of promoting an explosive deflagration inside a metal confined store has been examined using externally applied explosive donor charges. These have usually been made from Sheet Explosive (SX2), a high energy plastic explosive containing 88 percent RDX and 12 percent binder. The explosive is manufactured in tightly toleranced sheets, usually 3.2 mm thick. Composite donor charges have been made by cutting discs or squares out of the sheet explosive and assembling these on top of one another until the required thickness is obtained (Figure 1).

In each experiment, the disc or square of explosive was placed in intimate contact with the metal case of the explosive filled store at a specified distance from some notable feature, e.g., the base. The explosive donor charge was detonated and the extent of the break-up of the store being attacked was noted. The diameter, thickness, and position of the explosive donor was varied until a level of explosive deflagration

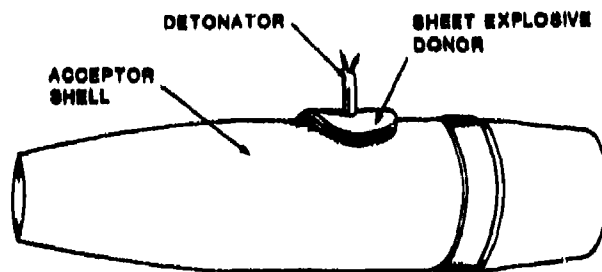


Figure 1. Experimental Arrangement to Shock-Induce Deflagrations in Shells



Figure 2. Fragmented M106 8 Inch Shells from Shock-Induced Deflagrations

occurred which shattered the store into a few major fragments (Figure 2). The damage done to the environment was slight; the explosive deflagrations produced only a few fragments which travelled tens, rather than hundreds, of meters. The explosive deflagrations did not produce a loud explosion, nor did they produce craters. In every case unreacted explosive remained after the deflagrative reaction. After the initial variation of the donor charge had served to identify a satisfactory combination of charge diameter, thickness, and position, the experiment was repeated until available explosive filled stores of that caliber had been exhausted. It was often possible to perform multiple attacks once confidence had been established in the technique. On numerous occasions shock-induced deflagration experiments were performed on up to 30 M106 8 inch shells at a time. On those occasions, the shells were aligned nose to tail in two staggered rows of 15. This configuration was chosen to minimize the chance of a single round detonating

the entire assembly of charges. Multiple initiations were arranged by coupling each individual donor/shell assembly with detonating cord. Each detonating cord termination used a booster assembly which comprised a detonator sized aluminum tube into which increments of RDX had been pressed. A low density increment was used for pick-up from the detonating cord, while two high density increments provided the output. Using these detonating cord boosters prevented a proliferation of initiators, and yet provided a discrete means of centrally initiating the sheet explosive donors.

#### Results of Shock-Induced Deflagrations Against M106 8 Inch Shell Filled TNT

The results of a typical series of firings against a previously untested caliber of projectile, the M106 8 inch shell, are shown in

Table 1. Initially, the diameter of the donor charge was held constant and the thickness of the charge was increased. These shots were performed sequentially on the same store. When this did not produce a deflagration, then the diameter of the charge was increased. After several attempts, an overly energetic reaction ensued, but still not a detonation. These energetic deflagrations consumed nearly all of the explosive filling, but projected large fragments of the casing a long way. By Firing 9 on shell number 4, a combination of diameter, thickness, and charge position had been found which produced an ideal level of disruption. This 'ideal' is a subjective level of response based upon generating sufficient free surface area of the explosive to allow a subsequent sustained deflagration, but without breaking up the shell body and scattering the explosive excessively.

*Table 1. Experimental Firings with Sheet Explosive Donors to Induce Deflagrations in M106 8 Inch Shell Filled TNT*

Firing Number	Shell Number	Donor Charge Details			Result
		Diameter (mm)	Thickness (mm)	Distance from Charge Center to Base of Shell (mm)	
1	1	63.5	3.2	304.8	No result
2	1	63.5	9.5	304.8	No result
3	1	63.5	12.7	304.8	No result
4	1	63.5	19.0	304.8	No result
5	1	95.2	9.5	406.4	Deflagration with excessive break up
6	2	95.2	9.5	406.4	Deflagration with excessive break up
7	3	95.2	3.2	355.6	No result
8	3	95.2	9.5	355.6	Deflagration, excessive break up
9	4	82.6	9.5	355.6	Deflagration, ideal break up
10 - 53	5 - 47	82.6	9.5	355.6	Deflagration, ideal break up
54 - 56	48 - 50	76.2*	9.5	355.6	Deflagration, ideal break up
57	51	82.6	12.7	355.6	Detonation

\*Square donor used.

Firings 10 to 53 used the preferred donor and produced acceptable levels of reaction. Firings 54 to 56 switched to a square donor with sides 76.2 mm by 76.2 mm and 9.5 mm thick. This was done principally to eliminate the need for special cutters in the field, but it also conserved explosive. Very similar results were obtained to those with the disc charges. Finally, Firing 57 was conducted to establish the charge size to cause detonation.

In subsequent days, a total of 700 M106 8 inch shells were disposed of using the shock-induced deflagration technique. There were five occasions when shells did not produce significant reactions on first application. These all produced adequate disruptive deflagrations on the second shot using an identical donor charge.

Once a batch of shells had been opened up using this technique, the carcasses were collected and loosely assembled into a heap containing 20 to 30 projectiles. These were then doused with kerosene and ignited remotely (qv earlier). It must be stressed that all such final clearances were conducted against unfused projectiles without boosters. The presence of even one initiator or booster element could cause mass detonation of the whole stack.

### Results of Shock-Induced Deflagrations Against Other Projectiles

The success of the shock-induced deflagration technique against M106 8 inch shell filled TNT prompted further experimentation against other projectiles. Four calibers of artillery shells, one naval shell, and two calibers of tank ammunition were available.

Each caliber was attacked with a sheet explosive donor. The position of the donor relative to the base of the projectile is shown in Figure 3.

The results against all calibers are shown in Table 2.

### Shock-Induced Deflagrations Produced in General Purpose Bombs

The previously described experiments demonstrated that satisfactory disruptive deflagrations could be caused in most calibers

of shell by detonating carefully controlled donor charges on the surface of the ordnance to be attacked. There was, however, a mixed response when this technique was applied to 1,000 lb (454 kg) GP bombs. Some bombs deflagrated, shattering the case into large fragments and leaving large quantities of unreacted explosive. However, some apparently detonated, producing craters and leaving no residual explosive. Varying the donor alone failed to achieve a level of shock input and subsequent deflagration that resulted in disruption of the case in a satisfactory manner.

A variation on the shock-induced technique was introduced to improve the chances of inducing deflagrations only. This involved the sequential firing of two explosive charges. The first explosive charge was used to cut a groove in the casing of the bomb. The shape of a rectangle was used in one method and a circle in another. A second charge was then placed within the perimeter of this weakened panel as a donor. When this was detonated, a deflagration was induced in the main explosive filling which generally vented by blowing out the pre-weakened section of the casing. Once access to the explosive filling had been obtained using this method, it could be burnt out as described in an earlier paragraph.

### Description of the Explosive Charges to Produce the Weakened Panels

The section of the bomb case was weakened by cutting a groove in the steel case in the shape of a rectangle 609 mm by 330 mm in one case or a circle 330 mm in diameter in the other. The groove was produced by detonating a length of boosted 80 g/meter CLC, shaped into the required configuration. Effectively, the first method used two meters of CLC and

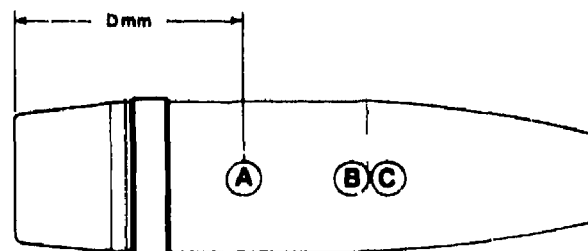


Figure 3. Position of Donor Charge

Table 2. Sizes and Positions of Donor Charges to Cause Shock-Induced Deflagration in Shells

Firing No.	Target	HE Filling	Shell Wall Thickness (mm)	Donor Size (mm)		Donor Position		Result/Comments
				Diameter	Thickness	A, B, or C	DMM	
1	76 mm	RDX/WAX	6	44.45	6.35	A	152.4	Detonation
2 - 30	76 mm	RDX/WAX	6	44.45	3.175	A	152.4	All deflagrations, ideal break-up
31 - 72	120 mm	RDX/WAX	7.5	50.8	6.35	A	254	All deflagrations, ideal break-up
73	105 mm	RDX/TNT 1A	11.5	57.15	6.35	A	228.6	Deflagrations, ideal break-up, 90 percent HE consumed
74 - 76	105 mm	RDX/TNT 1A	11.5	57.15	6.35	A	228.6	Deflagrations giving slightly more reaction than required
77 - 80	105 mm	RDX/TNT 1A	11.5	50.8	6.35	A	228.6	Deflagrations, ideal break-up, 90 percent HE consumed
81 - 88	155 mm	CW3	9	50.8	6.35	B	228.6	Deflagrations, ideal break-up
89	175 mm	RDX/TNT	-	63.5	6.35	A	558.8	Detonation
90	6"	RDX/TNT	25.5	57.15	6.35	B	381	Dent, no reaction
91	Previous	RDX/TNT	25.5	82.55	9.52	A	381	Detonation
92	6"	RDX/TNT	17.5	76.20	6.35	C	463.5	Dent, no reaction
93	Previous 6"	RDX/TNT	17.5	76.20	9.52	C	463.5	Deflagrations, ideal break-up
94	6"	RDX/TNT	25.5	76.20	9.52	B	381	Detonation
95	6"	RDX/TNT	25.5	76.20	6.35	B	381	Dent, no reaction
96	Previous 6"	RDX/TNT	25.5	63.50	9.52	B	381	Detonation
97 - 100	6"	RDX/TNT	25.5	63.50	9.52	B	381	Deflagration

the second, one meter. In each case, the cutting performance of the CLC was boosted by overlaying it with two 3.2 mm layers of sheet explosive. A layer of 6.3 mm expanded polythene foam was positioned between the cutting charge and the bomb case to reduce the transmission of shock into the bomb. Each charge was initiated by a single powerful detonator at the one point on its circumference.

### The Explosive Donor Charge to Produce Deflagration

A disc of sheet explosive (SX2) 9.5 mm thick and 117 mm in diameter was used to produce a deflagration in the filling of the bomb. In the case of the rectangular panel, the donor disc was placed inside the circumscribed area adjacent to one of the rear corners, with its center 89 mm from the two perpendicular grooves. With the circular weakened panel, the donor disc was placed with its center 89 mm from the circular groove. The SX2 donor charges were centrally initiated using standard demolition detonators.

### Types of General Purpose Bomb Used in These Experiments

Three types of GP bombs were used in these experiments. Their principal characteristics are shown in Table 3.

### Results of Firings

The SX2 boosted 80 g/meter CLC charges cut a groove into the bomb cases which varied in depth between 9.5 mm and 12.7 mm. The casing was intentionally never totally

penetrated. There were no explosive events generated in the bombs by this stage of the experiment.

The results of detonating the donor charges against the weakened panels and the subsequent disposals are shown in Table 4.

## DISCUSSION

### Experiments on Shell and Small Rocket Warheads

Previous studies<sup>1</sup> have shown that the violence of an event in a confined explosive store is dependent on both the innate deflagrative properties of the explosive composition and on the level of confinement that it experiences. The studies also showed that the deflagrative properties of the explosive compositions commonly used as munition fillings are far more influenced by their physical than their chemical characteristics. Frangible explosives, such as RDX/TNT and TNT, deflagrate

Table 3. Characteristics of 1,000 lb GP Bombs

Case Material	HE Filling	Weight of HE (kg)
Forged steel	TORPEX 4A or B RDX/TNT/Aluminum 20/55/25	186
Cast steel	TORPEX 4A or B RDX/TNT/Aluminum 20/55/25	186
Forged steel	RDX/Wax/Aluminum 71/9/20	185

Table 4. Experimental Firings With Sheet Explosive Donors to Induce Deflagrations in 1,000 lb (454 Kg) GP Bombs

Type of GP Bomb	2 m or 1 m Weakened Panel	Panel Separated/ Filling Burnt Out Non-Disruptively	Disruptive Event/ Subsequent Ignition	Detonation
MK 11 (TorpeX 4A)	2 m	10	0	0
MK 13 (RDX/Wax/Al)	2 m	0	1	0
MK 12 (TorpeX 4A)	1 m	12	3	2

more violently than some plastic bonded and waxed explosives, even though the detonative performance of the latter is greater. RDX/TNT 60/40 exhibits high levels of explosiveness in the RARDE Burning Tube test.<sup>1</sup> Nearly all the explosive is consumed in a violent deflagration that shatters the metal confining tube into 20 or more fragments. Velocities of the order of 1,400 meters/second have been measured in RDX/TNT charges over a 500 mm run. Further, it has been observed that a confined charge of RDX/TNT heated over a miniature fuel fire produces a more violent event generally than a deflagration induced in the material at ambient.<sup>1</sup>

The experiments described earlier with 155 mm shells ignited at the base of an empty fuse cavity showed no violent events. Each shell burned from the point of ignition near its nose until the whole 11.5 kg charge had been consumed. Examination of the shell cases after the event showed that they had been subjected to intense heat. The external paint had been blistered and burnt away. The burning surface of the explosive may have progressed down the charge completely linearly or perhaps, more likely, in a manner dependent on internal features of the charge, such as cracks or other weaknesses, such as the metal/explosive interface. Whichever way it progressed, it would seem likely that a considerable portion of the unreacted explosive would have been heated in the 30 minutes or so of burning time. However, this preconditioning did not seem to influence the burning rate significantly. The explosive burned with vigor, but the deflagration rate did not suddenly increase or decrease; neither did it transit from deflagration to detonation. This would seem to be further evidence for an observation made previously,<sup>1</sup> that there is a lower limit to confinement below which most secondary explosives or propellants will not sustain burning processes with significant damage potential.

The experiments with M107 155 mm shells filled with TNT indicate that chemistry cannot totally be disregarded when dealing with deflagrations. The poor oxygen balance of TNT results in the production of significant quantities of carbon when it burns. It would

seem that TNT chokes itself by producing an imbalance between solid and gaseous products of combustion when it is required to burn with a restricted free air surface. This imbalance is overcome once sufficient free air surface has been restored. At the moment it is only possible to speculate that the minimum diameter orifice to sustain a steady deflagration lies between 50 and 210 mm.

### Experiments With Large Rocket Warheads

The 130 kg rocket warheads were cylindrical, 744 mm long and 400 mm in diameter. The warheads were only lightly confined by a few millimeters of aluminum alloy. However, they were filled with RDX/TNT 60/40 which had glass fiber added to it to increase its structural strength. This effectively afforded the warhead considerable self confinement for any deflagration induced. Despite this, the events produced by firing the circumferential cutting charge were all steady, non-disruptive deflagrations. The use of the linear cutting charges to ignite the charge as well as removing the confinement is an elegant experimental variation. It would seem that matching the cutting capability of the charge to penetrate the case with very little residual overrun produces a reproducible means of igniting explosives that are particularly sensitive to impact. In more recent experiments, it has been shown that more modern and reproducible cutting charges, such as Explosive Cutting Tape,\* can be used to open even RDX/TNT filled charges without inducing ignitions.

The experiments with the rocket warheads again show that reduced confinement and a large free surface area can keep deflagrative events below the damaging level. Certainly, if there was going to be any risk of producing transitions from steady deflagrations across to explosive deflagrations or detonations, it was much more likely to occur with RDX/TNT 60/40 than many other munition fillings because of its demonstrated tendency to exhibit high levels of explosiveness.

---

\*Explosive Cutting Tape is manufactured by Royal Ordnance and North American Explosives.

### Experiments With General Purpose Bombs

The 1,000 lb GP bombs represent almost an extreme case of charge size and level of confinement that is likely to be encountered when dealing with accidental events in munitions. UK 1,000 lb bombs are generally filled with a variant of Torpex 4 (RDX/TNT/Al 20/55/25) or with RDX/Wax/Aluminum (71/9/20). From the percentage of RDX present, it might be assumed that RDX/Wax/Al would produce more violent deflagrative events than Torpex 4 derivatives. This is not the case, as RDX/Wax/Al exhibits considerably lower levels of explosiveness than Torpex 4.<sup>1</sup> Once again, however, these experiments illustrate that differences in explosiveness levels observed in totally confined systems are swamped by the overriding effects of low confinement when a significant free air surface is available. Any ignition at that free air surface progresses slowly driven probably more by the temperature generated by the exothermic reaction than by the generation of product gases. Those product gases are free to vent to the atmosphere and so do not act to pressurize the reaction front. Without that pressurization, there is no driving force other than temperature for the reaction rate to increase. Thermal losses serve to keep the reaction at a near steady state. The one bomb that went propulsive presumably did so through a buildup of solid Aluminum Oxide combustion product providing temporary confinement.

It must be stressed that, except for the exceptions dealt with later, there has only been that one occasion in our experiments, which now run into thousands, where ignitions at free air surfaces have lead to anything other than steady state deflagrations and on no occasions have they progressed to explosions or detonations. Nonetheless, all such ignition/deflagrations are performed remotely with observing personnel at a safe distance. The reasons for this, other than common prudence, are illustrated by two other incidents.

On the first occasion, considerable loose residual explosive had been collected after a series of experiments which had disrupted bomb cases. The explosive was arranged in normal burning ground manner so that it formed a continuous layer a few tens of millimeters thick. By mistake, booster elements consisting

of large tetryl pellets were included within the pile of explosive for disposal. The site was evacuated, personnel put under cover, and the explosive was ignited. After about five minutes, there was a detonation. Subsequent examination of the site showed that a significant proportion of the explosive had detonated. This may be because the tetryl pellets exceeded the critical length necessary to produce detonations when they are heated.<sup>1,3</sup> Once the heavy booster elements had detonated, then the explosive residue followed.

A further incident involved 140 kg Minol charges in Depth Charges. These were approximately 40 years old at the time of disposal. Many of the Minol charges burnt away in the manner of the rocket warheads described earlier. However, a significant proportion gave explosive deflagrations or detonations after a few minutes. Careful inspection before igniting the charges had made sure that there were no booster or initiatory elements present. It is known that the ammonium nitrate in Minol can evolve ammonia in the presence of moisture and that the presence of aluminum enhances that evolution. Ammonia reacts with TNT to give substances which are particularly sensitive to heat. It is, therefore, suggested that the unexpected explosive deflagrations and detonations that occurred in the Minol filled Depth Charges were caused by the formation of unstable compounds of ammonia and TNT formed over the 40 year life of these munitions.

### Shock-Induced Deflagrations on Shells

The promotion of "low order" explosive events using an explosive donor on the outside of a metal confined store was reported at the Fourth Detonation Symposium by Griffiths and Broom.<sup>4</sup> Their experiments were conducted against open ended cylinders and, finally, against GP bombs. Griffiths and Broom attempted to explain the phenomena of the "low order" reactions that they observed in terms of the reaction zone length of the compositions tested. However, the nature of the events observed in our experiments suggests to us that these "low order" events are deflagrations. Further, the violence of these events can be explained in terms of the explosiveness of the systems attacked.

The formation of deflagrations in an explosive acceptor purely from the shock from an explosive donor has been described by Tasker.<sup>5</sup> In his Low Amplitude Shock Initiation test, the explosive acceptor is unconfined, but separated from the donor charge by a PMMA barrier. Tasker has shown that there exists a definite zone of shock pressure inputs that result in deflagrations of the acceptor charge.

While the promotion of deflagration in the munitions that we have attacked may have been caused by shock alone, there is another possibility. Griffiths and Broom<sup>4</sup> noted that detonations of high energy sheet explosives on metal plates backed by air produced both plate deformation and a spall from the plate's rear surface. Examination of fragments recovered after our experiments has also shown considerable deformation of the case material and occasionally the formation of a spalled zone from the interior of the case. Howe et al.<sup>6</sup> has shown that incipient ignitions were occurring at sites within a shell filling after the shell had been impacted by a flying plate. Howe proposed that ignitions were occurring along shear planes in the relatively mechanically weak explosive which was failing in response to the deformation of the metal case. It is, therefore, suggested that mechanical deformation of the filling could also be causing ignitions.

The difference between the levels of reaction induced in these shells and those described earlier at a free air surface, can be explained by reference to the RARDE Burning Tube experiments.<sup>1</sup> In the shock-induced ignitions, the site of the initial burning reaction is totally confined. The response, therefore, is dependent on the deflagrative properties of the explosive, as well as the level of confinement that it experiences. Variations in the violence of the event observed with the shell reflect the ranking order of explosive compositions in the RARDE Burning Tube test. Higher levels of explosiveness have been observed with RDX/TNT filled shells than with TNT fillings. More violent events are produced, more of the explosive is consumed, and fragments from the event tend to be both smaller and projected further.

The use of the externally applied donor weakens the case material both by thinning and also occasionally by producing a spall from

the interior surface. It is likely that the ignition site is close to the area of weakness. Consequently, the case is inclined to fail early in the buildup of deflagration, with the result that the reduction in confinement quenches the reaction.

Insufficient experiments have been conducted on large, heavily cased shells such as the 6 inch Naval shells filled with RDX/TNT to come to any conclusive evidence. However, the indications are that the combination of confinement on these semi-armour piercing projectiles and the high levels of explosiveness exhibited by RDX/TNT combine against producing a satisfactory means of disposing of these shells using the shock-induced technique. However, the ability of RDX/TNT to burn from a small free air surface means that a non-detonative disposal technique is still possible.

Attempts have been made to predict the size of satisfactory donor charges for a "new" shell based on experiments with other projectiles. So far, this has not been successful. It seems that explosive type, case thickness, diameter of the projectile, and case material are all contributing parameters, but no simple formula has been found. However, as has been demonstrated with the example of the experiments with the M106 8 inch shells, on most occasions it has been possible to work up to a satisfactory level of deflagration within very few experiments.

#### **Shock-Induced Deflagrations in 1,000 lb (454 kg) General Purpose Bombs**

It is assumed that the sources of ignition in the bombs were very similar to the sources in the case of the shells. Therefore, by a combination of shock and mechanical deformation, ignitions are produced in the explosive. When the case has not been pre-weakened, then the ignition has both heavy confinement surrounding it and a large amount of explosive to involve in the reaction. The burning process evolves gas, which by simple kinetics, causes the burning reaction to accelerate. The increased burning rate produces more gas more rapidly, leading to further pressure rises. This cycle of increased reaction rate and pressure rise can then accelerate until either the pressure generated on the unreacted

explosive exceeds the shock initiation pressure, or the internal pressure exceeds the yield point of the bomb case. In consequence, when this sort of shock-induced event is produced in a store with an unweakened bomb case, then the heavy confinement and large explosive mass ensures that there is a possibility of a transition from deflagration to detonation.

Once the bomb case has been weakened, then the yield point of the case is reduced. High speed film of several of the events showed that the whole panel was projected from the bomb case at low velocity soon after the initiation of the donor charge. On some occasions, however, the case did not entirely disengage. This occurred most frequently with the bombs treated with the large circumscribed area. On these occasions, the deflagrative reaction induced in the filling faded so rapidly that insufficient disruptive power was generated to throw the panel clear. In none of the eleven occasions with the large circumscribed area did a violent explosion or detonation occur.

The level of reaction induced in the bombs with the small pre-weakening panel was markedly more violent. On two out of eighteen occasions, the bombs apparently detonated and in three others there was a violent deflagrative event with considerable disruption of both case and contents of the bomb. There would appear to be insufficient effect from the release of the smaller circumscribed area to prevent an excessive buildup of the deflagration. However, it does graphically illustrate the importance of the concept of explosiveness as identical stimuli produce wildly different levels of response. These experiments at the upper limit of normal munition size also show that explosive fillings behave in a similar way to their behavior in the RARDE Burning Tube test; ignitions of the explosive do not automatically transit to detonations because of scale factors. Further, confinement release mechanisms that occur naturally in munitions can be enhanced by purposely pre-weakening the case before inducing deflagrations.

## CONCLUSIONS

Recent experiments on a range of munitions, from shells to 1,000 lb GP bombs, have provided further evidence for the roles of

confinement and the innate deflagrative properties of the various explosive fillings on the level of violence of events ensuing from stimuli which produce ignitions. Experiments have been conducted on 105 mm, 4.5 inch, 155 mm shells filled with RDX/TNT and RDX/TNT analogs, such as CW3. With the fuse and booster pellet removed, the explosive main filling has been ignited by a small thermite charge placed at the base of the fuse cavity. The burning reaction so produced progresses through a steady deflagration until all the explosive contained in the shell has been consumed. The rate of burning does not increase, but remains relatively constant leaving the carcass of the shell body intact. The burning process consumed the 11.5 kg of RDX/TNT contained in the larger shells in approximately 30 to 40 minutes.

Similar caliber projectiles filled with TNT would not sustain a steady deflagration through the narrow orifice which remained once the fuse was removed.

Experiments on 130 kg charges of RDX/TNT contained within light alloy confinement have also been conducted. Linear cutting charges made from lead formed into a chevron cross-section have been used to cut through the case of the munition. The case afforded minimal confinement and was easily cut by the lead cutting charge. Having achieved penetration, the high speed residue from the explosive cutting charge caused the explosive filling to ignite. It deflagrated, but the burning process was non-disruptive and burned the explosive completely without explosion or detonation. The self-confinement afforded by the mass of explosive did not affect the level of the event. The experiment was repeated several hundred times with similar results.

Other ignition/deflagrations have been purposely induced in 1,000 lb GP bombs containing up to 186 kg of either RDX/TNT/Al or RDX/Wax/Al. These bombs were first modified by the removal of the base-plate. The explosive filling was then ignited at the free air surface using a thermite charge. The explosive again burned away vigorously without explosion or detonation, despite the heavy steel confinement.

This non-explosive deflagration of the explosive filling of munitions which have a free air surface has been observed in thousands of experiments. The few incidents of explosions or detonations reported are either ascribed to failure to remove initiatory elements or boost pellets from the munitions or from degradation products formed in old munitions, e.g., those containing ammonium nitrate, aluminum, and TNT.

Externally applied explosive donor charges have been used as an alternative means of promoting an explosive deflagration inside a metal confined store, such as a shell or bomb. Ignitions were caused in the explosive by a combination of the degraded shock and the mechanical deformation of the case material. The reproducibility of this process has been demonstrated on a wide variety of shell calibers and munition fillings ranging from 105 mm to 8 inch. Several thousand experiments have been conducted, the most spectacular of which involved the demilitarization of 700 8 inch shells filled with TNT. These were dealt with in batches of 30, the total explosive weight involved for each batch exceeding 740 kg (1,600 lbs). All produced deflagrations which consumed up to 30 to 40 percent of the explosive filling, disrupted the metal casing into a small number of large pieces, and produced only a localized effect on the surroundings. Fragment throw was reduced to tens of meters and noise kept to a minimum. The carcasses of the shells containing the residual TNT were loosely stacked together and burned. The large surface of explosive now available permitted the TNT to burn completely leaving non-contaminated metal.

The size and thickness of the explosive donor charge to induce a deflagration have been explored. Satisfactory charges have been found for most calibers between 105 mm and 8 inch, although no universal formula has been found to link satisfactorily the size of donor with the projectile to be attacked. Adjustments have to be made to accommodate changes in explosive filling type, shell wall thickness case material, and shell caliber. The use of explosive donor charges to shock-induce deflagrations in large iron bombs, e.g., 500 lb and 1,000 lb GP bombs, has been demonstrated.

However, the large mass of explosive and the heavy confinement afforded by the metal casing occasionally lead to deflagration/detonation transitions. Experiments have been conducted using flexible linear cutting charges to weaken the bomb case before using the explosive donor charges to induce the deflagration. Two sizes of weakened panel have been used, one produced by two meters of cutting charge and the other from using one meter. High speed framing camera pictures show the weakened panel failing in the early stages of the induced deflagration. The sudden pressure loss prevents the transition from deflagration to detonation. In repeated similar experiments with the large areas of weakness, no incidents of detonation have occurred. However, some incidents of detonation and violent deflagrations have occurred when only the smaller area was weakened.

Environmental pressure has made disposal of surplus ammunition by detonation extremely unpopular in the United Kingdom. While these techniques still require a safety radius to accommodate the small risk of detonation, disposal by deflagration techniques causes much less environmental impact than detonation. Blast and noise are significantly reduced, craters are avoided, and fragment radius is cut by an order of magnitude. None of the many thousands of experiments described has attracted adverse comment from members of the public. The phenomena described provide possible alternative methods for the demilitarization of explosive filled munitions, as well as throwing additional light on the deflagrative behavior of cased explosive charges.

## ACKNOWLEDGEMENTS

We gratefully acknowledge the guidance and practical assistance of Mr. S. T. Spooner and all the contributors, both Service and civilian, who have made the testing described here possible.

## REFERENCES

1. Dyer, A. S.; Hubbard, P. J.; Lee, P. R.; and Tisley, D. G., "Factors Affecting the Explosiveness of Munition Fillings," *Seventh Symposium (International) on Detonation*, Annapolis, MD, 1981.

2. Dyer, A. S.; Haskins, P. J.; Hubbard, P. J.; and Hutchinson, C. D., "The Growth and Decay of Explosive Deflagrations in Munitions in Simulated Factory Accident Scenarios," *Eighth Symposium (International) on Detonation*, Albuquerque, NM, 1985.
3. Hutchinson, C. D., "Experimental Studies Concerning the Response of Intermediate Explosives to Thermal Stimuli," *Eighth Symposium (International) on Detonation*, Albuquerque, NM, 1985.
4. Griffiths, N. and Broom, V. C., "Low Order Reactions in Shocked Explosives," *Fourth Symposium (International) on Detonation*, Washington, 1965.
5. Tasker, D. B., "Shock Initiation and Subsequent Growth of Reaction in Explosives and Propellants: The Low Amplitude Shock Initiation Test, LASI," *Seventh Symposium (International) on Detonation*, Annapolis, MD, 1981.
6. Howe, P. M.; Gibbons, G.; and Webber, P. E., "An Experimental Investigation of the Role of Shear in Initiation of Detonation by Impact," *Eighth Symposium (International) on Detonation*, Albuquerque, NM, 1985.

# INITIATION AND DETONATION MEASUREMENTS ON LIQUID NITRIC OXIDE

Garry L. Schott, William C. Davis, and William C. Chiles  
Los Alamos National Laboratory  
Los Alamos, New Mexico 87545

*Measurements are reported on detonations of homogeneous liquid nitric oxide initially at  $T = 119$  K,  $\rho_0 = 1.28$  g/cm<sup>3</sup>. Plane-shock initiation in mirror-covered wedges demonstrated detonation in preshocked material (superdetonation) that overtook the smooth input shock. Its transverse irregularities continued in the unsupported detonation. The input shock ran ca. 3 mm at  $U_1 = 3.8 \pm 0.2$  km/s. Behind it the fluid had  $u_p = 0.89 \pm 0.02$  km/s,  $p = 4.3 \pm 0.3$  GPa,  $\rho = 1.67 \pm 0.03$  g/cm<sup>3</sup>, and the superdetonation had  $D^*_{lab} \approx 6.9$  km/s. In 356-mm long graphite tubes with 25.4-mm inner diameter, measured detonation velocity is  $D = 5552 \pm 3$  m/s. Failure diameter in graphite is below 8 mm. Free-surface velocities of 1- and 2-mm aluminum plates terminating the detonation axis were near 1.5 km/s, approximately as predicted for CJ flow at  $D_{\infty} = 5564$  m/s,  $u_p = 1.34$  km/s impinging on aluminum. Electronic streak photography at  $d = 20.6$  mm in brass registered a smoothly convex detonation front with apparent brightness temperature of  $1735 \pm 40$  K as it reached an end window asynchronously.*

## INTRODUCTION

Liquid nitric oxide was studied as a prototype condensed-phase explosive in a multidisciplinary research program pursued during the 1980s at Los Alamos National Laboratory. Theoretical atomic/molecular treatments of this energetic, two-element substance and the products of its decomposition at condensed-phase density are simpler and correspondingly more mature than if carbon and/or hydrogen were included. Experiments with nitric oxide were favored by uniformly pure NO gas furnished as needed from the Laboratory's distillation facility operated for enrichment<sup>1</sup> of the stable isotopes of both O and N.

The present report assembles the dynamic measurements we completed on cryogenically liquefied nitric oxide functioning as a detonating, homogeneous high explosive. Precisely delayed initiation of detonation by a suitably weak input shock is demonstrated by a combination of orthodox wedge, impedance

mirror, and gas-gun techniques. The main results from long cylindrical charges are detonation velocity at selected diameters and on-axis acceleration of thin aluminum plates at the charge end. Finally, a single measurement by image-intensified, direct photography through a full-diameter window on a short cylinder is presented. This quantitatively demonstrates the convex shape and optical brightness of a detonation front in liquid nitric oxide. These measurements extend or supersede those we have published earlier.<sup>2,3,4</sup> The broad scope of the Laboratory's program included this work and related studies of nitric oxide, its constituent elements, and other oxidation states of nitrogen under static and transient conditions of high pressure and/or energy. Representative accounts are given in References 5-10.

The customary chemical formula of nitric oxide, NO, represents the diatomic molecular form of its gas phase under ambient conditions.

Cryogenic condensation to solid or liquid is accompanied by reversible dimerization to molecular  $N_2O_2$ . The substance melts at 109.5 K and boils at 121.4 K. In all of its states of aggregation, its energy of formation significantly exceeds that of the constituent elements,  $O_2$  and  $N_2$ , and of any of the other nitrogen oxides. We apply the name liquid nitric oxide to the homogeneous, neat explosive confined at temperatures near 119 K, and use one of the above chemical formulas when the molecular form or the gaseous state is pertinent.

## INITIATION OF DETONATION BY SHOCK

### Background

Earlier investigations<sup>2,11,12</sup> of occurrence of detonation in dense nitric oxide demonstrated its initiation in liquid or mixed phases by shocks from donor explosives or an equivalent projectile. The results were convincing that, in its susceptibility to detonation by accidental shock, condensed nitric oxide under technologically typical conditions more closely resembles nitroglycerine than it does the less sensitive liquid high explosives. However, the previously applied methods did not examine the detailed shock processes leading to detonation or subject the explosive only to plane or divergent flows. Also, each investigation was done with nitric oxide that contained different, small percentages of  $NO_2$ ,  $N_2O$ , and  $N_2$  accumulated from gradual, spontaneous decomposition of  $NO$  kept as a compressed gas.

In order to gain more precise information on initiation of detonation in liquid nitric oxide, we have aimed to control the shock geometry and the  $NO$  purity. Our preliminary experiments used plane-wave explosive systems as donors with uniform metal intermediate members to transmit and attenuate shocks at selected strength. Measurements included transit times through disk-shaped samples at a succession of depths and electro-optically intensified end-on streak photography across a diameter of a window-covered disk. An unsuccessful attempt was made to perform laser velocity interferometry at the impact surface, viewing through the liquid and window above it. The investigation was

culminated by two gas-gun shots that yielded clear streak-camera records of delayed detonation overtaking the steady input shock in wedges of homogeneous liquid explosive. The foregoing developments were reported in detail,<sup>4</sup> with emphasis on their qualitative features. Here we extend the earlier account of the wedge experiments by quantitative treatment of the wave velocities and the shocked state produced prior to the detonation.

### Wave Sequence

Figure 1 displays a record of initiation of detonation in a wedge of liquid nitric oxide. A very similar record from a second such shot and a schematic diagram of the gun target are shown in the appended posters and available elsewhere.<sup>4</sup> The shot configurations had a conventional wedge-shaped volume of explosive bounded downstream by a mirror-coated PMMA window surface inclined to the wave front. This interface was illuminated by an explosively shocked xenon lamp and photographed through the streak-camera slit. The initiating shock was introduced at the base plane of the liquid wedge by transmission from a smooth copper plate whose opposite face was struck by a matching copper impactor delivered from the gun muzzle.

Dynamic events at the mirrored interface alter its reflection at each position viewed by the slit, beginning when the first disturbance arrives. Advancing waves in the flow are recorded as continuous tracks with positive slope. Early in the record of Figure 1, where the explosive is thinnest, the input shock makes a smooth, straight track as it reaches the inclined mirror. Farther along, detonation makes a second track. The input-shock track terminates at a depth of 3 mm, and thereafter the single track is formed by detonation proceeding in original explosive. Before this transition point the detonation track appears in the sector to the left and identifies the beginning of detonation as a separate, fast wave in the compressed, moving material behind the input shock. In this domain the PMMA substrate of the mirror likewise is shocked, and the reflecting surface is reoriented to a decreased wedge angle. The separation between the waves and between

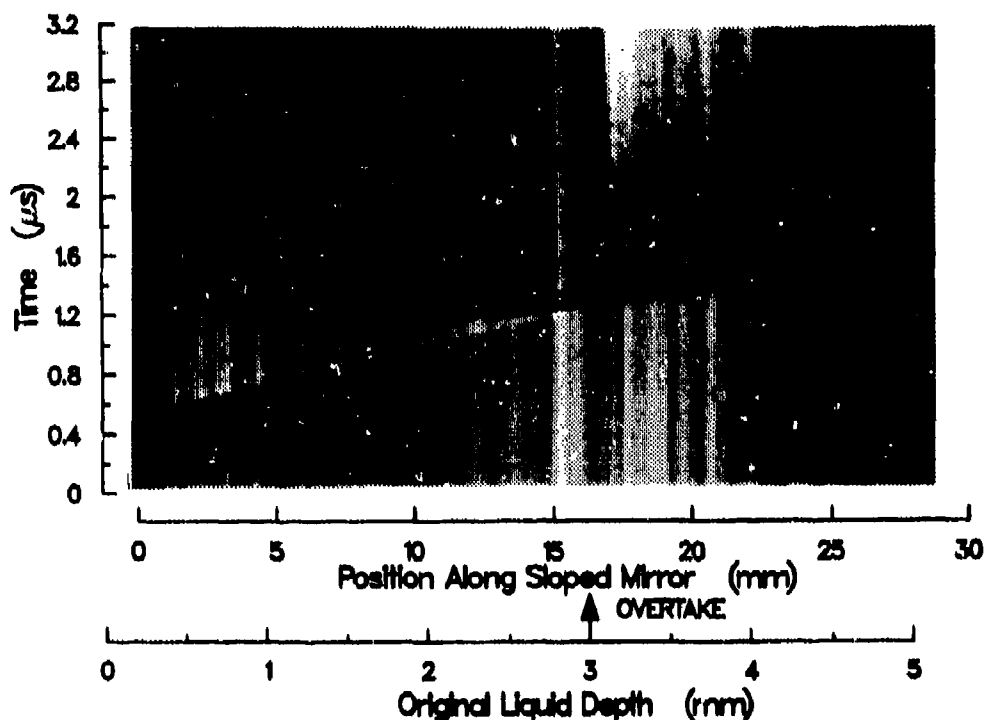


Figure 1. Annotated Streak Photograph of Delayed Initiation of Detonation in Wedge of Liquid Nitric Oxide. Time-axis origin is arbitrary; slit-axis projections/as shown.

their resulting tracks each diminishes linearly to zero when the input shock is overtaken supersonically from the rear. This event is pointed out in Figure 1.

The sequence of waves found here duplicates, at least qualitatively, the initiation mechanism witnessed repeatedly in liquid nitromethane and recognized in other homogeneous explosive media, including single crystals and doubly-shocked gases. The PMMA substrate supporting the mirrored wedge boundary has enabled our technique to record the three principal wave fronts and the transverse structure begun in the earliest detonation motion.

### Control of Conditions

The straight tracks of the frontmost waves recorded in Figure 1 determine a precise depth of overtake by their intersection and indicate sensibly constant velocities of the input shock front and later of the detonation propagating through original explosive liquid. For this

depth and these velocities to be interpreted, the strength and orientation of the input shock must be adequately uniform over the wedge section whose termination on the slant face is photographed. On the indication from Figure 1 that these criteria are met, we proceed to address the relevant material conditions.

The density of the initial nitric oxide liquid is governed by its temperature. Data from References 13-15 are represented between  $T = 110$  and  $130$  K by

$$\rho_{\text{liq}} (\text{g/cm}^3) = 1.274 + .00469(120.0 - T) \quad (1)$$

Under radiative heat load from gun components in both axial directions, the copper structure of the gas gun target attained an approximately uniform temperature after cool-down. A thermocouple in a blind well next to the explosive-filled space stably registered  $120.0 \pm 0.3$  K over times exceeding  $10^3$  s before firing each shot. The condition in the nitric oxide liquid was also measured by the

vapor pressure recorded during filling of the visible wedge volume. This indicated a somewhat lower temperature, 117.6 K. The average of these temperatures, 118.8 K, is taken to determine  $\rho = 1.28 \pm 0.005 \text{ g/cm}^3$ . Gravitational stratification is relied upon to keep nonuniformity within the horizontal wedge section less than the absolute uncertainty of the liquid density.

A test of our control of conditions that might influence the initiation of detonation was made by a duplicate experiment. The same target and impactor materials were used, and each face of the pure copper elements in the shock-forming path was diamond-tool machined to  $6 \times 10^{-6} \text{ mm}$  smoothness. The impact velocity from the gun was repeated to within 0.2 percent. The two shots used deliberately different batches of nitric oxide. Figure 1 is from the shot with the purest liquefied NO gas we could manage; absence of detectable infrared absorption through 100-mm path at 85 kPa gas pressure determined the sum of mass fractions of  $\text{N}_2\text{O}$  and  $\text{NO}_2$  to be below  $10^{-4}$ . However, the liquefied state appeared bluish and not as colorless as if the nitric oxide were ultrapure.<sup>16</sup> Because it was impractical to eliminate the triatomic constituents, we tested their possible influence upon initiation of detonation by increasing their concentrations to a total mass fraction near  $1 \times 10^{-3}$ , measured by infrared analysis. This alteration of composition was not enough to perceptibly influence the density, detonation velocity, or initial-shock Hugoniot of the liquid explosive. The increase in run to detonation that it produced, from 3.0 mm to 3.4 mm, is small enough that the apparent desensitization is of uncertain significance. The important indication is that impurities that accumulate in NO by its slow, spontaneous disproportionation do not profoundly alter the initiation of detonation of its liquid form.

### Primary Wave Velocities

In Figure 1 the arrival tracks for the input shock and the final detonation have positive slopes; their angular departures from the horizontal are respectively denoted  $\phi_I$  and  $\phi_D$ . The corresponding apparent velocities at which the respective waves in the wedge

progressed along the photographed band on the mirrored face are  $S_I = (W \cot \phi_I)/M_a$  and  $S_D = (W \cot \phi_D)/M_a$ , where  $W$  is the writing rate of the camera and  $M_a$  is the apparent magnification at which distances along the sloped object are projected through the camera slit and onto the film. These and other raw results of our two wedge experiments are assembled in Table 1.

Table 1. Liquid Nitric Oxide Wedge Parameters

Gas-Gun Shot No.	660	661
Photograph	Fig. 1	Ref. 4
Projectile Speed (km/s)	1.008	1.010
Wedge Angle, $\psi$ (rad)	0.172	0.173
$S_D$ (km/s)	35.9	33.8
$S_I$ (km/s)	24.0	22.8

To evaluate the wavefront velocities,  $U_I$  and  $D$ , from  $S_I$  and  $S_D$ , we assume as the ideal case that the waves are exactly parallel to the wedge base. We then consider that in reality there is small departure from ideal wave orientation caused by unintended tilt between the colliding surfaces of impactor and target. Coordinates are adopted with the  $x, y$  plane in the impact face of the wedge and the positive  $z$ -axis directed normally into the explosive. The axis of the photographic object band on the slant face lies in the  $x, z$  plane by definition, and has direction cosines  $(\cos \psi, 0, \sin \psi)$ , where  $\psi$  is the wedge angle. Planar waves, identified by subscript  $w$ , are oriented in this coordinate system by their unit normal vectors  $(a_w, b_w, c_w)$ . Waves that are ideally parallel to the wedge base have  $c_w = 1, a_w = b_w = 0$ , and their wave speed is simply  $U_w = S_w \sin \psi$ . For tilted waves,

$$U_w = S_w (a_w \cos \psi + c_w \sin \psi) . \quad (2)$$

Waves crossing  $z = z_0$  planes with a small delay gradient along the  $x$ - and/or  $y$ -directions possess small tilt components  $a_w$  and/or  $b_w$  that are proportional to  $U_w$  itself. For detonation following a slower input shock by a uniform time, this determines

$$a_D = a_1(U_D/U_1) \quad (3)$$

The analogous acceptor/donor relation between  $b_D$  and  $b_1$  is presumed, but is inconsequential.

Table 2 traces the application of these wave orientation relationships to the speeds of Table 1. The detonation speeds,  $D$ , in the "ideal" columns for the two shots differ from each other, and both are larger than the velocity near 5.55 km/s expected for unsupported detonation. The input shock speeds assuming ideal orientation are likewise unequal, whereas the gun projectile speed was duplicated. However, in each shot we find  $(U_1/D) = 0.67 \pm .01$ .

In the columns headed "tilted," we reconcile these results by considering first the tilt component  $a_D$  needed to adjust each detonation wave speed to an assumed value of 5.55 km/s. The effect upon  $c_D = \sqrt{1 - a_D^2 - b_D^2}$  of an unknown y-component,  $b_D$ , is ignored. Extending the adjustment to the input shock is less definite, and two naive estimates for  $a_1$  are evaluated. Taking  $a_1 = a_D$  gives values of  $U_1$  near 3.7 km/s from both shots. Considering the detonation as acceptor and input shock as donor according to Equation (3) diminishes the

Table 2. Wave Velocities in Liquid Nitric Oxide\*

	Shot 660		Shot 661	
	Ideal	Tilted	Ideal	Tilted
Detonation:				
$c_D$	(1.0)	.99985	(1.0)	.99996
$a_D$	(0.0)	-.0170	(0.0)	-.0084
$D$ (km/s)	6.15	(5.55)	5.82	(5.55)
Input Shock:				
$a_1 (= a_D)$	(0.0)	-.0170	(0.0)	-.0084
$U_1$ (km/s)	4.10	3.70	3.92	3.74
$a_1 (= a_D U_1/D)$		-.0117		-.0057
$U_1$ (km/s)		3.84		3.80

\* Assumed values in parentheses; symbols defined in text.

adjustment of each  $U_1$  from its "ideal" value, and the resulting values are both near 3.8 km/s.

### Hugoniot State and Superdetonation

$U_1 = 3.8 \pm 0.2$  km/s is adopted to determine the shocked state of nitric oxide fluid in which the superdetonations occurred. With the symmetric approximation for the shock and release of pressure and particle velocity in copper, the following properties are found from the conservation equations for the matching shock in the explosive: pressure  $p_1 = 4.3 \pm 0.3$  GPa; particle velocity,  $u_1 = 0.89 \pm 0.02$  km/s; density,  $\rho_1 = 1.67 \pm 0.03$  g/cm<sup>3</sup> = 1.305  $\rho_0$ ; specific internal energy,  $E_1 = E_0 + 0.40 \pm 0.02$  kJ/g.  $E_0$  for the original liquefied nitric oxide has the value  $+2.65 \pm 0.01$  kJ/g, relative to the elements O<sub>2</sub> and N<sub>2</sub> as ideal gases at zero K.<sup>8</sup> From the averages of the corresponding angles of the tracks registered by the superdetonations in Figure 1 and Reference 4 before they overtook the input shocks, we find  $S^* = 45.5$  km/s and  $D^*_{\text{net}} = 6.0$  km/s. This superdetonation velocity is in the frame of the compressed, moving material. In a Eulerian frame  $D^*_{\text{lab}}$  has the value  $6.0 + 0.9 = 6.9$  km/s. These values of  $D^*$  are subject to large uncertainty from tilt, and are presented primarily to illustrate the relationships applicable in the compressed wedge confined by a window with matching shock impedance.

### DETONATION PRESSURE AND VELOCITY MEASUREMENTS

The experimental arrangements have been described previously.<sup>3</sup> The tubes confining the explosive were made of graphite. They were cooled with liquid nitrogen in a bath with isopentane as the heat transfer fluid. With vigorous stirring, the temperature was maintained uniform along the length of the tube. Table 3 gives a list of temperatures. Except for the heat leak from the booster explosive warming the first thermocouple station, the temperature control is very good.

Graphite was chosen as the confining material because it is available commercially in the form of tubes, it has a relatively low shock impedance and offers minimal confinement, and it was thought that there would be

**Table 3. Temperature Uniformity Along Graphite-Walled Charges of Liquid Nitric Oxide**

Station Number	Distance from Booster (mm)	Temperature (°C)	
		Shot F-5730	Shot 8-184
1	25.4	-153.89	-153.75
2	76.2	-154.11	-154.05
3	127.0	-154.25	-154.10
4	177.8	-154.24	-154.14
5	228.6	-154.16	-154.05
6	279.4	-154.07	-154.06
7	330.2	-153.98	-154.01

no region of subsonic flow in the graphite that might cause a perturbation where the wave in the explosive intersects the tube wall. Later calculations have shown that the uncertainties in the equations of state are large enough that there could be a small subsonic region.

The detonation pressure is inferred from the measured free-surface velocity of a 6061 dural plate driven by the explosive at the end of its run through 355.6 mm of nitric oxide in the 25.4-mm diameter tube. The velocity was measured using the method described by Davis and Craig.<sup>17</sup> It has been shown by Davis and Venable<sup>18</sup> that the measured free-surface velocity is a linear function of  $(x/d)^{1/2}$ , where  $x$  is the thickness of the plate, and  $d$  is the diameter of the detonation tube. The data are plotted in Figure 2. The intercept with the axis gives the desired value of the free-surface velocity, which is then used to find the particle velocity in the dural at the instant it is contacted by the detonation wave.

Figure 3 is a plot in the pressure - particle velocity plane of the Hugoniot curve for dural and the reflected shock Hugoniot curve for the explosive. Their intersection should be at the point measured in the free-surface velocity experiments if the reflected shock Hugoniot curve is the correct one.

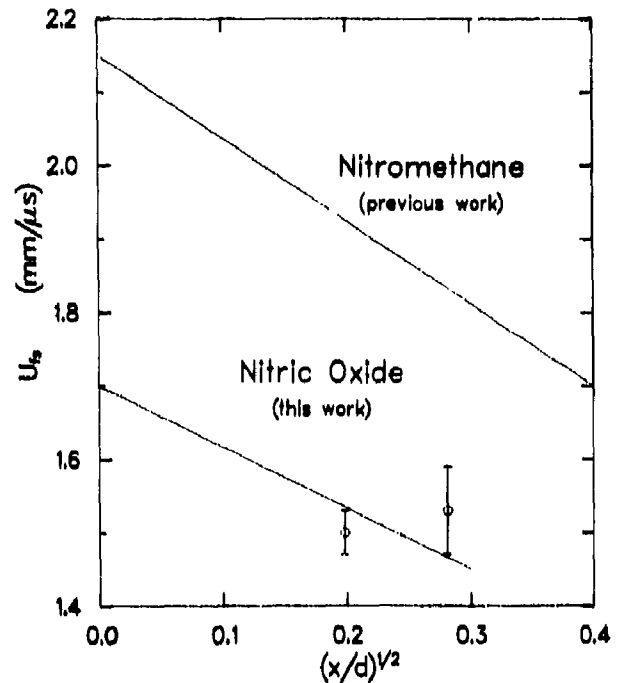


**Figure 2. Plot of Free-Surface Velocity vs. Plate Thickness for Nitromethane From Reference 18 and for the Measurements From Shots F-5730 and 8-184 Described Here. The extrapolation to zero plate thickness is made using the same fractional decrement for each.**

Within the accuracy of the experimental result, the curve is satisfactory.

An important reason for performing these measurements was to try to answer questions raised by speculation that real detonations are weak detonations, not Chapman-Jouguet (C-J) detonations. Nitric oxide is the only condensed phase material for which it has been possible to measure the equation of state of the detonation products in separate experiments that are not detonation experiments.<sup>8</sup> In Figure 3 the C-J state and its reflected-shock Hugoniot are the ones calculated from a semi-empirical equation of state of equilibrium products from liquid nitric oxide.<sup>8,19</sup> This is based on the measured shock Hugoniots of oxygen and nitrogen individually and of nitric oxide products in overdriven detonation states. Hence it is independent of assumptions about the nature of the unsupported detonation of nitric oxide. The measured point plotted in Figure 3 is not in disagreement with the assumption that the real detonation is a C-J detonation. The data

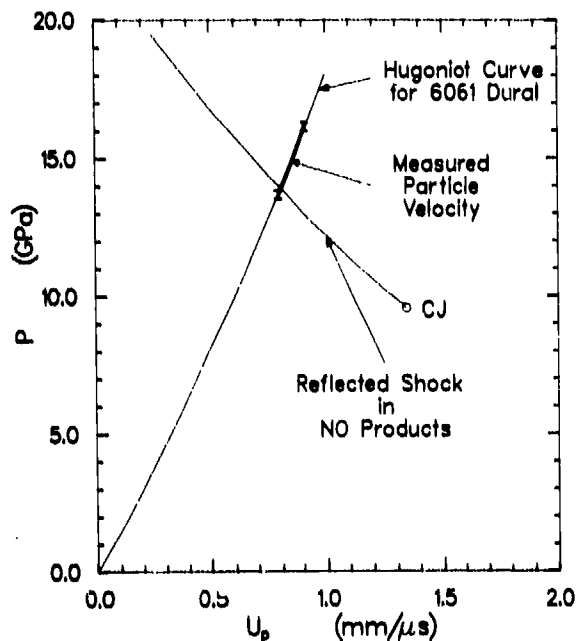


Figure 3. Matching of Nitric Oxide Detonation Products into the Dural Plate, Plotted in the Pressure vs. Particle Velocity Plane. The value of particle velocity inferred from the free-surface velocity measurements is plotted with estimated error span. There is no disagreement with the assumption that the detonation is a CJ detonation.

are not adequate to put any severe limit on the range of weak (or strong) detonations that might also be in agreement with the data.

Detonation velocity measurements were made incidental to the pressure measurements. A plot of detonation velocity versus charge diameter is shown in Figure 4. The infinite-medium detonation velocity is estimated to be 5564 m/s at a temperature of 119 K, corresponding to a density of 1.280 g/cm<sup>3</sup>.

## DETONATION FRONT PHOTOGRAPH

We had ambitiously intended to use measured wavefront shapes in long, detonating charges of several different diameters to determine rates of energy release in the reaction zone.<sup>10</sup> However, we completed only a prototype experiment demonstrating wavefront curvature. Electronically intensified cameras

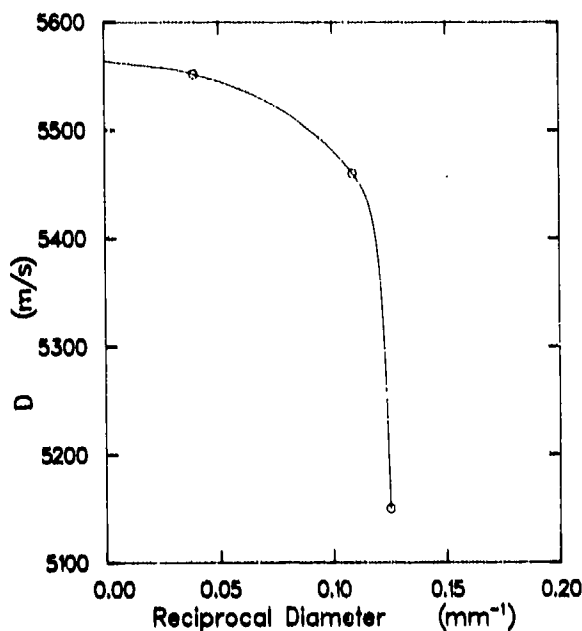


Figure 4. Plot of Detonation Velocity Versus Reciprocal Diameter for Nitric Oxide at 119 K and Density 1.280 g/cm<sup>3</sup>. The large decrement is unusual for a liquid explosive.

of two types, single-frame and streak, were used to photograph self-light from the transparent end of a detonating cylinder of N<sub>2</sub>O<sub>2</sub> capped by a flat PMMA window. The cylinder interior was 40 mm long and 20 mm in diameter, and detonation was initiated promptly by a flat, axially directed shock introduced from detonating TNT through the brass end wall opposite the window.

The streak photograph from this experiment is displayed in Figure 5, with axes to indicate the diametrical slit and advancing time,  $t$ . The midpoint of the streak record coincides with the framing picture exposure discussed below, and is taken as the time origin. Somewhat later, when the detonation reached the window, it abruptly intensified the otherwise slowly varying exposure on the film. The resulting arrival track appeared earliest at the charge axis ( $t_{\text{axis}} = 0.34 \mu\text{s}$ ) and formed a smooth, symmetric arc indicating that the detonation front is likewise curved and at the walls lagged by 0.09  $\mu\text{s}$ , or 0.5 mm ( $t_{\text{wall}} = 0.43 \mu\text{s}$ ). Transverse irregularity indicative of

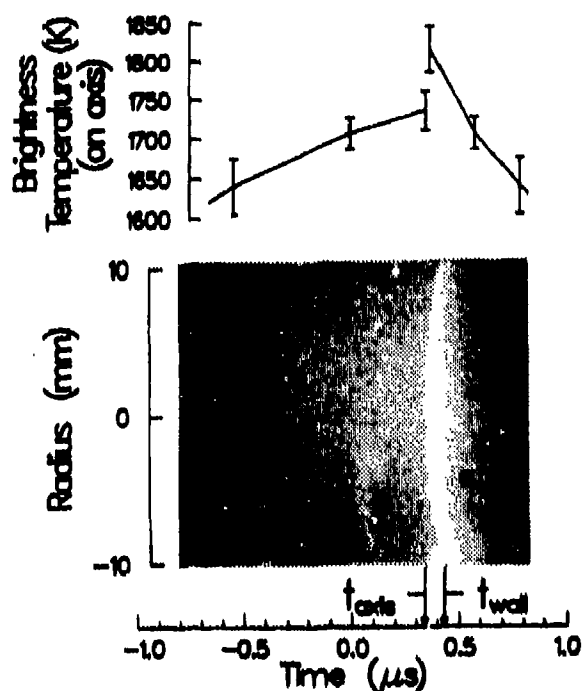


Figure 5. Electronic Streak Photograph of Self-Light from Convex Front of Liquid Nitric Oxide Detonation Reaching Full-Diameter PMMA Window. Brightness temperatures at zero radius plotted above to same time axis.

proximity to the failure diameter is absent, and any fine-scaled manifestations of non-laminar detonation flow are not resolved by our electronically intensified photography.

The single-frame picture, exposed for 30 ns, showed the full circular area of the approaching detonation when its front was still about 0.4  $\mu$ s, or 2 mm, from reaching the window surface. It showed a uniformly exposed disc whose apparent brightness we matched through the same photographic system by an incandescent tungsten-ribbon lamp. The equivalent black-body temperature of the tungsten source was  $1706 \pm 37$  K, and exposures at nearby temperatures indicated the film coefficient. Densitometry of the streak photograph showed that the brightness of the detonation increased steadily, and understandably, as the remaining depth of undisturbed, bluish-gray  $N_2O_2$  liquid diminished. The abrupt increase of brightness when the PMMA window was reached was followed by a steep, steady

decrease. The apparent brightness temperatures determined from the axial densitometric scan are plotted against time at the top of Figure 5.

All these brightness temperatures are far below the C-J temperature of approximately 2600 K we expect<sup>19</sup> from the equation of state of products from detonating  $N_2O_2$  at liquid initial density. The simplest interpretation, sufficient but not unique, is that the reaction zone and/or unreacted layer is significantly opaque and behaves in the limit as a black body near 1735 K. The effective emissivity of the detonation product state at or near C-J conditions remains unknown, as does the complex net effect of encountering the PMMA boundary.

## DISCUSSION

Here, in conjunction with the poster panels which appear elsewhere in this *Proceedings*, we expand our assessment of selected features of the measurements presented above.

The second poster panel includes a diagram of the instrumentation on the exterior of the long graphite tubes that led to the data in Table 3 and Figures 2 and 4. The precise detonation velocity of liquid nitric oxide found in 25.4-mm i.d. graphite at  $119.1 \pm 0.1$  K is  $D = 5552 \pm 3$  m/s. This was determined by means of the illustrated twisted pairs of thinly insulated magnet-wire sensors installed at the apexes of uniformly deep, exterior V-grooves in the tube walls. Figure 4 includes this value along with the less precisely determined<sup>3</sup> velocities of the slower detonations at two diameters below 10 mm.

The second and third poster panels contain abbreviated statements that extend our interpretations of Figures 3 and 5, respectively.

Mean results from the pairs of experiments represented in Tables 1 and 2 above, and of their consequences developed under the subheading "Hugoniot State and Superdetonation," are extended and arranged in tabular form in the fourth panel, under the heading: Wedge Initiation—Quantitative. The present collection of these results supersedes a previous, preliminary account.<sup>21</sup>

Our determination of superdetonation velocity,  $D^*$ , is admittedly compromised by somewhat uncertain effects of wave tilt and transmission of the input shock into the PMMA window. However, unlike many earlier determinations of  $D^*$  in nitromethane and other liquids,<sup>22,23</sup> it is based on the slope of the continuously recorded final segment of the superdetonation trajectory, rather than on the time differential associated with passage of the superdetonation from an inferred origin plane to the depth of the input shock at overtake.

The input shock in liquid nitric oxide that we have employed to achieve overtake in 3.0 - 3.4 mm has a combination of pressure and particle velocity that lies within the range of impedances found historically for PMMA.<sup>24</sup> We recognized this coincidence only as an outcome of our measurement on the liquid nitric oxide confined downstream by the PMMA that formed the solid member defining the slant face of the wedge near its toe. We have not pursued such refinements as allowing for the increased PMMA density at  $-153^\circ\text{C}$  or selecting PMMA stock in order to improve the impedance match. We simply note that fortuitously, our input-shock state for initiating detonation in homogeneous liquid nitric oxide was subject to only minor perturbation upon transmission of the shock front across the slant face of the wedge.

The fifth poster panel, headed Wedge Initiation—Qualitative, augments the streak records of wedge initiation with synthetic (computer-generated, color) snapshots of sections through the wedge in its initial configuration and at three representative times after the shock enters the wedge base. The static section is at the lower left; the lower right and upper left sectional snapshots show conditions prior to the overtake. The final snapshot, at the upper right, shows a condition after overtake, when detonation is occurring in original liquid explosive.

Our wedge initiation results exhibited in Figure 1 and amplified in Reference 4 show qualitatively how the wavefront of superdetonation evolves gradually in the interior of the shock layer. The superdetonation gains definition of its registration by the mirrored

confining boundary while its front advances through fluid layers initially situated from  $\leq 1$  mm to  $\geq 2$  mm from the copper surface at the wedge base. This result is in qualitative agreement with experimental<sup>25</sup> and theoretical<sup>26</sup> findings emphasized in the present symposium.

## ACKNOWLEDGEMENTS

This work was supported by Institutional Supporting Research and Development funds provided by the Los Alamos National Laboratory of the University of California under auspices of the U.S. Department of Energy, Contract W-7405-ENG-36. Many individuals within the Laboratory supplied their technical skill, knowledge, and effort to execute the measurements. We particularly acknowledge the indispensable contribution made by Dr. Tom Rivera toward unifying our otherwise fragmentary studies on diverse aspects of detonation.

## REFERENCES

1. McInteer, B. B. and Potter, R. M., "Nitric Oxide Distillation Plant for Isotope Separation," *Industrial and Engineering Chemistry Process Design and Development*, Vol. 4, 1965, pp. 35-42.
2. Ramsay, J. B. and Chiles, W. C., "Detonation Characteristics of Liquid Nitric Oxide," *Proceedings of the Sixth Symposium (International) on Detonation*, Coronado, CA, 24-27 Aug 1976, pp. 723-728.
3. Davis, W. C. and Chiles, W. C., "Detonation Properties of Liquid Nitric Oxide," *Proceedings of the Eighth Symposium (International) on Detonation*, Albuquerque, NM, 15-19 Jul 1985, pp. 422-424.
4. Schott, G. L. and Chick, K. M., "Photographically Observed Waves in Detonation of Liquid Nitric Oxide," Kuhl, A. L. et al., Eds., *Dynamics of Explosions Progress in Astronautics and Aeronautics*, American Institute of Aeronautics and Astronautics, Inc., Washington, D.C., Vol. 114, 1988, pp. 372-385.

5. Schmidt, S. C.; Moore, D. S.; Shaw, M. S.; and Johnson, J. D., "Vibrational Spectroscopy of Shock-Compressed Fluid N<sub>2</sub> and O<sub>2</sub>," Schmidt, S. C. and Holmes, N. C., Eds., *Shock Waves in Condensed Matter 1987*, North-Holland Physics Publishing, Amsterdam, 1988, pp. 489-492.
6. Blais, N. C. and Greiner, N. R., "Real-Time Analysis of the Reaction Products of Shocked Solid Nitric Oxide," *Journal of Energetic Materials*, Vol. 6, 1988, pp. 255-281.
7. Swanson, B. I.; Agnew, S. F.; and Greiner, N. R., "Static High Pressure Study of Nitric Oxide Chemistry: Proposed Mechanism for Nitric Oxide Detonation," *Proceedings of the Eighth Symposium (International) on Detonation*, Albuquerque, NM, 15-19 Jul 1985, pp. 715-724.
8. Schott, G. L.; Shaw, M. S.; and Johnson, J. D., "Shocked States From Initially Liquid Oxygen-Nitrogen Systems," *Journal of Chemical Physics*, Vol. 82, 1985, pp. 4264-4275.
9. Le Sar, R. and Shaw, M. S., "An Electron-Gas Plus Damped-Dispersion Calculation of the N<sub>2</sub>-N<sub>2</sub> Interaction," *Journal of Chemical Physics*, Vol. 84, 1986, pp. 5479-5485.
10. Rivera, T., "Fundamental Research on Explosives Program," *Industrial and Engineering Chemistry Product Research and Development*, Vol. 24, 1985, pp. 440-442.
11. Miller, R. O., "Explosions in Condensed-Phase Nitric Oxide," *Industrial and Engineering Chemistry Process Design and Development*, Vol. 7, 1968, pp. 590-593.
12. Ribovich, J.; Murphy, J.; and Watson, R., "Detonation Studies with Nitric Oxide, Nitrous Oxide, Nitrogen Tetroxide, Carbon Monoxide, and Ethylene," *Journal of Hazardous Materials*, Vol. 1, 1975-77, pp. 275-287.
13. Calado, C. G. and Staveley, L. A. K., "The Thermodynamics of the System Krypton—Nitric Oxide and Their Interpretation in Terms of Monomer-Dimer Association of the Oxide," *Fluid Phase Equilibria*, Vol. 3, 1979, pp. 153-166.
14. Adwentowski, K., "Behavior of Nitric Oxide at Low Temperatures," *Bulletin of the Academy of Sciences, Cracow*, 1909, pp. 742-767.
15. Kerr, E. C., I. *The Second Virial Coefficient of Argon at Low Temperatures and Low Pressures: II. The Heat Capacity of Liquid Nitric Oxide Above its Normal Boiling Point*, Ph.D. Dissertation, The Ohio State University, Columbus, Appendix I, 1957, pp. 60-67.
16. Mason, J., "The Nitric Oxide Dimer—Blue with Rectangular Molecules?," *Journal of Chemical Education*, Vol. 52, 1975, pp. 445-447.
17. Davis, W. C. and Craig, B. G., "Smear Camera Technique for Free-Surface Velocity Measurements," *Review of Scientific Instruments*, Vol. 32, 1961, pp. 579-581.
18. Davis, W. C. and Venable, D., "Pressure Measurements for Composition B-3," *Proceedings of the Fifth Symposium (International) on Detonation*, Pasadena, CA, 18-21 Aug 1970, pp. 13-21.
19. Shaw, M. S. and Johnson, J. D., "The Theory of Dense Molecular Fluid Equations of State with Applications to Detonation Products," *Proceedings of the Eighth Symposium (International) on Detonation*, Albuquerque, NM, 15-19 Jul 1985, pp. 531-539.
20. Engelke, R. and Bdzil, J. B., "A Study of the Steady-State Reaction-Zone Structure of a Homogeneous and a Heterogeneous Explosive," *Physics of Fluids*, Vol. 26, 1983, pp. 1210-1221.
21. Schott, G. L., "Initiation of Detonation From a Shocked State of Liquid Nitric Oxide," *Bulletin American Physical Society*, Series II., Vol. 33, Abstract No. J21-3, 1988, p. 536.
22. Campbell, A. W.; Davis, W. C.; and Travis, J. R., "Shock Initiation of

- Detonation in Liquid Explosives," *Physics of Fluids*, Vol. 4, 1961, pp. 498-510.
23. Travis, J. R.; Campbell, A. W.; Davis, W. C.; and Ramsay, J. B., "Shock Initiation of Explosives III. Liquid Explosives," *Les Ondes de Detonation*, Colloques Internationaux du Centre National de la Recherche Scientifique, Gif-sur-Yvette, France, No. 109, 1962, pp. 45-58.
24. Deal, W. E., "Shock Wave Research on Inert Solids," *Proceedings of the Fourth Symposium (International) on Detonation*, White Oak, MD, 12-15 Oct 1965, pp. 321-345.
25. Sheffield, S. A.; Engelke, R.; and Alcon, R. R., "In-Situ Study of the Chemically Driven Flow Fields in Initiating Homogeneous and Heterogeneous Nitromethane Explosives," *Proceedings of the Ninth Symposium (International) on Detonation*, Portland, OR, No. 54, 28 Aug-1 Sep 1989.
26. Kapila, A. K. and Dold, J. W., "A Theoretical Picture of Shock-to-Detonation Transition in a Homogeneous Explosive," *Proceedings of the Ninth Symposium (International) on Detonation*, Portland, OR, No. 138, 28 Aug-1 Sep 1989.

# INITIATION AND DETONATION MEASUREMENTS ON LIQUID NITRIC OXIDE

Garry L. Schott



William C. Davis



William C. Chilce



## DETONATION PROPAGATING IN CYLINDERS

Rate stick with graphite wall and imaged-wire  
measurement of end-plate velocity

Plate surface motion  
and detonation pressure

Detonation front brightness  
and convex shape

Detonation wave velocity versus  
reciprocal tube diameter

## DETONATION INITIATED IN WEDGES

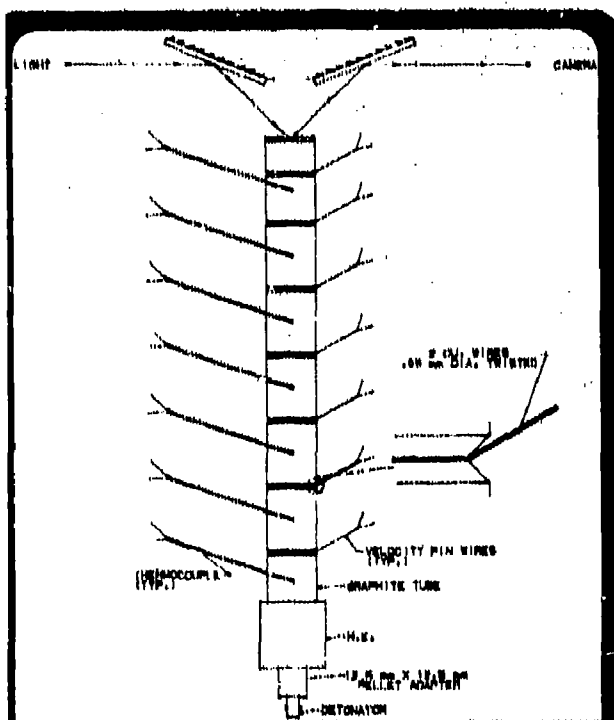
### QUANTITATIVE:

- Hugoniot state from input shock
- Detonation velocity reveals wave tilt

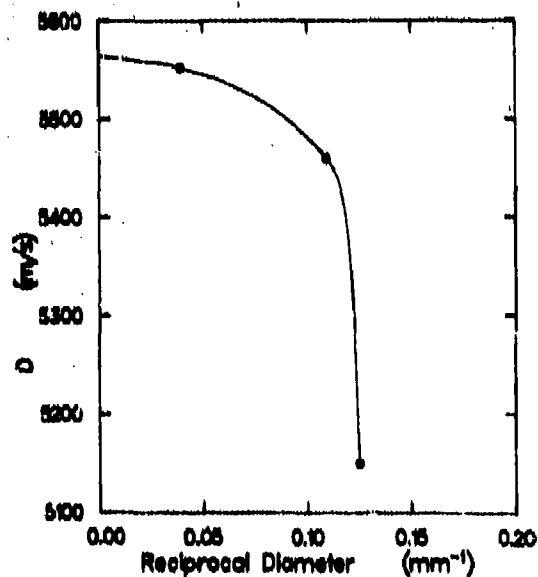
### QUALITATIVE:

- Superdetonation forms with transverse structure  
and overtakes smooth input shock
- Detonation continues, with structure

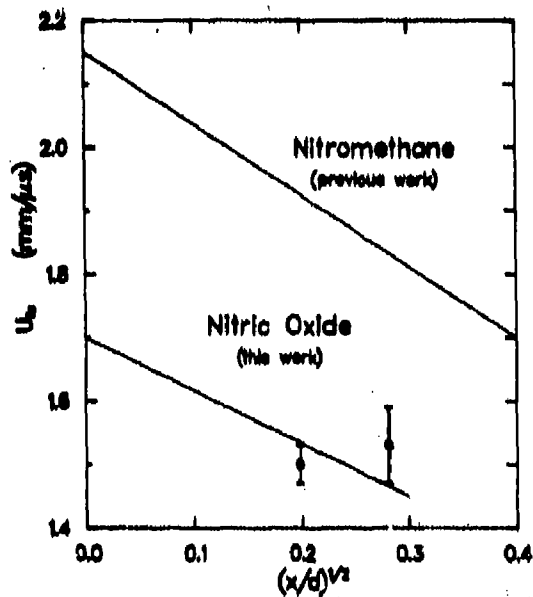
- Liquid nitric oxide has been the focus of concerted fundamental research on explosives, with multiple objectives in hydrodynamics, theory, and molecular properties.
- Nitric oxide is a prototype detonable liquid.
- Nitric oxide comprises only two chemical elements; its molecular makeup is simpler than other ML's.
- Products of nitric oxide decomposition are principally diatomic; equation of state of the product fluid is separately determined.
- Wave velocity plus pressure (or particle velocity) measured with sufficient accuracy in detonating liquid nitric oxide form a fundamental, quantitative test of the Chapman - Jouguet condition.
- Curved shape of detonation wavefront, observed for suitably confined cylinders, measures the axial zone of energy deposition.



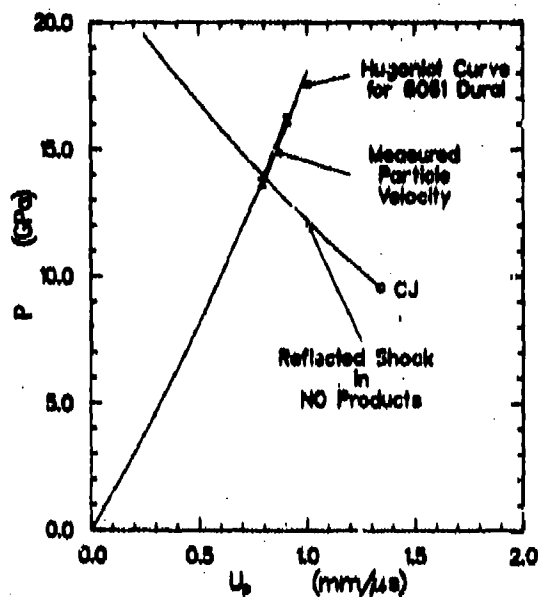
Mechanical configuration of liquid-filled assembly, terminated by aluminum free-surface plate, instrumented along length, for measuring uniformity of detonation velocity and preheat temperature. See Table 3 of Preprint.



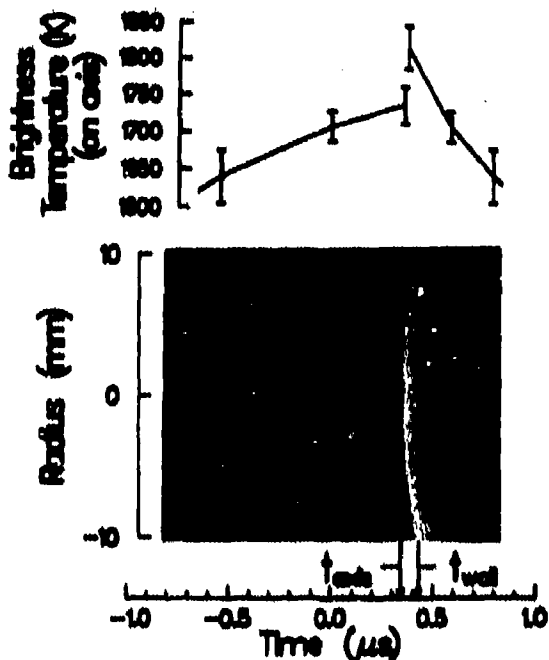
Effect of charge diameter on detonation velocity of liquid nitric oxide confined in graphite tubes. (Preprint Figure 4)



Free-surface velocity of aluminum plates, versus reduced distance, from image-wire streak records. (Preprint Figure 2)



Dynamic matching of nitric oxide detonation products propelling aluminum plate. (Preprint Figure 3)



Self-light from liquid nitric oxide detonation, in end-viewed streak photograph over full charge diameter, perturbed when flat end window is reached by convex wave. Brightness temperature on axis of charge also plotted to time scale of streak. (Preprint Figure 5)

### EXPLORATORY MEASUREMENTS OF WAVEFRONT LUMINOSITY SHOW:

- Convex wavefront in brass tube is macroscopically smooth, axially symmetric.
- Data not sufficient to determine reaction zone extent vs. radius.
- Frontal light intensity indicates  $1785 \pm 46$  K as apparent temperature.
- Brightness temperature may approximate Chapman - Jouguet temperature, estimated by BKW model as 1884 K.
- Brightness temperature may be seriously below C - J temperature, owing to opacity of shocked/ reacting zone.

## WEDGE INITIATION — QUANTITATIVE

Superdetonation behind input shock  
from 1.57 g/cm<sup>3</sup>

Detonation of liquid nitric oxide at rest  
from 1.59 g/cm<sup>3</sup>

Observed:

**Undetonated**

**Det. Wave**

**Detonation**

0.88 km/s

0.9 km/s

0.9 km/s

**Detonation Velocity**

0.88 ± 0.1 km/s

Estimated:

0.88 km/s

1.2 km/s

2.1 km/s

**Particle Velocity**

1.88 ± .07 km/s

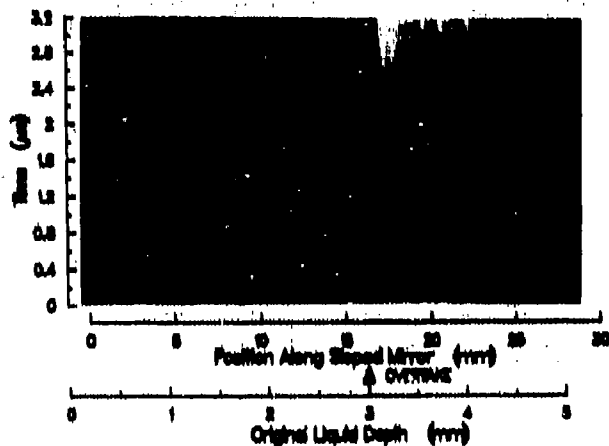
4.8 GPa

15. GPa

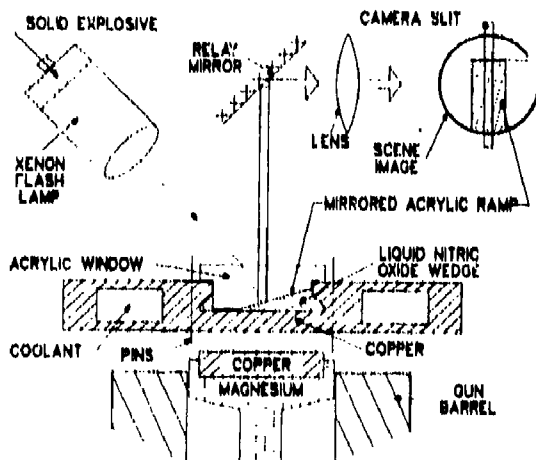
18.9 GPa

**Pressure**

9.8 ± 0.5 GPa



Delayed initiation of detonation in liquid nitric oxide; streak photograph. (Figure 1 of Preprint)



### HUGONIOT STATE OF NITRIC OXIDE FLUID

Shock Speed,  $U_s$  (km/s)     $2.8 \pm 0.2$

Particle Speed,  $U_p$  (km/s)     $0.88 \pm .02$

**Initial State**

$10^{-4}$     Pressure (GPa)     $4.8 \pm 0.8$

$1.58 \pm .01$     Density (g/cm<sup>3</sup>)     $1.67 \pm .02$

$+0.65 \pm .01$     Specific (kJ/g) Internal energy\*     $+0.08 \pm .02$

\*Reference State: N<sub>2</sub> and O<sub>2</sub> gases at 0.0 K.

Cryogenic target on gas gun; wedge-shaped volume filled with liquid, confined by impedance mirror and externally illuminated.

WEDGE INITIATION - QUALITATIVE

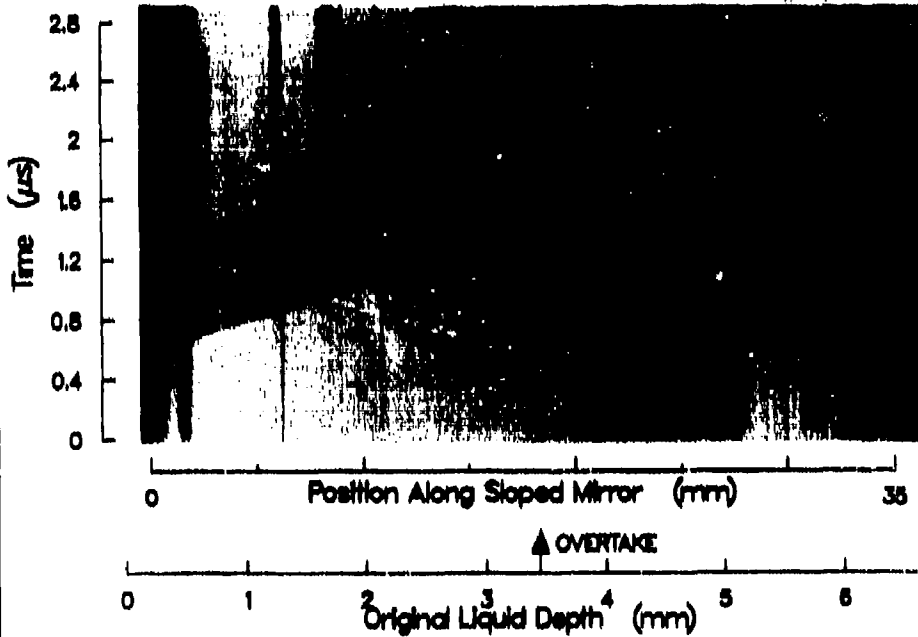


Superdetonation - Two Waves



Completed Initiation - One Wave

DELAYED DETONATION IN WEDGE of LIQUID NITRIC OXIDE



One Wave - Input Shock

# MECHANISMS OF DETONATION AND FAILURE IN WEAK CHEMICALLY SENSITIZED MINING SAFETY EXPLOSIVES

M. Kennedy and I. D. Kerr

Health and Safety Executive, Research and Laboratory Services  
Division, Harpur Hill, Buxton, Derbyshire, SK17 9JN, England, UNITED KINGDOM

*This paper discusses the experimental derivation of detonation reaction zone shapes, densities, pressures, and particle velocities in weak mining safety explosives of the powder type. It then shows how this information can be used to devise a model of the reaction zone processes, how compression of the explosive can affect detonation sufficiently to cause failure, and suggests a method of calculating failure diameters.*

## INTRODUCTION

Conditions can occur during shotfiring in mines in which detonation products from early shots in a delay round can pressurize, compress, and desensitize charges of later shots. Desensitization has become more important in recent years because the increased safety in gassy mines of weak mining safety explosives has been obtained by reductions in strength and sensitizer content.

This paper discusses and interprets X-ray photographs of freely suspended detonating cartridges of weak mining safety explosive of different diameters and densities, and outlines the methods used to obtain from them information concerning densities and pressures in detonation waves. This experimentally obtained information is used to devise a model of detonation in near failure conditions. The model is used to explain the desensitizing effects of increasing density, and for attempting a quantitative analysis of conditions in which detonation just fails in these types of explosives.

## COMPOSITIONS AND CHARACTERISTICS OF SAFETY EXPLOSIVES

Weak mining safety explosives are mostly sensitized by about ten percent by weight of mixtures of nitroglycerine and ethylene glycol

dinitrate. Proportions of ethylene glycol dinitrate in some mixtures vary between twenty and eight percent of the total. About eighty percent by weight of these explosives consists of finely divided inorganic compounds such as ammonium nitrate and alkali metal nitrates, sodium chloride as a flame inhibitor, and ammonium chloride as an ion-exchange component. The remainder consists of fuels, waterproofing agents, and anti-setting agents.

A substantial quantity of powder explosives is manufactured at densities in the region of 1.3 grams/cc. Component particle sizes are such that each gram of explosive will have a surface area in the range of 200 to about 600 sq. cm.

The maximum densities that these explosives can have, if all the air is expelled, is in the range 1.8 to 1.9 grams/cc, as calculated from the densities and quantities of each component of the composition.

## EXPERIMENTAL

Full details of the experimental arrangements have been published.<sup>1</sup> Figure 1 shows a typical arrangement of X-ray source, explosive cartridge, and photographic plate.

The X-ray source was a 300 kV type 730/2710 Field Emission Flash X-ray System, which is now supplied by Hewlett-Packard.

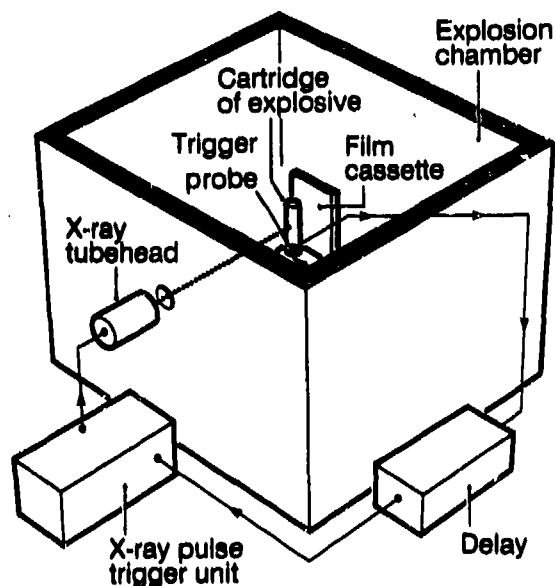


Figure 1. Typical Arrangement of X-Ray Source, Explosive, and Photographic Plate

Each cartridge was 120 mm long. The cartridge diameters were 18, 22, 26, or 32 mm. The densities of the cartridges were as received from the manufacturers, or compressed in a range up to about 85 percent of the voidless density of the explosive.

A trigger probe, which was used to initiate the X-ray flash at selected times after the detonation wave reached it, was always inserted in the cartridge 10 mm from the base charge of the detonator.

A calibration stepwedge was made by pressing a known weight of explosive of the same composition as that being investigated into a mould designed to produce five steps having thicknesses of one to five centimeters and of known density. This enabled optical densities in the X-ray photograph to be related to material densities.

## DERIVATION OF DENSITY DISTRIBUTIONS

Information concerning variations of average density in the detonation reaction zones of these explosives has been obtained from X-ray flash photographs of unconfined detonating cartridges of different diameters and densities.<sup>2</sup> The photographs were digitized and then processed using a microcomputer.

The average densities obtained are values of the integral of density with respect to distance through the explosive divided by the length of the path over which the integration is made.

## DENSITY VARIATIONS, PRESSURES, AND PARTICLE VELOCITIES

X-ray photographs have confirmed that in these low velocity detonations, wavefronts are curved. Density increases in the reaction zone at the charge axis are commonly only 10 to 20 percent of the initial density of the explosive, and mostly considerably less than voidless. Densities in planes perpendicular to the charge axis are approximately constant, but as distance behind the wavefront increases, densities reduce in magnitude as depicted in Figure 2.

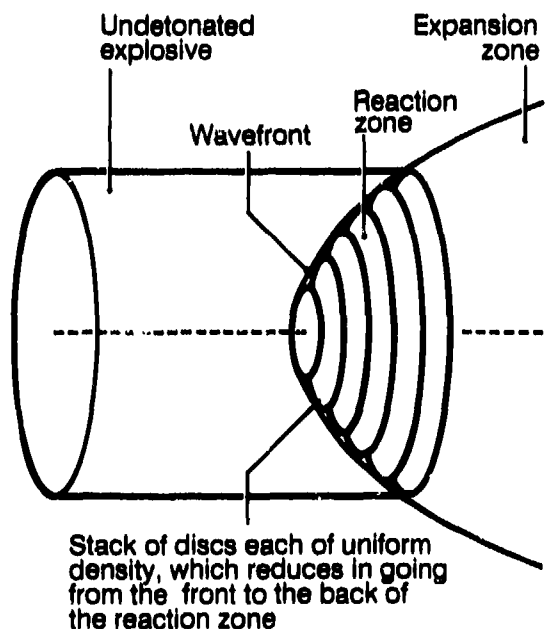


Figure 2. Density Distributions in the Reaction Zones of Detonating Safety Explosives

The pressures calculated on the basis of the observed density increases and detonation speeds lie in the range 0.1 to 1 GPa.

Some information on the dynamic compression, without detonation, of weak mining safety explosives is available.<sup>3</sup> Explosives were submitted to the compressive effects of dropping weights from a height of 5 meters

onto samples contained in a brass cylinder sealed at one end and closed at the other by a piston that was struck by a falling weight. If it is assumed that all the kinetic energy of the falling weight goes into compressing the explosive, and that the weight is uniformly decelerated as compression takes place, the pressure can be calculated. Although not all the kinetic energy of the falling weight goes into compressing the explosive, and the deceleration is not likely to be uniform, the assumptions employed probably give a reasonable estimate of the applied pressure. Pressures calculated on this basis for a range of mining safety explosives indicate that values of less than 0.1 GPa are required to effect compressions in excess of 20 percent. For example, a typical explosive of initial density 1.32 g/cc underwent a compression of 27 percent with an estimated pressure of 0.085 GPa. Another explosive of initial density 0.94 g/cc underwent a compression of 43 percent with an estimated pressure of 0.06 GPa.

The differences between the pressures reached in dynamic compression without detonation, and during detonation must arise from the fact that in one case there is no noticeable reaction, and in the other there is very noticeable reaction. It seems that in the detonation reaction zone, chemical reaction causes lower densities by preventing grains of explosive from compacting to the extent to which, in the absence of reaction, they should at the pressures reached. The implication of this is that reaction is initiated very quickly at the wavefront as a result of particles colliding violently.

For those explosives for which the pressures attained at the detonation wavefront are less than those required to exceed the mechanical strength of the grains in the reaction zone, the wavefront region probably extends over a distance of about a typical average explosive particle width. The likely width of the wavefront region, when flow is not particulate, is not clear, but will probably be smaller.

## PARTICLE COLLISIONS

High speed impacts between particles of explosives can cause effects which include sudden pressure increases, chemical reaction, intense friction, cracking into smaller pieces,

melting, compression, deformation, and vibration.

Where particles are initially in contact in the explosives, and particulate flow occurs, there are increases in pressure. Hot spots form at points where surface asperities rub together during the compaction process. The temperatures achieved at points of rubbing contact depend on the melting points of the particles and the applied pressure. In general, melting temperatures are raised by pressure, and at pressures up to one GPa, such as occur in mining safety explosives, the melting temperature could exceed that at which rapid reaction of the explosive can occur; then intergranular friction could be sufficient to initiate rapid reaction without melting. This suggests that pressure must be applied to initiate detonation, and this is confirmed by earlier studies.<sup>4</sup> Other effects such as compression, vibration and disintegration, are probably not by comparison with friction too important in the processes leading to the initiation of reaction. The possible formation of fast moving sensitizer particles is discussed later.

Approximate values of the times required to achieve maximum compression in the vicinity of the wavefront at the charge axis in weak mining safety explosives have been obtained. An average distance through which an average particle of explosive moves in the compaction process was estimated by assuming there are as many gas spaces as particles in the explosive. Then, further assuming that each particle moves at a constant speed, which can be calculated from plane wave hydrodynamic theory, the compaction time, as shown in Appendix 1, can be written as  $4.r.d_v/(3.d_0.D)$ ; where  $r$  is a representative average particle radius,  $D$  is the detonation velocity,  $d_v$  is the voidless density, and  $d_0$  the initial density. Using typical values for mining safety explosives; viz.  $D=1800$  meters/second,  $r=100$  microns,  $d_v=1.85$  grams/cc, and  $d_0=1.3$  grams/cc, a value of compression time of about  $10^{-7}$  seconds is obtained. This is clearly of the right order of magnitude, and illustrates the speed of the process.

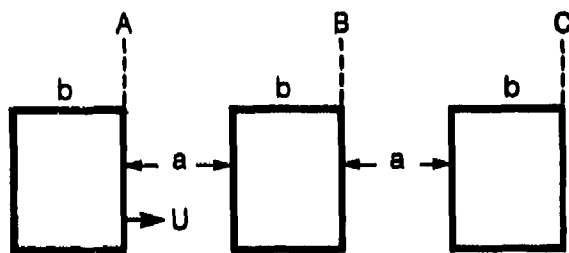
At maximum compression when the explosive's density is less than voidless, the interstices in the explosive must be filled with

gas at a pressure sufficient to prevent further compression taking place. This gas is generated by the reaction of one of the components of the explosive, which in this case is the sensitizer, because it reacts much more rapidly than the other components. An approximate value for the extent of reaction of the sensitizer of 25 percent was estimated by calculating the quantity of sensitizer required to fill the explosive's interstices with fully oxidized gases at the sensitizer explosion temperature, and a typical pressure of 0.4 GPa.

## THE RELATIONSHIP BETWEEN PARTICLE AND WAVE SPEEDS

In the vicinity of the detonation wavefront and when the mechanical strength of the explosive's grains is not exceeded, high speed reacting particles continually collide with stationary particles ahead of them. The speed of the reacting particles is considerably less than that of the wavefront. The reason for this appears to lie in the relationship between the sizes of the particles, the distances between them, the velocities imparted to them, and the compression to which they are subjected. A simple demonstration of this can be made by considering the following idealized situation.

A series of discs of thickness,  $b$ , are spaced a distance,  $a$ , apart as shown in Figure 3. If disc A is instantaneously imparted a velocity  $U$ , then it will take a time  $a/U$  to move a distance  $a$ . When disc A contacts disc B, it also is assumed to be instantaneously accelerated to a velocity  $U$ . However, the distance of the surface from the point at which disc A started moving is now  $a + b$ , whereas the time required for this surface to start moving is  $a/U$ . This process, if continued, would produce a wave of motion moving faster than each disc with a velocity given by the expression  $U(1 + b/a)$ . Writing the ratio  $b/a$  in terms of  $d_0$ , the initial density of the spaced out collection of discs, and  $d_c$ , the density of the discs when pushed together, gives for the wave velocity the expression  $U/(1 - d_0/d_c)$ . It is evident that the expression obtained is of the same form as that which is obtained on taking a mass balance for a detonation wave. However, the method of derivation emphasizes the collisional nature of the process. In the case of particulate flow, it is easy



Surface A is imparted a velocity  $U$  instantaneously  
*Figure 3. Diagram for Relating Wave to Particle Velocities in an Idealized Situation*

to understand how the wave arises as a continuous "knocking-on" between explosive particles, somewhat like a set of simply coupled boxcars being struck at one end by a locomotive.

## WAVEFRONT CURVATURE

Detonation wavefronts tend to become more curved as conditions for detonation failure are approached. In near failure conditions the detonation wavefront becomes highly curved, and flow divergence is reduced to such an extent that the flow behind the wavefront is almost plane.

A typical wave near to failure is shown in Figure 4. The divergence of the flow behind the reaction zone can be seen to be quite small.

Small divergence of flow  
 behind the reaction zone

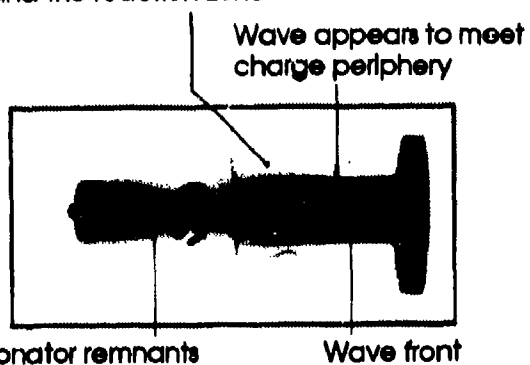
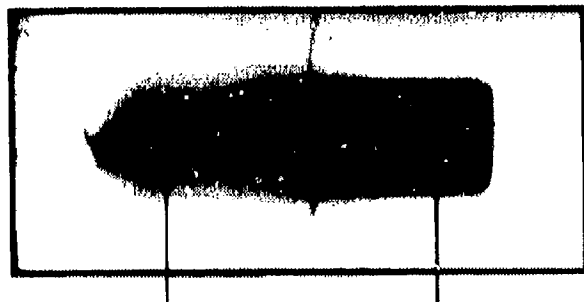


*Figure 4. X-Ray Photograph of a Highly Curved Detonation Wavefront*

Some wavefronts have a shape that is almost symmetrical about the charge axis, but many are not, and some are quite skew or have odd shapes as can be seen in Figure 5.



Detonator remnants      Position of Irregularity  
**Figure 5. X-Ray Photograph of an Oddly Shaped Detonation Wavefront**

The variations in waveshapes are thought to arise from variations in the distribution of the sensitizer, and its burning surface area, over a cross-section of a cartridge. The angle which a wavefront can make with a cartridge periphery cannot be less than or equal to 45 degrees because, as shown in Appendix B, there would be no compression, and the flow would not be divergent. The shapes of some wavefronts can be represented by a curve based on a parabola.

### THE SHAPE OF THE REACTION ZONE

The position of the back of the reaction zone, as assessed from discontinuities in plots of density versus distance behind the wavefront, lies approximately in a plane perpendicular to the charge axis, and cutting the charge periphery where the wavefront appears to meet it. Thus, the reaction zone has a shape that approximates that of a plano-convex lens.

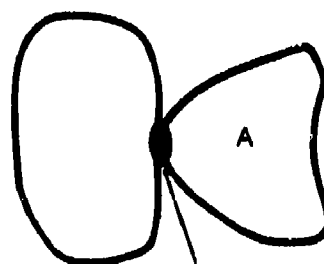
Wave curvature at the charge periphery is associated with material loss from the reaction zone which occurs by both lateral and radial expansion of the detonation products. When explosive is reacting rapidly, peripheral wave curvature appears small and tends to be restricted to extreme peripheral regions. Radial pressure gradients in the reaction zone induce radial transfers of detonating explosive. Diameter reductions increase the importance of radial losses, and cause pressure gradients to increase and penetrate deeper into the reaction zone. This leads to an overall reduction of pressures and reaction rates, and an extension of wave curvature to affect a greater proportion of the wavefront.

Waveshapes cannot be described in simple terms because they are the result of a complex interaction between reaction rates, flow conditions, and the initial condition of the explosive. Thus, waves will tend to assume different shapes depending on the precise conditions pertaining at any instant during detonation.

### A SUMMARY OF THE MAIN FEATURES OF THE DETONATION MODEL

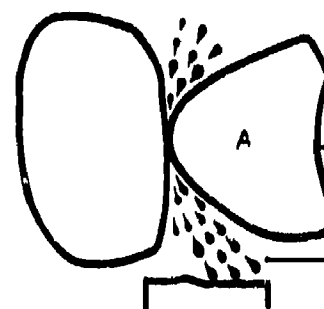
The observed reaction zone pressures are probably insufficient to exceed the mechanical strength of at least some of the granular components of the explosive, and so flow in the reaction zone is likely to be essentially particulate. The sudden compaction that occurs at the wavefront arises from the continuous collision of detonating particles with undetonated explosive. The collision processes cause substantial intergranular friction, and may also create many fast moving sensitizer droplets,<sup>5</sup> which impinge on adjacent sensitizer-coated surfaces in the explosive as depicted in Figure 6. This may contribute to the ignition of

BEFORE MOTION IS IMPARTED TO PARTICLE A



Sensitizer at point of contact

AFTER MOTION IS IMPARTED TO PARTICLE A



Motion imparted in this direction

Sensitizer droplets impinging on an adjacent surface

**Figure 6. The Formation of Fast Moving Sensitizer Droplets**

much of the sensitizer surface in under a microsecond. This seems to indicate that the wavefront region is likely to be about as wide as a typical particle of explosive, and that some reaction of the sensitizer takes place during the compaction process. Rapid reaction of the sensitizer in the wavefront region prevents densities increasing to at least voidless by filling the pores with high pressure gases.

The sensitizer layer burns erosively and is almost fully reacted at the end of the reaction zone at the charge axis, although this may not be the case for off-axis positions. Some breakage of the crystalline components of the explosive is also expected, arising from the frictional processes. Secondary components of the explosives are thought not to contribute significantly to the support of the detonation wave because they react too slowly in relation to the sensitizer.

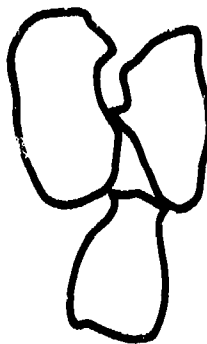
## EFFECTS OF COMPRESSION

When these types of explosives are slowly compressed in a press to a higher density than normal, the distances between constituent particles are reduced. In addition, the sensitizer must be gradually squeezed from between particles to form globules in the interstices as shown in Figure 7. Increasing the density of the explosives causes effects which include: reduction of the overall reaction rate by reducing the area of sensitizer available for erosive burning, reduction of the extent of frictional ignition, and reduction of the impulsive formation of sensitizer droplets so that there are fewer of them leading to less effective ignition. Together these processes reduce the ability of the explosive sensitizer to begin reacting and then to burn at a sufficient rate to support a detonation wave.

## MECHANISM OF DETONATION FAILURE

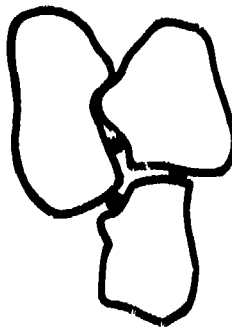
When a detonation wave is established in a cartridge of explosive of uniform density, diameter and sensitizer distribution, there is no reason for failure to occur. However, when a wave is travelling into explosive of increasing density and/or reducing diameter it will fail when the diameter becomes too small and/or the density becomes too large. When circumstances are such that detonation failure is

BEFORE COMPRESSION



Sensitizer distributed as a uniform layer

AFTER COMPRESSION



Dots indicate formation of globules of sensitizer

*Figure 7. Formation of Sensitizer Globules in Compressed Safety Explosives*

imminent only minor changes in conditions could lead to the failure process being initiated.

The detonation failure process is unlikely to be instantaneous since pressures and hence reaction rates are higher at the axis than the periphery of the charge, and so failure should take place from the periphery inwards. This may mean that during the course of failing, unstable waves having wavefronts of an apparently higher curvature than expected may be observed.

When failure occurs, the explosive particles at the wavefront are still moving in the direction of the wave and slam into undetonated explosive with a force that is sufficient to compact it to near voidless density. This compacted explosive is subsequently dispersed, but because it is relatively dense it appears on

sciagrams taken shortly after failure as accretions of dense material in the flow, as can be seen in Figure 8. The appearance of sciagrams of cartridges that have stopped detonating is characteristically different from those that are detonating, as can be seen by comparing Figures 4 and 8.

## A POSSIBLE METHOD OF ESTIMATING DETONATION FAILURE DIAMETERS

When detonation failure is imminent, experimental evidence indicates that the wavefront is approximately parabolic in shape, and appears to meet the charge periphery at very nearly 45 degrees. From this, and the geometry of a parabola that is symmetrical about the charge axis, it can be shown that the axial reaction zone length should be about a quarter of the length of the charge diameter. Flow divergence behind highly curved detonation wavefronts is very small, and so approximate estimates of axial reaction zone lengths, and hence failure diameters, might be made by applying plane wave detonation theory, although some allowance for reaction in the wavefront region might also be necessary.

## APPENDIX A

### Estimation of the Time Required to Achieve Maximum Compression in the Vicinity of the Wavefront

The volume of gas in one gram of explosive is given by:

$$V = 1/d_0 - 1/d_v \quad (A-1)$$

Where  $d_0$  is initial density and  $d_v$  is voidless density. The change in gas volume on changing the density from  $d_0$  to the compressed density  $d_c$  is  $D_v$  where:

$$D_v = 1/d_0 - 1/d_c \quad (A-2)$$

If there are  $n$  grains of explosive of typical average radius  $r$  in each gram of explosive, then the value of  $n$  is:

$$n = 3/(4 \cdot \pi \cdot r^3 \cdot d_v) \quad (A-3)$$

If it is assumed that there are as many gas spaces as particles in the explosive, then



Detonator remnants

Accretions of undetonated explosives

Figure 8. X-Ray Photograph of a Failed Detonation Wave Showing Accretions of Dense Material in the Flow

the change in volume of each gas space on changing density from  $d_0$  to  $d_c$  is  $V_g$  where:

$$V_g = 4 \cdot \pi \cdot r^3 \cdot d_v \cdot (d_c - d_0) / (3 \cdot d_0 \cdot d_v) \quad (A-4)$$

If the average cross-sectional area of a particle is  $a$ , and  $s$  is the distance moved to effect the volume change then:

$$s = V_g / a \quad (A-5)$$

If it is now assumed that the closing movement takes place at a constant velocity of  $U$ , where  $U$  can be written from detonation theory as:

$$U = D \cdot (d_c - d_0) / d_c \quad (A-6)$$

and  $T$  is the time taken for the compaction process to occur, then Equations (A-4), (A-5), and (A-6) lead to:

$$T = 4 \cdot r \cdot d_v / (3 \cdot d_0 \cdot D) \quad (A-7)$$

## APPENDIX B

### Flow Divergence Behind a Curved Detonation Wave in a Cylindrical Cartridge of Explosive

The divergence of flow at any given point behind a moving curved detonation wavefront in a cylindrical cartridge of explosive can be evaluated in terms of the

compressed density of the particle, and the initial density of the explosive.

Figure 9 shows a particle immediately behind the wavefront having a velocity  $V$ , and travelling in a direction  $AB$ , while the wavefront is travelling in the direction  $AC$  parallel to the axis of the cartridge. If the time required for the wavefront to move from  $A$  to  $C$  is  $dt$ , where  $dt$  is vanishingly small, then the distance moved by the wavefront along  $AC$  is  $Ddt$ , and the distance moved by the particle along  $AB$  is  $Vdt$ . Applying the sine rule to triangle  $ABC$  gives:

$$V \cdot \sin(180 - G - Q) = D \cdot \sin(G) \quad (B-1)$$

where  $G$  is the angle between sides  $AC$  and  $BC$  and is a measure of the divergence of the flow, and  $Q$  is the angle between the charge axis and the normal to the wavefront at point  $A$ .  $V$  is obtained by treating the wavefront as a connected set of small plane oblique shock waves, and applying mass momentum and energy balances to each as described by Shapiro.<sup>6</sup>  $V$  can be expressed as:

$$V = D \cdot (1 - d_0/d_c) \cdot \cos(Q) \quad (B-2)$$

where  $d_0$  is the initial density of the explosive, and  $d_c$  is the compressed density at point  $A$  of Figure 9.

Equations (B-1) and (B-2) give:

$$\tan(G) = (d_c - d_0) \cdot \tan(Q) / (d_0 + d_c \cdot \tan^2(Q)) \quad (B-3)$$

For constant values of  $d_0$  and  $d_c$  the value of  $G$  reaches a maximum value,  $G_m$  when  $Q$  reaches a value,  $Q_m$ , such that:

$$\tan(Q_m) = (d_0/d_c)^{1/2} \quad (B-4)$$

and

$$\tan(G_m) = (d_0/d_c - 1) \cdot \tan(Q_m) / 2 \quad (B-5)$$

It is clear from equation (B-4) that  $Q_m$  cannot have a value greater than 45 degrees, because for detonation to occur  $d_0$  must be greater than  $d_c$ . Also Equation (B-5) indicates that in conditions in which values of  $d_0$

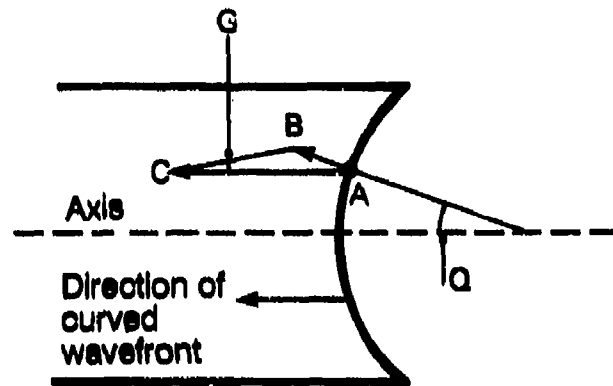


Figure 9. Diagram For Calculating Flow Divergence Behind a Curved Detonation Wavefront

approach values of  $d_0$ , such as when detonation is near to failure the value of  $G$ , the angle of divergence, approaches zero; that is the flow is almost plane.

## REFERENCES

1. Kennedy, M. and Kerr, I. D., "Studies of a Mechanism of Deflagration During Delay Round Firing in Coal," *Propellants and Explosives*, Vol. 5, 1980, pp. 29-33.
2. Kennedy, M. and Kerr, I. D., "Studies of Weakly Detonating Mining Safety Explosives," *Proceedings of the 17th International Conference of ICT, Karlsruhe, West Germany, 27-29 Jun 1986*, pp. 30-1 to 30-14.
3. Plant, J. and Barbero, L. P., *Deflagration and Detonation in Certain British Mining Safety Explosives*, Safety in Mines Research Establishment, Sheffield, England, Research Report No. 258, 1969.
4. Dauge, G.; Giraudu, J. P.; and Ficat, R., "Pressure Dependence of Solid Explosives Initiation," *Proceedings of the 15th Symposium (International) on Combustion, Tokyo, 25-31 Aug 1974*, p. 21.
5. Kennedy, M. and Kerr, I. D., "The Development of a Model of the Reaction Zones of Weakly Detonating Mining

**Safety Explosives Sensitized by Mixtures of Nitroglycerine and Ethylene Glycol Dinitrate," *Proceedings of the 19th International Conference of ICT*, Karlsruhe, West Germany, 29 Jun-1 Jul 1988, pp. 35-1 to 35-14.**

**6. Shapiro, A. H., *The Dynamics and Thermodynamics of Compressible Flow*, The Ronald Press Company, New York, Vol. 1, 1953, pp. 529-531.**

# EXPERIMENTAL STUDIES ON THE DETONATION OF AN EXPLOSIVE BY MULTI-POINT INITIATION

Yu Jun, Fu Xinghai, and Zhang Guanren  
Southwest Institute of Fluid Physics  
P.O. Box 523, Chengdu, CHINA

*This paper describes the experimental studies on the problem of multi-point initiation of detonation of an explosive slab. By means of flash gaps method, we obtained the shape of a flyer driving by the plane explosive and its velocity distribution. Through analysis of its average velocity, we conclude that there is a loss of energy for multi-point initiation while comparing with the full surface initiation.*

## INTRODUCTION

Multi-point initiation of detonation is a general method for obtaining surface initiation of explosives. References 1 and 2 are studies of the total time from multi-point initiation of a plane explosive, and the flying time of a flyer driven by the explosive by the method of fiber-optical pins. In this paper, we used the flash gaps method and a method of analysis to treat the experimental data, obtain the shape of the flyer, and the velocity distribution of the flyer under various thicknesses of the explosive. Then the average kinetic energy of the flyer was obtained. Obviously, this energy is the effective energy of the explosive imparted to the flyer.

## EXPERIMENTAL METHOD AND DATA TREATMENT

The experimental setup is shown in Figure 1; Line MM' is the slit for the high-speed camera. A layer of  $\text{Ba}(\text{NO}_3)_2$  powder is pasted on the surface of the flyer to give the initial light signal when the shock passes through it. Two successive air gaps can give two successive wave forms of the shock at two different places in the target. The thickness of the explosive H are 20 mm, 30 mm, 40 mm, and 50 mm, respectively. The flying distance of the flyer keeps constant as 35 mm. A typical photograph of the high-speed camera is shown in Figure 2. In order to prove the reliability of the method of our treatment of the

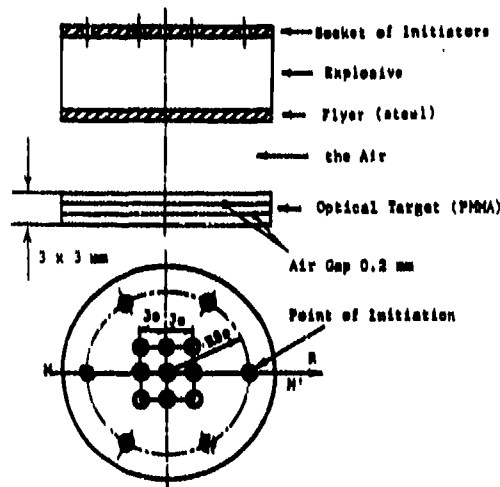


Figure 1. Schematic Diagram of Experimental Setup (Above: Experimental Setup; Below: Distribution of Multi-Point Initiation)

experimental data, we used a one-point initiation of the explosive to drive a flyer and measured the shape of the flyer by flash X-ray photographic method and the pressure with Mangarin gauges in the target, then compared them with the treated results.

### Method of Experimental Data Treatment

We suppose: (1) Neglect the attenuation of the shock wave between the two air gaps in the target; (2) The velocity of the shock wave in the target is perpendicular to the wave front; and (3) Neglect the attenuation of the velocity of the flyer during impact.



Figure 2. Photographs of the Shock Wave Form of One-Point Initiation (Above) and Multi-Point Initiation (Below)

### Determination of the Shock Wave Front<sup>3</sup>

In Figure 3, the shock wave form is two-dimensional; we drew a broken line AS to replace the curved front AQ, so the curved shock wave could be treated as a series of plane shock waves.

Thus, the local shock velocity  $D_2$  and its angle of inclination  $\beta$  at point A could be determined by the following formula:

$$D_2 = \frac{\Delta X}{t_{A1} - t_A} \sin \beta$$

$$\cos \beta = D_2(t_B - t_A) / h_2 \quad (1)$$

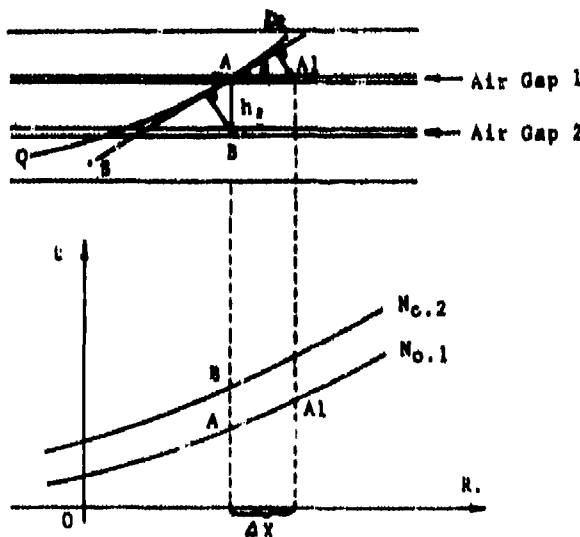


Figure 3. Schematic Diagram of Treatment of the Curved Shock Wave Front

Taking  $\Delta X$  as small as possible, then we get the all parameters of the shock wave.

### Determination of the Flyer at the Instant of Impact<sup>4</sup>

See Figure 4; by boundary conditions of the flyer and the target, we could get the relations of the flyer and the shock wave in the target by following:

$$C_{01} + \lambda_1 U_1 = W \cos \theta \sin(\alpha + \theta)$$

$$(C_{01} + \lambda_1 U_1) \operatorname{tg}(\alpha + \theta - \epsilon_1) = [C_{01} - (\lambda_1 - 1)U_1] \operatorname{tg}(\alpha + \theta)$$

$$P_1 = \rho_{01} U_1 (C_{01} + \lambda_1 U_1)$$

$$D_2 = W \sin \beta / \sin \theta$$

$$D_2 \operatorname{tg}(\beta - \epsilon_2) = (D_2 - U_2) \operatorname{tg} \beta$$

$$P_3 = \rho_{02} U_2 D_2$$

$$P_1 = P_3$$

$$\theta = \epsilon_1 + \epsilon_2 \quad (2)$$

Where  $C_{01}$ ,  $\lambda_1$ ,  $\rho_{01}$  are the sound speed; proportional constant in  $D, U$  linear relation; and density of the flyer, respectively;  $C_{02}$ ,  $\lambda_2$ , and  $\rho_{02}$  are those of the target;  $\beta$ ,  $\epsilon_1$ ,  $\epsilon_2$ , and  $\alpha$  are defined in Figure 4;  $W$  is the flyer velocity; and  $\theta$  is its impacting angle. There are eight equations and ten unknowns, if  $D_2$  and  $\beta$  were gotten from Equation (1), the system of equations would be solved.

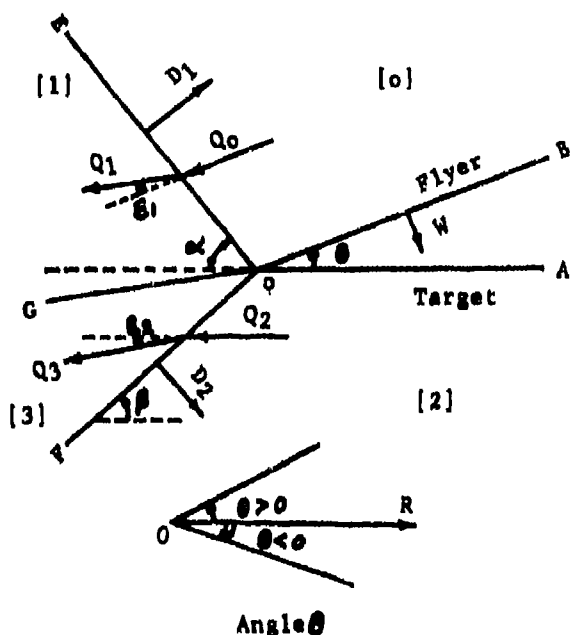


Figure 4. Schematic Diagram of the Wave System of the Flyer Impacting with the Target

After getting  $W$  and  $\theta$ , the shape of the flyer before impacting would be known. As Figure 3, from point to point, the whole shape of the flyer could be obtained.

## RESULTS

The results of one-point initiation, both treated by optical data and measured by Manganin gauges and flash X-rays, are listed in Tables 1 and 2. They are in good agreement, so the reliability of our method is approved.

For multi-point initiation, the results obtained from the above method are shown in Figures 5 through 7. We can see that the time of flight of the flyer in the air increases with a decrease of the explosive. In Figure 8, we drew

Table 1. Comparing the Treated Pressure in the Target with the Measured Pressure

One-Point initiation (H = 50 mm)				
R(mm)	5	25	35	55
$P_{mea.}$ (GPa)	9.99	7.60	6.95	6.28
$P_{tru.}$ (GPa)	9.42	7.79	7.06	5.93

the results of full surface initiation with one-dimensional calculation of the flyer in the same figure for comparison. It shows that their differences decrease with an increase of the thickness of the explosive which means the influence of the multi-point initiation decreases with the increase of the thickness of the explosive as well. There exists an energy loss in multi-point initiation for all cases.

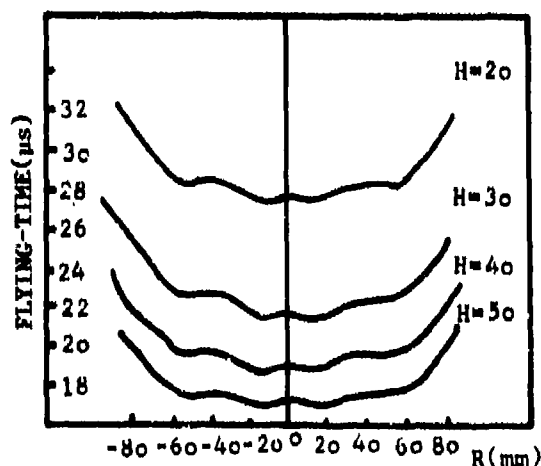


Figure 5. Time of the Flyers Flying in Given Distance

Table 2. Comparing the Shape of the Flyer Treated by Optical Data With that of the Flash X-Rays

R(mm)	-43.16	-38.49	-33.68	-28.10	-21.55	-4.75	0
$Y_{tre.}$ (mm)	4.14	3.38	2.67	2.03	1.31	0.11	0
$Y_{X-ray}$ (mm)	4.17	3.42	2.77	2.10	1.30	0.07	0
R(mm)	8.43	17.87	23.19	28.56	37.25	43.44	
$Y_{tre.}$ (mm)	0.29	0.98	1.43	2.18	3.32	4.25	
$Y_{X-ray}$	0.25	0.98	1.52	2.17	3.27	4.18	

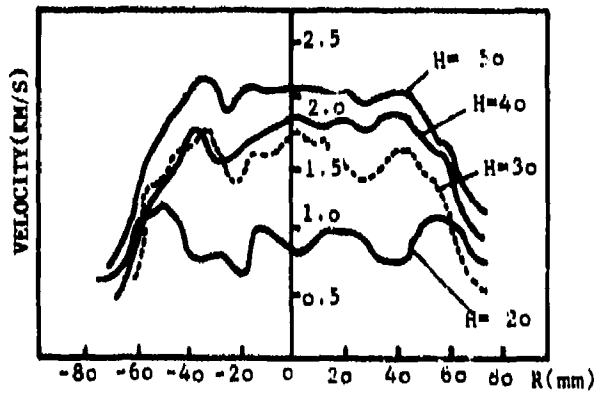


Figure 6. Impacting Velocity of the Flyers

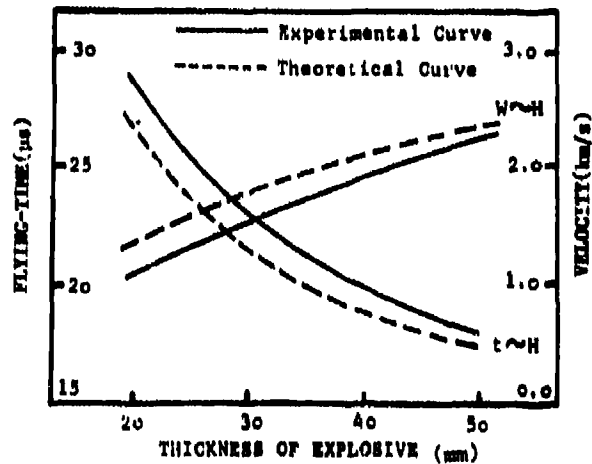


Figure 8.  $t \sim H, W \sim H$  Curves

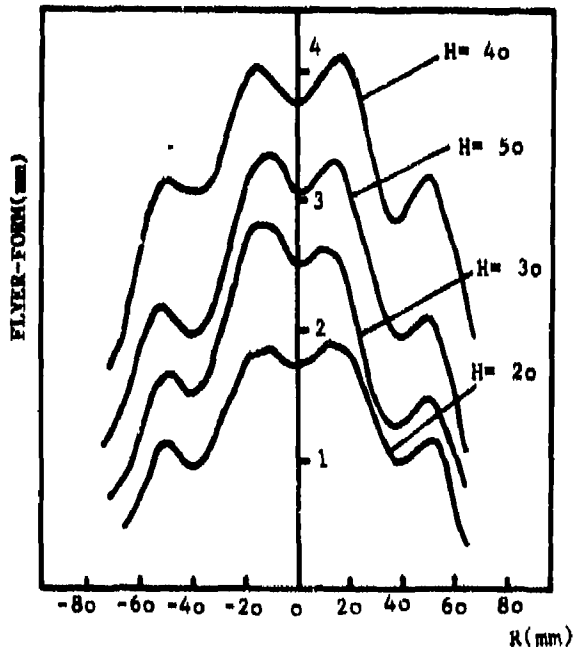


Figure 7. Shapes of the Flyers

## DISCUSSION

For multi-point initiation of detonation of a slab explosive, the initial detonation wave form is not a plane but a zigzag wave front with multi-spherical divergent forms. After interaction of spherical waves, the wave

front may be flattened a little in the explosive, but they still remain during flying in the air. They transport to the shock wave in the target as well. So we conclude that the initial zigzag pattern may keep at least for a long distance.

## REFERENCES

1. Guoqing, Y., "Experimental Studies on the Combined Detonation Profile in an Explosive Slab Initiated at Multiple Points," China Nuclear Science and Technology Report, CNIC-00103, 1987.
2. Guoqing, Y., et al., "The Energy Loss of a Flyer Driven by a Slab Explosive Initiated at Multiple Points," Proceedings of the Nineteenth International ICT Conference, 84-1-5, 1988.
3. Xinghai, F., "Measurement of Two-Dimensional Shock Wave Velocities and a Composite Probe," Proceedings of Eighth Symposium (International) on Detonation, (Preprint), 1985, pp. 528-532.
4. Fuqian, J., et al., *Introduction to the Experimental Equation of State*, First Edition, Science Publisher, China, 1986, pp. 136-140 and 307-310 (in Chinese).

# DETONATION PROPERTIES OF EXPLOSIVE FOAMS

C. J. Anderson\* and K. Von Rosen  
Mining Resource Engineering Limited  
Kingston, Ontario  
CANADA K7L 4V4

and

A. W. Gibb and I. O. Moen  
Defence Research Establishment Suffield  
Ralston, Alberta  
CANADA T0J 2N0

*This paper reports on the detonation properties of two types of explosive foams. The first foam consists of PETN dust dispersed evenly throughout a solid polyurethane foam matrix. Detonable 60/40 (weight percent) PETN/polyurethane foams with densities between 0.15 and 0.7 g/cc have been produced. The detonation velocities range from 1.5 to 3.0 km/s with corresponding pressures between 20 bar and 20 kbar. The second foam consists of liquid nitromethane that has been mixed with liquid surfactants and gassing agents. This foam has a consistency similar to shaving cream, with densities from 0.07 to 0.7 g/cc. The detonation velocities range from 1.8 to 4.4 km/s with corresponding pressures between 20 bar and 30 kbar. Detonation properties reported for each type of foam include detonability limits and theoretical/experimental detonation velocities and pressures as a function of density.*

## INTRODUCTION

The detonation properties of solid high density ( $\geq 1.0$  g/cc) explosives have been extensively investigated. These types of explosives have detonation pressures of several hundred kbar and detonation velocities up to 9 km/s. At the other end of the spectrum are fuel-air (or fuel-oxygen) explosives whose detonation pressures are less than 20 bar (50 bar) with detonation velocities less than 2 km/s (3 km/s). Explosive systems covering the entire range of detonation velocities and pressures between these two extremes are theoretically possible, but only a few such systems have been studied experimentally.

\* Person to whom correspondence should be addressed.

The most straightforward method of varying the detonation pressure and velocity is to vary the density of high explosive loading. Tullis<sup>1</sup> has shown that clouds of high explosive dusts dispersed into air can produce detonation pressures (100 bar) well in excess of those obtained in fuel-air or fuel-oxygen systems.

A potentially more effective method of producing explosive systems with low loading densities and uniform detonation properties is to disperse the high explosive in a high porosity foam matrix. An alternative method is to produce an explosive foam using a liquid explosive. This paper presents the results of an investigation of the detonation properties of two types of explosive foams: PETN dispersed in a polyurethane foam matrix, and nitromethane-based explosive foams. Detonation properties reported for each type of foam include detonability limits, and theoretical/experimental

detonation velocities and pressures as a function of density.

## EXPLOSIVE FOAMS

Detonable foams consisting of an open-cell structure urethane matrix impregnated with PETN were produced by Makomaski and Darling.<sup>2</sup> The explosive loading density of these foams was approximately 0.45 g/cc.

Tulis et al.<sup>3</sup> have investigated the feasibility of low explosive density detonation. An open-celled matrix, either ethyl cellulose or glass wool, contained 50-60 percent PETN with a density of approximately 0.1 g/cc. These explosive formulations failed to detonate. Earlier research by Austing and Tulis<sup>4,5</sup> using explosive dispersed in polyurethane foams had established the potential detonability of these low density systems.

Xueguo<sup>6</sup> has examined the detonation characteristics of PETN/polyurethane foam. PETN concentrations were 40 or 50 percent by weight, with foam densities ranging from 0.30 g/cc to 0.90 g/cc. The minimum PETN density for steady detonation was 0.27 g/cc. The charge diameter was 60 mm (2.4 inches).

The solid explosive foam used in the present investigation consists of a high explosive component (PETN) dispersed evenly throughout a polymeric foam matrix. The foam is produced from polyurethane, which produces low density foams having a uniform closed-cell foam structure. This structure helps prevent moisture desensitization of the explosive. The density of the foam is controlled through the addition of water (0-0.5 percent by weight). The PETN concentration, unless otherwise specified, is 60 percent by weight of the explosive foam. PETN particle size averaged 50-70 microns.

The nitromethane foam used in the present investigation is based on aerosol technology and emulsion science. Nitromethane is the explosive component, and generally comprises 78-92 percent by weight of the foam. This system is an example of a non-aqueous foam. Although not as thoroughly studied as aqueous foams, non-aqueous foams have received increasing interest due to the

problem of petroleum refining.<sup>7-10</sup> It appears that the non-aqueous foam may be stabilized by the presence of a liquid crystalline phase formed at the interface of the liquid/gas surface.

Pool<sup>11</sup> had previously developed a foamed liquid explosive composition based on nitromethane with added metal stearate surfactants. The liquid composition was whipped into a semi-stable foam. The foam density was approximately 0.5 g/cc. The foam drainage characteristics were rather poor. Alford<sup>12</sup> describes a liquid foamed explosive produced from an aerosol-type container. The foam is based on an aqueous solution which contains inorganic nitrates and PETN.

## EXPERIMENTAL

Polyurethane foams are produced by the exothermic reaction between a polyol and diisocyanate which crosslink and, under influence of a blowing agent, expand to produce a cellular structure. The PETN/polyurethane foam charges were formed by mixing the appropriate amounts of diisocyanate, polyol, and PETN to produce a foam that was 60 percent PETN by weight. The density of the foam was varied between 0.1 g/cc and 0.7 g/cc using polyols supplied by the manufacturer. The polyurethane system has a cream time of 1.5 minutes and a rise time of approximately 2 minutes.

Foam density was measured by cutting a sample of the foam, weighing it, and then determining the volume of water displaced by the foam. Detonation velocity of the foam was measured using a continuous resistance probe<sup>13</sup> implanted in the foam along the long axis. Detonation pressures of the PETN/polyurethane foamed explosive were measured using the aquarium technique outlined by Cook.<sup>14</sup>

Nitromethane foams were prepared by dissolving the appropriate amount of surfactant in the nitromethane, adding the thickening agent (and DETA if required), and then transferring the solution to a converted fire extinguisher. The desired amount of liquid propellant was then added. The solution was agitated for a period of 2 minutes which

ensured the generation of the necessary emulsion for foam formation. Density measurements were conducted by weighing a known volume of the foam. The detonation velocities of the nitromethane foams were measured using pin-switch probes.

Air-gap sensitivity tests on the nitromethane foam were conducted using 5 cm thick x 15 cm wide foams. The critical thickness of the foam is less than 5 cm. Donor charges were 38 cm long and were center initiated at one end. Receptor charges were 30 cm long. Masking tape was used to define the borders for these trials. A typical configuration is illustrated in Figure 1.

The thermohydrodynamic computer code TIGER was used for the calculation of theoretical detonation pressures and velocities.<sup>15</sup> The code used a modified, calibrated BKW equation of state.<sup>16,17</sup>

All charges were fired with a zero delay, 0.8 g (12 grains) PETN Electric Blasting Cap (hereafter referred to as EBC). Some trials used high explosive booster charges consisting of Composition C-4 (91 percent by weight RDX), or military plastic explosive DM12

(86 percent by weight PETN). Booster sizes varied between 3 g and 50 g.

## RESULTS AND DISCUSSION

### PETN/Polyurethane Foam

Figures 2 and 3 show the detonation velocities and pressures as a function of density for a 60/40 PETN/polyurethane foam system. The theoretical curves have been calculated using the thermohydrodynamic TIGER code, with a modified BKW equation of state. Pressures were approximated using the relationship:

$$N = (D/D^*)^2 = P/P^* \quad (1)$$

Here  $N$  is the degree or fraction reacted in the detonation,  $D$  is the measured velocity,  $D^*$  is the thermohydrodynamic velocity of detonation at the same density, and  $P^*$  is the thermohydrodynamic detonation pressure.  $D^*$  and  $P^*$  are calculated from TIGER. The above approximation is valid only if the ratio of particle velocity to detonation velocity is constant in an explosive foam at a given density.<sup>18</sup>

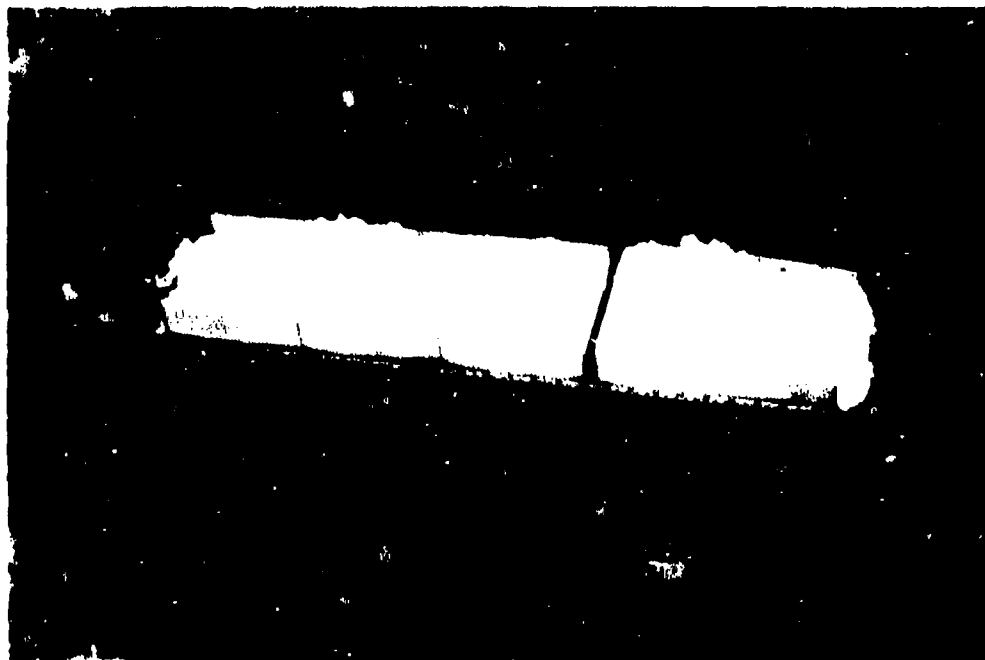


*Figure 1. Illustration of Typical Charge Setup for Determination of Air-Gap Sensitivity of Nitromethane Foam*

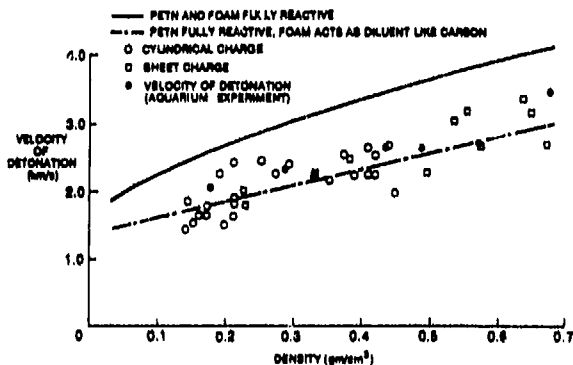


Figure 2. Detonation Velocity Versus Density for 60/40 PETN/Polyurethane Foam. The curves are calculated using the thermohydrodynamic code TIGER and a modified BKW equation of state. Charge configurations included slabs and cylinders

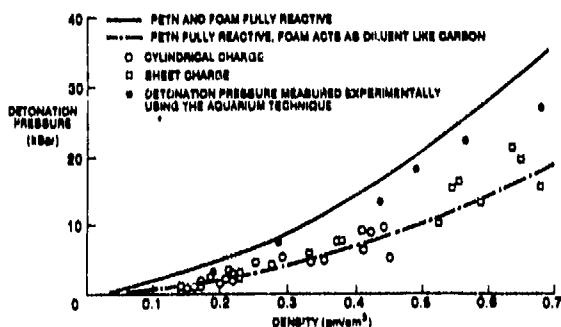


Figure 3. Detonation Pressure Versus Density for 60/40 PETN/Polyurethane Foam. The curves are calculated using the thermohydrodynamic code TIGER and a modified BKW EOS. Charge configurations included slabs and cylinders

The pressures measured with the aquarium technique (Figure 3) are consistently higher than the pressures calculated from Equation (1). The measured detonation velocities from the aquarium technique, however, are consistent with the detonation velocities measured for the slabs of foam. This discrepancy may be attributed to the non-ideal behavior of the foam, or to the non-validity of Equation (1). The scatter in the experimental data is likely due to the variation in explosive foam thickness.

There are also some questions concerning the validity of the aquarium test for determining the detonation pressure of low density explosives. Austing et al.<sup>4</sup> have noted a problem with impedance mismatch for materials of significantly different density. Tulis and Austing<sup>5</sup> have described a system which gives reasonable detonation pressure values for very low density explosive systems. The method utilizes a flash x-ray system, and measurement of the particle and shock velocities of the foamed explosive. The use of this method to determine experimentally the detonation properties of the PETN/polyurethane foams would provide a check on the experimental data obtained from the aquarium technique.

A series of experiments was carried out to determine the relationship between foam thickness and the critical foam density for successful initiation for two different primer strengths. Figure 4 illustrates the critical density for detonation propagation/failure as a function of thickness for a PETN/polyurethane foam slab 15 cm wide x 75 cm long lying on the ground surface. The slab was initiated by a

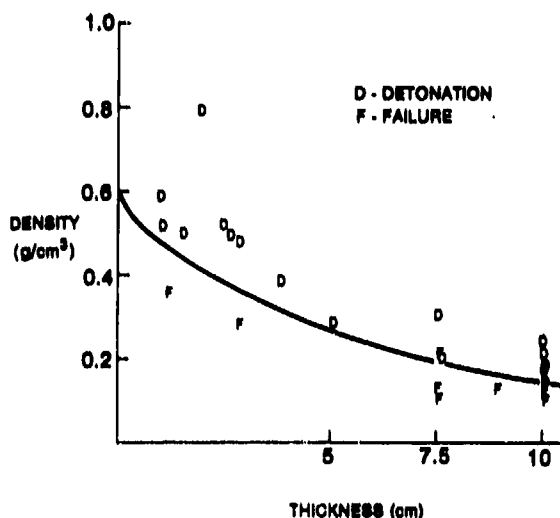


Figure 4. Critical Thickness and Density of 60/40 PETN/Polyurethane Foam. Initiating explosive was either an EBC or an EBC plus Composition C-4 booster.

single EBC. Critical density drops sharply for thicknesses up to 5 cm; the decline is less rapid for thicknesses between 7.5 cm and 10.0 cm. A number of tests were also conducted on end-initiated thin-walled cardboard tubes filled with explosive foam. The primer was an EBC plus 3 g of C-4. For tube inside diameters of 5.1 cm, 7.6 cm, and 10.2 cm, the critical densities were 0.33 g/cc, 0.21 g/cc, and 0.24 g/cc, respectively ( $\pm 0.02$  g/cc). These critical densities show the same general trend as, but are somewhat higher than, those observed for foam slabs at the same thickness (Figure 4). The lower critical thicknesses observed for the foam slabs with lower primer weight are likely due to the confining effect of the ground surface.

### Nitromethane Foam

It is well-known that nitromethane will detonate if exposed to the proper conditions of chemical treatment and shock. The pure organic liquid is relatively insensitive to detonation. Addition of 5-10 percent of ethylene diamine (ED) or other related amine, such as DETA, results in a cap-sensitive nitromethane solution in which a detonation will propagate reliably, even through small and changing diameters. Entrapment of air bubbles or suspension of glass microballoons will also significantly increase the sensitivity of nitromethane. A review of developments in nitromethane-based liquid explosives has been published by Egly.<sup>19</sup>

Figures 5 and 6 illustrate the dependence of detonation velocity and pressure on nitromethane foam density. The theoretical curves were calculated using the thermohydrodynamic code TIGER. The experimental scatter can be attributed to the different thicknesses of the foams and to the range of nitromethane concentration (80-90 percent). It is clear that detonation velocities and pressures of the order of 1.8 - 4.0 km/s and 20 bar - 30 kbar, respectively, can be generated by this foam system.

Figure 7 illustrates the effect of various sensitizers on the critical density of the nitromethane foam. It is clear that above a density of 0.2 g/cc the addition of sensitizers is unnecessary. It should also be noted that the foam is

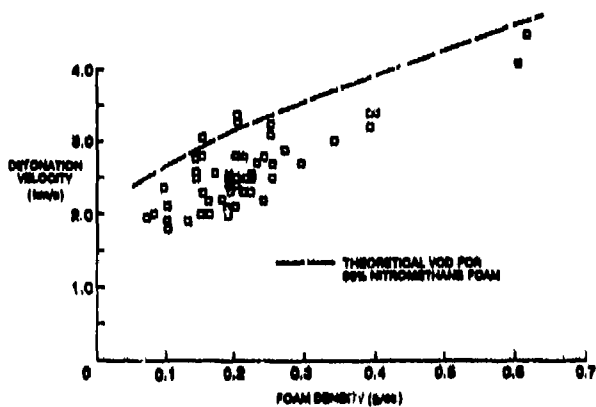


Figure 5. Detonation Velocity Versus Density for 80-94 Percent Nitromethane Foam. Theoretical curve calculated using the thermohydrodynamic code TIGER and a modified BKW EOS.

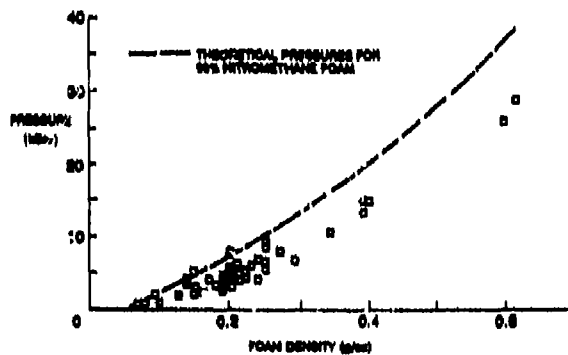


Figure 6. Detonation Pressure Versus Density for 80-94 Percent Nitromethane Foam. Theoretical curve calculated using the thermohydrodynamic code TIGER and a modified BKW EOS.

cap-sensitive above a density of 0.20 g/cc. Below this density unsensitized foams can be detonated provided a suitable booster charge and foam thickness are used. For example, a layer of nitromethane foam 5 cm thick, foam density 0.15 g/cc, can be detonated using an EBC and a booster charge of 50 g C-4 or DM12. As well, the EBC will detonate a nitromethane foam having a density of 0.25 g/cc and a thickness of 1.2 cm. These values can be compared with a critical diameter of the order of 0.5 cm for chemically sensitized liquid nitromethane initiated with an EBC.

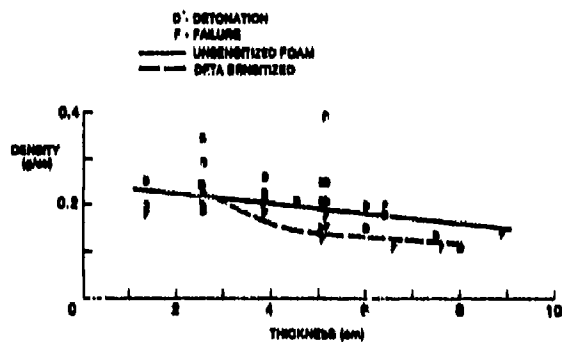


Figure 7. Critical Thickness and Density of 80-94 Percent Nitromethane Foam Slabs. The data includes foams containing 4 percent DETA (weight percent). Initiating explosive was either an EBC or an EBC plus Composition C-4 booster.

Figure 8 outlines the dependence of critical air-gap on density for a 5 cm thick layer of nitromethane foam. The trials at a density of 1.19 g/cc used a nitromethane gel composed of thickener and 1 percent microballoons. The microballoons generate the tiny "hot spots" necessary to sensitize the foam. As well, these voids simulate the voids generated by the gassing agent in the actual nitromethane foam. Detonation velocities in the receptor charges were recorded as a method of determining detonation/failure of the trial. The dependence of critical gap on foam density appears to be linear.

## CONCLUSIONS

Both the PETN/polyurethane foam and the nitromethane foam demonstrate the ability to offer variable density explosive systems which can be adjusted to obtain the required pressures. Detonable 60/40 (weight percent) PETN/polyurethane foams with densities between 0.15 and 0.7 g/cc have been produced. The detonation velocities range from 1.5 to 3.0 km/s with corresponding pressures between 20 bar and 20 kbar. The nitromethane foam has been examined for densities from 0.07 to 0.7 g/cc. The detonation velocities range from 1.8 to 4.4 km/s with corresponding pressures between 20 bar and 30 kbar. Detonation properties reported for each type of foam include detonability limits, and theoretical/

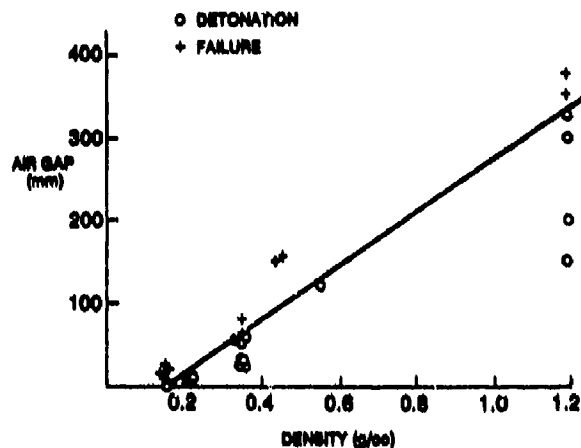


Figure 8. Dependence of Detonation/Failure on Air-Gap and Density for a 5 cm Thick Layer of Nitromethane Foam

experimental detonation velocities and pressures as a function of density.

Other research has established the feasibility of incorporating a reactive polymer matrix, and of developing a flexible foam matrix for use in the PETN/polyurethane foam system. As well, future research has targeted the use of sensitivity tests such as gap and projectile impact tests to further delineate useful parameters for these explosive systems.

## ACKNOWLEDGEMENTS

This work was performed under contract with the Canadian Department of National Defence for Defence Research Establishment Suffield. The authors are indebted to M. Baker of CXA Canada, who performed many of the initial trials; and for the leadership provided by the late Dr. A. Bauer, founder of Mining Resource Engineering Limited.

## REFERENCES

1. Tulis, A. J., "Analytical and Experimental Characterization of Explosives," *Proceedings of the 12th Symposium on Explosives and Pyrotechnics*, Mar 1984, p. 1-1.
2. Makomaski, A. H. and Darling, J. A., "A Method of Preparation of PETN-Impregnated Foams Capable of Initiation

- by Gaseous Detonation Waves," National Research Council of Canada, DME Mech. Eng. Report MT-60, Feb 1968.
3. Tulis, A. J.; Austing, J. L.; and Baker, D. E., "Open Matrix Very Low Density Explosive Formulations," *J. Hazardous Materials*, Vol. 5, 1982, p. 387.
  4. Austing, J. L.; Tulis, A. J.; and Johnson, C. D., "Detonation Characteristics of Very Low Density Explosive Systems," *Fifth Symposium (International) on Detonation*, ACR-184. ONR, 1970, p. 47.
  5. Tulis, A. J. and Austing, J. L., "Further Studies on the Detonation Characteristics of Very Low Density Explosive Systems," *Sixth Symposium (International) on Detonation*, 1976, p. 183.
  6. Xueguo. L., "Detonation Characteristics of Polyurethane Foamed Explosives," *Proceedings of the International Symposium on Intense Dynamic Loading and Its Effects*, Beijing, China, 1986, p. 173.
  7. Ross, S. and Nishioka, G., "Dynamic Foam: A Problem in Fraction and Distillation Towers," *Chemistry and Industry*, 1981, p. 47.
  8. Friberg, S. and Cox, J. M., "Stable Foams from Non-Aqueous Liquids," *Chemistry and Industry*, 1981, p. 50.
  9. Callaghan, I. and Neustadter, E., "Foaming of Crude Oils: A Study of Non-Aqueous Foam Stability," *Chemistry and Industry*, 1981, p. 53.
  10. Ottewill, R.; Segal, D.; and Watkins, R., "Studies on the Properties of Foams Formed from Non-Aqueous Dispersions," *Chemistry and Industry*, 1981, p. 57.
  11. Pool, J. E., U.S. Patent 2,967,099, 1961.
  12. Alford, S. C., "Explosives Foams," *Explosives Engineer*, 1985, p. 76.
  13. Ribovich, J.; Watson, R.; and Gibson, F., *AIAA J.*, Vol. 6, 1968, p.1260.
  14. Cook M. A., *The Science of Industrial Explosives*, IRECO Chemicals, Salt Lake City, 1974.
  15. Cowperthwaite, M. and Zwisler, W. H., *Theoretical and Mathematical Formulations for the Tiger Computer Program*, Stanford Research Institute, California, 1973.
  16. Mader, C. L., *Detonation Properties of Condensed Explosives Using the Becker-Kistiakowsky-Wilson Equation of State*, Los Alamos Scientific Laboratory, LA-2900, 1963.
  17. Katsabanis, P., *Studies on the Numerical Modelling of Explosives Performance and Sensitivity*, Ph.D. Dissertation, Queen's University, Kingston, Ontario, Canada, Oct 1987.
  18. Cook, M. A., *The Science of High Explosives*, Reinhold Publishing Co., 1958.
  19. Egly, R. S., "Recent Developments in Nitromethane-Based Liquid Explosives," *Proceedings of the Symposium on Military Applications of Commercial Explosives*, Defence Research Establishment, Val-Cartier, Quebec, Canada, 1972, p. 190.

# F. P. I. VELOCIMETRY TECHNIQUES APPLIED TO VARIOUS PROBLEMS IN DETONICS

P. Gimenez, J. P. Bedoch, C. Saint-Martin,  
G. Baudin, and Y. de Longueville  
Centre d'Etudes de Gramat  
46500 - Gramat, FRANCE

*Various applications of Fabry-Perot interferometry are described in order to show the possibilities of this technique applied in the field of detonics. First, usual tests in steady geometry demonstrate and begin to quantify the role of aluminum in a composite explosive. Then, three other examples show the possibilities of this technique in more difficult experimental conditions (with intrusive light, difficult access, and simultaneous measurements in divergent geometry).*

## INTRODUCTION

Velocimetry with a Fabry-Perot interferometer (F.P.I.) is a technique increasingly used in detonics and has recently been the subject of a detailed review article by McMillan, et al.<sup>1</sup> Currently available articles on the F.P.I. most often deal with their use in laboratory experiments such as plate push tests or cylinder tests.<sup>2</sup> In these cases, the advantage of using an F.P.I. lies in the wealth of information contained in a continuous velocity history compared with what can be obtained from classical chronometry. However, the F.P.I. also makes it possible to monitor more complex devices for which classical techniques are unsuitable. Our purpose here is to illustrate the advantages of this technique. First, there is a brief description of the F.P.I. used. The wealth of the information obtained is then illustrated in classical cylinder (C.T.) and symmetrical plane (S.P.T) tests which make it possible to study the influence of aluminum on the ballistic properties of an explosive. The last part describes three applications showing the scope of this technique in less usual tests.

## PRESENTATION OF THE F.P.I.

The F.P.I. used for the tests discussed below is outlined in Figure 1. The target is

illuminated by an argon-ion laser continuously providing about 5 watts.

The beam can be transported by mirror or by means of an optic fiber.<sup>3</sup> In the latter case, a single fiber is used for both the outgoing and return beam. The use of optic fibers for transport greatly simplifies the experimental setup, particularly in cases where several simultaneous measurements are to be taken.

Two paths of analysis of the return light are available allowing two simultaneous recordings of velocity history:

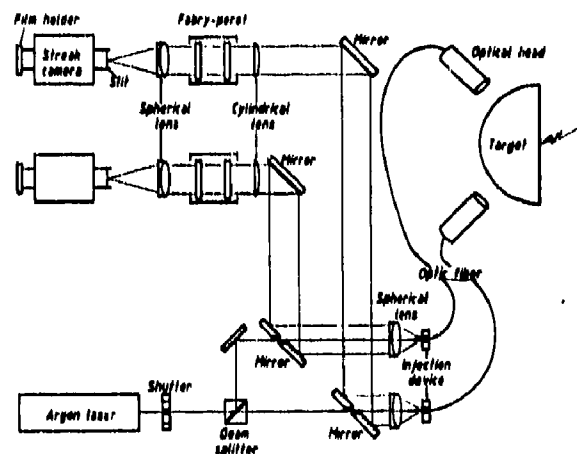


Figure 1. Description of the F.P.I. Used for This Study

- from the same point on the target with two different sensitivities or time resolutions,
- from two different points on the target.

The recording of the interference pattern is made by means of two electronic streak cameras.

The precision of the measurement and the time resolution are dependent on numerous parameters (spacing of the Fabry-Perot, sweep rate, method of analysis, etc.). In the test conditions used for the following examples, the velocity is considered to be measured to 1.5 percent and the time resolution to be about 50 ns to 100 ns.

### APPLICATION TO THE STUDY OF AN ALUMINIZED COMPOSITION<sup>4</sup>

The ballistic capacity of an explosive is generally measured in a steady configuration.

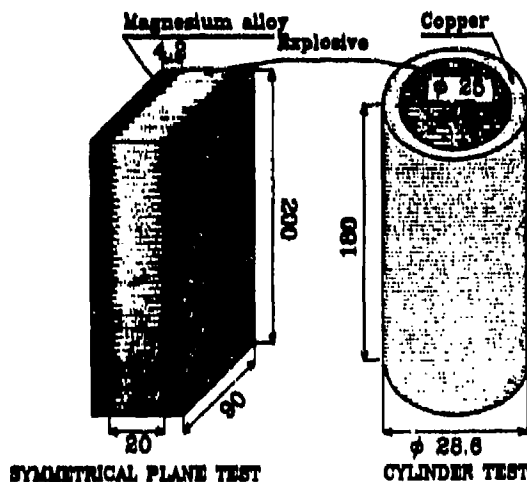


Figure 2. Layout of the Two Tests Used for the Study of the Role of Aluminum in the Ballistic Capacity of Explosives

It is thereby possible to avoid taking into account initiation conditions and to obtain a characteristic that is intrinsic to the explosive tested.

The cylinder test is the best known of this type of experiment. For various reasons shown in Reference 5, we have also developed a symmetrical plane test. The geometry of these two experiments, as used in this work, is shown in Figure 2. Monitored by F.P.I., these two tests provide a comparative classification of the compositions and make it possible to fit an equation of state for the detonation products.

The three compositions in Table 1 were subjected to both tests. The velocity histories obtained are shown in Figure 3.

A simple visual examination of the velocity histories reveals the unusual behavior of Comp 3 which continues to accelerate the walls until the end of the recordings, while the velocity limit is almost reached at the end of

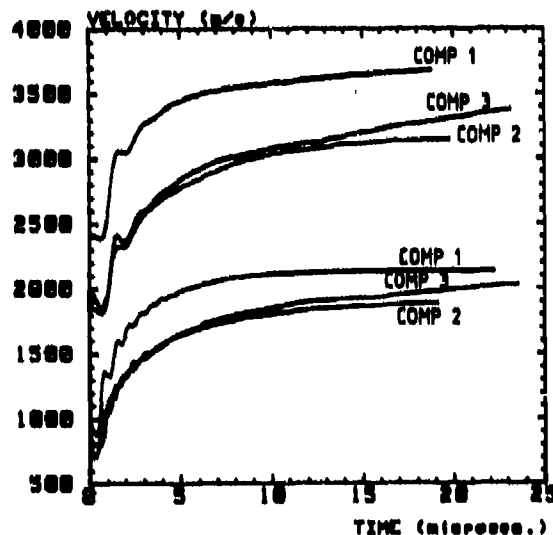


Figure 3. Velocity Histories Monitored by F.P.I. for the Three Compositions in Table 1. The three upper curves are for SPT and the three lower curves are for CT.

Table 1. Characteristics of Three Compositions Tested

Explosive	Composition	%Wt	Density (kg/m <sup>3</sup> )	Detonation Velocity (m/s)
Comp 1	HMX/Viton	96/4	1861	8850
Comp 2	RDX/PBHT Binder	88/12	1632	8180
Comp 3	HMX/AP/Al/ Binder	42/9/19/30	1830	7690

10  $\mu$ s in the case of compositions 1 and 2. This behavior is even more marked in the non-dimensionalized representation shown in Figures 4 and 5. Here, the results obtained are little dependent on the explosive, and the limit value gives the efficiency of the geometry. Thus, explosives 1 and 2 give close curves, although they have very different performances. After 10  $\mu$ s of motion, the curve for Comp 3 diverges from the other two. This divergence occurs mainly after the two other compositions have reached the limit value. To bring back the curve of Comp 3 to the efficiency level, the standardizing energy used should be progressively increased by  $\Delta Q$ , such as:

$$\Delta Q(t) = \left( \frac{E_{nd}(t)}{\eta} - 1 \right) Q_0 \quad (1)$$

where  $E_{nd}(t)$  is the non-dimensionalized energy of Figures 4 and 5,  $Q_0$  is the standardizing energy,  $\eta$  is the efficiency of the geometry (0.26 for SPT, 0.68 for CT).

One can reasonably suppose the  $\Delta Q(t)$  comes principally from the retarded combustion of the aluminum contained in Comp 3, which is likely to supply an energy  $Q_{Al}$  of about 3500 kJ per kilo of explosive.

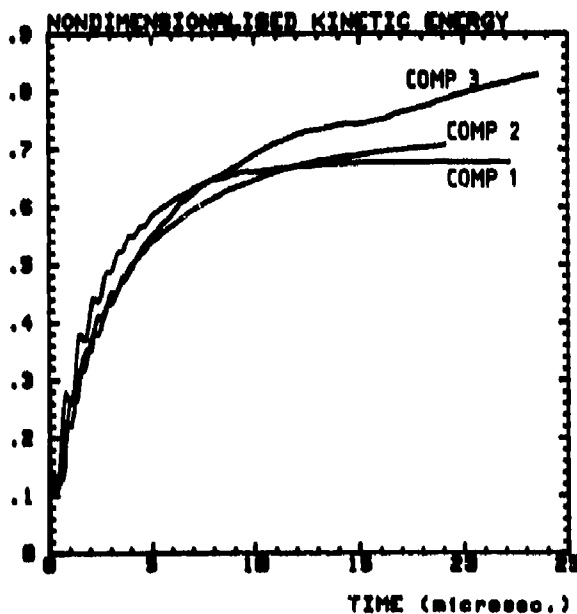


Figure 4. Experimental Results in Non-dimensionalized Form for CT. Standardizing energy =  $D^2/2(\Gamma^2-1) mx$  with  $\Gamma=3$  and  $mx =$  mass of the explosive.

From Equation (1) we can deduce a mass fraction of reacted aluminum:

$$\lambda(t) = \Delta Q(t) / Q_{Al} \quad (2)$$

The curves  $\lambda(t)$  thus obtained are shown in Figure 6 for the two tests. These two curves are very close, which seems reasonable as the two configurations give a similar expansion variation with respect to time.<sup>5</sup> There is an induction time of 10  $\mu$ s, and in the 12  $\mu$ s which follow, 25 percent of the aluminum reacts.

This approach has been made possible by the F.P.I., which gives the wall velocity directly. Figure 7 shows the displacement of the wall obtained by integration of the velocity history in the case of the cylinder test. It is this kind of information which is obtained with a streak camera, but the particular behavior of Comp 3 is not immediately visible in this representation. To be really useful, the streak camera recording must be derived to obtain the velocity; this is the approach used by M. Finger in 1970 in Reference 6. But, if  $\Delta x$  is the precision for the displacement, the error  $\Delta V$  on the velocity is given by:

$$\Delta V = 2\Delta X/t \quad (3)$$

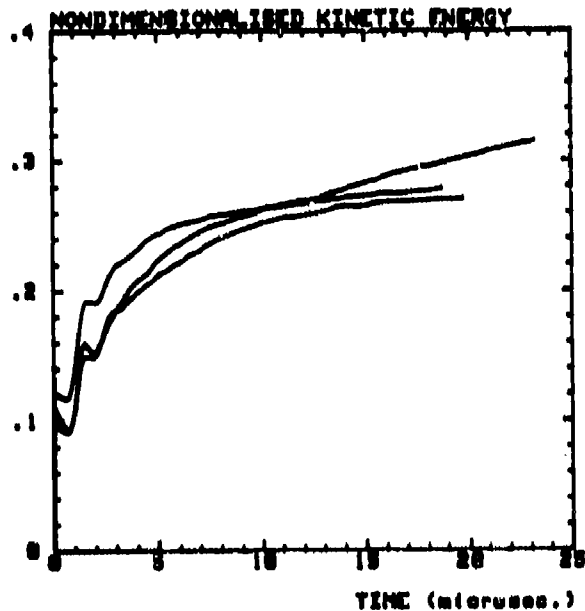


Figure 5. Experimental Results in Non-dimensionalized Form for SPT. Standardizing energy =  $D^2/2(\Gamma^2-1) mx$  with  $\Gamma=3$  and  $mx =$  mass of the explosive.

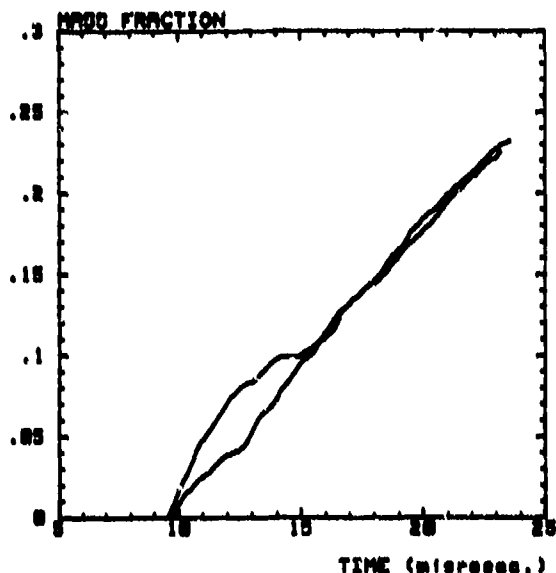


Figure 6. Mass Fraction for the Combustion of Aluminum Obtained Using Equation (2). The motion starts at  $t=0$ .

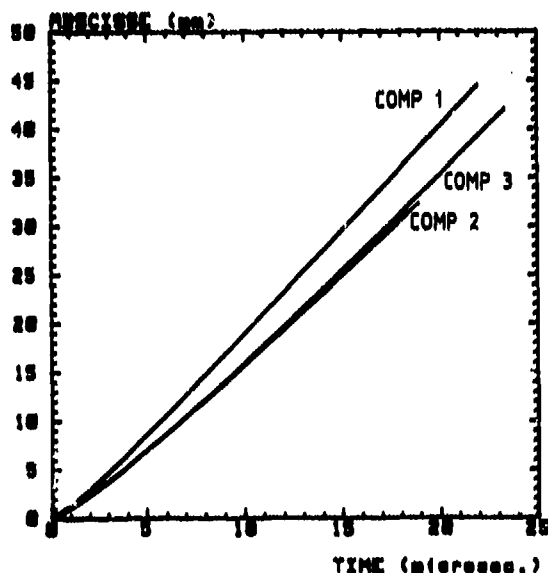


Figure 7. Displacements Versus Time Obtained by Integration of the Velocity Histories

where  $\tau$  is the interval of time separating the two points, that is the time resolution for the velocity. To obtain the velocities in the same conditions as with the F.P.I.,  $\Delta x$  must be of the order of 3 microns, which is difficult to achieve. With a more common value of  $\Delta x = 0.05$  mm,  $\Delta V$  will be the same as with the F.P.I. if  $\tau = 3 \mu s$

that is, 20 times the F.P.I.'s time resolution. The details of the velocity history, in particular the changes in the slope, would not be at all accessible using a streak camera.

For laboratory tests, it is therefore clear that the F.P.I. has the advantage of recording the velocity directly with a time resolution that is better by a factor of 20 than that given in classical chronometry. For applications requiring recording durations of less than several tens of microseconds, a higher sweep rate can be used and the time resolution of the F.P.I. can be less than 10 ns. A factor of 100 is gained, therefore, compared with chronometry techniques.

### OTHER EXAMPLES OF USE OF THE F.P.I.

The F.P.I. can also be used to monitor tests for which there would otherwise be few monitoring possibilities.

### VELOCITY OF FRAGMENTS IN A GROOVED CYLINDER TEST

These tests make possible evaluation of velocity loss due to the opening of the wall in a cylinder test. The geometry tested is described in Figure 8. The velocity histories of a fragment are given in Figure 9 for the 3 compositions in Table 1. In these tests the detonation products escape through the grooves immediately behind the detonation front. In spite of this early appearance, the recording durations are longer than 12  $\mu s$ , and an analysis of the most important part of the accelerating phase is therefore possible.

A streak camera would not give any information on the motion of the fragment, and this would be masked by the detonation products.

### FUNCTIONING OF A TRANSMITTING DEVICE<sup>7,8</sup>

This device is outlined in Figure 10. It is used to transmit pyrotechnic information through a wall. We recorded the velocity history of this wall using a F.P.I. and the results obtained are shown on Figure 10. The thickness of the wall determines whether or not there is plugging (piercing) expressed by a final velocity which is different from or equal to zero. Here, the F.P.I. makes it possible to obtain

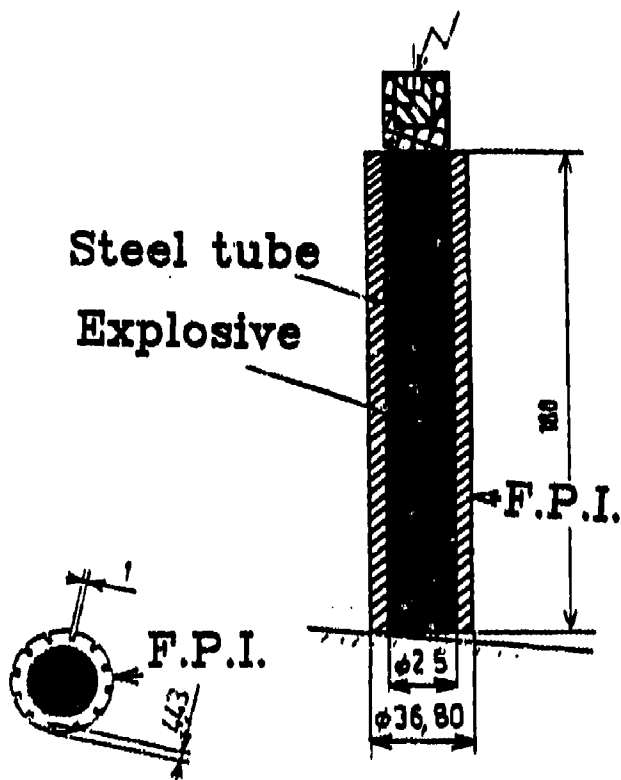


Figure 8. Layout of the Test for Evaluation of the Effect of Wall Opening in a Cylinder Test

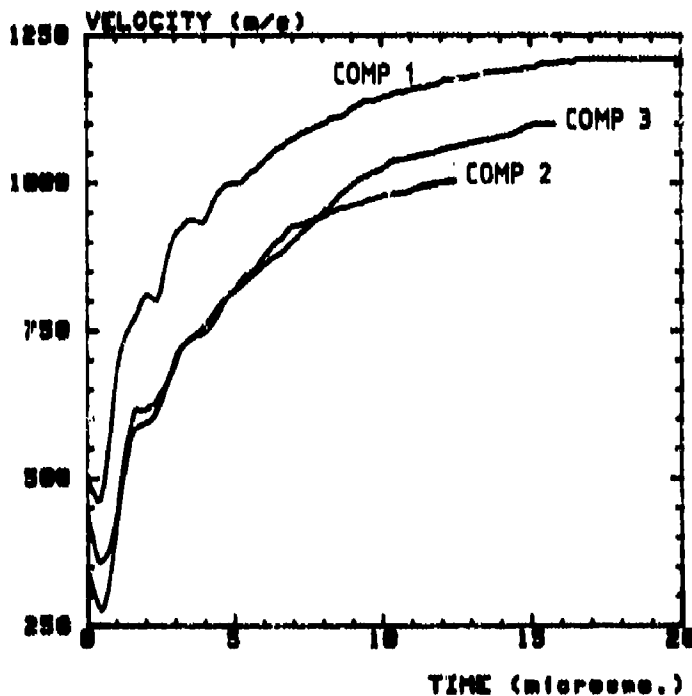


Figure 9. Velocity Histories Using the Grooved Cylinder Test for the Three Compositions of Table 1

information on small devices with difficult access subjected to non one-dimensional motion.

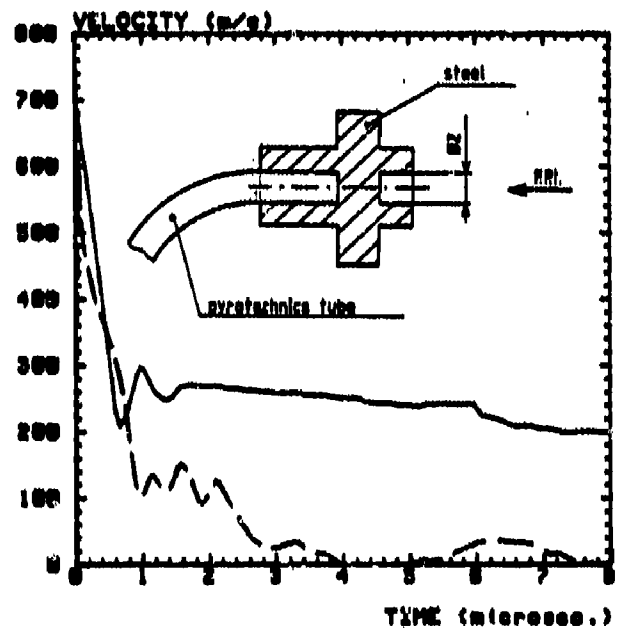


Figure 10. Monitoring of the Functioning of a Transmitting Device:

--: without plugging of the wall,  
—: with plugging of the wall

## CALIBRATION OF A DIVERGENT SPHERICAL GENERATOR

Such a generator is used to study the behavior of materials in regimes different from plane ones. It is shown in Figure 11. The calibration of this generator must give:

- the region where the flow is really one-dimensional,
- the pressure level in relation to the thickness of the intermediate material.

Part of this work can be done using a streak camera. However, these results are not very sensitive to the exact wave profile. A double F.P.I. measurement makes it possible to test more precisely both the one-dimensional character and the level of the wave produced by the generator. An example of the results is given in Figure 12.

This illustrates the F.P.I.'s capacity to take simultaneous measurements on non-planar geometries.

## CONCLUSION

It is clear that the F.P.I. gives valuable experimental results in laboratory tests

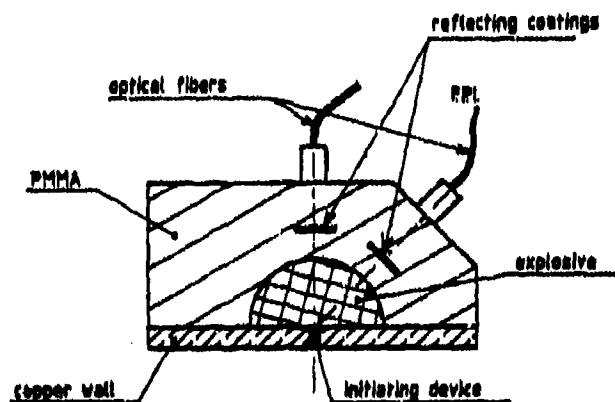


Figure 11. Calibration of a Diverging Spherical Generator

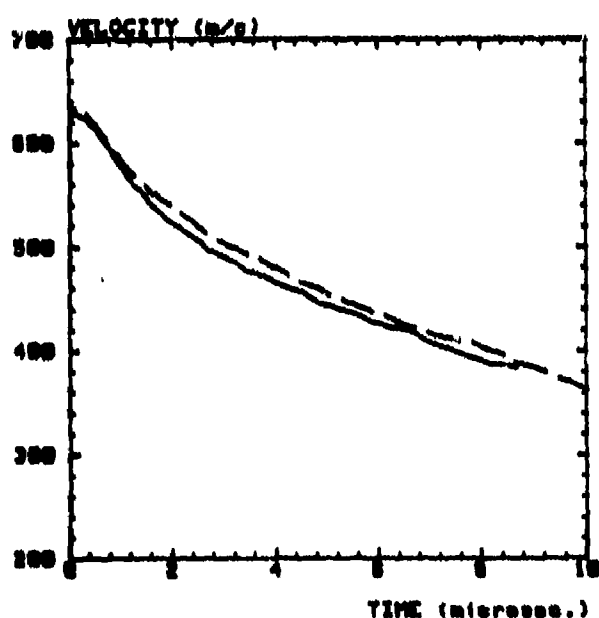


Figure 12. Velocity Histories Obtained for the Test Shown in Figure 11. The two recordings are obtained simultaneously on the axis (---) and at 45° from this axis (—).

involving simple geometries. In the application shown in this paper, the F.P.I. has enabled us to obtain information on the role of aluminum in the energy delivered by an explosive.

But the F.P.I. is not limited to this type of application and can also be used to monitor more complex geometries. At present its use is limited due to the available light power provided by monochromatic lasers. This limitation can now be overcome by, for

example, the use of a multi-line laser<sup>9</sup> enabling multiplication of the available power by a factor of 10 to 20. We can, therefore, expect that the F.P.I. will be used more and more in the field of detonics.

## REFERENCES

1. McMillan, C. F.; Goosman, D. R.; Parker, N. L.; Steinmetz, L. L.; Chau, H. H.; Huen, T.; Whipkey, R. K.; and Perry, S. J., "Velocimetry of Fast Surfaces Using Fabry-Perot Interferometry," *Rev. Sci. Instr.*, Vol. 59, No. 1, Jan 1988, pp. 1 and 20.
2. Lee, E. L.; Breithaupt, D.; McMillan, C.; Parker, N.; Kury, J.; Tarver, C.; Quirk, W.; and Walton, J., "The Motion of Thin Metal Walls and The Equation of State of Detonation Products," *Proceedings of The Eighth Symposium (International) on Detonation*, Albuquerque, NM, 15-19 Jul 1985, pp. 613-624.
3. Durand, M., "Emploi de Fibres Optiques pour la Mesure de Vitesse par Interférométrie Doppler-Laser avec Interféromètre de Fabry-Pérot," *16<sup>ème</sup> Congrès International de Photographie Rapide et de Photonique*, Strasbourg, France, 27-31 Aug 1984.
4. Work supported by French Ministry of Defense (Service Technique des Poudres et Explosifs).
5. Gimenez, P.; de Longueville, Y.; and Saint-Martin, C., "E.O.S. of Detonation Products Obtained from Symmetrical Deflection of Liners Investigated by Laser Interferometry Techniques," *Proceedings of the Eighth Symposium (International) on Detonation*, Albuquerque, NM, 15-19 Jul 1985, pp. 596-601.
6. Finger, M.; Hornig, H. C.; Lee, E. L.; and Kury, J. W., "Metal Acceleration by Composite Explosives" *Proceedings of the Fifth Symposium (International) on Detonation*, Pasadena, CA, 18-21 Aug 1970, pp. 137-151.
7. Work supported by Société Européenne de Propulsion.

8. Krassoulia, G. and Thinat, F., "Etouville à I.F.O.C. 3<sup>ième</sup> Congrès International de Pyrotechnie Spatiale," Juan les Pins, France, Jun 1987.

9. Gidon, S. and Behar, H., "Multiple-line Laser Doppler Velocimetry," Appl. Opt., Vol. 27, No. 11, Jun 1988, pp. 2315-2319.

# DETONATION PRODUCT EQUATION OF STATE FOR BARATOL\*

John W. Kury and R. Don Breithaupt  
Lawrence Livermore National Laboratory  
High Explosives Technology  
Livermore, California 94550

The metal acceleration ability of the composite explosive Baratol, was experimentally determined using a Fabry Perot velocimeter. The Baratol reaction zone has a von Neuman spike pressure of 23.5 GPa. The performance of Baratol was found to be geometry dependent which is attributed to the slow reaction of barium nitrate's oxygen with the TNT detonation products. About 35 percent of the oxygen reacted in the 7  $\mu$ sec available for metal acceleration. The experimental results were used to generate an equation of state "recipe" for use in hydrodynamic calculations of the wedge test.

## INTRODUCTION

A large number of wedge tests<sup>1</sup> have been performed, primarily by Dr. John Ramsay and others at Los Alamos National Laboratory, to measure the shock initiation behavior of both explosives and propellants. The experimental data are commonly summarized in plots of input pressure versus either time or run distance to detonation. These plots are also used to help calibrate reactive models describing the shock initiation behavior of the material tested.

There are difficulties with the above simple treatment. For given transition time, the actual transition to detonation can either be very rapid or gradual. Any implications of this difference to the reactive model are lost. Also, the input pressure in the wedge test is not constant but decreases significantly over the time of the experiment. The effect is particularly worrisome when using a highly pressure dependent reactive model.<sup>2</sup>

Hydrodynamic calculations to match wedge test distance-time data, can be used to

obtain a more precise description of the initiation behavior of the test material. To do this accurately, one requires good equations of state for the materials used in the driver systems (P081 lens and an explosive-inert material buffer - Figure 1). Precise data are available for the steel, PMMA, TNT, and Comp B used in the buffer. Almost no data, however, exists for Baratol which is used in the

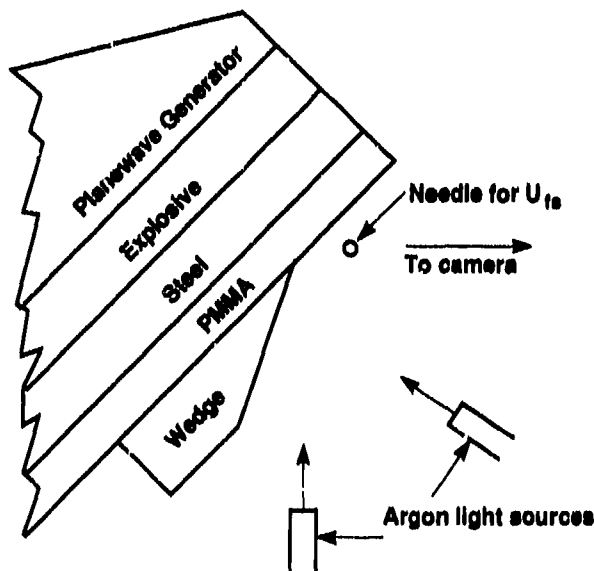


Figure 1. Los Alamos Wedge Test Geometry

\* Work performed under the auspices of the U.S. Department of Energy by the Lawrence Livermore National Laboratory under Contract No. W-7405-ENG-48

lens system and also in the low pressure buffer layer.

## EXPERIMENTAL

Baratol-containing lenses 50 mm, 100 mm, and 200 mm in diameter were used to accelerate tantalum plates. A Fabry Perot velocimeter<sup>6</sup> was used to measure the velocity-time history of the tantalum plates. The experimental geometries and pertinent dimensions are summarized in Table 1.

Table 1. Experimental Geometries

Experiment	Lens Designation	Length of Baratol in Lens	Tantalum Plate Thickness (mm)
BAR-3	P022	24 mm	0.264 mm
80Tu-1	P040	39 mm	1.630 mm
80Tu-2	P081	83 mm	2.606 mm

Experiment BAR-3, using a very thin plate (0.26 mm), was included to obtain an estimate of the von Neuman spike pressure and thickness of the reaction zone for this composite explosive containing 76 percent barium nitrate and 24 percent TNT by weight. The Fabry Perot record obtained in shot BAR-3 is shown in Figure 2. The time resolution is better than 10 nanoseconds. The tantalum free surface velocity-time histories for all three experiments are plotted in Figure 3.

## RESULTS AND DISCUSSION

### Pressure at the Detonation Front

The initial tantalum free surface velocities can be used to estimate the pressure behavior of Baratol near the detonation front. The one-dimensional Lagrangian hydrodynamic code KOVEC<sup>7</sup> was used to analyze the data. Initially, gamma law equations of state with the published<sup>3,4,5</sup> detonation pressures of 17 GPa, 16 GPa, or 14 GPa were used to calculate tantalum free surface velocities. These calculations underestimated the initial velocities, and it became apparent that a front pressure of over 20 GPa would be required to

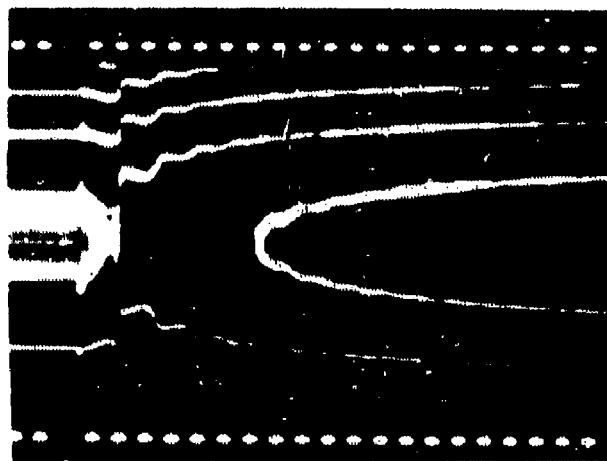


Figure 2. Fabry Perot Record for 0.26 mm Thick Tantalum Plate

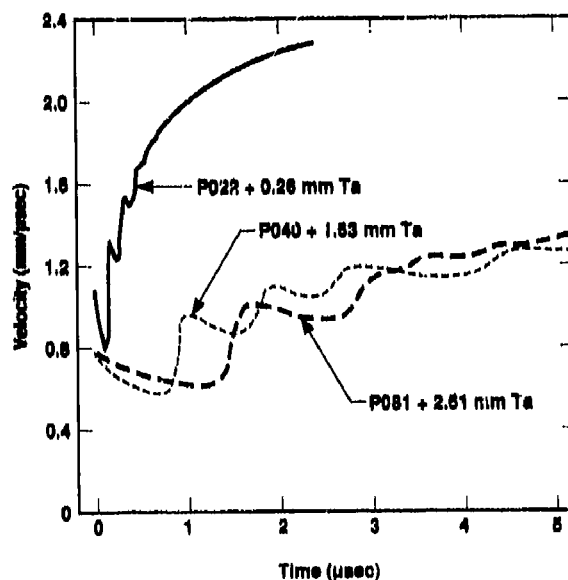


Figure 3. Experimental Tantalum Free Surface Velocities

obtain agreement. This indicated the presence of a significant von Neuman spike.

An attempt was first made to generate a single JWU equation of state that would describe both the high pressure spike and deliver approximately the correct total energy to the tantalum plates at late time. This was unsuccessful.

Tarver's<sup>2</sup> reactive model was then used with both inert and product JWU equations of state. The inert EOS for Baratol was based on a

fit to published Hugoniot data.<sup>8</sup> The product EOS was estimated from Tiger code<sup>9</sup> calculations and cylinder test results.<sup>10</sup> Many calculations with a wide range of reactive parameters were carried out. None produced a spike pressure high enough to match the experimental results.

A simple way to vary the Baratol pressure profile impacting the tantalum plate in a one-dimensional calculation is to use multiple explosive regions adjacent to the plate. The thickness of the regions and the product EOS can both be varied. This technique was used to generate the pressure profile presented in Figure 4. The spike pressure of 23.5 GPa drops to about 18 GPa in 15 nanoseconds, and then down to 15 GPa in another 100 nanoseconds. This pressure profile accurately predicts the initial free surface velocities for all three tantalum experiments. The comparison is shown in Figure 5.

#### Baratol Product Equation of State

Baratol is a composite explosive containing an oxidizer, barium nitrate, and an oxygen deficient explosive, TNT. Analysis of the three tantalum experiments with varying Baratol lengths shows that energetic reactions continue well behind the shock front. This geometry (time) dependent behavior is a dominant of the Baratol pressure history, and makes it extremely difficult to generate a simple EOS treatment for the products. As a compromise, two "recipes" have been formulated which are useful for calculations involving Baratol charges 100 mm in diameter by 100 mm long or larger. These "recipes" are based on the P081-tantalum experimental results.

A simple gamma law EOS with a detonation pressure of 12.2 GPa can be used to approximate the correct total energy transfer in both one-dimensional and two-dimensional hydrodynamic calculations. The gamma law constants are given in Table 2. The tantalum free surface velocity predicted by this EOS is compared to the experiment in Figure 6. Agreement is excellent except for the initial jump off velocity.

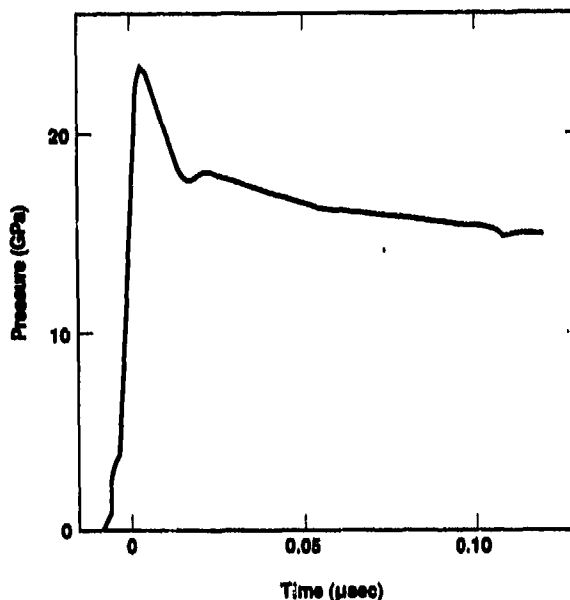


Figure 4. Baratol Pressure Spike Profile Deduced from Tantalum Plate Jump Off Velocities

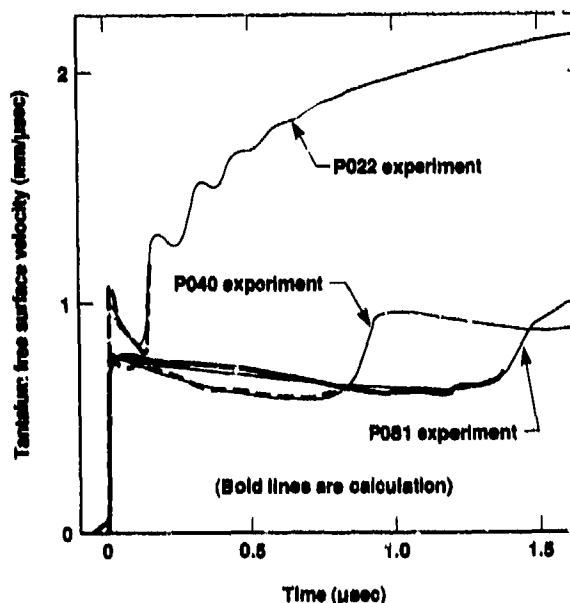
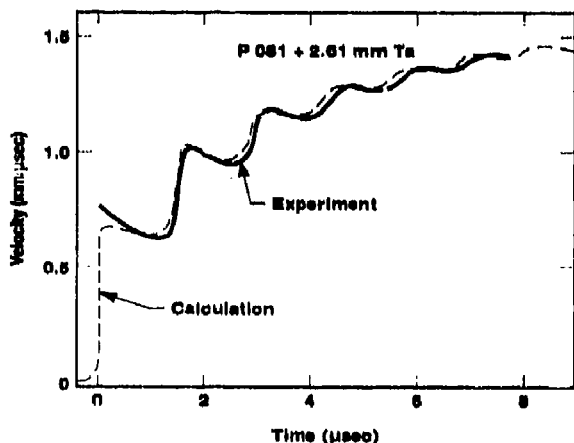


Figure 5. Comparison of Experimental Jump Off Velocities to those calculated with a 23.5 GPa Spike Pressure

**Table 2. Product EOS Recipe for Baratol Charges with Length (l) Greater than 100 mm**

Region	A*	B	C	One Region
Baratol Length (mm)	0.88 (0.40)	0.12 (0.40)	0.40	l
EOS Type	JWL	γ-law	γ-law	γ-law
$\rho_0$ (g/cc)	2.60	2.60	2.60	2.60
D (cm/μsec)	0.49	0.49	0.49	0.49
P (megabars)	0.110	0.165	0.240	0.122
γ	4.88	2.79	1.60	4.12
$\rho_0$ (megabar cc/cc)	0.0110	0.0462	0.200	0.0198
A	12.65			
B	0.0155			
$R_1$	5.80			
$R_2$	2.00			
ω	0.60			

\* Detonation progresses from Region A to C



**Figure 6. Tantalum Velocity Calculated with 12.2 GPa Gamma Law EOS Compared to Experiment**

A "recipe" for a more accurate description of the pressure for use in wedge test calculations and other one-dimensional geometries involves three different zones of explosive. All have the density and detonation velocity of Baratol but different equations of state. The EOS constants are given in Table 2. The region at the end of the Baratol, next to the

buffer layers (region C), is 0.4 mm long. The rest of the Baratol is split into region B, 12 percent the length of the charge, and region A described by a JWL EOS. A JWL EOS was required in region A to describe the products properly at large expansions. The tantalum free surface velocity predicted by this "recipe" is compared to experiment in Figure 7.

The three region EOS "recipe" was used to calculate the wedge test pressure for a typical explosive wedge at the PMMA - explosive interface for three commonly used P081 driver systems. The results are presented in Figure 8. Note the large drop in pressure with time, especially for the Comp B driver system.

Tarver's reactive model for LX-17<sup>2</sup> was used in one-dimensional calculations to estimate the difference in run distances to detonation that would be observed for a constant pressure input versus that shown in Figure 8 for the Comp B driver system. The decaying pressure for this driver system increased the run distance by 16 percent over that which would be observed with a constant pressure input.

### Amount of Barium Nitrate Reacted with TNT

The metal acceleration ability of Baratol can vary over a factor of two, depending on how much of the oxygen from barium nitrate reacts with the excess carbon produced by the TNT. Thermodynamic-hydrodynamic programs, such as BKW<sup>11</sup> or Tiger,<sup>9</sup> can be used to estimate the increase in energy as a function of the number of oxygen atoms from barium nitrate that react. These programs are not accurate in an absolute sense but can be used for relative comparison.<sup>12</sup> The tantalum experiments and cylinder test results were used to make such a comparison to the reference explosive nitromethane.

The performance of Baratol vs. nitromethane in the P081-tantalum geometry is shown in Figure 9. The tantalum velocity curve for nitromethane was calculated with KOVEC using a JWL EOS obtained from cylinder test experiments. Baratol delivers only 72 percent as much energy to the

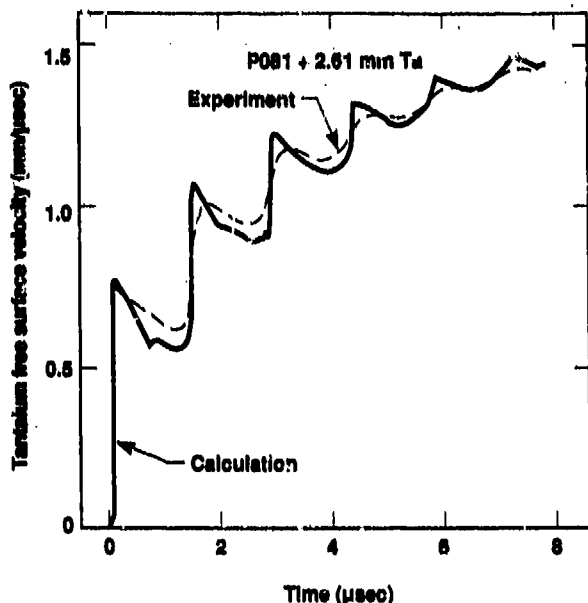


Figure 7. Tantalum Velocity Calculated with a 3 Region EOS "Recipe"

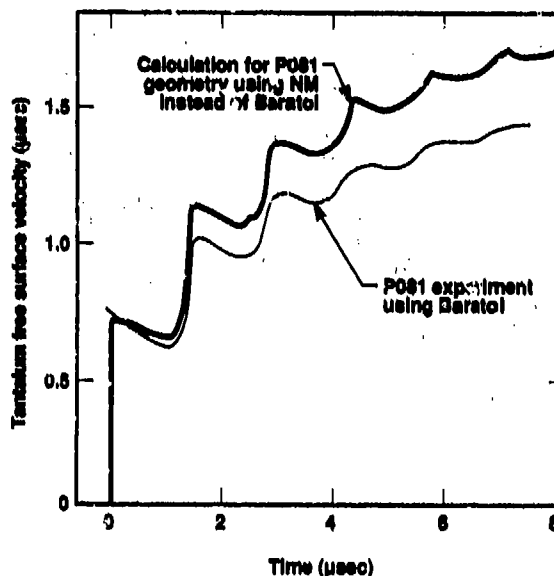


Figure 9. Baratol Performance Relative to Nitromethane

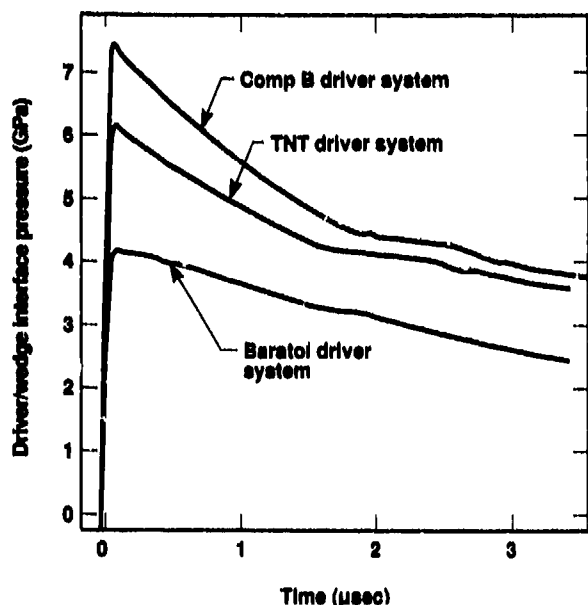


Figure 8. Calculated P081 Wedge Test Driver System Explosive Wedge Interface Pressure Vs. Time

tantalum plate as does nitromethane. Results from similar comparisons for the other experimental geometries are presented in Table 3.

For comparison, the Tiger code was used to calculate the energy released for isentropic

Table 3. Baratol Nitromethane Energy Comparisons

Baratol vs. NM	Relative Energy Delivered to the Metal
in P081 experiment	72%
in P040 experiment	68%
in P022 experiment	53%
in 1" cylinder test	55%

expansions to relative volumes up to 5. Calculations were done for nitromethane and Baratol with varying amounts of oxygen reacted. Baratol results were expressed in terms relative to nitromethane energy release. Table 4 presents the results for such a calculation, where only 50 percent of the oxygen in barium nitrate was allowed to react with barium to form barium oxide, and with excess carbon from TNT to form carbon oxides. The relative energy imparted to metal is a strong function of how far the detonation products expand. This results from the fact that Baratol has a much steeper isentrope (larger gamma) than does nitromethane.

**Table 4. Baratol Performance when 50 Percent of its Oxygen Reacts**

Relative Expansion Volume	Baratol Energy Relative to NM
1.2	-12%
1.6	-19%
2.0	-25%
2.4	-28%
3.0	-32%
5.0	-37%

Similar energy comparisons were made, allowing from 20 percent to 80 percent of barium nitrate's oxygen to react. The results for expansions to relative volumes of 1.2 and 2.4 are presented in Figure 10 as solid lines. The Baratol lens experiments sample the detonation products to relative volumes slightly greater than 1.2. The cylinder test data for Baratol sampled the products to a relative volume of 2.0.

The points in Figure 10 are the data in Table 3 plotted at the appropriate relative volumes. The P022 result indicates that only about 20 percent of the oxygen in barium nitrate reacted during this 1  $\mu$ sec experiment. This is in contrast to the 35 percent reacted in about 7  $\mu$ secs for the other three experiments.

## CONCLUSIONS

An equation of state "recipe" for Baratol has been derived from metal acceleration experiments, which allows accurate hydrodynamic calculations of wedge test experiments. It is now possible to calibrate shock initiation models in a manner which takes into account the significant decrease in pressure that occurs at the driver/test-sample interface during the course of an experiment.

## ACKNOWLEDGEMENTS

The authors wish to thank Mrs. Patricia Crawford for performing the Tiger calculations, and Dr. Edward Lee for his encouragement and helpful discussions.

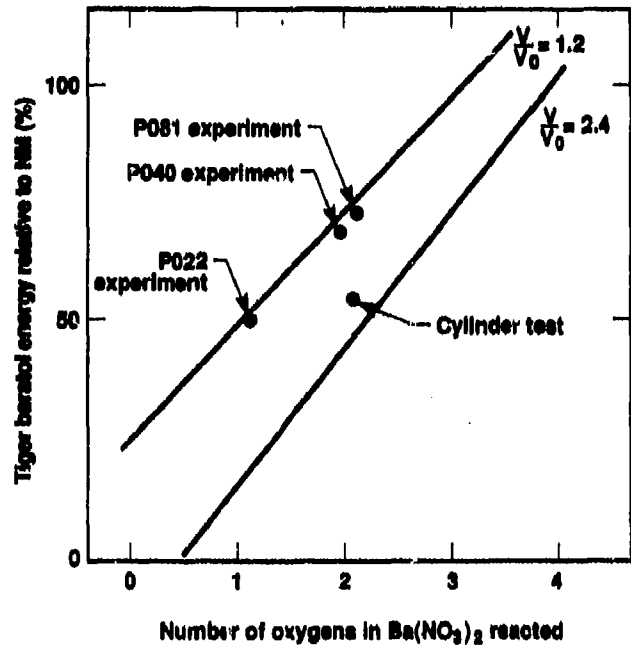


**Figure 10. Baratol Performance as a Function of the Amount of Ba(NO<sub>3</sub>)<sub>2</sub> Reacted**

## REFERENCES

1. Campbell, A. W.; Davis, W. C.; Ramsay, J. B.; and Travis, J. R., *Phys. Fluids*, Vol. 4, 1961, p. 511
2. Tarver, C. M. and Hallquist, J. O., "Modeling Shock Initiation and Detonation Wave Phenomena in PBX-9404 and LX-17," *Seventh Symposium (International) on Detonation*, NSWC MP 82-334, Annapolis, MD, Jun 1981, p. 488.
3. Burrow, K; Chilvers, D. K., Gyton, R.; Lamborn, R. D.; and Wallace, A. A., "Determination of Detonation Pressure Using a Manganin Wire Technique," *Sixth Symposium (International) on Detonation*, ACR-221, Coronado, CA, Aug 1976, p. 105.
4. Gardner, S. D. and Wackerle, J., "Interactions of Detonation Waves in Condensed Explosives," *Fourth Symposium (International) on Detonation*, ACR-125, Silver Spring, MD, Oct 1976, p. 154.
5. Kineke, Jr., J. H. and West, Jr., C. E., "Shocked States of Four Overdrive Explosives," *Fifth Symposium (International) on Detonation*, ACR-184, Pasadena, CA, Aug 1970, p. 533.

6. McMillan, C. F., et al., *Rev. Sci. Instrum.*, Vol. 59, 1988, p. 1.
7. Woodruff, J. P., "KOVEC User's Manual," Lawrence Livermore National Laboratory Report UCID-17306, Sep 1976.
8. *LASL Shock Hugoniot Data*, Stanley P. March, ed., University of California Press, Berkeley, CA, 1980.
9. Weibenson, W. E.; Zwisler, W. H.; Seely, L. B.; and Brinkley, Jr., S. R., "TIGER Documentation Volume," Stanford Research Institute (prepared for Ballistic Research Laboratory, Aberdeen, MD, Contract No. DA-04-200-AMC-3226 (X), Nov 1968, SRI Publication No. Z106.
10. Private communication from J. B. Ramsay, Los Alamos National Laboratory.
11. Mader, C. L., "FORTRAN BKW: A Code for Computing the Detonation Properties of Explosives," Los Alamos Scientific Laboratory Report No. LA-3705, Jul 1967.
12. Kury, J. W., et al., "Metal Acceleration by Chemical Explosives," *Fourth Symposium (International) on Detonation*, ACR-126, Silver Spring, MD, Oct 1965, p. 3.

# DESIGN AND DEVELOPMENT OF PRECISION LINEAR SHAPED CHARGES

Manuel G. Vigil  
Sandia National Laboratories  
Explosive Subsystems Division  
Albuquerque, New Mexico 87185

*The Precision Linear Shaped Charge (PLSC) design concept involves the independent fabrication and assembly of the liner (wedge of PLSC), the tamper / confinement, and explosive. The liner is the most important part of an LSC, and should be fabricated by a more quality controlled, precise process than the tamper material. Also, this allows the liner material to be different from the tamper material. The explosive can be loaded into the liner and tamper as the last step in the assembly process, rather than the first step as in conventional LSC designs. PLSC designs are shown to produce increased jet penetration in given targets, more reproducible jet penetration, and more efficient explosive cross-sections using a minimum amount of explosive. The Linear Shaped Charge Analysis Program (LSCAP) being developed at Sandia National Laboratories has been used to assist in the design of PLSCs. LSCAP predictions for PLSC jet penetration in aluminum targets, jet tip velocities, and jet-target impact angles are compared to measured data.*

## INTRODUCTION

Sandia National Laboratories (SNL)<sup>1</sup> is involved in the design of linear shaped charge (LSC) components varying in size from 10 to 300 grains per foot. These LSC components are required to perform such functions as rocket stage separation, parachute deployment, parachute system release, flight termination, system destruct and disablement. Most of the LSC components for these systems require precise and reproducible jet penetration, using the minimum explosive and total component weights.

Sandia National Laboratories is currently involved in a task to design Precision Linear Shaped Charges (PLSC).<sup>2-5</sup> The sweeping detonation and three-dimensional collapse process of an LSC is a complex phenomenon. The Linear Shaped Charge Analysis Program (LSCAP) is being developed at SNL to assist in the design of PLSC

components. Analytical output from the LSCAP code is presented and compared to experimental data for various PLSC designs in the 20 to 25 grain per foot explosive loading range. The LSCAP code models the motion of the LSC liner elements due to explosive loading, jet and slug formation, jet breakup, and target penetration through application of a series of analytical approximations, which are extensions of the standard one-dimensional modeling techniques for conical shaped charges. The structure of the code is intended to allow flexibility in LSC design, target configurations, and in modeling techniques. The analytical and experimental data presented includes LSC jet penetration in aluminum targets as a function of standoff, jet tip velocities, and jet-target impact angles. The measured velocity and angle data were obtained using a Cordin Model 114 rotating mirror camera at a turbine speed resulting in a 0.918-microsecond interframe time.

## GENERAL LINEAR SHAPED CHARGE

The parameters or variables for a general linear shaped charge cross-section are illustrated in Figure 1. The large number of variables defining a cross-section makes the design of "the" optimum LSC a very difficult task.

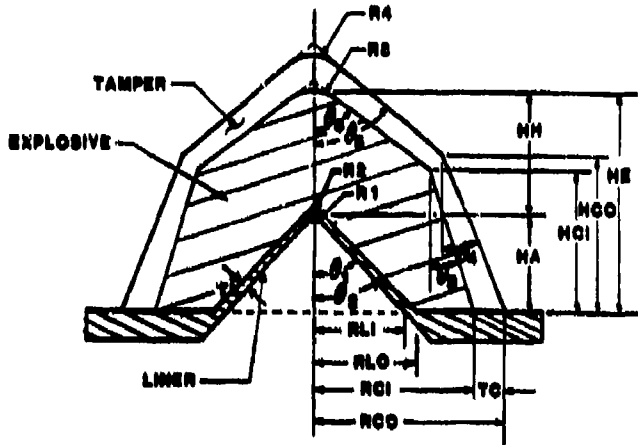


Figure 1. LSC Cross-Section Variables

The generic operational characteristics<sup>3-8</sup> of an LSC are shown in Figure 2. A metal tube or sheath containing explosive is formed so that a wedge is created on one side. The LSC is typically point or end initiated, and a detonation wave propagates along the axis. The wedge collapses on itself and forms a high velocity sheet of jet particles. In general, the jet particles are not projected perpendicular to the original direction of the liner, nor is the particle velocity perpendicular to the jet front.

The leading, relatively high velocity (3-5 mm/ $\mu$ s), main jet produces most of the penetration into the target. The slower (1-1.5 mm/ $\mu$ s), rear jet or slug is usually found embedded in the cavity generated in the target by the main jet. Severance of a finite thickness target results from both the penetration of the main jet and the fracture of the remaining target thickness. The fracture portion of the severed thickness usually varies,

and can be up to 50 percent depending on the target strength parameters.

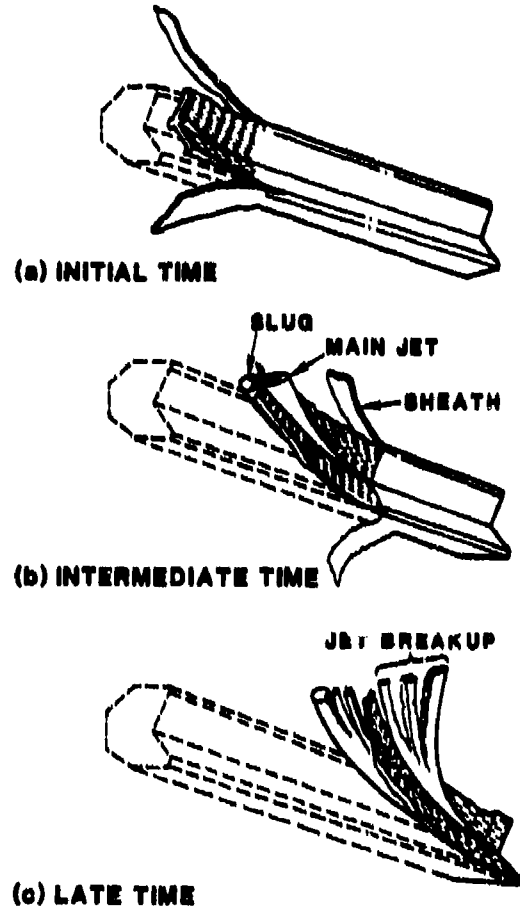


Figure 2. LSC Collapse and Jetting

## CONVENTIONAL LINEAR SHAPED CHARGE

Typically, conventional LSCs are fabricated by loading a cylindrical tube with granular explosives, and then roll or swage forming the loaded tube to the familiar chevron configuration illustrated in Figure 3.

Some of the disadvantages of conventional LSC designs are as follows:

1. Non-symmetrical cross-section,
2. Nonuniform explosive density,
3. Non-optimized explosive and sheath cross-sections, and
4. Historically designed for nonprecise jet cutting.

The explosive and sheath cross-section of a conventional 25 grain per foot, aluminum sheathed LSC loaded with HNS II explosive is shown in Figure 4. Figure 5 illustrates the

test to test variations in jet penetration of an aluminum target for the 25 grain per foot LSC shown in Figure 4.

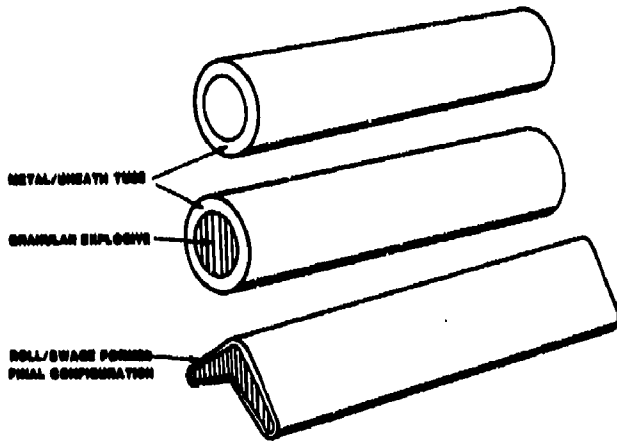


Figure 3. Conventional LSC Fabrication

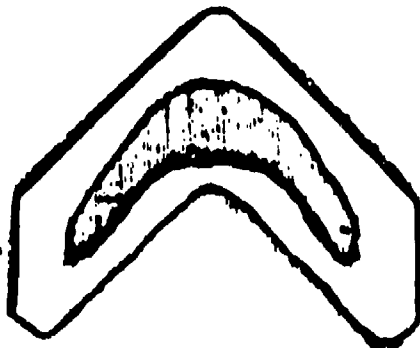


Figure 4. 25 GR/FT, HNS II, AL Sheathed LSC

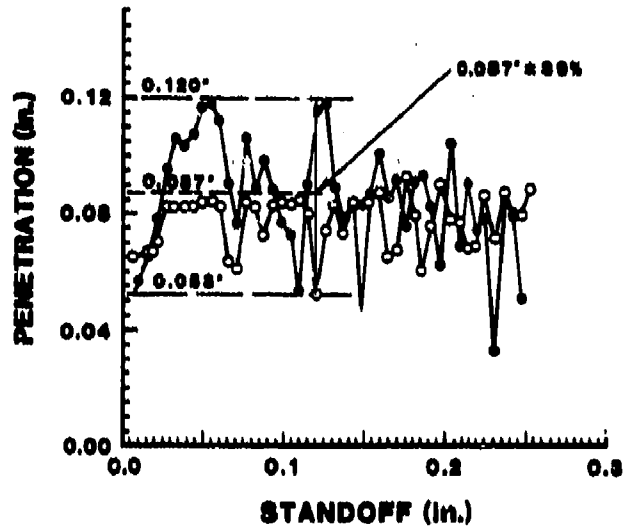


Figure 5. Reproducibility of 25 GR/FT LSC

### PRECISION LINEAR SHAPED CHARGE

For PLSC the liner, explosive, and tamper materials can be assembled as illustrated in Figure 6.

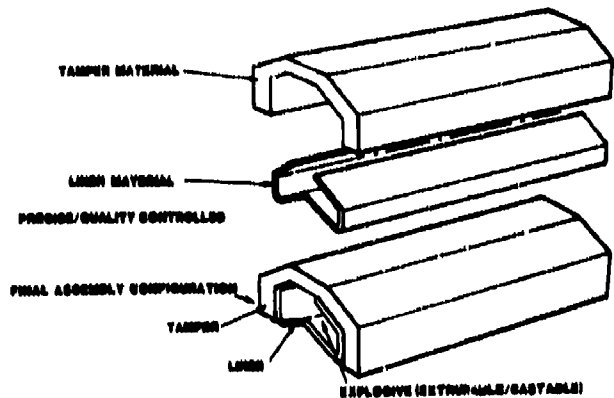


Figure 6. PLSC Fabrication

The liner, tamper, and explosive are manufactured independently to allow the required control of fabrication methods, which result in a more precise component. The

quality control of the liner is most important in the performance of LSC devices.

An extrudable or castable explosive is loaded or assembled with the liner and tamper components after these other two components are fabricated. The explosive can be loaded using single or multiple extrusions or by "buttering," a "toothpaste" like application technique, if necessary. Assembly aids, such as the use of vacuum, are also useful.

The LSCAP code has been used to improve the PLSC parameters. The explosive charge to liner mass ratio can be designed to optimize the transfer of energy from the detonation wave through the liner to the high-velocity jet. The explosive charge to tamper mass ratio can be designed to optimize the tamper material and thickness. The maximum tamper thickness is defined as that thickness beyond which no additional gain in the liner collapse velocity is obtained. The tamper can be made of different material than that for the liner in order to:

1. Fit different configurations
2. Allow for buttering of explosive
3. Allow selection of tamping characteristics in material
4. Allow for built-in shock mitigation properties
5. Allow for a built-in standoff housing free of foreign materials and water which degrade jet formation

## LINEAR SHAPED CHARGE ANALYSIS PROGRAM (LSCAP)

The modeling capabilities of the LSCAP code include:

1. Sweeping / tangential detonation propagation
2. Jet-target impact angles
3. Liner acceleration and velocity
4. Jet formation process
5. Jet penetration process including layered targets
6. Jet breakup stress model
7. Target strength modeling

The code is inexpensive relative to hydrocodes, can be easily used to conduct parametric studies, and is interactive.

The LSCAP modeling of half of an LSC cross-section is illustrated in Figure 7. Figure 8 shows sample LSCAP output illustrating an LSC with a variable standoff to an aluminum target, sweeping detonation, a jet front envelope of 26.7 degrees, jet particle path relative to the target, and a comparison of the predicted and experimental target-jet penetration at 8 and 24 microseconds, respectively.

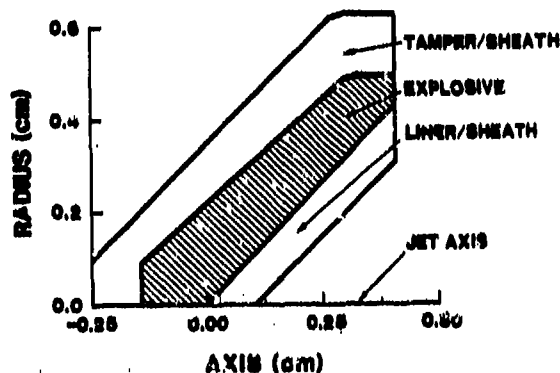


Figure 7. Model of LSC Cross-Section

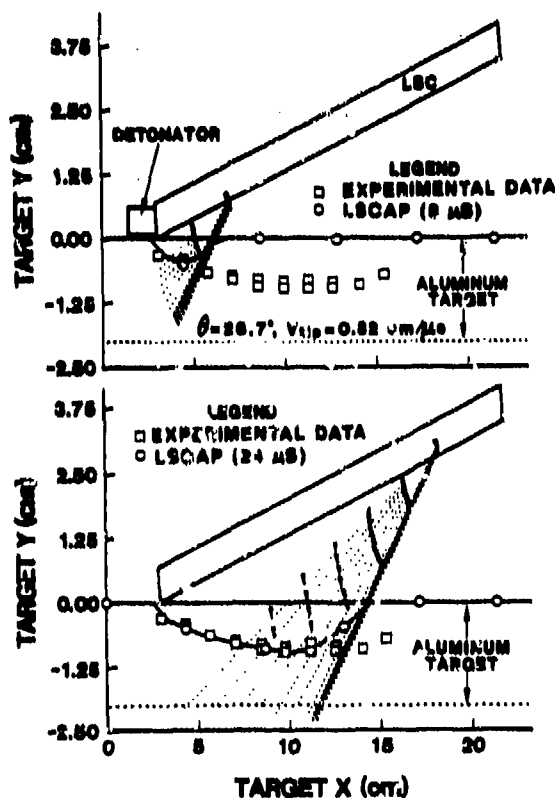


Figure 8. LSCAP Jet Penetration Graphics

## RESULTS

A parametric study was conducted incorporating the 25 grain per foot (gr/ft), LX-13 explosive, flange PLSC designs similar to Figure 9, and with the following variables:

1. Explosives
  - a. LX-13/XTX8003
  - b. PBXN301
2. Liner materials
  - a. Copper
  - b. Aluminum
  - c. Nickel
3. Tamper / confinement material  
Aluminum
4. PLSC Geometry
  - a. Liner apex angles:  
70, 75, 90, and 105 degrees
  - b. Liner thicknesses:  
.004, .007, .008, and .010 inches

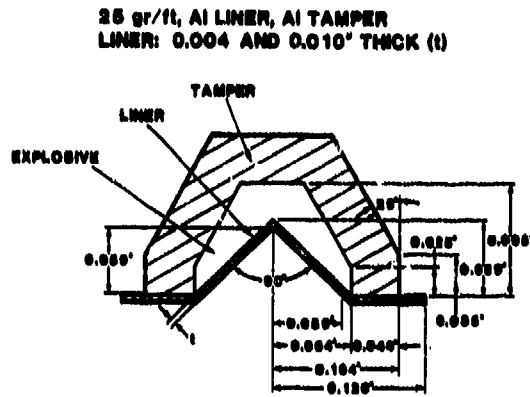


Figure 9. "Flange" PLSC Cross-Section

The PLSC materials, liner thickness ( $t$ ), and apex angles ( $\theta_a$ ) were varied as listed in Table 1. The PLSC jet tip velocity ( $V_j$ ), jet envelope angle ( $\theta$ ), jet-target angle ( $\alpha$ ), jet penetration into an aluminum 6061-T6 target

Table 1. LSCP Versus Experimental PLSC Parameter Comparisons

Liner Material	t (in.)	$\theta_a$ (in.)	$V_j$ (cm/us)		$\theta$ (deg)		$\alpha$ (deg)		P (in.)	S.O. (in.)
			Exp.	LSCAP	Exp.	LSCAP	Exp.	LSCAP		
Al	.004	70	.55	.65	49	55	62	63	.09	.07
Cu	.004	70	.36	.41	36	34	63	72	.11	.15
Al	.004	90	.42	.50	36	44	73	72	.11	.08
Cu	.004	90	.36	.33	27	27	77	77	.17	.10
Ni	.004	90	.28	.33	23	27	74	79	.13	.10
Al	.010	90	.32	.36	28	29	74	76	.15	.24
Cu	.010	90	.20	.20	16	16	78	82	.14	.19
Ni	.010	90	.17	.20	15	16	81	83	.09	.16
Al	.010	105	.28	.32	24	26	74	78	.13	.16
Cu	.010	105	.15	.17	15	13	86	83	.14	.21
Al	.004	105	.38	.46	31	37	84	75	.14	.11
Cu	.004	105	.26	.28	24	22	78	78	.16	.23
Cu	.010	70	.23	.25	19	20	80	81	.15	.16
Al	.010	70	--	.47	--	38	--	71	.18	.14

(P), and optimum standoff (S.O.) are listed in Table 1. The LSCAP predicted data are compared to the experimental values for most of the parameters. The effect on jet penetration versus standoff, due to variations in some of the PLSC cross-section parameters, are shown in Figures 10-14. The experimental data shown in Figures 10-14 were hand fitted to obtain the solid line curves.

The effect of varying materials is illustrated in Figures 10 and 11 for a 90 degree apex angle with 0.004 and 0.010 inch thick liners, respectively. The effect of varying apex angles is illustrated in Figures 12 and 13 for 0.004 and 0.010 inch thick aluminum liners, respectively. Figure 14 shows the penetration of 0.004 and 0.010 inch thick copper liners with apex angles of 70, 90, and 105 degrees.

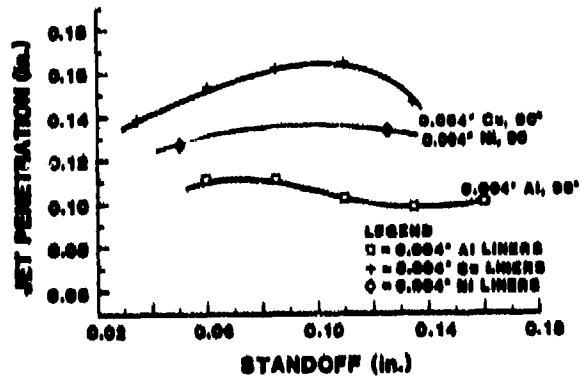


Figure 10. Effects of PLSC Liner Material (0.004" Liner, 90° APEX)

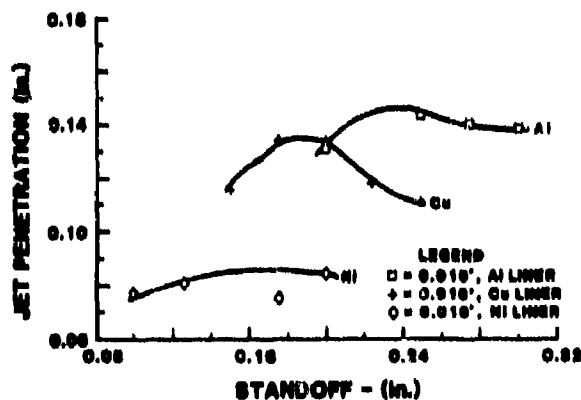


Figure 11. Effects of PLSC Liner Material (0.010" Liner, 90° APEX)

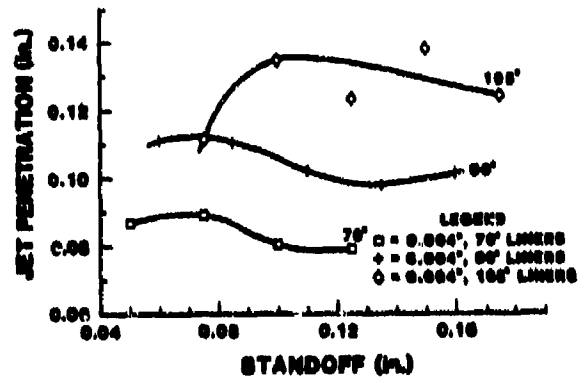


Figure 12. Effects of Al Liner APEX Angle (0.004" Liner)

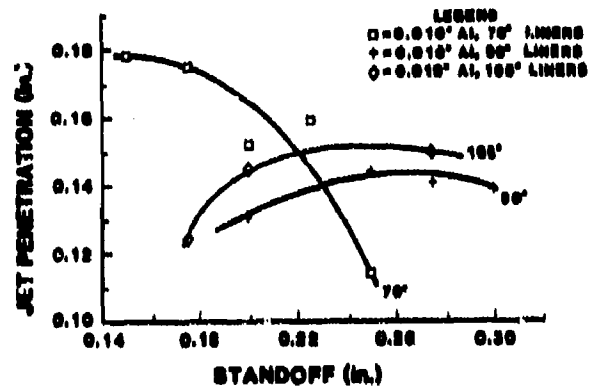


Figure 13. Effects of Al Liner APEX Angle (0.010" AL Liner)

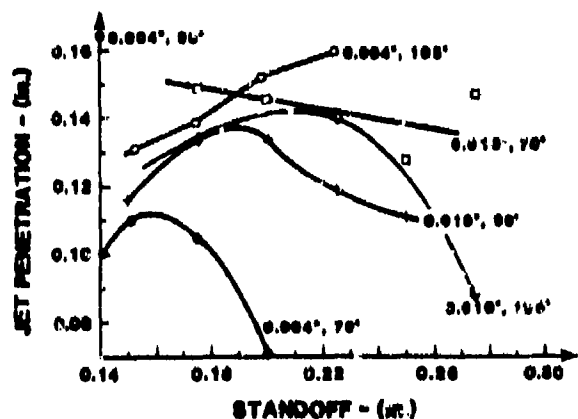


Figure 14. Effects of CU Liner Angle and Thickness (0.004" and 0.010" Liner)

Jet penetration versus standoff are illustrated in Figure 15 for the PLSC design shown in Figure 9 (0.010 in. thick liner), compared to the commercial LSC design shown in Figure 4. Both designs use aluminum liners (90 degree apex) and tampers. The LX-13 and HNS II explosives' metal driving ability is about the same.

Linear Shaped Charge Analysis Program predicted jet penetration versus standoff data are compared in Figure 16 to experimental data for the 25 gr/ft PLSC cross-section shown in Figure 9 using a 0.010 inch thick aluminum liner.

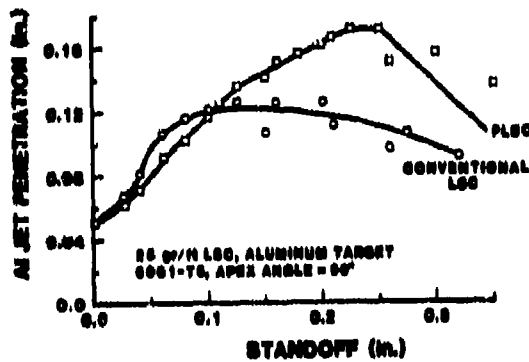


Figure 15. Measured PLSC Versus LSC Data

The LSCAP predicted jet penetration versus standoff data are compared in Figure 18 to experimental data for the 20 gr/ft PLSC cross-section shown in Figure 17 using a 0.008 inch thick copper liner. The "W" line configuration of the PLSC shown in Figure 17 can be more easily loaded with explosive than the PLSC shown in Figure 9. The reproducibility of jet penetration for one test versus position of distance along an aluminum 6061-T6 target is shown in Figure 19 for the 20 gr/ft PLSC cross-section of Figure 17 for both copper and aluminum liners 0.008 inch thick.

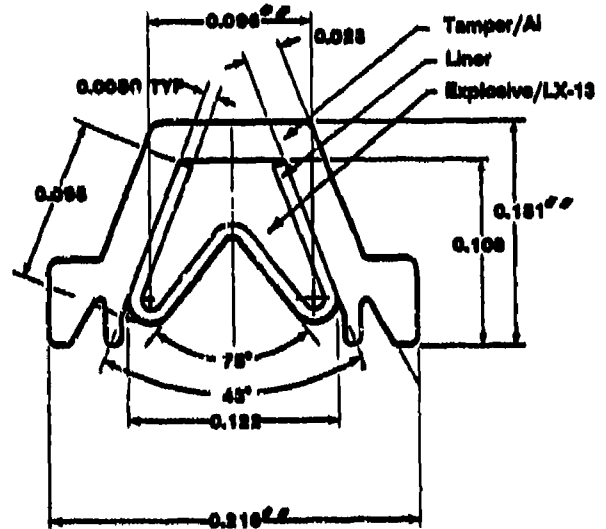


Figure 17. "W" PLSC Cross-Section

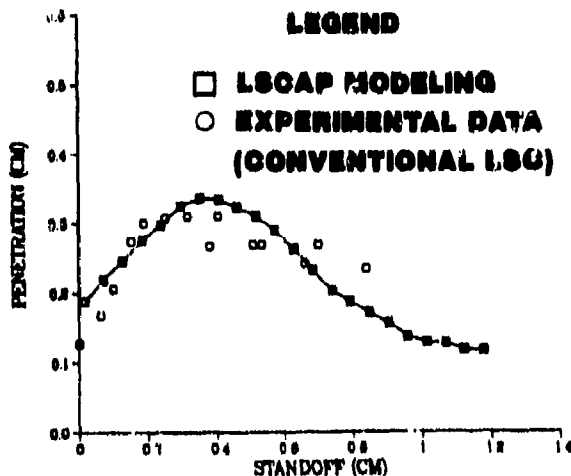


Figure 16. LSCAP Versus Experimental Data (Figure 9)

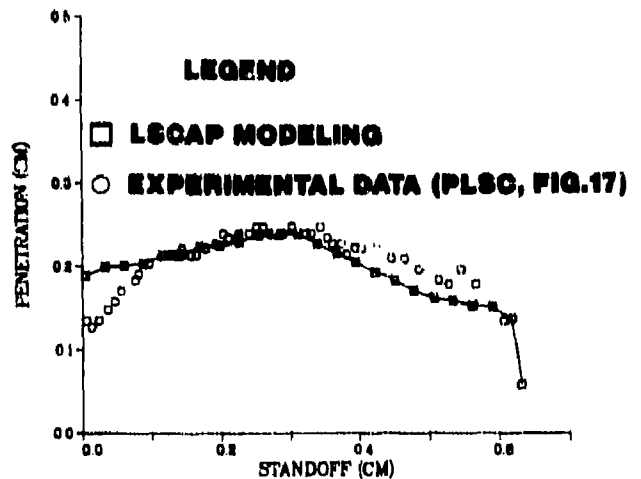


Figure 18. LSCAP Versus Data (Figure 17)

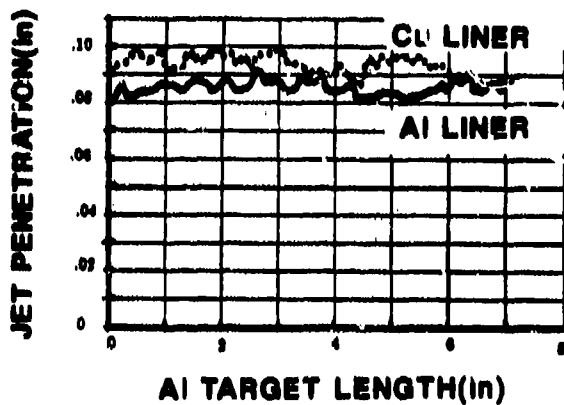


Figure 19. Reproducibility of PLSC (Figure 17)  
(Standoff = 0.100")

## CONCLUSIONS

PLSC liner, tamper, and explosive fabrication processes have been demonstrated to produce increased jet penetrations in aluminum targets, more reproducible jet penetrations, and more efficient explosive cross-sections compared to equivalent commercial LSCs.

The LSCAP predicted jet tip velocities are within 20 percent of the experimental values (Table 1). The predicted jet envelope angles relative to the PLSC are within 20 percent of the photometrically measured values (Table 1). The measured jet-target angles are within 11 percent of the predicted values (Table 1). Data for copper and aluminum PLSC jet penetration into an aluminum target was presented, demonstrating a 10 percent reproducibility for a given test (Figure 19). Data was presented to illustrate 40 percent improvement in jet penetration for a PLSC design, compared to an equivalent 25 gr/ft conventional LSC design (Figure 16).

The data of Figures 10-14 illustrate that similar jet penetrations can be obtained from various PLSC designs. A parametric study with the LSCAP code to determine "the" optimum PLSC design is very difficult because of the large number of interrelated variables. This does, however, emphasize the importance of LSCAP in obtaining a more optimized design than is currently available from conventional LSC designs. Currently, LSCAP is the only known linear shaped charge code in the USA.

PLSC designs similar to those presented here have recently been incorporated in Sandia National Laboratory (SNL) systems. The Explosive Subsystems Division plans to use PLSC designs in all future SNLA systems requiring jet severance of material, including Kevlar parachute suspension lines.

## ACKNOWLEDGEMENTS

The author wishes to thank Steve Hallett and Donnie Marchi for fabrication of test hardware, obtaining test measurements, and involvement in conducting tests. Mason & Hanger-Silas Mason Co., Inc. (Pantex Plant), and Ensign Bickford Aerospace Co. loaded the explosive in the PLSC hardware and conducted some of the tests.

## REFERENCES

1. Vigil, Manuel G. and Harlan, Jere G., *Optimal Design and Fabrication of Reproducible Linear Shaped Charges*, Sandia National Laboratories, SAND86-0982, 1986.
2. Robinson, Allen C. and Vigil, Manuel G., "An Analytical-Experimental Comparison of 150 and 220 Grain Per Foot Linear Shaped Charge Performance," *Tenth International Symposium on Ballistics*, San Diego, CA, Oct 27-29, 1987.
3. Robinson, A. C., *SCAP-A Shaped Charge Analysis Program - User's Manual for SCAP 1.0*, Sandia National Laboratories, SAND850708, Apr 1985.
4. Robinson, A. C., *Asymptotic Formulas for the Motion of Shaped Charge Liners*, Sandia National Laboratories, SAND841712, Sep 1984.
5. Robinson, S. C., *Multilayered Liners for Shaped Charge Jets*, Sandia National Laboratories, SAND852300, Dec 1985.
6. Hayes, G. A. and Horling, T. L., *Optical Metallography of Linear-Shaped Charge Fragments*, Naval Weapons Center, China Lake, CA, Report No. NWC TP 4859, Jul 1970.
7. Brown, George Elliott, Jr., *A New Optimized Theory for the End-Initiated Linear*

*Shaped Charge*, Naval Postgraduate School, Oct 1969.

8. Soper, W. G., *Performance of the Linear Shaped Charge*, Naval Weapons Laboratory Report 1946, AD-355352L, 1964.

## PRECISION LINEAR SHAPED CHARGE (PLSC)

### GOAL:

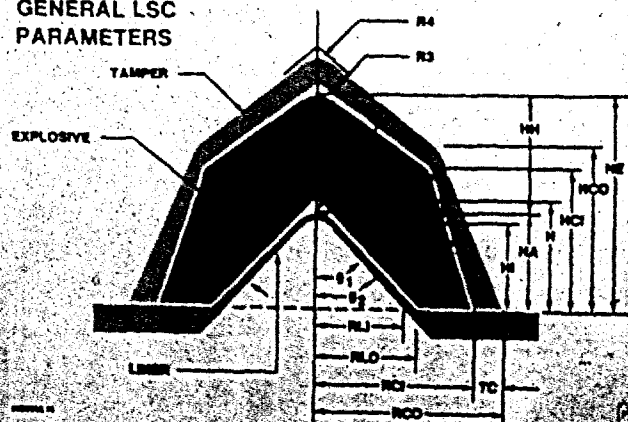
- DESIGN OPTIMUM PLSC
  - INCREASE JET PENETRATION
  - IMPROVE JET REPRODUCIBILITY
  - MORE EFFICIENT - MINIMUM EXPLOSIVE

## DESIGN AND DEVELOPMENT OF PRECISION LINEAR SHAPED CHARGES

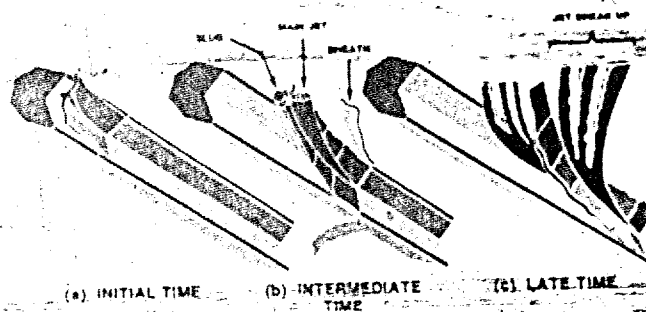
MANNY VIGIL

Sandia National Laboratories  
Albuquerque, New Mexico  
U.S.A.

### GENERAL LSC PARAMETERS



### GENERAL LSC JET FORMATION .



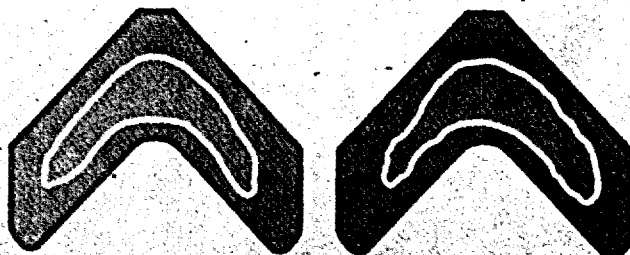
(a) INITIAL TIME (b) INTERMEDIATE TIME (c) LATE TIME

### CONVENTIONAL LINEAR SHAPED CHARGE (LSC)

#### • DISADVANTAGES:

- NON-REPRODUCIBLE JET PENETRATION,
  - NON-SYMMETRIC LSC CROSS-SECTIONS,
  - NON-UNIFORM EXPLOSIVE DENSITY,
  - NON-OPTIMIZED LSC CROSS-SECTION, AND
  - HISTORICALLY, FOR NON-PRECISE JET CUTTING.
- DEMOLITION WORK
- SEPARATION STAGES IN OLDER - LARGER SYSTEMS

### CONVENTIONAL 25 gr/ft ALUMINUM SHEATH, HNS EXPLOSIVE LSC CROSS-SECTIONS



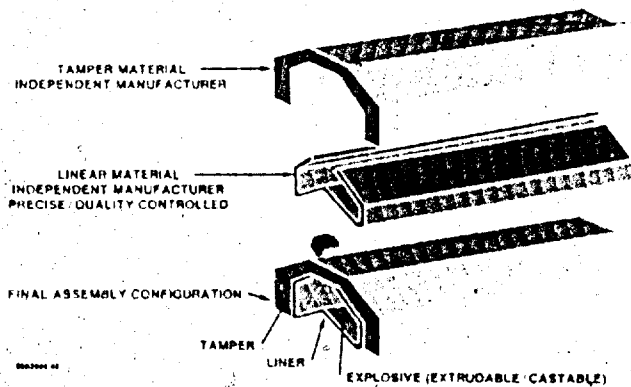
997000.23



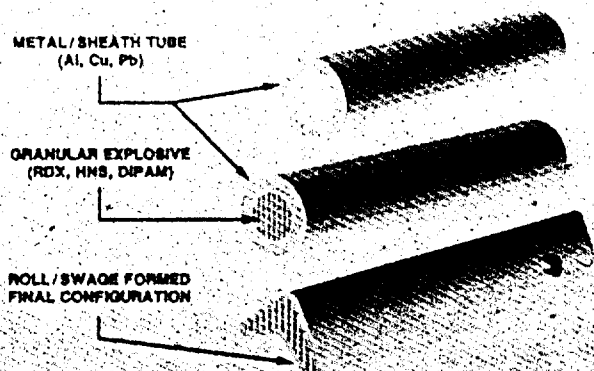
### PRECISION LINEAR SHAPED CHARGE (PLSC)

- OPTIMIZE PLSC COMPONENTS INDEPENDENTLY
  - LINER/WEDGE - PRECISION METAL
    - APEX ANGLE
    - THICKNESS
    - HIGH DENSITY
    - DUCTILE MATERIAL
    - STAMPING PROCESS
  - TAMPER/CONFINEMENT
    - THICKNESS
    - HIGH DENSITY
    - LESS PRECISE - EXTRUSION/OTHER PROCESS
  - EXPLOSIVE - EXTRUDABLE (LX-13,XTX8003, PBXN301, ECX, etc.)
    - UNIFORM EXPLOSIVE DENSITY
    - HIGH METAL DRIVING ABILITY
- PLSC COMPONENT ASSEMBLY - FINAL STEP

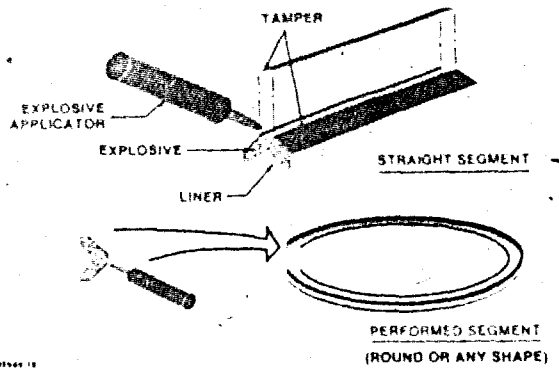
### PRECISION LINEAR SHAPED CHARGE FABRICATION



### CONVENTIONAL LINEAR SHAPED CHARGE FABRICATION



### PLSC EXPLOSIVE LOADING



### EXPERIMENTAL DATA PLSC LINER PARAMETERS

- MATERIAL:
  - ALUMINUM,
  - COPPER, AND
  - NICKEL.
- THICKNESS:
  - 0.004,
  - 0.007, AND
  - 0.010 INCH.
- APEX ANGLE:
  - 70,
  - 90, AND
  - 105 DEGREE.

FIGURE 11

### PLSC 90° APEX ANGLE CROSS-SECTION

MATERIALS

LINER - Al  
TAMPER - Al  
EXPLOSIVE - LX-13 (25 gr/lb)

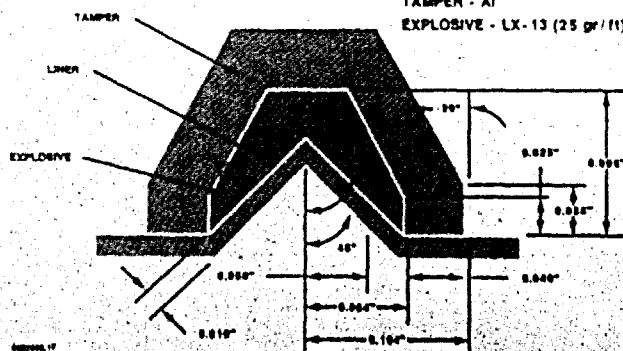
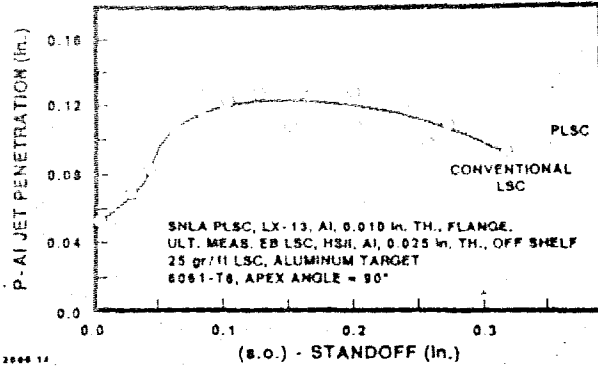


FIGURE 12

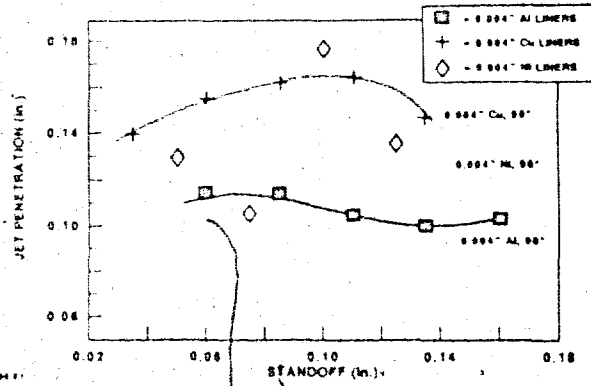


COMPONENT PLSC VS CONVENTIONAL LSC EXPERIMENTAL DATA



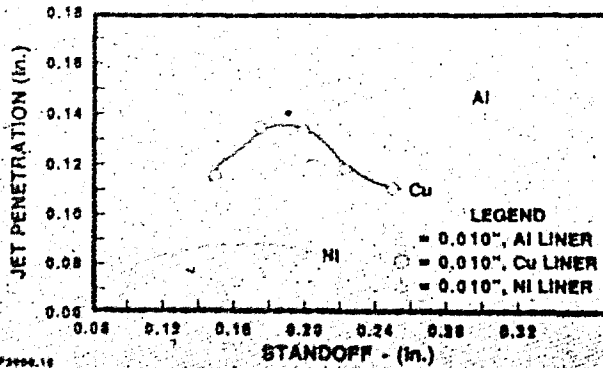
89F2000.14

0.004" ALUMINUM, COPPER AND NICKEL LINERS WITH A 90° APEX ANGLE



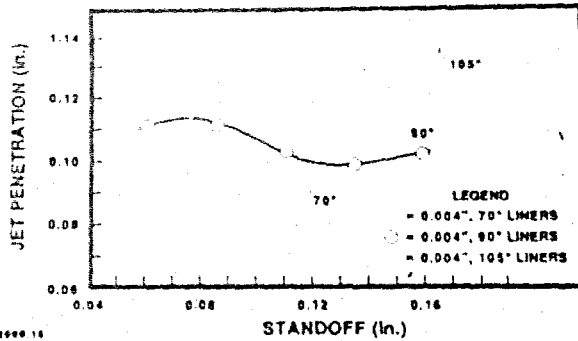
89F2000.14

FLANGE PLSC JET PENETRATION VERSUS STANDOFF FOR 0.010 INCH THICK Al, Cu, AND Ni LINERS

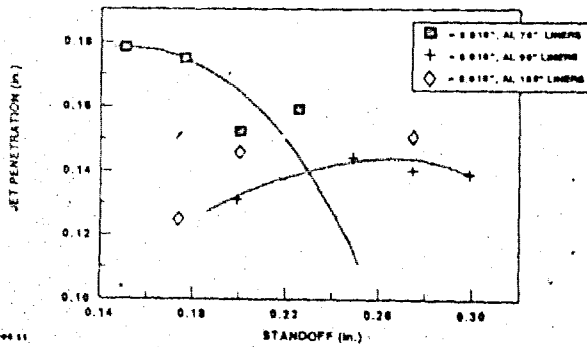


89F2000.14

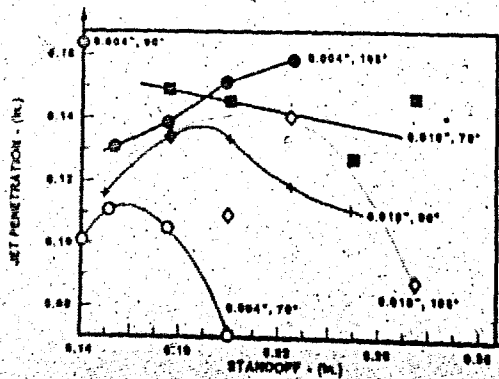
FLANGE PLSC JET PENETRATION VERSUS STANDOFFS FOR 0.004 INCH THICK ALUMINUM LINERS WITH 70°, 90° AND 105° APEX ANGLES



FLANGE PLSC JET PENETRATION VERSUS STANDOFF FOR 0.010" THICK AL LINERS WITH 70°, 90°, & 105° APEX ANGLES



0.004" and 0.010" COPPER LINERS WITH 70°, 90°, & 105° APEX ANGLES



EXPERIMENTAL ANALYTICAL PRECISION LINEAR SHAPED CHARGE (PLSC) PARAMETERS

PLSC: 25 gr. RDX, Al SHEATH Source: Eragn Bickford Camera: Cordin  
 Design: Flange liner Target: Aluminum  
 Tanker sheath: Aluminum

		V <sub>1</sub>	H <sub>1</sub>	T <sub>1</sub>	V <sub>2</sub>	H <sub>2</sub>	T <sub>2</sub>	P	S <sub>0</sub>
Al	004	70	55	65	49	55	67	83	09
Al	004	70	55	65	49	55	67	83	09
Al	004	70	42	50	36	44	71	72	13
Al	004	70	55	65	49	55	67	83	09
Al	010	90	29	13	23	27	74	79	18
Al	010	90	32	16	28	28	74	76	17
Al	010	90	37	20	36	36	74	80	13
Al	010	90	37	20	36	36	74	80	13
Al	010	105	28	32	24	26	74	76	13
Al	004	105	17	37	15	33	86	85	14
Al	004	105	24	44	31	37	84	79	14
Al	004	105	24	44	31	37	84	79	14
Al	010	110	23	25	19	20	80	81	15
Al	010	110	27	38	27	31	73	78	16

V<sub>1</sub> Jet tip velocity  
 H<sub>1</sub> Jet envelope angle relative to LSC  
 T<sub>1</sub> Linear apex angle  
 T<sub>2</sub> Linear thickness  
 P Maximum jet penetration in aluminum target  
 S<sub>0</sub> Jet target impact angle  
 S<sub>0</sub> Optimum standoff  
 Exp Experimental data  
 LSCAP LSCAP code prediction

PHOTOGRAPH OF 220 gr. ft., RDX, Al SHEATH, LSC JET



Fig 1000 10



PHOTOGRAPH OF 220 gr. ft., RDX, Al SHEATH, LSC JET

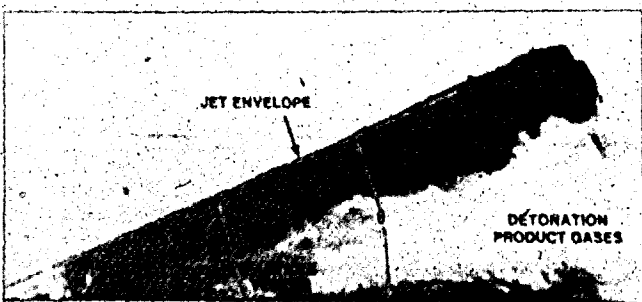


Fig 1000 10

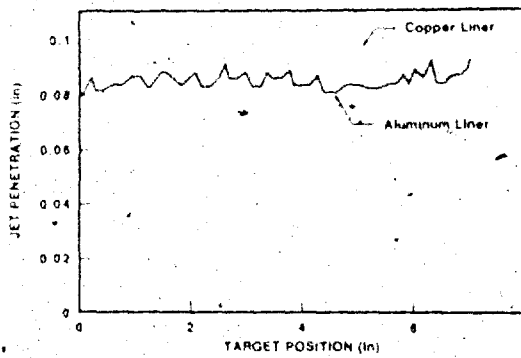


D9094-01

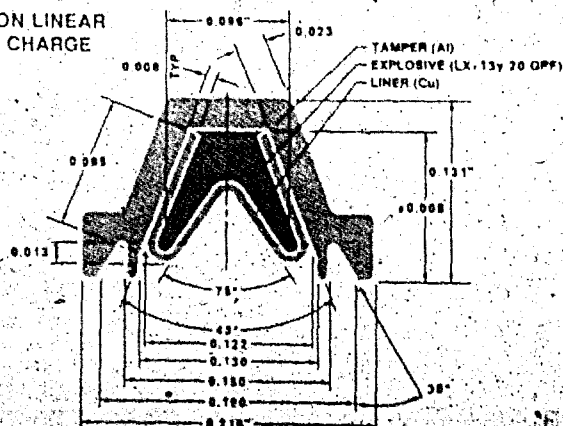
### LSCAP LINEAR SHAPED-CHARGE ANALYSIS PROGRAM

- EXPERIMENTAL CODE IN DEVELOPMENT
- MODELING FEATURES
  - SWEEPING / TANGENTIAL DETONATION-
  - LSC JET - TARGET IMPACT ANGLE
  - LINEAR ACCELERATION AND VELOCITY
  - JET FORMATION PROCESS
  - JET PENETRATION PROCESS / LAYERED TARGETS
  - VARIABLE AND CONSTANT STANDOFFS.
- ANALYTICAL CODE
  - INEXPENSIVE
  - PARAMETRIC STUDIES
  - INTERACTIVE

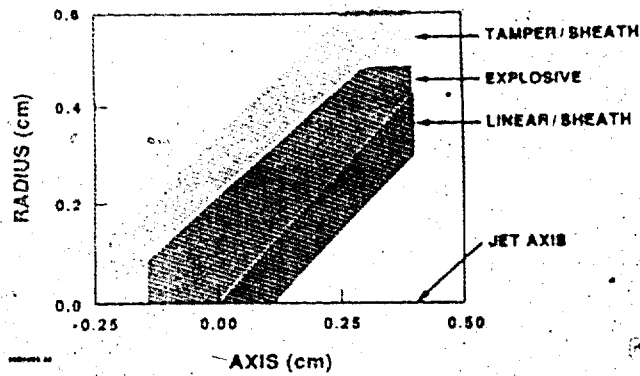
### REPRODUCIBILITY OF PLSC JET PENETRATION OF ALUMINUM 6061-76



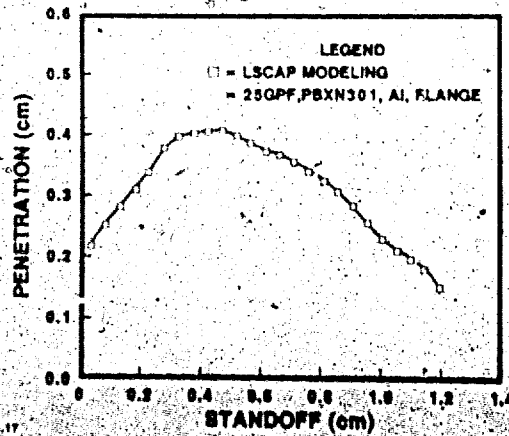
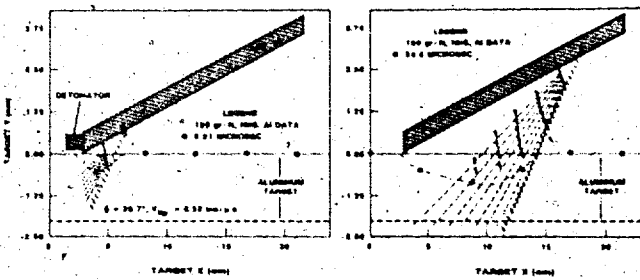
### PRECISION LINEAR SHAPE CHARGE



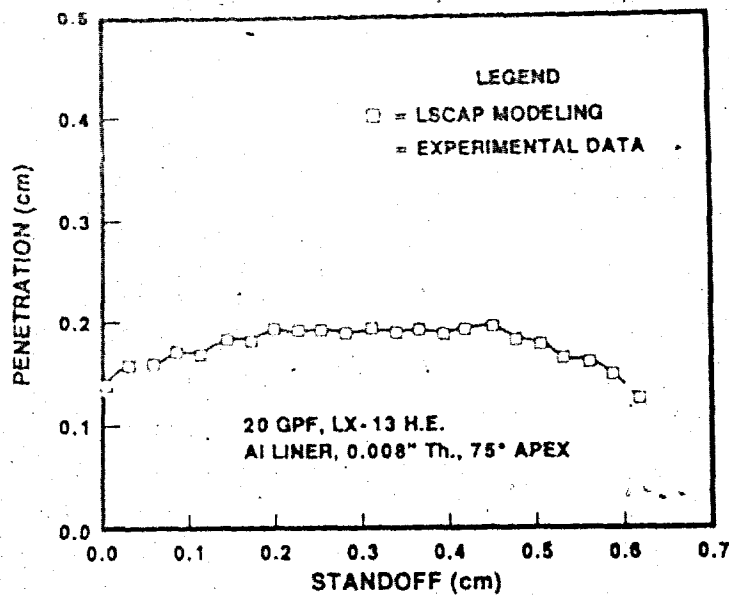
### LSCAP MODEL FOR LSC CROSS-SECTION



### LSCAP JET PENETRATION GRAPHICAL OUTPUT



## LSCAP VS. EXPERIMENTAL DATA



89F2000.16



## SUMMARY

89F2000.43

- PLSC HARDWARE FABRICATION PROCESSES DEMONSTRATED
- AUTOMATED EXPLOSIVE LOADING DEMONSTRATED
  - PANTEX PLANT
  - ENSIGN BICKFORD
- MORE OPTIMIZED PLSC DESIGN DEMONSTRATED
  - PLSC "W" DESIGN
    - LOCKHEED
  - PLSC "FLANGE" DESIGN
    - 40% MORE JET PENETRATION IN AL TARGET
  - JET PENETRATION REPRODUCIBILITY
    - ONE TEST - WITHIN 10%
    - TEST TO TEST - WITHIN 10%
- FUTURE ANALYTICAL WORK WITH LSCAP
  - IMPROVE YIELD STRESS - JET BREAKUP MODEL
  - IMPROVE YIELD STRESS JET - TARGET PENETRATION MODEL



# JET INITIATION MECHANISMS AND SENSITIVITIES OF COVERED EXPLOSIVES

M. Chick and T. J. Bussell  
Materials Research Laboratory  
Ascot Vale, Victoria 3032, AUSTRALIA

and

R. B. Frey and A. Bines  
Ballistic Research Laboratory  
Aberdeen Proving Ground, Maryland 21005

*The paper relates the computed pressure profile set up by jet penetration through a cover and underlying explosive to jet initiation characteristics. This method is used to assess likely initiation mechanisms. The analysis supports the proposal that the bow wave shock from jet penetration of the explosive is a major initiation mechanism and provides evidence for the existence of two previously unidentified initiation mechanisms. Jet penetration bow wave shock initiation is shown to occur in bare explosive for small diameter jets in certain situations and we demonstrate that spall from jet perforation of a cover does not contribute to the jet initiation of Composition B across an air gap.*

*A summary of likely jet initiation mechanisms, their operating regimes, and the appropriateness of predictive criteria for the detonation threshold is presented in tabular form. The study indicates jet diameter limitations in the application of  $V_j^2 d$  for predicting the detonation threshold.*

## INTRODUCTION

We have previously reported that a major mechanism for the metal jet initiation of covered explosive is via the bow wave shock set up by the jet penetration of the explosive<sup>1,2</sup> and a predictive criterion for the detonation threshold has been presented.<sup>3</sup> However, our recent investigations have suggested the existence of other initiation mechanisms and there is support<sup>4</sup> for the proposal<sup>2</sup> that for jets with small diameters with respect to the receptor's minimum detonation diameter the impact shock mechanism on bare explosive fails and initiation occurs via the jet penetration bow wave shock. Also, Held<sup>5</sup> has proposed that jet initiation of covered explosive is controlled by the stagnation pressure at the jet/explosive

interface, and that where there is an air gap under the cover, the spall from jet perforation contributes to jet initiation and, hence, affects the critical velocity for the detonation threshold.

This paper reports on a study aimed at assessing the alternative proposals for the jet initiation of covered explosive and on the status of predictive criteria for the detonation threshold. The approach has been to analyze the progressive pressure profile set-up by jet penetration through a cover and underlying explosive and relating the results to measured jet initiation characteristics. In this way, we examine the existence and regimes for different initiation mechanisms. The study includes further results on the effect of small diameter

jets on bare and covered explosive, and an experimental assessment of whether spall from the cover contributes to jet initiation across an air gap.

## METHOD OF COMPUTING JET PENETRATION PRESSURE PROFILES

We have calculated the general shape of the pressure profile of the jet penetration bow wave in different cover materials for a range of jet penetration velocities and cover thicknesses, deduced the corresponding pressure profile transmitted to the explosive, and assessed the general shape of the bow wave pressure profile set up in the jet penetration of the explosive. The analysis utilizes the standard jet penetration equation<sup>6</sup>

$$V_p = V_j \left( \frac{1}{1 + \gamma} \right) \quad (1)$$

where  $V_p$  is the jet penetration velocity,  $V_j$  is the jet velocity, and  $\gamma$  is the square root of the ratio of target density to jet density. Data from Reference 7 was used to determine the change in particle velocity,  $u$ , across the shock and the pressure change,  $P$ , across the shock was determined from the expression

$$P = \rho u V_p \quad (2)$$

where  $\rho$  is the target density. This assumes that the bow wave shock velocity is equal to the jet penetration velocity, which has been supported by experimental data.<sup>1</sup> Standard impedance match techniques were then used to compute the pressure delivered to the explosive.<sup>8</sup> The stagnation pressure  $P_b$ , in the target (cover or explosive) at the interface with the penetrating jet was determined from the Bernoulli relationship,<sup>6</sup>

$$P_b = \frac{1}{2} \rho V_p^2 \quad (3)$$

## GENERAL DESCRIPTION OF PRESSURE PROFILES

Jet impact on the cover forms a high pressure shock over a small area that can initiate explosive but is quickly quenched by lateral rarefactions. For example, a copper jet with a

velocity of 7 km/s produces an impact shock of 2600 kbar on a steel plate (which, unattenuated, produces a 1100 kbar shock in Composition B compared to a Large Scale Gap Test<sup>17</sup> initiation pressure of 25 kbar) but which is attenuated within a few jet diameters to a subcritical shock. The attenuation process has been demonstrated by Mader<sup>9</sup> in a numerical modeling study of a 1.5 mm diameter jet and is supported by the results from small diameter projectile initiation by Starckenberg et al.<sup>10</sup> The threshold for impact shock initiation of bare explosive is described by the Held<sup>11,12</sup> predictive criterion

$$V_j^2 d = k_1 \quad (4)$$

where  $d$  is the jet diameter and  $k_1$  is a sensitivity constant for the explosive receptor.

As the impact shock rapidly decays, it is overtaken by the formation of a pressure wave in front of the penetrating jet. If the penetration rate in the cover is supersonic, then the bow wave will form a shock with a velocity equal to the penetration rate. If the penetration rate is subsonic, the jet will be preceded by a ramped compression wave rather than a shock. For plexiglas covers, the bulk sound velocity estimated from Hugoniot data<sup>13</sup> is about 2.3 km/s and hence, for most practical situations ( $V_j > 3.5$  km/s), jet penetration will be supersonic and the bow wave will form a true shock front [pressure defined by Equation (2)] that ramps up to the stagnation pressure at the jet tip [pressure defined by Equation (3)]. For aluminum, the bulk sound velocity is about 5.4 km/s<sup>7</sup> and hence, for most practical situations ( $V_j < 6.4$  km/s), jet penetration will be subsonic and will be preceded by a compression wave that ramps up to the stagnation pressure. Thus, plexiglas and aluminum will transmit a shock and a compression wave respectively across the interface with the explosive.

However, the situation in steel is complicated. Steel has a high elastic sound velocity of about 6.0 km/s, but it may also have two distinct and slower plastic waves. The lower plastic wave has a minimum velocity of about 3.2 km/s, so for penetration rates between 3.2 and 6 km/s, steel may have a ramped elastic compression followed by a plastic bow wave

shock. This is shown schematically in Figure 1. We have used the analysis and results for steel covers to examine the processes responsible for the jet initiation of covered explosive.

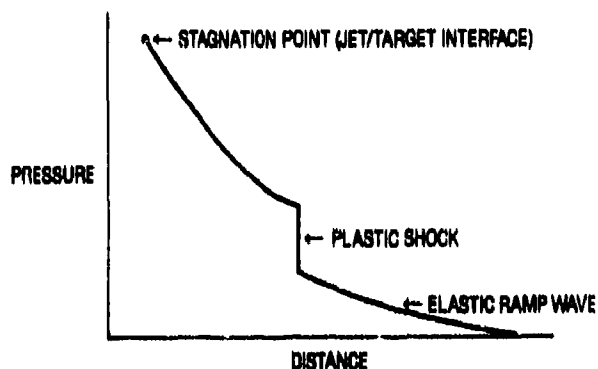


Figure 1. Schematic Graph of Pressure as a Function of Distance for a Bow Wave in Steel

### RELATIONSHIP OF PRESSURE PROFILE TO EXPLOSIVE INITIATION CHARACTERISTICS

If a bow wave shock exists in the cover plate it may cause initiation when transmitted into the explosive. Table 1 shows the calculated strength of the plastic bow wave in a steel cover as a function of jet velocity. The

pressure transmitted into Composition B is also shown. A likely example of this type of initiation is shown by the distance/time plot in Figure 2 produced by a 1.5 mm diameter jet striking a 12.5 mm thick steel cover. The data was obtained using multiple, orthogonal flash radiography by the method previously described.<sup>2</sup> Note that the jet had not reached the explosive when detonation commenced (thus precluding initiation from the jet penetration bow wave in the explosive) and the cover plate was about 8 jet diameters thick which would not be expected to support impact shock initiation. The jet velocity at the steel/explosive interface was 7.3 km/s which Table 1 suggests would deliver a pressure in Composition B from the bow wave in steel of about 17 kbar. This pressure is similar to, but a little lower than, typical shock initiation pressures.<sup>17</sup> This mechanism is unlikely to be responsible for defining a predictive criteria for the detonation threshold limit since initiation can take place at lower jet velocities by other mechanisms (see later).

In the explosive, the jet penetration rate is almost always supersonic, so a bow wave shock always forms. Table 2 shows the bow wave shock pressure as a function of jet velocity

Table 1. Properties of the Bow Wave in Front of a Copper Jet Penetrating Steel

Jet Velocity (km/s)	Penetration Rate (km/s)	Bow Wave Properties in Steel		Pressure Delivered to Composition B by Bow Wave in Steel	
		Pressure at end of ramp wave (kbar)	Change in pressure across plastic shock (kbar)	Pressure at end of ramp wave (kbar)	Change in pressure across shock (kbar)
4.0	2.06	*	*	*	*
5.0	2.58	*	*	*	*
6.0	3.09	*	*	*	*
6.5	3.35	133.0	3.6	36.0	2.0
7.0	3.60	133.0	22.0	36.0	11.0
7.5	3.87	133.0	45.0	36.0	21.0
8.0	4.12	133.0	69.0	36.0	32.0

\* No bow wave shock forms in the cover plate.

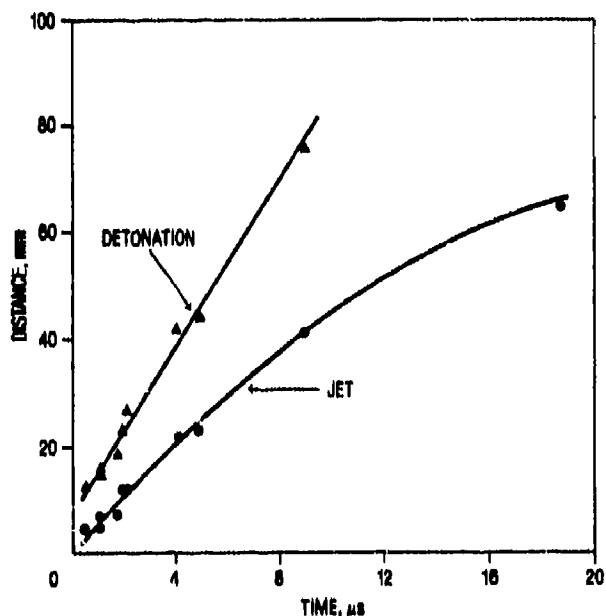


Figure 2. Space/Time Plot of a 1.5 mm Diameter Copper Jet Initiating Composition B Through a 12.5 mm Thick Steel Cover

Table 2. Properties of the Bow Wave in Front of a Copper Jet Penetrating Composition B

Jet Velocity (km/s)	Penetration Rate (km/s)	Bow Wave Shock Pressure (Kbar)
4	2.78	6.9
5	3.48	29.4
6	4.17	59.8
7	4.87	99.0
8	5.57	147.0

for Composition B. The calculations were done as described above, but the particle velocity behind the shock was determined from the Hugoniot given in Reference 7. The analysis results given in Tables 1 and 2 indicate that in most cases the bow wave which forms in the explosive produces a higher pressure in the explosive than does the bow wave from the steel cover plate. The data in Reference 2 confirms this conclusion, indicating that for Composition B covered with thick steel plates, it is the bow wave that forms in the explosive, not the bow wave which forms in the cover plate, which is responsible for initiation when

the jet velocity is close to the critical value for initiation. Since a bow wave shock will normally not occur in aluminum cover plates, one may presume that this is also the way initiation occurs in explosive covered with thick aluminum plates. Ramp compression waves are less efficient initiators than shock waves; this has been demonstrated by Setchell<sup>14</sup> experimentally for rise times of about 0.3 μs and theoretically by Frey.<sup>15</sup>

We should note that the bow wave shock pressure is not the highest pressure that the explosive sees. Behind the bow wave the pressure will rise to the stagnation pressure at the jet/target interface. The stagnation pressure is several times greater than the bow wave pressure. However, References 2 and 16 demonstrate that the stagnation pressure does not cause initiation. There are several reasons for this. First, if the bow wave does not initiate the charge, it may desensitize the explosive as is discussed in Reference 2. Second, at the critical condition the bow wave shock pressure is of sufficient magnitude to cause initiation (when compared to other shock initiation data) and it passes through a given plane in the explosive a few microseconds before the stagnation pressure. Third, the pressurization between a subcritical bow wave shock front and the stagnation point is a ramp formation which is not an efficient initiator.<sup>14,15</sup> After a jet enters the explosive, some time is required for the formation of a bow wave. This may account for the considerable distance required for this type of jet initiation of covered explosive. The proposed predictive criterion for the detonation threshold from bow wave shock initiation is similar to Equation (4) except that the sensitivity constant has a considerably higher value.<sup>3,4</sup>

We have examined the effect of the transition from supersonic to subsonic jet penetration in Composition B using the Ballistic Research Laboratory (BRL) 81 mm diameter shaped charge. The diameter of the jet was about 3 mm at the position of the study measurements. The approximate point of detonation breakout was assessed by measuring the time of arrival of either the jet, the bow wave, or the detonation wave at planes in the test charge which were spaced about 25.4 mm apart. The

test charges were made by stacking disks of Composition B with a thickness of about 25.4 mm. Time of arrival trigger screens were inserted between the disks. Two sets of tests were performed, one using Composition B disks with a diameter of 50.8 mm and the other using disks with a diameter of 101.6 mm.

The time of arrival data was plotted on a distance/time plot, as shown in Figure 3. In each test, there was a straight line portion corresponding to the relatively slow initial penetration of the jet, and a second straight line which corresponded to detonation. The point of intersection of these lines was taken as the point where detonation begins. Before detonation occurs we cannot be certain what triggers the screens. It could be the jet or the bow wave in front of the jet. However, since the bow wave should maintain a constant distance from the jet after an initial transient, the measured penetration rate may be nearly correct in either case.

The distance to detonation as a function of cover plate thickness is shown in Figure 4 for both sets of data. A separate scale on Figure 4 shows the calculated value of the average penetration rate of the jet in the first explosive disk. The distance to detonation is slightly longer for the smaller diameter samples. The smaller diameter sample fails to detonate at all for cover plates thicker than 229 mm. The larger diameter sample continues to detonate for 254 mm thick cover plates, but the distance to detonation increases markedly when the

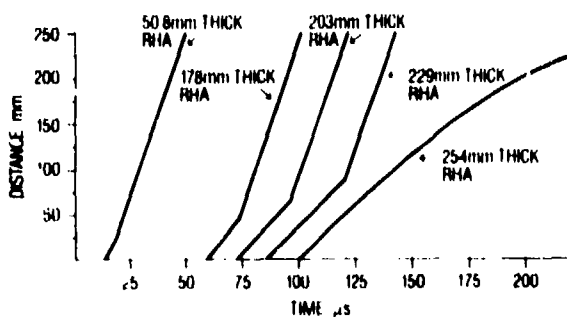
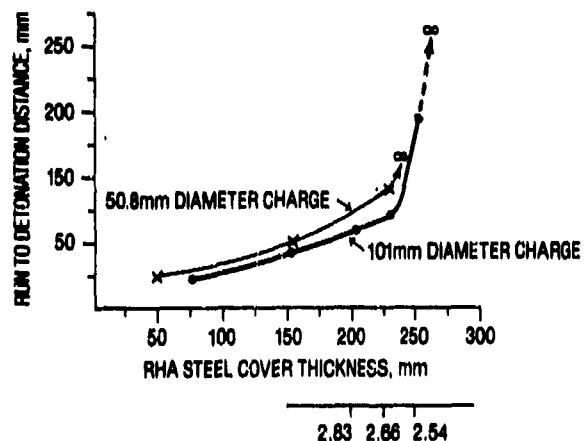


Figure 3. Run to Detonation Paths in 50.8 mm Diameter Composition B Covered by RHA Steel for a Jet from the 81 mm Diameter Shaped Charge



JET PENETRATION VELOCITY ENTERING COMPOSITION B, km/s

Figure 4. Run to Detonation Distance Vs. Cover Thickness and Jet Penetration Velocity Entering Composition B

cover plate increases from 229 to 254 mm. The bulk sound speed in Composition B has been reported to be between 2.5 and 2.7 km/sec.<sup>7</sup> The cover plate thickness, where the 50.8 mm explosive fails to detonate and where the 101.6 mm explosive shows the marked increase in distance to detonation, is the thickness which reduces the penetration rate to the sonic point. Thicker covers do not permit initiation by a bow wave shock, because no bow wave shock can form when the penetration rate is subsonic. Therefore, it is likely that the initiation which occurred in the larger diameter explosive with a 254 mm cover plate is due to a mechanism other than shock initiation; and the abrupt jump in distance to detonation is an indication of the change in mechanism. The very long run to detonation may indicate a type of deflagration to detonation process.

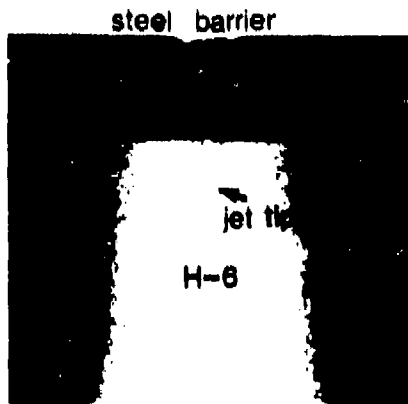
A non-shock mechanism suggests that jets at about 3 mm diameter may be the upper limit of the  $V_j^2 d = \text{constant}$  type of predictive criteria for the detonation threshold. There is insufficient data to consider an alternative predictive expression.

## SMALL DIAMETER JET INITIATION

We have recently reported<sup>4</sup> support for the proposal<sup>2</sup> that when the jet diameter is small with respect to the minimum detonation

diameter of a receptor explosive in the bare configuration the impact shock fails and detonation is produced by the jet penetration bow wave shock. This mechanism has been further investigated using a 0.75 mm diameter copper jet from a 15 mm diameter shaped charge, H-6 receptors and multiple, orthogonal flash radiography. The series of flash radiographs in Figures 5(a) to (d) show convincing evidence of the jet penetration bow wave shock initiation of bare H-6. In Figures 5(a) and (b)

the jet is observed penetrating into the bulk of bare H-6. Figure 5(c) shows the onset of detonation and in Figure 5(d) there can be seen a combination of established detonation and the detonation moving back through the H-6 that has been penetrated without initiation. This sequence of radiographs is similar to that reported for the 1.5 mm diameter jet initiation of steel covered Composition B.<sup>2</sup> Failure from the projectile impact shock has been extensively modeled by Mader and Pimbley.<sup>12</sup>



(a) *Jet Impact and Penetration of H-6 Without Sustained Detonation*



(b) *Jet Penetration into the Receptor Charge*



(c) *Onset of Detonation With a Run Distance of About 27 mm*



(d) *Detonation Established and Retonation Moving Back Through Penetrated H-6*

**Figure 5. Flash Radiographic Sequence of a 0.75 mm Diameter Copper Jet Initiating Bare H-6 Close to the Detonation Threshold Condition**

The run to detonation distance in H-6 close to the detonation threshold was about 27 mm, while the estimated critical jet penetration velocity was 3.8 km/s, which is well in excess of the bulk sound speed estimated from Hugoniot data<sup>13</sup> as 2.8 km/s, i.e., jet penetration is supersonic with bow wave shock formation. Previous firings<sup>3</sup> using steel covered H-6 and a 1.5 mm diameter copper jet gave a critical jet velocity of 4.9 km/s. This gives a  $V_j^2 d$  sensitivity constant of  $36 \text{ mm}^3/\mu\text{s}^2$  which would apply to jet penetration bow wave initiation. However, the data obtained with the 0.75 mm diameter jet and bare H-6 described above gave a critical jet velocity of 5.5 km/s (from Equation (1) where  $V_p = 3.8 \text{ km/s}$ ) and hence a significantly lower sensitivity constant of  $23 \text{ mm}^3/\mu\text{s}^2$ . The effect of the 0.75 mm diameter jet on the bow wave shock initiation threshold has been estimated for steel covered Composition B. The critical jet velocity was about 6.0 km/s ( $V_p = 4.2 \text{ km/s}$  in Composition B, i.e., supersonic penetration) to give a  $V_j^2 d$  sensitivity constant of about  $27 \text{ mm}^3/\mu\text{s}^2$ , which is significantly lower than the value of  $40 \text{ mm}^3/\mu\text{s}^2$  obtained for larger diameter jets. Thus, both the H-6 and Composition B results for the 0.75 mm diameter jet suggest that there is a lower limit to the use of  $V_j^2 d = \text{constant}$  criteria. In practice, the lower limit may not be generally exceeded since high velocity, coherent small diameter jets are difficult to produce since instabilities are readily formed by quite small fabrication inhomogeneities.

### CONTRIBUTION OF COVER PLATE SPALL TO JET INITIATION ACROSS AIR GAPS

We have previously demonstrated that air gaps between a cover or case and a solid energetic material significantly increase the filling's jet sensitivity, i.e., air gaps are highly sensitizing to jet initiation.<sup>1,2</sup> The effect was attributed to the air gap dissipating the desensitizing precursor waves (that travel ahead of the jet from the cover into the energetic material) and allowing the jet to produce impact initiation of the bare, unstressed filling on the far side of the air gap.<sup>2</sup> Recently, Held<sup>6</sup> confirmed our experimental observations using

Composition B receptors and proposed the alternative explanation that the filling across the air gap appears more sensitive because the jet is assisted in the initiation process by fragmentation spalling from the underside of the cover. If the latter explanation is correct, then current hazard analysis and predictive equations are inadequate to define the detonation threshold for air gap type systems. We have carried out two series of experiments to test the alternative proposals.

In the first series of experiments, the critical jet velocity was determined for Composition B separated from covers composed of steel and other materials by a 15 mm wide air gap. The jet was generated from a 38 mm diameter shaped charge. Critical velocities were determined by the method described in Reference 2.

Three types of covers were used and are illustrated in Figure 6. These consisted of: steel only; steel plus 5 mm of plexiglas glued to the underside of the steel and facing the Composition B; and steel with a 4 mm thick Kevlar plate separated from the underside of the steel by a 5 mm thick air gap, with the Kevlar facing the Composition B.

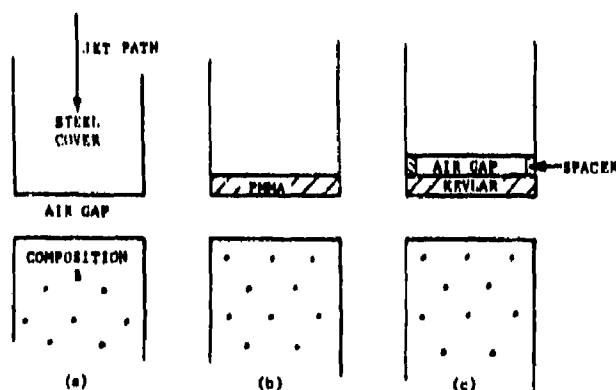


Figure 6. Experimental Arrangements for Assessing the Effect of Spall from Various Covers on Jet Initiation Across an Air Gap

The plexiglas will produce lower density spall than steel and if the spall is contributing to the initiation process, would be expected to be accompanied by a significant increase in the critical jet velocity. The Kevlar is a spall-reducing material, and its use would also be

expected to be accompanied by a significant increase in the critical jet velocity. Flash radiography showed that the small amount of steel spall produced was absorbed by the Kevlar. The measured critical jet velocities for each test arrangement given in Table 3 are similar within statistical limits and, hence, show no support for the spall-assisted mechanism.

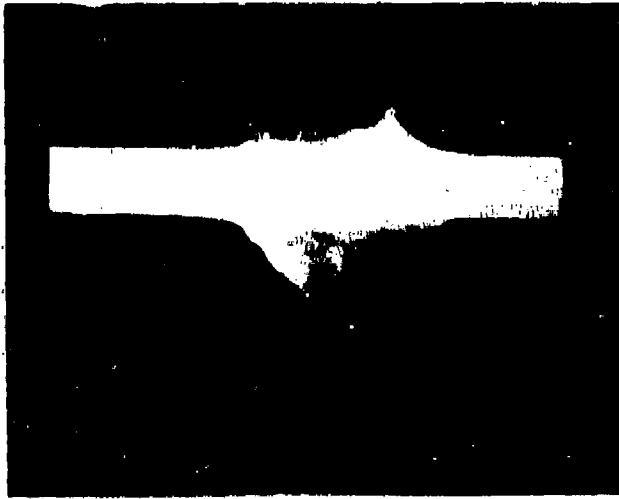
In the second series of tests two types of experiments were carried out whereby the jet was fired at 60° obliquity to the steel barrier. In one type of test the selected barrier thickness was thin (10 mm) in order to maximize the amount of spall. The Composition B receptor was positioned 15 mm directly under the spall, and the jet aimed to miss the explosive. This arrangement allowed investigation of massive spall (compared to that produced from critical jet velocity tests) but no jet impact on the explosive. In the other experiments the steel barrier was selected so that the jet path thickness produced a velocity marginally above the critical value (barrier thickness 65 mm, jet path length 130 mm), the explosive was placed on the projected jet axis and the spall arranged to miss the explosive. This arrangement allowed investigation of jet initiation without

spall (which, even so, would be minimal compared to that produced from the thin barrier).

The results of the massive spall/no jet explosive impact experiments are shown by the flash radiograph and illustration in Figures 7(a) and (b), respectively. The Composition B did not detonate but was recovered as lumps showing signs of surface melting. Figures 7(a) and (b) show that, although the jet missed the explosive, the spall cloud made direct impact with penetration of the surface (note the change in direction of the leading edge of the spall cloud on contact with the explosive). In these experiments the spall leading edge velocity in the direction of the axis of the Composition B cylinder was measured with flash radiography to be about 3 km/s. The exit hole in the steel barrier was directly above the Composition B and measured about 25 mm by 35 mm. In a variation of the massive spall/no jet impact experiment the plane of its top surface made an angle of about 60° to the steel plate. This arrangement was designed so that the leading edge of the spall cloud made an approximate planar impact with the Composition B. Again, the explosive failed to detonate or show significant reaction (see Figure 8).

*Table 3. Critical Steel Thicknesses and Jet Velocities for the Initiation of Composition B using the Experimental Arrangements Illustrated in Figure 6*

Cover System	Critical Steel Thickness		Critical Jet Velocity km/s
	Mean mm	σ 50% mm	
Steel only	156	8.8	3.0
Steel/5 mm PMMA	160	5.5	2.9
Steel/5 mm Air /4 mm Kevlar	145	4.7	3.1
Steel only (using different batch of explosive receptor charges)	138	2.6	3.2



(a) Flash Radiograph Showing that Intense Metal Spall from the Copper Jet Penetration of a Steel Plate Fails to Detonate Composition B. The jet missed the explosive.

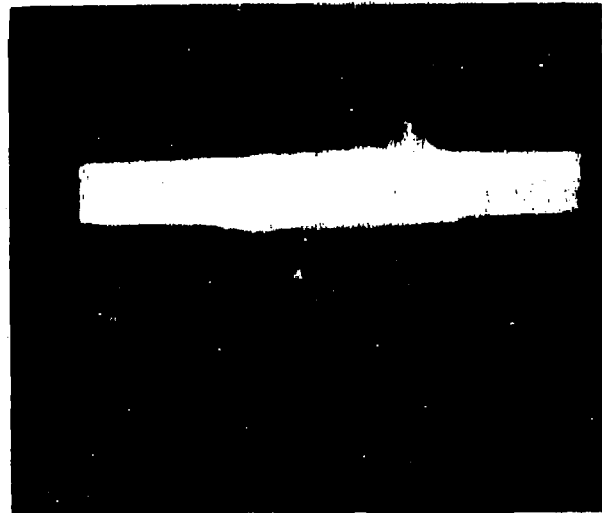
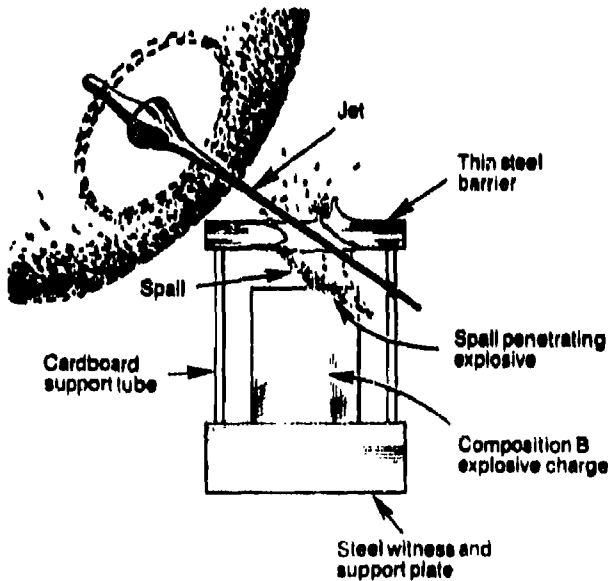


Figure 8. Flash Radiograph Showing Spall Making an Approximate Planer Impact on Composition B Which did not Detonate. The jet missed the explosive.



(b) Schematic Illustration of Result of Spall but not Jet Impact on Composition B

Figure 7. Flash Radiograph and Result of Spall

The jet only/no spall explosive impact experiments using thick barriers produced prompt detonation of the Composition B as shown by the flash radiograph and illustration in Figures 9(a) and (b). The exit hole was about 6 mm by 8 mm.

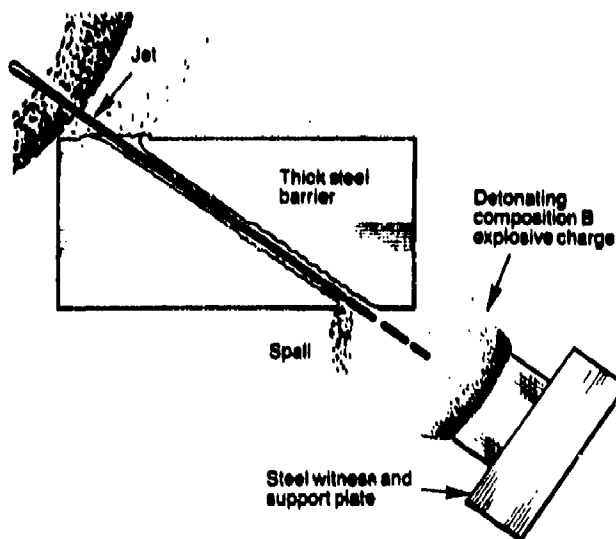
All of the tests reported above do not support the proposal that the spall from the cover contributes to the initiation of Composition B across an air gap and, hence, support the use of predictive criteria for the detonation threshold based on jet velocity and diameter. (The results shown in Figure 5 where small diameter jets were fired through steel across an air gap at bare H-6 to produce detonation deep in the explosive also support the proposal of initiation without spall.) Most of the tests were carried out at the critical condition where initiation of bare Composition B occurs promptly close to the surface. Thinner covers will allow higher velocity jets which will be even more effective initiators and thus spall from covers below the threshold thickness would also not be expected to contribute to the initiation process.

## CONCLUSION

The study supports the proposal that the bow wave shock from the jet penetration of the explosive is an important initiation mechanism for determining the detonation threshold of covered explosive. Evidence is presented for two previously unidentified initiation mechanisms; these are from the jet penetration bow wave shock transmitted from



(a) Flash Radiograph Demonstrating that a Jet Marginally Above the Critical Velocity Detonates Composition B Without the Presence of Spall



(b) Schematic Illustration of Result of Near Critical Jet Impact on Composition B Without Spall

Figure 9. Flash Radiograph and Result of Near Critical Jet Impact

the cover to the explosive and from large diameter jet subsonic penetration of the explosive. The latter process would appear to set the upper limit for the detonation threshold for large jets. A summary of likely jet initiation mechanisms and their possible operating

regimes is given in Table 4; the table also comments on the application of the appropriate criterion for predicting detonation. It is proposed that the  $V_j^2 d$  criteria operates over a limited range of jet diameters.

Jet penetration bow wave shock initiation of bare explosive is demonstrated using a small diameter jet and flash radiography. An experimental study supports the proposal that spall produced by the jet perforation of a cover does not contribute to jet initiation across an air gap.

## ACKNOWLEDGMENTS

We wish to record our thanks to Mrs. L. McVay of MRL for assistance with the experiments and to Drs. C. Mader and J. McAfee of LANL, USA, and to Dr. M. Held of MBB, FRG, for helpful discussions.

## REFERENCES

1. Chick, M. and Hatt, D. J., "The Mechanism of Initiation of Composition B by a Metal Jet," *Proceedings of the Seventh Symposium (International) on Detonation*, NSWC MP 82-334, 1981, p. 352.
2. Chick, M.; Macintyre, I. B.; and Frey, R. B., "The Jet Initiation of Solid Explosives," *Proceedings of the Eighth Symposium (International) on Detonation*, Albuquerque, NM, NSWC MP 86-194, 1985, p. 318.
3. Chick, M.; Bussell, T. J.; Frey, R. B.; and Boyce, G., "Initiation of Munitions by Shaped Charge Jets," *Proceedings of Ninth International Symposium on Ballistics*, Shrivenham, UK, 1986, pp. 2-421.
4. Chick, M. and Bussell, T. J., "The Effect of Minimum Detonation Diameter on the Mechanism of Jet Initiation of Bare Explosives," *J. Appl. Phys.*, Vol. 63, No. 9, 1988, p. 4761.
5. Held, M., "Discussion of the Experimental Findings from the Initiation of Covered but Unconfined High Explosive Charges with Shaped Charge Jets," *Propellants, Explosives, Pyrotechnics*, Vol. 12, 1987, p. 167.

*Table 4. Summary of Likely Initiation Mechanisms and Operating Criteria*

Mechanism	Regime and Predictive Criteria
1. Jet impact on bare explosive	<ol style="list-style-type: none"> <li>1. Detonation threshold determined by M. Held's <math>V_j^2 d = k_1</math> predictive equation.</li> <li>2. Occurs promptly close to explosive surface or not at all.</li> <li>3. Does not apply to jets with diameters small with respect to receptor explosive's minimum diameter for detonation, where jet penetration bow wave initiation occurs (see 4 below).</li> </ol>
2. Jet impact shock on cover	<ol style="list-style-type: none"> <li>1. Only for covers less than a few jet diameters thick.</li> <li>2. Requires increasing critical jet velocity with cover thickness above that predicted by <math>V_j^2 d = k_1</math> (see 1 above).</li> </ol>
3. Jet bow wave in cover transmitted into explosive	<ol style="list-style-type: none"> <li>1. Applies to thin covers.</li> <li>2. Appears to require the formation of a bow wave shock in cover.</li> <li>3. Hindered by ramp wave formation in cover which is desensitizing.</li> <li>4. Does not determine detonation threshold limit.</li> </ol>
4. Jet penetration of explosive	<ol style="list-style-type: none"> <li>1. Considered to be a major mechanism. Initiation by the jet penetration bow wave shock.</li> <li>2. Occurs over a wide range of cover thicknesses and materials.</li> <li>3. Within certain jet diameter limits detonation threshold predicted by <math>V_p^2 d = k_2</math> or <math>V_j^2 d = k_3</math>. Constants are much different from <math>k_1</math> in mechanism 1 listed above.</li> <li>4. Also applies to bare explosives where jet diameter small with respect to receptor explosive's minimum detonation diameter.</li> <li>5. Predictive criterion for small diameter jets appears to require an exponent for the velocity term greater than 2.</li> </ol>
5. Jet penetration bow waves reflected back into explosive filling	<ol style="list-style-type: none"> <li>1. Observed near critical jet initiation velocity for receptor charges of limited geometry.</li> <li>2. Requires confining rear surface; may be applicable to small confined rounds.</li> <li>3. Special case of mechanism 4.</li> </ol>
6. Subsonic jet penetration of explosives	<ol style="list-style-type: none"> <li>1. Applicable to larger diameter jets.</li> <li>2. Appears to be associated with a very long run to detonation.</li> <li>3. Limits the use of <math>V_j^2 d = k_1</math> (see 4 above) for predicting detonation threshold.</li> <li>4. No predictive criterion available for detonation threshold.</li> </ol>
7. Separate impacts from particulated jet penetration of explosive	<ol style="list-style-type: none"> <li>1. May require well separated jet particles.</li> <li>2. Does not appear to have been studied.</li> </ol>

6. Birkoff, G.; MacDougall, D.; Pugh, E. M.; and Taylor, G., "Explosives with Lined Cavities," *J. Appl. Phys.*, Vol. 9, 1948, p. 563.
7. Van Thiel, M.; Kusubov, A.; and Mitchell, C., Eds., "*Compendium of Shock Wave Data*," Lawrence Livermore Laboratory Report UCRL 50108, Vol. 1, 1966.
8. Duvall, G. F. and Fowles, R., "*Shock Waves*," Academic Press, R. S. Bradley, Ed., London, 1963, Chapter 9.
9. Mader, C., computer film and notes, Los Alamos National Laboratory, Los Alamos, NM, Jet impact shock initiation and desensitization, 1987.
10. Starckenberg, J. J.; Huang, Y. K.; and Arbuckle, A. L., "*A Numerical Study of Shock Initiation of Composition B by High Speed Impact of Small, Steel Projectiles*," ARBRL-TR-02548, BRL, Aberdeen Proving Ground, MD, 1984.
11. Held, M., "Initiating Explosives, a Multiple Problem of the Physics of Explosives," *Explosivstoffe*, Vol. 5, 1968, p. 121.
12. Mader, C. L. and Pimbley, G. H., "Jet Initiation and Penetration of Explosives," *J. Energetic Materials*, Vol. 1, 1983, p. 3.
13. Dobratz, B., Ed., *LLNL Explosives Handbook*, LLNL, Livermore, CA, 1981.
14. Setchell, R., "Ramp Wave Initiation of Granular Explosives," *Combustion and Flame*, Vol. 43, 1981, p. 255.
15. Frey, R. B., "Cavity Collapse in Energetic Materials," *Proceedings of the Eighth Symposium (International) on Detonation*, Albuquerque, NM, USA, NSWC MP 86-194, 1985, p. 68.
16. Chick, M.; Bussell, T. J.; and Frey, R. B., "Mechanisms of the Jet Initiation of Solid Explosives," *Proceedings 19th ICT International Conference*, Karlsruhe, FRG, 1988, p. 24.1.
17. Price, D.; Clairmont, A. R.; and Erkman, J. O., "*The NOL Large Scale Gap Test III. Compilation of Unclassified Data and Supplementary Information and Interpretation of Results*," NOLTR 74-40, NOL, White Oak, MD, 1974.

# INITIATION PHENOMENA WITH SHAPED CHARGE JETS

Manfred Held  
Messerschmitt-Bölkow-Blohm GmbH  
Research Department  
8898 Schrobenhausen, WEST GERMANY

*The initiability of unconfined high explosive charges by shaped charge jets can be well described with the  $v^2d$ -criterion. For covered, but still unconfined explosive charges, higher threshold values are measured. The reasons for this are preshocking, precompression, different loaded areas, and different pressure time histories of the acceptor charge in contact, compared to an arrangement with a larger air gap. Inversely, the threshold values are strongly decreasing by a confinement of the acceptor charge.*

## HISTORY

The initiation phenomena to shaped charge attack of high explosive charges in particular has been investigated over many years. But the number of papers published in the open literature is rather limited. In 1945, workers<sup>1</sup> in the United Kingdom reported on the use of flash radiography to study the initiation of bare tetryl pellets by a metal jet generated by a shaped charge.

In 1955, Zernov et al.,<sup>2</sup> using 42-mm and 105-mm diameter shaped charges, undertook a preliminary investigation into the jet initiation of Composition B charges of different length either bare, or with various thicknesses of steel cover plates and/or with side confinement. The study concluded that the coverplate thickness, explosive charge lengths, and degree of confinement affected the jet initiation of the explosive. Photography of the exterior of the charge indicated that as steel cover plate thickness was increased, the onset of detonation occurred further down the charge. The limited nature of the investigation did not allow this observation to be explained. Interpretation of the results was complicated by the spread of results obtained for a given cover plate thickness and length of explosive.

In 1968, Held<sup>3</sup> reported the initiation of bare high explosive charges by jets from

shaped charges of 22 mm, 32 mm, 64 mm, and 96 mm diameter. It was found that the threshold velocity,  $v$ , of the jet particles was related to the jet diameter,  $d$ , by the relationship  $v^2d = \text{constant}$ . Held<sup>4</sup> has also shown that the  $v^2d$ -criterion for detonation has been generally confirmed in other work on blunt-projectile and flying foil impact tests against various high explosives.

In 1981, Mader and Pimbley<sup>5</sup> reported work by Campbell using bare PBX-9404 and PBX-9502. The results supported Held's  $v^2d$ -critical initiation criterion for particulated jets. Mader modeled the process numerically by treating the jet as a solid cylinder of metal impacting the bare explosive.

Mader<sup>6</sup> (1986) has well summarized recent advances in numerical modeling of jet initiation and penetration of explosives using the two-dimensional Eulerian hydrodynamic code 2 DE, with the shock initiation of heterogeneous explosive and the Forest Fire burn model. He confirmed theoretically the critical jet or projectile velocity for initiation propagating detonation using the projectile diameter and the Held<sup>3,4</sup> critical  $v^2d$  expression.

Chick and Hatt<sup>7-10</sup> (1981-1985), using X-ray flash radiography, have reported on the initiation of covered, but otherwise unconfined, high explosive charges by means of the jet of a 38-mm shaped charge, the high explosive.

being in direct contact with the cover material in some of the experiments, but with a 15-mm air gap between in others. It was found that an unconfined high explosive, which is in contact with the barrier, requires a higher jet velocity for initiation than one with an air gap. The  $v^2d$ -criterion for attack of bare charges was also confirmed with jets of 38-mm and 81-mm shaped charges,<sup>11</sup> and replaced for covered charges by  $ud$ , where  $u$  is the crater velocity. Critical steel cover thicknesses and critical jet velocities for creamed and pressed TNT, Composition B, H-6, and pressed tetryl were also measured. A summary of the Australian opinion on jet initiation mechanism for covered, but unconfined high explosive charges is given by Chick, Wolfsan, and Learmonth<sup>12</sup> (1986).

Vigil<sup>13</sup> (1985) has made initiation tests with very small shaped charges (1.73 mm to 3.46 mm cone diameter) against a few types of acceptor charges.

Held<sup>14,16</sup> (1987) has reproduced the tests made by Chick and Hatt<sup>7,10</sup> with similar size shaped charges and with acceptor high explosive charges having a similar geometry and sensitiveness. However, this time the diagnostic instrument was not FXR, but a simultaneous framing and streak recording rotating mirror camera. To demonstrate the different effects, the air gaps between the barriers and/or the acceptor charges were spaced and/or interrupted by air gaps.

McAfee<sup>19</sup> (1987) has obtained similar streak records to find the build-up distances or corner-turning distances (CTD) for the initiation of PBX-9502 by the copper jet from the LAW warhead (66 mm diameter, 42° angle). Detailed streak measurements are much more accurate than the use of witness plates only to indicate the promptness of the initiation (Campbell<sup>20</sup>).

## TEST SETUP

The test setup for the measurement of the initiability of an unconfined high explosive charge, covered by a steel block either in direct contact with the explosive or with a specified air gap between, and of a confined high explosive charge is shown in Figure 1. The

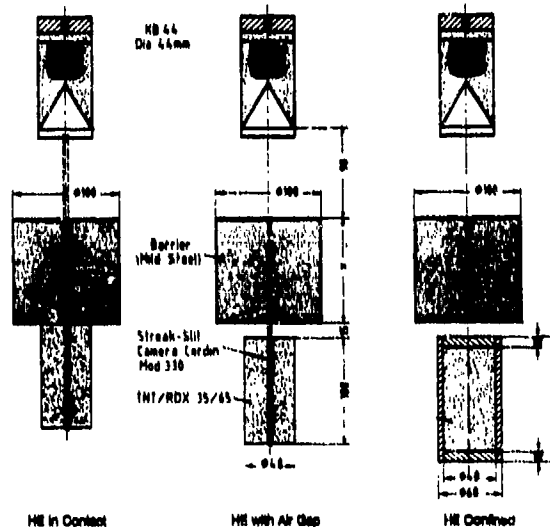


Figure 1. Experimental Setup of Shaped Charge with 44 mm Diameter, Barrier, and Acceptor Charge, Either Unconfined in Contact to the Barrier or with 15 mm Airgap, or Confined

tests with unconfined charges are solely to establish the threshold between a "reaction" and a "detonation" of the acceptor charge, i.e., a measure of the ease of initiation or "initiability" by a shaped charge jet. With confined high explosive charges one can get also the threshold for no reaction/reaction—which happens only for very insensitive high explosive charges—or the threshold for less powerful reactions. Figures 2 through 5 show selected frames and the corresponding streak records of unconfined high explosive charges in contact, respective with an air gap after barriers with different thicknesses.

## RESULTS WITH UNCONFINED ACCEPTOR CHARGES

The experimental results regarding the build-up distances,  $\Delta s$ , the run-up times,  $\Delta t$ , and the initiation times,  $t_i$ , for the two different arrangements of the barrier relative to the unconfined acceptor charge, as a function of the residual jet tip velocity after the barrier are summarized in Figure 6 for the unconfined acceptor charge in direct contact with the

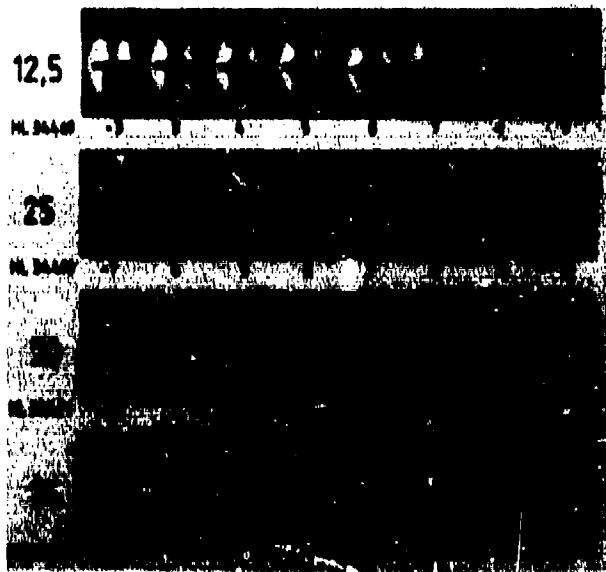


Figure 2. Example of Individual Frames of Different Barriers as Recorded With the Cordin Model 330 Rotating-Mirror Camera at About  $10^6$  Frames per Second. The barrier thicknesses are indicated to the left of the picture.

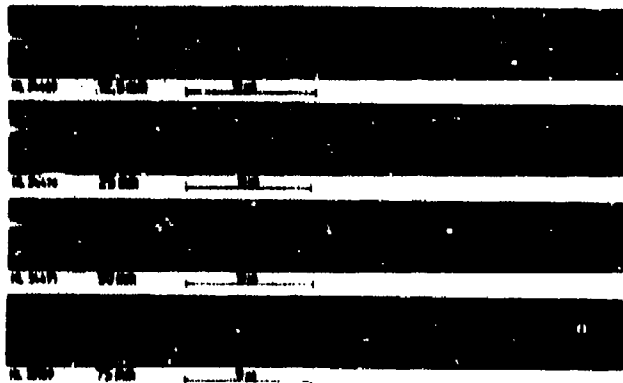


Figure 3. Streak Records of the Shaped Charge Jet Hitting the Barrier (Left in the Picture), and Delayed Appearance of a Detonation in the Acceptor Charge. These records were obtained simultaneously with the individual frames (Figure 2).

barrier, and in Figure 7, for a 15-mm air gap between the unconfined acceptor charge and the steel barrier.<sup>16</sup> Chick and Hatt<sup>7-9</sup> (1981) also have roughly determined, with the help of FXRs, the build-up distances and delay times for the initiation of unconfined Composition B as a function of the cover plate thickness. The build-up distances  $\Delta s$  and/or the initiation



Figure 4. Samples of Individual Frames of the Initiation of Acceptor Charges Arranged 15 mm Behind Barriers of Different Thickness

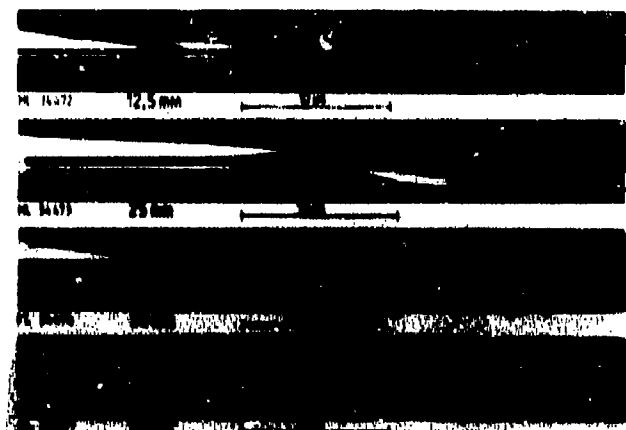


Figure 5. Streak Records of Shaped Charge Jet Impact on a Barrier (Left in the Individual Pictures), Exit of the Jet from the Barrier, and Initiation of the Acceptor Charge. Records were obtained simultaneously with the individual frames of Figure 4.

times  $t_i$  of the tests with the charges in contact with the barrier (only for these were data from Chick and Hatt available) are in fairly good agreement.

Initiation time  $t_i$  is defined from measured run-up time  $\Delta t$  minus the time  $t_1$ , which is necessary for the detonation wave to

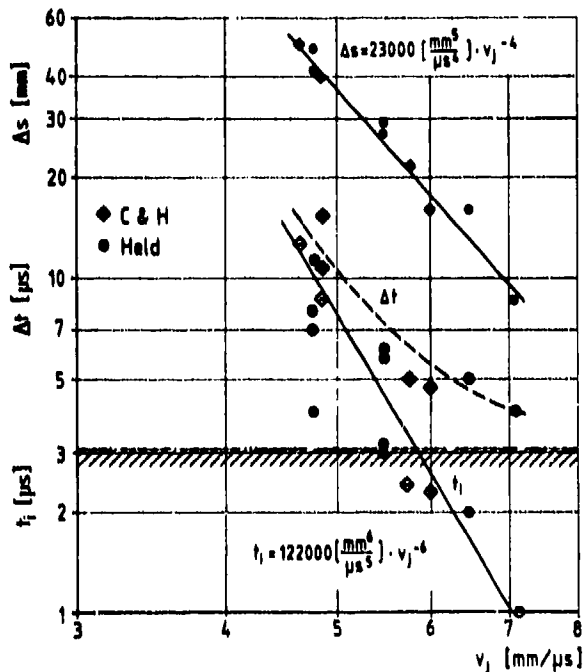


Figure 6. Build-up Distance  $\Delta s$ , Run-up Times  $\Delta t$ , and Initiation Times  $t_i$  as Function of the Residual Jet Velocity  $v_j$ , for the Arrangement with the Unconfined High Explosive Charge in Contact with the Barrier

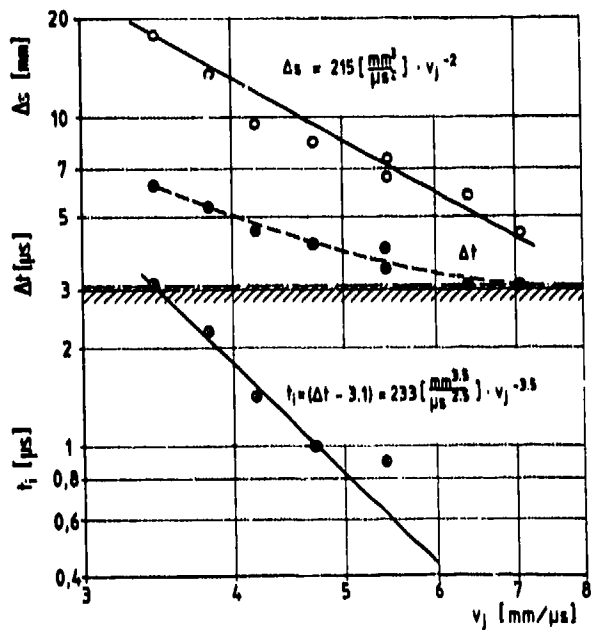


Figure 7. Build-up Distances  $\Delta s$ , Run-up Times  $\Delta t$ , and Initiation Times  $t_i$  as Function of the Residual Jet Velocity  $v_j$ , for the Arrangement with a 15-mm Air Gap Between the Unconfined High Explosive Charge and the Barrier

propagate from the axis to the surface of the charge. ( $t_i$ ) = R/D, where R = radius and D = detonation velocity of the acceptor charge.)

The unconfined high explosive charge directly in contact with the barrier is less easily initiated than the one with an air gap between. The reasons for this are as follows:

- the acceptor charge is being pre-shocked by preceding waves (in the author's opinion, this is only of minor importance, because these shock waves are comparatively weak);
- the high explosive is pre-compressed by the bulging of the barrier plate as the shaped charge jet perforates it;
- relatively slow loading of the test charge generated by the bulging target plate and by the pressure of the cratering jet and there is no such high,

one-dimensional pressure as in the case of a free jet; and

- the high explosive charge in contact with the barrier is exposed in a smaller area than the charge with an air gap between, because the emerging shaped charge jet forms a large-area spray of fragments.

The three listed effects appear to be responsible for the differences in initiability of a covered and an uncovered acceptor charge. However, the test setup and the sensitivity of the acceptor charge might also play a critical role as to which of these three effects will be more or less dominant.

The values of the particulation time,  $t_p$ , and the particulated jet diameter,  $d_p$ , are measured,  $v_j$  and  $t_j$  for the exiting jet after the barrier were calculated. So the diameter,  $d_j$ , of

the exiting jet can be calculated from the following equation:

$$d_j = d_p (t_p / t_j)^{0.5}$$

In Figure 8, a representation is given of the build-up distance,  $\Delta s$ , of the measured delay times,  $\Delta t$ , and of the initiation time,  $t_i$ , as a function of  $v_j^2 d_j$  for the given acceptor charge in contact with the barrier, and Figure 9 shows analogous relationships for the acceptor charge at an air gap of 15 mm behind the barrier.

Surprisingly, such a log-log representation gives a straight line in first approximation, and  $\Delta s$  and  $t_i$  can be written as follows for the case of the high explosive charge in contact (Figure 8):

$$\Delta s = 160 \times 10^3 (v_j^2 d_j)^{-2}$$

$$t_i = 16.8 \times 10^3 (v_j^2 d_j)^{-2}$$

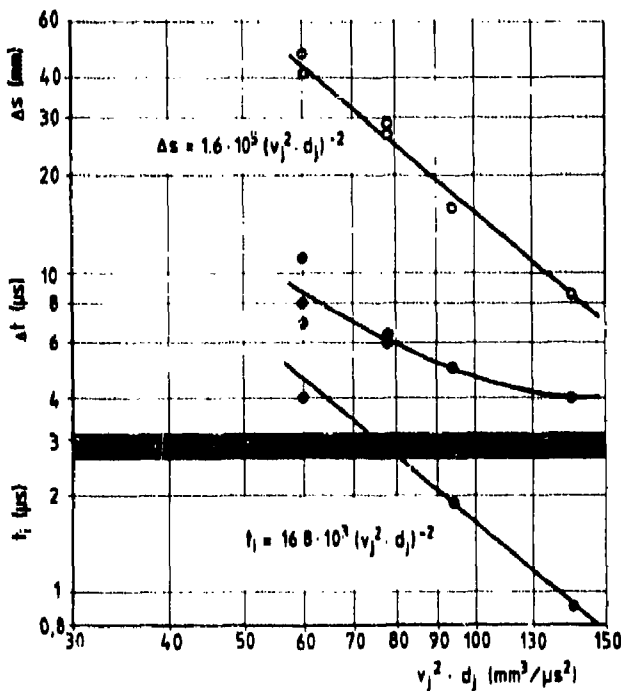


Figure 8.  $\Delta s$ ,  $\Delta t$ , and  $t_i = f(v_j^2 d)$  for the Arrangement With the Unconfined High Explosive Charge in Contact With the Barrier

With a good fit of the measured points, the result for the 15-mm air gap arrangement is (Figure 9)

$$\Delta s = 373 (v_j^2 d_j)^{-0.91}$$

or, still in fair agreement with a perhaps more plausible exponent:

$$\Delta s = 560 (v_j^2 d_j)^{-1}$$

The measured initiation times,  $t_i$ , which show an even greater dispersion, can be described approximately by the equations

$$t_i = 205 (v_j^2 d_j)^{-1.25}$$

$$t_i = 3600 (v_j^2 d_j)^{-2}$$

## RESULTS WITH CONFINED ACCEPTOR CHARGES

A few tentative trials were made in order to determine how the initiation behavior would change if the acceptor charge were fully

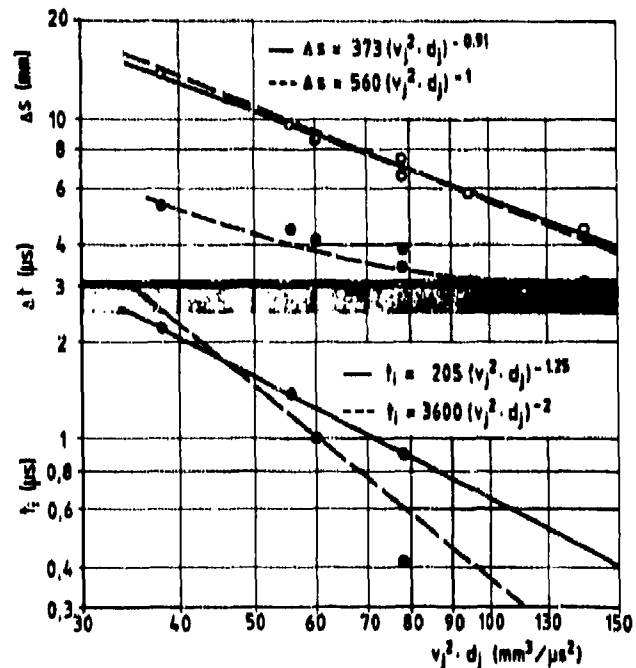


Figure 9.  $\Delta s$ ,  $\Delta t$ , and  $t_i = f(v_j^2 d)$  for the Arrangement With a 15-mm Air Gap Between the Unconfined High Explosive Charge and the Barrier

confined, and where the threshold between reaction and no reaction of the acceptor charge would lie in such a case.

Results of four trials are listed in the table below:

Barrier with Confinement [mm]	$v_j$ [mm/ $\mu$ s]	Type of Reaction
110	4.1	Det.
150	3.5	Det.
175	3.2	Defl.
200	2.9	Defl.

An "unconfined" high explosive charge behind a 100-mm barrier and in contact with a 10-mm cover plate, showed no detonation, whereas the confined charge came to a full detonation. The same occurred also after a total of 150 mm had been perforated (Figure 10). A violent reaction occurred even after a total distance of 175 mm had been perforated, and an only slightly less violent reaction even after a total perforation thickness of 200 mm.

These results show that the confined test charge will be detonated by a lower velocity residual jet than the unconfined charge. The limit of initiation of the unconfined charge, being in contact with the barrier, by this type of shaped charge was found to be 4.8 mm/ $\mu$ s, while the confined charge is still initiated by a jet having a velocity as low as 3.5 mm/ $\mu$ s. A very violent reaction occurs even at a jet velocity of approximately 3.1 mm/ $\mu$ s, the evidence being the type of fragments generated; a full deflagration is still obtained with jet velocity 2.8 mm/ $\mu$ s (Figure 11).

The times for a reaction in the case of an unconfined charge must be relatively short. The high explosive charge must react before it is broken up by the perforating jet and/or by the pressure developing internally from reaction around the jet path. Under confinement, the charge has much more time to react and can come to full detonation through a DDT process.

These preliminary tests with confined acceptor charges and the comparison with unconfined acceptor charges demonstrated the

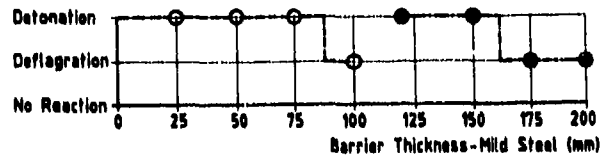


Figure 10. Type of Reaction as a Function of Barrier Thickness for Unconfined  $\circ$  and Confined  $\bullet$  Acceptor Charges

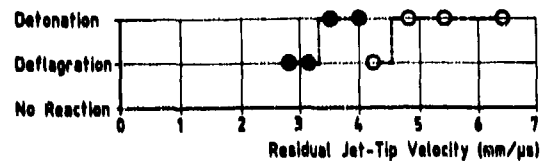


Figure 11. Type of Reaction as a Function of Jet Velocity for Unconfined  $\circ$  and Confined  $\bullet$  Acceptor Charges

important fact that unconfined charges are suitable only for establishing the initiability, because the perforating jet and the internal reaction it causes will rapidly destroy the test charge.

Confinement holds the test charge together for a considerably longer time, so that a reaction that starts more slowly can still run up to a full detonation. Therefore, the threshold between detonation and reaction, and the threshold between reaction and no reaction, will in the case of a confined charge, of course, be at considerably lower jet penetration velocities.

## RESULTS WITH PROPELLANTS

In the open literature, few tests are published relating to shaped charge attack against propellants. The behavior of charges of different types of propellant under shaped charge attack has been investigated by the author.

With high content in sensitivity materials, the whole of the composition comes to full detonation (Figure 12 (a)). If the propellant was less sensitive, only that part of the sandwich which has a smaller angle between the jet- and detonation-direction, came to full

detonation (upper part in Figure 12 (b)) and, finally, with much less energetic materials reaction occurred only around the jet (Figure 12 (c)).

The conclusion from these tests is that, depending on the sensitiveness, the composition can come to a full detonation, or a partial detonation, or only a reaction in a limited region around the jet impact.

No doubt, the initiability is also correlated with the critical detonation diameter of the tested material. The jet is generally very



(a)



(b)



(c)

Figure 12 (a) through (c). The Three Possible Types of Reaction of Solid Propellants Under Shaped Charge Jet Attack: "Full Detonation," "Partial Detonation" (in the Upper Region of Figure 12 (b) Only), and "Partial Reaction"

small in diameter. The "stagnation" pressure decreases radially and follows the penetrating jet. If, over a dimension less than the critical detonation diameter of the material, the shock pressure in the bow wave around the jet becomes less than the initiation threshold pressure, a high-order reaction of the propellant cannot be expected.<sup>22</sup>

If no detonation results from the shaped charge impact and perforation, no doubt exists that a burning reaction of the propellant will occur. Asay, Ramsay, and Campbell<sup>23</sup> have described this behavior quite adequately. They have given a good schematic model (Figure 13) which helps to define the regions of interest in the case of detonation failure.

### $v^2d$ CRITERION

The  $v^2d$  criterion gives the critical threshold velocity for the initiation of charges of different high explosives as a function of the diameter of shaped charge jets or projectiles (Figure 14). Experiments with flying foils of different diameters and theoretical predictions are also included.

The following table is summarizing the values and gives the used references.

In early experiments<sup>3</sup> (1968) with shaped charges, having different base diameters and, hence, also different jet diameters, which were fired against unconfined charges of TNT/RDX-35/65, the critical velocity of impact was found to be inversely proportional to the square root of the jet diameter.

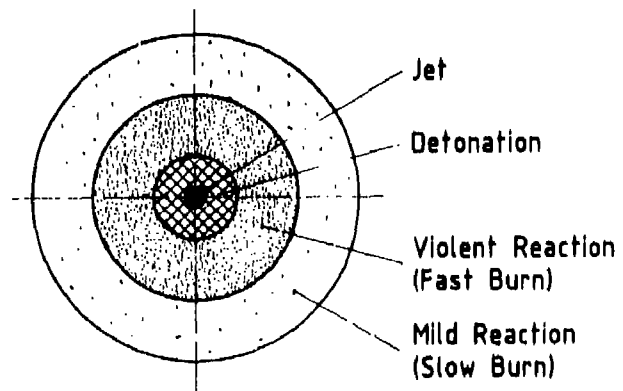
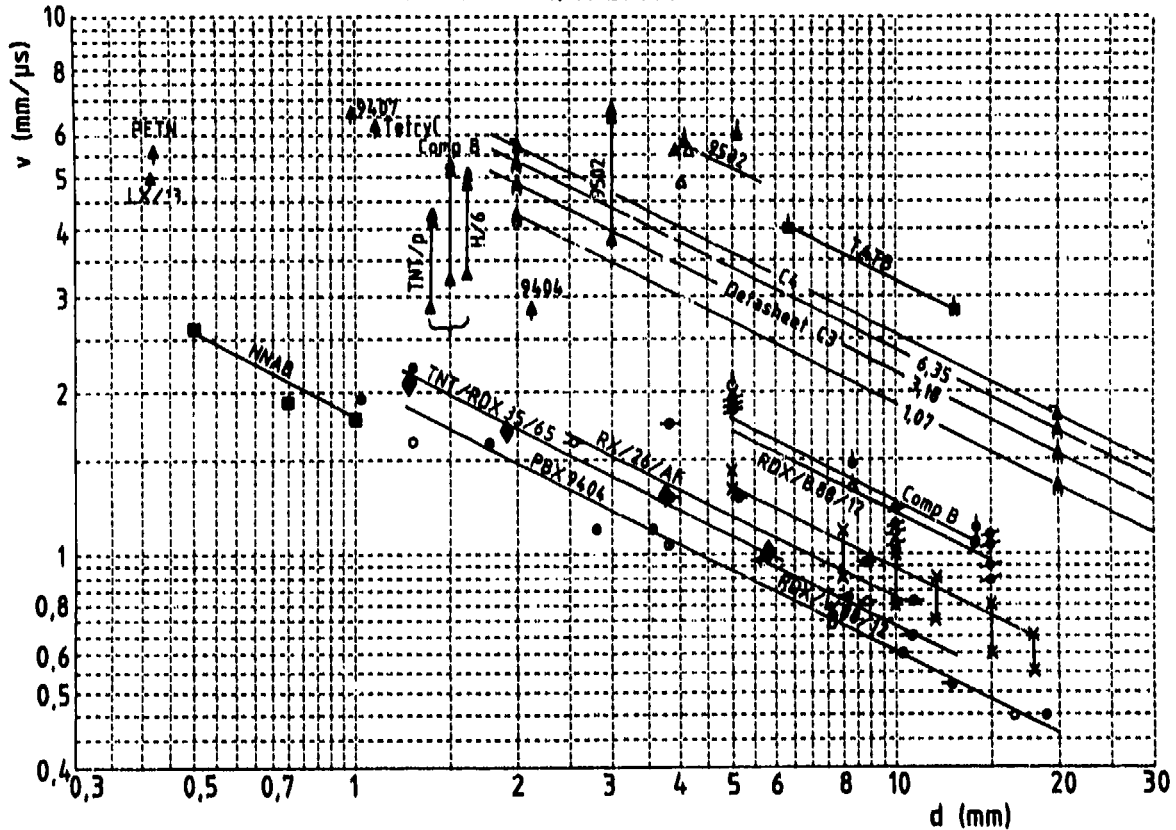


Figure 13. Failure in Propellant Subject to Shaped Charge Attack

### $v^2 d$ - Criterion



□ ○ etc., no initiation, ■ ● etc., initiation

Figure 14. Threshold Impact Velocity as a Function of the Diameter of Shaped Charge Jets, Projectiles or Flyer Foils for Different High Explosive Charges

Table: Initiation Criterion  $v^2 d$

Type of HE	$v^2 d$ (mm <sup>3</sup> /μs)	Reference	Sign in Figure 14
HNAB	3	Hasman e.a. <sup>29</sup>	■
PBX 9404	4	Bahl et.al <sup>24</sup>	●
RDX/Wax 88/12	5	Griffiths e.a. <sup>25</sup>	◐
TNT/RDX 38/65	6	Neld <sup>3</sup>	◆
PETN (1.77)	13	Vigil <sup>13</sup>	▲
Comp. B	16	Chick e.a. <sup>11</sup>	▲
		Moulard <sup>27</sup>	●
H6	16.5	Chick e.a. <sup>11</sup>	▲
Detasheet C3	36-53	Weickert <sup>24</sup>	▲
9407	40	Vigil <sup>13</sup>	▲
Tetryl	44	Vigil <sup>13</sup>	▲
C4	64	Weickert <sup>24</sup>	▲
TATB	108	Weingart e.a. <sup>28</sup>	■
9502	128	Campell <sup>17,18</sup>	▲

Campbell carried out tests in 1978 and 1979.<sup>17</sup> A summary of these tests was given in 1988.<sup>18</sup>

Vigil<sup>13</sup> (1985) has used jets of very small shaped charges to initiate four different secondary explosives. The jet velocities varied between 3.6 and 6.5 mm/μs. The jet tip diameters ranged from 0.041 mm to 1.1 mm. The lateral confinement of the acceptor explosive was minimal. The threshold initiation parameter  $v^2 d$  for LX-13 (80 percent PETN and 20 percent Sylgard), PETN, PBX-9407, and Tetryl were experimentally determined to be 11, 13, 31, and 44 mm<sup>3</sup>/μs, for copper jets impacting bare explosive acceptors. The lower values for the LX-13 and PETN indicate that these two explosives are more sensitive to jet initiation than PBX-9407 and Tetryl explosives.

Chick, Bussell, Frey, and Boyco<sup>11</sup> (1986) have also examined Composition B, H-6, PBX-9502, and pressed TNT with jets from 38-mm and 81-mm diameter shaped charges. They looked at the sensitivity of bare and covered unconfined acceptors. The jet diameter was not measured for each firing; a diameter of 1.5 mm was assumed for all small shaped charge jets, and one of 3 mm for the large shaped charge jets. Nevertheless, the values are within the range of the other data (Figure 12). Important is the fact that they have shown for the first time that bare high explosive charges can be initiated by a jet at about half the tip velocity required by a covered, but unconfined charge attacked by a similar jet.

Weickert<sup>24</sup> (1987) has also confirmed the  $v^2d$  criterion using four different shaped charge diameters, namely 25.4-mm, 50.8-mm, 76.2-mm, and 101.6-mm against relatively thin layers of confined high explosive charges in metal/explosive/metal sandwiches. Two types of high explosive layers were used, consisting of Detasheet C with thicknesses of 1.07 mm, 3.18 mm, and 6.35 mm; and Composition C-4, 3.18 mm thick. He is reporting that his shaped charge jet particles were very irregular in shape, or were multiple particles. Still, the Detonation/No Detonation results indicate that the relation  $v^2d = \text{constant}$  can be used for the shaped charge jet initiation confined high explosive in explosive/metal sandwich arrangements.

The  $v^2d$  criterion has also been confirmed for projectile impact on bare high explosive charges. Griffiths, Laidler, Spooner<sup>25</sup> (1967) have published earlier work of Whitbread on the threshold velocities with projectiles of 12.7-mm, 10.67-mm, 8.13-mm, and 5.60-mm diameter against charges of RDX/Wax 88/12. It was shown that the length of the projectile did not affect the probability of detonation. They have tried to find a correlation between  $v$  and  $r^2$ . But the four points do not make a convincing straight line on the diagram.

Bahl, Vantine, and Weingart<sup>26</sup> (1981) have measured the initiation threshold of bare and covered PBX-9404 and an HMX/TATB explosive, called RX-26-AF. Steel projectiles of flat and rounded fronts were used in the

velocity range of 0.5 - 2.2 mm/ $\mu$ s. All their experimental values for bare high explosive charges of PBX-9404 and RX-26-AF are presented in Figure 14. The regression line gives a straight correlation for the  $v^2d$ -criterion. Projectiles with rounded front also give the  $v^2d$ -criterion, but with a constant twice as high (but they are not presented in Figure 14).

Moulard<sup>27</sup> (1981) has made additional tests with projectiles of rectangular and ring-shaped front ends. If these areas are transformed into diameters (representing the area) then the corresponding points are also on the  $v^2d$ -line.

Foil tests also demonstrate the  $v^2d$ -criterion if the flying foil thickness, related to the diameter, is not too small. The ratio should be greater than 1/5. Two velocities have been added to Figure 14 from published papers by Weingard<sup>28</sup> (1976) who had used 0.255-mm thick flyers of Mylar against TATB. Hasman<sup>29</sup> (1986) has published the critical energy for initiation, using flyer diameters of 0.5 and 1 mm, and 76- $\mu$ m thick Mylar foils against HNAB of 5 m grain size and 1.6 g/cm<sup>3</sup> density.

The experimental values of the  $v^2d$ -criterion also are confirmed by the numerical two-dimensional simulations of Mader<sup>5-6</sup> and Starkenberg, Huang, and Arbuckle.<sup>30-31</sup> The latter values are also given in Figure 14 for Composition B, and correlate very well with the trend, but not so well with the constants compared to the experimental data for Composition B. Also, Green<sup>32</sup> has made relatively simple considerations for the shock and release wave behavior and has found a good correlation to the  $v^2d$ -criterion.

## CONCLUSION

In conclusion, one can say that for "jet attack" against unconfined high explosive charges, the  $v^2d$ -criterion in fact describes the detonation threshold—initiability—of the high explosive charges in terms of the threshold velocity as a function of jet diameter. This is confirmed by "projectile" impact results which, however, involve larger diameters and correspondingly lower velocities and also by "flying foils," if the ratio of the flying foil

thickness to the diameter is larger than 1/5. This criterion is also confirmed by simulation of the high explosive charge behavior with numerical codes.

## REFERENCES

1. "The Initiation of an Exploder by a Munroe Jet (Flash Radiography)," Armament Research Department, ARD Met. Report 45, Apr 1945.
2. Zernow, L.; Liebermann, I.; and Kronman, S., "An Exploratory Study of the Initiation of Steel-Shielded Composition B by Shaped Charge Jet," BRL Memo Report 944, Oct 1955.
3. Held, M., "Initiierung von Sprengstoffen, ein vielschichtiges Problem der Detonationsphysik," *Explosivstoff*, Vol. 5, 1968, pp. 2-17.
4. Held, M., "Critical Area for the Initiation of High Explosive Charges," *Shock Waves in Condensed Matter*, Santa Fe, NM, [Proc.] Chapter XII., 1983, pp. 555-557.
5. Mader, C. L. and Pimbley, G. H., "Jet Initiation of Explosives," LANL-Report 8647, 1981; "Jet Initiation and Penetration of Explosives," *Journal of Energetic Materials*, Vol. 1, 1983, pp. 3-44.
6. Mader, C. L., "Recent Advances in Numerical Modeling of Detonations," *Propellants, Explosives, Pyrotechnics*, Vol. 11, 1986, pp. 163-166.
7. Chick, M. C. and Hatt, D. J., "The Mechanism of Initiation of Composition B by a Metal Jet," *Proceedings of the Seventh Symposium (International) on Detonation*, 1981, pp. 352-281.
8. Chick, M. C. and Hatt, D. J., "Metal Jet Initiation of Bare and Covered Explosives; Summary of the Mechanism, Empirical Model and Some Applications," Department of Defence, Material Research Laboratories, Melbourne, Victoria, Australia, Report, MRL-R-830, 1981.
9. Chick, M. C. and Hatt, D. J., "The Initiation of Covered Composition B by a Metal Jet," *Propellants, Explosives, Pyrotechnics*, Vol. 8, 1983, pp. 121-126.
10. Chick, M. C. and MacIntyre, J. B., "The Jet Initiation of Solid Explosives," *Proceedings of the Eighth Symposium (International) on Detonation*, 1985, pp. 318-329.
11. Chick, M. C.; Bussell, T.; Fey, R. B.; and Boyce, G., "Initiation of Munitions by Shaped Charge Jets," *Ninth International Symposium on Ballistics*, Vol. 2, 1986, pp. 421-430.
12. Chick, M. C.; Wolfsan, M. G.; and Learmonth, L. A., "A Calibrated Test for the Assessment of the Sensitivity of Explosives to Shaped Charge Jets," MRL-Report-1016, 1986.
13. Vigil, M. G., "Explosive Initiation by Very Small Conical Shaped Charge Jets," *Proceedings of the Eighth Symposium (International) on Detonation*, 1985, pp. 1091-1101.
14. Held, M., "Experiments of Initiation of Covered, but Unconfined High Explosive Charges by Means of Shaped Charge Jets," *Propellants, Explosives, Pyrotechnics*, Vol. 12, 1987, pp. 35-40.
15. Held, M., "Experiments of Initiation of Covered, but Unconfined HE Charges Under Different Test Conditions by Shaped Charge Jets," *Propellants, Explosives, Pyrotechnics*, Vol. 12, 1987, pp. 97-100.
16. Held, M., "Discussion of the Experimental Findings from the Initiation of Covered, but Unconfined High Explosive Charges with Shaped Charge Jets," *Propellants, Explosives, Pyrotechnics*, Vol. 12, 1987, pp. 167-174.
17. Campbell, A. W., "Jet Attack of PBX-9502," LANL Int. Report M-3-QR-78-4, 1978 and M-3-QR-79-1, 1979.
18. Campbell, A. W., "Jet Attack of PBX-9502," LA-UR-88-458, 1988.
19. McAfee, J. M., "Jet Initiation of PBX-9502," LA-UR-87-3169, 1987.

20. Campbell, A. W., "The Use of Witness Plates to Assess the Promptness of Initiation of PBX-9502 by Jets," LA-UR-81-3545, 1981.
21. Held, M.; Schedelbauer, F.; and Schubert, H., "Aktive Schicht für Schutzanordnungen gegen Hohlladungs- und Wuchtgeschosse," Patent DBP 2 831 415, 1978.
22. Chick, M. C. and Bussel, T. J., "The Importance of Critical Detonation Diameter in Determining the Response of a Munition Filling to Shaped Charge Jets," Second Australian Explosive Safety Seminar, Canberra, 1987.
23. Asea, B. W.; Ramsay, J. B.; and Campbell, A. W., "Response of Propellants to Hypervelocity Attack," LA-UR-87-3171, 1987.
24. Weikert, C., "Jet Initiation of Explosive/Metal Sandwiches," *Proceedings of the Tenth International Symposium on Ballistics*, 1987.
25. Griffiths, N.; Laidler, R. McN.; and Spooner, S. T., "Some Aspects of the Shock Initiation of Condensed Explosives," *Combustion and Flame*, Vol. 7, 1963, pp. 347-352.
26. Bahl, K. L.; Vantine, H. C.; and Weingart, R. C., "The Shock Initiation of Bare and Covered Explosives by Projectile Impact," *Proceedings of the Seventh Symposium (International) on Detonation*, 1981, pp. 325-335.
27. Moulard, H., "Une Condition de Surface Critique pour l'Armorage par Onde de Choc des Explosifs Solides," *Propellants and Explosives*, Vol. 6, 1981, pp. 63-66.
28. Weingart et al., "Acceleration of Thin Flyers by Exploding Metal Foils: Application to Initiation Studies," *Proceedings of the Sixth Symposium (International) on Detonation*, 1976, pp. 653-663.
29. Hasman, E.; Gvishi, M.; and Carmel, Y., "Measurement of Shock Initiation Threshold of HNAB by Flyer Plater Impact," *Propellant, Explosives, Pyrotechnics*, Vol. 11, 1986, pp. 144-149.
30. Starckenberg, J. J.; Huang, Y. K.; and Arbuckle, A. L., "Numerical Modeling of Projectile Impact Shock Initiation of Bare and Covered Composition B,"
  - Technical Report ARBRI-TR-02576, 1984.
  - *Journal of Energetic Materials*, Vol. 2, 1984, pp. 1-42.
31. Huang, Y. K.; Starckenberg, J. J.; and Arbuckle, A. L., "Some New Computed Results for Projectile-Impact Shock Initiation of Solid Explosives," *Proceedings of the Eighth Symposium (International) on Detonation*, 1985, pp. 307-317.
32. Green, L., "Shock Initiation of Explosives by the Impact of Small Diameter Cylindrical Projectiles," *Proceedings of the Seventh Symposium (International) on Detonation*, 1981, pp. 273-277.

# SPHERICAL PROJECTILE IMPACT ON EXPLOSIVES

Eric N. Ferm and John B. Ramsay  
Los Alamos National Laboratory  
Los Alamos, New Mexico 87545

*A simple relationship between the critical velocity and the radius of a spherical projectile that initiates an explosive charge is derived by further developing the shock initiation description previously used to describe flat-ended projectiles. The criterion agrees with spherical impact initiation experiments done on PBX-9404 and Comp B-3. The validity is limited in that it considers only shock initiation from the contact shock and does not account for shock wave divergence or growth into a larger bow-wave structure. It is also limited to projectile diameters larger than the failure diameter of the explosive. The criterion requires Hugoniot data for the projectile and unreacted explosive, the failure diameter of the explosive, and a run-to-detonation/shock pressure relationship. The calculation can easily be extended to other smooth, blunt projectile shapes. The simplicity illustrates the basic phenomena associated with contact shock initiation of bare explosive.*

## INTRODUCTION

Many experiments on the initiation of explosives by projectile impact have been conducted. The results of these tests are critical conditions of projectile shape, diameter, and velocity that will initiate a given explosive. For projectile impacts on bare explosive (no intervening plate in contact with the explosive), experiments have shown that the conditions for initiation can be fit to the form\*  $Ru^n \geq k$ , where  $R$  is the radius and  $u$  the velocity of the projectile. The parameters  $n$  and  $k$  vary with the explosive and the shape of the projectile. For example, in the initiation of bare PBX-9404 charges, the initiation region for flat-ended rods is  $Ru^{2.0} \geq 2.0$ , whereas for spherical-ended rods it is  $Ru^{2.5} \geq 9.5$ . In this paper, we develop a simple analytical initiation criterion for spherical projectile impact, based on existing initiation

\*Standard terminology is  $v^2d$ , where  $v$  is the velocity and  $d$  is the diameter of the projectile. We have elected to use  $u$  for the velocity and  $R$  for the radius to maintain consistency within the paper.

data for large, well-supported plane-wave initiation. We show that for projectile diameters larger than the explosive failure diameter, the initiation of bare explosives is well described as a simple shock initiation process emanating from the initial contact between the projectile and the explosive.

Green<sup>1</sup> described a simple model for the initiation of explosive by flat-ended rod impact. He included the areal expansion of the shock front, coupled with the decaying mean shock pressure. If these effects led to initiation of the explosive over a diameter larger than the failure diameter at the distance specified by the run to detonation for the average shock pressure, the model would predict that the explosive would propagate. Otherwise, the impact led to failure. This idea was the basis for the development of the spherical projectile impact.

## THE MODEL

During the impact between a sphere and a plane surface, the phase velocity of the intersection locus is initially infinite and then decreases as the angle between the two



There are two release mechanisms to consider in impact initiation. The first is a release from the edges (lateral rarefactions) that travel in at the sound speed along the shock. Another release wave enters through the interface between the acceptor and donor. The effect of this latter rarefaction is generally modeled with a  $P^2t$  relationship, where  $t$  is some characteristic time thickness of the shock. We have made two assumptions about the effect of these rarefactions: (1) the rear rarefaction does not reach the shock before the lateral rarefactions, and (2) the effect of the lateral rarefaction is to completely quench the initiation at the affected shock front.

In the limit of small  $u_i/c_0 > 0$ , Equation (6) reveals that a relation of the form

$$Ru_i^{(1+a)} = f(u_i) \quad (7)$$

is appropriate, where  $f(u_i)$  is a continuous function. As  $u_i$  approaches 0,  $f(u_i)$  approaches the value

$$f(0) = c_0 b((\rho_0 c_0)^{-1} + (\rho_i c_i)^{-1})^a,$$

where  $\rho$  is the density. For large  $u_i$ ,  $R$  approaches the failure radius,  $r_f$ . The relation  $Ru_i^{(1+a)}$  is quite similar to typical experimental relations and  $1+a$  is about the right size for the exponent (for PBX-9404, it is 2.54, compared with an experimental value of about 2.5). However,  $f(0)$  is nearly twice the typical experimental value (for PBX-9404,  $f(0) = 15$  instead of an experimental value of 9.5). With  $f(u_i)$  varying so much, use of approximations to evaluate Equation (6) would create significant errors. To obtain a correct comparison with the experimental data, Equation (6) has been evaluated by simple substitution of  $u_i$  and  $X^* = bP^a$ , where  $P$  is the shock match pressure corresponding to an impact velocity  $u_i$ .

## COMPARISON WITH EXPERIMENTAL DATA

Comparison between the calculation and experiment is limited because no body of experimental data exists that includes both impact of spherical projectiles above failure diameter and Hugoniot and shock initiation data for the same explosive. Figure 2 presents the results obtained by this simple model and

experimental data for steel spheres impacting PBX-9404 reported by Bahl, Vantine, and Weingart,<sup>2</sup> and by Rice.<sup>3</sup> One datum for ball initiation of Comp B-3 was reported by Rice<sup>3</sup> and it is compared with the model in Figure 3. The parameters used for the calculations are presented in Table 1. The agreement between the experiment and the calculation for Comp B-3 could be improved if initiation parameters were changed to give shorter runs to detonation, as Rice found necessary to

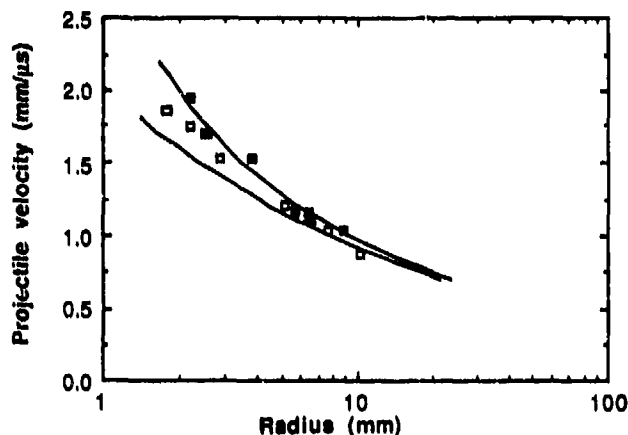


Figure 2. Comparison of Model to Experimental Data for PBX-9404. The upper curve is for a failure radius of 0.59 mm and the lower curve for 0 mm radius. The solid and open squares are the go and nogo points from Bahl et al., and the solid triangle is the go point from Rice.

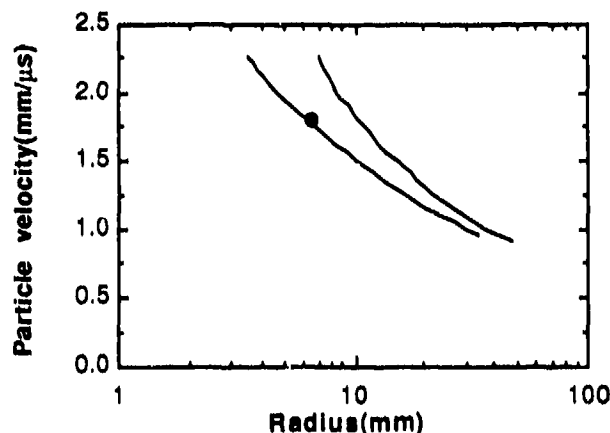


Figure 3. Comparison of Model with Experimental Datum for Composition B. The experimental value was obtained at Ballistic Research Laboratory and reported by Rice. The upper curve is for a failure radius of 2.14 mm and the lower curve for 0 mm.

obtain agreement between his numerical calculations and the experimental data for Comp B-3. The values used for  $r_f$  are for unconfined explosive. The values appropriate to the model may be smaller because of confinement provided by the shocked explosive. The effect of  $r_f$  on the model is shown in Figures 2 and 3 with plots for  $r_f = 0$ .

## DISCUSSION

The model highlights the physical phenomena connected with the contact shock initiation realm of projectile impact. It was not intended to address the questions associated with radii less than the failure radius, nor does it address the possibility of the formation of a Mach stem. Chick, Bussel, and Frey<sup>6</sup> show convincing evidence of contact shock initiation when the ratio of failure diameter-to-projectile diameter is larger than five. The classic  $Ru^2$  relationship does not extrapolate to the plane initiation conditions in the large-projectile-diameter limit. The current model shows how this transition occurs. Green's model for flat-end impact required modeling of the evolution of the shock wave to match experimental data. With this hemispherical impact model, it has not been necessary to include the expansion to obtain reasonable agreement for radii larger than failure radius. The model can be used to estimate behavior for attack by ogival-shaped

(off-centered spherical) projectiles whose diameter is larger than failure diameter and with velocities such that the intersection phase velocity is greater than sound velocity in the explosive.

## REFERENCES

1. Green, LeRoy, "Shock Initiation of Explosives by the Impact of Small Diameter Cylindrical Projectiles," *Proceedings of the 7th Symposium (International) on Detonation*, Annapolis, MD, 16-19 Jun 1981, pp. 273-277.
2. Bahl, K. L.; Vantine, H. C.; and Weingart, R. C., "The Shock Initiation of Bare and Covered Explosives by Projectile Impact," *Proceedings of the 7th Symposium (International) on Detonation*, Annapolis, MD, 16-19 Jun 1981, pp. 325-335.
3. Rice, M. H., "Penetration of High Explosives by Inert Projectiles," SSS-R-78-3512, Systems, Science, and Software, P.O. Box 1620, La Jolla, CA, Nov 1977.
4. Marsh, S. P., Ed., *LASL Shock Hugoniot Data*, Los Alamos Series on Dynamic Material Properties, University of California Press, 1980.
5. Gibbs, T. R. and Popolato, A., *LASL Explosive Property Data*, Los Alamos

Table 1. Parameters of Materials Used in Projectile Impact Model

Material	Density (g/cm <sup>3</sup> )	$c_0$ (mm/ $\mu$ s)	$U_p$ - $u_p$ Slope	Pop-Plot <sup>a</sup>		$r_f$ (mm)
				Exponent	Constant	
Stainless steel <sup>b</sup>	7.896	4.569	1.49	---	---	---
PBX-9404 <sup>c</sup>	1.84	2.494	2.093	1.54	51	0.59
Comp B-3 <sup>d</sup>	1.72	2.31	1.83	1.34	96	2.14

<sup>a</sup> The Pop-plot form is  $P^*X^* = b$ , where P is pressure in GPa,  $X^*$  the distance to detonation in mm, and a and b are parameters.

<sup>b</sup> Reference 4.

<sup>c</sup> Reference 5.

<sup>d</sup> Reference 3.

**Series on Dynamic Material Properties,  
University of California Press, 1980.**

- 6. Chick, M. C.; Bussell, T. J.; and Frey, R. B., "Mechanisms of the Jet Initiation of Solid Explosives," *Combustion and Detonation Phenomena*, 19th International**

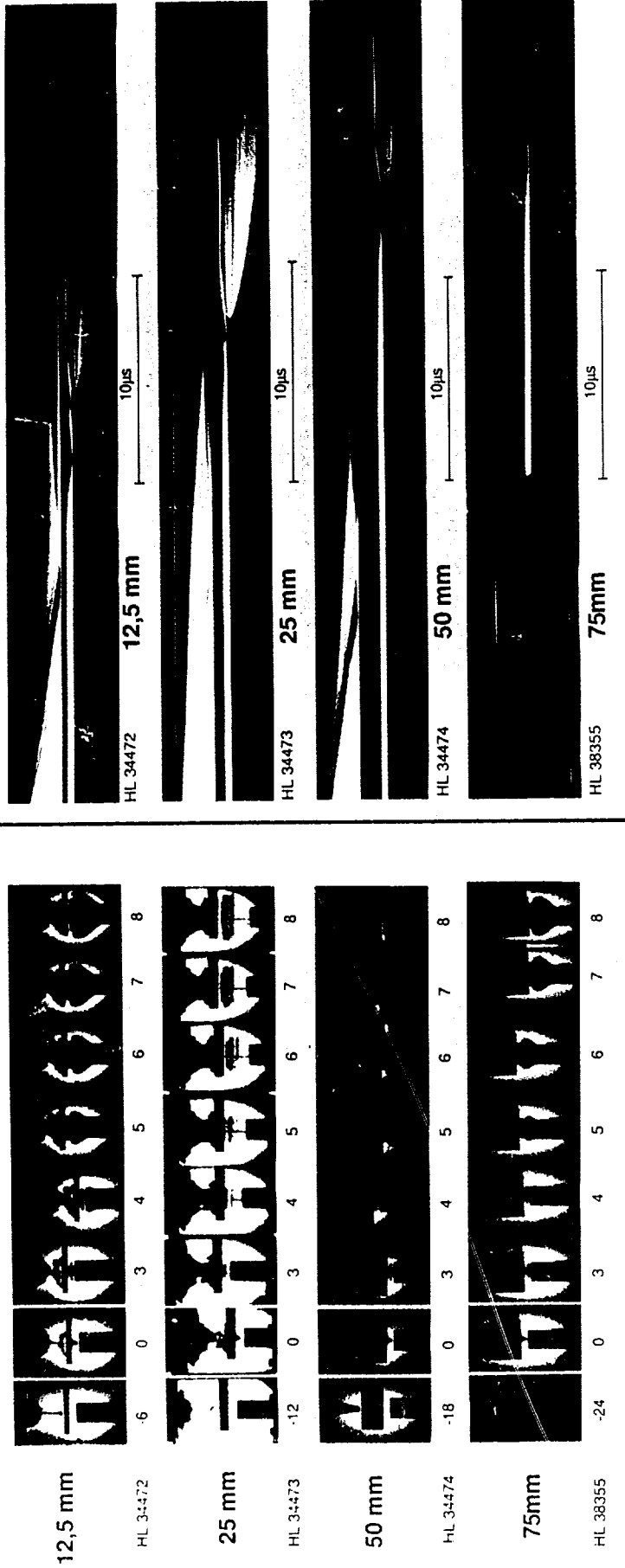
**Annual Conference of ICT 1988,  
Fraunhofer-Institut für Chemische Tech-  
nologie, Karlsruhe, Federal Republic of  
Germany, 29 Jun-1 Jul 1988, pp. 24.1-  
24.14**

# INITIATION PHENOMENA WITH SHAPED CHARGE JETS

***MBB***

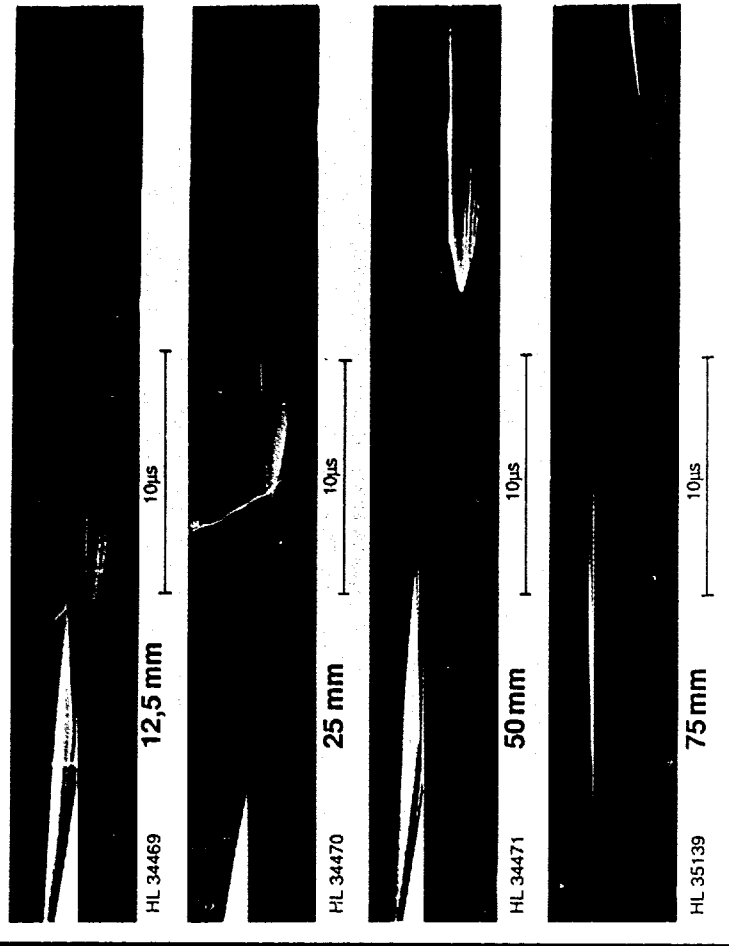
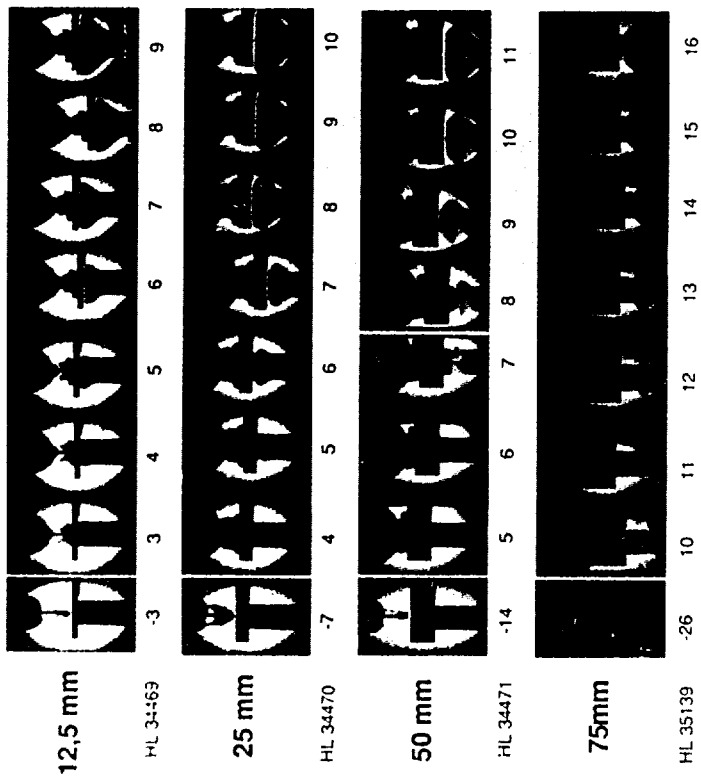
The initiability of unconfined high explosive charges by shaped charge jets can be well described with the  $v^2d$  - criterion. For covered, but still unconfined explosive charges, higher initiation threshold values are measured. The main reason for this is precompression and a different pressure time history in the acceptor charge in contact with the cover, as compared with an arrangement with a larger air gap. Preshocking and differences in the impacted areas seem to have less influence. But confining the acceptor charge reduces the initiation threshold noticeably.

*Manfred Held*



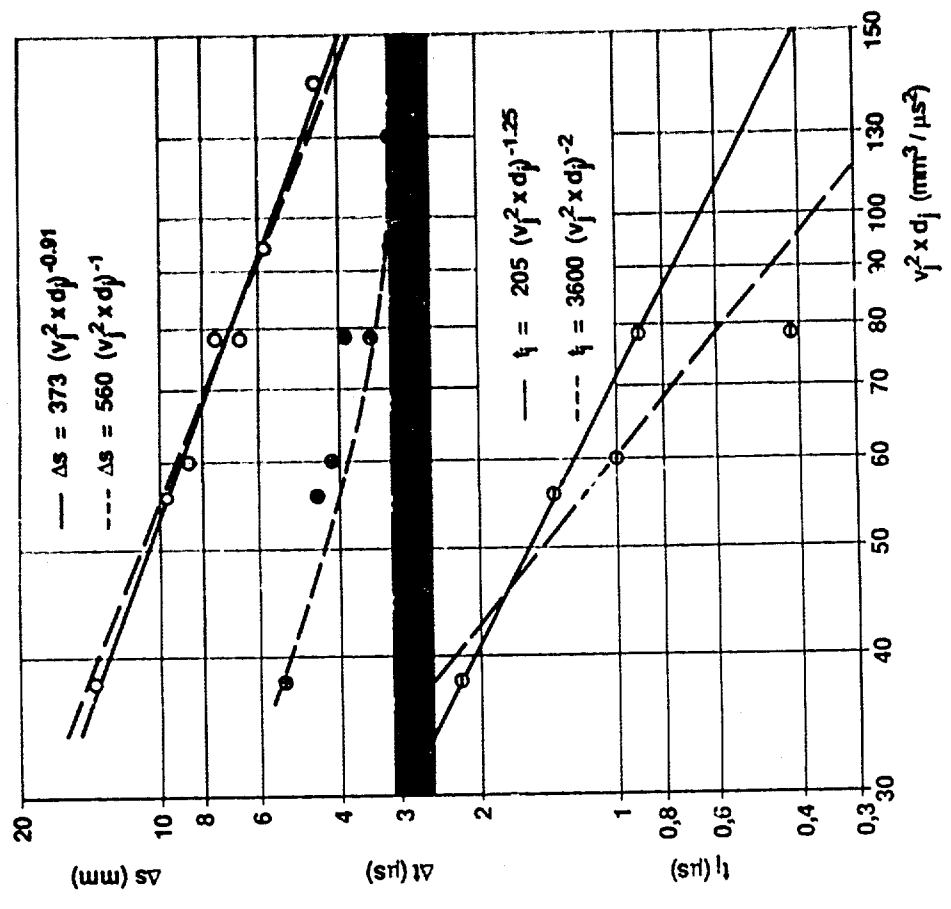
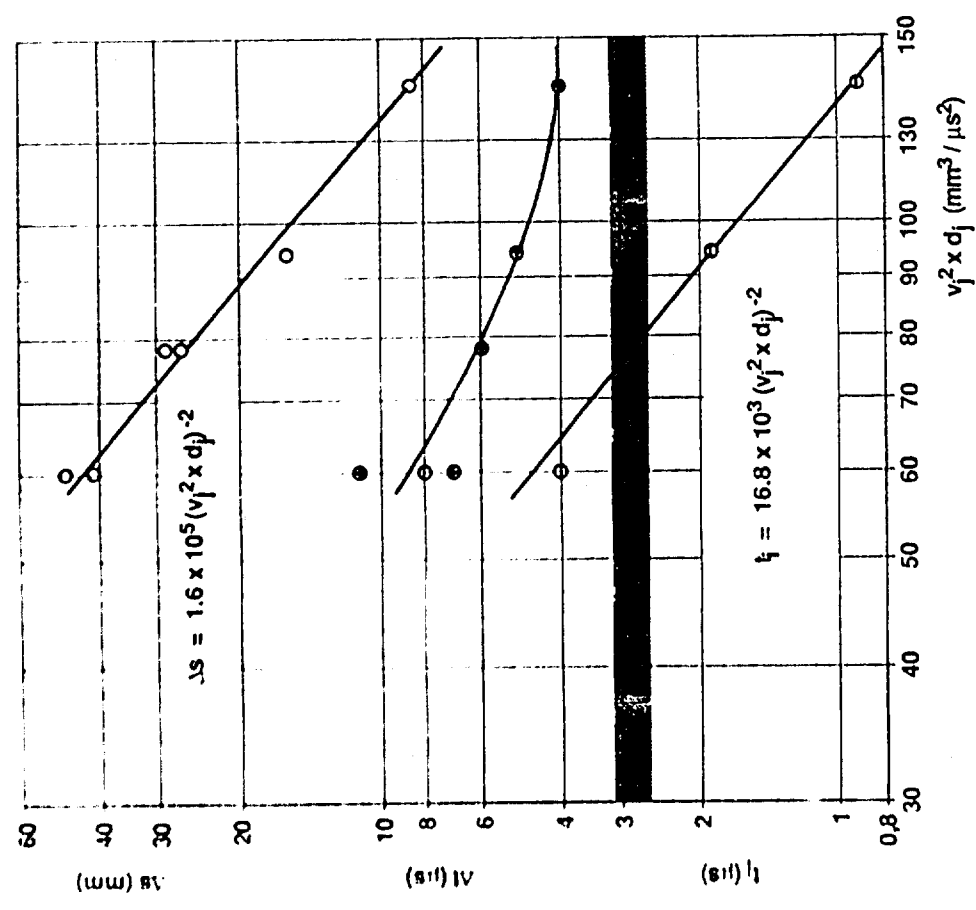
Acceptor charge with an air gap to the barrier

Frames and streak records of the initiation of acceptor charges arranged 15 mm behind barriers of different thickness. The simultaneously obtained streak records show the impact of the shaped charge jet on the barrier (left in the records), exit of the jet from the barrier, the impact on the HE-charge and the initiation of the acceptor charge.

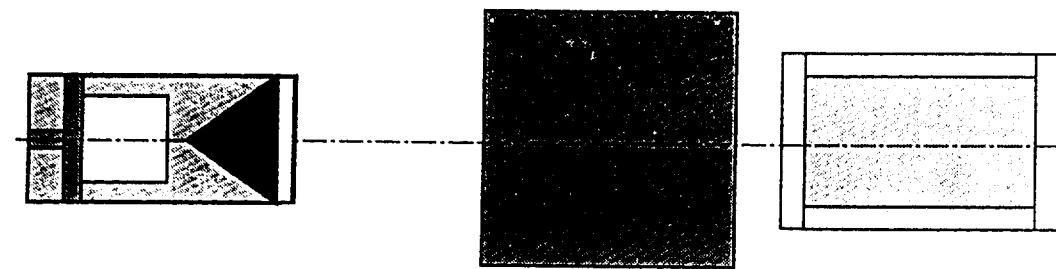


Accepter charge in contact with the barrier

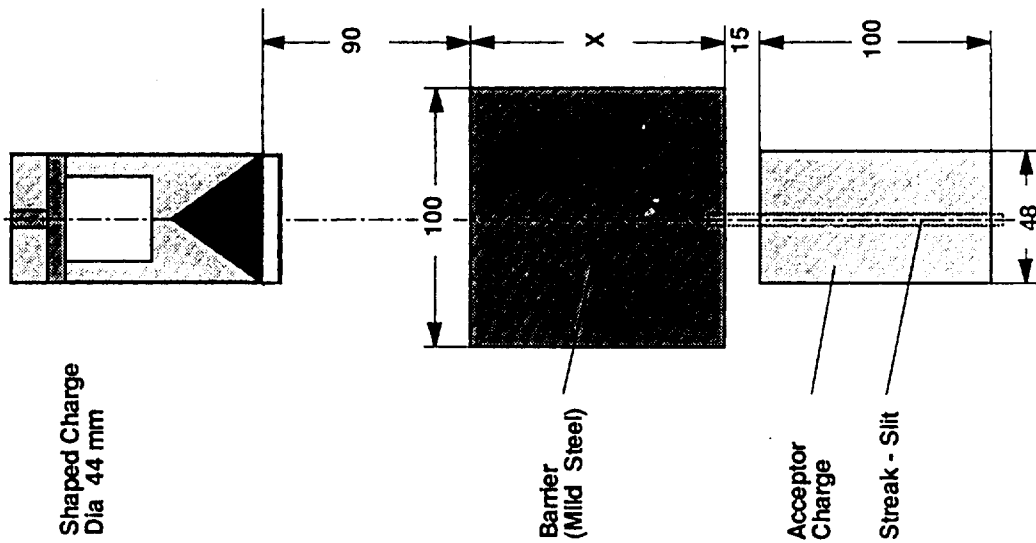
Frames and streak records of jet initiation tests with different barriers, recorded with the Cordin Model 330 rotating - mirror camera at about  $10^6$  frames per second and about  $4.5 \text{ mm}/\mu\text{s}$  writing velocity. The barrier thicknesses are indicated to the left of the pictures. The simultaneously obtained streak records show the impact of the shaped charge jet on the barrier (left in the picture), and the delayed onset of detonation in the acceptor charge, with detonation and retonation waves.



Build-up distances  $\Delta s$ , run-up times  $\Delta t$  and initiation times  $t_i = f(v^2 d)$  for the arrangements with the unconfined high explosive charge in contact with the barrier (left) and with a 15 mm air gap between the unconfined high explosive charge and the barrier (right). These values have been obtained from the above streak records.



HE in Contact

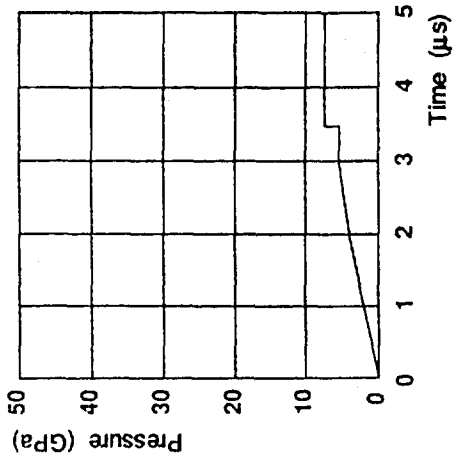


HE with Air Gap

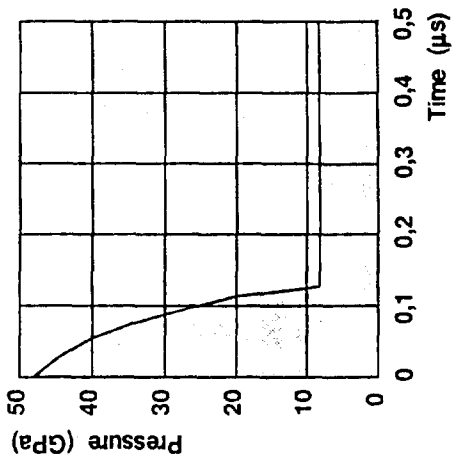
HE Confined

Test set - ups of the 44 mm shaped charge with the barrier and the TNT / RDX 35 / 65 acceptor charge unconfined - either in contact with the barrier or with a 15 mm air gap - and confined.

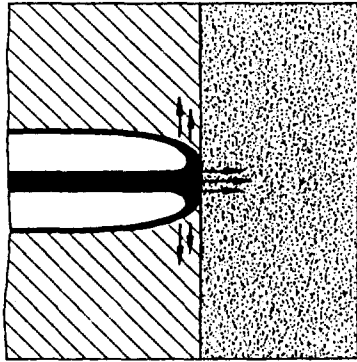
Covered HE



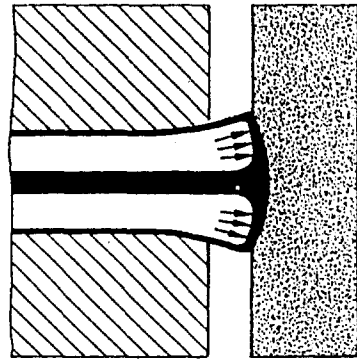
Uncovered HE



Contact



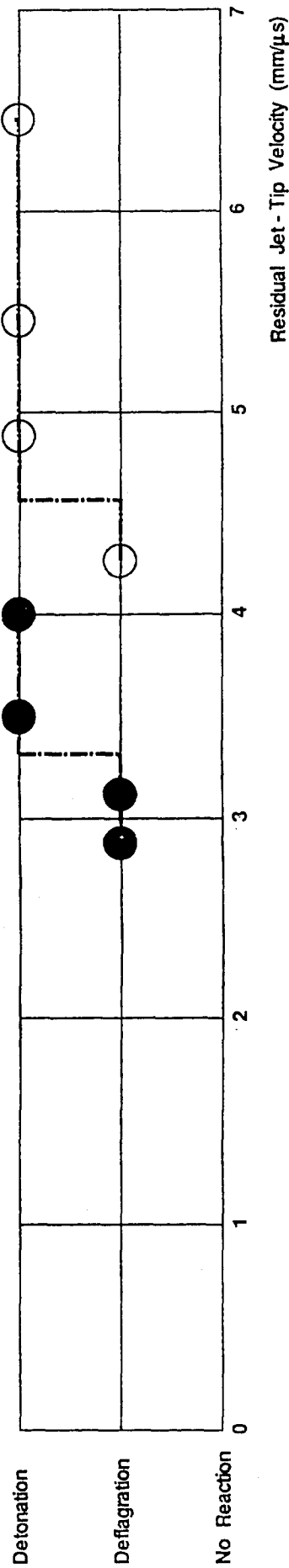
Air Gap



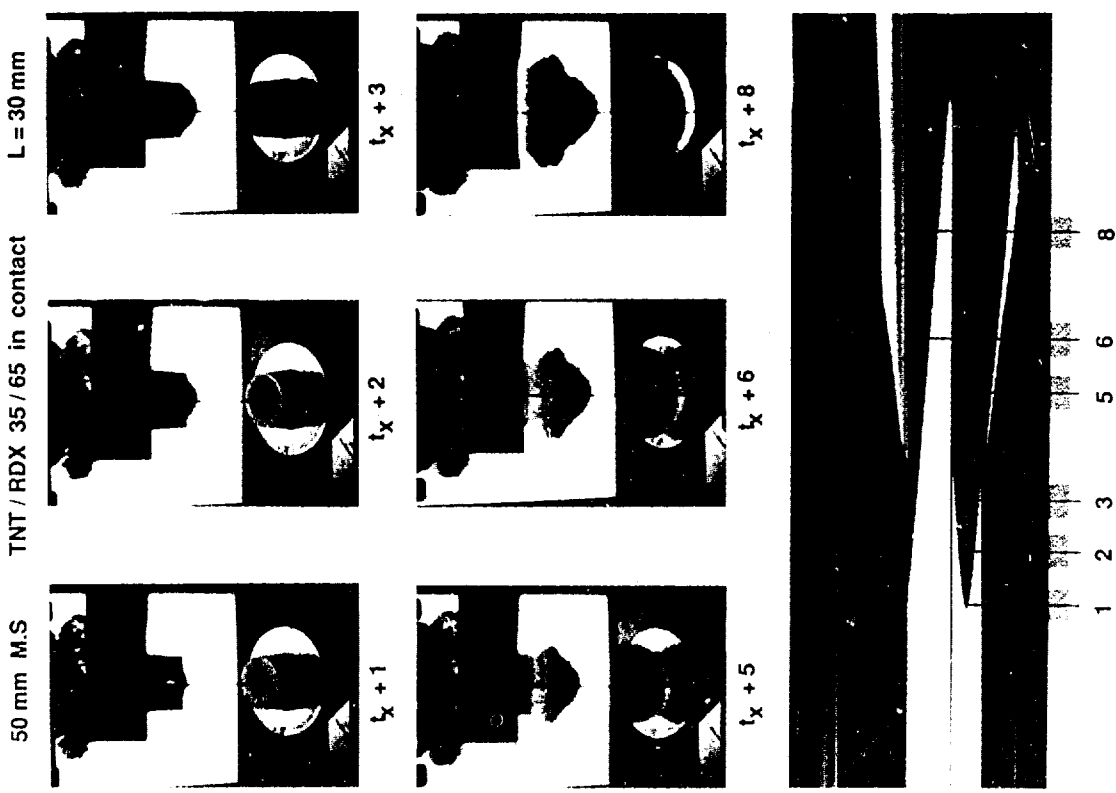
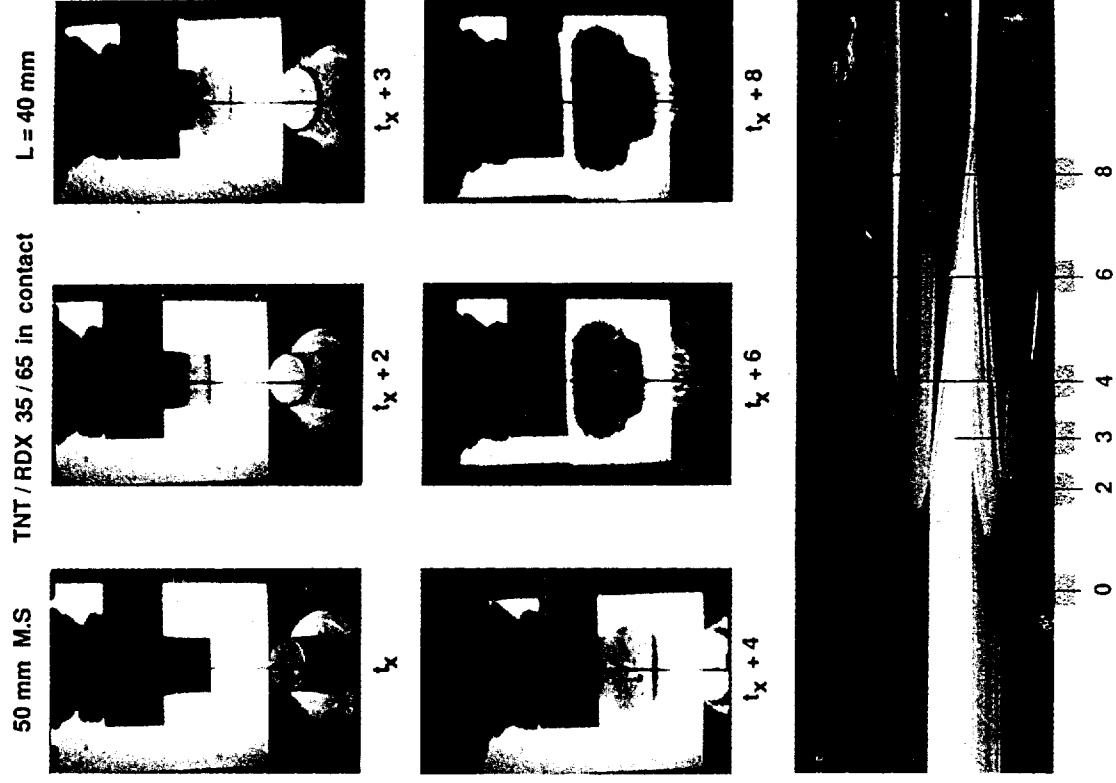
Pressure - time history of an impacting and a penetrating shaped charge jet for the two cases:

- HE - charge in contact with the barrier (left)
- HE - charge with a larger air gap to the barrier (right).

Precompression of the acceptor charge arranged in contact (and therefore loaded on a smaller area)(left), in comparison to the arrangement with a larger air gap (right).

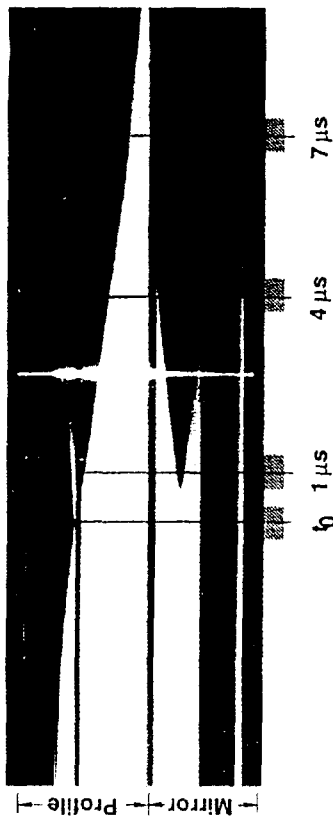
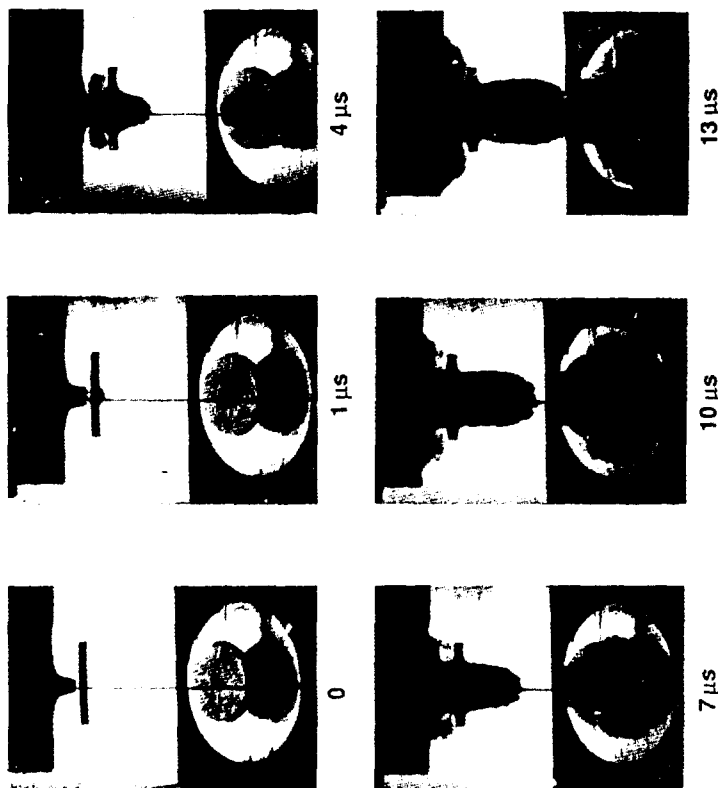


Initiation / Reaction threshold for unconfined ○ and confined ● acceptor charges.

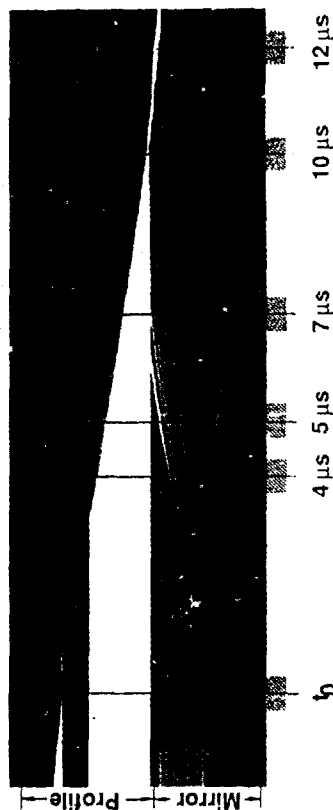
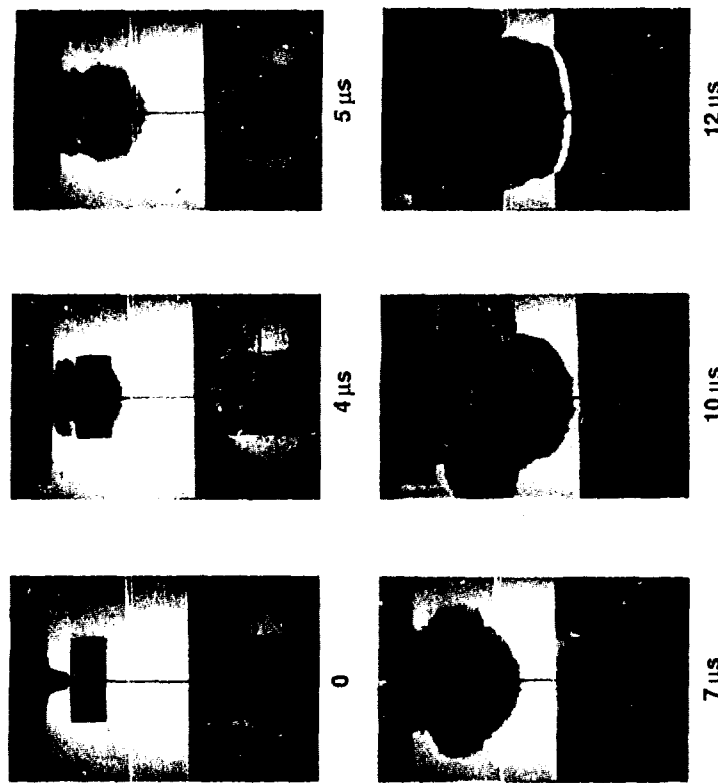


Selection of 6 frames and the associated streak records obtained simultaneously, showing the reaction behavior of an acceptor charge in contact with a 50 mm thick steel barrier exposed to the impact of a shaped charge jet ( $v_{j, res.} = 5.5 \text{ mm}/\mu\text{s}$ ). In a 30 mm long HE - charge the induced reaction stays low order (left), whereas in a 40 mm long HE - charge it builds-up to a detonation (right).

100 mm M.S TNT / RDX 35 / 65 at 15 mm air - gap L = 5 mm



100 mm M.S TNT / RDX 35 / 65 at 15 mm air - gap L = 20 mm



In the arrangement with a 15 mm air gap between the barrier (here 100 mm thick, corresponding to  $v_{j, res.} = 4.2 \text{ mm}/\mu\text{s}$ ) the initiation starts at much shorter build-up distances  $\Delta s$  and run-up times  $\Delta t$ , but it is not instantaneous! No detonation in a 5 mm thick HE charge (left) and detonation in one 20 mm thick (right). The upper frames and upper portions of the streak records have been taken from the direct view, and the lower ones over a mirror facing the exit surface of the shortened acceptor charge.



# PROJECTILE IMPACT INITIATION OF EXPLOSIVE CHARGES

**M. D. Cook and P. J. Haskins**

**Royal Armament Research and Development Establishment  
Fort Halstead, Sevenoaks, Kent TN14 7BP  
UNITED KINGDOM**

and

**H. R. James**

**Atomic Weapons Establishment, Foulness Island, Essex SS3 9XE  
UNITED KINGDOM**

*In this paper we report the results of an experimental and theoretical study of projectile impact into covered secondary explosive charges. Flat-ended steel projectiles in two diameters (13.15 and 20 mm) were employed to determine thresholds for detonation in charges covered by steel, PMMA, and aluminum barrier plates. Our results indicate that for impacts through barriers below a critical thickness a shock initiation mechanism dominates, and that this can be modelled using an energy-per-unit-area criterion. For barriers in excess of the critical thickness, our results provide strong evidence for initiation by a non-shock process.*

## INTRODUCTION

Studies of projectile impact on explosives are of direct relevance to weapon vulnerability and explosive ordnance disposal studies. For these reasons many investigators have carried out projectile impact studies on explosives and there have been a number of attempts at modelling or interpreting the results of such experiments. Despite these efforts, there are still many unknown factors concerning the response of explosives to projectile impact, particularly when the explosive is cased or covered by a barrier plate. In this paper we report new experimental data on detonation thresholds through barrier plates. In addition, we propose a theoretical interpretation of those results which fall in the shock initiation regime, and discuss the possible mechanisms which may be responsible for initiation outside this regime.

The response of a bare or covered explosive (covered implying no confinement apart from a protective barrier) to the attack of a flat-faced projectile is determined by the initial impact shock. This response is usually either 'no reaction,' which may consist of some local burning

but no blast output, or detonation. This is in contrast to a cased explosive, which can give a range of blast outputs up to and including detonation from a variety of stimuli. These stimuli include the initial impact shock, but also include such phenomenon as the rapid plastic working of the explosive material near the site of impact due to projectile penetration and case distortion. The confinement of the explosive allows the buildup of reaction that results from such phenomenon to grow, while the same reaction would be quickly released in a bare charge. Consequently, a cased charge has a far greater complexity of response to the impact of a flat-faced projectile than its bare or covered counterparts. Although the majority of experiments discussed in this paper were carried out with cased charges, it is only the detonation/nondetonation threshold with which we concern ourselves here, and we do not discuss the subdetonative responses. Similarly, in the shock initiation regime, we have attempted to predict the detonation/nondetonation threshold, but not the level of response associated with nondetonation.

## EXPERIMENTAL

PE4 (a plastic explosive containing 88 percent RDX) has been the principal explosive used in this study, although some additional work has also been carried out with tetryl and RDX/TNT (60:40). The target charges were 114 mm long x 57 mm diameter, and were contained in a 9 mm thick mild steel cylindrical casing open at one end. The end of the charge subjected to impact was either bare or covered by a chosen barrier plate. Three barrier materials have been investigated, namely mild steel, aluminum, and PMMA. The projectiles employed were flat-ended rods of two diameters (13.15 and 20 mm) but constant mass (27 g), and were made from hardened steel (condition W). The projectiles were housed in a nylon sabot and fired from a rifled 30 mm RARDEN gun. This system enabled velocities in the range 800 - 2000 m/s to be investigated with very few projectile stability problems. From a limited number of direct comparison experiments we have conducted between rifled and smooth bore gun systems, it would appear that detonation thresholds are not significantly influenced by projectile spin, but problems with yaw are greatly reduced.

The event was backlit by flashbulbs and the projectile flight and explosive reaction were filmed using a 1/4 height Fastax camera operating at ca. 30000 fps. In addition to providing a measurement of projectile velocity, the film record gave an indication of the response of the explosive and enabled a check to be made for projectile yaw.

## THEORETICAL PREDICTION OF EXPLOSIVE RESPONSE

The theory employed is based on the critical energy criterion for bare explosives postulated by Walker and Wasley,<sup>1</sup> and developed by James<sup>2</sup> to cope with projectiles such as flat-ended cylindrical rods. It is assumed that the theory is valid for covered explosives providing that:

- a) The initial impact shock can be transmitted into the explosive.
- b) The shock mechanism is the most efficient mechanism for initiating explosives

within the region defined by a), i.e., it is not possible for a non-shock stimulus, produced by a projectile which is below the requirements for the shock threshold, to cause detonation.

If either a) or b) does not hold, then the detonation threshold is not defined by a shock mechanism, and is not described by the theory given below.

The theory requires the explosive to have a critical value of energy-per-unit-area ( $E_c$ ) which, if exceeded by conditions within the initial shock, causes detonation. It is postulated that the value of  $E_c$  for a given explosive is constant, regardless of whether the charge is bare, covered, or cased. Hence, to predict the detonation threshold the theory needs a value for  $E_c$  (from bare charge impacts), the values of shock parameters in the explosive, and a knowledge of how quickly they are released by rarefactions from free surfaces. The importance of the latter requirement is that it determines the time at which the maximum impact shock energy is deposited in the explosive, which in turn is the time at which the energy-per-unit-area ( $E$ ) is calculated.<sup>2</sup> The detonation threshold for the covered explosive is theoretically determined by impacts which give  $E$  equal to  $E_c$ .

It should be noted that in bare charge experiments the  $E_c$  criterion has been found not to apply to some explosives,<sup>3</sup> or to only apply over a limited impact velocity range in others.<sup>4</sup> Obviously these limitations also apply to covered experiments. However, the criterion does apply to a sufficient number of commonly used explosives to make its adaptation to covered charges worthwhile.

## THE CALCULATION OF ENERGY-PER-UNIT-AREA

The energy-per-unit-area deposited by the impact shock in the explosive is calculated in three stages. By knowing the Hugoniot for the projectile, barrier plate, and charge material, and also by knowing the impact velocity, the shock parameters in the explosive can be calculated. These parameters, plus the barrier thickness and projectile diameter, allow the shock diameter at the case/explosive interface to be calculated at the start of shock transmission into the explosive. Finally, by

finding the main release mechanism for the shock volume in the explosive, the time at which the maximum shock energy is deposited in the charge is found. The value of E is calculated at this point and compared to  $E_c$  to predict the explosive's response.

This calculation is complicated by the presence of several factors. The main one is identified as being the effect that the rarefaction in the barrier has on the behavior of the release wave in the explosive.

The release of the shock in the explosive is determined by both the rarefaction in the barrier reaching the barrier/explosive interface, and those release waves generated at the periphery of the shocked explosive moving radially inwards. The relative importance of these two sets of rarefactions in determining this shock boundary will be discussed in the following sections.

### CALCULATION OF SHOCK CONDITIONS IN THE EXPLOSIVE

Provided that Hugoniot are known for the explosive, barrier, and projectile, the shock conditions in the barrier and explosive can be calculated. If all three materials obey a linear shock/particle velocity relationship, a straightforward algebraic solution can be obtained.

Let the projectile, barrier, and explosive be identified by subscripts 1, 2, and 3 respectively. Then the shock/particle velocity relationships are:

$$w_i = a_i + b_i u_i \quad (i = 1, 2, 3) \quad (1)$$

where  $w$  is shock velocity,  $u$  is particle velocity, and  $a$ ,  $b$  are constants for the particular material.

The constants used to obtain the Hugoniot of materials discussed in this paper are listed in Table 1, and sound speeds,  $c_i$ , have been calculated using the Jacobs approximation.<sup>5</sup>

### CALCULATION OF RELEASE WAVES IN THE BARRIER

The time  $T$  taken for the initial shock to reach the barrier/explosive interface is given by:

Table 1. Hugoniot Data

Material	Density (Mg/m <sup>3</sup> )	a (km/s)	b	Ref.
PBX9404	1.834	2.46	2.53	9
RDX/Wax 88/12	1.55	2.5**	2.0**	.
PE4	1.6	2.5**	2.0**	.
Mild Steel	7.84*	3.596	1.6863	10
Tantalum	16.656	3.43	1.19	11
Aluminum	2.68	5.27	1.37	12
PMMA	1.196	3.07	1.12	11+
Polythene	0.9	2.9	1.48	12+

- \* Densities for PE4 experiments were 7.81 Mg/m<sup>3</sup> for the rod and 7.78 Mg/m<sup>3</sup> for the barrier.
- \*\* Estimated values-- probably close to actual values. However, values of  $E_c$  derived from this should not be treated as absolute values.
- + Values for  $a$  and  $b$  derived from data in this reference.

$$T = d/w_2 \quad (2)$$

where  $d$  is the original thickness of the case. The case thickness  $d'$  at time  $T$  is

$$d' = d (w_2 - u_2)/w_2 \quad (3)$$

Taking a set of axes that are stationary relative to the rod/barrier interface (and so moving at  $u_2$  relative to laboratory axes), the rarefaction from the rod periphery forms an arc of radius  $c_2 T$  at time  $T$ , providing  $c_2$  is greater than or equal to  $c_1$ . This arc is centered on the position of the rod periphery at the time of impact. Where the arc cuts the barrier/explosive interface it defines the shock radius ( $R_c$ ) at the start of shock transmission into the explosive. Hence the general equation for the arc is:

$$(c_2 T)^2 = x^2 + (R_0 - R)^2 \quad (4)$$

where  $x$  is the vertical distance from the rod/barrier interface,  $R_0$  is the initial rod radius and  $R$  is the radius corresponding to  $x$ . Substituting  $d'$  for  $x$  and rearranging allows  $R_c$  to be found:

$$R_c = R_0 - \{c_2^2 - (w_2 - u_2)^2\}^{1/2} d/w_2 \quad (5)$$

The critical case thickness ( $d_c$ ), beyond which no initial impact shock is transmitted into the explosive is then given by:

$$d_c = R_0 w_2 / (c_2^2 - [w_2 - u_2]^2)^{1/2} \quad (6)$$

It is assumed that  $d_c$  defines the limit of the shock initiation regime for a given combination of both rod and barrier materials, impact velocity, and rod radius. It should be noted that detonation due to shock will cease at a thickness that is slightly less than  $d_c$ , if the  $E_c$  criterion is applied. The reason for this is that a given value of  $E_c$  requires a finite shock radius at a given impact velocity ( $d_c$  corresponds to zero radius), and radii that are less than this (produced by barriers of thickness just below  $d_c$ ) will produce a nondetonation.

If  $c_1$  is greater than  $c_2$ , then the overall shape of the head of the rarefaction in the barrier is changed. However, that portion of the rarefaction that initially intersects the explosive interface still originates at  $R_0$ , and hence, is still defined by (5) for all practical examples studied by the present authors.

The importance of  $R_0$  is that it defines the maximum radius of initial impact shock that will be seen by the explosive. Consequently,  $R_c$  plays the same role in covered charges as  $R_0$  does in bare impacts. However, unlike  $R_0$ ,  $R_c$  decreases due to two sets of rarefactions running radially inwards. The first set originates in the explosive at the periphery of  $R_c$ , and is analogous to those found in bare impacts. The second set is composed of the rarefactions already present in the barrier at time  $T$ . The curvature of the head of the release wave in this second set ensures a high initial release rate along the explosive interface as the expanding rarefaction intersects this boundary. At early times after  $T$  the release along the interface is usually driven by this rarefaction. Only at later times can rarefactions in the explosive take over.

## CALCULATION OF SHOCK VOLUME IN THE EXPLOSIVE

The volume of the initial (i.e., 1D) impact shock in the explosive is determined by the depth of explosive penetrated by the shock, and

the radial contraction caused by the rarefactions in the explosive and case. The critical energy criterion requires that the energy-per-unit-area  $E$  is calculated at the time when this volume reaches a maximum,<sup>2</sup> i.e., when the maximum amount of initial shock energy has been transferred to the explosive.

The depth  $L$  of shock penetration is

$$L = (w_3 - u_3)t \quad (7)$$

where  $t$  is the time after the shock has reached the explosive interface.

The calculation of the radial shape of the volume is rather more complicated since two sets of rarefactions are involved. However, a study of the experimental evidence suggests that a simple approximation allows a reasonable estimate of  $E_c$  to be made for impacts at the initiation threshold.

Figure 1 shows experimental threshold data<sup>6</sup> for steel rods impacting bare and covered PBX 9404. Shock pressure in the explosive ( $P$ ) is plotted against the "effective diameter" of the projectile, i.e., either  $D_0$  or  $D_c$  ( $D$  indicating diameter, with the subscripts as for  $R$ ), depending on whether the impact was against bare or covered explosive. It can be seen that to a first approximation, the relationship between  $P$  and  $D_0$  is the same as that between  $P$  and  $D_c$ .

If the barrier rarefaction played a significant role in releasing the shock conditions in the explosive, it would be expected that the pressure/diameter relationships would differ between bare and covered impacts, since the release mechanisms would be different. The fact that the relationships are so similar suggests that it is the rarefactions in the explosive that largely determine the explosive's response. This is reinforced by the experimental observation that materials that have high sound speeds do not necessarily provide the best protection against shock initiation resulting from projectile attack, for example, References 7 and 8 (and the current work--see next section) show aluminum as not providing as good a protection as the same thickness of steel.

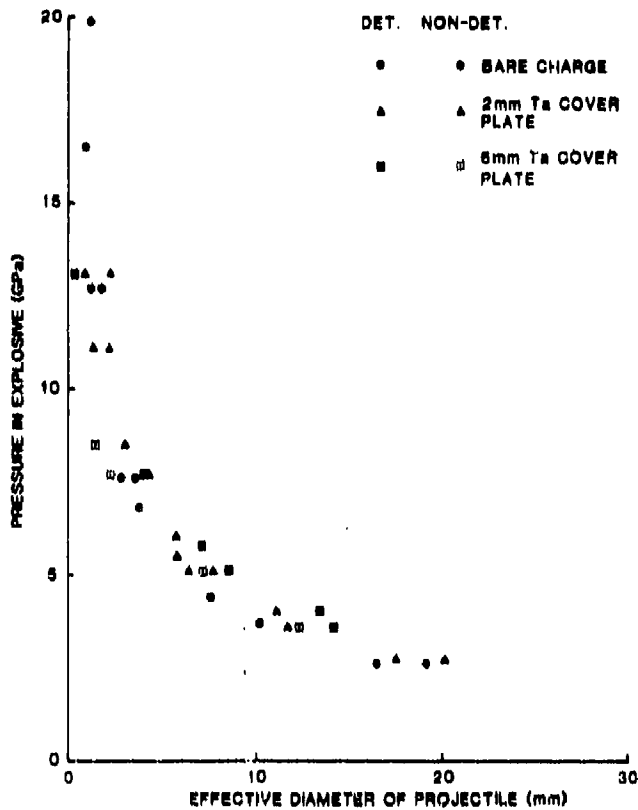


Figure 1. Steel Flat-Nosed Rod Impacts into Bare and Covered PBX 9404

At the initiation threshold the critical energy criterion requires:

$$E = E_c = P u_3 t \quad (8)$$

where  $t$  is the time of maximum shocked volume,<sup>2</sup> in this instance the time being relative to the arrival of the shock at the barrier/explosive interface. For bare impacts  $t$  has been shown to be  $R_0/(3c_3)$ . As a result of the similarity between the bare and covered relationships, it is assumed that to a first approximation

$$t = R_c/(3c_3) \quad (9)$$

for covered impacts. Hence,

$$E = P u_3 R_c/(3c_3) \quad (10)$$

and  $E = E_c$  for threshold impacts.

The relationship for  $t$  described by (9) is based on a cylindrical 1D shock volume contracting radially at constant velocity from an

initial radius  $R_c$ , while at the same time growing in length at velocity  $w_3-u_3$ . Although the growth in length is correct, both the constant radial velocity and cylindrical nature of the volume are known to be approximations. Hence (10) should be used with care.

From the previous section it must be realized that the assumption that  $t$  has no dependence on barrier rarefactions is an oversimplification. The release of the shock volume at times soon after  $T$  almost certainly depends to some extent on the barrier rarefaction. Although the experimental results indicate that the overall effect of this rarefaction cannot be great, some effect is present, as a close study of Figure 1 shows. Any initiation boundary drawn through the data in this figure would almost certainly fail to completely separate detonations from nondetonations. The problem lies in determining how much of this is due to experimental uncertainties, and how much is due to differences in the release mechanism.

The strengths and limitations of the simplified model described above are demonstrated below, where its predictions are compared with experimental data.

## RESULTS

We have divided the presentation of our results into two sections. In the first, we describe the experimental results appropriate to the shock regime and compare these with predictions based on the theory described above. In the second section, we discuss the results obtained with barriers thicker than  $d_c$ , i.e., the non-shock regime.

### THE SHOCK REGIME-- COMPARISON OF THEORY WITH EXPERIMENT

Figure 2 compares the simple theory with experimental data for steel flat-nosed rod impacts into PE4 protected by steel and aluminum barriers. In addition to the barrier, the explosive was contained in a steel case as described above. For bare impacts, only the barrier was removed, the case having little or no effect on the threshold velocity.

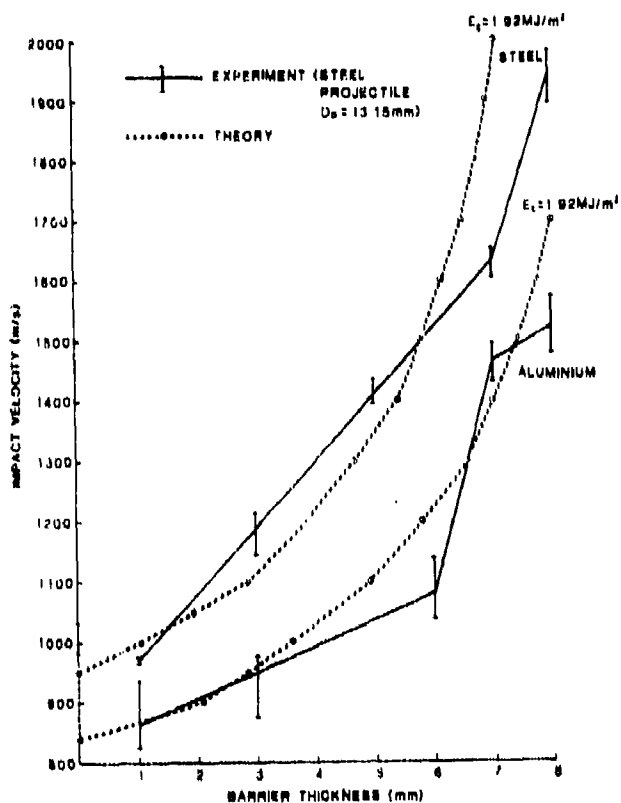


Figure 2. Comparison of Theory with Experiment in the Shock Regime for Steel and Aluminum Barriers Covering PE4

In the figure it can be seen that the experimental data follows a similar pattern for both barriers. Initially there is a linear or near linear increase in threshold velocity with increasing barrier thickness, followed by a sharp rise in threshold velocity for a small increase in thickness. Beyond this region the velocity levels out, giving a slower increase at greater thicknesses. However, the discussion here concentrates on the first two parts of this curve, as it will be postulated that these constitute the shock initiation regime.

The threshold velocity for the bare charge impact lies in the range 982-1034 m/s, which corresponds to  $E_c$  values of 2.04-2.25 MJ/m<sup>2</sup>. Since the constants for the linear shock/particle velocity relationship had to be estimated for PE4, it should be noted that these values of  $E_c$  are only useful for comparing different types of impact which use the same explosive (although the absolute value of  $E_c$  is probably not far from that given above). The theoretical curves shown (in Figure 2) for

both barriers use  $E_c = 1.92$  MJ/m<sup>2</sup>, which corresponds to a threshold velocity for a bare charge of 950 m/s, and generates the best overall fit to the data. The shape of the theoretical curve follows the changes in the experimental data very well. The steep rise in the latter stages being the asymptote of the theoretical curve to the critical thickness  $d_c$ . From this follows the postulate that detonations beyond this thickness lie outside the shock initiation regime.

The quantitative predictions of the theory are reasonably good over the linear portion of the experimental data, but tend to diverge from experiment in the region where the curve steepens. In this region shock volumes are small and their behavior may be heavily influenced by the rarefaction in the barrier. Alternatively, the energy content of the partly released portion of the shocked explosive may start to play a role in such circumstances, or the critical diameter of the explosive could be affecting the results. Further work is needed to identify which, if any, of these factors contributes to this portion of the response curve.

It should be noted in Figure 2 that the experimental value of threshold velocity for the 1 mm aluminum barrier lies significantly below the bare charge value, and yet appears to be consistent with data from thicker barriers. The theory shows the same anomaly, which is explained by an examination of the Hugoniot of the various materials involved. Figure 3 gives a diagrammatic representation of these Hugoniot in the pressure, particle velocity plane.

The mirror image of the steel Hugoniot is used to represent the rod since it has already acquired a velocity at zero pressure, i.e., it can be considered as already having been shocked and released to a free surface velocity during launch. On impact with a bare explosive the conditions jump from A to B; this latter point defining the 1D shock conditions in the explosive. If a steel barrier is placed in contact with the explosive, the conditions jump from A to C in the rod, and from O to C in the barrier. The conditions in the barrier undergo further change when the shock reaches the explosive interface. They change along the mirror image of the barrier line about C, i.e., along the rod line. Hence, the final conditions in barrier and

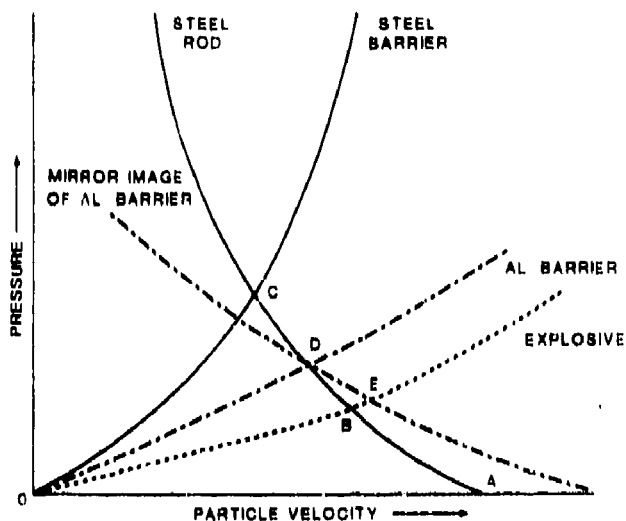


Figure 3. Illustration of Hugoniot Plots for Covered Charges

explosive (for calculating the 1D shock) are again to be found at B. However, if an aluminum barrier is used, then the initial jump is from A to D, and the second change is along the mirror image of the aluminum line about D. This produces a 1D shock condition, represented by E, in the explosive which has a higher pressure and particle velocity than conditions at B. Hence, for thin barriers, where  $R_c$  is only slightly less than  $R_0$ , the enhanced value of  $Pu_3$  means a lower velocity than that needed for the bare charge impact will ensure that  $E_c$  is exceeded.

The above arguments will apply to any barrier material whose Hugoniot lies between the Hugoniots of the projectile and explosive. Thin barriers of all such materials would, therefore, be expected to yield enhanced sensitivity to shock. In fact, the term thin could be misleading. It should be noted from Figure 2 that some 4-5 mm of aluminum is required before a threshold velocity comparable to the bare charge value is reached.

Figure 4 shows that the theory appears to cope well with changes in projectile diameter. The barrier was aluminum for both diameters of projectile, and  $E_c = 1.92 \text{ MJ/m}^2$  was used for the comparison of theory with the two sets of experimental data. It can be seen, for both projectile diameters, that detonations continue to be observed at barrier thicknesses which are

clearly in excess of  $d_c$ . The possible mechanisms operating in this regime are discussed in the next section.

The use of PMMA barriers (Figure 5) illustrate some limitations of the simple theory. Although good agreement has been achieved between the shapes of the theoretical and experimental curves, the theory needed a value of  $E_c = 1.70 \text{ MJ/m}^2$  in order to obtain quantitative agreement. This is equivalent to a bare charge threshold velocity of 890 m/s, which is about 10 percent lower than the bottom of the experimental range. Although some of this may be accounted for by experimental uncertainties, it seems probable that, at least for this material, barrier plate rarefactions do have a role in determining the behavior of the shock volume.

To check the accuracy of the simple model in dealing with different materials, experimental data<sup>6</sup> for a different explosive was compared with theory. The explosive was RDX/Wax 88/12, and flat-nosed steel rods ( $D_0 = 12.7 \text{ mm}$ ) were used to impact charges protected by a variety of cover plate materials ( $d = 3.175 \text{ mm}$ ). The range of  $E_c$  values (again not absolute) was found to be  $0.70\text{-}0.90 \text{ MJ/m}^2$  from the impacts of four different diameters of projectile into the bare explosive. Table 2 lists the experimental data for the covered impacts, and compares it with the predicted threshold velocity found by the simple theory using  $E_c = 0.82 \text{ MJ/m}^2$  (the average value of the bare charge data).

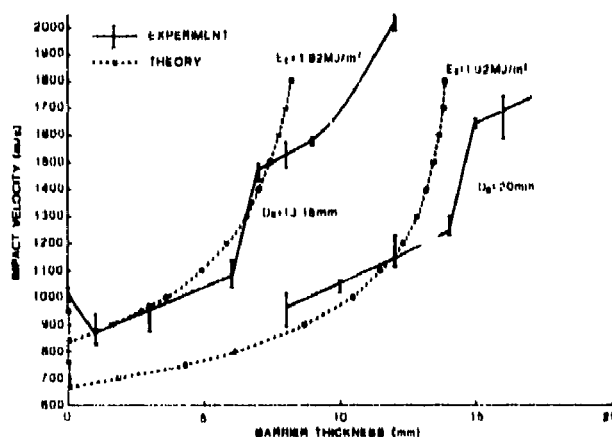


Figure 4. Steel Projectiles of Two Diameters Impacting PE4 Covered by Aluminum Barriers

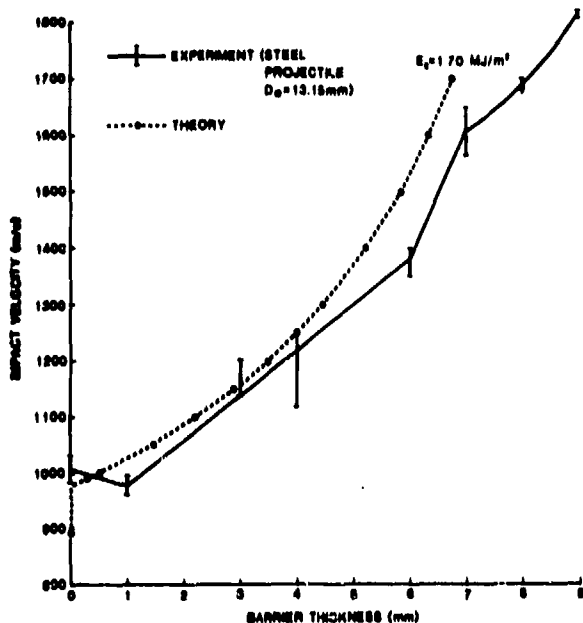


Figure 5. Comparison of Theory with Experiment for PMMA Barriers Covering PE4

Table 2. Comparison of Theory with Experiment for Impacts into Covered RDX/WAX

Cover Material	Experimental Threshold Vel. (m/s)	Predicted Threshold Vel. (m/s)	% Difference
PMMA	750	790	+ 5.3
Polythene	826	905	+9.6
Steel	847	730	-13.8
Aluminum	719	615	-14.5

The predicted threshold velocity lies within the range  $\pm 15$  percent when compared with experimental values--too large for accurate work, but adequate for a first approximation.

## THE NON-SHOCK REGIME

The experimental results for PE4 covered by aluminum barriers (shown in Figure 4), provide the clearest evidence to date for a change in mechanism from a shock to a non-shock process. Both the shape of the curves and the theoretical interpretation given earlier, strongly suggest that the detonations

obtained with the thickest barriers (i.e.,  $>7$  mm for a 13.15 mm projectile and  $>15$  mm for a 20 mm projectile) were not as a result of shock initiation. The data for PE4 covered by PMMA barriers (Figure 5) shows almost identical behavior, with detonations again being observed at barrier thicknesses too great for a primary shock mechanism to be operating.

A considerable number of experiments have also been carried out with RDX/TNT (60:40) and tetryl using the 13.15 mm projectiles. Although complete curves of the type shown in Figures 2, 4, and 5 are not yet available, detonations have again been observed outside the shock initiation regime. With RDX/TNT (open cast to a density of  $1.65 \text{ Mg/m}^3$ ) detonations were observed with a 10 mm thick steel barrier (threshold velocity ca. 2000 m/s)--clearly well outside the shock regime. Similarly, tetryl (pressed to a density of  $1.58 \text{ Mg/m}^3$ ) has been detonated when covered by a 15 mm steel barrier (threshold velocity: 1605-1537 m/s).

The experiments described above were all carried out on steel cased charges, as detailed in Section 2. To see if this casing was influencing the detonation threshold in the non-shock regime an experiment was conducted on PE4 contained only in a light plastic tube, but covered with an 8 mm aluminum barrier. Using a 13.15 mm projectile, detonation was achieved at ca. 1605 m/s. While more experiments are needed, this is sufficiently close to the threshold observed for the cased charges to suggest that the casing has not influenced the initiation to any significant extent. As a consequence of this result, it would appear that neither interactions with the back plate nor the confinement afforded by the steel casing play a significant part in the initiation process. The lack of any apparent dependence on confinement suggests that onset of detonation must be reasonably prompt. The Fastax camera records show detonation occurring within 1 frame after projectile impact, which puts an upper bound on the delay before detonation of ca. 33  $\mu\text{s}$ ., but higher speed instrumentation will be needed to explore this question further.

Howe<sup>13</sup> has reviewed the evidence from earlier studies, which have indicated that a non-shock process may be controlling the initiation

of detonation. Howe concludes that a macroscopic shear process is probably the mechanism in many of these cases. The new results we have presented here are certainly consistent with such a mechanism, but considerably more work is needed before any firm conclusions can be drawn.

## CONCLUSIONS

The experimental and theoretical results we have given provide strong evidence that at least two mechanisms can be responsible for the projectile initiation of detonation in some secondary explosives. For impacts through thin barriers, the evidence for a shock initiation mechanism is almost conclusive, but for thick barriers there is still considerable research needed before shear or some other process can be identified with any certainty. Our future experiments will concentrate on a more detailed examination of initiation in this non-shock regime.

We have shown that in the shock regime the simple model we have proposed can provide a qualitative explanation of trends observed in the experimental data, and a first approximation for a quantitative fit to this data over a large portion of the experimental curve. This fit was achieved using a criterion that depended on a single empirical constant which may be derived from bare charge impacts. The major weakness of the model being that a poor quantitative prediction is obtained at large barrier thicknesses.

The model has given a good basis for understanding some of the detailed processes present in shock initiation. Even with the scatter in predicted velocities seen above, it still appears that case rarefactions are a correction rather than a dominating feature. Work is underway to refine the model and, hopefully, further reduce the errors in prediction.

## REFERENCES

1. Walker, F. E. and Wasley, R. J., "Critical Energy for Shock Initiation of Explosives," *Explosivesoffe*, Vol. 17, 1969, p. 9.
2. James, H. R., "Critical Energy Criterion for the Shock Initiation of Explosives by

Projectile Impact," *Propellants, Explosives, Pyrotechnics*, Vol. 13, 1988, p. 35.

3. de Longueville, Y.; Fauquignon, C.; and Moulard, H., "Initiation of Several Condensed Explosives by a Given Duration Shock Wave," *Sixth Symposium (International) on Detonation*, San Diego, CA, 24-27 Aug 1976, pp. 105-114.
4. Honodel, C. A.; Humphery, J. R.; Weingart, R. C.; Lee, R. S.; and Kramer, P. E., "Shock Initiation of TATB Formulations," *Seventh Symposium (International) on Detonation*, Annapolis, MD, 15-19 Jun 1981, pp. 425-434.
5. Allison, F. E., "Thermodynamic States for Aluminium and Polystyrene," BRL Report 1294, Ballistic Research Laboratories, Aberdeen Proving Ground, MD, 1965.
6. Bahl, K. L.; Vantine, H. C.; and Weingart, R. C., "The Shock Initiation of Bare and Covered Explosives by Projectile Impact," *Seventh Symposium (International) on Detonation*, Annapolis, MD, 15-19 Jun 1981, pp. 325-335.
7. Slade, D. C. and Dewey, J., "High Order Initiation of Two Military Explosives by Projectile Impact," BRL Report 1021, Ballistic Research Laboratories, Aberdeen Proving Ground, MD, 1967.
8. Griffiths, N.; Laidler, R. McN.; and Spooner, S. T., "Some Aspects of the Shock Initiation of Condensed Explosives," *Combustion and Flame*, Vol. 7, 1963, p. 347.
9. Ramsay, J. B. and Popolato, A., "Analysis of Shock Wave and Initiation Data for Solid Explosives," *Fourth Symposium (International) on Detonation*, White Oak, MD, 12-15 Oct 1965, pp. 233-238.
10. Burrows, K. D., AWE Foulness, Private Communication.
11. Marsh, S. P., ed., "LASL Shock Hugoniot Data," University of California Press, 1980.
12. van Thiel, M., ed., "Compendium of Shock Wave Data," Lawrence Radiation Laboratory Report UCRL-50108, Vol. 1, 1966.

13. Howe, P. M., "On the Role of Shock and Shear Mechanism in the Initiation of Detonation by Fragment Impact," *Eighth Symposium (International) on Detonation*, Albuquerque, NM, 15-19 Jul 1985, pp. 1150-1159.

• Controller HMSO, London, 1989.

# CORRELATION OF EXPLOSIVE SENSITIVITY TO COMPRESSIONAL INPUTS

M. Kornhauser  
3C Systems, Inc.  
Wynnewood, Pennsylvania 19096

*Sensitivity of explosives and propellants to compressional pulses is considered to depend primarily on the  $P^2t$  and  $P$  parameters of the inputs that define the thresholds of reaction. The methodology of plotting sensitivity curves in the  $P^2t$  vs.  $P$  format is shown to lead to curves with two asymptotes, each of which represents a fundamental property of the explosive or propellant. Although the integral of  $P^2dt$  does not remain constant along the sensitivity curve, it is shown that the integral of  $(P-P_c)^2dt$  does, where  $P_c$  is a critical pressure above which the explosive is no longer elastic. Using this methodology, models of the various sensitivity tests are used to generate sensitivity curves for the explosives and propellants for which there are sufficient test data.*

## INTRODUCTION

A fundamental question to be answered when working with the parameters of explosive sensitivity is how to express sensitivity data. Bullet impact velocity at the threshold of reaction may be the quantity measured, but is hardly a fundamental property of the explosive since it depends on many properties of the bullet. Likewise, a gap test threshold cannot be considered an explosive sensitivity parameter since it depends on at least the details of donor geometry and on gap material of the particular gap test employed. What is proposed here is a methodology of treating compressionally induced threshold data with  $P^2t$  and  $P$  as the parameters most directly linked to fundamental properties of explosives and propellants. Other parameters such as  $dP/dt$  are also significant, but they have lesser quantitative influence. Further, correlations and presentations of data become unduly complex if more than two parameters are considered simultaneously. Another factor favoring the selection of  $P^2t$  and  $P$  is that the typical plot of experimental data in the  $P^2t$  vs.  $P$  format leads to two asymptotes, each of

which proves to be a physically satisfying property of the explosive.

In the past several years  $P^2t$  or  $P^{nt}$  has gained acceptance as a criterion of explosive reaction thresholds. However, the  $P^2t$  data developed by flyer plate tests does not necessarily agree with  $P^2t$  threshold data obtained from the various gap tests, nor with bullet impact data, nor with aquarium test data. In general, the  $P^2t$  threshold values appear to increase as the loading duration increases or as the peak input pressure decreases. In this paper, the  $P^2t$  criterion is modified (as has been done by Stresau and Kennedy in Reference 1) to account for the phenomenon that compressive energy is not absorbed appreciably by the explosive until the pressure exceeds some threshold value,  $P_c$ , perhaps equal to the Hugoniot Elastic Limit. When the threshold test data are correlated using the integral of  $(P-P_c)^2dt$ , with  $P_c$  of the order of 0.1-0.3 GPa for COMP B, PBX-9404, TNT, and Tritonal, this integral is fairly constant for the various laboratory tests cited above. Further evidence for the existence and magnitude of  $P_c$  is afforded by the fact that a simple compressive model of the long duration

Premature Simulator predicts pre-reaction stresses and decelerations accurately using the explosive's elastic bulk modulus until the reaction thresholds are reached at pressures of the order of 0.3 GPa. It is after the elastic portion of the explosive column's compression that plastic deformation occurs and thermal energy is deposited in the explosive. Integration of  $P^2 dt$  results in very high values, but integration of  $(P - P_c)^2 dt$  yields results close to those obtained by short duration tests such as flyer plate tests.

In order to deal directly with experimental data and not be forced to make assumptions on the magnitude of  $P_c$ , a method of presentation of sensitivity data has been developed for the purpose of presentation in a format that permits superposition of explosive sensitivity and input parameters and also for the purpose of correlating threshold data produced by experiments with a variety of laboratory test devices. Reaction threshold data resulting from the various tests are expressed in terms of  $P^2 t$  and  $P$ , leading to sensitivity plots with two asymptotes. The  $P$  asymptote is of the order of 0.3 GPa for many explosives, but it may be much higher for some insensitive propellants, and it is approached by test data from long duration devices such as the Army's Activator or the Navy's Premature Simulator. The  $P^2 t$  asymptote is approached by flyer plate data, gap test data, and bullet impact data. The sensitivity curve between the asymptotes may be based on test data from bullet impact tests, gap tests, and the aquarium test.

Another utilitarian value of the  $P^2 t$  vs.  $P$  plot of an explosive's sensitivity is that a munition's inputs to the explosive in an operational situation (target impact, sympathetic detonation, etc.) may be plotted parametrically in the same format. Intersections of the munition input plot and the explosive's sensitivity curve permit rapid estimation of the thresholds of explosive reaction.

### THE $P^2 t$ - $P$ SENSITIVITY CURVE

Figure 1 contains a sensitivity curve for Comp B, expressed in terms of the peak pressure and loading duration inputs to the explosive. The curve approaches a

15 GPa<sup>2</sup>-microsecond asymptote and an approximately 0.4 GPa asymptote. Input compressive pulses with  $P^2 t$  and  $P$  lying in the zone above and to the right of these asymptotes will elicit energetic reactions; those in the zone below and to the left of the asymptotes will not produce reactions.

Note that two data points are shown in the short duration (less than one microsecond), high pressure region, one point in the intermediate region, and one point in the long duration, low pressure region. These points represent test data obtained from flyer plate tests, gap tests, and Premature Simulator tests, respectively. Figure 2 contains plots of

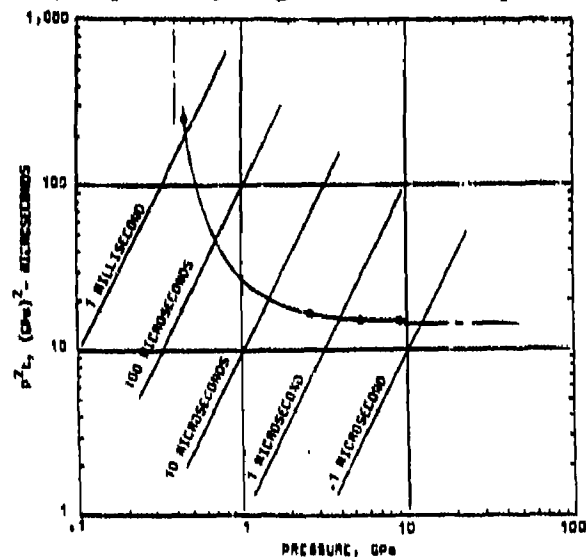


Figure 1. Explosive Sensitivity Curve for Comp B

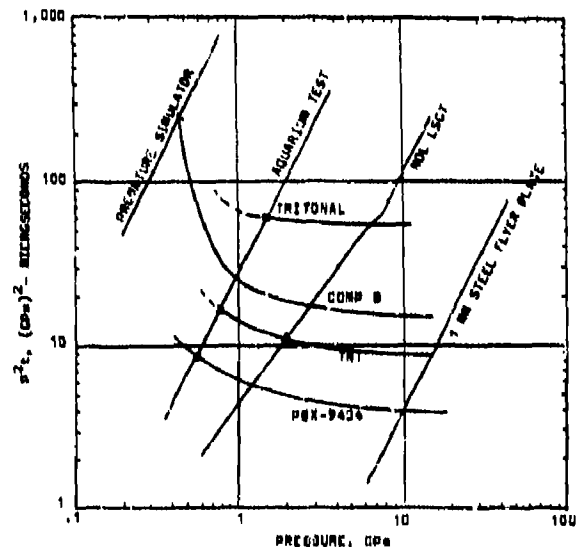


Figure 2. Cross-Plots of Laboratory Test Outputs and Explosive Sensitivity Curves

the  $P^2t$  vs.  $P$  inputs delivered by various test devices, as well as sensitivity curves for several explosives in addition to Comp B. The laboratory tests represented in Figure 2 are considered to deliver primarily compressional energy to the explosive being tested; therefore, their test results may be correlated for purposes of establishing empirical values of critical  $P^2t$  and  $P$  for each explosive.

## MODELS OF THE SENSITIVITY TESTS

In order to locate threshold sensitivity test data on the  $P^2t$ - $P$  plot, as in Figure 2, it was necessary to develop engineering models of the various laboratory tests. The flyer plate model is the simplest, with pressures defined by the Hugoniot relationships of the flyer plate material and the explosive being impacted, and duration,  $t$ , defined as follows:

$$t = 2h/C \quad (1)$$

where  $h$  is plate thickness and  $C$  is stress wave velocity in the plate material. Note that the curves in Figure 2 have been faired through many threshold datum points, including a wealth of flat-bullet-induced data on PBX-9404 reported by Bahl et al. in the Seventh Symposium (International) on Detonation. The details are reported in Reference 8.

The NOL Large Scale Gap Test, shown schematically in Figure 3, has been calibrated thoroughly for  $P$  vs. width of the PMMA gap, as reported in Reference 2. Loading durations have not been well calibrated. Therefore, a semi-empirical model of  $t$  (loading duration) has been developed by making use of data (from Reference 3) on total impulse delivered to an extended plane slab by detonation of a cylindrical charge in contact with the plane. Figure 4 contains a curve of impulse vs.  $L/D$  of the cylindrical charge, taken from data obtained with  $\frac{1}{4}$  - 2 pound charges of pressed TNT and reported in Reference 3 together with correction factors to be applied when using other explosives. Effective loading duration, also shown in Figure 4, has been calculated from the impulse data assuming an exponential decay from 25 GPa to the pressure when 90 percent of the impulse has been

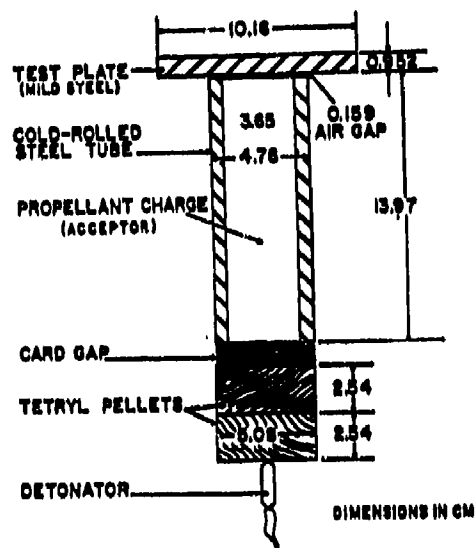


Figure 3. Charge Assembly for NOL-LSGT

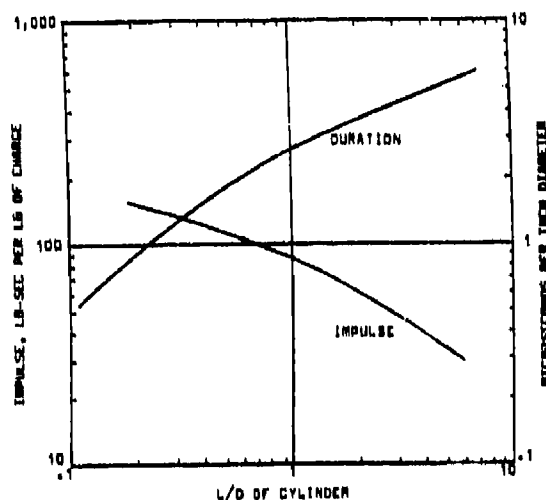


Figure 4. Duration of Loading in Gap Tests

delivered to the plate. In addition, it was assumed the loading area on the extended plane slab grew from the original area of contact to an area consistent with expansion of the cylinder according to gamma equal to 2.85. The loading duration curve for Figure 4 was used to develop the  $P^2t$  curve for the NOL LSGT as presented in Figure 2.

The aquarium test utilizes a sphere of cast pentolite as a pressure source, as shown in Figure 5. Acceptors are held at various distances from the donor charge, with  $R/R_0$  ranging from approximately 2 to 5. Photographic observations of the donor's shock wave and the acceptor's reactions are

used to calculate the pressure delivered to the acceptor and the onset of reaction of the acceptor. Initiation thresholds may be estimated by plotting the data and by extrapolating the curves down to zero, as shown in Figure 6 (taken from Reference 4). Pressure in the explosive vs.  $R/R_0$ , as well as  $t/R_0$  (from Reference 5, where  $t$  is the time for the incident wave to decay exponentially from  $P_0$  to  $P_0/e$ ), are plotted in Figure 7. These curves are used to calculate the  $P^2t$  vs.  $P$  curve in Figure 2 for the aquarium test.

The Premature Simulator was developed by the U.S. Navy (Reference 6) to simulate the mechanical shock experienced during setback accelerations on gun launch. Figure 8 shows schematically the one-pound sample

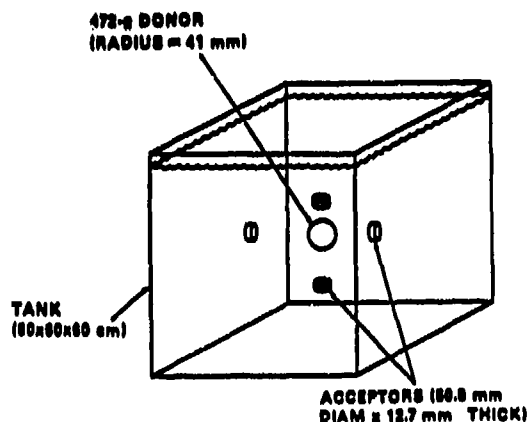


Figure 5. The Aquarium System

of explosive inside the test projectile. It is a free fall drop tester. When the projectile strikes the steel plate anvil (on which may be placed various stopping pads designed to lengthen the pressure-time pulse delivered to the explosive) the projectile is brought to rest quickly, and the explosive sample is compressed as the vehicle's large mass (in the 300 to 1,100 pound range) is brought to rest more gradually using the explosive as a "cushion." Pressures as high as 1 GPa can be developed, with pressure buildup times from about 1 to 15 milliseconds, measured by the pressure gauge shown in the plunger. For steel-on-steel drops, the following analysis assumes deformations of only the explosive sample.

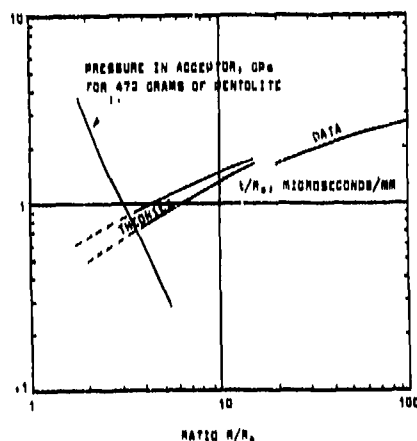


Figure 7. Pressure and Duration in Aquarium Test

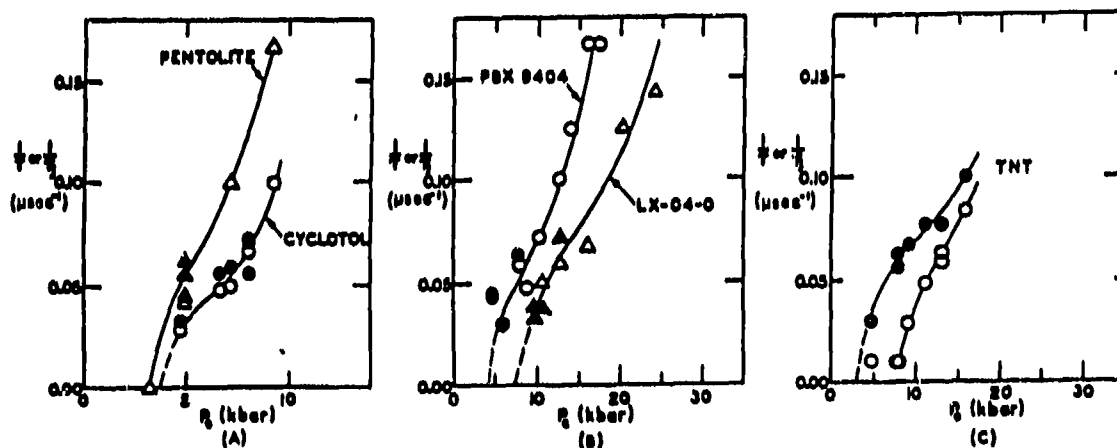


Figure 6. Aquarium Data on Reaction Thresholds

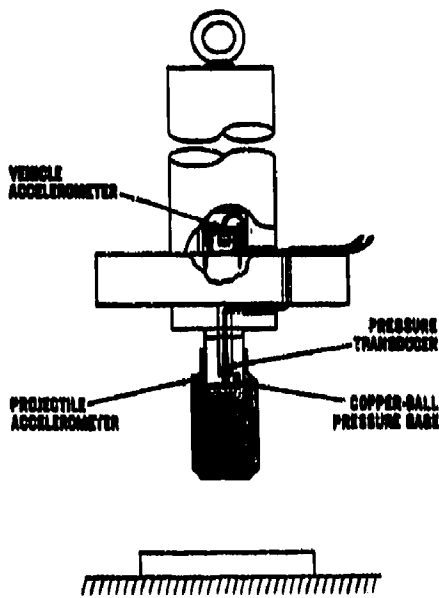


Figure 8. The Premature Simulator

When the simulator assembly strikes the steel anvil, the assumption is made that the test projectile containing the explosive sample is brought to rest instantaneously while the massive body, acting through the plunger, continues downward at velocity  $V_0$ . The steel plunger with density  $\rho_s$  and wave speed  $C_s$  strikes the explosive with density  $\rho_e$  and wave speed  $C_e$ , generating a stress wave in the explosive with pressure  $P_w$ , as follows:

$$P_w = \frac{\rho_s C_s V_0}{1 + \rho_s C_s / \rho_e C_e} \quad (2)$$

For a 40 foot drop with  $V_0 = 50.6$  ft/sec with  $\rho_s = 7.8$ ,  $C_s = 17,000$  ft/sec,  $\rho_e = 1.7$ , and  $C_e = 6,000$  ft/sec,  $P_w = .045$  GPa. The low intensity of this stress wave insures that there will be small losses of energy as the wave progresses down the explosive sample's length. When this first wave strikes the base of the steel test projectile, a reflected wave is generated in the explosive with the following intensity:

$$P_r / P_w = \frac{1 - \rho_e C_e / \rho_s C_s}{1 + \rho_e C_e / \rho_s C_s} = 0.86$$

Until this reflected wave reaches the explosive-plunger interface, the plunger has been decelerating under a pressure of

0.045 GPa. After two transit times (of the order of 100 microseconds) of stress waves in the 4.76 inch column of explosive, the plunger experiences an added pressure of 0.033 GPa, for a total of 0.078 GPa. As soon as waves reflect from the rear of the body and plunger, however, the plunger loses some velocity and then generates less than the initial 0.045 GPa input to the explosive. In this fashion the plunger is decelerated approximately exponentially, with discontinuous jumps in deceleration amplitude about every 100 microseconds. Analyses of such deceleration processes have been made by Cauchy, Poisson, St. Venant, and others in the 1860 - 1885 era, as described in Reference 7.

During the period when the plunger is being decelerated, the explosive sample experiences similar stepwise increases in pressure due to the reflected waves, and finally decreases in pressure as the plunger mass is being brought to rest. This discontinuous process can be shown to be approximated reasonably well by treating the column of explosive as an elastic spring and the plunger as a rigid body. If the initial height of the column of explosive is  $h$ , its cross-sectional area is  $A$ , and its modulus of elasticity is  $E$ , the pressure in the explosive is related to its deflection  $X$  as follows:

$$P = EX/h \quad (3)$$

The equation of motion of the mass,  $M$ , is as follows:

$$d^2X/dt^2 + AEX/hM = 0 \quad (4)$$

Solving this equation with the initial conditions  $X = 0$  and  $dX/dt = V$  when  $t = 0$ :

$$X = V \sin \omega t / \omega \quad (5)$$

where  $\omega = (AE/hM)^{1/2}$ . The peak pressure is reached when the mass is brought to rest at time  $t_1$ :

$$t_1 = \pi/2\omega = \frac{1}{2}\pi(hM/AE)^{1/2} \quad (6)$$

$$P_1 = EV/\omega h = (2gHEM/Ah)^{1/2} \quad (7)$$

where  $H$  is the height of drop.

For the one pound sample of explosive used in the premature simulator,  $h = 4.76$  inches and  $A = 3.90$  square inches (an average of areas that vary from 4.40 to 2.90 square inches). Modulus  $E$  is taken as 800,000 psi. Figure 9 shows the comparison of Equation (6) for rise time and Equation (7) for peak pressure with experimental calibration data.

The Premature Simulator's energy output may be calculated with the pressure vs. time relationship  $P_2/P_1 = \sin \frac{1}{2}nt/t_1$ , where the integral of  $P^2 dt$  is equal to  $\frac{1}{2}P_1^2 t_1$ . The  $P^2 t$  vs.  $P$  plot for the 1,100 pound Premature Simulator is shown on Figure 2.

### THE THEORETICAL SENSITIVITY CURVE

It is postulated that an explosive responds elastically to compressional inputs (as is assumed by using the elastic modulus  $E$  in the analysis of the Premature Simulator) until the pressure reaches a critical pressure,  $P_c$ , above which compressive energy is absorbed until the integral of  $(P - P_c)^2 dt$  reaches a critical value for that explosive, at which time an energetic reaction occurs. Figure 10 illustrates this process for half-sine compressive inputs, showing threshold input pulses and the resulting sensitivity plot which makes use of the integral of  $P^2 dt$ . The question to be answered by theoretical analysis is whether or not there is a value of  $P_c$  for which the integral of  $(P - P_c)^2 dt$  is constant over a wide range of peak input pressures. For  $P/P_1 = \sin \pi t/t_1$  (appropriate for the Premature Simulator), this integral is as follows:

$$\int (P - P_c)^2 dt / P_1^2 t_1 = \frac{1}{2} (1 - 2t_c/t_1) (1 + 2P_c^2/P_1^2) + (1/2n) \sin n(1 - 2t_c/t_1) - (4P_c/nP_1) \sin \frac{1}{2}n(1 - 2t_c/t_1) \quad (8)$$

Figure 11 is a plot of input  $P_1^2 t_1$  vs.  $P_1$ , both normalized, that produce constant values of the integral of  $(P - P_c)^2 dt$  between  $t_c$  and  $t_1 - t_c$ . This plot may be used to evaluate the adequacy of the model by correlating the

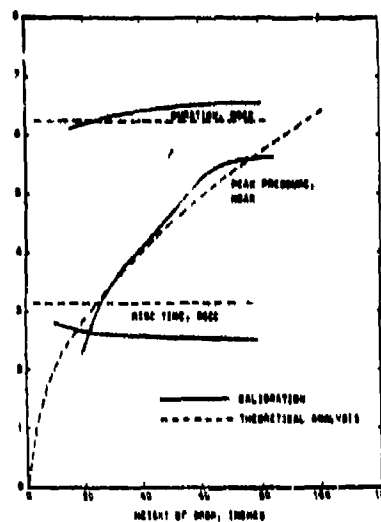


Figure 9. Outputs of Premature Simulator, Steel Anvil, 1100 Pounds, Filler E

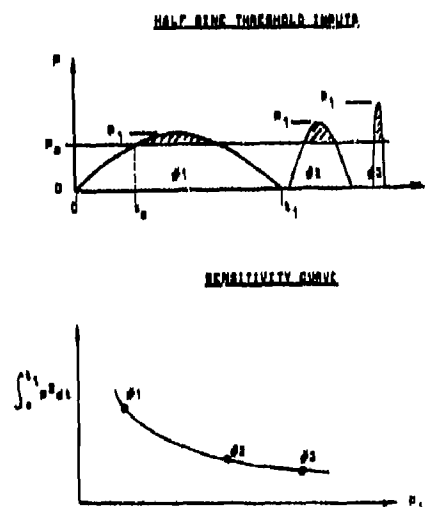


Figure 10. Threshold Inputs and Sensitivity Curve

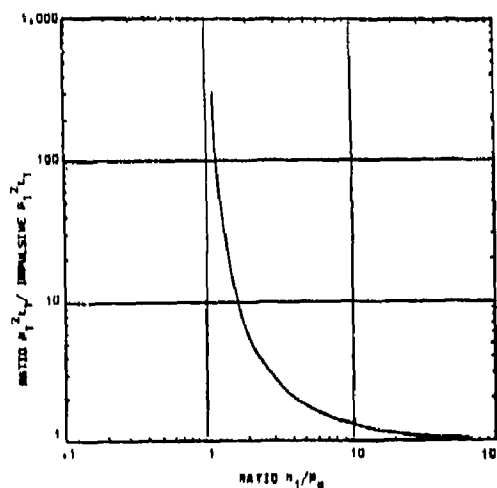


Figure 11.  $P^2 t$  for Constant Integral of  $(P - P_c)^2 dt$ , Half-Sine Pulses

empirical explosive sensitivity data presented in Figure 2. Note that these sensitivity curves pass through more data points in the short duration regime, where flyer plate data are available, than in the long duration regime which depends primarily on Premature Simulator data. This is the rationale for normalizing the ordinate of Figure 11 by dividing by impulsive (very-short-duration)  $P_1^2 t_1$ , which is estimated as the asymptotic value. To calculate  $P_c$  from the sensitivity curve data, values of  $P_1$  and  $P_1^2 t_1$  are taken from the empirical curves of Figure 2,  $P_1^2 t_1$  is divided by the asymptotic value of  $P_1^2 t_1$ , Figure 11 is entered at this ratio in order to obtain  $P_1/P_c$ , and  $P_c$  is calculated with the appropriate value of  $P_1$ .

Figure 12 contains plots of  $P_c$  vs.  $P_1$  for each of the four explosives of Figure 2, calculated in this manner. The solid curves correspond to the data on the plots of Figure 2. Since the calculated  $P_c$ 's are not constant, and since the plotted values follow systematic trends, the curves are extrapolated down into the low pressure regime in order to find each curve's intersection with the  $P_c = P_1$  line. The results are highly approximate, for at least the following reasons:

- (1) Each datum point on each sensitivity curve of Figure 2 was obtained by testing explosive samples with somewhat different properties, since the

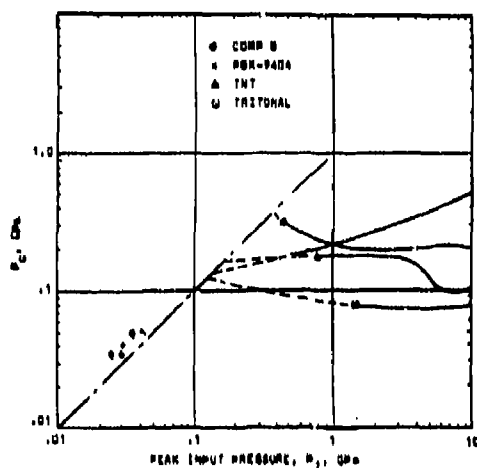


Figure 12. Estimation of  $P_c$  from Explosive Sensitivity Curves

samples were prepared at different facilities at different times.

- (2) The curves presented in Figure 2 were faired through the scatter of the three or four points of data for each explosive.
- (3) The Premature Simulator delivers half-sine pressure pulses to the test samples, the flyer plates deliver square waves, while the NOL-LSGT and the aquarium test deliver compressive pulses with less idealized shapes. To evaluate the constancy of  $P_c$ , the half-sine model was applied to all points along the sensitivity curves of Figure 2. This procedure introduces a source of error into the correlation process, since Equation (8) and Figure 11 apply only to the half-sine pulse shape.

Because of these sources of inaccuracy, the curves in Figure 12 must be considered order-of-magnitude estimates, with  $P_c$  estimated to be in the 0.1-0.3 GPa range for these four explosives.

## SOME EFFECTS OF FRICTION COMBINED WITH COMPRESSION

Poster No. 8 contains a sketch taken from the patent application of the newly patented "SHARP SHIELD," consisting of wedges placed with the sharp wedge apex in contact with the acceptor's casing. (All posters can be found in the Poster Session section of this publication.) When bullets or fragments strike the SHARP SHIELD the wedges may damage the acceptor by piercing its casing, but the very early advent of rarefaction waves generated from what may be considered a very small-radius bullet will greatly reduce the  $t$  in  $P^2 t$  (also note the equation for bullet-loading duration at the bottom of Poster No 2. If  $r$  approaches zero,  $t$  approaches zero.). Note that there will be friction and inertially-induced pressures generated as the wedge is driven into the acceptor's explosive, both of which can induce reactions even when shock wave pressures are minimized. To study these effects, tests were conducted with bullets

having conical and wedge-shaped noses. Test data are reported in Posters No. 4, 5, 7, and 9.

The curves on Poster No. 4 show that frictional effects become more significant relative to compressive pressure effects at the smaller cone angles. This observation is based on the predictions of the cone model, which is based on reactions to pressures alone, resulting in curves that tend to rise above the test data at small cone angles. The empirical reactions at relatively lower impact velocities are attributed to frictional heating of particles of explosive as they slide from the cone's apex to the cone's base.

Poster No. 6 summarizes the theoretical prediction that  $Q$  of the bullet material (where  $Q$  is the product of density times thermal conductivity times specific heat) is the significant parameter that affects the heat transferred to the explosive, expressed as  $E_p/E_f$  (explosive energy divided by frictional energy). This prediction is borne out by the data presented in Poster No. 7 showing low order reaction thresholds for H-6 impacted by bullets with a wide range of the quantity  $Q$ .

Additional data on cones and wedges are presented in Poster No. 9. It is apparent that much experimental and theoretical work remains to be done to quantify the roles of friction and shear when combined with pressure, during impacts by cones and wedges with various profiles and various thermal properties.

## CONCLUSIONS

Based on these preliminary correlations made with the severely limited amount of empirical data available, it may be concluded that the concept of explosive initiation depending on a constant value of the integral of  $(P-P_c)^2 dt$  for each explosive is promising but not yet validated on a firm quantitative basis. Much more empirical data will be required on a variety of explosives and propellants, using laboratory tests with a range of loading durations, particularly in the low pressure, long duration regime. At present, however, the use of the  $P^2 t$  vs.  $P$  plot to correlate data on explosive sensitivity appears to be a very

useful methodology for presentation of data and for prediction of reaction thresholds of full scale munitions.

## ACKNOWLEDGEMENTS

This document was prepared in connection with work supported by the Small Business Innovative Research (SBIR) program under contracts with the U.S. Navy, NAVSEA, and with the U.S. Air Force Armament Laboratory.

The author also wishes to express appreciation for very helpful suggestions by Dr. C. S. Coffey of the Naval Surface Warfare Center, White Oak Laboratory.

## REFERENCES

1. Stresau, R. H. and Kennedy, J. E., "Critical Conditions for Shock Initiation of Detonation in Real Systems," *Proceedings of the Sixth Symposium (International) on Detonation*, San Diego, CA, 24-27 Aug 1976, pp. 68-75.
2. Price, D. et al, *The NOL Large Scale Gap Test III*, NOLTR 74-40, NSWC, White Oak, MD, Mar 1974.
3. OSRD, *Effects of Impact and Explosion*, Summary Technical Report of Div. 2, NDRC, Vol. 1, Washington, DC, 1946.
4. Liddiard, T. P. Jr., "The Initiation of Burning in High Explosives by Shock Waves," *Proceedings of the Fourth Symposium (International) on Detonation*, U.S. Naval Ordnance Laboratory, White Oak, Silver Spring, MD, 12-15 Oct 1965, pp. 487-495.
5. Walker, W. A. and Sternberg, H. M., "The Chapman-Jouguet Isentrope and the Underwater Shockwave Performance of Pentolite," *Proceedings of the Fourth Symposium (International) on Detonation*, U.S. Naval Ordnance Laboratory, White Oak, Silver Spring, MD, 12-15 Oct 1965, pp. 27-38.
6. Devost, V. F., *Premature Simulator (Final Progress Report)*, NOLTR 74-178, NSWC, White Oak, MD, Oct 1974.

7. Timoshenko, S., *Theory of Elasticity*, First Edition, McGraw-Hill Book Co., Inc., New York, NY, 1934, pp. 389-395.
8. Kornhauser, M., "Engineering Methods of Calculating Munition Sensitivity to

Impact by Bullets and Fragments,"  
Phase I SBIR Report to NAVSEA, U.S.  
Navy, 15 Jul 1987.

# SENSITIVITY OF SEVERAL EXPLOSIVES TO IGNITION IN THE LAUNCH ENVIRONMENT

John Starckenberg, Doenec L. McFadden, Deborah L. Pilarski,  
Kelly J. Benjamin, Vincent M. Boyle, and Ona R. Lyman  
U. S. Army Ballistic Research Laboratory  
Aberdeen, Maryland 21005-5066

*We have recently completed testing of the sensitivity of several explosives to ignition by the combined effects of air compression and deformation. These are Composition B (Comp B), TNT, Composition A3 (Comp A3) Type II, LX-14, PBXW-113, PBX-0280, and PBX-0280/PE. Comp B exhibits one of the highest sensitivity levels and responds violently. The data for TNT provide no reason to believe that it is less sensitive to ignition than Comp B. Comp A3 Type II may be considered the least sensitive explosive tested. It exhibits a moderately high level of response violence. LX-14 exhibits a sensitivity intermediate between those of Comp B and Comp A-3 Type II and reacts very violently. PBXW-113, is by far the most sensitive in this test. It also produces the mildest response. The sensitivity of PBX-0280 is generally greater than that of Comp B. PBX-0280/PE, on the other hand, appears quite insensitive. Our results can be explained most satisfactorily in terms of each explosive's tendency to deconsolidate, or break up into small particles, during cavity collapse.*

## INTRODUCTION

Experimental studies aimed at clarifying the mechanisms involved in the premature ignition of high explosives in the launch environment have been pursued for a number of years at the Ballistic Research Laboratory (BRL).<sup>1-6</sup> This work was done using an apparatus referred to as the activator. Investigators at the Naval Surface Weapons Center have concentrated on simulating projectile geometries and developing statistical data in a large-scale drop-weight simulator.<sup>7-9</sup> This work has not been pursued recently due to the high cost, which severely limits the amount of data that can be collected, and to the fact that a sufficiently accurate representation of the launch environment has still not yet been obtained. Much of the early work has been summarized by Fishburn.<sup>10</sup> Our investigations have focused on ignition of explosives due to compression of occluded air, deformation of the explosive during the collapse of included cavities and a combination of these. Boyle and

his coworkers have also considered shear under pressure.<sup>11</sup>

Results obtained with the activator indicate that none of these mechanisms can ignite explosives at or near nominal launch pressures or pressurization rates. Rather, these parameters must be amplified by about an order of magnitude before ignition is observed. This is to be expected, as premature explosions are uncommon. We believe that when a premature explosion occurs the explosive is locally subjected to the same stimulus level generated in our experiments. In general, the explosive must be subject to a minimum heating rate per unit surface area if an ignition is to occur. In the case of air compression heating, the heating rate is roughly proportional to the product of the air pressurization rate and a representative cavity dimension while the surface area depends on how the cavity collapses. In the case of frictional or shear heating, the heating rate is roughly proportional to the product of the (pressure dependent) viscosity and the

square of the shear strain rate. In both cases, many other factors are also important. Pressurization rates and peak pressures measured external to projectile bases or inferred from acceleration histories and explosive column heights appear insufficient to produce the required stimulus. The maximum sliding velocity produced by projectile rotation is somewhat below that required for ignition observed in activator experiments which isolate frictional heating. Amplification of these stimulus levels may occur in a number of ways. In the case of air compression heating, one way is to amplify the pressurization rate. This can occur if a loose charge impacts the base, or if a cavity fails to collapse during the early portion of pressurization and then collapses very rapidly when a critical pressure has been reached. A cavity collapse geometry which concentrates heated air on a small portion of the explosive surface also amplifies the stimulus level. In addition, as a cavity collapses, shear heating may combine with air compression heating to produce an ignition.

The relationship between the local heating rate experienced by an explosive fill, the mechanical properties of the explosive, and the acceleration history of the projectile is complicated and has not been established. We have not pursued this avenue. Rather, we have tried to determine the parameters which govern ignition by the most likely mechanisms and to develop ignition threshold data for explosives including Comp B and TNT. Vietnam-era field experience has shown that Comp B exhibits a relatively high (usually unacceptable) incidence of in-bore premature explosions while TNT exhibits a relatively low incidence. We felt that the susceptibility of other explosives to premature ignition might be assessed by comparing their ignition thresholds to those of Comp B and TNT. However, the issue is complicated by the fact that the explosiveness of the burning response is also a factor. It has been speculated that the infrequency of reported prematures with TNT may be due to its relatively slow burning response rather than a lower ignitability. This would lead to the premature explosion occurring down range rather than in the gun tube. If this

is the case, the sensitivity assessment is more difficult as both ignitability and explosiveness must be considered.

We have recently completed testing of the sensitivity of a number of different explosives to ignition by the combined mechanisms and have used the results to assess their relative sensitivities. Results for Comp B were reported previously.<sup>4,6</sup> Additional explosives tested include TNT, Comp A3 Type II, LX-14, PBXW-113, PBX-0280, and PBX-0280/PE. In this paper we discuss the pertinent ignition mechanisms, describe the experimental approach, review some of the early activator results, compare the data obtained for all of the explosives, and provide an interpretation of the observations.

## IGNITION MECHANISMS

### Gas Compression

When a small volume of air is compressed very rapidly such that no energy transport can occur, a high temperature reservoir is created which may subsequently heat an adjacent explosive layer to the point of ignition. This process is referred to as ignition by adiabatic compression of the air. If, on the other hand, the air is compressed very slowly, no temperature increase occurs and no explosive ignition can follow. Between these limits lies the compressive heating regime in which the compression occurs sufficiently slowly that considerable energy is transported by conduction and convection during the process. The ignitions observed by Bowden and his associates in the 10- to 100-microsecond time range properly belong to this latter category.<sup>12</sup> For adiabatic compression in the shock wave regime, the heating due to gas compression does not appear to influence sensitivity since other heating mechanisms dominate.<sup>13-15</sup> Compressive heating has, therefore, received attention primarily as a source of ignition which is active when the observed time to ignition is in the 10-microsecond to 10-millisecond range, a time scale which is typical of events during the setback of the explosive fill in a projectile during launch.

## Shear

The shear mechanism has also received considerable attention. This mechanism is active when shearing flows are produced by cavity collapse or by motion relative to a surface such as the interior of the projectile casting. These flows tend to localize deformation in shear bands leading to the production of high local temperatures as discussed by Frey.<sup>16</sup> The action of friction under pressure (in the absence of air compression) has been considered by Boyle.<sup>11</sup> Our earlier results show that this mechanism is also active during cavity collapse, but that air compression is usually the dominant mechanism.<sup>4,6</sup>

## DESCRIPTION OF THE EXPERIMENTS

### The Activator

The experimental investigation was conducted using an apparatus, referred to as the activator, which was originally designed at Picatinny Arsenal for use as a laboratory-scale artillery setback simulator.<sup>17</sup> The activator, as presently used at BRL, is illustrated schematically in Figure 1. The test section consists of a 63.5-mm (2.5-inch) diameter mild steel, heavy confinement cylinder with a 12.7-mm (.5-inch) diameter bore hole enclosing the explosive sample and a hardened steel driving piston. A hardened steel gauge block on which a manganin foil pressure gauge is mounted is tightly bolted to the back of the confinement cylinder and the explosive sample is inserted into the bore adjacent to the gauge. A gap or cavity of some type is formed adjacent to or in the end of the sample. The gauge block rests against a rigid stop which incorporates an

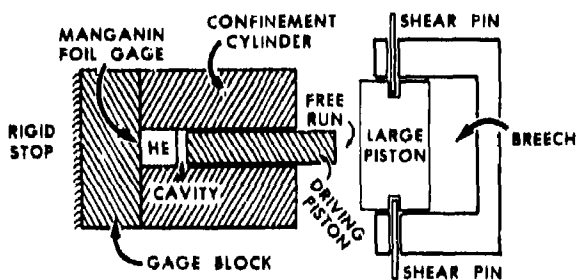


Figure 1. Activator Schematic

adjustment screw to accommodate test fixtures of different lengths and to allow easy installation. The driving piston is activated by a larger piston which is initially held in place using shear pins. The large piston is set in motion by pressure developed in the breech which is instrumented with a pressure transducer. The free run allowed between the large piston and the driving piston is used to set the stimulus level to be applied.

In order to conduct a test, the breech is pressurized using compressed air until the shear pins fail. The large piston accelerates through the free run and impacts the driving piston. The momentum developed by the pistons is transformed to an impulse delivered to the sample. This impulse is as much as 0.6 GPa in amplitude and approximately 0.5 ms in duration, producing an average pressurization rate as high as 2.5 GPa/ms. The pistons may then rebound and strike the explosive again delivering a second, smaller impulse. The breech pressure begins at the shear pin failure pressure and drops linearly with time during the test to a value associated with the final volume of the breech.

A disadvantage of this test configuration is that extrusion of explosive between the gauge block and the confinement cylinder may occur at the higher free runs because the loading action tends to increase the space there. Extrusion of explosive between the driving piston and confinement cylinder is avoided by maintaining tight tolerances on the clearance. Ignitions caused by extrusion are sometimes identifiable as late events on the pressure records. Extrusion ignition is an artifact of the experimental procedure which is not relevant to ignition in the launch environment. Generally, there exists a free run below which extrusion does not occur. Our experience indicates that testing with solid samples to determine this free run is advisable. Determination of ignition thresholds due to cavity collapse at lower stimulus levels is then possible. This procedure was followed for all the explosives we tested, except Comp B and TNT.

### Dimple Tests

The dimple test is the procedure currently in use. The experimental configuration is

shown schematically in Figure 2. In this test, a cylindrical cavity or "dimple" of controlled depth and diameter is cast or machined into one end of the explosive sample. The sample is inserted, dimple up, into the confinement cylinder. A thin polyethylene film attached to the face of the driving piston improves the seal against the face of the explosive sample. Both air compression and deformation heating mechanisms are active in the standard dimple test.

### Sample Preparation

Figure 3 shows Comp B samples before and after activator testing. Dimples begin at a nominal depth of 0.38 mm (.015 inch) and increase in steps of 0.38 mm to a maximum depth of 1.91 mm (.075 inch). The actual depths vary somewhat from the nominal values and must be measured. Dimple diameters of 6.4 mm

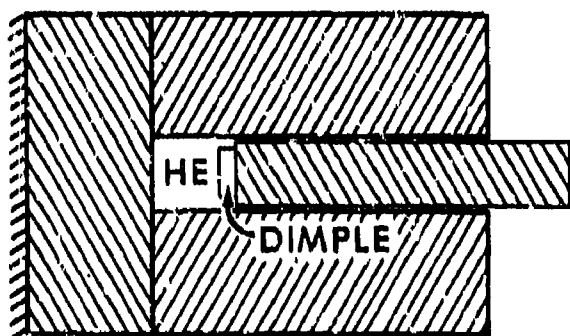


Figure 2. Dimple Test Schematic



Figure 3. Composition B Samples Before and After Activator Testing

(.25 inch) and 8.6 mm (.34 inch) were used in testing Comp B. Only 6.4-mm diameter dimples were used in testing of all the other explosives.

The Comp B and TNT samples were prepared at BRL by casting short 12.7-mm diameter cylinders. In order to prepare dimpled samples, a casting plate with cylindrical protrusions of adjustable height was used beneath the mold. For undimpled samples, a flat polished casting plate was used. All samples were finished to a length of 12.7 mm by cutting and polishing the opposite end.

The LX-14, Comp A3 Type II, and PBXW-115 samples were prepared by Honeywell, Inc. The PBX-0280 and PBX-0280/PE samples were prepared at Picatinny Arsenal. Dimples in these samples were produced by machining. Other details of their preparation are unknown.

Sample dimensions, including dimple depth and diameter, and sample weight were measured and the density of each sample was computed. All samples were inspected radiographically and any sample appearing to have internal voids was rejected.

The unclassified formulations and the average percentages of theoretical maximum density (TMD) of the explosive samples tested are summarized in Table 1.

Table 1. Summary of Explosive Formulations

	% TNT	% RDX	% HMX	% Estane	% Poly-Ethylene	Average % TMD
TNT	100	-	-	-	-	96.8
Comp B	40	60	-	-	-	97.9
Comp A3 Type II	-	91	-	-	8	98.4
LX-14	-	-	95	5	-	97.0
PBX-0280	-	95	-	5	-	96.8
PBX-0280/PE	-	95	-	-	5	96.5

### Characterization of the Stimulus Level

In our earlier tests with cavities external to the explosive, pressure conditions in the vicinity of the cavity could be inferred from the pressure records from the manganin gauge at

the base of the sample. This provided us with a pertinent characterization of the stimulus level. In the dimple test, however, the conditions as the cavity collapses are complicated and the heating rate bears no simple relation to the pressure record. The best measure of applied stimulus level must be judged, therefore, by the degree to which it segregates ignitions and ignition failures in a plot of stimulus level versus cavity size. Several measures of stimulus level are available. The most successful of these is the free run of the activator. The stimulus generally increases with increasing free run. Our previous results indicated that free run is the only parameter producing good data segregation in all three tests.<sup>4,6</sup> Thus, results of activator testing are usually given as an ignition threshold in the free run - dimple depth plane.

## OBSERVATIONS FROM PREVIOUS STUDIES

### Compressive Heating

Compressive heating ignition has been the subject of extensive analytical<sup>1,3</sup> and experimental<sup>2,3,5</sup> study at BRL. In this work, cavities external to the explosive in a soft material were used. The activator was used in its original form in preliminary experiments to produce data which revealed the role of air in causing ignitions during compression. Subsequently, the activator was modified and further instrumented so that more definitive data could be extracted from the tests and direct comparisons to the predictions obtained from analytical models could be made. In particular, the activator was used to explore ignition of Comp B, TNT, and LX-14 (as well as a number of other explosives) caused by the rapid compression of air trapped in contact with the explosive.

A number of observations from our study of air compression heating are pertinent to the present study. As a result of our earlier testing, we learned that this is indeed a viable mechanism for ignition at relatively mild stimulus levels and we established pressurization rate and cavity size as the principal governing parameters. We found that sensitivity is substantially influenced by

the geometry of cavity collapse and by the state of the explosive surface. Convergent geometries, such as hemispherical bubbles, which concentrate heated air on a small portion of the explosive surface, promote ignition. A series of tests with LX-14 pressed to different densities showed that nonporous surfaces also promote ignition by enhancing retention of heated air at the ignition site.

### Cavity Collapse Heating

In the earliest work, care was taken to completely decouple the local stimulus level from the explosive mechanical properties by using cavities external to the explosive which collapse without its mechanical failure. Subsequently, we turned our attention to a series of experiments in which shallow cylindrical cavities (dimples) in cast Comp B were subjected to deformation both with and without simultaneous air compression as well as air compression without deformation. This series of tests was used to explore the role of explosive deformation in ignition.<sup>4,6</sup> In particular, we were interested in determining whether deformation produces sufficient heating to cause ignition or simply acts to increase the local air pressurization rate. This approach, of course, does not account for the complete role of explosive mechanical properties in the actual launch environment.

We found that when the air compression and deformation heating mechanisms are combined the dominant ignition mechanism is compressive heating of air strongly influenced by the cavity collapse geometry and by alteration of the state of the exposed explosive surface during collapse. This result is in agreement with Frey's theoretical assessment,<sup>18</sup> which indicates that the air compression mechanism dominates for large cavities at low pressurization rates. Comp B seemed to exhibit a "maximum tolerable" dimple depth below which ignitions could not be obtained. The observations suggest that the cavity in the explosive may close in at least two different ways depending on dimple depth. Cavity closure for shallow dimples presumably occurs by axial flow and results in low sensitivity. The sudden transition above the maximum tolerable dimple depth observed in

the tests was interpreted as marking a transition to radial cavity closure, a highly sensitive mode for which dimple depth independence would be expected. Our compressive heating results indicated that increasing surface porosity leads to decreased sensitivity. One would expect the brittle explosives to break up into particles during cavity collapse, thus reducing sensitivity. The presence of particles can also be sensitizing if they are fine enough. This occurs when the nominal diameter of the particles is less than twice the thickness of the heated explosive layer. However, our planar computations showed that this heated-layer thickness is 25  $\mu\text{m}$  or less when ignition occurs.<sup>1</sup> Thus, the sensitizing effect should not be expected to appear unless a significant number of particles are 50  $\mu\text{m}$  or less in diameter. Results from tests conducted under vacuum indicate that heating due to deformation alone is the dominant ignition mechanism only for relatively deep dimples.

## RESULTS

### General Observations

The pressure histories observed may be generally categorized according to the nature of the rising portion of the impulse. When undimpled samples were used, the pressure was observed to rise in a series of steps. The pressurization rate between the plateaus was roughly the same. With dimpled explosives, however, the pressure was frequently observed to rise and fall quite markedly during pressurization. The pressure was usually seen to drop back, after a short pressurization, to a considerably lower pressure before continuing to rise to its maximum value. This occurred for both ignitions and ignition failures and is probably associated with cavity collapse. Samples that were recovered after firing almost always showed the dimple to be completely closed as shown in Figure 3.

Burning may begin during the rising portion of the pressure history, be delayed until after the pressure has peaked, be delayed until much later when the pressure has returned to ambient or occur on the second strike of the driving piston. Where possible, ignitions have been classified as either prompt

(when they occur during the stimulus impulse) or late (when they occur substantially after the stimulus impulse). In a few cases, when the pressure record was lost and an ignition clearly occurred, the result is identified simply as an ignition.

As described in the following sections, we believed that Comp B and TNT were sometimes igniting due to extrusion between the gauge block and the confinement cylinder. Because of this, we decided to screen the subsequently tested explosives using undimpled samples, which are assumed to be ignited only by extrusion.

The violence of reactive responses varied from explosive to explosive and ranged from partial reaction with recovery of significant amounts of explosive to extremely rapid reaction characterized by the splitting of the confinement cylinder into several pieces. These results have been associated with response levels in Table 2.

*Table 2. Response Violence Levels*

Level	Response Violence
1	Partial reaction. Partially burned explosive sample is recovered or unburned explosive is extruded past gauge block.
2	Complete reaction. Damage to confinement cylinder limited to enlargement of bore hole.
3	Complete reaction. Confinement cylinder split open.
4	Complete reaction. Confinement cylinder split into two or more pieces.

### Composition B

Results for Comp B with two different dimple diameters were previously reported.<sup>4,6</sup> The 8.6-mm diameter dimples are considered too large to eliminate substantial influence of the sample diameter. Therefore, testing of other explosives was limited to the 6.4-mm diameter dimples. The data for the smaller

diameter is reproduced in Figure 4. No tests on solid samples to determine the extrusion limit were conducted. However, late ignitions (of the type usually associated with extrusion) were observed with shallow dimples at free runs exceeding 22 mm. Two threshold curves have been indicated on the plot in the dimple depth - free run plane. Only ignitions were observed above the upper curve and only ignition failures were observed below the lower curve. A region of mixed results lies between the curves. The results indicate that extremely high stimulus levels are required to produce ignition with the shallowest dimples. The free run required drops rapidly with increased dimple depth until a minimum is reached. Surprisingly, further increase in the dimple depth appears to reduce sensitivity. This behavior allows us to roughly define a maximum tolerable dimple depth at about 0.5 mm, below which ignition requires very high stimulus levels, and a maximum tolerable stimulus level at about 10 mm free run, below which no ignitions occur. When Comp B ignited, the response was fairly violent, often splitting the cylinder. Several of the samples

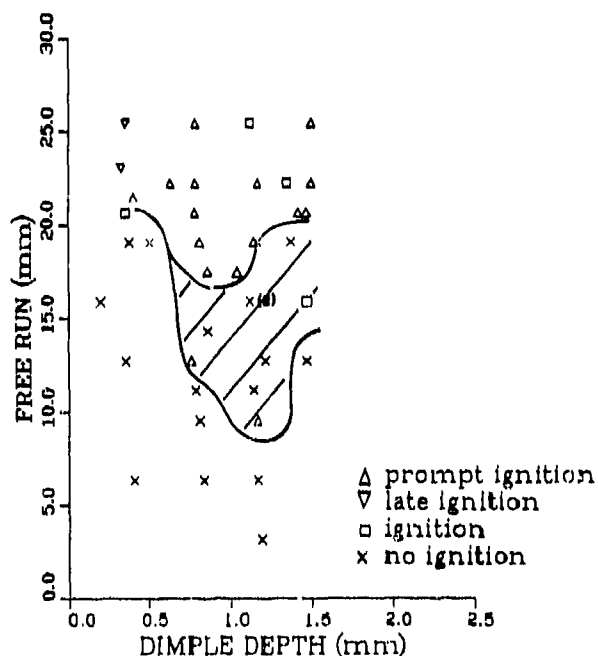


Figure 4. Ignition Threshold for Composition B in the Dimple Depth - Free Run Plane. Duplicate data points are indicated by (2).

which failed to ignite were recovered and sectioned. The cavities were observed to be filled with porous explosive which, for dimples deeper than about 0.4 mm, apparently originated in the shoulder of the dimple. In addition, cone-shaped regions of deformation were observed below the floors of the dimples. The shallowest dimples, on the other hand, were observed to close from the bottom up. This transition of cavity closure mode is believed to account for the rapid change of sensitivity observed as the dimple depth is reduced to its smallest values. There may be some other such transition which accounts for the decrease in sensitivity for the deepest dimples.

### TNT

We experienced considerable difficulty in obtaining definitive data for TNT and a broader variety of responses was observed. Virtually all ignitions occurred slightly after peak pressure had been reached. In several cases, reaction was extinguished leaving partially burned samples. In many cases in which incipient reaction was extinguished, burning was observed to begin at the circumference of the dimple. In other cases, at moderate free runs, the samples appeared to melt and extrude past the gauge block without any evidence of reaction. These responses are represented in the plot shown in Figure 5. It is difficult to distinguish ignition, failure, and mixed regions as with Comp B. Unfortunately, no rapid decrease in the free run required to produce ignition as dimple depth increased may be observed (probably because no tests were conducted with the shallowest dimples) so that no effective maximum tolerable dimple depth can be determined. However, no ignitions were produced at free runs less than about 12 mm. TNT is known to have a relatively low intrinsic reaction rate. The activator's stimulus duration may be too short to appropriately test such a slow burning explosive. The response violence was considerably lower with TNT and the confinement cylinders were not observed to split.

### Composition A3 Type II

Using undimpled Comp A3 Type II samples, we found that extrusion ignition

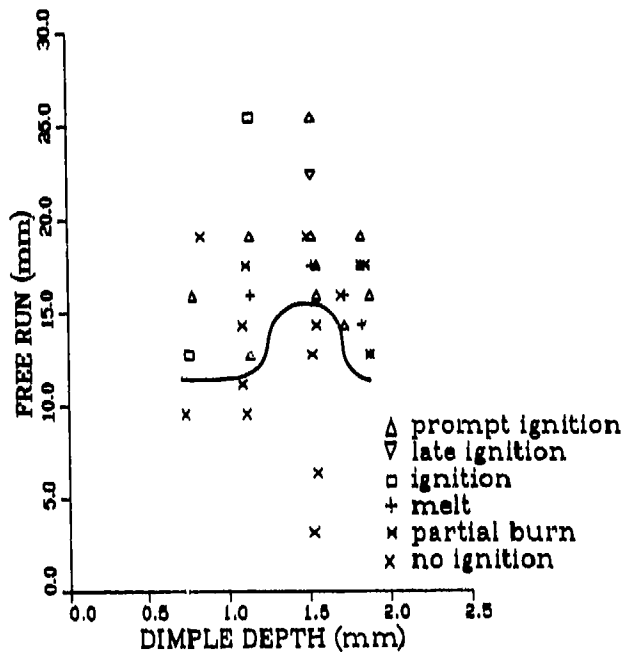


Figure 5. Ignition Threshold for TNT in the Dimple Depth - Free Run Plane

occurred at free runs greater than 20 mm. Fewer tests were conducted than with Comp B or TNT, but the ignitions and failures segregate nicely in the dimple depth - free run plane as shown in Figure 6. The maximum tolerable dimple depth is about 1.1 mm but no minimum in required stimulus level is realized. Response violence was greater than that of Comp B and the cylinder was usually split, sometimes into two pieces. In some cases, the shallowest dimples did not close, even at moderate free runs. This was not observed with any other explosive. Examination of recovered samples suggests a possible cavity collapse mode transition between dimple depths of 1.1 mm (corresponding to the maximum tolerable dimple depth) and 1.5 mm.

#### LX-14

Testing with undimpled LX-14 samples also indicated that free run should be limited to about 20 mm. Again, the number of tests were few but the data segregation is fairly good as shown in Figure 7. However, establishment of a more reliable threshold curve would require some additional data. The maximum

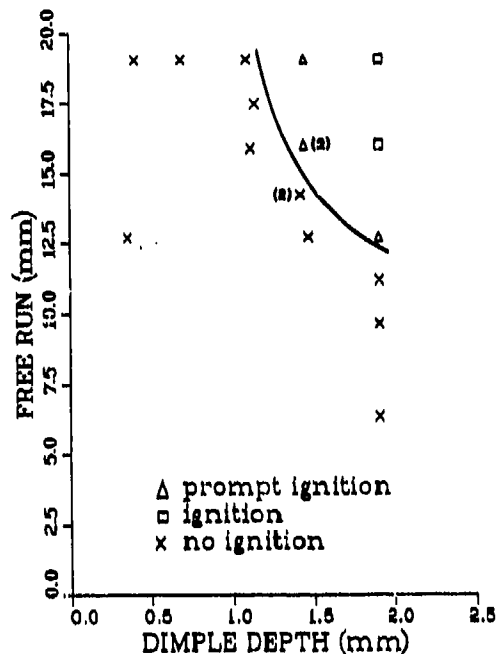


Figure 6. Ignition Threshold for Composition A-9 Type II in the Dimple Depth - Free Run Plane. Duplicate data points are indicated by (2).

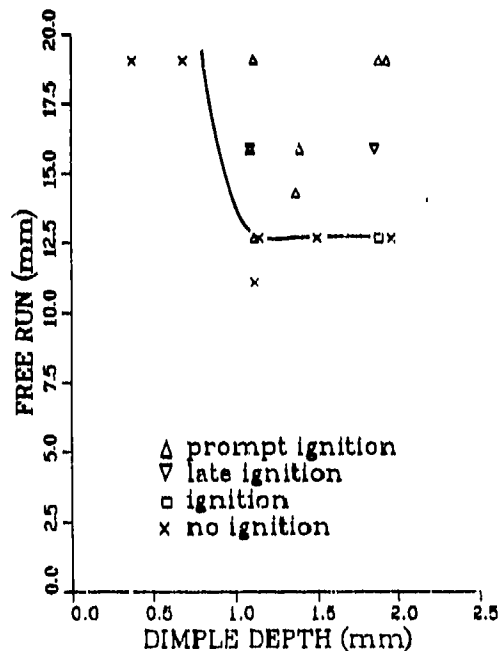


Figure 7. Ignition Threshold for LX-14 in the Dimple Depth - Free Run Plane

tolerable dimple depth is about 0.8 mm and the maximum tolerable free run is about 12 mm. The late ignitions observed occurred on the second strike of the driving piston as evidenced by the manganin gauge record. The reactive response following ignition was very violent. The confinement cylinder was often split into two or more pieces and the bolts holding the gauge block were sometimes broken. Recovered samples appear to show a transition from bottom-up to radial-inward closure above a depth of about 0.8 mm.

### PBXW-113

PBXW-113 is a soft rubbery explosive. We found that it responds considerably differently than the other explosives. When no dimples were present, the explosive exhibited an extrusion limit at about 19 mm of free run. However, when dimples of any size were present, testing always produced ignition, even at the shortest possible free run. With one exception, these ignitions occurred very late (often being audibly distinguishable from the stimulus impulse) and were very mild (varying amounts of explosive were usually found to remain). Explosive was often seen to have been sprayed out between the confinement cylinder and the gauge block and could be found in the bolt holes. The results do not lend themselves to the usual presentation in the dimple depth - free run plane. Rather, they are summarized in Table 3, which lists each test. The mild events observed may be a result of the activator's short pulse. The one burn that occurred during the high pressure portion of the pulse was quite violent, splitting the confinement cylinder. During gun launch, the pressure may be maintained for a longer time, allowing a more violent burn with this explosive. Since all dimpled samples ignited, the mode of cavity closure could not be assessed.

### PBX-0280

Five undimpled samples of PBX-0280 were tested in an attempt to determine the extrusion ignition limit. The results, however, were inconclusive. Delayed ignitions were observed in three tests at free runs of 19, 22, and 25 mm while ignition failures were observed in two tests at free runs of 22 and

Table 3. Summary of Results with PBXW-113

Dimple Depth (mm)	Free Run (mm)	Ignition?	Explosive Remaining
no dimple	12.7	no	all
no dimple	12.7	no	all
no dimple	15.9	no	all
no dimple	19.1	no	all
no dimple	19.1	late	most
no dimple	22.2	late	half
no dimple	22.2	late	most
no dimple	25.4	late	trace
no dimple	25.4	late	trace
0.38	3.2	late	trace
0.38	6.4	late	none
0.38	6.4	late	?
0.38	12.7	late	most
0.76	19.1	late	some
1.14	19.1	late	none
1.91	3.2	late	trace
1.91	9.5	late	?
1.91	12.7	late	?
1.91	19.1	prompt	none
1.91	19.1	late	?

25 mm. Dimple tests were then conducted on the remainder of the samples. The dimples in these samples appeared to be machined. Their edges were of only fair quality, showing considerable crumbling. The results of the tests are plotted in the free run - dimple depth plane in Figure 8. Only a few ignition failures (for shallow dimples or low stimulus levels) were observed. In the region of the plane where ignitions appear, considerable mixing of prompt and delayed ignitions were observed. Nonetheless, an ignition threshold can be reasonably well defined. Ignitions frequently resulted in split confinement cylinders. No observations of recovered samples were made.

### PBX-0280/PE

The five undimpled PBX-0280/PE samples were tested at free runs of 19, 22, and 25 mm. Two ignition failures were observed at 19 mm, one prompt ignition and one failure were observed at 22 mm, and one prompt ignition was observed at 25 mm. The machined dimples in these samples appeared to be of somewhat better quality than those in the

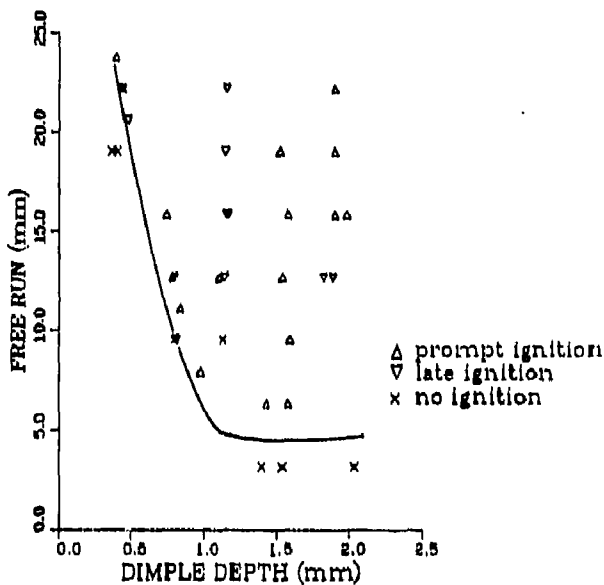


Figure 8. Ignition Threshold for PBX-0280 in the Dimple Depth - Free Run Plane

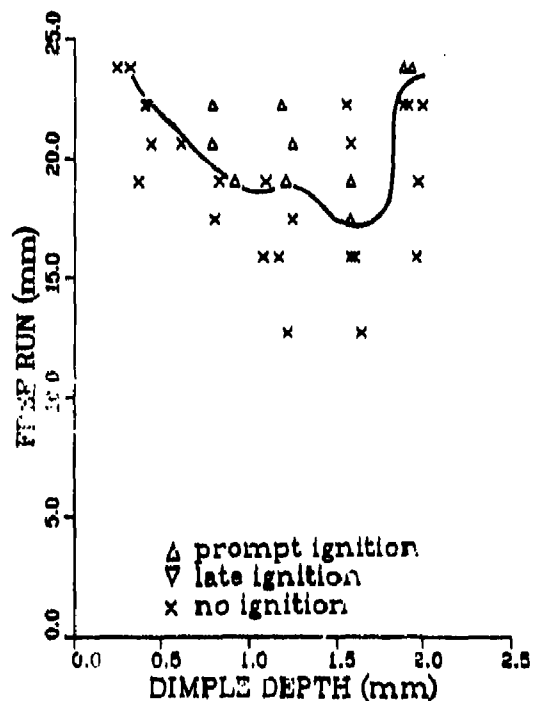


Figure 9. Ignition Threshold for PBX-0280/PE in the Dimple Depth - Free Run Plane

PBX-0280 samples. The results indicate that 19 mm of free run is a safe upper limit in the dimple tests. However, definition of an ignition threshold in the free run - dimple depth plane required tests at free runs in excess of this value as illustrated in Figure 9. Seven tests with dimples shallower than 0.7 mm produced only one delayed ignition at free runs varying between 19 and 25 mm. Only one test at a dimple depth of 1.5 mm yielded an ignition at a free run shorter than 19 mm. The results produce a relatively well-defined ignition threshold. The response of this explosive was a little less violent than that of PBX-0280, producing split cylinders less often. Again, no observations of recovered samples were made.

#### Comparison of Sensitivity and Response Violence

The threshold curves for all the explosives (except PBXW-113) are shown together in Figure 10. Many of the explosives exhibit decreasing sensitivity with the deepest dimples used. In most cases, two simple measures of sensitivity for each explosive may be extracted

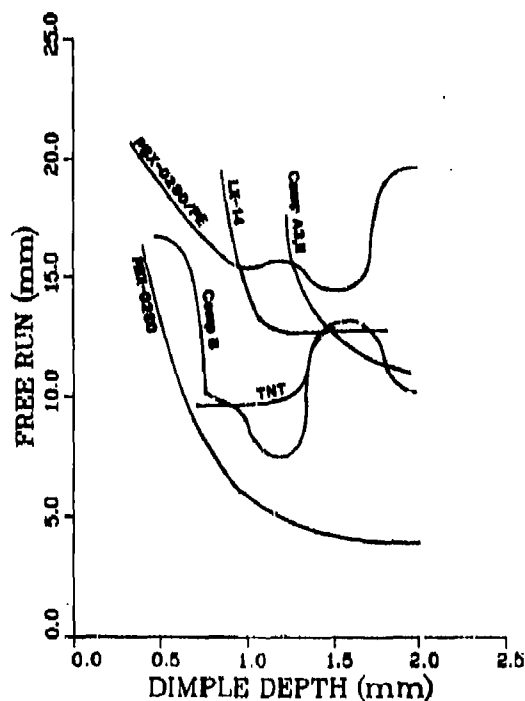


Figure 10. Comparison of Ignition Thresholds in the Dimple Depth - Free Run Plane

from the data: the maximum tolerable dimple depth (for which no ignition is produced at any free run) and the maximum tolerable free run (for which no ignition is produced at any dimple depth). Table 4 lists the explosives in order of increasing values of the maximum dimple depth tolerated. The reaction violence level is also shown in the table.

*Table 4. Relative Sensitivity of Explosives*

Explosive	Maximum Tolerable		Reaction Violence
	Free Run (mm)	Dimple Depth (mm)	
PBXW-113	0	0.0	1*
PBX-0280	7	0.5	3
Comp B	10	0.5	2,3
TNT	12	0.5?	1,2
PBX-0280/PE	17	0.5*-0.9	3,4
LX-14	12	1.0	4
Comp A3, II	12	1.4	3,4

\* delayed ignition ignored      \* violent reaction ignored

The results exhibit some tendency toward an increase in reaction violence with decreasing ignition sensitivity. PBXW-113 is by far the most sensitive in this test. It also produces the mildest response. Comp B exhibits one of the highest sensitivity levels among the brittle explosives and responds violently. Although the data for TNT do not permit definition of a complete ignition threshold, they provide no reason to believe that TNT is less sensitive to ignition than Comp B. This lends support to the interpretation that the higher frequency of premature explosions observed with Comp B filled rounds is due to its higher explosiveness. Comp A3 Type II may be considered the least sensitive explosive tested (based on maximum tolerable dimple depth). It exhibits a moderately high level of response violence. Its maximum tolerable dimple depth is considerably greater than that for Comp B but no decrease in sensitivity with deeper dimples is observed leading to an apparent crossover of the thresholds for deep cavities. LX-14 exhibits a sensitivity intermediate between those of Comp B and Comp A-3 Type II and reacts very violently. Its threshold also crosses over that of Comp A-3 Type II for deep dimples. The

sensitivity of PBX-0280 is generally greater than that of Comp B. It ignites at lower stimulus levels and tolerates roughly the same dimple depth as Comp B. PBX-0280/PE, on the other hand, appears quite insensitive in terms of the stimulus level tolerated. Although it was observed to ignite with relatively shallow dimples, this was at very high stimulus levels and may have been due to extrusion. The difference in sensitivity between these two explosives is remarkable since they both contain 85 percent RDX and were tested at almost exactly the same percentage of theoretical maximum density. The principal differences are the binder material and the particle size of the RDX used. The less sensitive explosive uses polyethylene as a binder and much coarser RDX.

Our results can be explained most satisfactorily in terms of each explosive's tendency to deconsolidate, or break up into small particles, during cavity collapse. Evidence of deconsolidation is apparent in samples which failed to ignite. Such breakup produces competing effects on the sensitivity to ignition. It desensitizes by presenting greater explosive surface area to a limited quantity of heated air. This is the same mechanism that accounts for the decreased sensitivity previously observed at low pressing density. At the same time, deconsolidation sensitizes by raising the explosive-air interface temperature for particles that are sufficiently small compared to the heated layer thickness. Only one of the explosives tested is made with a significant number of particles which are smaller than the 50  $\mu$ m size suggested by our earlier analysis.<sup>1,3</sup> Thus, in most cases, it appears that the desensitizing effect dominates. In addition, the increased surface area manifests itself in a more violent response when ignition does occur. The results are, of course, influenced by each explosive's intrinsic sensitivity to pure thermal stimulus and the amount of energy released in decomposition.

The mechanical properties of PBXW-113 render it the most resistant to deconsolidation and it shows the greatest sensitivity and the lowest reaction violence. TNT might be expected to break up less readily than the other brittle explosives because it is a single

phase cast material. It exhibits a relatively high ignition sensitivity and is the second lowest in reaction violence. Comp B, as a multiphase cast explosive, is somewhat higher in reaction violence and has about the same sensitivity as TNT. Here, the slower energy release of TNT is also a factor. The remaining explosives are multiphase pressed materials and (with the exception of PBX-0280) exhibit lower sensitivities and higher reaction violence levels. The order of sensitivity of PBX-0280 and PBX-0280/PE are not consistent with the dominance of the desensitizing effect. However, the more sensitive PBX-0280 contains class 5 RDX (virtually all particles less than 50  $\mu\text{m}$ ) and class 7 RDX. It can be expected to produce a significant quantity of very small particles upon deconsolidation. This might explain its high sensitivity. The binder difference could also have some effect on sensitivity by influencing the explosive's mechanical properties and, in turn, the degree of deconsolidation and the mode of cavity collapse.

## CONCLUSIONS

The path toward more premature-resistant explosives is not clear. Velicky, Voigt, and Voreck<sup>19</sup> have suggested that an explosive's mechanical strength should be increased to reduce the probability of collapse of casting flaws. However, it seems likely that this will have little effect on cavities large enough to present a problem since the launch acceleration environment appears to produce stresses well above those required to collapse larger cavities. Because of the importance of the gas pressurization rate, increasing mechanical strength might even have a negative effect. Delaying cavity collapse until higher stress levels have been reached could increase the pressurization rate. Cavities in a softened material, meanwhile, might collapse during the very early portion of launch, thus resisting ignition. On the other hand, they might better trap hot air, thus promoting ignition. In the latter case, the low ignited surface area can be expected to yield low initial reaction rates which may sufficiently delay any violent response. Approaches which reduce the incidence of flaws in explosive fills, reduce the ignitability of the explosive or

retard the burning response of the explosive are, of course, desirable. Because of the complexity of the issues involved, characterization of explosives through testing is the only available approach to discovering premature resistant formulations. Long term field experience is the only reliable measure of success.

Our observations indicate that field experience cannot be correlated with the results of ignition sensitivity tests. Thus, both ignitability and explosiveness should be considered in assessing an explosive's resistance to launch-induced explosion. In the controversy between brittle and soft explosives, our ignition sensitivity results are biased in favor of the brittle materials. For this reason, we do not believe that explosives should be rejected on the basis of exhibiting high ignition sensitivity in the activator unless the reaction violence levels are also high. The activator may be limited in its ability to appropriately measure explosiveness since it generates a considerably shorter pulse than that produced in the launch environment. This could inhibit violent reaction for explosives which do not burn rapidly either because insufficient surface area is produced during cavity collapse or because of relatively slow chemical kinetics. Clearly, our approach tells only part of the story since the applied stimulus level in the activator is partially independent of explosive mechanical properties and the testing may not reflect all the ways in which the mechanical properties influence the stimulus amplification mechanism. In spite of all this, the activator, when used with care, remains the best available tool for assessing an explosive's resistance to launch-induced premature explosions.

## REFERENCES

1. Starckenberg, J., "Analytical Models for the Compressive Heating Ignition of High Explosives," Ballistic Research Laboratory Technical Report ARBRL-TR-02225, Mar 1980.
2. Taylor, B. C.; Starckenberg, J.; and Ervin, L. H., "An Experimental Investigation of Composition-B Ignition under Artillery Setback Conditions," Ballistic Research Laboratory Technical Report ARBRL-TR-02276, Dec 1980.

3. Starkenberg, J., "Ignition of Solid High Explosives by the Rapid Compression of an Adjacent Gas Layer," *Seventh Symposium (International) on Detonation*, Jun 1981, pp. 3-16.
4. Starkenberg, J.; McFadden, D. L.; and Lyman, O. R., "Cavity Collapse Ignition of Composition B in the Launch Environment," *Eighth Symposium (International) on Detonation*, Jul 1985.
5. Starkenberg, J.; Ervin, L. H.; and McFadden, D. L., "Air Compression Heating Ignition of High Explosives in the Launch Environment," Ballistic Research Laboratory Technical Report BRL-TR-2709, Feb 1986.
6. Starkenberg, J.; McFadden, D. L.; and Lyman, O. R., "Cavity Collapse Ignition of Composition B in the Launch Environment," Ballistic Research Laboratory Technical Report BRL-TR-2714, Feb 1986.
7. DeVost, V. F., "Premature Simulator (Final Progress Report)," Naval Ordnance Laboratory Technical Report 74-178, Oct 1978.
8. Meyers, T. F. and Hershkowitz, J., "The Effect of Base Gaps on Setback-Shock Sensitivities of Cast Composition B and TNT as Determined by the NSWC Setback-Shock Simulator," *Seventh Symposium (International) on Detonation*, Jun 1981.
9. Soper, W. O., "The NSWC Setback Simulator: Stress Environment for Explosive," Naval Surface Weapons Center Technical Report TR-84-65, Apr 1984.
10. Fishburn, B. D., "Ignition of Explosive Fills by Setback Acceleration Forces During Launch," U.S. Army Armament Research and Development Center Technical Report ARLCD-TR-85010, May 1985.
11. Boyle, V.; Pillarski, D. L.; and Blake, O. H., "Combined Pressure-Shear Ignition Sensitivity Test," Ballistic Research Laboratory Technical Report BRL-TR-2927, Jul 1988.
12. Bowden, F. P. and Yoffe, A. D., *Initiation and Growth of Explosion in Liquids and Solids*, Cambridge University Press, 1952.
13. Chick, M. C., "The Effect of Interstitial Gas on the Shock Sensitivity of Low Density Explosive Compacts," *Fourth Symposium (International) on Detonation*, 1965, pp. 349-358.
14. Koldunov, S. A.; Shvedov, K. K.; and Dremin, A. N., "Decomposition of Porous Explosives under the Effect of Shock Waves," *Combustion, Explosion and Shock Waves*, Vol. 9, 1973, pp. 255-262.
15. Anderson, W. H. and Gillespie, F. L., "Surface Ignition of Explosives and Propellants by a Hot, Stagnant Gas Pocket," *Combustion Science and Technology*, Vol. 24, 1980, pp. 34-42.
16. Frey, R. B., "The Initiation of Explosive Charges by Rapid Shear," *Seventh Symposium (International) on Detonation*, Jun 1981, pp. 36-42.
17. Schimmel, R. T., "Setback Sensitivity of Composition B Under Conditions Simulating Base Separation in Artillery Projectiles," Picatinny Arsenal Technical Report 3857, 1969.
18. Frey, R. B., "Cavity Collapse in Energetic Materials," *Eighth Symposium (International) on Detonation*, Jul 1985.
19. Velicky, R. W.; Voigt, H. W.; and Voreck, W. E., "The Effect of Some Additives on the Closed Bomb Burning and Ignitability of RDX/TNT (60/40)," *Journal of Energetic Materials*, Vol. 3, Jun 1985, pp 129-148.

# SENSITIVITY OF SEVERAL EXPLOSIVES TO IGNITION IN THE LAUNCH ENVIRONMENT

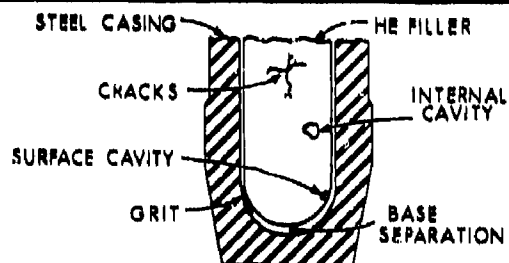
STARKENBERG

THE CONSEQUENCES OF IN-BORE EXPLOSIONS OF HE-FILLED PROJECTILES ARE UNDESIRABLE



## PROPOSED IGNITION MECHANISMS INCLUDE :

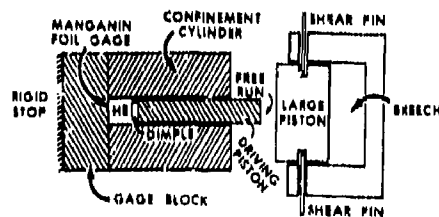
- HEATING DUE TO COMPRESSION OF OCCLUDED AIR
- EXPLOSIVE DEFORMATION DURING CAVITY COLLAPSE
- FRICTIONAL HEATING OF EXPLOSIVE AT CASING INTERFACE
- COMBINATIONS OF THE ABOVE



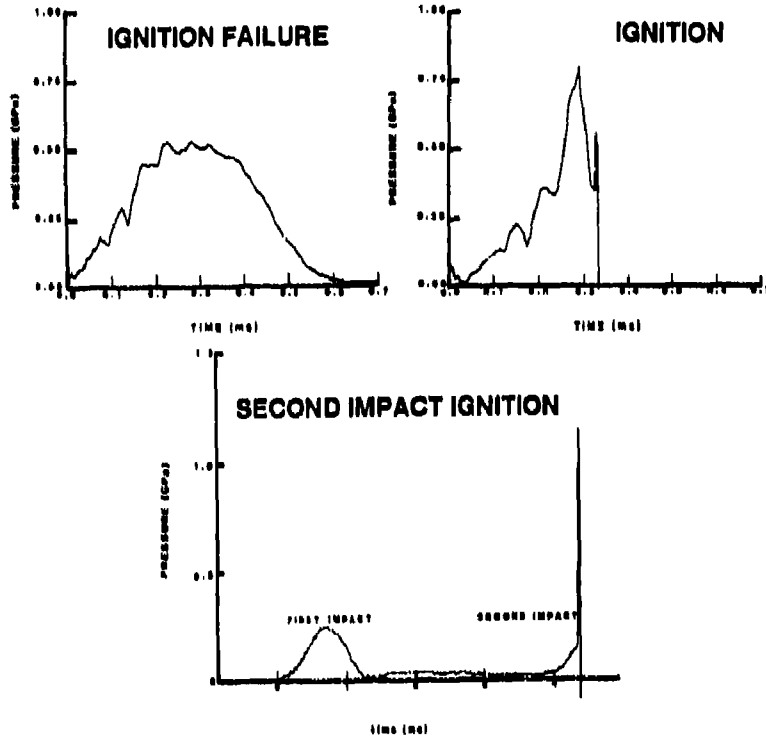
## PREVIOUS STUDIES INDICATE :

- AIR COMPRESSION IN COMBINATION WITH DEFORMATION HEATING IS A LIKELY IGNITION SOURCE
- STIMULUS LEVELS SIGNIFICANTLY HIGHER THAN ASSOCIATED WITH THE NOMINAL LAUNCH ENVIRONMENT ARE REQUIRED TO PRODUCE IGNITION
- POROUS EXPLOSIVE SURFACES REDUCE SENSITIVITY TO IGNITION BY THESE MECHANISMS

## THE ACTIVATOR



## TYPICAL MANGANIN GAUGE RECORDS



## EXPLOSIVE SAMPLES



COMPOSITION B SAMPLES  
BEFORE AND AFTER

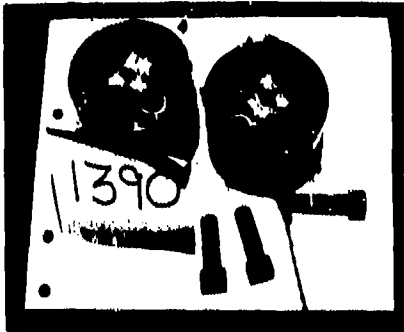
## FORMULATIONS OF EXPLOSIVES TESTED

	% TNT	% RDX	% HMX	% ESTANE	% POLY- ETHYLENE	AVERAGE % TMD
TNT	100					96.6
Composition B	40	60				97.9
Composition A3 Type II		91			9	98.4
LX-14			95	5		97.0
PBX-0280		95		5		96.8
PBX-0280/PE		95			5	96.5
PBXW-113						

## RESPONSE VIOLENCE LEVELS

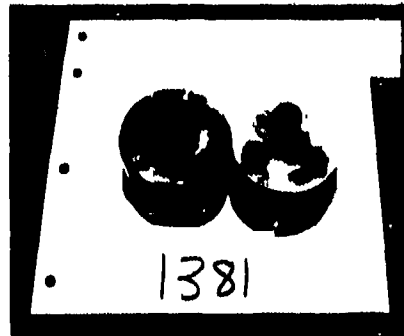
### LEVEL 1 RESPONSE

Partial reaction. Partially burned explosive sample is recovered or unburned explosive is extruded past gauge block.



### LEVEL 2 RESPONSE

Complete reaction. Minimal damage to confinement cylinder.



### LEVEL 3 RESPONSE

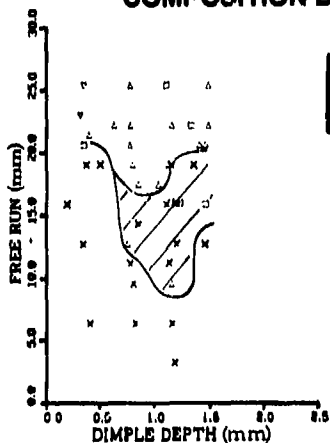
Complete reaction. Confinement cylinder split open

### LEVEL 4 RESPONSE

Complete reaction. Confinement cylinder split into two or more pieces.

**IGNITION THRESHOLDS**

**COMPOSITION B**

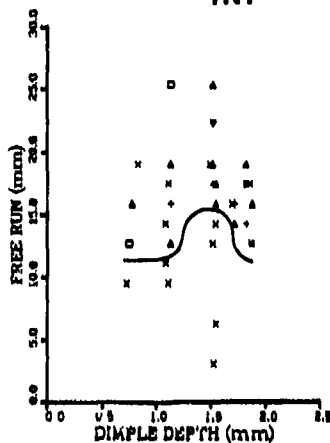


- △ prompt ignition
- ▽ late ignition
- ignition
- × no ignition



**COMP B IS VERY SENSITIVE AND REACTS VIOLENTLY**

**TNT**

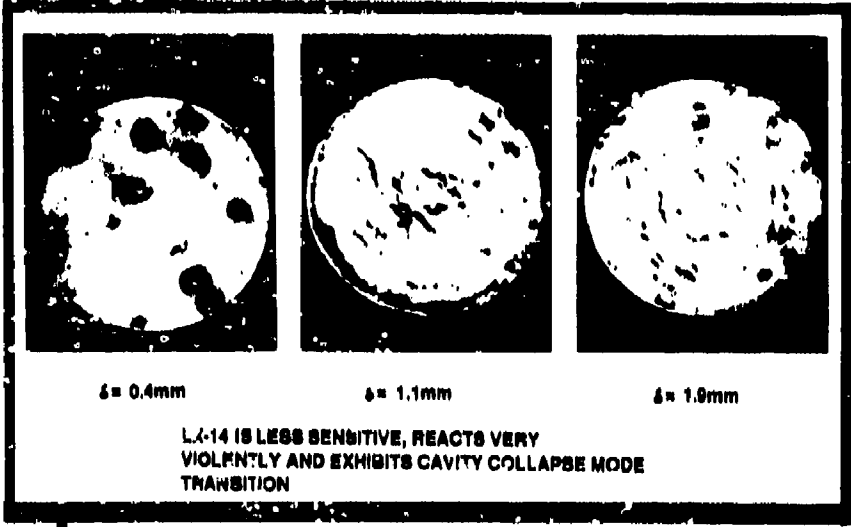
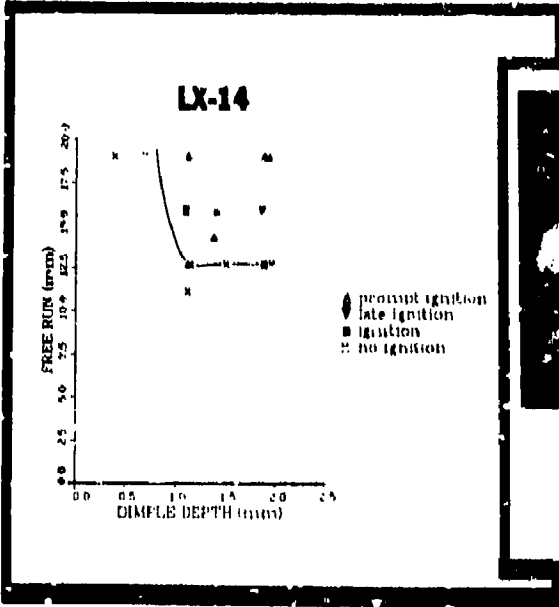
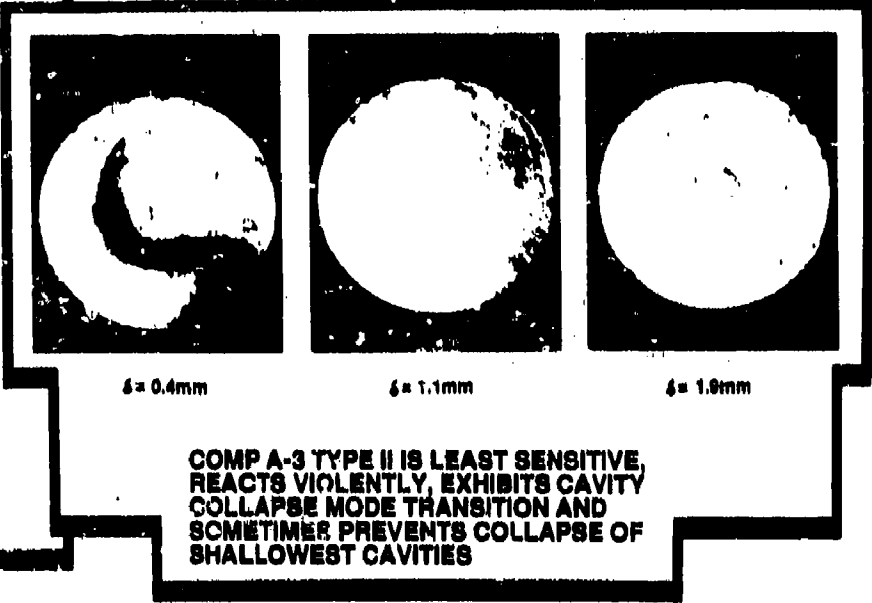
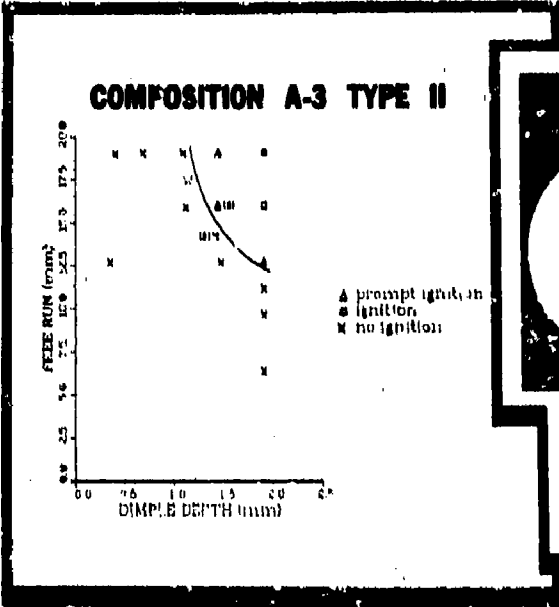


- △ prompt ignition
- ▽ late ignition
- ignition
- + melt
- × partial burn
- × no ignition

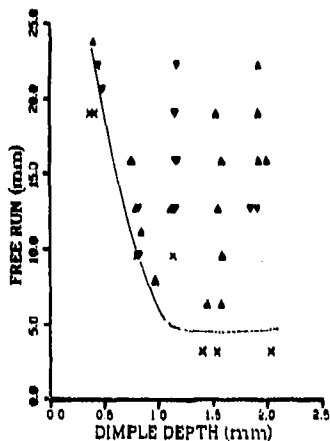


**TNT EXHIBITS PARTIAL REACTIONS AND DOES NOT APPEAR LESS SENSITIVE THAN COMP B**

# IGNITION THRESHOLDS



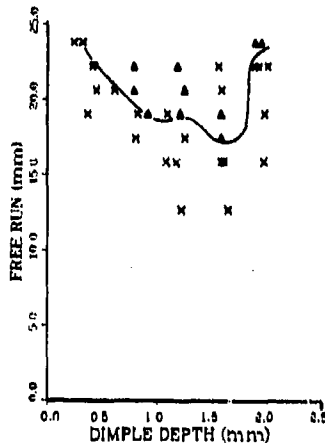
**PBX-0280**



▲ prompt ignition  
▼ late ignition  
x no ignition

**PBX-0280 CONTAINS FINE  
(CLASSES 5 & 7) RDX  
WITH ECOTANE BINDER**

**PBX-0280/PE**



▲ prompt ignition  
▼ late ignition  
x no ignition

**PBX-0280/PE CONTAINS  
COARSE (CLASS 1) RDX  
WITH POLYETHYLENE BINDER**

**PBX-0280 IS SIGNIFICANTLY MORE SENSITIVE THAN  
PBX-0280/PE ALTHOUGH EACH CONTAINS 95 PERCENT RDX**

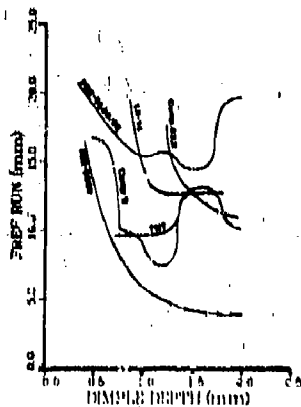
**PBXW-113**

**SUMMARY OF RESULTS WITH PBXW-113**

DIMPLE DEPTH (mm)	FREE RUN (mm)	IGNITION ?	EXPLOSIVE REMAINING
no dimple	12.7	no	all
no dimple	12.7	no	all
no dimple	15.9	no	all
no dimple	19.1	no	all
no dimple	19.1	late	most
no dimple	22.2	late	half
no dimple	22.2	late	most
no dimple	25.4	late	trace
no dimple	25.4	late	trace
0.38	3.2	late	trace
0.38	6.4	late	none
0.38	6.4	late	?
0.38	12.7	late	most
0.76	19.1	late	some
1.14	10.1	late	none
1.91	3.2	late	trace
1.91	9.5	late	?
1.91	12.7	late	?
1.91	19.1	PROMPT	NONE & LEVEL 4 RESPONSE
1.91	19.1	late	?

**PBXW-113 IGNITES WITH ANY  
CAVITY AT ANY FREE RUN BUT  
YIELDS MILDEST RESPONSE**





**MAXIMUM TOLERABLE**

EXPLOSIVE	FREE RUN (mm)	DIMPLE DEPTH (mm)	REACTION VIOLENCE
PBXW-113	0	0.0	1 <sup>†</sup>
Comp B	10	0.6	2,3
TNT	12	0.5 <sup>†</sup>	1,2
PBX-0280	7	0.5	3
PBX-0280/PE	17	0.5 <sup>†</sup> -0.8	3,4
LX-14	12	1.0	4
Comp A3, II	12	1.4	3,4

\* delayed ignition ignored  
<sup>†</sup> violent reaction ignored

**RESULTS CAN BE EXPLAINED IN TERMS OF EACH EXPLOSIVE'S TENDENCY TO DECONSOLIDATE OR BREAK UP INTO FINE PARTICLES DURING CAVITY COLLAPSE.**

**DECONSOLIDATION UNDER LOADING. . . .**

**DESENSITIZES BY PRESENTING GREATER EXPLOSIVE SURFACE AREA TO A LIMITED QUANTITY OF HEATED AIR**

**SENSITIZES BY RAISING THE EXPLOSIVE-AIR INTERFACE TEMPERATURE FOR SUFFICIENTLY SMALL PARTICLES (< 50 μm)**

**INCREASES THE REACTION VIOLENCE BY INCREASING SURFACE AREA**

**THE DESENSITIZING EFFECT APPEARS TO DOMINATE EXCEPT FOR PBX-0280 WHICH CONTAINS VERY FINE RDX**

# STUDY OF EXPLOSIVE SHELL FILLINGS WITH DEFECTS IN SIMULATED GUN LAUNCH CONDITIONS

C. Bélanger  
Defence Research Establishment  
Valcartier, Québec, CANADA

*Experiments were carried out using the DREV Setback Simulator to study defects which can be found in shell fillings as a cause of premature explosion during gun launch. The testing parameters studied were base separations and surface cavities for the 105-mm M1 shell at different accelerations. The stimulus of an adiabatic compression of air from a base separation of 0.50 mm caused consecutive reactions in CX-84A, and also in TNT and Composition B, but under specific conditions. However, the effect of explosive shear and deformation from a surface cavity was found to be a severe stimulus for CX-84A and for TNT-based explosives when a high deformation rate was tested.*

## INTRODUCTION

The conditions under which the launch of a shell from a gun results in a premature initiation of its explosive charge (hereafter referred to simply as "a premature") are not yet well understood. Although the frequency of their occurrence is fairly low, these reactions are known to result in catastrophic consequences and their numbers could increase with the development of more powerful launching systems. These undesirable initiations have been the object of many investigations conducted in several countries. However, additional studies are required to identify which among the launch parameters have a dominant effect on the explosive fillings under setback conditions.

For economical and practical reasons, it would be difficult to conduct experiments leading to prematures in the guns themselves. An alternative is to simulate the setback stresses applied to the explosive filling during gun launch. A setback simulator was designed at the Defence Research Establishment of Valcartier (DREV) for reproducing most setback conditions during gun launch for specific shells, with different explosive fillings and acceleration levels, and with their corresponding setback durations. The effects of

most filling defects which can be found in shells have been studied as causes of premature initiation. The stimuli present for each of these defects were assessed separately in order to evaluate their relative sensitizing effect on explosive fillings.

## EXPERIMENTS

The experimental method is described briefly in this paper. A more complete description of the DREV Setback Simulator was reported previously in Reference 1. This apparatus, shown schematically in Figure 1, was designed to reproduce as realistically as possible most of the conditions present in shell fillings during gun launch. Its design originated from the theoretical study in Reference 2.

Realistic simulations are based on two major characteristics of this apparatus. First, the setback stresses are applied on a representative explosive specimen by a piston with a mass-to-area ratio identical to that of the shell explosive filling considered. Second, the desired launch conditions are reproduced by using a square wave force with selected intensity and duration. The duration considered is the time when the acceleration of the selected shell in a gun is higher than 50 percent of its

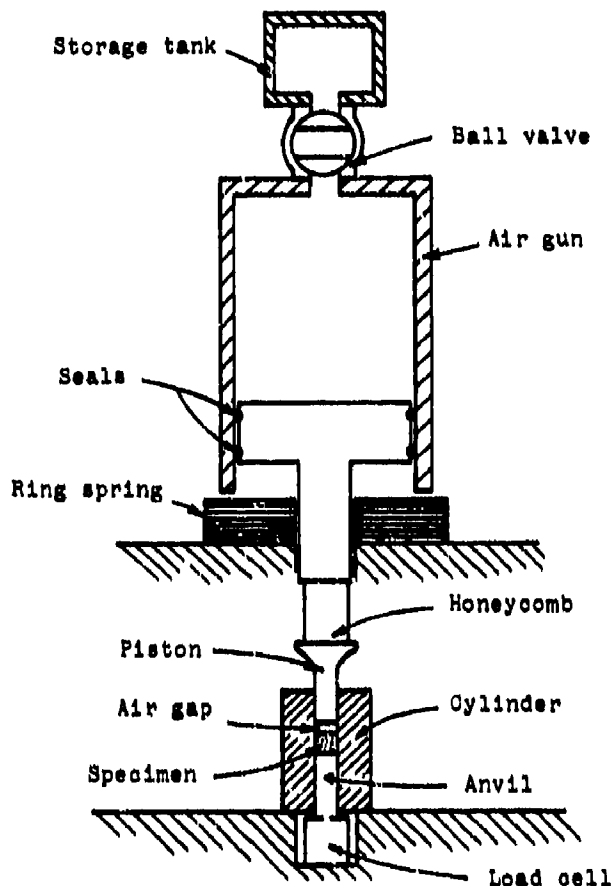


Figure 1. Schema of the DREV Setback Simulator

maximum value. Thus, the piston applies stresses reproducing the specific setback conditions desired to a specimen. The explosive specimen, with a diameter of 25.40 mm and 25.40 mm in length, is precisely located in a rigid steel cylinder between the piston and an anvil, as shown in Figure 2.

The square wave force is obtained by crushing a piece of honeycomb made of corrugated aluminum. This crushing gives a constant force over a major portion of its initial height. The honeycomb is crushed by a 75-kg hammer driven as a projectile in an air gun. The hammer velocity was always greater than that acquired by the piston during the test. A system of ring springs stops the hammer when the test is complete in order to prevent the crushing of the honeycomb beyond the point of constant crushing force. The ring spring was

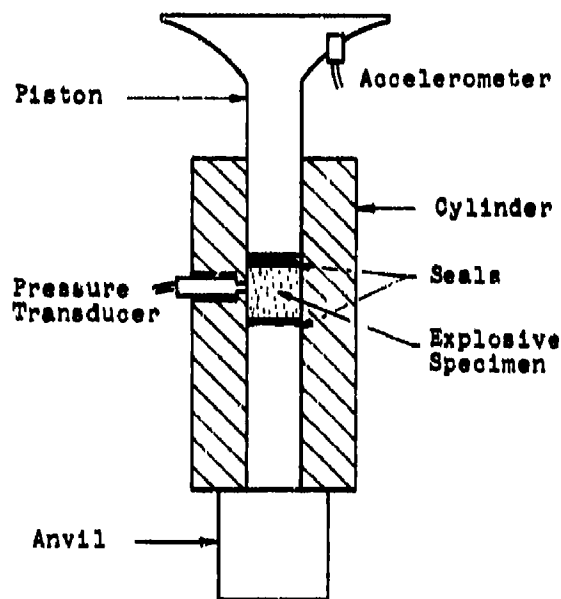


Figure 2. Enlarged View of the Specimen Mounting

designed such that the friction between the rings eliminates any significant recoil of the hammer.

The instrumentation of the simulator monitors the testing conditions. A load cell records the force applied to the specimen in addition to the reaction peak, if any, including its delay. The velocity of the hammer is also measured for each test and occasionally the acceleration of the piston and the pressure applied to the specimen are measured using transducers. All signals are collected and processed by a microcomputer through transient waveform recorders.

Experiments have been carried out to study the effect of base separations, surface cavities (explosive/steel interface), internal cavities, and different TNT crystallizations. From these defects, the adiabatic compression of air, shear and deformation of the explosive, and friction at explosive/steel interface were studied either together or as a single stimulus. These parameters were tested for a 105-mm M1 shell accelerated at 20,000 and 25,000  $g_n$ . The explosives tested were cast TNT and Composition B Grade A (RDX/TNT/WAX-59.5/39.5/1) with densities of  $1.56 \pm .005$  and  $1.68 \pm .005 \text{ Mg/m}^3$  respectively, Composition A-3

pressed at  $1.59 \pm .005 \text{ Mg/m}^3$  and CX-84A, a cast-cured plastic bonded explosive (PBX) developed at DREV.<sup>3</sup> CX-84A consists of 84 percent RDX and 16 percent HTPB binder and has a density of  $1.55 \pm .003 \text{ Mg/m}^3$ . Tetryl, pressed at  $1.66 \pm .005 \text{ Mg/m}^3$ , was also tested for comparison.

The tests reported here were carried out under conditions where any motion of the explosive filling inside the shell occurred at or very close to the maximum acceleration specified. Also, the filling defects mentioned were assumed to be at the base of the 105-mm M1 shell. In general, five tests were carried out under each condition except when three consecutive reactions were obtained.

## RESULTS AND DISCUSSIONS

### Base Separations

Air gaps of 2.50, 1.50, 1.00, 0.50, 0.33, and 0.19 mm thick were tested to simulate base separations. Table 1 shows the results obtained for the effect of the adiabatic compression of air under the setback conditions mentioned. Those with gaps larger than 0.50 mm are not included because reactions were always obtained for all explosives tested, even at 20,000  $g_n$ .

Composition A-3 was the least sensitive to adiabatic compression. In increasing order of sensitivity, Composition A-3 was followed by TNT, Composition B, tetryl, and CX-84A. As shown, tetryl and CX-84A resulted in at least one reaction with the separation of 0.33 mm, but none were obtained with the 0.19-mm gap. An effect of base separations for TNT and Composition B shell fillings was studied by Myers and Hershkowitz.<sup>4</sup> Although the number of experiments is limited for TNT and the density is not specified, the results suggest that the sensitivity of TNT is lower than that of Composition B, as in the present study.

The effect of the adiabatic compression of air was also studied for TNT with large crystals. TNT castings with larger crystals, corresponding to a density of  $1.54 \pm 0.005 \text{ Mg/m}^3$ , were found to be more sensitive to the effect of a base separation of 0.50 mm than TNT with finer crystals, and significantly more sensitive

than Composition B or even tetryl. The effect of crystallization on sensitivity to adiabatic compression of air is of interest and will be the object of future studies.

The effect of the adiabatic compression of a base separation of 0.50 mm was studied with a small hemispherical cavity of 1.50-mm diameter adjacent to the air gap. As shown in Table 2, the sensitivity of Composition B was appreciably increased by the addition of this small cavity, whereas that of Composition A-3 was slightly increased and that of TNT remained unchanged. Except where specified otherwise TNT refers to normal crystallization. An explanation for the difference in the results when that small cavity was added is probably that the cavity concentrated or focused the energy available, and not because of the additional air volume which is less than one percent of that of the air gap tested. Thus, for launch at 20,000  $g_n$ , the adiabatic compression of a base separation of 0.50 mm, when a small surface cavity is adjacent, can be the cause of premature for a shell filled with Composition B, but not for those filled with TNT.

These results simulating the launch at 20,000  $g_n$  of a 105-mm M1 shell with base separations indicate that a separation of 0.50 mm can be the cause of premature of CX-84A, TNT with large crystals, and Composition B, particularly when a small cavity is adjacent. By comparison, when loaded with Composition A-3, shell premature could be obtained at accelerations of 25,000  $g_n$  if a small surface cavity is adjacent to the 0.50-mm base separation.

### Surface Cavities

Cavities at the surface of the explosive, i.e., at the explosive/steel interface in a shell, were studied. These cavities of fairly large volume were cylindrical with a diameter of 8.0 mm and a length of 5.0 mm and hemispherical with a diameter of 7.0 mm. The stimuli assessed when testing these cavities were the adiabatic compression of air combined with the shear and deformation of the explosive. The individual effect of shear and deformation of the explosive material was studied by conducting tests under vacuum.

**Table 1. Results of Tests Simulating the Launch of 105-mm Shell With Base Separation**

Explosive	Separation (mm)	Acceleration (g <sub>n</sub> )	Reactions	
			Frequency	Type
Comp A-3	0.50	25,000	1/20	E
	0.33	25,000	0/5	N
	0.50	20,000	0/5	N
TNT	0.50	25,000	1/5 (3/3)*	PP
	0.33	25,000	0/5 (0/5)*	N
	0.50	20,000	1/5 (4/5)*	PP
Comp B	0.50	25,000	3/5	E
	0.33	25,000	0/5	N
	0.50	20,000	0/5	N
Tetryl	0.50	25,000	3/5	PP
	0.33	25,000	1/5	PP
	0.19	25,000	0/5	N
	0.50	20,000	1/5	PP
	0.33	20,000	0/5	N
	0.19	20,000	0/5	N
CX-84A	0.50	25,000	5/5	P
	0.33	25,000	1/5	P
	0.19	25,000	0/5	N
	0.50	20,000	5/5	P
	0.33	20,000	1/5	P
	0.19	20,000	0/5	N

\* TNT: with large crystals  
 P: light partial reaction      E: explosion  
 PP: heavy partial reaction    N: no reaction

**Table 2. Results of Tests Simulating the Launch of 105-mm Shell with a Base Separation of 0.50 mm Adjacent to a 1.50-mm Diameter Cavity**

Explosive	Acceleration (g <sub>n</sub> )	Reactions	
		Frequency	Type
TNT	25,000	1/5	PP
	20,000	0/5	N
Comp A-3	25,000	3/5	E
	20,000	0/5	N
Comp B	25,000	4/5	E
	20,000	3/3	E

Furthermore, a friction effect at the explosive/steel interface was added to the previous stimuli when the cavity was located at the bottom of the specimen instead of the top.

The results obtained for the cylindrical cavity are shown in Table 3. The combined effect of adiabatic compression of air and shear and deformation of the explosive material was very severe; it led to consecutive reactions for all the explosives tested at 25,000 g<sub>n</sub> and even at 20,000 g<sub>n</sub> for Composition B and CX-84A. When friction at the explosive/steel interface was added (cavity at the bottom) to the previous stimuli, the conditions were found to be significantly more severe for Composition A-3, but less severe for Composition B. The results for the individual effect of shear and deformation of the explosive material (tests under vacuum) indicated that Composition A-3 was not affected by this stimulus even at an acceleration of 25,000 g<sub>n</sub> (contrary to TNT, Composition B, and CX-84A) which led to the same number of reactions as when air was present in the cavity. These results suggest

**Table 3. Results of Tests Simulating the Launch of 105-mm Shell With a Cylindrical Cavity of 0.25 cm<sup>3</sup>**

Explosive	Cavity Dia: 8, H: 5 mm	Acceleration (g <sub>n</sub> )	Reactions	
			Frequency	Type
Comp A-3	top	25,000	3/3	E
	top	20,000	2/5	E
	bottom	20,000	3/3	E
	top (vacuum)	25,000	0/5	N
	top (vacuum)	20,000	0/5	N
	bottom (vacuum)	25,000	1/5	E
	bottom (vacuum)	20,000	0/5	N
TNT	top	25,000	3/3	PP
	top	20,000	4/5	PP
	bottom	20,000	3/3	PP
	top (vacuum)	25,000	3/3	PP
	top (vacuum)	20,000	4/5	PP
	bottom (vacuum)	25,000	3/3	PP
	bottom (vacuum)	20,000	4/5	PP
Comp B	top	20,000	3/3	E
	bottom	20,000	2/5	E
	top (vacuum)	20,000	3/3	E
	bottom (vacuum)	25,000	3/3	E
	bottom (vacuum)	20,000	4/5	E
CX-84A	top	20,000	3/3	P
	top (vacuum)	20,000	3/3	P
	bottom (vacuum)	20,000	3/3	P

that the shear and deformation of the explosive in setback conditions was the main cause of reactions in TNT, Composition B, and CX-84A, but not Composition A-3. However, the results obtained with the hemispherical cavity did not entirely confirm this observation.

With a hemispherical cavity 7.0 mm in diameter, the results in Table 4 in comparison to those with the cylindrical cavity, indicated that the stimuli were still quite severe for all explosives tested at 25,000 g<sub>n</sub>, but not for TNT at 20,000 g<sub>n</sub>. When the friction effect was added, the stimuli was not increased but reduced for Composition A-3, TNT, and particularly for Composition B. Whereas the individual effect of shear and deformation did not ignite any TNT, even at 25,000 g<sub>n</sub>, nor any Composition B at 20,000 g<sub>n</sub>, this stimulus remained very severe for CX-84A. Results on the effect of friction at the explosive/steel

interface were not conclusive, further studies will be carried out in the future.

An explanation for the difference in results between the cylindrical and spherical cavities tested seems to be related to their volume rather than their shape. The volume of the hemispherical cavity is 0.09 cm<sup>3</sup> in comparison to 0.25 cm<sup>3</sup> for the cylindrical cavity. The volume ratio is almost three to one.

Thus, in the presence of a cavity of 0.25 cm<sup>3</sup>, the individual effect of shear and deformation of the explosive under setback conditions at accelerations of 20,000 g<sub>n</sub> is likely to cause a premature of CX-84A, Composition B, and TNT, but not Composition A-3 shell fillings. With a cavity of 0.09 cm<sup>3</sup>, this stimulus is not likely to cause a premature of TNT, in addition to Composition A-3 fillings, under launch conditions at 25,000 g<sub>n</sub> and of

**Table 4. Results of Tests Simulating the Launch of 105-mm Shell With a Hemispherical Cavity of 0.09 cm<sup>3</sup>**

Explosive	Cavity 3.5 mm Radius	Acceleration (g <sub>n</sub> )	Reactions	
			Frequency	Type
Comp A-3	top	25,000	4/5	E
	top	20,000	3/5	E
	bottom	25,000	2/5	E
	top (vacuum)	25,000	0/5	N
	bottom (vacuum)	25,000	1/5	E
TNT	top	25,000	3/5	PP
	top	20,000	1/5	PP
	bottom	25,000	2/5	PP
	bottom	20,000	3/5	PP
	top (vacuum)	25,000	0/5	N
	bottom (vacuum)	25,000	4/5	PP
Comp B	top	20,000	3/3	E
	bottom	25,000	4/5	E
	bottom	20,000	0/5	N
	top (vacuum)	25,000	3/5	E
	top (vacuum)	20,000	0/5	N
	bottom (vacuum)	25,000	2/5	E
CX-84A	top	20,000	3/3	P
	bottom	20,000	3/3	P
	top (vacuum)	20,000	4/5	P
	bottom (vacuum)	20,000	3/3	P

Composition B fillings at accelerations not exceeding 20,000 g<sub>n</sub>. A cavity volume would have to be reduced to slightly under 0.09 cm<sup>3</sup> to avoid premature of Composition B fillings at 25,000 g<sub>n</sub> and a further decrease would be required to meet this objective for CX-84A fillings.

The results with the hemispherical cavity indicate also that the combined effect of adiabatic compression of air and explosive shear and deformation was a significantly more severe stimulus for Composition A-3 and TNT than each effect considered individually. In Tables 1 and 2, Composition A-3 and TNT were not found to be very sensitive to the adiabatic compression of an air gap of 0.50 mm which represents a volume of 0.14 cm<sup>3</sup>; furthermore, these explosives were not found to be sensitive to shear and deformation either, as shown in Table 4 for the vacuum tests. By comparison, Composition B and CX-84A were

found to be very sensitive to each individual stimulus. These explosives resulted in almost consecutive reactions to adiabatic compression as discussed previously (Tables 1 and 2) and the effect of shear and deformation became a major stimulus when a high deformation rate was tested either for high accelerations such as 25,000 g<sub>n</sub> or large deformations such as 0.25 cm<sup>3</sup>. Thus, a minimum rate of shear and deformation seems to be required to produce a reaction in Composition B. This observation also applies in part to TNT, but not to Composition A-3. This minimum rate would explain the reduction in sensitivity observed for Composition B in Tables 3 and 4 when friction at the explosive/steel interface was added. That friction of the specimen on the steel walls led to a slower velocity than when the piston was accelerated freely; thus, reducing the rate of shear and deformation of the explosive.

## Internal Cavities

Tests were carried out on specimens with internal cavities of diameters from 0.25 to 0.40 mm, 0.60 to 0.80 mm, and 1.2 to 1.8 mm. These experiments were conducted on cast Composition B. In general, in each category, the specimen had a minimum of one cavity at the maximum size mentioned, and a maximum of ten cavities within the range specified. The size and number of the cavities were identified by radiographs. The effect of micro-porosity—many cavities smaller than 0.1 mm—was also studied.

The results obtained are presented in Table 5. The effect of internal cavities from 0.60 to 0.80 mm in diameter was to consecutively ignite Composition B while simulating the launch of a shell at 25,000  $g_n$ . Under the same conditions, the effect of smaller cavities, from 0.25 to 0.40 mm, and the micro-porosity did not produce any reactions in five tests each. A significant effect due to the acceleration level was indicated when cavities from 1.20 to 1.80 mm were tested. Only one reaction was obtained for five tests at 20,000  $g_n$  in comparison to three consecutive reactions at 25,000  $g_n$  for significantly smaller cavities (0.60 to 0.80 mm). For these tests, the stimuli considered were the adiabatic compression of air in the cavity combined with shear and deformation of Composition B.

These results indicate that internal cavities from 0.60 to 0.80 mm in diameter are likely to be the cause of a premature of Composition B filled shells when launched at

Table 5. Results of Tests Simulating the Launch of 105-mm Shell Filled with Composition B with Internal Cavities

Cavity size (mm)	Acceleration (gn)	Reactions	
		Frequency	Type
Micro-porosity	25,000	0/5	N
0.24 to 0.40	25,000	0/5	N
0.60 to 0.80	25,000	3/3	E
1.2 to 1.8	20,000	1/5	E

25,000  $g_n$ , but not those smaller than 0.40 mm. In contrast, at 20,000  $g_n$ , cavities as large as 1.8 mm are not likely to cause a premature.

A summary of all the results obtained is given in Figure 3. It shows that Composition A-3 or TNT fillings, depending on the testing conditions considered, are the least likely to result in a premature during gun launch of 105-M1 shells with the filling defects mentioned. They are followed, in increasing order of sensitivity, by Composition B and CX-84A, the most sensitive explosive tested. This figure indicates that a base separation of 1.0 mm is more severe than a cylindrical cavity of 0.25  $cm^3$ , and a base separation of 0.33 mm is the least important defect tested.

## Explosiveness

The explosiveness of each explosive was also evaluated under different setback conditions in addition to their sensitivity. For each individual explosive, its explosiveness remained the same under all the conditions tested. Their explosiveness was assessed by analyzing load cell recordings and examining the components upon dismantling the specimen mounting pieces, including any residual portion of the specimen.

Composition B led to the most violent reactions, with reaction peaks higher than 400 kN on load cell recordings. The cylindrical portion of the piston was broken in parts and the cylinder was usually reduced to three or four large pieces. Only explosions (E) were obtained, no trace of explosive was found and ignition delays were always shorter than 0.15 ms.

Composition A-3 resulted in explosions slightly less violent than Composition B. Reaction peaks were between 300 and 400 kN and the cylindrical portion of the piston was broken. Reaction delays varied from 0.20 to 0.40 ms. In comparison, TNT led to heavy partial reactions (PP) consuming up to 80 percent of the specimen. Reaction peaks were between 100 and 200 kN and they occurred with delays from 0.30 to 0.80 ms. CX-84A resulted in the least violent reactions. Only light partial reactions (P) were obtained, consuming less than 15 percent of the specimen and often only a few crystals were burnt on one

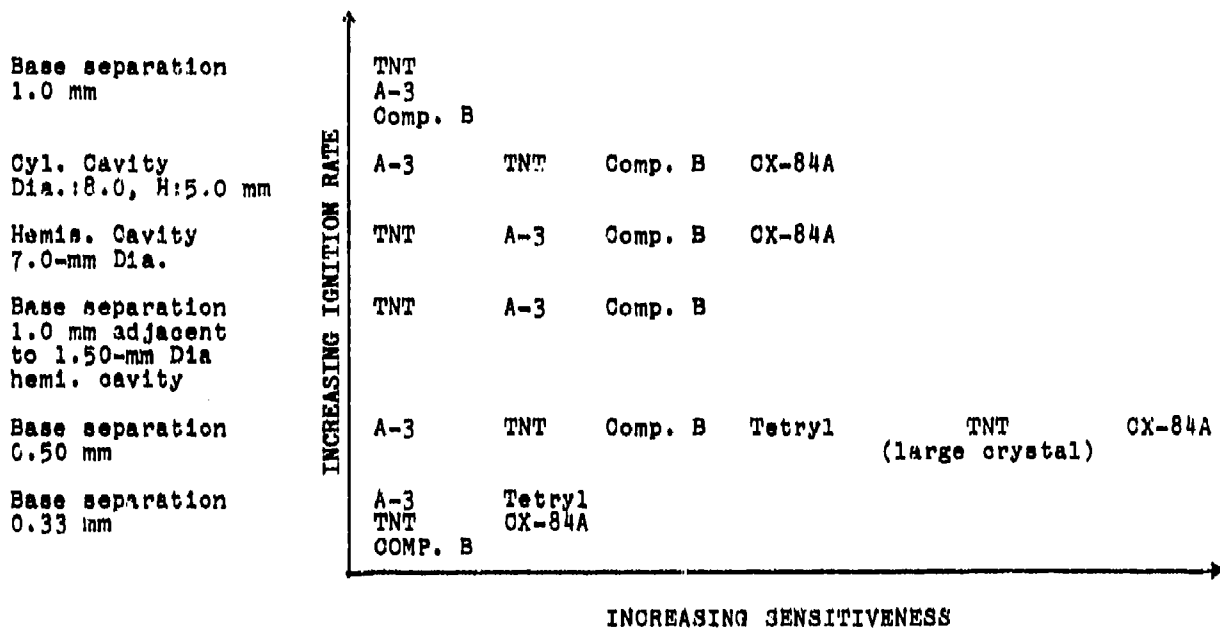


Figure 3. Summary of Setback Results Simulating the Launch of 105-mm Shell

face of the specimen. The reactions were so feeble that the reaction peaks were barely seen on the recordings. Reaction delays were always longer than 2.0 ms. Tetryl, tested for comparison, led to heavy partial reactions very similar to those of TNT.

In summary, the results indicated that Composition A-3 or TNT, depending on the setback conditions, were the least likely, among the explosives tested, to result in a premature explosion during gun launch. They are followed, in increasing order, by Composition B and CX-84A.

However, the CX-84A behavior was different than that of the other explosives tested. Although it was found to be the most sensitive to all the stimuli studied, it showed the greatest resistance to the propagation of a reaction. No significant reaction growth was obtained even for setback stresses up to 250 MPa applied for about 6 ms. Although these results suggest that the gun launch of a 105-mm M1 shell filled with CX-84A involving defects, such as those tested in this paper, could lead to a premature for accelerations higher than 20,000  $g_n$ , unlike Composition B, a CX-84A premature will not have catastrophic consequences. The feeble reactions obtained,

combined with rather long reaction delays, suggest that a shell could have reached the end of the gun tube before the reaction has grown enough to eject the fuze or if this event occurred in the gun barrel, the consequences would be mild if not negligible.

## CONCLUSIONS

The experiments carried out simulating the gun launch of a 105-mm M1 shell with filling defects have shown that Composition A-3 or TNT, depending on the conditions tested, would be the least likely to have premature explosions. They are followed in increasing order by Composition B and CX-84A. Although the PBX CX-84A was found to be the most susceptible to premature, its unique resistance to reaction growth would lead to the mildest consequences.

The effect of an adiabatic compression of air from the collapse of a base separation of 0.50 mm simulating a 20,000  $g_n$  launch caused consecutive reactions of CX-84A, TNT with large crystals, and also Composition B when a small cavity was adjacent to the separation. This stimulus can be the cause of a premature of 105-mm shells filled with these explosives during launch under those conditions.

The single effect of explosive shear and deformation was found to be a very severe stimulus for CX-84A and also for TNT based explosives when a high deformation rate is obtained either from a fairly large cavity such as 0.25 cm<sup>3</sup> at a moderate acceleration or a high acceleration of 25,000 g<sub>n</sub> with a smaller cavity. Thus, this stimulus can be the cause of a premature of shells filled with CX-84A, TNT, and Composition B, but not those filled with Composition A-3 during launches under the conditions mentioned.

Internal cavities with diameters from 0.60 to 0.80 mm are likely to cause a premature of Composition B filled shells when launched at 25,000 g<sub>n</sub>, whereas those smaller than 0.40 mm are negligible.

The sensitivity of cast TNT to the adiabatic compression of an air gap is increased significantly when its crystal size is increased.

The combined effect of the adiabatic compression of air with the explosive shear and deformation from a surface cavity of 0.09 cm<sup>3</sup>, was found to be a more severe condition in Composition A-3 and TNT than each stimulus tested individually. However, CX-84A was

found very sensitive to each of these stimuli and similar behavior was obtained with Composition B, but to a lesser degree.

## REFERENCES

1. Bélanger, C. and Walker, G. R., *DREV Setback Simulator: Design and Performance*, DREV Report 4274/82, DREV, Quebec, Canada, Nov 1982.
2. Pasman, H. J., *Shell Prematures by Compression Ignition and their Laboratory Simulation*, DREV Report 707/75, DREV, Quebec, Canada, Apr 1975.
3. Drolet, J.-F.; Lavertu, R. R.; Bélanger, C.; and Walker, G. R., *Castable Plastic Bonded Explosive CX-84A*, DREV Memorandum 3564/81, DREV, Quebec, Canada, Oct 1981.
4. Myers, T. F. and Hershkowitz, J., "The Effect of Base Gaps on Setback-Shock Sensitivities of Cast Composition B and TNT as Determined by the NSWC Setback-Shock Simulator," *Proceedings of the Seventh Detonation Symposium*, U. S. Naval Academy, Annapolis, MD, 16 Jun 1981, pp. 914-923.

# A COMPUTATIONAL ASSESSMENT OF THE ROLE OF SHIELDING IN PREVENTING THE SYMPATHETIC DETONATION OF MUNITIONS

J. Starckenberg, T. M. Dorsey,  
K. J. Benjamin, and A. L. Arbuckle  
Ballistic Research Laboratory  
Aberdeen Proving Ground, MD 21005-5066

*In order to reduce the vulnerability of stored ammunition, shielding between rounds has been used to prevent initiation of detonation in a round (the acceptor) when one of its neighbors (the donor) detonates. We have conducted a study of the role of shielding in reducing the initiation stimulus for a simplified two-dimensional representation of the problem using the STEALTH code. Mechanisms associated with compression caused by impact and massive deformation of the acceptor were considered. Three shield materials were used: steel, Lucite, and tungsten. Three types of shields were considered: single-layered slabs, multilayered slabs, and rods. Conclusions regarding the effectiveness of shielding that may be drawn from the computed results depend upon the mechanism(s) that are regarded as contributing to initiation of the acceptor. We found that, for unshielded rounds, interround separation has an effect on the peak pressure and deformation rate stimuli which is consistent with experimental observations while maximum deformation decreases somewhat as interround separation increases. Single-layered metal shields are superior to multilayered and rod-shaped shields in reducing the initial peak pressure and the average deformation rate. They also do well in reducing the late time pressure. Single-layered plastic shields are not as effective. Multilayered shields do a superior job of increasing the initial compression rise time and reducing maximum deformation. They can also be effective in reducing the average deformation rate and late time pressure. While the multilayered shields perform best only with respect to maximum deformation, they are a close second with respect to every other measure of sympathetic detonation stimulus. Rod-shaped shields are most effective in increasing the initial rise time but produce high late time pressures, higher maximum deformations than no shield at all, and average deformation rates which are greater than those with any of the other shields.*

## INTRODUCTION

Experience with sympathetic detonation of munitions has led to the interpretation that, for unprotected rounds, the primary propagation mechanism at close range is shock initiation due to casing impact while at longer range, fragment penetration is the primary

mechanism. In order to reduce the vulnerability of stored ammunition, shielding between rounds has been used to prevent initiation of detonation in a round (the acceptor) when one of its neighbors (the donor) detonates.<sup>1-3</sup> The shielding serves primarily to prevent direct impact of the donor casing or its fragments on the acceptor, thus reducing the

initiation stimulus. When shields are used, the shock and penetration mechanisms may be eliminated but propagation of violent reaction still often occurs. Considerable delays in the response of the acceptor have frequently been observed in the presence of shielding. The mechanism in this case is apparently related to the rapid deformation of the round and is not well understood. Work by Howe, Gibbons, and Webber has demonstrated that the gross deformation of a munition leads to the formation of a region of severe damage in the explosive near the impact point and to shear concentrations in the remainder of the explosive.<sup>4</sup>

Numerical simulation of detonation propagation in somewhat simplified geometries has been successful in guiding the design of shields to eliminate the shock mechanism. We have already simulated round-to-round detonation propagation, with and without shielding,<sup>5,6</sup> using the reactive 2DE code and shielding effectiveness in reducing shock initiation stimulus levels in one dimension<sup>7,8</sup> using the STEALTH<sup>9</sup> code. The reactive models may be of interest in predicting the response of acceptors to pure shock stimuli but are generally inadequate to describe reaction in the complex environment associated with sympathetic detonation. Use of these models serves only to obscure the stimuli generated. For the present investigation, we have extended the nonreactive STEALTH simulation of shielding effectiveness to two dimensions in order to study shield influence on mechanisms associated with both compression and deformation of the acceptor explosive and to address additional shield design considerations.

## SIMULATION DESCRIPTION

The problem elements are the donor, the shield, and the acceptor as illustrated in Figure 1. Symmetry about the x and y axes leads to a simulation of a single center-initiated donor flanked by shields and acceptors on either side. The donor consists of a steel casing 10 mm thick and 105 mm in outside diameter with a Composition B (Comp B) fill which is caused to detonate in order to initiate the computation. The shield configuration is varied. It may consist of a single layer of one material, multiple layers of two materials, or a

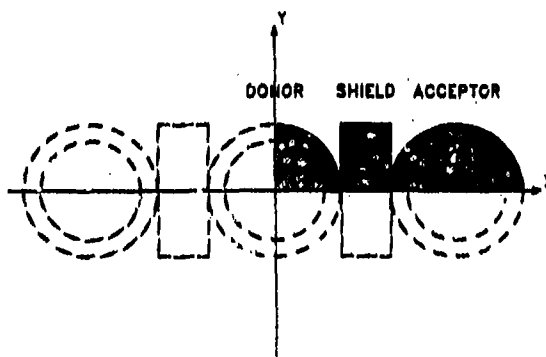


Figure 1. Physical Configuration of Shielding Simulation

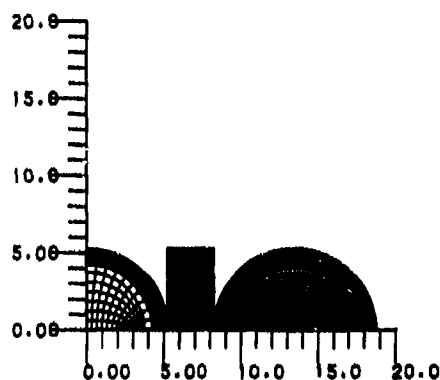


Figure 2. Typical Zoning. Pressure monitored at filled cells.

cylindrical rod. Unshielded configurations were also considered. The acceptor representation is similar to that of the donor except that the fill is "inert" TNT.

Hyperbolicelliptic computational grids were generated for explosive fills. Casings are described by polar grids. Rectangular grids were used for the slab shields and an external program was used to generate grids for rod-shaped shields. Typical zoning is illustrated in Figure 2. Explosive fill grids are 10 by 7 zones for the donor and 40 by 10 zones for the acceptor. Casing grids are 20 zones per quadrant by 5 zones. Shield grids are 5 zones per 10 mm by 5 zones per 10 mm. The grids interact with one another without imparting frictional forces. We attempted to run each problem to 120  $\mu$ s after donor initiation and were successful in most cases.

The detonation Comp B is simulated using the built-in "LLNL HE Burn" model which incorporates the JWL equation of state to describe the products. The inert TNT is described by Lee's unreacted JWL equation of state<sup>10</sup> and all other materials by Wilkins' model<sup>9</sup> with 304 steel used for the casings.

In order to provide a baseline from which to evaluate the stimulus reduction provided by shielding, we made several computations without shielding in which interround separation was varied. We then proceeded to computations in which we used three different shield materials: steel, Lucite, and tungsten. For steel and Lucite, the effect of shield thickness, lateral extent, and of spaces between the shield and the rounds were considered. Computations with multilayered shields consisting of steel and Lucite were also made. Some of the multilayered shields considered simulate configurations for which experimental data is available. Additional computations consider variations in the order of shield material at constant areal density and the substitution of tungsten for steel. Finally, we also considered rod-shaped shields of different materials. All of the computations are summarized in Table 1.

## STIMULUS CHARACTERIZATIONS

Several measures of sympathetic detonation stimulus levels corresponding to different ignition mechanisms have been extracted from the computations. These are associated with either the pressures generated in the acceptor explosive or its deformation. Of particular importance to ignition are the strength of the initial compression and its rise time, as well as the rate at which the acceptor explosive is deformed. The maximum deformation produced may also be of some importance, particularly as it relates to the degree of damage to the explosive. Finally, the general pressure levels produced are important since they influence the burning rate regardless of the ignition mechanism.

### Compression

In all of our computations, pressure was monitored at a number of points in the acceptor explosive as indicated in Figure 2. Pressure

Table 1. Summary of Problem Configurations

Shield Material	Interround Spacing (mm)	Shield Thickness (mm)
unshielded	0.0	--
unshielded	10.0	--
unshielded	20.0	--
unshielded	30.0	--
tungsten	30.0	30.0
steel	30.0	30.0
Lucite	30.0	30.0
steel	20.0	20.0
steel	30.0	20.0
Lucite	30.0	20.0
Lucite	30.0	20.0
Luc-st-Luc	30.0	12.0-6.0-12.0
Luc-st-Luc	30.0	10.0-10.0-10.0
Luc-st-Luc	30.0	9.0-12.0-9.0
Luc-st-Luc	30.0	7.5-15.0-7.5
st-Luc-st	30.0	10.0-10.0-10.0
st-Luc-st	30.0	9.0-12.0-9.0
st-Luc-st	30.0	7.5-15.0-7.5
Luc-W-Luc	30.0	10.0-10.0-10.0
Luc-W-Luc	30.0	9.0-12.0-9.0
Luc-W-Luc	30.0	7.5-15.0-7.5
W-Luc-W	30.0	10.0-10.0-10.0
W-Luc-W	30.0	9.0-12.0-9.0
W-Luc-W	30.0	7.5-15.0-7.5
steel rod	30.0	30.0
Lucite rod	30.0	30.0
tungsten rod	30.0	30.0

histories for all monitored points with and without shielding are shown in Figure 3. In general, these configurations do not give rise to discontinuous shock waves. Rather, the initial waves are ramps with various rise times and peak pressures. The initial peak pressure is highest and the rise time shortest at the near-side casing interface at or near the centerline. The pressure decreases and the rise time increases approximately as the distance from the near-side centerline increases. In order to simplify matters, the pressure history of the point in the acceptor explosive just inside the casing on the centerline is assumed to be representative of the overall loading of the

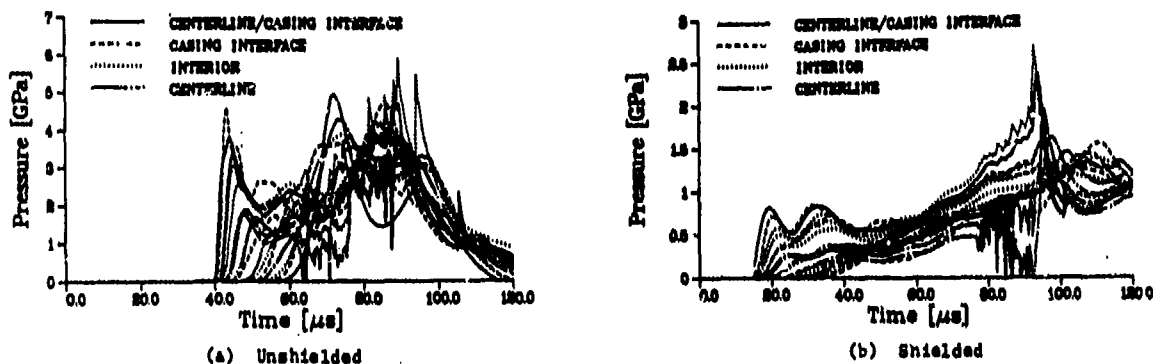


Figure 3. Typical Acceptor Explosive Pressure Histories

acceptor explosive (especially in the region in which ignition has been observed) and has been used in the rest of this report to characterize the compression stimulus. Generally, we saw an initial compression followed after some time by reflected waves. The initial wave is of particular interest since it is usually implicated in initiation when no shielding is present. When shielding sufficient to inhibit shock initiation is present, the later time pressure history may be important, especially insofar as it influences the rate of burning. Both the amplitude and rise time of the initial compression are considered to be factors influencing sensitivity. Rise times in the numerical solutions may, in part, be artifacts of the numerical shock representation. The computed rise time associated with a genuine shock wave is governed by the artificial viscosity and the zone size. This seemed to be about 2  $\mu$ s or less in our computations. Thus, rise times longer than this may be considered to result from the geometry and loading of the problem and are not simply artifacts. The critical energy criterion, often expressed in terms of  $f_p 2dt$ , has not been used because it is not generally applicable to complex waveforms.

### Deformation

Deformation may produce shear concentrations within the acceptor explosive or slip at the casing interface leading to ignition and/or damage to the charge which enhances burn propagation. We have simply characterized deformation using the change in length of the acceptor explosive fill along the x axis normalized with respect to its original length. The

average rate of change of this parameter with time has also been considered. This is defined as the average rate of change of the deformation as it varies from 5 to 95 percent of its maximum value. It is assumed that the mechanisms affecting sensitivity of the acceptor are directly related to these parameters. In particular, the shear strain rates associated with ignition of the explosive should be generally proportional to the deformation rate for all geometrically similar problems.

## RESPONSE OF UNSHIELDED ACCEPTORS

### Compression

Four problems with separations between rounds of 0, 10, 20, and 30 mm were considered. The 30 mm spacing corresponds to impact at the maximum casing velocity achieved in the absence of fragmentation. Pressure histories in the acceptor explosive at the casing interface on the centerline are shown in Figure 4. The time axis has been shifted for each computation such that the initial compression appears at about the same time in the plot.

In the contact case, no normal casing impact occurs and a 2.4 GPa compression with a rise time of about 4  $\mu$ s is produced. In the cases where there is an initial separation, impact of the donor casing on the acceptor produces somewhat stronger initial pulses with amplitudes ranging from 3.5 to 4.1 GPa and rise times of less than 4  $\mu$ s. For these cases, the variation of peak pressure with separation is

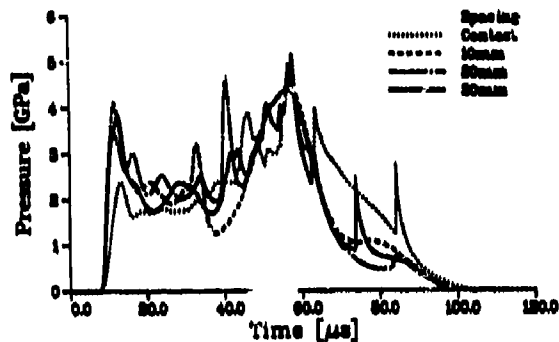


**Figure 4. Effect of Separation on Acceptor Explosive Pressure History for Unshielded Rounds**

weak and no specific trend may be observed. The value of approximately 3.8 GPa for the 30 mm spacing compares favorably with an experimental measurement of 4.4 GPa.<sup>11</sup> This pressure is sufficient to promptly initiate a Comp B fill).

Subsequent compressions arise from reflections from rear portions of the acceptor casing or the y axis symmetry plane. The curved nature of the former interface produces incremental reflections which arrive at the monitored cell over a period of time. This produces a compression with a long rise time which is about as strong as the initial shock. Since the cell being monitored lies in the acceptor fill at the casing interface, we observe this wave as it is being reflected again, accounting for the high pressure. The arrival time of the reflection from the symmetry plane varies with the interround separation. These shocks appear as spikes in the plot following the initial shock by about 20 to 80  $\mu$ s. The pressures generated by the shock reflections are not significantly higher than the initial shock pressures, and detonation would presumably have occurred long before any of these reflections could have any effect. In all these

cases, the pressure has dropped essentially to 0 by about 90  $\mu$ s after initial shock entry. The general pressure levels following the initial compression are similar in all four cases.

### Deformation

The sequence of grid plots in Figure 5 shows the typical physical configuration of the rounds as a function of time. Deformation is plotted as a function of time for the four unshielded cases in Figure 6. Deformation increases with time until a maximum is reached and then decreases. The maximum deformations and average deformation rates are summarized in Table 2. Maximum deformation shows some mitigation at the larger separations. The deformation rate, on the other hand, is lowest for rounds in contact and does not vary significantly when an initial separation is present.

### Interpretation

The peak pressure and deformation rate are minimized for rounds in contact. Thus, both the compression and shear mechanisms are consistent with experimental observations of suppression of sympathetic detonation for rounds in contact. It appears that deformation rate must be considered along with "shock" as an active mechanism for unshielded rounds.

## SHOCK AND DEFORMATION MITIGATION BY SHIELDS

### Results with Single-Layered Shields

We have considered three different shield materials: steel, Lucite (representing a low-density, low-impedance material), and tungsten (representing a high-density, high-impedance material). Figure 7 shows pressure history plots for rounds shielded by 30 mm thick slabs

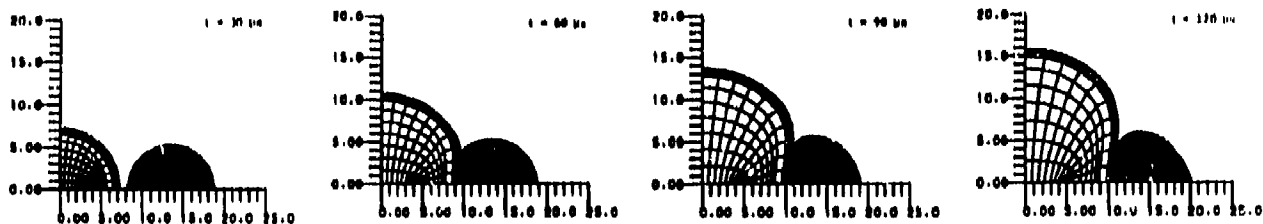


**Figure 5. Sequence of Grid Plots for Unshielded Rounds With an Initial Separation of 30 mm**

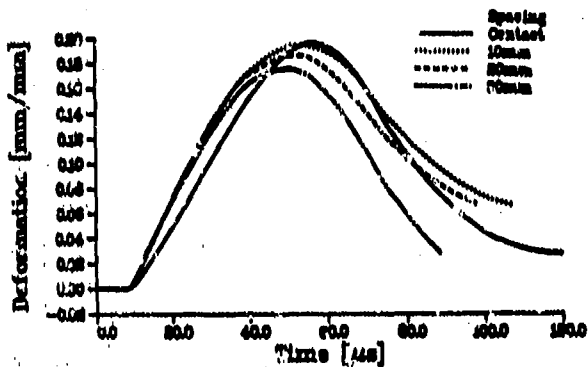


Figure 6. Effect of Separation on Acceptor Explosive Deformation History for Unshielded Rounds

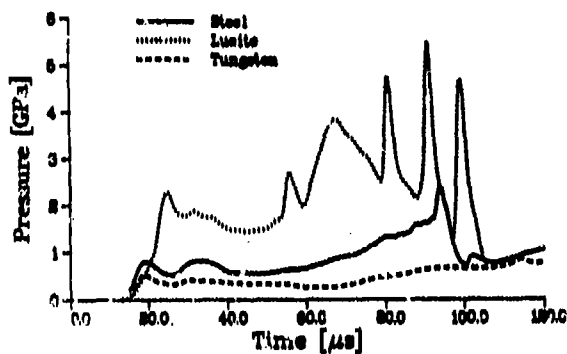


Figure 7. Effect of Single-Layered Shield Material on Acceptor Explosive Pressure History

Table 2. Effect of Interround Separation on Maximum Deformation and Average Deformation Rate for Unshielded Rounds

Interround Separation (mm)	Maximum Deformation (mm/mm)	Average Deformation Rate (mm/mm/ms)
0	0.196	4.63
10	0.194	5.13
20	0.186	5.13
30	0.175	5.08

of each material extending laterally to the full round diameter and in contact with both the donor and acceptor.

With steel and tungsten, the initial peak pressures were reduced to 0.8 and 0.5 GPa, respectively, and the rise times remained at about 4  $\mu$ s. In the case of the steel shield, a second compression with approximately the same strength and rise time follows the first after about 15  $\mu$ s. With the tungsten shield, there is a relatively weak second compression. With the Lucite shield, the pressure was reduced only to 2.3 GPa but the rise time was increased to about 8  $\mu$ s. This pressure is considerably higher than the measured value of 0.7 GPa with polyethylene shields.<sup>11</sup> Notably, the value is close to that computed for rounds in contact. At late times, there are several strong reflected waves generated by the impedance discontinuities between the Lucite shield and steel casings. The flow in this region is more

nearly one-dimensional at late times as can be seen in the grid plot sequence. This type of reflection is not observed with steel or tungsten shields. Reflected compressions appear only very late for the steel shield and are quite weak for the tungsten shield. Thus, the tungsten shield is most effective in reducing late-time pressure. In these problems, the pressures have not dropped back to zero by the end of the computation.

A sequence of grid plots for the steel shield is shown in Figure 8, while Figure 9 shows the deformation as a function of time associated with all three shields. The maximum deformations and average deformation rates are summarized in Table 3. The Lucite shield allows the greatest maximum deformation and deformation rate. The deformation shows some "ripples" near the peak associated with the reflected shocks. The steel and tungsten shields do not produce markedly different maximum deformations but the deformation rate is much lower for tungsten.

#### Results with Multilayered Shields

Shields with multiple layers provide additional impedance discontinuities which were effective in breaking transmitted shocks up into a series of weaker shocks or producing increased rise times in our one-dimensional study. We have also examined the effectiveness of three-layered shields composed of alternate layers of steel and Lucite as well as of alternate layers of tungsten and Lucite in the present two-dimensional study. The order of

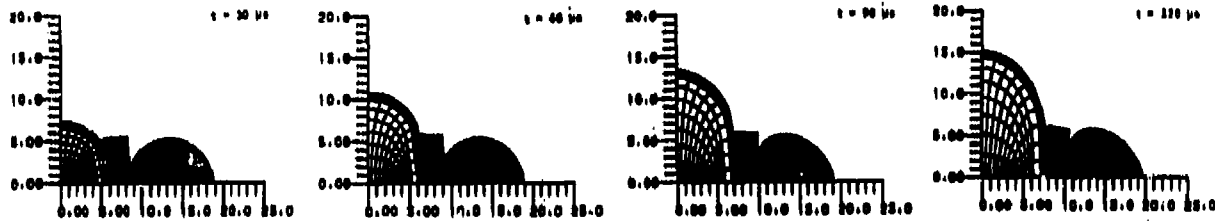


Figure 8. Sequence of Grid Plots for Rounds Shielded by a 30 mm Thick Steel Slab

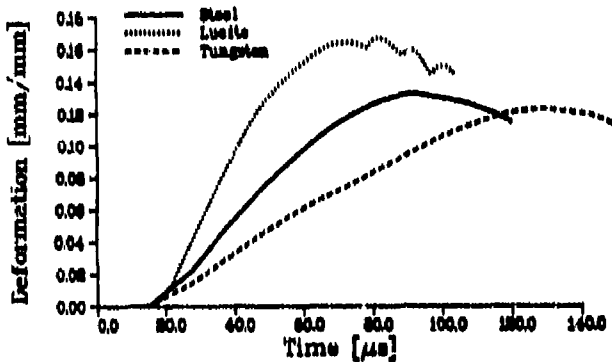


Figure 9. Effect of Single-Layered Shield Material on Acceptor Explosive Deformation History

Table 3. Effect of Shield Material on Maximum Deformation and Average Deformation Rate for 30 mm Thick Single-Layered Shield

Shield Material	Maximum Deformation (mm/mm)	Average Deformation Rate (mm/mm/ms)
Lucite	0.167	0.167
steel	0.132	0.132
tungsten	0.123	0.123

the materials and the relative thicknesses of the layers were varied but all of the shields were 30 mm thick and symmetry was always maintained. We did not generally observe "shock" breakup in the two-dimensional computations (because the principal compression is created downstream of the shield by its impact on the acceptor casing), but we did see a significant increased rise time effect. Pressure histories from these computations are shown in Figures 10 through 13.

Some of the computations were designed to simulate experimental configurations in

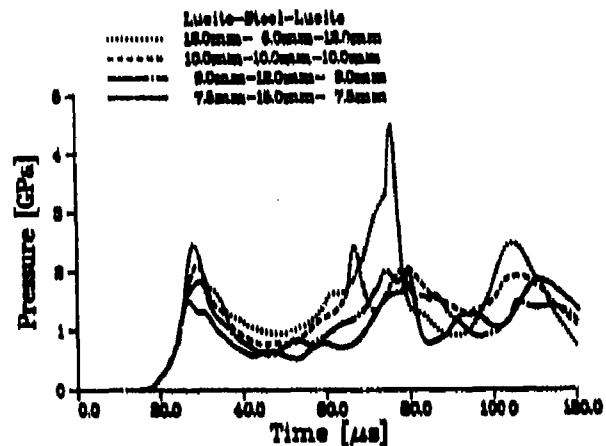


Figure 10. Effect of Layer Thickness on Acceptor Explosive Pressure History for Multilayered Lucite-Steel-Lucite Shields

which polyethylene was used instead of Lucite as the outer layer of the shield and steel was used as the inner layer. We considered inner layer thicknesses of 6, 10, 12, and 15 mm with a 30 mm total shield thickness. The pressure histories for these are shown in Figure 10. These computations showed an increase in initial compression rise time to about 8 to 10  $\mu$ s. An experimental measurement is available for a configuration comparable to the shield with the 6 mm thick steel layer. The experimental value of 0.4 GPa is considerably lower than the computed value of 2.4 GPa. Shield performance improves at both early and late times with increasing steel content consistent with the experimental results.

Results with steel as the outer layer are shown in Figure 11. Inner layer thicknesses of 10, 12, and 15 mm were considered. These shields produce a substantial increase in rise time to about 15  $\mu$ s. At early times, there is only a slight effect of steel content on the

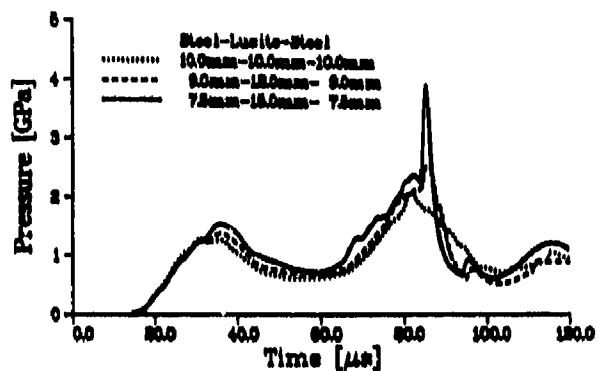


Figure 11. Effect of Layer Thickness on Acceptor Explosive Pressure History for Multilayered Steel-Lucite-Steel Shields

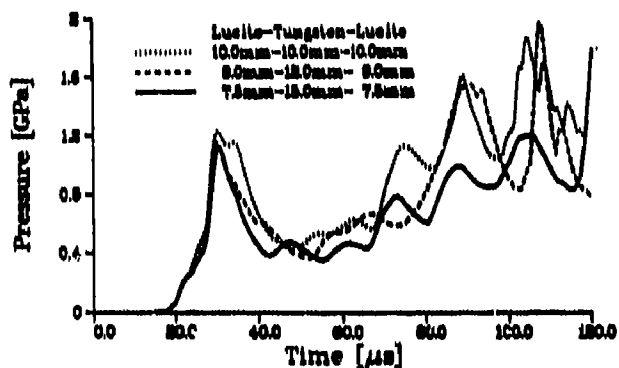


Figure 12. Effect of Layer Thickness on Acceptor Explosive Pressure History for Multilayered Lucite-Tungsten-Lucite Shields

initial peak pressure but, at late times, considerably lower pressures are produced when more steel is present in the shield. The wave structure is simplified considerably.

Results with tungsten as the inner layer are shown in Figure 12. Inner layer thicknesses of 10, 12, and 15 mm were considered. Again, pressure levels are substantially lower. The rise time of the initial compression is about 10  $\mu$ s in each case and the peak pressure is relatively insensitive to the tungsten content. At late times, lower pressures are produced when more tungsten is present in the shield.

Results with tungsten as the outer layer are shown in Figure 13. Inner layer thicknesses of 10, 12, and 15 mm were considered. These shields exhibit even longer rise times of

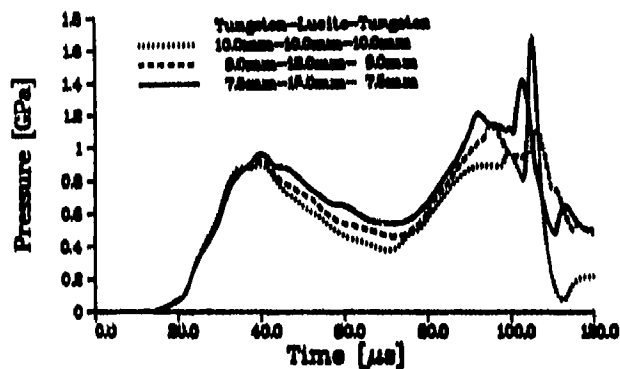


Figure 13. Effect of Layer Thickness on Acceptor Explosive Pressure History for Multi-Layered Tungsten-Lucite-Tungsten Shields

about 15 to 20  $\mu$ s. The pressure histories are remarkably insensitive to variations in the tungsten content.

Results obtained when the order of the shield materials is reversed while maintaining a constant shield mass per unit area (using a 15 mm thick inner layer) are illustrated in Figure 14 for steel and in Figure 15 for tungsten. For steel, the peak pressure is essentially unchanged, but the rise time is increased to about 17  $\mu$ s when steel is the outer component. However, this configuration produces a relatively high late pressure. The results are similar for tungsten but some pressure reduction accompanies the rise time increase from 10 to 20  $\mu$ s with tungsten as the outer component.

When tungsten is substituted for steel in either the inner or outer layers, the initiation stimulus is generally reduced as shown in the pressure histories in Figures 16 and 17. Rise times are somewhat longer and initial peak pressures and late time pressures are substantially reduced.

Effective deformation mitigation is also achieved with multilayered shields. A sequence of grid plots for a steel-Lucite-steel shield is shown in Figure 18. All of the results for three-layered shields are summarized in Table 4. For shields containing steel, the performance improves with increasing steel content. For shields having a 50 percent steel content, results are better when the steel is in the inner layer. (This is the opposite of the effect on initial compression rise time.) When tungsten

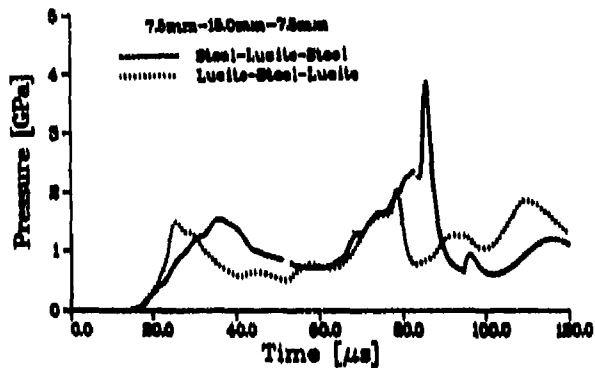


Figure 14. Effect of Material Order on Acceptor Explosive Pressure History for Multilayered Steel-Lucite Shields

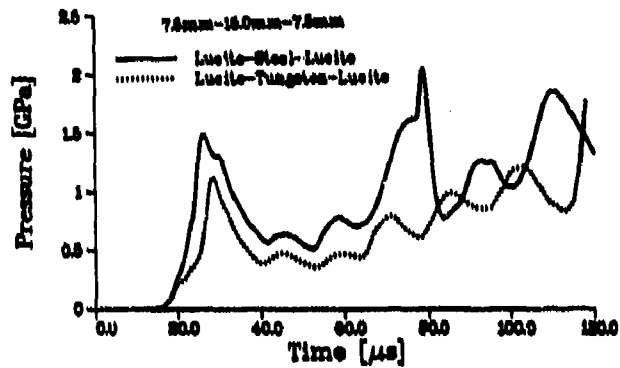


Figure 16. Effect of Inner Layer High Impedance Material on Acceptor Explosive Pressure History for Multilayered Shields

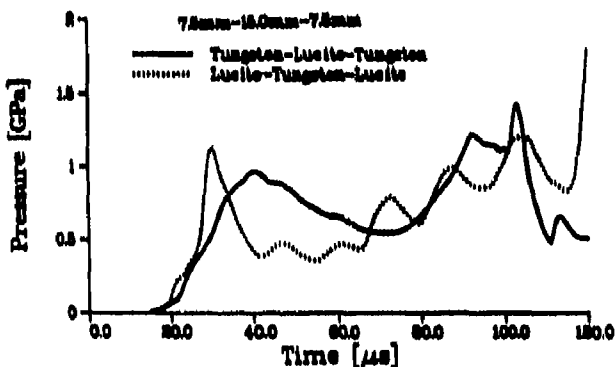


Figure 15. Effect of Material Order on Acceptor Explosive Pressure History for Multilayered Tungsten-Lucite Shields

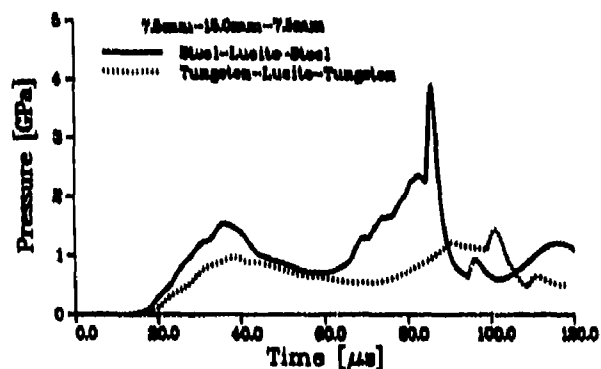


Figure 17. Effect of Outer Layer High Impedance Material on Acceptor Explosive Pressure History for Multilayered Shields

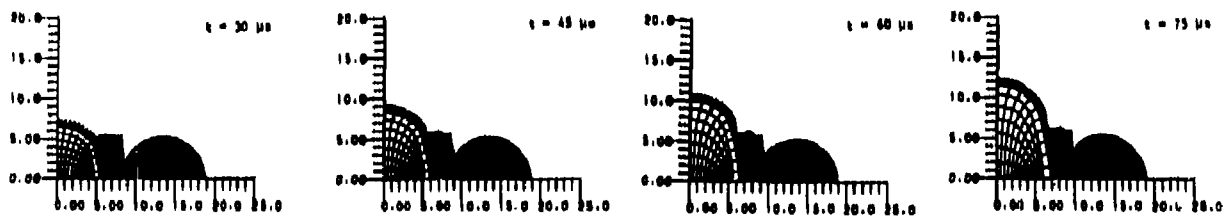


Figure 18. Sequence of Grid Plots for Rounds Shielded by a 30 mm Thick Steel-Lucite-Steel Slab

**Table 4. Effect of Shield Configuration on Maximum Deformation and Average Deformation Rate for 30 mm Thick Multilayered Shields**

Material Configuration	Layer Dimensions (mm-mm-mm)	Maximum Deformation (mm/mm)	Average Deformation Rate (mm/mm)
Luc-st-Luc	12.0-8.0-12.0	0.142	3.10
Luc-st-Luc	10.0-10.0-10.0	0.140	2.83
Luc-st-Luc	9.0-12.0-9.0	0.127	2.53
Luc-st-Luc	7.5-15.0-7.5	0.127	2.02
st-Luc-st	10.0-10.0-10.0	*	~2.1
st-Luc-st	9.0-12.0-9.0	0.129	2.48
st-Luc-st	7.5-15.7.5	0.138	2.46
Luc-W-Luc	10.0-10.0-10.0	0.121	1.83
Luc-W-Luc	9.0-12.0-9.0	0.119	1.70
Luc-W-Luc	7.5-15.0-7.5	0.121	1.48
W-Luc-W	10.0-10.0-10.0	0.113	1.97
W-Luc-W	9.0-12.0-9.0	0.117	2.11
W-Luc-W	7.5-15.0-7.5	0.120	2.31

\* Computation terminated before maximum deformation.

is substituted for steel further improvement in both the maximum deformation and average deformation rate is obtained. As an outer layer material, tungsten produces smaller maximum deformations but higher average deformation rates than as an inner layer material.

#### Results with Rod-Shaped Shields

Computations were made with 30 mm diameter rod-shaped steel, Lucite, and tungsten shields. The Lucite problem failed at about 40  $\mu$ s. The pressure histories are compared in Figure 19. The pressure rises relatively slowly and is initially independent of rod material. At late times, however, strong shocks of uncertain

origin may be observed. Pressure histories are also compared with those for corresponding 30 mm thick full-extent shields in Figures 20 through 22. Although the initial compression is slow with rods, the ultimate pressure levels are generally much higher than with slabs, with the possible exception of Lucite.

A grid plot sequence for the steel rod is shown in Figure 23. The maximum deformations and average deformation rates are even greater than those produced without shielding. No significant differences between the materials are obvious. The results are summarized in Table 5.

#### Summary and Comparison of Shields

In Table 6, we compare all of the shields on the basis of the ranges of values of the important parameters obtained for each general category of shield. Specifically considered are: the peak pressure of the initial compression, the associated rise time, the maximum deformation produced, and the average rate of deformation. The results for shields constructed of Lucite only indicate that low-density plastic materials generally provide inadequate protection. Shields containing tungsten, on the other hand, provide excellent

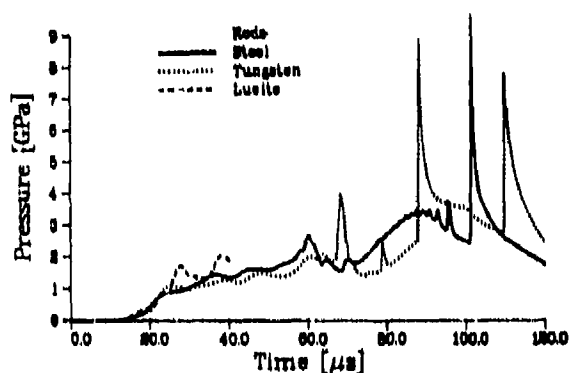


**Figure 19. Effect of Rod-Shaped Shield Material on Acceptor Explosive Pressure History**

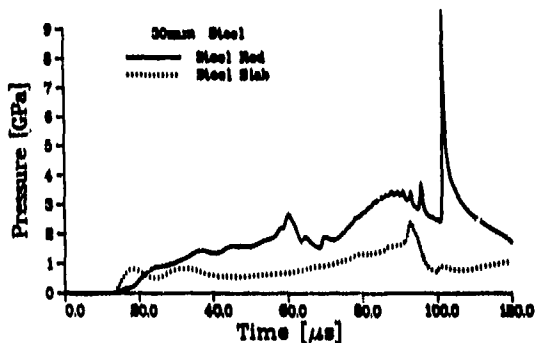


Figure 20. Comparison of the Pressure History for a Steel Rod with that for a Steel Slab

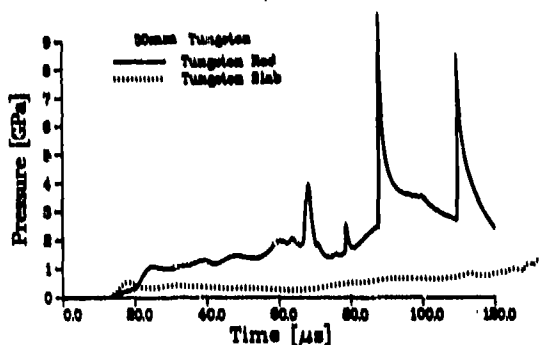


Figure 21. Comparison of the Pressure History for a Tungsten Rod with that for a Tungsten Slab

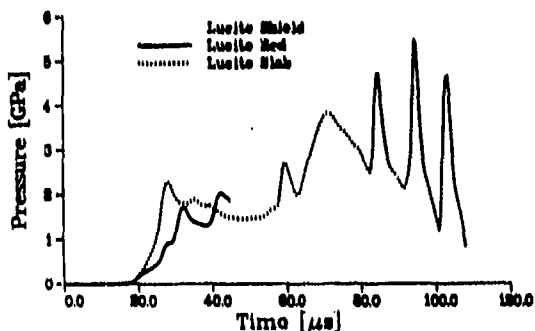


Figure 22. Comparison of the Pressure History for a Lucite Rod with that for a Lucite Slab

protection but are almost always impractical due to cost and weight considerations. Special attention, then, should be given to the shields which incorporate steel. The best such shields for reducing the peak pressure are the single-layered slabs. The rise time is most favorably affected by rod-shaped shields. Multilayered shields provide the greatest mitigation of maximum deformation while the slabs are best for reducing deformation rate. While the multilayered shields perform best only with respect to maximum deformation, they are a close second with respect to every other measure of sympathetic detonation stimulus. This makes them an attractive choice, especially in consideration of the uncertainty about what mechanism may be dominant in any particular case. Although the rod-shaped shields perform well in one respect, their overall poor performance makes them unlikely candidates.

## CONCLUSION

Conclusions regarding the effectiveness of shielding that may be drawn from the computed results depend upon the mechanism(s) that are regarded as contributing to initiation of the acceptor. We found that, for unshielded rounds, interround separation has an effect on the compression and deformation rate stimuli which is consistent with experimental observations while deformation decreases somewhat as interround separation increases. Because the net deformation cannot generally be related to a heating rate, we favor the use of the pressure history and the deformation rate to assess shielding effectiveness. Both of these contribute, and shields which reduce both are expected to be most effective. At least three aspects of the pressure history are of interest: the initial peak pressure, the initial compression rise time (and/or pressurization rate), and the late time pressure. We have also considered the average deformation rate and, for completeness, the maximum deformation.

Single-layered metal shields are superior to multilayered and rod-shaped shields in reducing the initial peak pressure and the average deformation rate. They do well in reducing the late time pressure. They should be chosen if initial rise time turns out to be an

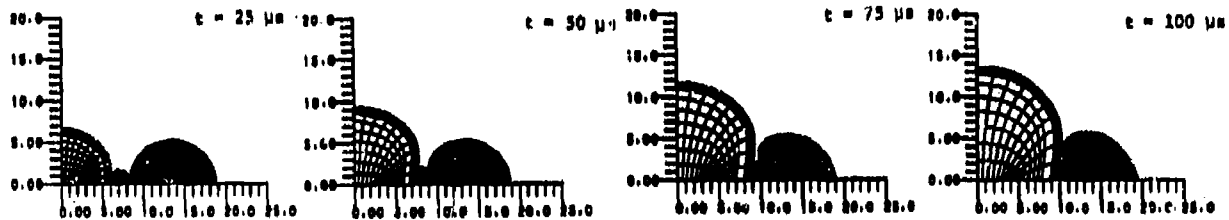


Figure 23. Sequence of Grid Plots for Rounds Shielded by a 30 mm Diameter Steel Rod

Table 5. Effect of Shield Material on Maximum Deformation and Average Deformation Rate for 30 mm Diameter Rod-Shaped Shields

Shield Material	Maximum Deformation (mm/mm)	Average Deformation Rate (mm/mm/ms)
Lucite	*	~3.9
Steel	0.242	4.02
Tungsten	0.262	3.71

\* Computation terminated before maximum deformation.

unimportant consideration. Single-layered plastic shields are not as effective. Multi-layered shields do a superior job of increasing the initial compression rise time and maximum deformation. They can also be effective in reducing the average deformation rate and late time pressure. Their choice may be dictated when reduction of the initial compression rise time is more important than reduction of the initial peak pressure. Because they perform well with respect to all types of stimulus, they should be considered when the sympathetic detonation mechanisms are most uncertain. Rod-shaped shields are most effective in increasing the initial rise time but produce

Table 6. Comparison of Shield Types Based on Typical Values

Shield	Peak Pressure (GPa)	Rise Time (μs)	Maximum Deformation (mm/mm)	Average Deformation Rate (mm/mm/ms)
Unshielded:				
contact	2.4	3.9	0.20	4.6
noncontact	3.5-4.1	2.2-3.5	0.19-0.19	5.1
Slabs:				
steel	*0.8-1.5	4.0-6.0	0.13-0.16	*1.9-2.4
Lucite	1.6-2.7	5.9-8.3	0.16-0.19	2.9-4.0
tungsten	0.5-1.0	3.8-4.2	0.12	1.2-2.2
Multilayer:				
Luc-st-Luc	1.5-2.5	7.8-9.4	*0.13-0.14	2.0-3.1
st-Luc-st	1.3-1.5	13.1-17.1	*0.13-0.14	2.1-2.5
Luc-W-Luc	1.1-1.2	9.9-10.6	0.12	1.5-1.8
W-Luc-W	0.9-1.0	15.3-20.0	0.11-0.12	2.0-2.3
Rods:				
steel	1.5	*20.0	0.24	4.0
Lucite	1.7	12.3	**	~3.9
tungsten	1.1	9.9	0.26	3.7

\* Best steel configuration.

\*\* Computation terminated before maximum deformation.

high late pressures, higher maximum deformations than no shield at all, and average deformation rates which are greater than those with any of the other shields. Their use can only be envisioned in the event that compression rise time is the only important consideration.

## REFERENCES

1. Gibbons, G., *Multiple Round Fragmentation Hazards and Shielding*, ARBRL-TR-02329 (AD B058793L), Ballistic Research Laboratory, Aberdeen Proving Ground, MD, Jun 1981.
2. Walker, E. H. and Gibbons, G., U.S. Army Ballistic Research Laboratory, Aberdeen Proving Ground, MD, personal communication concerning shielding designs, 1983 and 1986.
3. Walker, E. H., *A Model of Antifratricide Shield Interaction with Jets Formed by Multiple Artillery Round Detonations*, ARBRL-TR-02466, Ballistic Research Laboratory, Aberdeen Proving Ground, MD, Jan 1983.
4. Howe, P. M.; Gibbons, G.; and Webber, P., "An Experimental Investigation of the Role of Shear in Initiation of Detonation by Impact," in *Eighth Symposium (International) on Detonation*, Jul 1985.
5. Howe, P. M.; Huang, Y. K.; and Arbuckle, A. L., "A Numerical Study of Detonation Propagation Between Munitions," in *Seventh Symposium (International) on Detonation*, Jun 1981, pp. 1055-1061.
6. Starkenberg, J.; Huang, Y. K.; and Arbuckle, A. L., *A Two-Dimensional Numerical Study of Detonation Propagation Between Munitions by Means of Shock Initiation*, ARBRL-TR-02522 (AD A133680), Ballistic Research Laboratory, Aberdeen Proving Ground, MD, Sep 1983.
7. Starkenberg, J.; Dorsey, T. M.; and Benjamin, K. J., "A Computational Investigation of the Effect of Shielding in Mitigating Shock Initiation Stimuli Produced by Impact," in *Eighth Symposium (International) on Detonation*, Jul 1985.
8. Starkenberg, J.; Dorsey, T. M.; and Benjamin, K. J., *A Computational Investigation of the Effect of Shielding in Mitigating Shock Initiation Stimuli Produced by Impact*, BRL-TR-2672 (AD A159506), Ballistic Research Laboratory, Aberdeen Proving Ground, MD, Sep 1983.
9. *STEALTH- A Lagrange Explicit Finite Difference Code for Solids, Structural, and Thermohydraulic Analysis*, Electric Power Research Institute, Nov 1981.
10. Lee, E. L. and Tarver, C. M., "Phenomenological Model of Shock Initiation in Heterogeneous Explosives," *Physics of Fluids*, Vol. 23, No. 12, Dec 1980, pp. 2362-2372.
11. Gibbons, G. and Walker, E. H., *A Stowage System for 120 mm Tank Gun Ammunition*, Draft Report, Ballistic Research Laboratory, Aberdeen Proving Ground, MD.

# A COMPUTATIONAL ASSESSMENT OF THE ROLL OF SHIELDING IN PREVENTING THE SYMPATHETIC DETONATION OF MUNITIONS

STARKENBERG

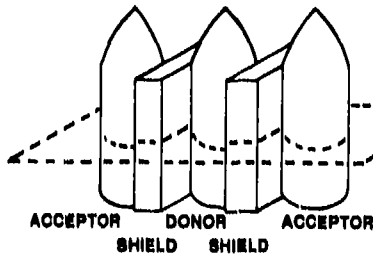
## MECHANISMS FOR SYMPATHETIC DETONATION INCLUDE . . .

shock initiation at close range  
fragment penetration at long range  
shearing flow induced by rapid deformation

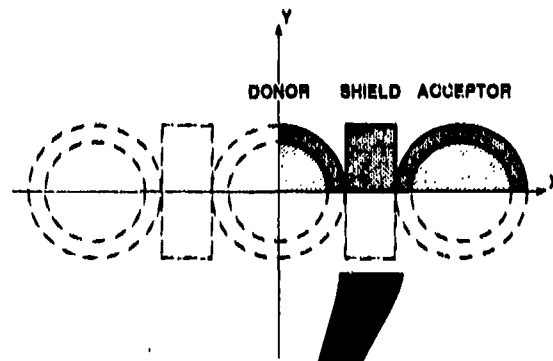
## THE INFLUENCE OF SHIELDING ON THESE MECHANISMS IS . . .

mitigation of shock strength, rise time and duration  
the prevention of discrete fragment impact  
reduction of deformation and deformation rates

## SIMULATION DESCRIPTION



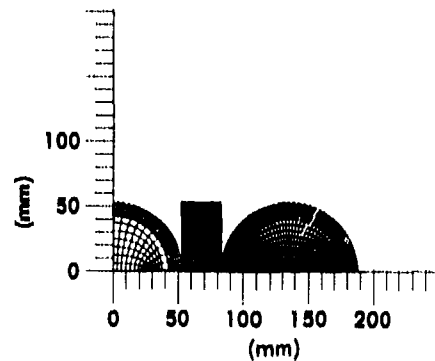
## 2-D REPRESENTATION



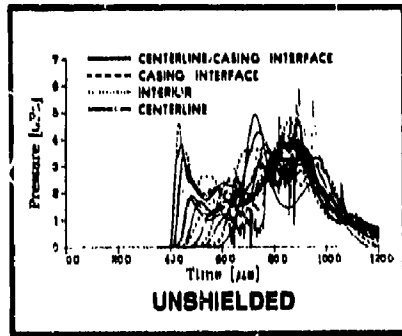
## STIMULUS CHARACTERIZATIONS

### COMPRESSION . . .

of the explosive is manifest in finite rise-time waves rather than discontinuous shocks. The loading may be characterized by the peak pressure, rise time and late time pressure at a point in the explosive just within the casing.

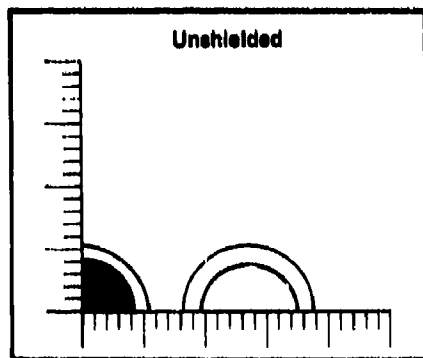
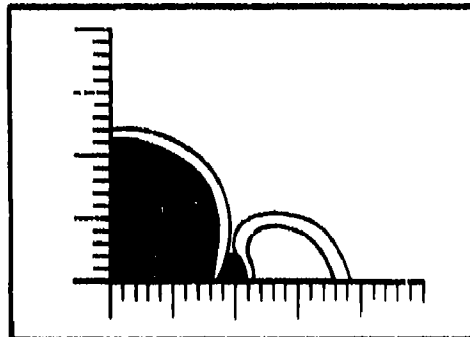
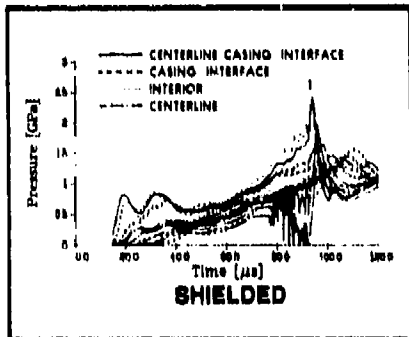


COMPUTATIONAL GRID -  
PRESSURE WAS MONITORED  
AT FILLED CELLS

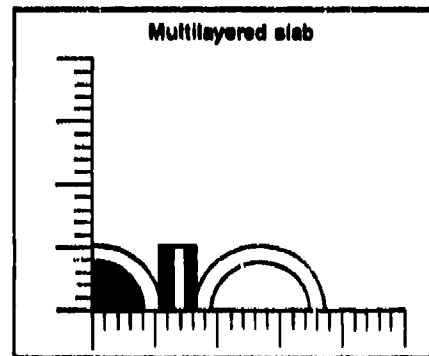
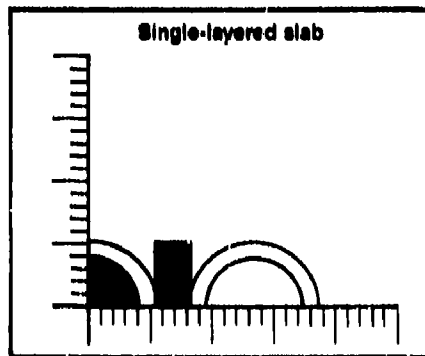
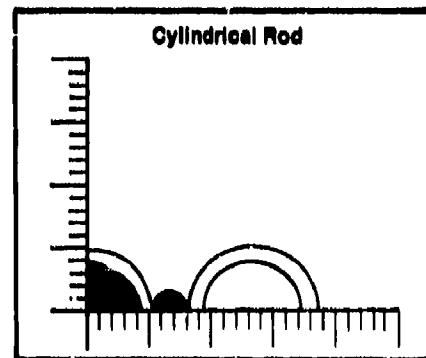


**DEFORMATION . . .**

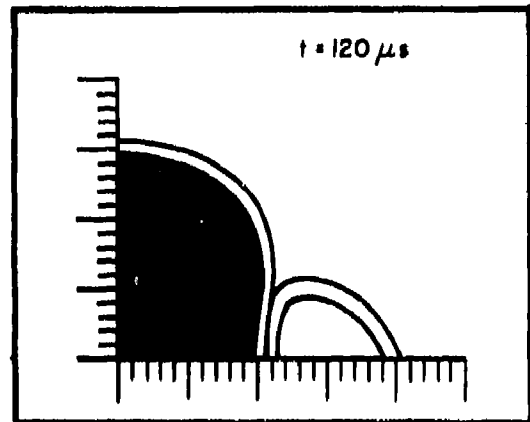
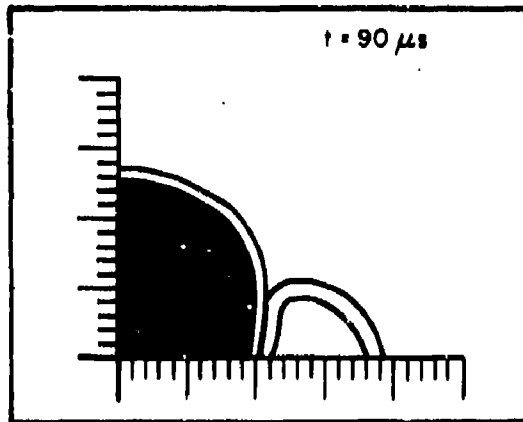
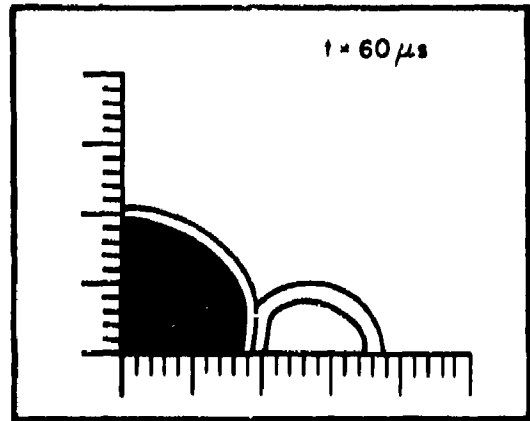
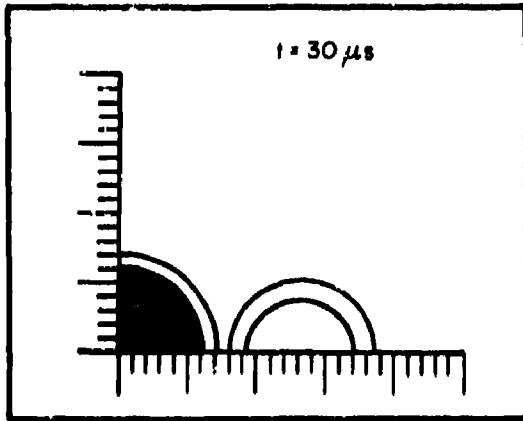
may produce shear concentrations leading to ignition of the explosive. It may be simply characterized by an engineering strain defined by the change in diameter of the acceptor fill divided by its original diameter. The average rate of deformation is another important parameter characterizing the ignition stimulus.



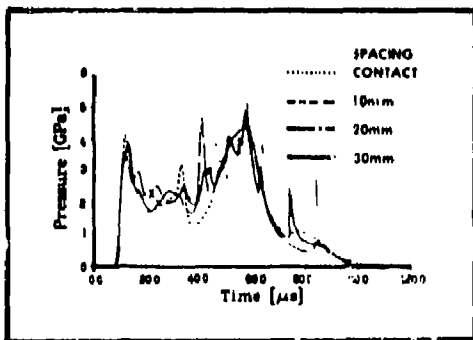
**CONFIGURATIONS**



**RESPONSE OF UNSHIELDED ACCEPTORS - EFFECT OF SEPARATION BETWEEN ROUNDS**

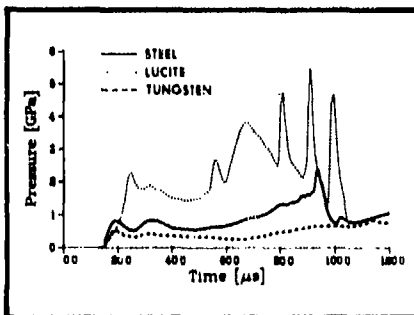
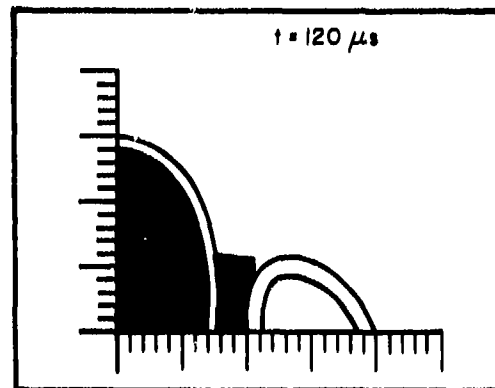
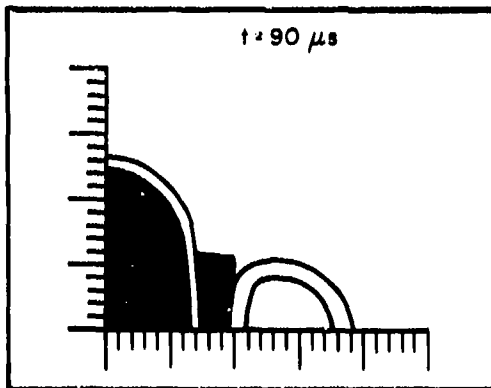
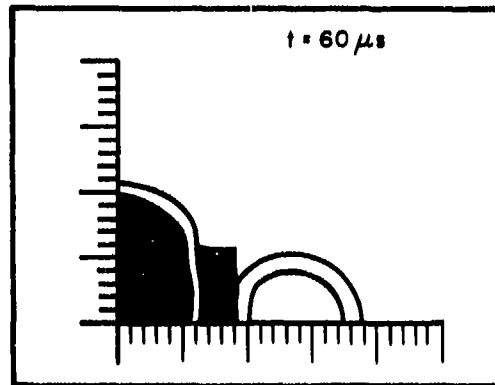
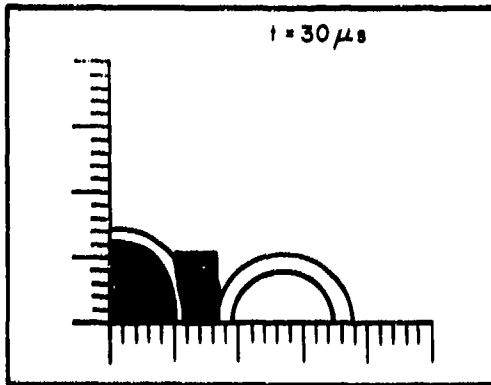


INTERROUND SEPARATION (mm)	PEAK PRESSURE (GPa)	RISE TIME ( $\mu s$ )	MAXIMUM DEFORMATION (mm/mm)	AVERAGE DEFORMATION RATE (mm/mm/ms)
0	2.4	3.9	0.196	4.63
10	4.1	2.6	0.194	5.13
20	3.5	2.2	0.186	5.13
30	3.8	3.5	0.175	5.08



Both peak pressure and average deformation rate are minimum for rounds in contact consistent with some experimental observations of suppression of sympathetic detonation for rounds in contact.

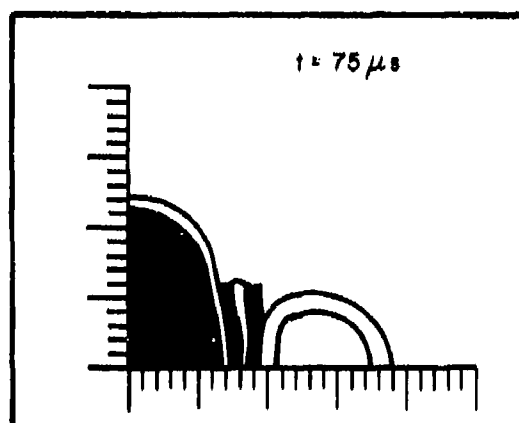
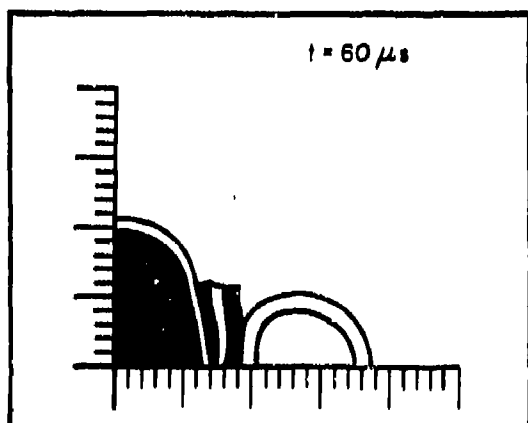
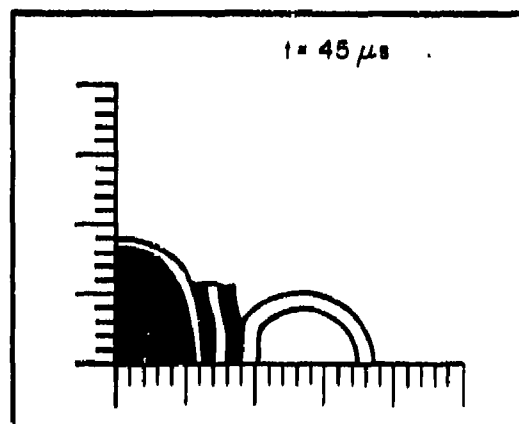
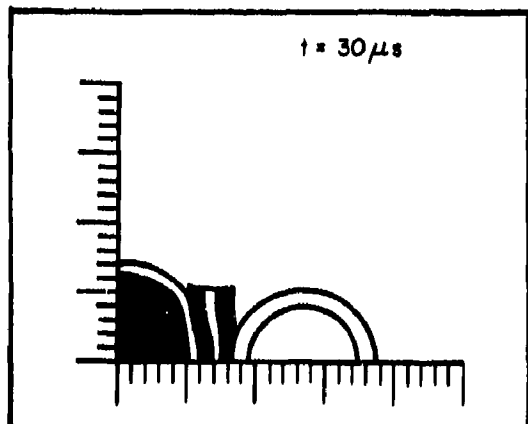
# RESULTS WITH SINGLE-LAYERED SHIELDS - EFFECT OF SHIELD MATERIAL



SHIELD MATERIAL (mm)	PEAK PRESSURE (GPa)	RISE TIME ( $\mu s$ )	MAXIMUM DEFORMATION (mm/mm)	AVERAGE DEFORMATION RATE (mm/mm/ms)
lucite	2.3	8.0	0.167	3.37
steel	0.8	4.0	0.132	1.94
tungsten	0.5	4.2	0.123	1.18

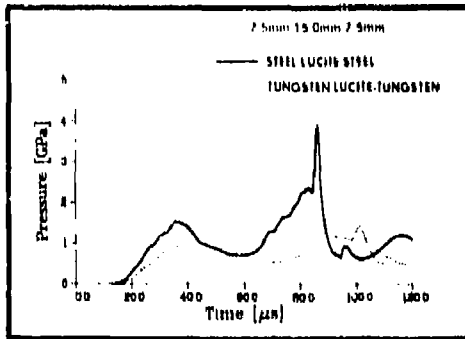
Pressures, maximum deformation, and average deformation rates generally decrease with increasing shield density

# MULTILAYERED SHIELDS



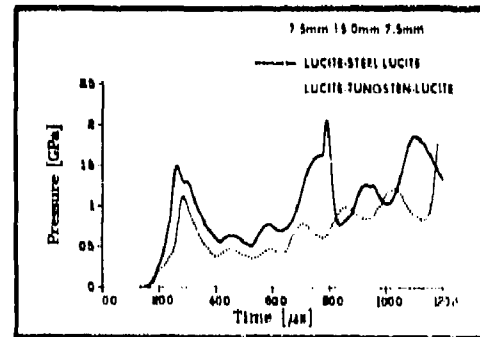
CONFIGURATION (7.5mm - 15.0mm - 7.5mm)	PEAK PRESSURE (GPa)	RISE TIME ( $\mu s$ )	MAXIMUM DEFORMATION (mm/mm)	AVERAGE DEFORMATION RATE (mm/mm/ms)
lucite - steel - lucite	1.5	7.8	0.127	2.02
steel - lucite - steel	1.5	17.1	0.138	2.46
lucite - tungsten - lucite	1.1	10.5	0.121	1.48
tungsten - lucite - tungsten	1.0	19.6	0.120	2.31

## RESULTS WITH MULTILAYERED SHIELDS - EFFECT OF SHIELD MATERIALS

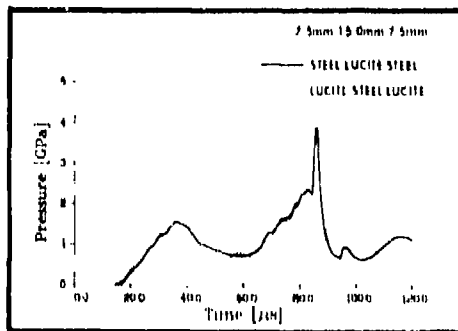


\* PRESSURES ARE GENERALLY LOWER WITH TUNGSTEN LAYERS

- \* MAXIMUM DEFORMATIONS ARE GENERALLY LOWER WITH TUNGSTEN LAYERS
- \* DEFORMATION RATES ARE GENERALLY LOWER WITH TUNGSTEN LAYERS

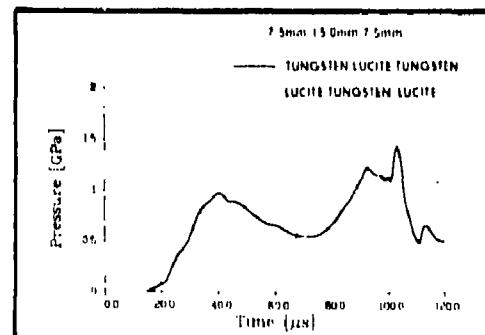


## RESULTS WITH MULTILAYERED SHIELDS - EFFECT OF MATERIAL ORDER

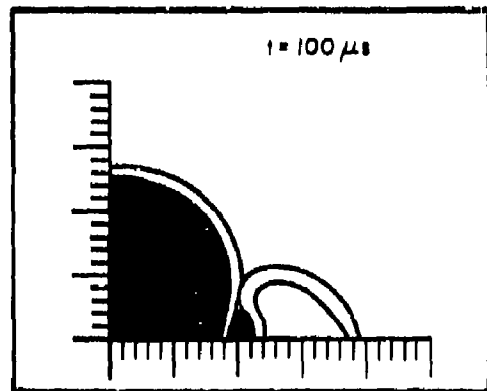
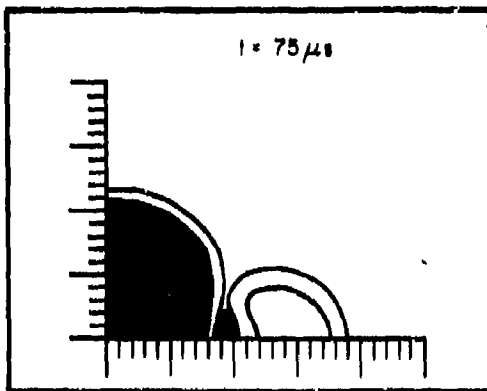
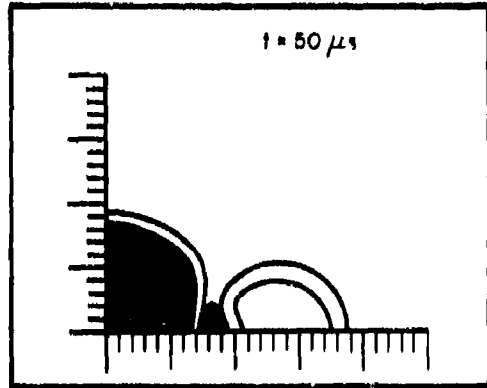
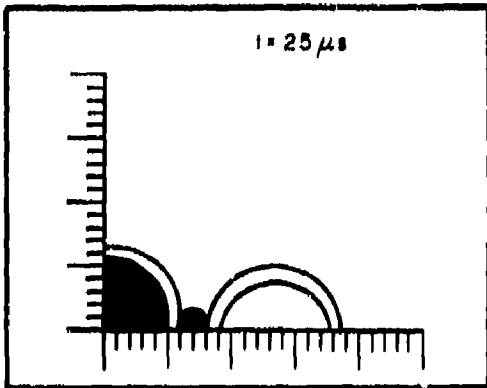


\* RISE TIMES ARE GENERALLY LONGER WITH HIGH-DENSITY OUTER LAYERS

- \* DEFORMATION RATES ARE GENERALLY LOWER WITH LOW-DENSITY OUTER LAYERS



# RESULTS WITH ROD-SHAPED SHIELDS

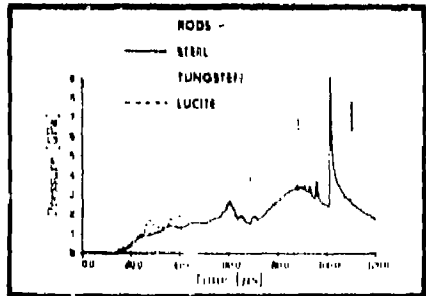


SHIELD MATERIAL (mm)	PEAK PRESSURE (GPa)	RISE TIME ( $\mu s$ )	MAXIMUM DEFORMATION (mm/mm)	AVERAGE DEFORMATION RATE (mm/mm/ms)
lucite	1.7	12.3	*	$\sim 3.9$
steel	0.9	10.0	0.242	4.02
tungsten	1.1	9.9	0.262	3.71

\* computation terminated before maximum deformation

**\* ROD SHIELDS GENERALLY PRODUCE...**

- LONG RISE TIMES
- VERY HIGH MAXIMUM DEFORMATIONS
- VERY HIGH DEFORMATION RATES
- VERY HIGH LATE-TIME PRESSURES



## **CONCLUSIONS. . . .**

- \* **PEAK PRESSURE AND DEFORMATION RATE TRENDS ARE CONSISTENT WITH EXPERIMENTAL OBSERVATIONS FOR UNSHIELDED MUNITIONS**
- \* **VERY HIGH DENSITY SHIELD MATERIALS GENERALLY PROVIDE THE GREATEST SYMPATHETIC DETONATION STIMULUS MITIGATION**
- \* **SINGLE-LAYERED SLABS PROVIDE STIMULUS MITIGATION WHICH INCREASES WITH INCREASING DENSITY EXCEPT FOR RISE TIME**
- \* **MULTILAYERED SHIELDS PROVIDE THE BEST RISE TIME AND DEFORMATION MITIGATION AND VERY GOOD PEAK PRESSURE AND DEFORMATION RATE MITIGATION**
- \* **ROD-SHAPED SHIELDS PROVIDE VERY GOOD RISE TIME MITIGATION BUT PRODUCE LARGE DEFORMATIONS AND DEFORMATION RATES AND VERY HIGH LATE TIME PRESSURE**

# OUTPUT MEASUREMENTS AND MODELING OF HNS MILD DETONATING FUSE

R. G. Jungst and M. E. Klpp  
Sandia National Laboratories  
Albuquerque, New Mexico 87185

*The explosive output characteristics of HNS in aluminum sheath mild detonating fuse (MDF) have been measured with VISAR and compared to results from HNAB in aluminum or PETN in lead sheath MDF. Peak particle velocities generated in PMMA windows by detonating HNS MDF were found to decrease for smaller sample diameters and pulse widths narrowed to approximately 0.35  $\mu$ s at half maximum for a 2-grain/foot core load. Implications of this pulse shape for acceptor initiation from MDF are discussed. A trailing peak whose separation from the detonation front increased regularly with increasing sample diameter was consistently present in the particle velocity records. Numerical calculations revealed that a reflected wave from the inner wall of the MDF sheath converges on the axis behind the detonation front to form this feature. The effect of sheath material properties and detonation front curvature on the amplitude and position of this trailing peak were also investigated.*

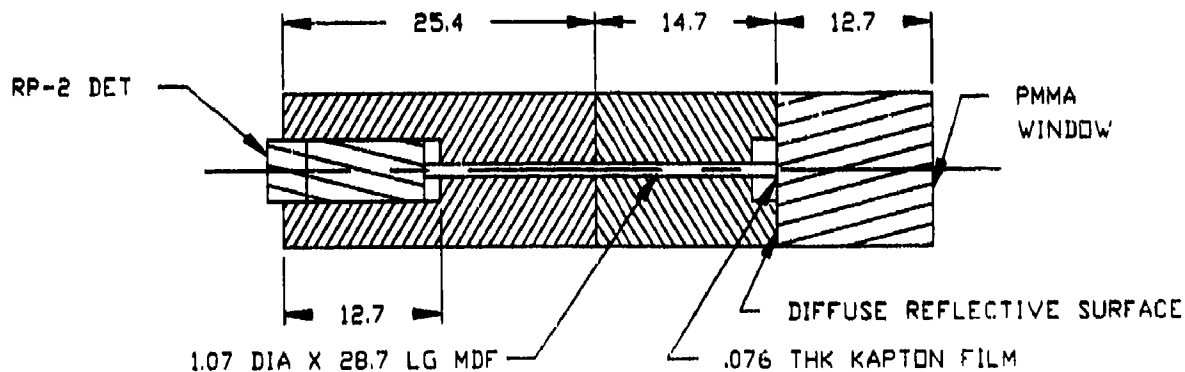
## INTRODUCTION

Mild detonating fuse (MDF) is used in a variety of applications, including explosive transfer lines, delays, and precision timing trains. The explosives PETN, RDX, HNAB and HNS are all commonly found in this type of product, but HNS is of particular interest currently due to its improved thermal stability over these other materials. In some cases, the desired explosive core load is only a few grains per foot which raises questions as to the effects of the small diameter on explosive propagation and the characteristics of the explosive output into acceptor charges. Detonation velocity (VOD) measurements on HNS MDF have shown no explosive propagation effect from reducing explosive column diameters down to 0.33 mm (a 1-grain/foot core load),<sup>1</sup> but output has not been studied in detail.

The duration of the pressure pulse produced in an acceptor from MDF would be expected to decrease as the MDF diameter is

reduced. Since the relative initiation sensitivities of acceptor explosives are commonly pulse width dependent, knowledge of the pulse shape produced by MDF would aid in selecting materials and particle sizes for acceptor charges which would optimize interface performance margins. Such information was not previously available for small diameter MDF samples, mainly because of experimental difficulties inherent in studying these small explosive cross sections.

In this work, Velocity Interferometer System for Any Reflector (VISAR) instrumentation<sup>2</sup> was used to record the particle velocity produced in PMMA windows by detonation of different core loads of HNS in aluminum sheath MDF. For comparison, samples containing HNAB in aluminum and PETN in lead were also evaluated. Numerical simulations of the experimental configuration were employed to provide insight into mechanisms responsible for unexpected structure observed on the particle velocity records.



NOTE: ALL DIMENSIONS ARE IN MILLIMETERS

Figure 1. MDF Output Test Fixture

## EXPERIMENTAL

Figure 1 shows the test fixture used in the VISAR data acquisition. All samples were initiated with RP-2 detonators. Although Figure 1 shows a piece of 2-grain /foot MDF set up for test, the same configuration bored out to a suitable diameter was used for a variety of core loads. A 2 mm length of MDF was left unsupported just in front of the window for all tests. The total length of the MDF sample was approximately 30 mm which served to isolate the results from detonator effects. Slicing with a razor blade while supporting the MDF in a metal block gave a reasonably square, flat end which would minimize air gaps at the window interface. One face of the 12.7-mm thick PMMA window was lapped to give a diffuse surface and then approximately 5000 Å of aluminum was vapor deposited on that face to provide a reflector for the VISAR laser beam. The aluminum was protected from erosion by detonation products during the shot with a 0.076-mm thick Kapton buffer.

Alignment of the VISAR laser beam on the part of the window directly opposite the explosive core of the MDF was critical to recording useful data. The laser beam diameter was about 0.25 mm at the target, which is half the diameter of the explosive core in the smallest sample studied. Since the aluminized

window is opaque, beam alignment was carried out with a clear window of the same dimensions in place. This accounts for beam skewing due to refraction in the window material. The sample fixture was held in a heavy metal block so that no movement could occur when the windows were exchanged. Repeated switching of the windows with no observable change in alignment verified that this was actually the case. A thin layer of grease around the outer edge of the window held it in contact with the fixture during test firing. Grease at the center of the window was avoided since it was found to generally cause reflected light levels to fluctuate enough during a shot that VISAR data were often lost.

A dual leg VISAR system operating at 1 mm/μs velocity per fringe was used to measure particle velocity at the PMMA window interface. For each shot, 512 data points were recorded with a time resolution of either 2 or 4 nanoseconds per point. Missing fringes needed to resolve velocity differences when reducing the two VISAR data legs were added in the first 5 ns of data.

Core loads for all the MDF samples were derived from the measured weight loss when the explosive was dissolved using dimethylformamide or acetone. The actual explosive density was calculated from this weight and

**Table 1. MDF Sample Matrix and Measured Characteristics**

Core Load (grain/foot)	Explosive	Sheath Material	Explosive Density (g/cm <sup>3</sup> )	OD (mm)	ID (mm)
1.95	PETN	Lead	1.37	1.27	0.66
2.01	HNAB	Aluminum	1.46	1.09	0.61
2.03*	HNAB	Aluminum	1.69	1.02	0.56
2.12	HNS-II	Aluminum	1.31	1.07	0.66
2.13*	HNS-II	Aluminum	1.69	1.02	0.58
10.1	PETN	Lead	1.50	2.64	1.47
14.6	HNS-II	Aluminum	1.47	2.67	1.63
19.1	PETN	Lead	1.45	3.10	2.01
29.1	PETN	Lead	1.45	3.66	2.46
79.9	HNS-II	Aluminum	1.45	5.41	3.96

\*Pressurized at 60 kpsi

the volume of the sheath cavity as determined by filling an empty piece with a fluid of known density (glycerol). The largest core load MDF would not retain glycerol long enough for a weighing, so the cavity volume in this case was obtained from the outer dimensions and a sheath volume based on the sheath weight and density.

## RESULTS AND DISCUSSION

### Visar Experiments

Table 1 lists the matrix of MDF samples which was studied with the VISAR. Figure 2 shows typical particle velocity profiles recorded when firing MDF samples containing HNS explosive. A decrease in pulse width from 1.45  $\mu$ s at half maximum in the 80 grain/foot case to 0.35  $\mu$ s for the 2-grain/foot sample was observed. The largest peak particle velocity also declined from 2.30 km/s to 1.69 km/s. Some variability was noted in the amplitude results from duplicate samples, but the pulse widths and the overall wave shape were, in general, quite reproducible. Lower particle velocities could have been caused in some cases by slight gaps at the explosive/window interface due to some roughness remaining in the explosive surface. Figure 3 compares the 2-grain/foot HNS MDF output to those from similar core loads of HNAB and PETN in MDF. The largest peak particle velocity found was similar for all three materials once

variations due to the dominant explosive core density effect were discounted. The 1.69 km/s peak particle velocity (10.4 GPa pressure) generated in the PMMA window by the 1.95-grain/foot PETN sample was unexpectedly low. PETN was predicted to generate larger particle velocities in the VISAR experiment than HNS at the same density, based on simple overlaps of detonation product adiabats with Hugoniot's for unreacted Kapton and PMMA.<sup>3</sup> At larger diameters, the experimental PETN MDF output was close to predicted values. The fact that PETN has a smaller critical diameter than HNS argues against diameter as the sole cause for the disagreement between experimental and predicted particle velocities. PETN explosive propagation should have been affected less (if at all) by the small size of the 2-grain/foot MDF than that of HNS. Table 2 gives particle velocity results for all of the samples.

The pulse widths were similar for all the 2-grain/foot samples, which was expected considering the similarity in column diameters. This width is intermediate between that typical of large booster pellets and that generated by flying plates.<sup>4</sup> This implies that the initiation sensitivities of acceptor explosives from 2-grain/foot MDF ought to also be intermediate to their sensitivities in typical long and short pulse situations. In the case of HNS, large particle size material is more sensitive to long pressure pulses such as in the

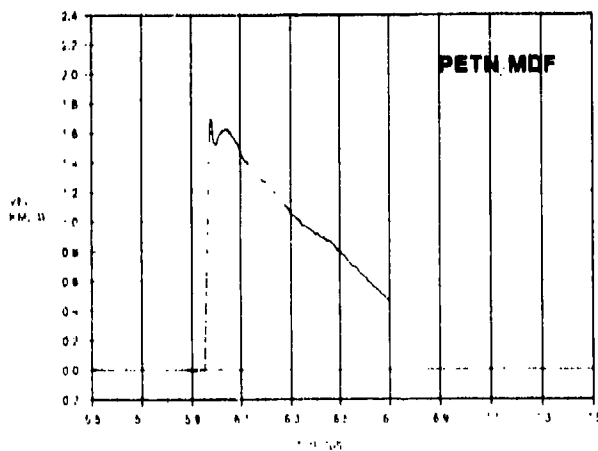
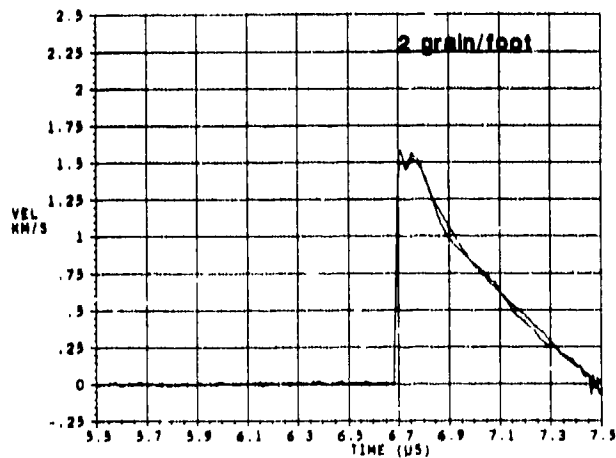
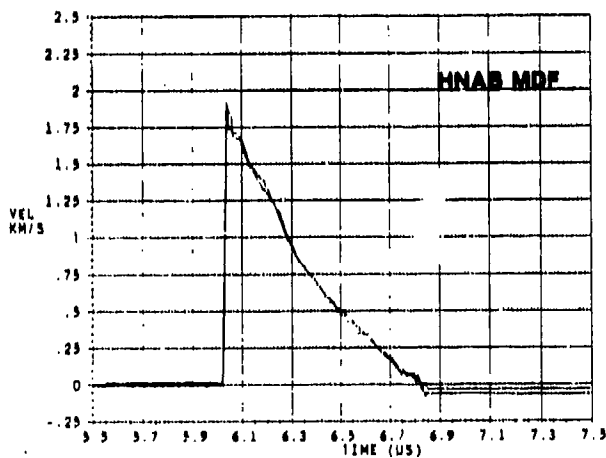
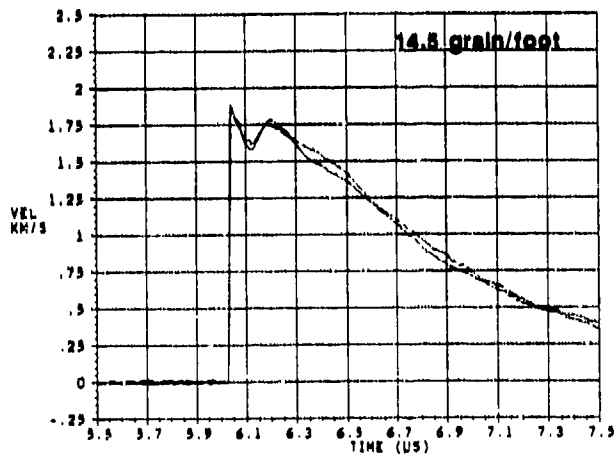
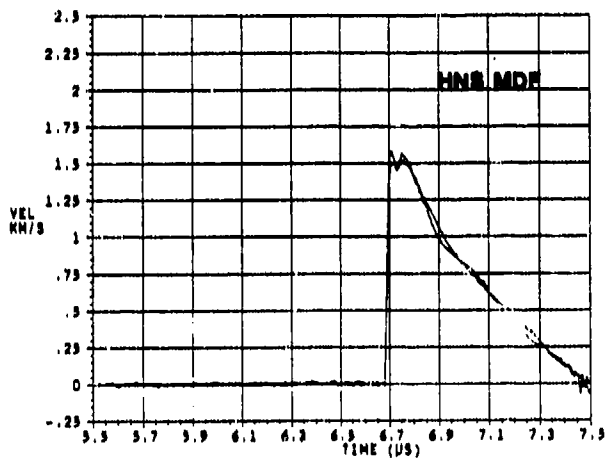
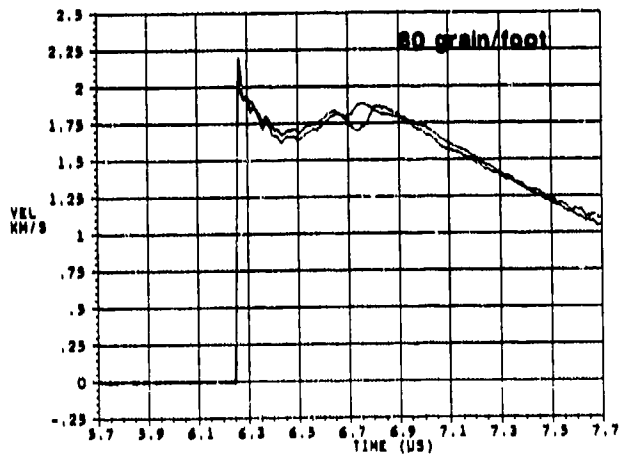


**Figure 2. VISAR Records of PMMA Particle Velocities Generated by Different Nominal Core Loads of HNS in Al MDF (Unpressurized)**

**Figure 3. Comparison of PMMA Particle Velocity Profiles Generated by 2-Grain/Foot MDF Containing Different Explosives**

**Table 2. PMMA Particle Velocities Generated by MDF Samples**

Core Load (grain/foot)	Explosive Type	Explosive Density (g/cm <sup>3</sup> )	Particle Velocity (km/s)		Pressure in PMMA (GPa)
			Predicted	Observed	
1.95	PETN	1.37	2.06	1.69	10.4
2.01	HNAB	1.46	2.06	1.91	12.5
2.03*	HNAB	1.69	2.29	2.23	15.9
2.12	HNS-II	1.31	1.76	1.69	10.4
2.13*	HNS-II	1.69	2.35	2.13	14.8
10.1	PETN	1.50	2.30	2.21	15.7
14.6	HNS-II	1.47	2.00	1.95	12.9
19.1	PETN	1.45	2.21	2.23	15.9
29.1	PETN	1.45	2.21	2.27	16.4
79.9	HNS-II	1.45	1.96	2.30	16.7

\*Pressurized at 60 kpsi

gap test, while a fine particle size has been found to perform better in short pulse cases.<sup>6</sup> Gap tests using 2-grain/foot HNS MDF donors and HNS acceptors with various particle sizes confirm that fine particle material is slightly more sensitive to the MDF output<sup>6</sup> and, therefore, this situation is near a crossover point for optimum acceptor particle size.

Pressurized samples of HNS and HNAB MDF did give higher outputs than their unpressurized analogs due to the higher explosive core densities. Pulse widths were not significantly affected by pressurization. The pressurized 2-grain/foot HNS samples contained higher explosive core densities than the 80-grain/foot HNS MDF, but the peak particle velocities were still lower in the small diameter case. This suggests a diameter effect on the peak pressure, but could also be partly caused by an inability of the VISAR to record the true peak for the sharper particle velocity profiles exhibited by the small diameter samples.

Instead of a simple detonation wave transmitted into the window, some additional structure was nearly always present on the particle velocity records. The feature consistently observed was a second peak trailing the detonation front whose position appeared related to the sample diameter as shown in Figure 4. Changing the explosive core material did not seem to affect its location

significantly. This second peak does broaden the pulse delivered, particularly for small diameter MDF, and therefore could have some influence on acceptor initiation margins. There were perceived to be two possible sources of this second peak: (1) The diagnostic technique used to obtain the particle velocity histories might be intrusive, the sample fixture itself being responsible for reflections

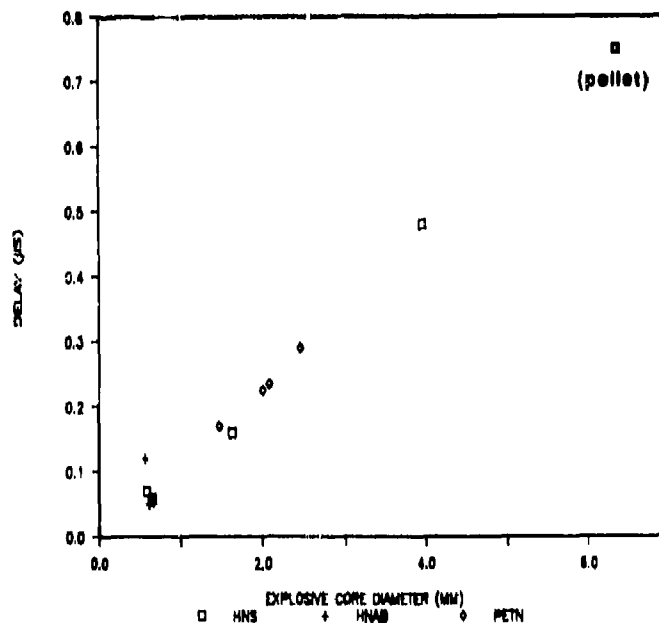


**Figure 4. Diameter Dependence of Separation of Second Particle Velocity Peak from Detonation Front**

causing the peak to form, or (2) The peak forms in the MDF and is being accurately acquired by the diagnostic technique. Developing insight as to the origin of this feature was the motivating factor for the accompanying numerical studies.

### Numerical Simulations

There were two approaches to the numerical simulations: (1) a reactive kinetics model, and (2) programmed burn techniques. A homogeneous reactive kinetics model has recently been developed for very fine-grained HNS,<sup>7</sup> and the initial modeling work focused on using this with a recent version<sup>8</sup> of the TOODY shockwave propagation code to simulate detonation in 2-grain/foot HNS MDF. The homogeneous model was developed for  $1.6 \text{ g/cm}^3$  HNS with a grain size of about 1 - 2  $\mu\text{m}$ . While this is not very similar to the 25 - 30  $\mu\text{m}$  mean grain size of the HNS-II used to initially load the MDF fill tubes, considerable fracturing of the explosive particles does occur while the MDF is being reduced to its final diameter. HNS MDF cross sections do not generally show well-defined explosive crystal boundaries, so the precise particle size in the MDF is not known. These calculations, of the 2.13-grain/foot HNS core load, showed no evidence of trailing wave formation in the MDF during steady detonation and pressure contour plots indicated that there was very little curvature of the detonation front. However, these calculations did make it clear that reflections from the window or buffer in the fixture for the VISAR experiment were not responsible for the formation of the second wave.

As a consequence of uncertainty as to whether the reactive model was really suited to analyze the behavior of this particular HNS, a programmed burn detonation definition in TOODY was used to prescribe the curvature in the detonation front. A series of calculations in which the curvature varied indicated that, as the radius of curvature decreased, there appeared on the MDF axis a trailing peak whose strength depended on the radius of curvature (Figure 5).

An example of the internal reflections that lead to this structure is shown in a

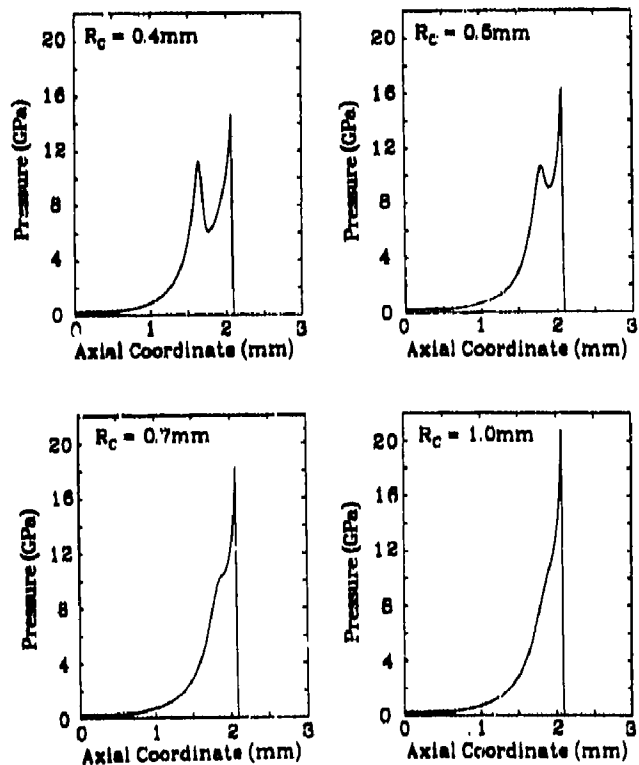
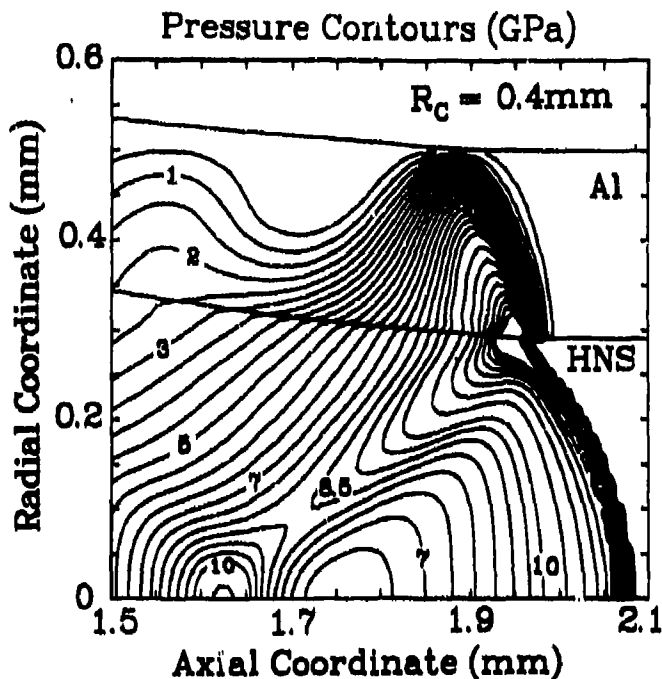
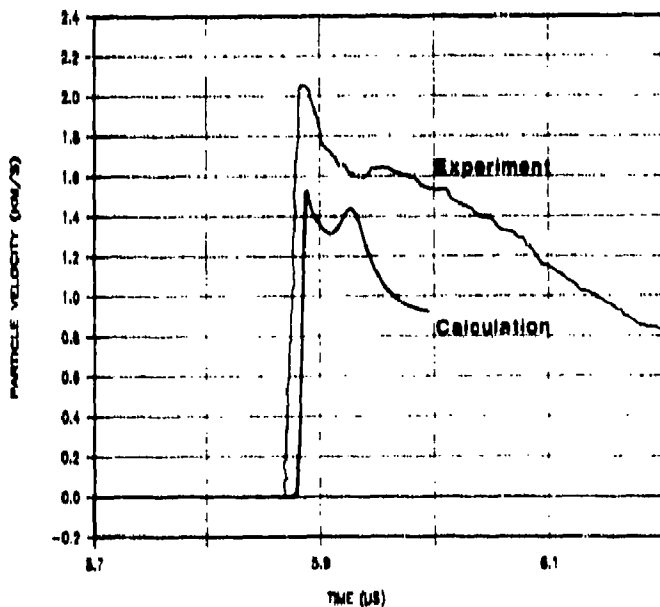


Figure 5. Calculated Pressure Contours on the Axis of 2-Grain/Foot HNS in Aluminum Sheath MDF Showing the Effect of Increasing Radius of Reaction Front Curvature

pressure contour plot in Figure 6 for the case of curvature radius 0.4 mm (the axial pressure distribution corresponds to  $R_c = 0.4$  mm in Figure 5). The interaction of the detonation front with the inner wall of the MDF sheath produces a steady reflected wave which projects rearward into the reaction products. For shallow curvature, the reflected wave amplitude is small and the waves do not extend far enough to converge on the MDF axis. At some threshold curvature, the reflected waves attain enough intensity to converge and the trailing pulse appears. The separation between the two peaks is primarily determined by the MDF core diameter, but, as illustrated in Figure 5 for 2-grain/foot samples, is also controlled by the curvature. Figure 7 compares calculated and experimental PMMA particle velocity profiles resulting from detonation of 2-grain/foot HNS MDF. Although the match is not perfect, similar pulse shapes were obtained and no attempt has been made to refine the curvature for a best fit. The amplitude of the calculated



**Figure 6.** Calculated Pressure in Detonating 2-Grain/Foot HNS in Aluminum MDF with a Detonation Front Curvature of 0.4 mm Radius. The pressure contours in one-half the axially symmetric MDF cross section show a reflected wave from the sheath wall and the trailing peak near 1.6 mm on the axis.



**Figure 7.** Particle Velocity Profile at the PMMA Window Interface from Detonating 2-Grain/Foot HNS in Aluminum Sheath MDF. Experimental VISAR record is from a pressurized MDF sample containing HNS at 1.69 g/cm<sup>3</sup> density. Calculated curve was obtained with a 0.5 mm radius detonation front and 1.6 g/cm<sup>3</sup> HNS detonation parameters.

curve is expected to be less than that of the experiment since a somewhat lower HNS density was used in the simulation. It should also be noted that the actual amplitude of the measured particle velocity could possibly be less than shown here, due to divergent wave effects in the PMMA window.<sup>9</sup> A quantitative evaluation of this is not possible without more detailed characterization of the detonation front curvature.

Additional simulations were carried out to define what combinations of sheath material properties and detonation front curvature would cause a substantial second pulse to form. The favorable combinations proved to be fairly limited. For example, maintaining a sheath material impedance similar to aluminum, but reducing the sound velocity and increasing the density (antimony material properties) significantly reduced the amplitude of the trailing pulse as shown in Figure 8. Use of PMMA as the confining material led to a detonation wave with a large curvature even with the reactive kinetics model. However, the reflected waves were of such small amplitude in this case that a second pulse did not appear to form. This is somewhat at odds with VISAR data on 6.35 mm diameter HNS pellets pressed into PMMA sleeves where a second wave was experimentally observed 0.75 μs after the detonation front.<sup>3</sup> The position of this peak followed the same diameter dependence as the MDF samples (see Figure 4). The difference in scale between the calculation with small diameter PMMA confinement and the experiments with pellets in 6.35 mm PMMA sleeves may account for the disagreement.

## CONCLUSIONS

VISAR measurements have found the output of 2-grain/foot HNS MDF to be intermediate in pulse width to pressure pulses from booster pellets and thin flying plates. Output amplitude was also somewhat reduced for small core load MDF as compared to larger diameter samples. This may at least partially be due to uncertainties in recording the initial sharp peak in the particle velocity profiles generated by small diameter samples. These results imply that fine particle HNS acceptor charges should optimize initiation margins at

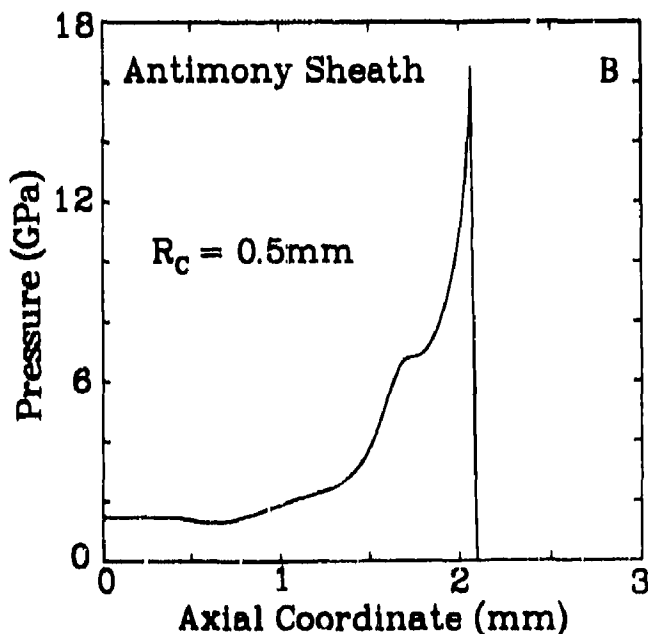
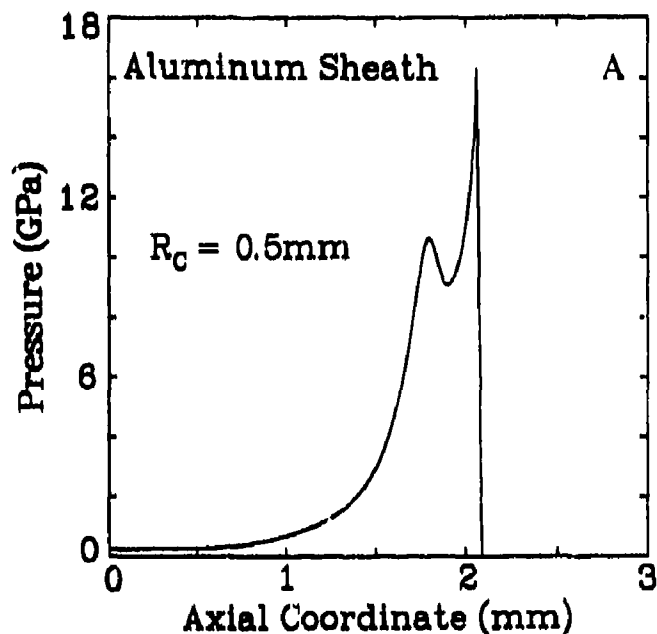


Figure 8. Calculated Pressure Profiles on the Axis of Detonating 2-Grain/Foot HNS MDF. Detonation front radius of curvature is fixed at 0.5 mm. A) Aluminum sheath; B) Antimony sheath.

interfaces with very small diameter HNS MDF donors. The beginning of this trend has been confirmed by experiments with 2-grain/foot HNS MDF. Numerical modeling of the VISAR test has revealed that a secondary pressure pulse trailing the detonation front originates within the MDF and that its relative position and amplitude are related to the particular material properties of the MDF sheath and the degree of curvature of the detonation front. This combination of measurement and simulation has led to an enhanced understanding of details regarding MDF output. In addition, MDF offers a rather unique two-dimensional test which may aid in evaluation of new reaction kinetics models for explosive detonation.

### ACKNOWLEDGEMENTS

We are pleased to acknowledge the contributions to this work by S. G. Hallett, R. D. Wickstrom, A. C. Robinson, and P. E. Kramer. This work by Sandia National Laboratories was performed with support from the U.S. Department of Energy under contract number DE-AC04-76DP00789.

### REFERENCES

1. Schwartz, A. C., *Applications of Hexanitrostilbene (HNS) in Explosive Components*, SC-RR-71 0673, Sandia National Laboratories, Albuquerque, NM, May 1972.
2. Barker, L. M. and Hollenbach, R. E., "Laser Interferometer for Measuring High Velocities of Any Reflecting Surface," *Journal of Applied Physics*, Vol. 43, 1972, p. 4669.
3. Jungst, R. G.; Hallett, S. G.; and Wickstrom, R. D., *Explosive Output Characteristics of Mild Detonating Fuse*, SAND88-0621, Sandia National Laboratories, Albuquerque, NM, Jan 1989.
4. Schwartz, A. C., *Study of the Factors Which Influence the Shock-Initiation Sensitivity of Hexanitrostilbene*, SAND80-2372, Sandia National Laboratories, Albuquerque, NM, Mar 1981.
5. Schwartz, A. C., "Shock Initiation Sensitivity of Hexanitrostilbene (HNS),"

- Proceedings of the Seventh Symposium (International) on Detonation*, U.S. Naval Academy, Annapolis, MD, 16-19 Jun 1981, pp. 1024-1028.
6. Jungst, R. G., telephone conversation with P. E. Kramer, Development Division, Pantex Plant, Mason & Hanger - Silas Mason Co., Inc., concerning MDF gap tests, 4 Apr 1988.
  7. Kipp, M. E. and Setchell, R. E., "A Shock Initiation Model for Fine-Grained Hexanitrostilbene," *Proceedings of the Ninth Symposium (International) on Detonation*, Portland, OR, 28 Aug - 1 Sep 1989.
  8. Swegle, J. W., *ARTOO—An Automatically Rezoning Two-Dimensional Lagrangian Finite Difference Wave Code*, SAND 81-2235, Sandia National Laboratories, Albuquerque, NM, Dec 1981.
  9. Wackerle, J.; Stacy, H. L.; and Dallman, J. C., "Refractive Index Effects for Shocked Windows in Interface Velocimetry," *Proceedings of SPIE, Vol. 832 High Speed Photography, Videography, and Photonics V*, San Diego, CA, 17-19 Aug 1987, pp. 72-82.



**Sandia National Laboratories**

## **OUTPUT MEASUREMENTS AND MODELING OF HNS MILD DETONATING FUSE**

**Rudolph G. Jungst and Marlin E. Kipp**  
**Sandia National Laboratories**  
**Albuquerque, New Mexico 87185**

### **MOTIVATION**

Characterize small diameter MDF donors to optimize interface margins with various acceptors in explosive trains.

### **APPROACH**

- Use VISAR diagnostics to measure particle velocity profiles generated in PMMA windows by detonating MDF.
- Model VISAR experiment to clarify the mechanism responsible for structure of the pressure pulse.

### **CONCLUSIONS**

- Pressure pulse widths generated by 2 grain foot MDF samples are intermediate to those from booster pellets or thin flying plates.
- Fine particle acceptor material is indicated to optimize the interface to very small diameter MDF donors.
- A trailing pressure pulse is observed whose position is related to the MDF diameter.
- Numerical simulations indicate that the trailing pressure pulse originates within the MDF.

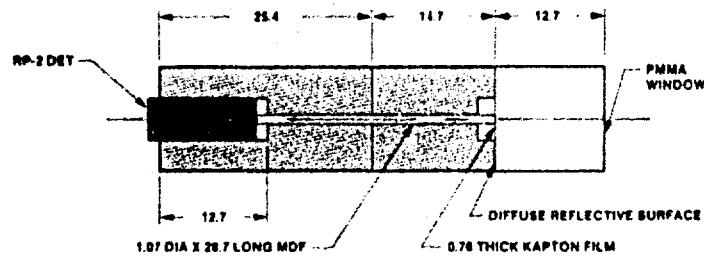
# EXPERIMENT

## Velocity Interferometer System for Any Reflector (VISAR)



Operating Parameters:  
 Laser spot size 0.25mm  
 Velocity per fringe 1mm/ $\mu$ s  
 Number of data points 512  
 Time resolution 2 or 4 ns

## MDF Test Fixture



NOTE: ALL DIMENSIONS ARE IN MILLIMETERS

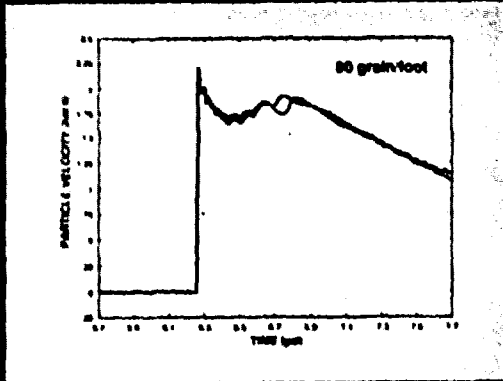
## Sample Matrix and Output Results

CORE LOAD (gr-7)	EXPLOSIVE TYPE	EXPLOSIVE DENSITY (g/cm <sup>3</sup> )	SHEATH MATERIAL	OUTER DIAMETER (mm)	INNER DIAMETER (mm)	PARTICLE VELOCITY (mm/ $\mu$ s)		PRESSURE IN PMMA (GPa)
						PREDICTED	OBSERVED	
1.95	PETN	1.37	LEAD	1.27	0.86	2.06	1.89	10.4
2.01	HNAB	1.48	ALUMINUM	1.09	0.81	2.06	1.91	12.5
2.03	HNAB	1.89	ALUMINUM	1.02	0.56	2.29	2.23	15.9
2.12	HNS	1.31	ALUMINUM	1.07	0.56	1.78	1.69	10.4
2.13	HNS	1.89	ALUMINUM	1.02	0.58	2.35	2.11	14.8
10.1	PETN	1.50	LEAD	2.64	1.47	2.30	2.21	15.7
14.6	HNS	1.47	ALUMINUM	2.67	1.83	2.00	1.95	12.8
19.1	PETN	1.45	LEAD	3.10	2.01	2.21	2.23	15.9
24.1	PETN	1.45	LEAD	3.46	2.48	2.21	2.27	16.4
79.9	HNS	1.45	ALUMINUM	5.41	3.96	1.96	2.30	16.7

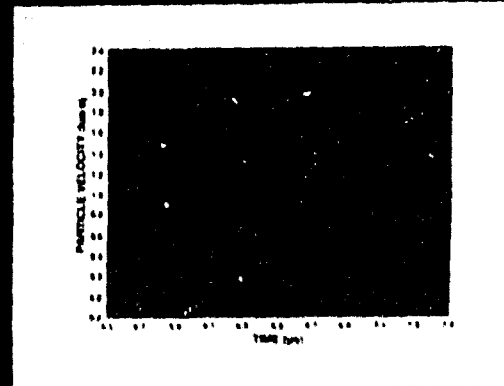
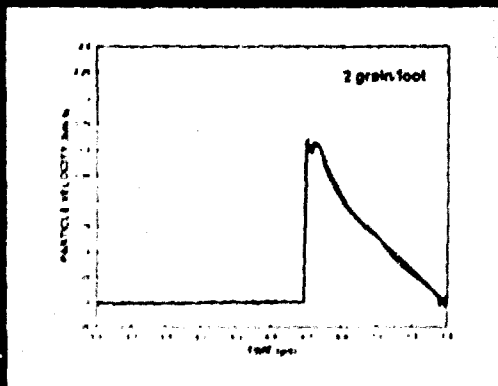
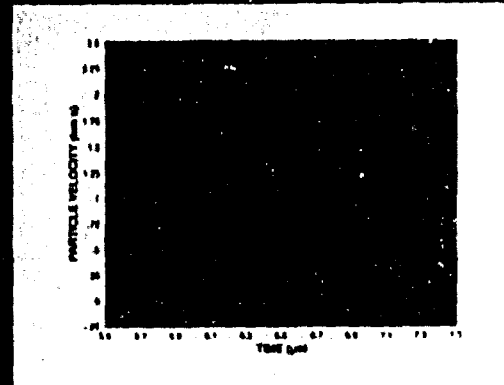
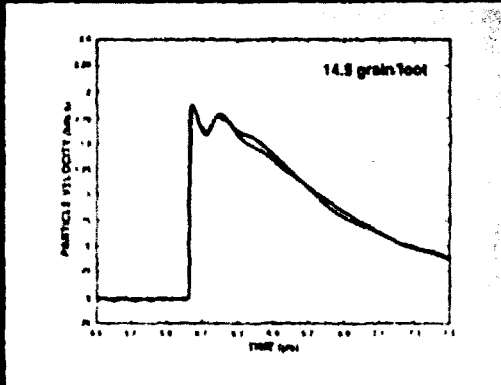
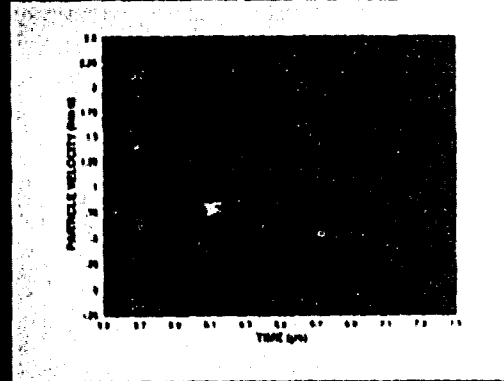
\* PRESSURIZED AT 0.41 GPa

# EXPERIMENT

**Output Amplitude and Pulse Width from HNS in Al Sheath MDP Decrease with Core Load**



**Output Shows Little Dependence on Explosive**



# SIMULATION

## 2-D Wave Propagation Studies

Code: ARTOO (J. W. Swegle, 1981)  
2-D Finite Difference, Lagrangian Code.

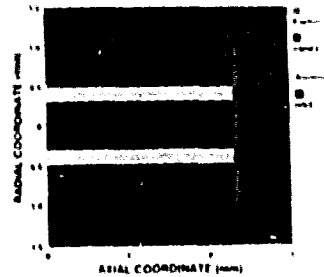
### Material Equations of State:

- HNS explosive: JWL (Jones, Wilkins, Lee)
- Solid components: Mie Gruneisen
- Programmed burn: Prescribed radius of curvature at detonation front

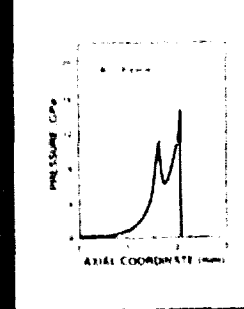
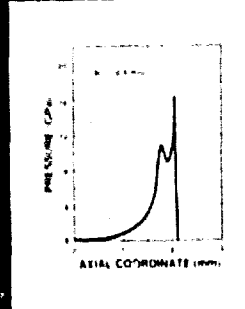
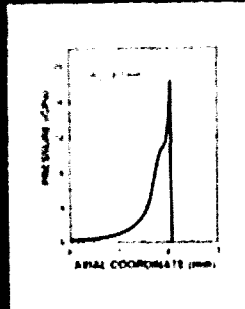
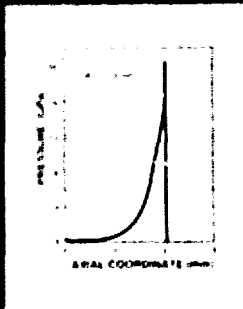
### Summary of Calculation Results:

- Formation of trailing wave not related to diagnostic window.
- Reflection of curved detonation front from tube wall forms second pressure pulse.
- Amplitude and separation of trailing wave a function of detonation front curvature and confinement material.

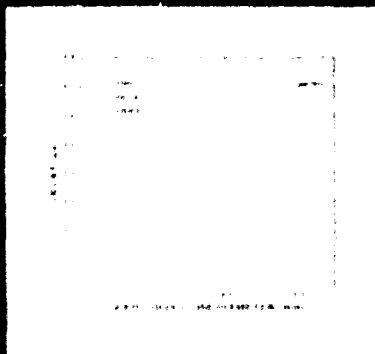
## Computational Setup



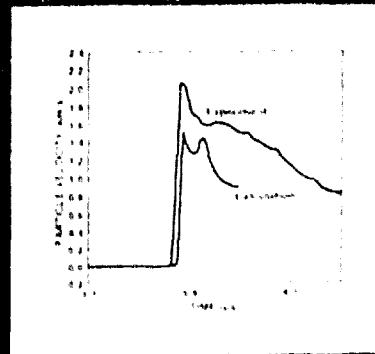
## Detonation Front Curvature Affects Calculated Shape of Pressure Wave in MDF



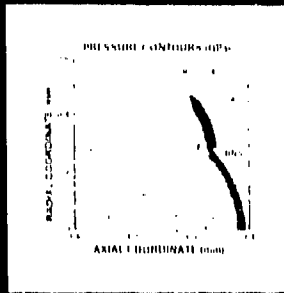
## Experimental Delay of Trailing Wave Depends on MDF Diameter



## Experimental Versus Simulated VISAR Particle Velocity from 2 Grain/Foot HNS MDF

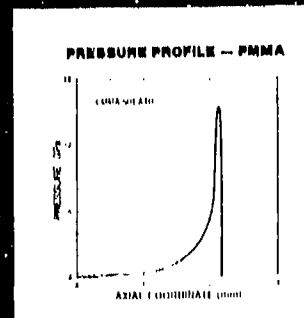
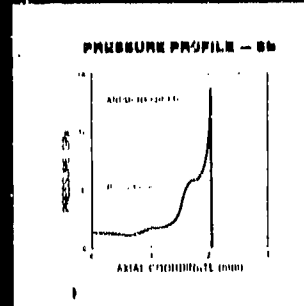
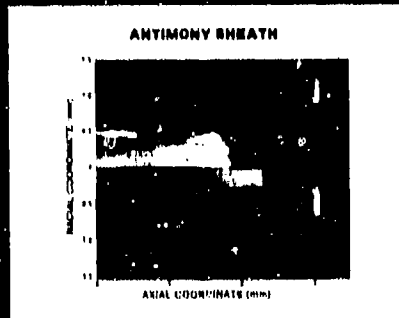
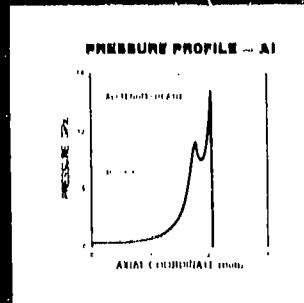
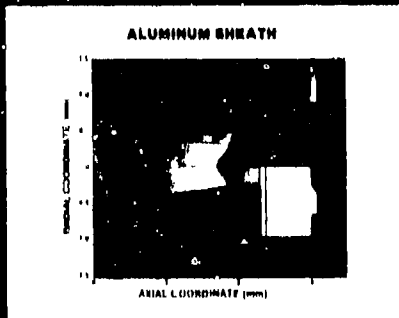


# SIMULATION



Structure on the pressure wave in the MDF results from internal reflections at the explosive/sheath interface

## Sheath Material Properties Affect the Trailing Pulse Amplitude



lets to deploy T-64 reactive armour

# JET INITIATION MECHANISMS AND SENSITIVITIES OF COVERED EXPLOSIVES



M. Chick and T.J. Brunell  
Materials Research Laboratory,  
DSTO, Melbourne, Australia.

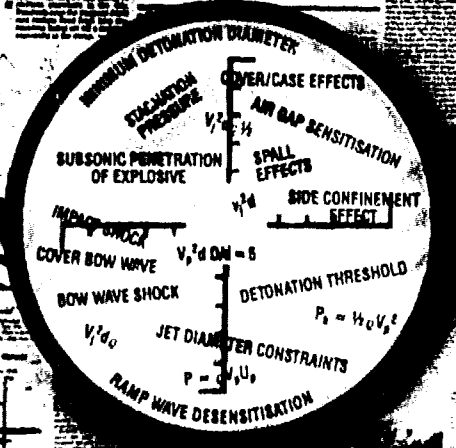
R.R. Frey and A. Bines  
Ballistic Research Laboratory,  
APG, Maryland, USA.

## STUDY OBJECTIVE

For jet strike on covered solid explosives:

1. Identify the various initiation mechanisms and their operating regimes.
2. Determine predictive criteria for the detonation threshold and any limiting conditions.

## CRACKERS FOR TOUGHER NUTS



# JET INDUCED PRESSURE PROFILES Computational Method and Results

## 1. Method

a. Jet impact pressure on target given by jet velocity, Hugoniot data and impedance matching across jet/target surface.

b. Assume bow wave velocity in cover equal to penetration velocity, given by

$$V_b = V_j \left( \frac{1}{1 + \gamma} \right)$$

c. Pressure change across bow wave shock, given by

$$P = \rho V_b^2$$

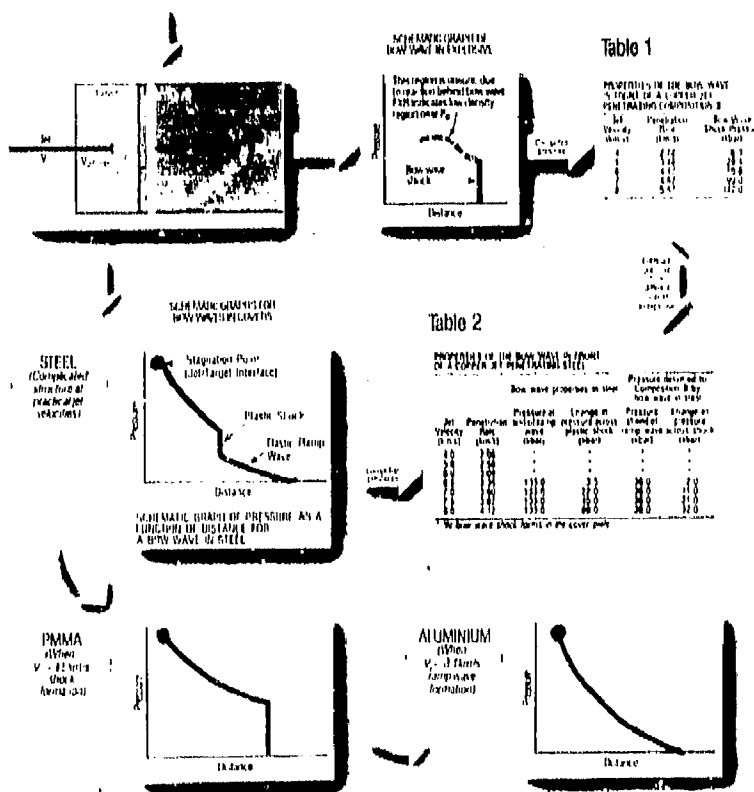
d. Bow wave pressure transmitted from rear cover surface to explosive, determined by impedance matching techniques.

e. Stagnation pressure at jet/target interface given by Bernoulli relationship

$$P_b = \frac{1}{2} \rho V_b^2$$

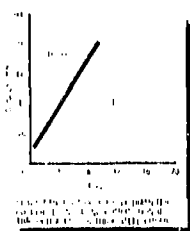
f. For jet penetration of explosive, steps 'b' and 'c' give bow wave shock pressure.

## 2. Results



## IDENTIFIED INITIATION MECHANISMS Which Ones Are Important?

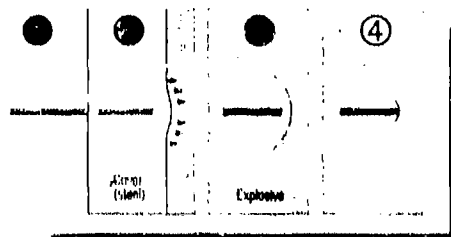
- Initiation from jet impact shock, small impact area and immediate side rarefactions limit it to covers less than a few jet diameters thick. Prediction based on Heik's  $V_p^2 d = k_1$
- Initiation from jet bow wave shock in cover transmitted into Composition B.



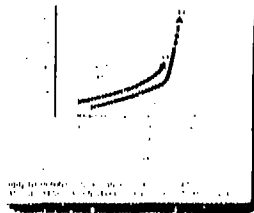
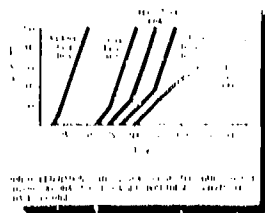
*Supported by*

- a. Detonation onset prior to jet entry into Composition B thus not from jet penetration of explosive
- b. Cover - B jet diameters thick impact shock attenuated to become subcritical
- c. Computed pressure in Composition B = 17 kbar - Similar to shock initiation pressures from other tests
- d. Unlikely to determine detonation threshold

- Initiation by jet penetration bow wave in explosive
  - a. Tables 1 and 2 show bow wave formed in explosive has a greater pressure than that transmitted from a bow wave in steel.
  - b. Although stagnation pressure is higher than bow wave pressure, it occurs too late (few  $\mu$ s), critical bow pressures are sufficient to cause initiation, subcritical bow waves may cause desensitisation of explosive. Predictive criteria are based on:  
our  $V_p^2 d = k_1$  or  $V_p d^{1/2} = k_2$



- ④ Initiation by subsonic jet penetration of Composition B.
  - a. Indicated by sharp jump to a very long run to detonation, penetration velocity reduced to sonic point (2.5 to 2.7 km/s).
  - b. Suggests change from shock to detonation to detonation initiation.
  - c. Occurs for larger diameter jets and may be the upper limit for  $V_p^2 d = k$  type predictive equations



# QUERIES

## 1. How do small diameter jets fit the picture?

### a. BARE EXPLOSIVES

Normally initiated by impact shock but here we present support for a proposal that in some situations it is replaced by jet penetration bow wave initiation. The transition can be linked to the ratio of jet diameter and minimum detonation diameter.



FLASH RADIOGRAPHIC SEQUENCE OF A 0.25mm DIAMETER COPPER JET PENETRATING BARE H-6 CLOSE TO THE DETONATION THRESHOLD CONDITION

### b. PREDICTIVE CRITERIA

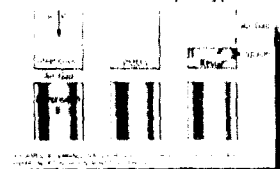
Critical velocities for 0.75mm diameter copper jet bow wave initiation.

$$\text{Steel covered Composition B: } V_j = 6.0\text{km/s} \rightarrow V_j^{2.2} d = 40\text{mm}^3/\mu\text{s}^2$$

$$\text{Bare H-6: } V_j = 5.5\text{km/s} \rightarrow V_j^{2.3} d = 36\text{mm}^3/\mu\text{s}^2$$

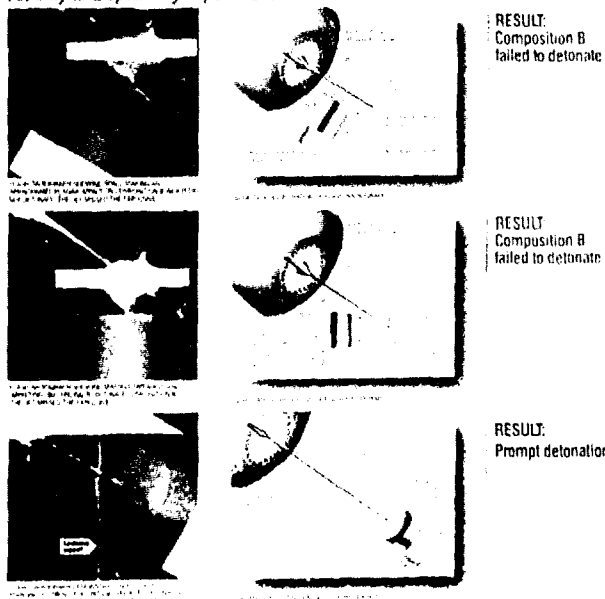
## 2. Does spall contribute to behind-the-plate jet initiation?

### a. Effect of variation of spall type on critical jet velocity.



Spall system	Critical jet velocity (km/s)	
	Steel covered	Bare H-6
Steel only	6.0	5.5
Steel with H-6A	5.5	5.0
Steel with H-6B	5.5	5.0
Steel with H-6C	5.5	5.0
Steel with H-6D	5.5	5.0
Steel with H-6E	5.5	5.0

### b. Jet only and spall only experiments.



THUS SPALL DOES NOT CONTRIBUTE TO JET INITIATION OF COMPOSITION B AT THE DETONATION THRESHOLD - IT CAN BE IGNORED IN PREDICTIVE CRITERIA AND HAZARD ANALYSIS.

SOVIET INTELLIGENCE  
 COUNCIL OF THE USSR  
 Soviet reactive tank armour updated

# CONCLUSION

Soviet Armour in Transitional Efforts Focused on Automated Systems

Soviets to deploy 1

## LIKELY INITIATION MECHANISMS and OPERATING CRITERIA

Results relative to some variables are shown in the following graphs. The graphs show the relationship between the velocity of the jet and the diameter of the jet. The graphs show that the velocity of the jet is a function of the diameter of the jet. The graphs show that the diameter of the jet is a function of the velocity of the jet. The graphs show that the velocity of the jet is a function of the diameter of the jet. The graphs show that the diameter of the jet is a function of the velocity of the jet.

The graphs show the relationship between the velocity of the jet and the diameter of the jet. The graphs show that the velocity of the jet is a function of the diameter of the jet. The graphs show that the diameter of the jet is a function of the velocity of the jet. The graphs show that the velocity of the jet is a function of the diameter of the jet. The graphs show that the diameter of the jet is a function of the velocity of the jet.

The graphs show the relationship between the velocity of the jet and the diameter of the jet. The graphs show that the velocity of the jet is a function of the diameter of the jet. The graphs show that the diameter of the jet is a function of the velocity of the jet. The graphs show that the velocity of the jet is a function of the diameter of the jet. The graphs show that the diameter of the jet is a function of the velocity of the jet.

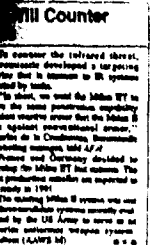
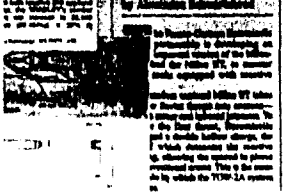
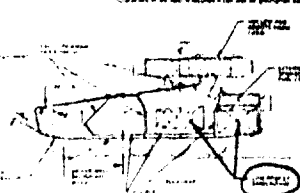
MECHANISM	REGIME AND PREDICTIVE CRITERIA
1. Jet impact on bare explosive	<ol style="list-style-type: none"> <li>1. Detonation threshold determined by M. Heil's <math>V/d = k_1</math></li> <li>2. Occurs promptly close to explosive surface or not at all.</li> <li>3. Does not apply to jets with diameters small with respect to receptor explosive's minimum diameter for detonation, where jet penetration bow wave initiation occurs (see 4 below).</li> </ol>
2. Jet impact shock on cover	<ol style="list-style-type: none"> <li>1. Only for covers less than a few jet diameters thick</li> <li>2. Requires increasing critical jet velocity with cover thickness above that predicted by <math>V/d = k_1</math> (see 1 above)</li> </ol>
3. Jet bow wave in cover transmitted into explosive	<ol style="list-style-type: none"> <li>1. Applies to thin covers</li> <li>2. Appears to require the formation of a bow wave shock in cover.</li> <li>3. Hindered by ramp wave formation in cover which is desensitizing.</li> <li>4. Other mechanisms will generally determine detonation threshold limit.</li> </ol>
4. Jet penetration of explosive	<ol style="list-style-type: none"> <li>1. Considered to be a major mechanism. Initiation by the jet penetration bow wave shock.</li> <li>2. Occurs over a wide range of cover thicknesses and materials.</li> <li>3. Within certain jet diameter limits detonation threshold predicted by <math>V/d = k_2</math> or <math>V/d = k_3</math> or <math>V/d = k_4</math>. Constants are much different to <math>k_1</math> in mechanism 1 listed above.</li> <li>4. Also applies to bare explosives where jet diameter small with respect to receptor explosive's minimum detonation diameter.</li> <li>5. Predictive criterion for small diameter jets appears to require an exponent for the velocity term greater than 2.</li> </ol>
5. Jet penetration bow waves reflected back into explosive filling	<ol style="list-style-type: none"> <li>1. Observed near critical jet initiation velocity for receptor charges of limited geometry</li> <li>2. Requires confining rear surface, may be applicable to small confined rounds.</li> <li>3. Special case of mechanism 4</li> </ol>
6. Subsonic jet penetration of explosives	<ol style="list-style-type: none"> <li>1. Applicable to larger diameter jets</li> <li>2. Appears to be associated with a very long run to detonation.</li> <li>3. Limits the use of <math>V/d = k_1</math> (see 4 above) for predicting detonation threshold.</li> <li>4. No predictive criterion available for detonation threshold.</li> </ol>
7. Separate impacts from particulated jet penetration of explosive	<ol style="list-style-type: none"> <li>1. May require well separated jet particles</li> <li>2. Does not appear to have been studied</li> </ol>

ARMOUR PERSONNEL  
 in fact, the Soviet Army is not a homogeneous force. It is a collection of units with different levels of training and equipment. The Soviet Army is a collection of units with different levels of training and equipment. The Soviet Army is a collection of units with different levels of training and equipment. The Soviet Army is a collection of units with different levels of training and equipment.

ARMOUR PERSONNEL  
 in fact, the Soviet Army is not a homogeneous force. It is a collection of units with different levels of training and equipment. The Soviet Army is a collection of units with different levels of training and equipment. The Soviet Army is a collection of units with different levels of training and equipment. The Soviet Army is a collection of units with different levels of training and equipment.

ARMOUR PERSONNEL  
 in fact, the Soviet Army is not a homogeneous force. It is a collection of units with different levels of training and equipment. The Soviet Army is a collection of units with different levels of training and equipment. The Soviet Army is a collection of units with different levels of training and equipment. The Soviet Army is a collection of units with different levels of training and equipment.

ARMOUR PERSONNEL  
 in fact, the Soviet Army is not a homogeneous force. It is a collection of units with different levels of training and equipment. The Soviet Army is a collection of units with different levels of training and equipment. The Soviet Army is a collection of units with different levels of training and equipment. The Soviet Army is a collection of units with different levels of training and equipment.



# DETONATOR RESPONSE MEASUREMENTS WITH A STANDARDIZED PIEZOELECTRIC POLYMER (PVDF) GAUGE

L. M. Moore

Explosive Projects and Diagnostics Division, 2514

R. A. Graham

Structural Physics and Shock Chemistry Division, 1153

R. P. Reed

Field Measurements Division, 7116

Sandia National Laboratories

P.O. Box 5800

Albuquerque, New Mexico 87185

and

L. M. Lee

Ktech Corporation

901 Pennsylvania Avenue, NE

Albuquerque, New Mexico 87110

*Time-resolved measurements of pressure profiles from the detonation of explosive devices can provide critical information on device performance. The special problems presented by the small size of the piezoelectric polymer gauges and nonplanar impacts are studied over a range of impact conditions. The response of PVDF gauges under precisely controlled impacts shows highly reproducible results to pressures of 20 GPa. Under approximately planar loading with small detonator flyer plates, the PVDF signals appear to be reduced by about 15 percent. For highly nonplanar flyer impacts the PVDF signals are reduced by about 35 percent. In all stress environments, high quality, time-resolved current pulses are observed.*

## INTRODUCTION

Knowledge of the response of explosives and explosive devices is, in large part, based on measurements describing the detonation process or the resulting stress pulses produced by the explosive event. Although relatively crude measurements can be used to indicate that a detonation event has occurred, modeling of detonation processes and quantitative design of explosive devices requires time-resolved measurement. At present, most of the time-resolved observations are made with particle velocity measurements with the VISAR or electromagnetic particle velocity gauges, or stress measurements with the Manganin or other piezoresistant gauges.<sup>1</sup>

Over the last few years, there has been considerable work in progress to study the features of the piezoelectric polymer film polyvinylidene fluoride (PVDF) under high pressure shock loading.<sup>2-4</sup> Although full characterization of the material is not complete, it is clear that if the material is prepared with careful attention to the mechanical processing (stretching) and to the electrical processing (electrical poling), highly reproducible responses can be achieved to shock pressures of over 40 GPa. The range of pressure accessible for measurement, the unobtrusive nature of the thin film, the simplicity of the circuitry, and the large signal levels from such PVDF gauges are highly desirable features for a

gauge. In addition, if the output of the gauge is monitored in a "current mode," the measured current provides a measure of the stress-rate. Thus, a far more sensitive measure of details of the stress profile can be obtained with PVDF than heretofore possible.

Present interests in detonator performance require measurements over dimensions smaller than about 5 mm; thus, a gauge for such a measurement must not be larger than about 1 mm. With a typical film thickness of 25 microns, two-dimensional electrical field fringing is expected to influence both the electrical poling process in gauge preparation and gauge measurements.

The purpose of the present study is to characterize the shock-compression response of a 1 mm x 1 mm active area PVDF gauge that is subject to standardized gauge-preparation processes. The shock response is studied in both compressed-gas gun, controlled impact loading, and in detonator loading configurations. In the present paper, a brief summary of standardization processes will be described, followed by a description of the controlled impact loading and the detonator-response measurements.

## PVDF PIEZOELECTRIC POLYMER MATERIAL<sup>5</sup>

Although a chemical characterization of the present material as PVDF indicates a common basis for a starting material, it does not adequately describe electrical, mechanical, and other physical properties. Both mechanical and electrical processing have a strong influence on the structure of PVDF. The piezoelectric and pyroelectric properties desired for most uses of the polymer derive from processing that produces a polar crystalline phase, designated  $\beta$  phase. Well prepared film may have up to 50 percent crystalline material, but the composition of any film depends upon the mechanical processing which is accomplished with mechanical stretching. The largest concentrations of  $\beta$ -phase PVDF are achieved with biaxial stretching, which has been found to be essential to produce high quality film.

Once formed by the mechanical treatment, the  $\beta$ -phase crystallites must be aligned

electrically to achieve a state of remanent ferroelectric polarization. As a typical ferroelectric, the treated film has physical properties controlled substantially by the remanent polarization, which may typically vary from 2 to  $9 \mu\text{C}/\text{cm}^2$ . Even in a high remanent-polarization state, it should be recognized that the film is heterogeneous, both mechanically and electrically, due to the presence of both amorphous and  $\beta$ -phase material and internal fields due to heterogeneous distribution of polarization. At best, high quality PVDF film is substantially more complicated than piezoelectric crystals, such as quartz<sup>6</sup> or lithium niobate,<sup>7</sup> which have been used in the past for time-resolved measurements of shock-compression stress pulses.

In order to achieve a highly reproducible material, Francois Bauer of the Institut de Saint-Louis in France has developed a patented process<sup>8-9</sup> to electrically treat good mechanical-quality PVDF film to achieve a reproducible and internally uniform state of electrical polarization. As shock gauges are destroyed in use and must be studied over an extended period of time to characterize the response, such reproducible starting material must be in hand before a credible shock gauge can be developed. In a cooperative program with Bauer, our laboratory has worked to standardize a PVDF gauge sensing element and carry out its characterization under high pressure shock loading. As there is no unique set of properties for PVDF without specifying the processing, it is necessary to designate a particular grade of PVDF which follows the processing procedures recommended by Bauer.

## STANDARDIZED PVDF GAUGE

The principal features of the standardized Bauer PVDF shock gauge are:

1. High quality, biaxially-stretched PVDF film.
2. Polymer film thickness of nominally 25 micron.
3. Sputtered gold-over-platinum strip electrodes and leads.
4. Remanent ferroelectric polarization of  $9.2 \mu\text{C}/\text{cm}^2$ .

5. Quantitative specification of physical and electrical characteristics.
6. Bauer electrical poling process.

For the gauge elements of the present report, the film was formulated and biaxially-stretched by the Rhone Poulenc Company of Lyon, France, in a batch of material designated RPA by our working group. The electrode plating and electrical poling was carried out by the Metravib Company of Lyon, France at a laboratory in Saint-Louis, France. A batch of 100 gauges was produced with a remanent polarization of  $9.15 \pm 0.15 \mu\text{C}/\text{cm}^2$ ,  $d_{33} = 20.2 \pm 1.4 \text{ pC}/\text{N}$  and relative dielectric constant  $12.7 \pm 0.7$ . Both controlled projectile impact and detonator response studies were carried out on this batch of gauges. Other batches of biaxially-stretched film from this supplier have been found to achieve the standardized polarization and other material constants within similar ranges.

## COMPRESSED-GAS-GUN EXPERIMENTS

The experimental arrangement used to characterize the Bauer PVDF gauge elements is similar to that used previously for study of quartz<sup>6</sup> and lithium niobate<sup>7</sup> gauge crystals, in that standard materials are used for impactors and targets under planar low-tilt projectile impact configurations. Impact velocities are measured to an accuracy of less than 0.1 percent. A schematic drawing of the arrangement is shown in Figure 1.

For the stress range from about 2 to 7 GPa, z-cut quartz crystals are used as impactors and targets for standards to establish the stress imposed on the PVDF. For the stress range of about 5 to 18 GPa, z-cut sapphire crystals are used for standards. These two crystalline materials remain elastic to stresses approaching 20 GPa. With the use of such high quality single crystals, material properties are reproducible within a few tenths of a percent and the release-wave behavior is not influenced by elastic-plastic response. For stresses less than 2 GPa, the polymer Kel-F is used as the standard. Although reproducibility of shock properties of such a polymer will not approach that achieved by quartz and sapphire, there is sufficient data in the literature to support an

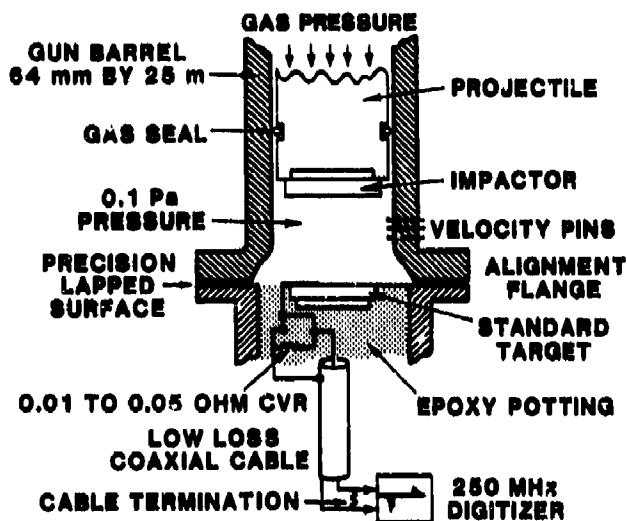


Figure 1. Impact Loading Configuration

accurate stress calculation. Kel-F matches the shock impedance of PVDF to a good approximation. At stresses higher than 20 GPa, a tungsten carbide, Kennametal 68, is used for the standard. The properties of this material are under study.

To achieve well-defined impact conditions, the gauge elements are bonded directly on the impact surfaces of the targets. For the tungsten carbide targets, a 12 micron thick film of PTFE (Teflon) is placed on either side of the PVDF film for electrical insulation. PTFE does not shock-polarize at the stress levels encountered. In this configuration, the gauge element is subjected to an initial stress determined by the shock impedances of the impactor and gauge element and, subsequently, "rings-up" to a final pressure determined by the shock impedances of the target and impactor. At low pressure, the transit time is typically 11 nsec, and at higher pressure, the time is typically 5 nsec. Because the loading is rapid relative to the transit time, the loading in this configuration produces a lower temperature rise from shock-induced heating than in a direct shock to the peak pressure.

The electrical response of the PVDF elements is recorded on LeCroy 6880 digitizers with a digitizing rate of 0.742 nsec, a vertical resolution of 8 bits and a frequency response of 250 MHz. Other digitizers have been found to be inadequate to accurately record the very

rapidly varying signals. Signals are transmitted from the gauge element to the digitizer through a length of about 13 meters of Andrews LDF-50; a low-loss coaxial cable (2.4 dB/100 feet at 1 GHz).

The recorded current-versus-time pulses are integrated and processed in a special data-reduction program which has been compared to another program developed independently by Bauer. Comparison of data processed by either program has been found to agree within a range of  $\pm 2$  percent.

A summary of the experimental configurations and piezoelectric response data is shown in Table 1. The plot of shock-induced piezoelectric current observed at various peak shock pressures is shown in Figure 2 for  $1 \text{ mm}^2$  active area gauges studied in this work. For comparison, earlier reported data on larger gauges ( $9 \text{ mm}^2$  active area) which are much less influenced by electrical field fringing are shown.

## DETONATOR RESPONSE EXPERIMENTS

Two types of detonators were used in this series of experiments. Both devices use the explosive compound 2-(5-cyanotetrazolato) pentaamminocobalt (III) perchlorate (abbreviated CP<sup>10</sup>) which undergoes a deflagration-to-detonation transition (DDT<sup>11</sup>). The first device to be tested will be referred to as the Mod E test detonator.<sup>12</sup> It was designed to meet the need for a relatively simple test device which could be used for studies of design parameters for the application of the explosive CP. The detonator consists of two pressings of energetic material in the igniter region and four in the output region for a nominal total mass of 130 milligrams. The second device to be tested will be referred to as the 4 mm (the diameter of the flyer) system detonator. Also, six pressings of CP are used in this detonator. There are three pressings in the igniter region and three in the output region for a nominal total mass of 180 milligrams of CP.

### Experimental Arrangements

A fixture has been developed to precisely mount and align the PVDF gauge and the detonator. Figure 3 shows an exploded component

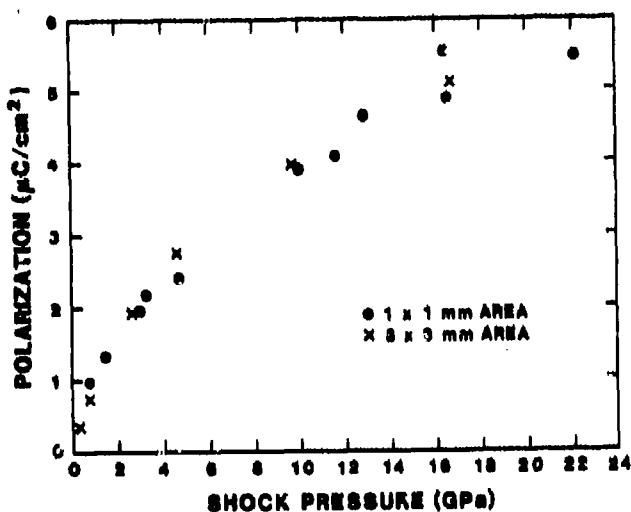


Figure 2. PVDF Gauge Charge as a Function of Stress

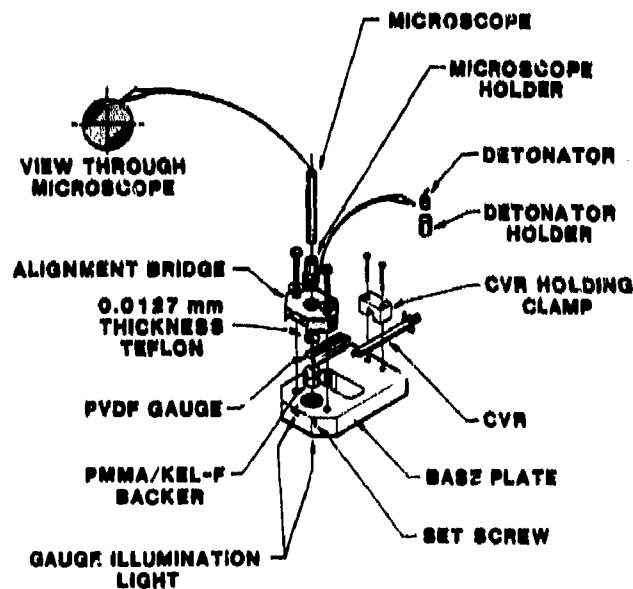


Figure 3. Mounting Fixture for Detonator and PVDF Gauge

view of the gauge assembly, the base plate, and the alignment bridge. A 12 micron thick Teflon film is used to electrically isolate the gauge from the stainless-steel closure disk placed on the end of the detonator. A thin-film Hysol epoxy (2038 resin and 3404 hardener) is used to bond the Teflon film to the gauge, and the gauge to the backing material. The backing material (the flyer target material) is either of the two polymers, Kel-F or PMMA. These materials are chosen for their known shock-Hugoniot properties.

**Table 1. Piezoelectric Polymer (PVDF) Impact Response Measurements  
(1x1 mm Active Area)**

Experiment Number	Configuration <sup>a</sup> Impactor → Target	Impact Velocity km/sec	Initial Stress <sup>b</sup> GPa	Peak Stress <sup>c</sup> GPa	Electrical Charge μC/cm <sup>2</sup>
2259	Vac/Kel-F → PVDF/Kel-F/Air 5.08/4.73 .025/3.12	0.292	0.70	0.70	0.961
2260	Vac/Kel-F → PVDF/Kel-F/Air 5.08/4.74 .025/3.13	0.535	1.40	1.40	1.33
2233	Vac/ZSiO <sub>2</sub> → PVDF/ZSiO <sub>2</sub> /Air 5.08/4.77 .025/3.19	0.320	1.27	2.79	1.96
2263	Vac/Kel-F → PVDF/Kel-F/Air 5.08/4.75 .025/3.10	1.021	3.11	3.11	2.19
2239	Vac/ZSiO <sub>2</sub> → PVDF/ZSiO <sub>2</sub> /Air 5.08/4.76 .025/3.18	0.503	2.14	4.47	2.41
2240	Vac/ZA12O <sub>3</sub> → PVDF/ZA12O <sub>3</sub> /Air 5.08/4.75 .025/3.18	0.416	2.07	9.50	3.92
2241	Vac/ZA12O <sub>3</sub> → PVDF/ZA12O <sub>3</sub> /Air 5.08/4.75 .025/3.18	0.485	2.48	11.1	4.09
2256	Vac/ZA12O <sub>3</sub> → PVDF/ZA12O <sub>3</sub> /Air 5.08/1.57 .025/4.74	0.537	2.83	12.3	4.65
2251	Vac/ZA12O <sub>3</sub> → PVDF/ZA12O <sub>3</sub> /Air 5.08/4.67 .025/3.18	0.683	3.80	15.7	5.53 <sup>d</sup>
2242	Vac/ZA12O <sub>3</sub> → PVDF/ZA12O <sub>3</sub> /Air 5.08/4.74 .025/3.18	0.690	3.87	15.8	4.90
2243	Vac/WC → PTFE/PVDF/WC/Air 5.08/3.17 .012/.025/3.18	0.466	—	21.1 <sup>e</sup>	5.47

<sup>a</sup> Impactor and target thicknesses are listed in millimeters.

<sup>b</sup> The initial stress is that produced by the impact of the impactor on the gauge whose Hugoniot is taken as corresponding to Kel-F.

<sup>c</sup> The peak stress is taken as that achieved by the direct impact of impactor and target. It is achieved by the reverberation of the initial shock between target and impactor.

<sup>d</sup> The active area of this gauge was not confirmed prior to use and may have been in error.

<sup>e</sup> Hugoniot properties of the WC (tungsten carbide, Kennametal 68, 15.0 Mg/m<sup>3</sup>) are being refined at this time.

For assembly, the gauge is approximately centered on the backer, bonded to the backer, and the assembly is cured at ambient temperature under pressure overnight. A microscope (20X) and holder, mounted in an alignment bridge, are then used for precise alignment of the detonator and gauge active area. The insert shown in Figure 3 indicates the view seen through the microscope. After alignment, the bolts holding the bridge to the base plate

are firmly tightened. This procedure centers the detonator over the active area of the gauge to within .15 mm. A detonator with its holder then replaces the microscope/holder. The unit can be set in contact with the gauge for direct contact use or a Teflon spacer may be used to position the detonator for use in the flyer-plate mode. The holders are destroyed in each shot, but the assembly is designed for reuse of the bridge/base-plate unit.

It is important to observe that in this configuration the PVDF gauge surface is within 12 microns of the impact surface and that its sensing area is about one-quarter of the flyer diameter.

## INSTRUMENTATION

The instrumentation used in these experiments is shown in the block diagram of Figure 4. The current pulse from the gauge is split at a current viewing resistor (CVR) with an N type Tee so that a primary and secondary channel may be recorded. Each cable is terminated with its characteristic impedance of 50 Ohms. The vertical amplifier sensitivity of the primary channel is normally set to achieve good resolution with the secondary channel set less sensitively to assure recording of the signal without clipping.

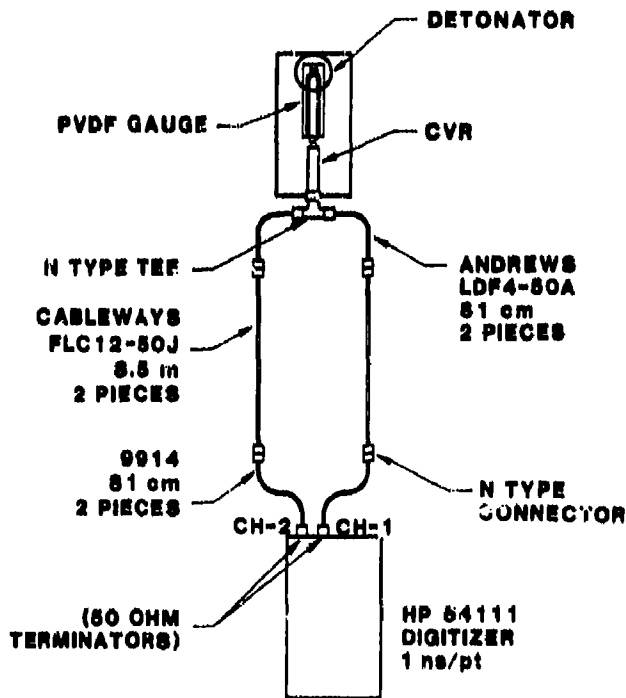


Figure 4. Instrumentation Block Diagram for Detonator Tests

Low-loss coaxial cables, such as Cableways FLC12-50J (1.37 dB/100 feet at 1 GHz), are used to prevent distortion of the several nanosecond duration current pulses. A Hewlett-Packard 54111 waveform digitizer was used to

record the signal at 1 nanosecond/point sampling rate. This digitizer has a 6-bit vertical resolution and a 250 MHz frequency response. Control of the waveform digitizer, as well as analysis of the data, is done by a Hewlett-Packard desktop computer.

The experimental arrangement shown is conceptually simple, with the electrical signal to noise ratio large and easy to record. Nevertheless, the signals are typically pulses whose durations and period are tens of nanoseconds wide signals, and details of the digitizer capabilities can influence the recording.

A typical current-time trace observed for the MODE test detonator is shown in Figure 5. Note that the current pulse follows the *stress-rate*, and is, therefore, a very sensitive indicator of the pulse. Upon integration, the stress-time pulse is obtained, as shown in Figure 6.

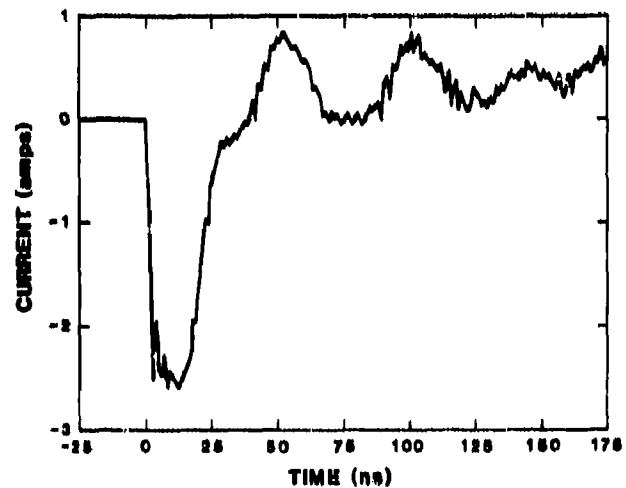


Figure 5. Typical Current Vs. Time Waveform for MODE Test Detonator. Each of the positive current pulses represent a wave reverberation through the flyer.

An important tool for our comparison experiments was the VISAR<sup>13</sup> (Velocity Interferometer System For Any Reflector). Both free surface and particle velocity measurements were done for comparison information. This measurement monitors a laser beam that is typically 100 microns in diameter, reflected at a local surface to provide a time-resolved particle velocity profile.

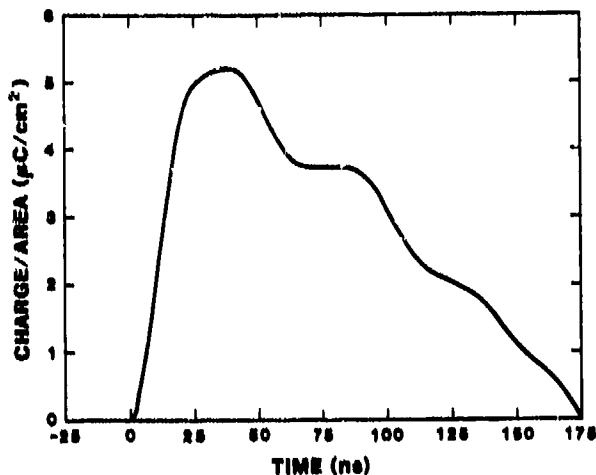


Figure 6. Typical Charge/Area Vs. Time Waveform for MOD E Test Detonator.

### Mod E Test Detonator

The Mod E test detonators are single bridgewire units in which the CP explosive is pressed in a precisely controlled operation. They are positioned 1 mm ( $\pm 0.025$  mm) above the gauge active area using a Teflon spacer. This distance corresponds to the flight distance at which the flyer velocity is evaluated with VISAR measurements. A 3.3 mm diameter by 127 micron thick stainless-steel closure disk is welded on the end of the detonator. This closure disk is the flyer propelled by the detonation. Five independent measurements of flyer velocity at 1 mm show a mean value of 2.52 km/sec, with a variability of 3 percent. Errors in the flyer travel distance of 25 microns will produce an error in velocity of no more than 2.5 percent.

The averaged measured charge/unit area from the PVDF gauges for these four detonator flyer plate responses is found to be  $5.2 \mu\text{C}/\text{cm}^2$ , with a variability of 0.1. The mean pressure computed from the charge measurements in the gas-gun responses is 18.8 GPa. The measured flyer velocity was used to compute a pressure, assuming the gauge/Teflon cover to be impedance-matched to the Kel-F backer. This idealized, one-dimensional shock pressure of 22.4 GPa assumes steady, planar conditions within the measuring space. Thus, the PVDF gauge appears to indicate a pressure about

15 percent lower than the expected value under the loading conditions of this detonator.

### Four mm System Detonator

The 4 mm detonators are typical of those detonators produced in large scale production. They were tested in the flyer mode in the same manner as the previous detonators. Even though the configuration of the energetic material is the same in this device as in the MOD E test detonator, they were initiated asymmetrically by one of two bridgewires in the device. Because of this single-wire initiation, the flyer is strongly nonplanar in flight and at impact. Measurements of the planarity by T. Warren<sup>14</sup> at the Pantex Plant of Mason & Hanger are summarized in Figure 7 and show the loading edge of the flyer impacts on a point near the outer edge of the PVDF gauge. The following surface of the flyer completes the impact about 25 nsec later. The planarity data of Figure 7 also show that the MOD E test detonator (label precision in Figure 7) and the dual-bridgewire ignited 4 mm system detonator show significantly better planarity.

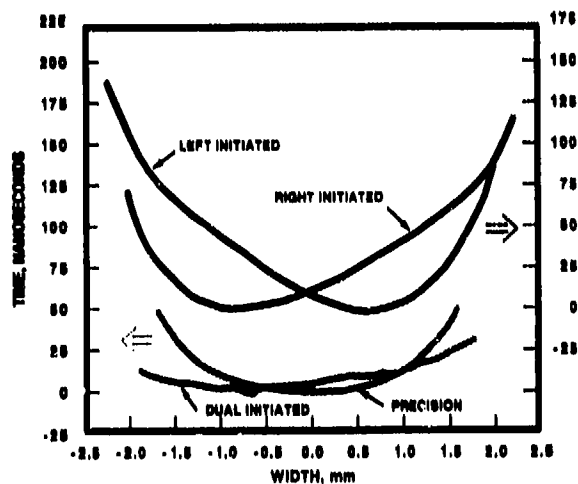


Figure 7. Flyer Planarity for the Mod E Test Detonator, the Single Bridge and Dual Bridge Ignited 4 mm System Detonator

Seven VISAR flyer velocity measurements showed a mean flyer velocity of 2.49 km/sec, with a variability of 4 percent. In the experiments on this detonator, transparent PMMA

backers were used so that "in-material" particle velocity measurements could be carried out by VISAR simultaneously with PVDF gauge measurements. The VISAR particle velocity measurements were found to have a much larger spread (12 percent) than the variability in flyer velocity, and were found to be about 3 percent lower than that predicted from the idealized flyer impact conditions.

The average pressure measured by the PVDF gauge (using the PVDF gas-gun response data for conversion of charge/unit area to pressure) was found to be 10.4 GPa, with a spread in value of about 10 percent. This value of average pressure under these high nonplanar conditions is about 35 percent lower than that predicted from the flyer-velocity measurements and that measured in the "in-material" VISAR particle velocity measurements. In every case, however, a well characterized, repeatable current pulse was observed, with features corresponding to release waves in the flyer after impact.

## CONCLUSIONS

In the present work the response of small diameter PVDF piezoelectric polymer gauges has been investigated under a wide range of impact conditions. They include ideal, precisely controlled impact conditions, less ideal but approximately planar, small diameter flyer impact conditions, and highly nonplanar small diameter flyer impacts. The present PVDF gauge response data provide the basis for an identification of problems to be encountered in a variety of device response environments.

In the compressed-gas gun response measurements, it has been established that the basic response properties of small size gauges prepared by the Bauer process are highly reproducible. Differences of about 2 percent observed under precise impact conditions are thought to be accounted for by ambiguities in the data recording and analysis, as well as in materials response. These experiments show that the PVDF gauge will prove useful over a wide range of pressure and will, therefore, prove useful for a wide variety of measurement problems. Although these projectile impact data are obtained under precise conditions, it

should be recognized that the peak pressures are obtained under "ring-up" conditions in which the rise time to peak pressure is typically 60 nsec. Thus, under a more rapidly rising pulse in which the peak pressure is obtained in a single shock, there may be differences in response due to a higher shock-induced temperature rise. This point requires further study.

The nearly planar detonator flyer-plate response measurements show a reduced output compared to idealized, one-dimensional pressure calculations. Even though this flyer is substantially more nonplanar than in the gun-impact studies, the 15 percent reduced outputs seem larger than can be accounted for by the nonplanar conditions. It remains to be seen whether direct shock measurements to similar pressure values can account for the observed differences.

The strongly nonplanar, detonator flyer-plate response measurements show a very strong effect due to the three-dimensional nature of the loading, amounting to about a 35 percent reduction in signal. Whether this difference is due to a real difference in average pressure over the volume of the gauge or is due to an inherent reduced output in three-dimensional stress fields requires further study. When one considers that the measurement is made within 12 microns of the impact surface, it is remarkable that any type measurement is possible. Indeed, the presence of the reduced gauge output provides a direct measure of the strongly nonplanar impact conditions.

Because the gauge response is composed of such short duration current pulses, there is concern for the adequacy of digitizer responses. The LeCroy 6880 digitizer appears to have adequate vertical resolution with its 8-bit design, but the 6-bit resolution of the Hewlett-Packard digitizer may not be fully adequate for some of the narrower current pulses. Preliminary measurements in the gun-impact configuration suggest that gauge output of charge/area may be reduced with the Hewlett-Packard digitizer as much as 7 percent. Comparisons of the LeCroy digitizer measurements with independent measurements at our laboratories and in the laboratory of Francois Bauer show good agreement. This point requires further study.

It should be emphasized that the PVDF gauge provided sensitive, time-resolved measurements in all cases investigated. The measurement of the stress-rate provides a far more sensitive measurement of such stress pulses than available in any other shock-measurement technique. The unobtrusive nature of the gauge, its very large signal output, its wide pressure operating range, and its capability to measure stress-rate make it a far more useful gauge than previously developed piezoelectric gauges.

## ACKNOWLEDGEMENTS

The authors are pleased to acknowledge the excellent technical assistance of F. Horine, M. Anderson, D. Wackerbarth, D. Sanchez, and M. Wing. Discussions with and encouragement from F. Bauer, R. Weinmeister, and L. Bonzon were critical to the success of the present work. The authors are very appreciative of T. Warren for permitting use of his flyer planarity measurements prior to publication.

## REFERENCES

1. Chhabildas, L. C. and Graham, R. A., "Developments in Measurement Techniques for Shock-Loaded Solids, *Techniques and Theory of Stress Measurement for Shock Wave Applications*, eds., Stout, R. B.; Norwood, F. R.; and Fourney, M. E., AMD Vol. 83, American Society of Mechanical Engineers, NY, 1987, pp. 1-18.
2. Bauer, F., "Behavior of Ferroelectric Ceramics and PVF<sub>2</sub> Polymers Under Shock Loading," *Shock Waves in Condensed Matter-1981*, eds., Nellis, W. J.; Seaman, L.; and Graham, R. A., American Institute of Physics, 1982, pp. 251-267.
3. Graham, R. A.; Lee, L. M.; and Bauer, F., "Response of Bauer Piezoelectric Polymer Stress Gauges (PVDF) to Shock Loading," *Shock Waves in Condensed Matter 1987*, eds., Schmidt, S. C. and Holmes, N. C., Elsevier, 1988, pp. 619-622.
4. Graham, R. A.; Bauer, F.; Lee, L. M.; and Reed, R. P., "Standardized Bauer Piezoelectric Polymer Shock Gauge," *Shock Wave Compression of Condensed Matter*, 1988, pp. 47-50.
5. Bauer, F., "Properties and High Pressure Shock Loading Response of Poled Ferroelectric PVF<sub>2</sub> Polymer Gauges," Stout, et al., loc cit.
6. Graham, R. A.; Neilson, F. W.; and Benedick, W. B., "Piezoelectric Current from Shock-Loaded Quartz-A Submicrosecond Stress Gauge," *Journal of Applied Physics*, Vol. 36, 1965, pp. 1775-1783.
7. Graham, R. A., "Second- and Third-Order Piezoelectric Stress Constants of Lithium Niobate as Determined by the Impact-Loading Technique," *Journal of Applied Physics*, Vol. 48, 1977, pp. 2153-2163.
8. Bauer, F., "Method and Device for Polarizing Ferroelectric Materials," U. S. Patent 4,611,260, 9 Sep 1986.
9. Bauer, F., "Device for Polarizing Ferroelectric Materials," U. S. Patent 4,684,337, 4 Aug 1987.
10. Stanton, P. L.; Igel, E. A.; Lee, L. M.; Mohler, J. M.; and West, G. T., "Characterization of the DDT Explosive, CP," *Seventh Symposium (International) on Detonation*, Annapolis, Maryland, Jun 1981, p. 865.
11. Bernecker, R. R. and Price, D., "Studies in the Transition from Deflagration to Detonation in Granular Explosives-III. Proposed Mechanisms for Transition and Comparison with Other Proposals in the Literature," *Combust Flame*, Vol. 22, 1974, p. 161.
12. Fleming, W.; Fronabarger, J. W.; and Lieberman, M. L., "CP DDT Detonators: I. Design Sensitivity Study," *Proceedings 12th Symposium on Explosives and Pyrotechnics*, Mar 1984.
13. Barker, L. M. and Hollenback, R. E., "Laser Interferometer for Measuring High Velocities of Any Reflecting Surface," *J Appl Physics*, Vol. 43, 1972, p. 11.
14. Warren, T. W., written communication, Development Division, Mason & Hanger-Silas Mason Company, Inc., Till of Detonator Flyer Plate, 5 Jan 1989.



**Sandia National Laboratories**

**DETONATOR RESPONSE  
MEASUREMENTS WITH A  
STANDARDIZED PIEZOELECTRIC  
POLYMER (PVDF) GAUGE**

**Larry M. Moore, R. A. Graham,  
R. P. Reed**

**Sandia National Laboratories  
Albuquerque, New Mexico 87185**

**Larry M. Lee**

**Ktech Corporation  
Albuquerque, New Mexico 87110**

**OVERVIEW**

- INTRODUCTION
- STANDARDIZED PVDF GAUGE
- COMPRESSED-GAS GUN EXPERIMENTS
- EXPERIMENTAL SETUP
- DETONATOR MEASUREMENTS
- TWO FACTORS THAT INFLUENCE DETONATOR MEASUREMENTS
- CONCLUSIONS

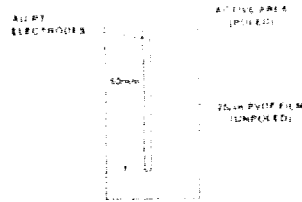
**INTRODUCTION**

- COOPERATIVE EFFORT FOR PVDF GAUGE DEVELOPMENT
  - SANDIA NATIONAL LABORATORIES
  - INSTITUT SAINT LOUIS
- GOAL
  - REPRODUCIBLE MATERIAL
  - STANDARDIZED GAUGE
- ADVANTAGES OF PVDF GAUGE
  - CURRENT MEASURE OF STRESS RATE
  - UNOBTRUSIVE LARGE SIGNAL OUTPUT
  - WIDE PRESSURE RANGE
- PURPOSE OF THIS WORK
  - FEASIBILITY OF PVDF PRESSURE MEASUREMENTS ON SMALL DETONATORS

# STANDARDIZED PVDF GAUGE

## Standardized PVDF Gauge

- BIAXIALLY-STRETCHED FILM
- POLYMER FILM THICKNESS — NOMINAL 25 MICRONS
- SPUTTERED GOLD-OVER-PLATINUM ELECTRODES & LEADS
- REMANENT FERROELECTRIC POLARIZATION OF  $9.2 \text{ } \mu\text{C}/\text{cm}^2$  USING BAUER PROPRIETARY PROCESS
- QUANTITATIVE PHYSICAL/ELECTRICAL CHARACTERISTICS

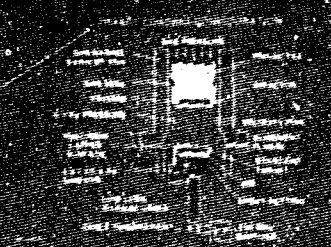


PHYSICAL PROPERTIES OF PVDF GAUGE

PROPERTY	VALUE	UNITS	STANDARD DEVIATION (%)
Thickness	25.4	μm	0.5
Area	1.0	cm <sup>2</sup>	0.2
Remanent Polarization	9.2	μC/cm <sup>2</sup>	0.5
Dielectric Constant	12.0		0.5
Electrical Resistance	1.0	Ω	0.5
Impedance	1.0	Ω	0.5

- Small percent standard deviation shows reproducibility needed for commercial scale production

# COMPRESSED-GAS GUN EXPERIMENTS

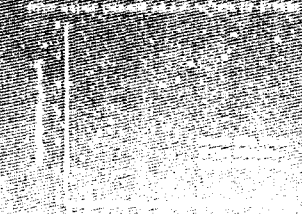


- Symmetric impact experiments using KBr, s-cut quartz, s-cut sapphire and tungsten carbide for standard target and impactor
- Gauge "rings-up" to final pressure determined by shock impedances of target and impactor

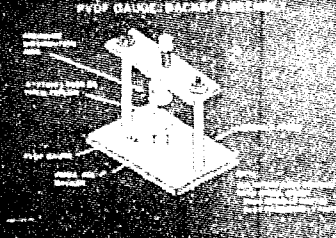
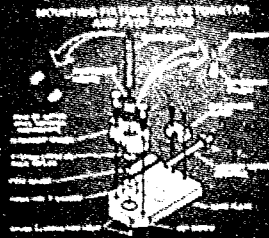
... of the gauge ...

... of the gauge ...

... of the gauge ...



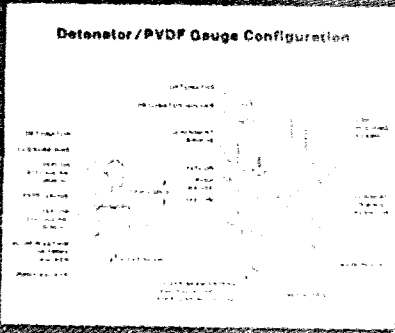
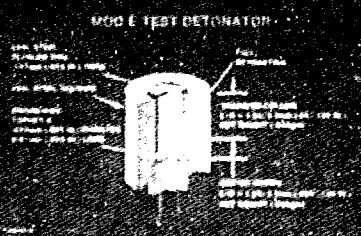
## EXPERIMENTAL SETUP



- 12.7  $\mu\text{m}$  Teflon used to provide electrical isolation for gauge
- Detonator: must be centered over active area of gauge

- Simple instrumentation for measuring gauge output
- Low-loss coaxial cable used to minimize distortion of nanosecond current pulses

## DETONATOR MEASUREMENTS

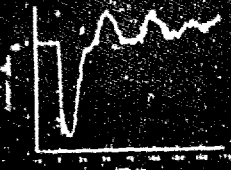


- Precision fixture used to align gauge and detonator

- Precision fixture used to align gauge and detonator
- Precision fixture used to align gauge and detonator

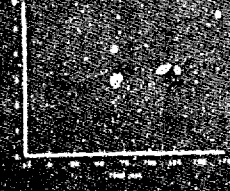
# DETONATOR MEASUREMENTS

TYPICAL CURRENT VS TIME WAVEFORM FOR MOD E TEST DETONATOR



• Each of the positive current pulses represents a wave reverberation through the flyer

TYPICAL CHARGE AREA VS TIME WAVEFORM FOR MOD E TEST DETONATOR



• Integration of the current waveform yields the charge waveform from which stress can be deduced using the calibration curve

FLYER VELOCITY SUMMARY

FLYER	VELOCITY (mm/μs)	CHARGE AREA (μs)	STRESS (GPa)	FLYER THICKNESS (mm)	FLYER DENSITY (g/cm³)
MOD E	2.52	1.1	1.1	0.1	1.8
4 mm SYSTEM	2.49	1.1	1.1	0.1	1.8

FLYER VELOCITY MEASURED BY VISAR TO DEFINE PRESSURE

MOD E Detonator 2.52 mm/μs  
4 mm System Detonator 2.49 mm/μs

Pressure used to determine charge/area for gauge from calibration curve

Predicted charge/area from flyer measurement can be compared to measured charge/area from experiments

• Flyer velocity measured by VISAR to define pressure

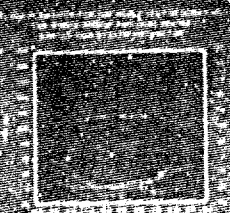
MOD E Detonator 2.52 mm/μs  
4 mm System Detonator 2.49 mm/μs

• Pressure used to determine charge/area for gauge from calibration curve

• Predicted charge/area from flyer measurement can be compared to measured charge/area from experiments

## TWO FACTORS THAT INFLUENCE DETONATOR MEASUREMENT

### PLANARITY



• Mod E test detonator single bridgewise device

• 4 mm system detonator two bridgewise devices

• Equalization of 4 mm system detonator significantly improves planarity



# INDEXES FOR THE PROCEEDINGS OF THE SYMPOSIA (INTERNATIONAL) ON DETONATION-1951 THROUGH 1985

Sharon L. Crane, William E. Deal,  
John B. Ramsay, and Bruce E. Takala\*  
Los Alamos National Laboratory  
Los Alamos, New Mexico 87545

*The Proceedings of the eight Detonation Symposia have become the major archival source of information on international research in explosive phenomenology, theory, experimental techniques, numerical modeling, and high-rate reaction chemistry. In many cases, they contain the original reference or the only reference to major progress in this field. For some papers, the information is more complete than the complementary article appearing in a formal journal, yet for others, authors elected to publish only an abstract in the Proceedings. For the large majority of papers, the Symposia Proceedings provide the only published reference to a body of work. However, no indexes exist for any of the Proceedings, making it difficult to locate a reference or to perform a preliminary literature search. This report indexes the eight existing Proceedings of the Detonation Symposia by paper titles, topic phrases, authors, and first appearance of acronyms and code names. It is a dynamic effort that we expect to supersede by future versions.*

## INTRODUCTION

The index of the eight preceding Symposia Proceedings which appears following this paper was prepared as a useful reference tool for both new and experienced researchers in the field of detonation research.

"Researching" the published Proceedings of the eight previous Symposia (International) on Detonation is time consuming because no indexes exist, either collectively or individually. Including the *Proceedings of the 8th Symposium*, a collective 580 papers have been published. *Chemical Abstracts Services* provides abstracts as part of its topic coverage of "Explosives and Pyrotechnics," but when a researcher merely remembers that a paper was presented at a Detonation Symposium, that is insufficient information to find the reference in

*Chemical Abstracts*. In the past, some of us have spent much effort locating a paper about which we vaguely remembered, knowing only that it had appeared in a past Symposium. Our perception is that much research is being redone because research workers are unaware that a particular question has already been addressed. Thus, we were led to produce a set of indexes.

This index has also been published as a Los Alamos National Laboratory report.<sup>1</sup>

The indexes comprise four parts: (A) a listing of the paper titles and authors in order of appearance in each Symposium Proceedings, (B) an alphabetical listing of topic phrases, (C) an index of all authors, and (D) an index of first appearance of acronyms and code names of compositions and components that are defined. Each index also lists the Symposium number and page number of the reference. For the Proceedings of the First and Second Symposia, the page numbers quoted

\* Major, US Army.

are for the single volume reprinted by the Detonation Symposium Committee in 1987 (NSWC MP 87-194), not the original page numbers.

The entries were initially entered on a structured database program (dBASE III+®). The compilation was edited for printing in WordPerfect 5.0®. Future revisions will be entered into the original database file.

## A. TITLES INDEX

In the first index, the chronological order of the papers has been preserved, beginning with the first symposium and the first paper presented. We list the Symposium number, paper number, paper title, all co-authors, and the nation of the first author.

## B. TOPIC PHRASE INDEX

Here we list the topic phrases alphabetically with reference to the symposium number and page number. We considered using key words, which are cryptic and more mnemonic, rather than the longer and more descriptive topic phrases, but we decided on the latter because they provide more information for selecting the correct reference. The compilers have used their own judgment in selecting and defining the topic phrases and hope that the phrases are self-explanatory. At the present time, a significant cross-referencing capability is lacking within the index, and users are cautioned to check several different topics when searching.

## C. AUTHOR INDEX

This index is a simple listing of all authors, giving the symposium number and first-page number references. All except family names were contracted to initials. We have attempted to combine different presentations of an author's name (e.g., J. Ramsay and J. B. Ramsay) into a uniform entry. Please notify the compilers of errors.

## D. ACRONYM AND CODE NAME INDEX

This index is an attempt to cite the first use of this acronym or code name for neat explosives, ingredients, or formulations, in which a definition of the term is also provided. The names of some explosive compositions that were "known to everyone" in 1950 are no longer commonly used, particularly within the

international community. For example, the names MEDINA and DINA were used in at least one instance with no recognized chemical name or formula given. Rather interestingly, no definition of RDX was located within the Proceedings until the Fifth Symposium.

Many explosive compounds and compositions are named as contractions of the chemical names (e.g., TNT); for others, the histories of the names are lost in research laboratories (e.g., HMX\*); and others have no relationship to the composition (e.g., X-0290). A large number of papers within the Symposia Proceedings refer to compositions only by acronym or code name, with no formal definition of the composition. Composition B (Comp B) is cited in many papers, yet at least 10 citations for Comp B provide similar but different compositions. Also, in some instances, the same explosive compound was defined by three or more acronyms.

We intended that each citation be the earliest reference within the eight Proceedings for the use of the acronym, coupled with a meaningful chemical definition. Errors in finding and entering the citations may have occurred. If readers detect errors, please contact one of the compilers.

## FUTURE REVISIONS

The compilers intend to continue the process of updating the indexes of the Proceedings of the Symposia. A revision of the database will begin as soon as the published version of the Ninth Symposium Proceedings is available. Individuals interested in obtaining copies of the revised indexes should contact one of the authors.

## REFERENCES

1. Crane, S. L.; Deal, William E.; Ramsay, John B.; and Takala, Bruce E., *Indexes for the Proceedings of the Symposia (International) on Detonation*, Los Alamos National Laboratory Report LA-11570-MS, UC-741, Aug 1989.

\*Ray Walker has told JBR that HMX most probably stands for High Melting eXplosive, but Walker has also heard a reasonable statement that the initials may have been derived from Holston Military eXplosive. It does not stand for His Majesty's eXplosive.

# A. TITLES INDEX

## By Symposium Page

<b>SYM PAGE</b>	<b>TITLE, AUTHORS, NATION</b>
1 3	RECENT STUDIES IN BURORD; BRUNAUER, S.; USA
1 9	RECENT WORK ON DETONATION AT ABERDEEN; DEWEY, J. M.; USA
1 12	STUDIES ON DETONATION PHENOMENA; GIBSON, F. C.; MASON, C. M.; USA
1 22	RECENT WORK AT NOL.; PRICE, D.; USA
1 31	RECENT STUDIES AT THE NAVAL ORDNANCE TEST STATION; RINEHART, J. S.; USA
1 39	SOME RECENT STUDIES IN CANADA; WALKER, G. R.; CANADA
1 43	CHEMICAL ASPECTS OF DETONATION; LEWIS, B.; USA
1 45	NONSTATIONARY DETONATION WAVES IN GASES; KISTIAKOWSKY, G. B.; USA
1 52	DURATION OF THE REACTION IN A DETONATING EXPLOSIVE; JACOBS, S. J.; USA
1 57	EXPERIMENTS ON THE TRANSITION FROM DEFLAGRATION TO DETONATION; ROTH, J.; USA
1 71	PHYSICAL ASPECTS OF DETONATION; KIRKWOOD, J. G.; USA
1 72	THE EQUATION OF STATE FOR DETONATION GASES; BRINKLEY, S. R.; USA
1 79	CONVERGENT SHOCK WAVES; KANTROWITZ, A.; USA
1 88	SHOCK WAVES IN SOLIDS; ABLARD, J. E.; USA
1 93	INTERACTIONS OF DETONATION WAVES WITH MATERIAL BOUNDARIES; PARLIN, R. B.; EYRING, H.; USA
1 105	PROBLEMS AND FUTURE DEVELOPMENTS; KISTIAKOWSKY, G. B.; USA
1 107	THEORETICAL DEVELOPMENTS IN DETONATION; KIRKWOOD, J. G.; USA
2 119	CHARGE PREPARATION FOR PRECISE DETONATION VELOCITY STUDIES; JAMES, E.; USA
2 136	TECHNIQUE FOR THE MEASUREMENT OF DETONATION VELOCITY; CAMPBELL, A. W.; MALIN, M. E.; BOYD, T. J.; HULL, J. A.; USA
2 151	A MICROWAVE TECHNIQUE FOR MEASURING DETONATION VELOCITIES; SCYD, T. J.; FAGAN, P.; USA
2 157	MEASUREMENT OF DETONATION TEMPERATURES; GIBSON, F. C.; BOWSER, M.; SUMMERS, C. R.; SCOTT, F. H.; COOPER, J. C.; MASON, C. M.; USA

## A. TITLES INDEX (Continued)

<b>SYM</b>	<b>PAGE</b>	<b>TITLES, AUTHORS, NATION</b>
2	168	A NEW CINE MICROSCOPE AND ITS APPLICATION TO DETONATION PHENOMENA; COURTNEY-PRATT, J. S.; UK
2	187	THE MEASUREMENT OF DENSITY CHANGES IN GASEOUS DETONATIONS; KISTIAKOWSKY, G. B.; KYDD, P. H.; USA
2	198	THE ATTAINMENT OF THERMODYNAMIC EQUILIBRIUM IN DETONATION WAVES; KISTIAKOWSKY, G. B.; ZINMAN, W. G.; USA
2	216	ON THE STRUCTURE OF A DETONATION WAVE; GILKERSON, W. R.; DAVIDSON, N.; USA
2	231	HIGH TEMPERATURE THERMODYNAMIC AND GASEOUS DETONATIONS IN MIXTURES OF CYANOGEN, OXYGEN, AND NITROGEN; PEEK, H. M.; THRAP, R. G.; USA
2	251	DETONATION IN GASES AT LOW PRESSURE; BENNET, A. L.; WEDAA, H. W.; USA
2	266	MEASUREMENTS ON GASEOUS DETONATION WAVES; NICHOLLS, J. A.; MORRISON, R. B.; CULLEN, R. E.; USA
2	281	STUDIES ON GASEOUS DETONATION; GREIFER, B.; GIBSON, F. C.; MASON, C. M.; USA
2	295	CONDENSATION SHOCKS AND WEAK DETONATIONS; REED, S. G.; HEYBEY, W. H.; USA
2	312	THE STRUCTURE OF A STEADY-STATE PLANE DETONATION WAVE WITH FINITE REACTION RATE; KIRKWOOD, J. G.; WOOD, W. W.; USA
2	327	THE MEASUREMENT OF CHAPMAN-JOUQUET PRESSURE FOR EXPLOSIVES; DEAL, W. E.; USA
2	343	MEASUREMENT OF THE CHAPMAN-JOUQUET PRESSURE AND REACTION ZONE LENGTH IN A DETONATING HIGH EXPLOSIVE; DUFF, R. E.; HOUSTON, E.; USA
2	358	THE DETONATION ZONE IN CONDENSED EXPLOSIVES; MALLORY, H. D.; JACOBS, S. J.; USA
2	383	CALCULATION OF THE DETONATION PROPERTIES OF SOLID EXPLOSIVES WITH THE KISTIAKOWSKY-WILSON EQUATION OF STATE; FICKETT, W.; COWAN, R. D.; USA
2	404	A SOLID-STATE MODEL FOR DETONATIONS; PARLIN, R. B.; GIDDINGS, J. C.; USA
2	424	DIAMETER EFFECT IN CONDENSED EXPLOSIVES. THE RELATION BETWEEN VELOCITY AND RADIUS OF CURVATURE OF THE DETONATION WAVE; WOOD, W. W.; KIRKWOOD, J. G.; USA
2	439	THE DETONATION BEHAVIOR OF LIQUID TNT; IGEL, E. A.; SEELY, L. B.; USA
2	454	DETONATION IN HOMOGENEOUS EXPLOSIVES; CAMPBELL, A. W.; MALIN, M. E.; HOLLAND, T. E.; USA

## A. TITLES INDEX (Continued)

<b>SYM</b>	<b>PAGE</b>	<b>TITLES, AUTHORS, NATION</b>
2	478	PARTICLE SIZE EFFECTS IN ONE- AND TWO-COMPONENT EXPLOSIVES; MALIN, M. E.; CAMPBELL, A. W.; MAUTZ, C. W.; USA
2	500	DETONATION WAVE FRONTS IN IDEAL AND NON-IDEAL DETONATION; COOK, M. A.; USA
2	519	DETERMINATION OF REACTION RATE OF SODIUM NITRATE AND THE EQUATION OF STATE OF 50/50 TNT- $\text{NaNO}_3$ ; COOK, M. A.; URSENBACH, W. O.; USA
2	529	THE DECOMPOSITION OF ALPHA-LEAD AZIDE; GROOCCOCK, J. M.; UK
2	547	THE DETONATION OF AZIDES BY LIGHT; COURTNEY-PRATT, J. S.; ROGERS, G. T.; UK
2	561	DETONATION IN AZIDES WHEN THE DIMENSIONS ARE COMPARABLE WITH THE LENGTH OF THE REACTION ZONE; BOWDEN, F. P.; MCLAREN, A. C.; UK
2	571	ORIGIN OF LUMINOSITY IN DETONATION WAVES; JONES, E.; UK
2	582	THE ROLE OF GAS POCKETS IN THE PROPAGATION OF LOW VELOCITY DETONATION; GURTON, O. A. J.; UK
2	601	SENSITIVENESS TO DETONATION; JONES, E.; CUMMING, I. G.; UK
2	612	INITIATION OF MILITARY EXPLOSIVES BY PROJECTILE IMPACT; DEWEY, J. M.; USA
2	620	FACTORS AFFECTING THE TRANSMISSION OF DETONATION BETWEEN SMALL EXPLOSIVE CHARGES; HAMPTON, L. D.; SAVITT, J.; STARR, L. E.; STRESAU, R. H. F.; USA
2	643	THE CORRELATION OF THE SENSITIVENESS OF EXPLOSIVES WITH COMBUSTION DATA; WHITBREAD, E. G.; WISEMAN, L. A.; UK
2	695	PROBLEMS OF INITIATION IN TESTS OF SENSITIVENESS; WHITBREAD, E. G.; UK
2	711	LEAD AZIDE PRECIPITATED WITH POLYVINYL ALCOHOL; BLAKE, T. G.; SEEGAR, D. E.; STRESAU, R. H. F.; USA
2	733	THERMO-HYDRODYNAMICS AND THE REACTION KINETICS IN SOME METALIZED EXPLOSIVES; COOK, M. A.; FILLER, A. S.; KEYES, R. T.; PARTRIDGE, W. S.; URSENBACH, W. O.; USA
2	749	CONDITIONS BEHIND THE REACTION ZONE OF CONFINED COLUMNS OF EXPLOSIVE--NOTIONS DERIVED FROM PLATE DENT EXPERIMENTS; SLIE, W. M.; STRESAU, R. H. F.; USA
3	1	A COLLIDING BALL HIGH EXPLOSIVE IMPACT SENSITIVITY TESTING MACHINE; BEAN, C. M.; CACHIA, G. P.; KIRKHAM, J.; UK
3	10	A PHOTOGRAPHIC STUDY OF EXPLOSIONS INITIATED BY IMPACT; WENOGRA, J.; USA
3	24	PURE ENVIRONMENTAL SHOCK TESTING OF CONDENSED PHASES; ERIKSON, T. A.; USA

## A. TITLES INDEX (Continued)

SYM	PAGE	TITLES, AUTHORS, NATION
3	42	ON THE MEMORY EFFECT IN THE THERMAL INITIATION OF EXPLOSIVES; HESS, W. R.; LING, R. C.; USA
3	50	THE THERMAL DECOMPOSITION OF $[\text{Co}(\text{NH}_3)_6](\text{N}_3)_3$ ; JOYNER, T. B.; VERHOEK, F. H.; USA
3	60	THE BEHAVIOR OF EXPLOSIVES AT VERY HIGH TEMPERATURES; WENOGRAD, J.; USA
3	77	THE RAPID BURNING OF SECONDARY EXPLOSIVES BY A CONVECTIVE MECHANISM; TAYLOR, J. W.; UK
3	88	ELECTRICAL INITIATION OF RDX; MULLER, G. M.; MOORE, D. B.; BERNSTEIN, D.; USA
3	112	DETONATION STUDIES IN ELECTRIC AND MAGNETIC FIELDS; ALLISON, F. E.; USA
3	120	ELECTRICAL MEASUREMENTS IN DETONATING PENTOLITE AND COMPOSITION B; JAMESON, R. L.; USA
3	139	ON THE ELECTRICAL CONDUCTIVITY OF DETONATING HIGH EXPLOSIVES; HAYES, B.; USA
3	150	IONIZATION IN THE SHOCK INITIATION OF DETONATION; CLAY, R. B.; COOK, M. A.; KEYES, R. T.; SHUPE, O. K.; UDY, L. L.; USA
3	184	CHEMICAL FACTORS IN EXTERNAL DETONATION-GENERATED PLASMAS; COOK, M. A.; FUNK, A. G.; USA
3	202	DETONATION PLASMA; KEYES, R. T.; KENDREW, E. L.; WHITBREAD, E. G.; UK
3	205	ENERGY TRANSFER TO A RIGID PISTON UNDER DETONATION LOADING; AZIZ, A. K.; HURWITZ, H.; STERNBERG, H. M.; USA
3	226	A COMPUTER PROGRAM FOR THE ANALYSIS OF TRANSIENT AXIALLY SYMMETRIC EXPLOSION AND SHOCK DYNAMICS PROBLEMS; ORLOW, T.; PIACESI, D.; STERNBERG, H. M.; USA
3	241	PRESSURE PROFILES IN DETONATING SOLID EXPLOSIVE; HAUVER, C. E.; USA
3	253	DECAY OF EXPLOSIVELY-INDUCED SHOCK WAVES IN SOLIDS AND SPALLINGS OF ALUMINUM; ERKMAN, J. O.; USA
3	267	EFFECTS OF BOUNDARY RAREFACTIONS ON IMPULSE DELIVERED BY EXPLOSIVE CHARGE; TAYLOR, B. C.; USA
3	285	EXPERIMENTAL DETERMINATION OF STRESSES GENERATED BY AN ELECTRIC DETONATOR; RINEHART, J. S.; USA
3	304	COMMENTS ON HYPERVELOCITY WAVE PHENOMENA IN CONDENSED EXPLOSIVES; CHAIKEN, R. F.; USA

## A. TITLES INDEX (Continued)

SYM	PAGE	TITLES, AUTHORS, NATION
3	309	NONIDEAL DETONATION OF AMMONIUM NITRATE-FUEL MIXTURES; SADWIN, L. D.; STRESAU, R. H. F.; SAVITT, J.; USA
3	327	THE DETONATION VELOCITY OF PRESSED TNT; URIZAR, M. J.; JAMES, E.; SMITH, L. C.; USA
3	357	MEASUREMENT OF DETONATION, SHOCK, AND IMPACT PRESSURES; KEYES, R. T.; URSENBACH, W. O.; USA
3	386	LOW PRESSURE POINTS ON THE ISENTROPES OF SEVERAL HIGH EXPLOSIVES; DEAL, W. E.; USA
3	396	STRONG SHOCKS IN POROUS MEDIA; AUSTING, J. L.; NAPADENSKY, H. S.; STRESAU, R. H. F.; SAVITT, J.; USA
3	420	THE BEHAVIOR OF EXPLOSIVES AT IMPULSIVELY INDUCED HIGH RATES OF STRAIN; NAPADENSKY, H. S.; STRESAU, R. H. F.; SAVITT, J.; USA
3	436	INITIATION AND GROWTH OF DETONATION IN LIQUID EXPLOSIVES; GIBSON, F. C.; SUMMERS, C. R.; MASON, C. M.; VAN DOLAH, R. W.; USA
3	455	INITIATION CHARACTERISTICS OF MILDLY CONFINED, BUBBLE-FREE NITROGLYCERINE; WINNING, C. H.; USA
3	469	SHOCK INITIATION OF DETONATION IN LIQUID EXPLOSIVES; CAMPBELL, A. W.; DAVIS, W. C.; TRAVIS, J. R.; USA
3	499	SHOCK INITIATION OF SOLID EXPLOSIVES; CAMPBELL, A. W.; DAVIS, W. C.; RAMSAY, J. B.; TRAVIS, J. R.; USA
3	520	SHOCK INDUCED SYMPATHETIC DETONATION IN SOLID EXPLOSIVE CHARGES; SULTANOFF, M.; BOYLE, V. M.; PASZEK, J.; USA
3	534	GROWTH OF DETONATION FROM AN INITIATING SHOCK; ENIG, J. W.; USA
3	562	INITIATION OF A LOW-DENSITY PETN PRESSING BY A PLANE SHOCK WAVE; SEAY, G. E.; SEELY, L. B.; USA
3	574	THE TRANSITION FROM SHOCK WAVE TO DETONATION IN 60/40 RDX/TNT; KENDREW, E. L.; WHITBREAD, E. G.; USA
3	584	DETERMINATION OF THE SHOCK PRESSURE REQUIRED TO INITIATE DETONATION OF AN ACCEPTOR IN THE SHOCK SENSITIVITY TEST; JAFFE, I.; BEAUREGARD, R.; AMSTER, A. B.; USA
3	606	A COMPUTATIONAL TREATMENT OF THE TRANSITION FROM DEFLAGRATION TO DETONATION IN SOLIDS; ZOVKO, C. T.; MACEK, A.; USA
3	635	A METHOD OF DETERMINATION OF DETONABILITY OF PROPELLANTS AND EXPLOSIVES; WACHTELL, S.; MCKNIGHT, C. E.; USA

## A. TITLES INDEX (Continued)

SYM	PAGE	TITLES, AUTHORS, NATION
3	659	SENSITIVENESS TESTING AND ITS RELATION TO THE PROPERTIES OF EXPLOSIVES; WHITBREAD, E. G.; UK
3	671	SENSITIVITY RELATIONSHIPS; KAMLET, M. J.; USA
3	693	A STATISTICAL CORRELATION OF IMPACT SENSITIVITY WITH OXYGEN BALANCE FOR SECONDARY EXPLOSIVES; ALSTER, J.; USA
3	706	THE ELECTRIC-SPARK INITIATION OF MIXTURES OF HIGH EXPLOSIVES AND POWDERED ELECTRICAL CONDUCTORS; LIDDIARD, T. P.; DRIMMER, B. E.; USA
3	721	DETONATION AND SHOCK REVIEW; WILKINS, M. L.; USA
3	725	DETONATION PERFORMANCE CALCULATIONS USING THE KISTIAKOWSKY-WILSON EQUATION OF STATE; MADER, C. L.; USA
3	738	ENERGY RELEASE FROM CHEMICAL SYSTEMS; KURY, J. W.; DOROUGH, G. D.; SHARPLES, R. E.; USA
3	761	THE DETONATION PROPERTIES OF (1,3-DIAMINO, 2,4,6-TRINITROBENZENE); COLEBURN, N. L.; DRIMMER, B. E.; LIDDIARD, T. P.; USA
3	784	NON-STEADY DETONATION - A REVIEW OF PAST WORK; JACOBS, S. J.; USA
3	813	THE SHOCK INITIATION OF DETONATION IN LIQUID EXPLOSIVES; GEY, W. A.; KINAGA, K.; USA
3	822	SENSITIVITY OF PROPELLANTS; BRANDON, W. W.; OCKERT, K. F.; USA
3	833	SOME STUDIES ON THE SHOCK INITIATION OF EXPLOSIVES; CLARK, E. N.; SCHWARTZ, F. R.; USA
3	842	THE INFLUENCE OF ENERGY ON THE DECOMPOSITION OF THE TRANSITION FROM INITIATION TO DETONATION; HARVALIK, Z. V.; USA
4	3	METAL ACCELERATION BY CHEMICAL EXPLOSIVE; KURY, J. W.; HORNIG, H. C.; LEE, E. L.; MCDONNELL, J. L.; ORNELLAS, D. L.; FINGER, M.; STRANGE, F. M.; WILKINS, M. L.; USA
4	14	THE MOTION OF PLATES AND CYLINDERS DRIVEN BY DETONATION WAVES AT TANGENTIAL ANGLES; HOSKIN, N. E.; ALLAN, J. W. S.; BAILEY, W. A.; LETHABY, J. W.; SKIDMORE, I. C.; UK
4	27	THE CHAPMAN-JOUGUET ISENTROPE AND THE UNDERWATER SHOCKWAVE PERFORMANCE OF PENTOLITE; WALKER, W. A.; STERNBERG, H. M.; USA
4	39	DETONATION OF A CYLINDRICAL CHARGE-STUDY OF THE FLOW OF BURNED GASES; FAUQUIGNON, C.; PROUTEAU, M.; VERDES, G.; FRANCE
4	47	THE EQUATION OF STATE OF DETONATION PRODUCTS BEHIND OVERDRIVEN DETONATION WAVES IN COMPOSITION B; SKIDMORE, I. C.; HART, S.; UK

## A. TITLES INDEX (Continued)

SYM	PAGE	TITLES, AUTHORS, NATION
4	52	AN EQUATION OF STATE OF DETONATION PRODUCTS AT PRESSURE BELOW 30 KILOBARS; ALLAN, J. W. S.; LAMBOURN, B. D.; UK
4	67	STRUCTURE, CHEMISTRY, AND INSTABILITY OF DETONATION IN GASES; SCHOTT, G. L.; USA
4	78	THEORETICAL CONSIDERATIONS ON THE PROPAGATION OF SHOCK AND DETONATION WAVES; CHERET, R.; FRANCE
4	84	FAILURE OF THE CHAPMAN-JOUQUET THEORY FOR LIQUID AND SOLID EXPLOSIVES (abstract only); DAVIS, W. C.; CRAIG, B. G.; RAMSAY, J. B.; USA
4	86	RADIUS OF CURVATURE EFFECT ON DETONATION VELOCITY; GREEN, L. G.; JAMES, E.; USA
4	92	LATERAL SHOCK PRESSURE MEASUREMENTS AT AN EXPLOSIVE COLUMN; SADWIN, L. D.; JUNK, N. M.; USA
4	96	STUDIES ON THE DIAMETER-DEPENDENCE OF DETONATION VELOCITY IN SOLID COMPOSITE PROPELLANTS. I. Attempts to Calculate Reaction-Zone Thickness; PANDOW, M. L.; OCKERT, K. F.; SHUEY, H. M.; USA
4	102	STUDIES OF THE DIAMETER-DEPENDENCE OF DETONATION VELOCITY IN SOLID COMPOSITE PROPELLANTS II. Prediction of Failure Diameter; PANDOW, M. L.; OCKERT, K. F.; PRATT, T. H.; USA
4	107	NON-IDEAL DETONATION WITH CONSTANT LATERAL EXPANSION; WECKEN, F.; FRANCE
4	117	DETONATIONS IN LIQUID EXPLOSIVES--THE LOW VELOCITY REGIME; WATSON, R. W.; SUMMERS, C. R.; GIBSON, F. C.; VAN DOLAH, R. W.; USA
4	126	DETONATION OF NITROMETHANE-TETRANITROMETHANE MIXTURES: LOW AND HIGH VELOCITY WAVES; AMSTER, A. B.; MCEACHERN, D. M.; PRESSMAN, Z.; USA
4	135	OBSERVATION AND STUDY OF THE CONDITIONS FOR THE FORMATION OF MACH DETONATION WAVES; ARGOUS, J. P.; PEYRE, C.; THOUVENIN, J.; FRANCE
4	142	MACH INTERACTION OF TWO PLANE DETONATION WAVES; LAMBOURN, B. D.; WRIGHT, P. W.; UK
4	153	INTERACTION OF OBLIQUE DETONATION WAVES WITH IRON (abstract only); STERNBERG, H. M.; PIACESI, D.; USA
4	154	INTERACTIONS OF DETONATION WAVES IN CONDENSED EXPLOSIVES (abstract only); GARDNER, S. D.; WACKERLE, J.; USA
4	156	AXIAL INITIATION OF MULTI-COMPONENT EXPLOSIVES CHARGES; DEFFET, L.; FOSSE, C.; BELGIUM
4	167	A DETONATION CALORIMETER AND THE HEAT OF PRODUCTS OF DETONATION OF PENTA-ERYTHRITOL TETRANITRATE (PETN) (abstract only); ORNELLAS, D. L.; CARPENTER, J. H.; GUNN, S. R.; USA

## A. TITLES INDEX (Continued)

<u>SYM</u>	<u>PAGE</u>	<u>TITLES, AUTHORS, NATION</u>
4	168	ANOMALOUS ISENTROPE RESULTS OBTAINED WITH THE RUBY COMPUTER PROGRAM; HERSHKOWITZ, J.; USA
4	176	FRONT AND MASS VELOCITY AT DETONATION IN EVACUATED CHAMBERS; LUNDBORG, N.; SWEDEN
4	179	DETONATION LIMITS IN CONDENSED EXPLOSIVES; GORDON, W. E.; USA
4	198	SUMMARY OF PAPERS ON CONDENSED PHASE DETONATION; DUFF, R. E.; USA
4	205	EVALUATION OF THE GRUNEISEN PARAMETER FOR COMPRESSED SUBSTANCES - I. METALS; ANDERSEN, W. H.; USA
4	213	THE EQUATION OF STATE OF 1060 ALUMINUM FROM SHOCK WAVE MEASUREMENTS (abstract only); ANDERSON, G. D.; FAHRENBRUCH, A. L.; FOWLES, G. R.; USA
4	214	THE COMPRESSION OF POLYMETHYL METHACRYLATE BY LOW AMPLITUDE SHOCK WAVES; LIDDIARD, T. P.; USA
4	222	SHOCK WAVE COMPRESSION OF PLEXIGLAS FROM 3 TO 20 KILOBARS; HALPIN, W. J.; GRAHAM, R. A.; USA
4	233	ANALYSIS OF SHOCK WAVE AND INITIATION DATA FOR SOLID EXPLOSIVES; RAMSAY, J. B.; POPOLATO, A.; USA
4	239	LOW-PRESSURE HUGONIOTS OF SOLID EXPLOSIVES (abstract only); WASLEY, R. J.; O'BRIEN, J. F.; USA
4	240	THE UNREACTED HUGONIOT EQUATIONS-OF-STATE OF SEVERAL EXPLOSIVES (abstract only); COLEBURN, N. L.; LIDDIARD, T. P.; USA
4	241	DETERMINATION OF SHOCK HUGONIOTS FOR SEVERAL CONDENSED PHASE EXPLOSIVES; BOYLE, V. M.; JAMESON, R. L.; SULTANOFF, M.; USA
4	248	SHOCK INDUCED PHASE TRANSITIONS; DUVALL, G. E.; HORIE, Y.; USA
4	258	EFFECT OF A SHOCK WAVE ON A POROUS SOLID; THOUVENIN, J.; FRANCE
4	266	SHOCK BEHAVIOR OF SOME NON-REACTING POROUS SOLIDS; REMPEL, J. R.; SCHMIDT, D. N.; USA
4	277	ELASTOPLASTIC EFFECTS IN THE ATTENUATION OF SHOCK WAVES; ERKMAN, J. O.; USA
4	289	HYDRODYNAMIC ELASTIC PLASTIC THEORY AND PLANE SHOCK WAVES IN METALS. I. THEORY (abstract only); PEARSON, J. C.; USA
4	290	THE ELASTO-PLASTIC RELEASE BEHAVIOR OF MAGNESIUM AT 80 Kb; FULLER, P. J. A.; PRICE, J. H.; UK
4	295	THE INFLUENCE OF MECHANICAL PROPERTIES ON WAVE PROPAGATION IN ELASTIC-PLASTIC MATERIALS; BUTCHER, B. M.; MUNSON, D. E.; USA

## A. TITLES INDEX (Continued)

<b>SYM</b>	<b>PAGE</b>	<b>TITLES, AUTHORS, NATION</b>
4	305	THE INSTABILITY OF AN INTERFACE BETWEEN TWO FLUIDS UNDER VARIABLE NORMAL ACCELERATION; CAMERON, I. G.; PIKE, H. H. M.; UK
4	316	CALCULATION OF THE GROWTH OF INTERFACE INSTABILITIES BY A LAGRANGIAN MESH METHOD; ELLIOT, L. A.; UK
4	321	SHOCK WAVE RESEARCH ON INERT SOLIDS; DEAL, W. E.; USA
4	349	THE EFFECT OF INTERSTITIAL GAS ON THE SHOCK SENSITIVITY OF LOW DENSITY EXPLOSIVE COMPACTS; CHICK, M. C.; UK
4	359	SHOCK INITIATION OF LOW-DENSITY PRESSINGS OF AMMONIUM PERCHLORATE; EVANS, M. W.; REESE, B. O.; SEELY, L. B.; USA
4	373	INITIATION OF A SOLID EXPLOSIVE BY A SHORT-DURATION SHOCK; GITTINGS, E. F.; USA
4	381	OBLIQUE IMPACT OF A LAYER OF EXPLOSIVE BY A METAL PLATE; DAVID, F.; FAUQUIGNON, C.; BERNIER, H.; POTAU, J.; FRANCE
4	386	EXPERIMENTAL OBSERVATIONS OF INITIATION OF NITROMETHANE BY SHOCK INTERACTIONS AT DISCONTINUITIES; TRAVIS, J. R.; USA
4	394	INITIATION OF DETONATION BY THE INTERACTION OF SHOCK WITH DENSITY DISCONTINUITIES (abstract only); MADER, C. L.; USA
4	395	AN EQUATION OF STATE AND DERIVED SHOCK INITIATION CRITICALITY CONDITIONS FOR LIQUID EXPLOSIVES (abstract only); ENIG, J. W.; PETRONE, F. J.; USA
4	399	THE EFFECT OF WAX ON THE SHOCK SENSITIVITY OF EXPLOSIVE COMPACTS; EADIE, J.; UK
4	404	DIRECT CONTACT DETONATION SENSITIVITY; SAVITT, J.; LEONE, CAPT. N.; KYSELKA, C.; USA
4	412	THE EFFECT OF PHYSICAL AND CHEMICAL PROPERTIES ON THE SENSITIVITY OF LIQUID EXPLOSIVES; HAY, J. E.; RIBOVICH, J.; SCOTT, F. H.; GIBSON, F. C.; USA
4	426	RETONATION CAUSED BY THE REFLECTION OF DIVERGENT WAVES; MARLOW, W. R.; UK
4	432	COMPARISON BETWEEN SHOOTING AND BARRIER TESTS; LUNDBORG, N.; SWEDEN
4	435	THE INITIATION PROPERTIES OF BOOSTERS IN EXPLOSIVES WITH LOW SENSITIVITY; JOHANSSON, C. H.; SJOLIN, T.; SWEDEN
4	442	SIZE FACTORS IN DETONATION TRANSFER; STRESAU, R. H. F.; USA
4	449	CONFINEMENT EFFECTS IN EXPLODING BRIDGEWIRE INITIATION OF DETONATION; STRESAU, R. H. F.; HILLYER, R. M.; KENNEDY, J. E.; USA

## A. TITLES INDEX (Continued)

<b>SYM</b>	<b>PAGE</b>	<b>TITLES, AUTHORS, NATION</b>
4	461	SURFACE RATE PROCESSES AND SENSITIVITY OF HIGH EXPLOSIVES (abstract only); CHAIKEN, R. F.; CHESELSKE, F. J.; USA
4	462	LOW ORDER REACTIONS IN SHOCKED EXPLOSIVE; GRIFFITHS, N.; BROOM, V. C.; UK
4	473	INITIATION OF EXPLOSIVES BY LOW VELOCITY IMPACT; NAPADENSKY, H. S.; USA
4	477	FURTHER STUDIES ON THE IGNITION OF EXPLOSIVES; GREEN, L. G.; DOROUGH, G. D.; USA
4	487	THE INITIATION OF BURNING IN HIGH EXPLOSIVES BY SHOCK WAVES; LIDDIARD, T. P.; USA
4	496	MECHANICAL AND DETONATION PROPERTIES OF RUBBER BONDED SHEET EXPLOSIVES; KEGLER, W.; SCHALL, R.; FRANCE
4	502	EXPLICIT SOLUTIONS FOR UNSTEADY SHOCK PROPAGATION IN CHEMICALLY REACTING MEDIA; ADAMS, G. K.; COWPERTHWAIT, M.; UK
4	512	SUMMARY PAPER ON INITIATION, IGNITION AND GROWTH OF REACTION; CACHIA, G. P.; UK
4	519	THE USE OF ONE- AND TWO-DIMENSIONAL HYDRODYNAMIC MACHINE CALCULATIONS IN HIGH EXPLOSIVE RESEARCH; WILKINS, M. L.; USA
4	527	CALCULATION OF UNSTEADY 2-D FLOWS BY VARIOUS NUMERICAL METHODS; VIDART, A.; BEATRIX, P.; CHEVALIER, Y.; BOUCHON, H.; FRANCE
4	538	THE CALCULATION OF HYDRODYNAMIC BEHAVIOR OF PLANE ONE DIMENSIONAL EXPLOSIVE/METAL SYSTEMS; LAMBOURN, B. D.; HARTLEY, J. E.; UK
4	555	A METHOD FOR THE STUDY OF PROPERTIES OF SOLID EXPLOSIVES AND OTHER SOLID (INCLUDING POROUS) MATERIALS WHEN SUBJECTED TO SHOCK WAVES; MURRY, W. L.; PLANT, J.; UK
4	566	EXPERIMENTAL METHOD FOR THE ANALYSIS OF THE STRUCTURE OF A SHOCK WAVE IN A SOLID; PEYRE, C.; PUJOL, J.; THOUVENIN, J.; FRANCE
4	573	A TECHNIQUE FOR THE PRECISE MEASUREMENT OF THE MOTION OF A PLANE FREE SURFACE; EDEN, G.; WRIGHT, P. W.; UK
4	584	A MICROWAVE TECHNIQUE FOR STUDYING DETONATION PHENOMENA; JOHNSON, E. G.; USA
4	595	ON ELECTRICAL CONDUCTIVITY IN DETONATION PRODUCTS; HAYES, B.; USA
4	602	A TECHNIQUE FOR DETAILED TIME-RESOLVED RADIATION MEASUREMENTS IN THE REACTION ZONE OF CONDENSED EXPLOSIVES; PERSSON, P.-A.; ANDERSSON, B.; STAHL, S. O.; SWEDEN
4	609	ELECTRICAL TRANSDUCER STUDIES OF INITIATION OF LIQUID EXPLOSIVES; TRAVIS, J. R.; USA

## A. TITLES INDEX (Continued)

<b>SYM</b>	<b>PAGE</b>	<b>TITLES, AUTHORS, NATION</b>
4	616	ELECTRICAL PROBE TECHNIQUE FOR MEASUREMENT OF DETONATION AND DEFLAGRATION VELOCITIES; PITTS, L. D.; USA
4	627	ANOMALOUS THERMOELECTRIC EFFECT IN THE SHOCK REGIME AND APPLICATION TO A SHOCK PRESSURE TRANSDUCER; CROSNIER, J.; JACQUESSON, J.; MIGAULT, A.; FRANCE
4	639	PERMEX APPLICATIONS TO STUDIES OF DETONATION WAVES AND SHOCK WAVES; VENABLE, D.; BOYD, T. J.; USA
5	3	FLASH X-RAY OBSERVATION OF MARKED MASS POINTS IN EXPLOSIVE PRODUCTS; RIVARD, W. C.; VENABLE, D.; FICKETT, W.; DAVIS, W. C.; USA
5	13	PRESSURE MEASUREMENTS FOR COMPOSITION B-3; DAVIS, W. C.; VENABLE, D.; USA
5	31	DIVERGENT SPHERICAL DETONATION WAVES IN A SOLID EXPLOSIVE; CHERET, R.; VERDES, G.; FRANCE
5	34	SHOCK VELOCITY MEASUREMENTS IN INERT MONITORS PLACED ON SEVERAL EXPLOSIVES; JAMESON, R. L.; HAWKINS, A.; USA
5	41	A COMPARISON OF SPHERICAL, CYLINDRICAL AND PLANE DETONATION VELOCITIES IN SOME CONDENSED AND GASEOUS EXPLOSIVES; BROCHET, C.; BROSSARD, J.; MANSON, N.; CHERET, R.; VERDES, G.; FRANCE
5	47	DETONATION CHARACTERISTICS OF VERY LOW DENSITY EXPLOSIVE SYSTEMS; AUSTING, J. L.; TULIS, A. J.; JOHNSON, C. D.; USA
5	59	AN ANALYSIS OF THE "AQUARIUM TECHNIQUE" AS A PRECISION DETONATION PRESSURE MEASUREMENT GAGE; RIGDON, J. K.; AKST, I. B.; USA
5	67	EFFECTS OF PRECOMPRESSION UPON THE DETONATION PROPERTIES OF LIQUID AND SOLID EXPLOSIVES; ANDERSEN, W. H.; ZERNOW, L.; MOTTET, A. L.; RANDALL, R. R.; USA
5	81	THE STABILITY OF LOW-VELOCITY DETONATION WAVES; WATSON, R. W.; RIBOVICH, J.; HAY, J. E.; VAN DOLAH, R. W.; USA
5	89	FAILURE DIAMETER, SENSITIVITY AND WAVE STRUCTURE IN SOME BIS-DIFLUOROAMINO ALKANES; SEELY, L. B.; BERKE, J. G.; SHAW, R.; TEGG, D.; EVANS, M. W.; USA
5	99	THE FAILURE DIAMETER THEORY OF DREMIN; ENIG, J. W.; PETRONE, F. J.; USA
5	105	WALL TRACES OF DETONATION IN NITROMETHANE-ACETONE MIXTURES; URTIEW, P. A.; KUSABOV, A. S.; USA
5	115	A PHOTOGRAPHIC TECHNIQUE FOR MAPPING FAILURE WAVES AND OTHER INSTABILITY PHENOMENA IN LIQUID EXPLOSIVES DETONATION; PERSSON, P.-A.; BJARNHOLT, G.; SWEDEN

## A. TITLES INDEX (Continued)

<u>SYM</u>	<u>PAGE</u>	<u>TITLES, AUTHORS, NATION</u>
5	119	ON THE DYNAMICS OF SHOCK INTERACTIONS; OPPENHEIM, A. K.; SMOLEN, J. J.; KWAK, D.; URTIEW, P. A.; USA
5	137	METAL ACCELERATION BY COMPOSITE EXPLOSIVES; FINGER, M.; HORNIG, H. C.; LEE, E. L.; KURY, J. W.; USA
5	153	LIGHT EMISSION DURING INITIATION OF LIQUID EXPLOSIVES; PERSSON, P.-A.; SJOLIN, T.; SWEDEN
5	169	DARK WAVES IN LIQUID EXPLOSIVE SYSTEMS: THEIR ROLE IN DETONATION FAILURE; WATSON, R. W.; USA
5	177	NUMERICAL CALCULATIONS OF DETONATION FAILURE AND SHOCK INITIATION; MADER, C. L.; USA
5	185	THE ROLE OF THE MATRIX IN DETERMINING THE SHOCK INITIATION CHARACTERISTICS OF COMPOSITIONS CONTAINING 60% BY VOLUME OF HMX; MARSHALL, W. W.; UK
5	191	EFFECT OF PULSE DURATION ON THE IMPACT SENSITIVITY OF SOLID EXPLOSIVES; TROTT, B. D.; JUNG, R. G.; USA
5	207	SHOCK SENSITIVITY, A PROPERTY OF MANY ASPECTS; PRICE, D.; USA
5	219	SHOCK SENSITIVITY AND SHOCK HUGONIOTS OF HIGH-DENSITY GRANULAR EXPLOSIVES; ROTH, J.; USA
5	231	EXPERIMENTAL STUDY OF THE TRANSITION FROM BURNING TO DETONATION; CALZIA, J.; CARABIN, H.; FRANCE
5	237	SHOCK INITIATION OF NITROMETHANE, METHYL NITRITE, AND SOME BIS DIFLUORO ALKANES; BERKE, J. G.; SHAW, R.; SEELY, L. B.; USA
5	247	THE ROLE OF INTERSTITIAL GAS IN THE DETONATION BUILD-UP CHARACTERISTICS OF LOW DENSITY GRANULAR HMX; MARSHALL, W. W.; UK
5	251	THE SHOCK HUGONIOT OF UNREACTED EXPLOSIVES; BOYLE, V. M.; SMOTHERS, W. G.; ERVIN, L. H.; USA
5	259	EFFECT OF PARTICLE SIZE ON SHOCK INITIATION OF PETN, RDX, AND TETRYL; SCOTT, C. L.; USA
5	267	EXPLOSIVE BEHAVIOR OF METHYLNITRATE AND ITS MIXTURES WITH LIQUID DILUENTS; KUSAKABE, M.; FUJIWARA, S.; JAPAN
5	279	THE THERMAL INITIATION AND GROWTH OF REACTION IN SECONDARY EXPLOSIVES UNDER TRANSIENT CONFINEMENT; BEEDHAM, K.; DYER, A. S.; HOLMES, W. I.; UK
5	291	INITIATION OF DETONATION BY FRICTION ON A HIGH EXPLOSIVE CHARGE; DYER, A. S.; TAYLOR, J. W.; UK

## A. TITLES INDEX (Continued)

<u>SYM</u>	<u>PAGE</u>	<u>TITLES, AUTHORS, NATION</u>
5	301	DEFLAGRATION IN SINGLE CRYSTALS OF LEAD AZIDE; CHAUDHRI, M. M.; FIELD, J. E.; UK
5	311	THE INFLUENCE OF SURFACE MELTING OF CRYSTALS ON THE BURNING OF SOLID EXPLOSIVE UNDER RISING PRESSURE CONDITIONS (abstract only); TAYLOR, J. W. UK
5	313	DEFORMATION OF A CYLINDER OF EXPLOSIVE MATERIAL IN UNCONFINED IMPACT; NAPADENSKY, H. S.; EICHLER, T. V.; KOT, C. A.; ZAKER, T. A.; USA
5	321	DECOMPOSITION OF A SHOCKED SOLID EXPLOSIVE; CRAIG, B. G.; MARSHALL, E. F. USA
5	331	THERMAL DECOMPOSITION OF HIGH EXPLOSIVES AT STATIC PRESSURE 10-50 KILOBARS; LEE, E. L.; SANBORN, R. H.; STROMBERG, H. D.; USA
5	339	EXPERIMENTAL OBSERVATIONS OF INITIATION OF PRIMARY EXPLOSIVES BY A HOT WIRE; LEOPOLD, H. S.; USA
5	351	EQUATION-OF-STATE INVESTIGATION OF GRANULAR EXPLOSIVES USING A PULSED ELECTRON BEAM; SHEA, J. H.; MAZZELLA, A.; AVRAMI, L.; USA
5	361	CREATION OF AN INTENSE SHOCK IN SOLID DEUTERIUM BY A PULSED LASER BEAM; FAUQUIGNON, C.; FRANCE
5	369	QUARTZ GAUGE TECHNIQUE FOR IMPACT EXPERIMENTS; INGRAM, G. E.; GRAHAM, R. A.; USA
5	387	SHOCK-INDUCED ELECTRICAL SIGNALS FROM DIELECTRICS; HAUVER, G. E.; USA
5	399	THE MECHANISM OF ELECTRICAL CONDUCTIVITY OF LIQUID DIELECTRICS IN SHOCK WAVES; DREMIN, A. N.; YAKUSHEV, V. V.; USSR
5	403	ELECTRICAL EFFECT OF BIMETALLIC AND METAL SEMICONDUCTOR JUNCTIONS UNDER SHOCK; JACQUESSON, J.; ROMAIN, J. P.; HALLOUIN, M.; DESOYER, J. C.; FRANCE
5	413	EXPERIMENTAL STUDY OF THE ELECTROMAGNETIC VELOCITY-GAGE TECHNIQUE; JACOBS, S. J.; EDWARDS, D. J.; USA
5	427	DETERMINATION OF CONSTITUTIVE RELATIONSHIPS WITH MULTIPLE GAGES IN NON-DIVERGENT WAVES; COWPERTHWAIT, M.; WILLIAMS, R. F.; USA
5	429	SHOCK-INDUCED ELECTRICAL POLARIZATION OF A SOLID EXPLOSIVE; MORVAN, J.; PUJOLS, H.; FRANCE
5	435	QUARTZ GAUGE STUDY OF UPSTREAM REACTION IN A SHOCKED EXPLOSIVE; KENNEDY, J. E.; USA
5	447	MEASUREMENT OF MASS MOTION IN DETONATION PRODUCTS BY AN AXIALLY-SYMMETRIC ELECTROMAGNETIC TECHNIQUE; HAYES, B.; FRITZ, J. N.; USA

## A. TITLES INDEX (Continued)

<u>SYM</u>	<u>PAGE</u>	<u>TITLES, AUTHORS, NATION</u>
5	457	EXPLOSIVE DEFLECTION OF A LINER AS A DIAGNOSTIC OF DETONATION FLOWS; DEFOURNEAUX, M.; JACQUES, L.; FRANCE
5	467	ELASTIC-PLASTIC BEHAVIOR OF POROUS BERYLLIUM; EDEN, G.; SMITH, C. P. M.; UK
5	477	NUMERICAL ANALYSIS OF A DIVERGING SHOCK WAVE IN PLEXIGLAS CYLINDERS; KAMEGAI, M.; ERKMAN, J. O.; USA
5	487	A CODE METHOD FOR CALCULATING HYDRODYNAMIC MOTION IN HE DETONATIONS; NEEDHAM, C. E.; USA
5	493	A REALISTIC APPROACH FOR DESCRIBING THE EXPLOSION-GENERATED AXI-SYMMETRIC WAVE PROPAGATING IN A HALF-SPACE; SAKURAI, A.; USA
5	501	THE COMPUTATION OF GENERAL PROBLEMS IN ONE DIMENSIONAL UNSTEADY FLOW BY THE METHOD OF CHARACTERISTICS (abstract only); LAMBOURN, R. D.; HOSKIN, N. E.; UK
5	503	EQUATION OF STATE OF DETONATION PRODUCTS; HORNIG, H. C.; LEE, E. L.; FINGER, M.; KURRLE, J. E.; USA
5	513	OPTICAL PROPERTIES OF DETONATION WAVES (OPTICS OF EXPLOSIVES); BUSCO, M.; ITALY
5	523	HYDRODYNAMIC BEHAVIOR AND EQUATION OF STATE OF DETONATION PRODUCTS BELOW THE CHAPMAN-JOUGUET STATE; ROSLUND, L. A.; COLEBURN, N. L.; USA
5	533	SHOCKED STATES OF FOUR OVERDRIVEN EXPLOSIVES; KINEKE, J. H.; WEST, C. E.; USA
5	547	VAPORIZATION OF URANIUM AFTER SHOCK LOADING; DE BEAUMONT, P.; LEYGONIE, J.; FRANCE
5	559	OBSERVATIONS OF DETONATION IN A HIGH VACUUM; HAY, J. E.; PETERS, W. C.; WATSON, R. W.; USA
5	567	PLANE SPALLING OF COPPER; DAVID, F.; VACELLIER, J.; PROUTEAU, F.; LEGRAND, J.; CHERET, R.; FRANCE
5	573	SPALLING UNDER OBLIQUE IMPACT; SKIDMORE, I. C.; LETHADY, J. W.; UK
5	581	INTERACTIONS OF SPHERICAL SHOCK WAVES IN WATER; COLEBURN, N. L.; ROSLUND, L. A.; USA
5	589	THE SPEED OF PROPAGATION OF RELEASE WAVES IN POLYMETHYL METHACRYLATE; SCHULER, K. W.; USA
5	597	ARTIFICIAL VISCOSITY METHOD CALCULATION OF AN UNDERWATER DETONATION; STERNBERG, H. M.; WALKER, W. A.; USA
5	599	SPHERICAL EXPLOSIONS IN WATER; HANTEL, L. A.; DAVIS, W. C.; USA

## A. TITLES INDEX (Continued)

SYM	PAGE	TITLES, AUTHORS, NATION
6	3	SEPARATION OF IGNITION AND BUILDUP TO DETONATION IN PRESSED TNT; TAYLOR, B. C.; ERVIN, L. H.; USA
6	11	SHOCK INITIATION AND THE CRITICAL ENERGY CONCEPT; HOWE, P. M.; FREY, R. B.; BOYLE, V. M.; USA
6	20	SHOCK INITIATION OF HIGH DENSITY PETN; WACKERLE, J.; JOHNSON, J. O.; HALLECK, P. M.; USA
6	29	ON SHOCK WAVE EXPLOSIVE DECOMPOSITION; DREMIN, A. N.; SHVEDOV, K. K.; USSR
6	36	INVESTIGATION OF SOME CAST TNT PROPERTIES AT LOW TEMPERATURE; TITOV, V. M.; SILVESTROV, V. V.; KRAVTSOV, V. V.; STADNITSHENKO, I. A.; USSR
6	47	MODES OF SHOCK WAVE GROWTH IN THE INITIATION OF EXPLOSIVES; NUNZIATO, J. W.; KENNEDY, J. E.; HARDESTY, D. R.; USA
6	62	GEOMETRICAL SHOCK FOCUSING AND FLYING PLATE INITIATION OF SOLID EXPLOSIVES; SEARCY, J. Q.; SCHWARZ, A. C.; USA
6	66	CRITICAL CONDITIONS FOR SHOCK INITIATION OF DETONATION IN REAL SYSTEMS; STRESAU, R. H. F.; KENNEDY, J. E.; USA
6	76	A P <sup>nt</sup> DETONATION CRITERION FROM THERMAL EXPLOSION THEORY; HAYES, D. B.; USA
6	105	INITIATION OF SEVERAL CONDENSED EXPLOSIVES BY A GIVEN DURATION SHOCK WAVE; DE LONGUEVILLE, Y.; FAUQUIGNON, C.; MOULARD, H.; FRANCE
6	115	INITIATION OF DETONATION IN INSENSITIVE LIQUID EXPLOSIVES BY LOW-AMPLITUDE COMPRESSION WAVES; HAY, J. E.; WATSON, R. W.; USA
6	124	CELLULAR STRUCTURE OF DETONATION IN NITROMETHANE CONTAINING ALUMINUM PARTICLES; YATO, Y.; BROCHET, C.; FRANCE
6	133	EFFECTS OF LIQUID DILUENTS ON DETONATION PROPAGATION IN NITROMETHANE; KUSAKABE, M.; FUJIWARA, S.; JAPAN
6	143	SHOCK-INDUCED ELECTRICAL POLARIZATION OF HOMOGENEOUS EXPLOSIVES; DREMIN, A. N.; ANT'PENKO, A. G., YAKUSHEV, V. V.; USSR
6	151	SOME APPLICATIONS OF THE ELECTRICAL JUNCTION EFFECT IN EXPERIMENTAL SHOCK STUDIES; ROMAIN, J. P.; JACQUESSON, J.; FRANCE
6	162	THE JCE EQUATIONS OF STATE FOR DETONATION PRODUCTS AND THEIR INCORPORATION IN THE TIGER CODE; COWPERTHWAIT, M.; ZWISLER, W. H.; USA
6	173	SYMPATHETIC DETONATION OF AMMONIUM PERCHLORATE BY SMALL AMOUNTS OF NITROGUANIDINE; TULIS, A. J.; USA
6	183	FURTHER STUDIES ON THE DETONATION CHARACTERISTICS OF VERY LOW DENSITY EXPLOSIVE SYSTEMS; TULIS, A. J.; AUSTING, J. L.; USA

## A. TITLES INDEX (Continued)

SYM	PAGE	TITLES, AUTHORS, NATION
6	195	DEFLAGRATION RATE OF COMPOSITE HIGH EXPLOSIVE AND COMPOSITE PROPELLANTS AT PRESSURES ABOVE 1 KILOBAR; BENHAIM, P.; GOLIGER, J.; FRANCE
6	204	EFFECTS OF CONFINEMENT AND INITIAL PRESSURE ON THE DEFLAGRATION OF SOME HIGH EXPLOSIVES; LISTH, O.; SWEDEN
6	214	THE THERMAL DECOMPOSITION AND REACTION OF CONFINED EXPLOSIVE; CATALANO, E.; ORNELLAS, D. L.; WRENN, E.; LEE, E. L.; WALTON, J.; MCGUIRE, R. R.; USA
6	225	RETARDED DETONATION; HELD, M.; LUDWIG, D.; NIKOWITSCH, P.; WEST GERMANY (FRG)
6	291	DEFLAGRATION TO DETONATION TRANSITION STUDIES FOR TWO POTENTIAL ISOMETRIC CAST PRIMARY EXPLOSIVES; TARVER, C. M.; GOODALE, T. C.; SHAW, R.; COWPERTHWAIT, M.; USA
6	250	ON THE MECHANISM OF DEFLAGRATION TO DETONATION TRANSITION IN GAS-PERMEABLE HIGH EXPLOSIVE; SULIMOV, A. A.; ERMOLAEV, B. S.; BORISOV, A. A.; KOROTKOV, A. I.; KHASAINOV, B. A.; KHRAPOVSKY, V. E.; USSR
6	258	A COMPARISON OF MODEL PREDICTIONS AND EXPERIMENTAL RESULTS OF DDT TESTS; PILCHER, D. T.; CHRISTENSEN, L. W.; BECKSTED, M. W.; KING, A. J.; USA
6	267	SHOCKS RETARDATION AND PRESENCE OF CRACKS IN MATERIALS; BELGAUMKAR, B. M.; INDIA
6	272	SENSITIVITY OF EXPLOSIVE SUBSTANCES, A MULTIVARIATE APPROACH; EK, S.; SWEDEN
6	281	INSTABILITY OF HETEROGENEOUS DEFLAGRATION WAVES; DE LUCA, L.; ITALY
6	290	THE GROWTH OF REACTION IN SECONDARY EXPLOSIVES UNDER TRANSIENT CONFINEMENT; COLEY, G. D.; UK
6	299	PROPELLANT DETONATION RISK TESTING; PASMAN, H. J.; CRUYSBERG, E. E. A.; GROOTHUIZEN, T. M.; NETHERLANDS
6	305	VOLUME AND PRESSURE DEPENDENCE OF SOME KINETIC PROCESSES IN EXPLOSIVES; PASTINE, D. J.; KAMLET, M. J.; JACOBS, S. J.; USA
6	312	THE RELATIONSHIP OF IMPACT SENSITIVITY WITH STRUCTURE OF ORGANIC HIGH EXPLOSIVES. I. POLYNITROALIPHATIC EXPLOSIVES; KAMLET, M. J.; USA
6	325	INITIATION OF VIOLENT REACTION BY PROJECTILE IMPACT; FREY, R. B.; MELANI, G.; CHAWLA, M.; TRIMBLE, J.; USA
6	336	A NUMERICAL STUDY OF IMPACT PHENOMENA IN EXPLOSIVES AND PROPELLANTS; KOT, C. A.; WIEDERMANN, A. H.; NAPADENSKY, H. S.; SHIKARI, Y. A.; USA

## A. TITLES INDEX (Continued)

SYM	PAGE	TITLES, AUTHORS, NATION
6	344	A KINETIC LATTICE APPROACH TO DETONATION IN HETEROGENEOUS EXPLOSIVES; CHAIKEN, R. F.; EDWARDS, J. C.; USA
6	352	PERTURBATION METHODS APPLIED TO PROBLEMS IN DETONATION PHYSICS; BDZIL, J. B.; USA
6	371	A SIMPLE MODEL FOR THE SIMULATION OF THE INITIATION OF DETONATION BY A SHOCK WAVE IN HETEROGENEOUS EXPLOSIVE; SCHILPEROORD, A. A.; NETHERLANDS
6	379	CHEMICAL KINETIC AND CURVATURE EFFECTS ON SHOCK WAVE EVOLUTION IN EXPLOSIVES; CHEN, P. J.; KENNEDY, J. E.; USA
6	389	THE HUGONIOT AND SHOCK INITIATION THRESHOLD OF LEAD AZIDE (abstract only); DAVIES, F. W.; ZIMMERSCHIED, A. B.; BORGARDT, F. G.; AVRAMI, L.; USA
6	390	ELECTRIC FIELD INITIATION OF EXPLOSIVE AZIDES; GORA, T.; DOWNS, D. S.; FAIR, H. D.; MARK, P.; USA
6	396	ADIABATIC ELASTIC MODULI OF SINGLE CRYSTAL PENTAERYTHRITOL TETRANITRATE (PETN); MORRIS, C. E.; USA
6	405	TWO DIMENSIONAL HOMOGENEOUS AND HETEROGENEOUS DETONATION WAVE PROPAGATION; MADER, C. L.; USA
6	414	HIGH RESOLUTION PHOTOGRAPHY OF TRANSVERSE WAVE EFFECTS IN THE DETONATION OF CONDENSED EXPLOSIVES; PERSSON, P.-A.; PERSSON, G.; SWEDEN
6	426	DEFLAGRATION TO DETONATION TRANSITION BEHAVIOR OF TETRYL; BERNECKER, R. R.; PRICE, D.; ERKMAN, J. O.; CLAIRMONT, A. R.; USA
6	439	IMPROVEMENT OF PERFORMANCE OF COMPOSITE EXPLOSIVES CONTAINING AMMONIUM NITRATE BY PHYSICAL SYNTHESIS; HERSHKOWITZ, J.; AKST, I. B.; USA
6	450	HOMOGENEOUS LIQUID EXPLOSIVES CONTAINING UREA PERCHLORATE; FUJIWARA, S.; KUSAKABE, M.; SHIINO, K.; JAPAN
6	455	A NEW EXPLOSIVE FOR LOW VOLTAGE DETONATOR APPLICATIONS; LESLIE, W. B.; DIETZEL, R. W.; SEARCY, J. Q.; USA
6	460	BTX - A USEFUL HIGH TEMPERATURE EBW DETONATOR EXPLOSIVE; DINEGAR, R. H.; CARLSON, L. A.; COBURN, M. D.; USA
6	466	PHYSICAL, STABILITY, AND SENSITIVITY PROPERTIES OF LIQUID EXPLOSIVES; SCRIBNER, K.; ELSON, R. E.; FYFE, R. R.; CRAMER, J. P.; USA
6	477	DYNAMIC DETECTION OF THE ONSET OF SPALLING IN STAINLESS STEEL ON COMP. B; SMITH, C. P. M.; EDEN, G.; LAMBOURN, B. D.; UK
6	489	THE CRITICAL ANGLE FOR MACH BRIDGE FORMATION BETWEEN OPPOSING SHOCK WAVES IN POLYURETHANE FOAM; JAMES, R. M.; MOORE, P. W. J.; LAMBOURN, B. D.; UK

## A. TITLES INDEX (Continued)

<u>SYM</u>	<u>PAGE</u>	<u>TITLES, AUTHORS, NATION</u>
6	502	ON BLAST WAVES IN LIQUIDS; KAMAL, M. M.; ABOUSEIF, G. E.; GUIGUIS, R. H.; FARAG, S. A.; OPPENHEIM, A. K.; EGYPT
6	510	EFFECTS OF ALUMINUM AND LITHIUM FLUORIDE ADMIXTURES ON METAL ACCELERATION ABILITY OF COMP B; BJARNHOLT, G.; SWEDEN
6	521	ACCELERATION OF SPHERICAL METAL SHELLS BY HIGH EXPLOSIVES: DETONATION VELOCITY ALONG THE SHELL SURFACE AND EFFICIENCY OF ENERGY TRANSFER; FREUND, H. V.; GEIGER, W.; HONCIA, G.; WEST GERMANY (FRG)
6	528	CALCULATED SPHERICAL SHOCK WAVES PRODUCED BY CONDENSED EXPLOSIVES IN AIR AND WATER; STERNBERG, H. M.; HURWITZ, H.; USA
6	540	EXPLOSIVE EXPANSION WORKS IN UNDERWATER DETONATIONS; BJARNHOLT, G.; HOLMBERG, R.; SWEDEN
6	551	OPTIMISATION OF EXPLOSIVES FOR USE UNDERWATER; HICKS, A. N.; UK
6	561	THE EFFECT OF EXPLOSIVE PROPERTIES ON THE SHOCK WAVE PARAMETERS OF UNDERWATER EXPLOSIONS; LAMBOURN, B. D.; UK
6	570	THE UNSTEADY REGULAR AND MACH REFLECTION RESULTING FROM THE INTERACTION OF SPHERICAL EXPLOSION SHOCK WAVES IN WATER; ENIG, J. W.; USA
6	590	THE PROBLEM OF STRONG POINT EXPLOSION IN A COMBUSTIBLE MEDIUM; EIDELMAN, S.; TIMNAT, Y. M.; BURCAT, A.; ISRAEL
6	602	PERPENDICULAR EXPLOSIVE DRIVE AND OBLIQUE SHOCKS; NEAL, T. R.; USA
6	612	LASER INITIATION OF INSENSITIVE HIGH EXPLOSIVES; YANG, L. C.; MENICHELLI, V. J.; USA
6	625	DETERMINATION OF DETONATION PRESSURE USING A MANGANIN WIRE TECHNIQUE; BURROWS, K.; CHILVERS, D. K.; GYTON, R.; LAMBOURN, B. D.; WALLACE, A. A.; UK
6	637	MAGNETIC PROBE MEASUREMENTS OF PARTICLE VELOCITY PROFILES; DAVIS, W. C.; USA
6	642	THE DIAMETER EFFECT IN HIGH-DENSITY HETEROGENEOUS EXPLOSIVES; ENGELKE, R.; CAMPBELL, A. W.; USA
6	653	ACCELERATION OF THIN FLYERS BY EXPLODING METAL FOILS: APPLICATION TO INITIATION STUDIES; WEINGART, R. C.; LEE, R. S.; JACKSON, R. K.; PARKER, N. L.; USA
6	664	MULTIPLE-EXPOSURE IMAGE INTENSIFIER CAMERA; WINSLOW, O. G.; DAVIS, W. C.; CHILES, W. C.; USA
6	668	THE USE OF A DUAL-DELAY-LEG VELOCITY INTERFEROMETER WITH AUTOMATIC DATA REDUCTION IN A HIGH-EXPLOSIVE FACILITY; LEDERER, R. A.; SHEFFIELD, S. A.; SCHWARZ, A. C.; HAYES, D. B.; USA

## A. TITLES INDEX (Continued)

<b>SYM PAGE</b>	<b>TITLES, AUTHORS, NATION</b>
6 673	WIDE RANGE VELOCITY INTERFEROMETER; AMERY, B. T.; UK
6 682	ASSESSMENT METHODS OF THE IMPACT IGNITION SENSITIVITY OF DIFFICULTLY-DETONABLE EXPLOSIVES; ANDERSEN, W. H.; LOUIE, N. A.; USA
6 691	SHAPED CHARGE TEMPERATURE MEASUREMENT; VON HOLLE, W. G.; TRIMBLE, J.; USA
6 700	THE HYDROSTATIC COMPRESSION OF EXPLOSIVES & DETONATION PRODUCTS TO 10 GPa (100 KBARS) AND THEIR CALCULATED SHOCK COMPRESSION: RESULTS FOR PETN, TATB, CO <sub>2</sub> & H <sub>2</sub> O; OLINGER, B.; CADY, H. H.; USA
6 710	THE EFFECT OF ELEMENTAL COMPOSITION ON THE DETONATION BEHAVIOR OF EXPLOSIVES; FINGER, M.; LEE, E. L.; HELM, F. H.; HAYES, B.; HORNIG, H. C.; MCGUIRE, R. R.; KAHARA, M.; GUIDRY, M.; USA
6 723	DETONATION CHARACTERISTICS OF LIQUID NITRIC OXIDE; CHILES, W. C.; RAMSAY, J. B.; USA
6 729	CHARACTERIZATION OF COMMERCIAL, COMPOSITE EXPLOSIVES; FINGER, M.; HELM, F. H.; LEE, E. L.; CHEUNG, H.; HAYES, B.; PENN, L.; WALTON, J.; BOAT, R.; USA
6 740	THE EQUATION OF STATE AND SHOCK INITIATION OF HNS II; DAVIES, F. W.; SHRADER, J.; ZIMMERSCHIED, A. B.; RILEY, J. F.; USA
6 748	THE EQUATION OF STATE AND CHEMICAL KINETICS FOR HEXANITROSTILBENE (HNS) EXPLOSIVE; SHEFFIELD, S. A.; MITCHELL, D. E.; HAYES, D. B.; USA
6 755	INITIATION AND DETONATION CHARACTERISTICS OF TATB; JACKSON, R. K.; GREEN, L. G.; BARLETT, R. H.; HOFER, W. W.; KRAMER, P. E.; LEE, R. S.; NIDICK, E. J.; SHAW, L. L.; WEINGART, R.; USA
6 766	COMPUTED AND EXPERIMENTAL HUGONIOTS FOR UNREACTED POROUS HIGH EXPLOSIVES; ERKMAN, J. O.; EDWARDS, D. J.; USA
6 777	THE INFLUENCE OF INERT CASES ON AIRBLAST: AN EXPERIMENTAL STUDY; FILLER, W. S.; USA
6 786	A MULTIPLE LAGRANGE GAGE STUDY OF THE SHOCK INITIATION PROCESS IN CAST TNT; COWPERTHWAIT, M.; ROSENBERG, J. T.; USA
7 3	IGNITION OF SOLID HIGH EXPLOSIVE BY THE RAPID COMPRESSION OF AN ADJACENT GAS LAYER; STARKENBERG, J.; USA
7 17	THE INFLUENCE OF THE DYNAMIC COMPRESSIVE STRENGTH PROPERTIES OF HE FORMULATIONS ON THE GROWTH OF REACTION; COLEY, G. D.; WHATMORE, C. E.; UK
7 24	EFFECT OF POLYMERS ON THE DROP-WEIGHT SENSITIVENESS OF EXPLOSIVENESS; SWALLOWE, G. M.; FIELD, J. E.; UK
7 36	THE INITIATION OF EXPLOSIVE CHARGES BY RAPID SHEAR; FREY, R. B.; USA

## A. TITLES INDEX (Continued)

<b>SYM</b>	<b>PAGE</b>	<b>TITLES, AUTHORS, NATION</b>
7	43	THERMAL EXPLOSION HAZARD OF THIN LAYERS OF GELATINE DYNAMITE; PERSSON, A.; JERBERYD, L.; SWEDEN
7	50	ELECTRON BEAM INITIATION OF HIGH EXPLOSIVES; STOLOVY, A.; AVILES, J. B.; JONES, E. C.; NAMENSON, A. I.; USA
7	56	CHEMICAL DECOMPOSITION MODELS FOR THE THERMAL EXPLOSION OF CONFINED HMX, TATB, RDX, AND TNT EXPLOSIVES; MCGUIRE, R. R.; TARVER, C. M.; USA
7	65	MOLECULAR ELECTRONIC STRUCTURE AND INITIATION OF SECONDARY EXPLOSIVES; DELPUECH, A.; CHERVILLE, J.; MICHAUD, C.; FRANCE
7	75	THERMAL DECOMPOSITION OF RDX BELOW THE MELTING POINT; PUGH, H. L.; DAVIS, L. P.; WILKES, J. S.; CARPER, W. R.; DOREY, R. C.; USA
7	84	SOME COMMENTS REGARDING THE SENSITIVITIES, THERMAL STABILITIES, AND EXPLOSIVE PERFORMANCE CHARACTERISTICS OF FLUORODINITROMETHYL COMPOUNDS; KAMLET, M. J.; ADOLPH, H. G.; USA
7	93	THE ROLE OF EXCITED ELECTRONIC STATES IN THE BOND-SCISSION PROCESS IN DETONATION REACTIONS; BARDO, R. D.; USA
7	107	STUDIES ON TRANSITION FROM DEFLAGRATION TO DETONATION IN HIGH EXPLOSIVES AT VERY SMALL DIAMETERS; THIVET, R.; GUY, L. R.; FRANCE
7	119	DEFLAGRATION-TO-DETONATION TRANSITION STUDIES OF POROUS EXPLOSIVE CHARGES IN PLASTIC TUBES; BERNECKER, R. R.; SANDUSKY, H. W.; CLAIRMONT, A. R.; USA
7	139	DEFLAGRATION DETONATION TRANSITION IN WAXED RDX; SAMIRANT, M.; FRANCE
7	143	EFFECTS OF IGNITER AND COMPACTION ON DDT RUN UP IN PLASTIC PIPES; BUTCHER, A. G.; KEEFE, R. L.; ROBINSON, N. J.; BECKSTED, M. W.; USA
7	151	EXPERIMENTAL STUDY OF DEFLAGRATION TO DETONATION TRANSITION CASE OF AMMONIUM PERCHLORATE; MAURIN, C.; DERRIEN, J. C.; DENEUVILLE, P.; MONTEAGUDO, P.; FRANCE
7	164	TRANSITIONS FROM LAMINAR BURNING FOR POROUS CRYSTALLINE EXPLOSIVES; FIFER, R. A.; COLE, J. E.; USA
7	175	DEFLAGRATION FROM AN IGNITION SITE OF A CONFINED EXPLOSIVE CHARGE AS A FUNCTION OF VENTING BY ORIFICE FLOW; HERSHKOWITZ, J.; CHANG, L. M.; HUDGINS, H. E.; USA
7	186	IMPROVED PREDICTION OF FLAME SPREADING DURING CONVECTIVE BURNING IN SOLID PROPELLANT CRACKS; KOVACIC, S. M.; KUMAR, M.; KUO, K. K.; USA
7	198	A MECHANISM FOR THE BURNING RATE OF HIGH DENSITY, POROUS ENERGETIC MATERIALS; KOOKER, D. E.; ANDERSON, R. D.; USA

## A. TITLES INDEX (Continued)

<u>SYM</u>	<u>PAGE</u>	<u>TITLES, AUTHORS, NATION</u>
7	216	ROLE OF GAS PHASE REACTIONS IN DEFLAGRATION-TO-DETONATION TRANSITION; BOGGS, T. L.; PRICE, C. F.; ATWOOD, A. I.; ZURN, D. E.; DERR, R. L.; USA
7	225	PHENOMENOLOGY OF THE DEFLAGRATION TO DETONATION TRANSITION IN PROPELLANTS AND EXPLOSIVES; COWPERTHWAITTE, M.; USA
7	234	BURNING AND DETONATION; FOREST, C. A.; USA
7	247	NONDETONATIVE EXPLOSIONS IN CONFINED EXPLOSIVE CHARGES; FREY, R. B.; TRIMBLE, J.; USA
7	256	DELAYED DEFLAGRATION IN PROPELLANTS FROM LOW VELOCITY IMPACT; GREEN, L. G.; JAMES, F.; LEE, E. L.; CHAMBERS, E. S.; TARVER, C. M.; WESTMORELAND, C.; WESTON, A. M.; BROWN, B.; USA
7	265	DELAYED DETONATION IN CARD GAP TESTS; KEEFE, R. L.; USA
7	273	SHOCK INITIATION OF EXPLOSIVES BY THE IMPACT OF SMALL DIAMETER CYLINDRICAL PROJECTILES; GREEN, L. G.; USA
7	278	SHOCK INITIATION IN GAP TEST CONFIGURATIONS; FOAN, G. C. W.; COLEY, G. D.; UK
7	285	SHOCK INITIATION AND SUBSEQUENT GROWTH OF REACTION IN EXPLOSIVES AND PROPELLANTS; THE LOW-AMPLITUDE SHOCK INITIATION TEST, LASI; TASKER, D. G.; UK
7	299	AN INSTRUMENTED SHOTGUN FACILITY TO STUDY IMPACT-INITIATED EXPLOSIVE REACTIONS; JENSEN, R. C.; BLOMMER, E. J.; BROWN, B.; USA
7	308	INITIATION OF BURNING AND DETONATION IN CAST H-6 AND CAST PBXW-109; LIDDIARD, T. P.; FORBES, J. W.; USA
7	316	CRITICAL CONDITIONS FOR SHOCK INITIATION OF DETONATION BY SMALL PROJECTILE IMPACT; MOULARD, H.; FRANCE
7	325	THE SHOCK INITIATION OF BARE AND COVERED EXPLOSIVES BY PROJECTILE IMPACT; BAHL, K. L.; VANTINE, H. C.; WEINGART, R. C.; USA
7	336	THE SENSITIVITY TO INITIATION OF HE-WAX COMPOUNDS AT DIFFERENT TEMPERATURES; KLEE, CH.; LUDWIG, D.; WEST GERMANY (FRG)
7	343	FORMATION AND DISTRIBUTION OF HOT SPOTS IN SLURRY EXPLOSIVES UNDER PROJECTILE IMPACT; FENG, K. K.; CHUNG, W. K.; YU, J. M.; LU, B. C.-Y.; CANADA
7	352	THE MECHANISM OF INITIATION OF COMPOSITION B BY A METAL JET; CHICK, M. C.; HATT, D. J.; AUSTRALIA
7	362	INVESTIGATION OF TRANSIENT PROCESSES AT INITIATION OF HIGH EXPLOSIVES; TITOV, V. M.; LOBANOV, V. F.; BORDZILOVSKY, S. A.; KARAKHANOV, S. M.; USSR

## A. TITLES INDEX (Continued)

SYM PAGE	TITLES, AUTHORS, NATION
7 373	EFFECT OF CAVITATION ON THE SHOCK SENSITIVITY OF LIQUID EXPLOSIVES; MOHAN, V. K.; HAY, J. E.; INDIA AND USA
7 385	SHOCK INITIATION OF POROUS TATB; ANDERSON, A. B.; GINSBERG, M. J.; SEITZ, W. L.; WACKERLE, J.; USA
7 394	HOT SPOT INITIATION OF HETEROGENEOUS EXPLOSIVES; KIPP, M. E.; NUNZIATO, J. W.; SETCHELL, R. E.; WALSH, E. K.; USA
7 408	DIVERGING DETONATIONS IN RDX- AND PETN- BASED CAST-CURED PBX; BONTHOUX, F.; DENEUVILLE, P.; DE LONGUEVILLE, Y.; FRANCE
7 416	SHOCK CHARACTERIZATION OF HEXANITROAZOBENZENE (HNAB); LEE, L. M.; SCHWARZ, A. C.; USA
7 425	SHOCK INITIATION OF TATB FORMULATIONS; HONODEL, C.; HUMPHREY, J.; WEINGART, R. C.; LEE, R. S.; KRAMER, P. E.; USA
7 435	TWO-PHASE VISCO-PLASTIC MODEL OF SHOCK INITIATION OF DETONATION IN HIGH-DENSITY PRESSED EXPLOSIVES; KHASAINOV, B. A.; BORISOV, A. A.; ERMOLAEV, B. S.; KOROTKOV, A. I.; USSR
7 448	THE INITIATION TRANSIENT IN DILUTE EXPLOSIVES; FICKETT, W.; USA
7 459	MODEL OF IMPACT IGNITION AND EXPLANATION OF CRITICAL SHOCK INITIATION ENERGY. II. Application; ANDERSEN, W. H.; USA
7 466	THE ACCURACY OF REACTION RATES INFERRED FROM LAGRANGE ANALYSIS AND IN-SITU GAUGE MEASUREMENTS; VANTINE, H. C.; RAINSBERGER, R. B.; CURTIS, W. D.; LEE, R. S.; COWPERTHWAIT, M.; ROSENBERG, J. T.; USA
7 479	NUMERICAL MODELING OF SHOCK SENSITIVITY EXPERIMENTS; BOWMAN, A. L.; FOREST, C. A.; KERSHNER, J. D.; MADER, C. L.; PIMBLEY, G. H.; USA
7 488	MODELING TWO-DIMENSIONAL SHOCK INITIATION AND DETONATION WAVE PHENOMENA IN PBX 9404 AND LX-17; TARVER, C. M.; HALLQUIST, J. O.; USA
7 498	A CONSTITUTIVE MODEL FOR CALCULATING CHEMICAL ENERGY RELEASE RATES FROM THE FLOW FIELDS IN SHOCKED EXPLOSIVES; COWPERTHWAIT, M.; USA
7 506	A VOID COLLAPSE MODEL FOR SHOCK INITIATION; PARTOM, Y.; ISRAEL
7 517	MODELING STUDIES OF THE PERFORMANCE CHARACTERISTICS OF COMPOSITE EXPLOSIVES; WESTMORELAND, C.; LEE, E. L.; USA
7 523	HOT SPOT AND BULK TEMPERATURE INDUCTION IN SHOCK COMPRESSED EXPLOSIVES; FRANKEL, M. J.; PASTINE, D. J.; USA
7 531	DETONATION PRESSURES OF PBX-9404, COMPOSITION B, PBX-9502, AND NITROMETHANE; DAVIS, W. C.; RAMSAY, J. B.; USA

## A. TITLES INDEX (Continued)

<b>SYM</b>	<b>PAGE</b>	<b>TITLES, AUTHORS, NATION</b>
7	540	COMPARISON OF TATB AND DINGU EXPLOSIVE PROPERTIES; DENEUVILLE, P.; GAUDIN, C.; DE LONGUEVILLE, Y.; MALA, J.; FRANCE
7	548	DETONATION IN INTERMOLECULAR EXPLOSIVES; CHARACTERISTICS OF SOME EUTECTIC FORMULATIONS; AKST, I. B.; USA
7	560	INFLUENCE OF INERT BINDERS ON DETONATION PROPERTIES OF CAST-CURED PBX; DE LONGUEVILLE, Y.; DELCLOS, A.; GAUDIN, C.; MALA, J.; FRANCE
7	566	CUSTOMIZED EXPLOSIVES BASED ON PLASTIC-BONDED MIXTURES TO TATB AND HMX; CAMPBELL, A. W.; FLAUGH, H. L.; POPOLATO, A.; RAMSAY, J. B.; USA
7	575	ON THE LOW-VELOCITY DETONATION OF NITROMETHANE; SCHILPEROORD, A. A.; NETHERLANDS
7	583	INFLUENCE OF ADDITIVES ON NITROMETHANE DETONATION CHARACTERISTICS; PRESLES, H. N.; BROCHET, C.; KATO, Y.; TANAKA, K.; FRANCE AND JAPAN
7	589	A THEORY TO PREDICT THE VELOCITY-DIAMETER RELATION OF EXPLOSIVES; CHAN, S. K.; UK
7	602	SOME RESULTS ON THE CONVERGING SPHERICAL DETONATION IN A SOLID EXPLOSIVE; CHERET, R.; CHAISSE, F.; ZOE, J.; FRANCE
7	608	NUMERICAL SIMULATION OF DETONATION FAILURE IN NITROMETHANE; KIPP, M. E.; NUNZIATO, J. W.; USA
7	620	NONIDEAL DETONATION AND INITIATION BEHAVIOR OF A COMPOSITE SOLID ROCKET PROPELLANT; DICK, J. J.; USA
7	624	CORNER-TURNING IN TATB; COX, M.; CAMPBELL, A. W.; USA
7	634	THE CHAPMAN-JOUQUET DETONATION AND ITS ACCELERATION FOR A PERFECT FLUID WITHOUT CONDUCTION; DAMAMME, G.; FRANCE
7	641	SIMULATION OF THE REACTION ZONE OF HETEROGENEOUS EXPLOSIVES; DAMAMME, G.; MISSONIER, M.; FRANCE
7	646	POSTDETONATION BEHAVIOR OF CONDENSED HIGH EXPLOSIVES BY MODERN METHODS OF STATISTICAL MECHANICS; REE, F. H.; USA
7	661	INFLUENCE OF THE REACTION ZONE ON THE STATE OF DETONATION IN A STEADY AXIAL WAVE; THOUVENIN, J.; FRANCE
7	669	DETONATION WAVE INTERACTIONS; MADER, C. L.; USA
7	678	EXPLOSIVE EQUATION OF STATE DETERMINATION BY THE AWRE METHOD; BAILEY, W. A.; BELCHER, R. A.; CHILVERS, D. K.; EDEN, G.; UK
7	686	AN ELEMENTARY SOLUTION FOR THE EQUATIONS OF THE ZEROth ORDER INTERNAL STRUCTURE OF A STRONG DETONATION IN A SOLID HIGH EXPLOSIVE; CHAISSE, F.; CHERET, R.; PAUL, S.; SEPVAS, J. M.; FRANCE

## A. TITLES INDEX (Continued)

SYM	PAGE	TITLES, AUTHORS, NATION
7	695	NUMERICAL SIMULATIONS OF NONIDEAL DETONATIONS OF A HETEROGENEOUS EXPLOSIVE WITH THE TWO-DIMENSIONAL EULERIAN CODE C.E.E.; DONGUY, P.; LEGRAND, N.; FRANCE
7	703	DETONATION PROPERTIES OF CONDENSED EXPLOSIVES CALCULATED WITH AN EQUATION OF STATE BASED ON INTERMOLECULAR POTENTIALS; CHIRAT, R.; PITTION-ROSSILLON, G.; FRANCE
7	716	THEORETICAL EOS FOR REACTION PRODUCTS OF RDX; JONES, H. D.; USA
7	721	DEVELOPMENT OF A SINGLE SPECIES EQUATION OF STATE FOR DETONATION PRODUCTS SUITABLE FOR HYDROCODE CALCULATIONS; SENTMAN, L. H.; STREHLOW, R. A.; HAEFFLE, B.; ECKSTEIN, A.; USA
7	735	LOW ENERGY LASER INITIATION OF SINGLE CRYSTALS OF beta-LEAD AZIDE; HAGAN, J. T.; CHAUDHRI, M. M.; UK
7	746	MESH-INITIATED LARGE-AREA DETONATOR WITH MAGNETIC FLUX COMPRESSION CURRENT GENERATOR AS SOURCE; SANG, W.; ZHANG, G.-R.; CHINA (PRC)
7	751	INVERSE MULTI-STREAK TECHNIQUE; HELD, M.; NIKOWITSCH, P.; WEST GERMANY (FRG)
7	759	DETONATION TEMPERATURE OF SOME LIQUID EXPLOSIVES; BURTON, J. T. A.; HAWKINS, S. J.; HOOPER, G.; UK
7	763	BRIGHTNESS TEMPERATURE OF DETONATION WAVE IN NITROMETHANE-TETRANITROMETHANE MIXTURES AND IN GASEOUS MIXTURES AT A HIGH INITIAL PRESSURE; KATO, Y.; BAUER, P.; BROCHET, C.; BOURIANNES, R.; JAPAN AND FRANCE
7	777	COMPARISON OF MOLECULAR DYNAMICS CALCULATIONS WITH OBSERVED INITIATION PHENOMENA; WALKER, F. E.; KARO, A. M.; HARDY, J. R.; USA
7	789	ON DECOMPOSITION REACTION KINETICS IN SHOCK WAVE FRONT; DREMIN, A. N.; KLIMENKO, V. Y.; MICHAILJUK, K. M.; TROFIMOV, V. S.; USSR
7	795	A SHORT SURVEY OF DETONATION RESEARCH IN CHINA; DING, J.; CHINA (PRC)
7	801	EUTECTIC COMPOSITE EXPLOSIVES CONTAINING AMMONIUM NITRATE; STINECIPHER, M. M.; USA
7	811	THE ACCELERATION OF TWO METAL PLATES IN AN HE-METAL SANDWICH; HOSKIN, N. E.; LAMBURN, B. D.; UK
7	826	THE PLANAR FLYER PLATE DRIVEN BY DETONATION PRODUCT CONVERGENT FLOW; TAN, B.-S.; JING, F.-Q.; CHINA (PRC)
7	834	AN IMPROVED APPROXIMATE MODEL OF EXPLOSIVE CASING EXPANSION; KORNHAUSER, M.; USA
7	843	COMPACTION OF POROUS BEDS OF INERT MATERIALS; SANDUSKY, H. W.; ELBAN, W. L.; KIM, K.; BERNECKER, R. R.; GROSS, S. P.; CLAIRMONT, A. R.; USA

## A. TITLES INDEX (Continued)

<u>SYM</u>	<u>PAGE</u>	<u>TITLES, AUTHORS, NATION</u>
7	857	SHORT-PULSE SHOCK INITIATION OF GRANULAR EXPLOSIVES; SETCHELL, R. E.; USA
7	865	CHARACTERIZATION OF THE DDT EXPLOSIVE, CP; STANTON, P. L.; IGEL, E. A.; LEE, L. M.; MOHLER, J. H.; WEST, G. T.; USA
7	877	PRECURSORS IN DETONATIONS IN POROUS EXPLOSIVES; SPAULDING, R. L.; USA
7	887	CORRELATION OF THE RESULTS OF SHOCK INITIATION TESTS; WESTON, A. M.; KINCAID, J.; JAMES, E.; LEE, E. L.; GREEN, L. G.; WALTON, J.; USA
7	898	ANOMALOUS BURNING RATE CHARACTERISTICS OF COMPOSITION B AND TNT; VELICKY, R. W.; HERSHKOWITZ, J.; USA
7	906	SHOCK IGNITION SENSITIVITY OF MULTIPLY-SHOCKED PRESSED TNT; BOYLE, V. M.; PILARSKI, D. L.; USA
7	914	THE EFFECT OF BASE GAPS ON SETBACK-SHOCK SENSITIVITIES OF CAST COMPOSITION B AND TNT AS DETERMINED BY THE NSW SETBACK-SHOCK SIMULATOR; MYERS, T. F.; HERSHKOWITZ, J.; USA
7	924	EXPLODING FOIL SHOCK SENSITIVITY TEST; VORECK, W. E.; VELICKY, R. W.; USA
7	930	THE ROLE OF AIR AND OTHER GASES IN FLYER PLATE INITIATION OF EXPLOSIVES; HARLAN, J. G.; RICE, J. K.; ROGERS, J. W.; USA
7	940	DETONATION CHEMISTRY: AN INVESTIGATION OF FLUORINE AS AN OXIDIZING MOIETY IN EXPLOSIVES; MCQUIRE, R. R.; ORNELLAS, D. L.; HELM, F. H.; COON, C. L.; FINGER, M.; USA
7	952	SIMPLIFIED METHODS FOR PREDICTING EXPLOSIVE PERFORMANCE PARAMETERS INCLUDING EREMENKO'S RELATIVE DETONATION IMPULSES; SHORT, J. M.; ADOLPH, H. G.; KAMLET, M. J.; USA
7	958	FINE STRUCTURE IN NITROMETHANE/ACETONE DETONATION; DAVIS, W. C.; USA
7	965	LABORATORY-SCALE SENSITIVITY TESTING OF INSENSITIVE HIGH EXPLOSIVES; BROSSE, J. M.; KASSEL, C.; MICHAUD, C.; POULARD, S.; FRANCE
7	970	EXPERIMENTAL INVESTIGATION OF HOT SPOTS PRODUCED BY HIGH RATE DEFORMATION AND SHOCKS; COFFEY, C. S.; FRANKEL, M. J.; LIDDIARD, T. P.; JACOBS, S. J.; USA
7	976	MICROHARDNESS STUDY OF RDX TO ASSESS LOCALIZED DEFORMATION AND ITS ROLE IN HOT SPOT FORMATION; ELBAN, W. L.; ARMSTRONG, R. W.; USA
7	986	FLASH X-RAY CINERADIOGRAPHY @ 100,000 FPS; TRIMBLE, J. J.; ASELTINE, C. L.; USA
7	993	TEMPERATURE MEASUREMENT OF SHOCKED EXPLOSIVES BY TIME-RESOLVED INFRARED RADIOMETRY--A NEW TECHNIQUE TO MEASURE SHOCK-INDUCED REACTION; VON HOLLE, W. G.; TARVER, C. M.; USA

## A. TITLES INDEX (Continued)

<u>SYM</u>	<u>PAGE</u>	<u>TITLES, AUTHORS, NATION</u>
7	1004	THERMOCOUPLE TEMPERATURE MEASUREMENTS IN SHOCK-INITIATED PBX-9404; BLOOMQUIST, D. D.; SHEFFIELD, S. A.; USA
7	1010	RAMAN SCATTERING TEMPERATURE MEASUREMENT BEHIND A SHOCK WAVE; BOISARD, F.; TOMBINI, C.; MENIL, A.; FRANCE
7	1016	AQUARIUM TESTS ON ALUMINIZED ANFO; GOLDSTEIN, S.; JOHNSON, J. N.; USA
7	1024	SHOCK INITIATION SENSITIVITY OF HEXANITROSTILBENE (HNS); SCHWARZ, A. C.; USA
7	1029	INTERPOLATION OF DETONATION PARAMETERS FROM EXPERIMENTAL PARTICLE VELOCITY RECORDS; HAYES, B.; TARVER, C. M.; USA
7	1040	FACTORS AFFECTING THE EXPLOSIVENESS OF MUNITIONS FILLINGS; DYER, A. S.; HUBBARD, P. J.; LEE, P. R.; TISLEY, D. G.; UK
7	1048	THE RESPONSE OF CONFINED EXPLOSIVE CHARGES TO FRAGMENT ATTACK; HOWE, P. M.; WATSON, J. L.; FREY, R. B.; USA
7	1055	A NUMERICAL STUDY OF DETONATION PROPAGATION BETWEEN MUNITIONS; HCWE, P. M.; HUANG, Y. K.; ARBUCKLE, A. L.; USA
7	1062	THE ELECTROMAGNETIC VELOCITY GAUGE; USE OF MULTIPLE GAUGES, TIME RESPONSE, AND FLOW PERTURBATIONS; ERICKSON, L. M.; JOHNSON, C. B.; PARKER, N. L.; VANTINE, H. C.; WEINGART, R. C.; LEE, R. S.; USA
7	1072	LAGRANGE GAGE STUDIES IN IDEAL AND NON-IDEAL EXPLOSIVES; COWPERTHWAITTE, M.; ROSENBERG, J. T.; USA
8	3	THE RELATIONSHIP BETWEEN THE SHOCK SENSITIVITY AND THE SOLID PORE SIZES OF TATB POWDERS PRESSED TO VARIOUS DENSITIES; LEE, R. S.; BLOOM, G.; VON HOLLE, W. G.; WEINGART, R. C.; ERICKSON, L. M.; SANDERS, S.; SLETTEVOLD, C.; MCGUIRE, R. R.; USA
8	15	EXPERIMENTAL STUDIES OF CHEMICAL REACTIVITY DURING SHOCK INITIATION OF HEXANITROSTILBENE; SETCHELL, R. E.; USA
8	26	THE EFFECTS OF MATERIAL MICROSTRUCTURE ON THE SHOCK SENSITIVITY OF POROUS GRANULAR EXPLOSIVES; TAYLOR, P. A.; USA
8	35	MODELING GRANULAR EXPLOSIVE DETONATIONS WITH SHEAR BAND CONCEPTS; KIPP, M. E.; USA
8	42	THE THREE-DIMENSIONAL HYDRODYNAMIC HOT-SPOT MODEL; MADER, C. L.; KERSHNER, J. D.; USA
8	52	MODELING HETEROGENEOUS HIGH EXPLOSIVE BURN WITH AN EXPLICIT HOT-SPOT PROCESS; TANG, P. K.; JOHNSON, J. N.; FOREST, C. A.; USA
8	62	HOT SPOT PRODUCTION BY MOVING DISLOCATIONS IN A RAPIDLY DEFORMING CRYSTALLINE EXPLOSIVE; COFFEY, C. S.; USA

## A. TITLES INDEX (Continued)

<u>SYM</u>	<u>PAGE</u>	<u>TITLES, AUTHORS, NATION</u>
8	68	CAVITY COLLAPSE IN ENERGETIC MATERIALS; FREY, R. B.; USA
8	83	HUGONIOTS AND REACTION RATES FROM EMV GAUGE MEASUREMENTS AND LAGRANGE ANALYSIS; JIAO, Q.; DING, J.; LIANG, Y.; HUANG, Z.; ZHAO, H.; CHINA (PRC)
8	89	MEASUREMENT OF TWO-DIMENSIONAL SHOCK WAVE VELOCITIES AND A COMPOSITE PROBE; FU, X.; CHINA (PRC)
8	93	RETONATION PHENOMENON IN SOLID EXPLOSIVES; DING, J.; BI, Z.; HU, D.; DENG, Q.; CHINA (PRC)
8	99	REACTION RATES FROM ELECTROMAGNETIC GAUGE DATA; VORTHMAN, J.; ANDREWS, G.; WACKERLE, J.; USA
8	111	LAGRANGE GAGE STUDIES OF DETONATION IN SOME INTERMOLECULAR EA-BASED EXPLOSIVES; COWPERTHWAITTE, M.; ROSENBERG, J. T.; USA
8	123	DETONATION REACTION ZONE STUDIES ON TATB EXPLOSIVES; SEITZ, W. L.; STACY, H. L.; WACKERLE, J.; USA
8	135	EXPERIMENTS AND NUMERICAL SIMULATION OF HIGH EXPLOSIVE DELAYED AND LOWED DETONATION; VANPOPERYNGHE, J.; SOREL, J.; PUJOLS, H. C.; FRANCE
8	143	PRESSURE VARIATION UPON INITIATION OF CAST RDX/TNT 50/50 CHARGE BY DIVERGING SHOCK WAVE; TITOV, V. M.; KARAKHANOV, S. M.; BORDZILOVSKY, S. A.; USSR
8	151	EXPERIMENTAL STUDY OF SPHERICALLY DIVERGING DETONATION WAVES; AVEILLE, J.; BACONIN, J.; CARION, N.; ZOE, J.; FRANCE
8	159	A THEORETICAL ANALYSIS OF THE SHAPE OF A STEADY AXISYMMETRICAL REACTIVE SHOCK FRONT IN CYLINDRICAL CHARGES OF HIGH EXPLOSIVE, A CURVATURE-DIAMETER RELATIONSHIP; CHAISSE, F.; SERVAS, J. M.; AVEILLE, J.; BACONIN, J.; CARION, N.; BONGRAIN, P.; FRANCE
8	168	A GENERALIZED C-J CONDITION FOR SIMPLE AXIAL FLOW WITH A SPHERICAL SHOCK FRONT: ITS APPLICATION TO THE SLURRY EXPLOSIVES; MATSUI, H.; MORITANI, A.; YONEDA, K.; ASABA, T.; JAPAN
8	176	A SMALL DIVERGENT DETONATION THEORY FOR INTERMOLECULAR EXPLOSIVES; KIRBY, I. J.; LEIPER, G. A.; SCOTLAND, UK
8	187	DETERMINATION OF REACTION RATES IN INTERMOLECULAR EXPLOSIVES USING THE ELECTROMAGNETIC PARTICLE VELOCITY GAUGE; LEIPER, G. A.; KIRBY, I. J.; HACKETT, A.; SCOTLAND, UK
8	196	DETERMINATION OF TRANSIENT AND KINETIC CHARACTERISTICS IN SIMULATING RDX/TNT 50/50 CHARGE INITIATION; TITOV, V. M.; LOBANOV, V. F.; BORDZILOVSKY, S. A.; KARAKHANOV, S. M.; USSR
8	207	THE INFLUENCE OF REACTIVE CASES ON AIRBLAST FROM HIGH EXPLOSIVES; FILLER, W. S.; USA

## A. TITLES INDEX (Continued)

SYM	PAGE	TITLES, AUTHORS, NATION
8	211	THE GROWTH AND DECAY OF EXPLOSIVE DEFLAGRATIONS IN MUNITIONS IN SIMULATED FACTORY ACCIDENT SCENARIOS; DYER, A. S.; HASKINS, P. J.; HUBBARD, P. J.; HUTCHINSON, C. D.; UK
8	228	AN EIGHT-INCH-DIAMETER, HEAVILY CONFINED CARD GAP TEST; FOSTER, J.; FORBES, K.; GUNGER, M.; CRAIG, B. G.; USA
8	243	CHEMICAL REACTION OF EXPLOSIVES AND GUN PROPELLANT DURING HIGH ACCELERATION; LANZEROTTI, M. Y. D.; PINTO, J.; USA
8	251	THE EFFECT OF SOME ADDITIVES ON THE CLOSED BOMB BURNING AND IGNITABILITY OF RDX/TNT; VELICKY, R. W.; VOIGHT, H. W.; VORECK, W. E.; USA
8	262	RESPONSE OF CONFINED EXPLOSIVE CHARGES TO FRAGMENT IMPACT; BARKER, M. A.; BASSET, J. F.; CONNER, J.; HUBBARD, P. J.; UK
8	274	PRESSURE-SHEAR LOADING OF PBX-9404; CHHABILDAS, L. C.; KIPP, M. E.; USA
8	284	ENERGETIC RESPONSE OF PROPELLANTS TO HIGH-VELOCITY IMPACT; GREEN, L. G.; JAMES, E.; LEE, E. L.; USA
8	294	AN EXPERIMENTAL INVESTIGATION OF THE ROLE OF SHEAR IN INITIATION OF DETONATION BY IMPACT; HOWE, P. M.; GIBBONS, G.; WEBBER, P. E.; USA
8	307	SOME NEW COMPUTED RESULTS FOR PROJECTILE IMPACT SHOCK INITIATION OF SOLID EXPLOSIVES; HUANG, Y. K.; STARKENBERG, J.; ARBUCKLE, A. L.; USA
8	318	THE JET INITIATION OF SOLID EXPLOSIVES; CHICK, M. C.; MACINTYRE, I. B.; FREY, R. B.; AUSTRALIA & USA
8	330	SUPERPOSITION OF SHOCK WAVES AND REACTION WAVES FOR THE INITIATION OF HIGH EXPLOSIVE CHARGES; HELD, M.; WEST GERMANY (FRG)
8	337	NUMERICAL SIMULATION OF JET PENETRATION OF HMX AND TATB EXPLOSIVES; PIROTAIS, D.; PLOTARD, J. P.; BRACONNIER, J. C.; FRANCE
8	351	SENSITIVITY AND PERFORMANCE CHARACTERIZATION OF DINGU; STINECIPHER, M. M.; STRETZ, L. A.; USA
8	361	SHOCK SENSITIVITY STUDY OF THE CURABLE PLASTIC BONDED EXPLOSIVES; BELANGER, C.; DROLET, J. F.; PELLETIER, P.; CANADA
8	372	EFFECT OF CONFINEMENT ON FAILURE IN 95 TATB/5 Ke1-F; RAMSAY, J. B.; USA
8	380	RUN TO DETONATION IN TATB; GRIEF, D.; WARD, S. H.; COLEY, G. D.; UK
8	390	THE USE OF THE DOUBLE PIPE TEST TO INVESTIGATE THE RUN-UP AND RUN-DOWN FROM INITIATION IN PNEUMATICALLY LOADED ANFO; DU PLESSIS, M. P.; LOWNDS, C. M.; SOUTH AFRICA
8	399	SIMULATING THE INITIATION OF HIGH EXPLOSIVE BY EXPLOSIVE TRAINS; LEIBUNDGUT, F.; SWITZERLAND

## A. TITLES INDEX (Continued)

<u>SYM</u>	<u>PAGE</u>	<u>TITLES, AUTHORS, NATION</u>
8	409	INFLUENCE OF AIR GAPS ON DETONATION PROPAGATION IN CHARGES CONSISTING OF STACKED BLOCKS OF CAST TNT; GIBB, A. W.; CANADA
8	422	DETONATION PROPERTIES OF LIQUID NITRIC OXIDE; DAVIS, W. C.; CHILES, W. C.; USA
8	425	CHARACTERIZATION OF STRONG DETONATION WAVES IN NITROMETHANE; SELLAM, M.; BROCHET, C.; CHERET, R.; FRANCE
8	431	CONTINUOUS OBSERVATION OF MACH BRIDGE AND MACH PHENOMENA; PRESLES, H. N.; SOULETIS, J.; GROUX, J.; FRANCE
8	440	DISPLACEMENT GRADIENT METHOD FOR MEASURING DETONATION PARAMETERS USING FLASH X-RAY PHOTOGRAPHY; LI, H.; HUANG, Z.; DING, J.; CHINA (PRC)
8	447	THE STUDY OF BOOSTER MATERIALS WITH ELECTROMAGNETIC PARTICLE VELOCITY GAUGES; PHILIPART, D. A.; UK
8	460	APPLICATIONS OF FIBER OPTICS TO DETONATION EVENTS; LU, P.; NAIMAN, E.; VORECK, W. E.; USA
8	468	VISAR: INTERFEROMETER QUADRATURE SIGNAL RECORDING BY ELECTRONIC STREAK CAMERA; HEMSING, W. F.; USA
8	473	LASER AS A TOOL IN SENSITIVITY TESTING OF EXPLOSIVES; OSTMARK, H.; SWEDEN
8	485	MICROWAVE INTERFEROMETER TECHNIQUES FOR DETONATION STUDY; STANTON, P. L.; VENTURINI, E. L.; DIETZEL, R. W.; USA
8	501	DETONATION BEHAVIOR OF LX-14 AND PBX-9404: THEORETICAL ASPECT; REE, F. H.; VAN THIEL, M.; USA
8	513	COMPARISON OF EXPERIMENTAL DATA ON DETONATION VELOCITY AND CHAPMAN-JOUQUET PRESSURE VS INITIAL HE DENSITY WITH PREDICTIONS FROM REE'S MODEL EQUATION OF STATE; STEINBERG, D. J.; USA
8	521	WHICH EQUATION OF STATE FOR CARBON IN DETONATION PRODUCTS?; BAUTE, J.; CHIRAT, R.; FRANCE
8	531	THE THEORY OF DENSE MOLECULAR FLUID EQUATIONS OF STATE WITH APPLICATION TO DETONATION PRODUCTS; SHAW, E. S.; JOHNSON, J. D.; USA
8	540	THEORETICAL EQUATIONS OF STATE FOR THE DETONATION PRODUCTS OF EXPLOSIVES; KERLEY, G. I.; USA
8	548	DETONATION PROPERTIES OF HIGH EXPLOSIVES CALCULATED BY REVISED KIHARA-HIKITA EQUATION OF STATE; TANAKA, K.; JAPAN
8	558	DETONATION TEMPERATURE OF NITROMETHANE AND SOME SOLID HIGH EXPLOSIVES; KATO, Y.; MORI, N.; SAKAI, H.; TANAKA, K.; SAKURAI, T.; HIKITA, T.; JAPAN

## A. TITLES INDEX (Continued)

- | SYM | PAGE | TITLES, AUTHORS, NATION   |
|-----|------|---|
| 8   | 567  | THE MEASUREMENT OF DETONATION TEMPERATURE OF CONDENSED EXPLOSIVES WITH TWO-COLOUR OPTICAL FIBER PYROMETER; HE, X.; HAN, C.; KANG, S.; CHINA (PRC)   |
| 8   | 577  | DETONATION PRODUCTS OF INSENSITIVE CAST HIGH EXPLOSIVES; VOLK, F.; BATHELT, H.; SCHEDLBAUER, F.; WAGNER, J.; WEST GERMANY (FRG)   |
| 8   | 587  | THE SUPRACOMPRESSION OF LX-07, LX-17, PBX-9404, AND RX-26-AF AND THE EQUATIONS OF STATE OF THE DETONATION PRODUCTS; GREEN, L. G.; LEE, E. L.; MITCHELL, A.; TARVER, C. M.; USA                  |
| 8   | 596  | EOS OF DETONATION PRODUCTS OBTAINED FROM SYMMETRICAL DEFLECTION OF LINERS INVESTIGATED BY LASER INTERFEROMETRY TECHNIQUES; GIMENEZ, P.; DE LONGUEVILLE, Y.; SAINT-MARTIN, C.; FRANCE            |
| 8   | 602  | MODELS OF EXPLOSIVELY DRIVEN METAL; DEHN, J. T.; USA  |
| 8   | 613  | THE MOTION OF THIN METAL WALLS AND THE EQUATION OF STATE OF DETONATION PRODUCTS; LEE, E. L.; BREITHAUP, D.; MCMILLAN, C.; PARKER, N. L.; KURY, J. W.; TARVER, C. M.; QUIRK, W.; WALTON, J.; USA |
| 8   | 625  | INFLUENCE OF TEST CONDITIONS ON THE BALLISTIC CLASSIFICATION OF EXPLOSIVES; SOULETIS, J.; MALA, J.; FRANCE  |
| 8   | 635  | MECHANICAL PROPERTIES OF FBX'S AND THEIR BEHAVIOUR DURING DROP WEIGHT IMPACT; FIELD, J. E.; PALMER, S. J. P.; POPE, P. H.; GUNRARAJAN, R.; SWALLOWE, G. M.; UK                                  |
| 8   | 645  | THE STRAIN RATE BEHAVIOR OF COARSE HMX POROUS BED COMPACTION; COYNE, P. J.; ELBAN, W. L.; CHIARITO, M. A.; USA  |
| 8   | 658  | DEFLAGRATION-TO DETONATION TRANSITION (DDT) STUDIES OF A DOUBLE-BASE PROPELLANT; BERNECKER, R. R.; SANDUSKY, H. W.; CLAIRMONT, A. R.; USA   |
| 8   | 669  | MODELLING OF DDT IN GRANULAR EXPLOSIVES; VERBEEK, H. J.; NETHERLANDS  |
| 8   | 678  | ON THE MECHANISM OF THE REACTION "HOT SPOTS" ORIGIN AT LIQUID EXPLOSIVES DETONATION; DREMIN, A. N.; KLIMENKO, V. Y.; KOSIREVA, I. Y.; USSR  |
| 8   | 691  | TIME-RESOLVED SPECTROSCOPIC STUDIES OF DETONATING HETEROGENEOUS EXPLOSIVES; TRCOTT, W. M.; RENLUND, A. M.; USA  |
| 8   | 701  | REAL TIME ANALYSIS OF PETN DETONATION PRODUCTS; BLAIS, N. C.; VALENTINI, J. J.; USA   |
| 8   | 710  | FAST SPECTROSCOPIC ANALYSIS OF LASER INITIATED DECOMPOSITION REACTIONS IN EXPLOSIVES; LEEUW, M. W.; ROOIJERS, A. J. T.; VAN DER STEEN, A. C.; NETHERLANDS                                       |
| 8   | 715  | STATIC HIGH PRESSURE STUDY OF NITRIC OXIDE CHEMISTRY: PROPOSED MECHANISM FOR NITRIC OXIDE DECOMPOSITION; SWANSON, B. I.; AGNEW, S. F.; GREINER, N. R.; USA                                      |

## A. TITLES INDEX (Continued)

<b>SYM</b>	<b>PAGE</b>	<b>TITLES, AUTHORS, NATION</b>
3	725	SUB-IGNITION REACTIONS AT MOLECULAR LEVELS IN EXPLOSIVES SUBJECTED TO IMPACT AND UNDERWATER SHOCK; SHARMA, J.; HOFFSOMMER, J. C.; GLOVER, D. J.; COFFEY, C. S.; FORBES, J. W.; LIDDIARD, T. P.; ELBAN, W. L.; SANTIAGO, F.; USA
8	734	PARAMAGNETIC DECOMPOSITION PRODUCTS FROM ENERGETIC MATERIALS; PACE, M. D.; BRITT, A. D.; MONIZ, W. B.; STEC, D.; USA
8	742	PARAMAGNETIC RESONANCE OF RADICALS IN DECOMPOSED TRINITROAROMATICS; OWENS, F. J.; USA
8	751	AN EXTENSIVE APPLICATION OF WCA4 EQUATION OF STATE FOR EXPLOSIVES; CHIRAT, R.; BAUTE, J.; FRANCE
8	762	THE EQUATION OF STATE OF DETONATION PRODUCTS AND THEIR INCORPORATION INTO THE QUATUOR CODE; HEUZE, O.; BAUER, P.; PRESLES, H. N.; BROCHET, C.; FRANCE
8	770	SENSITIVITY ANALYSIS OF THE IDEAL DETONATION STATE TO ERRORS IN MOLECULAR PROPERTIES AND INTERMOLECULAR FORCE PARAMETERS; BROWN, W. B.; UK
8	773	DERIVATIVES OF THE CHAPMAN-JOUQUET STATE; LAMBOURN, B. D.; UK
8	785	EQUATION OF STATE FOR DETONATION PRODUCTS; DAVIS, W. C.; USA
8	796	DETONATION PROPERTIES OF CONDENSED EXPLOSIVES COMPUTED WITH THE VLW EQUATION OF STATE; WU, X.; CHINA (PRC)
8	805	CALCULATION OF DETONATION PRODUCTS BY MEANS OF THE CS HARD-SPHERE EQUATION OF STATE; FENG, K. K.; CHUNG, W. K.; LU, B. C.-Y.; CANADA
8	815	EXPANSION ISENTROPES OF TATB COMPOSITIONS RELEASED TO ARGON; PINEGRE, M.; AVEILLE, J.; LEROY, M.; PROTAT, J. C.; CHERET, R.; CAMARCAT, N.; FRANCE
8	827	QUANTUM CHEMICAL STUDIES OF ENERGETIC MATERIALS; HASKINS, P. J.; COOK, M. D.; UK
8	839	ELECTRON DENSITY DISTRIBUTION ANALYSIS FOR NITROGUANIDINE; FITCHIE, J. P.; CROMER, D. T.; RYAN, R. R.; STEWART, R. F.; WASSERMAN, H. J.; USA
8	847	A MOLECULAR MECHANISM FOR THE INITIATION OF SECONDARY EXPLOSIVES. INFLUENCE OF A SHOCK LIGHT-COUPLING; DUFORT, S.; DELPUECH, A.; FRANCE
8	855	CALCULATED REACTION PATHWAYS FOR NITROMETHANE AND THEIR ROLE IN THE SHOCK INITIATION PROCESS; BARDO, R. D.; USA
8	864	THE DYNAMICS OF SHOCK-INDUCED ENERGY FLUX IN MOLECULAR BONDS; KARO, A. M.; MEHLMAN, M. H.; HARDY, J. R.; USA
8	870	SIMULATION OF THE INITIATION OF DETONATION IN AN ENERGETIC MOLECULAR CRYSTAL: THE OVERDRIVEN CASE; TREVINO, S. F.; TSAI, D. H.; USA

## A. TITLES INDEX (Continued)

SYM	PAGE	TITLES, AUTHORS, NATION
8	881	COMPRESSIVE REACTION IN POROUS BEDS OF ENERGETIC MATERIALS; SANDUSKY, H. W.; BERNECKER, R. R.; USA
8	892	SHOCK INITIATION OF TATB AND HMX EXPLOSIVE COMPOSITIONS; VANPOPERYNGHE, J.; SOREL, J.; AVEILLE, J.; ADENIS, J. C.; FRANCE
8	902	THE EFFECT OF RDX PARTICLE SIZE ON THE SHOCK SENSITIVITY OF CAST PBX FORMULATIONS; MOULARD, H.; KURY, J. W.; DELCLOS, A.; FRANCE
8	914	MODELING 1-D DEFLAGRATION TO DETONATION TRANSITION (DDT) IN POROUS EXPLOSIVE; WESTON, A. M.; LEE, E. L.; USA
8	926	MODELING OF REACTION BUILDUP PROCESS IN SHOCKED POROUS EXPLOSIVE; KIM, K.; SOHN, C. H.; KOREA
8	934	MODELING THE DEFLAGRATION TO DETONATION TRANSITION IN POROUS BEDS OF PROPELLANT; PRICE, C. F.; BOGGS, T. L.; USA
8	943	A SEMI-ANALYTICAL APPROACH TO SHOCK INITIATION IN HETEROGENEOUS EXPLOSIVES; HUANG, Y. K.; ARBUCKLE, A. L.; USA
8	951	MODELING SHORT PULSE DURATION SHOCK INITIATION OF SOLID EXPLOSIVES; TARVER, C. M.; HALLQUIST, J. O.; ERICKSON, L. H.; USA
8	962	A MODEL FOR SHOCK INITIATION OF POROUS PROPELLANTS BY RAMP-INDUCED COMPRESSION PROCESSES; KRIER, H.; CUDAK, C. A.; STEWART, J. R.; BUTLER, P. B.; USA
8	972	DDT IN RDX AND BALL POWDER: BEHAVIOR OF THE POROUS BED; SAMIRANT, M.; FRANCE
8	979	DETONATION IN TUNGSTEN-LOADED HMX; GOLDSTEIN, S.; MADER, C. L.; USA
8	985	CALCULATION OF THE BLASTING PERFORMANCE OF SOME COMMERCIAL EXPLOSIVES; PERSSON, A.; PERSSON, P.-A.; SWEDEN
8	993	DETONATION BEHAVIOR OF EMULSION EXPLOSIVES CONTAINING GLASS MICROBALLS; YOSHIDA, M.; IIDA, M.; TANAKA, K.; FUJIWARA, S.; KUSAKADE, M.; SHIINO, K.; JAPAN
8	1001	INTERMOLECULAR EXPLOSIVES; AKST, I. B.; USA
8	1011	THE DETONATION REACTION OF HETEROGENEOUS COMPOSITE EXPLOSIVE; GUO, Y.; PENG, G.; SONG, J.; XU, L.; WANG, A.; ZOU, Q.; CHINA
8	1018	COMPOSITE EXPLOSIVES FOR METAL ACCELERATION: THE EFFECT OF DETONATION TEMPERATURE; MCGUIRE, R. R.; FINGER, M.; USA
8	1025	A MODEL SOLUTION FOR NONIDEAL ONE-DIMENSIONAL DETONATION WAVES; COWPERTHWAIT, M.; USA

## A. TITLES INDEX (Continued)

<u>SYM PAGE</u>	<u>TITLES, AUTHORS, NATION</u>
8 1035	THE INFLUENCE OF FORMULATION VARIABLES ON THE GROWTH OF REACTION IN PLASTIC BONDED EXPLOSIVES; FLEMING, K. A.; BIRD, R.; BURT, M. W. G.; WHATMORE, C. E.; UK
8 1045	INITIATION STUDIES ON LX-17 EXPLOSIVE; BAHL, K. L.; BLOOM, G.; ERICKSON, L. M.; LEE, R. S.; TARVER, C. M.; VON HOLLE, W. G.; WEINGART, R. C.; USA
8 1057	THE SHOCK DESENSITIZATION OF PBX 9404 AND COMPOSITION B-3; CAMPBELL, A. W.; TRAVIS, J. R.; USA
8 1069	ON DETONATION DRIVEN AIR SHOCKS IN THE AIR GAP BETWEEN A CHARGE AND ITS CONFINEMENT; BJARNHOLT, G.; SMEDBERG, U.; SWEDEN
8 1080	CAVITY COLLAPSE IGNITION OF COMPOSITION B IN THE LAUNCH ENVIRONMENT; STARKENBERG, J.; MCFADDEN, D. L.; LYMAN, O. R.; USA
8 1091	EXPLOSIVE INITIATION BY VERY SMALL CONICAL SHAPED CHARGE JETS; VIGIL, M. G.; USA
8 1105	EXPERIMENTAL STUDIES CONCERNING THE RESPONSE OF INTERMEDIATE EXPLOSIVES TO THERMAL STIMULI; HUTCHINSON, C. D.; UK
8 1119	DERIVATION OF THE $P^2t$ DETONATION CRITERION; WALKER, E. H.; UK
8 1126	SHOCK INITIATION OF HNAB BY ELECTRICALLY DRIVEN FLYER PLATES; HASMAN, E.; GVISHI, M.; SEGALOV, Z.; CARMEL, Y.; AYALON, D.; SOLOMONOVICI, A.; ISRAEL
8 1131	SHOCK SENSITIVITY AND PERFORMANCE OF SEVERAL HIGH EXPLOSIVES; KROH, M.; THOMA, K.; ARNOLD, W.; WOLLENWEBER, U.; WEST GERMANY (FRG)
8 1139	A COMPUTATIONAL INVESTIGATION OF THE EFFECT OF SHIELDING IN MITIGATING SHOCK INITIATION STIMULI PRODUCED BY IMPACT; STARKENBERG, J.; DORSEY, T. M.; BENJAMIN, K. J.; USA
8 1150	ON THE ROLE OF SHOCK AND SHEAR MECHANISM IN THE INITIATION OF DETONATION BY FRAGMENT IMPACT; HOWE, P. M.; USA

# B. TOPIC PHRASE INDEX

## Alphabetically

SUBJECT	SYM PAGE	SUBJECT	SYM PAGE
ABEL CO-VOLUMES, COMPUTED VELOCITY	2 237	ALUMINIZED BLASTING AGENTS, CHARACTERIZATION	6 734
ABEL EOS, HARD-SPHERE GAS MODEL, LOW DENSITY LIMITS IN HOMOGENEOUS EXPLOSIVES	2 406	ALUMINIZED HE, ELECTRIC SPARK INITIATION	3 706
P(V- $\alpha$ ) = RT, CURVATURE EFFECTS	4 190	EXPANSION WORK	6 547
SIMPLIFIED van der WAALS', COOK'S	1 94	FOR UNDERWATER BOMBS	1 111
ABH, DETONATION PROPERTIES, CARBON EOS	1 72	LOW BRISANCE, HIGH BLAST	2 733
ACCELERATION WAVE SPEEDS, PMMA, CALCULATED	8 528	vs PERFLUORINATED HE	7 949
ACCEPTOR EXPLOSIVE PRESSURE HISTORIES	5 589	ALUMINIZED HMX, DDT STUDIES	7 119
ACCIDENT SCENARIO SIMULATIONS	8 1144	ALUMINUM COMP B, EFFECT ON VELOCITY	6 510
ACCIDENT SCENARIO, TANK CARB OF LIQUID HE	8 211	ALUMINUM SILICOFLUORIDE, LIGHT ENHANCEMENT	3 833
ACETYLENE-O <sub>2</sub> MIXTURES	6 116	ALUMINUM, 6061, EFFECT ON WAVE PROPAGATION	4 295
ACETYLENE-O <sub>2</sub> MIXTURES, D vs CALCULATIONS	2 236	CONCENTRATION EFFECT, NM/PMMA/AL	6 129
ACOUSTIC APPROXIMATION, CJ DETONATION	2 198	DETONATION PERFORMANCE EFFECT	8 1004
CJ PRESSURE CALC.	4 523	ENDOTHERMIC EFFECT AT CJ PLANE	2 736
ACOUSTIC IMPEDANCE, SHOCK TRANSMISSION	2 394	EXPLODING FOILS, INITIATION STUDIES	6 654
ACTIVATION ENERGIES, NM PARAMETERS	2 629	INCLUSIONS, INCREASED SHOCK EFFECTS	4 393
STEADY FLOW	8 856	PREHEATED, PRESHOCKED, P-V-E DATA	4 213
TIME-TO-EXPLOSION PLOTS	6 406	SHOCK WAVE PHOTO	4 570
ADDF, LIQUID HE, CHARACTERIZATION	8 1115	SPALL FROM OBLIQUE SHOCK WAVES	3 253
ADDITIVE DENSITY, DIAMETER EFFECTS IN NM	6 467	ALUMINUM-COPPER COMPOSITES, SHOCK LOADING	6 151
ADDITIVES IN RDX/TNT, ASBESTOS, ALUMINA, ETC.	7 583	AMATEX 20, DIAMETER-EFFECT PARAMETERS	6 647
ADIABATIC & HUGONIOT CURVES FOR MIXED PHASES	5 465	PARTICLE VELOCITIES, LAGRANGE GAUGE	7 1072
ADIABATIC COLLAPSE, BUBBLES TO HOT SPOTS	4 248	AMATOL 60/40, CURVATURE EFFECT ON SHOCK WAVE	1 99
ADIABATIC COMPRESSION OF GASES, SENSITIVITY	7 373	AMATOL, PLATE DENT AND CYLINDER TEST DATA	7 550
ADIABATIC CURVES, THEORETICAL EXPLOSIVES	7 7	WAVE SHAPE STUDIES, R/d	2 503
ADIABATIC ELASTIC MODULI OF PETN	6 533	AMINE NITRATE (mq.), THRESHOLD V, BURN RATE	6 119
ADIABATIC EXPANSION, DETONATION PRODUCTS	6 396	AMMONIA EFFECTS, COBALT AMINE AZIDE	3 54
ADIABATIC FURNACE, DYNAMITE PACKAGING HAZARD	8 602	AMMONIT, BOOSTER STUDY, CRITICAL DIAM & MASS	4 435
ADIABATIC GAMMA = 3, FLOW TO RIGID PISTON	7 43	AMMONIUM DYNAMITE, CRITICAL PRESSURE/DENSITY	4 185
ADIABATIC GAMMA, PREDICTED	3 207	AMPLITUDE-TIME DEPENDENCE FOR GO/NO GO	3 798
ADIABATS IN MIXED PHASE, COMPRESSIBILITY	7 646	AN, EFFECT IN RDX/TNY	5 465
ADNT, EUTECTIC COMPOSITE EXPLOSIVE	4 250	EUTECTICS	7 801
AERATING EXPLOSIVE GELATINE, LOW-V DETONATION	7 801	EXPERIMENTAL vs COMPUTED HUGONIOTS	6 773
AIR BUBBLE EFFECT, SENSITIZING NITROGLYCERIN	2 582	IMPROVED PERFORMANCE, COSOLIDIFICATION	6 439
AIR GAP EFFECT, INITIATOR & MAIN CHARGE, MODEL PROPAGATING IN CAST TNT	3 455	SENSITIVITY, CAVITATION EFFECT	7 373
AIR GAP SENSITIVITY TEST	8 399	AN-BASED HE, VERY SMALL REACTION ZONE LENGTH	8 993
AIR GAP SENSITIVITY vs LOADING DENSITY, TETRYL	8 409	AN/ADNT MIXES, SENSITIVITY OF EUTECTICS	7 801
AIR MIXTURE, CALCULATED SHOCK PARAMETERS	1 24	AN/AL, V-d CURVES, WAVE SHAPE vs D, KINETICS	2 733
AIR SHOCK PRESSURES FROM DONOR CHARGES, GAP	2 631	AN/HMTA, LIMIT DATA, DIFFUSION EFFECTS	4 184
AIR SHOCKS IN AIR GAP (PERIPHERAL)	3 389	AN/TNM, BKW MODEL & PERFORMANCE DATA	3 731
AIR SHOCKS, CAMERA RECORDS	3 794	AN/TNT, DENSITY, D, CD, P	3 376
CAMERA RECORDS	8 1069	AN/TNT/AL, AXIAL INITIATION vs BOOSTER	4 156
SYMPATHETIC DETONATION	1 9	ANDERSEN-PARLIN EOS, HARMONIC OSCILLATOR	2 406
AIR vs VACUUM, EFFECTS OF AP SENSITIVITY	3 390	ANFO, ALUMINIZED, AQUARIUM TESTS	7 1016
AIR-CHAMBERS PROBE, SPHERICAL DETONATION	3 531	AXIAL FUSE INITIATION vs NORMAL BOOSTER	4 156
AIR-MATCH POINTS, DEAL'S	4 359	BUBBLE ENERGY, UNDERWATER EXPANSION	6 546
AIR-REACTION PRODUCTS INTERFACE, P vs U <sub>p</sub>	5 32	CALCULATED BLASTING PERFORMANCE	8 987
AIRBLAST EFFECTS, PREDICTION FROM SHELL MODEL	4 63	CHEMISTRY OF EXTERNAL PLASMAS	3 186
REACTIVELY CASSED HE	3 386	CRITICAL DENSITY, DIAMETER EFFECT	4 179
SHOCK PRESSURE VARIATION	5 491	DENSITY, CD, D, EXPERIMENTAL PRESSURE	3 381
AL(CIO <sub>4</sub> ) <sub>3</sub> /HMX FORMULATIONS, CYLINDER TESTS	8 207	EXPLOSIVE PERFORMANCE CHARACTERIZED	6 729
Al <sub>2</sub> O <sub>3</sub> FORMED AS PRODUCT	6 777	LATERAL SHOCK PRESSURE MEASUREMENTS	4 95
Alex 20 & 32, BKW MODEL & PERFORMANCE DATA	5 137	NONIDEAL DETONATION	3 309
ALIEN, 2D LAGRANGIAN MODEL, INITIATION	4 168	PNEUMATICALLY LOADED, DOUBLE PIPE	8 390
ALIPHATIC COMPOUNDS, OB/100, SENSITIVITY TEST	3 731	SELF-LUMINOSITY PHOTOS, KERR CELL	6 424
ALLISON POLARIZATION, SHOCK-INDUCED SIGNALS	8 399	ANFO-TYPE BOOSTER, PROPERTIES	4 435
ALUMINA EFFECT IN RDX/TNT	3 677	ANFOAL, BUBBLE ENERGY, UNDERWATER EXPANSION	6 546
ALUMINIZED ANFO, AQUARIUM TESTS	5 387	ANGLE OF EXPANSION, CALCULATED FOR TNT	2 451
	5 465	ANGULAR DISTRIBUTION OF DETONATOR IMPULSE	3 300
	7 1016	ANOMALOUS ISENTROPE FROM RUBY PROGRAM	4 168

## B. Topic Phrase Index (Continued)

SUBJECT	SYM PAGE	SUBJECT	SYM PAGE
ANTIMONY, HUGONIOT DATA	6 602	B 2174 [HMx/AP/Pb(NO <sub>3</sub> ) <sub>2</sub> /PU], MACH STUDY	8 431
ANVIL, AL, THERMAL DECOMPOSITION, CONFINED HE SENSITIVITY TEST, LOW-VELOCITY IMPACT	6 214 4 473	B 2190, (PETN/HTPB), MACH PHENOMENA	8 431
AP, DDT STUDIES	7 151	B 2191, [HMx/AP/Pb(NO <sub>3</sub> ) <sub>2</sub> /PU], MACH STUDY	8 431
DIAMETER EFFECT, D vs 1/d, LIMIT DATA	4 183	B 2192, [HMx/AP/Pb(NO <sub>3</sub> ) <sub>2</sub> /PU], MACH STUDY	8 431
DIAMETER EFFECT, REACTION ZONE THICKNESS	4 97	B 3003, (HMx/NC-NGL), MACH PHENOMENA	8 431
GROWTH TO DETONATION, INTERFEROMETRY	4 584	BALL-BEARING IMPACT SENSITIVITY TEST	3 1
HUGONIOT CURVE WITH RAYLEIGH LINE	4 188	BALLISTIC CAPACITY vs SHAPED CHARGE	8 630
MECHANICAL PROPERTIES, DROP WEIGHT	8 642	BALLISTIC MORTAR TEST, MN SENSITIVITY	5 268
PERFORMANCE MODEL	7 517	BALLISTITE TRANSITION, DDT IN AP	7 156
PROPELLANTS, PROPERTIES, PARAMETERS	7 191	BARATOL, DENSITY, SHOCK & PARTICLE VELOCITIES	4 245
SHOCK INITIATION OF LOW-DENSITY PRESSINGS	4 359	DIAMETER-EFFECT PARAMETERS	6 647
SYMPATHETIC DETONATION BY NG	6 173	FREE-SURFACE MOTION, PRECURSOR WAVES	4 579
AP-LOADED EBW INITIATION	4 452	IN MODIFIED GAP TEST	7 279
AP/AL/NC PROPELLANT, CARD GAP SENSITIVITY	3 822	OVERDRIVEN SHOCKED STATES	5 533
AQUARIUM TECHNIQUE, DETONATION PRESSURE	5 59	P-t PROFILE, SULFUR CONDUCTIVITY	3 241
P, STREAK CAMERA TRACE	3 382	PERPENDICULAR DRIVER, ALUMINUM, X RAY	6 602
AQUARIUM TEST, ALUMINIZED ANFO	7 1016	PLATE IMPACT PRESSURE PROFILES	3 246
ANFO, NONIDEAL DETONATION	3 315	WAVE SHAPE STUDIES, R/d	2 503
DETONATION PERFORMANCE	7 801	WAX-GAP TEST	1 23
DETONATION PRESSURE IN EA	7 549	BARATOL/AL WAVE DIAGRAMS, MANGANIN GAUGE STUDY	6 631
LATERAL SHOCK PRESSURE	4 92	BARATOL/COMP B PLANE WAVE SHAPER, RETONATION	4 426
MAPPING FAILURE WAVES	5 115	BARATOL/TNT, DENSITY, D, CD, P	3 376
ONE TO SEVERAL HUNDRED kbars P	3 357	BARTLETT'S TEST, LEAST SQUARES FITS	3 335
SHOCK PRESSURE < DETONATION	3 152	BASE GAP EFFECT ON COMP B, TNT SENSITIVITY	7 914
SUBIGNITION REACTIONS	8 727	BENZENE/TNM, BKW MODEL & PERFORMANCE DATA	3 728
TATB/HMX	7 573	BENZOYL PEROXIDE, THERMAL DECOMPOSITION	7 27
X-0233, DETONATION BEHAVIOR	8 979	BERYLLIUM, ELASTIC-PLASTIC BEHAVIOUR	5 467
ARGON, THERMODYNAMIC PROPERTIES	8 815	BH-1, (RDX+), DETONATION PARAMETERS	8 440
AROMATIC NITRO COMPOUNDS, SENSITIVITY & OR	3 700	HUGONIOTS, VELOCITY/PRESSURE DATA	8 83
ARP PROPELLANT, DETONABILITY IN DDT STUDY	3 642	BICHROMATOR, TEMPERATURE, RAMAN BAND	7 1010
ARRHENIUS CONSTANTS, NG, TATB, HMX, PETN	8 43	BIMETALLIC & METAL SEMICONDUCTORS, SHOCKED	5 403
ARRHENIUS KINETICS, INITIATION & PROPAGATION	6 405	BIMETALLIC EMS GENERATION IN SHOCKS	5 403
ARRHENIUS PARAMETERS, THERMAL DECOMPOSITION	7 91	BIMODAL VELOCITY DISTRIBUTION, ANFO	3 325
ARRHENIUS PLOTS, INTERMEDIATE RADICAL GROWTH	7 80	BIMOLECULAR DECOMPOSITION	6 308
ARRHENIUS RATE, SHOCK-STRENGTH MODIFIED	7 385	BINARY MIXTURES, MELTING POINTS (EUTECTICS)	6 470
ARTIFICIAL VISCOSITY CALCULATION, UNDERWATER	5 597	BINDER, EFFECT ON EXPLOSIVENESS	8 1035
ASBESTOS EFFECT IN RDX/TNT	5 465	IMPROVED INERT, DETONATION EFFECTS	7 560
ASM PROBE, PARTICLE VELOCITIES, TEST SETUP	6 637	BIPLANAR OBSERVATION, DETONATIVE CENTERS	8 330
ASM PROBE, RECORD	5 451	BIS- & TRIS-DIFLUORAMINO PERFLUOROBUTANE	7 940
ATMOSPHERE EFFECT, CIRCUIT-RECORDED VOLTAGE	2 142	BIS-DIFLUORAMINO ALKANES, CRITICAL DIAMETER	5 89
ATTENUATING SHOCK WAVES, ELASTOPLASTIC EFFECT	4 277	SHOCK INITIATION	5 237
ATTENUATOR HUGONIOT AND RAREFACTION LOCUS	3 501	BISMUTH PHASE TRANSITION, ELECTRICAL JUNCTION	6 151
AUTOIGNITION AFTER TRAVEL, ZELDOVICH	1 49	BKW CALCULATIONS AND CYLINDER TEST RESULTS	8 1137
AXIAL CURVE vs REACTION ZONE vs DIAMETER	8 159	BKW CALCULATIONS FOR RDX/TNT MIXTURES	6 517
AXIAL INITIATION vs NORMAL BOOSTER INITIATION	4 136	BKW CALCULATIONS, DETONATION PERFORMANCE	3 725
AXIAL INITIATION, MULTICOMPONENT HE CHARGES	4 156	BKW CODE, SPHERICAL EXPLOSIONS UNDERWATER	5 603
AXISYMMETRIC DETONATION WAVE VELOCITIES	8 155	BKW EOS, CARBON CALC IN DETONATION PRODUCTS	4 599
AXISYMMETRIC ELECTROMAGNETIC PROBE (AGM)	5 447	QUATUOR CODE	8 763
AXISYMMETRIC EXPLOSION ANALYSIS CODE	3 226	BKW EQUATION, EOS FOR DETONATION GASES	1 73
AXISYMMETRIC FLOW, SPHERICAL SHOCK, SLURRY	8 168	BKW MODEL, HMx/AP/AL PROPELLANT	7 620
AXISYMMETRIC IMPACT, PROPELLANTS D AND E	8 285	HOT SPOT TEMPERATURE	7 348
AXISYMMETRIC WAVE PROPAGATING IN A HALF-SPACE	5 493	POSTDETONATION BEHAVIOR	7 646
AZIDES, DETONATION VELOCITY, SIZE EFFECTS	2 561	BKW-HOM EOS vs DATA, 1D CALIBRATION, COMP B-3	5 8
EXPLOSIVE, ELECTRICAL INITIATION	6 390	BLACKBODY RADIATION IN LIQUID HE	7 759
PHOTOLYSIS & THERMOLYSIS (N <sub>3</sub> , EXCITON)	3 843	BLACKBODY SPECTRAL INTENSITIES, 3000-6000 K	1 15
B 2141, DIVERGING DETONATIONS	7 408	BLAST WAVES IN LIQUIDS, INITIAL STAGES	6 502
FLYER PLATE, CRITICAL SURFACE AREA	7 320	BLASTING CAPS, STRESSES GENERATED	3 285
B 2142, BALLISTIC CLASSIFICATION	8 626	BLASTING PERFORMANCE, COMMERCIAL EXPLOSIVES	8 985
DIVERGING DETONATIONS	7 408	DO-1, HMX EXPLOSIVE, RETONATION EFFECT	8 93
B 2161, (HMx/AP/AL/PU), MACH PHENOMENA	8 431	BOLTZMANN EOS, QUATUOR CODE	8 764
BALLISTIC CLASSIFICATION	8 626	BOLTZMANN VIBRATIONAL TEMPERATURES, CALCULATED	8 691
B 2169, (PETN/PU), MACH PHENOMENA STUDY	8 431	BOMB TESTS, TNT IN DDT STUDY	3 637
B 2174, BALLISTIC CLASSIFICATION	8 626	BOND POLARITY AND DECOMPOSITION	7 69
		BOND SCISSION REACTIONS, UNIMOLECULAR	8 827

B. Topic Phrase Index (Continued)

SUBJECT	SYN PAGE	SUBJECT	SYN PAGE
BOND SCISSION, EXCITED ELECTRONIC STATE	7 93	BURNING OF SECONDARY HE BY CONVECTION	3 77
BOOSTER HE, EMP VELOCITY GAUGES	8 447	BURNING TUBE TEST DATA, RARDE, EXPLOSIVENESS	7 1040
BOOSTER PROPERTIES, CRITICAL DIAM vs MASS	4 435	BURNING, SUPERFAST REGRESSION	7 168
BOOSTER SENSITIVITY TEST SETUP, SCALING TESTS	2 623	BURSTING PRESSURE RATIO vs VELOCITY	2 223
BOOSTER STUDIES, TATB INITIATION, MODEL	8 1045	BUTANE DIOL DINITRATE, SENSITIVENESS	2 699
BOOSTING EFFECT ON STEADY DETONATION VELOCITY	6 642	BUTANE ISOMERS, FAILURE DIAM & SENSITIVITY	5 89
BOREHOLE, CHARGE WITH AIR SHOCK AHEAD OF FRONT	8 1070	BUTYLENE, SENSITIVENESS, Q, m	2 648
BOUNDARY CONDITIONS CORRESPONDING TO PISTON	3 541	C-3, MEASURED DETONATION VELOCITY, 0-60 kpsf	5 73
BOUNDARY CONDITIONS, STRONG POINT EXPLOSION	6 591	C-4, DIAMETER EFFECT, REACTION ZONE THICKNESS	4 97
BOUNDARY RAREFACTION EFFECTS, RELEASE WAVE	3 267	C.E.E. 2D MODEL, NONIDEAL DETONATIONS	7 695
BOW WAVE, DESENSITIZING EFFECT	8 318	CABLE CALIBRATION SUMMARY, PINS, DELAY SYSTEM	2 441
EFFECTS ON DETONATION	3 802	CABLE DELAY TIMING FILM, VELOCITY DATA FILM	2 445
BRAZILIAN TEST GEOMETRY, DROP WEIGHT TEST	8 635	CABLE DELAY TIMING SYSTEM, PIN RECORDS	2 441
BRIDGEWIRE (CU & NICHROME) INITIATION, RDX	3 89	CALCULE BALLISTICQ, SIMPLER PREDICTION	7 953
BRIGHTNESS TEMPERATURE, MEAN, LIQUID HE	7 762	CALIBRATED SHOCK WAVE TEST, FLYER PLATE	8 361
NITROMETHANE	7 760	CALIBRATING SENSITIVITY TESTS, LASER	8 473
NITROMETHANE FLYERS	7 1002	CALIBRATION CURVES, SHOCK TUBE	3 30
OVERDRIVEN NM	8 427	CALORIMETRY, MIXING TESTS, HE <sub>s</sub> , MODEL	8 1019
BRISANCE DEFINED, ALUMINIZED EXPLOSIVES	2 734	DETONATION, AN/ADNT	7 807
BRISANCE FACTORS IN DONORS	2 628	CAMERA RECORD, INVERSE MULTISTREAK	7 753
BRITTLE-TYPE FRACTURES IN STEEL PLATES	1 37	LASER INITIATION, LEAD AZIDE	7 738
BRUCETON METHOD DESCRIBED, 50% FIRING	2 622	RETONATION, DIVERGENT WAVES	4 428
BRUCETON METHOD, IMPACT VELOCITY, 50% PROBABLE	6 682	STREAK, CHINESE	7 749
BRUCETON TEST, DROP-WEIGHT IMPACT TEST	3 1	CARBON MONOXIDE/O <sub>2</sub> , NORMAL DETONATION WAVE	1 45
HE-WAX SENSITIVITY	7 337	CARBON TETRACHLORIDE, NM DILUENT	6 133
BRUCETON-TYPE DIRECT-CONTACT SENSITIVITY TEST	4 407	CARBON, HUGONIOT DATA, GRAPHITE AND DIAMOND	8 552
BTF, CJ PROPERTIES, OXYGEN BALANCE	8 547	CARD GAP TEST, DELAYED DETONATION	7 265
EXPERIMENTAL & CALCULATED CJ PARAMETERS	6 713	LOW-PRESSURE, LONG DURATION	8 228
BTFMA, LIQUID HE, CHARACTERIZATION	6 467	SETUP	3 824
BTNEN, ADIABATS CALCULATED FOR ENERGY RELEASE	3 740	SPHF PLATE SHOCK PRESSURE	3 150
IMPACT SENSITIVITY, CRITICAL TEMP	3 69	CARNAHAN-STARLING (CS) EOS, QUATUOR CODE	8 764
BTX, HIGH-TEMPERATURE EBW DETONATOR EXPLOSIVE	6 460	CARNAHAN-STARLING (CS) HARD-SPHERE EOS	8 805
BUBBLE & SPIKE INTERFACE, 2 FLUIDS	4 305	CASE EFFECT ON AIRBLAST OF PETN/TNT	6 777
BUBBLE EFFECTS, CAVITY INITIATION, GAP TEST	2 676	CASE, EXPANSION MODEL	7 834
COMPRESSIVE HEATING	7 9	EXPANSION MODEL, CYCLONE CODE	3 226
LVD STUDY	5 86	PENETRATION EFFECT, MODELS	7 273
SHOCK WAVE INTERACTION, NM	3 489	CASED CHARGES, AIRBLAST EFFECT	8 207
UNDERWATER EXPLOSIONS	1 8	FRAGMENT IMPACT RESPONSE	8 262
BUBBLE ENERGIES, UNDERWATER DETONATIONS	6 540	CASTING EMP VELOCITY GAUGES IN EXPLOSIVE	7 1072
BUBBLE PRESSURE vs TIME, LIQUID IHE MODEL	6 121	CASTING, PRESSING, AND MACHINING HE CHARGES	2 119
BUBBLE PULSATION ENERGY, FRACTION OF ORIGINAL	6 559	CAVITATED LIQUID IHE MODEL, DDT FROM BURN RATE	6 115
BUCKINGHAM POTENTIAL, INTERMOLECULAR ENERGY	2 437	CAVITATION EFFECT ON SENSITIVITY OF LIQUID HE	7 373
MODIFIED FOR EOS MODEL	7 716	CAVITATION IN SOLIDS & LIQUIDS, FRACTURING	3 805
BUILDUP TO DETONATION, IMPACTED HMX, TATB	8 346	CAVITATION MODEL OF LOW-VELOCITY DETONATION	5 81
SMEAR CAMERA, RDX/AL	3 708	CAVITATION THRESHOLD AS LIMITING FACTOR IN HE	4 413
BULLET IMPACT, RESULTS, SENSITIVENESS	2 703	CAVITY COLLAPSE IGNITION, COMP R	8 1080
SINGLE-CRYSTAL SENSITIVITY	2 471	CAVITY COLLAPSE IN ENERGETIC MATERIALS	8 68
SENSITIVENESS vs GAP TEST	2 644	CHAIN INITIATION, RADICALS IN UNREACTED GAS	2 229
TEST, SETUP	6 684	CHANNEL EFFECT, PRECOMPRESSED EXPLOSIVE	8 1069
TEST, SGL-CRYSTAL SENSITIVITY	2 471	CHANNEL PLATE DETONATIVE CENTERING	8 330
TEST, TATB/HMX MIXTURES	7 572	CHARACTERISTICS METHOD, NIP CODE	4 538
BURN FRACTION IN EULERIAN COORDINATES	3 724	CHARGE DIAMETER EFFECT, DETONATION VELOCITY	8 906
BURN MODEL, COMPRESSIBLE SOLIDS & GASES	7 234	CHARGE DIAMETER, DETONATION WAVE CURVE	7 592
EXPLICIT HOT SPOTS	8 52	VELOCITY DEPENDENCE IN LVD	5 86
HYDRODYNAMIC MOTION	5 487	CHARGE LENGTH EFFECT, L/d < 3, L/d = 15.5, TNT	2 504
NONDETONATIVE, VENTING	7 175	CHARGE PREPARATION, DETONATION VELOCITY TESTS	2 119
SLURRIES AND EMULSIONS	8 985	CHARGE RADIUS, STEADY VELOCITY DEPENDENCE	6 642
BURN PRESSURE IN UNDERWATER & GAP TESTS	4 494	CHARGE SIZE EFFECT ON PLATE DENT DEPTH	2 752
BURN PROBABILITY vs IMPACT VELOCITY, AMMO	6 689	CHARGE-SEPARATION HYPOTHESIS, WAVE/GROUND	2 142
BURN RATE ANOMALIES, COMP B, TNT, M30A1	7 898	CHD-3, 1D LAGRANGE MODEL, CHINESE	8 94
BURN RATE PARAMETERS vs PRESSURE EXPONENT	5 191	CHEMICAL ASPECTR OF DETONATION	1 43
BURN RATE vs PRESSURE, DDT	3 635	CHEMICAL COMPOSITION EFFECT ON PERFORMANCE	6 710
BURN RATES AT HIGHER PRESSURES	3 78	CHEMICAL DECOMPOSITION MODEL, CONFINED HE	7 56
BURN RATES OF SOLID HE, SENSITIVENESS	2 651	LAGRANGE GAUGES	7 498

## B. Topic Phrase Index (Continued)

SUBJECT	SYM	PAGE	SUBJECT	SYM	PAGE
CHEMICAL ENERGY RELEASE EQUATION, 1D MODEL	3	614	CJ PROPERTIES, HIGH-CARBON CHNO, MODEL	8	521
CHEMICAL ENERGY, UNLOADING RATE EFFECT	7	857	CJ STATE CALCULATIONS, BKW MODEL	3	726
CHEMICAL IONIZATION MASS SPECTROMETRY (CIMS)	8	725	CS HARD-SPHERE EOS	8	805
CHEMICAL KINETICS IN DETONATION	4	75	CJ STATE DERIVATIVES, JWL EOS	8	778
CHEMICAL KINETICS, C.E.E. 2D MODEL	7	695	CJ STATE, INITIAL STATE VARIATION	8	778
CHEMICAL REACTION, MODEL, SHOCK WAVE INIT	6	371	PBX, INERT BINDER EFFECTS, WAVES	7	560
RATE, PBX 9404 vs LX-17	8	953	RDX, TNT: JCZ EOS	6	162
RESULT OF FRACTURE	8	243	VARIATION OF MOLECULAR PARAMETERS	8	774
SHOCKED HNS	8	15	CJ SURFACE LOCATION REACTION RATE INFLUENCES	2	494
CHEMICAL REACTION/TRANSVERSE WAVES, DARK WAVE	6	414	CJ TEMPERATURES, FIVE LIQUID EXPLOSIVES	7	759
CHEMIONIZATION, SOURCE OF PLASMA LUMINOSITY	3	187	CJ THEORY, 1ST APPROXIMATION OF D (VELOCITY)	5	41
CHEG, CHEMICAL EQUILIBRIUM MODEL	8	302	CYANOGEN, O <sub>2</sub> , N <sub>2</sub> MIXTURE	2	231
CHICANERY, RETARDED DETONATION	6	225	FAILURE IN LIQUID & SOLID HE	4	84
CHINESE DETONATION RESEARCH, SURVEY	7	795	CJ VELOCITY, FRONT, TAYLOR WAVE	5	4
CINE-MICROSCOPE, NEW, DETONATION PHENOMENA	2	168	CJ VOLUME BURN vs TWO-PHASE BURN, GAMMA vs JWL	8	948
CINERADIOGRAPHY, FLASH X RAY(100,000 fpe)	7	986	CJ WAVE, STEADY STATE, CALCULATED FLOW	7	504
CISSOIDAL DETONATION WAVE, VERTEX, MACH WAVE	4	135	CLASSICAL DETONATION WAVE MODEL	8	487
CJ ADIABAT, KINETIC ENERGY OF WATER, BUBBLES	6	561	CLOSED-BOMB TEST RESULTS, COMP B	8	252
P-u <sub>p</sub> FOR HBX-1	5	523	CLOSED-VESSEL DEFLAGRATION, HE + PROPELLANTS	6	195
CJ CONDITION, AXIAL FLOW, SPHERICAL FRONT	8	168	CO <sub>2</sub> LASER, IGNITION OF PROPELLANTS	7	217
CALC., LOW-DENSITY HE SYSTEMS	5	56	CO <sub>2</sub> vs CF <sub>2</sub> AS DETONATION PRODUCTS	7	949
CYLINDRICAL OR SPHERICAL FLOW	4	78	CO <sub>2</sub> , TEST AND CALCULATED HUGONIOT	8	551
HYDRODYNAMICAL STUDIES	1	107	COAL-MINING EXPLOSIVES, CRITICAL DETONATION P	4	556
INITIAL CONDITIONS FOR FLOW	6	603	LUMINOSITY	2	571
POINT OF COMPLETE REACTION	1	55	COBALT AMINE AZIDES, THERMAL DECOMPOSITION	3	50
CJ DEFLAGRATION, SHOCK = CJ DETONATION	3	793	COLLIDING-BALL HE IMPACT SENSITIVITY TEST	3	1
WAVE MODEL, DDT STUDY	6	238	COMBUSTION DATA CORRELATED WITH SENSITIVENESS	2	643
CJ DETONATION, ACCELERATION, NO CONDUCTION	7	634	COMBUSTION ENERGIES, OXIDES AND FLUORIDES	7	941
PRESSURE, ZND AND CJ MODELS	7	531	COMBUSTION IN A CAVITY, CALCULATION	2	687
CJ EQUATION DERIVED, PRECOMPRESSION EFFECTS	5	69	COMBUSTION MODEL, STRESS WAVE PROPAGATION	7	208
CJ EXPANSION ADIABAT, FROM CYLINDER TEST DATA	7	646	COMBUSTION WAVE TRANSFORMATION, HIGH ORDER	1	43
CJ GAMMA DEFINED, ADIABAT FOR ENERGY RELEASE	3	739	COMMERCIAL BLASTING AGENTS, CHARACTERIZATION	6	729
CJ HYPOTHESIS, D = u + C	1	88	COMP A, DIAMETER-EFFECT PARAMETERS	6	647
CJ ISENTROPE & UNDERWATER PENTOLITE TESTS	4	27	MODIFIED, DETONATION VELOCITY, RATES	2	130
CJ ISENTROPES MEASURED FOR X2, T2	8	753	COMP A-5, EXPLODING-FOIL SHOCK SENSITIVITY	7	928
CJ MODEL, ASM PROBE PRESSURE DATA	6	639	SENSITIVITY AND EXPLOSIVENESS	8	265
SHOCK AMPLITUDE EVOLUTION	6	383	COMP B AND COMP B-4, DEFLAGRATION, VENTING	7	175
CJ PARAMETERS, (P, T, m, D FROM TIGER MODEL)	8	965	COMP B, AIR HUGONIOT AND CJ ISENTROPES	8	1076
DATA & CALCULATED	6	713	AL & LIF EFFECTS ON ACCELERATION	6	510
EOS CONSTANTS, LX-14	8	618	ANOMALOUS BURN RATE CHARACTERISTICS	7	898
POLYTROPIC EOS, 2D MODEL	7	589	BASE GAP EFFECT ON SENSITIVITY	7	914
RELEASE ISENTROPES, CALCULATED	7	1072	BKW MODEL & PERFORMANCE DATA	3	728
CJ PARTICLE DENSITY EFFECT ON CJ PERFORMANCE	3	735	CAMERA RECORD, IMPACT TO INITIATION	3	423
CJ PARTICLE VELOCITY BY EMV GAUGE	5	421	CARD GAP (SPHF), P-x CURVES, IONIZING	3	152
CJ PLANE, COINCIDING WITH COMBUSTION WAVE	1	44	CASED AND BARE, JET INITIATION	8	318
CONDUCTION ZONE BEHIND	3	117	CAVITY COLLAPSE IGNITION	8	1080
EQUILIBRIUM, STEADY STATE	2	200	CHEMICAL DECOMPOSITION MODELS	7	56
CJ POINT, DENSITY OF SOLIDS AFFECTS PRESSURE	1	112	CJ POINT, CJ ISENTROPE, ERROR %	7	709
TEMPERATURE, PRESSURE	1	21	CONDUCTING ZONE, ELECTRICAL EFFECTS	3	120
VELOCITY MEASUREMENTS, HMX/TNT/INERT	4	56	CONDUCTIVITY PROFILE, PIN SIGNALS	3	140
CJ PRESSURE & GAMMA (CALC) vs DURAL DATA	3	394	CONDUCTIVITY PROFILES, C PRECIPITATION	4	599
CJ PRESSURE & REACTION ZONE LENGTH MEASURED	2	343	CONFINED, AFTER FIRING, DEFLAGRATION	6	204
CJ PRESSURE, CALCULATED: TNT, COMP B, OCTOL...	5	23	CORNER TURNING MODEL, PHERMEX PROFILES	6	410
EFFECT, AWRE EOS DETERMINATION	7	682	CRYSTAL STRUCTURE, SENSITIVENESS	3	666
ESTIMATED FROM JONES EQUATION	2	380	CYLINDER TEST RESULTS	4	5
HIGH-DENSITY RDX, TNT, ROX/TNT	2	383	DENSITY, D, CD, EXPERIMENTAL PRESSURE	3	377
HIGHEST IN DETONATION WAVE	3	382	DENSITY, SHOCK AND PARTICLE VELOCITIES	4	245
MEASURED IN EXPLOSIVES	2	327	DETONABILITY, PROPELLANTS & EXPLOSIVES	3	639
NEW AQUARIUM TECHNIQUE (CHINESE)	7	795	DETONATION PRESSURE DATA	7	531
CJ PRODUCTS AS HIGH-DENSITY LATTICE STRUCTURE	2	405	DETONATION PRODUCTS, TEST, CALCULATIONS	8	581
CJ PROPERTIES, AN & AL-LOADED EXPLOSIVES	8	555	DETONATION PROPERTIES, CARBON EOS	8	528
AN- & EDD-LOADED HE, MODEL	7	555	DETONATION-DRIVEN PLATES & CYLINDERS	4	23
AP, RUBY CODE	4	360	DIAMETER-EFFECT PARAMETERS	6	647
CJ PROPERTIES, CHNO & CNO EXPLOSIVES	8	554	COMP B, DURAL, U <sub>10</sub>	7	535

## B. Topic Phrase Index (Continued)

SUBJECT	SYM PAGE	SUBJECT	SYM PAGE
COMP B, DYNAMIC DETECTION OF SPALLING	6 477	COMPACTION, EFFECTS ON FLAME TRAVEL, DDT	7 143
EMF GENERATED BY CONDUCTION ZONE	3 116	HEAT GENERATION IN HOT SPOTS	8 926
ENERGY THRESHOLD, p-t PLOT	6 106	POROUS BEDS OF INERTS	7 843
EUTECTIC WITH TNT, STRAIN-FREE CASTING	2 119	COMPACTION, WAVES, PISTON-PROPELLANT IMPACT	7 261
EXPLODING-FOIL SHOCK SENSITIVITY	7 928	COMPOSITE HE, Al PERCHLORATES/HMX	5 137
EXPLOSIVELY DRIVEN METAL, MODEL	8 610	CALCULATED IGNITION DATA	7 462
FLYER PLATE CRITICAL SURFACE AREA	7 316	DETONATION MODEL	7 517
FREE-SURFACE MOTION STUDIES	4 577	METAL ACCELERATION	8 1018
GAP TEST RESULTS, VARIABLE DONOR	7 279	COMPOSITION F.209, SPHERICAL DETONATION WAVE	5 31
GAP TEST, LOW-PRESSURE LONG DURATION	8 228	COMPRESSED-GAS GUN, SHORT-PULSE SHOCKS	7 857
HEAT OF DETONATION $q$ , $D$ , $P_{0j}$	3 744	COMPRESSIBILITY, WEAKER SHOCKS CAUSE REACTION	2 629
HIGH-VACUUM DETONATION	5 561	COMPRESSION WAVES, CHARACTERISTICS, SHIELDING	8 1145
IGNITION BY AIR GAP COMPRESSION	7 3	PROPAGATING, CAMERA RECORD	3 420
IMPACT INITIATION, .30-CAL CYLINDERS	2 612	COMPRESSION, RAMP-INDUCED, SHOCKED PROPELLANTS	8 962
INITIATION BY METAL JET, x-t PLOTS	7 352	COMPRESSIVE (HOT SPOT) BURNING STAGE, DDT	8 666
ISENTROPES, KNT vs JWJ	8 556	COMPRESSIVE HEATING, CAVITY COLLAPSE, COMP B	8 1080
JET TEMPERATURES, IR RADIOMETER	6 691	IGNITION MODEL	7 3
LOW-ORDER EXPLOSIONS AFTER IMPACT	6 328	COMPRESSIVE SHOCK & ACCELERATION (RAMP) WAVES	7 394
LOW-ORDER WAVE, RETONATION, WAVE EXIT	3 833	CONDENSATION SHOCK, CENTERED WAVE EXPANSION	2 308
LOW-PRESSURE POINT ON ISENTROPE	3 389	CONDENSATION SHOCKS & WEAK DETONATIONS	2 295
MACH INTERACTION, TWO WAVES	4 142	CONDENSATION SHOCKS IN 1D UNSTEADY FLOW	2 300
MEASURED DETONATION PRESSURE, AQUARIUM	5 65	CONDENSED PHASE WITH CAVITIES, CALC INITIATION	2 689
NONDETONATIVE EXPLOSION	7 246	CONDENSED-PHASE DETONATION, SUMMARY OF PAPERS	4 198
ON DURAL, $U_{10}$	2 334	CONDENSED-PHASE REACTIONS, NITRIC OXIDE	8 715
ON SPHERICAL Al SHELLS, VELOCITIES	6 521	CONDUCTANCE, NORMALIZED APPROX, HEMI PROBE	4 596
OVERDRIVEN DETONATION WAVES, EOS	4 47	CONDUCTANCE-DISTANCE CURVES, SPHF (CARD GAP)	3 164
OVERDRIVEN SHOCKED STATES	5 533	CONDUCTION TRACES, COMP B AND PENTOLITE	3 129
PARTICLE SIZES, FINITE & INFINITE DIAM	2 479	CONDUCTION ZONE BEHIND CJ PLANE	3 117
PARTICLE VELOCITIES	7 1072	CONDUCTIVE (LAMINAR) TO CONVECTIVE BURN	7 164
PHYSICAL PARAMETERS	7 593	CONDUCTIVE AND CONVECTIVE BURNING, DDT STUDY	8 665
PLEXIGLAS MONITOR, SHOCK VELOCITY	5 23	CONDUCTIVITY, DETONATING HE	3 139
POP PLOTS, BURN RATE MODEL	7 481	PROFILES vs C CONTENT, PRODUCTS	4 595
PRESSURE TIME PROFILES, MANGANIN GA.	6 625	PROFILES, ELECTRODES IN PROPANE	3 122
PULSE DURATION SENSITIZING EFFECT	5 191	PROBE RECORDS, SPHF PLATES	3 150
RADIATION & BLACKBODY TEMPERATURES	7 879	CONFINED CHARGES, 2D METAL & GAS FLOW, MODEL	3 226
RELEASE WAVE, BOUNDARY RAREFACTIONS	3 267	FUEL FIRE, MINITRIAL	7 1040
S. STEEL, INTERFACE VELOCITY, MODEL	4 545	STEEL YOKE SETUP	6 204
SENSITIVITY vs GAP THICKNESS	7 920	CONFINED DROP HAMMER TEST, IHE	7 965
SHOCK-INDUCED ELECTRICAL POLARIZATION	5 429	CONFINED HE, CHEMICAL DECOMPOSITION MODFL	7 56
SHOCKED, THERMAL FILM RECORD	7 973	PROPAGATING DETONATION MODEL	7 1055
SYMPATHETIC DETONATION	3 790	CONFINED HEATING, TATB/HMX MIXTURES	7 571
TRANSMISSION OF SHOCK WAVES IN Al	1 90	CONFINED TNT CHARGES, FINAL VELOCITIES	3 337
VELOCITY-DIAMETER CURVES	7 589	CONFINED-CHARGE RESPONSE TO FRAGMENTS	7 1048
W, Fe, Al, Al-Mg, & Be (MODEL)	7 796	CONFINEMENT & PRESSURE EFFECTS, DEFLAGRATION	6 204
WAX-GAP TEST	1 23	CONFINEMENT EFFECTS, CONTACT SENSITIVITY	4 408
X RAYS OF DETONATION	8 322	EBW INITIATION	4 449
COMP B-3, DROP-WEIGHT IMPACT TEST	3 6	ENERGY PREDICTION	8 176
IMPACT RESPONSE, MODEL AND TESTS	7 273	GAP TEST, DISCONTINUITY	3 805
ISENTROPES CALIBRATED FROM DATA	5 9	LOW-VELOCITY DETONATION	7 575
LOW-VELOCITY IMPACT IGNITION	4 478	PBX 9502, Mg, Al, PHMA	8 376
MEASURED PRESSURES, FOUR TESTS	3 14	PROPELLANTS DETONATING	3 823
OBLIQUE SHOCKS, PERPENDICULAR DRIVE	6 602	SMALL PETN & TNT CHARGES	2 768
PARTICLE VELOCITIES, MAGNETIC PROBE	6 637	SUBSONIC FLOW, MODEL	6 368
PRESSURE DATA, PHEMEX, $U_{10}$	5 13	VELOCITY, ANFO	3 316
PULSE DURATION SENSITIZING EFFECT	5 191	CONICAL IMPLOSION GENERATOR, Cu & U	5 548
SHOCK DESENSITIZATION	8 1057	CONSERVATION EQUATIONS, 1D, SPHERIC SYMMETRY	6 590
SHOCK WAVE DECAY IN Al	3 254	GASEOUS DETONATION	2 266
THERMAL INITIATION AND GROWTH	5 280	MASS, ENERGY, MOMENTUM	1 88
COMP B/AN, DIAMETER EFFECT, D vs 1/d	4 182	CONSTANT-CURRENT GENERATOR SETUP, TRIGGER	4 621
COMP C, DROP WEIGHT IMPACT TEST	8 640	CONSTANT-GAUGE RECORDS, LOW-ORDER DETONATION	6 330
COMP C-4, GAP TEST SENSITIVITY	3 830	CONTINUITY EQUATION, SPHERICAL DETONATION WAVE	1 93
GROWTH TO DETONATION, INTERFEROMETRY	4 584	CONTINUOUS RATE PROBE, LVD IN NITROMETHANE	7 577
SHOCK WAVE DECAY IN Al	3 254	CONVECTIVE BURN (CB), GAS PENETRATIVE, DDT	6 250
COMPACTION, DISTANCE vs XTMD	8 938	CONVECTIVE BURN MODEL, REGRESSION RATES	7 164

## B. Topic Phrase Index (Continued)

SUBJECT	SYN PAGE	SUBJECT	SYN PAGE
CONVECTIVE BURN MODEL, SOLID PROPELLANT CRACKS	7 186	CRYSTAL SIZE EFFECTS, THERMAL INIT OF AZIDES	2 563
CONVECTIVE BURNING, EXPLOSIVE POWDERS	3 77	CRYSTAL STRUCTURE, HMX POLYMORPH SENSITIVITY	3 665
CONVERGENT CYLINDRICAL SHOCK WAVES	1 79	CRYSTAL THICKNESS vs VELOCITY, LEAD AZIDE	5 301
CONVERGING (SONIC) DETONATION WAVES	7 638	CRYSTALLOGRAPHIC DATA, HQ	8 841
CONVERGING 1D SPHERICAL DETONATION	7 602	CS EOS, DETONATION TEMPERATURE vs DENSITY	8 805
CONVERGING FLOW DRIVER, PLANAR FLYER PLATES	7 826	CTPB AND HTPB BINDERS, DIAMETER EFFECTS	7 561
COPPER, PLANE SPALLING, 1D CALCULATION	5 567	CTX-1, SENSITIVITY AND EXPLOSIVENESS	8 265
RADIANCE RATIO & BLACKBODY RATIO	6 692	CU-CTE JUNCTIONS, SHOCK WAVE EFFECT	5 404
CORDITE SENSITIVENESS, GAP TEST SCALE	2 702	CUO-Hg, DEFLAGRATION VELOCITY, ELECTRIC PROBE	4 616
CORIOLIS ACCELERATION, FRICTIONAL HEAT	8 247	CURABLE PLASTIC-BONDED HE, CX-84A	8 361
CORNER-TURNING, COMP B, IMAGE INTENSIFIER	6 666	CURVATURE EFFECTS, DETONATION FRONT, HMX	4 86
MODEL	8 52	SHOCK WAVE EVOLUTION	6 379
MODEL, PBX 9404 & LX-17	7 488	STABLE DETONATION WAVES	1 93
TATB	7 624	CURVATURE OF AXIS EFFECT, DETONATION VELOCITY	1 53
COURANT CRITERION, ARTIFICIAL VISCOSITY	6 337	CURVE FITS, FIVE METHODS, SHOCK VELOCITY	5 62
COWAN-FICKETT DATA, EFFECTIVE GAMMAS, BETAS	3 721	CURVED-FRONT THEORY, NONPLANAR SHOCK WAVE	8 168
CP, DDT CALCULATION OF FLAME, CORNER TURNING	8 675	REACTION RATE, TNT/NANO	2 519
DDT, CHARACTERIZATION	7 865	WAVE SHAPE vs RATE	2 501
NEW EXPLOSIVE FOR LOW-VOLTAGE DETONATORS	6 455	CUSTOMIZED EXPLOSIVES, TATB- & HMX-BASED	7 566
CRACK EFFECT ON OCTOL, HOT PLATE & HOT WIRE	5 284	CX-84A, CURABLE PLASTIC-BONDED EXPLOSIVE	8 361
CRITICAL ACCELERATION FOR SHOCK GROWTH	6 47	CYANOGEN-O <sub>2</sub> MIXTURES, HIGH-TEMP THERMODYNAMICS	2 231
CRITICAL ACCELERATION, RADIUS OF CURVATURE	6 387	CYCLONE MODEL, TRANSIENT 2D FLOW	3 227
CRITICAL AIR GAP, LEAD AZIDE/TETRYL	2 626	CYCLOTOL 75/25, FREE-SURFACE VELOCITY	2 335
TETRYL ACCEPTOR DENSITY	1 25	CYCLOTOL, BKW MODEL & PERFORMANCE DATA	3 728
CRITICAL ANGLE FOR MACH BRIDGE, SHOCKS, FOAM	6 489	CYLINDER TEST RESULTS	4 5
CRITICAL BARRIER THICKNESS, COMP B CHARGE	7 354	DIAMETER-EFFECT PARAMETERS	6 647
CRITICAL BOOSTER DIAMETER & MASS	4 435	LOW-PRESSURE POINT ON ISENTROPE	3 389
CRITICAL CAPACITOR VOLTAGE, CONFINED CHARGES	6 207	MEASURED DETONATION PRESSURE	5 65
CRITICAL CONDITIONS, IMPACT INITIATION	7 316	UNDERWATER SHOCK-TO-BURN TESTS	4 489
SHOCK INITIATION	6 68	WEDGE TEST WITH SMEAR CAMERA RECORD	3 504
CRITICAL DIAMETER, ADDITIVE DENSITY EFFECT, NM	7 583	WEDGE TEST WITH SMEAR CAMERA RESULT	3 504
AN/AL MIXTURES	2 744	CYLINDER ENERGY, SIMPLER PREDICTION	7 953
AP, SYMPHETIC DETONATION	6 174	CYLINDER TEST, ALUMINIZED HE EFFECTS, SETUP	7 949
CONFINED CHARGES OF NM	7 609	BURNED GASES ISENTROPE & FLOW	4 39
NM-DILUENT MIXTURE	6 135	CP IN CU	7 869
THRESHOLD FOR PROPAGATION	5 207	EA EUTECTIC AND OTHERS	7 553
WAVE FRONT SHAPE	7 792	EA SYSTEMS	8 1004
CRITICAL ENERGY FLUENCE, CRITERION, PRESSURES	7 887	EUTECTICS OF AMMONIUM NITRATE	7 801
MOLECULAR DYNAMICS	7 778	IDEAL EXPLOSIVE PREDICTIONS	6 446
CRITICAL ENERGY, CONCEPT, SHOCK INITIATION	6 11	LX-14, VELOCITIES	8 616
DERIVED FROM GAP TEST DATA	8 1136	METAL ACCELERATION	4 3
IMPACT ON TETRYL, COMP B	6 327	NF <sub>2</sub> PERFORMANCE	7 940
INITIATION BEHAVIOR	7 459	OFF-CENTER INITIATION	7 755
TNT DETONATION	6 4	RDX/TNT MIXTURES	6 516
CRITICAL IMPACT CRITERIA, SHOCK INITIATION	7 857	TEMPERATURE, PARTICLE SIZE	8 1018
CRITICAL IMPACT VELOCITY, FRACTURE STRESS	1 35	TWO-PART, AWR EOS METHOD	7 678
SHOTGUN FACILITY	7 299	CYLINDRICAL CONVERGING DETONATION, D vs 1/r	7 602
vs LENGTH	4 474	CYLINDRICAL DIVERGING DETONATIONS, MODEL	7 669
CRITICAL JET INITIATION ENERGY	8 1091	CYLINDRICAL SHOCK TUBE, CONVERGING WAVES	1 81
CRITICAL PARTICLE VELOCITY, INIT THRESHOLD	5 227	CYLINDRICAL TUBE CELL FOR GAS FLOW MODEL	8 915
CRITICAL SHOCK DURATION, REACTION KINETICS	6 105	CYLINDRICALLY SYMMETRIC HOT BOUNDARY IN WAVE	4 83
CRITICAL SHOCK INITIATION ENERGY MODEL	7 459	DAGMAR MODEL, CORRELATION WITH SHOCK DATA	8 108
CRITICAL SHOCK INTENSITY, SHOCKED LIQUID HE	3 820	REFLECTED SHOCK, RAREFACTION	7 385
CRITICAL SHOCK PRESSURE EQUATIONS	8 1123	DARK WAVES, DETONATION FRONT	7 958
CRITICAL SHOCK, NM, MMAN, TNT, AN, DNT, DNB	7 382	HOMOGENEOUS HE DETONATION, PHOTOS	6 414
CRITICAL SURFACE AREA, BOT PARAMETER	7 316	LIQUID HE, FAILURE EFFECTS	5 169
CRITICAL TEMPERATURE SCALING, CONFINED HE, DDT	6 218	DARK ZONE IN SHOCK INITIATION	3 786
CRITICAL TEMPERATURE TESTS, t TO EXPLOSION	8 1114	DARK-WAVE FAILURE OF 1,2-DP, REINITIATION	5 97
CRITICAL THICKNESS OF DETONATION PROPAGATION	8 904	DARK-WAVE MODE OF FAILURE & REINITIATION	5 89
CRITICAL THICKNESSES FOR SHEET INCLUSIONS, NM	4 391	DATB, DETONATION PROPERTIES	3 761
CRITICAL TRANSFER CHARGE DIAMETER	8 334	DETONATION PROPERTIES, CARBON EOS	8 528
CRYSTAL BREAKUP IN REACTION OF SOLIDS	3 794	RADICALS IN DECOMPOSITION PRODUCTS	8 742
CRYSTAL GROWTH, PETN, ELASTIC MODULI	6 396	THERMAL INITIATION AND GROWTH	5 280
CRYSTAL MELTING EFFECT ON BURNING HMX	5 311	DAUTRICHE EFFECT, DETONATION WAVES COLLIDING	7 757

## B. Topic Phrase Index (Continued)

SUBJECT	SYN PAGE	SUBJECT	SYN PAGE
DAUTRICHE METHOD, D FOR CONFINED TNT	3 354	DECOMPOSITION REACTION KINETICS	7 789
D, UNREPRODUCIBLE RESULTS	1 9	DECOMPOSITION REACTION KINETICS, LEAD AZIDE	2 529
TEST SETUP	2 586	DEFLAGRATING EXPLOSIVES OR PROPELLANTS	3 799
DBA-1, -2, -3, DENSITIES, D, CD, P	3 381	DEFLAGRATION & DETONATION VELOCITIES, PROBE	4 616
DDNP, BURN RATE, SENSITIVENESS	2 651	DEFLAGRATION MODEL, FRAGMENT IMPACT	7 175
DEFLAGRATION BEFORE DDT	1 59	DEFLAGRATION RATE, HE + PROPELLANTS, > 1 kbar	6 195
DROP-WEIGHT INITIATION TEST	3 12	DEFLAGRATION WAVES, UNSTABLE, HETEROGENEOUS	6 281
DDT EXPERIMENTS, TEST FOR EXISTING THEORIES	1 57	DEFLAGRATION, ACCIDENT SIMULATIONS	8 211
DDT IN CP STUDY	6 455	BEFORE DETONATION, PHOTOS	1 57
DDT IN NITROGLYCERIN, BUBBLE EFFECT	3 455	CO-O <sub>2</sub> EXPLOSION, x-t PLOT	2 288
DDT IN PETN & RDX, FREE-RUN LASER INITIATION	6 612	DEUTERIUM, LASER DRIVEN	5 361
DDT IN PROPELLANTS & EXPLOSIVES, QUANTITATIVE	3 635	FROM EBW-INITIATED CAPACITOR	6 205
DDT IN PROPELLANTS, RISK TESTING	6 299	INDUCED AT AMBIENT	8 216
DDT IN RDX AND BALL POWDER, POROUS BEDS	8 972	PRINCIPAL MEANS OF PROPAGATION	3 433
DDT IN SOLIDS, CHEMICAL KINETICS, CALCULATIONS	3 606	SCHLIEREN PHOTO, CO/O <sub>2</sub> /H <sub>2</sub> /H <sub>2</sub> O	2 286
DDT MODEL, COMPACTED POROUS HE	7 198	DEFLAGRATION-TO-SHOCK TRANSITION (DST)	7 225
GRANULAR EXPLOSIVES	8 669	DEFORMATION AS THERMAL ENERGY SOURCE	8 926
PROPAGATING FLAME, CASED PROPELLANT	7 143	DEFORMATION HEATING, HIGH ASPECT RATIO DIMPLE	8 1080
PROPELLANT, CAST-GRANULAR INTERFACE	8 962	DEFORMATION, ROLE IN HOT-SPOT FORMATION	7 976
DDT STAGES FOR POROUS CHARGES	8 658	VELOCITY DISTRIBUTION PROFILES	7 347
DDT STUDY, AP + PYRIDINE IN STEEL TUBE	7 151	DEGRN, RADIANCE	7 762
CP CHARACTERIZATION	7 865	SENSITIVENESS, m x Q	2 700
DOUBLE-BASED PROPELLANT	8 658	DEKAZENE IN HYDRAZINE, GAP TEST SENSITIVITY	3 830
DREMIN'S DECOMPOSITION MECHANISMS	6 29	DELAYED AND LOW DETONATION, MODEL AND TESTS	8 135
HIGH-HMX SOLID PROPELLANTS	7 256	DELAYED DETONATION, CARD GAP TESTS	7 265
POROUS HE IN PLASTIC TUBES	7 119	LOW-VELOCITY IMPACT	7 256
RDX, "RETONATION" WAVE	5 231	DELAYED-DETONATION TRANSITION (XDT)	7 258
SMALL DIAMETERS IN RDX, HMX & HNS	7 107	DENSE FLUID EOS	8 785
STEEL-CONFINED RDX/WAX	7 139	DENSE MOLECULAR FLUIDS THEORY vs MODEL	8 531
TETRYL, FINE & COARSE, <85% TMD	6 426	DENSITY CHANGES IN GASEOUS DETONATIONS	2 187
DDT TEST DATA vs KRIER/VAN TASSELL GUN MODEL	6 258	DENSITY DISCONTINUITY, HMX/ZnCl <sub>2</sub> STUDY	5 187
DDT TUBE SETUP, PROPELLANT STUDY	8 659	HOT-SPOT FORMATION	5 177
DDT TUBE TESTS, BALL POWDER, MODEL	8 938	SHOCK INTERACTION	4 394
DDT, CONDUCTION PULSE PEAK TO INITIATION	3 156	SHOCK INTERACTION, NH	4 386
CP, SUMMARY OF PROPERTIES	7 865	DENSITY EFFECT, DDT	7 113
DIRECT OBSERVATION IN GLASS TUBES	7 873	DDT	7 166
DYNAMIC COMPACTION OF INERTS	7 843	DETONATION FRONT	7 768
DYNAMIC COMPACTION, INTRAGRANULAR STRESS	8 645	GAP TEST	7 336
EARLY WORK	3 788	HNS-SF SENSITIVITY	7 1026
GAS EVOLUTION & GAS ESCAPE vs PRESSURE	1 110	INITIAL, SCALED RADIUS	6 564
GAS-PHASE REACTIONS	7 216	RUN TIME AND PRESSURE	3 514
IGNITER AND COMPACTION EFFECTS	7 143	STRETCHED/UNSTRETCHED HE	4 500
LAMINAR TO CONVECTIVE BURNING	7 164	UNDERWATER	6 561
POROUS BEDS OF PROPELLANT, MODEL	8 934	DENSITY FLUCTUATION CONSTRUCTION SCHEME	8 680
POROUS EXPLOSIVE, CONSUMABLE	8 914	DENSITY SURFACE CONTOURS, TAB MODEL	8 50
POROUS HE, HIGH STRAIN RATE DEFORMATION	8 881	DENSITY, STRONGEST PRESSURE INFLUENCE	4 179
SCHLIEREN PHOTOS & PLOTS, CO/O <sub>2</sub> /H <sub>2</sub> /etc.	2 284	DENT & DETONATION VELOCITY TESTS, 3/8-in. DIAM	6 441
TWO ISOMERIC CAST PRIMARY EXPLOSIVES	6 231	DENT TEST RESULTS, AZIDE/PETN DETONATORS	2 723
WALL TRACE RECORDS FOR NM-ACETONE	5 105	DEPTH OF INITIATION vs BRASS U <sub>10</sub>	3 567
DE LAVAL NOZZLE, FLOW CONDITIONS	2 754	DESENSITIZATION BY PRESHOCKING HE	8 47
DEAD PRESSING	3 785	DESENSITIZATION BY SHOCKING	3 805
DEAD PRESSING, NO BURN TO DETONATION	2 629	DETSHEET C, PHYSICAL PROPERTIES	8 363
DEAL'S AIR-MATCH POINTS	4 63	DETONABILITY OF PROPELLANTS & EXPLOSIVES	3 635
DEBONDING & CRYSTAL FRACTURE vs EXPLOSIVENESS	7 20	DETONABILITY TEST SETUP, PRESHOCKED HE	8 1058
DEBRIS 13AS, SENSITIVITY AND EXPLOSIVENESS	8 265	DETONATING DIATOMIC LATTICES (MD)	8 864
DEBRIS 2, EMP VELOCITY GAUGES	8 447	DETONATION BEHAVIOR OF LIQUID TNT	2 439
DEBYE CONTINUUM THEORY, SHOCK COMPRESSION	7 523	DETONATION CALORIMETER, PETN DETONATION HEAT	4 167
DECAY OF SHOCK WAVES, SOLIDS & AL SPALLINGS	3 253	DETONATION CALORIMETRY, FLUORINE OXIDIZER	7 942
DECAY ZONES NEAR FRONT OF DETONATION WAVE	5 18	DETONATION CHEMISTRY, FLUORINE OXIDIZERS	7 940
DECOMPOSITION ENERGY, HEAT, RADIATION	3 843	DETONATION CRITERION, P <sup>n</sup> <sub>T</sub> = const	6 76
DECOMPOSITION FRONT REACTION	7 789	DETONATION FAILURE & SHOCK INITIATION MODEL	5 177
DECOMPOSITION KINETICS, EMISSION SPECTRA	8 710	DETONATION FAILURE, NM, 2D SIMULATION	7 608
DECOMPOSITION PRODUCTS, EMISSION SPECTRA	8 712	VELOCITY DIAMETER THEORY	7 589
DECOMPOSITION RATE vs PRESSURE (FOREST FIRE)	6 409	DETONATION FRONT PHOTOS: NM, NM/ACETONE	7 958

## B. Topic Phrase Index (Continued)

SUBJECT	SYM PAGE	SUBJECT	SYM PAGE
DETONATION FRONT STRUCTURE, GASEOUS, REACTION	2 216	DETONATORS, M29 & M47, DEVELOPMENT	2 712
DETONATION FRONT, SHAPED CHARGE, RECORD	7 751	DETOVA MODEL, DDT, DYNAMIC COMPACTION	7 850
DETONATION HEAD MODEL, WAVE SHAPES	2 501	DEUTERIUM SHOCKED BY PULSING Nd LASER	5 361
DETONATION HEAD SHAPES, SPHERICAL IGNITION	6 525	DFB, FAILURE DIAM, TIMES	5 89
DETONATION HEAD THEORY, REACTION RATE, TNT/SN	2 519	LIQUID HE, CHARACTERIZATION	6 467
DETONATION IF BURN SURFACE V > SOUND SPEED	2 695	DF, LIQUID HE, CHARACTERIZATION	6 467
DETONATION IN GASES AT LOW PRESSURE	2 251	DFNT, LIQUID HE, CHARACTERIZATION	6 467
DETONATION IN HIGH VACUUM	5 559	DIAMETER EFFECT, CJ PARAMETERS, KHT EOS	8 996
DETONATION IN HOMOGENEOUS EXPLOSIVES	2 454	CONDENSED EXPLOSIVES	2 424
DETONATION LIGHT, BUBBLES IN NM, CAMERA RECORD	3 481	DETONATION VELOCITIES	2 202
DETONATION LIMITS IN CONDENSED EXPLOSIVES	4 179	DETONATION VELOCITY	3 791
DETONATION PARAMETERS, AMATEX 20 & COMP B	7 1082	DETONATION VELOCITY, ZND	1 105
NM/DILUENT	6 136	DIVERGING DETONATION WAVES	8 1046
ONE EMBEDDED FOIL	8 440	EYRING THEORY, LIMITS	4 180
DETONATION PERFORMANCE CALCULATIONS, KW EOS	3 725	HI-DENSITY HETEROGENEOUS HE	6 642
DETONATION PRESSURE, FUNCTION OF LENGTH	5 59	LIQUID TNT, DURAL & PYREX	2 449
NM DRIVING DURAL, "DECAY"	5 18	NM, JONES & EYRING THEORIES	2 454
PBX 9404, COMP B, NM,	7 531	NONIDEAL DETONATIONS MODEL	7 699
SIMPLER PREDICTION	7 953	ON DDT	7 110
X RAY OF WAVE vs TIME	5 13	ON WAVE SHAPE, IDEAL HE	2 505
DETONATION PROCESS IN p-v PLANE, CJ POINT	2 345	PBX 9404, COMP B, PBX 9502	7 533
DETONATION PRODUCTS (ELEMENTS) EFFECT ON HE	6 710	REACTION ZONE THICKNESS	4 96
DETONATION PRODUCTS BELOW THE CJ STATE	5 523	SLURRY	8 168
DETONATION PRODUCTS STUDY, APPARATUS	8 702	TATB/HMX MIXTURES	7 567
DETONATION PROPERTIES, KHT EOS MODEL	8 548	THEORIES, EARLY WORK	3 801
DETONATION RESEARCH IN CHINA, SURVEY	7 795	THEORY & EXPERIMENT	8 168
DETONATION STATE, SERIES OF Ta FOILS	5 5	VARIOUS THEORIES COMPARED	2 482
DETONATION TEMPERATURE, 4-COLOR PYROMETER	8 558	DICHLORO-TNT, RADICALS, DECOMPOSITION PRODUCTS	8 742
CHARGE-CORE RADIATION	2 157	DIELECTRIC LIQUID EXPLOSIVES, TRANSDUCERS	4 609
LIQUID HEs	7 759	DIELECTRICS (LIQUID) IN SHOCK WAVES	5 399
THEORY, TNT & TETRYL	2 165	DIFFERENCE EQUATIONS, 1D FLOW, ISENTROPE + E	3 608
DETONATION THRESHOLD DATA, TNT-FILLED TARGETS	7 1051	DIFFUSION EFFECT IN COMPOSITE EXPLOSIVES	4 193
DETONATION THRESHOLD VELOCITY, IMPACT EFFECT	7 273	DIFFUSION LAYER CALCULATION	8 1012
DETONATION THRESHOLDS, PBX 9404 & RX-26-AF	7 325	DIFFUSION METHOD FOR GROWING LEAD AZIDE	7 736
DETONATION TUBE, STANDARD (FRENCH), PHOTO	6 126	DIFFUSION-CONTROLLED REACTION RATE MODEL	7 520
DETONATION VELOCITY, ANFO, TNT, EMULITE,...	8 987	DILUENT EFFECT ON METHYL NITRATE SENSITIVITY	5 271
CALCULATED, CJ, EOS, .	1 107	DILUENT EFFECT ON PROPAGATION OF NM	6 133
CURVATURE FUNCTION	7 602	DIMENSIONLESS EXPLOSIVE/JET PARAMETER	8 1091
CURVED LINER EFFECT	6 503	DIMPLE TESTS, THREE VARIATIONS, COMP B	8 1080
DENSITY, ANFO	3 314	DINA, BKW MODEL & PERFORMANCE DATA	3 728
DENSITY, DATB	3 764	CONFINED EFFECTS, FAILURE DIAMETER	3 800
DIAMETER STUDY	2 133	ELECTRICAL TRANSDUCER STUDIES	4 609
DIVERGING	8 151	NM, TNT, DITHEKITE SHOCK INITIATION	3 469
FROM HUGONIOT MINIMUM	2 387	TIME DELAY vs TEMP RECIPROCAL, DECOMP	3 68
LINEAR vs DENSITY	2 416	DINGU, SENSITIVITY AND PERFORMANCE	8 351
MEASUREMENT, PIN METHOD	2 136	SYNTHESIS	8 351
OSCILLOGRAPH TRACE, PETN	1 13	vs TATB, COMPARISON OF PROPERTIES	7 540
RADIUS (D vs 1/r)	2 480	DIRECT-CONTACT DETONATION SENSITIVITY TEST	4 404
RADIUS (D vs 1/r)	3 311	DISCONTINUITIES IN HE-DRIVEN PLATE TESTS	4 645
SIMPLER PREDICTION	7 953	DISCONTINUITIES IN MODELS, q & LAX METHODS	3 615
SPHERE, CYLINDER, PLANE	5 41	DISCONTINUITY ANGLE OF SHOCK WAVE	4 258
vs CHARGE DENSITY	5 74	DISCREPANCIES IN LOS, ADD FORMIC ACID	8 540
vs INITIAL DENSITY	2 390	DISK STANDOFF DISTANCE EFFECT, VELOCITY	7 306
DETONATION WAVE, FRONTS, IDEAL/NONIDEAL	2 500	DISLOCATION DYNAMICS, CRACKS IN ELASTIC MEDIA	6 268
GENERATORS, FAMILIES, TYPES	5 517	DISPLACEMENT GRADIENT METHOD, FLASH X RAY	8 440
INTERACTIONS, MODELING	5 487	DISSOCIATION ENERGY vs DETONATION VELOCITY, N <sub>2</sub>	2 244
INTERACTIONS, MODELING	7 669	DISTANCE-TIME PLOT, BUILDUP TO DETONATION	5 248
SUBSONIC, CONTAINER VELOCITY	5 85	DISTANCE-TO-DETONATION TESTS	7 888
THEORY, CHINESE	7 795	DISTANCE vs PRESSURE PLOTS, PETN, 2 DENSITIES	6 371
INTERACTING WITH INERTS	1 93	DITHEKITE, DINA, TNT, NM SHOCK INITIATION	3 469
DETONATION ZONE, CONDENSED EXPLOSIVES	2 358	PLASMA, STREAK CAMERA	3 200
PEAK LUMINOSITY MEASUREMENT	1 39	SENSITIVENESS, q, m	2 648
DETONATOR DESIGN & FABRICATION	2 720	DIVERGENT SPHERICAL DETONATION WAVES, SOLID HE	5 31
DETONATOR STRESSES, MOMENTUM, TIME, DISTANCE	3 285	DIVERGENT WAVE, FLOW DERIVATIVES, HEAT	8 148

## B. Topic Phrase Index (Continued)

SUBJECT	SYM	PAGE	SUBJECT	SYM	PAGE
DIVERGING DETONATIONS, RDX & PETN-BASED PBX	7	408	EDNA, IMPACT SENSITIVITY AND OS/100	3	674
DIVERGING SHOCK WAVE IN PLEXIGLAS CYLINDERS	5	477	LIMIT DATA, HIGH REACTION ZONE	4	184
DIVERGING SHOCK WAVE INITIATION, RDX/TNT	8	143	SENSITIVITY AND OXYGEN BALANCE DATA	3	699
DNP, DETONATION PROPERTIES	6	100	WAVE CURVATURE vs CHARGE LENGTH	2	506
SENSITIVITY, CAVITATION EFFECT	7	373	EDNP, LIQUID HE, CHARACTERIZATION	6	467
THERMAL DECOMPOSITION AT P = 10-50 kbars	5	331	EFFICIENT TEMPERATURE, > SHOCK PRESSURE OF EOS	6	105
DNPP, LIQUID HE, CHARACTERIZATION	6	467	EQO, SENSITIVENESS, Q,m	2	649
DNPTB, IMPACT SENSITIVITY, CRITICAL TEMP	3	39	SENSITIVENESS,m x Q	2	700
DNT, DIAMETER EFFECT, D vs 1/D, LIMIT DATA	4	182	EGON, BUBBLE ENERGY, UNDERWATER EXPANSION	6	546
RADICALS IN DECOMPOSITION PRODUCTS	8	742	LIGHT EMISSION DURING INITIATION	3	133
SENSITIVITY	7	373	EIE, FRENCH ION-EXCHANGED EXPLOSIVE	4	156
THRESHOLD VELOCITY, BURN RATE	6	119	EINSTEIN VIBRATIONAL FREQUENCY, PARTITION f	2	407
DOERING-KIRKWOOD-WOOD, INCREASE IN VELOCITY	2	198	ELA 2D MODEL, AWARE EOS DETERMINATION	7	678
DONOR CHARGES INITIATING ACCEPTOR CHARGES	2	621	ELA 2D STEADY-STATE CODE	4	14
DOPPLER LASER INTERFEROMETRY, VELOCITY STUDY	8	815	ELASTIC HALF-SPACE, WATER SURFACE DETONATION	5	497
DOPPLER SHIFT VELOCITY INTERFEROMETER, RECORD	6	673	ELASTIC MODULI, PETN CRYSTALS	6	400
DOUBLE WEDGE TEST, TATB AND HMX	8	892	ELASTIC PRECURSOR DECAY MODEL, WITH CRACKS	6	267
DOUBLE-BASE PROPELLANT, CASTING SOLVENTS	4	421	ELASTIC PRECURSOR WAVES IN IRON AND QUARTZ	4	569
DDT STUDY	3	658	ELASTIC PRECURSOR WAVES IN LVD, CAVITATION	5	85
GAP TEST SENSITIVITY	3	830	ELASTIC PRECURSOR WAVES IN SHOCKED BERYLLIUM	5	467
DOUBLE-CARTRIDGE TEST, SENSITIVENESS	2	604	ELASTOPLASTIC EFFECTS, ATTENUATING SHOCK WAVE	4	277
DOUBLE PIPE TEST (DPT), ANFO IN 40-mm DIAM	8	390	ELASTOPLASTIC RELEASE OF Mg AT 80 kbars	4	290
DOUBLY SHOCKED HMX, SHEAR CAMERA RECORD	3	511	ELECTRIC BOUNDARY VALUES, LAPLACE'S EQUATION	4	596
DOWNSTREAM MACH NUMBER PLOTS	5	131	ELECTRIC FIELD INITIATION, EXPLOSIVE AZIDES	6	390
1-2 DP, EXPERIMENTAL & CALC CJ PARAMETERS	6	713	ELECTRIC GUN TEST SETUP	8	1126
DREV GAP TEST, SHOCK SENSITIVITY	8	361	ELECTRIC GUN, INITIATING TATB, SHORT SHOCK	8	380
DROP HAMMER, IHE TEST, LABORATORY SCALE	7	965	ELECTRIC PROBE TECHNIQUE, DETONATION & DEFLAG	4	616
DROP WEIGHT APPARATUS, EXPLOSIVENESS, SKID	6	291	ELECTRICAL CONDUCTIVITY, DETONATION PRODUCTS	4	595
DROP WEIGHT IMPACT TEST, COLLIDING BALL	3	1	LIQUID DIELECTRICS	5	399
HOT SPOTS, SHEAR	7	970	ELECTRICAL EFFECTS IN PIN METHOD, VELOCITY	2	141
POLYMER EFFECTS	7	24	ELECTRICAL INITIATION OF RDX	3	88
TATB/HMX	7	570	ELECTRICAL JUNCTION EFFECT, SHOCKED METALS	6	151
DROP WEIGHT IMPACT, MECHANICAL PROPERTIES	8	635	ELECTRICAL RESISTANCE OF IONIZED ZONE	3	112
TRANSPARENT ANVILS	3	635	ELECTRICALLY ACCELERATED FLYER PLATE SYSTEM	6	653
DTA FOR BTX, NEW HIGH-TEMP EBW EXPLOSIVE	6	460	ELECTROCHEMICAL ELECTRODE EFFECT, LAB STOCK	5	399
DUAL VELOCITIES OF DETONATION: HG, TNT, TETRYL	2	583	ELECTRODE INTERFACE EFFECTS, LEAD AZIDE	6	393
DUAL-DELAY-LEG VELOCITY INTERFEROMETER (VIVAR)	6	668	ELECTRON BEAM HEATING, STRESS PULSE MEASURED	3	351
DUST PARTICLES INTERACTING WITH AIRBLAST	6	784	ELECTRON BEAM INITIATION	7	50
DYN2D MODEL, FAILURE RADII & CORNER TURNING	7	488	ELECTRON BOMBARDMENT DECOMPOSITION, AZIDES	2	531
DYN2D, EXPLICIT HOT-SPOT MODEL	8	58	ELECTRON DENSITY DISTRIBUTION ANALYSIS, HQ	8	839
DYNAMIC COMPACTION, POROUS BEDS OF INERTS	7	843	ELECTRON PARAMAGNETIC RESONANCE (EPR)	8	734
DYNAMIC COMPRESSIVE PROPERTIES, HMX COMPOUNDS	8	1037	ELECTRON PARAMAGNETIC RESONANCE (EPR) SPECTRA	8	742
DYNAMIC COMPRESSIVE STRENGTH EFFECTS	7	17	ELECTRONIC EXCITED STATES, BOND SCISSION	7	93
DYNAMIC DETECTION, SPALLING, STAINLESS, COMP B	6	477	ELECTROSTATIC POTENTIAL MAP, HQ	8	845
DYNAMIC IMPACT MODEL, 2D LAGRANGIAN	6	336	EMBEDDED FOILS, DETONATION STATE MEASURES	5	4
DYNAMIC RADIOGRAPHS, SPHERICAL DETONATION	5	36	X-RAY PHOTOS, FITS TO	5	16
DYNAMIC STABILITY BOUNDARIES, DEFLAGRATION	6	281	EMBEDDED GAUGE MEASUREMENTS vs RFLA	7	466
DYNAMIC STRESS-STRAIN DATA, CAMERA RECORD	3	420	EMBEDDED GAUGES, LX-17	8	1053
DYNAMITE, CALCULATED BLASTING PERFORMANCE	8	987	MANGANIN, TATB INITIATION	7	385
EXPLOSIVE PERFORMANCE CHARACTERIZED	6	729	EMF STATIC & DYNAMIC LOADING, C.T.E./CU JUNCT	4	633
LATERAL SHOCK PRESSURE TESTS	4	95	EMISSION INTENSITY, REACTIVITY INDICATOR	8	15
THERMAL HAZARD	7	45	EMISSION SPECTRA, DETONATING HNS	8	694
EA, EUTECTIC OF EDD AND AN, PERFORMANCE TESTS	7	548	Hg(CNO) <sub>2</sub> & C <sub>6</sub> H(NO <sub>2</sub> ) <sub>3</sub> (O <sub>2</sub> Pb)	8	710
EAK AND EAKL, INTERMOLECULAR EXPLOSIVES	8	111	EMP GAUGES, STEADY-STATE VELOCITIES	8	187
EAK, EUTECTIC, NON-STEADY-STATE EFFECTS	8	1001	EMULITE, AIR HUGONIOT & ISENTROPES, MODEL	8	1077
GAP TEST RESULTS	8	232	CALCULATED BLASTING PERFORMANCE	8	987
LOW EXPLOSIVITY BUT NOT LOW SENSITIVITY	8	1005	PRECURSOR AIR SHOCK IN AIR GAP	8	1072
EAR (EDD/AN/RDX) PLATE DENT TEST DATA	7	551	EMULSION EXPLOSIVES, PERFORMANCE TESTS, MODEL	8	985
EARLY-MOTION TEST, AWARE CYLINDER TEST	7	680	EMULSIONS, GLASS MICROBALLOONS, PERFORMANCE	8	993
EBW DETONATOR, HIGH TEMP, NEW EXPLOSIVE (BTX)	6	460	ENV GAUGE, ASSEMBLIES, (ELECTROMAGNETIC VEL)	8	102
EBW, CAUSE OF ENERGY LIMIT	4	449	HUGONIOTS, POROUS TNT	6	766
ILLUMINATION IN I <sup>2</sup> C PHOTOS, PBX 9404	6	666	RISE TIME, FLOW PERTURBATION	7	1062
EDD, EUTECTICS	7	548	SCHEMATIC, PARTICLE VELOCITIES	5	413
EDGE EFFECT STEADY-STATE DETONATION	6	356	ENV GAUGE, TECHNIQUE, PMMA	5	413

## B. Topic Phrase Index (Continued)

SUBJECT	SYM PAGE	SUBJECT	SYM PAGE
EN, BURN RATE, SENSITIVENESS	2 651	EOS, URANIUM AFTER SHOCK LOADING	5 547
RADIANCE & DETONATION TEMPS	7 762	WATER	3 357
SENSITIVENESS	2 699	WATER	4 27
SENSITIVENESS, Q. m	2 648	WATER, TWIN SPHERE INTERACTION	5 581
SHOCK COMPRESSION THROUGH INERT, DCT	3 813	WCA4	8 521
ENERGY BAND DIAGRAM, SCHOTTKY-BARRIER CONTACT	6 391	EPR RESONANCE, TRINITROAROMATICS	8 742
ENERGY DELAY EFFECT ON BLAST WAVE	7 729	EPR SPECTRA OF TETRYL, TNT, DNT, AND DABT	8 742
ENERGY EFFECT ON DECOMPOSITION OF DDT	3 842	EPR THEORY, DECOMPOSITION OF RDX & HMX	8 734
ENERGY FRACTIONG, BUBBLE, HEAT, MECHANICAL, ...	6 554	RADICAL IDENTIFICATION	8 734
ENERGY RELEASE, CHEMICAL SYSTEMS	3 738	EPR, HIGH-ACCELERATION CHEMICAL REACTION	8 243
RATE MODEL, FLOW FIELDS	7 498	THERMAL DECOMPOSITION OF NITRAMINES	7 75
ENERGY THRESHOLD vs SHOCK PRESSURE	6 112	EQUATION OF MOTION, CURVATURE EFFECTS	1 95
ENERGY TRANSFER EFFICIENCY, PLATES & CYLINDERS	4 21	EQUILIBRIUM IN C <sub>2</sub> H <sub>2</sub> /O <sub>2</sub> /N <sub>2</sub> ; PROOF OF C <sub>v</sub> THEORY	2 238
ENERGY TRANSFER TO RIGID PISTON AFTER IMPACT	3 205	EREMENKO'S RELATIVE DETONATION IMPULSES	7 952
ENERGY TRANSFER vs MASS RATIO, SPHERES, MODELS	6 526	ERYTHROSIN IN AZIDE PHOTOCHEMICAL INITIATION	2 554
ENHANCED THERMAL DIFFUSIVITY, SHOCKED PBX 9404	7 1006	ET, P <sub>cj</sub> , D	3 744
ENVIRONMENTAL SHOCK TESTING, CONDENSED PHASES	3 24	ETARC CODE, CHEMICAL EQUILIBRIUM MODEL	7 705
EOS & CRITICALITY CONDITIONS FOR LIQUID HE	4 395	EULERIAN, LAGRANGIAN COORDINATES COUPLED, MODEL	4 529
EOS DETERMINATION, AWRE METHOD	7 678	EUTECTIC, AN-BASED HE	8 997
EOS, 1060 ALUMINUM, SHOCK WAVE MEASUREMENT	4 213	AN-COMPOSITE EXPLOSIVES	7 801
ALUMINUM	2 354	AN, CONSOLIDIFICATION, INDICES	6 448
ALUMINUM	3 358	m.p. OF BINARY MIXTURES, LIQUID HE	6 470
AN-BASED HE	8 997	EVANS' LIMITS IN HOMOGENEOUS EXPLOSIVES	4 190
ANTIMONY	6 602	EXCESS TRANSIT TIME vs FLYER VELOCITY	6 660
ARGON, EXPANSION ISENTROPES OF TATB	8 816	EXCIMER LASER INITIATION, SPECTROGRAPHY	8 710
BASED ON INTERMOLECULAR POTENTIALS	7 703	EXPANSION ISENTROPES, TATB COMPOSITIONS	8 815
CALIBRATION METHOD	8 794	EXPANSION WAVE BEHIND DETONATION FRONT, IMPACT	4 560
CARBON	8 521	EXPLODING-FOIL SHOCK SENSITIVITY TEST	7 924
CAST PBX (HMX/POLYURETHANE)	8 599	EXPLODING-WIRE DETONATOR, PETN SURROUNDING IT	1 7
CHNO EXPLOSIVES PROPERTIES MODEL	7 703	EXPLOSIVE DEFLECTION OF A LINER	5 457
CJ CONDITIONS (K-W)	4 27	EXPLOSIVE GRAINS, GUMP B, TNT, H30A1	7 899
COMP B	4 3	EXPLOSIVE PARAMETERS, CONICAL SHAPED CHARGES	8 1093
DETONATION GASES	1 72	EXPLOSIVE SHOCK ADIABAT, COMPRESSIBILITY	7 791
DETONATION PARAMETERS, CHINESE	7 795	EXPLOSIVE WEDGE TEST, SETUP & STREAK RECORD	6 22
DETONATION PRODUCTS, AT P < 30 kbars	4 52	EXPLOSIVE-DRIVEN HE, SHOCK WAVES IN X RAYS	4 646
DETONATION PRODUCTS, C vs HCOOH	8 540	EXPLOSIVE-DRIVEN METAL, MODELS	8 602
DETONATION PRODUCTS, COMP B	4 47	EXPLOSIVE FILLED TRANSDUCER, CHARGE ASSEMBLY	4 611
DETONATION PRODUCTS, GASES	4 29	EXPLOSIVE-PLATE INTERFACE, VELOCITY, COMP B/SS	4 545
DETONATION PRODUCTS, INTRODUCTION	8 785	EXPLOSIVENESS, AWRE LABSET TEST	7 17
DETONATION PRODUCTS, VLV EOS	8 796	MUNITION FILLINGS	7 1040
ELASTOPLASTIC MATERIALS, AL, CU, C-7	4 280	RARDE BURNING TUBE, CONFINED HE	7 1040
GAS & LIQUID, LENNARD-JONES-DEVONSHIRE	1 108	RESPONSE, HMX-BASED PBXs	8 1035
GRANULAR HE, PULSED ELECTRON BEAM	5 351	SMALL-SCALE SKID TEST	6 290
GRAPHITE AT TNT CJ POINT	2 401	vs MINIMUM IMPACT VELOCITY	8 268
H <sub>2</sub> -O <sub>2</sub> DETONATIONS	2 221	EXPLOSOPHOROUS BONDS, SENSITIVITY, C-NO <sub>2</sub>	7 66
HBX-1	5 531	EXTX, MINIMUM PRIMING CHARGE TEST MODEL	7 479
HMX/POLYURETHANE	7 678	EXTRUDABLE HE, 36 NEW LIQUID CARRIERS	6 466
HMX/TNT	4 24	EYRING'S CURVED-FRONT THEORY	3 310
HNAB, RATE MODELING	7 416	EYRING'S CYLINDER DETONATION, DIAMETER EFFECT	3 787
LUCITE	3 584	EYRING'S EQUATION FOR UNCONFINED CHARGES	2 461
NITROMETHANE	7 609	EYRING'S THEORY & TECHNIQUE DISCOUNTED	2 452
PBX 9404	7 407	FABRY-PEROT INTERFEROMETER, SCHEMATIC	8 124
PETN DETONATION PRODUCTS	5 503	U <sub>fs</sub>	8 596
PLEXIGLAS	5 477	FABRY-PEROT vs ROTATING-MIRROR RESULTS	3 617
PMMA	5 477	FAILURE & REIGNITION PROCESSES, NM/PMMA/AL	6 130
POLYTROPIC, CJ PARAMETERS vs AREA	7 589	FAILURE CONE AND FAILURE WEDGE SETUPS	8 980
POROUS MATERIAL (INSULBOARD)	3 396	FAILURE DIAMETER, BIS-DIFLUOROAMINO ALKANES	5 89
RDX	7 716	CHARGE SETUP	5 91
REACTIVE MIXTURES, POSTDETONATION	7 650	FOR PBAA PROPELLANTS (RDX)	4 105
SOLID EXPLOSIVE (TAIT) + ISENTROPE	3 610	NITRIC OXIDE, SHOT SETUP	6 724
TNT, BURN MODEL FROM LSZK EOS	5 420	RDX ADDITION	4 97
TNT, IMPACTED, UNCONFINED	5 316	SOLID COMPOSITE PROPELLANT	4 102
TNT/NaNO <sub>3</sub> 50/50	2 519	THEORY, APPROX. DELETED	5 99
EOS, UNREACTED EXPLOSIVE	3 542	FAILURE EFFECTS, DARK WAVES IN LIQUID HE	5 169

B. Topic Phrase Index (Continued)

SUBJECT	SYM	PAGE	SUBJECT	SYM	PAGE
FAILURE LIMIT CURVES, TNT, DIAM vs DENSITY	5	211	FLYER PLATE, SLAPPERS, AIR & GAS EFFECTS	7	930
FAILURE OF CJ THEORY FOR SOLID & LIQUID HE	4	84	TEST SETUP, ISL (FRANCE)	8	368
FAILURE RADII, DATA & MODEL, HOT SPOTS	6	411	FLYER VELOCITY CALIBRATION CURVES	6	658
FAILURE RADII, TESTS, PBX 9404 & LX-17	7	488	FLYER VELOCITY vs BURST CURRENT DENSITY	8	1127
FAILURE WAVES, PHOTO MAPPING TECHNIQUE	5	115	FLYING-FOIL TESTS IN METHANE & VACUUM, 9404	4	376
FALLING HAMMER TEST, MN SENSITIVITY	5	268	FOAMED HE, DETONATION CHARACTERISTICS	5	47
FAST-BURNING REACTION, PETN, FRAMING CAMERA	3	16	FOAMED PETN CHARGE, LOW-DENSITY HE SYSTEMS	6	183
FDA, LIQUID HE, CHARACTERIZATION	6	467	FOAMS, SHOCKED, HEATED, PRESSURE WAVES	4	266
FDEE, LIQUID HE, CHARACTERIZATION	6	467	FOIL-MOTION METHOD, CJ CONDITIONS, LOW DENSITY	6	185
FDEK (AN/ADNT/EDD/KN) SENSITIVITY	7	804	FOILS, CONFINEMENT, REDUCING FAILURE DIAMETER	2	474
FDNE-A, -H, -S, LIQUID HE, CHARACTERIZATION	6	467	FOREST FIRE BURN MODEL vs TEST DATA	7	479
FDNEP, LIQUID HE, CHARACTERIZATION	6	467	FOREST FIRE MODEL, TARGET GAUGE RECORDS	6	27
FEFO, EXPERIMENTAL & CALCULATED CJ PARAMETERS	6	713	FOUR-SHOCK CONFIGURATION, OBLIQUE, REFLECTED	6	572
LIQUID HE, CHARACTERIZATION	6	467	FRACTURE IN HE-METAL SYSTEM, SCABBING/SPALLING	1	33
FIBER OPTIC DETECTORS USED WITH STREAK CAMERA	8	381	FRACTURE PATTERNS, IMPACTS AT DIFFERING ANGLES	5	575
FIBER OPTICS ASSEMBLY, SHAPED-CHARGE TEST	8	462	FRACTURE PHENOMENA, FROM SUDDEN RELEASE	1	35
FIBER OPTICS, GASED DEVICE, ARRIVAL TIME	8	460	HIGH ACCELERATION	8	243
FICKETT & WOOD EOS, STRAIGHT-LINE CJ ADIABAT	4	52	XPS (SPECTROSCOPY)	8	243
FICKETT-JACOBS CYCLE	8	794	FRACTURE ZONE LIMITS vs ANGLE OF INCIDENCE	5	578
FILM CONTACT, ANVIL, IMPACT SENSITIVITY MACHINE	3	11	FRAGMENT ATTACK TEST, SENSITIVENESS	2	696
FILM, SPRAYED-ON HE, LARGE-AREA DETONATOR	7	746	FRAGMENT IMPACT EFFECTS, PLATE & PLUG	7	1048
FINITE-DIFFERENCE MESH, 2 CHARGES UNDERWATER	6	584	FRAMING CAMERA, COMP B & DITHEKITE PLASMA	3	189
FINITE-DIFFERENCE METHOD, FLOW TO PISTON	3	205	RECORD, NM/PMMA/AL, WAVES	6	129
FINITE-DIFFERENCE SCHEME IN LAURANGIAN COORD.	4	528	FREE RADICALS, HMX DECOMPOSITION	8	737
FITS TO P-U POINTS FOR HMX/TNT	4	61	RDX DECOMPOSITION	8	737
FITTING FORM DESIGN, ISENTROPE	8	792	FREE-RADICAL SHOCK INITIATION MODEL	7	778
FIVONITE, WAX-GAP TEST	1	23	FREE-SURFACE MOTION, PREDICTION & DATA	4	295
FLAME ANALYSIS, TETRYL, PETN, NITROGLYCERIN	2	572	STREAK CAMERA READINGS	4	573
FLAME AS REACTIVE DISCONTINUITY	7	223	FREE-SURFACE ROTATION, OBLIQUE SHOCK	4	566
FLAME HEIGHT PREDICTIONS, HMX IN DDT	7	169	FREE-SURFACE VELOCITY, = ?(PARTICLE VELOCITY)	1	91
FLAME PROPAGATION, CONVECTIVE BURN MODEL	7	186	FLAT TOP	2	381
FLAME SPREAD THROUGH PROPELLANT, DDT	7	143	IRON IMPACTED, 25 GPa	6	672
FLAME TRAJECTORY, CALCULATED	7	227	vs PLATE THICK, PINS	2	349
FLASH X RAY, CINEPADIOGRAPHY, HIGH SPEED	7	986	vs PLATE THICKNESS	2	330
COMP B, JET INITIATION	7	358	vs PLATE THICKNESS	4	547
INSTRUMENTED SHOTGUN, DEF, XOT	7	299	vs TIME, PBX 9404	5	324
PERMEX	4	639	vs(PLATE THICK/CD) <sup>1/2</sup>	5	20
FLASH-GAP TECHNIQUE, DETONATION PRESSURE	5	13	FREE-VOLUME INCREASE, SLOWER REACTION, LOWER P	2	629
FLAT PLATE TEST, ELECTRIC GUN INITIATION	8	614	FREE-VOLUME THEORY, FLUIDS, LENNARD-JONES-...	1	107
FLO, PRESSURE-BASED, REACTIVE FLOW 2D MODEL	7	328	FRICTION INITIATION APPARATUS	5	291
FLOW BEHIND REACTION ZONE, PLATE DENT RESULTS	2	749	FRICTION TEST, SENSITIVENESS TESTING	3	660
FLOW BOUNDARY & SHOCK WAVE IN AIR, PHOTO	5	461	FRONT & MASS VELOCITY IN EVACUATED CHAMBERS	4	176
FLOW FIELD MEASUREMENTS, EXPLOSIVE STRUCTURE	5	33	FTE, LIQUID HE, CHARACTERIZATION	6	467
FLOW FIELDS, CALCULATION, RFLA TECHNIQUE	7	466	FULL-MOTION TEST, AWRE CYLINDER TEST	7	679
FLOW GAUGES, CONSTITUTIVE RELATIONSHIPS	5	427	FUNDAMENTAL RESEARCH ON EXPLSIVES, NO	8	422
FLOW VELOCITY, EMV & VELOCIMETER	7	1064	FUZE DESIGNS & TECHNOLOGY	2	720
FLUID MODEL, 1D, COMPRESSIBLE, REACTIVE FLOW	2	313	GAMMA & CJ PRESSURE (CALC) vs DURAL DATA	3	394
FLUORINE AS OXIDIZER IN EXPLOSIVES	7	940	GAMMA LAW HE, DETONATION PARAMETER RELATIONS	3	754
FLUORODINITROMETHYL COMPOUNDS, SENSITIVITY	7	84	GAMMA LAW, (P-V BEHAVIOR), COMP B	4	8
FLUOROMETHYL- SYNTHESIS, HISTORY	7	84	CALCULATIONS, HE PARAMETERS	8	946
FLUORONITROALIPHATIC SENSITIVITY, OXYGEN BAL	7	87	EOS vs DATA, CJ PRESSURE	5	8
FLYER ACCELERATION, EXPLODING METAL FOILS	6	653	EOS, P-Up ISENTROPE FROM CJ STATE	3	387
FLYER PLATE, COLLISION, PERMEX RADIOGRAPH	4	645	GAMMAS, GRUNEISEN AND ADIABATIC	8	791
CONVERGENT FLOW DRIVER	7	826	GAP TEST, 6-in.-DIAM CONFINED, INSTRUMENTED	8	228
CRITICAL SURFACE AREA CONCEPT	7	316	CARD, PROPELLANTS, CONFINEMENT	3	823
ENERGY vs REACTION RESPONSE	6	7	CAVITATION EFFECT ON SENSITIVITY	7	373
EXPLODING FOIL, SENSITIVITY TEST	7	924	CRITICAL FAILURE DIAMETER	3	800
IMPACT SIMULATION	8	52	CRITICAL SHOCK INITIATION	7	278
IMPACT TEST, HE SENSITIVITY	6	105	CYLINDRICAL	4	462
LIMITING VELOCITY	7	798	DATA vs FRAGMENT IMPACT DATA	8	1151
METAL-HE-METAL ACCELERATION	7	811	ERDE, SENSITIVENESS	2	646
OBLIQUE IMPACT	4	381	HISTORICAL WORK	3	785
SCHEMATIC, HNS SENSITIVITY TEST	7	1025	INITIATION THRESHOLD, TNT	6	36
FLYER PLATE, SHOCK FOCUSING	6	62	GAP TEST, INTERSTITIAL GAS EFFECTS	5	247

B. Topic Phrase Index (Continued)

SUBJECT	SYM	PAGE	SUBJECT	SYM	PAGE
GAP TEST, LIQUID MONOPROPELLANTS	3	436	GAUGE, QUARTZ, TECHNIQUE FOR IMPACT TESTS	5	369
LOW-AMP SHOCK INITIATION (LASI)	7	285	QUARTZ, THICK, PMMA	4	222
LOW-ORDER REACTIONS IN SHOCKED HE	4	462	RECORDS, PERFECT vs MODEL	7	472
MODEL vs LANL & NOL RESULTS	7	479	GBFO, LIQUID HE, CHARACTERIZATION	6	467
MODIFIED	8	1131	G <sub>0</sub> AND B1, COMPLEX SHOCK WAVES	3	408
MODIFIED, LOW-VELOCITY DETONATION	7	575	GELIGNITE, SHOCK PARAMETERS, MINING EXPLOSIVE	4	559
MODIFIED, UNDERWATER SHOCK TO BURN	4	488	GEM-DINITRO COMPOUNDS, IMPACT TESTS, OB/100	3	676
MORE RELIABLE FOR MONOPROPELLANTS	2	695	GEOMETRICAL SHOCK FOCUSING	6	62
NM, 50X GAP > WITH Al CONFINEMENT	3	798	GIBBS FREE ENERGY, EQUILIBRIUM COMPOSITION	4	168
NOL, SHOCK PRESSURE TO INITIATION	3	584	GITTINGS' FLYING FOIL RESULTS, VACUUM/METHANE	8	1061
PERPENDICULAR, LOW-ORDER REACTIONS	4	463	GLASS MICROCALLOONS, EMULSION EXPLOSIVES	8	993
SCHEMATIC CROSS SECTION	5	220	GLASS MOUSETRAP PLANE-WAVE GENERATOR	8	447
SENSITIVENESS TESTING	3	660	GLYCOL DINITRATE, DILUENT EFFECTS IN NM	7	583
SENSITIVENESS, CONSTANT PRIMER	2	602	GRAIN BURNING, BUILDUP TO DETONATION	6	11
SENSITIVITY, LIQUID HE SYSTEMS	4	412	GRAIN-BURNING MODEL, REACTION ZONE MODEL	3	310
SETUP, TATB AND HMX COMPOUNDS	8	897	GRANULAR DECOMPOSITION, LAMINAR GRAIN BURNING	7	394
SETUP, VACUUM vs AIR	7	5	GRANULAR HE DETONATIONS MODEL	8	55
SHOCK WAVE SENSITIVITY IN LIQUIDS	7	575	GRANULAR HE, PRESSED, SHOCK TO INITIATION	3	562
SHOCKED H-6 & PBXW-109	7	308	GRANULOMETRY EFFECT ON MACH REFLECTION	8	437
SMALL-SCALE TEST SETUP	5	261	GRAPHITE FCW EFFECT ON D vs INITIAL DENSITY	2	392
TATB FORMULATIONS, PANTEX	7	430	GRIT EFFECT ON FRICTIONAL INITIATION	5	295
WAX vs INERT BARRIER	3	787	GROWTH OF DETONATION FROM INITIATING SHOCK	3	534
WAX EFFECTS ON SENSITIVITY	4	401	GROWTH OF REACTION IN SMALL CHARGES, TESTS	6	290
WAX, SENSITIVITY, PRESSED/CAST	1	22	GROWTH TO DETONATION IN ACCEPTOR, HIGH ORDER	2	626
GAP THICKNESS, COMPRESSIVE HEATING IGNITION	7	3	GROWTH TO DETONATION, C-4 & AP, INTERFEROMETRY	4	504
GAS BUBBLE, SCREENING EFFECT, DELAYED ARRIVAL	6	587	GRUNEISEN COEFFICIENT FOR GRANULAR EXPLOSIVES	5	351
GAS DETONATION, STRUCTURE & INSTABILITY	4	67	GRUNEISEN EOS, COEFFICIENTS, Cu AND Al	8	615
GAS EFFECTS ON FLYER INITIATION	7	931	UNREACTED POROUS TNT	6	767
GAS EVOLUTION AND GAS ESCAPE vs PRESSURE	1	110	GRUNEISEN GAMMA ALONG CJ ADIABAT, HNB	7	655
GAS FRACTIONS, PYROLYSIS & FINAL GAS FRACTION	8	938	GRUNEISEN PARAMETER, EVALUATION, METALS	4	203
GAS GUN, HUGONIOT, LEAD AZIDE	6	389	MEASUREMENT, HNS II	6	742
TESTS, PLANAR SUSTAINED SHOCKS	7	385	PRECOMPRESSION EFFECTS	5	68
GAS IMPERFECTION FACTOR F DEFINED, K-W EOS	2	385	GURIT CHARGE, PRECURSOR AIR SHOCK, DET FRONT	8	1071
GAS IN SUPERSONIC NOZZLE FLOW, SHOCK-LIKE	2	295	GURNEY CONSTANT, SIMPLER PREDICTION	7	952
GAS NONIDEALITY IN CJ STATE, SCHMIDT EQUATION	2	204	GURNEY CURVE vs CALCULATED EFFICIENCIES	7	824
GAS PASSING THROUGH SHOCK FRONT INTO REACTION	1	43	GURNEY ENERGY vs INITIAL DENSITY FOR CP	7	870
GAS POCKETS IN LOW-VELOCITY DETONATION	2	582	GURNEY MODEL AND THOMAS' SYNTHESIS	8	602
GAS SHOCK VELOCITIES, HMX/TNT/INERT	4	57	GURNEY MODEL, FRAGMENT VELOCITIES	4	19
GAS-DYNAMICAL MODEL, RDX/TNT INITIATION	8	196	GURNEY VELOCITY, CASING EXPANSION MODEL	7	834
GAS-PHASE REACTIONS IN DDT	7	216	H-6, ANOMALOUS INVERSE SENSITIVITY, LASI	7	293
GASDYNAMIC FLOW FUNCTIONS, DIMENSIONLESS	6	592	BURNING AND DETONATION, GAP TEST	7	308
GASEOUS DETONATION WAVES, AIR CYCLE CALC	2	266	HUGONIOT DATA FOR UNREACTED EXPLOSIVE	5	251
GASEOUS DETONATION, PHOTOS, O <sub>2</sub> -H <sub>2</sub> , O <sub>2</sub> -CO	2	281	HARDNESS NUMBERS, GROWTH SURFACE OF RDX	7	930
RAPID DENSITY CHANGES	2	187	HAZARD CLASSES, VELOCITIES OF PROPELLANTS	6	303
GASEOUS FLOW FROM METAL TUBE (2D), CODE	3	226	HAZARD POTENTIAL, LIQUID HE, LARGE MASA	6	122
GAUGE CALIBRATION, PRESSURE, CARBON RESISTOR	5	54	HBX, MEASURED DETONATION VELOCITY, 0-54 kpsi	5	73
GAUGE RECORDS, PERFECT vs MODEL	7	472	V-d CURVES, WAVE SHAPE vs d, KINETICS	2	733
GAUGE RISE TIME & PARTICLE VELOCITY (EMV)	7	1064	HBX-1, DENSITY, CD, D, EXPERIMENTAL PRESSURE	3	376
GAUGE, ELECTROMAGNETIC VELOCITY TECHNIQUE	5	413	ELECTRON-BEAM INITIATION	7	50
EM, REACTION RATES	8	99	STABILITY & EXPANSION BEHAVIOR	5	523
EM, REACTION RATES FROM	8	83	HBX/TNT/Al, V-d CURVES, WAVE SHAPE vs d	2	733
EMBEDDED vs VISAR IN REACTIVE FLOW	8	955	HEAT CAPACITIES, CALC, C, O, N, CN, CO, O <sub>2</sub> ,...	2	239
EMP, INTERMOLECULAR HE REACTION	8	187	HEAT OF EXPLOSION x MASS BURN = SENSITIVENESS	2	643
IONIZATION & PIEZOELECTRIC	2	201	HEAT PULSE, FORMATION & TRANSMISSION	3	575
MANGANIN WIRE, PRESSURE MEASUREMENT	6	625	HEAT RELEASE, PLANE AND HEMISPHERICAL WAVES	8	147
MANGANIN, LOW RESISTANCE	7	386	RATE ALONG SHOCK TRAJECTORY	8	143
MANGANIN, MULTIPLY EMBEDDED	6	21	vs VELOCITY, CAREFUL DETONATION	2	268
MANGANIN, STRAIN COMPENSATED	6	330	HEAT TRANSFER, FROM (p,v,e)	7	504
MULTIPLE LAGRANGE, TNT	6	786	HEAT TRANSFER FACTOR IN INITIATION	3	793
MULTIPLE, STUDIES IN SITU	7	1062	HEAT-SENSITIVE FILM RECORD, HOT SPOTS, SHEAR	7	970
PARTICLE VELOCITY, NEW	8	447	HEATS OF FORMATION, AT 298 K, EXPLOSIVES	3	608
PBX 0501 EJECTA	7	883	CN, C <sub>2</sub> N <sub>2</sub> , C, N, O	2	240
PRESSURE, CARBON RESISTOR	5	47	MAXIMUM RATE OF BURN	2	683
GAUGE, QUARTZ, STUDY, UPSTREAM OF SHOCKED HE	5	435	HEATS OF FORMATION, RDX, TNT, ...	2	388

## B. Topic Phrase Index (Continued)

SUBJECT	SYN PAGE	SUBJECT	SYN PAGE
HELMHOLTZ FREE-ENERGY CALCULATION, HNS	6 751	HMX, SELF-PRESSURIZING BOMB EXPERIMENTS	7 172
HELMHOLTZ INSTABILITY, 2D, FLUIDS' INTERFACE	4 305	SHOCK IGNITION CHARACTERISTICS	7 463
HEMP MODEL, HE CHARGE INSIDE CU CYLINDER	4 520	SHOCK INITIATION, TESTS AND MODELS	8 892
HEMP, 2D ELASTIC-PLASTIC CODE, DIVERGING WAVE	5 477	SPECTROSCOPIC STUDY OF DETONATION	8 591
HENRY MODEL, GURNEY VELOCITY, HE CASING	7 834	STEADY-STATE BURN RATES	7 217
HERRMANN MODEL, COMPACTED POROUS MATERIAL	7 428	SURFACE MELTING CRYSTALS EFFECT ON BURN	5 311
PARAMETERS FOR 5 POROUS HES	6 772	TEMPERATURE, MEASURED AND CALCULATED	8 534
HETEROGENEOUS COMPOSITE HE (H.C.X.)	8 1011	THERMAL DECOMPOSITION AT P = 10-50 kbars	5 331
HETEROGENEOUS DETONATION WAVE PROPAGATION, 2D	6 405	THERMAL INITIATION AND GROWTH	5 280
HETEROGENEOUS HE REACTION ZONE, MODEL	7 641	TUNJSTEN-LOADED, X-0233, DETONATION TESTS	8 979
HETEROGENEOUS SHOCK-HEATING EFFECT	6 76	WEDGE TEST, SHEAR CAMERA RECORD	3 311
HEXATOL, HEXOTONAL, HEXOTOL IF DATA	6 513	X-RAY AND INFRARED STUDIES, BONDS	7 779
HMX/SEN WAX/BALLISTITE GENERATOR, DDT	7 157	HMX-BASED CUSTOMIZED EXPLOSIVES	7 566
HEXOTOL, BUBBLE ENERGY, UNDERWATER EXPANSION	6 546	HMX-BASED PPKs, EXPLOSIVE RESPONSE, AWRE TEST	8 1035
HEXOTONAL, BUBBLE ENERGY, UNDERWATER EXPANSION	6 546	HMX/AL/VITON, PERCHLORATES, CYLINDER TESTS	5 140
HIGH-DENSITY INCLUSIONS, SMALL THERMAL EFFECT	6 336	HMX/AP MIXTURES, COMPOSITE HE MODEL	7 517
HIGH-DENSITY POLYTHENE (HDPE) BINDER	7 34	NONIDEAL DETONATION	7 620
HIGH-ORDER DETONATION, ONSET & TRANSITION	3 517	HMX/BINDERS, EXPLOSIVENESS EFFECT, LABSET	8 1039
SURFACE DISCONTINUITY	3 520	EXPLOSIVENESS, LABSET	7 17
HIGH-OXYGEN HE, D vs INITIAL DENSITY	1 28	HMX/INERT, BEST FITS TO TAYLOR WAVES	6 633
HIGH-SPEED FRAMING CAMERA, IMPACT INITIATION	2 10	HMX/NC/CEP, ELECTRON BEAM INITIATION	7 53
HIGH-SPEED PARTICLE INITIATION, AZIDES	2 565	HMX/NG & HMX/TNT, LIGHT EMISSION TESTS	5 158
HIGH-TEMP DETONATOR STUDY, BTX IN SE-1	6 460	HMX/NYLON, ENERGY THRESHOLD, p-t PLOT	6 108
HIGH-TEMP EFFECTS, TIME TO EXPLOSION	3 60	HMX/PS, SENSITIVITY AND PERFORMANCE, SDDT	8 1132
HIGH-TEMP THERMODYNAMICS & GASEOUS DETONATION	2 231	HMX/POLYURETHANE, AWRE EOS METHOD	7 679
HIGH-VACUUM DETONATION, SPECIES SEPARATION	5 559	HMX/TATB, CHEMICAL DECOMPOSITION MODEL	7 56
HIGH-VELOCITY METAL JETS	8 318	HMX/TATB/BTF, TEMPERATURE, CYLINDER TEST DATA	8 1020
HMX, 3D HYDRODYNAMIC HOT-SPOT MODEL	8 44	HMX/TNT, DIVERGENT WAVES & RETONATION	4 426
BUBBLE ENERGY, UNDERWATER EXPANSION	6 546	POLYTROPIC GAMMA, ENERGIES, VELOCITY	5 462
CHEMICAL DECOMPOSITION MODEL	7 56	HMX/TNY/INERT, CJ POINT FROM VELOCITIES	4 56
CJ PROPERTIES, OXYGEN BALANCE	8 547	PLATE & CYLINDER DRIVER	4 23
CONFINEMENT INFLUENCE ON SENSITIVITY	7 966	HMX/Viton, RADIUS OF CURVATURE EFFECT	4 86
CONTENT, EFFECT ON EXPLOSIVENESS	8 1035	HMX/WAX, SURFACE COAT EFFECT ON SENSITIVITY	4 399
CONVECTIVE BURN AT HIGHER PRESSURES	3 77	HMX/ZnCl <sub>2</sub> , TEMP & CONC EFFECT ON SENSITIVITY	5 185
CONVERGING SPHERICAL DETONATION	7 603	HNB, HUGONIOT DATA	7 416
D(km/s), DENSITY	8 514	INITIATION BY ELECTRICALLY DRIVEN FLYER	8 1126
DDT MODEL, TIGER CODE	8 672	POLYMORPHIC FORMS (I,II), THRESHOLDS	8 1126
DDT PHENOMENA IN SMALL DIAMETERS	7 107	HNB, CJ PROPERTIES, OXYGEN BALANCE	8 547
DDT STUDY, PLASTIC TUBES	7 119	DETONATION VELOCITIES	8 538
DETONATION TEMPERATURE, PYROMETER	8 574	ISENTROPE BEHAVIOR, FLUORINE OXIDIZER	7 942
DOPPLER LASER INTERFEROMETER STUDY	8 135	POSTDETONATION PROPERTIES, CJ POINTS	7 647
EXPERIMENTAL & CALCULATED CJ PARAMETERS	6 713	HNS II, EOS & SHOCK INITIATION	6 740
HMX/Kel-F CYLINDER TEST RESULTS	4 5	HNS, CHEMICAL REACTION, SHOCK-INITIATED	8 15
HOT-SPOT INITIATION	7 398	CJ PROPERTIES, OXYGEN BALANCE	8 547
IGNITION DATA IN DDT	7 217	DDT STUDIES, SMALL DIAMETERS	7 107
IMPACT SENSITIVITY AND OS/100	3 674	DETONATION PROPERTIES, CARBON EOS	8 528
INTERSTITIAL GAS EFFECTS ON SENSITIVITY	5 247	ENHANCED TEMPERATURE AND PRESSURE	6 62
INTERSTITIAL GASES, SENSITIVITY	4 349	EOS & CHEMICAL KINETICS	6 748
JET PENETRATION MODEL	8 337	IMPACT SENSITIVITY AND OS/100	3 681
LAMINAR TO CONVECTIVE BURNING, DDT	7 164	I <sub>2</sub> COMP B, REDUCED THERMAL HAZARD	8 252
LASER IGNITION TEST	8 476	INITIATION THRESHOLD, HIGH T <sub>0</sub>	6 44
MECHANICAL PROPERTIES	8 637	LASER IGNITION TEST	8 476
PARAMAGNETIC DECOMPOSITION PRODUCTS	8 734	MECHANICAL PROPERTIES, DROP WEIGHT	8 642
PARTICLE SIZE DISTRIBUTIONS, MICROGRAPHS	8 1036	MICROSTRUCTURE EFFECT ON SENSITIVITY	8 26
PARTICLE SIZE, EFFECT ON EXPLOSIVENESS	8 1035	OPTICAL ABSORPTION	7 935
PERFORMANCE MODEL	7 517	SENSITIVITY	7 1024
PHYSICAL PROPERTIES	7 33	SENSITIVITY AND PERFORMANCE, SDDT MODEL	8 1132
POLYMORPHS, DIFFERING SENSITIVITY	3 665	SHOCK HUGONIOTS & INITIATION THRESHOLD	5 219
POROUS BED COMPACTION, STRAIN RATE	8 645	SPECTROSCOPIC STUDY OF DETONATION	8 691
POROUS, POP PLOT, MODEL vs TEST DATA	8 967	HOLLOW CHARGES, MULTIPROFILE STREAK TECHNIQUE	7 751
PRECURSORS IN DETONATION	7 877	HOLOGRAPHY, PULSED LASER, HMX IN DDT	7 165
QUASI-STATIC COMPACTION	8 645	HOM EOS, UNDERWATER SHOCKS, MACH STEM PRESSURE	6 570
RETARDED DETONATION, TRICKS (CHICANERY)	6 226	HOM-SG EOS, DECOMPOSITION ESTIMATE	6 25
HMX, RUBBER-BONDED SHEET EXPLOSIVE	4 496	HOMOGENEOUS DETONATIONS, 2D MODEL	6 405

## B. Topic Phrase Index (continued)

SUBJECT	SYN PAGE	SUBJECT	SYN PAGE
HOMOGENEOUS HE, TECHNIQUES TO ENSURE THEM	2 119	HULL EULERIAN CODE, COMPOSITE HE MODEL	7 517
HONDO/KRIER, COMBUSTION MODEL + DYNAMICS CODE	6 258	HV4, THERMAL INITIATION AND GROWTH	5 280
HOOK EFFECT, CORNER-TURNING PROPAGATION	7 625	HW4, GROWTH OF REACTION, SKID TEST	6 290
HOOK EFFECT, DARK ZONE, RAREFACTIONS	3 802	HW4, THERMAL INITIATION AND GROWTH	5 280
OBSERVATIONS, THEORY, RAREFACTIONS	3 786	HYDRAZINE MONONITRATE, DETONATION VELOCITY	1 8
HOPKINSON BAR, APPARATUS, STRAIN RATE DATA	8 635	REACTION TIME	1 56
SHOCK PRESSURE TEST	2 657	WAX-GAP TEST	1 23
HOT BOUNDARY OF 1D DETONATION WAVE ( $\Sigma$ )	4 82	HYDRAZINE NITRATE (HN), HIGH-VACUUM DETONATION	5 559
HOT PLATE AND HOT WIRE SENSITIVITY TESTS	5 280	HYDRAZOIC ACID, UNIMOLECULAR DECOMPOSITION	8 828
HOT SPOTS, CAVITY INITIATION	2 643	HYDROCODE RUBY, ALUMINIZED HMX, PERCHLORATES	5 141
COMP B, IN-BORE EXPLOSIONS	8 252	HYDROCODES, ZDE, HOT SPOTS, RAREFACTIONS	5 177
DDT, COMPACTION OF POROUS HE	8 881	HYDRODYNAMIC CODES, 1D & 2D, USED WITH TESTS	4 519
DECOMPOSITION AT LOW PRESSURE	6 29	HYDRODYNAMIC ELASTIC PLASTIC THEORY IN METALS	4 289
FORMATION MECHANISMS	6 69	HYDRODYNAMIC MOTION, ZDE SHELL CODE	5 487
FORMATION, EXPLOSIVE CRYSTALS	8 62	HYDRODYNAMIC SOLUTION, REFLECTED SHOCK, fs	3 264
GAS INCLUSIONS CAUSE OF	6 336	HYDRODYNAMICS, HIX 1DL MODEL, DURATION EFFECT	5 191
HIGH RATE DEFORMATION & SHOCKS	7 970	PHERMEX RADIOGRAPHY, RAREFACTION	4 642
INITIATION, MICROHARDNESS OF RDX	7 976	HYDROGEN INCREASES PERFORMANCE > CARBON	8 1003
INITIATION, VARYING PLANAR FIGURES	7 797	HYDROGEN PEROXIDE-GLYCEROL, LVD & HVD, GAP	4 412
INTERACTING SHOCK IN NM, MODEL	5 180	HYDROGEN-OXYGEN, DETONATION, SCHLIEREN PHOTO	2 284
LOW IMPACT & LOW AMPLITUDE	7 970	MIXTURES, STOICHIOMETRIC	2 258
MODEL, Al & VOID IN NM CYLINDER	4 394	HYDROSTATIC COMPRESSION OF HE, THEIR PRODUCTS	6 700
MODEL, CAVITY COLLAPSE	8 68	HYDROXYL-TERMINATED BUTADIENE (HTPB)	7 17
MODEL, EMP VELOCITY GAUGE DATA	8 190	HYPERVELOCITY IMPACT DATA, STEEL, Al, Pb	8 1153
MODEL, HETEROGENEOUS HE	7 394	HYPERVELOCITY WAVE PHENOMENA, CONDENSED HE	3 304
MODEL, INITIATES BULK REACTION	6 371	IDEAL AND NONIDEAL DETONATIONS	8 988
MODEL, REACTION CENTERS, PRESSED H	7 435	IDEAL GAS, ADIABATIC COMPRESSION, EQUATION	2 584
MODEL, REACTION SPOTS ORIGIN	8 678	IDEAL/NONIDEAL HE, WAVE SHAPE MEASUREMENT	2 500
MODEL, SHEAR BAND NUCLEATION	8 35	IGNITER COMPACTION OF INERTS	7 843
MODEL, SHOCK-COMPRESSED HE	7 523	IGNITERS, DDT EFFECTS IN PLASTIC TUBES	7 143
MODEL, THERMAL ENERGY, PORE COLLAP	8 26	IGNITION & GROWTH OF REACTION, SUMMARY	4 512
MODEL, TEMP DEPENDENT, 3 TERMS	8 951	IGNITION AND GROWTH MODEL, 2D LAGRANGIAN	7 488
MODEL, VOID COLLAPSE	7 506	DYNA2D	7 1035
MODEL, CHEMICAL, PRESSURE LOADING	8 926	POKOUS HE	7 234
SHOCK CAUSES THERMAL REACTIONS	3 518	PROPELLANT CRACKS	7 186
SHOCKS + DENSITY DISCONTINUITIES	6 405	TATB EOS	8 588
SIZE, CRITICAL, PROPAGATING NM	4 395	THREE TERMS	8 902
SLURRY HE UNDER IMPACT, MODEL	7 343	IGNITION BY RAPID COMPRESSION OF AIR	7 3
SURFACE BURNING IN POROUS SOLIDS	3 801	IGNITION STUDIES, MECHANICAL & CHEMICAL	4 477
THEORY, FIRST PROPOSED	3 842	IGNITION TESTS, RDX/TNT	8 255
THERMALLY DECOMPOSED INTERMEDIATES	8 725	THE LAB-SCALE SENSITIVITY TESTING	7 965
VOLUME FRACTION	6 372	IMAGE DISSECTION MULTIPLE-FRAME PHOTOGRAPHY	2 169
HOT-WIRE INITIATION OF PRIMARY EXPLOSIVES	5 339	IMAGE INTENSIFIER CAMERA, MULTIPLE EXPOSURE	6 664
HTPB/PDL BINDERS	7 17	IMPACT (PLATE) INITIATION, RDX/TNT MODEL	8 198
HUGONIOT, (THEORETICAL) OF METALS vs DATA	4 209	IMPACT HEIGHTS (50%) vs OB/100 VALUES	6 317
BRASS, PRESSURE vs $U_p$	3 567	IMPACT IGNITION MODEL	7 459
CONDENSED-PHASE EXPLOSIVES	4 241	IMPACT INITIATION, CRITICAL CONDITIONS	7 316
DATA, LEAST-SQUARE FITS	5 222	LOW-ORDER EXPLOSIVES	6 325
DETONATION & DEFLAGRATION BRANCHES	6 238	MILITARY EXPLOSIVES	2 612
ELASTIC LIMITS IN Al-Cu ALLOYS	6 151	IMPACT MACHINE, ERL, HIGH RATE DEFORMATION	7 970
EQUATION, DETONATION PRODUCTS	2 386	FRAMING-CAMERA STUDY	3 10
EXPERIMENTS, SDT, SMALL POWDER GUN	8 907	SENSITIVENESS TESTS	3 660
INSULBOARD	3 401	IMPACT ON HEAVILY CONFINED HE TARGETS	8 294
LAMELLAR Al-Cu COMPOSITES	6 155	IMPACT PHENOMENA, EXPLOSIVES & PROPELLANTS	6 336
LIQUID $N_2$ , $CO_2$ , $O_2$	7 649	IMPACT RESPONSE, CONFINED CHARGES	8 262
LOW PRESSURE, OF SOLID HE	4 239	FLAT & ROUND-NOSED vs CODE	7 325
POLYURETHANE FOAMS	6 492	FRAGMENT ATTACK	7 1048
SHOCK INITIATION THRESHOLD, $Pb(N_3)_2$	6 389	INSTRUMENTED SHOTGUN TESTS	7 299
STEAM	2 307	LOW-AMPLITUDE & LOW-IMPACT	7 970
UNREACTED EXPLOSIVES	5 251	MOLECULAR DYNAMICS STUDY	7 783
UNREACTED POROUS HIGH EXPLOSIVES	6 766	SMALL CYLINDERS, THRESHOLDS	7 273
UNREACTED, EOS, < 90 kbars	4 240	TWO MECHANISMS	8 1150
WITH TOO MUCH Al, ENVELOPES	1 114	IMPACT SENSITIVITY, & OB/100, 78 EXPLOSIVES	6 314
HUGONIOTS-RAYLEIGH LINE INTERSECTION, STEAM	2 298	CRITICAL AIR GAP	2 628

## B. Topic Phrase Index (Continued)

SUBJECT	SYM	PAGE	SUBJECT	SYM	PAGE
IMPACT SENSITIVITY, MACHINE, COLLIDING BALL	3	1	INTERMOLECULAR HE, EAK, WEDGE TESTS	8	1001
ORGANIC HE STRUCTURE	6	312	REACTION, EMP GAUGES	8	187
OXYGEN BALANCE	3	693	SMALL DIVERGENCE	8	176
TESTS, EA EUTECTICS	7	548	INTERSTITIAL GAS EFFECT, LOW-DENSITY COMPACTS	4	349
THERMAL EXPLOSION TIME	3	69	SENSITIVITY & TIMES	5	247
IMPACT WITH TRANSIENT CONFINEMENT	5	279	INTRAGRANULAR STRESS, COMPACTION OF INERTS	7	843
IMPACT, TANDEM AND AXISYMMETRIC, PROPELLANT	8	287	vs PLASTIC STRAIN RATE	8	643
IMPACT-FACE STRESS RECORDS	7	867	INVERSE METHOD, CJ PRESSURE,	5	75
IMPACT-LOADED VOID MODEL	7	783	INVERSE MULTISTREAK TECHNIQUE, WH SYMMETRY	7	751
IMPACTING SURFACES, ALIGNING & ADJUSTING	5	384	IODINE IN H <sub>2</sub> -O <sub>2</sub> , LIGHT ABSORPTION OF FRONT	2	217
IMPEDANCE EFFECTS ON DETONATION FAILURE	8	378	ION PROBE ASSEMBLY, DIAMETER EFFECT TESTS	4	97
IMPEDANCE MATCH DETERMINES PARTICLE VELOCITY	5	251	ION-EXCHANGED EXPLOSIVE (EIE), AXIAL FUSE	4	156
IMPEDANCE MATCHES, SHOCK WAVES	7	908	IONIZATION & PIEZOELECTRIC GAUGES	2	201
IMPEDANCE MATCHING PLATE & HE, REFLECTION = 0	1	91	IONIZATION IN SHOCK INITIATION	3	150
IMPEDANCE-MISMATCHED SYSTEMS	2	363	IR EMISSION, TEMPERATURE OF SHOCKED HE	7	993
IMPULSE & ENERGY FLUXES, CALCULATED	6	557	IRON, ELASTIC PRECURSOR & SHOCK WAVE PHOTOS	4	569
IN-BORE THERMAL EXPLOSIONS, COMP B	8	251	IRON-CONSTANTAN THERMOCOUPLES, NM TEMPERATURE	2	456
INCLUSION GEOMETRY EFFECTS ON INITIATION	4	386	ISENTROPE PRESSURE EFFECT ON CYLINDER TEST	4	7
INDUCTION PERIOD, GASEOUS DETONATION	1	49	ISENTROPES, X-0233, GAMMA LAW AND BKW	8	983
INDUCTION PERIODS, MEMORY EFFECT	3	42	ISENTROPIC COMPRESSION, PERPENDICULAR DRIVE	6	608
INDUCTION TIME DEPENDENCE ON SHOCK PRESSURE	3	487	ISENTROPIC EXPANSIONS	6	717
INDUCTION TIME $\tau$ vs THICKNESS OF INCLUSIONS	4	389	ISENTROPIC UNSTEADY 3DE FLOW, SURFACE, MODEL	4	78
INDUCTION ZONE IN TNT, VARIABLE DENSITIES	2	370	ISOBAR CROSS SECTIONS, TRIPLE WAVE	7	672
INERT ADDITIVES, EFFECT ON HE	5	464	ISOBARS, ISOTHERMS, ISOWS, NM CALCULATIONS	5	179
INERT BINDER EFFECTS ON CAST-CURED PBX	7	560	ISOMERIC CAST PRIMARY EXPLOSIVES, DDT STUDIES	6	231
INERT GAS EFFECT IN GAS REACTION ZONE	2	196	ISOPHORONE DI-ISOCYANATE (IPDI) BINDER	7	17
INERT SOLIDS, SHOCK WAVE RESEARCH ON	4	321	ISOTHERMAL COMPRESSION OF HE & THEIR PRODUCTS	6	700
INERT WITNESS FOAMS, LOW-DENSITY HE SYSTEMS	6	183	ISOTHERMS, GAS BUBBLES IN RADIUS-TIME PLANE	6	342
INERT-HE INTERFACE, DECOMPOSITION EFFECT	6	29	JACOBS EQUATIONS OF STATE	6	162
INFINITE CONFINEMENT FOR NM IN METAL TUBES	2	455	JACOBS-COMPERTHWAITTE-ZWISLER (JCZ) EOS	6	163
INFINITE CONFINEMENT IN 0.1-in. PYREX TUBES	2	439	JACOBS-ROBLUND FORMULA THRESHOLD VELOCITY	7	332
INFINITE DIAMETER DETONATION VELOCITY, C <sub>2</sub> H <sub>2</sub>	2	236	JCZ EOS, DETONATION PRODUCTS, TIGER CODE	6	162
TNT	3	327	SINGLE SPECIES FOR HYDROCODES	7	721
INFINITE DIAMETER VELOCITY, AI CONCENTRATION	6	124	JCZ3 EOS, FOR TIGER	6	166
INFINITE DIAMETER vs DENSITY, DEVIATIONS, TNT	3	345	POSTDETONATION BEHAVIOR MODEL	7	646
INFRARED RADIOMETRY, TIME-RESOLVED	7	993	QUATUOR MODEL	8	765
INFRARED SPECTRA, NM, HIGH-PRESSURE	5	331	JCZ3P EOS, DETONATION PROPERTIES OF CHNO HE	7	713
INFRARED-SENSITIVE PHOTOMULTIPLIER TUBE	5	339	JET INITIATION, CHARACTERISTICS, BARE HF	8	323
INITIABILITY TEST, HMX BY PBX 9404	8	1064	COMP B	7	352
INITIAL DECAY TIME CONSTANTS, UNDERWATER	6	556	CONICAL SHAPED CHARGES	8	1091
INITIATING POWER vs SENSITIVENESS, d	2	608	SOLID EXPLOSIVES	8	318
INITIATION, ADIABATIC CAVITY COMPRESSION	2	645	vs 2DE, FOREST FIRE MODELS	7	479
CENTERING DEVICE	8	336	JET PENETRATION OF HMX AND TATB, MODEL	8	337
CRITERIA, PARTICLE VELOCITY	6	71	JETTING INTERACTION OF DETONATING GRAINS	7	885
CRITERIA, PRESSURE vs PULSE LGNTH	7	429	JONES & EYRING THEORIES CONTRADICTED	2	451
DELAYED, OPAQUE RAREFACTION ZONE	3	468	JONES NOZZLE THEORY FOR UNCONFINED EXPLOSIVES	2	483
GRADIENTS IN METASTABLE COMPOUND	3	842	JONES' DETONATION THEORY	1	26
IGNITION & GROWTH SUMMARY	4	512	JONES' EOS FOR DETONATION GASES	1	76
IHE BY LOW-AMP COMPRESSION	6	115	JUMP CONDITIONS, BOUNDARY OF PISTON, REACTIVE	4	503
MOLECULAR CRYSTAL (MO)	8	870	FLOW VELOCITY IN SHOCK	1	54
POROUS PROPELLANT	8	293	JUMP DISTANCE, GAMMA, MEAN FREE PATH	4	194
TRANSIENT IN DILUTE EXPLOSIVES	7	448	JWL CALCULATION, HE PARAMETERS	8	947
INSENSITIVENESS vs OXYGEN BALANCE, CHNO HE	3	697	JWL EOS, COEFFICIENTS, INTERFEROMETER TEST	8	596
INSTABILITY OF INTERFACE, TWO FLUIDS	4	305	CYLINDER TEST DATA & ELA CODE	7	678
INTERACTING DETONATION WAVES IN CONDENSED HE	4	154	DETONATION PERFORMANCE IN HMX	8	914
INTERFACE CALCULATION, AI/HE, ACOUSTIC APPROX	4	524	PARAMETERS	8	909
INTERFACE EQUATION SOLUTION, GRAPHICAL MODEL	5	254	REACTION RATE PARAMETERS	7	488
INTERFACE INSTABILITIES, LAGRANGIAN MESH	4	316	vs DATA, 1D CALIBRATION, COMP B-3	5	8
INTERFACE VELOCITY HISTORIES	8	123	JWL ISENTROPE, P-V, THREE TERMS	8	598
INTERFEROGRAM OF REACTIVE MACH STEM IN GAS	4	71	K-W (KISTIAKOWSKY-WILSON) EOS	4	27
INTERFEROMETER DEVELOPMENT, DOPPLER SHIFT	6	673	K-W EOS, APPLICABILITY TO PRODUCT GASES	4	173
INTERFEROMETER QUADRATURE SIGNAL	8	468	CJ ISENTROPE, PENTOLITE SPHERES	4	27
INTERFEROMETRY, GAUGE RISE TIME IN PMMA	7	1063	KAMLET'S METHOD, EXPLOSIVE PERFORMANCE	7	952
INTERMOLECULAR HE, EA EUTECTIC TESTS	7	548	KANTROWITZ RELATION, SHOCK PATH EQUATION	2	301

## B. Topic Phrase Index (Continued)

SUBJECT	SYM	PAGE	SUBJECT	SYM	PAGE
KDNBF, MIE-GRUNEISEN EOS, ELECTRON BEAM HEAT	5	352	LATERAL SHOCK PRESSURE IN CYLINDRICAL CHARGE	4	92
KERR CELL CAMERA DEVELOPMENT	1	31	LATTICE DISSOCIATION, 2D SYSTEMS	7	781
KERR-CELL PHOTOS, NM TRANSVERSE-WAVE EFFECTS	6	415	LATTICE STRUCTURE, CJ PRODUCTS, HIGH DENSITY	2	405
KHT EOS, EQUILIBRIUM CALCULATION AT CJ STATE	8	997	LAUE BACK-REFLECTION PHOTO, RDX CRYSTAL	7	978
QUATUOR MODEL	8	764	LAX METHOD, DISCONTINUITIES IN 1D HYDROCODES	3	615
KIHARA-HIKITA EOS, REVISED (KHT)	8	548	UNSTEADY 1D FLOW	3	534
KINETIC LATTICE MODEL, HETEROGENEOUS HE	6	344	LAYZER'S SOLUTION, ACCELERATION, 2 FLUIDS	4	305
KINETIC PARAMETERS, N-NITRO, C-NITRO COMPOUNDS	6	318	LEAD AZIDE, B, LASER INITIATION	7	735
KINETICS OF DETONATION WITH SOLID REACTANT	1	107	CJ DEFLAGRATION MODEL, DDT STUDY	6	244
KIRKWOOD PROPAGATION THEORY, CJ CONDITIONS	1	107	CRYSTAL SIZE EFFECTS, SIZE EFFECT	2	561
KIRKWOOD THEORY, SHOCK WAVE PARAMETERS	1	8	DDT STUDY	1	60
KIRKWOOD-WOOD DISCUSSION, von NEUMANN'S MODEL	2	312	DECOMPOSITION REACTION	2	529
KISTIAKOWSKY'S THEORY OF INITIATION	1	57	DEFLAGRATION IN SINGLE CRYSTALS	5	301
KISTIAKOWSKY-WILSON (KW) EOS, PERFORMANCE	3	725	ELECTRIC FIELD INITIATION	6	390
KISTIAKOWSKY-WILSON EOS FOR COMP B, CYCLOTOL	3	721	ENVIRONMENTAL SHOCK TEST	3	24
KISTIAKOWSKY-WILSON EOS, MODEL OF SOLID HE	2	383	FAST BURNING, IMPACT MACHINE	3	10
KISTIAKOWSKY-WILSON EQUATION FOR PARAMETERS	1	30	HIGH-VACUUM DETONATION	5	561
KNOOP TESTING, PLASTIC ANISOTROPY, CRYSTAL	7	977	HOT-WIRE INITIATION	5	339
KOENEN TEST, SENSITIVITY & RISK EVALUATION	6	274	HUGONIOY & SHOCK INITIATION, GUN	6	389
KP/AL, DEFLAGRATION VELOCITY, ELEC PROBE	4	616	LINEAR MEMORY EFFECT	3	47
KRAKATOA MODEL, DELAYED DETONATION	8	135	PRECIPITATED W/ POLYVINYL ALCOHOL	2	711
KRAKATOA SHOCK INITIATION MODEL, 1D & 2D	8	892	LEAD OXIDE EFFECT IN RDX/TNT	5	465
KRIER/VAN TASSELL GUN COMBUSTION CODE, DDT	6	258	LEAD SPREAD ORIENTATION EFFECT IN TESTS	7	1065
KWB EOS FOR 50/50 TNT/AN	2	520	LEAD STYPHNATE, BURN RATE, SENSITIVENESS, Q	2	651
LABORATORY-SCALE EXPLOSIVENESS TEST (LABSET)	8	1035	DDT STUDY	1	60
LABSET SETUP, EXPLOSIVENESS TEST	8	1037	HOT-WIRE INITIATION	5	339
LAGRANGE 1D MODEL, GAS FLOW, COMPACTION,...	8	914	LASER INITIATION STUDY	8	710
LAGRANGE ANALYSIS TECHNIQUE, CHINESE	8	83	LEAST SQUARES METHOD, RATE STICK TESTS	2	131
LAGRANGE ANALYSIS, SHOCKED TATB	7	386	LENNARD-JONES PARAMETERS, CALCULATED VELOCITY	2	237
LAGRANGE FINITE DIFFERENCE METHOD, FLOW	4	317	LENNARD-JONES-DEVONSHIRE EOS, GAS & LIQUID	1	108
LAGRANGE GAUGE, EA-BASED EXPLOSIVE	8	111	LENNARD-JONES-DEVONSHIRE FREE-VOLUME EOS	2	389
IN SITU CASTING, FLOW MODEL	7	1072	LIAHOV EQUATION FOR SLURRY HE DENSITY	7	346
STUDIES, FLOW FIELDS	7	498	LIF EFFECT ON COMP B'S ACCELERATION OF METAL	6	510
LAGRANGE PARTICLES, PHASE TRAJECTORIES	8	201	LIF, MATERIAL PROPERTY VALUES	8	65
LAGRANGE SOUND VELOCITY	7	791	LIF-HE INTERFACE DETONATION PRODUCTS	8	133
LAGRANGIAN 1D FINITE DIFFERENCE CODE, WONDY	7	394	LIGHT EMISSION, COMPRESSED GAS AROUND CHARGE	3	203
LAGRANGIAN 2D MODEL, CYLINDER, LVD IMPACT	5	313	INITIATION OF LIQUID HE	5	153
LAGRANGIAN 2D UNSTEADY MODEL OF IMPACT	6	336	LIGHT INITIATION OF CRYSTALLINE AZIDES	2	547
LAGRANGIAN COORDINATES, POROUS HE MODEL	7	442	LIGHT INTENSITY AT CHARGE-PERSPEX INTERFACE	4	431
SLURRY HE MODEL	7	344	LIGHT PATTERNS IN POWDER & PLASTIC HE, PHOTOS	6	422
LAGRANGIAN MESH 2D CALCULATION, INSTABILITIES	4	316	LIGHT PIPE, DETECTORS OF HOT-WIRE INITIATION	5	340
LAGRANGIAN WAVE PROPAGATION MODELS, NM	7	609	LIGHT-GAS GUN EXPERIMENTAL SETUP	6	16
LAME'S CONSTANTS, ELASTIC STRAIN RATE	4	296	LIGHT-GAS GUN, MULTIPLE SHOCKS TO TNT	7	907
LAMELLAR COMPOSITE MATERIALS (AL-CU), SHOCKED	6	151	SUPRACOMPRESSION, TATB EOS	8	587
LAMINAR REACTIVE FLOW, CONFINED HE	7	958	LIGHT-SCATTERING PROCESSES, SCHEMATIC	7	1011
LAMINAR-CONVECTIVE BURN, POROUS, CRYSTALLINE	7	164	LINEAR BURN RATE, THEORY & CALCULATION	3	655
LARGE-CALIBER CHARGES, TNT, NQ, AN, AL	8	577	LINER DEFLECTION, SYMMETRIC, INTERFEROMETER	8	596
LARGE-SCALE GAP TEST, CORRELATING OTHER TESTS	7	880	LINER VELOCITY vs POLAR ANGLE, PINS IN SPHERES	6	524
CRITICAL DIAMETER, TNT	5	207	LINER VELOCITY, INTERFEROMETER DATA	8	597
MODEL, TEST SETUP	7	480	LIQUID HE, 36 NEW, CHARACTERIZATION STUDY	6	466
NSWC, PENTOLITE/PMMA	6	768	CAVITATION EFFECTS	7	373
NUMERICAL MODEL	5	477	DECOMPOSITION, THERMAL EXPLOSION	6	29
TATB & HMX MIXTURES	7	569	DETONATION, HOT SPOT MODEL	8	678
LASER BEAM FLUX CALCULATION	7	797	INITIATION & GROWTH OF DETONATION	3	436
LASER BEAM SHOCK IN SOLID DEUTERIUM	5	361	NM FAILURE PROCESS	2	462
LASER IGNITION TEST	8	473	SENSITIVENESS, m x Q	2	699
LASER INITIATION, INSENSITIVE HIGH EXPLOSIVE	6	612	SENSITIVENESS, Q, m	2	648
LEAD AZIDE CRYSTALS	7	735	LITHIUM NIOBATE PRESSURE TRANSDUCERS, AQUARIUM	7	1016
LASER INTERACTION, DAMAGE TO MATERIALS	6	613	LOGOSPHERE EXPLOSIVE DEVICE, SETUP	8	152
LASER INTERFEROMETRY, LINER DEFLECTION	8	596	LONG PRESSURE PULSES, 102mm GUN TESTS	8	11
LASER SPECKLE, TENSILE STRENGTH AND STRAIN	8	635	LOW DETONATION VELOCITY, HMX/AP/AL	7	620
LASER-INITIATED DECOMPOSITION, SPECTROGRAPHY	8	710	LOW-AMPLITUDE SHOCK INITIATION (LASI) TEST	7	285
LATERAL EXPANSION, PRANDTL-MEYER FLOW	6	602	LOW-AMPLITUDE SHOCKS, HOT SPOTS	7	973
LATERAL RAREFACTIONS, OBLIQUE IMPACT EFFECTS	5	578	LOW-DENSITY EXPLOSIVES, D, P, CJ CONDITIONS	5	47

### 3. Topic Phrase Index (Continued)

SUBJECT	SYM	PAGE	SUBJECT	SYM	PAGE
LOW-DENSITY HE SYSTEMS (<0.25 g/cm <sup>3</sup> )	6	183	MACH BRIDGE, WHITMAN'S METHOD MODIFIED	4	142
LOW-ENERGY LASER INITIATION, LEAD AZIDE	7	735	MACH BRIDGE, INTERACTING TWIN SPHERES IN WATER	5	585
LOW-IMPACT TESTS, HOT SPOTS GENERATED	7	971	MACH DETONATION WAVES	1	40
LOW-ORDER DECOMPOSITION (SYMPATHETIC DET)	3	520	MACH DETONATION WAVES, FORMATION CONDITIONS	4	135
LOW-ORDER DETONATION, CAVITATION, NG/EGDN	3	451	MACH INTERACTION, CRITICAL ANGLE	6	498
EARLY HISTORICAL WORK	3	786	TWO PLANE DETONATION WAVES	4	142
RAPID BURN, STEADY STATE	3	607	MACH PHENOMENA, CONTINUOUS OBSERVATION	8	431
TNT, PARTICLE SIZES	2	479	TWO INTERACTING WAVES	4	138
LOW-ORDER INITIATION, RETONATION, COMP B	3	833	MACH REFLECTION, AIR SHOCK AFTER IMPACT	8	1075
VELOCITY vs MASS	6	328	CONDENSED EXPLOSIVE	4	154
LOW-ORDER REACTIONS IN SHOCKED EXPLOSIVES	4	462	DETONATION WAVES	7	669
LOW-PRESSURE EFFECT IN DDT	7	143	DIAGRAMMATIC SKETCH	1	80
LOW-PRESSURE HUGONIOTS OF SOLID EXPLOSIVES	3	239	IRON	4	153
LOW-PRESSURE POINTS ON ISENTROPE OF HE	3	386	OBLIQUE FLOW ACROSS SHOCK	6	571
LOW-VELOCITY, 1D IMPACT ON SHOCKED SOLID HF	4	239	OF DETONATION WAVES	7	756
IMPACT INITIATION, ANVIL TEST	4	473	MACH STEM, IN WATER, PARAMETERS, DATA & MODEL	6	382
IMPACT, SUSAN TEST	4	477	ZERO & NONZERO GROWTH ANGLES	6	574
NONDETONATIVE EXPLOSION	7	248	MACROKINETICS EQUATIONS OF DECOMPOSITION	7	362
LUCITE, SHOCK VELOCITY vs SHOCK PRESSURE	3	372	MAGNESIUM, ELASTOPLASTIC RELEASE AT 30 kbar	4	290
LUMINOSEC, DETONATION FLAMES	2	571	MAGNETIC & ELECTRIC FIELDS IN DETONATION	3	844
RADIATION ENERGY, FOR DETONATION	1	15	MAGNETIC FLUX COMPRESSION GENERATOR SOURCE	7	746
LUMINOSEC-TIME CURVES, DETONATION TEMPERATURE	2	158	MAGNETIC PROBE DATA, PARTICLE VELOCITIES	7	534
LVD, (LOW VELOCITY DETONATION), CAVITATION	7	373	MAGNETIC PROBE MEASURE OF PARTICLE VELOCITIES	6	637
CONDENSED HE	6	344	MANGANIN GAUGE, MULTIPLY EMBEDDED	6	21
DDT STUDY	6	250	PRESSURE RECORDS, DIMPLE TEST	8	1085
GAS EFFECTS	2	582	RECORDS, LOW-ORDER DETONATION	6	330
HVD IN LIQUID HE, CARD GAP TEST	4	412	SETUP, LOW RESISTANCE	7	386
HVD IN UREA PERCHLORATE MIXTURES	6	450	SETUP, RECORDS	6	625
LIQUID HE, CAMERA	4	117	MANSOORI-CANFIELD-ROSS PROCEDURE, POLYATOMIC	7	648
METHYL NITRATE	5	267	MAPPING FAILURE WAVES IN LIQUID HE DETONATION	5	115
NG-EGDN, CAGED	5	81	MASS FRACTION CONTOURS, FROM 2DE MODEL	8	314
NITROMETHANE	7	575	PBX 9502, CORNER	8	59
NM, WINDOWS	4	126	MASS FRACTION PROFILES, X-0219 IN AIR, 2D	6	411
SCREENING TEST	6	470	MASS MOTION IN DETONATION PRODUCTS (ASM)	5	447
WALL EFFECTS	4	117	MASS POINTS IN HE, MARKED, X RAYS, ANALYSIS	5	3
WALL EFFECTS	4	126	MASS RATE OF COMBUSTION, SENSITIVENESS	2	643
WAVE STABILITY, TESTS	5	81	MASS SPECTROMETER, DETONATION PRODUCTS	8	701
WITNESS PLATES	6	473	MATRIX PROPERTIES, SHOCK SENSITIVITY	5	182
LX-04, -07 CYLINDER TEST RESULTS	4	5	McSKIMIN PHASE COMPARISON TECHNIQUE, TRANSIT	6	398
CURVATURE RADIUS EFFECTS	4	88	MECHANICAL PROPERTIES, EFFECT ON EXPLOSIVENESS	8	1037
LOW-VELOCITY IMPACT SENSITIVITY, PINCH	4	478	MEDIA, IMPACT SENSITIVITY AND OB/100	3	674
MEASURED DETONATION PRESSURE, AQUARIUM	5	65	MELAMINE, COMPACTION IN POROUS BEDS	7	843
THERMAL DECOMPOSITION OF CONFINED HE	6	214	MELT KETTLE DESIGN, HOMOGENEOUS HE CHARGES	2	121
UNDERWATER SHOCK-TO-BURN TESTS	4	489	MEMORY EFFECT, THERMAL INITIATION	3	42
LX-06, MEASURED DETONATION PRESSURE, AQUARIUM	5	65	MERCURY FULMINATE, BURN RATE, Q, m x Q	2	651
LX-07, CYLINDER TEST RESULTS, 2-in. DIAM	5	140	CONTACT FILM RECORD	3	10
EOS ABOVE CJ PRESSURE	8	587	DEFLAGRATION BEFORE DDT	1	58
MEASURED DETONATION PRESSURE, AQUARIUM	5	65	LASER INITIATION STUDY	8	710
LX-10, CYLINDER TEST RESULTS, 2-in. DIAM	5	140	MERCURY INTRUSION POROSIMETRY, TATS	8	3
MEASURED DETONATION PRESSURE, AQUARIUM	5	65	MESH-INITIATED DETONATOR, MFG AS SOURCE	7	746
THERMAL DECOMPOSITION OF CONFINED HE	6	214	METAL (Al) FOILS, ELECTRICALLY EXPLODED	6	553
LX-14, CJ ADIABATS, HUGONIOTS	8	504	METAL ACCELERATION BY CHEMICAL EXPLOSIVES	4	3
DYNAMIC HIGH-RESOLUTION TESTS	8	613	METAL ACCELERATION BY COMPOSITE HE	5	157
POSTDETONATION BEHAVIOR THEORY	8	501	METAL-SEMICONDUCTOR BLOCKING CONTACT, E LEVEL	6	391
LX-17, 2D IGNITION MODEL, CORNER TURNING	7	488	METALLURGICAL PROPERTIES, SHOCK PROPAGATION	4	295
CALCULATED & TEST PARTICLE VELOCITIES	7	1034	METHYL NITRATE & MIXTURES, DETONABILITY	5	267
EOS ABOVE CJ PRESSURE	8	587	METHYL NITRATE, BURN RATE, SENSITIVENESS, Q	2	651
TATS COMPOSITIONS, INITIATION STUDIES	8	1045	DILUENT EFFECT ON NM	7	583
M29 & M47 DETONATORS, VA LEAD AZIDE	2	712	METHYL NITRITE, SHOCK INITIATION, GAP TEST	5	237
M30 A1 BURN RATE	7	899	METHYL-5-NITRAZOLE (1-MNT)&(2-MNT), DDT STUDY	6	231
M30, CHEMICAL REACTION, FRACTURE RESULT	8	243	METHYLNITRAMINE, MOLECULAR GEOMETRY, AS INITIO	8	828
MA, LIQUID HE, CHARACTERIZATION	6	467	MF, LIQUID HE, CHARACTERIZATION	6	467
MACEK'S MODEL, MODIFIED, FOR DDT IN CAST HE	6	236	MFDNB, LIQUID HE, CHARACTERIZATION	6	467
MACH BRIDGE, CRITICAL ANGLE, SHOCK WAVES	6	489	MFF, LIQUID HE, CHARACTERIZATION	6	467

## B. Topic Phrase Index (Continued)

SUBJECT	SYM PAGE	SUBJECT	SYM PAGE
MICHELSON-REYLAIN LINE, P-V PLANE	7 791	MURNAGHAN EOS AND EXPONENT	7 503
MICROBALLOONS, EMULSION HE, PERFORMANCE	8 993	MURNAGHAN EOS, CONSTANTS FOR C-7, Al, Cu, Au	4 279
NG, INITIATION EFFECTS	3 460	NB POWDER, POLARIZATION & RELAXATION SIGNALS	6 145
MICROCRACKS IN CAST HE, BURN RATE EFFECT	7 904	NB-40, EXPERIMENTAL vs COMPUTED HUGONIOTS	6 772
MICROGRAPHS, SHEAR AND FRACTURE DAMAGE	8 297	NC, DETONATION CHARACTERISTICS	5 47
MICROHARDNESS STUDY, RDX, DEFORMING HOT SPOTS	7 976	EFFECT, CHEMICAL DECOMPOSITION	7 58
MICROSTRUCTURE EFFECT ON SENSITIVITY	8 26	MECHANICAL PROPERTIES, DROP WEIGHT	8 642
MICROWAVE INTERFEROMETER, WAVE FORM, TNT	3 147	NONDETONABILITY THRU TRANSITION, EXPLAINED	3 636
MICROWAVE INTERFEROMETRY TECHNIQUES	4 584	NC/NG DETONATION CHARACTERISTICS, LOW DENSITY	5 47
MICROWAVE INTERFEROMETRY TECHNIQUES	8 485	NF <sub>2</sub> CALORIMETRY STUDIES	7 940
MICROWAVE TECHNIQUE FOR DETONATION VELOCITIES	2 151	NG, BKW MODEL & PERFORMANCE DATA	3 728
MICROWAVE VELOCIMETER, HE-FILLED WAVEGUIDE	2 151	BUBBLE-FREE, LOW SENSITIVITY	3 455
MIE-GRUNEISEN EOS, DETONATION PRODUCTS	5 67	BURN RATE, SENSITIVENESS, Q, m x Q	2 651
HE & DETONATION PRODUCTS	7 362	CJ PROPERTIES, OXYGEN BALANCE	8 547
SHOCK LOADING Cu & U	5 554	DETONATION FLAME ANALYSIS	2 573
THEORY	4 205	HIGH- & LOW-VELOCITY DETONATION, AERATION	2 582
UNBURNED MATERIAL	5 196	LIGHT EMISSION IN INITIATION	5 153
MILITARY EXPLOSIVES, IMPACT INITIATION	2 612	POLARIZATION & RELAXATION	6 144
MINIMUM PRIMING CHARGE TEST, CORRELATIONS	7 888	RADIANCE, DETONATION TEMPERATURE	7 762
MINIMUM DETONATOR TEST FOR SENSITIVENESS	2 602	SENSITIVENESS, m x Q	2 699
MINIMUM PRIMING CHARGE TEST, ASSEMBLY	7 698	SENSITIVENESS, Q, m	2 648
MODEL	7 479	STREAK CAMERA RECORD, 5.2-DIAM CYLINDER	3 814
MODEL	8 954	TIME DELAY vs TEMP RECIPROCAL	3 68
PROPELLANTS	8 285	NG/EGDN, GAP TEST, CAMERA RECORD	3 440
MINIMUM SHOCK PRESSURE TO START REACTION	6 3	LOW-VELOCITY DETONATION	4 117
MINIMUM SHOCK-LOADED SURFACE AREA	7 316	LVD & HVD IN LIQUID HE, GAP TEST	4 412
MINOL, LOW-ORDER REACTIONS--REACTION ZONE	4 462	NG/EGDN/TA, SHOCK SENSITIVITY GAP TEST DATA	4 416
MINOL-2, CURVATURE EFFECT ON SHOCK WAVE	1 99	NIP MODEL, PLANE WAVE DRIVING PLATE, SPALL	4 538
MIXER CIRCUIT, CAPACITORS & RESISTORS, D	2 139	NITRAMINE DECOMPOSITION, EPR SPECTRA	8 734
MODEL OF 3D SPINNING DETONATION WAVE FRONT	4 74	NITRAMINE PROPELLANTS, GAS PHASES IN DDT	7 217
MOLECULAR DYNAMICS (MD), DIATOMIC XTALS	8 864	NITRAMINES & NITRAMIDES, SENSITIVITY TESTS	3 673
EXOTHERMIC XTALS	8 870	NITRAMINES, ELECTRONIC STRUCTURE	7 65
MOLECULAR DYNAMICS METHODS	7 777	IMPACT SENSITIVITY vs OB	3 696
MOLECULAR DYNAMICS METHODS	7 789	NITRATE ESTER (aq.), THRESHOLD V, BURN RATE	6 119
MOLECULAR DYNAMICS SIMULATIONS, N <sub>2</sub> & CO <sub>2</sub>	8 531	NITRIC ESTERS, ELECTRONIC STRUCTURES	7 65
MOLECULAR DYNAMICS, JCZ EOS	7 721	NITRIC OXIDE, CJ PROPERTIES, OXYGEN BALANCE	8 547
MOLECULAR INITIATION, BUCKINGHAM POTENTIAL	7 716	DETONATION CHARACTERISTICS	6 723
SECONDARY EXPLOSIVES	7 65	DETONATION PROPERTIES	8 422
MOLECULAR KINETICS, V & P DEPENDENCE	6 305	DETONATION VELOCITIES	8 538
MOLECULAR ORBITAL CALCULATIONS, AB INITIO, HE	8 827	POSTDETONATION PROPERTIES	7 647
MOLECULAR SUBIGNITION, UNDERWATER SHOCK	8 725	STATIC HIGH PRESSURE STUDY	8 715
MONEL BOMB WALLS, HF-PRODUCING HE	7 942	NITROALIPHATIC COMPOUNDS, SENSITIVITY vs OB	3 696
MONOMETHYLAMINE NITRATE (MMAN) SENSITIVITY	7 373	NITROALIPHATIC HE, HEATS OF DETONATION	6 320
MONOMODAL CAST PBX FORMULATIONS, RDX	8 903	THERMAL DECOMPOSITION	5 331
MONOMOLECULAR DECOMPOSITION	6 306	IMPACT SENSITIVITY & OB/100	7 87
MONOPROPELLANT, CARD GAP SENSITIVITY TEST	3 822	NITROAROMATIC COMPOUNDS, OB/100, SENSITIVITY	3 680
REACTION MODEL	7 517	NITROAROMATICS, ELECTRONIC STRUCTURE	7 65
MONTE CARLO AND THEORETICAL ISOTHERMS	8 523	NITROGEN, EQUIVALENT EQUATION	8 1011
MULTI-INITIATOR EXPLOSIVE INITIATION	7 671	ISOTHERMS AND HUGONIOT	8 534
MULTILAYERED SHIELDS, IMPEDANCE VARIATIONS	8 1143	TEST & CALCULATED HUGONIOT	8 551
MULTIPHASE DETONATION, FUEL-AIR	7 799	NITROHETEROCYCLES, AMMONIUM SALTS	7 801
MULTIPLE FLASH GAP, DETONATION PRESSURE	7 409	NITRONYL NITROXYL RADICAL, DECOMPOSITION	8 740
MULTIPLE LAGRANGE GAUGES, CONDENSED HE	7 1072	NITROSOL, DENSITY, SHOCK & PARTICLE VELOCITIES	4 245
TNT	6 786	NM & NM/TNM GAP TEST RESULTS, SENSITIVITY	4 417
MULTIPLE SHOCK CALCULATIONS FOR PBX 9404	8 1063	NM & NM/TNM, BKW MODEL & PERFORMANCE DATA	3 728
MULTIPLE-EXPOSURE IMAGE-INTENSIFIER CAMERA	6 464	NM, ZDE MODEL, FAILURE & SHOCK INITIATION	5 177
MULTIPLE-GAUGE STUDIES, IN SITU EMV SYSTEMS	7 1062	AQUARIUM TESTS, PHOTOS OF FAILURE WAVES	5 115
MULTIPROBE DETONATION BUILDUP TESTS	5 249	BRIGHTNESS TEMPERATURES	7 1000
MULTIPROFILE STREAK TECHNIQUE, WH SYMMETRY	7 751	BUBBLE ENERGY, UNDERWATER EXPANSION	6 546
MULTISTREAK CAMERA RECORD, SHAPED CHARGE	8 464	CAVITATION SENSITIVITY	7 373
MULTISTREAK TECHNIQUE, DETONATION FRONT	8 330	CJ PROPERTIES, OXYGEN BALANCE	8 547
MUNITIONS ACCIDENTS, ANALYSIS AND TESTS	8 211	CONDUCTIVITY PROFILES, C PRECIPITATION	4 500
MUNITIONS, PROPAGATING DETONATION MODEL	7 1055	CYLINDER TEST RESULTS	4 5
MUNROE JET, FORMATION & EQUILIBRIUM IN X RAY	4 644	NM, DARK WAVE STRUCTURE, CAMERA RECORDS	5 170

## B. Topic Phrase Index (Continued)

SUBJECT	SYM	PAGE	SUBJECT	SYM	PAGE
NM, DECOMPOSITION KINETICS	6	95	NONEQUILIBRIUM MOLECULAR DYNAMIC METHOD	8	680
DECOMPOSITION, KAMLET'S METHOD	6	96	NONIDEAL 1D DETONATION WAVES, MODEL	8	1025
DETONATION PRESSURE DATA	7	531	NONIDEAL BEHAVIOR, HMX/AP/AI PROPELLANT	7	620
DETONATION TEMPERATURE, PYROMETER	8	558	NONIDEAL DETONATION, ANFO MIXTURES	3	309
DETONATION TEMPERATURE, TEST SETUP	8	569	C.E.E. 2D MODEL	7	695
DETONATION VELOCITY MEASUREMENTS	5	41	EMULSION, MODEL	8	1069
DIAMETER-EFFECT PARAMETERS	6	647	KINETIC LATTICE MODEL	6	344
DILUENT EFFECT ON DETONATION	7	583	LATERAL EXPANSION	4	107
DINA, TNT, DITHEKITE, SHOCK INITIATION	3	469	NONLAMINAR FLOW EFFECTS IN GASES	4	70
EARLY RESEARCH	3	789	NONREACTIVE RAREFACTION FAN SOLUTION	8	1027
EOS CONSTANTS	7	619	NONSTATIONARY DETONATION WAVES IN GASES	1	45
EXPERIMENTAL & CALCULATED CJ PARAMETERS	5	713	NONSTEADY BEHAVIOR AND RATE, EOS MODEL	7	703
EXPERIMENTAL DETONATION VELOCITY DATA	5	74	NONSTEADY DETONATION, REVIEW	3	784
FAILURE DIAMETERS, INITIAL TEMPERATURES	5	102	NONSTEADY EFFECTS, LIQUIDS & SINGLE CRYSTALS	3	791
FAILURE WAVES, FOILS, TRANSIENT WAVES	3	791	NONSTEADY STATE DETONATION VELOCITY, MICROWAVE	2	151
FAILURE, RAREFACTION COOLING, 2D MODEL	6	405	NOVA MODEL, GUN INTERIOR BALLISTICS CODE	7	850
FREE-SURFACE VELOCITY DATA	7	537	NOZZLE CONCEPT, LONG CYLINDRICAL CHARGES	2	759
INTERNAL/EXTERNAL VELOCITY, CAMERA RECORD	3	473	NOZZLE THEORY (H. JONES), DIAMETER EFFECT	3	342
LIGHT EMISSION, EST. SHOCK TEMPERATURES	5	153	NOZZLE THEORY, 1D MODEL, SLURRY	8	168
LIGHT EMITTED FROM REACTION ZONE	4	604	REACTION RATE OF TNT/NaNO <sub>3</sub>	2	519
LIQUID DILUENTS EFFECT ON PROPAGATION	6	133	NO, 3D HYDRODYNAMIC HOT-SPOT MODEL	2	44
LVD & HVD IN LIQUID HE, CARD GAP TEST	4	412	BOND LENGTHS, CRYSTALLOGRAPHIC DATA	8	841
MIXTURES, PROPERTIES	7	584	CJ PROPERTIES, OXYGEN BALANCE	8	547
POLARIZATION & RELAXATION SIGNALS	6	144	DIRECT-CONTACT SENSITIVITY TEST	4	404
PREDICTED TIMES, REACTION ZONES, E,P,V	4	395	ELECTRON DENSITY DISTRIBUTION ANALYSIS	8	839
RADIANCE AND DETONATION TEMPERATURE	7	762	EUTECTIC COMPOSITE EXPLOSIVES	7	803
REACTION PATHWAYS IN SHOCK INITIATION	8	855	GAS PUCKETS IN LOW-VELOCITY DETONATION	2	584
SENSITIVITY CAVITATION EFFECT	7	374	RETARDED DETONATION, TRICKS (CHICANERY)	6	226
SHOCK COMPRESSION THROUGH INERT, DDT	3	813	SYMPATHETIC DETONATION OF AP	6	173
SHOCK INTERACTION WITH DISCONTINUITIES	4	386	NO/AP COMPOSITES, DETONATION PARAMETERS	6	178
SHOCK WAVE GROWTH MODES	6	47	NUCLEAR WEAPON SIMULATION WITH TNT TEST	8	418
STABLE LOW-VELOCITY DETONATION WAVE	7	575	NUMERICAL CODES, 1D & 2D, ALONG WITH TESTS	4	519
STRONG DETONATION WAVES	8	425	2D, UNSTEADY FLOW	4	527
TEMPERATURE & DIAMETER EFFECTS	2	454	O-NITROANISOLE, SHOCK-INDUCED ELECTRIC SIGNAL	5	387
TEMPERATURE BEHIND SHOCK, RAMAN SCATTERING	7	1010	OB/ICO, OXIDANTS IN SENSITIVITY RELATIONSHIPS	3	671
TEMPERATURE EFFECTS, GAP TEST	5	237	OBLIQUE DETONATION WAVES INTERACTING, IRON	4	153
THERMAL DECOMPOSITION AT P = 10-50 kbars	5	331	OBLIQUE IMPACT, LARGE CHARGES	5	296
THRESHOLD VELOCITY, BURN RATE	6	119	METAL PLATE ON EXPLOSIVE	4	381
TIME-RESOLVED EMISSION	7	953	OBLIQUE SHOCK, DETONATION WAVE PERPENDICULAR	6	602
UNIMOLECULAR DECOMPOSITION	8	828	INITIATION OF PELLETS	3	791
VELOCITY-DIAMETER RELATION, MODEL	7	589	OCTOL, CHEMICAL DECOMPOSITION MODEL	7	56
NM-CARBORUNDUM, INHOMOGENEOUS MIXTURE, EFFECTS	3	512	CYLINDER TEST RESULTS	4	5
NM-TNM MIXTURES, LOW & HIGH-VELOCITY WAVES	4	126	DENSITY, SHOCK & PARTICLE VELOCITIES	4	245
NM/ACETONE DETONATIONS, FINE STRUCTURE	7	958	DIAMETER-EFFECT PARAMETERS	6	647
NM/ACETONE MIXTURES, WALL TRACES OF DETONATION	5	105	JET TEMPERATURE, IR RADIOMETER	6	691
NM/ACETONE, TRIPLE-POINT TRAJECTORIES	5	126	LOW-ORDER EXPLOSIONS AFTER IMPACT	6	328
NM/PMMA/AI, CELLULAR STRUCTURE OF DETONATION	6	124	LOW-PRESSURE POINT ON ISENTROPE	3	389
NM/SiO <sub>2</sub> VELOCITY/DIAMETER RELATION, MODEL	7	589	NONDETONATIVE EXPLOSIVE	7	248
NM/TNM MIXTURES, DETONATION WAVE TEMPERATURES	7	768	PLEXIGLAS MONITOR, SHOCK VELOCITY	5	23
NO <sub>2</sub> , MOLECULAR EXCITATION ENERGIES	7	100	OCTOL-A, -B, THERMAL INITIATION & GROWTH	5	280
NOL GAP TEST, MODEL	8	233	GROWTH OF REACTION	6	290
NOL LARGE-SCALE CARD GAP TEST	7	265	ONE-DIMENSIONAL STEADY DETONATION WAVE MODEL	5	24
NOL LARGE-SCALE GAP TEST, MODIFIED (LASI)	7	285	ONE-DIMENSIONAL TIME TO EXPLOSION (ODTX) TEST	7	56
MODIFIED (MGT)	7	308	ONE-FLUID van der Waals MIXTURE MODEL	7	646
NOL SHOCK SENSITIVITY TEST, SHOCK PRESSURE	3	584	OPEN CAMERA DETONATION LIGHT RECORDS, NM	5	116
NOL SMALL-SCALE GAP TEST REPLACEMENT	7	924	OPTICAL FIBER/PHOTOCELL DDT TUBE	7	120
NONA, INITIATION THRESHOLD, HIGH T <sub>0</sub>	6	44	OPTICAL PROPERTIES OF DETONATION WAVES	5	513
SHOCK HUGONIOTS & INITIATION THRESHOLD	5	219	OPTICAL REGION, HOMOGENEOUS HE CYLINDERS	5	515
NONDETONATIVE EXPLOSIONS, CONFINED CHARGES	7	247	OPTICAL SYSTEM, VISAR/EMISSION MEASURED	8	17
H6 & PBXW-109	7	308	OPTICAL TECHNIQUE, DETONATION FRONT TEMP	7	759
VENTING EFFECT, MODEL	7	175	OPTICS, DETONATION WAVE GENERATORS	5	513
NONDIMENSIONAL PROFILES, NONIDEAL DETONATION	8	1029	MULTIFRAME MICROSCOPE PHOTOGRAPHY	2	172
NONEQUILIBRIUM FLOW, WAVE PROPAGATION	7	795	OPTO-ELECTRONIC PLASTIC OPTICAL FIBER	8	465
NONEQUILIBRIUM IN SHOCK COMPRESSION ZONE	7	789	ORVIS VELOCIMETER	7	1084

## B. Topic Phrase Index (Continued)

SUBJECT	SYM	PAGE	SUBJECT	SYM	PAGE
OSCILLOGRAMS, INERT-HE VELOCITY, u(t)	6	30	PBX 9404, 1D PRESSURE-SHEAR LOADING	8	274
OSCILLOGRAMS, SHOCK-INDUCED POLARIZATION	6	145	2D MODEL, INITIATION AND GROWTH	7	488
OSCILLOGRAPH vs LIGHT ABSORPTION, SHOCK FRONT	2	225	2DE MODEL, WAVE PROPAGATION, CORNERS	6	406
OSCILLOSCOPE RECORDS, DROP WEIGHT TEST OUTPUT	6	292	3-TERM IGNITION AND GROWTH MODEL	8	951
OSCILLOSCOPE TRACES, SHAPED-CHARGE TEMP	6	696	AQUARIUM TEST DATA, d = 7.2 cm	5	64
OTTO, LIQUID HE, CHARACTERIZATION	6	467	BARE & COVERED, SHOCKED	7	325
OVERDRIVEN AND MACH REFLECTION OF WAVES	7	796	CAMERA RECORD, IMPACT TO INITIATION	3	426
OVERDRIVEN DETONATIONS, SETUP FOR NM	8	425	CENTRAL DETONATION, AIR & WATER	6	528
OVERDRIVEN EXPLOSIVES, SHOCKED STATES	5	533	CHEMICAL DECOMPOSITION MODELS	7	56
OVERDRIVEN PRESSURE DECREASES TO CJ POINT	1	56	CJ ADIABATS, HUGONIOTS	8	503
OXIDANT BALANCE, OB/100, DECOMPOSITION	6	312	CYLINDER TEST RESULTS	4	5
IMPACT HEIGHT, SENSITIVITY	3	671	DAGMAR vs SHORT-SHOCK DATA	8	107
OXYGEN BALANCE, IMPACT SENSITIVITY	3	693	DETONATION CRITERION STUDY	6	78
OB EXPLOSIVE, PARTICLE SIZES	8	1011	DETONATION PRESSURE DATA	7	531
PLASMA, DETONATION VELOCITY	3	192	DETONATION THRESHOLD PARAMETERS	6	72
SOLID CARBON (C8 FOS)	8	809	DETONATION WAVE INTERACTIONS	7	669
OXYGEN RATIO EFFECT ON DETONATION FRONT	7	768	DIAMETER-EFFECT PARAMETERS	6	647
OXYGEN-BALANCED, -DEFICIENT CHMO EXPLOSIVES	6	548	DRIVER OF BERYLLIUM	6	602
P 2100 B, BALLISTIC CLASSIFICATION	6	626	ELECTRON BEAM INITIATION	7	53
P-V DIAGRAM FOR STEADY, 1D OZONE DETONATION	4	69	ELECTRON BEAM, INITIATION	7	50
PALLET FIRES, SINGLE AND MULTIPLE SHELLS	8	214	EOS ABOVE CJ PRESSURE	8	587
PARALLEL PROCES, CONDUCTIVITY, SPHF PLATES	3	156	EOS CONSTANTS	7	407
PARAMAGNETIC DECOMPOSITION PRODUCTS, SPECTRA	8	734	EOS FOR HOT AND COLD SOLIDS	8	38
PARAMETER EFFECTS, IDEAL DETONATION STATE	8	774	FLYER PLATE, CRITICAL SURFACE AREA	7	316
PARTIALLY REACTED HE, HUGONIOT STATES	8	943	GROWTH OF REACTION, SKID TEST	6	290
PARTICLE & GRADIENT WITH MOVING GRID	4	527	HEAT OF DETONATION Q, D, P <sub>0j</sub>	3	744
PARTICLE SIZE EFFECTS ON HOT-SPOT TEMPERATURE	5	220	HOT-SPOT INITIATION MODEL	7	394
PARTICLE SIZE EFFECTS, 1- & 2-COMPONENT HE	2	478	HUGONIOT CURVES & SOUND VELOCITY	4	235
ANFO	3	312	HUGONIOT DATA FOR UNREACTED HE	5	251
AP/HQ	6	175	IMPACT RESPONSE, MODEL & TESTS	7	273
COBALT AMINE AZIDES	3	50	INITIATION THRESHOLD, HIGH TEMP	6	44
CRITICAL DIAMETER	8	902	1°C PHOTO, LINE DETONATION, EBWs	6	666
DDT	7	107	LOW-ORDER EXPLOSIONS AFTER IMPACT	6	328
DDT	7	119	LOW-VELOCITY IMPACT SENSITIVITY	4	478
DDT	7	166	OBLIQUE SHOCKS, PERPENDICULAR DRIVE	6	602
DETONATION WAVES	8	1047	PARTICLE VELOCITIES, MAGNETIC PROBE	6	637
EA EUTECTIC	7	549	PHYSICAL PARAMETERS	7	593
NEGATIVE OB EXPLOSIVES	8	1011	PLEXIGLAS MONITOR, SHOCK VELOCITY	5	23
ON DETONATION VELOCITY	3	791	POLYTROPIC, JWJ, CONSTANT BETA EOSs	6	566
ON HMX/WAX	4	399	POP PLOT, 1D & 2D MODELS	8	59
ON SENSITIVITY, RDX	8	902	POP PLOTS, HIGHEST DENSITY MODEL	7	237
OXIDIZERS, PROPELLANTS	3	825	POSTDETONATION BEHAVIOR THEORY	8	501
PETN, RDX, & TETRYL	5	259	PRESSURE EFFECTS ON INITIATION	5	321
RUN TIME vs PRESSURE	3	515	PULSE DURATION SENSITIZING EFFECT	5	191
TATB INITIABILITY	8	1047	RADIUS OF CURVATURE EFFECTS	4	88
TETRYL, DDT STUDY	6	426	REE'S PREDICTION vs DATA	8	513
PARTICLE VELOCITIES, CAMERA RECORD, MEASURED	3	420	SHOCK DESENSITIZATION	8	1057
FREE-SURFACE, DIFFERENCE	6	637	SHOCK FRONT TEMPERATURE	7	1005
IMPACTED PMMA	5	592	SHOCK HUGONIOTS & INIT THRESHOLD	5	219
MAGNETIC PROBE	6	637	SHOCK WAVE GROWTH MODES, INITIATION	6	47
TEST & MODEL	7	1034	SHOCKED QUARTZ GAUGES, UPSTREAM	5	435
TNT, LAGRANGE GAUGE	6	787	SHOCKED, IR EMISSION MEASUREMENTS	7	993
vs DISTANCE, MODEL	6	355	SHOCKED, PRESSURES, MODEL AND TEST	8	931
vs TIME, ACCEPTOR HEs	5	484	SHORT-DURATION SHOCK INITIATION	4	373
PARTICLE VELOCITY, DISTANCE DIAGRAMS, DDT	6	239	SHORT-PULSE SHOCK INITIATION	7	859
EM GAUGE, IN SITU	7	1062	THERMAL INITIATION AND GROWTH	5	280
GAUGE SYSTEM, NEW	8	447	UNDERWATER SHOCK-TO-BURN TESTS	4	489
HISTORIES, HNS	8	19	VELOCITY-DIAMETER PREDICTION	7	589
STRESS CALC, GAUGES	5	427	VELOCITY-DIAMETER RELATION, MODEL	7	589
PATERSON EOS, LONG-RANGE MOLECULAR FORCES	3	722	WAVE SURFACE CURVATURE EFFECTS	6	379
PB-HMX-9404, OVERDRIVEN, SHOCKED STATES	5	533	WAVEFORMS, MICROWAVE RECORD	8	491
PBX 9010, PBX 9011 CYLINDER TEST RESULTS	4	5	PBX 9404/DURAL, FREE-SURFACE VELOCITY	7	536
PBX 9311, LOW-VELOCITY IMPACT SENSITIVITY	4	478	PBX 9407, EXPLODING-FOIL SHOCK SENSITIVITY	7	928
PBX 9205, UNDERWATER SPHERICAL EXPLOSIONS	5	599	PBX 9501, AQUARIUM TEST RECORDS	8	981

## B. Topic Phrase Index (Continued)

SUBJECT	SYM	PAGE	SUBJECT	SYM	PAGE
PBX 9501, COMPOSITION, DENSITIES	7	567	PETN, ADIABATIC ELASTIC MODULI, SINGLE CRYSTAL	6	396
DIAMETER-EFFECT PARAMETERS	6	647	BUBBLE ENERGY, UNDERWATER EXPANSION	6	546
GAUGE RECORD ANALYSIS, EJECTA	7	883	BURN RATE, SENSITIVENESS, $Q, m \times Q$	2	651
SUSTAINED-SHOCK HISTORIES	8	104	CALC & TEST DETONATION VELOCITIES, $P_{CJ}$	2	418
PBX 9502, COMPOSITION, DENSITIES	7	567	CALC vs TEST CJ PRESSURE & VELOCITIES	5	503
CONFINEMENT EFFECT ON FAILURE	8	372	CJ POINT, CJ ISENTROPE, ERROR %	7	709
CORNER-TURNING DATA	7	630	CJ PROPERTIES vs INITIAL DENSITY	8	553
DESENSITIZATION CALCULATIONS	8	47	CJ PROPERTIES, OXYGEN BALANCE	8	547
DETONATION PRESSURE DATA	7	531	CONTACT FILM, FRAMING-CAMERA STUDY	3	10
DETONATION REACTION ZONE STUDY	8	123	CONVECTIVE BURN AT HIGHER PRESSURES	3	77
ELECTRON BEAM INITIATION	7	52	CRITICAL LENGTH vs CRITICAL VELOCITY	4	432
TENSILE PROPERTIES	8	637	CYLINDER TEST RESULTS	4	5
TRIPLE SHOCK-WAVE INTERACTION	7	669	DDT STUDY, CONVECTIVE BURN, LVD	6	250
$U_{10}$ , MAGNETIC PROBE	7	538	DEFLAGRATION BEFORE DDT	1	60
PBX 9503, DETONATION REACTION ZONE STUDY	8	123	DETONATION FLAME ANALYSIS	2	572
PBX, BEHAVIOR DURING DROP WEIGHT IMPACT	8	635	DETONATION HEAT, DETONATION CALORIMETER	4	167
CAST-CURED, BEHAVIORAL MODEL	7	560	DETONATION PRODUCTS, REAL-TIME ANALYSIS	8	701
CAST-CURED, EFFECTS OF INERT BINDERS	7	560	DETONATION TEMPERATURE, PYROMETER	8	574
PBXN-5 SENSITIVITY CROSSOVER, PRESSURE	6	74	DETONATION VELOCITIES (30- $\mu$ m SIZE)	1	14
PBXW-109, BURNING & DETONATION, GAP TEST	7	308	DETONATION VELOCITY, ELECTRIC PROBE	4	616
PE4, SENSITIVITY AND EXPLOSIVENESS	8	265	DROP WEIGHT IMPACT TEST	8	641
PEAK PRESSURE, EFFECT, CRITICAL ENERGY	6	12	EOS CALCULATIONS AND TEST RESULTS	5	503
& PARTICLE VELOCITIES, Al & Cu	4	284	EXPERIMENTAL & CALCULATED CJ PARAMETERS	6	713
POSITIVE IMPULSE, SPHERES	6	533	EXPERIMENTAL vs COMPUTED HUGONIOTS	6	773
TRANSMITTED BY FOAMS	4	273	EXPLODING-FOIL SHOCK SENSITIVITY	7	928
PENTANEX, BUBBLE ENERGY, UNDERWATER EXPANSION	6	546	EXPLOSIVE-ETCHED CU MESH INITIATOR	7	746
PENTOLITE, ARTIFICIAL VISCOSITY CALCULATION	5	597	FOAMED, LOW DENSITY, CHARACTERISTICS	5	47
CASE EFFECT ON AIRBLAST	6	777	FREEZE-OUT TEMPERATURE	4	167
CONDUCTING ZONE, ELECTRICAL EFFECT	3	120	HEAT OF DETONATION, CONFINED/UNCONFINED	3	750
DEFLAGRATION WAVES, ODT STUDY	6	241	HIGH-DENSITY SHOCK INITIATION	6	20
DENSITY & VELOCITIES	4	245	HIGH-VACUUM DETONATION	5	559
DENSITY, D, CD, EXPERIMENTAL P	3	377	IMPACT-FACE PRESSURE, POROSITY MODEL	7	443
DETONATION VELOCITIES	1	14	IN METHANE, LOW-VELOCITY DETONATION	2	585
EMF GENERATED BY CONDUCTION ZONE	3	114	INITIATION THRESHOLD, HIGH $T_0$	6	44
GROWTH TO DETONATION, INTERFEROMETER	4	584	INTERSTITIAL GASES, SENSITIVITY	4	349
HIGH-DENSITY GAS, ELECTRODE, X RAY	3	136	ISOTHERMAL LINEAR & VOLUME COMPRESSION	6	700
HIGH-VACUUM DETONATION	5	561	JCZ STATE, MOLECULAR PARAMETERS	7	721
INERT MONITOR, SHOCK VELOCITY	5	23	LASER AND SHOCK INITIATION	7	797
INITIATION BY AIR SHOCK, DELAY TIME	3	790	LASER IGNITION TEST	8	476
LATERAL SHOCK PRESSURE TESTS	4	95	LINEAR MEMORY EFFECT	3	47
MEASURED DETONATION PRESSURE	5	65	LINEAR SURFACE REGRESSION TO 500°C	4	461
SHOCKED SYMPATHETIC DETONATION	3	521	LOW-VELOCITY DETONATION, CONFINED	7	575
SHOCKED, THERMAL FILM RECORD	7	974	MIE-GRUNEISEN EOS, PULSED ELECTRON BEAM	5	351
SLURRY, CONTACT FILM RECORD	3	18	MOLECULAR ELECTRONIC STRUCTURE	7	65
SPHERICAL EXPLOSIONS IN WATER	6	570	PARTICLE SIZE EFFECTS, SMALL-SCALE GAP	5	259
SPHERICAL SHOCKS IN WATER, INITIATE	3	790	PHYSICAL PROPERTIES	7	33
UNDERWATER SHOCK-TO-BURN TESTS	4	489	POLYMERS ADDED, DROP-WEIGHT IMPACT	7	25
UNDERWATER SHOCK-WAVE PERFORMANCE	4	27	POP PLOTS OF HIGHEST DENSITY	7	237
vs PBX 9404 SHOCK WAVE DATA, MODEL	6	528	PRECURSORS IN DETONATIONS	7	877
WAVE CURVATURE vs CHARGE LENGTH	2	506	PRESSURE PROFILES, POP PLOTS	6	22
WAX-GAP TEST	1	23	RECEPTORS IN GAP TESTS	7	279
PERCUS YEVICK (PY) EOS, QUATUOR CODE	8	764	RETARDED DETONATION, TRICKS (CHICANERY)	6	226
PERFECT GAS, SHOCK POLARS, DEFLECTION ANGLE	5	129	RUBBER-BONDED SHEET EXPLOSIVE	4	496
PERFLUORINATED ALKYLAMINES, SYNTHESIS	7	941	SHOCK HUGONIOT	3	570
PERFORMANCE PARAMETERS, EASIER PREDICTION	7	952	SHOCK HUGONIOTS & INITIATION THRESHOLDS	5	219
PERFORMANCE TESTS, PLATE DENT, BURN	8	353	SHOCK WAVE INITIATION MODEL	6	371
PERIPHERAL DETONATION, WAVEGUIDE DESIGN	1	31	SHOCKED, PRESSURE vs DISTANCE DATA	5	225
PERPENDICULAR EXPLOSIVE DRIVE, OBLIQUE SHOCKS	6	602	SIMULATIONS IN HOT-SPOT MODEL	7	506
PERSPEX MOUSETRAPS, SHOCK TO DETONATION	8	447	SINGLE-CRYSTAL TESTS, PROPERTIES	2	470
PERSPEX TUBES, BURN VELOCITY MEASUREMENTS	3	83	SPECTROSCOPIC STUDY OF DETONATION	8	691
PERTURBATION METHODS IN DETONATION PHYSICS	6	352	SPRAYED ON COPPER MESH ON MYLAR	7	746
PERTURBATION ON INNER SURFACE OF SHELL, 2DL	4	316	SURROUNDING EXPLODING WIRE INITIATOR	1	12
PETN, 2D SIMULATION OF CHNO CHAIN	7	784	TEMPERATURE, MEASURED AND CALCULATED	8	558
3D HYDRODYNAMIC HOT-SPOT MODEL	8	44	PETN, THERMAL DECOMPOSITION, $P = 10-50$ kbars	5	331

B. Topic Phrase Index (Continued)

SUBJECT	SYM	PAGE	SUBJECT	SYM	PAGE
PETN, THERMAL INITIATION & GROWTH	5	280	PLANE LATERAL DRIVING TESTS	8	625
THERMODYNAMIC PROPERTIES, 293 K, 0 GPa	6	704	PLANE SHOCK INITIATION, DILUTE HE	7	448
TIME DELAY vs TEMP RECIPROCAL, DECOMP	3	67	PLANE SHOCK RESPONSE, CRITICAL ACCELERATION	6	387
TNT REACTION ZONE LENGTHS	2	755	PLANE SPALLING OF COPPER, 1D CALCULATIONS	5	567
WEDGE-BRASS INTERFACE, 1 g/cm <sup>3</sup>	3	562	PLANE vs DIVERGING DETONATION WAVES	8	143
PETN-POLYURETHANE, DETONATION PROPERTIES	7	530	PLANE WAVE GENERATOR SETUP, X RAY, PHERMEX	5	4
PETN/BENZOYL PEROXIDE DECOMPOSITION	7	27	PLANE WAVE GENERATORS, MACH PHENOMENA	8	431
PETN/NaCl, AIR SHOCKS IN AIR GAP	8	1072	PLANE WAVE SHEAR CAMERA RECORD, AP	4	365
PETN/POLYURETHANE, DIVERGING DETONATIONS	7	408	PLANE WAVE, HEAT RELEASE, FLOW DERIVATIVES	8	148
PETN/TNT, POLYTROPIC GAMMA, ENERGIES, VELOCITY	5	462	PLASMA IN PROPANE, CO <sub>2</sub> , Ne, & IN VACUUM	3	202
PETRIN ACRYLATE PROPELLANT, SENSITIVITY	3	830	PLASMAS, DILUTE, DETONATION GENERATED, FACTORS	3	184
PHASE CHANGE WITHIN SHOCK WAVE	3	358	PLASTIC DEFORMATION, CRYSTALLINE SOLIDS	8	62
PHASE DIAGRAMS, P-T, CARBON	8	528	MECHANISM	7	241
PHASE SHIFT vs SEAL THICKNESS, TRANSIT TIME	6	399	METALS	1	37
PHASE TRANSFORMATION OF HNAS, DSC MEASUREMENT	8	1129	PLASTIC FLOW CONDITIONS OF METALS	1	33
PHASE TRANSITIONS, SHOCKED; Bi, Fe, QUARTZ	4	248	PLASTIC PROPELLANTS, GAP SENSITIVENESS	2	653
TYPES & BOUNDARIES	4	249	PLASTIC WORK vs PROJECTILE VELOCITY, DIAMETER	6	332
PHASE VELOCITY OF PROPAGATION DEFINED	4	258	PLASTISOL, CARD GAP SENSITIVITY, PROPELLANTS	3	825
PERMEX APPLICATIONS, DETONATION & SHOCK WAVES	4	639	PLASTISOL-NITROCELLULOSE PROPELLANTS	4	99
PERMEX MACHINE, NEW, FLOW BEHIND WAVE, FRONT	5	3	PLASTISOL-NITROCELLULOSE PROPELLANTS	4	103
PERMEX RADIOGRAPHIC FACILITY, HE STUDY	6	409	PLATE & CYLINDER MOTION, ELA MODEL	4	14
PHONON-DRAG EFFECT, THERMOELECTRIC	4	636	PLATE ACCELERATION IN HE-METAL SANDWICH	7	811
PHOTOCCELL MONITOR, LIGHT EMITTED BY IMPACT	6	682	PLATE DENT DEPTH vs DETONATION VELOCITY	2	753
PHOTOCHEMICAL INITIATION OF SILVER AZIDE	2	547	PLATE DENT PHOTOS, BTX & PETN ON DURAL	6	463
PHOTOELASTIC SUBSTANCES, TRANSIENT STRESSES	1	31	PLATE DENT RESULTS, AREA BEHIND REACTION ZONE	2	749
PHOTOGRAPHY, HIGH-RESOLUTION, WAVE EFFECTS	6	414	PLATE DENT TEST, (SMALL-SCALE) SETUP	3	745
PHOTOLYSIS & THERMOLYSIS OF METAL AZIDES	3	843	EA EUTECTIC & OTHERS	7	549
PHOTOLYSIS OF BARIUM & POTASSIUM AZIDES	2	530	HMX/AP/AL PROPELLANT	7	622
PHOTOMULTIPLIER & OSCILLOSCOPE, REACTION ZONE	4	602	PLATE IMPACT TEST, PRESSURE PROFILES	3	246
PHOTOMULTIPLIER DETECTOR, DENSITY CHANGES	2	192	PLATE IMPACT, CASE FAILURE, NO IGNITION	7	1048
LIQUID HE	7	759	PLATE TRAJECTORY, NEGATIVE PRESSURE REGIONS	4	544
PHOTOSENSITIZATION OF HE ACCEPTORS	7	938	PLATE-PUSH TEST, DISK SHOT FROM MORTAR	3	780
PHYSICAL SYNTHESIS, AN COMPOSITE HE	6	439	PLEXIGLAS, SHOCK COMPRESSION DATA	4	225
PIC (PARTICLE-IN-CELL) METHOD, HYDRODYNAMICS	5	177	PMMA, COMPRESSION BY LOW-AMPLITUDE SHOCK WAVE	4	214
VISCOSITY ADDED	4	528	ENHANCED EXPLOSIVE EFFECT ON IMPACT	7	308
PICRAMIDE, RADICALS IN DECOMPOSITION PRODUCTS	8	742	HUGONIOT FOR PLEXIGLAS vs AP	4	363
PICRIC ACID, CALC & TEST DET VELOCITIES	2	418	HUGONIOTS, PETN EOS TESTS	5	507
CURVATURE EFFECTS ON SHOCK WAVE	1	99	PARTICLE VELOCITY, EMV GAUGE STUDIES	5	414
IMPACT SENSITIVITY, OB/100	3	681	PHYSICAL PROPERTIES	7	33
MECHANICAL PROPERTIES	8	642	PHYSICAL PROPERTIES, SHOCK HUGONIOT	4	326
SENSITIVENESS OF PRESSED CHARGES	2	643	PROPAGATION SPEED OF RELEASE WAVES	5	589
SENSITIVITY AND OXYGEN BALANCE	3	700	SHOCK WAVE COMPRESSION, 3-20 kbars	4	222
PICRYLAZOLES, ELECTRONIC STRUCTURE	7	66	SURFACE-VELOCITY TESTS: FOIL TECHNIQUE	4	215
PIEZOELECTRIC PRESSURE GAUGES, CASING EFFECT	6	777	U <sub>0</sub> , INITIATING PBX 9404, 2DL MODEL	5	322
PIEZORESISTIVE GAUGES, GAP TESTS	7	280	POINT EXPLOSION SELF-SIMILAR PROBLEM	6	594
PIKE EQUATION, AIR-MATCH POINT ABOVE ADIABAT	4	53	POLAR (LIBBAJOUS) PLOT, PUSH/PULL VISAR	8	470
PIN ARRAY, DETONATION FRONT VELOCITY, SPHERES	6	522	POLAR ANGLE vs FRONT & LINER VELOCITIES	6	521
PIN METHOD, MEASURING DETONATION VELOCITY	2	136	POLAR INITIATION, COMP B ON AL SPHERES	6	521
VELOCITY DETERMINATION, TOA	2	440	POLARIZATION OF HOMOGENEOUS HE, SHOCK INDUCED	6	143
PIN SIGNAL RECORD, CONDUCTIVITY, TOA SIGNALS	3	139	POLARIZATION SIGNALS, DETONATION INDUCED	5	429
PIN SWITCH CONSTRUCTION, DETONATION VELOCITY	2	140	LIQUID DIELECTRICS	5	399
PIN TECHNIQUES, MEASURING PARTICLE VELOCITY	1	107	POLARIZATION TEST SETUP, DIELECTRICS	5	308
PIN-CONTACTOR TECHNIQUE, SHOCKED SOLID HE	4	373	POLARIZATION, SHOCK INDUCED IN SOLID HE	5	429
PIPE BOMBS, VARYING IGNITION METHODS	7	248	POLYCARBONATE (PC), BINDER EFFECTS, PROPERTIES	7	25
PISTON IMPACT, LOW VELOCITY, DELAYED DET	7	256	POLYESTER, PHYSICAL EFFECTS	7	25
POROUS ENERGETIC MATERIALS	8	882	POLYETHYLENE, SHOCK-INDUCED ELECTRICAL SIGNAL	5	387
PISTON IN FLUID, HEAT FROM CHEMICAL REACTION	4	502	POLYMER EFFECT ON DROP-WEIGHT RESULTS	7	24
PISTON VELOCITY, FLOW AFTER IMPACT, GAMMA = 3	3	205	POLYINITROALIPHATIC EXPLOSIVES, SENSITIVITY	3	672
INERT AGAINST HE SLAB	3	534	SENSITIVITY	6	312
PLANAR 1D EXPLOSIVE-METAL MODEL, CJ STATES	4	538	POLYINITROAROMATIC COMPOUNDS, SENSITIVITY	3	680
PLANAR IMPACT GUN TEST, SHOCK PROFILE DETECTOR	5	369	POLYINITROSTILBENES, SENSITIVITY AND OB/100	3	684
PLANAR SHOCK INITIATION, SOLID HE	3	499	POLYPROPYLENE BINDER, PHYSICAL PROPERTIES	7	33
PLANE DETONATIONS vs CYLINDRICAL, SPHERICAL	5	41	POLYSULFONE BINDER, PHYSICAL PROPERTIES	7	25
PLANE ELASTIC PRECURSOR DECAY MODEL, CRACKS	4	267	POLYSULFONE COATING, DECREASED SENSITIVITY	8	257

## B. Topic Phrase Index (Continued)

SUBJECT	SYM	PAGE	SUBJECT	SYM	PAGE
POLYTROPIC EOS, CHANGES, SHOCK PULSE IN WATER	6	561	PRESSURE EFFECT, INITIATING, NM & TNT, IN NG	5	156
SHOCK MOTION OF A LINER	3	275	LOW-VELOCITY DETONATION	2	585
POLYTROPIC GAMMA FROM $[\rho_0 D^2 / P_0] - 1$	5	56	MOLECULAR DECOMPOSITION	8	835
POP PLOT, COMP B, PBX 9404, TATB	7	487	OCTOL, HOT WIRE, HOT PLATE	5	283
EAKs vs COMP B, TETRYL, TNT, PBXs	8	1008	PRESSURE ENTERING RECEPTOR, MODEL	4	555
LOW-DENSITY TATB	7	386	PRESSURE EVOLUTION, TRANSIENT ZONE	8	143
PETN, HIGH DENSITY	7	237	PRESSURE GAUGE (SHOCK), CARBON RESISTOR	5	47
SHOCK INITIATION BEHAVIOR	8	945	PRESSURE GRADIENTS ACROSS WAVE FRONT	2	514
SHOCK WAVE & INITIATION DATA	4	237	PRESSURE HISTORIES, SHOCKED METALS, WAVE FORMS	4	271
XDT, THREE MODELS, PBX 9404	8	932	PRESSURE MEASUREMENT BY MANGANIN WIRE GAUGE	6	625
PORE COLLAPSE AND COMPRESSION MODEL	7	523	PRESSURE PEAK & TIME BEHIND THE SHOCK, DECAY	3	795
PORE COLLAPSE FROM SHOCK LOADING	8	26	PRESSURE PROBE RECORD, NOL GAP TEST	3	590
PORE SURFACE HEATING BY VISCOUS FLOW	7	435	PRESSURE PROFILE, DETONATING SOLID EXPLOSIVE	3	241
POROSITY EFFECT, LOW-DENSITY CHARGES, ANDREEV	3	794	DETONATION WAVE vs AL PLATE	2	372
PRESSED HE, BURN RATE	7	904	DETONATION WAVE, NM	6	138
STRONG SHOCKS, EOS (CALC)	3	396	DETONATION WAVE, P vs x	2	327
POROSITY vs IGNITION ENERGY, HUGONIOT CURVE	4	181	FOR REACTION ZONES, SOLID HE	2	345
POROSITY-DEPENDENT SHEAR MODULUS	7	201	REACTION ZONE IN AL PLATE	4	525
POROUS BED BURNING, DDT MODEL	7	234	PRESSURE PULSES, x-t PLOT	6	106
POROUS BED COMPACTION, HMX STRAIN RATE	8	654	PRESSURE RATIOS AT CRIT CAL BETA, CALCULATED	6	578
INERT MATERIALS	7	843	PRESSURE RISE IN CONFINED CHARGES	6	211
POROUS BED MATERIALS, TMO, AVE. PARTICLE SIZE	8	883	PRESSURE SIGNATURES, CALCULATED, UNDERWATER	6	556
POROUS BEDS OF HE, COMPRESSIVE REACTION	8	881	PRESSURE SPECTROSCOPIC STUDIES, NO	8	716
POROUS CHARGE, DETONATING PRECURSORS	7	877	PRESSURE TRANSDUCER, SULFUR, CALIBRATION	3	241
HMX REGRESSION RATES	7	173	PRESSURE vs EULERIAN POSITION $\theta$ , TIME $\tau$	3	551
SHOCK-INDUCED HEATING	7	523	PRESSURE vs EXCESS TRANSIT TIME, SOLID HE	4	237
POROUS SOLID, SHOCK PROPAGATION	4	258	PRESSURE vs $P_0$ , OVERDRIVEN COMP B	4	51
POROUS, NONREACTIVE MATERIALS, RESPONSE	6	766	PRESSURE vs PARTICLE VELOCITY, ISENTROPE	3	387
POSTPEAK IGNITION (PPI) TRACES, GAP TEST	7	916	PRESSURE vs PULSE LENGTH, INITIATION CRITERIA	7	429
POTASSIUM PICRATE, BURN RATE, SENSITIVENESS	2	651	PRESSURE vs TIME, ACCEPTOR HEs	5	485
POTENTIAL ENERGY SURFACES, BOND SCISSION	8	827	PRESSURE, 293 K vs RELATIVE VOLUMES NaCl, NaF	6	702
POWDER MORPHOLOGY EFFECT, HNS	7	938	DETONATION, SHOCK, IMPACT, AQUARIUM	3	357
POWDER TRAIN TIME-DELAY ELEMENT	1	32	VICINAL, FAR FROM BUBBLE	6	120
PRANDTL-MEYER EXPANSION, "SIMPLE" WAVE FLOW	3	578	PRESSURE-DISTANCE CURVES: $q$ , LAX, ANALYTIC	3	619
PRANDTL-MEYER FAN, EXPLOSIVE EDGE CALCULATION	4	16	PRESSURE-PARTICLE VELOCITY DATA, HMX-1	5	528
PRANDTL-MEYER FLOW BEHIND DETONATION WAVE	3	787	PRESSURE-PARTICLE VELOCITY FITS, HMX/TNT	4	61
PRANDTL-MEYER SINGULARITY, STEADY DETONATION	6	356	PRESSURE-SHEAR LOADING (1D) OF PBX 9404	8	274
PRECOMPRESSING CHARGES, QUENCHING AIR SHOCK	3	798	PRESSURE-TIME PROFILES, INHOMOGENEITIES	6	341
PRECOMPRESSION EFFECTS, FLYERS	7	938	LOW-ORDER INITIATION	6	325
LIQUID & SOLID HE	5	67	PRESSURE-VELOCITY SLOPES, PHASE TRANSITIONS	4	256
TNT & COMP B	7	3	PRESSURE-WAVE REFLECTION EFFECT ON BURN	7	186
PRECURSOR AIR SHOCK, PISTON EFFECT OF HE	8	1069	PRESSURE-WAVE VELOCITY IN MAPLE	1	31
PRECURSOR WAVE DETECTOR, STREAK CAMERA, PRISM	4	573	PRESSURIZED HE, MEASURED DETONATION VELOCITIES	5	73
PRECURSOR WAVE, FLUID & AIR CAVITATION EFFECT	4	117	PRESTRESSING SHOCK, METAL-HE INTERFACE	4	383
WATER-CONTROL TESTS	5	81	PRIMACORD, DETONATION VELOCITIES	1	14
PRECURSOR, DETONATING POROUS HE	7	877	EXPLODING-WIRE INITIATORS	1	9
SHOCK DEFENSITIZATION	7	352	LATERAL SHOCK PRESSURE TESTS	4	95
PREDETONATION COLUMN LENGTH (PCL)	7	107	PRESSURE-TIME PROFILES	3	317
PREDETONATION COLUMN LENGTH, COMPACTION EFFECT	6	433	PRIMAKOF SIMILARITY SOLUTION, SHOCKED INERT	4	510
PREDETONATION TRANSIENT WAVES	7	248	PRIMERS, INITIATING POWER, NUMERICAL QUANTITY	2	602
PREDICTING PERFORMANCE PARAMETERS, SIMPLIFIED	7	952	PRISM TEST, CONFINEMENT EFFECT ON FAILURE	8	372
PREHEATING EFFECT ON DETONATING LEAD AZIDE	2	569	PROBE, COAXIAL, OPTICAL AND ELECTRICAL	8	89
PRESHOCKED PBX 9404 AND COMP B-3	8	1057	CONDUCTIVITY, EFFECTS & SUITABILITY	2	443
PRESHOCKING SOLID HE TO MAKE IT INSENSITIVE	3	785	SHAPE CHANGES, MODEL & TESTS	4	597
PRESSING $\mu$ , VACUUM MOLDING CHARGES	2	123	PROBIT TESTS, CARD GAP TESTS	7	265
PRESSURE & DENSITY IN SHOCKED SOLIDS, MODEL	4	555	PROFILE STREAK TECHNIQUE, WAVE PROFILES	8	330
PRESSURE AT IMPACT vs TEMPERATURE, PBX 9404	7	1007	PROGRESSIVE DECONSOLIDATION MODE, DDT	7	168
PRESSURE CONTOURS, SHOCKED LX-17, MODEL	7	491	PROJECTILE ATTACK TEST, SENSITIVENESS TESTING	3	660
PRESSURE DEFLAGRATION RATE, CLOSED VESSEL	6	195	PROJECTILE IMPACT, MODEL	7	175
PRESSURE DEFLECTION CURVES, FLOW DIAGRAMS	4	382	MODEL	7	325
PRESSURE DEPENDENCE ON LOADING DENSITY	6	714	MODEL	7	343
PRESSURE EFFECT, BONDS, REACTION, MODEL	7	93	SENSITIVITY, AMMUNITION	6	682
ELECTRONIC STRUCTURE	8	827	TESTS	7	316
PRESSURE EFFECT, HE DECOMPOSITION	5	331	PROJECTILE IMPACT, TESTS, RDX PARTICLE SIZE	8	907

B. Topic Phrase Index (Continued)

SUBJECT	SYN	PAGE	SUBJECT	SYN	PAGE
PROJECTILE VELOCITY, THREE LASER BEAMS	7	300	RADIOGRAPHY, PHERMEX, RAREFACTION WAVES	4	642
BARRIER LENGTH	4	433	RADIOMETER, 2-COLOR IR, SHAPED CHARGES TEMPS	6	691
PROJECTILE-IMPACT SHOCK INITIATION MODEL	8	307	RADIUS-OF-CURVATURE EFFECT ON DET VELOCITY	4	86
PROPAGATING DEFLAGRATION, CONFINEMENT EFFECT	6	204	RADIUS-TIME HISTORY, CU CYLINDERS, COMP B	4	4
PROPAGATING DETONATION FRONT IN TATS	6	762	RAMAN MEASUREMENTS, REACTION ZONE LENGTH	8	691
PROPAGATING DETONATION MODEL, MUNITIONS	7	1055	RAMAN SCATTERING TEMPERATURE, SHOCK WAVE	7	1010
PROPAGATING DETONATION THRESHOLD	5	207	RAMAN SPECTRA, PETN AND HMX, SINGLE PULSES	8	696
PROPAGATING FAST REACTION, LEAD AZIDE CRYSTALS	5	301	SHOCKED RDX, PETN XTALS	8	847
PROPAGATING SHOCK & DETONATION WAVES	4	79	SOLID NITRIC OXIDE	8	719
PROPAGATION RATE, IMPACT MACHINE, PHOTOGRAPHS	3	10	RAMAN SPECTROSCOPY, EXPERIMENTAL SETUP	7	1013
TNT, AIR GAP EFFECT	8	409	RAMP WAVE RISE TIME EFFECT ON RUN-UP DISTANCE	8	970
PROPAGATION TEST vs GAP TEST RESULTS	2	656	RAMP WAVES, PBX 9404	7	394
PROPAGATION THEORY, KIRKWOOD/BRINKLEY	1	107	RAMP-INDUCED COMPRESSION, PROPELLANT INIT	8	962
PROPANE ISOMERS, FAILURE DIAM & SENSITIVITY	5	89	RANDOM CHOICE METHOD, DETONATION SIMULATION	7	799
PROPANE, DETONATION VELOCITY MEASUREMENTS	5	44	RANKINE-HUGONIOT CONDITION, DISCONTINUITIES	2	317
PROPANE-IMPREGNATED HE, DETONATION TEMPS	2	166	PRESSURE MODEL	6	604
PROPELLANT, ACCELERATION SIMULATOR	7	915	VECTOR IN EOS.	2	426
BURN, REFLECTION & RECIRCULATION	7	186	RANKINE-HUGONIOT CURVE IN MIXED PHASE	4	252
CAMERA & X RAYS, SHOTGUN FACILITY	7	302	RANKINE-HUGONIOT EQUATIONS, 1D STEADY STATE	3	305
D & E, PROPERTIES	8	285	P, V FLUID	2	219
DELAYED DETONATION IN GRANULAR	7	256	PRECOMPRESSION	5	68
DIAMETER EFFECT, REACTION ZONE	4	97	REFLECTED SHOCK	3	215
DUAL THRESHOLDS IN GAP TEST	7	267	SHOCK COMPRESSION	4	207
EXPLOSIVENESS, RARDE BURNING TUBE	7	1040	RARDE BURNING TUBE-TEST, LOW EXPLOSIVES	8	211
FAILURE DIAMETER PREDICTION	4	102	RARDE SMALL-SCALE BOOSTER COOK-OFF TEST SETUP	8	1107
GAP SENSITIVENESS	2	653	RARDE SMALL-SCALE BURNING-TUBE TEST	8	262
HIGH-VELOCITY IMPACT RESPONSE	8	284	RARDE SMALL-SCALE FUEL-FIRE TEST	8	211
LARGE-SCALE INITIATION STUDY	7	887	RAREFACTION EFFECT ON MACH BRIDGE	4	144
NONIDEAL DETONATION, HMX/AP/AL	7	620	RAREFACTION WAVES IN EXPLOSIVE PRODUCTS, X RAY	5	14
POROUS BED DDT STUDY vs MODEL	6	258	RAREFACTION WAVES RESTRICTING ACCELERATION	3	579
SENSITIVITY, CARD GAP TEST	3	822	RAREFACTION-OVERTAKE MODEL vs INITIATION DATA	7	431
SHOCKED & DESENSITIZED, HOT SPOTS	3	796	RAREFACTIONS FROM METAL-HE INTERFACE, AL	2	379
TEMP IS RATE-DETERMINING FACTOR	2	741	RASTER CHRONOGRAPH, DETONATION VELOCITY	2	137
PROPYL NITRATE, THRESHOLD VELOCITY, BURN RATE	6	119	RATE OF EXPANSION & $\tau$ FOR PEAK STRESSES	4	492
PTFE INSULATOR, MANGANIN GAUGE, PRESSURE	6	626	RATE PARAMETERS, CRITICAL DIAMETER & VELOCITY	7	589
PULSE DURATION EFFECT, COMP B, B-3, PBX 9404	5	191	RATE STICK, ASSEMBLY, JOINTS EFFECTS	6	642
PYRIDINE, EFFECTS ON DDT, AMMONIUM PERCHLORATE	7	153	ANALYZED BY DIFFERENCE METHOD	3	334
PYROMETER, DETONATION PRODUCT TEMPERATURE	8	567	COMP B, PARTICLE SIZE EFFECTS	2	480
FOUR-COLOR	8	558	FAILURE RADII, 2D MODEL	7	488
FOUR-COLOR, BRIGHTNESS IN NM-TNM	7	768	PLATE DENT, UNCONFINED AM COMP	7	806
TWO-COLOR OPTICAL FIBER	8	567	PRODUCTION	2	120
P <sup>2</sup> -T DETONATION CRITERION, DERIVATION	8	1119	PROPELLANT, NONIDEAL BEHAVIOR	7	620
Q METHOD, CALCULATION, UNDERWATER FLOW	4	33	RATES OF REACTION, ESTIMATES, IR EMISSION	7	993
MODEL, CONFINED DEFLAGRATION	3	606	RAYL DEFINITION, SHOCK IMPEDANCE OF ACCEPTOR	2	633
Q-SWITCHED LASER PULSE INITIATION	6	612	RAYLEIGH LINE-HUGONIOT, STEAM CONDENSATION	2	298
QUARTZ GAUGE, FRONT-BACK SETUP, PETN	6	21	RDX, AXIAL FUSE INITIATION vs NORMAL BOOSTER	4	156
RECORDS, HNAB HUGONIOT	7	419	SKW MODEL AND PERFORMANCE DATA	3	728
SANDIA, CONSTRUCTION & TESTING	5	369	BURN RATE, SENSITIVENESS, Q, m x Q	2	651
TECHNIQUE FOR IMPACT TESTS	5	369	CALC & TEST DETONATION VELOCITIES	2	418
THICK, SHOCKED PMMA, RECORDS	4	222	CHEMICAL DECOMPOSITION MODEL	7	56
UPSTREAM OF SHOCKED HE	5	435	CJ POINT, THEORETICAL EOS MODEL	7	716
QUARTZ, ELASTIC PRECURSOR & SHOCK WAVE PHOTOS	4	569	CJ PRESSURE vs INITIAL DENSITY	8	519
QUASI-SONIC DISCONTINUITY, CJ DETONATION	7	635	CJ PROPERTIES, OXYGEN BALANCE	8	547
QUASI-STATIC COMPACTION OF INERTS	7	843	CONTACT FILM, FAST-BURNING MODE	3	13
QUASI-STATIC STRESS-STRAIN CURVES: AL, STEEL	4	298	CONVECTIVE BURN AT HIGHER PRESSURES	3	77
QUATUOR CODE, DETONATION THERMOCHEMISTRY	8	762	CRYSTAL GROWTH AND MORPHOLOGY	7	977
RADIAL VELOCITIES, COLLAPSING CAVITIES	8	78	CURVATURE EFFECT ON SHOCK WAVE	1	99
RADIANCE SIGNALS, HE-LOADED COPPER PLATES	6	693	D (km/s), DENSITY	8	514
RADIANCES, NG, NM, DEGM, EN, 2-NE	7	764	DDT PHENOMENA, VERY SMALL DIAMETERS	7	107
RADIATION EFFECT ON PROPELLANTS	1	32	DDT STUDY, "RETONATION" WAVE	5	231
RADIATION MEASUREMENTS IN REACTION ZONE	4	602	DENSITY, CD, D, EXPERIMENTAL PRESSURE	3	376
RADIATION SIGNAL DURING DETONATION	2	144	DIAMETER EFFECT, REACTION ZONE THICKNESS	4	97
RADIATIVE vs HOT-GAS IGNITION	8	481	DURAL, U <sub>9</sub>	2	336
RADIOGRAPHS, DETONATION ZONE	4	162	RDX, ELECTRICAL INITIATION	2	88

## B. Topic Phrase Index (Continued)

SUBJECT	SYM	PAGE	SUBJECT	SYM	PAGE
RDX, ELECTRON PARAMAGNETIC RESONANCE	7	75	RDX/TNT, LASI GAP TEST	7	291
ENERGY THRESHOLD, p-t PLOT	6	106	LIGHT EMITTED FROM REACTION ZONE	4	604
EXPERIMENTAL vs COMPUTED HUGONIOTS	6	773	LOW-ORDER REACTIONS--REACTION ZONE	4	462
EXPLODING-FOIL SHOCK SENSITIVITY	7	928	POLYSULFONE-COATING, IGNITION	8	253
HIGH-VACUUM DETONATION	5	559	POLYTROPIC EXPONENT GAMMA, ENERGIES	5	459
HOT-SPOT TEMPERATURES, MODEL	7	524	SENSITIVITY AND EXPLOSIVENESS	8	265
IMPACT SENSITIVITY & OXYGEN BALANCE	3	699	SHOCK WAVE TO DETONATION TRANSITION	3	574
IMPACT SENSITIVITY AND OB/100	3	674	SIMULATED ACCIDENT	8	211
INITIATION THRESHOLD, HIGH TO	6	44	RDX/TNT/AL/WAX, ELECTRON BEAM INITIATION	7	50
INITIATION, PHOTOMULTIPLIER RECORDS	3	109	RDX/TNT/AN, CYLINDER TESTS vs BKW EOS (TIGER)	6	439
INTERMEDIATE RADICAL, ACTIVATION ENERGY	7	75	RDX/TNT/WAX (COMP B), SHAPED CHARGE	7	352
JCZ STATE, MOLECULAR PARAMETERS	7	721	RDX/WAX, DDT, POROUS BED, MECHANICS/CHEMISTRY	8	972
KINETIC PARAMETERS	7	75	RUNUP DISTANCE AND GAP TEST	7	336
LASER IGNITION TEST	8	476	STEEL CONFINEMENT, DDT STUDIES	7	139
LIGHT EMISSION DURING INITIATION	5	158	RDX/WAX/C, DETONATING CENTERING DEVICE	8	332
LINEAR SURFACE REGRESSION TO 500°C	4	461	REACTANTS, PRODUCT & DETONATION PARAMETERS	8	1005
MECHANICAL PROPERTIES, DROP WEIGHT	8	642	REACTION BUILDUP IN SHOCKED POROUS EXPLOSIVES	8	926
MICROHARDNESS, DEFORMATION, HOT SPOTS	7	976	REACTION CENTERS, HOT SPOTS	7	435
MIE-GRUNEISEN EOS, ELECTRON BEAM HEATING	5	352	REACTION CHEMISTRY, NITRIC OXIDE	8	715
MOLECULAR ELECTRONIC STRUCTURE	7	65	REACTION COMMUNICATION DISTANCE	6	47
MOLECULAR GEOMETRY, BOND LENGTHS, AB INIT	8	831	REACTION GROWTH OR DECAY, LOW-AMP SHOCKS	7	970
PARAMAGNETIC DECOMPOSITION PRODUCTS	8	734	REACTION PHASES: GRANULAR, BINDER, GASEOUS	7	396
PARTICLE SIZE EFFECT, CAST PBX	8	902	REACTION RATE ACCURACY, LAGRANGE ANAL, GAUGE	7	466
PARTICLE SIZE EFFECT, SMALL-SCALE GAP	5	259	REACTION RATE LAW, NITROMETHANE MODELING	7	611
PARTICLE SIZES, RATE STICK VELOCITIES	2	131	REACTION RATE THEORIES, D vs d, 3 EXTANT	2	519
PRESSURE AND HEAT RISE EFFECTS, MODEL	7	523	REACTION RATES, ELECTROMAGNETIC GAUGES	8	99
REACTION PRODUCTS, THEORETICAL EOS	7	716	EM GAUGE DATA	8	83
RETARDED DETONATION, TRICKS (CHICANERY)	6	226	LAGRANGE & IN SITU GAUGES	7	466
RUBBER-BONDED SHEET EXPLOSIVE	4	496	NOZZLE, CURVED FRONT, D HEAD	2	522
SENSITIVITY WITH AMMONIUM NITRATE	7	804	REACTION ZONE, CAST TNT	2	376
SENSITIVITY, GAS COMPRESSION	7	7	CONDENSED HE, PMT & SCOPE	4	602
SHOCK HUGONIOTS & INITIATION THRESHOLD	5	219	DETONATION HEAD OF HIGH-P GAS	2	749
SINGLE-CRYSTAL TESTS, PROPERTIES	2	470	EFFECT, STEADY AXIAL WAVE	7	661
SOLID, IN MODIFIED GAP TEST	7	310	ESTIMATE FROM SURFACE VELOCITY	1	92
SPECTRA, UNDER SHOCK AND AT REST	7	73	H <sub>2</sub> -O <sub>2</sub> & ACETYLENE-O <sub>2</sub> MIXTURES	2	193
STEEL-CONFINED, DDT STUDIES	7	139	HETEROGENEOUS EXPLOSIVES	7	641
STRUCTURE AND PROPERTIES	7	546	LENGTH	3	327
TEMPERATURE, MEASURED AND CALCULATED	8	558	LENGTH, & CJ PRESSURE MEASURED	2	343
THERMAL DECOMPOSITION < MELTING POINT	7	75	LENGTH, & TEMPERATURE VARIANCE	1	53
THERMAL INITIATION AND GROWTH	5	280	LENGTH, CURVED WAVE FRONT, D	1	96
TUNGSTEN FLYER, CONVERGENT FLOW	7	826	LENGTH, EFFECT ON CURVATURE	2	509
V-d CURVES, WAVE SHAPE vs d, KINETICS	2	733	LENGTH, TATB FORMULATIONS	6	652
VOLUME DISPLACED BY DROP-IMPACTED SAMPLE	3	8	LENGTH, TATB, FRONT CURVATURE	6	642
WAVE CURVATURE vs CHARGE LENGTH	2	506	LENGTH, TATB, HMX, WAVE CURVATURE	8	159
WEDGE TEST WITH SHEAR CAMERA RESULTS	3	504	LENGTH, CD & CURVATURE RADIUS	2	424
X-RAY AND INFRARED STUDIES, BONDS	7	779	PARAMETERS, ANALYSIS & MODEL	7	362
XTALS, FINE & COARSE, PHOTOMICROGRAPHS	8	904	PRESSURE = CJ PRESSURE	3	396
RDX-LOADED EBW INITIATION	4	452	PREVENTING CJ PRESSURE DATA	4	526
RDX/AL, DEFLAGRATION VELOCITY, ELECTRIC PROBE	4	616	PROFILES IN DETONATING HE	7	1029
ELECTRIC SPARK INITIATION TESTS	3	706	SEPARATION--WAVE FRONT, EFFECT	6	414
RDX/AL/PBX, SENSITIVITY & PERFORMANCE, SDDT	8	1132	STRUCTURE, NONIDEAL IN GAS	4	107
RDX/AN/MAN, CYLINDER TESTS vs BKW EOS (TIGER)	6	439	THICKNESS CALCULATION	4	96
RDX/AP PROPELLANT, INPUT PARAMETERS	6	350	THICKNESS DATA, CURVATURE TEST	4	90
RDX/BORON, V vs d, REACTION KINETICS	2	733	WIDTH, PREDICTED FOR NM	4	395
RDX/HTPB BINDER, DIVERGING DETONATIONS	7	400	REACTIVE CASES, AIRBLAST EFFECT FROM HE	8	207
RDX/POLYBUTADIENE, CX-84 EXPLOSIVE	8	361	REACTIVE EULERIAN HYDRODYNAMIC CODE, 3DE	7	649
FRENCH EXPLOSIVE	7	316	REACTIVE EXPLOSION MODEL	8	209
RDX/TNETB, DESENSITIZATION WITH WAX, OB/100	3	688	REACTIVE FLOW, LAGRANGE ANALYSIS (RFLA)	7	466
RDX/TNT, ADDITIVES, BURNING AND IGNITABILITY	8	251	MATHEMATICAL ANALOG	7	448
AL OR LIF ADMIXTURES, EFFECTS	6	510	REACTIVE HEAT FLOW MODELS, HMX, TATB, RDX, TNT	7	56
CRYSTAL STRUCTURE, SENSITIVENESS	3	666	REACTIVE HYDRODYNAMIC (2D) CALCULATIONS	6	405
INITIATION, PRESSURE VARIATION	8	143	REACTIVE MULTIPHASE MIXTURES	8	501
KINETIC PARAMETERS	7	75	REACTIVE SHOCK WAVES, MODEL	8	943
RDX/TNT, KINETICS OF SIMULATED INITIATION	8	196	REE'S PBX-9404 MODEL vs DATA	8	513

## B. Topic Phrase Index (Continued)

SUBJECT	SYN PAGE	SUBJECT	SYN PAGE
REFLECTED SHOCK, PRESSURES & ANGLES, CALC	5 587	SABOT, AI, FRAGMENT-CAUSED VULNERABILITY	7 326
RAREFACTION, X-T PLOT	4 540	SAFETY CERTIFICATE TESTING, SENSITIVENESS	3 459
TATS STUDY AND MODEL	8 138	SANDWICH RESISTANCE WIRE WALL PROBE, TRACE, DDT	4 618
REFLECTED WAVE VELOCITY vs PARTICLE VELOCITY	2 377	SAP, IDL SPHERICALLY SYMMETRIC BURN CODE	5 487
REFLECTED WAVES IN OVERDRIVEN COMP B	4 49	SAPPHIRE FLYER, SHORT-PULSE INITIATION	7 860
REFLECTED-WIRE TECHNIQUE, DETONATION P	8 422	SAPPHIRE WINDOW, FLYER, VACUUM OR GAS SHOTS	7 931
REFLECTION AND RAREFACTION TESTS, PBX 9404	8 591	SCANNING ELECTRON MICROGRAPHS, BTX	6 462
REFLECTION-CHANGE FLASH GAP TEST, D, P	5 13	EUTECTICS	7 550
REGRESSION RATE, DEFLAGRATION AT >1 kbar	6 195	SCHIPPEL EFFECT, STRETCHED SHEET EXPLOSIVES	4 499
REGRESSIVE BURNING RATE, PRESSURE EFFECT	7 168	SCHLIEREN PHOTOS, INITIATION, ACETYLENE-O <sub>2</sub>	2 270
REINITIATION IN A DARK WAVE, PROPANES	5 97	PRECURSOR SHOCK, PETN/NaCl	8 1072
RELATIVE DETONATION IMPULSES, PREDICTION	7 954	SCHOTTKY-BARRIER REGION, CONTACT, MODEL	6 390
RELEASE STRESS-STRAIN PATH, ELASTOPLASTICITY	4 290	SCOTCHLITE PHOTOS, CASING EFFECT ON AIRBLAST	6 782
RELEASE WAVE APPROXIMATION, POLYTROPIC EOS	3 275	SDT, INSTRUMENTED SHOTGUN TESTS	7 301
RELEASE WAVES IN PMMA, PROPAGATION SPEED	5 589	POP PLOTS FOR FOUR TATS COMPOUNDS	8 380
REGLIT, BOOSTER STUDY, CRITICAL DIAM & MASS	4 435	POROUS HE CHARGES IN PLASTIC TUBES	7 301
RESISTIVITY, ELECTRICAL EFFECTS OF DETONATION	3 120	RELATED TO DDT	7 139
ELECTRICAL/MAGNETIC FIELD	3 112	THIN-PLATE IMPACTS, PROJECTILES, WEDGES	8 902
SHOCKED, INHOMOGENEOUS SOLID HE	3 505	THRESHOLD, CRITICAL INITIATING PRESSURE	5 207
vs TEMP CURVE, HE AT HIGH TEMPS	3 63	TWO-PHASE MULTICOMPONENT, PBX 9404	8 943
RETARDED DETONATION, VELOCITIES > BURN RATES	6 225	SDT/DDT COMBINED MODEL	8 962
RETONATION PHENOMENON, SOLID EXPLOSIVES	8 93	SE-1 DETONATOR, MODIFIED, BTX STUDY	6 462
RETONATION WAVE EFFECT, POSITIVE/NEGATIVE, DDT	1 48	SECONDARY EXPLOSIVES, NITRATED, BOND POLARITIES	7 71
RETONATION, REFLECTION OF DIVERGENT WAVES	4 426	SELF-PRESSURIZING BOMB EXPERIMENTS	7 172
RETARDED DETONATION, RCHIKANES	6 225	SELF-SUSTAINING DETONATION, EAK & EAKL	8 116
SHOCK, DETONATION CURVES	7 355	SEMICONDUCTOR JUNCTIONS, SHOCK EFFECTS	5 403
REVERBERATION TIME, SPALLED & NONSPALLED AREAS	6 486	SENSITIVENESS, BULLET TEST	2 660
REX-20, LIQUID HE, CHARACTERIZATION	6 467	COMBUSTION DATA	2 643
RQPA, SENSITIVITY AND EXPLOSIVENESS	8 265	DETONATION, HE, TESTS	2 601
RICHTMYER-VON NEUMANN "q" METHOD	3 615	ENERGY RELEASE RATE	2 695
RICSHAW MODEL, 1D UNSTEADY FLUID DYNAMICS	6 629	HEAT OF EXPLOSION Q	2 643
Be ELASTIC PRECURSOR WAVE	5 470	LIMIT, PRESHOCKED RECEPTORS	3 176
RICSHAW, 1D UNSTEADY COMPRESSIBLE FLUID FLOW	6 477	TESTS, EXPLOSIVE PROPERTIES	3 659
1D UNSTEADY FLOW MODEL	5 501	SENSITIVITY ANALYSIS, EOS PARAMETERS	8 770
RIEMANN PROBLEM, MESH CELL SPACING	7 799	SENSITIVITY AND PERFORMANCE DATA, GAP, MODEL	8 1131
RIGIDITY EFFECT ON SHOCK WAVES IN Al & Cu	4 277	SENSITIVITY OF LIQUID HE, NM, TM, etc.	4 412
RISE TIME, MAGNETIC DIFFUSION EFFECTS	7 1068	SENSITIVITY RELATIONSHIPS, MOLECULAR, OB/100	3 671
RISK EVALUATION, EXPLOSIVES' SENSITIVITY	6 272	SENSITIVITY TEST, BURNING, GAP, 30-kg IMPACT	7 541
RISK TESTING, SINGLE- & DOUBLE-BASE PROPELLANT	6 299	CO <sub>2</sub> LASER	8 473
RMX-11-AV, MEASURED DETONATION PRESSURE	5 65	COLLIDING-BALL HE IMPACT	3 1
ROTATING-MIRROR CAMERA, SPLIT CHARGE & WEDGE	4 242	DIRECT CONTACT WITH SHOCKS	4 404
ROTATING-MIRROR SMEAR CAMERA, U <sub>fa</sub>	2 330	FLYER IMPACTS HE ON ANVIL	3 420
ROTATING-MIRROR STREAK CAMERA, SCHEMATIC	8 124	IHE, LABORATORY SCALE	7 965
ROTTER PROCEDURE, IMPACT MACHINE TECHNIQUE	3 660	IMPACT, HENKIN, WEDGE, PLATE	7 804
RUBBER-BONDED PETN SHEET EXPLOSIVES	4 496	IMPACT, THERMAL, SPARK GAP	8 353
RUBY CODE, CJ ISENTROPE FROM K-W EOS	4 31	MULTIVARIATE APPROACH	6 272
EXPLOSIVES PERFORMANCE vs COMP B'S	4 3	SENSITIVITY, BOND POLARITY EFFECTS	7 68
RUN DISTANCE vs PRESSURE & TIME, SOLID HE	4 237	IMPACT vs OB/100	3 674
RUN TO DETONATION IN TATR, POP PLOTS	8 380	MATHEMATICAL DEFINITION	3 40
RUNAWAY BURNING, TNT, COMP B, RDX MODELS	7 175	NOT ABSOLUTE CRITERION	1 109
RUNUP DISTANCE, HE-WAX SENSITIVITY	7 336	vs DELAY TIMES	3 60
RX-03-BB, 2D SHOCK MODEL	7 488	SENSITIZING EFFECT OF POLYMERS	7 24
RX-04, -05, -09 CYLINDER TEST RESULTS	4 5	SERVICE LEAD AZIDE vs DEXTRINATED LEAD AZIDE	2 711
RX-04-P-1, CURVATURE RADIUS EFFECTS	4 88	SETBACK SIMULATION, ACTIVATOR TESTS	8 1080
RX-23, CJ PROPERTIES, OXYGEN BALANCES	8 547	SETBACK-SHOCK SIMULATOR, BASE GAP EFFECT	7 914
RX-23-AA, -AB ISENTROPE BEHAVIOR	7 942	SHAPE FACTOR IN DIAMETER FOR INITIATION	7 273
-AB, -AC CJ PARAMETERS	6 713	SHAPED CHARGES, BALLISTIC COEFFICIENT	8 630
RX-23-AB, POSTDETONATION PROPERTIES	7 647	DETONATION WAVE FRONT	7 751
RX-26-AE (HMx/TATB), CHEMICAL DECOMPOSITION	7 56	INITIATION, COMP B	7 352
RX-26-AF (HMx/TATB), SHOCKED	7 325	INITIATION, TEST AND MODEL	8 337
RX-26-AF, EOS ABOVE CJ PRESSURE	8 587	LINER COLLAPSE, LIGHT TRACER	1 31
RX-26-AY DETONIC PROFILES	7 1032	TEMPERATURE MEASUREMENT	6 691
RX-36, HMx/TATB/BTF, CYLINDER TEST DATA	8 1020	TO DISRUPT AND DETONATE	8 318
S-W EOS FOR UNDERWATER SHOCK WAVES	6 570	SHARP SHOCK CALCULATION, SPHERICAL SHOCK WAVE	6 528

## B. Topic Phrase Index (Continued)

SUBJECT	SYM	PAGE	SUBJECT	SYM	PAGE
SHARP SHOCK, LAGRANGIAN ARTIFICIAL VISCOSITY	6	529	SHOCK INITIATION, THRESHOLD DATA, TATB	8	5
SHEAR BAND FORMATION, SHOCK LOADING, COMP B	8	1119	THRESHOLDS, HI-DENSITY HE	5	219
SHEAR BAND NUCLEATION, GRANULAR HE	8	35	TWO-DIMENSIONAL MODEL	7	488
SHEAR BANDS, THERMAL MODEL	7	36	TWO-PHASE MODEL	7	435
SHEAR DEFORMATION, FRAGMENT ATTACK, CONFINED HE	7	1048	SHOCK INSENSITIVITY OF MQ, ELECTRON DENSITY	8	839
SHEAR IN IMPACT INITIATION	8	294	SHOCK INTERACTION, THEORY vs RESULTS	6	496
SHEAR MECHANISM, IMPACT INITIATION	8	1150	DENSITY DISCONTINUITIES	4	394
SHEAR VELOCITY AT THERMAL EXPLOSION	7	41	SHOCK INTERSECTIONS, COLLISION EFFECTS	5	119
SHEAR VELOCITY IN DI-CONSTITUENT EXPLOSIVES	8	1120	SHOCK LOCUS, SONIC LOCUS CALCULATIONS	6	352
SHEAR, CHEMICAL REACTION, FRACTURE RESULT	8	246	SHOCK PASS-HEAT FILTER TEST, MOL CARD GAP	7	266
ROLE IN HOT-SPOT GENERATION	7	970	SHOCK POLARS FOR PERFECT GAS, GAMMA = 1.4	5	129
SHEAR-INITIATED IGNITION	7	144	SHOCK POLARS, 2 MACH STEMS, X > 0	6	574
SHEAR-RELATED IGNITION MECHANISM	7	1050	SHOCK PRESSURE, AQUARIUM TESTS	7	1016
SHEET EXPLOSIVE, RUBBER-BONDED PETN, RDX, TNT	4	496	HIGH FOR CHEMICAL REACTION	3	840
SHELL, 2DE CYLINDRICALLY SYMMETRIC CODE	5	487	INCIDENCE vs REFLECTION ANGLE	6	497
SHIELDING EFFECTS, 1D MODEL	8	1139	WATER, END & LATERAL	4	95
SYMPATHETIC DETONATION	7	1059	SHOCK PROFILES (RADIAL vs AXIAL DISTANCES)	5	483
SHIELDING MATERIALS, HIGH vs LOW IMPEDANCE	8	1139	SHOCK PROPAGATION, CONDENSED MATERIAL	7	780
SHOCK AMPLITUDE, GROWTH & DECAY CONDITIONS	6	379	LOW INTENSITY SHOCK	8	893
SHOCK AND DETONATION WAVE INTERACTIONS	7	669	SHOCK REACTION TIME TEST SETUP	5	95
SHOCK AND LASER INITIATION	7	797	SHOCK RELATIONS TO GET PRESSURE, SHOCK FRONT	2	433
SHOCK AND SHEAR MECHANISM, FRAGMENT IMPACT	8	1150	SHOCK RETARDATION IN ELASTIC MEDIA, CRACKS	6	268
SHOCK ATTENUATION IN LUCITE AND WATER	3	589	SHOCK SENSITIVITY TEST	7	479
SHOCK BEHAVIOR OF NONREACTING POROUS SOLIDS	4	266	SHOCK SENSITIVITY, 50X THRESHOLDS, PREHEATING	5	223
SHOCK BREAKUP BY IMPROVED SHIELDING	8	1139	CARD GAP TEST	7	278
SHOCK COMPRESSION, SOLID & POROUS HE	6	5	EXPLODING FOIL	7	924
SHOCK DESENSITIZATION MODEL	8	52	GAP TESTS	8	228
SHOCK DESENSITIZATION OF PBX 9404 & COMP B-3	8	1057	NUMERICAL MODELING	7	479
SHOCK DISCONTINUITY ZONE, CHEMICAL ACTION	7	791	REACTION THRESHOLDS	8	1135
SHOCK EFFECT ON AROMATICS AND ALIPHATICS	7	793	TATB/HMX MIXTURES	7	573
SHOCK ENERGY FLUENCE, SHORT PULSE EFFECT	6	68	THRESHOLDS	5	207
SHORT-PULSE EFFECT	6	68	TNT, MULTIPLE SHOCKS	7	906
SHOCK FRONT, ANGLE C <sub>0</sub> /D, 7000 m/s, NONPLANAR	1	53	vs PARTICLE SIZES	8	3
CURVATURE, TEST SETUP, PMMA	5	478	SHOCK STRENGTH, CRITICAL FOR INITIATION	4	179
ENERGY, REACTIVE/NONREACTIVE	4	584	SHOCK TEMPERATURE vs PARTICLE VELOCITY, TNT	2	371
PRESSURE vs MATERIAL THICKNESS	2	328	SHOCK TEMPERATURE vs VELOCITY, DIAMETER	6	332
VELOCITY BY STREAK CAMERA RECORD	4	440	SHOCK TUBE PROFILE & SETUP, LEAD AZIDE	3	24
SHOCK GENERATION IN DEUTERIUM, LASER PULSE	5	361	SHOCK VELOCITY, INERT MONITORS ON HE	5	23
SHOCK HEATING, MECHANISMS OF	8	68	LUCITE & WATER, SHEAR DATA	3	593
SHOCK HUGONIOT OF UNREACTED EXPLOSIVES	5	251	PMMA vs DISTANCE	4	219
SHOCK IMPEDANCE & PRESSURE BOUNDARIES	4	274	SCHLIEREN PHOTOS	4	555
SHOCK IMPEDANCE MEASUREMENTS OF CJ STATE	5	526	vs DISTANCE, TNT, COMP B,...	5	25
SHOCK IMPEDANCE MISMATCH EQUATION, PRESSURE	3	359	vs PARTICLE VELOCITY, PMMA	4	231
SHOCK INITIATION, & DETONATION FAILURE MODEL	5	177	vs PRESSURE, OVERDRIVEN HE	5	533
AND P <sub>r</sub>	6	82	SHOCK WAVE, & INITIATION DATA FOR SOLID HE	4	233
BURN, UNDERWATER, SOLID HE	4	487	COMPRESSION OF PLEXIGLAS, 3-20 kbar	4	222
CORRELATING RESULTS	7	887	CONVERGING CYLINDRICAL	1	79
CRITICAL CONDITIONS	7	316	DECAY IN SOLIDS & AL SPALLINGS	3	253
DENSITY FUNCTION, TATB	7	429	EFFECT ON POROUS SOLID	4	258
H-6 & PBXW-109	7	308	EVOLUTION, CHEMICAL KINETICS	6	379
HISTORICAL WORK	3	786	EXPLOSIVE DECOMPOSITION	6	29
IN LIQUID EXPLOSIVES	3	813	FOLLOWING COMPRESSION WAVE, PHOTO	4	372
LOW-DENSITY PRESSINGS, AP	4	359	GROWTH MODES, HE INITIATION	6	47
MECHANISM	6	89	INITIATION MODEL, HETEROGENEOUS HE	6	371
MODEL, EVALUATING NEW	7	857	INTERACTION WITH CONDENSED HE	7	778
MODEL, HOT-SPOT BASED	7	459	INTERACTIONS, FRAMING CAMERA RECORD	6	581
MODEL, HOT-SPOT BASED	7	506	PARAMETERS FOR 4 PBX 9404 MODELS	6	568
NM, HYPERVELOCITY WAVE	3	304	PARAMETERS FOR MACH WAVES IN WATER	5	588
NM, LIQUID TNT, DINA,	3	469	PERSPEX, PRESSURE EFFECTS	4	156
NONIDEAL, PROPELLANT	7	620	PRESSURE, ATTENUATOR/HE INTERFACE	3	500
PBX 9404, HMX/TATB	7	325	PROPAGATION VELOCITY, MEASURED	3	420
PLOT, SHORT DURATION	4	376	RESEARCH ON INERT SOLIDS	4	321
SOLID EXPLOSIVES	3	499	SOLIDS, Al = COMP B, TNT	1	88
SHOCK INITIATION, TATB AND HMX COMPOUNDS	8	892	SHOCK WAVE, STRUCTURE IN SOLIDS, EXPERIMENTAL	4	566

## B. Topic Phrase Index (Continued)

SUBJECT	SYM	PAGE	SUBJECT	SYM	PAGE
SHOCK WAVE, TEMPERATURE, RAMAN SCATTERING	7	1011	SMALL-SCALE GAP TEST, SETUP, AXIAL AIR GAPS	2	623
UNDERWATER, TWIN SPHERES	5	581	SMALL-SCALE PLATE DENT TEST, ENERGY RELEASE	3	744
SHOCK WIDTH & IMPULSE vs Q & GAMMA	6	563	SMALL-SCALE THERMAL TEST, IHE SENSITIVITY	7	965
SHOCK-FOCUSING MECHANISM, HOT SPOTS	6	371	SHEAR CAMERA RECORD, 1D & 2D TESTS	4	269
SHOCK-IMPEDANCE-MATCHING INFRARED WINDOW	7	993	CYCLOTOL WEDGE, U <sub>0</sub>	3	502
SHOCK-INDUCED BOND SCISSION	7	779	NITROMETHANE INITIATION	3	485
SHOCK-INDUCED DECOMPOSITION, FOREST FIRE MODEL	7	234	SMOKELESS POWDER (E.C. BLANK FIRE), DDT STUDY	1	60
SHOCK-INDUCED ELECTRICAL POLARIZATION IN HE	5	429	SODATOL, WAVE SHAPE STUDIES, R/d	2	503
SHOCK-INDUCED PHASE TRANSITIONS	4	248	SODIUM NITRATE (SN), EOS OF TNT/NaNO <sub>3</sub> 50/50	2	519
SHOCK-INDUCED POLARIZATION, HOMOGENEOUS HE	6	143	SODIUM SULFATE ADDITIVE IN RDX/TNT	5	465
SHOCK-INDUCED REACTION, IR EMISSION	7	993	SOLID HE & OTHER SOLIDS, PROPERTIES, MODEL	4	555
SHOCK-INDUCED SIGNALS FROM DIELECTRICS	5	387	SOLID HE DECOMPOSITION, HOT-SPOT REACTION	6	29
SHOCK-INDUCED SYMPATHETIC DETONATION, SOLID HE	3	520	SOLID HE, PLANE SHOCK WAVE INITIATION	3	499
SHOCK-INDUCED THERMAL RISE MODEL	6	89	SOLID-STATE MODEL FOR DETONATIONS	2	404
SHOCK-TO-DEFLAGRATION TO DETONATION (SDDT)	8	1131	SOLID/LIQUID RATIOS (S/L) OF HE, MODEL	7	343
SHOCK-TO-DETONATION TRANSITION, (SDT)	7	265	SONIC ANGLES CALCULATED FOR COMP B & NH	4	154
1D MODEL	3	792	SONIC OR QUASI-SONIC DISCONTINUITY	7	635
RESULTS	8	307	SONIC POINT IN STEADY AXIAL WAVE	7	664
LIGHT EMISSION	4	607	SOPHY GAP TEST DATA FOR AAB 3267	7	892
SHOCK-WAVE LUMINOSITY/PRODUCT LUMINOSITY	2	576	SOUND SPEED c DEFINED, THERMODYNAMIC IDENTITY	3	543
SHOOTING vs BARRIER TEST RESULTS, VELOCITIES	4	432	SOUND VELOCITY, (EULER'S) DETONATION GASES	1	74
SHORT- & LONG-PULSE INITIATION THRESHOLD, HNS	6	745	POROUS BED UNLOADING	8	653
SHORT-, LONG-, SUSTAINED-PULSE INITIATION, TATB	6	757	SPACE vs TIME, SHOCK INITIATION IN SOLID HE	4	233
SHORT-DURATION SHOCK INITIATION OF SOLID HE	4	373	SPACE-TIME HISTORY, PROPAGATION DETONATION	5	108
SHORT-PULSE SHOCK INITIATION, GRANULAR HE	7	857	SPALL CALCULATIONS FOR AL, SCALING LAWS	3	253
SOLID HE, MODEL	8	951	SPALL, MESH CALCULATION & WAVE DIAGRAM	4	548
SHORT-PULSE SHOCK SENSITIVITY TESTS	7	924	SPALLING (SCABBING), STRESS WAVE RESULT	1	33
SHORT-SHOCK INITIATION MODEL	8	52	SPALLING DETECTION, COMP B TESTS & MODEL	6	477
SHORT-SHOCK INITIATION OF TATB	7	385	SPALLING IN NICKEL PLATE, PHERMEX RADIOGRAPH	4	646
SHOTGUN TEST, 2DE & FOREST FIRE MODELS	7	479	SPALLING MECHANISM, CALCULATION, FOR COPPER	5	567
SHOTGUN, INSTRUMENTED FACILITY, PROPELLANTS	7	299	SPALLING UNDER OBLIQUE IMPACT	5	573
SILICA IMPACTOR, SHORT-PULSE SHOCK STUDY	7	860	SPARK INITIATION IN ALUMINIZED HE	3	706
SILVER AZIDE DETONATION BY LIGHT	2	547	SPECIFIC HEAT RATIO EFFECTS ON LIQUID HE	7	374
SILVER AZIDE, HOT-WIRE INITIATION	5	339	SPECTRAL DISTRIBUTION OF LIGHT, INITIATION	5	153
SIMILARITY SOLUTION, REACTIVE TAYLOR WAVE	8	1026	SPECTRAL RESPONSE AND EMISSION FOR FLYER	7	934
SINGLE CUBICAL AIR-HOLE STUDY	8	45	SPECTROGRAMS OF SHOCKS IN ARGON & AIR	1	86
SINGLE-CRYSTAL DETONATION, PREPARATION, TESTS	2	469	SPECTROSCOPY, REAL-TIME, DETONATING HE	8	691
SINGLE-CRYSTAL EXPERIMENTS, EARLY WORK	3	791	TIME-RESOLVED IN VACUUM	5	560
SINGLE-PORE DEFORMATION, MODEL	7	436	SPECTRUM, OPTICAL ABSORPTION, LEAD AZIDE	7	740
SINGLE-SHOCKED SUPRACOMPRESSION TESTS	8	590	SPHERICAL DETONATION, CONVERGING, SOLID HE	7	602
SINGLE-SPECIES EQUIVALENT, JC23 EOS	7	721	DIVERGENT WAVES	5	31
SIZE FACTORS IN DETONATION TRANSFER	4	442	SURFACE, LINER VELOCITY	6	521
SKID TEST (AWRE) vs LABSET RESPONSE	7	19	WAVE INTERACTIONS	7	671
SKID TEST RESULTS, TATB/HMX MIXTURES	7	570	SPHERICAL EXPLOSION SHOCK WAVES IN WATER	6	570
SKID TEST vs LABSET DATA, EXPLOSIVENESS, HMX	8	1039	SPHERICAL INITIATORS & CHARGES, UNDERWATER	5	600
SLAPPER DEVICE, AIR/GAS EFFECTS	7	930	SPHERICAL PORE COMPACTION CELL MODEL, P vs V	8	915
SLIC METHOD, ADVECTED VOLUME, TRANSPORT MODEL	7	696	SPHERICAL SHOCK WAVES IN CONDENSED HE, MODEL	6	528
SLIPPAGE ROUTINE IN LAGRANGIAN FLOW, MODEL	3	234	SPHERICAL SHOCK WAVES IN WATER, TWIN SPHERES	5	581
SLURRY BLASTING AGENTS, CHARACTERIZATION	6	729	SPHERICAL vs CYLINDRICAL vs PLANE DETONATION	5	41
SLURRY EXPLOSIVE, AXIAL INITIATION STUDY	4	159	SPHERICAL WAVE FRONTS, WAVE SHAPE STUDY	2	504
COOK-TYPE, BOOSTER	4	435	SPHERICALLY DIVERGING DETONATION WAVES	8	151
CS EOS	8	805	SPHERICITY ANALYSIS, STREAK CAMERA RECORD	5	32
DIAMETER EFFECT	8	168	SPIN DETONATION, VISCOSITY EFFECT	7	796
ELEMENTAL COMPOSITION	8	810	SPIN FREQUENCY AS FUNCTION OF TUBE DIAMETER	1	51
IMPACTED, HOT SPOTS MODEL	7	343	SPIN HAMILTONIAN PARAMETERS, NITRUSO RADICALS	8	745
PERFORMANCE, REACTION MODEL	8	985	SPIN TRAPPING SPECTRAL DATA	8	737
SMALL DIVERGENT DETONATION THEORY	8	176	SPIN, SPOT SPIRALING ALONG TUBE, COMBUSTION	1	44
SMALL-CALIBER CASELESS AMMUNITION SENSITIVITY	6	682	SPINNING DETONATION, PROPAGATING H <sub>2</sub> -O <sub>2</sub>	2	269
SMALL-SCALE DENT TEST, SETUP	2	760	RETONATION WAVE	1	48
SMALL-SCALE GAP TEST, ASSEMBLY	4	401	SPIS-44 (HMX/AP/AL) PROPELLANT, NONIDEAL	7	620
CORRELATING	7	888	SPLIT-CHARGE EXPERIMENT, LOWER PRESSURE	4	241
INTERSTITIAL GAS	4	349	SQUIB- & PISTON-INITIATED HMX MODEL	8	914
MECHANISM OF INITIATION	3	794	SQUIB-IGNITED DDT TUBE, BOX COMPACTION	8	917
SMALL-SCALE GAP TEST, RESULTS, HMX/Viton	4	90	SRI-1,-2,-3,-4,-5, LIQUID HE CHARACTERIZATION	6	469

## B. Topic Phrase Index (Continued)

SUBJECT	SYM	PAGE	SUBJECT	SYM	PAGE
STABILITY OF PLANAR, STEADY WAVE FRONT	4	73	SUSAN TEST, ENERGY RELEASE vs IMPACT VELOCITY	6	753
STABILITY PROPERTIES OF NEW LIQUID HES	6	471	LOW-VELOCITY IMPACT SENSITIVITY	4	477
STAGGER SCHEME, SHOCK & CONSTANT STATE POINTS	3	214	SENSITIVITY OF IHE	7	965
STARTEX (DITeU) BOOSTERS, CRITICAL DIAM & MASS	4	435	TATB/HMX MIXTURES	7	570
STATIC PORE COLLAPSE MODEL	8	964	SYEP, LIQUID HE, CHARACTERIZATION	6	469
STATIC STABILITY BOUNDARY, DEFLAGRATION WAVES	6	283	SYMPATHETIC DETONATION, 2DE MODEL	7	1055
STATISTICAL MECHANICAL THEORY, CHEG MODEL	8	502	AP BY NO	6	173
STATISTICAL MECHANICS, POSTDETONATION	7	646	MODEL	7	479
STEADY AXIAL PLANE, REACTION ZONE EFFECT	7	661	PROPELLANTS	6	302
STEADY AXIAL WAVE, DETONATION STATE LOCI	7	666	SHOCK INDUCED	3	520
STEADY CONDENSATION AIR SHOCKS, WATER VAPOR	2	296	SYNCHRO-STREAK TECHNIQUE, SHAPED CHARGE	7	751
STEADY DETONATION IN 2D FLOW, SLAB & CYLINDER	1	52	T1, EXPERIMENTAL ISENTROPE DATA	8	815
STEADY PLANE REACTION ZONE, 2ND MODEL	7	532	T2 (TATB), EOS CALCULATION	8	751
STEADY vs OVERDRIVEN WAVES, ACETYLENE-O <sub>2</sub> MIX	2	203	T2, EXPERIMENTAL ISENTROPE DATA	8	820
STEADY-STATE DETONATION WAVE, FINITE RATE	2	312	TAIT EOS, PRESSURE PROFILES, LIQUID BLASTS	6	502
STEADY-STATE DETONATION, TIME-DEPENDENT MODEL	4	520	TAIT EQUATION, SHOCK TRANSMISSION THROUGH AL	1	91
STEADY-STATE PLANE DETONATION WAVE (SSPD)	2	425	TANDEM SINGLE IMPACT, PROPELLANTS D AND E	8	286
STEADY-STATE PLANE DETONATION WAVE STRUCTURE	3	791	TANTALUM-COVERED PROJECTILE, IMPACTED	7	325
STEEL, 4340, EFFECT ON WAVE PROPAGATION	4	295	TARGET GAUGE ASSEMBLIES, QUARTZ GAUGE STUDY	5	376
STEP SHOCK SOLUTION IN PLANAR FLOW	4	503	TATB, 3D HYDRODYNAMIC HOT-SPOT MODEL	8	44
STILBENES, IMPACT SENSITIVITY AND OS/100	3	681	CHEMICAL DECOMPOSITION MODEL	7	56
STONG POINT EXPLOSION IN A COMBUSTIBLE MEDIUM	6	590	CJ POINT, CJ ISENTROPE, ERROR %	7	709
STRAIN RATE SENSITIVITY, HMX	8	645	CJ PROPERTIES, OXYGEN BALANCE	8	547
STRAIN RATE vs STRAIN CURVES FOR COMP B	3	432	CORNER-TURNING DATA	7	624
STRAIN WAVE, CONFINED, SUBSONIC & PLASTIC	7	253	CRASH-PRECIPIATED PORE-SIZE TESTS	8	3
STRAIN-TIME PLOTS, TETRYL, DDT STUDY	6	428	CRYSTALLOGRAPHIC CELL PARAMETERS	6	705
STRAND BURNER, PRESSURE VESSEL	3	80	DETONATION PARAMETERS, INTERPOLATION	7	1029
STREAK CAMERA RECORD, COMP B, POLARIZATION	5	432	DETONATION PROPERTIES, CARBON EOS	8	528
CONVECTIVE BURN OF PETN	6	253	DETONATION REACTION ZONE STUDIES	8	123
CYLINDER TEST	6	512	DOPPLER LASER INTERFEROMETER STUDY	8	135
DARK WAVES IN NM	6	417	EB INITIATION, TWO EXOTHERMIC REACTIONS	7	50
DDT STUDY	5	235	EXPANSION ISENTROPES	8	815
DIGITAL FILTERING	7	296	FLYER PLATE INITIATION	6	756
FLYER IMPACT	6	656	FRONT CURVATURE, REACTION ZONE LENGTH	6	642
MACH REFLECTION	8	433	INITIATION & DETONATION CHARACTERISTICS	6	755
SHOCK CURVATURE	8	190	INITIATION STUDIES OF LX-17 & PBX 9502	8	1045
SPHERICITY ANALYSIS	5	32	ISOTHERMAL LINEAR & VOLUME COMPRESSION	6	700
WAVE DIAGRAM	7	680	JET PENETRATION MODEL	8	337
STREAK CAMERA RESULTS vs CURVE FITS	5	60	LOW DENSITY, SHOCK INITIATION	7	385
STREAK SCHLIEREN INTERFEROGRAM, REFLECTED	4	71	PARTICLE SIZE DISTRIBUTION EFFECTS	8	3
STREAM TUBE EXPANSION, JACOBS vs EYRING	1	54	PLANAR SHOCK INITIATION, GAUGES, WEDGES	7	385
STRESS HISTORIES IN SHOCKED PBX 9404	5	438	POROUS, SHOCK INITIATION	7	385
STRESS WAVE INTERACTIONS, x-c, Fe/FREE SURFACE	6	672	REACTION ZONE, STEADY AXIAL WAVE	7	661
STRESS WAVES, LONGITUDINAL, LEAD AZIDE	5	302	SCANNING ELECTRON PHOTOMICROGRAPHS	7	427
STRESS-STRAIN DATA, DYNAMIC RECORD	3	420	SDT, RUN TO DETONATION	8	380
STRESS-TIME PROFILES OF SHOCK & RELEASE WAVES	4	290	SENSITIVITY WITH AMMONIUM NITRATE	7	804
STRESS-WAVE PROPAGATION, SCHEMATIC	7	1052	SENSITIVITY, SHORT & LONG PULSES	7	425
STRESSES GENERATED BY ELECTRIC DETONATORS	3	285	SHOCK INITIATION, TESTS AND MODELS	8	892
STRETCHED HE, EFFECT ON DETONATION VELOCITY	4	500	SHORT-PULSE SENSITIVITY	7	390
STROBOSCOPIC LASER-SCHLIEREN RECORDS, SHOCKS	5	125	STANDARD GAP TEST, BURN MODEL	7	482
STRUCTURE, CHEMISTRY, & INSTABILITY IN GASES	4	67	SYNTHESIS	7	425
SULFUR CONDUCTIVITY PRESSURE DEPENDENCE	3	241	THERMAL DECOMPOSITION OF CONFINED HE	6	214
SULFUR PRESSURE TRANSDUCER, CALIBRATION, PERF	3	241	vs DINGU, COMPARISON OF PROPERTIES	7	540
SUPER GAP TEST SETUP	8	230	vs HMX, CONFINED DROP HAMMER TEST	7	966
SUPER-VELOCITY REACTION WAVE MODEL	3	307	TATB-BASED CUSTOMIZED EXPLOSIVES	7	566
SUPRACOMPRESSION, TATB, EOS OF PRODUCTS	8	587	TATB/AP, CYLINDER TEST DATA, TEMPERATURE	8	1020
SURFACE AREA INCREASE, IGNITABILITY & BURN	2	629	TATB/HMX COMPOSITIONS, CUSTOMIZED PBX	7	567
SURFACE BURNING EQUATION, EYRING'S, CALC TIME	2	526	TATB/Kel-F, CONFINEMENT EFFECT ON FAILURE	8	372
SURFACE BURST, UNDERWATER, HALF-SPACE MODEL	5	493	DOUBLE DISCONTINUITY MODEL, GAP	7	294
SURFACE FILM EFFECTS ON EXTERNAL PLASMAS	3	188	ELECTRON BEAM INITIATION	7	52
SURFACE HEAT DISSIPATED vs IMPACT SENSITIVITY	4	461	RECEPTORS IN GAP TESTS	7	279
SURFACE HEAT RELEASE, DEFLAGRATION WAVES	6	284	TATB/Kel-F, SUSTAINED PULSE INITIATION, WEDGE	6	764
SURFACE RATE PROCESSES & SENSITIVITY OF HE	4	461	TATB/Viton, TRANSPORT MODEL	7	697
SURFACE-TO-VOLUME RATIO OF PROPELLANT	7	143	TAYLOR ANALYSIS OF A TUBULAR BOMB	8	604

## B. Topic Phrase Index (continued)

SUBJECT	SYM	PAGE	SUBJECT	SYM	PAGE
TAYLOR INSTABILITY, SAME AS LANDAU'S (RUSSIAN)	1	105	TETRYL, RADICALS IN DECOMPOSITION PRODUCTS	8	742
TAYLOR MODEL SIMPLIFIED AND EXTENDED	8	602	RETARDED DETONATION, TRICKS (CHICANERY)	6	226
TAYLOR WAVE CALCULATED FOR PENTOLITE	4	33	SINGLE-CRYSTAL TESTS, PROPERTIES	2	470
TAYLOR WAVE FITS, RIGSHAW MODEL, MANGANIN GA.	6	625	TEMPERATURE, MEASURED AND CALCULATED	8	558
TAYLOR WAVE IN PRESSURE-TIME CURVE	3	249	HEAT OF DETONATION, UNCONFINED/CONFINED	3	750
TAYLOR WAVE P-T, PYROMETER, IN SITU GAUGE	8	564	TETRYL/WAX, x-t PLOT, STRAIN-t PLOT, DDT EFFECT	6	434
TAYLOR WAVE REGION, NONSTEADY 1D FLOW	7	531	TFA, LIQUID HE, CHARACTERIZATION	6	469
TAYLOR WAVE, ENERGY TRANSFER TO RIGID PISTON	3	206	TFMA, LIQUID HE, CHARACTERIZATION	6	469
INERT BINDERS EFFECT	7	564	TFMDA, LIQUID HE, CHARACTERIZATION	6	469
TDPF, LIQUID HE, CHARACTERIZATION	6	469	TFMFF, LIQUID HE, CHARACTERIZATION	6	469
TEFLON 7C TESTS, STRAIN RATES OF HMX	8	648	TFNA & TFENA, BKW MODEL & PERFORMANCE DATA	3	731
TEFLON 7C, COMPACTION IN POROUS BEDS	7	843	THERMAL DECOMPOSITION OF $[\text{Co}(\text{NH}_3)_6](\text{NO}_3)_3$	3	50
SOUND VELOCITIES vs % TMD	7	204	THERMAL DECOMPOSITION RATE CONSTANTS	5	166
TEGDN, GAP TEST SENSITIVITY IN PROPELLANTS	3	830	THERMAL DECOMPOSITION REACTION, CONFINED HE	6	214
TEMPERATURE DEPENDENCE OF DENSITY FOR NM	2	455	THERMAL DECOMPOSITION VELOCITIES, SENSITIVITY	3	60
TEMPERATURE EFFECT, COBALT AMINE AZIDES	3	53	THERMAL EXPLOSION THEORIES, GASEOUS SYSTEMS	2	563
COMPOSITE HE	8	1018	THERMAL EXPLOSION THEORY, REACTION RATE	6	76
DETONATION VELOCITY OF NM	2	455	THERMAL EXPLOSION TIME AT m.p. vs PRESSURE	7	37
DIAMETER EFFECT, NM	2	461	THERMAL EXPLOSION TIMES, CRITICAL DIAMETER	5	102
DIVERGING DETONATION WAVE	8	1047	THERMAL EXPLOSIONS, EB HEATING, HEAT FLOW OVEN	7	62
GAP TEST	7	336	THERMAL HAZARD OF DYNAMITE, MODELING	7	43
PRECOMPRESSION STUDY	5	77	THERMAL INITIATION & REACTION, SECONDARY HE	5	279
PROPELLANTS	3	828	THERMAL INITIATION, ELECTRON BEAM, MODEL	7	50
SECONDARY EXPLOSIVES	5	279	MEMORY EFFECT	3	42
SHOCK IGNITION	7	459	THERMAL RESPONSE OF INTERMEDIATE EXPLOSIVES	8	1105
SHOCK INITIATION	5	219	THERMAL TEST, SENSITIVENESS TESTING	3	660
TEMPERATURE IN REACTION ZONE, LIGHT INTENSITY	4	602	SENSITIVITY TEST, SMALL SCALE	7	965
TEMPERATURE VARIATION, INITIATION OF LIQUID HE	5	153	THERMAL WAVE, ENERGY MOTION	5	361
TEMPERATURE, OPTICAL SYSTEM FOR MEASUREMENT	1	17	THERMO-HYDRODYNAMICS IN METALIZED EXPLOSIVES	2	733
SHOCK WAVE ENVIRONMENTS	7	1004	THERMOCOUPLE CONFIG, THERMOELECTRIC STUDY	4	628
SHOCKED HE, IR RADIOMETRY	7	993	THERMOCOUPLE DESIGN FOR SHOCK WAVE LOCUS	7	1005
TEMPERATURE-TIME CURVES, IDEAL GAS vs BKW	7	348	THERMODYNAMIC EQUILIBRIUM IN DETONATION WAVES	2	198
TENSION CONTOURS vs OBSERVED FRACTURE PATTERN	5	579	THERMODYNAMIC FUNCTIONS, DETONATION PRODUCTS	8	799
TENSOR MODEL, HOT SPOTS IN SLURRY HE	7	344	GAS & SOLID PHASES	2	384
TETRAZOLES, ELECTRONIC STRUCTURE	7	71	THERMODYNAMIC PARAMETERS DISTRIBUTION	7	789
TETRYL, BOOSTER REPLACEMENTS	8	1105	THERMODYNAMIC PATH IN (P,V) PLANE	7	693
BURN RATE, SENSITIVENESS, Q, m x Q	2	651	THERMODYNAMIC PROPERTIES, INVERSE METHOD, EOS	2	522
CALC & TEST DETONATION VELOCITIES	2	418	THERMODYNAMIC STATE FROM DETONATION VELOCITY	1	72
CONTACT FILM, DROP-WEIGHT IMPACT TEST	3	13	THERMODYNAMICS OF DETONATION PRODUCTS	7	759
DDT STUDIES, PLASTIC TUBES	7	119	THERMODYNAMICS, INFLUENCE ON HYDRODYNAMICS	8	788
DENSITY, DET. VELOCITY, PRESSURE	3	378	THERMOELECTRIC EFFECT, SHOCK PRESS TRANSDUCER	4	627
DETONATING CENTERING DEVICE	8	332	THERMOKINETIC PARAMETERS, TETRYL, RDX, HNS, HMX	8	1112
DETONATION FLAME ANALYSIS	2	572	THERMOMECHANICAL COEFFICIENT vs AMPLITUDE	6	386
DETONATION PROPERTIES, CARBON EOS	8	528	THIN FOILS CONFINING DETONATION WAVE	6	406
DETONATION TEMPERATURE vs DENSITIES	8	573	THIN METAL FILMS, CONFINED, SHOCKS GENERATED	6	614
DIAMETER EFFECT, D vs 1/d	4	182	THIN-LAYER CHROMATOGRAPHY (TLC), SUBIGNITION	8	725
DIRECT-CONTACT DETONATION SENSITIVITY	4	405	THIN-PULSE INITIATION, LX-17, VELOCITIES	8	1051
EMP VELOCITY GAUGES	8	447	THREE-DIMENSIONAL (3DE) HOT-SPOT MODEL	8	42
EMV GAUGE, PRESSURES & TIMES	5	413	THRESHOLD GAP VALUES, CAVITATION EFFECTS	7	376
EXPERIMENTAL vs COMPUTED HUGONIOTS	6	773	THRESHOLD INITIATION, LX-13, PEIN, PBX 9407, ...	8	1091
EXPLODING-FOIL SHOCK EFFECT	7	928	THRESHOLD PRESSURE vs RECIPROCAL CHARGE DIAM	4	446
GAP TEST CALIBRATION RESULTS	7	288	THRESHOLD VELOCITY DATA, COMP B, TNT, TETRYL	8	1151
GAP TEST FOR LIQUID HE, HQ/EGDN	3	438	THURSTON'S STRESS GRADIENT MODEL, SPALL STUDY	6	487
GAS POCKETS, LOW-VELOCITY DETONATION	2	584	TIGER CALCULATION PARAMETERS, BKW, BKWR, JC23	6	720
HIGH-VACUUM DETONATION	5	561	TIGER JC23 ADIABATS, EMULITE vs AIR, P-U <sub>p</sub>	8	1077
IMPACT INITIATION, .30-CAL. CYLINDERS	2	612	TIGER MODEL, CP DETONATION PROPERTIES	7	870
IMPACT SENSITIVITY AND OB/100	3	674	DETONATION PRESSURE CALCULATIONS	5	28
IMPACT SENSITIVITY, CRITICAL TEMP	3	69	MATCHED TO CJ FROM JC2 EOS	7	725
LASER IGNITION TEST	8	476	NITROMETHANE EOS	7	610
LINEAR MEMORY EFFECT	3	47	TIGER/BKWR EOS FOR EUTECTICS OF EDD AND AN	7	555
LINEAR SURFACE REGRESSION, 500°C	4	461	TILT CONTROL OF IMPACT SURFACES	5	382
MECHANICAL PROPERTIES, DROP WEIGHT	8	642	TIME DEPENDENCE vs METHOD OF CHARACTERISTICS	4	520
PARTICLE SIZE EFFECTS, SMALL-SCALE GAP	5	259	TIME-DEPENDENT 1D UNSUPPORTED DETONATION	6	352
TETRYL, PELLET INITIATORS IN NOL GAP TEST	3	585	TIME-DEPENDENT BEHAVIOR, COMPOSITE EXPLOSIVES	6	729

## B. Topic Phrase Index (Continued)

SUBJECT	SYM	PAGE	SUBJECT	SYM	PAGE
TIME-DEPENDENT DETONATION WAVES, CURVATURES	1	99	TNT, IGNITION BY AIR GAP COMPRESSION	7	3
TIME-DEPENDENT FLOW BEHIND DETONATION FRONT	6	637	IMPACT SENSITIVITY AND OB/100	3	681
TIME-RESOLVED INFRARED RADIOMETRY	7	993	IMPACT SENSITIVITY AND OXYGEN BALANCE	3	701
TIME-RESOLVED RADIATION IN REACTION ZONE	4	602	INERT-EXPLOSIVE INTERFACE STUDY	6	29
TMETH, SHOCK COMPRESSION THROUGH INERT, DDT	3	813	INITIATION AND PROPAGATION, MODEL	7	362
TNB, DIRECT-CONTACT DETONATION SENSITIVITY	4	407	JCZ STATE, MOLECULAR PARAMETERS	7	721
TIME DELAY vs TEMP RECIPROCAL, DECOMP	3	68	LARGE-SCALE GAP TEST, CRITICAL DIAMETER	5	207
TNETB, IMPACT SENSITIVITY, CRITICAL TEMP	3	69	LASER IGNITION TEST	8	476
TNM, DETONATION VELOCITIES	8	538	LINEAR SURFACE REGRESSION TO 500°C	4	461
LVD & HVD IN LIQUID HE, CARD GAP TEST	4	412	LIQUID, MODIFIED GAP TEST	7	310
TNM/AL ISENTROPIC BEHAVIOR	7	942	LIQUID/SOLID, ENERGY THRESHOLD, p-t PLOT	6	106
TNM/C, CYLINDER TEST DATA, TEMPERATURE EFFECT	8	1022	LOW-PRESSURE POINT ON ISENTROPE	3	389
TNT, 500-TON HEMISPHERE, PHOTOGRAPH	8	410	LOW-PRESSURE, LOW-VELOCITY SHOCKS	4	239
AIR GAP EFFECT ON PROPAGATION	8	409	LOW-TEMPERATURE INITIATION	6	36
ANOMALOUS BURN RATE CHARACTERISTICS	7	898	LUMINOSECURITY RECORDS, DETONATION TEMPS	2	158
BASE GAP EFFECT ON SENSITIVITY, NSWC TEST	7	914	MEASURED DETONATION PRESSURE, AQUARIUM	5	65
BKW MODEL & PERFORMANCE DATA	3	728	MECHANICAL PROPERTIES, DROP WEIGHT	8	642
BUBBLE ENERGY, UNDERWATER EXPANSION	6	546	MOLECULAR GEOMETRY, BOND LENGTHS, AB INIT	8	830
BURN RATE, SENSITIVENESS, Q, m x Q	2	651	MULTIPLY SHOCKED, SENSITIVITY EFFECT	7	906
CALC & TEST DETONATION VELOCITIES	2	418	OBLIQUE SHOCKS, PERPENDICULAR DRIVE	6	602
CALCULATED DETONATION TEMPERATURE	1	74	OVERALL ENERGY BALANCE	6	559
CALCULATED PRESSURE PULSE SHAPES	7	910	OVERDRIVEN SHOCKED STATES	5	533
CAST, LOW-TEMPERATURE PROPERTIES	6	36	PARTICLE VELOCITIES, LAGRANGE GAUGES	7	1074
CAST, MULTIPLE LAGRANGE GAUGE STUDY	6	786	PHYSICAL PROPERTIES, GRAIN GROWTH	1	32
CAST, SHOCK COMPRESSIBILITY DIFFERENCES	7	793	PLEXIGLAS MONITOR, SHOCK VELOCITY	5	23
CHEMICAL DECOMPOSITION MODEL	7	56	POROUS, RESPONSE, MODEL & DATA	6	766
CHEMICAL REACTION, FRACTURE RESULT	8	243	PRESSED, DETONATION VELOCITY vs DIAMETER	3	327
CJ DATA & CALCULATED CJ PARAMETERS	6	713	PRESSED, JET INITIATION	8	318
CJ POINT, CJ ISENTROPE, ERROR %	7	709	PRESSED, LIGHT-GAS GUN IMPACT	6	3
CJ PROPERTIES, OXYGEN BALANCE	8	547	PRESSED, PHYSICAL CHARACTERISTICS	6	6
CJ STATE FOR CAST, MODEL	7	364	PRESSED, WEDGE TEST & SHEAR CAMERA DATA	3	504
COMP B, BURN RATE ANOMALIES	7	898	PRESSURE PULSES, FREE-SURFACE VELOCITIES	7	910
CONDUCTIVITY PROFILES, C PRECIPITATION	4	599	PROPERTIES COMPARED WITH THOSE OF DATB	3	769
CONFINED, AFTER FIRING, DEFLAGRATION	6	204	RADICALS IN DECOMPOSITION PRODUCTS	8	742
CRITICAL LENGTH vs CRITICAL VELOCITY	4	432	REACTION ZONE LENGTH CALCULATED	5	23
CRYSTAL STRUCTURE IN CAST BLOCK	8	412	RECEPTORS IN GAP TESTS	7	279
CRYSTAL STRUCTURE, SENSITIVENESS	3	666	RETARDED DETONATION, TRICKS (CHICANERY)	6	226
CURVATURE EFFECT ON SHOCK WAVE	1	99	SENSITIVENESS OF LIQUID & PRESSED GRAINS	2	643
CYLINDER TEST RESULTS	4	5	SENSITIVITY	7	373
CYLINDER WITH AIR BUBBLE, DEFORMATION	6	340	SENSITIVITY AND EXPLOSIVENESS	8	265
DEFLAGRATION RATE, MODELING	7	175	SENSITIVITY AND PERFORMANCE DATA, SDDT	8	1132
DENSITY, D, CD, EXPERIMENTAL PRESSURE	3	376	SENSITIVITY WITH AMMONIUM NITRATE	7	804
DENSITY, SHOCK & PARTICLE VELOCITIES	4	245	SHOCK COMPRESSION THROUGH INERT, DDT	3	813
DETONABILITY IN PROPELLANTS & EXPLOSIVES	3	637	SHOCK FRONT VELOCITY IN VACUUM	4	176
DETONATION BEHAVIOR OF LIQUID	2	439	SHOCK TEMPERATURE IN MODEL	7	463
DETONATION DECAY VELOCITY	1	15	SHOCK WAVE TRANSMISSION THROUGH AL	1	90
DETONATION PARAMETERS, CHINESE TEST	8	440	SHOCK-INDUCED PHASE CHANGE	5	257
DETONATION PROPAGATION DATA, GAP TEST	6	40	SHOCKED, HEAT-SENSITIVE FILM RECORD	7	973
DETONATION PROPERTIES, CARBON EOS	8	528	SINGLE-CRYSTAL TESTS, PROPERTIES	2	470
DETONATION TEMPERATURE, PYROMETER	8	574	SLURRY, CALCULATED BLASTING PERFORMANCE	8	987
DIAMETER-EFFECT PARAMETERS	6	647	SNOW-FLAKED PACKED, CJ PRESSURES	2	380
DIRECT-CONTACT DETONATION SENSITIVITY	4	406	TEMPERATURE, MEASURED AND CALCULATED	8	558
DROP-WEIGHT IMPACT TEST	3	6	THERMAL DECOMPOSITION AT P = 10-50 kbars	5	331
DURAL, U <sub>10</sub>	2	333	THERMAL DECOMPOSITION OF CONFINED HE	6	214
EMV GAUGE, DETONATION PRESSURES & TIMES	5	413	THERMAL INITIATION AND GROWTH	5	280
ENERGY vs REACTION RESPONSE	6	3	TIME DELAY vs TEMP RECIPROCAL, DECOMP	3	67
ENERGY vs REACTION RESPONSE	6	7	TNT/TNM, ELECTRICAL TRANSDUCER STUDIES	4	609
EOS AND THERMAL DECOMPOSITION RATE	3	352	UNCONFINED CYLINDER, TEST, 2DL MODEL	5	313
EXPLODING-FOIL SENSITIVITY EFFECT	7	928	UNDERWATER SHOCK-TO-BURN TESTS	4	489
EXPLOSIVELY DRIVEN METAL, MODEL	8	610	WAVE CURVATURE vs CHARGE LENGTH, L/d < 3	2	504
GAS POCKETS IN LOW-VELOCITY DETONATION	2	584	WAX-GAP TEST	1	23
HUGONIOT CURVES AND SOUND VELOCITIES	4	235	ZND PROOF, INDUCTION/CHEMICAL REACTION	2	358
HUGONIOT DATA FOR UNREACTED EXPLOSIVE	5	251	TNT-LOADED EBW INITIATION	4	452
TNT, HUGONIOTS, DERIVATIVES ALONG SHOCK PATH	6	791	TNT/AN + AL, DETONATION PRODUCTS ANALYZED	8	577

B. Topic Phrase Index (continued)

SUBJECT	SYM	PAGE	SUBJECT	SYM	PAGE
TNT/AN, DIAMETER EFFECT, D vs 1/d, LIMIT DATA	4	182	UNDERWATER SENSITIVITY TEST, HOT SPOTS	7	973
V-d CURVES, WAVE SHAPE vs d, KINETICS	2	733	UNDERWATER SHOCK, INITIATION TO BURN	4	487
TNT/NQ (N <sub>2</sub> O) + Al, DETONATION PRODUCTS	8	577	METHODS	3	795
TNT/NQ/WAX, GAP TEST RESULTS	8	228	MOLECULAR SUBIGNITION TESTS	8	725
TNT/RDX/WAX, RUNUP DISTANCE AND GAP TEST	7	336	PRESSURE P <sub>1</sub> vs R/R <sub>0</sub>	6	587
TNT/SALT MIXTURES, QUENCHING EFFECT OF SALT	2	509	WAVES FROM PENTOLITE	4	27
TNT/WAX, GAP TEST RESULTS	8	228	UNDERWATER TESTS, ANFO, NONIDEAL DETONATION	3	315
TNT, BURN RATE, SENSITIVENESS, Q, m x Q	2	651	UNSTEADY & REGULAR MACH REFLECTION, WATER	6	570
TOODY MODEL, NITROMETHANE FAILURE	7	609	UNSTEADY 1D SHOCK WAVES IN SOLID HE	3	535
TORCHING EXPERIMENTS, SIMULATIONS	8	215	UNSTEADY CONDENSATION 3D SHOCKS, JET FORMED	2	304
TORPEX 2B, SENSITIVITY AND EXPLOSIVENESS	8	265	UNSTEADY DETONATION GROWTH, SOLID HE	3	534
TORPEX, LOW-ORDER REACTIONS--REACTION ZONE	4	462	UNSTEADY FLOW EQUATIONS, EULERIAN, LAGRANGIAN	6	582
TRANBA SUBROUTINE TO RUBY PROGRAM, ISENTROPES	4	168	UNSTEADY FLOW, PLANE, LAGRANGIAN EQUATIONS	3	213
TRANSDUCER STUDIES, INITIATION OF LIQUID HE	4	609	UNSTEADY MOTION OF PERFECT FLUID, 1D MODEL	4	503
TRANSIENT COMBUSTION PROCESS, MODEL	8	940	UNSTEADY SHOCK PROPAGATION IN REACTIVE MEDIA	4	502
TRANSIT TIMES = SOUND SPEEDS & INITIAL SLOPES	4	240	UP, PROPERTIES OF COMPOUNDS	6	450
TRANSIT TIMES IN HE CHARGES, PIN METHOD	2	136	URANIUM, CONICAL IMPLOSION, VAPORIZATION	5	547
TRANSITION PRESSURES AND SLOW BURN	3	85	UV-IRRADIATED HMX, SHOCK TRANSIT TIME	8	847
TRANSMISSION & GROWTH OF DETONATION	2	620	VACUUM DETONATION, TNT/NQ AND TNT/AN	8	579
TRANSPARENT ANVIL, DROP WEIGHT APPARATUS	8	635	VACUUM GAP TEST SETUP	7	5
TRANSPARENT LIQUID-HE OPTICAL EMISSION	8	15	VACUUM, EXPLOSIVES, FRONT VELOCITIES	4	176
TRANSPORT MODEL, SLIC METHOD, ADVECTED	7	696	VAPORIZING URANIUM AFTER SHOCK LOADING	5	547
TRANSPORT PHENOMENA, DETONATION WAVE EFFECT	3	537	VELOCITIES, D & PLASMA, vs OXYGEN BALANCE	3	192
TRANSPORT-CONTROLLED REACTION, MODEL	7	521	DETONATION & DEFLAGRATION, PROBE	4	616
TRANSVERSE DISPLACEMENT TEST SETUP	2	637	VELOCITY RECORD, OSCILLOGRAPH TRACE, PETN	1	13
TRANSVERSE WAVE EFFECTS, CONDENSED HE, PHOTOS	6	414	VELOCITY vs CURVATURE RADIUS, DETONATION WAVE	2	424
TRAPEZOIDAL PRISM SHOT ASSEMBLY, PBX 9502	8	373	VELOCITY-DIAMETER DEPENDENCE, CRITICAL DIAM	6	344
TRAUZL TEST, METHYL NITRATE SENSITIVITY	5	268	VELOCITY-DIAMETER PREDICTED RELATIONSHIP	7	589
TRINITROANILINES, EPR SPECTRUM	8	746	VELOCITY-PRESSURE DATA, AQUARIUM TESTS	5	65
TRINITROAROMATICS, UV & THERMAL DECOMPOSITION	8	742	VENTING BY ORIFICE FLOW, DEFLAGRATION MODEL	7	175
TRINITROMETHYL COMPOUNDS	7	90	VIBRATING SOLID, PARTITION FUNCTION	2	406
TRINITROMETHYL COMPOUNDS, IMPACT TESTS, OB/100	3	675	VICKERS HARDNESS TEST, RDX DEFORMATION	7	977
TRIPLE SPHERE, WAVE FORMS, VELOCITIES	8	89	VISAR, DIAL-DELAY LEG, DIGITAL RECORDERS	6	669
TRIPLE-WAVE INITIATION MODEL, INSENSITIVE HE	7	373	ELECTRONIC STREAK CAMERA RECORD	8	468
TRITONAL & HBX, VELOCITY-DIAMETER CURVES	2	737	MULTIPLE RELEASE RATES, UNLOADING	7	857
TRITONAL, GAP TEST RESULTS	8	228	PARTICLE VELOCITY, HE/WINDOW INTERFACE	8	16
HUGONIOT DATA FOR UNREACTED HE	5	251	PARTICLE VELOCITY-TIME RECORDS FOR CP	7	871
TTF, LIQUID HE, CHARACTERIZATION	6	469	vs EMBEDDED GAUGE vs REACTIVE FLOW	8	955
TUBE-WALL MOTION, FLASH X-RAY PHOTOGRAPH	7	799	VISAR-MEASURED WAVEFORMS	7	402
TUNGSTEN STRIKERS, OSCILLOSCOPE TRACES	2	562	VISCOPLASTIC MODEL, HOT SPOTS IN SHOCKED HE	7	435
TUNGSTEN, SHOCK WAVE vs PARTICLE WAVE VELOCITY	7	831	VISCOPLASTIC WORK, COLLAPSING CAVITIES	8	68
TURBULENCE EFFECTS ON GAS DETONATION IN TUBES	2	255	VISCOSITY & HEAT TRANSFER EFFECTS IN CODES	3	803
TWO-DIMENSIONAL INITIATION MODEL	7	316	VISCOSITY EFFECT IN GROWTH OF DETONATION	3	534
TWO-DIMENSIONAL SHOCK WAVE VELOCITY	8	89	VISCOSITY EFFECT, DETONATION WAVE THEORY	7	795
ULTRACENTRIFUGE TESTS, FRACTURE RESULTS	8	243	VISCOSITY vs TEMPERATURE, 3 LIQUID HEs	6	470
ULTRASONIC MEASUREMENT OF D & TEMP	1	31	VISCOUS HEATING, EFFICIENT FOR SHOCK CONDITION	8	68
ULTRASONIC WAVE VELOCITY, ELASTIC MODULI, PETN	6	396	VLW EOS, CJ CALCULATIONS FOR CHNO EXPLOSIVES	8	796
ULTRASONIC WELDING HAZARD	7	43	COMPARISON WITH BKW AND LJD	8	796
ULTRAVIOLET LIGHT INITIATION OF AZIDES	2	547	VOID & GAS BUBBLE EFFECTS, SURFACE REACTION	3	518
UNCONFINED TNT CHARGES, FINAL VELOCITIES	3	339	VOID COLLAPSE MODEL, SHOCK INITIATION	7	506
UNDERWATER DEFLAGRATION, LEAD AZIDE CRYSTALS	5	305	VOID MODEL, DYNAMIC COMPACTION PROCESS	8	929
UNDERWATER DETONATION, ACOUSTIC HALF-SPACE	5	493	VOID VOLUME EFFECT, SURFACE REACTION MECHANISM	4	402
ARTIFICIAL VISCOSITY	5	597	VOIDS, DECREASED VELOCITY AND PRESSURE	2	629
BUBBLE EXPANSION	6	540	VOLUME & PRESSURE DEPENDENCE, KINETICS OF HE	6	305
DENSITY EFFECTS	6	561	VON NEUMANN DETONATION THEORY, 2D EXTENSION	2	424
SPHERICAL INTERACTION	5	581	VON NEUMANN MODEL, ANALYSIS & PROOF	2	312
SURFACE BURST MODEL	5	493	VON NEUMANN SPIKE, CJ CONDITION	1	107
UNDERWATER EXPLOSIONS, BUBBLE EFFECTS	1	8	DENSITY, ESTIMATING	4	78
SHOCK WAVE EFFECTS	6	561	IN PRESSURE-TIME CURVE	3	249
SIMPLE ANALYSIS	6	502	OXIDATION REACTION ZONE	2	212
SPHERES. CALIBRATION	5	599	PRESSURE, PMMA DISKS ON HE	4	244
UNDERWATER EXPLOSIVES, OPTIMIZING FLOW	6	551	VON NEUMANN-RICHTMEYER Q METHOD IN HYDROCODE	3	226
UNDERWATER GAP TEST, CALIBRATION, PBX 9205	5	599	VON NEUMANN-RICHTMEYER Q METHOD, 1D, 2D MODELS	3	723
UNDERWATER HE USE, SHOCK WAVE & BUBBL:	1	107	VOY PROPELLANT IN DDT STUDIES	7	146

## B. Topic Phrase Index (Continued)

SUBJECT	SYM PAGE	SUBJECT	SYM PAGE
WALKER-WASLEY CRITERION, FLYER PLATE IMPACT	8 1093	WOOD-KIRKWOOD DIAMETER EFFECTS	2 424
WALL TRACES OF DETONATION, NM, TEST METHODS	5 105	WOOD-KIRKWOOD EQUATIONS, CURVATURE EFFECT, D	4 86
WALL VELOCITIES CALCULATED FROM FIT TO DATA	6 518	WOOD-KIRKWOOD RESULTS, DIAMETER EFFECTS STUDY	6 651
WATER, ISENTROPES & ISOTHERMS, CALCULATED	4 30	WOOD-KIRKWOOD THEORY EXTENDED, 2D DETONATION	7 589
SHOCK PRESSURE vs SHOCK VELOCITY	3 369	X-0204, CYLINDER TEST RESULTS	4 5
WATER-CONTROL TESTS, PRECURSORS IDENTIFIED	5 81	X-0219, 2D. WAVE PROPAGATION, MODEL vs DATA	6 411
WAVE CURVATURE FILM, WAVE TRACE	2 446	FRONT CURVATURE, REACTION ZONE LENGTH	6 650
WAVE CURVATURE INCREASE, REACTION ZONE WIDTH	6 405	WAVE SURFACE CURVATURE EFFECTS	6 379
WAVE CURVATURE MEASUREMENT METHOD, LIQUID TNT	2 443	X-0233, TUNGSTEN-LOADED HMX, DETONATION TESTS	8 979
WAVE CURVATURE vs DIAMETER & DENSITY, IDEAL HE	2 500	X-0290, DIAMETER-EFFECT PARAMETERS	6 647
WAVE DIAGRAMS, SPALLING CALCULATIONS	6 482	FAILURE RADII, DATA & MODEL	6 412
WAVE FRONT PATTERNS, IMPACTING PLATES, DIAGRAM	5 576	<sup>13</sup> C PHOTO, INITIATION ON BACK FACE	6 667
WAVE FRONT SOLUTION, NONIDEAL 1D MODEL	8 1026	PARTICLE VELOCITIES, MAGNETIC PROBE	6 637
WAVE PROPAGATION, 2D HETERO- & HOMOGENEOUS	6 405	X-0319, COMPOSITION, DENSITY	7 567
AFTER SHOCK INITIATION, x-t	3 306	X-0320, COMPOSITION, DENSITY	7 567
ELASTIC-PLASTIC MATERIALS	4 295	X-0321, COMPOSITION, DENSITY	7 567
SINGLE CRYSTALS, PETN	6 397	X-0341, COMPOSITION, DENSITY	7 567
WAVE REFLECTIONS IN TARGET, COMP B/Al	2 368	X-0342, COMPOSITION, DENSITY	7 567
WAVE SHAPE EFFECTS FROM INERT ADDITIVES	2 508	X-0343, COMPOSITION, DENSITY	7 567
WAVE SHAPE MEASUREMENTS IN ALUMINIZED HE	2 739	X-0344, COMPOSITION, DENSITY	7 567
WAVE SHAPE vs PARTICLE SIZE, d, NONIDEAL	2 512	TENSILE PROPERTIES	8 637
WAVE STRUCTURE, ROTATING-MIRROR CAMERA	5 97	X-0407, DETONATION REACTION ZONE STUDY	8 123
WAVE SURFACE CURVATURE EFFECTS, SHOCK WAVES	6 379	X-RAY ABSORPTION PHOTOMETER, DETONATION TUBE	2 188
WAVE VELOCITIES, ULTRASONIC, ELASTIC MODULI	6 396	X-RAY INITIATION OF AZIDES	2 565
WAVE VELOCITY-ELASTIC STIFFNESS MODULUS	6 398	X-RAY PHOTOELECTRON SPECTROSCOPY (XPS)	8 243
WAVEFORM RECORDS, CONDUCTANCE, FLAT PROBES	4 598	X-RAY PHOTOELECTRON SPECTROSCOPY (XPS)	8 725
WAVEFORMS, PBX 9404 MODELS AND TESTS	8 932	X-RAY TOPOGRAPHY, LIF STRAIN FIELDS	7 982
WAX, DESENSITIZING AGAINST CAVITY INITIATION	2 681	X2 (HMX), EOS CALCULATION	8 751
EFFECTS ON SENSITIVITY	7 336	XDT DEFINITION, REACTIONS	7 265
EFFECTS ON SENSITIVITY OF HMX/wax COMPAC	4 399	XDT REACTION, INSTRUMENTED SHOTGUN TESTS	7 301
WAX-GAP SENSITIVITY TEST, NOL, SETUP & DATA	1 22	THRESHOLD VELOCITIES	7 259
WC 231, DOUBLE-BASED PROPELLANT, DDT STUDY	8 658	XDT, ANFO, DOUBLE-PIPE TEST	8 390
WCA SELF-CONSISTENT EOS MODELS	8 521	DISTANCE TO DETONATION DATA	8 888
WCA THEORY, SIMPLIFIED IN BKW-EOS	7 704	PROPELLANTS, RAREFACTION, AND COMPACTION	8 284
WCA4 EOS, CJ CALCULATION, CHNO EXPLOSIVE	8 751	XENON ARC IMAGE FURNACE, PROPELLANT STUDY	7 217
INTERMOLECULAR POTENTIALS	7 703	XPS SPECTRA, RDX, TNT, AP, TAB	8 728
WCA4-CALCULATED CJ PRESSURE	7 716	XPS, HE REACTION PRODUCT, SUBIGNITION REGIME	8 725
WEAK CONDENSATION DETONATIONS, GAS FLOW	2 295	XTX-8003, DIAMETER-EFFECT PARAMETERS	6 647
WEAK DETONATION SOLUTION, TAYLOR, FRIEDRICHS	2 304	YAG LASER, TEMPERATURE BEHIND SHOCK WAVE	7 1010
WEDGE EXPERIMENTS WITH NM, TNT	6 13	YIZUM, 1D LAGRANGIAN INITIATION MODEL	7 506
WEDGE TEST, BRASS-PETN, 2.5-kbar INITIATION	3 563	Z-TACOT, DETONATION PROPERTIES, CARBON EOS	8 528
DATA, BETTER	4 234	ZELDOVICH REACTION ZONE, PRESSURE vs DISTANCE	1 46
NEW, NO CONFINEMENT EFFECT	8 372	ZELDOVICH-von NEUMANN PRIORITY CLAIM	1 105
NO RETONATION, CAMERA RECORD	3 504	ZERO-PRESSURE LIM OF HUGONIOT vs SOUND SPEED	4 344
PARAMETERS & SETUP, DATB, (NOL)	3 770	ZEROTH-ORDER INTERNAL STRUCTURE, SOLID HE	7 686
PLANE WAVE, SCHEMATIC	5 221	ZND DETONATION SPIKE POINT, NM STUDY	7 610
SETUP, STREAK CAMERA RECORDS	8 905	ZND MODEL, CHEMICAL REACTION ZONE	7 369
VELOCITY vs TIME, H <sub>2</sub> -O <sub>2</sub> MIXES	2 270	CHEMICAL REACTION ZONE	7 641
WEDGE TESTS & RATE STICKS, HMX/AP/Al	7 620	CHINESE DETONATION RESEARCH	7 795
WEIERSTRASSIAN ELLIPTIC FUNCTION, FLOW CALC.	4 16	PARTICLE VELOCITY HISTORIES	7 488
WELDING, JETLESS & JET FORMING WITH SHEET HE	4 499	SHOCK AMPLITUDE EVOLUTION	6 382
WG2 & 4, MMAN SENSITIVE WATERGELS	6 546	STEADY DETONATION REACTION	7 531
WHITHAM'S METHOD, PROPAGATING SHOCK WAVES	4 145	ZND PRESSURE, NITROMETHANE MIXTURES	7 586
WHITHAM'S RULE, EXTENDED, UNDERWATER BLASTS	6 502		
WIDE-RANGE VELOCITY INTERFEROMETER	6 673		
WIEN'S RADIATION EQUATION, DETONATION TEMP	2 157		
WILKINS EOS, MODIFIED, DIP BELOW CONSTANT GAMMA	4 54		
WILKINS FORM OF EOS, DIP IN CJ ADIABAT	4 24		
WIRE BRIDGE IN EBW INITIATOR	4 450		
WITNESS FOAM, CJ CONDITIONS IN FOAMED PETN	6 188		
WITNESS PLATE DENT FROM PRISM TEST	8 374		
WITNESS PLATES, HIGH-DENSITY EFFECTS ON TESTS	5 47		
WONDY MODEL, NITROMETHANE FAILURE	7 609		
WONDY, 1D LAGRANGIAN MODEL, SHOCK & RAMP	7 394		

# C. AUTHOR INDEX

## Alphabetically

NAME	SYM	PAGE	NAME	SYM	PAGE
ABLARD, J. E.	1	88	BACONIN, J.	8	159
ABOUSEIF, G. E.	6	502	BAHL, K. L.	7	325
ADAMS, G. K.	4	502		8	1045
ADENIS, J. C.	8	892	BAILEY, W. A.	4	14
ADOLPH, H. G.	7	84		7	678
	7	952	BARDO, R. D.	7	93
AGNEW, S. F.	8	715		8	855
AKST, I. B.	5	59	BARKER, M. A.	8	262
	6	499	BARLETT, R. H.	6	755
	7	548	BASSET, J. F.	8	262
	8	1001	BATHELT, H.	8	577
ALLAN, J. W. S.	4	14	BAUER, P.	7	768
	4	52		8	762
ALLISON, F. E.	3	112	BAUTE, J.	8	521
ALSTER, J.	3	693		8	751
AMERY, B. T.	6	673	BDZIL, J. B.	6	352
AMSTER, A. B.	3	584	BEAN, C. M.	3	1
	4	126	BEATRIX, P.	4	527
ANDERSEN, W. H.	4	205	BEAUREGARD, R.	3	584
	5	67	BECKSTED, M. W.	6	258
	6	682		7	143
	7	459	BEEDHAM, K.	5	279
ANDERSON, A. B.	7	385	BELANGER, C.	8	361
ANDERSON, G. D.	4	213	BELCHER, R. A.	7	678
ANDERSON, R. D.	7	198	BELGAUMKAR, B. M.	6	267
ANDERSSON, B.	4	602	BENHAIM, P.	6	195
ANDREWS, G.	8	99	BENJAMIN, K. J.	8	1139
ANTIPENKO, A. G.	6	143	BENNET, A. L.	2	251
ARBUCKLE, A. L.	7	1055	BERKE, J. G.	5	89
	8	307		5	237
	8	943	BERNECKER, R. R.	6	426
ARGOUS, J. P.	4	135		7	119
ARMSTRONG, R. W.	7	976		7	843
ARNOLD, W.	8	1131		8	658
ASABA, T.	8	168		8	881
ASELTINE, C. L.	7	986	BERNIER, H.	4	381
ATWOOD, A. I.	7	216	BERNSTEIN, D.	3	88
AUSTING, J. L.	3	396	BI, Z.	8	93
	5	47	BIRD, R.	8	1035
	6	183	BJARNHOLT, G.	5	115
AVEILLE, J.	8	151		6	510
	8	159		6	540
	8	815		8	1069
	8	892	BLAIS, N. C.	8	701
AVILES, J. B.	7	50	BLAKE, T. G.	2	711
AVRAMI, L.	5	351	BLOMMER, E. J.	7	299
	6	389	BLOOM, G.	8	3
AYALON, D.	8	1126		8	1045
AZIZ, A. K.	3	205	BLOOMQUIST, D. D.	7	1004
BACONIN, J.	8	151	BOAT, R.	6	729

### C. AUTHOR INDEX (Continued)

NAME	SYM	PAGE	NAME	SYM	PAGE
BOGGS, T. L.	7	216	CALZIA, J.	5	231
	8	934	CAMARCAT, N.	8	815
BOISARD, F.	7	1010	CAMERON, I. G.	4	305
BONGRAIN, P.	8	159	CAMPBELL, A. W.	2	136
BONTHOUX, F.	7	408		2	454
BORDZILOVSKY, S. A.	7	362		2	478
	8	143		3	469
	8	196		3	499
BORGARDT, F. G.	6	389		6	642
BORISOV, A. A.	6	250		7	566
	7	435		7	624
BOUCHON, H.	4	527		8	1057
BOURIANNES, R.	7	768	CARABIN, H.	5	231
BOWDEN, F. P.	2	561	CARION, N.	8	151
BOWMAN, A. L.	7	479		8	159
BOWSER, M.	2	157	CARLSON, L. A.	6	460
BOYD, T. J.	2	136	CARMEL, Y.	8	1126
	2	151	CARPENTER, J. H.	4	167
	4	639	CARPER, W. R.	7	75
BOYLE, V. M.	3	520	CATALANO, E.	6	214
	4	241	CHAIKEN, R. F.	3	304
	5	251		4	461
	6	11		6	344
	7	906	CHAISSÉ, F.	7	602
BRACONNIER, J. C.	8	337		7	686
BRANDON, W. W.	3	822		8	159
BREITHAUP, D.	8	613	CHAMBERS, E. S.	7	256
BRINKLEY, S. R.	1	72	CHAN, S. K.	7	589
BRITT, A. D.	8	734	CHANG, L. M.	7	175
BROCHET, C.	5	41	CHAUDHRI, M. M.	5	301
	6	124		7	735
	7	583	CHAWLA, M.	6	325
	7	768	CHEN, P. J.	6	379
	8	425	CHERET, R.	4	78
	8	762		5	31
BROOM, V. C.	4	462		5	41
BROSSARD, J.	5	41		5	567
BROSSE, J. M.	7	965		7	602
BROWN, B.	7	256		7	686
	7	299		8	425
BROWN, W. B.	8	770		8	815
BRUNAUER, S.	1	3	CHERVILLE, J.	7	65
BURCAT, A.	6	590	CHESELSKE, F. J.	4	461
BURROWS, K.	6	625	CHEUNG, H.	6	729
BURT, M. W. G.	8	1035	CHEVALIER, Y.	4	527
BURTON, J. T. A.	7	759	CHHABILDAS, L. C.	8	274
BUSCO, M.	5	513	CHIARITO, M. A.	8	645
BUTCHER, A. G.	7	143	CHICK, M. C.	4	349
BUTCHER, B. M.	4	295		7	352
BUTLER, P. B.	8	962		8	318
CACHIA, G. P.	3	1	CHILES, W. C.	6	664
	4	512		6	723
CADY, H. H.	6	700		8	422

### C. AUTHOR INDEX (Continued)

NAME	SYM PAGE	NAME	SYM PAGE
CHILVERS, D. K.	6 625	CRAIG, B.G.	5 321
	7 678		8 228
CHIRAT, R.	7 703	CRAMER, J. P.	6 466
	8 521	CROMER, D. T.	8 839
	8 751	CROSNIER, J.	4 627
CHRISTENSEN, L. W.	6 258	CRUYSBERG, E. E. A.	6 299
CHUNG, W. K.	7 343	CUDAK, C. A.	8 962
	8 805	CULLEN, R. E.	2 266
CLAIRMONT, A. R.	6 426	CUMMING, I. G.	2 601
	7 119	CURTIS, W. D.	7 466
	7 843	DAMAMME, G.	7 634
	8 658		7 641
CLARK, E. N.	3 833	DAVID, F.	4 381
CLAY, R. B.	3 150		5 567
COBURN, M. D.	6 460	DAVIDSON, N.	2 216
COFFEY, C. S.	7 970	DAVIES, F. W.	6 389
	8 62		6 740
	8 725	DAVIS, L. P.	7 75
COLE, J. E.	7 164	DAVIS, W. C.	3 469
COLEBURN, N. L.	3 761		3 499
	4 240		4 84
	5 523		5 3
	5 581		5 13
COLEY, G. D.	6 290		5 599
	7 17		6 637
	7 278		6 664
	8 380		7 531
CONNER, J.	8 262		7 958
COOK, M. A.	2 500		8 422
	2 519		8 785
	2 733	DE BEAUMONT, P.	5 547
	3 150	DE LONGUEVILLE, Y.	6 105
	3 184		7 408
COOK, M. D.	8 827		7 540
COON, C. L.	7 940		7 560
COOPER, J. C.	2 157		8 596
COURTNEY-PRATT, J. S.	2 168	DE LUCA, L.	6 281
	2 547	DEAL, W. E.	2 327
COWAN, R. D.	2 383		3 386
COWPERTHWAIT, M.	4 502		4 321
	5 427	DEFFET, L.	4 156
	6 162	DEFORNEAUX, M.	5 457
	6 231	DEHN, J. T.	8 602
	6 786	DELCLOS, A.	7 560
	7 225		8 902
	7 466	DELPUECH, A.	7 65
	7 498		8 847
	7 1072	DENEUVILLE, P.	7 151
	8 111		7 408
	8 1025		7 540
COX, M.	7 624	DENG, Q.-N.	8 93
COYNE, P. J.	8 645	DERR, R. L.	7 216
CRAIG, B. G.	4 84	DERRIEN, J. C.	7 151

### C. AUTHOR INDEX (Continued)

NAME	SYM	PAGE	NAME	SYM	PAGE
DESOYER, J. C.	5	403	ENIG, J. W.	3	534
DEWEY, J. M.	1	9		4	395
	2	612		5	99
DICK, J. J.	7	620		6	570
DIETZEL, R. W.	6	455	ERICKSON, L. M.	7	1062
	8	485		8	3
DINEGAR, R. H.	6	460		8	951
DING, J.	7	795		8	1045
	8	83	ERIKSON, T. A.	3	24
	8	93	ERKMAN, J. O.	3	253
	8	440		4	277
DONGUY, P.	7	695		5	477
DOREY, R. C.	7	75		6	426
DOROUGH, G. D.	3	738		6	766
	4	477	ERMOLAEV, B. S.	6	250
DORSEY, T. M.	8	1139		7	435
DOWNES, D. S.	6	390	ERVIN, L. H.	5	251
DREMIN, A. N.	5	399		6	3
	6	29	EVANS, M. W.	4	359
	6	143		5	89
	7	789	EYRING, H.	1	93
	8	678	FAGAN, P.	2	151
DRIMMER, B. E.	3	706	FAHRENBRUCH, A. L.	4	213
	3	761	FAIR, H. D.	6	390
DROLET, J. F.	8	361	FARAG, S. A.	6	502
DU PLESSIS, M. P.	8	390	FAUQUIGNON, C.	4	39
DUFF, R. E.	2	343		4	381
	4	198		5	361
DUFORT, S.	8	847		6	105
DUVALL, G. E.	4	248	FENG, K. K.	7	343
DYER, A. S.	5	279		8	805
	5	291	FICKETT, W.	2	383
	7	1040		5	3
	8	211		7	448
EADIE, J.	4	399	FIELD, J. E.	5	301
ECKSTEIN, A.	7	721		7	24
EDEN, G.	4	573		8	635
	5	467	FIFER, R. A.	7	164
	6	477	FILLER, A. S.	2	733
	7	678	FILLER, W. S.	6	777
EDWARDS, D. J.	5	413		8	207
	6	766	FINGER, M.	4	3
EDWARDS, J. C.	6	344		5	137
EICHLER, T. V.	5	313		5	503
EIDELMAN, S.	6	590		6	710
EK, S.	6	272		6	729
ELBAN, W. L.	7	843		7	940
	7	976		8	1018
	8	645	FLAUGH, H. L.	7	566
	8	725	FLEMING, K. A.	8	1035
ELLIOT, L. A.	4	316	FOAN, G. C. W.	7	278
ELSON, R. E.	6	466	FORBES, J. W.	7	308
ENGELKE, R.	6	642		8	725

## C. AUTHOR INDEX (Continued)

NAME	SYM PAGE	NAME	SYM PAGE
FORBES, K.	8 228	GREEN, L. G.	4 86
FOREST, C. A.	7 234		4 477
	7 479		6 755
	8 52		7 256
FOSSE, C.	4 156		7 273
FOSTER, J.	8 228		7 887
FOWLES, G. R.	4 213		8 284
FRANKEL, M. J.	7 523		8 587
	7 970	GREIFER, B.	2 281
FREUND, H. V.	6 521	GREINER, N. R.	8 715
FREY, R. B.	6 11	GRIEF, D.	8 380
	6 325	GRIFFITHS, N.	4 462
	7 36	GROOCKOCK, J. M.	2 529
	7 247	GROOTHUIZEN, T. M.	6 299
	7 1048	GROSS, S. B.	7 843
	8 68	GROUX, J.	8 431
	8 318	GUIDRY, M.	6 710
FRITZ, J. N.	5 447	GUIGUIS, R. H.	6 502
FU, X.	8 89	GUNGER, M.	8 228
FUJIWARA, S.	5 267	GUNN, S. R.	4 167
	6 133	GUO, Y.	8 1011
	6 450	GURTON, O. A. J.	2 582
	8 993	GUY, L. R.	7 107
FULLER, P. J. A.	4 290	GVISHI, M.	8 1126
FUNK, A. G.	3 184	GYTON, R.	6 625
FYFE, R. R.	6 466	HACKETT, A.	8 187
GARDNER, S. D.	4 154	HAEFFELE, B.	7 721
GAUDIN, C.	7 540	HAGAN, J. T.	7 735
	7 560	HALLECK, P. M.	6 20
GEIGER, W.	6 521	HALLOUIN, M.	5 403
GEY, W. A.	3 813	HALLQUIST, J. O.	7 488
GIBB, A. W.	8 409		8 951
GIBBONS, G.	8 294	HALPIN, W. J.	4 222
GIBSON, F. C.	1 12	HAMPTON, L. D.	2 620
	2 157	HAN, C.	8 567
	2 281	HANTEL, L. A.	5 599
	3 436	HARDESTY, D. R.	6 47
	4 117	HARDY, J. R.	7 777
	4 412		8 864
GIDDINGS, J. C.	2 404	HARLAN, J. G.	7 930
GILKERSON, W. R.	2 216	HART, S.	4 47
GIMENEZ, P.	8 596	HARTLEY, J. E.	4 538
GINSBERG, M. J.	7 385	HARVALIK, Z. V.	3 842
GITTINGS, E. F.	4 373	HASKINS, P. J.	8 211
GLOVER, D. J.	8 725		8 827
GOLDSTEIN, S.	7 1016	HASMAN, E.	8 1126
	8 979	HATT, D. J.	7 352
GOLIGER, J.	6 195	HAUVER, G. E.	3 241
GOODALE, T. C.	6 231		5 387
GORA, T.	6 390	HAWKINS, A.	5 34
GORDON, W. E.	4 179	HAWKINS, S. J.	7 759
GRAHAM, R. A.	4 222	HAY, J. E.	4 412
	5 369		5 81

### C. AUTHOR INDEX (Continued)

NAME	SYM	PAGE	NAME	SYM	PAGE
HAY, J. E.	5	559	HU, D.	8	93
	6	115	HUANG, Y. K.	7	1055
	7	373		8	307
HAYES, B.	3	139		8	943
	4	595	HUANG, Z.	8	83
	5	447		8	440
	6	710	HUBBARD, P. J.	7	1040
	6	729		8	211
	7	1029		8	262
HAYES, D. B.	6	76	HUDGINS, H. E.	7	175
	6	668	HUILING, L.	8	440
	6	748	HULL, J. A.	2	136
HE, X.	8	567	HUMPHREY, J.	7	425
HELD, M.	6	225	HURWITZ, H.	3	205
	7	751		6	528
	8	330	HUTCHINSON, C. D.	8	211
HELM, F. H.	6	710		8	1105
	6	729	IGEL, E. A.	2	439
	7	940		7	865
HEMSING, W. F.	8	468	IIDA, M.	8	993
HERSHKOWITZ, J.	4	168	INGRAM, G. E.	5	369
	6	439	JACKSON, R. K.	6	653
	7	175		6	755
	7	898	JACOBS, S. J.	1	52
	7	914		2	358
HESS, W. R.	3	42		3	784
HEUZE, O.	8	762		5	413
HEYBEY, W. H.	2	295		6	305
HICKS, A. N.	6	551		7	970
HIKITA, T.	8	558	JACQUES, L.	5	457
HILLYER, R. M.	4	449	JACQUESSON, J.	4	627
HOFER, W. W.	6	755		5	403
HOFFSOMMER, J. C.	8	725		6	151
HOLLAND, T. E.	2	454	JAFFE, I.	3	584
HOLMBERG, R.	6	540	JAMES, E.	2	119
HOLMES, W. I.	5	279		3	327
HONCIA, G.	6	521		4	86
HONODEL, C.	7	425		7	256
HOOPER, G.	7	759		7	887
HORIE, Y.	4	248		8	284
HORNIG, H. C.	4	3	JAMES, R. M.	6	489
	5	137	JAMESON, R. L.	3	120
	5	503		4	241
	6	710		5	34
HOSKIN, N. E.	4	14	JENSEN, R. C.	7	299
	5	501	JERBERYD, L.	7	43
	7	811	JIAO, Q.	8	83
HOUSTON, E.	2	343	JING, F.-Q.	7	826
HOWE, P. M.	6	11	JOHANSSON, C. H.	4	435
	7	1048	JOHNSON, C. B.	7	1062
	7	1055	JOHNSON, C. D.	5	47
	8	294	JOHNSON, E. G.	4	584
	8	1150	JOHNSON, J. D.	8	531

### C. AUTHOR INDEX (Continued)

NAME	SYM PAGE	NAME	SYM PAGE
JOHNSON, J. N.	7 1016	KINCAID, J.	7 887
	8 52	KINEKE, J. H.	5 533
JOHNSON, J. O.	6 20	KING, A. J.	6 258
JONES, E.	2 571	KIPP, M. E.	7 394
	2 601		7 608
JONES, E. C.	7 50		8 35
JONES, H. D.	7 716		8 274
JOYNER, T. B.	3 50	KIRBY, I. J.	8 176
JUNG, R. G.	5 191		8 187
JUNK, N. M.	4 92	KIRKHAM, J.	3 1
KAHARA, M.	6 710	KIRKWOOD, J. G.	1 71
KAMAL, M. M.	6 502		1 107
KAMEGAI, M.	5 477		2 312
KAMLET, M. J.	3 671		2 424
	6 305	KISTIAKOWSKY, G. B.	1 45
	6 312		1 105
	7 84		2 187
	7 952		2 198
KANG, S.	8 567	KLEE, C.	7 336
KANTROWITZ, A.	1 79	KLIMENKO, V. Y.	7 789
KARAKHANOV, S. M.	7 362		8 678
	8 143	KOOKER, D. E.	7 198
	8 196	KORNHAUSER, M.	7 834
KARO, A. M.	7 777	KOROTKOV, A. I.	6 250
	8 864		7 435
KASSEL, C.	7 965	KOSIREVA, I. Y.	8 678
KATO, Y.	6 124	KOT, C. A.	5 313
	7 583		6 336
	7 763	KOVACIC, S. M.	7 186
	8 558	KRAMER, P. E.	6 755
KEEFE, R. L.	7 143		7 425
	7 265	KRAVTSOV, V. V.	6 36
KEGLER, W.	4 496	KRIER, H.	8 962
KENDREW, E. L.	3 202	KROH, M.	8 1131
	3 574	KUMAR, M.	7 186
KENNEDY, J. E.	4 449	KUO, K. K.	7 186
	5 435	KURRLE, J. E.	5 503
	6 47	KURY, J. W.	3 738
	6 68		4 3
	6 379		5 137
KERLEY, G. I.	8 540		8 613
KERSHNER, J. D.	7 479		8 902
	8 42	KUSABOV, A. S.	5 105
KEYES, R. T.	2 733	KUSAKABE, M.	5 267
	3 150		6 133
	3 202		6 450
	3 357		8 993
KHASAINOV, B. A.	6 250	KWAK, D.	5 119
	7 435	KYDD, P. H.	2 187
KHRAPOVSKY, V. E.	6 250	KYSELKA, C.	4 404
KIM, K.	7 843	LAMBOURN, B. D.	4 52
	8 926		4 142
KINAGA, K.	3 813		4 538

### C. AUTHOR INDEX (Continued)

NAME	SYM PAGE	NAME	SYM PAGE
LAMBOURN, B. D.	5 501	LIDDIARD, T. P.	4 487
	6 477		7 308
	6 489		7 970
	6 561		8 725
	6 625	LING, R. C.	3 42
	7 811	LISTH, O.	6 204
	8 778	LOBANOV, V. F.	7 362
LANZEROTTI, M. Y. D.	8 243	LOBANOV, V. F.	8 196
LEDERER, R. A.	6 668	LOUIE, N. A.	6 682
LEE, E. L.	4 3	LOWNDS, C. M.	8 390
	5 137	LU, B. C.-Y.	7 343
	5 331		8 805
	5 503	LU, P.	8 460
	6 214	LUDWIG, D.	6 225
	6 710		7 336
	6 729	LUNDBORG, N.	4 176
	7 256		4 432
	7 517	LYMAN, O. R.	8 1080
	7 887	MACEK, A.	3 606
	8 284	MACINTYRE, I. B.	8 318
	8 587	MADER, C. L.	3 725
	8 613		4 394
	8 914		5 177
LEE, L. M.	7 416		6 405
	7 865		7 479
LEE, P. R.	7 1040		7 669
LEE, R. S.	6 653		8 42
	6 755		8 979
	7 425	MALA, J.	7 540
	7 466		7 560
	7 1062		8 625
	8 3	MALIN, M. E.	2 136
	8 1045		2 454
LEEuw, M. W.	8 710		2 478
LEGRAND, J.	5 567	MALLORY, H. D.	2 358
LEGRAND, N.	7 695	MANSON, N.	5 41
LEIBUNDGUT, F.	8 399	MARK, P.	6 390
LEIPER, G. A.	8 176	MARLOW, W. R.	4 426
	8 187	MARSHALL, E. F.	5 321
LEONE, CAPT. N.	4 404	MARSHALL, W. W.	5 185
LEOPOLD, H. S.	5 339		5 247
LEROY, M.	8 815	MASON, C. M.	1 12
LESLIE, W. B.	6 455		2 157
LETHABY, J. W.	4 14		2 281
	5 573		3 436
LEWIS, B.	1 43	MATSUI, H.	8 168
LEYGONIE, J.	5 547	MAURIN, C.	7 151
LI, H.	8 440	MAUTZ, C. W.	2 478
LIANG, Y.	8 83	MAZZELLA, A.	5 351
LIDDIARD, T. P.	3 706	MCDONNELL, J. L.	4 3
	3 761	MCEACHERN, D. M.	4 126
	4 214	MCFADDEN, D. L.	8 1080
	4 240	MCGUIRE, R. R.	6 214

### C. AUTHOR INDEX (Continued)

NAME	SYM	PAGE	NAME	SYM	PAGE
MCGUIRE, R. R.	6	710	NUNZIATO, J. W.	7	608
	7	56	O'BRIEN, J. F.	4	239
	7	940	OCKERT, K. F.	3	822
	8	3		4	96
	8	1018		4	102
MCKNIGHT, C. E.	3	635	OLINGER, B.	6	700
MCLAREN, A. C.	2	561	OPPENHEIM, A. K.	5	119
MCMILLAN, C.	8	613		6	502
MEHLMAN, M. H.	8	864	ORLOW, T.	3	226
MELANI, G.	6	325	ORNELLAS, D. L.	4	3
MENICHELLI, V. J.	6	612		4	167
MENIL, A.	7	1010		6	214
MICHAILJUK, K. M.	7	789		7	940
MICHAUD, C.	7	65	OSTMARK, H.	8	473
	7	965	OWENS, F. J.	8	742
MIGAULT, A.	4	627	PACE, M. D.	8	734
MISSONIER, M.	7	641	PALMER, S. J. P.	8	635
MITCHELL, A.	8	587	PANDOW, M. L.	4	96
MITCHELL, D. E.	6	748		4	102
MOHAN, V. K.	7	373	PARKER, N. L.	6	653
MOHLER, J. H.	7	865		7	1062
MONIZ, W. B.	8	734		8	613
MONTEAGUDO, P.	7	151	PARLIN, R. B.	1	93
MOORE, D. B.	3	88		2	404
MOORE, P. W. J.	6	489	PARTOM, Y.	7	506
MORI, N.	8	558	PARTRIDGE, W. S.	2	733
MORITANI, A.	8	168	PASMAN, H. J.	6	299
MORRIS, C. E.	6	396	PASTINE, D. J.	6	305
MORRISON, R. B.	2	266		7	523
MORVAN, J.	5	429	PASZEK, J.	3	520
MOTTET, A. L.	5	67	PAUL, S.	7	686
MOULARD, H.	6	105	PEARSON, J. C.	4	289
	7	316	PEEK, H. M.	2	231
	8	902	PELLETIER, P.	8	361
MULLER, G. M.	3	88	PENG, G.	8	1011
MUNSON, D. E.	4	295	PENN, L.	6	729
MURRY, W. L.	4	555	PERSSON, A.	7	43
MYERS, T. F.	7	914		8	985
NAIMAN, E.	8	460	PERSSON, G.	6	414
NAMENSON, A. I.	7	50	PERSSON, P.-A.	4	602
NAPADENSKY, H. S.	3	396		5	115
	3	420		5	153
	4	473		6	414
	5	313		8	985
	6	336	PETERS, W. C.	5	559
NEAL, T. R.	6	602	PETRONE, F. J.	4	395
NEEDHAM, C. E.	5	487		5	99
NICHOLLS, J. A.	2	266	PEYRE, C.	4	135
NIDICK, E. J.	6	755		4	566
NIKOWITSCH, P.	6	225	PHILIPART, D. A.	8	447
	7	751	PIACESI, D.	3	226
NUNZIATO, J. W.	6	47		4	153
	7	394	PIKE, H. H. M.	4	305

### C. AUTHOR INDEX (Continued)

NAME	SYM	PAGE	NAME	SYM	PAGE
PILARSKI, D. L.	7	906	RILEY, J. F.	6	740
PILCHER, D. T.	6	258	RINEHART, J. S.	1	31
PIMBLEY, G. H.	7	479		3	285
PINEGRE, M.	8	815	RITCHIE, J. P.	8	839
PINTO, J.	8	243	RIVARD, W. C.	5	3
PIROTAIS, D.	8	337	ROBINSON, N. J.	7	143
PITTION-ROSSILLON, G.	7	703	ROGERS, G. T.	2	547
PITTS, L. D.	4	616	ROGERS, J. W.	7	930
PLANT, J.	4	555	ROMAIN, J. P.	5	403
PLOTARD, J. P.	8	337		6	151
POPE, P. H.	8	635	ROOIJERS, A. J. T.	8	710
POPOLATO, A.	4	233	ROSENBERG, J. T.	6	786
	7	566		7	466
POTAU, J.	4	381		7	1072
POULARD, S.	7	965		8	111
PRATT, T. H.	4	102	ROSLUND, L. A.	5	523
PRESLES, H. N.	7	583		5	581
	8	431	ROTH, J.	1	57
	8	762		5	219
PRESSMAN, Z.	4	126	RYAN, R. R.	8	839
PRICE, C. F.	7	216	SADWIN, L. D.	3	309
	8	934		4	92
PRICE, D.	1	22	SAINT-MARTIN, C.	8	596
	5	207	SAKAI, H.	8	558
	6	426	SAKURAI, A.	5	493
PRICE, J. H.	4	290	SAKURAI, T.	8	558
PROTAT, J. C.	8	815	SAMIRANT, M.	7	139
PROUTEAU, F.	5	567		8	972
PROUTEAU, M.	4	39	SANBORN, R. H.	5	331
PUGH, H. L.	7	75	SANDERS, S.	8	3
PUJOL, J.	4	566	SANDUSKY, H. W.	7	119
PUJOLS, H.	5	429		7	843
PUJOLS, H. C.	8	135		8	658
QUIRK, W.	8	613		8	881
RAINSBERGER, R. B.	7	466	SANG, W.	7	746
RAMSAY, J. B.	3	499	SANTIAGO, F.	8	725
	4	84	SAVITT, J.	2	620
	4	233		3	309
	6	723		3	396
	7	531		3	420
	7	566		4	404
	8	372	SCHALL, R.	4	496
RANDALL, R. R.	5	67	SCHEDLBAUER, F.	8	577
RENLUND, A. M.	8	691	SCHILPEROORD, A. A.	6	371
REE, F. H.	7	646		7	575
	8	501	SCHMIDT, D. N.	4	266
REED, S. G.	2	295	SCHOTT, G. L.	4	67
REESE, B. O.	4	359	SCHULER, K. W.	5	589
REMPEL, J. R.	4	266	SCHWARTZ, F. R.	3	833
RIBOVICH, J.	4	412	SCHWARZ, A. C.	6	62
	5	81		6	668
RICE, J. K.	7	930		7	416
RIGDON, J. K.	5	59		7	1024

### C. AUTHOR INDEX (Continued)

NAME	SYM PAGE	NAME	SYM PAGE
SCOTT, C. L.	5 259	SMITH, L. C.	3 327
SCOTT, F. H.	2 157	SMOLEN, J. J.	5 119
	4 412	SMOTHERS, W. G.	5 251
SCRIBNER, K.	6 466	SOHN, C. H.	8 926
SEARCY, J. Q.	6 62	SOLOMONOVICI, A.	8 1126
	6 455	SONG, J.	8 1011
SEAY, G. E.	3 562	SOREL, J.	8 135
SEEGAR, D. E.	2 711		8 892
SEELY, L. B.	2 439	SOULETIS, J.	8 431
	3 562		8 625
	4 359	SPAULDING, R. L.	7 877
	5 89	STACY, H. L.	8 123
	5 237	STADNITSHENKO, I. A.	6 36
SEGALOV, Z.	8 1126	STAHL, S. O.	4 602
SEITZ, W. L.	7 385	STANTON, P. L.	7 865
	8 123		8 485
SELLAM, M.	8 425	STARKENBERG, J.	7 3
SENTMAN, L. H.	7 721		8 307
SERVAS, J. M.	7 686		8 1080
	8 159		8 1139
SETCHELL, R. E.	7 394	STARR, L. E.	2 620
	7 857	STEC, D.	8 734
	8 15	STEINBERG, D. J.	8 513
SHARMA, J.	8 725	STERNBERG, H. M.	3 205
SHARPLES, R. E.	3 738		3 226
SHAW, L. L.	6 755		4 27
SHAW, M. S.	8 531		4 153
SHAW, R.	5 89		5 597
	5 237		6 528
	6 231	STEWART, J. R.	8 962
SHEA, J. H.	5 351	STEWART, R. F.	8 839
SHEFFIELD, S. A.	6 668	STINECIPHER, M. M.	7 801
	6 748		8 351
	7 1004	STOLOVY, A.	7 50
SHIINO, K.	6 450	STRANGE, F. M.	4 3
	8 993	STREHLOW, R. A.	7 721
SHIKARI, Y. A.	6 336	STRESAU, R. H. F.	2 620
SHORT, J. M.	7 952		2 711
SHRADER, J.	6 740		2 749
SHUEY, H. M.	4 96		3 309
SHUPE, O. K.	3 150		3 396
SHVEDOV, K. K.	6 29		3 420
SILVESTROV, V. V.	6 36		4 442
SJOLIN, T.	4 435		4 449
	5 153		6 68
SKIDMORE, I. C.	4 14	STRETZ, L. A.	8 351
	4 47	STRONBERG, H. D.	5 331
	5 573	SULIMOV, A. A.	6 250
SLETTEVOLD, C.	8 3	SULTANOFF, M.	3 520
SLIE, W. M.	2 749		4 241
SMEDBERG, U.	8 1069	SUMMERS, C. R.	2 157
SMITH, C. P. M.	5 467		3 436
	6 477		4 117

### C. AUTHOR INDEX (Continued)

NAME	SYM PAGE	NAME	SYM PAGE
SUNDARARAJAN, R.	8 635	TROTT, B. D.	5 191
SWALLOWE, G. M.	7 24	TROTT, W. M.	8 691
	8 635	TSAI, D. H.	8 870
SWANSON, R. I.	8 715	TULIS, A. J.	5 47
TAN, B.	7 826		6 173
TANAKA, K.	7 583		6 183
	8 548	UDY, L. L.	3 150
	8 558	URIZAR, M. J.	3 327
	8 993	URSENBACH, W. O.	2 519
TANG, P. K.	8 52		2 733
TARVER, C. M.	6 231		3 357
	7 56	URTIEW, P. A.	5 105
	7 256		5 119
	7 488	VACELLIER, J.	5 567
	7 993	VALENTINI, J. J.	8 701
	7 1029	VAN DER STEEN, A. C.	8 710
	8 587	VAN DOLAH, R. W.	3 436
	8 613		4 117
	8 951		5 81
	8 1045	VAN THIEL, M.	8 501
TASKER, D. G.	7 285	VANPOPERYNGHE, J.	8 135
TAYLOR, B. C.	3 267		8 892
	6 3	VANTINE, H. C.	7 325
TAYLOR, J. W.	3 77		7 466
	5 291		7 1062
	5 311	VELICKY, R. W.	7 898
TAYLOR, P. A.	8 26		7 924
TEGG, D.	5 89		8 251
THIVET, R.	7 107	VENABLE, D.	4 639
THOMA, K.	8 1131		5 3
THOUVENIN, J.	4 135		5 13
	4 258	VENTURINI, E. L.	8 485
	4 566	VERBEEK, H. J.	8 669
	7 661	VERDES, G.	4 39
THRAP, R. G.	2 231		5 31
TIMNAT, Y. M.	6 590		5 41
TISLEY, D. G.	7 1040	VERHOEK, F. H.	3 50
TITOV, V. M.	6 36	VIDART, A.	4 527
	7 362	VIGIL, M. G.	8 1091
	8 143	VOIGHT, H. W.	8 251
	8 196	VOLK, F.	8 577
TOMBINI, C.	7 1010	VON HOLLE, W. G.	6 691
TRAVIS, J. R.	3 469		7 993
	3 499		8 3
	4 386		8 1045
	4 609	VORECK, W. E.	7 924
	8 1057		8 251
TREVINO, S. F.	8 870		8 460
TRIMBLE, J.	6 325	VORTHMAN, J.	8 99
	6 691	WACHTELL, S.	3 635
	7 247	WACKERLE, J.	4 154
TRIMBLE, J. J.	7 986		6 20
TROFIMOV, V. S.	7 789		7 385

### C. AUTHOR INDEX (Continued)

NAME	SYM	PAGE	NAME	SYM	PAGE
WACKERLE, J.	8	99	WILKINS, M. L.	4	3
	8	123		4	519
WAGNER, J.	8	577	WILLIAMS, R. F.	5	427
WALKER, E. H.	8	1119	WINNING, C. H.	3	455
WALKER, F. E.	7	777	WINSLOW, O. G.	6	664
WALKER, G. R.	1	39	WISEMAN, L. A.	2	643
WALKER, W. A.	4	27	WOLLENWEBER, U.	8	1131
	5	597	WOOD, W. W.	2	312
WALLACE, A. A.	6	625		2	424
WALSH, E. K.	7	394	WRENN, E.	6	214
WALTON, J.	6	214	WRIGHT, P. W.	4	142
	6	729		4	573
	7	887	WU, X	8	796
	8	613	XU, L.	8	1011
WANG, A.	8	1011	YAKUSHEV, V. V.	5	399
WARD, S. H.	8	380		6	143
WASLEY, R. J.	4	239	YANG, L. C.	6	612
WASSERMAN, H. J.	8	839	YONEDA, K.	8	168
WATSON, J. L.	7	1048	YOSHIDA, M.	8	993
WATSON, R. W.	4	117	YU, J. M.	7	343
	5	81	ZAKER, T. A.	5	313
	5	169	ZERNOW, L.	5	67
	5	559	ZHANG, G.-R.	7	746
	6	115	ZHAO, H.	8	83
WEBBER, P. E.	8	294	ZIMMERSCHIED, A. B.	6	389
WECKEN, F.	4	107		6	740
WEDAA, H. W.	2	251	ZINMAN, W. G.	2	198
WEINGART, R. C.	6	653	ZOE, J.	7	602
	6	755		8	151
	7	325	ZOU, Q.	8	1011
	7	425	ZOVKO, C. T.	3	606
	7	1062	ZURN, D. E.	7	216
	8	3	ZWISLER, W. H.	6	162
	8	1045			
WENOGRAD, J.	3	10			
	3	60			
WEST, C. E.	5	533			
WEST, G. T.	7	865			
WESTMORELAND, C.	7	256			
	7	517			
WESTON, A. M.	7	256			
	7	887			
	8	914			
WHATMORE, C. E.	7	17			
	8	1035			
WHITBREAD, E. G.	2	643			
	2	695			
	3	202			
	3	574			
	3	659			
WIEDERMANN, A. H.	6	336			
WILKES, J. S.	7	75			
WILKINS, M. L.	3	721			

# D. ACRONYM and CODE NAME INDEX

## Alphabetically, First Reference

NAME	SYM	PAGE	MAKEUP
A-5	7	551	97 RDX/3 wax
A-589	5	139	86 HMX/14 PB
A-590	5	139	80.3 HMX/5.9 AP/13.8 PB
A-591	5	139	69 HMX/17 AP/14 PB
A-592	5	139	57 HMX/29 AP/14 PB
AAB 3189	7	892	9.2 RDX/60.8 AP/15 Al/15 binder
AAB 3225	7	892	7.1 RDX/62.9 AP/15 Al/15 binder
AAB 3267	7	892	5 RDX/65 AP/15 Al/15 binder
ABH	8	528	$C_{24}H_6N_{14}O_{24}$
ADDF	6	467	1,4,4,10,10,13-hexafluoro-1,1,7,7,13,13-hexanitro-3,5,9,11-tetraoxotridecane
ADNT	7	801	ammonium salt of 3,5-dinitro-1,2,4-triazole
AFX-521	8	1106	95 PYX/5 Kel-F 800
Amatex 20	6	647	20 RDX/40 TNT/40 AN
Amatol	5	501	20-60% AN/80-40% TNT
Amatol	7	801	$N^{15}$ -labeled ammonium nitrate (AN/TNT)
AN	6	439	ammonium nitrate
ANFO	3	186	94.6 AN/5.4 fuel oil
ANFOAL-10	6	546	87.4 AN/2.6 fuel oil/10 aluminum
AP	5	139	ammonium perchlorate
B 2141	7	409	88 RDX/12 HTPB
B 2142	7	409	77 PETN/23 PU
B 2161	8	437	40 HMX/30 AP/20 Al/10 polyurethane binder
B 2169	8	437	83 PETN/17 polyurethane
B 2174	8	437	47 HMX/30 AP/11 lead nitrate/12 polyurethane
B 2190	8	437	30 PETN/70 HTPB
B 2191	8	437	37 HMX/40 AP/11 lead nitrate/12 polyurethane
B 2192	8	437	27 HMX/50 AP/11 lead nitrate/12 polyurethane
B 3003	8	437	80 HMX/20 NC-NGI
Baratol	6	629	72 barium nitrate/28 TNT
Baratol	3	563	76 barium nitrate/24 TNT
Baratol	4	361	70 barium nitrate/30 TNT
Baratol 76	6	647	76 barium nitrate/24 TNT
BH-1	8	83	plastic-bonded RDX
BO-1	8	93	plastic-bonded HMX, similar to PBX 9404
BTF	6	712	benzotrifuroxane
BTFMA	6	467	1-fluoro-1,1-dinitro-4,4-bis(trifluoromethyl)-3,5-dioxohexane
BTNEN	3	70	bis-(2,2,2-trinitroethyl)nitramine
BTX	6	460	5,7-dinitro-1-picrylbenzotriazole
BTZ	8	1019	bitetrazole
BWX	2	661	beeswax
BX1	8	1106	60 TATB/35 (95 RDX/5 HMX)/5 Kel-F

## D. ACRONYM AND CODE NAME INDEX (Continued)

NAME	SYM PAGE	MAKEUP
BX2	8 1106	60 TATB/35 (95 RDX/5 HMX)/5 PTFE
BX3	8 1106	60 TATB/35 (90 RDX/10 HMX)/5 Kel-F
BX4	8 1106	60 TATB/35 (90 RDX/10 HMX)/5 PTFE
C-4	4 97	91 RDX/9 wax
CACTP	6 455	catena- $\mu$ -cyanotetraammine cobalt(III) perchlorate
CEF	4 5	tris $\beta$ -chloroethylphosphate
Comp A	3 687	91 RDX/9 wax
Comp A	6 647	92 RDX/8 wax
Comp A 5	8 265	98.5 RDX/1.5 stearic acid
Comp A-5	7 551	97 RDX/3 wax
Comp A-5	7 928	98 RDX/2 stearic acid
Comp B	2 479	60 RDX/40 TNT, wax and other additives (1 to 1.5%)
Comp B	4 48	60 RDX/40 TNT
Comp B	6 493	60 RDX/40 TNT/1 wax
Comp B	6 629	59.5 RDX/39.5 TNT/1 beeswax
Comp B	6 647	63 RDX/36 TNT/1 wax
Comp B	7 353	45 RDX/55 TNT/1 wax
Comp B (ISL)	7 317	65 RDX/35 TNT
Comp B, Grade A	4 5	64 RDX/36 TNT
Comp B, Grade A	5 198	59.5 RDX/39.5 TNT/1.0 wax
Comp B-3	5 4	60 $\pm$ 1.5 RDX/40 $\pm$ 1.5 TNT
Comp B-3	4 361	64 RDX/36 TNT
Comp B-3 (ISL)	7 317	60 RDX/40 TNT
Comp B3 (waxed)	5 280	60 RDX/40 TNT/1 wax
Comp B4	7 900	60 RDX/40 TNT, no wax
CP	6 455	1-(5-cyanotetrazolato)pentaammine cobalt(III) perchlorate
CTX-1	8 265	15 RDX/40 AP/23 Al/22 TNT + additives
CX-84	8 366	84 RDX/9.7 R45-HT/5.6 DOA/0.7 TDI
Cyclonite	3 437	RDX
Cyclotol	3 502	65 RDX/35 TNT
Cyclotol	5 65	72 RDX/25 TNT
Cyclotol 77/23	6 647	77 RDX/23 TNT
DATB	3 761	1,3-diamino-2,4,6-trinitrobenzene
1,2-DB	5 237	1,2-bis(difluoramino)butane
2,2-DB	5 237	2,2-bis(difluoramino)butane
DDNP	3 12	diazodinitrophenol
Debrix 18AS	8 265	95.5 RDX/2.5 wax/2 additives
Debrix-2	8 1106	95 RDX/5 wax
DEGDN	7 762	diethylene glycol dinitrate
DFB	6 467	2,2-difluoro-2-nitroethyl-5,5-difluoro-2-(3',3'-difluoro-3'-nitro-1-oxopropyl)-5,5-dinitro-3-oxopentanoate
DFF	6 467	bis(2-fluoro-2,2-dinitroethyl)difluoroformal
DFNT	6 467	2,2-difluoro-2-nitroethyl-trifluoromethane-sulfonate
DHE	8 365	2-hydroxymethyl dimethylhydantoin

## D. ACRONYM AND CODE NAME INDEX (Continued)

NAME	SYM	PAGE	MAKEUP
DINA	3	66	di- $\beta$ -nitroxyethyl nitramine
DINGU	7	540	dinitroglucuril
DiTeU	4	435	dinitroethyl-uric ( <i>sic</i> )
Dithekite	3	186	a mixture of 82.8% nitric acid, nitrobenzene, and water
Dithekite 13/20	2	648	dithekite with 13/20 wt% water
Dithekite 13	3	493	63 nitric acid/24 nitrobenzene/13 water
DNP	7	374	dinitrophenol
DNPA	4	5	2,2-dinitropropylacrylate
DNPF	3	685	bis-dinitropropyl fumarate
DNPP	6	467	2,2-dinitropropyl perchlorate
DNPTB	3	70	2,2-dinitropropyl 4,4,4-trinitrobutyrate
DNT	7	374	dinitrotoiuene
DNT	7	802	3,5-dinitro-1,2,4-triazole
DOA	8	363	dioctyl adipate
DOP	4	5	dioctylphthalate
1,1-DP	5	90	1,1-bis(difluoroamino)propane
1,2-DP	5	237	1,2-bis(difluoroamino)propane
1,3-DP	5	90	1,3-bis(difluoroamino)propane
2,2-DP	5	237	2,2-bis(difluoroamino)propane
DREV-Explosive	8	363	84 RDX/16 polybutadiene
EA	7	548	50 EDD(ethylenediamine dinitrate)/50 AN
EAK	8	1002	46 ethylenediamine dinitrate/46 ammonium nitrate/ 8 potassium nitrate
EAR	7	551	42.5 EDD/42.5 AN/15 RDX
EARK	7	551	42.5 EDD/36.1 AN/15 RDX/6.4 potassium nitrate
EARL-1	7	551	40.3 EDD/40.3 AN/14.2 RDX/5.2 Al
EARL-2	7	551	36.2 EDD/36.2 AN/12.8 RDX/14.8 Al
EDD	6	439	ethylenediamine dinitrate
EDNA	6	314	ethylenedinitramine
EDNP	5	139	ethyl-4,4-dinitropentanoate w/1% Cab-O-Sil gelling agent
EGD	3	456	ethylene glycol dinitrate
EGDN	3	438	ethylene glycol dinitrate
EGN	2	659	ethylene glycol dinitrate
EIE	4	159	exchanged-ion explosive (10 NG/90 stoichiometric ammonium chloride-potassium nitrate mixture)
Emulite	8	1071	AN/FO/water with gas-filled microspheres
EN	3	813	ethyl nitrate
Estane	4	5	trademark for polyester-urethane of adipic acid 1,4-butanediol, diphenylmethane diisocyanate
ET	3	744	homogeneous mixture of ethyldecaborane in tetranitromethane
EtDP	4	5	ethyl 4,4-dinitropentanoate
FDA	6	467	bis(2-fluoro-2,2-dinitroethyl) acetal
FDE	6	467	1,1,4-trifluoro-1,4,4-trinitro-3-oxobutane
FDEE	6	467	1,5,-difluoro-1,1,5,5-tetranitro-3-oxopentane

## D. ACRONYM AND CODE NAME INDEX (Continued)

NAME	SYN	PAGE	MAKEUP
FDEK	7	804	2.55 AN/0.3 ADNT/1 EDD/0.36 potassium nitrate (Note! These numbers are vol%)
FDNE-A	6	467	1,9-difluoro-1,1,5,5,9,9-hexanitro-3,7-dioxononane
FDNE-N	6	467	2-fluoro-2,2,-dinitroethyl nitrate
FDNE-S	6	467	bis(2-fluoro-2,2-dinitroethyl)sulfate
FDNEP	6	467	2-fluoro-2,2-dinitroethyl perchlorate
FEFO	6	467	bis(2-fluoro-2,2-dinitroethyl)formal
FNR	4	5	tetrafluoroethylene-trifluoro-nitroso methane copolymer
FC	6	546	86 fuel oil
FTE	6	467	1,1,1,4-tetrafluoro-4,4-dinitro-3-oxobutane
GBFO	6	467	1,12-difluoro-1,1,12,12-tetranitro- 3,5,8,10-tetraoxododecane
GMB	8	993	glass microballoons
Gurit	8	1071	NG/EGDN/SiO <sub>2</sub>
H-6	5	255	45 RDX/30 TNT/20 Al/5 wax
HAV-10	5	139	74.7 HMX/10.6 Al/14.7 Viton
HAV-20	5	139	65.7 HMX/18.9 Al/15.4 Viton
HBX	5	73	75 Composition B/25 Al
HBX	2	737	45 RDX/30 TNT/25 Al
HBX-1	5	524	40 RDX/38.1 TNT/17.1 Al/4.8 Wax
HCX	8	1011	heterogeneous composite explosive
HDBA	8	365	4-hydroxy-N-N-dimethylbutyramide
HEP	8	883	high-energy propellant
Hexatol 60/40	6	546	59 RDX/40 TNT/1 wax
Hexatonal 15	6	546	42.1 RDX/42.1 TNT/0.8 wax/15 Al
Hexogen	4	159	RDX
Hexotol 60/40	6	511	60 RDX/40 TNT
Hexotolif 15	6	511	42.5 RDX/42.5 TNT/15 LiF
Hexotonal 15	6	511	42.5 RDX/42.5 TNT/15 Al
HMTA	4	184	hexamethylenetetramine
HMX	6	712	cyclotetramethylene tetranitramine
HN	1	27	hydrazine mononitrate
HNAB	7	416	hexanitroazobenzene
HNB	7	647	hexanitrobenzene
HNS	5	222	hexanitrostilbene
HTPB	8	1036	hydroxyl-terminated polybutadiene
HV4	5	280	85 HMX/15 Viton
HW4	5	280	95 HMX/5 wax
IBA	5	237	1,2-bis(difluoramino)-2-methylpropane (isobutylene adduct)
ICCP	6	455	isothiocyanatopentaammine cobalt(III) perchlorate
IPDI	8	1036	isophorone diisocyanate
KP	5	139	potassium perchlorate
LP	5	139	lithium perchlorate
LS	8	711	lead styphnate, Pb(C <sub>6</sub> O <sub>9</sub> N <sub>3</sub> H <sub>3</sub> )
LX-04-1	4	489	85 HMX/15 Viton, "1" denotes fine-particle-sized HMX

## D. ACRONYM AND CODE NAME INDEX (Continued)

NAME	SYM	PAGE	MAKEUP
LX-07	5	65	90 HMX/10 Viton
LX-07-0	4	5	90 HMX/10 Viton
LX-09	5	65	93.3 HMX/4.2 DNPA/2.5 FEFO
LX-10	5	65	95 HMX/5 Viton
LX-11	5	139	80 HMX/20 Viton
LX-13	8	1091	80 PETN/20 Sylgard (see XTX-8003)
LX-14	8	614	95.5 HMX/4.5 Estane 5702-F1
LX-15	8	1106	95 HNS/5 Kel-F 800
LX-17	7	488	92.5 TATB/7.5 Kel-F (formerly RX-03-BB)
M-FEFO	6	467	1,7-difluoro-4-(1-oxomethyl)-1,1,7,7-tetranitro-3,5-dioxoheptane
MA	6	467	1,1,7-trifluoro-4-methyl-1,7,7-trinitro-3,5-dioxoheptane
MAN	6	439	methylammonium nitrate
MEDINA	3	674	CH <sub>4</sub> N <sub>4</sub> O <sub>4</sub> , methylene dinitramine
MF	6	467	1,1,7-trifluoro-1,7,7-trinitro-3,5-dioxoheptane
MF	8	711	mercury fulminate, Hg(ONC) <sub>2</sub>
MFDNB	6	467	methyl-4-fluoro-4,4-dinitrobutyrate
MFF	6	467	1,4,4,7,7-pentafluoro-1,1,7-trinitro-3,5-dioxoheptane
Minol 2	4	463	aluminized ammonium nitrate/TNT
MMAN	7	374	monomethylamine nitrate
MN	5	267	methylnitrate
1-MNT	6	232	1-methyl-5-nitrotetrazole
2-MNT	6	232	2-methyl-5-nitrotetrazole
NB-40	6	771	60 pyroxyline/40 nitroglycerine
NC	4	5	nitrocellulose
2-NE	7	762	2-nitroethanol
NG	3	66	nitroglycerin
NGI	7	43	nitroglycol
Nigu	8	577	nitroguanidine
Nitromixture	2	648	83% nitromethane/17 2-nitropropane
NM	4	126	nitromethane
NONA	5	222	nonanitroterphenyl
NQ	7	566	nitroguanidine
Octol	6	647	77 HMX/23 TNT
Octol	4	5	78 HMX/22 TNT
Octol-A	5	280	80 HMX/20 TNT/1 Wax
Octol-B	5	280	70 HMX/30 TNT/1 Wax
OTTO	6	467	1,1,1,7,7,13,13,13-octafluoro-4,4,10,10-tetranitro-2,6,8,12-tetraoxotridecane
P2100 B	8	626	88 HMX/12 HTPB
PA	3	700	picric acid
PB	5	139	hydroxyterminated polybutadiene
PB	8	1132	polybutadiene
PBX 9205	5	599	92 RDX/6 polystyrene/2 dioctyl phthalate
PBX 9404	5	60	94 HMX/3 nitrocellulose/3 tris-β-chloroethyl phosphate
PBX 9407	7	928	94 RDX/6 EXON 461

## D. ACRONYM AND CODE NAME INDEX (Continued)

NAME	SYM	PAGE	MAKEUP
PBX-9010	4	5	90 RDX/10 Kel-F
PBX-9011	4	5	90 HMX/10 Estane
PBX-9404-03	4	5	94 HMX/3 NC/3 CEF
PBX-9501	6	647	95 HMX/2.5 Estane/1.25 BDNPA/1.25 BDNPF
PBX-9502	7	52	95 TATB/5 Kel-F 800 (formerly X-0290)
PBX-9503	8	1106	80 TATB/15 HMX/5 Kel-F 800
PBXN-5	7	928	95 HMX/5 Viton A
PBXW	8	883	RDX/inert binder
Pc	3	323	Primacord
PE	6	543	86 PETN/14 wax
PE 6	5	139	6-polyethylene
PE4	8	265	88 RDX/12 plasticizer
Pentanex	6	546	45 PETN/37 AN/2 glycol/15.5 water/0.5 guar
Pentolite	1	14	50 PETN/50 TNT
PETN	3	12	pentaerythritol tetranitrate
Polystyr	4	5	polystyrene
PTFE	6	626	polytetrafluoroethylene
PVA	2	712	polyvinyl alcohol
PYX	8	1106	2,6-bis(picrylamino)-3,5-dinitropyridine
QMAN	6	439	tetramethylammonium nitrate
RDX	7	928	1,3,5-trinitro 1,3,5-tetrazacyclohexane
RDX	5	222	cyclotrimethylenetrinitramine
REX-20	6	467	2,2,2-trifluoroethyl-4-fluoro-4,4-dinitrobutyrate
RGPA	8	265	70 RDX/19 plasticizer/5.5 polyurethane/5.5 ?
RX-03-BB	7	488	92.5 TATB/7.5 Kel-F (new name is LX-17)
RX-04-AT	4	5	88 HMX/12 carborane-fluorocarbon copolymer
RX-04-AU	5	139	92 HMX/8 Viton
RX-04-AV	4	5	92 HMX/8 PE
RX-04-BM	5	139	81.6 HMX/4 Al/14.4 Viton
RX-04-BN	5	139	79 HMX/6.6 Al/14.3 Viton
RX-04-BO	5	139	72.7 HMX/13.3 Al/14.0 Viton
RX-04-BT	5	139	76 HMX/10 LIF/14 Viton
RX-04-BY	4	5	86 HMX/14 FNR
RX-04-DS	5	139	81 HMX/9.9 Al/9.1 Viton
RX-04-P1	4	5	80 HMX/20 Viton
RX-05-AA	4	5	80 RDX/8 polystyrene/2 DOP
RX-09-AA	4	5	93.7 HMX/5.7 DNPA/0.6 EtDP
RX-11-AF	5	139	52 HMX/43 KP/5 PE
RX-11-AI	5	139	52 HMX/43 KP/5 PE
RX-11-AJ	5	139	52 HMX/43 KP/5 PE
RX-11-AW	5	139	51 HMX/35 KP/14 PB
RX-11-AX	5	139	51 HMX/35 KP/14 PB
RX-11-AY	5	139	33.4 HMX/53.4 KP/13.2 PB
RX-11-AZ	5	139	33.4 HMX/53.4 KP/13.2 PB
RX-11-BA	5	139	51 HMX/39 AP/10 Viton
RX-18-AB	5	139	51 HMX/20 AP/29 EDNP

## D. ACRONYM AND CODE NAME INDEX (Continued)

NAME	SYN	PAGE	MAKEUP
RX-18-AE	5	139	51 HMX/20 AP/29 EDNP
RX-18-AG	5	139	51 HMX/20 AP/29 EDNP
RX-18-AH	5	139	71 HMX/29 EDNP
RX-18-AJ	5	139	52.6 HMX/34.7 KP/12.7 PB
RX-18-BA	5	139	31 HMX/45 KP/24 EDNP
RX-22-AG	5	139	73.6 HMX/26.4 LP
RX-23-AA	6	712	79 hydrazine nitrate/21 hydrazine
RX-23-AB	6	712	70 hydrazine nitrate/5.9 hydrazine/24.1 water
RX-23-AC	6	712	30 hydrazine nitrate/70 hydrazine
RX-25-AA	5	139	22 HMX/58 AP/10 Al/10 Viton
RX-25-AF	7	59	49.3 HMX/46.6 TATB/4.1 Estane
RX-30 AD	6	731	47.1 KP/51.3 NM/guar 1.6
RX-30-AA	6	731	60.8 AP/38 NM/1.2 guar
RX-30-AB	6	731	61.1 AP/37.9 NM/1 guar
RX-30-AC	6	731	47.6 KP/50.8 NM/1.6 guar
RX-30-AE	6	731	57.9 AN/40.8 NM/1.3 guar
RX-30-AF	6	731	57.9 AN/40.8 NM/1.3 guar
RX-31-AA	6	731	28.8 AN/47 NM/22.8 Al/1.4 guar
RX-31-AB	6	731	43.2 AN/47 NM/8.3 Al/1.5 guar
RX-36-AA	8	1020	1 HMX/1 TATB/1 BTF, note mole ratios
RX-36-AB	8	1020	1 TATB/1 BTF, note mole ratios
RX-36-AC	8	1020	4 HMX/1 TATB/1 BTF, note mole ratios
RX-36-AD	8	1020	1 HMX/3 TATB/1 BTF, note mole ratios
RX-36-AE	8	1020	1 HMX/1 BTF, note mole ratios
RX-36-AF	8	1020	1 HMX/1 TATB, note mole ratios
RX-36-AG	8	1020	1 HMX/1 TATB/3 BTF, note mole ratios
RXAC	8	802	70 hydrazine/30 hydrazine nitrate
s-TCB	7	425	symmetrical 1,3,5-trichlorobenzene (precursor to TATB)
SPIS-44	7	620	20 HMX/49 AP/21 Al/10 binder
SRI-1	6	467	1,1,1-trifluoro-4,4,4-trinitro-2-oxobutane
SRI-2	6	467	1,1,1,4-tetrafluoro-4,4-dinitro-2-oxobutane
SRI-3	6	468	1,1,1-trifluoro-4,4-dinitro-2-oxopentane
SRI-4	6	468	1,1,1,7,7,7-hexafluoro-4,4-dinitro-2,6-dioxoheptane
SRI-5	6	468	1-fluoro-1,1,3,3-tetranitro-5-oxohexane
SX-2	6	493	RDX/filler, sheet explosive
SYEP	6	468	4,4-bis(difluoramino)-1,7-difluoro-1,1,7,7-tetranitro-3,5-dioxoheptane
T	7	697	95.5 TATB/4.5 Viton
T1	8	151	95.5 TATB/?
T2	8	151	97 TATB/?
TA	2	659	triacetin
TATB	6	659	1,3,5-triamino-2,4,6-trinitrobenzene
TCE	7	374	trichloroethylene
TCTNB	7	425	1,3,5-trichloro-2,4,6-trinitrobenzene (precursor for TATB)
TDI	8	363	toluenediisocyanate

## D. ACRONYM AND CODE NAME INDEX (Continued)

NAME	SYM	PAGE	MAKEUP
TDPF	6	468	1,1,1,13,13,13-hexafluoro-4,4,10,10-tetranitro-2,6,8,12-tetraoxotridecane
Tetryl	6	427	N-methyl-N-nitro-2,4,6-trinitroaniline
TFA	6	468	1,7,difluoro-1,1,7,7-tetranitro-4-trifluoromethyl-3,5-dioxoheptane
TFMA	6	468	1-fluoro-1,1-dinitro-4-trifluoromethyl-3,5-dioxohexane
TFMDA	6	468	1-fluoro-4-difluoronitromethyl-1,1-dinitro-4-trifluoromethyl-3,5-dioxoheptane
TFMFF	6	468	1,1,1,4,4,7-hexafluoro-7,7-dinitro-3,5-dioxoheptane
TFNA	8	802	1,1,1-trifluoro-3,5,5-trinitro-3-azahexane
TMETN	3	813	trimethylolethane trinitrate
TNA	8	746	trinitroaniline, picramide
TNB	3	66	1,3,5 trinitrobenzene
TNETB	3	70	2,2,2-trinitroethyl-4,4,4-trinitrobutyrate
TNM	4	126	tetranitromethane
TNT	3	66	2,4,6-trinitrotoluene
TNTAB	8	802	1,3,5-triazido-2,4,6-trinitrobenzene
Torpex	4	463	aluminized RDX/TNT
Torpex 2B	8	265	42 RDX/40 TNT/18 Al/5 desensitizer
Tritonal	2	735	80 TNT/20 Al
TTF	6	468	1,1,1-trifluoro-7,7,7-trinitro-3,5-dioxoheptane
UP	6	450	ureamonoperchlorate
UPS	6	450	90 wt% aqueous solution of UP
Viton	5	199	vinylidene fluoride-hexafluoropropylene copolymer
WC 231	8	883	75 NC/25 NG "commercial reloading powder"
WG-2	6	546	MMAN-sensitized watergel explosive 7% Al
WG-4	6	546	MMAN-sensitized watergel explosive 13% Al
X-0204	4	5	83 HMX/17 Teflon
X-0219	6	647	90 TATB/10 Kel-F 800
X-0233	8	979	85.48 tungsten/13.22 HMX/0.8 polystyrene/0.5 DOP
X-0290	6	637	95 TATB/5 Kel-F 800 (changed to PBX 9502)
X-0319	7	567	50 TATB/45 HMX/5 Kel-F 800
X-0320	7	567	60 TATB/35 HMX/5 Kel-F 800
X-0321	7	567	75 TATB/20 HMX/5 Kel-F 800
X-0341	7	567	90.25 TATB/4.75 HMX/5 Kel-F 800
X-0342	7	567	85.5 TATB/9.5 HMX/5 Kel-F 800
X-0343	7	567	80.75 TATB/14.25 HMX/5 Kel-F 800
X-0344	7	567	71.25 TATB/23.75 HMX/5 Kel-F 800
X-0407	8	123	70 TATB/25 PETN/5 Kel-F
X1	8	151	96 HMX/?
XTX-8003	6	647	80 PETN/20 silicone rubber
Z TACOT	8	528	C <sub>12</sub> H <sub>4</sub> N <sub>8</sub> O <sub>8</sub>

## 9TH DETONATION SYMPOSIUM REGISTRANTS

Stephen F. Agnew  
Los Alamos National Laboratory  
P.O. Box 1663, MS C346  
Los Alamos, NM 87545

M. Ahadd  
AL QAQAA State Establishment  
P.O. Box 5134  
Baghdad, Iraq

Irving Akst  
Los Alamos National Laboratory  
P.O. Box 1663, M-8, MS J960  
Los Alamos, NM 87545

Fernando Alcalde  
Union Española De Explosivos  
Claudio Coello, 124  
Madrid, 28006 Espana

David F. Aldis  
Lawrence Livermore National  
Laboratory  
P.O. Box 808, L-364  
Livermore, CA 94550

Richard M. Aire  
Lawrence Livermore National  
Laboratory  
P.O. Box 808, L-282  
Livermore, CA 94550

Allan B. Anderson  
Los Alamos National Laboratory  
P.O. Box 1663, P952  
Los Alamos, NM 87545

C. J. Anderson  
Mining Resource Engineering Ltd  
1555 Sydenham Rd., RR 8  
Kingston, Ontario Canada K7L 4V4

James Aplin  
USAF Armament Laboratory  
AFATL/MNE  
Eglin AFB, FL 32542-6009

Mary E. Arce  
U.S. Air Force Astronautics Lab  
AL(AFSC)RKPL  
Edwards AFB, CA 93523-5000

Werner A. Arnold  
MBB Schrobenuhausen  
Hagenauer Forst  
Schrobenuhausen, D-8898 FRG

Blaine W. Assy  
Los Alamos National Laboratory  
P.O. Box 1663, M-8, MS J960  
Los Alamos, NM 87545

Alice I. Atwood  
Naval Weapons Center  
Code 3891  
China Lake, CA 94555-6001

Jean Avelle  
Commissariat a l'Energie Atomique  
CEVMBP No. 7  
Courtry, 77181 France

Joseph E. Backofen  
Brigs Co.  
2668 Petersborough St.  
Herndon, VA 22071

Mel R. Baer  
Sandia National Laboratories  
P.O. Box 5800, Div. 1512  
Albuquerque, NM 87185

Kerry L. Bahl  
Lawrence Livermore National  
Laboratory  
P.O. Box 808, L-281  
Livermore, CA 94550

Richard Bardo  
Naval Surface Warfare Center  
10901 New Hampshire Ave.  
Silver Spring, MD 20903-5000

Peter Barnes  
Ministry of Defence - Navy  
CINO 64B Ensign  
Bath, Avon UK

Edward J. Barr  
Vanderbilt University  
Box 6019, Station B  
Nashville, TN 37235

Jude Barry  
Aerojet Solid Propulsion  
P.O. Box 15699C  
Sacramento, CA 95608

Pascal A. Bauer  
ENSMA, Lab Detonique  
Rue Guillaume VII  
Poitiers, 86036 France

John B. Bdzil  
Los Alamos National Laboratory  
P.O. Box 1663, M-9, P952  
Los Alamos, NM 87545

Bruce Beard  
Naval Surface Warfare Center  
10901 New Hampshire Ave.  
Silver Spring, MD 20903-5000

Raymond L. Beauregard  
Applied Ordnance Tech, Inc.  
2001 Jefferson Davis Hwy  
Arlington, VA 22202

Alain Becuwe  
Societe Nationale des Poudres et  
Explosifs BP No. 2  
Vert-le-Petit, 91710 France

Anthony J. Bedford  
Embassy of Australia  
1601 Massachusetts Avenue N.W.  
Washington, DC 20036

Clifford D. Bedford  
Naval Surface Warfare Center  
10901 New Hampshire Ave.  
Silver Spring, MD 20903-5000

Donald A. Bednar  
U.S. Air Force Armament Laboratory,  
AFATL/MNW  
Eglin AFB, FL 32542-5434

Lawrence Behrmann  
Schlumberger Well Services  
P.O. Box 1590  
Rosharon, TX 77459

Conrad Belanger  
Defence Research Establishment  
Valcartier P.O. Box 8800  
2459 pie XI Blvd North,  
Courcelletta, Quebec, Canada

Robert Belmas  
Commissariat a l'Energie Atomique  
CEVMBP No. 7  
Courtry, 77181 France

David V. Bent  
RARDE  
Fort Halstead, Bldg. X3  
Sevenoaks, Kent UK TN 167 BP

Didier Bergues  
Commissariat a l'Energie Atomique  
Center de Etudes de Gramat  
GRAMAT, 46500 France

Nicholas Berkholz  
Honeywell Proving Ground  
23100 Sugar Bush Road NW  
Elk River, MN 55330

Richard R. Bernacker  
Naval Surface Warfare Center  
10901 New Hampshire Ave.  
Silver Spring, MD 20903-5000

James P. Billingsley  
U.S. Army Missile Command  
DRSMI-RHC  
Redstone Arsenal, AL 35898

A. Birnboim  
Rafael Ballistic Center  
P.O. Box 2250 (24)  
Haifa, Israel

Gert O. Bjarnholt  
Swedish Defense Research  
Establishment  
Dept of Weapons Tech. Sve DeFo  
Stockholm, 10254 Sweden

George Bloom  
Lawrence Livermore National  
Laboratory  
P.O. Box 808, L-281  
Livermore, CA 94550

Thomas L. Boggs  
Naval Weapons Center  
Code 3891  
China Lake, CA 94555-6001

Jacques Boileau  
Societe Nationale des Poudres et  
Explosifs (SNPE)  
12 Quai Henri IV  
75004 Paris, France

Paul R. Bolduc  
U.S. Air Force Armament Laboratory  
AFATL/MNE  
Eglin AFB, FL 32542-5434

Lloyd L. Bonzon  
Sandia National Laboratories  
P.O. Box 5800, Div. 2514  
Albuquerque, NM 87185

Mark B. Boslough  
Sandia National Laboratories  
P.O. Box 5800, Div. 1153  
Albuquerque, NM 87185

Michel Bosse-Platiere  
Schlumberger  
26 Rue de la Cavee  
Clamart, 92140 France

Ronald B. Boulet  
U.S. Air Force Armament Laboratory  
AFATL/MNF  
Eglin AFB, FL 32542-5434

Nell K. Bourne  
University of Cambridge  
Madingley Road, G787  
Cambridge, CB3 0HE UK

Allen L. Bowman  
Los Alamos National Laboratory  
P.O. Box 1663  
Los Alamos, NM 87545

Philippe G. Boyce  
DCAN-SDEB-GERBY  
BP 77  
Toulon Naval, 83800 France

Larry R. Boyer  
Naval Weapons Center  
Code 3891  
China Lake, CA 93555

Vincent M. Boyle  
U.S. Army Ballistic Research  
Laboratory, SLCBR-TB-E  
3419 Walnut Rd  
Aberdeen, MD 21001

Martin Braithwaite  
ICI Explosives  
Nobel House Stevenston  
Ayrshire KA20 3LN UK

R. Don Breithaupt  
Lawrence Livermore National  
Laboratory  
P.O. Box 808, L-282  
Livermore, Ca 94550

Thomas B. Brill  
University of Delaware  
Dept. of Chemistry  
Newark, NJ 19716

John R. Brinkman  
EG&G Mound Applied Technology  
P.O. Box 3000  
Miamisburg, OH 45343-3000

Louis Brun  
Commissariat a l'Energie Atomique  
CEVMB No. 7  
Courtry, 77181 France

Jacques Brunet  
Societe Nationale des Poudres et  
Explosifs CRB BP 2  
Vert-le-Petit, France

Michael A. Bucher  
Naval Weapons Station  
Code 321  
Concord, CA 94520

Francois I. Bugaut  
Commissariat a l'Energie Atomique  
CEV-MB 7  
77181 Courtry, France

Bruce G. Bukiet  
Department of Mathematics  
New Jersey Institute of Technology  
Newark, NJ 07102

Gregory A. Buntain  
Los Alamos National Laboratory  
P.O. Box 1663, C920  
Los Alamos, NM 87545

Keith D. Burrows  
Ministry of Defence  
AWE Foulness, Southend on Sea,  
Essex SS3 9XE UK

A. Garn Butcher  
Hercules Inc.  
P.O. Box 98  
Magna, UT 84037

W. Byers Brown  
University of Manchester  
Department of Chemistry  
Manchester, M13 9PL UK

Daniel Calef  
Lawrence Livermore National  
Laboratory  
P.O. Box 808, L-282  
Livermore, CA 94550

Dalton E. Canty  
Lockheed, Org. 54-60  
1111 Lockheed Way  
Sunnyvale, CA 94088-3504

Dorn W. Carlson  
Naval Surface Warfare Center  
10901 New Hampshire Avenue  
Silver Spring, MD 20903-5000

Kim E. Carlson  
Naval Surface Warfare Center  
10901 New Hampshire Ave.  
Silver Spring, MD 20903-5000

Stacey Carswell  
U.S. Air Force Armament Laboratory  
AFATL/MNE  
Eglin AFB, FL 32542

Rendell L. Carver  
Los Alamos National Laboratory  
P.O. Box 1663, B295  
Los Alamos, NM 87545

Francis Chaisse  
Commissariat a l'Energie Atomique  
CEV-MB 7  
Courtry, 77181 France

May L. Chan  
Naval Weapons Center  
Code 3891  
China Lake, CA 93555

Lonnie B. Chapman  
Los Alamos National Laboratory  
P.O. Box 1663, MS C920  
Los Alamos, NM 87545

Mohammad M. Chaudhri  
University of Cambridge  
Madingley Road  
Cambridge, Cambridgeshire UK

Roger Cheret  
Commissariat a l'Energie Atomique 33  
Rue de la Federation  
Paris, 75015 France

Christopher Cherry  
Naval EOD Tech. Center  
Indian Head, MD 20640

Pei Chi Chou  
Dyna East Corporation  
3201 Arch Street  
Philadelphia, PA 19014

David A. Ciaramitaro  
Naval Weapons Center  
Code 3891  
China Lake, CA 93555

Dorothy A. Cichra  
Naval Surface Warfare Center  
10901 New Hampshire Ave.  
Silver Spring, MD 20903-5000

Rochelle E. Clements  
Lawrence Livermore National  
Laboratory  
P.O. Box 808, L-283  
Livermore, CA 94550

Steve C. Coffey  
Naval Surface Warfare Center  
10901 New Hampshire Ave.  
Silver Spring, MD 20903-5000

C. P. Constantinou  
University of Cambridge  
Cavendish Lab., Madingley Rd  
Cambridge, CB 3 0HE UK

Malcolm D. Cook  
RARDE, NPI Division  
Fort Halstead  
Sevenoaks, Kent TN16/BP UK

John Cooper  
ICI Explosives, FGTC  
Stevenson, Ayrshire, Scotland, UK

Paul W. Cooper  
Sandia National Laboratories  
P.O. Box 5800, Div. 7133  
Albuquerque, NM 87185

Marc S. Costantino  
Lawrence Livermore National  
Laboratory  
P.O. Box 808, L-369  
Livermore, Ca 94550

James D. Costello  
U.S. Air Force Armament Laboratory  
Eglin AFB, FL 32542

Albert L. Course  
Naval Weapons Station  
Code 321  
Concord, CA 94520

Michael Cowperthwaite  
SRI International  
333 Ravenswood  
Menlo Park, CA 94025

Bobby G. Craig  
56 Hidden Cove  
Valparaiso, FL 32580

Sharon L. Crane  
Los Alamos National Laboratory  
P.O. Box 1663, J960  
Los Alamos, NM 87545

Patricia C. Crawford  
Lawrence Livermore National  
Laboratory  
P.O. Box 808, L-353  
Livermore, CA 94550

James Culver  
Strategic Systems Programs  
U.S. Navy/SP-2731  
1931 Jefferson Davis Highway  
Washington, DC 20376-5002

John C. Cummings  
Sandia National Laboratories  
P.O. Box 5800, Div. 1512  
Albuquerque, NM 87185

Ian Dagley  
Naval Surface Warfare Center  
10901 New Hampshire Avenue  
Silver Spring, MD 20903-5000

C. James Dahn  
Safety Consulting Engineers, Inc.  
5240 Pearl St.  
Rosemont, IL 60018

John C. Dallman  
Los Alamos National Laboratory  
P.O. Box 1663, MS P952  
Los Alamos, NM 87545

Frank W. Davies  
General Research Corporation  
5383 Hollister Avenue  
Santa Barbara, CA 93160-6770

William C. Davis  
Los Alamos National Laboratory  
P.O. Box 1663, P952  
Los Alamos, NM 87545

William E. Deal  
Los Alamos National Laboratory  
P.O. Box 1663, P915  
Los Alamos, NM 87545

Scott Delter  
Naval Surface Warfare Center  
10901 New Hampshire Ave.  
Silver Spring, MD 20903-5000

Alain Delclos  
Societe Nationale des Poudres et  
Explosifs RP No.2  
Vert-le-Petit, 91710 France

Susan C. DeMay  
Naval Weapons Center  
Code 3205  
China Lake, CA 93555

David Demske  
Naval Surface Warfare Center  
10901 New Hampshire Ave.  
Silver Spring, MD 20903-5000

Pierre Deneuille  
Societe Nationale des Poudres et  
Explosifs BP No. 2  
Vert-le-Petit, 91710 France

Didier Devynck  
Applied Concepts Corp.  
P.O. Box 1096  
Aberdeen, MD 21001

Charles Dickinson  
Naval Surface Warfare Center  
10901 New Hampshire  
Silver Spring, MD 20903-5000

Peter M. Dickson  
University of Cambridge  
Madingley Road  
Cambridge, CB3 0HE UK

Ding Jing  
CETR  
New Mexico Tech.  
Socorro, NM 87801

Brigitta Dobratz  
Los Alamos National Laboratory  
P.O. Box 1663, C920  
Los Alamos, NM 87545

Ruth M. Doherty  
Naval Surface Warfare Center  
Bldg 30 Room 110  
Silver Spring, MD 20904

Q. Dong  
Southwest Institute of Fluid Physics  
P.O. Box 5231  
Chengdu, China

Paul J. Dotson  
Los Alamos National Laboratory  
P.O. Box 1663, MS B214  
Los Alamos, NM 87545

Steve Downey  
Northwest Technical Industries  
547 Diamond Point Rd.  
Sequim, WA 98382

David R. Dreitzler  
U.S. Army Redstone Arsenal,  
AMSMI-RD-PR-E  
Huntsville, AL 35898-5249

A. N. Dremim  
Institute of Chemical Physics  
USSR Academy of Sciences  
Moscow Region, USSR

Serge Dufort  
Commissariat a l'Energie Atomique  
Boite Postale No. 16  
Monts, France

Michael Dufour  
Establishment Technique de Bourges  
B7712-18015 Bourges Cedex  
Bourges, 18 France

Maurice E. Dunand  
Laboratoire d'Energetique et de  
Detonique (ENSMA)  
Poitiers, France

Mark Elert  
U.S. Naval Academy  
Chemistry Department  
Annapolis, MD 21402

Julius W. Enig  
Enig Associates, Inc.  
11120 New Hampshire Ave.  
Silver Spring, MD 20904

Kenneth L. Erickson  
Sandia National Laboratories  
P.O. Box 5800, Div. 1512  
Albuquerque, NM 87185

Alain Fergat  
DCAN-SDEE-Gerry  
BP 77  
Toulon Naval, 83800 France

Rocco Farinaccio  
Defence Research Establishment  
Valcartier P.O. Box 8800  
2459 pie XI Blvd North  
Courcellette, Quebec, G0A 1R0 Canada

Claude Fauquignon  
Institut Saint-Louis (ISL)  
12, Rue de l'Industrie  
Saint Louis 68301, France

Eric N. Fern  
Los Alamos National Laboratory  
P.O. Box 1663, J960  
Los Alamos, NM 87545

John E. Field  
University of Cambridge  
Madingley Rd.  
Cambridge, CB 3 0H UK

Milton Finger  
Lawrence Livermore National  
Laboratory  
P.O. Box 808, L-11  
Livermore, CA 94550

Susan Fischer  
Sandia National Laboratories  
P.O. Box 5800, Div. 2513  
Albuquerque, NM 87185

Barry D. Fishburn  
U.S. Army ARDEC  
Picatinny Arsenal  
Dover, NJ 07801-5000

Michael M. Fitz  
Machine Design Engineers  
714 S. Homer St.  
Seattle, WA 98108

Thomas G. Floyd  
U.S. Air Force Armament Laboratory,  
AD/AFATL/MNE  
Eglin AFB, FL 32542

M. Frances Foltz  
Lawrence Livermore National  
Laboratory  
P.O. Box 808, L-282  
Livermore, CA 94550

Jerry W. Forbes  
Naval Surface Warfare Center  
10901 New Hampshire Ave.  
Silver Spring, MD 20903-5000

Charles A. Forest  
Los Alamos National Laboratory  
P.O. Box 1663, MS P952  
Los Alamos, NM 87545

Geoff Foster  
Hadland Photonics, Inc.  
NewHouse Road, Bovingdon  
Hemel Hempsted, Herts, HP3 OEL UK

Joseph C. Foster  
U.S. Air Force Armament Laboratory,  
AFATL  
Eglin AFB, FL 32542

Martin C. Foster  
Ensign Bickford Aerospace Co.  
P.O. Box 427  
Simbury, CT 06070

Eugene C. Francis  
United Technologies  
P.O. Box 49028  
San Jose, CA 95161-9028

Alan M. Frank  
Lawrence Livermore National  
Laboratory  
P.O. Box 808, L-281  
Livermore, CA 94550

Alain Freche  
Societe Nationale des Poudres et  
Explosifs BP No.2  
Vert-le-Petit, 91710 France

Robert B. Frey  
U.S. Army Ballistic Research  
Laboratory  
Aberdeen Proving Ground, MD 21005

Wolfgang Fucke  
Battelle Institut e.V.  
AM Roemerhof 35  
6000 Frankfurt 90, FRG

Douglas Garrett  
Mason & Hanger, Pantex  
P.O. Box 30020  
Amarillo, TX 79177

Michael George  
Los Alamos National Laboratory  
P.O. Box 1663, P940  
Los Alamos, NM 87545

A. W. Gibb  
Defense Research Establishment  
Balston,  
Alberta T1C 1G3 Canada

Robert C. Gill  
Naval Surface Warfare Center  
Bldg. 600  
Indian Head, MD 20640

Patrick Gimenez  
Ministere de la Defense  
Centre d'Etudes de Gramat  
GRAMAT, 46500 France

Albert Ginzburg  
Rafael Ballistic Center  
P.O. Box 2250 (24)  
Haifa, Israel

Brian C. Glancy  
Naval Surface Warfare Center  
10901 New Hampshire Avenue  
Silver Spring, MD 20903-5000

Robert Glascock  
Tektronix, Inc.  
1258 Ortiz Dr. S.E.  
Albuquerque, NM 87108

Joseph G. Glenn  
U.S. Air Force Armament Laboratory,  
AFATL/MNE  
Eglin AFB, FL 32542

Stanley Goddard  
Battelle Memorial Institute  
505 King Avenue  
Columbus, OH 43201

Raymond Gogolewski  
Lawrence Livermore National  
Laboratory  
P.O. Box 808, L-321  
Livermore, CA 94550

Kenneth Graham  
Atlantic Research Corporation  
5945 Wellington Road  
Gainesville, VA 22065

Richard H. Granholm  
IRECO Inc.  
3000 West 8600 South  
West Jordan, UT 84088

LaRoy G. Green  
Lawrence Livermore National  
Laboratory  
P.O. Box 808, L-282  
Livermore, CA 94550

Gordon A. Greene  
Naval Weapons Center  
Code 32103  
China Lake, CA 93555

Roy Greiner  
Los Alamos National Laboratory  
P.O. Box 1663, MS G740  
Los Alamos, NM 87545

Ludwig A. Gritz  
Los Alamos National Laboratory  
P.O. Box 1663, A120  
Los Alamos, NM 87545

Harold J. Gryting  
Gryting Energetics Sciences Co.  
1324 Klondike  
San Antonio, TX 78245

Raafat H. Guirguis  
Naval Surface Warfare Center  
10901 New Hampshire Ave.  
Silver Spring, MD 20903-5000

Y. M. Gupta  
Washington State University  
Dept. of Physics, Shock Dynamics  
Pullman, WA 99164-2814

Steven G. Hallett  
Mason & Hanger, Pantex  
P.O. Box 30020  
Amarillo, TX 79177

Andrew Hanlon  
Westinghouse Marine Division  
401 East Hendy Ave. M/S 21-12  
Sunnyvale, CA 94088

Steven M. Harris  
Sandia National Laboratories  
P.O. Box 5800, Div. 2513  
Albuquerque, NM 87185

Richard C. Harrison  
U.S. Army Ballistic Research  
Laboratory  
SLCBB-TM-EE  
Aberdeen Proving Ground, MD  
21005

Peter J. Haskins  
RARDE  
Fort Halstead, NPI Division  
Sevenoaks, Kent TN147BP UK

Michael Hayek  
Rafael Ballistic Center  
P.O. Box 2250 (24)  
Haifa, 31021 Israel

Dennis B. Hayes  
Sandia National Laboratories  
P.O. Box 5800, Div. 1530  
Albuquerque, NM 87185-5800

Manfred Held  
MBB Schrobhausen  
D-8898 Schrobhausen,  
FRG

Frank H. Helm  
Lawrence Livermore National  
Laboratory  
P.O. Box 808, L-282  
Livermore, CA 94550

Steve Henderson  
Jet Research Center, Inc.  
7170 Rendon Bloodworth Rd.  
Ft. Worth, TX 76140

Robert W. Hermsen  
United Technologies  
P.O. Box 49028  
San Jose, CA 95161

Walter Herrmann  
Sandia National Laboratories  
P.O. Box 5800, Div. 1500  
Albuquerque, NM 87185

Joseph Hershkowitz  
Geo-Centers  
305 Passaic Avenue  
West Caldwell, NJ 07006

Robert G. Hickman  
Lawrence Livermore National  
Laboratory  
P.O. Box 808, L-365  
Livermore, CA 94550

Floyd J. Hildebrandt  
U.S. Army ARDEC  
Picatinny Arsenal, NJ 07806

Sook-Ying Ho  
Weapons Systems Research Lab  
P.O. Box 1700 SA 5108  
Salisbury, Australia

Ronald E. Hollands  
Royal Ordnance PLC  
Glascoed, USK  
Gwent, Wales UK NP5 1XL

Neil C. Holmes  
Lawrence Livermore National  
Laboratory  
P.O. Box 808, L-281  
Livermore, CA 94550

Charles A. Honodel  
Lawrence Livermore National  
Laboratory  
P.O. Box 808, L-35  
Livermore, CA 94550

Henry L. Horak  
Los Alamos National Laboratory  
P.O. Box 1663, C936  
Los Alamos, NM 87532

Gerald L. Houston  
EG&G Mound Applied Technologies  
P.O. Box 3000  
Miamisburg, OH 45343-3000

Philip M. Howe  
Los Alamos National Laboratory  
P.O. Box 1663  
ATAC, K574  
Los Alamos, NM 87545

Carl T. Hsieh  
Naval Surface Warfare Center  
10901 New Hampshire Ave.  
Silver Spring, MD 20903-5000

S. Huang  
Institute of Applied Physics  
University of Science and Technology  
Chengdu, China

Peter J. Hubbard  
RARDE, EC3 Division  
Fort Halstead  
Sevenoaks, Kent, UK TN 147 BK

Lewis C. Hudson III  
Naval Surface Warfare Center  
10901 New Hampshire Ave.  
Silver Spring, MD 20903-5000

James R. Humphrey  
Lawrence Livermore National  
Laboratory  
P.O. Box 808, L-125  
Livermore, CA 94550

Christopher D. Hutchinson  
Atomic Weapons Establishment  
Building B8C, Aldermaston  
Reading, Berkshire, RG7 4PR UK

S. Ibrahim  
AL QAQA State Establishment  
P.O. Box 5134  
Baghdad, Iraq

Edward S. Idar  
Los Alamos National Laboratory  
P.O. Box 1663, G787  
Los Alamos, NM 87545

Sigmund J. Jacobs  
Advanced Technology and Research  
1208 Ruppert Road  
Silver Spring, MD 20903-5000

Edward James  
Lawrence Livermore National  
Laboratory  
P.O. Box 808, L-282  
Livermore, CA 94550

Hugh R. James  
Atomic Weapons Establishment  
Foulness Island, Southend on Sea  
Essex, SS3 9XE UK

Jay T. Janton  
Westinghouse Corp.  
401 E. Hedy Ave., Box 3499  
Sunnyvale, CA 94088-3499

Leif A. Jerberyd  
Swedish Defence Material  
Administration  
S-11588 Stockholm, Sweden

F. Jing  
China Academy of Engineering Physics  
P.O. Box 501  
Chengdu, China

James N. Johnson  
Los Alamos National Laboratory  
P.O. Box 1663, B221  
Los Alamos, NM 87545

Robert C. Johnson  
Mason & Hanger, Pantex  
P.O. Box 30020  
Amarillo, TX 79177

Jack L. Johnston  
Naval Ordnance Station  
Yorktown, VA 23691-5110

David A. Jones  
Materials Research Laboratory  
P.O. Box 50 Ascot Vale,  
Victoria, 3032 Australia

Dennis L. Jones  
Kaman Sciences Corporation  
2560 Huntington Ave., Suite 100  
Alexandria, VA 22303

Dwight J. Jones  
Thiokol  
P.O. Box 400006  
Huntsville, AL 35815-1506

Hermenzo Jones  
Naval Surface Warfare Center  
10901 New Hampshire Ave.  
Silver Spring, MD 20903-5000

Timothy A. Jordan  
BDM International, Inc.  
950 Explorer Blvd.  
Huntsville, AL 35806

Larry H. Josephson  
Naval Weapons Center  
Code 321  
China Lake, CA 93555

Rudolph G. Jungst  
Sandia National Laboratories  
P.O. Box 5800, Div. 2512  
Albuquerque, NM 87185

Ashwani K. Kapila  
Rensselaer Polytechnic Institute  
Dept. of Math Sciences  
Troy, NY 12180-3590

Arnold Karo  
Lawrence Livermore National  
Laboratory  
P.O. Box 808, L-325  
Livermore, CA 94550

Yukio Kato  
Nippon Oil and Fats Co., Ltd.  
82-Nishimon, Taketoyo-cho  
Aichi 470-23, Japan

Panagiotis Katsabanis  
Queen's University  
Goodwin Hall  
Kingston, ONT K7L 3N6 Canada

Eleonore G. Kayser  
Naval Surface Warfare Center  
10901 New Hampshire Ave.  
Silver Spring, MD 20903-5000

Bennett W. Kelley  
P.E. Consultant  
6201 St. Croix Trail North  
Stillwater, MN 55082

David L. Kennedy  
ICI Australian Operations PTY, LTD  
Newsom Street  
Ascot Vale, 3032 Australia

James E. Kennedy  
Los Alamos National Laboratory  
P. O. Box 1663, P950  
Los Alamos, NM 87545

Michael Kennedy  
Health & Safety Executive House  
HSE, Harpur Hill  
Buxton, Derbyshire, UK

Gerald I. Kerley  
Sandia National Laboratories  
P.O. Box 5800, Div. 1533  
Albuquerque, NM 87195

James D. Kershner  
Los Alamos National Laboratory  
P. O. Box 1663, B214  
Los Alamos, NM 87545

Dong-Soo Kim  
Korea Explosives Co., Ltd  
50 KO-Jan Dong, Nam-Dong Ku  
Incheon, Korea

Kibong Kim  
Naval Surface Warfare Center  
10901 New Hampshire Ave.  
Silver Spring, MD 20903-5000

Martin E. Kipp  
Sandia National Laboratories  
P.O. Box 5800, Div. 1533  
Albuquerque, NM 87185

Hans R. Kleinhanss  
Universitaet Duesseldorf  
Universitaetsstr 1  
Duesseldorf, D-4000 FRG

Edward M. Kober  
Los Alamos National Laboratory  
P.O. Box 1663, MS B214  
Los Alamos, NM 87545

Douglas E. Kooker  
U.S. Army Ballistic Research  
Laboratory  
Aberdeen Proving Ground, MD 21005-  
5066

Murray Kornhauser  
3C Systems, Inc.  
620 Argyle Rd.  
Wynnewood, PA 19096

Frederick Kovar  
Lawrence Livermore National  
Laboratory  
P.O. Box 808, L-24  
Livermore, CA 94550

Richard A. Krajcik  
Los Alamos National Laboratory  
P.O. Box 1663, P664  
Los Alamos, NM 87545

Kurtis Kuhlits  
Mason & Hanger, Pantex  
P.O. Box 30020  
Amarillo, TX 79177

John W. Kury  
Lawrence Livermore National  
Laboratory  
P.O. Box 808, L-282  
Livermore, CA 94550

Gerald R. Laib  
Naval Surface Warfare Center  
10901 New Hampshire Ave  
Silver Spring, MD 20903-5000

David Lambert  
U.S. Air Force Armament Laboratory  
Eglin AFB, FL 32542

Brian D. Lambourn  
Atomic Weapons Establishment  
Aldermaston (AWE)  
Reading, RG7 4PR UK

Sam Lambrakos  
Naval Research Laboratory  
4555 Overlook Ave., SW  
Washington, DC 20375

Detlev Langner  
Bundesamt für Wehrtechnik und  
Beschaffung Postfach 7360  
5400 Koblenz, FRG

Dr. Y Lanzerotti  
U.S. Army ARDEC  
SMCAR-AEE-WW, B3022  
Picatinny Arsenal, NJ 07806-5000

Thomas E. Larson  
Los Alamos National Laboratory  
P.O. Box 1663, C920  
Los Alamos, NM 87545

Chang-Gi Lee  
Korea Explosives Co., Ltd  
#50 Ko-Jan Dong, Nam-Dong Ku  
Incheon, S. Korea

Edward L. Lee  
Lawrence Livermore National  
Laboratory  
P.O. Box 808, L-282  
Livermore, CA 94550

Jaimin Lee  
Center for Explosive Technology  
Research  
P.O. Box 2007  
Socorro, NM 87801

Jun Wung Lee  
Agency for Defense Dev.  
Dae-Jeon P.O. Box 35  
Dae-Jeon, 300-600, Republic of Korea

Larry M. Lee  
Ktech Corporation  
901 Pennsylvania NE  
Albuquerque, NM 87110

Richard Lee  
Naval Surface Warfare Center  
10901 New Hampshire Ave.  
Silver Spring, MD 20903-5000

Robert E. Lee  
Lawrence Livermore National  
Laboratory  
P.O. Box 808, L-262  
Livermore, CA 9455

Ronald S. Lee  
Lawrence Livermore National  
Laboratory  
P.O. Box 808, L-281  
Livermore, CA 94550

Woodrow Lee  
Naval Surface Warfare Center  
10901 New Hampshire  
Silver Spring, MD 20903-5000

Carl-Otto Leiber  
Bundesinstitut für Chemisch-Technische  
Untersuchungen Grosses Cent  
Swisttal 1, D-5357 FRG

Graeme A. Leiper  
ICI Explosives  
Nobels Explosives Co., Ltd  
Stevenson, Ayrshire, KA20 3LN UK

Ray Lemar  
Naval Surface Warfare Center  
10901 New Hampshire Ave.  
Silver Spring, MD 20903-5000

Thomas Liddiard  
Naval Surface Warfare Center  
10901 New Hampshire Ave.  
Silver Spring, MD 20903-5000

Morton L. Lieberman  
Sandia National Laboratories  
P.O. Box 5800, Div. 2363  
Albuquerque, NM 87185

Hendrik Lips  
Rheinmetall GMBH  
Dusseldorf, FRG

Pai Lu  
U.S. Army ARDEC  
Picatinny Arsenal, B3022  
Dover, NJ 07806-5000

Mary Ann Lucero  
Los Alamos National Laboratory  
P.O. Box 1663, J960  
Los Alamos, NM 87545

Roy A. Lucht  
Los Alamos National Laboratory  
P.O. Box 1663, J960  
Los Alamos, NM 87545

Dieter H. Ludwig  
Dornier G.m.b.H  
P.O. Box 1420  
D7990 Friedrichshafen 1, FRG

Michael D. Lundquist  
Mason & Hanger  
Iowa Ammunition Plant  
Middletown, IA 52638

Eric Lundstrom  
Naval Weapons Center  
Code 3891  
China Lake, CA

Gabi Luttwak  
Rafael Ballistics Center  
P.O. Box 2250 (24)  
Haifa, 31021 Israel

Lawrence J. Lyon  
Hercules Inc.  
P.O. Box 549  
Desoto, KA 66018

Oldrich Machacek  
Thermex Energy Corp.  
13601 Preston Rd., Suite 1007W  
Dallas, TX

Gay Maestas  
Lawrence Livermore National  
Laboratory  
P.O. Box 808, L-360  
Livermore, CA 94550

H. Mahd  
AL QAQAA State Establishment  
P.O. Box 5134  
Baghdad, Iraq

Joel J. Mala  
Societe Nationale des Poudres et  
Explosifs  
BP No. 2  
Vert-le-Petit, 91710 France

David Mann  
U.S. Army Research Office  
P.O. Box 1221  
Research Triangle Park, NC 27709

Ernesto C. Martinez  
Los Alamos National Laboratory  
P.O. Box 1663, P950  
Los Alamos, NM 87545

Jean-Claude Massal  
Pilot NATO Insensitive Munition  
Information Ctr, Applied Physics Lab  
Johns Hopkins University  
Laurel, MD 20707-6099

John M. McAfee  
Los Alamos National Laboratory  
P.O. Box 1663, P950  
Los Alamos, NM 87545

Beverly McCollough  
Lawrence Livermore National  
Laboratory  
P.O. Box 808, L-325  
Livermore, CA 94550

Charles R. McCulloch  
ERDCCO/ADPA  
550 Phara Rd. NE  
Atlanta, GA 30305

Olin K. McDaniel  
2156 5th St.  
Livermore, CA 94550

Raymond R. McGuire  
Lawrence Livermore National  
Laboratory  
P.O. Box 808, L-394  
Livermore, CA 94550

Yoav Me-Bar  
Rafael Ballistic Center  
P.O. Box 2250 (24)  
Haifa, 31021 Israel

David T.C. Meade  
Ministry of Defence, Royal Arsenal  
West,  
Woolwich  
London, SE18 6TD UK

Anna Meck  
Westinghouse Corp.  
401 East Hendy Ave.  
Sunnyvale, CA 94088

Arthur M. Mellor  
Vanderbilt University  
Box 6019, Station B  
Nashville, TN 37235

Arthur Metzner  
Naval Ordnance Station  
Code 2031  
Indian Head, MD 20640

Walt H. Meyers  
Los Alamos National Laboratory  
P.O. Box 1663, P950  
Los Alamos, NM 87545

Christian Michot  
CERCHAR  
Verneuil-en-Halatte, 60550 France

Philip J Miller  
Naval Surface Warfare Center  
10901 New Hampshire Ave.  
Silver Spring, MD 20903-5000

Robert W. Milton  
U.S. Army MICOM  
Redstone Arsenal, AMSNI-2D-PR-P  
Huntsville, AL 35898-5249

I. B. Mishra  
KANAN Associates  
2925 Churchville Rd.  
Churchville, MD 21028

Dennis E. Mitchell  
Sandia National Laboratories  
P.O. Box 5800, Div. 2513  
Albuquerque, NM 87185

Atsumi Miyake  
Dept. of Safety Engineering  
Tokiwadai, Hodagaya-ku  
Yokohama, 240 Japan

Andrzej W. Miziolek  
U.S. Army Ballistic Research  
Laboratory, SLCBR-IB-1  
Aberdeen Proving Ground, MD 21005-  
5066

Krishna Mohan  
IDL Chemicals Limited  
Post Bag 397  
Mallewaram, 560-003 India

David S. Moore  
Los Alamos National Laboratory  
P.O. Box 1663, MS J567  
Los Alamos, NM 87545

Larry M. Moore  
Sandia National Laboratories  
P.O. Box 5800, Div. 2514  
Albuquerque, NM 87185

Wanda Morat  
Naval Surface Warfare Center  
10901 New Hampshire Avenue  
Silver Spring, MD 20903-5000

Jerry A. Morgan  
Los Alamos National Laboratory  
P.O. Box 1663, MS P940  
Los Alamos, NM 87545

Charles E. Morris  
Los Alamos National Laboratory  
P.O. Box 1663, MS J970  
Los Alamos, NM 87545

James L. Morse  
Lawrence Livermore National  
Laboratory  
P.O. Box 808, L-384  
Livermore, CA 94550

Henry H.P. Moulard  
Institut Saint-Louis (ISL)  
12, Rue De l'Industrie  
Saint Louis, 68300 France

Michael J. Murphy  
Lawrence Livermore National  
Laboratory  
P.O. Box 808, L-321  
Livermore, CA 94550

Mas Nakano  
Lockheed Missiles & Space Co.  
Box 504  
Sunnyvale, CA 94088

Hyla Napadensky  
Napadensky Energetics Inc.  
650 Judson Ave.  
Evanston, IL 60202-2551

Barry T. Neyer  
EG&G Mound  
P.O. Box 3000  
Miamisburg, OH 45343

Helena Nilsson-Bergman  
Swedish Defense Research  
Establishment  
S-10254 Stockholm, Sweden

Edward S. Norton  
Pilot NATO Insensitive Munition  
Information Ctr, Applied Physics Lab  
John Hopkins University  
Laurel, MD 20707-6099

Bruno Nouguez  
Societe Nationale des Poudres et  
Explosifs BP. No 2  
Vert-le-Petit, 91710 France

Simone Odier  
Universite Pierre et Marie Curie  
D.R.P. Tour 22, 4 Place Jussieu  
Paris 75252 France

Douglas B. Olson  
Center for Explosive Technology  
Research, N.M. Tech.  
Campus Station  
Socorro, NM 87801

Elsine Oran  
Naval Research Laboratory  
4555 Overlook Ave., SW  
Washington, DC 20375

Donald L. Ornellas  
Lawrence Livermore National  
Laboratory  
P.O. Box 808, L-282  
Livermore, CA 94550

Henric Ostmark  
Swedish Defense Research  
Establishment  
S-10254 Stockholm, Sweden

D. Ouyang  
Southwest Institute of Fluid Physics  
P.O. Box 523  
Chengdu, China

Marvis D. Pace  
Naval Research Laboratory  
4555 Overlook Ave., SW  
Washington, DC 20375-5000

Dennis L. Paisley  
Los Alamos National Laboratory  
P.O. Box 1663, P950  
Los Alamos, NM 87545

Jack M. Pakulak  
Naval Weapons Center  
Code 3212  
China Lake, CA 9355

Christian M. Paquet  
Ministry of Defence  
ETBS BP 712  
Bourges, 18015 France

Gary H. Parsons  
U.S. Air Force Armament Laboratory  
Eglin AFB, FL 32542

H J. Pasma  
TNO Prins Maurits Laboratory  
P.O. Box 45  
Rijswijk, 2280 AA The Netherlands

Michael A. Patrick  
U.S. Air Force Armament Laboratory  
Eglin AFB, FL 32542

Gianfranco Paziienza  
Oto Melara Spa  
Loc. Barcara P.O. Box 71  
54011 Aulla, MS Italy

Timothy S. Pendergrass  
Kaman Sciences Corporation  
600 Boulevard South, Suite 208  
Huntsville, AL 35802

Steven L. Perkins  
Ensign Bickford Aerospace Co.  
640 Hopmeadow Street  
Simsbury, CT 06070

Algot Persson  
Swedish Detonic Research Foundation  
Box 32058, S-12611  
Stockholm, Sweden

Per-Anders Persson  
Center for Explosive Technology  
Research  
Campus Station  
Socorro, NM 87801

Santo Petralia  
c/o Italian Embassy  
2110 Leroy Place NW  
Washington, DC 20008

Lee S. Phillips  
Naval Research Laboratory  
4555 Overlook Ave., SW  
Washington, DC 20009

Jack R. Polson  
Mason & Hanger  
Iowa Ammunition Plant  
Middletown, IA 52638

Edward C. Poston, Jr.  
U.S. Air Force Armament Laboratory  
Eglin AFB, FL 32542-5434

Henri N. Presles  
ENSM  
Rue Guillaume VII  
Poitiers, 86034 France

Channon F. Price  
Naval Weapons Center  
Code 3891  
China Lake, CA 93555

Donna Price  
Advanced Technology and Research  
10901 New Hampshire Ave.  
Silver Spring, MD 20903-5000

M. Quidot  
Societa Nazionale des Poudres et  
Explosifs  
BP2 Le Bouchet  
Vert-Le-Petit, 91710 France

William J. Quirk  
Lawrence Livermore National  
Laboratory  
P.O. Box 808, L-35  
Livermore, CA 94550

John B. Ramsay  
Los Alamos National Laboratory  
P.O. Box 1663, J960  
Los Alamos, NM 87545

Francis H. Ree  
Lawrence Livermore National  
Laboratory  
P.O. Box 808, L-299  
Livermore, CA 94550

Starlin Reid  
Halliburton Logging Services  
P.O. Box 42800  
Houston, TX 77242

Joseph D. Renick  
Weapons Lab (AFSC)  
Kirtland AFB, NM 87117-6008

Anita M. Renlund  
Sandia National Laboratories  
P.O. Box 5800, Div. 2515  
Albuquerque, NM 87185

Ashley H. Rezaie  
Schlumberger Well Services  
14910 Airline Rd.  
Rosharon, TX 77583

Steven F. Rice  
Sandia National Laboratories  
P.O. Box 969  
Livermore, CA 94550

Jeffrey H. Richardson  
Lawrence Livermore National  
Laboratory  
P.O. Box 808, L-326  
Livermore, CA 94550

William B. Richardson  
Martin Marietta  
P.O. Box 179  
Denver, CO 80201

Herbert P. Richter  
Naval Weapons Center  
Code 3891  
China Lake, CA 93555

Robert S. Riggs  
Jet Research Center, Inc.  
7170 Rendon Bloodworth Rd.  
Ft. Worth, TX 76140

James P. Ritchie  
Los Alamos National Laboratory  
P.O. Box 1663, B214  
Los Alamos, NM 87545

Thomas Rivera  
Los Alamos National Laboratory  
P.O. Box 1663, C920  
Los Alamos, NM 87545

Alita M. Roach  
Los Alamos National Laboratory  
P.O. Box 1663, P915  
Los Alamos, NM 87545

Struan H. Robertson  
Oxford University  
P.C.L. South Parks Rd.  
Oxford, OX1 302 UK

Leslie A. Roslund  
Naval Surface Warfare Center  
10901 New Hampshire Ave.  
Silver Spring, MD 90203-5000

Julius Roth  
Consultant  
308 Canyon Drive  
Portola Valley, CA 94025

Lewis R. Rothstein  
Mason & Hanger, Consultant  
124 Selden Rd  
Newport News, VA 23606

James W. Routh  
Lawrence Livermore National  
Laboratory  
P.O. Box 808  
Livermore, CA 94550

Lippe D. Sadwin  
Israeli Military Industries  
Kefar Pines, 37920 Israel

Naoko Sakata  
Japan

Michel M. Samirant  
Institut Saint-Louis (ISL)  
Rue De l'Industrie  
Saint Louis, 68301 France

Luis Sanchez  
Union Espanola De Explosivos  
Claudio Coello, 124  
Madrid, 28006 Espana

Frederick W. Sandstrom  
Center for Explosive Technology  
Research  
Campus Station  
Socorro, NM 87801

Harold W. Sandusky  
Naval Surface Warfare Center  
10901 New Hampshire Ave.  
Silver Spring, MD 20903-5000

John S. Sarracino  
Los Alamos National Laboratory  
P.O. Box 1663, X-4, MS-F664  
Los Alamos, NM 87545

Robert S. Sarracino  
AECI, Research Dept.  
P.O. Modderfontein  
TVL INS 1645 South Africa

Siegfried F. Schaefer  
Test Center Meppen  
Postfach 1280  
4470 Meppen, FRG

Dale R. Schaeffer  
EG&G Mound Applied Technologies  
P.O. Box 3000  
Miamisburg, OH 45343

Fritz Schedlbauer  
Fraunhofer Institut für Chemische Tech  
(ICT)  
Joseph-von-Fraunhofer-Strasse  
D-7507 Pfinztal-Berghausen, FRG

George J. Schlenker  
U.S. AMCCOM  
AMSMC-SAS  
Rock Island, IL 61299-6000

Stephen C. Schmidt  
Los Alamos National Laboratory  
P.O. Box 1663, M-6, J970  
Los Alamos, NM 87545

Guenther Schniedermann  
Bundesinstitut für Chemisch-Technische  
Grosses Cent  
Swisttal 1, D-5357 FRG

Paul R. Schomber  
U.S. Air Force Armament Laboratory  
AFATLMNE  
Eglin AFB, FL 32542-5434

Garry L. Schott  
Los Alamos National Laboratory  
P.O. Box 1663, MS P952  
Los Alamos, NM 87545

Diana Schroen  
Vitric Technologies, Ltd.  
326 Rawson, G-3  
Dundee, MI 49131

Hilmar Schubert  
Fraunhofer Institut für Chemische Tech  
(ICT)  
D 7507 Bad.-Würtbg, FRG

Wendell L. Seitz  
Los Alamos National Laboratory  
P.O. Box 1663, MS P952  
Los Alamos, NM 87545

Robert E. Setchell  
Sandia National Laboratories  
P.O. Box 5800, Div. 5166  
Albuquerque, NM 87185

Milton S. Shaw  
Los Alamos National Laboratory  
P.O. Box 1663, T-14, B214  
Los Alamos, NM 87545

Stephen Sheffield  
Los Alamos National Laboratory  
P.O. Box 1663, M-9, MS 952  
Los Alamos, NM 87545

Howard Sheinfeld  
U.S. Army Foreign Science &  
Technology Center  
220 7th St. NE  
Charlottesville, VA 22901-5396

Leo Sten  
Hewlett-Packard  
1700 South Baker Street  
McMinnville, OR 97128

James M. Short  
Naval Surface Warfare Center  
10901 New Hampshire Ave., R12  
Silver Spring, MD 20903-5000

Randall L. Simpson  
Lawrence Livermore National  
Laboratory  
P.O. Box 808, L-282  
Livermore, CA 94550

Michael E. Sitzmann  
Naval Surface Warfare Center  
10901 New Hampshire Ave.  
Silver Spring, MD 20903-5000

Per G. Sjöberg  
Nobel Chemicals AB/University of  
New Orleans  
Department of Chemistry  
New Orleans, LA 70122

Russell D. Skocypec  
Sandia National Laboratories  
P.O. Box 5800, Div. 1512  
Albuquerque, NM 87185

Steven Smith  
U.S. Air Force Armament Laboratory  
AFATLMNF  
Eglin AFB, FL 32542-5434

Vernon Smith  
Kaman Sciences Corp.  
P.O. Box 7463  
Colorado Springs, CO 80933

So-Young Song  
Agency for Defense Dev.  
P.O. Box 35  
Dae-Jeon, 300-600 Korea

Laurent L. N. Soulard  
Institut Saint-Louis (ISL)  
12, Rue De l'Industrie  
Saint Louis, 68300 France

Patrick F. Spahn  
Naval Surface Warfare Center  
10901 New Hampshire St.  
Silver Spring, MD 20903-5000

Kathy Spivey  
Wilfred Baker Engineering  
8700 Crownhill, Suite 310  
San Antonio, TX 78209

Karen Spurlin  
Lawrence Livermore National  
Laboratory  
P.O. Box 808, L-282  
Livermore, CA 94550

Philip L. Stanton  
Sandia National Laboratories  
P.O. Box 5800, Div. 2514  
Albuquerque, NM 87185

John Starckenberg  
U.S. Army Ballistic Research  
Laboratory  
Aberdeen Proving Ground, MD 21005-  
5066

Raymond D. Steele  
Los Alamos National Laboratory  
P.O. Box 1663, C920  
Los Alamos, NM 87545

Roy Stenson  
Ministry of Defence  
Lillie Rd.  
London, SW6-1TR UK

James W. Straight  
Los Alamos National Laboratory  
P.O. Box 1663, J960  
Los Alamos, NM 87545

Gerald Stribling  
EPDS - Mas Bel Air  
St. Gilles, 30800 France

Walter B. Sudweeks  
IRECO Inc.  
3000 West 8600 South  
West Jordan, UT 84088-9699

Gerrit T. Sutherland  
Naval Surface Warfare Center  
10901 New Hampshire Ave.  
Silver Spring, MD 20903-5000

Ray T. Swanson  
SFAT America, Inc.  
824 N. Victory Blvd.  
Burbank, CA 91502

Bruce E. Takala  
Los Alamos National Laboratory  
P.O. Box 1663, J960  
Los Alamos, NM 87545

Katsumi Tanaka  
National Chemical Lab for Industry  
Explosives Chemistry Section  
Tsukuba Ibaraki, 305 Japan

Pier K. Tang  
Los Alamos National Laboratory  
P.O. Box 1663, F664  
Los Alamos, NM 87545

William C. Tao  
Lawrence Livermore National  
Laboratory  
P.O. Box 808, L-282  
Livermore, CA 94550

Craig M. Tarver  
Lawrence Livermore National  
Laboratory  
P.O. Box 808, L-282  
Livermore, CA 94550

Douglas G. Tasker  
Naval Surface Warfare Center  
10901 New Hampshire Ave.  
Silver Spring, MD 20903-5000

Wayne A. Tenbrink  
Naval Weapons Station  
Code 321  
Concord, CA 94520

W. B. Thomas  
Thiokol  
P.O. Box 400006  
Huntsville, AL 35815

James Thoreen  
Air Force Armament Laboratory  
AFATLMN  
Eglin AFB, FL 32542-5000

James R. Travis  
Los Alamos National Laboratory  
P.O. Box 1663, P915  
Los Alamos, NM 87543

Radoslaw R. Trebinski  
Technical Military Academy  
01-489 Warszawa 49  
Warsaw, Poland

Wayne M. Trott  
Sandia National Laboratories  
P.O. Box 5800, Dov. 1164  
Albuquerque, NM 87185-5800

Allen J. Tulis  
IIT Research Institute  
10 W 35th St.  
Chicago, IL 60616

Richard Turcotte  
ICI  
Richelieu Bldg.  
McMasterville, QU Canada

Paul A. Urtiew  
Lawrence Livermore National  
Laboratory  
P.O. Box 808, L-282  
Livermore, CA 94550

Albert C. van der Steen  
TNO Prins Maurits Laboratory  
P.O. Box 45  
Rijswijk, 2280 AA The Netherlands

Robert W. Van Dolah  
Consultant  
202 Cherokee Rd.  
Pittsburgh, PA 15241

Lawrence Vande Kieft  
U.S. Army Ballistic Research  
Laboratory, SLCBR-1B  
Aberdeen Proving Ground, MD 21005-  
5066

Mathias vanThiel  
Lawrence Livermore National  
Laboratory  
P.O. Box 808, L-299  
Livermore, CA 94550

Ronald E. Varosh  
Reynolds Industrial Systems  
3420 Fostoria Drive  
San Ramon, CA 94583

Ries J. Verbeek  
TNO Prins Maurits Laboratory  
P.O. Box 45  
Rijswijk, 2280 AA The Netherlands

Manual G. Vigil  
Sandia National Laboratories  
P.O. Box 5800, Div. 1512  
Albuquerque, NM 87185

Andre Vlahov  
Institut Boris Kidric e Vinca  
Box 522  
11001 Belgrade, Yugoslavia

H. William Voigt  
U.S. Army ARDEC  
Picatinny Arsenal  
Dover, NJ 07801

Fred Volk  
Fraunhofer Institut fur Chemische Tech  
Joseph-von-Fraunhofer-Strasse  
7507-Pfingztal, FRG

William G. Von Holle  
Lawrence Livermore National  
Laboratory  
P.O. Box 808, L-281  
Livermore, CA 94550

Wallace E. Voreck  
Schlumberger Well Services  
2006 San Sebastian, 304B  
Houston, TX 77058

Jerry D. Wackerle  
Los Alamos National Laboratory  
P.O. Box 1663, MS P952  
Los Alamos, NM 87545

David R. Wagnon  
Air Force Armament Laboratory  
Eglin AFB, FL 32542

W M. Walasinski  
Hercules Inc.  
Radford, VA 24141

Franklin E. Walker  
Interplay  
18 Shadow Lake Road  
Danville, CA 94526

Raymond F. Walker  
Walker Associates  
13660 Greenview Dr.  
Sun City West, AZ 85375

John R. Walton  
Lawrence Livermore National  
Laboratory  
P.O. Box 808, L-282  
Livermore, CA 94550

Paul Wanninger  
MBB Schrobenuhausen  
Postfach 1340  
8898 Schrobenuhausen, BA FRG

Donald E. Warne  
Science Applications Int. Corp  
10260 Campus Point Drive  
San Diego, CA 92121

James W. Watt  
Advanced Technology and Research  
14900 Sweitzer Lane, Suite 104  
Laurel, MD 20707

Ulrich Weigel  
Ministry of Defense  
5300 Bonn  
Sinzig, Rhein Pfoolz 5485 FRG

Lawrence J. Weirick  
Sandia National Laboratories  
P.O. Box 5800, Div. 2514  
Albuquerque, NM 87185

Albert M. Weston  
KMI/Lawrence Livermore National  
Laboratory, P.O. Box 808, L-282  
Livermore, CA 94550

William W. Whaley  
Los Alamos National Laboratory  
P.O. Box 1663, P915  
Los Alamos, NM 87545

Michael Wieland  
U.S. Bureau of Mines  
Cochran's Mill Road  
Pittsburgh, PA 15236

Andrew E. Williams  
Naval Research Laboratory  
4555 Overlook Ave., SW  
Washington, DC 20375

William H. Wilson  
Naval Surface Warfare Center  
10901 New Hampshire Ave.  
Silver Spring, MD 20903-5000

Curt Wittig  
University of Southern California  
Department of Chemistry  
Los Angeles, CA 90089-0482

Edward Wlodarczyk  
Technical Military Academy  
01-489 Warszalia 49  
Warsaw, Poland

Kenneth L. Woods  
Naval Weapons Center  
Code 3894  
China Lake, CA 93555-6001

Diana L. Woody  
Naval Surface Warfare Center  
10901 New Hampshire Ave.  
Silver Spring, MD 20903-5000

Delbert F. Wright  
Lawrence Livermore National  
Laboratory  
P.O. Box 808, L-389  
Livermore, CA 94550

Gaymond Yes  
Science Applications International  
160 Spear St., Suite 1250  
San Francisco, CA 94105

Frank J. Zerilli  
Naval Surface Warfare Center  
10901 New Hampshire Ave.  
Silver Spring, MD 20903-5000

Louis Zernow  
Zernow Technical Services Inc.  
425 W. Bonita Ave.  
San Dimas, CA 91773

J. Zhu  
Institute of Applied Physics and  
Computational Mathematics  
P.O. Box 8009  
Beijing, China

## AUTHOR INDEX\*

Agnew, S. F.	1019	Boyer, L. R.	1295
Alcon, R. R.	39	Boyle, V. M.	3, 897, 1460
Akst, I. B.	478	Braithwaite, M.	513
Aldis, D. F.	112, 280	Brazell, N.	1131
Alexander, K. E.	498	Breithaupt, R. D.	133, 525, 1378
Anderson, C. J.	1364	Brill, T. B.	228
Andrew, M. I.	1253	Brun, L.	757
Andriot, P.	506	Brush, P. J.	228
Anisichkin, V. F.	407	Bugaut, F.	489
Arbuckle, A. L.	1489	Bukiet, B. G.	751
Armstrong, R. W.	1260	Buntain, G. A.	1037
Asay, B. W.	265, 537	Bussell, T. J.	1404
Atwood, A. I.	363	Butler, P. B.	906
Aubert, S. A.	1284	Byers Brown, W.	513
Austing, J. L.	972		
Aveill�, J.	506, 842	Campbell, A. W.	265, 537
		Campos, J.	925
Baer, M. R.	293, 906	Capellos, C.	1084
Bahl, K. L.	133	Carion, N.	506, 842
Bai Chunhua	879	Carlson, D. W.	626, 1260
Bainville, D.	1070	Castille, C.	1070
Baker, D. E.	972	Chaisse, F.	506, 757
Baker, R. N.	806	Chan, M. L.	566
Bardo, R. D.	235	Chapman, L. B.	1001
Baudin, G.	1371	Chaudhri, M. M.	857
Bauer, P.	925, 933	Chen Fumei	816
Bdzil, J. B.	730, 773	Chen Peiqi	142
Beard, B. C.	897	Cheret, R.	246
Becuwe, A.	1008	Cherin, H.	1271
Bedoch, J. P.	1371	Chick, M.	1404
Beitel, F. P., Jr.	585	Chiles, W. C.	1335
B�langer, C.	1480	Chirat, R.	489
Belcher, R. A.	831, 1253	Cichra, D. A.	633
Belmas, R.	1070	Clements, R. E.	641
Benjamin, K. J.	1460, 1489	Coffey, C. S.	58, 897, 1243
Bernard, S.	489	Cook, M. D.	1027, 1441
Bernecker, R. R.	354	Cooper, J.	197
Bhasu, V. C. Jyothi	1276	Cooper, P. W.	379
Bines, A.	1404	Costantino, M. S.	1310
Blais, N.	953	Cowperthwaite, M.	89, 388
Blake, O.	3	Craig, B. G.	573
Boggs, T. L.	363	Crane, S. L.	1543
Boslough, M. B.	1199	Crawford, P. C.	25
Bourne, N. K.	869	Crouch, L. D.	798

\*Pages 1 through 854 appear in Volume I and pages 855 through 1646 appear in Volume II.

## AUTHOR INDEX (Cont.)\*

Davidova, O. N.	724	Gimenez, P.	1371
Davis, W. C.	1335	Ginsberg, M. J.	537
Deal, W. E.	1543	Glancy, B. C.	341, 1260
Deiter, J. S.	626	Glenn, J. G.	1284
Delclos, A.	1008	Gohar, P.	1271
Delpuech, A. E.	172	Graham, K. J.	1295
Demske, D.	1131	Graham, R. A.	1529
DeVost, D. F.	1243	Green, L. G.	670, 701
Dick, J. J.	683	Green, N. J. B.	1193
Dickson, P. M.	1100	Greiner, N. R.	953, 1170
Dimas, P.	1076	Groux, J.	1217
Ding Jing	77, 252, 879	Guo Yuxian	554
Doherty, R. M.	626, 633	Guri, G.	506
Dold, J. W.	219		
Dong Haishan	995	Han Chengbang	947
Dorsey, T. M.	1489	Hannaford, C. E.	1076
Dremin, A. N.	724	Haskins, P. J.	1027, 1441
Dufort, S.	1271	Hattori, K.	640
Dunand, M.	933	Held, M.	1416
		Helm, F. H.	25
Eden, G.	831, 1253	Hermes, R.	1170
Elban, W. L.	1260	Heuzé, O.	925, 933
Engelke, R.	39, 657	Hikita, T.	939
Erickson, K. L.	1140	Ho, S. Y.	1052
Erickson, L. M.	112	Holmes, N. C.	190
Erskine, D. J.	670	Hrdina, D. J.	972
		Hsieh, T.	329
Fanget, A.	1047	Huan Shi	77, 252
Farley, W. E.	1131	Huang Lihong	947
Ferm, E. N.	1427	Hubbard, P. J.	1322
Fickett, W.	730	Huntley, J. M.	886
Field, J. E.	869, 886, 1100, 1276	Hutchinson, C. D.	123
Foan, G. C. W.	123		
Forbes, J. W.	806, 897, 1235	Iida, M.	621
Forest, C. A.	683	Ishikawa, N.	621
Fortov, V. E.	50	Iwata, L.	1084
Fortova, T. N.	50		
Frank, A. M.	641	James, H. R.	1441
Frey, R. B.	3, 1404	Jia Quansheng	816
Fu Kinghai	1360	Johnson, J. D.	417
Fujiwara, S.	621	Jones, A. G.	123
Fukatsu, Y.	640	Jones, H. D.	461
		Jungst, R. G.	1510
Gibb, A. W.	853, 1364		

\*Pages 1 through 854 appear in Volume I and pages 855 through 1646 appear in Volume II.

## AUTHOR INDEX (Cont.)\*

Kanel, G. I.	50	Lyman, O. R.	1460
Kang, J.	906	Mader, C. L.	693
Kang Shufang	947	Mal'kov, I. Yu.	407
Kapila, A. K.	219	Malyrenko, S. I.	50
Kato, Y.	640, 939	Marlow, W. R.	1253
Kennedy, D. L.	1224	McAfee, J. M.	265
Kennedy, M.	1351	McCandless, P.	190
Kenney, I.	1019	McFadden, D. L.	1460
Kenney, J.	1019	McKinney, T. L.	1037
Kerihuel, M. T.	506	Meulenbrugge, J. J.	83
Kerley, G. I.	443	Miller, P. J.	341, 498
Kerr, I. D.	1351	Miller, S.	1131
Kershner, J. D.	693	Mishra, I. B.	1084
Kim, K.	329, 593	Miyake, A.	560
Kinney, J. H.	868	Moen, I. O.	1364
Kipp, M. E.	209, 1510	Mohan, V. Krishna	1276
Kleinhanß, H. R.	66	Moore, D. S.	180
Klimenko, V. Yu.	724	Moore, L. M.	1529
Kober, E. M.	1185	Mori, N.	640, 939
Kodde, H. H.	560	Moulard, H.	18
Kolodney, K.	1084	Murphy, M. J.	525
Kooker, D. E.	306		
Kornhauser, M.	1451	Nakayama, Y.	621
Krall, A. D.	341	Nanut, V.	98
Kury, J. W.	25, 1378	Nilsson, H.	162, 1151
		Nunziato, J. W.	293
Lambourn, B. D.	784		
Lambrakos, S. G.	713	Oran, E. S.	713
Lanzerotti, M. Y. D.	918	Ornellas, D. L.	1162, 1310
Larson, T. E.	1076	Östmark, H.	162, 1151
Lawn, H. R.	123	Otani, G.	190
Lee, E. L.	280	Ouyang DENGHuan	142
Lee, J.	573		
Lee, J. W.	471	Pace, M. D.	987
Lee, L. M.	1529	Paisley, D. L.	1110
Lee, R. J.	396	Palmer, S. J. P.	886
Lee, R. S.	798	Parry, M. A.	886, 1100
Leiper, G. A.	197, 1224	Parsons, G. H.	1284
Lemar, E. R.	806	Persson, P.-A.	545, 573
Lepie, A. H.	1295	Pettit, D. R.	683
Leroy, M.	506	Peyrard, M.	713
Liddiard, T. P.	1235	Pilarski, D. L.	1460
Lind, C. D.	566	Pilling, M. J.	1193
de Longueville, Y.	1371	Pinto, J. J.	918
Loupias, C.	1047	Politzer, P.	566
Lungenstraß, F.	66		

\*Pages 1 through 854 appear in Volume I and pages 855 through 1646 appear in Volume II.

## AUTHOR INDEX (Cont.)\*

Powers, P. S.	1084	Song, S. Y.	471
Presles, H. N.	925, 933	Spear, R. J.	98
Price, C. F.	363	Stacy, H. L.	657
Price, D.	1235	Stanton, P. L.	1118
Quidot, M.	1217	Starkenber, J.	604, 1460, 1489
Ramsay, J. B.	265, 537, 1427, 1543	Steele, R. D.	1014
Reddy, G. Om	585	Stewart, D. S.	730, 773
Ree, F. H.	425, 743	Stretz, L. A.	1014
Reed, R. P.	1529	Sumida, W. K.	972
Reisler, H.	1084	Sun Chengwei	142
Renick, J. D.	545	Sun Jian	435
Renlund, A. M.	153, 1118	Swanson, B. I.	1019
Reynier, P.	1070	Swift, D. C.	784
Rice, S. F.	190	Takala, B. E.	1543
Richter, H. P.	1295	Taliancich, A. G.	89
Ringbloom, V.	626	Tanaka, K.	621
Ritchie, J. P.	1185	Tang, P. K.	657
Rivera, T.	1014, 1037	Tao, W. C.	641, 798, 868, 1310
Robertson, S. H.	1193	Tarver, C. M.	112, 133, 525, 670, 701
Rosenberg, J. T.	89	Tasker, D. G.	396
Saint-Martin, C.	1371	Taylor, G. W.	1014, 1037
Sakai, H.	939	Thoreen, J. L.	1284
Sakurai, T.	939	Titov, V. M.	407
Samirant, M.	259	Tokita, K.	640
Sanchez, J. A.	545	Tomlinson, R.	1322
Sandstrom, F. W.	573	Torii, A.	640
Sandusky, H. W.	341, 1260	Trebinski, R.	766
Schedlbauer, F.	962	Trofimov, V. S.	250
Schmidt, S. C.	180	Trott, W. M.	153, 1118
Schott, G. L.	1335	Trzcinski, W.	766
Seitz, W. L.	657	Tulis, A. J.	972
Servas, J. M.	842	Utkin, A. V.	50
Setchell, R. E.	209	Urtlew, P. A.	112
Sharma, J.	897	Vacellier, J.	842
Shaw, M. S.	452	van der Steen, A. C.	83, 320, 560
Sheffield, S. A.	39, 683	van Thiel, M.	425, 743
Shepherd, J. E.	641	Verbeek, H. J.	83, 320
Shi Huisheng	947	Vigil, M. G.	1385
Simpson, R. L.	25, 280, 525	Volk, F.	962
Sitzmann, M. E.	1162	Von Holle, W. G.	133
Skocypiec, R. D.	1140		

\*Pages 1 through 854 appear in Volume I and pages 855 through 1646 appear in Volume II.

## AUTHOR INDEX (Cont.)\*

Von Rosen, K.	1364	Woody, D. L.	1243
Wackerle, J.	657, 683	Wu Xiong	435
Wang Tinzheng	816	Xiao Lianjie	435
Warnes, R.	1131	Yoshida, M.	621
Warren, T. W.	822	Yu Jun	1360
Weinmaster, R. R.	822	Zhao Feng	142
Weirick, L. J.	1060	Zerilli, F. J.	461
Weston, A. M.	280	Zhang Guanren	1360
Wilmot, G. B.	626	Zöllner, H.	66
Witkowski, W.	766	Zoludeva, T. A.	724
Wittig, C.	1084	Zwierzchowski, N. G.	1295
Wlodarczyk, E.	766		
Wolfe, A.	918		

\*Pages 1 through 854 appear in Volume I and pages 855 through 1646 appear in Volume II.

# REPORT DOCUMENTATION PAGE

*Form Approved*  
OMB No. 0704-0188

Public reporting burden for this collection of information is estimated to average 1 hour per response, including the time for reviewing instructions, searching existing data sources, gathering and maintaining the data needed, and completing and reviewing the collection of information. Send comments regarding this burden estimate or any other aspect of this collection of information, including suggestions for reducing this burden, to Washington Headquarters Services, Directorate for Information Operations and Reports, 1215 Jefferson Davis Highway, Suite 1204, Arlington, VA 22202-4302, and to the Office of Management and Budget, Paperwork Reduction Project (0704-0188), Washington, DC 20503.

<b>1. AGENCY USE ONLY (Leave blank)</b>		<b>2. REPORT DATE</b> Aug 28 through Sep 1, 1989	<b>3. REPORT TYPE AND DATES COVERED</b> Proceedings, 8/28-9/1/89	
<b>4. TITLE AND SUBTITLE</b> Proceedings of the Ninth Symposium (International) on Detonation, Volume II			<b>5. FUNDING NUMBERS</b>	
<b>6. AUTHOR(S)</b> Wanda J. Morat, editor				
<b>7. PERFORMING ORGANIZATION NAME(S) AND ADDRESS(ES)</b> Naval Surface Warfare Center 10901 New Hampshire Avenue Silver Spring, MD 20903-5000			<b>8. PERFORMING ORGANIZATION REPORT NUMBER</b>	
<b>9. SPONSORING/MONITORING AGENCY NAME(S) AND ADDRESS(ES)</b> Office of Naval Research 800 North Quincey Street Arlington, VA 22217-5000			<b>10. SPONSORING/MONITORING AGENCY REPORT NUMBER</b>  OCNR-113291-7	
<b>11. SUPPLEMENTARY NOTES</b>				
<b>12a. DISTRIBUTION/AVAILABILITY STATEMENT</b>  Approved for public release; distribution is unlimited.			<b>12b. DISTRIBUTION CODE</b>	
<b>13. ABSTRACT (Maximum 200 words)</b> This book is the second of two volumes that document the proceedings of the Ninth Symposium (International) on Detonation which was held August 28 through September 1, 1989, at the Red Lion Inn, Portland, Oregon. Papers presented in this publication cover special problems in the field of energetic materials, particularly detonation phenomena in solids and liquids. General subject areas include shock-to-detonation transition, time resolved chemistry, initiation modeling, deflagration-to-detonation transition, equation of state and equation of state and performance, composites and emulsions, and composites and emulsions/underwater explosives, reaction zone, detonation wave propagation, hot spots, detonation products, chemistry and compositions, and special initiation.  ↑				
<b>14. SUBJECT TERMS</b> Detonation Energetic materials Time resolved chemistry			Explosives Composites and emulsions Special initiation	Shock-to-detonation transition Hot spots
			<b>15. NUMBER OF PAGES</b> 819	<b>16. PRICE CODE</b>
<b>17. SECURITY CLASSIFICATION OF REPORT</b> UNCLASSIFIED	<b>18. SECURITY CLASSIFICATION OF THIS PAGE</b> UNCLASSIFIED	<b>19. SECURITY CLASSIFICATION OF ABSTRACT</b> SAR	<b>20. LIMITATION OF ABSTRACT</b> SAR	

## GENERAL INSTRUCTIONS FOR COMPLETING SF 298

The Report Documentation Page (RDP) is used in announcing and cataloging reports. It is important that this information be consistent with the rest of the report, particularly the cover and its title page. Instructions for filling in each block of the form follow. It is important to *stay within the lines* to meet optical scanning requirements.

### Block 1. Agency Use Only (Leave blank).

**Block 2. Report Date.** Full publication date including day, month, and year, if available (e.g. 1 Jan 88). Must cite at least the year.

**Block 3. Type of Report and Dates Covered.** State whether report is interim, final, etc. If applicable, enter inclusive report dates (e.g. 10 Jun 87 - 30 Jun 88).

**Block 4. Title and Subtitle.** A title is taken from the part of the report that provides the most meaningful and complete information. When a report is prepared in more than one volume, repeat the primary title, add volume number, and include subtitle for the specific volume. On classified documents enter the title classification in parentheses.

**Block 5. Funding Numbers.** To include contract and grant numbers; may include program element number(s), project number(s), task number(s), and work unit number(s). Use the following labels:

C - Contract	PR - Project
G - Grant	TA - Task
PE - Program Element	WU - Work Unit Accession No.

**BLOCK 6. Author(s).** Name(s) of person(s) responsible for writing the report, performing the research, or credited with the content of the report. If editor or compiler, this should follow the name(s).

**Block 7. Performing Organization Name(s) and Address(es).** Self-explanatory.

**Block 8. Performing Organization Report Number.** Enter the unique alphanumeric report number(s) assigned by the organization performing the report.

**Block 9. Sponsoring/Monitoring Agency Name(s) and Address(es).** Self-explanatory.

**Block 10. Sponsoring/Monitoring Agency Report Number. (If Known)**

**Block 11. Supplementary Notes.** Enter information not included elsewhere such as: Prepared in cooperation with...; Trans. of...; To be published in... . When a report is revised, include a statement whether the new report supersedes or supplements the older report.

**Block 12a. Distribution/Availability Statement.** Denotes public availability or limitations. Cite any availability to the public. Enter additional limitations or special markings in all capitals (e.g. NOFORN, REL, ITAR).

DOD - See DoDD 5230.24, "Distribution Statements on Technical Documents."  
DOE - See authorities.  
NASA - See Handbook NHB 2200.2  
NTIS - Leave blank.

### Block 12b. Distribution Code.

DOD - Leave blank.  
DOE - Enter DOE distribution categories from the Standard Distribution for Unclassified Scientific and Technical Reports.  
NASA - Leave blank.  
NTIS - Leave blank.

**Block 13. Abstract.** Include a brief (*Maximum 200 words*) factual summary of the most significant information contained in the report.

**Block 14. Subject Terms.** Keywords or phrases identifying major subjects in the report.

**Block 15. Number of Pages.** Enter the total number of pages.

**Block 16. Price Code.** Enter appropriate price code (*NTIS only*)

**Blocks 17.-19. Security Classifications.** Self-explanatory. Enter U.S. Security Classification in accordance with U.S. Security Regulations (i.e., UNCLASSIFIED). If form contains classified information, stamp classification on the top and bottom of the page.

**Block 20. Limitation of Abstract.** This block must be completed to assign a limitation to the abstract. Enter either UL (unlimited) or SAR (same as report). An entry in this block is necessary if the abstract is to be limited. If blank, the abstract is assumed to be unlimited.